M. N. Berdichevsky
V. I. Dmitriev

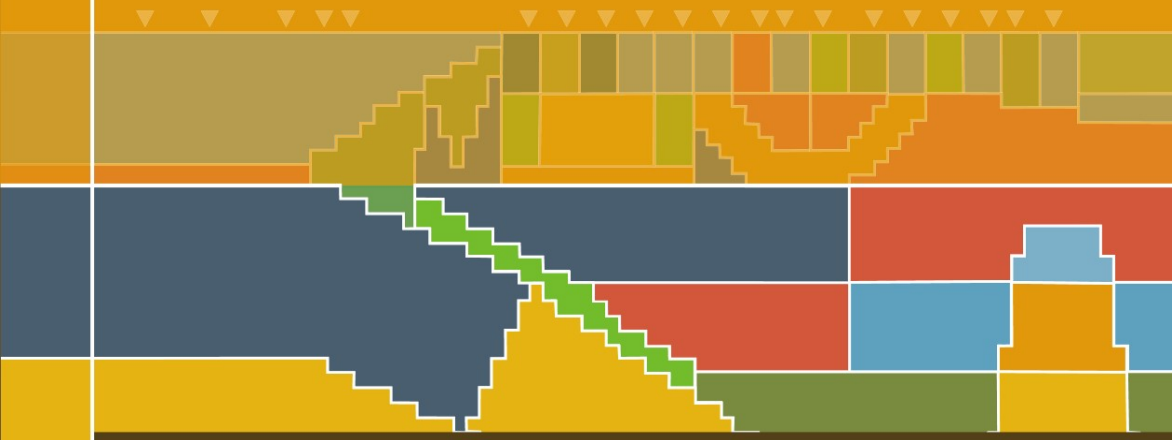

Models and Methods of Magnetotellurics

Springer

Models and Methods of Magnetotellurics

Mark N. Berdichevsky · Vladimir I. Dmitriev

Models and Methods of Magnetotellurics

Springer

Prof. Mark N. Berdichevsky
Moscow State University
Geological Department
Vorobjovy Gory
Moscow
Russia 119999
mark.berd@mtu-net.ru

Lomonosov
Moscow State University
Vorobjovy Gory
MOSKAU GSP1 19991
RUSSISCHE FÖDERATION

Prof. Vladimir I. Dmitriev
Moscow State University
Dept. Computational
Mathematics & Cybernetics
Vorobjovy Gory
Moscow
Russia 119899
dmitriev@cs.msu.su

Polish Academy of Sciences
Institute of Geophysics
ul. Ks. Janusza 64
101-452 Warsaw
Poland

ISBN: 978-3-540-77811-0 e-ISBN: 978-3-540-77814-1

Library of Congress Control Number: 2008926519

Cover design: deblik, Berlin

Camera-ready by the Editorial Office of the Institute of Geophysics, Polish Academy of Sciences, Warsaw, Poland

Printed on acid-free paper

9 8 7 6 5 4 3 2 1

springer.com

LOOKING FOR NEW WAYS
TO DO OLD JOBS
MEANS PROGRESS

Foreword

During the past decades the geophysical methods using the magnetotelluric field passed through a phase of fast development. Geophysical journals were overflown with papers dedicated to different facets of industrial and academic magnetotellurics. When writing the book, we tried to systemize this disembodied knowledge and reduce it to all-sufficient and self-consistent philosophy that can provide the best way to the efficient interpretation of magnetotelluric and magnetovariational soundings.

This book may be regarded as a continuation of Berdichevsky-Dmitriev's monograph (Berdichevsky and Dmitriev, 2002), which presents the foundations of the one-dimensional magnetotellurics. The subject matter of the present book is the two-dimensional and three-dimensional magnetotellurics. We discuss the methods of integrated interpretations of magnetotelluric and magnetovariational soundings and show that a rational use of the magnetovariational data is the key ingredient of progress in magnetotellurics.

The book is arranged in three parts.

In Part I we consider a model of the inhomogeneous Earth with plane-wave primary field and establish the deterministic nature of the magnetotelluric and magnetovariational response functions – the impedance tensor, telluric and magnetic tensors, phase tensor, tipper vector. On this basis we examine the properties of the response functions and describe the methods of their analysis.

Part II presents a set of basic two-dimensional and three-dimensional models that demonstrate the magnetotelluric anomalies caused by typical near-surface and deep geoelectric structures. Analyzing these models, we estimate the informativeness of the magnetotelluric and magnetovariational data.

Part III introduces the reader to a broad range of approaches to the magnetotelluric and magnetovariational interpretation. Using synthetic and experimental data, we show that the most meaningful and complete solution to the ill-posed multicriterion inverse problem may be obtained in the interactive mode including the hypotheses test and successive partial inversions with magnetovariational and impedance phase priority, which keeps out the destructive effects of near-surface inhomogeneities.

Some semantic and terminological remarks need to be made:

(1) All formulas in the book are given in SI units.
(2) Throughout the book, we use the time-factor $e^{-i\omega t}$ and a default plane model of the Earth excited by a vertically propagating plane monochromatic electromagnetic wave impinging on the Earth's surface. The Earth is supposed to be nonmagnetic with vacuum permeability $\mu_o = 4\pi \cdot 10^{-7}$henry/m.
(3) In describing the magnetotelluric field, we follow the tradition of Russian magnetotelluric school and use the magnetic field **H** instead of **B**.
(4) Geophysicists vary somewhat in their terminology concerning geoelectric studies based on observation of geomagnetic variations. Two terms are embedded in the geophysical literature: geomagnetic sounding, and magnetovariational sounding. In our book preference is given to more adequate term "magnetovariational sounding".

Our work has been initiated and supported by the Institute of Geophysics of Polish Academy of Sciences. It is a great pleasure for us to thank prof. J. Jankovsky, the former director of this Institute, for friendly discussions which helped to build a scenario of the book and formulate its basic statements. We wish gratefully acknowledge the exceptional efforts of A. Dziembowska, the chief of the information department of the IGF, for correcting our English and preparing the manuscript for publication. We are deeply indebted to our colleagues from Moscow State University and Geophysical Company North-West and particularly to V. Khmelevskoy, A. Bulychev and A. Jakovlev for creating a climate which favored our work. We cordially thank all our colleagues, both those in the Russian geoelectric community and those from abroad, whose interest has stimulated our work on the book. Our special gratitude is to L. Vanyan, U. Schmucker, P. Weidelt, and M. Zhdanov for encouraging talks on difficulties that emerged in the course of our work. We are indebted to N. Golubtsova, P. Pushkarev, V. Kuznetsov, and D. Jakovlev for assistance in computer work and drawing graphical illustrations. Grants 05-05-65082, 07-05-00523, 08-05-00345 from Russian Foundation of Basic Researches are gratefully acknowledged.

Moscow

Mark Berdichevsky
Vladimir Dmitriev

Contents

Part III Interpretation of Magnetotelluric and Magnetovariational Data

Basic Notations

$\bar{a}$	complex conjugate of scalar a
$\bar{\mathbf{A}}$	complex conjugate of vector $\mathbf{A}$
$\overline{[\mathbf{A}]}$	conjugate of matrix $[\mathbf{A}]$
$[\mathbf{A}]^{\mathrm{T}}$	transpose of matrix $[\mathbf{A}]$
$\mathbf{1}_x, \mathbf{1}_y, \mathbf{1}_z$	unit vectors of Cartesian basis
$\mathbf{E}(E_x, E_y, E_z)$	electric field
$\mathbf{H}(H_x, H_y, H_z)$	magnetic field
$\mathbf{E}_\tau(E_x, E_y)$	horizontal electric field
$\mathbf{H}_\tau(H_x, H_y)$	horizontal magnetic field
$\mathbf{E}^{\mathrm{N}}, \mathbf{H}^{\mathrm{N}}$	normal field
$\mathbf{E}^{\mathrm{A}}, \mathbf{H}^{\mathrm{A}}$	anomalous field
$[\mathbf{G}^{\mathrm{E}}], [\mathbf{G}^{\mathrm{H}}]$	electric and magnetic Green tensors
$J, \mathbf{j}$	electric current, current density
ρ, σ	electric resistivity, electric conductivity
μ_{o}	magnetic permeability of free space
Z	Tikhonov-Cagniard impedance
Z_{N}	normal impedance
Z_{n}	locally normal impedance
Z_{eff}	effective impedance
Z_{brd}	Berdichevsky impedance
Z_{rms}	root-mean-square impedance
$[\mathbf{Z}]$	impedance tensor
$\left[\overset{\leftrightarrow}{\mathbf{Z}}\right]$	Adam impedance tensor
$\det[\mathbf{Z}]$	determinant of matrix $[\mathbf{Z}]$
$\mathrm{tr}\,[\mathbf{Z}]$	trace of matrix $[\mathbf{Z}]$
$[\mathbf{Y}]$	admittance tensor
ρ_{A}	apparent resistivity
ρ_{N}	normal apparent resistivity
ρ_{n}	locally normal apparent resistivity
ρ_{xy}, ρ_{yx}	apparent resistivities oriented in x- and y-directions

$\rho^{\parallel}, \rho^{\perp}$	longitudinal and transverse apparent resistivity
ρ_{eff}	effective apparent resistivity
ρ_{brd}	Berdichevsky apparent resistivity
ρ_{rms}	root-mean-square apparent resistivity
S	conductance (integral conductivity)
R	resistance (integral resistivity)
h	thickness of a layer
h_{eff}	effective penetration depth
k	wave number of a medium
λ	electromagnetic wave length
δ	skin-depth
T, ω	period, cyclic frequency
$[\mathbf{D}]$	Doll tensor
$[\mathbf{M}]$	horizontal magnetic tensor
$[\mathbf{\Phi}]$	phase tensor, Tikhonov functional
$[\mathbf{S}]$	Schmucker tensor
$[\mathbf{S}_\tau]$	horizontal Schmucker tensor
$[\mathbf{W}]$	Wiese-Parkinson matrix
$[\mathbf{S}_z]$	Schmucker matrix
ε	ellipticity
P	polarization ratio
$[\mathbf{R}(\alpha)]$	rotation matrix
$[\mathbf{I}]$	identity matrix, misfit functional
$[\mathbf{\Omega}]$	stabilizing functional
$skew_S$	Swift skew
$skew_B$	Bahr skew
$skew_{CBB}$	Caldwell-Bibby-Brown skew
$skew_{mv}$	magnetovariational skew
N_{mt}	magnetotelluric inhomogeneity parameter
N_{mv}	magnetovariational inhomogeneity parameter
$\mathbf{W}$	Wiese-Parkinson tipper
$\mathbf{V}$	Vozoff tipper
$\mathbf{S}_z$	Schmucker tipper
pv	principal value of an integral in the Cauchy sense
mod	modulo
δ	skin-depth
$[F]_S$	jump of a function F at the boundary S
Δ	Laplace operator
$\|u\|_C$	norm of the function u in the space C
$\|u\|_{L_2}$	norm of the function u in the space L_2
$\|u\|_R$	norm of the function u in the space R

Introduction

We address this book to those readers
who not only want to know "how"
but who also want to understand "why".

Modern magnetotellurics consists of two interwoven branches: (1) the magnetotelluric sounding, MT sounding, MTS, based on simultaneous measurements of time variations in the electric (telluric) and magnetic (geomagnetic) fields of the Earth, and (2) the magnetovariational sounding, MV sounding, MVS, (sometimes referred to as geomagnetic depth sounding, GDS) which is restricted to measurements of time variations only in the magnetic field.

Behind the MT and MV soundings we have a common model with a plane electromagnetic wave vertically incident on a plane horizontally inhomogeneous Earth (Berdichevsky and Zhdanov, 1984). The electromagnetic field $\mathbf{E}_\tau\,(E_x, E_y)$ and $\mathbf{H}(H_x, H_y, H_z)$ observed at the Earth's surface $z = 0$ is divided into the normal and anomalous parts. The normal field $\mathbf{E}_\tau^{\mathrm{N}}\,(E_x^{\mathrm{N}}, E_y^{\mathrm{N}})$, $\mathbf{H}_\tau^{\mathrm{N}}(H_x^{\mathrm{N}}, H_y^{\mathrm{N}})$ reflects the horizontally homogeneous layered background. The anomalous field $\mathbf{E}_\tau^{\mathrm{A}}\,(E_x^{\mathrm{A}}, E_y^{\mathrm{A}})$, $\mathbf{H}^{\mathrm{A}}(H_x^{\mathrm{A}}, H_y^{\mathrm{A}}, H_z^{\mathrm{A}})$ arises due to horizontally inhomogeneous structures.

The basic response functions in MTS are the impedance tensor

$$[\mathbf{Z}] = \begin{bmatrix} Z_{xx} & Z_{xy} \\ Z_{yx} & Z_{yy} \end{bmatrix}$$

defined from relations between the horizontal components of the electric and magnetic fields at an observation site (Berdichevsky and Zhdanov, 1984):

$$\begin{aligned} E_x(\mathbf{r}) &= Z_{xx}H_x(\mathbf{r}) + Z_{xy}H_y(\mathbf{r}), \\ E_y(\mathbf{r}) &= Z_{yx}H_x(\mathbf{r}) + Z_{yy}H_y(\mathbf{r}), \end{aligned}$$

and the apparent resistivities

$$\rho_{xy} = \left|Z_{xy}\right|^2/\omega\mu_{\mathrm{o}} \qquad \rho_{yx} = \left|Z_{yx}\right|^2/\omega\mu_{\mathrm{o}}$$

calculated from the components Z_{xy}, Z_{yx} of the secondary diagonal of the impedance tensor $[\mathbf{Z}]$.

The basic response functions in MVS are the tipper vector (the Wiese–Parkinson vector)

$$\mathbf{W} = W_{zx}\mathbf{1}_x + W_{zy}\mathbf{1}_y$$

defined from relations between the vertical component of the magnetic field and its horizontal components at an observation site (Parkinson, 1983):

$$H_z(\mathbf{r}) = H_z^{\mathrm{A}}(\mathbf{r}) = W_{zx}H_x(\mathbf{r}) + W_{zy}H_y(\mathbf{r})$$

and the magnetic tensor

$$[\mathbf{M}] = \begin{bmatrix} M_{xx} & M_{xy} \\ M_{yx} & M_{yy} \end{bmatrix}$$

defined from relations between the horizontal components of magnetic fields at an observation site and at a base (reference) observation site, B (Berdichevsky and Zhdanov, 1984):

$$H_x(\mathbf{r}) = M_{xx}H_x(\mathbf{r}_B) + M_{xy}H_y(\mathbf{r}_B),$$
$$H_y(\mathbf{r}) = M_{yx}H_x(\mathbf{r}_B) + M_{yy}H_y(\mathbf{r}_B).$$

Using Schmucker's concept (Schmucker, 1970), the magnetic tensor $[\mathbf{M}]$ and the tipper vector $\mathbf{W}$ are represented as the perturbation tensor

$$[\mathbf{S}] = \begin{bmatrix} S_{xx} & S_{xy} \\ S_{yx} & S_{yy} \\ S_{zx} & S_{zy} \end{bmatrix}$$

transforming the normal magnetic field $\mathbf{H}^{\mathrm{N}} = \mathbf{H}(\mathbf{r}_B)$ observed at a base site, B, into the anomalous field $\mathbf{H}^{\mathrm{A}}(\mathbf{r}) = \mathbf{H}(\mathbf{r}) - \mathbf{H}^{\mathrm{N}}(\mathbf{r}_B)$ observed at an observation site:

$$H_x^{\mathrm{A}}(\mathbf{r}) = S_{xx}H_x^{\mathrm{N}}(\mathbf{r}_B) + S_{xy}H_y^{\mathrm{N}}(\mathbf{r}_B),$$
$$H_y^{\mathrm{A}}(\mathbf{r}) = S_{yx}H_x^{\mathrm{N}}(\mathbf{r}_B) + S_{yy}H_y^{\mathrm{N}}(\mathbf{r}_B),$$
$$H_z^{\mathrm{A}}(\mathbf{r}) = S_{zx}H_x^{\mathrm{N}}(\mathbf{r}_B) + S_{zy}H_y^{\mathrm{N}}(\mathbf{r}_B),$$

where

$$S_{xx} = M_{xx} - 1, \quad S_{xy} = M_{xy}, \quad S_{yx} = M_{yx}, \quad S_{yy} = M_{yy} - 1,$$
$$S_{zx} = W_{zx}M_{xx} + W_{zy}M_{yx}, \quad S_{zy} = W_{zx}M_{xy} + W_{zy}M_{yy}.$$

The MTS method has its origin in famous papers by Tikhonov (1950), Cagniard (1953) and Weidelt (1972). The MVS method came into being due to works by Parkinson (1959), Wiese (1965), Schmucker (1970), Jankovski (1972), Vozoff (1972), Rokityansky (1975, 1982).

In the traditional scheme of electromagnetic sounding applying magnetotelluric field, the MTS method plays a leading part (stratification of the medium, geoelectric zoning, mapping of underground topography, detection of conductive zones in the Earth crust and upper mantle, recognition of deep faults), whereas the MVS method helps in tracing horizontal conductivity gradients, localizing geoelectric structures, determining their strike. Such a partition of MT and MV methods is reflected even

in the magnetotelluric nomenclature: if the MT studies are referred to as magnetotelluric soundings, the MV studies are consider as magnetovariational profiling (Rokityansky, 1982).

This scheme is widely and rather successfully applied throughout the world. It provides an unique information on the Earth's interior (porosity, permeability, graphitization, sulfidizing, dehydration, melting, fluid regime, ground-water mineralization, reological characteristics, thermodynamic and geodynamic processes).

Let us make a retrospective journey into the history of the MTS method treated customarily as a basic method of magnetotellurics.

Following a common practice for geoelectric surveys, Tikhonov and Cagniard (Tikhonov, 1950; Cagniard, 1953) designed the magnetotelluric sounding as a method for studying the vertical variations in the electrical conductivity of the Earth. In their initial studies, they did not go beyond the one-dimensional model (Tikhonov–Cagniard model) charactertized by the scalar impedance $Z = Z_{xy} = -Z_{yx}$, $Z_{xx} = Z_{yy} = 0$ and rotationally invariant apparent resistivity $\rho_A = \rho_{xy} = \rho_{yx}$. Alas, the very first experiments showed that horizontal geoelectric inhomogeneities might drastically distort the results of MT-sounding (Tikhonov and Berdichevsky, 1966). Neglecting these distortions, we impair the accuracy of magnetotelluric interpretation – the essential information on the Earth's interior may be lost and even false geoelectric layers and structures may appear. It was just in the early 1960s when it became evident that magnetotellurics dramatically needs a theory considering the electromagnetic field within the horizontally inhomogeneous (two-dimensional, three-dimensional) Earth. In the Russian magnetotelluric school this theory received the name the theory of distortions.

The first results in the distortion theory came from the pioneering papers of Berdichevsky (1961), Obukhov (1962), D'Erceville and Kunetz (1962), Mann (1964), Kaufman and Taborovsky (1969). A groundwork for the distortion theory was laid by the Tikhonov–Dmitriev paper (1969), which exposed physical mechanisms of the field distortions and suggested criteria to estimate their intensity. Starting from the concepts of excess charges and excess currents appearing in the inhomogeneous medium (Kaufman, 1961, 1974), the electromagnetic anomalies are divided into two parts: the galvanic (Coulomb's) part generated by the excess charges and the induction (Faraday's) part which reflects the inductive interaction between the excess currents. The galvanic and induction parts of the anomalous field are responsible for galvanic and induction distortions of the MTS data. The main difference between galvanic and induction distortions is that the galvanic distortions (even caused by near-surface inhomogeneities) manifest themselves over a wide frequency range and do not vanish with lowering frequency, while the induction distortions appear at high frequencies and vanish at low frequencies.

The last decades of XX century were marked by rapid progress in computing electrodynamics (Dmitriev and Zakharov, 1970; Vasseur and Weidelt, 1973; Weidelt, 1975; Hohmann, 1975; Tikhonov et al., 1977; Fainberg and Singer, 1980; Ting and Hohmann, 1981; Singer and Fainberg, 1985; Wannamaker et al., 1987; Weaver, 1994; Mackie et al., 1994; Avdeev et al., 1997; Spichak, 1999). Advances in mathematics opened the way to systematic studies in the distortion theory. Many

geophysicists from the world geoelectric community participated in this work. Nowadays we have a comprehensive idea of the two-dimensional distortions and greatly proceeded in understanding of the three-dimensional distortions. Using criteria of the distortion theory, we could recognize the lateral effects and (if possible) present the results of MT soundings in a form that allows for one-dimensional interpretation. The most spectacular result of that kind has been obtained by Russian geophysicists in Western Siberia, in the vicinity of the Urengoy fur-trading station (Fig. 1). Here, the vast Purovsky uplift of the Paleozoic basement (indicated by the arrow) was outlined by one-dimensional interpretation of MTS data and this stimulated the discovery of the Urengoy gas field, one of the largest gas field in the World. However, such a one-dimensional normalization of MTS data is not always reliable and nearly always leads to the loss of some part of information.

The challenging problem of present-day magnetotellurics is the two and three-dimensional interpretation of MTS data. This trend of development can be found in the works by Adam (1964), Jupp and Vozoff (1977), Dmitriev (1987), Barashkov and Dmitriev (1987, 1990), deGroot-Hedlin and Constable (1990), Smith and Booker (1991), Mackie and Madden (1993), Oldenburg and Ellis (1993), Golubev and Varentsov (1994), Berdichevsky et al. (1998), Varentsov (1999), Siripunvaraporn and Egbert (2000), Novozhynski and Pushkarev (2001), Zhdanov (2002).

Considerable progress has been made in the two-dimensional interpretation. Nowadays we have at hand effective fast programs for 2D inversion of MTS data in the classes of smooth inhomogeneous and piece-wise homogeneous (blocky) media with fixed geometry of blocks. In modern geophysical journals we find varied examples of successful 2D interpretation of MT soundings carried out in geological provinces with rather complex geoelectric structure. Let us show, for instance, the European-Asiatic map of the crustal conductivity reproduced by Zhamaletdinov (1996) from data of 1D and 2D interpretation (Fig. 2). The map covers vast expanses of eastern Europe and northern Asia. It depicts numerous linear zones and large areas of high conductivity in the Earth's crust. The well-known arc-shaped Carpathian anomaly (13) borders the Pannonian Basin. Its nature up to now remains a subject of discussion (fluid? graphites?). Remarkable is the linear Kirovograd anomaly (10),

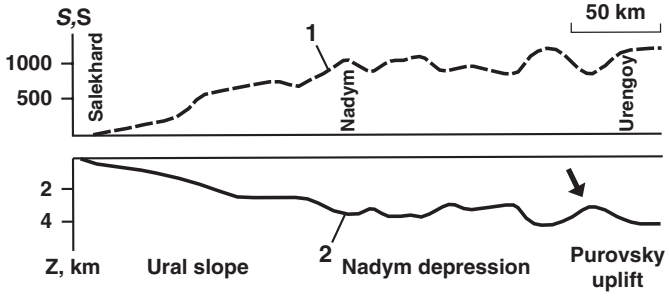

Fig. 1 Magnetotelluric soundings along the profile Salekhard-Urengoy; one-dimensional interpretation; 1 – conductance of the Mesozoic–Cenozoic sediments, 2 – relief of the Paleozoic basement

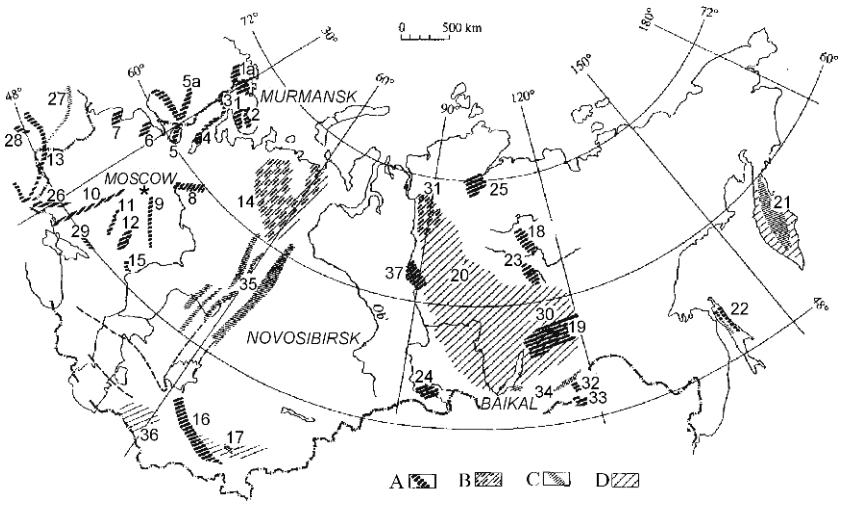

Fig. 2 Map of crustal conductivity anomalies over the territory of the former Soviet Union. Crustal anomalies of the presumably electron-conduction origin: (**A**) linear high-conductive zones, (**B**) vast high-conductive areas. Crustal anomalies of presumably fluid origin: (**C**) linear conductive zones, (**D**) conductive areas. Names of anomalies (arabic numbers): (1) Pechenga-Varguza, (1a) Lapland, (2) Keivskaya, (3) Tiksheozerskaya, (4) Onega, (5) Ladoga, (5a) Bothnian, (6) Chudskaya, (7) Baltic, (8) Vologda, (9) Tambov, (10) Kirovograd, (11) Kursk, (12) Vorontsovskaya, (13) Carpathian, (14) Timano-Pechorskaya, (15) Frolovskaya, (16) Tien Shan, (17) Fergana, (18) Anabar, (19) Bodaibinskaya, (20) Siberian, (21) Kamchatka, (22) Sakhalin, (23) Viluis, (24) Minusinskaya, (25) Khatanga, (26) Izmail-Poltava, (27) North-German, (28) Pannonian, (29) Donbass, (30) East-Siberian, (31) Norilsk, (32) Undino-Baleiskaya, (33) Kurunzulaiskaya, (34) Mongolia-Okhotskaya, (35) Urals, (36) Kopet Dagh, (37) Tungusskaya (Zhamaletdinov, 1996)

which can be traced for 600 km from the Crimea to the Moscow syneclise. It is interpreted as a belt of graphitization and/or dehydration caused by recent tectonic activity. Considerable attention should be given to the concept, which attributes the Kirovograd anomaly to the early stage of the continental rifting (Gordienko, 2002). One of the most intensive anomalies is the Tien-Shan anomaly (16), caused by graphite-bearing formations. High crustal conductivity can be observed within the Baikal rift zone, the Tungus syneclise, and the Vilyuis syneclise. This is the Siberian anomaly (20), which is assigned to crustal fluids forming a deep hydrosphere. Evidently, the information on the deep electric conductivity may give a good grounds for regional prognoses of the mineral resources.

Let us show an instructive result obtained on profiles crossing the Carpathian anomaly. Figure 3 displays the V_p-velocity section along the seismic CELO5 Profile and the resistivity section along the magnetotelluric PREPAN Profile. One can see here an astonishingly good correlation of the high conductive zone in the Carpathian arc ($\rho = 4 \div 7$ Ohm $\cdot$ m) and low velocities zone ($V_p = 5.2$ km/s). Geoelectric and seismic indications nicely supplement each other. Correlation of low resistivities and low velocities testifies that the Carpathian anomaly has the fluid nature (Jankowski et al., 2005).

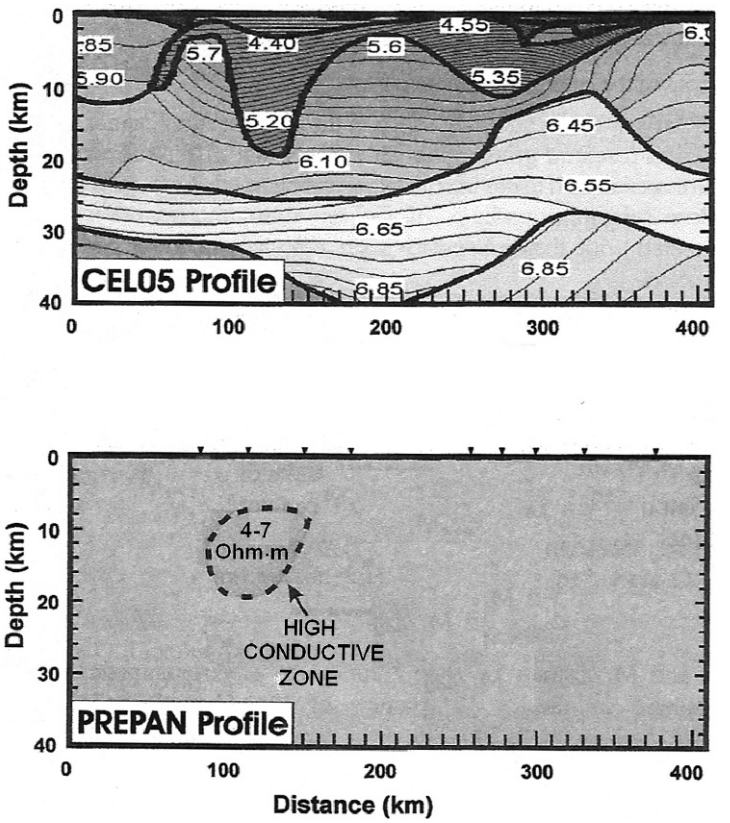

Fig. 3 Geoelectric and seismic models supplement each other (Jankovski et al., 2005)

We close our review of magnetotelluric developments by mentioning the successes of surveys carried out in continental and global scale (Schultz et al. 1998; Semenov 1998). We associate the progress in the three-dimensional interpretation with development of methods of fast 3D modelling and application of quasi-one-dimensional approaches reducing the three-dimensional inversion to an iterative sequence of one-dimensional inversions corrected by the 3D misfit. Nowadays due to the promising results obtained by Zhdanov (2002) we are looking forward to the elaborating of new mehods providing immediate three-dimensional inversion.

The weak point of the electromagnetic sounding with MTS priority is that inhomogeneities in the uppermost layers may severely distort the electric field and consequently the impedance tensor along with the apparent resistivities. The distortions are of galvanic nature – they extend over the whole range of low frequencies, causing static ("conformal") shifts of the apparent resistivity curves. The near-surface inhomogeneities affect the apparent resistivities, no matter how low the frequency is. They can destroy the information on the deep conductivity. There is a plethora of techniques for correcting these distortions (Bahr, 1988;

Jones, 1988; Groom and Bailey, 1989; Vozoff, 1991; Singer, 1992; Berdichevsky et al., 1998). But all these techniques are fraught with rough approximations (with information losses) or even with subjective (sometimes erroneous) decisions resulting in false structures.

We can considerably improve the MT ÷ MV complex by realising in full measure the potentials of the magnetovariational sounding. An advantage of MVS is that at lower frequencies the induced currents penetrate deeper and deeper into the Earth, so that their magnetic field and consequently the tipper and magnetic tensor are less and less distorted by near-surface inhomogeneities. This remarkable property of the magnetic field gives us the chance to save the electromagnetic sounding from the static-shift problem (no electric field is measured). But excluding the electric field, we face the problem of informativeness of the MV sounding. And here we hit upon one of the most dramatic magnetotelluric delusion. It is commonly supposed that "MV studies determine only horizontal conductivity gradients, while the vertical conductivity distribution is not resolved" (Simpson and Bahr, 2005). Is it true? It is true if MV studies are carried out in the narrow frequency range (in the profiling mode) and it is not true in the case of MV studies carried out in the broad frequency range (in the sounding mode). Let us consider a two-dimensional model with an inclusion of higher conductivity in the upper layer resting on the resistive strata and the conductive basement (Fig. 4). A depth to the conductive basement changes from 25 to 150 km. Compare the longitudinal apparent-resistivity curves ρ_{xy}, measured outside the inclusion (site O_1), with the real-tipper curves $|\mathrm{Re}W_{zy}|$,measured at the same site O_1, and with the magnetic-perturbation curves $|S_{yy}|$, measured over the

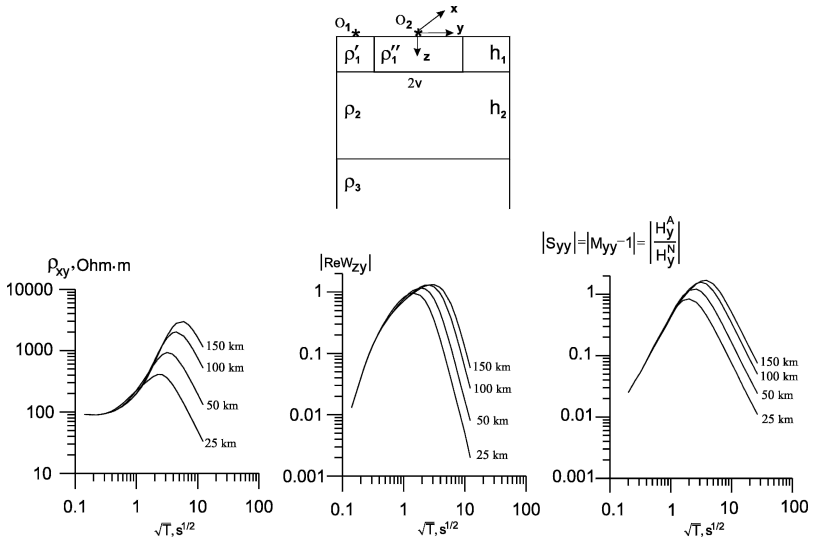

Fig. 4 Illustrating the resolution of magnetotelluric and magnetovariational soundings. Model parameters: $\rho_1' = 100$ Ohm·m, $\rho_1'' = 10$ Ohm·m, $v = 8$ km, $h_1 = 1$ km, $\rho_2 = 10,000$ Ohm·m, $h_2 = 24, 49, 99, 149$ km, $\rho_3 = 1$ Ohm·m. The ρ_{xy}-curves and $|ReW_{zy}|$-curves are measured at a site $O_1(y = -9)$, the $|S_{yy}|$-curves are measured at a site $O_2(y = 0)$. Curve parameter: $h = h_1 + h_2$

inclusion (site O_2). In the model under consideration the bell-shaped magnetovariational curves of $|\mathrm{Re}W_{zy}|$ and $|S_{yy}|$ quite distinctly resolve the vertical distribution of conductivity (in the same way as the customary apparent-resistivity curves of ρ_{xy}!). Proceeding from this model, we should correct statement from (Simpson and Bahr, 2005) and say that the MV sounding reveals not only horizontal variations in the Earth's conductivity but the vertical variations as well. The physical meaning of this unexpected result is rather simple. Naturally, the MV sounding of horizontally homogeneous media with zero magnetovariational anomalies makes no sense. But in the case of the horizontally inhomogeneous medium we observe the anomalous magnetic field, which reflects the distribution of the excess currents. It hardly needs proving that intensity of the excess currents is defined by the electric field depending on the conductivity distribution $\sigma(x, y, z)$. It follows from these relations that magnetovariational response functions contain information on $\sigma(x, y, z)$. So, the MV sounding can be considered as a common frequency sounding using the magnetic field of excess currents distributed within a local horizontal inhomogeneity, which plays a role of the buried source.

Studies in the integrated interpretation of MTS and MVS data are conducted along two lines.

Firstly, methods for transforming the magnetic field into synthetic electric field slightly distorted by near-surface inhomogeneities are elaborated. The idea of such a transformation was proposed by Vanyan (Osipova et al., 1982). The first experiments in this direction were carried out in the early 1980s (Osipova et al., 1982; Burjanov et al., 1983). Recently Vanyan et al. (1997, 1998) suggested the algorithms and computing programs for the two-dimensional transformation of the magnetic field and successfully applied this approach for interpretation of MVS data obtained in the Juan de Fuca subduction zone (western coast of the USA). These studies played a vital role in the history of the experiment EMSLAB (Wannamaker et al., 1989a, b), since they confirmed the existence of the continental asthenosphere.

Secondly, a strategy of straightforward MV inversion based on the minimization of the tipper and magnetic tensor misfit in a wide frequency range is elaborated. This approach goes back to the magnetotelluric experiments that were carried out in 1988–1990 in the Kirghiz Tien Shan by geophysical teams of the Institute of High Temperatures, Russian Academy of Sciences (Trapeznikov et al., 1997; Berdichevsky and Dmitriev, 2002). These measurements were made on a profile characterized by strong local and regional distortions of apparent resistivities that dramatically complicated the interpretation of observation data. The situation has been resolved only with MV soundings. Figure 5 shows the real tippers, Re W_{zy}, and the geoelectric model fitting these observation data. The model contains an inhomogeneous crustal conductive layer (a depth interval of 25÷55 km) and vertical conductive zones connected with the known faults, the Nikolaev line (NL) and the Atbashi-Inylchik faults (AIF). The figure also presents the model constructed from seismic tomography data. The geoelectric model coincides remarkably well with the seismic model. Low resistivities are reliably correlated with lower velocities. This correlation confirms the validity of geoelectric reconstructions based on MVS data. The studies in the mountains of Tien Shan indicate that MVS not only outlines crustal conductive zones but also stratifies the lithosphere. Developing this

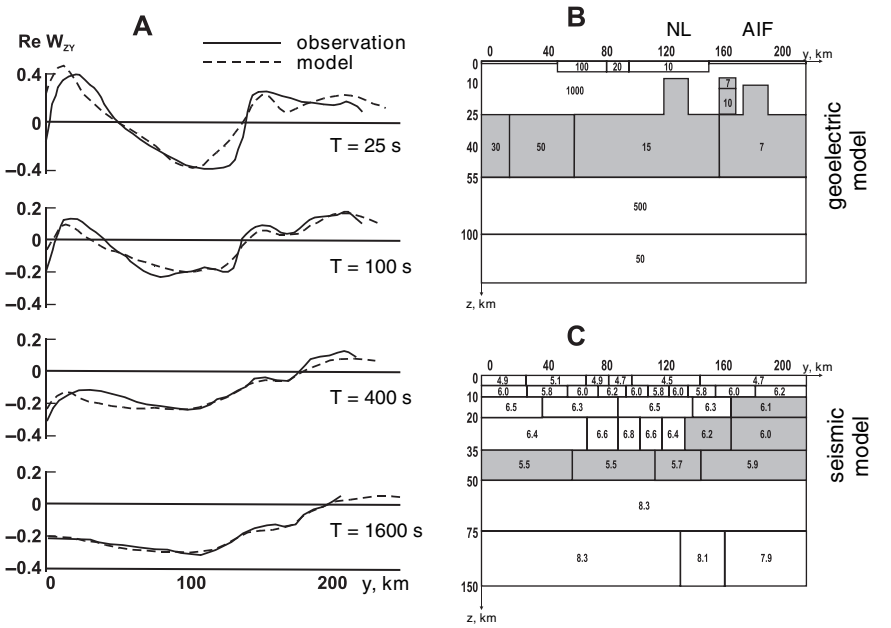

Fig. 5 Magnetovariational sounding in the Kirghiz Tien Shan Mountains. (**A**) Real tipper Re W_{zy} along a profile crossing the Kirghiz Tien Shan. (**B**) The resistivity section from magnetovariational data (Trapeznikov et al., 1997); NL – Nikolaev line, AIF – Atbashi-Inylchek faults; the resistivity values in Ohm·m are given within blocks; the lower-resistivity crustal zones ($\rho \leq 50$ Ohm $\cdot$ m) are shaded. (**C**) The velocity section from seismic tomography data (Roecker et al., 1993); values of P-wave velocities in km/s are gven within blocks; the low-velocity crustal zones ($V_P \leq 6.2$ km/s) are shaded

inference, one can propose a new scheme of electromagnetic sounding in which MVS yields a basic reliable information on the Earth's interior, whereas MTS is applied for editing and extending the MVS results. Studies in this field are favored by appearance of programs combining MT and MV automatized inversions (Golubev and Varentsov, 1994; Varentsov, 1999; Siripunvaraporn and Egbert, 2000; Novozhynski and Pushkarev, 2001). The main virtue of such a strategy is that difficulties caused by near-surface distorting effects may arise only at the MTS stage and we can constraint these distortions using reliable low-frequency references derived from the inversion of MVS data. Here we would like to stress that Dmitriev has proved the uniqueness theorem for two-dimensional inverse magnetovariational problem (Berdichevsky et al., 2000, 2003) and this encouraging result determines the future prospect of the electromagnetic sounding with MVS priority.

We believe that magnetovariational sounding with its rather high sensitivity to horizontal and vertical conductivity variations and rather high immunity to near-surface galvanic distortion should be considered as an efficient tool of the modern geoelectrics. Geophysicists have every reason for developing new interpretation technique that would realize the potentials of the magnetic field, especially in the deep geoelectric studies.

Part I
Magnetotelluric and Magnetovariational Response Functions

Chapter 1
The Magnetotelluric Response Functions

1.1 On the Deterministic Nature of the Impedadance Tensor

At the heart of the *magnetotelluric sounding* is a one-dimensional model named after Tikhonov and Cagniard. The *Tikhonov–Cagniard model* is very simple (Tikhonov, 1950; Cagniard, 1953). A plane vertically incident monochromatic electromagnetic wave illuminates the plane Earth consisting of homogeneous isotropic layers with horizontal boundaries. Introduce a standard reference frame with horizontal axes x, y directed northwards and eastwards respectively, and vertical axis z directed downwards. On the Earth's surface

$$\mathbf{E}_\tau = \begin{bmatrix} 0 & Z \\ -Z & 0 \end{bmatrix} \mathbf{H}_\tau = Z \begin{bmatrix} 0 & 1 \\ -1 & 0 \end{bmatrix} \mathbf{H}_\tau, \tag{1.1}$$

where

$$\mathbf{E}_\tau = \begin{bmatrix} E_x \\ E_y \end{bmatrix}, \qquad \mathbf{H}_\tau = \begin{bmatrix} H_x \\ H_y \end{bmatrix}$$

are the horizontal components of the magnetotelluric field and Z is the scalar complex-valued *Tikhonov–Cagniard impedance*. In expanded form

$$E_x = ZH_y, \qquad E_y = -ZH_x, Z = \frac{E_x}{H_y} = -\frac{E_y}{H_x}. \tag{1.2}$$

Here the complex electric and magnetic vectors, $\mathbf{E}_\tau$ and $\mathbf{H}_\tau$, are linearly polarized in the mutually perpendicular directions.

The rotationally invariant impedance Z is a functional of the Earth's resistivity ρ. The reciprocals of Z and ρ are the admittance $Y = 1/Z$ and the conductivity $\sigma = 1/\rho$. The inverse MTS problem reduces to reconstruction of $\rho(z)$ or $\sigma(z)$ from the parametric dependence of the impedance $Z(z = 0, \omega)$ or the admittance $Y(z = 0, \omega)$ upon the frequency ω.

M. Berdichevsky, V.I. Dmitriev, *Models and Methods of Magnetotellurics*,
DOI 10.1007/978-3-540-77814-1_1, © Springer-Verlag Berlin Heidelberg 2008

The question of physical validity of the Tikhonov–Cagniard model seemed to be the controversial one. The discussion was opened by Wait (1954, 1962) and Price (1962, 1967). They referred to the strong horizontal nonuniformity of the external magnetic field and pointed to the necessity of serious limitations for MT sounding. These limitations have been removed by Dmitriev and Berdichevsky (1979) and Berdichevsky and Dmitriev (2002). They showed that the Tikhonov–Cagniard model covers a broad class of magnetotelluric fields with anyhow fast but quasi-linear variations of $\mathbf{H}_\tau$ over distances comparable to the threefold field-penetration depth. This considerably extends the boundaries of practical applicability of the MT sounding. Moreover, in that class of fields the Tikhonov–Cagniard impedance may be determined by the *gradient magnetovariational sounding* (Berdichevsky et al., 1969; Schmucker, 1970; Weidelt, 1978; Berdichevsky and Dmitriev, 2002):

$$Z = -i\omega\mu_0 \frac{H_z}{\partial H_x/\partial x + \partial H_y/\partial y}. \tag{1.3}$$

The experiments carried out in the late 1950s showed that the real magnetotelluric field may dramatically differ from (1.2). The impedance Z was being determined with large (occasionally very large!) scatter. What's more, it depended on the direction of the measurement axes x, y.

Berdichevsky (1960, 1963) and Cantwell (1960) attributed these effects to the influence of lateral inhomogeneity of the Earth's layers and went from the scalar impedance measurements to the tensor ones. The validity of the tensor approach has been confirmed by extensive magnetotelluric observations over many years.

Behind the tensor approach is the long-standing question on the existence and nature of linear algebraic relations between horizontal components of the electromagnetic field in inhomogeneous media. Would we have to consider the magnetotelluric linear relationships as a postulate verified by statistics of numerous observations? Or, more properly, can we turn to the common principles of classic electrodynamics and derive the linear relations directly from the Maxwell equations?

The general theory of this question has been suggested by Berdichevsky and Zhdanov (1984). They proved that the existence of invariant linear relationships with coefficients reflecting the Earth's conductivity is a special property of the electromagnetic field stemming from the structure of its generators. Electromagnetic fields having this property are said to be fields of algebraic type. Considering fields of algebraic type we can deduce the linear relationships between the field components directly from the equations of Maxwell's electrodynamics. The form of these relationships depends on the number of degrees of freedom characterizing the primary field.

In our book we will follow the work by Berdichevsky and Dmitriev (1997) and use a field excited by a primary plane wave propagating vertically from the ionosphere. This is the simplest field of algebraic type having two degrees of freedom corresponding to two different polarizations of the primary plane. We are going to

start from the Maxwell equations and construct a model with a functionally deterministic magnetotelluric impedance tensor.

Let a plane elliptically polarized monochromatic wave with the components E_x, E_y and H_x, H_y be incident vertically on the Earth's surface $z = 0$ (Fig. 1.1) The air is an ideal insulator. The Earth with magnetic permittivity μ_o of vacuum consists of horizontally homogeneous isotropic layers with normal conductivity $\sigma_N(z)$ and contains a bounded inhomogeneous domain V with excess electric conductivity $\Delta\sigma(x, y, z) = \sigma(x, y, z) - \sigma_N(z)$. The problem is solved in a quasi-stationary approximation.

The electromagnetic field within the Earth meets the equations

$$\begin{aligned} curl\,\mathbf{H} &= \sigma\mathbf{E} = \sigma_N\mathbf{E} + \mathbf{j} \\ curl\,\mathbf{E} &= i\omega\mu_o\mathbf{H}\,, \end{aligned} \tag{1.4}$$

where $\mathbf{j} = \Delta\sigma\,\mathbf{E}$ is the density of excess currents distributed within inhomogeneous domain V.

We will represent $\mathbf{E}$, $\mathbf{H}$ as the sum of the normal field $\mathbf{E}^N$, $\mathbf{H}^N$, and the anomalous field $\mathbf{E}^A$, $\mathbf{H}^A$:

$$\mathbf{E} = \mathbf{E}^N + \mathbf{E}^A, \qquad \mathbf{H} = \mathbf{H}^N + \mathbf{H}^A.$$

The *normal field* $\mathbf{E}^N(E_x^N,\ E_y^N, 0)$, $\mathbf{H}^N(H_x^N,\ H_y^N, 0)$ is a horizontally uniform field observed within the host Earth in the absence of the inhomogeneities. It satisfies the equations

$$\begin{aligned} curl\,\mathbf{H}^N &= \sigma_N\mathbf{E}^N, \\ curl\,\mathbf{E}^N &= i\omega\mu_o\mathbf{H}^N\,. \end{aligned} \tag{1.5}$$

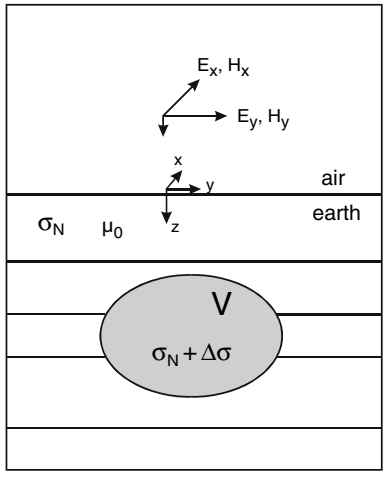

Fig. 1.1 A layered model with an inhomogeneous three-dimensional domain *V*

In the presence of lateral inhomogeneities, the *anomalous field* $\mathbf{E}^{\mathrm{A}}(E_x^{\mathrm{A}}, E_y^{\mathrm{A}}, E_z^{\mathrm{A}})$, $\mathbf{H}^{\mathrm{A}}(H_x^{\mathrm{A}}, H_y^{\mathrm{A}}, H_z^{\mathrm{A}})$, $E_z^{\mathrm{A}}\big|_{z=0} = 0$ appears. Subtracting (I.5) of (I.4), we arrive at equations for the anomalous field:

$$\begin{aligned} curl\,\mathbf{H}^{\mathrm{A}} &= \sigma_{\mathrm{N}}\mathbf{E}^{\mathrm{A}} + \mathbf{j}, \\ curl\,\mathbf{E}^{\mathrm{A}} &= i\omega\mu_{\mathrm{o}}\mathbf{H}^{\mathrm{A}}. \end{aligned} \tag{1.6}$$

From these equations we deduce the integral representations for the anomalous field:

$$\begin{aligned} \mathbf{E}^{\mathrm{A}}(\mathbf{r}) &= \iiint_{\mathrm{V}} \left[\mathbf{G}^{\mathrm{E}}(\mathbf{r}|\mathbf{r}_v)\right]\mathbf{j}\,(\mathbf{r}_v)\;dV, \\ \mathbf{H}^{\mathrm{A}}(\mathbf{r}) &= \iiint_{\mathrm{V}} \left[\mathbf{G}^{\mathrm{H}}(\mathbf{r}|\mathbf{r}_v)\right]\mathbf{j}\,(\mathbf{r}_v)\;dV, \end{aligned} \tag{1.7}$$

where $[\mathbf{G}^{\mathrm{E}}]$ and $[\mathbf{G}^{\mathrm{H}}]$ are the electric and magnetic *Green tensors* for horizontally layered medium:

$$[\mathbf{G}^{\mathrm{E}}] = \begin{bmatrix} G_{xx}^{\mathrm{E}} & G_{xy}^{\mathrm{E}} & G_{xz}^{\mathrm{E}} \\ G_{yx}^{\mathrm{E}} & G_{yy}^{\mathrm{E}} & G_{yz}^{\mathrm{E}} \\ G_{zx}^{\mathrm{E}} & G_{zy}^{\mathrm{E}} & G_{zz}^{\mathrm{E}} \end{bmatrix}, \qquad [\mathbf{G}^{\mathrm{H}}] = \begin{bmatrix} G_{xx}^{\mathrm{H}} & G_{xy}^{\mathrm{H}} & G_{xz}^{\mathrm{H}} \\ G_{yx}^{\mathrm{H}} & G_{yy}^{\mathrm{H}} & G_{yz}^{\mathrm{H}} \\ G_{zx}^{\mathrm{H}} & G_{zy}^{\mathrm{H}} & G_{zz}^{\mathrm{H}} \end{bmatrix}. \tag{1.8}$$

The Green tensors satisfy the equations

$$\begin{aligned} curl[\mathbf{G}^{\mathrm{H}}(\mathbf{r}|\,\mathbf{r}_v)] &= \sigma_{\mathrm{N}}\,[\mathbf{G}^{\mathrm{E}}(\mathbf{r}|\mathbf{r}_v)] + [\boldsymbol{\delta}\,(\mathbf{r}-\mathbf{r}_v)], \\ curl[\mathbf{G}^{\mathrm{E}}(\mathbf{r}|\mathbf{r}_v)] &= i\omega\mu_{\mathrm{o}}\,[\mathbf{G}^{\mathrm{H}}(\mathbf{r}|\mathbf{r}_v)], \end{aligned} \tag{1.9}$$

where $[\boldsymbol{\delta}]$ is the diagonal matrix consisting of the scalar Dirac δ-functions:

$$[\boldsymbol{\delta}\,(\mathbf{r}-\mathbf{r}_v)] = \begin{bmatrix} \delta\,(\mathbf{r}-\mathbf{r}_v) & 0 & 0 \\ 0 & \delta(\mathbf{r}-\mathbf{r}_v) & 0 \\ 0 & 0 & \delta(\mathbf{r}-\mathbf{r}_v) \end{bmatrix}.$$

Here we should clarify how the *curl* of Green's tensor is calculated. Let us write [G] in the form

$$[\mathbf{G}] = [\mathbf{G}_x\;\;\mathbf{G}_y\;\;\mathbf{G}_z]\,,$$

where

$$\mathbf{G}_x = \begin{bmatrix} G_{xx} \\ G_{yx} \\ G_{zx} \end{bmatrix}, \qquad \mathbf{G}_y = \begin{bmatrix} G_{xy} \\ G_{yy} \\ G_{zy} \end{bmatrix}, \qquad \mathbf{G}_z = \begin{bmatrix} G_{xz} \\ G_{yz} \\ G_{zz} \end{bmatrix} .$$

Then

$$\begin{aligned} curl\,[\mathbf{G}] &= [curl\ \mathbf{G}_x \quad curl\ \mathbf{G}_y \quad curl\ \mathbf{G}_z] \\ &= \begin{bmatrix} curl_x \mathbf{G}_x & curl_x \mathbf{G}_y & curl_x \mathbf{G}_z \\ curl_y \mathbf{G}_x & curl_y \mathbf{G}_y & curl_y \mathbf{G}_z \\ curl_z \mathbf{G}_x & curl_z \mathbf{G}_y & curl_z \mathbf{G}_z \end{bmatrix} \\ &= \begin{bmatrix} \frac{\partial G_{zx}}{\partial y} - \frac{\partial G_{yx}}{\partial z} & \frac{\partial G_{zy}}{\partial y} - \frac{\partial G_{yy}}{\partial z} & \frac{\partial G_{zz}}{\partial y} - \frac{\partial G_{yz}}{\partial z} \\ \frac{\partial G_{xx}}{\partial z} - \frac{\partial G_{zx}}{\partial x} & \frac{\partial G_{xy}}{\partial z} - \frac{\partial G_{zy}}{\partial x} & \frac{\partial G_{xz}}{\partial z} - \frac{\partial G_{zx}}{\partial x} \\ \frac{\partial G_{yx}}{\partial x} - \frac{\partial G_{xx}}{\partial y} & \frac{\partial G_{yy}}{\partial x} - \frac{\partial G_{xy}}{\partial y} & \frac{\partial G_{yz}}{\partial x} - \frac{\partial G_{xz}}{\partial y} \end{bmatrix} . \end{aligned} \tag{1.10}$$

Now let us divide the normal field $\mathbf{E}^{\mathrm{N}}$,$\mathbf{H}^{\mathrm{N}}$ into two partial waves linearly polarized in orthogonal directions.

The first polarization offers the wave with components E_x^{N}, H_y^{N}. Normalizing this wave to magnetic field on the Earth's surface, we get:

$$\widehat{E}_x^{\mathrm{N}}(z) = \frac{E_x^{\mathrm{N}}(z)}{H_y^{\mathrm{N}}(0)}, \qquad \widehat{H}_y^{\mathrm{N}}(z) = \frac{H_y^{\mathrm{N}}(z)}{H_y^{\mathrm{N}}(0)} .$$

The second polarization offers the wave with components E_y^{N}, H_x^{N}. Normalizing this wave to magnetic field on the Earth's surface, we get:

$$\widehat{E}_y^{\mathrm{N}}(z) = \frac{E_y^{\mathrm{N}}(z)}{H_x^{\mathrm{N}}(0)}, \qquad \widehat{H}_x^{\mathrm{N}}(z) = \frac{H_x^{\mathrm{N}}(z)}{H_x^{\mathrm{N}}(0)} .$$

The normal fields satisfy (1.2). Thus, on the Earth's surface:

$$\begin{aligned} \widehat{E}_x^{\mathrm{N}}(0) &= Z_{\mathrm{N}} & \widehat{H}_y^{\mathrm{N}}(0) &= 1 \\ \widehat{E}_y^{\mathrm{N}}(0) &= -Z_{\mathrm{N}} & \widehat{H}_x^{\mathrm{N}}(0) &= 1 , \end{aligned} \tag{1.11}$$

where Z_{N} is the *normal impedance*, that is, the Tikhonov–Cagniard impedance of the horizontally layered host medium. Within the inhomogeneous domain V, the normalized field $\widehat{\mathbf{E}}^{\mathrm{N}}$, $\widehat{\mathbf{H}}^{\mathrm{N}}$ excites the excess currents with densities $\mathbf{j}_1$ (the first polarization) and $\mathbf{j}_2$ (the second polarization).

Consider a normal field with arbitrary magnetic components $H_{x\mathrm{o}} = H_x^{\mathrm{N}}(0)$ and $H_{y\mathrm{o}} = H_y^{\mathrm{N}}(0)$ on the Earth's surface. Using the principle of superposition and summing the effects of excess currents, we determine the associated anomalous field. According to (1.7):

$$\mathbf{E}^{\mathrm{A}}(\mathbf{r}) = H_{x\mathrm{o}} \iiint\limits_{\mathrm{V}} \left[\mathbf{G}^{\mathrm{E}}(\mathbf{r}|\mathbf{r}_v)\right]\mathbf{j}_2(\mathbf{r}_v)dV + H_{y\mathrm{o}} \iiint\limits_{\mathrm{V}} \left[\mathbf{G}^{\mathrm{E}}(\mathbf{r}|\mathbf{r}_v)\right]\mathbf{j}_1(\mathbf{r}_v)dV,$$

$$\mathbf{H}^{\mathrm{A}}(\mathbf{r}) = H_{x\mathrm{o}} \iiint\limits_{\mathrm{V}} \left[\mathbf{G}^{\mathrm{H}}(\mathbf{r}|\mathbf{r}_v)\right]\mathbf{j}_2(\mathbf{r}_v)dV + H_{y\mathrm{o}} \iiint\limits_{\mathrm{V}} \left[\mathbf{G}^{\mathrm{H}}(\mathbf{r}|\mathbf{r}_v)\right]\mathbf{j}_1(\mathbf{r}_v)dV\,.$$

In compact form

$$\begin{aligned} \mathbf{E}^{\mathrm{A}}(\mathbf{r}) &= H_{x\mathrm{o}}\mathbf{J}^{\mathrm{E}2}(\mathbf{r}) + H_{y\mathrm{o}}\mathbf{J}^{\mathrm{E}1}(\mathbf{r}), \\ \mathbf{H}^{\mathrm{A}}(\mathbf{r}) &= H_{x\mathrm{o}}\mathbf{J}^{\mathrm{H}2}(\mathbf{r}) + H_{y\mathrm{o}}\mathbf{J}^{\mathrm{H}1}(\mathbf{r}), \end{aligned} \tag{1.12}$$

where

$$\mathbf{J}^{\mathrm{F}\lambda}(\mathbf{r}) = \iiint\limits_{\mathrm{V}} \left[\mathbf{G}^{\mathrm{F}}(\mathbf{r}|\mathbf{r}_v)\right]\mathbf{j}_\lambda(\mathbf{r}_v)dV$$

with F(field) = E, H and λ (polarization) = 1, 2.

And finally, taking into account (1.11), we get

$$\begin{aligned} E_x &= E_x^{\mathrm{N}} + E_x^{\mathrm{A}} = H_{x\mathrm{o}}J_x^{\mathrm{E}2} + H_{y\mathrm{o}}\left(Z_{\mathrm{N}} + J_x^{\mathrm{E}1}\right) && a \\ E_y &= E_y^{\mathrm{N}} + E_y^{\mathrm{A}} = H_{x\mathrm{o}}\left(-Z_{\mathrm{N}} + J_y^{\mathrm{E}2}\right) + H_{y\mathrm{o}}J_y^{\mathrm{E}1} && b \\ H_x &= H_x^{\mathrm{N}} + H_x^{\mathrm{A}} = H_{x\mathrm{o}}\left(1 + J_x^{\mathrm{H}2}\right) + H_{y\mathrm{o}}J_x^{\mathrm{H}1} && c \\ H_y &= H_y^{\mathrm{N}} + H_y^{\mathrm{A}} = H_{x\mathrm{o}}J_y^{\mathrm{H}2} + H_{y\mathrm{o}}\left(1 + J_y^{\mathrm{H}1}\right) && d \end{aligned} \tag{1.13}$$

Eliminating $H_{x\mathrm{o}}$, $H_{y\mathrm{o}}$ from (1.13*c*, *d*) and substituting these values in (1.13*a, b*), we establish:

$$\begin{aligned} E_x &= Z_{xx}H_x + Z_{xy}H_y, \\ E_y &= Z_{yx}H_x + Z_{yy}H_y, \end{aligned} \tag{1.14}$$

where

$$Z_{xx} = \frac{J_x^{E2} - Z_N J_y^{H2} + \left(J_x^{E2} J_y^{H1} - J_x^{E1} J_y^{H2}\right)}{1 + J_x^{H2} + J_y^{H1} + \left(J_x^{H2} J_y^{H1} - J_x^{H1} J_y^{H2}\right)},$$

$$Z_{xy} = \frac{Z_N \left(1 + J_x^{H2}\right) + J_x^{E1} + \left(J_x^{E1} J_x^{H2} - J_x^{E2} J_x^{H1}\right)}{1 + J_x^{H2} + J_y^{H1} + \left(J_x^{H2} J_y^{H1} - J_x^{H1} J_y^{H2}\right)},$$

$$Z_{yx} = \frac{-Z_N \left(1 + J_y^{H1}\right) + J_y^{E2} + \left(J_y^{E2} J_y^{H1} - J_y^{E1} J_y^{H2}\right)}{1 + J_x^{H2} + J_y^{H1} + \left(J_x^{H2} J_y^{H1} - J_x^{H1} J_y^{H2}\right)},$$

$$Z_{yy} = \frac{J_y^{E1} + Z_N J_x^{H1} + \left(J_y^{E1} J_x^{H2} - J_y^{E2} J_x^{H1}\right)}{1 + J_x^{H2} + J_y^{H1} + \left(J_x^{H2} J_y^{H1} - J_x^{H1} J_y^{H2}\right)} .$$

Thus, we have deduced the complex-valued *impedance tensor* $[\mathbf{Z}]$ that transforms the horizontal magnetic field $\mathbf{H}_\tau$ into the horizontal electric field $\mathbf{E}_\tau$:

$$\mathbf{E}_\tau = [\mathbf{Z}]\,\mathbf{H}_\tau\,, \tag{1.15}$$

where

$$\mathbf{E}_\tau = \begin{bmatrix} E_x \\ E_y \end{bmatrix}, \qquad [\mathbf{Z}] = \begin{bmatrix} Z_{xx} & Z_{xy} \\ Z_{yx} & Z_{yy} \end{bmatrix}, \qquad \mathbf{H}_\tau = \begin{bmatrix} H_x \\ H_y \end{bmatrix}.$$

The impedance tensor is functionally deterministic, being independent of the normal field intensity and polarization. It reflects the electrical structure of the Earth.

Now we can explain why the earliest magnetotelluric experiments were doomed to failure. Applying the Tikhonov–Cagniard relations (1.1), (1.2) to the field observed over the horizontally inhomogeneous Earth, we get a pseudoimpedance

$$Z_{\text{pseudo}} = \begin{cases} \dfrac{E_x}{H_y} = Z_{xy} + Z_{xx}\dfrac{H_x}{H_y} \\ -\dfrac{E_y}{H_x} = -Z_{yx} - Z_{yy}\dfrac{H_y}{H_x} \end{cases}$$

that depends on an arbitrary ratio between magnetic components. With unstable field polarization, Z_{pseudo} may dramatically change.

The impedance tensor $[\mathbf{Z}]$ has a second-order square matrix with Z_{xx}, Z_{yy} on the principal diagonal (on the "diagonal") and Z_{xy}, Z_{yx} on the secondary diagonal (on the "antidiagonal"). By virtue of (1.14) these response functions depend on the normal impedance Z_N characterizing the one-dimensional layered background and on the three-dimensional integrals J summing the effects of excess currents arising within inhomogeneities. Clearly Z_{xx}, Z_{yy} and Z_{xy}, Z_{yx} carry the information on vertical and horizontal variations in the Earth's conductivity. Note, however, that the basic information on the vertical distribution of the conductivity is given by

the components Z_{xy} and Z_{yx} on the secondary diagonal, while the components Z_{xx} and Z_{yy} on the principal diagonal indicate the geoelectric asymmetry of the medium. By way of example consider (1.1) and (1.2) describing the horizontally homogeneous layered model. Here $Z_{xy} = -Z_{yx} = Z$ and $Z_{xx} = Z_{yx} = 0$. No wonder that Z_{xy} and Z_{yx} are sometimes said to be principal impedances, whereas Z_{xx} and Z_{yy} are referred to as secondary impedances. Such a paradoxical peculiarity of the impedance tensor [**Z**] can be easily removed by rotating the magnetic field through $\pi/2$ (Adam, 1964) and writing the impedance relation as

$$\mathbf{E}_\tau = [\mathbf{Z}]\,\mathbf{H}_\tau = [\mathbf{Z}][\mathbf{R}(-\pi/2)[\mathbf{R}(\pi/2)]\,\mathbf{H}_\tau = [\overleftrightarrow{\mathbf{Z}}]\,\overleftrightarrow{\mathbf{H}}_\tau\,, \tag{1.16}$$

where

$$[\mathbf{R}(\alpha)] = \begin{bmatrix} \cos\alpha & \sin\alpha \\ -\sin\alpha & \cos\alpha \end{bmatrix}$$

$$\overleftrightarrow{\mathbf{H}}_\tau = [\mathbf{R}(\pi/2)]\,\mathbf{H}_\tau = \begin{bmatrix} 0 & 1 \\ -1 & 0 \end{bmatrix} \begin{bmatrix} H_x \\ H_y \end{bmatrix} = \begin{bmatrix} H_y \\ -H_x \end{bmatrix} = \begin{bmatrix} \overleftrightarrow{H}_x \\ \overleftrightarrow{H}_y \end{bmatrix}$$

and:

$$[\overleftrightarrow{\mathbf{Z}}] = [\mathbf{Z}][\mathbf{R}(-\pi/2)] = \begin{bmatrix} Z_{xx} & Z_{xy} \\ Z_{yx} & Z_{yy} \end{bmatrix} \begin{bmatrix} 0 & -1 \\ 1 & 0 \end{bmatrix} = \begin{bmatrix} Z_{xy} & -Z_{xx} \\ Z_{yy} & -Z_{yx} \end{bmatrix} = \begin{bmatrix} \overleftrightarrow{Z}_{xx} & \overleftrightarrow{Z}_{xy} \\ \overleftrightarrow{Z}_{yx} & \overleftrightarrow{Z}_{yy} \end{bmatrix}.$$

Here $[\overleftrightarrow{\mathbf{Z}}]$ is the *Adam impedance tensor.* In this representation, the basic information on the vertical distribution of the conductivity is given by the components $\overleftrightarrow{Z}_{xx} = Z_{xy}$ and $\overleftrightarrow{Z}_{yy} = -Z_{yx}$ on the principal diagonal, while the components $\overleftrightarrow{Z}_{xy} = -Z_{xx}$ and $\overleftrightarrow{Z}_{yx} = Z_{yy}$ on the secondary diagonal indicate the geoelectric asymmetry of the medium. Turning back to the horizontally homogeneous model described by (1.1) and (1.2), we see that in the representation $\mathbf{E}_\tau = [\overleftrightarrow{\mathbf{Z}}]\overleftrightarrow{\mathbf{H}}_\tau$ the electric and magnetic fields are collinear.

The components of the impedance tensor [**Z**] can be transformed into *apparent resistivities*. In the horizontally homogeneous model the transform $\rho_A = |Z|^2/\omega\mu_o$ gives a vivid qualitative picture of vertical resistivity profile. This useful property of the one-dimensional impedance is inherited by components Z_{xy}, Z_{yx} of the impedance tensor (though with some distortions) and hardly by components Z_{xx}, Z_{yy}. So, it would appear natural to calculate the amplitude and phase MT-curves related to x, y-axes as

$$\begin{aligned} \rho_{xy} &= \frac{|Z_{xy}|^2}{\omega\mu_o} & \rho_{yx} &= \frac{|Z_{yx}|^2}{\omega\mu_o} \\ \varphi_{xy} &= \operatorname{Arg} Z_{xy} & \varphi_{yx} &= \operatorname{Arg} Z_{yx}\,. \end{aligned} \tag{1.17}$$

Along with the impedance tensor $[\mathbf{Z}]$ we can introduce its inverse

$$[\mathbf{Y}] = [\mathbf{Z}]^{-1}, \tag{1.18}$$

which is the *admittance tensor* transforming the horizontal electric field E_τ into the horizontal magnetic field $\mathbf{H}_\tau = [\mathbf{Y}]\,\mathbf{E}_\tau$.

In the matrix form

$$[\mathbf{Y}] = \begin{bmatrix} Y_{xx} & Y_{xy} \\ Y_{yx} & Y_{yy} \end{bmatrix}, \tag{1.19}$$

where

$$Y_{xx} = \frac{Z_{yy}}{Z_{xx}Z_{yy} - Z_{xy}Z_{yx}}, Y_{xy} = -\frac{Z_{xy}}{Z_{xx}Z_{yy} - Z_{xy}Z_{yx}},$$
$$Y_{yx} = -\frac{Z_{yx}}{Z_{xx}Z_{yy} - Z_{xy}Z_{yx}}, Y_{yy} = \frac{Z_{xx}}{Z_{xx}Z_{yy} - Z_{xy}Z_{yx}},$$

and

$$H_x = Y_{xx}E_x + Y_{xy}E_y,$$
$$H_y = Y_{yx}E_x + Y_{yy}E_y.$$

The impedance and admittance tensors carry the same information about the geoelectric structure of the Earth, and from this point of view, it makes no difference which of them is used as fundamental. Cagniard chose the impedance and apparent resistivity, and this suited geophysicists who got accustomed to the apparent resistivity measured with the DC vertical sounding method. There is little point in abandoning this tradition, though we have to realize that the layered Earth constitutes a system consisting of parallel-connected conductors (the Earth's layers), and the most natural way of characterizing such a system would seem to be as an admittance, and therefore, as an apparent conductivity. It is not an accident that in many magnetotelluric problems, it is easier to deal with the admittance (Berdichevsky and Dmitriev, 2002). Consider, for instance, a one-dimensional model where the admittance constitutes the weighted complex conductance :

$$Y = \int_0^\infty \sigma(z)\, e^{i\omega\mu_0 \int_0^z Y(z)\,dz}\, dz.$$

In concluding we note that model under consideration offers the linear relationships between the electric fields measured at different sites of the Earth's surface. Let us consider horizontal electric fields $\mathbf{E}_\tau$ at two sites: at an observation site and at a base (reference) site B. According to (1.13)

$$
\begin{aligned}
E_x(\mathbf{r}) &= E_x^{\mathrm{N}} + E_x^{\mathrm{A}}(\mathbf{r}) = H_{x\mathrm{o}} J_x^{\mathrm{E2}}(\mathbf{r}) + H_{y\mathrm{o}} \left[Z_{\mathrm{N}} + J_x^{\mathrm{E1}}(\mathbf{r}) \right], \\
E_y(\mathbf{r}) &= E_y^{\mathrm{N}} + E_y^{\mathrm{A}}(\mathbf{r}) = H_{x\mathrm{o}} \left[-Z_{\mathrm{N}} + J_y^{\mathrm{E2}}(\mathbf{r}) \right] + H_{y\mathrm{o}} J_y^{\mathrm{E1}}(\mathbf{r}),
\end{aligned}
\tag{1.20}
$$

$$
\begin{aligned}
E_x(\mathbf{r}_{\mathrm{B}}) &= E_x^{\mathrm{N}} + E_x^{\mathrm{A}}(\mathbf{r}_{\mathrm{B}}) = H_{x\mathrm{o}} J_x^{\mathrm{E2}}(\mathbf{r}_{\mathrm{B}}) + H_{y\mathrm{o}} \left[Z_{\mathrm{N}} + J_x^{\mathrm{E1}}(\mathbf{r}_{\mathrm{B}}) \right], \\
E_y(\mathbf{r}_{\mathrm{B}}) &= E_y^{\mathrm{N}} + E_y^{\mathrm{A}}(\mathbf{r}_{\mathrm{B}}) = H_{x\mathrm{o}} \left[-Z_{\mathrm{N}} + J_y^{\mathrm{E2}}(\mathbf{r}_{\mathrm{B}}) \right] + H_{y\mathrm{o}} J_y^{\mathrm{E1}}(\mathbf{r}_{\mathrm{B}}).
\end{aligned}
\tag{1.21}
$$

Eliminating $H_{x\mathrm{o}},\ H_{y\mathrm{o}}$ from (1.20) and (1.21), we get

$$
\mathbf{E}_\tau(\mathbf{r}) = [\mathbf{D}\,(\mathbf{r}|\mathbf{r}_{\mathrm{B}})]\ \mathbf{E}_\tau(\mathbf{r}_{\mathrm{B}}),
\tag{1.22}
$$

where

$$
\mathbf{E}_\tau(\mathbf{r}) = \begin{bmatrix} E_x(\mathbf{r}) \\ E_y(\mathbf{r}) \end{bmatrix}, \qquad \mathbf{E}_\tau(\mathbf{r}_{\mathrm{B}}) = \begin{bmatrix} E_x(\mathbf{r}_{\mathrm{B}}) \\ E_y(\mathbf{r}_{\mathrm{B}}) \end{bmatrix}
$$

and

$$
[\mathbf{D}\,(\mathbf{r}|\mathbf{r}_{\mathrm{B}})] = \begin{bmatrix} D_{xx}(\mathbf{r}|\mathbf{r}_{\mathrm{B}}) & D_{xy}(\mathbf{r}|\mathbf{r}_{\mathrm{B}}) \\ D_{yx}(\mathbf{r}|\mathbf{r}_{\mathrm{B}}) & D_{yy}(\mathbf{r}|\mathbf{r}_{\mathrm{B}}) \end{bmatrix}
$$

$$
= \begin{bmatrix} J_x^{E2}(\mathbf{r}) & Z_{\mathrm{N}} + J_x^{E1}(\mathbf{r}) \\ -Z_{\mathrm{N}} + J_y^{E2}(\mathbf{r}) & J_y^{E1}(\mathbf{r}) \end{bmatrix} \begin{bmatrix} J_x^{E2}(\mathbf{r}_{\mathrm{B}}) & Z_{\mathrm{N}} + J_x^{E1}(\mathbf{r}_{\mathrm{B}}) \\ -Z_{\mathrm{N}} + J_y^{E2}(\mathbf{r}_{\mathrm{B}}) & J_y^{E1}(\mathbf{r}_{\mathrm{B}}) \end{bmatrix}^{-1}.
$$

Recall that the tensor $[\mathbf{D}\,(\mathrm{r}|\mathrm{r}_{\mathrm{B}})]$ was introduced by Doll into the telluric current method about 70 years ago. We will refer it as the *Doll tensor*. The basic result of a telluric prospecting was given in a map showing *effective electric intensity* defined as

$$
D_{\mathrm{eff}} = \sqrt{|\det[\mathbf{D}\,(\mathrm{r}|\mathrm{r}_{\mathrm{B}})]\,|}\,.
\tag{1.23}
$$

Summing up, we should say some words about stability of the impedance relations. The experience of manifold MTS-soundings carried out at the middle and low latitudes in the frequency range from 10^2 to 10^{-4} Hz suggests that modern noise-suppressing methods of MT-date processing (mathematical filtration, admittance control, remote reference magnetotellurics, robust statistics, monitoring of impedance scattering) may provide the impedance estimation with a scattering of 2–3% in modulus and 2–3° in phase (Gamble et al., 1979; Chave et al.,1987; Jones et al., 1989; Berdichevsky et al., 1989a; Larsen, 1989; Larsen et al., 1996). The most reliable and stable result can be obtained using the MT-data processing which reinforces the remote reference magnetotellurics with robust statistics.

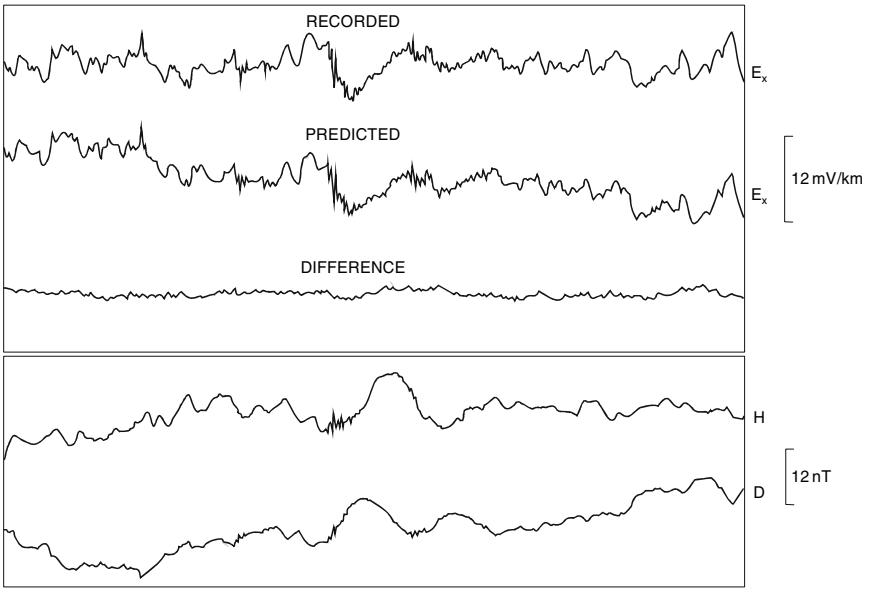

Fig. 1.2 Comparison between recorded and predicted variations in the E_x-component (Wielondek and Ernst, 1977)

Let us exemplify the stability of the impedance relation by experiments carried out on the southeast of Poland (Wielondek and Ernst, 1977). Figure 1.2 shows the observed variations in the E_x-component of electric field and the same variations predicted from the variations in H- and D-components of magnetic field convolved with the previously determined impedance [**Z**]. The predicted variations look like a replica of the recorded variations including small details.

1.2 Rotation of the Impedance Tensor

Let us orient the components $Z_{xx},\ Z_{xy}, Z_{yx}, Z_{yy}$ of the impedance tensor [**Z**] in the direction corresponding to their first subscript. It means that $Z_{xx},\ Z_{xy}$ are oriented in the x-direction, and Z_{yx}, Z_{yy} are oriented in the y-direction. The orientation of the impedance components complies with the orientation of the corresponding electric field components.

How do the components of the impedance tensor [**Z**] change as a frame of reference rotates? Let α be a clockwise rotation angle (Fig. 1.3). Consider the transition from the old axes x, y to the new axes x', y' and conversely.

The direct and converse rotation matrices are

$$[\mathbf{R}(\alpha)] = \begin{bmatrix} \cos\ \alpha & \sin\ \alpha \\ -\sin\ \alpha & \cos\ \alpha \end{bmatrix}, \qquad [\mathbf{R}(\alpha)\,]^{-1} = \begin{bmatrix} \cos\ \alpha & -\sin\ \alpha \\ \sin\ \alpha & \cos\ \alpha \end{bmatrix}. \quad (1.24)$$

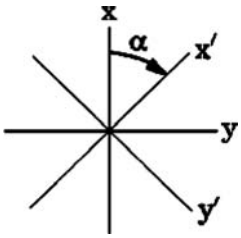

Fig. 1.3 Rotation of a reference frame

Thus,

$$\mathbf{E}_\tau(\alpha) = [\mathbf{R}(\alpha)]\mathbf{E}_\tau = [\mathbf{R}(\alpha)][\mathbf{Z}]\ \ \mathbf{H}_\tau = [\mathbf{R}(\alpha)][\mathbf{Z}]\ [\mathbf{R}(\alpha)]^{-1}[\mathbf{R}(\alpha)]\mathbf{H}_\tau$$
$$= [\mathbf{Z}(\alpha)]\ \mathbf{H}_\tau(\alpha),$$

where

$$[\mathbf{Z}(\alpha)] = [\mathbf{R}(\alpha)][\mathbf{Z}][\mathbf{R}(\alpha)\,]^{-1}. \tag{1.25}$$

In full form, we have

$$\begin{aligned}
Z_{xx}\,(\alpha) &= Z_{xx}\cos^2\alpha + Z_{yy}\sin^2\alpha + (\,Z_{xy} + Z_{yx}\,)\sin\alpha\cos\alpha \\
Z_{xy}\,(\alpha) &= Z_{xy}\cos^2\alpha - Z_{yx}\sin^2\alpha - (\,Z_{xx} - Z_{yy}\,)\sin\alpha\cos\alpha \\
Z_{yx}\,(\alpha) &= Z_{yx}\cos^2\alpha - Z_{xy}\sin^2\alpha - (\,Z_{xx} - Z_{yy}\,)\sin\alpha\cos\alpha \\
Z_{yy}\,(\alpha) &= Z_{yy}\cos^2\alpha + Z_{xx}\sin^2\alpha - (\,Z_{xy} + Z_{yx}\,)\sin\alpha\cos\alpha
\end{aligned} \tag{1.26}$$

or

$$\begin{aligned}
Z_{xx}(\alpha) &= Z_2 + Z_3\sin 2\alpha + Z_4\cos 2\alpha \\
Z_{xy}(\alpha) &= Z_1 + Z_3\cos 2\alpha - Z_4\sin 2\alpha \\
Z_{yx}(\alpha) &= -\,Z_1 + Z_3\cos 2\alpha - Z_4\sin 2\alpha \\
Z_{yy}(\alpha) &= Z_2 - Z_3\sin 2\alpha - Z_4\cos 2\alpha\,,
\end{aligned} \tag{1.27}$$

where

$$Z_1 = \frac{Z_{xy} - Z_{yx}}{2} \quad Z_2 = \frac{Z_{xx} + Z_{yy}}{2}$$
$$Z_3 = \frac{Z_{xy} + Z_{yx}}{2} \quad Z_4 = \frac{Z_{xx} - Z_{yy}}{2}\ .$$

One can readily see that

$$\begin{aligned}
Z_{xx}(\alpha) &= Z_{xx}\,(\alpha + \pi) = Z_{yy}\,(\alpha + \pi/2) \\
Z_{xy}(\alpha) &= Z_{xy}\,(\alpha + \pi) = -\,Z_{yx}\,(\alpha + \pi/2) \\
Z_{yx}(\alpha) &= Z_{yx}\,(\alpha + \pi) = -\,Z_{xy}(\alpha + \pi/2) \\
Z_{yy}(\alpha) &= Z_{yy}(\alpha + \pi) = Z_{xx}(\alpha + \pi/2).
\end{aligned} \tag{1.28}$$

The principal *rotational invariants* of the magnetotelluric impedance tensor are (Berdichevsky, 1968; Sharka and Menvielle, 1997):

$$\begin{aligned}
&\mathbf{I}_1 = \mathrm{tr}\,[\mathbf{Z}] = Z_{xx} + Z_{yy} && a \\
&\mathbf{I}_2 = \det\,[\mathbf{Z}] = Z_{xx}Z_{yy} - Z_{xy}Z_{yx} && b \\
&\mathbf{I}_3 = \mathrm{tr}\,[\overleftrightarrow{\mathbf{Z}}] = \mathrm{tr}\,[\mathbf{Z}][\mathbf{R}(-\pi/2)] = \overleftrightarrow{Z}_{\mathrm{xx}} + \overleftrightarrow{Z}_{yy} = Z_{xy} - Z_{yx}, && c
\end{aligned} \tag{1.29}$$

where tr [**Z**] and det [**Z**] are the trace and determinant of the impedance tensor [**Z**], while tr $[\overleftrightarrow{\mathbf{Z}}]$ is the trace of the Adam impedance tensor $[\overleftrightarrow{\mathbf{Z}}]$.

Using (1.29), we introduce the effective impedance Z_{eff} and the Berdichevsky impedance Z_{brd}:

$$\begin{aligned}
Z_{\mathrm{eff}} &= \sqrt{Z_{xx}Z_{yy} - Z_{xy}Z_{yx}}, \\
Z_{\mathrm{brd}} &= Z_1 = \frac{Z_{xy} - Z_{yx}}{2} \quad .
\end{aligned} \tag{1.30}$$

These three independent invariants can be supplemented with the quadratic invariant derived from (1.29):

$$\mathrm{I}_4 = \mathrm{I}_1^2 + \mathrm{I}_3^2 - 2\mathrm{I}_2 = \mathrm{tr}\,[\mathbf{C}] = Z_{xx}^2 + Z_{xy}^2 + Z_{yx}^2 + Z_{yy}^2\,, \tag{1.31}$$

where tr [**C**] is the trace of the tensor $[\mathbf{C}] = [\mathbf{Z}][\mathbf{Z}]^{\mathrm{T}}$, T denotes the transposition.

Since [**Z**] is determined by eight independent real-valued elements, the number of independent real rotational invariants should be less than eight. Sharka and Menvielle (1997) proved that the maximum number of the real independent invariants is equal to seven. They suggested the following standard set of independent rotational invariants:

$$\begin{aligned}
J_1 &= 2\mathrm{Re}\;Z_{\mathrm{brd}} = \mathrm{Re}\;\mathrm{I}_3 = \mathrm{Re}\;Z_{xy} - \mathrm{Re}\;Z_{yx} && a \\
J_2 &= 2\mathrm{Im}\;Z_{\mathrm{brd}} = \mathrm{Im}\;\mathrm{I}_3 = \mathrm{Im}\;Z_{xy} - \mathrm{Im}\;Z_{yx} && b \\
J_3 &= \mathrm{tr}\,[\mathrm{Re}\;\mathbf{Z}] = \mathrm{Re}\;\mathrm{I}_1 = \mathrm{Re}\;Z_{xx} + \mathrm{Re}\;Z_{yy} && c \\
J_4 &= \mathrm{tr}\,[\mathrm{Im}\;\mathbf{Z}] = \mathrm{Im}\;\mathrm{I}_1 = \mathrm{Im}\;Z_{xx} + \mathrm{Im}\;Z_{yy} && d \\
J_5 &= \det\,[\mathrm{Re}\;\mathbf{Z}] = \mathrm{Re}\;Z_{xx}\mathrm{Re}\;Z_{yy} - \mathrm{Re}\;Z_{xy}\mathrm{Re}\;Z_{yx} && e \\
J_6 &= \det\,[\mathrm{Im}\;\mathbf{Z}] = \mathrm{Im}\;Z_{xx}\mathrm{Im}\;Z_{yy} - \mathrm{Im}\;Z_{xy}\mathrm{Im}\;Z_{yx} && f \\
J_7 &= \mathrm{Im}\;\det\,[\mathbf{Z}] = \mathrm{Im}\,(\,Z_{xx}Z_{yy} - Z_{xy}Z_{yx}\,), && g
\end{aligned} \tag{1.32}$$

where

$$[\mathrm{Re}\;\mathbf{Z}] = \begin{bmatrix} \mathrm{Re}\;Z_{xx} & \mathrm{Re}\;Z_{xy} \\ \mathrm{Re}\;Z_{yx} & \mathrm{Re}\;Z_{yy} \end{bmatrix}, \qquad [\mathrm{Im}\;\mathbf{Z}] = \begin{bmatrix} \mathrm{Im}\;Z_{xx} & \mathrm{Im}\;Z_{xy} \\ \mathrm{Im}\;Z_{yx} & \mathrm{Im}\;Z_{yy} \end{bmatrix}.$$

From (1.29) and (1.32) we can derive another real-valued invariants:

$$
\begin{aligned}
J_8 &= J_5 - J_6 = \det\,[\mathrm{Re}\,\mathbf{Z}] - \det\,[\mathrm{Im}\,\mathbf{Z}] = \mathrm{Re}\,\det\,[\mathbf{Z}] && a \\
J_9 &= \sqrt{\mathrm{Re}^2\,\mathrm{I}_3 + \mathrm{Re}^2\,\mathrm{I}_1 - 2\,J_5} \\
&= \sqrt{\mathrm{Re}^2\,Z_{xx} + \mathrm{Re}^2\,Z_{xy} + \mathrm{Re}^2\,Z_{yx} + \mathrm{Re}^2\,Z_{yy}} = \|\mathrm{Re}\,\mathbf{Z}\| && b \\
J_{10} &= \sqrt{\mathrm{Im}^2\,\mathrm{I}_3 + \mathrm{Im}^2\,\mathrm{I}_1 - 2\,J_6} \\
&= \sqrt{\mathrm{Im}^2\,Z_{xx} + \mathrm{Im}^2\,Z_{xy} + \mathrm{Im}^2\,Z_{yx} + \mathrm{Im}^2\,Z_{yy}} = \|\mathrm{Im}\,\mathbf{Z}\| && c \\
J_{11} &= \sqrt{|\mathrm{I}_1|^2 + |\mathrm{I}_3|^2 - 2(J_5 + J_6)} \\
&= \sqrt{|Z_{xx}|^2 + |Z_{xy}|^2 + |Z_{yx}|^2 + |Z_{yy}|^2} = \|\mathbf{Z}\|\,, && d
\end{aligned}
\tag{1.33}
$$

where $\|Re\,\mathbf{Z}\|$, $\|\mathrm{Im}\,\mathbf{Z}\|$, $\|\mathbf{Z}\|$ are the Euclidean norms of the matrices [Re **Z**], [Im **Z**], [**Z**] respectively.

Two more real-valued rotational invariant are

$$J_{12} = \mathrm{Im}\,(Z_{xy}\,\bar{Z}_{yy} + Z_{xx}\,\bar{Z}_{yx}), \tag{1.34}$$

$$J_{13} = \mathrm{Im}\,(Z_{xx}\,\bar{Z}_{xy} + Z_{yx}\,\bar{Z}_{yy}), \tag{1.35}$$

where the bars denote the complex conjugation.

With all these invariants one can construct a standard set of parameters that help to reveal and classify the geoelectric structures of the Earth.

1.3 Dimensionality of the Impedance Tensor

The general properties of the impedance tensor depend on the dimensionality D of the magnetotelluric model, that is, on the number of coordinates required for its description.

We deal with one-dimensional (1D), two-dimensional (2D) and three-dimensional (3D) models as well as with superimposition (2D + 3D, 3D + 3D, 2D + 2D) models. Respectively, we consider the one-dimensional, two-dimensional and three-dimensional impedance tensors as well as the superimposition impedance tensor.

The number n of real quantities which determine the complex-valued impedance tensor are considered as a number of degrees of its freedom. A simple relation holds between n and D:

$$n = 2^D. \tag{1.36}$$

1.3.1 The One-Dimensional Impedance Tensor

In the 1D-model the conductivity $\sigma(z)$ varies only with depth z. Here D = 1 and $n = 2$. The one-dimensional impedance tensor assumes the form

$$[\mathbf{Z}] = Z \begin{bmatrix} 0 & 1 \\ -1 & 0 \end{bmatrix} = \mathrm{Re}\, Z \begin{bmatrix} 0 & 1 \\ -1 & 0 \end{bmatrix} + i\,\mathrm{Im}\, Z \begin{bmatrix} 0 & 1 \\ -1 & 0 \end{bmatrix}, \tag{1.37}$$

where scalar Z is the Tikhonov–Cagniard impedance (no mater how axes x, y are directed):

$$Z = i\omega\mu_o \frac{E_x}{dE_x/dz} = i\omega\mu_o \frac{E_y}{dE_y/dz} = -\frac{1}{\sigma}\frac{dH_y/dz}{H_y} = -\frac{1}{\sigma}\frac{dH_x/dz}{H_x}. \tag{1.38}$$

The necessary condition for the one-dimensionality is

$$Z_{xx} = Z_{yy} = 0, \qquad Z_{xy} = -Z_{yx}\,. \tag{1.39}$$

This is the simplest magnetotelluric model. The one-dimensional impedance Z and admittance $Y = 1/Z$ meet the Riccati equations

$$\frac{dZ}{dz} - \sigma Z^2 = i\omega\mu_o, \qquad \frac{dY}{dz} + i\omega\mu_o Y^2 = -\sigma, \tag{1.40}$$

where $\mathrm{Re}\, Z \geq 0$ and $\mathrm{Im}\, Y \geq 0$, while $0 \leq \arg Z \leq -\pi/2$ and $0 \geq \arg Y \leq \pi/2$. When lowering frequency, the impedance module, $|Z|$, monotonically descends.

The apparent resistivity is

$$\rho_A = \frac{|Z|^2}{\omega\mu_o} = \frac{1}{\omega\mu_o\,|Y|^2}. \tag{1.41}$$

The slope of apparent-resistivity curves plotted on log–log scale is bounded by $\pm \arctan 2$.

From (1.38) we readily derive

$$\begin{aligned} |E_x(z)| &= |E_x(0)| \exp\left(-\omega\mu_o \int_0^z \mathrm{Im}\, Y(z)\, dz\right), \\ \left|H_y(z)\right| &= \left|H_y(0)\right| \exp\left(-\int_0^z \sigma(z)\mathrm{Re}\, Z(z)\, dz\right), \end{aligned} \tag{1.42}$$

where $H_y(0) = 2\,H^p(0)$ is the double primary magnetic field $H^p(0)$ impinging on the Earth's surface $z = 0$. Analysis of (1.42) shows that in any layered one-dimensional model, electric and magnetic fields descend monotonically with depth and the faster, the higher the frequency is.

Let us consider a three-layered K-type model with $\rho_2 >> \rho_1,\ h_2 >> h_1,\ \rho_3 = 0$. This generalized model characterizes the typical geoelectric structure of the upper Earth's layers. The first layer represents conductive sedimentary strata, the second layer relates to the resistive lithosphere, and the third layer simulates the highly conductive mantle.

Solving the Riccati equation, we get

$$Z = \frac{E_x}{H_y} = -\frac{E_y}{H_x} = -\frac{\omega\mu_o}{k_1}\ \tan\ h\left\{ik_1h_1 + \tan\ h^{-1}\frac{k_1}{k_2}\ \tan\ hik_2h_2\right\}, \qquad (1.43)$$

where $k_1 = \sqrt{i\omega\mu_o/\rho_1}$ and $k_2 = \sqrt{i\omega\mu_o/\rho_2}$, $\mathrm{Im}\, k > 0$ (Berdichevsky and Dmitriev, 2002). The apparent-resistivity and impedance-phase curves, ρ_A and φ, calculated for ρ_1 = 10 Ohm·m, h_1 = 1 km, ρ_2 = 10000 Ohm·m, h_2 = 49 km, ρ_3 = 0 are shown in Fig. 1.4. Examine the informativeness of different portions of these curves.

The low-frequency asymptotics of the impedance Z gives

$$Z = -\frac{i\omega\mu_o h}{1 - i\omega\mu_o S_1 h_2}, \quad \text{when } \rho_2 >> \rho_1,\ h_2 >> h_1 \text{ and } \omega << \frac{1}{\mu_o S_1 h_1}, \qquad (1.44)$$

where $S_1 = h_1/\rho_1$ and $h = h_1 + h_2$. Here two frequency intervals are of specific interest.

If $\omega\mu_o S_1 h_2 >> 1$, then

$$Z = \frac{1}{S_1}. \qquad (1.45)$$

This frequency interval corresponds to the ascending branch of the ρ_A-curve. It contains information on the conductance S_1 of the upper layer. Its title is the S_1-interval. Within the S_1-interval the ρ_A-curve merges with the S_1-line, while the impedance phase nears to zero. According to (1.45), equation for the S_1-line is

$$\rho_A = \frac{(\sqrt{T})^2}{2\pi\mu_o S_1^2}.$$

In bilogarithmic coordinates, this is

$$\log\rho_A = 2\log\sqrt{T} - \log 2\pi\mu_o S_1^2.$$

Evidently, the S_1-line is tilted at an angle of $\arctan 2 = 63.43^o$ to the axis of $\sqrt{T}$. It intersects the line $\rho_A = 1$ Ohm · m at $\sqrt{T_{S_1}}$, from which we can determine

$$S_1 = \frac{1}{\sqrt{2\pi\mu_o}}\sqrt{T_{S_1}} \quad \text{or} \quad S_1(\text{siemens}) = 356\sqrt{T_{S_1}(\text{second})}.$$

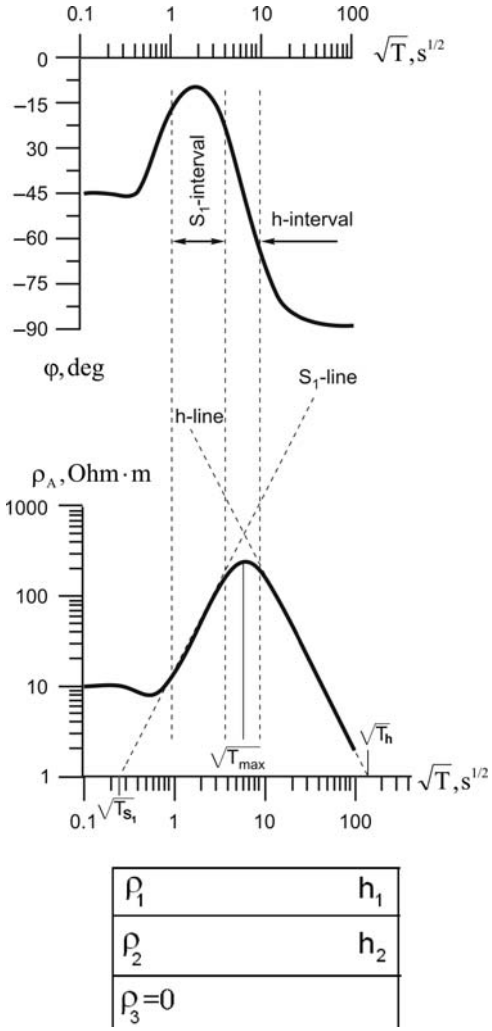

Fig. 1.4 Three-layered apparent-resistivity and impedance-phase curves characterizing the geoelectric structure of the tectonosphere. Model parameters: $\rho_1 = 10\,\text{Ohm}\cdot\text{m}$, $h_1 = 1\,\text{km}$, $\rho_2 = 10\,000\,\text{Ohm}\cdot\text{m}$ $h_2 = 49\,\text{km}$, $\rho_3 = 0$

If $\omega\mu_0 S_1 h_2 << 1$, then

$$Z = -i\omega\mu_o h. \tag{1.46}$$

This frequency interval corresponds to the descending branch of the ρ_A-curve. It contains information on the total thickness h of the layers underlaid with conductive basement. Its title is the *h-interval*. Within the h-interval the ρ_A-curve merges with the h-line, while the impedance phase nears to $-\pi/2$. According to (1.46), equation for the h-line is

$$\rho_A = \frac{2\pi\mu_o h_1^2}{(\sqrt{T})^2}.$$

In bilogarithmic coordinates, we have

$$\log \rho_A = -2\log\sqrt{T} + \log 2\pi\mu_o h_1^2.$$

Evidently, the h-line is tilted at an angle of -arctan $2 = -63.43^o$ to the axis of $\sqrt{T}$. It intersects the line $\rho_A = 1$ Ohm $\cdot$ m at $\sqrt{T_h}$, from which we can determine

$$h = \frac{1}{\sqrt{2\pi\mu_o}}\sqrt{T_h} \quad \text{or} \quad h(\text{kilometer}) = 0.356\sqrt{T_h(\text{second})}.$$

The remarkable property of the h-interval is that the depth h to the perfect conductor can be obtained immediately from the impedance, $h = |Z|/\omega\mu_o$, without any additional information. Applying this formula for an arbitrary layered medium, we get at any frequency so-called *effective penetration depth* h_{eff}. Following Weidelt (1972), we draw analogy with a center of masses and consider h_{eff} as the depth to the center of currents induced in the Earth:

$$h_{\text{eff}} = \frac{|Z|}{\omega\mu_o} = \sqrt{\frac{\rho_A}{\omega\mu_o}} = \frac{1}{\omega\mu_o}\left|\frac{E_x(0)}{H_y(0)}\right| = \left|\frac{\int_0^\infty H_y\,dz}{\int_0^\infty j_x\,dz}\right| = \left|\frac{\int_0^\infty z\frac{dH_y}{dz}\,dz}{\int_0^\infty j_x\,dz}\right| = \left|\frac{\int_0^\infty z\,j_x\,dz}{\int_0^\infty j_x\,dz}\right|. \tag{1.47}$$

Note that in the homogeneous half-space of resitivity ρ the *effective penetration depth* h_{eff} is proportional to the *skin-depth* δ:

$$h_{\text{eff}} = \frac{1}{\sqrt{2}}\delta = \sqrt{\frac{\rho}{\omega\mu_o}},$$

where

$$\delta = \sqrt{\frac{2\rho}{\omega\mu_o}}.$$

The h-interval is separated from the S_1-interval by a transition zone embracing the maximum of the ρ_A-curve. The position of the maximum can be defined from the approximate equation $\omega_{\max}\mu_0 S_1 h_2 \approx 1$ whence

$$T_{\max} \approx 2\pi\mu_o S_1 h_2. \tag{1.48}$$

Thus, with $T << T_{\max}$ we obtain information on S_1 and with $T >> T_{\max}$ we obtain information on h. The informativeness of apparent resistivities depends on parameter $\omega\mu_o S_1 h_2$. Note that this parameter reflects the distribution of current induced in the Earth. With some work it is shown that

$$\omega\mu_o S_1 h_2 \approx \left|\frac{J_1}{J_3}\right|, \tag{1.49}$$

where J_1 and J_3 are currents induced in the upper layer and in the conductive basement (Berdichevsky and Dmitriev, 2002).

More detailed consideration of the one-dimensional model can be found in the basic works by Weidelt (1972, 1978) and Weidelt and Kaikkonen (1994) as well as in the books by Kaufman and Keller (1981), Whittall and Oldenburg (1992) and Berdichevsky and Dmitriev (2002).

1.3.2 The Two-Dimensional Impedance Tensor

In the 2D-model the conductivity varies along the vertical axis z and one of the horizontal axes, x or y, perpendicular to the model strike. The magnetotelluric field splits into two independent modes: (1) the *TM-mode* (transverse magnetic mode – the magnetic field is transverse to vertical direction), and (2) the *TE-mode* (transverse electric mode – the electric field is transverse to vertical direction). The TM- and TE-modes are frequently referred to as the *H-polarization* (the magnetic field is polarized along the model strike) and the *E-polarization* (the electric field is polarized along the model strike).

Let the x-axis run along the strike. Then the TM-mode is presented by components E_y, E_z, H_x, where H_x obeys the equation

$$div\left(\frac{1}{\sigma} grad\, H_x\right) + i\omega\mu_o H_x = 0 \tag{1.50}$$

and

$$E_y = \frac{1}{\sigma}\frac{\partial H_x}{\partial z}, \qquad E_z = -\frac{1}{\sigma}\frac{\partial H_x}{\partial y}\ , \tag{1.51}$$

while the TE-mode is presented by components E_x, H_y, H_z, where E_x obeys the equation

$$div\, grad\, E_x + i\omega\mu_o\sigma E_x = \Delta E_x + i\omega\mu_o\sigma E_x = 0 \tag{1.52}$$

and

$$H_y = \frac{1}{i\omega\mu_o}\frac{\partial E_x}{\partial z}, \qquad H_z = -\frac{1}{i\omega\mu_o}\frac{\partial E_x}{\partial y}\ . \tag{1.53}$$

It is common for the magnetotelluric theory to ignore galvanic coupling between the ionosphere and the Earth and accept that the electric conductivity of the air is zero (Berdichevsky and Dmitriev, 2002). If this is the case, we assume that

on the lower side of the Earth's surface $E_z = 0$ and, according to (1.51), get a simple boundary condition, for the TM-mode, $H_x|_{z=0} = const$. The constant is taken as double primary magnetic field $2H^p$ and thus it fits with the normal (one-dimensional) magnetic field observed at a great distance from the inhomogeneous region.

The horizontal directions along and across the strike of the 2D-model are labeled as the *longitudinal direction* (notation "||") and the *transverse direction* (notation "⊥"). It is plain that any transverse vertical plane is a plane of the mirror symmetry. Then, $J_y^{\mathrm{E1}},\ J_x^{\mathrm{E2}},\ J_x^{\mathrm{H1}},\ J_y^{\mathrm{H2}}$ and according to (1.14),

$$[\mathbf{Z}] = \begin{bmatrix} 0 & Z_{xy} \\ Z_{yx} & 0 \end{bmatrix} = \begin{bmatrix} 0 & Z^{\parallel} \\ -Z^{\perp} & 0 \end{bmatrix} = \begin{bmatrix} 0 & \mathrm{Re}\, Z^{\parallel} \\ -\mathrm{Re}\, Z^{\perp} & 0 \end{bmatrix} + i \begin{bmatrix} 0 & \mathrm{Im}\, Z^{\parallel} \\ -\mathrm{Im}\, Z^{\perp} & 0 \end{bmatrix}, \tag{1.54}$$

where $Z^{\parallel} = Z_{xy}$ is the longitudinal impedances (TE-impedance) and $Z^{\perp} = -Z_{yx}$ is the transverse impedance (TM-impedance):

$$Z^{\parallel} = \frac{Z_{\mathrm{N}} + J_x^{\mathrm{E1}}}{1 + J_y^{\mathrm{H1}}}, \qquad Z^{\perp} = \frac{Z_{\mathrm{N}} - J_y^{\mathrm{E2}}}{1 + J_x^{\mathrm{H2}}}.$$

Here, D = 2 and $n = 4$.

Considering longitudinal and transverse impedances, we can calculate the longitudinal and transverse apparent resistivities and phases:

$$\begin{aligned} \rho^{\parallel} &= \frac{\left|Z^{\parallel}\right|^2}{\omega\mu_{\mathrm{o}}} & \rho^{\perp} &= \frac{\left|Z^{\perp}\right|^2}{\omega\mu_{\mathrm{o}}} \\ \varphi^{\parallel} &= \arg Z^{\parallel} & \varphi^{\perp} &= \arg Z^{\perp}. \end{aligned} \tag{1.55}$$

Now rotate axes x, y clockwise through an angle α. With (1.27) we obtain

$$\begin{aligned} Z_{xx}(\alpha) &= \frac{Z^{\parallel} - Z^{\perp}}{2} \sin 2\alpha \\ Z_{xy}(\alpha) &= \frac{Z^{\parallel} + Z^{\perp}}{2} + \frac{Z^{\parallel} - Z^{\perp}}{2} \cos 2\alpha \\ Z_{yx}(\alpha) &= -\frac{Z^{\parallel} + Z^{\perp}}{2} + \frac{Z^{\parallel} - Z^{\perp}}{2} \cos 2\alpha \\ Z_{yy}(\alpha) &= -\frac{Z^{\parallel} - Z^{\perp}}{2} \sin 2\alpha, \end{aligned} \tag{1.56}$$

whence, with account for (1.29*a*),

$$Z_{xx}(\alpha) + Z_{yy}(\alpha) = \mathrm{tr}\,[\mathbf{Z}] = \mathrm{I}_1 = 0, \tag{1.57}$$

and

$$\tan 2\alpha = \frac{Z_{xx}(\alpha) - Z_{yy}(\alpha)}{Z_{xy}(\alpha) + Z_{yx}(\alpha)}\,. \tag{1.58}$$

One can see that the 2D-impedance has zero trace. But it should meet an additional condition

$$\mathrm{Im}\,\frac{Z_{xx}(\alpha) - Z_{yy}(\alpha)}{Z_{xy}(\alpha) + Z_{yx}(\alpha)} = 0$$

to ensure α to be real. On rearrangement with account for (1.57), this condition can be written as

$$\mathrm{Im}\,(Z_{xy}\bar{Z}_{yy} + Z_{xx}\bar{Z}_{yx}) = J_{12} = 0, \tag{1.59}$$

where J_{12} is a rotational invariant defined by (1.34).

Generally the invariants I_1 and J_{12} characterize the geoelectric asymmetry (the skewness) of the medium. If $\mathrm{I}_1 = 0$ and $J_{12} = 0$, then a model has a vertical plane of mirror symmetry of $\sigma(x, y, z)$ that passes through the observation point. Following Swift (1967) and Bahr (1988), we use these asymmetry parameters in normalized form. The *Swift skew* is

$$skew_S = \left|\frac{\mathrm{I}_1}{\mathrm{I}_3}\right| = \left|\frac{Z_{xx} + Z_{yy}}{Z_{xy} - Z_{yx}}\right| \tag{1.60}$$

and the *Bahr skew* is

$$skew_B = \frac{\sqrt{|J_{12}|}}{|\mathrm{I}_3|} = \frac{\sqrt{\left|\mathrm{Im}\,(Z_{xy}\,\bar{Z}_{yy} + Z_{xx}\,\bar{Z}_{yx})\right|}}{\left|Z_{xy} - Z_{yx}\right|}. \tag{1.61}$$

Note that the parameter $skew_B$ differs from the asymmetry parameter η initially introduced by Bahr. We have $skew_B = \eta/\sqrt{2}$.

In the 2D-model, asymmetry parameters $skew_S$ and $skew_B$ are equal to zero:

$$skew_S = 0, \qquad skew_B = 0\,. \tag{1.62}$$

This is the necessary condition for the two-dimensionality. With this condition, we can turn to (1.58) and determine an angle α defining the strike of the two-dimensional structure (modulo $\pi/2$). Rotating the reference frame counterclockwise through the angle α, we obtain the impedance tensor (1.54) with components $Z^{\parallel}$, $Z^{\perp}$ on the secondary diagonal. Such a tensor with zero principal diagonal and nonzero secondary diagonal will be specified as an *antidiagonal tensor*.

1.3.3 The Three-Dimensional Impedance Tensor

In the 3D-model the conductivity varies in all three directions, that is, along the x, y, z-axes. Here $D = 3$ and $n = 8$.

Generally

$$[\mathbf{Z}] = \begin{bmatrix} Z_{xx} & Z_{xy} \\ Z_{yx} & Z_{yy} \end{bmatrix} = \begin{bmatrix} \text{Re } Z_{xx} & \text{Re } Z_{xy} \\ \text{Re } Z_{yx} & \text{Re } Z_{yy} \end{bmatrix} + i \begin{bmatrix} \text{Im } Z_{xx} & \text{Im } Z_{xy} \\ \text{Im } Z_{yx} & \text{Im } Z_{yy} \end{bmatrix}. \quad (1.63)$$

Let $skew_S \neq 0$ and $skew_B \neq 0$. This indicates that the three-dimensional medium has no vertical plane of mirror symmetry.

From the variety of 3D-models we set off the symmetric models with a vertical plane of mirror symmetry. If the observation point is on this symmetry plane, then, in line with (1.62), $skew_S = 0$ and $skew_B = 0$. Here we have the impedance tensor [Z] that can be reduced to the antidiagonal form.

Among three-dimensional symmetric models we identify the axisymmetric models, with a vertical axis of symmetry. Here $skew_S$ and $skew_B$ are everywhere equal to zero, and the tensor [**Z**] can be reduced to the antidiagonal form at any observation point. Considering an axisymmetric model, we establish two characteristic directions: the *radial direction* (notation "*r*") and the *tangential direction* (notation "*t*"). Let the x-axis run in the radial direction. Then we have a tensor [**Z**] with $Z_{xx} = 0$, $Z_{xy} = Z_r$, $Z_{yx} = -Z_t$, $Z_{yy} = 0$ where Z_r and Z_t are the radial and tangential impedances which yield the radial and tangential apparent resistivities and phases:

$$\begin{aligned} \rho_r &= \frac{|Z_r|^2}{\omega\mu_o} & \rho_t &= \frac{|Z_t|^2}{\omega\mu_o} \\ \varphi_r &= \arg Z_r & \varphi_t &= \arg Z_t. \end{aligned} \quad (1.64)$$

We see that (1.62) is also the necessary condition for the axisymmetric three-dimensionality.

In the special case that observation point lies on the axis of symmetry, the impedance tensor assumes the same form as in the 1D-model:

$$[\mathbf{Z}] = Z_c \begin{bmatrix} 0 & 1 \\ -1 & 0 \end{bmatrix} = \text{Re } Z_c \begin{bmatrix} 0 & 1 \\ -1 & 0 \end{bmatrix} + i\,\text{Im } Z_c \begin{bmatrix} 0 & 1 \\ -1 & 0 \end{bmatrix}, \quad (1.65)$$

where scalar Z_c is the *central impedance*.

We have examined some simple effects concerned with symmetry of the 2D and 3D-medium. It is believed that in the 3D-models we may observe more complicated effects, for instance, the *quasi-symmetry effect* indicated by zero $skew_S$ and nonzero $skew_B$:

$$skew_S = 0, \qquad skew_B \neq 0\,. \quad (1.66)$$

1.3.4 The Superimposition Impedance Tensor

Let the host horizontally homogeneous layered medium contain local near-surface two- or three-dimensional inhomogeneities over a regional two- or three-dimensional structure. This model will be referred to as the *superimposition model.* It simulates conditions encountered in many provinces of our planet where small-scale (local) near-surface inhomogeneities are superimposed on large-scale (regional) structures.

Following Wannamaker et al. (1984) and Zhang et al. (1987), we look for relationships between fields $\mathbf{E}_\tau^{\mathrm{S}}$, $\mathbf{H}_\tau^{\mathrm{S}}$ and impedance $[\mathbf{Z}^{\mathrm{S}}]$, observed in the superimposition model, and fields $\mathbf{E}_\tau^{\mathrm{R}}$, $\mathbf{H}_\tau^{\mathrm{R}}$ and impedance $[\mathbf{Z}^{\mathrm{R}}]$, observed in the regional model (Fig. 1.5). The superimposition model contains local inhomogeneities $\mathrm{V_{loc}}$ and a regional structure $\mathrm{V_{reg}}$, while the regional model contains only the regional structure $\mathrm{V_{reg}}$.

Let the superimposition and regional models be excited by the same elliptically polarized plane monochromatic wave with components $H_{x\mathrm{o}}$, $H_{y\mathrm{o}}$ on the Earth's surface. By virtue of (1.12)

$$
\begin{aligned}
E_x^{\mathrm{R}} &= E_x^{\mathrm{N}} + E_x^{\mathrm{A^R}} = H_{x\mathrm{o}} J_x^{\mathrm{E^R}2} + H_{y\mathrm{o}} \left(Z_{\mathrm{N}} + J_x^{\mathrm{E^R}1} \right) && a \\
E_y^{\mathrm{R}} &= E_y^{\mathrm{N}} + E_y^{\mathrm{A^R}} = H_{x\mathrm{o}} \left(-Z_{\mathrm{N}} + J_y^{\mathrm{E^R}2} \right) + H_{y\mathrm{o}} J_y^{\mathrm{E^R}1} && b \\
E_x^{\mathrm{S}} &= E_x^{\mathrm{N}} + E_x^{\mathrm{A^S}} = H_{x\mathrm{o}} J_x^{\mathrm{E^S}2} + H_{y\mathrm{o}} \left(Z_{\mathrm{N}} + J_x^{\mathrm{E^S}1} \right) && c \\
E_y^{\mathrm{S}} &= E_y^{\mathrm{N}} + E_y^{\mathrm{A^S}} = H_{x\mathrm{o}} \left(-Z_{\mathrm{N}} + J_y^{\mathrm{E^S}2} \right) + H_{y\mathrm{o}} J_y^{\mathrm{E^S}1} && d \\
H_x^{\mathrm{S}} - H_x^{\mathrm{R}} &= H_x^{\mathrm{A^S}} - H_x^{\mathrm{A^R}} = H_{x\mathrm{o}} \left(J_x^{\mathrm{H^S}2} - J_x^{\mathrm{H^R}2} \right) + H_{y\mathrm{o}} \left(J_x^{\mathrm{H^S}1} - J_x^{\mathrm{H^R}1} \right) && e \\
H_y^{\mathrm{S}} - H_y^{\mathrm{R}} &= H_y^{\mathrm{A^S}} - H_y^{\mathrm{A^R}} = H_{x\mathrm{o}} \left(J_y^{\mathrm{H^S}2} - J_y^{\mathrm{H^R}2} \right) + H_{y\mathrm{o}} \left(J_y^{\mathrm{H^S}1} - J_y^{\mathrm{H^R}1} \right), && f
\end{aligned}
\tag{1.67}
$$

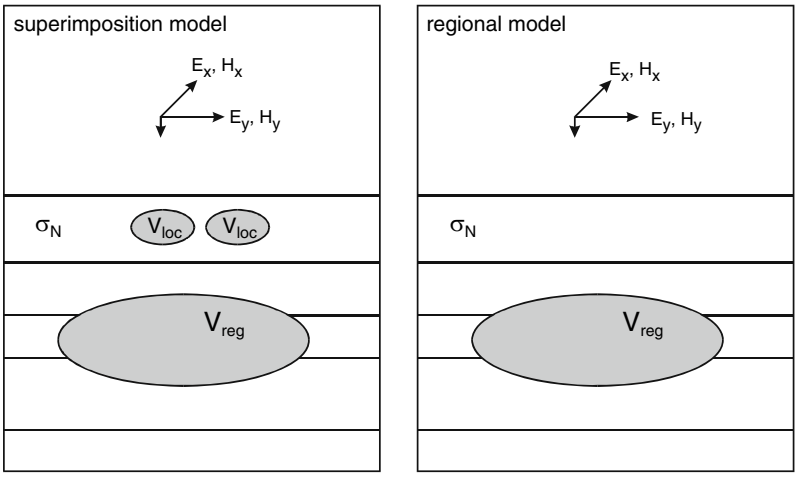

Fig. 1.5 Superimposition model and regional model

where Z_N is the normal impedance of the horizontally layered host medium and $\mathbf{J}^{\mathrm{F\,M}\,\lambda}$ are convolutions

$$\mathbf{J}^{\mathrm{F\,M}\,\lambda}(\mathbf{r}) = \iiint\limits_{\mathrm{V^M}} \left[\mathbf{G}^{\mathrm{F}}(\mathbf{r}|\mathbf{r}_v)\right] \mathbf{j}_\lambda(\mathbf{r}_v) dV$$

with F (field) = E, H , M (model) = S (superimposition), R (regional), λ (polarization) = 1, 2.

Eliminating $H_{x\mathrm{o}}$, $H_{y\mathrm{o}}$ from (1.67*a,b*) and substituting these values into (1.67 *c,d* and *e, f*), we obtain

$$\mathbf{E}_\tau^{\mathrm{S}} = [\mathbf{e}]\,\mathbf{E}_\tau^{\mathrm{R}} \qquad \mathbf{H}_\tau^{\mathrm{S}} = \mathbf{H}_\tau^{R} + [\tilde{\mathbf{h}}]\mathbf{E}_\tau^{\mathrm{R}} = \{[\mathbf{I}] + [\tilde{\mathbf{h}}]\,[\mathbf{Z}^{\mathrm{R}}]\}\mathbf{H}_\tau^{\mathrm{R}} = [\mathbf{h}]\,\mathbf{H}_\tau^{\mathrm{R}}, \tag{1.68}$$

where $[\mathbf{I}]$ is the identity matrix

$$[\mathbf{I}] = \begin{bmatrix} 1 & 0 \\ 0 & 1 \end{bmatrix}$$

and $[\mathbf{e}]$, $[\tilde{\mathbf{h}}]$, $[\mathbf{h}]$ are matrices of electric and magnetic distortions caused by local near-surface inhomogeneities:

$$[\mathbf{e}] = \begin{bmatrix} e_{xx} & e_{xy} \\ e_{yx} & e_{yy} \end{bmatrix}, \qquad [\tilde{\mathbf{h}}] = \begin{bmatrix} \tilde{h}_{xx} & \tilde{h}_{xy} \\ \tilde{h}_{yx} & \tilde{h}_{yy} \end{bmatrix} \tag{1.69}$$

and

$$[\mathbf{h}] = [\mathbf{I}] + [\tilde{\mathbf{h}}][\mathbf{Z}^{\mathrm{R}}] = \begin{bmatrix} 1 + \tilde{h}_{xx} Z_{xx}^{\mathrm{R}} + \tilde{h}_{xy} Z_{yx}^{\mathrm{R}} & \tilde{h}_{xx} Z_{xy}^{\mathrm{R}} + \tilde{h}_{xy} Z_{yy}^{\mathrm{R}} \\ \tilde{h}_{yx} Z_{xx}^{\mathrm{R}} + \tilde{h}_{yy} Z_{yx}^{\mathrm{R}} & 1 + \tilde{h}_{yx} Z_{xy}^{\mathrm{R}} + \tilde{h}_{yy} Z_{yy}^{\mathrm{R}} \end{bmatrix}. \tag{1.70}$$

The components of distortion matrices $[\mathbf{e}]$ and $[\tilde{\mathbf{h}}]$ are

$$\begin{aligned}
e_{xx} &= \frac{Z_{\mathrm{N}}^2 + Z_{\mathrm{N}}\left(J_x^{\mathrm{E^S}1} - J_y^{\mathrm{E^R}2}\right) + J_x^{\mathrm{E^S}2} J_y^{\mathrm{E^R}1} - J_x^{\mathrm{E^S}1} J_y^{\mathrm{E^R}2}}{Z_{\mathrm{N}}^2 + Z_{\mathrm{N}}\left(J_x^{\mathrm{E^R}1} - J_y^{\mathrm{E^R}2}\right) + J_x^{\mathrm{E^R}2} J_y^{\mathrm{E^R}1} - J_x^{\mathrm{E^R}1} J_y^{\mathrm{E^R}2}} \\
e_{xy} &= \frac{Z_{\mathrm{N}}\left(J_x^{\mathrm{E^R}2} - J_x^{\mathrm{E^S}2}\right) + J_x^{\mathrm{E^R}2} J_x^{\mathrm{E^S}1} - J_x^{\mathrm{E^S}2} J_x^{\mathrm{E^R}1}}{Z_{\mathrm{N}}^2 + Z_{\mathrm{N}}\left(J_x^{\mathrm{E^R}1} - J_y^{\mathrm{E^R}2}\right) + J_x^{\mathrm{E^R}2} J_y^{\mathrm{E^R}1} - J_x^{\mathrm{E^R}1} J_y^{\mathrm{E^R}2}} \\
e_{yx} &= \frac{Z_{\mathrm{N}}\left(J_y^{\mathrm{E^S}1} - J_y^{\mathrm{E^R}1}\right) + J_y^{\mathrm{E^R}1} J_y^{\mathrm{E^S}2} - J_y^{\mathrm{E^S}1} J_y^{\mathrm{E^R}2}}{Z_{\mathrm{N}}^2 + Z_{\mathrm{N}}\left(J_x^{\mathrm{E^R}1} - J_y^{\mathrm{E^R}2}\right) + J_x^{\mathrm{E^R}2} J_y^{\mathrm{E^R}1} - J_x^{\mathrm{E^R}1} J_y^{\mathrm{E^R}2}} \\
e_{yy} &= \frac{Z_{\mathrm{N}}^2 + Z_{\mathrm{N}}\left(J_x^{\mathrm{E^R}1} - J_y^{\mathrm{E^S}2}\right) + J_x^{\mathrm{E}R2} J_y^{\mathrm{E^S}1} - J_x^{\mathrm{E^R}1} J_y^{\mathrm{E^S}2}}{Z_{\mathrm{N}}^2 + Z_{\mathrm{N}}\left(J_x^{\mathrm{E^R}1} - J_y^{\mathrm{E^R}2}\right) + J_x^{\mathrm{E^R}2} J_y^{\mathrm{E^R}1} - J_x^{\mathrm{E^R}1} J_y^{\mathrm{E^R}2}}
\end{aligned} \tag{1.71}$$

and

$$
\begin{aligned}
\tilde{h}_{xx} &= \frac{\left(Z_{\mathrm{N}} - J_y^{\mathrm{E^R}2}\right)\left(J_x^{\mathrm{H^S}1} - J_x^{\mathrm{H^R}1}\right) + J_y^{\mathrm{E^R}1}\left(J_x^{\mathrm{H^S}2} - J_x^{\mathrm{H^R}2}\right)}{Z_{\mathrm{N}}^2 + Z_{\mathrm{N}}\left(J_x^{\mathrm{E^R}1} - J_y^{\mathrm{E^R}2}\right) + J_x^{\mathrm{E^R}2}J_y^{\mathrm{E^R}1} - J_x^{\mathrm{E^R}1}J_y^{\mathrm{E^R}2}} \\
\tilde{h}_{xy} &= \frac{\left(Z_{\mathrm{N}} + J_x^{\mathrm{E^R}1}\right)\left(J_x^{\mathrm{H^R}2} - J_x^{\mathrm{H^S}2}\right) + J_x^{\mathrm{E^R}2}\left(J_x^{\mathrm{H^S}1} - J_x^{\mathrm{H^R}1}\right)}{Z_{\mathrm{N}}^2 + Z_{\mathrm{N}}\left(J_x^{\mathrm{E^R}1} - J_y^{\mathrm{E^R}2}\right) + J_x^{\mathrm{E^R}2}J_y^{\mathrm{E^R}1} - J_x^{\mathrm{E^R}1}J_y^{\mathrm{E^R}2}} \\
\tilde{h}_{yx} &= \frac{\left(Z_{\mathrm{N}} - J_y^{\mathrm{E^R}2}\right)\left(J_y^{\mathrm{H^S}1} - J_y^{\mathrm{H^R}1}\right) + J_y^{\mathrm{E^R}1}\left(J_y^{\mathrm{H^S}2} - J_y^{\mathrm{H^R}2}\right)}{Z_{\mathrm{N}}^2 + Z_{\mathrm{N}}\left(J_x^{\mathrm{E^R}1} - J_y^{\mathrm{E^R}2}\right) + J_x^{\mathrm{E^R}2}J_y^{\mathrm{E^R}1} - J_x^{\mathrm{E^R}1}J_y^{\mathrm{E^R}2}} \\
\tilde{h}_{yy} &= \frac{\left(Z_{\mathrm{N}} + J_x^{\mathrm{E^R}1}\right)\left(J_y^{\mathrm{H^R}2} - J_y^{\mathrm{H^S}2}\right) + J_x^{\mathrm{E^R}2}\left(J_y^{\mathrm{H^S}1} - J_y^{\mathrm{H^R}1}\right)}{Z_{\mathrm{N}}^2 + Z_{\mathrm{N}}\left(J_x^{\mathrm{E^R}1} - J_y^{\mathrm{E^R}2}\right) + J_x^{\mathrm{E^R}2}J_y^{\mathrm{E^R}1} - J_x^{\mathrm{E^R}1}J_y^{\mathrm{E^R}2}}\,.
\end{aligned}
\tag{1.72}
$$

Now we can derive relation between the superimposition impedance, $[\mathbf{Z}^{\mathrm{S}}]$, and the regional impedance, $[\mathbf{Z}^{\mathrm{R}}]$. Following Zhang et al. (1987), we write:

$$
\mathbf{E}_\tau^{\mathrm{S}} = [\mathbf{e}]\,\mathbf{E}_\tau^{\mathrm{R}} = [\mathbf{e}]\,[\mathbf{Z}^{\mathrm{R}}]\,\mathbf{H}_\tau^{\mathrm{R}} = [\mathbf{e}]\,[\mathbf{Z}^{\mathrm{R}}]\,[\mathbf{h}]^{-1}\mathbf{H}_\tau^{\mathrm{S}} = [\mathbf{Z}^{\mathrm{S}}]\,\mathbf{H}_\tau^{\mathrm{S}}\,, \tag{1.73}
$$

where

$$
[\mathbf{Z}^{\mathrm{S}}] = [\mathbf{e}]\,[\mathbf{Z}^{\mathrm{R}}]\,[\mathbf{h}]^{-1}. \tag{1.74}
$$

Thus we expand the superimposition impedance, $[\mathbf{Z}^{\mathrm{S}}]$, in components of the regional impedance, $[\mathbf{Z}^{\mathrm{R}}]$. This decomposition reduces to the left and right-multiplication of the regional impedance $[\mathbf{Z}^{\mathrm{R}}]$ by the matrices $[\mathbf{e}]$ and $[\mathbf{h}]^{-1}$ reflecting electrical and magnetic anomalies caused by local inhomogeneities. It will be referred to as the *local-regional decomposition*, LR-decomposition.

Chave and Smith (1994) considered the local-regional decomposition in terms of the localized Born approximation (Habashy et al., 1993). They believe that the local-regional decomposition is valid if the regional field is uniform across the distorting local inhomogeneity. However, in our consideration the regional field does not need any restriction. Thus, the local-regional decomposition can be applied to rather wide class of superimposition models.

An important point is that at low frequencies the local-regional decomposition can be significantly simplified (Bahr, 1985). If the skin-depth is much larger than dimensions of near-surface inhomogeneities, we can neglect the local induction and take into account only quasi-static effects caused by excess charges. With this simplification, the electric and magnetic distortion matrices, $[\mathbf{e}]$ and $[\tilde{\mathbf{h}}]$, are treated as real-valued and frequency-independent. Furthermore, we can assume that $[\mathbf{Z}^R] \to 0$ and $[\mathbf{h}] \to [\mathbf{I}]$ as $\omega \to 0$. Hence, the magnetic anomalies caused by small-scale near-surface inhomogeneities decay and the low-frequency local-regional decomposition may be written in the truncated form

$$[\mathbf{Z}^S] = [\mathbf{e}]\,[\mathbf{Z}^R]. \tag{1.75}$$

It would be instructive to evaluate, at least roughly, the frequencies that allow for truncating the LR-decomposition. Let us consider a three-layered K-type model describing a one-dimensional normal background with $\rho_2 >> \rho_1$, $h_2 >> h_1$ $\rho_3 = 0$. According to (1.45) and (1.46),

$$Z = \frac{E_x}{H_y} \approx \begin{cases} \dfrac{1}{S_1} & \text{in the } S_1 - \text{interval} \\ -i\omega\mu_o h & \text{in the } h - \text{interval}, \end{cases} \tag{1.76}$$

whence

$$\frac{E_x S_1}{H_y} = \frac{J_1}{H_y} = \widehat{J}_1 \approx \begin{cases} 1 & \text{in the } S_1 - \text{interval} \\ -i\omega\mu_o S_1 h_2 & \text{in the } h - \text{interval}, \end{cases} \tag{1.77}$$

where $J_1 = E_x S_1$ is the current induced in the upper layer and $\widehat{J}_1$ is its normalized value. From (1.77), taking into account (1.48), we get

$$\left| \frac{\widehat{J}_1(h - \text{interval})}{\widehat{J}_1(S_1 - \text{interval})} \right| \approx \frac{T_{\max}}{T}, \tag{1.78}$$

where $T_{\max}$ is a period of the maximum of the apparent resistivity curve. To estimate the magnetic anomalies caused by a near-surface inhomogeneity, we assume that their intensity varies proportionally with the normalized current $\widehat{J}_1$ induced in the first layer. Within the S_1-interval, anomalies in horizontal components of the magnetic field do not usually exceed $25 \div 50\%$. Thus, according to (1.78), at $T > 10T_{\max}$ we observe negligibly small magnetic anomalies ($2.5 \div 5\%$) allowing for the truncated decomposition.

For more precise estimates we have to examine the superimposition models numerically. To this end, an approximate hybrid method suggested by Berdichevsky and Dmitriev (1976) can be used.

Let us examine a (3D + 2D)-superimposition model shown in Fig. 1.6. It consists of three layers: conductive sediments (ρ_1), resistive lithosphere (ρ_2) and highly conductive mantle (ρ_3). The model contains a local three-dimensional inhomogeneous inclusion L of width w in the sediments and a regional two-dimensional homogeneous prism R of width w_R in the lithosphere, the strike of the prism being along the $x-$axis. Here $w_L << w_R$ so that the regional field can be assumed uniform in the area of the local inclusion.

The problem is solved in three stages.

At the first stage, we solve the two-dimensional problem for the prism R in the absence of the inclusion L and over the middle of the prism determine the regional impedance with longitudinal and transverse antidiagonal components:

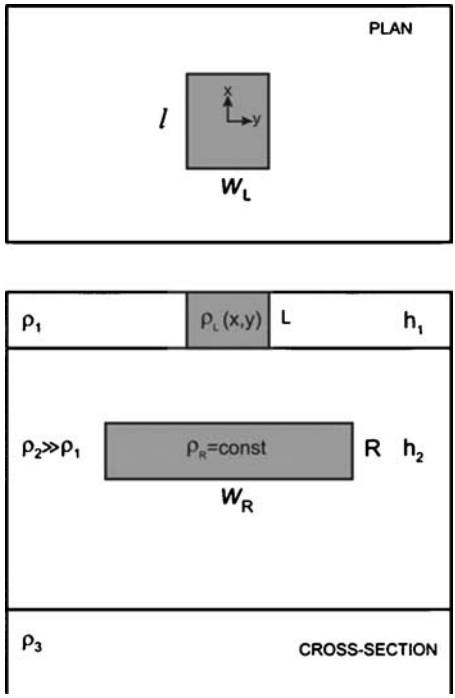

Fig. 1.6 Illustrating the construction of a (3D + 2D)-superimposition model by Berdichevsky–Dmitriev's hybrid method

$$[\mathbf{Z}^{\mathrm{R}}] = \begin{bmatrix} 0 & Z^{\parallel} \\ -Z^{\perp} & 0 \end{bmatrix}. \tag{1.79}$$

At the second stage, we determine the electric and magnetic distortion tensors [**e**] and [**h**], solving the three-dimensional problem for the inclusion L and the prism R with $w_R \to \infty$. Using the low-frequency thin-sheet approximation, we find

$$[\mathbf{e}] = \begin{bmatrix} e_{xx} & e_{xy} \\ e_{yx} & e_{yy} \end{bmatrix}. \tag{1.80}$$

To find the magnetic distortion tensor, we evaluate the excess current in the sediments:

$$\begin{aligned} &\mathbf{J} = S\,\mathbf{E}_{\tau}^{\mathrm{S}} - S_1\mathbf{E}_{\tau}^{\mathrm{R}} \\ &S = \begin{cases} S_1 = h_1/\rho_1 & \text{outside L} \\ S_{\mathrm{L}} = h_1/\rho_{\mathrm{L}} & \text{inside L} \end{cases} \end{aligned} \tag{1.81}$$

and calculate the anomalous magnetic field from conditions of its discontinuity at the current layer:

$$\begin{aligned}\mathbf{H}_\tau^{\mathrm{A}} &= \frac{1}{2}[\mathbf{R}(-\pi/2)]\,\mathbf{J} = \frac{1}{2}[\mathbf{R}(-\pi/2)]\,\left(S\,\mathbf{E}_\tau^{\mathrm{S}} - S_1\mathbf{E}_\tau^{\mathrm{R}}\right)\\ &= \frac{1}{2}[\mathbf{R}(-\pi/2)]\,(S\,[\mathbf{e}] - S_1[\mathbf{I}])\mathbf{E}_\tau^{R} = [\tilde{\mathbf{h}}]\,\mathbf{E}_\tau^{\mathrm{R}},\end{aligned} \tag{1.82}$$

where

$$[\tilde{\mathbf{h}}] = \frac{1}{2}[\mathbf{R}(-\pi/2)]\,(S\,[\mathbf{e}] - S_1[\mathbf{I}])$$

and $[\mathbf{R}]$, $[\mathbf{I}]$ are rotationl and identity matrices:

$$[\mathbf{R}(-\pi/2)] = \begin{bmatrix} 0 & -1 \\ 1 & 0 \end{bmatrix}, \qquad [\mathbf{I}] = \begin{bmatrix} 1 & 0 \\ 0 & 0 \end{bmatrix}.$$

Finally, with account for (1.68) and (1.70), we write

$$\mathbf{H}_\tau^{S} = [\mathbf{h}]\,\mathbf{H}_\tau^{R}, \tag{1.83}$$

where

$$[\mathbf{h}] = [\mathbf{I}] + [\tilde{\mathbf{h}}]\,[\mathbf{Z}^R]. \tag{1.84}$$

The components of magnetic distortion tensor $[\mathbf{h}]$ are

$$\begin{aligned} h_{xx} &= 1 + \frac{1}{2}(S e_{yy} - S_1)Z^{\perp} \qquad h_{xy} = -\frac{1}{2}S e_{yx} Z^{\parallel}\\ h_{yx} &= -\frac{1}{2}S e_{xy} Z^{\perp} \qquad\qquad h_{yy} = 1 + \frac{1}{2}(S e_{xx} - S_1)\,Z^{\parallel}\,. \end{aligned} \tag{1.85}$$

At the final stage, we go to (1.74) with (1.79), (1.80), (1.84) and synthesize the LR-decomposition:

$$[\mathbf{Z}^S] = [\mathbf{e}]\,[\mathbf{Z}^R]\,[\mathbf{h}]^{-1}.$$

The truncated decomposition, $[\mathbf{Z}^S] = [\mathbf{e}]\,[\mathbf{Z}^R]$, is admissible if

$$\begin{aligned} &\frac{1}{2}\left|(S e_{yy} - S_1)\right|\left|Z^{\perp}\right| << 1 \qquad &&\frac{1}{2}S\left|e_{yx} Z^{\parallel}\right| << 1\\ &\frac{1}{2}\left|(S e_{xx} - S_1)\right|\left|Z^{\parallel}\right| << 1 \qquad &&\frac{1}{2}S\left|e_{xy} Z^{\perp}\right| << 1. \end{aligned} \tag{1.86}$$

The arithmetic suggests that near-surface magnetic anomalies can be neglected in the period range $T > 100\,\mathrm{s}$ providing $S \le 300\mathrm{S}$ and $\rho_2 \ge 1000$ Ohm·m, $h_2 \le 100$ km, $\rho_3 \le 100$ Ohm·m.

1.4 Impedance Polar Diagrams

The dependence of the impedances upon orientation of the measurement axes may be displayed graphically by polar diagrams. No structural or frequency limitations are required in constructing the impedance polar diagrams.

1.4.1 Polar Diagrams of the Impedance Tensor

This techniques has been suggested in (Berdichevsky, 1968; Berdichevsky et al., 1993).

Let the tensor [**Z**] be obtained on the measurement axes x, y. We will introduce new axes x', y' rotated through a clockwise angle α. In view of (1.27), (128)

$$
\begin{aligned}
|Z_{xx}(\alpha)| &= \left|Z_{yy}(\alpha+\pi/2)\right| = \ |\, Z_2 + Z_3 \sin 2\alpha + Z_4 \cos\ 2\alpha\,|\,,\\
\left|Z_{xy}\,(\alpha)\right| &= \left|Z_{yx}\,(\alpha+\pi/2)\right| = |\, Z_1 + Z_3 \cos 2\alpha - Z_4 \sin 2\,\alpha\,|\,,\\
\left|\arg Z_{xy}(\alpha)\right| &= \left|\arg Z_{yx}(\alpha+\pi/2)\right| = \left|\arctan \frac{\mathrm{Im}\,(Z_1 + Z_3\cos 2a - Z_4 \sin 2a)}{\mathrm{Re}\,(Z_1 + Z_3\cos 2a - Z_4 \sin 2a)}\right|.
\end{aligned}
\tag{1.87}
$$

Plot these values on the x'-axis. As α changes from 0 to 2π, the resultant points describe closed curves known under the name of *impedance polar diagrams*. The diagrams of $\left|Z_{xx}\right|$, $\left|Z_{xy}\right|$ are amplitude polar diagrams. The diagram of $\left|\arg Z_{xy}\right|$ is a phase polar diagram. One can see from (1.28) that the amplitude and phase polar diagrams are antisymmetric about any straight line passing through the origin.

The conditions for extrema of polar diagram radii are

$$
\frac{d\,|Z_{xx}(\alpha)|}{d\alpha} = 0, \quad \frac{d\left|Z_{xy}(\alpha)\right|}{d\alpha} = 0, \quad \frac{d\left|\arg Z_{xy}(\alpha)\right|}{d\alpha} = 0.
$$

This yields equations of degree 4 in $\tan\alpha$. Therefore, the interval $0 \le \alpha \le 2\pi$ can contain four maxima and four minima of $|\,Z_{xx}\,|$, $|\,Z_{xy}\,|$, $\left|\arg Z_{xy}\right|$. Clearly, the impedance polar diagrams may have, at most, four petals.

Examples of impedance polar diagrams for 1D, 2D and 3D-models are shown in Fig. 1.7. Configuration of the impedance polar diagrams is a good indicator of the dimensionality of geoelectric structures.

In the 1-D model the diagram of $|Z_{xx}|$ degenerates into a point, while the diagrams of $|\,Z_{xy}\,|$ and $\left|\arg Z_{xy}\right|$ are circles of radii $|Z|$ and $|\arg Z|$, where Z is Tikhonov–Cagniard's impedance.

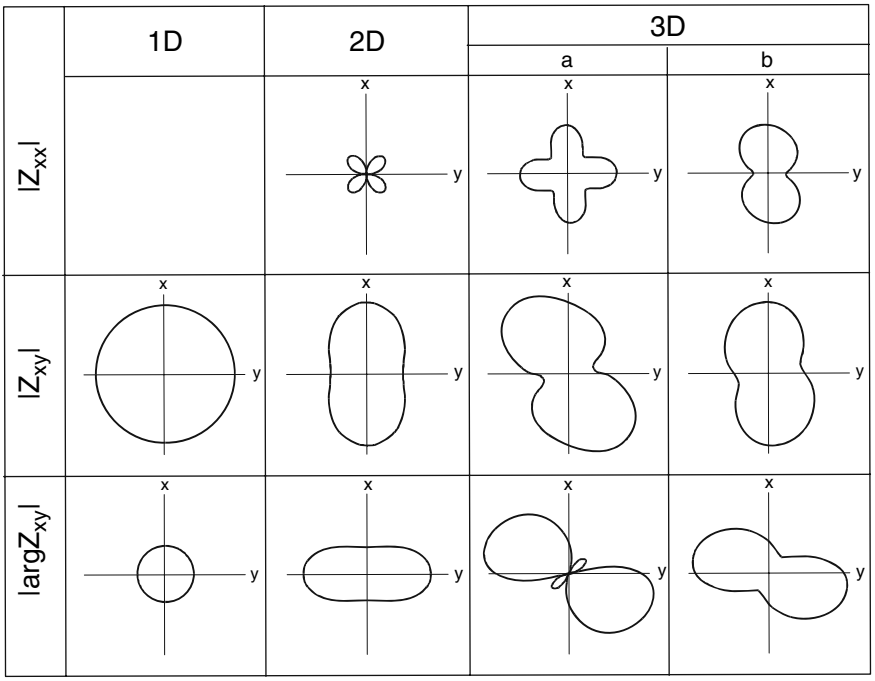

Fig. 1.7 Polar diagrams of the impedance tensor

1D: $Z = 4 - 2i$

2D: $[\mathbf{Z}] = \begin{bmatrix} 0 & 4-2i \\ -1+2i & 0 \end{bmatrix}, \quad skew_S = 0, \quad skew_B = 0$

3D: **a)** $[\mathbf{Z}] = \begin{bmatrix} -0.5-3i & 4-2i \\ -1+2i & 0.5-3i \end{bmatrix}, \quad skew_S = 0, \quad skew_B = 0.47$

b) $[\mathbf{Z}] = \begin{bmatrix} -0.5-3i & 4-2i \\ -1+2i & 0.1-i \end{bmatrix}, \quad skew_S = 0.63, \quad skew_B = 0.44$

Consider the 2D-model ($skew_S = 0$, $skew_B = 0$) striking along the x-axis. According to (1.49) and (1.87),

$$
\begin{aligned}
|\, Z_{xx}\,(\alpha)| &= \left|\left(Z^{\parallel} - Z^{\perp}\right) \sin\alpha \cos\alpha \,\right|, \\
|\, Z_{xy}\,(\alpha)| &= \left|\, Z^{\parallel} \cos^{\,2}\alpha + Z^{\perp} \sin^2\alpha \right|, \\
\left|\arg Z_{\mathrm{xy}}(\alpha)\right| &= \left| \arctan \frac{\mathrm{Im}\,(Z^{\parallel}\cos^2\alpha + Z^{\perp}\sin^2\alpha)}{\mathrm{Re}\,(Z^{\parallel}\cos^2\alpha + Z^{\perp}\sin^2\alpha)} \right|,
\end{aligned}
\tag{1.88}
$$

where $Z^{\parallel}$ and $Z^{\perp}$ are the longitudinal and transverse impedances. The diagram of $|Z_{xx}|$ looks like a flower with four identical petals. The lines bisecting the angles

between these petals are oriented in the longitudinal and transverse directions. The diagrams of $\left|Z_{xy}\right|$ and $\left|\arg Z_{xy}\right|$ have the form of a regular oval. Their principal diameters $2\left|Z^{\parallel}\right|$, $2\left|Z^{\perp}\right|$ and $2\left|\arg Z^{\parallel}\right|$, $2\left|\arg Z^{\perp}\right|$ are oriented in the longitudinal and transverse directions.

Similar form of the impedance polar diagrams would be found in the axially symmetric 3D-models ($skew_S = 0$, $skew_B = 0$). Here bisectrices of diagram of $|Z_{xx}|$ and principal diameters $2\,|Z_r|$, $2\,|Z_t|$ and $2\,|\arg Z_r|$, $2\,|\arg Z_t|$of diagrams of $\left|Z_{xy}\right|$ and $\left|\arg Z_{xy}\right|$ are oriented in the radial and tangential directions.

If the 3D-model is asymmetric, the regular form of polar diagrams is violated, and they can take rather whimsical form. But in the special case of quasi-symmetry (3D,a), when $skew_S = 0$ and $skew_B \neq 0$, the $|Z_{xx}|$-diagram is cross-shaped, while diagrams of $\left|Z_{xy}\right|$ and $\left|\arg Z_{xy}\right|$ are shaped into oblique figures eight with or without small petals. In the general event (3D,b) that $skew_S \neq 0$ and $skew_B \neq 0$, all diagrams look like oblique figure eight with more or less narrow waist.

1.4.2 Polar Diagrams of H- and E-Polarized Impedances

This technique has been advanced in (Berdichevsky and Logunovich, 2005). It is based on the decomposition of the electromagnetic field in conjugate and associate directions suggested by Counil et al. (1986).

The Counil-Le Mouel-Menvielle decomposition is associated with so called "*induction intensity*" and "*current intensity*". But this terminology is vulnerable to criticism. The electric current and electromagnetic induction are interconnected via the Ampere, Faraday, and Ohm laws. An electric current generates a magnetic field that in turn induces an electric field producing an electric current. The intensity of electromagnetic induction depends on the intensity of the inducing current, and the intensity of the induced current depends on the intensity of electromagnetic induction. The separation of these phenomena is scarcely constructive and only complicates their mathematical description. The formulation of the problem is significantly simplified if the construction of polar diagrams involves the formal terminology, reflecting the mathematical meaning of the values to be determined.

Following Yee and Paulson (1987), we introduce a scalar indicator defined as the ratio between the Euclidean norms $\|\mathbf{E}_\tau\|$ and $\|\mathbf{H}_\tau\|$ of electric and magnetic fields $\mathbf{E}_\tau(E_x, E_y)$ and $\mathbf{H}_\tau(H_x, H_y)$,the magnetic field being linearly polarized at an angle α_H to the original x axis:

$$Z_H(\alpha_H) = \frac{\|\mathbf{E}_\tau\|}{\|\mathbf{H}_\tau\|} = \sqrt{\frac{\mathbf{E}_\tau \cdot \overline{\mathbf{E}_\tau}}{\mathbf{H}_\tau \cdot \overline{\mathbf{H}_\tau}}} = \sqrt{\frac{E_x \bar{E}_x + E_y \bar{E}_y}{H_x \bar{H}_x + H_y \bar{H}_y}} = \sqrt{\frac{|E_x|^2 + \left|E_y\right|^2}{|H_x|^2 + \left|H_y\right|^2}}$$

$$= \sqrt{\frac{\left|Z_{xx} H_x + Z_{xy} H_y\right|^2 + \left|Z_{yx} H_x + Z_{yy} H_y\right|^2}{|H_x|^2 + \left|H_y\right|^2}}$$

$$
\begin{aligned}
&= \sqrt{\frac{\left|Z_{xx} + Z_{xy}\tan\alpha_H\right|^2 + \left|Z_{yx} + Z_{yy}\tan\alpha_H\right|^2}{1+\tan^2\alpha_H}} \\
&= \sqrt{\frac{k_1\tan^2\alpha_H + k_2\tan\alpha_H + k_3}{1+\tan^2\alpha_H}} \\
&= \sqrt{k_1\sin^2\alpha_H + k_2\sin\alpha_H\cos\alpha_H + k_3\cos^2\alpha_H},
\end{aligned}
\tag{1.89}
$$

where

$$
k_1 = \left|Z_{xy}\right|^2 + \left|Z_{yy}\right|^2, \qquad k_2 = 2\mathrm{Re}\left(Z_{xx}\bar{Z}_{xy} + Z_{yx}\bar{Z}_{yy}\right), \qquad k_3 = |Z_{xx}|^2 + \left|Z_{yx}\right|^2.
$$

The scalar indicator Z_H can be naturally called a H-polarized impedance. It is a function of the angle α_H defining the direction of the magnetic field polarization axis.

Determine α_H, at which the H-polarized impedance has a maximum and minimum. The condition

$$
\frac{d\,Z_H}{d\alpha_H} = 0
$$

gives the equation

$$
\tan 2\alpha_H = \frac{k_2}{k_3 - k_1}, \tag{1.90}
$$

which has two solutions, $\alpha_H^{\max}$ and $\alpha_H^{\min}$, differing by $\pi/2$.

Similar to the H-polarized impedance Z_H, we introduce a scalar indicator Z_E defined as the ratio between the Euclidean norms $\|\mathbf{E}_\tau\|$ and $\|\mathbf{H}_\tau\|$ of electric and magnetic fields $\mathbf{E}_\tau(E_x, E_y)$ and $\mathbf{H}_\tau(H_x, H_y)$,the electric field being linearly polarized at an angle α_E to the original x axis:

$$
\begin{aligned}
Z_E(\alpha_E) &= \frac{\|\mathbf{E}_\tau\|}{\|\mathbf{H}_\tau\|} = \sqrt{\frac{\mathbf{E}_\tau\cdot\mathbf{E}_\tau}{\mathbf{H}_\tau\cdot\mathbf{H}_\tau}} = \sqrt{\frac{E_x\bar{E}_x + E_y\bar{E}_y}{H_x\bar{H}_x + H_y\bar{H}_y}} = \sqrt{\frac{|E_x|^2 + \left|E_y\right|^2}{|H_x|^2 + \left|H_y\right|^2}} \\
&= \sqrt{\frac{|E_x|^2 + \left|E_y\right|^2}{\left|Y_{xx}E_x + Y_{xy}E_y\right|^2 + \left|Y_{yx}E_x + Y_{yy}E_y\right|^2}} \\
&= \sqrt{\frac{1+\tan^2\alpha_E}{\left|Y_{xx} + Y_{xy}\tan\alpha_E\right|^2 + \left|Y_{yx} + Y_{yy}\tan\alpha_E\right|^2}},
\end{aligned}
\tag{1.91}
$$

where $Y_{xx}, Y_{xy}, Y_{yx}, Y_{yy}$ are the components of the admittance tensor determined by (1.19). Substituting (1.19) into (1.91), we get

$$Z_E(\alpha_E) = \sqrt{\frac{1+\tan^2\alpha_E}{l_1\tan^2\alpha_E - l_2\tan\alpha_E + l_3}} = \sqrt{\frac{1}{l_1\sin^2\alpha_E - l_2\sin\alpha_E\cos\alpha_E + l_3\cos^2\alpha_E}}, \tag{1.92}$$

where

$$l_1 = \frac{|Z_{xx}|^2 + |Z_{xy}|^2}{|Z_{xx}Z_{yy} - Z_{xy}Z_{yx}|^2}, \quad l_2 = \frac{2\mathrm{Re}(Z_{xx}\bar{Z}_{yx} + Z_{yy}\bar{Z}_{xy})}{|Z_{xx}Z_{yy} - Z_{xy}Z_{yx}|^2} \quad l_3 = \frac{|Z_{yy}|^2 + |Z_{yx}|^2}{|Z_{xx}Z_{yy} - Z_{xy}Z_{yx}|^2}.$$

The scalar indicator Z_E can be called a *E-polarized impedance.* Determine α_E, at which the *E*-polarized impedance has a maximum and minimum. The condition

$$\frac{d\,Z_E}{d\alpha_E} = 0$$

gives the equation

$$\tan 2\alpha_E = \frac{l_2}{l_1 - l_3}, \tag{1.93}$$

which has two solutions, $\alpha_E^{\max}$and $\alpha_E^{\min}$, differing by $\pi/2$.

Let us plot a value $Z_H(\alpha_H)$ on the polarization axis of the magnetic field. As the angle α_H varies from 0 to 2π, the resultant point describes a closed curve that is the *polar diagram of H-polarized impedance*. The polar diagram of $Z_H(\alpha_H)$ is a regular oval determined by (1.89). Its inversion $Y_H(\alpha_H) = 1/Z_H(\alpha_H)$ gives an ellipse defined by equation

$$k_1 Y_H^2 \sin^2\alpha_H + k_2 Y_H^2 \sin\alpha_H\cos\alpha_H + k_3 Y_H^2\cos^2\alpha_H = 1. \tag{1.94}$$

Now plot a value $Z_E(\alpha_E)$ on the polarization axis of the electric field. As the angle α_E varies from 0 to 2π, the resultant point describes a closed curve that is the *polar diagram of the E-polarized impedance*. The polar diagram of $Z_E(\alpha_E)$ is an ellipse determined by the equation

$$l_1 Z_E^2 \sin^2\alpha_E - l_2 Z_E^2 \sin\alpha_E\cos\alpha_E + l_3 Z_E^2\cos^2\alpha_E = 1. \tag{1.95}$$

Following (Counil et al., 1986), we introduce an *angular skew parameter* in accordance with (1.90) and (1.93):

$$skew_{CLM} = \alpha_E^{\max} - \alpha_H^{\min} = \alpha_H^{\max} - \alpha_E^{\min} = \arctan \operatorname{Re} \frac{Z_{xx} + Z_{yy}}{Z_{yx} - Z_{xy}}. \qquad (1.96)$$

This parameter characterizes the mutual orientation of polar diagrams of the *H*- and *E*-polarized impedances. Here, the angles $\alpha_E^{\max}$, $\alpha_E^{\min}$ and $\alpha_H^{\max}$, $\alpha_H^{\min}$ define the directions of the maximum and minimum diameters of the polar diagrams. Note that $skew_{CLM} = 0$ if $skew_S = 0$. So, in symmetric and quasi-symmetric models the diagrams of the *H*- and *E*-polarized impedances are elongated in perpendicular directions.

Examples of polar diagrams of the *H*- and *E*-polarized impedances typical of 1D, 2D, and 3D-models are presented in Fig. 1.8.

The Z_H and Z_E diagrams in a 1D-model are circles of the radius $|Z|$, where Z is the Tikhonov–Cagniard 1D-impedance.

Consider a 2D-model with the strike along the *x*-axis. According to (1.54), we have

$$Z_{xy} = 0,\ Z_{xy} = Z^{\parallel},\ Z_{yx} = -Z^{\perp},\ Z_{yy} = 0,$$

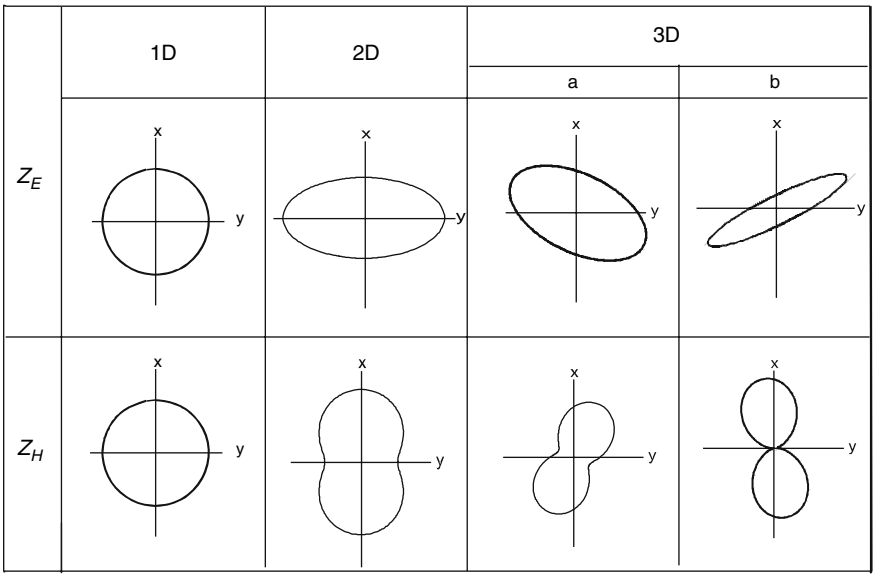

Fig. 1.8 Polar diagrams of the ***E***-polarized (Z_E) and ***H***-polarazed (Z_H) impedances

1D: $Z = 4 - 2i$

2D: $[\mathbf{Z}] = \begin{bmatrix} 0 & 4-2i \\ -1+2i & 0 \end{bmatrix}$, $skew_S = 0,\ skew_{CLM} = 0$, $skew_B = 0$

3D: **a)** $[\mathbf{Z}] = \begin{bmatrix} -0.5-3i & 4-2i \\ -1+2i & 0.5+3i \end{bmatrix}$, $skew_S = 0,\ skew_{CLM} = 0$, $skew_B = 0.47$

b) $[\mathbf{Z}] = \begin{bmatrix} -0.2+0.2i & -1+3i \\ 0.7-0.5i & 0.5-1.4i \end{bmatrix}$, $skew_S = 0.63,\ skew_{CLM} = 20^{\circ}$, $skew_B = 0.44$

here $Z^{\parallel}$ and $Z^{\perp}$ are the longitudinal and transverse impedances. Substituting (1.54) into (1.89) and (1.92), we find

$$Z_H(\alpha_H) = \sqrt{\left|Z^{\parallel}\right|^2 \sin^2 \alpha_H + \left|Z^{\perp}\right|^2 \cos^2 \alpha_H}$$

$$Z_E(\alpha_E) = \sqrt{\frac{1}{\dfrac{\sin^2 \alpha_E}{\left|Z^{\perp}\right|^2} + \dfrac{\cos^2 \alpha_E}{\left|Z^{\parallel}\right|^2}}}. \tag{1.97}$$

Polar diagrams of the H- and E-polarized impedances are a regular oval with a waist and an ellipse, respectively. Their principal diameters $2\left|Z^{\parallel}\right|$ and $2\left|Z^{\perp}\right|$ are oriented along and across the strike of the model. The Z_H and Z_E diagrams in an axisymmetric 3D-model have similar shape, with their principal diameters $2|Z_r|$ and $2|Z_t|$ being oriented along the radial and tangential directions.

In a quasi-symmetric 3D-model with $skew_S = skew_{CLM} = 0$, the diagrams of Z_H and Z_E retain a regular shape and are elongated in perpendicular directions (3D,a). In an asymmetric 3D-model with $skew_{CLM} \neq 0$, a regular shape of the Z_H and Z_E diagrams is preserved but the angle between their elongation directions can deviate significantly from the right angle (3D,b). This is the only feature of the Z_H and Z_E diagrams that can be used as an indicator distinguishing an asymmetric 3D medium from a 2D or an axisymmetric 3D medium.

1.5 Dispersion Relations in the Impedance Tensor

The dispersion relations were first derived by Kramers and Kronig in the theory of dispersion of optic rays (Mathews and Walker, 1964). These integral relations are the direct consequence of the principle of causality.

The Kramers–Kronig dispersion relations were introduced in geoelectrics by Kaufman (1960) and Vanyan et al. (1961). These authors used the dispersion relations to convert the apparent resistivity curves of frequency sounding into the phase curves.

In 1972, Weidelt published his famous paper that laid the groundwork for the mathematical theory of magnetotelluric sounding (Weidelt, 1972). In this paper he gave rigorous analytical proof for the existence of the dispersion relations in the Tikhonov–Cagniard one-dimensional model.

Following Weidelt, we will consider the dispersion relations of two kinds.

1. The dispersion relations of the first kind. These relations connect the real and imaginary parts of the normalized impedance. They assume the form

$$\begin{aligned} R(\omega_o) &= \frac{2}{\pi} \mathrm{pv} \int_0^{\infty} \frac{X(\omega)}{\omega^2 - \omega_o^2} \omega d\omega, \\ X(\omega_o) &= -\frac{2\omega_o}{\pi} \mathrm{pv} \int_0^{\infty} \frac{R(\omega)}{\omega^2 - \omega_o^2} d\omega\,, \end{aligned} \tag{1.98}$$

where pv means that integral is taken in the sense of the Cauchy principal value, and

$$R = \mathrm{Re}\frac{Z}{i\omega\mu_o}, \qquad X = \mathrm{Im}\frac{Z}{i\omega\mu_o}.$$

These relations exist if the impedance Z has no poles in the upper half-plane of the complex frequency $\Omega = \omega + i\lambda$.

2. The dispersion relations of the second kind. They relate the apparent resistivities and impedance phases. These relations are in the form:

$$\begin{aligned} \varphi(\omega_o) &= -\frac{\pi}{4} - \frac{\omega_o}{\pi}\mathrm{pv}\int_0^\infty \ln\,\rho_A(\omega)\frac{d\omega}{\omega^2-\omega_o^2}, \\ \ln\frac{\rho_A(\omega_o)}{\rho_A(\infty)} &= \frac{4}{\pi}\mathrm{pv}\int_0^\infty\left[\frac{\pi}{4}+\varphi(\omega)\right]\frac{\omega d\omega}{\omega^2-\omega_o^2}\ , \end{aligned} \tag{1.99}$$

where $\rho_A(\infty)$ is the high-frequency asymptotic value of the apparent resistivity. These relations exist if the impedance Z satisfies the condition of the minimum phase, that is, if it has neither poles nor zeros in the upper half-plane of the complex frequency $\Omega = \omega + i\lambda$.

The existence of the dispersion relations in the two- and three-dimensional models is among the most controversial subjects of magnetotellurics.

Weidelt and Kaikkonen (1994) gave rigorous proof to the validity of the dispersion relations of both kinds in the *H*-polarized 2D-models. We examined numerically a lot of the *E*-polarized 2D-models with different characteristic structures (dyke, ledge, horst, graben, canyon) and revealed that all these models met the dispersion relations of both kinds.

Yee and Paulson (1988) considered the impedance tensor of the heterogeneous Earth as a linear casual operator and on this ground state that the dispersion relations of both kinds hold good in all models, including 3D ones. But this consideration is vulnerable to criticism since the electrical and magnetic fields interact with each other and we hardly can say that one of these fields is a cause and another is an effect (Svetov, 1991). The magnetelluric system is casual in the sense that the electrical and magnetic fields are effects of the same cause, for instance, of ionospheric or magnetospheric currents.

Many people were involved in this discussion (Fischer and Schnegg, 1980, 1993; Egbert, 1990; Svetov, 1991; Berdichevsky and Pokhotelov, 1997a, b). Nowadays it is evident that we have to leave room for the possibility of violation of dispersion relations in the *E*-polarized 2D-models and 3D-models. The discussion makes a clear practical sense: if the Kramers–Kronig relations are violated, our philosophy of amplitude-phase inversion of MT-data should be revised. This is seen from the following example. Take a regional elongated (quasi 2D) depression with local near-surface 3D inhomogeneities that violate the dispersion relations. Here the separate inversions of transverse apparent resistivity and phase curves in the class of *H*-polarized 2D-models may yield conflicting geoelectric structures.

Meantime the magnetotelluric observations give a good deal of examples with dramatic violation of MT dispersion relations (Berdichevsky et al., 1996; Vanyan et al., 2002a; Chouteau and Tournerie, 2002). Figure 1.9 presents apparent-resistivity and phase curves obtained in the mountains of the Lesser Caucasus (Berdichevsky et al., 1996). Here the accuracy of the phase measurements seems to be rather high (good spatial correlation!), but we see in Fig. 1.10 that the difference between observed and calculated φ-curves amounts up to 35°.

The key to an understanding these phenomena lies with mathematical modelling.

Berdichevsky and Pokhotelov (1997b) revealed the dramatic violation of the Kramers–Kronig relations in a (3D + 2D)-superimposition model shown in Fig. 1.11. The model contains a two-dimensional deep conductive prism R of half-width v and a near-surface resistive cylinder L of radius a ($a << v$). The calculations have been carried out by an approximate hybrid method given in Sect. 1.3.4. Here

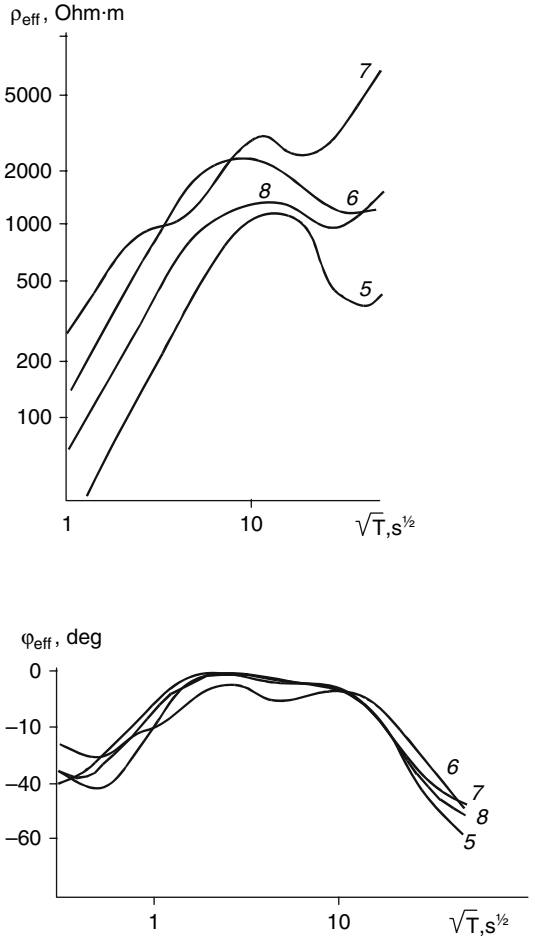

Fig. 1.9 Magnetotelluric curves in the mountains of the Lesser Caucasus; 5,6,7, . . . observation sites

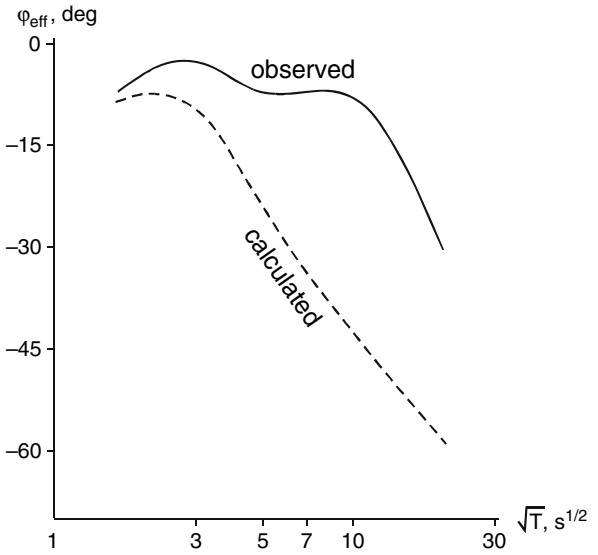

Fig. 1.10 Violation of the dispersion relation in MTS-6; solid line – observed phase curve, broken line – phase curve computed by (1.99)

the two-dimensional problem for the regional inhomogeneity, R, has been solved numerically by program of Wannamaker et al. (1987), while the real-valued electric distortion tensor [**e**] has been determined from the well-known problem on a cylinder in the stationary uniform electric field (Smythe, 1950). Introduce polar coordinates r, θ with angle θ measured clockwise from the x-axis. At an arbitrary site O(r, θ) we have

$$e_{xx} = \begin{cases} 1 - \frac{a^2}{r^2} m \cos 2\theta & r > a \\ 1 + m & r < a \end{cases} \quad e_{xy} = \begin{cases} -\frac{a^2}{r^2} m \sin 2\theta & r > a \\ 0 & r < a \end{cases}$$
$$e_{yx} = \begin{cases} -\frac{a^2}{r^2} m \sin 2\theta & r > a \\ 0 & r < a \end{cases} \quad e_{yy} = \begin{cases} 1 + \frac{a^2}{r^2} m \cos 2\theta & r > a \\ 1 + m & r < a, \end{cases} \tag{1.100}$$

where

$$m = \frac{\rho_L - \rho_1}{\rho_L + \rho_1}.$$

Figure 1.12 demonstrates the apparent resistivity and impedance-phase curves obtained in the immediate vicinity of the cylinder L. Note that, relative to the cylinder, the $\rho_{x'y'}$- and $\varphi_{x'y'}$-curves are oriented in a direction close to the radial one, while the $\rho_{y'x'}$- and $\varphi_{y'x'}$-curves are oriented in a direction close to the tangential one. It is remarkable that the near-radial $\rho_{x'y'}$-curve lies three decades

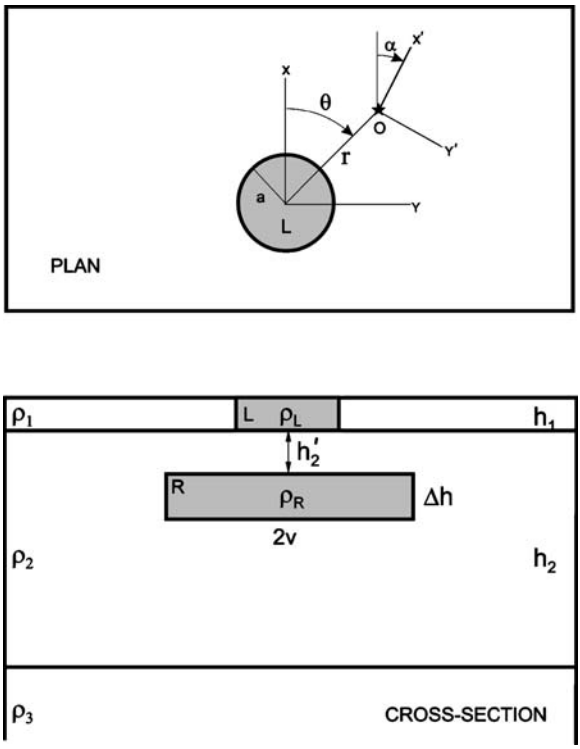

Fig. 1.11 A superimposition model with a near-surface resistive cylinder and a 2D deep regional conductive prism; O-observation site. Model parameters: $\rho_1 = 10$ Ohm·m, $h_1 = 0.5$ km, $\rho_L = \infty$, $a = 0.125$ km, $\rho_2 = \infty$, $h_2 = 100$ km, $\rho_R = 10$ Ohm·m, $h'_2 = 10$ km, $\Delta h = 10$ km, $v = 20$ km, $\rho_3 = 0$

below the near-tangential $\rho_{y'x'}$-curve. This relationship can be readily explained by effect of current flowing around the resistive cylinder L. On the other hand, the relationship between the near-radial and near-tangential phase curves is rather strange: the near-tangential $\varphi_{y'x'}$-curve does not leave the fourth quadrant, whereas the near-radial $\varphi_{x'y'}$-curve passes over all the quadrants, making a total phase rotation.

The Kramers–Kronig transforms of the first kind relating the real and imaginary parts of the near-tangential and near-radial impedances are shown in Fig. 1.13. We see that relations (1.98) provide for rather accurate transition from the real part of the impedance to its imaginary part and vice versa. Here the dispersion relations of the first kind obviously hold and we can say that the near-tangential and near-normal impedances have no poles in the upper half-plane of the complex frequency Ω.

Now we turn to Fig. 1.14 that presents the Kramers–Kronig transforms of the second kind relating the apparent resistivities and impedance phases. The

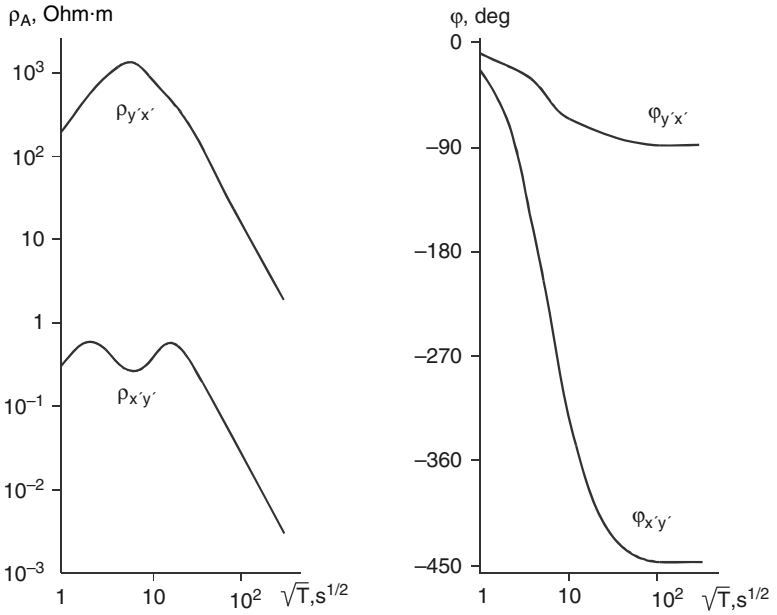

Fig. 1.12 Curves of the apparent-resistivity and impedance-phase at a point O with coordinates $r = 0.129$ km, $\theta = 45^\circ$, $\alpha = 50^\circ$; calculated for a model shown in Fig. 1.11

near-tangential $\rho_{y'x'}$- and $\varphi_{y'x'}$-curves exhibit a reasonably good agreement with the dispersion relations: here the initial curves and curves calculated by (1.99) virtually coincide. So, we can say that the near-tangential impedance has no zeros in the upper half-plane of the complex frequency Ω. Another picture is characteristic of the near-radial $\rho_{x'y'}$- and $\varphi_{x'y'}$-curves: here the initial curves and curves calculated by (1.99) are close to each other in the high-frequency range but abruptly diverge with lowering frequency. We observe a crude violation of the dispersion relations of the second kind. Clearly the near-radial impedance has a zero (or a few zeros) in the upper half-plane of the complex frequency Ω.

Recently the violation of dispersion relations of the second kind has been detected in the two-dimensional model with an anisotropic layer (Heise et al., 2002) and in the 2D coast-effect model (Alekseev et al., 2006).

Calculations verify the reality of anomalous phenomena that are exhibited in violation of dispersion relations. But we know less than nothing about these phenomena. To fill the gap, we need field experiments and model studies. It would be useful to include a special test controlling the dispersion relations into existing programs of MT data processing and inversion.

What can be done if MT data exhibit discrepancy between apparent resistivity and phase curves? Let us recall the sorrowful letter that many of us have received from Alan Jones when Leonid Vanyan passed away:

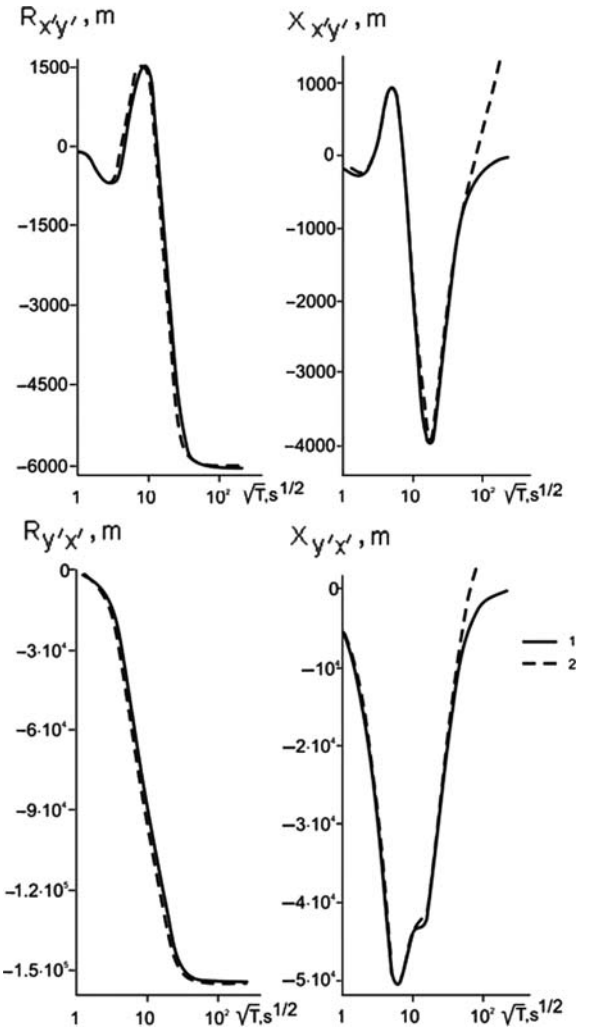

Fig. 1.13 Dispersion relations between the real, R, and imaginary, X, parts of normalized impedance $Z/i\omega\mu_0$ at a point O with coordinates $r = 0.129$ km, $\theta = 45^\circ$, $\alpha = 50^\circ$; solid line – initial curve, broken line – curve compuded by (1.98); calculated for a model shown in Fig. 1.11

Dear colleagues,
The loss of our colleague and my friend Leonid Vanyan is truly sad, and I am personally devastated by the news. Just two weeks ago Leo sent me this email message, with the germ of an idea for how to make "old" apparent resistivity and phase data useful by requiring them to be consistent using an iterative approach. He and I were going to work on this together, but that will not happen now. Rather than work on this alone, I would like to share this idea with you all. If any of you should find it useful, please name it the *Vanyan correction* in Leonid's honor. Those of you who were at Victoria in 1982 will smile at Leonid's comment about our agreement on the importance of comparing ρ and φ. Alan Jones

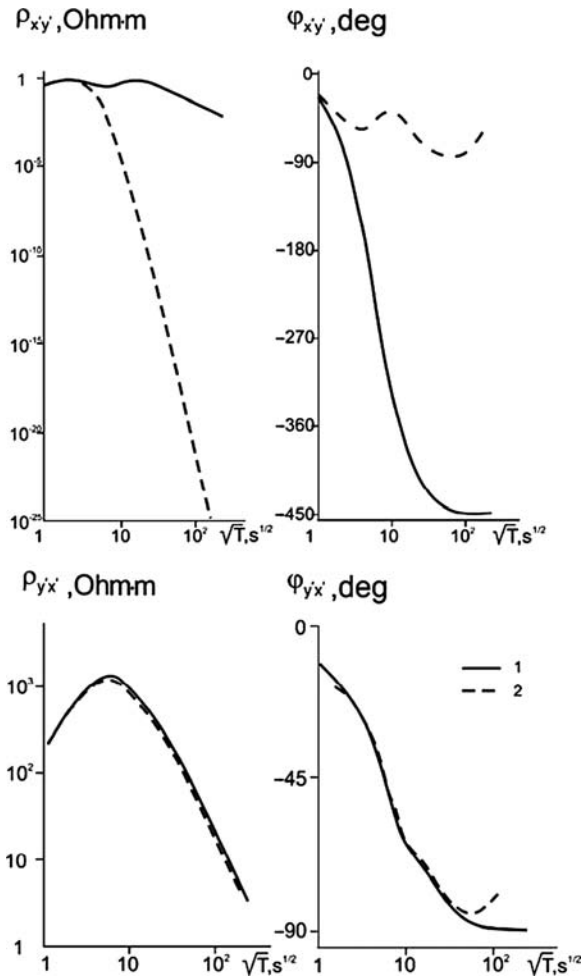

Fig. 1.14 Dispersion relations between the apparent resistivity and impedance phase at a point O with coordinates $r = 0.129$ km, $\theta = 45^\circ$, $\alpha = 50^\circ$; solid line – initial curve, broken line – curve computed by (1.99); calculated for a model shown in Fig. 1.11

Dear Alan,
A few years ago you and me agreed in importance of a comparison of measured φ and the same calculated from ρ. Couple weeks ago I asked Mark Berdichevsky: -Do you use this technique? -Yes. -And what do you do if there is a discrepancy? -I put data in trash. But sometimes we have a limited amount of curves. It is a pity to put them in trash. Perhaps, there are structures that produce ρ and φ away of Hilbert transform. But definitely there are cases when discrepancy is due to noises, poor data processing etc. For those cases an idea appeared. Look: Initial data -ρ_1, φ_1. First step -ρ_1 gives φ_2 (by Hilbert). Second step – $\varphi_3 = (\varphi_1 + \varphi_2)/2$. Third step – φ_3 gives ρ_2 (by Hilbert). Fourth step -$\log \rho_3 = (\log \rho_1 + \log \rho_2)/2$. Fifth step – ρ_3 gives φ_4 ...etc. After 3–4 iterations we have a pair of self-consistent ρ, φ. Best wishes! Yours Leonid

1.6 On the Magnetotelluric Anomalies

We consider models, in which the horizontally homogeneous Earth of normal electric conductivity $\sigma_N(z)$ contains two-dimensional or three-dimensional inhomogeneities $\Delta\sigma(y, z)$ or $\Delta\sigma(x, y, z)$, causing *magnetotelluric anomalies* (distortions). Magnetotelluric anomalies carry information on geoelectric structures.

The *normal field* $\mathbf{E}^N$, $\mathbf{H}^N$ is a field observed within the host Earth in the absence of the lateral inhomogeneities. In such a one-dimensional model the currents flow along layers, charges do not arise, the magnetic field has no vertical component, leading mechanism is the electromagnetic induction.

Considering the normal field, we determine the *normal impedance*, $Z_N = E_x^N / H_y^N = -E_y^N / H_x^N$, and the *normal apparent resistivity*, $\rho_N = |Z_N|^2 / \omega\mu_o$, that are independent of orientation of coordinate axes and reflect vertical variations in conductivity.

In the presence of the inhomogeneities the *anomalous field* $\mathbf{E}^A$, $\mathbf{H}^A$ appears. Magnetotelluric anomalies caused by lateral geoelectric inhomogeneities distort the normal impedance and normal apparent resistivity. Now we determine the impedance tensor and oriented apparent resistivities that reflect not only vertical, but also horizontal variations in conductivity.

Take the real Earth with three-dimensional conductivity distribution $\sigma(x, y, z)$. Let the apparent esistivity, $\rho_A(x_o, y_o)$, and impedance phase, $\varphi(x_o, y_o)$, be obtained at a point $M_o(x_o, y_o)$ on the Earth's surface. We will juxtapose these distorted values with the *locally normal apparent resistivity* $\rho_n(x_o, y_o)$ and *locally normal phase* $\varphi_n(x_o, y_o)$,calculated from the *locally normal impedance* $Z_n(x_o, y_o)$ corresponding to the one-dimensional model $\sigma_n(z) = \sigma(x_o, y_o, z)$, where $\sigma_n(z)$ is a local conductivity-depth profile at the point M_o. The value

$$\Delta\rho_A(x_o, y_o) = \log\frac{\rho_A(x_o, y_o)}{\rho_n(x_o, y_o)} \tag{1.101}$$

is a measure of distortion of the apparent resistivity. Similarly

$$\Delta\varphi(x_o, y_o) = \varphi(x_o, y_o) - \varphi_n(x_o, y_o) \tag{1.102}$$

is a measure of distortion of the impedance phase.

With strong anomalies, that is, with large $\Delta\rho$, $\Delta\varphi$ the apparent-resistivity and impedance-phase curves depend heavily on orientation of the measurement axes. For each observation site we can plot a lot of conflicting curves. It is evident that the formal one-dimensional interpretation of such magnetotelluric curves is senseless.

We classify the magnetotelluric anomalies by their depth, scale, dimensionality and physical nature.

1. The geoelectric medium can be divided into near-surface and deep parts. According to this specification, we differentiate the *near-surface inhomogeneities* and *deep inhomogeneities***,** which cause the *near-surface anomalies* and *deep anomalies***.** Traditionally, we associate the near-surface anomalies with sediments (partially or in full) and the deep anomalies with consolidated crust and mantle.

2. Classifying the anomalies by their scale, we discern the continental, regional and local anomalies. The effects caused by electromagnetic interaction between oceans and continents are considered as *continental anomalies.* The effects connected with influence of the first- and second-order tectonic structures (mountain ridges and valleys, shields, crystalline massifs, platforms, vast depressions and elevations) are designated as *regional anomalies.* These anomalies are observed at distances numbered in the hundreds or even thousands of kilometers. Third-order structures (minor folds, salt domes, traprocks, permafrost lenses, small-scale inclusions) produce the *local anomalies*. These effects create mosaic pattern with characteristic dimensions from tens of meters to kilometers. If their dimension is much less than the measurement spacing, the local anomalies are considered as noninterpretable *geoelectric noise*.

3. Anomalies generated by elongated inhomogeneities with great aspect ratio (their length is much larger than their width) are considered as *quasi-two-dimensional anomalies* ("two-dimensional" anomalies). Mathematical modelling enables one to establish criteria for quasi-two-dimensionality that are valid in the central part of the inhomogeneity. Anomalies that do not satisfy the quasi-two-dimensionality criteria are taken as *three-dimensional anomalies*.

4. The most difficult is to classify the anomalies by their physical nature. We observe complicated phenomena, in which the sources and vortices of the anomalous field interact with each other. For simplicity we separate the vortex-free (potential) and vortex (solenoidal) mechanisms of the excitation of the anomalous field. Using the terminology suggested by Kaufman (1961, 1974), we divide the anomalous electromagnetic field into two parts: the galvanic (Coulomb's) part which is generated by the excess charges and the induction (Faraday's) part which is generated inductively by the closed excess currents. The galvanic and induction parts of the anomalous field are responsible for *galvanic distortions* and *induction distortions* of the magnetotelluric and magnetovariational response functions.

The galvanic distortions are most pronounced at low frequencies when the penetration depth of the normal field far exceeds the depth and dimensions of the inhomogeneities. Here the inductive influence of the excess currents is too weak to reveal itself, while the galvanic part of the anomalous field obeys the direct current laws. Inasmuch as the anomalous field is proportional to the normal field, both the fields have the same phases and in the same ways depend on frequency. The galvanic anomalies manifest themselves in *static shift* of the low-frequency parts of the apparent-resistivity curves and do not affect the corresponding parts of the impedance-phases curves. These effects extend over entire spectrum of sufficiently low frequencies and do not attenuate even as $\omega \to 0$. The structure of the galvanic anomalies is vividly imaged in the current pattern: electric currents flow around resistive zones and gather within conductive zones.

Quite different are the regularities of the induction distortions caused by the excess currents. These effects manifest themselves at high frequencies when the Faraday induction in the inhomogeneous medium is sufficiently intensive. Here anomalous and normal fields have different phases and in different ways depend on frequency. With lowering frequency the induction effects vanish. The characteristic

feature of the induction anomalies is the horizontal skin effect: high-frequency electric currents are concentrated in the vicinity of resistive zones.

This simple classification of magnetotelluric anomalies is built on phenomenological base. Can we construct a self-consistent theory of galvanic and induction effects?

Turn back to the model shown in Fig. 1.1. According to (1.6) the anomalous field meets the equations

$$curl\mathbf{H}^{\mathrm{A}} = \sigma_{\mathrm{N}}\mathbf{E}^{\mathrm{A}} + \mathbf{j}$$

$$curl\mathbf{E}^{\mathrm{A}} = i\omega\mu_{\mathrm{o}}\mathbf{H}^{\mathrm{A}},$$

where

$$\mathbf{j}(M) = \begin{cases} \mathbf{j}(M) = \Delta\sigma\mathbf{E} & M \in V \\ 0 & M \notin V \end{cases}$$

is the density of excess electric current filling the inhomogeneous domain V.

Let us divide the excess current into potential, $\mathbf{j}_{\mathrm{p}}$, and solenoidal, $\mathbf{j}_{\mathrm{s}}$, parts:

$$\mathbf{j} = \mathbf{j}_{\mathrm{p}} + \mathbf{j}_{\mathrm{s}}, \tag{1.103}$$

where

$$\begin{cases} curl\,\mathbf{j}_{\mathrm{p}} = 0 \\ div\,\mathbf{j}_{\mathrm{p}} = div\,\mathbf{j} \end{cases} \qquad \begin{cases} curl\,\mathbf{j}_{\mathrm{s}} = curl\,\mathbf{j} \\ div\,\mathbf{j}_{\mathrm{s}} = 0\ . \end{cases} \tag{1.104}$$

The parts $\mathbf{j}_{\mathrm{p}}$ and $\mathbf{j}_{\mathrm{s}}$ are readily determined.

We will start with the potential part $\mathbf{j}_{\mathrm{p}}$. Define $\mathbf{j}_{\mathrm{p}}$ as

$$\mathbf{j}_{\mathrm{p}}(M) = \begin{cases} -grad\,U(M) & M \in V \\ 0 & M \notin V. \end{cases} \tag{1.105}$$

Here U is the scalar potential of the field $\mathbf{j}_{\mathrm{p}}$. It satisfies the equation

$$\Delta U(M) = -div\,\mathbf{j}_{\mathrm{p}}(M) = div\,\mathbf{j}(M) \qquad M \in V \tag{1.106}$$

with condition $U|_S = 0$ on the surface S bounding the inhomogeneous domain V. Solving (1.106), we find

$$U(M) = \iiint_V G(M, M_v)\,div\,\mathbf{j}(M_v)\,dV, \tag{1.107}$$

where $G(M, M_v)$ is the Green function for the Dirichlet problem:

$$\Delta G(M, M_v)| = -\delta(r_{MM_v}) \qquad G(M, M_v)|_S = 0. \tag{1.108}$$

Thus,

$$\mathbf{j}_{\mathrm{p}}(M) = \begin{cases} -grad \iiint\limits_V G(M, M_v) div\, \mathbf{j}\,(M_v)\, dV & M \in V \\ 0 & M \notin V. \end{cases} \tag{1.109}$$

Next we will pass on to the solenoidal part $\mathbf{j}_s$. Define $\mathbf{j}_{\mathrm{s}}$ as

$$\mathbf{j}_s(M) = \begin{cases} curl\, \mathbf{I}(M) & M \in V \\ 0 & M \notin V, \end{cases} \tag{1.110}$$

where $\mathbf{I}$ can be considered as the magnetization of a magnetic body that is equivalent to the solenoidal current of the density $\mathbf{j}_{\mathrm{s}}$ distributed within the domain V. Note that (1.110) does not provide the unique determination of $\mathbf{j}_s$. Evidently $\mathbf{j}_s$ can be also taken as

$$\mathbf{j}_{\mathrm{s}}(M) = curl\, \mathbf{I}'(M) \qquad M \in V, \tag{1.111}$$

where

$$\mathbf{I}'(M) = \mathbf{I}(M) + grad\, \Psi(M)$$

and Ψ is arbitrary scalar function. But we eliminate such an arbitrariness by imposing the requirement that $div\, \mathbf{I} = 0$. So, we write

$$curl\, \mathbf{I}(M) = \mathbf{j}_{\mathrm{s}}(M) \qquad div\, \mathbf{I}(M) = 0 \qquad M \in V, \tag{1.112}$$

whence, with due regard for (1.104),

$$\Delta\, \mathbf{I}(M) = -curl\, \mathbf{j}_{\mathrm{s}}(M) = -curl\, \mathbf{j}(M). \tag{1.113}$$

Now, using the Green function introduced by (1.108), we find

$$\mathbf{I}(M) = \begin{cases} \iiint\limits_V G(M, M_v) curl\, \mathbf{j}\,(M_v)\, dV & M \in V \\ 0 & M \notin V. \end{cases} \tag{1.114}$$

Here the $curl$ may be taken out of the integral. Since $div\, \mathbf{I} = 0$, we express $\mathbf{I}$ as $\mathbf{I} = curl\, \mathbf{P}$, where $\mathbf{P}$ is a vector field. Then (1.113) assumes the form $\Delta \mathbf{P} = -\mathbf{j}$, whence

$$\mathbf{P}(M) = \begin{cases} \iiint\limits_V G(M, M_v) \mathbf{j}\,(M_v)\, dV & M \in V \\ 0 & M \notin V. \end{cases} \tag{1.115}$$

and along with (1.114) we get

$$\mathbf{I}(M) = \begin{cases} curl \iiint\limits_V G(M, M_v)\mathbf{j}\,(M_v)\,dV & M \in V \\ 0 & M \notin V. \end{cases} \tag{1.116}$$

Finally

$$\mathbf{j}_s(M) = \begin{cases} curl \iiint\limits_V G(M, M_v) curl\,\mathbf{j}\,(M_v)\,dV & M \in V \\ 0 & M \notin V \end{cases} \tag{1.117}$$

or

$$\mathbf{j}_s(M) = \begin{cases} curl\, curl \iiint\limits_V G(M, M_v)\mathbf{j}\,(M_v)\,dV & M \in V \\ 0 & M \notin V. \end{cases} \tag{1.118}$$

Thus, we have separated the electric excess current into potential and solenoidal parts, $\mathbf{j}_p$ and $\mathbf{j}_s$. Each part of the excess current is responsible for its own anomalous field.

Potential part of the electric excess current consists of currents that close upon the excess charges arising at inhomogeneities. It excites the anomalous field $\mathbf{E}^e$, $\mathbf{H}^e$ of the electric type described by equations

$$\begin{aligned} curl\ \mathbf{H}^e &= \sigma_N \mathbf{E}^e + \mathbf{j}_p \\ curl\ \mathbf{E}^e &= i\omega\mu_o \mathbf{H}^e\,. \end{aligned} \tag{1.119}$$

At low frequencies these galvanic effects are of static nature. They follow the direct-current laws.

Solenoidal part of the excess electric current consists of currents that close upon themselves. It excites the anomalous field $\mathbf{E}^m$, $\mathbf{H}^m$ of the magnetic type described by equations

$$\begin{aligned} curl\ \mathbf{H}^m &= \sigma_N \mathbf{E}^m + \mathbf{j}_s = \sigma_N \mathbf{E}^m + curl\ \mathbf{I} \\ curl\ \mathbf{E}^m &= i\omega\mu_o \mathbf{H}^m\ , \end{aligned} \tag{1.120}$$

where $\mathbf{I}$ is the magnetization of the equivalent magnetic body. Eliminating from $\mathbf{H}^m$ the contribution of the electric excess current, we get a magnetic field $\tilde{\mathbf{H}}^m = \mathbf{H}^m - \mathbf{I}$. Substitution of $\tilde{\mathbf{H}}^m$ into (1.120) gives

$$\begin{aligned} curl\ \tilde{\mathbf{H}}^m &= \sigma_N \mathbf{E}^m \\ curl\ \mathbf{E}^m &= i\omega\mu_o \tilde{\mathbf{H}}^m + \mathbf{j}_s^m\,, \end{aligned} \tag{1.121}$$

where $\mathbf{j}_s^m = i\omega\mu_o \mathbf{I}$ is the density of excess fictitious magnetic current equivalent to the excess electric current. Note that the magnetic excess current is proportional

to ω. These induction effects appear at high frequencies and they attenuate with lowering frequency.

The most simple situation we have in the two-dimensional model. Let the x-axis run along the strike. Considering the TE-mode with components E_x, H_y, H_z and the TM-mode with components E_y, E_z, H_x, we separate the galvanic and induction anomalies.

The TE-mode is excited by the excess electric current of density $\mathbf{j}\,(j_x, 0, 0)$ with a single component $j_x(y, z) = \Delta\sigma E_x(y, z)$. Here

$$div\,\mathbf{j} = \frac{\partial j_x}{\partial x} = 0, \qquad curl\,\mathbf{j} = \frac{\partial j_x}{\partial z}\mathbf{1}_y - \frac{\partial j_x}{\partial y}\mathbf{1}_z \neq 0.$$

We see that the field $\mathbf{j}$ is solenoidal, $\mathbf{j}_\mathrm{p} = 0$ and $\mathbf{j} = \mathbf{j}_\mathrm{s}$. The TE-mode is distorted solely by the induction effects (currents flow along the strike and do not charge the medium). Let us find the equivalent magnetic current, $\mathbf{j}^m_\mathrm{s}$, responsible for the induction distortions. By virtue of (1.116) and (1.121)

$$\left.\begin{aligned} j^m_{sx} &= 0 \\ j^m_{sy} &= i\omega\mu_\mathrm{o}\tfrac{\partial}{\partial z}\iiint\limits_V G(M, M_v)\, j_x\,(M_v)\, dV \\ j^m_{sz} &= -i\omega\mu_\mathrm{o}\tfrac{\partial}{\partial y}\iiint\limits_V G(M, M_v)\, j_x\,(M_v)\, dV \end{aligned}\right|_{M\in V.} \tag{1.122}$$

The TM-mode is excited by the excess electric current of density $\mathbf{j}\,(0, j_y, j_z)$ where $j_y(y, z) = \Delta\sigma E_y(y, z)$ and $j_z(y, z) = \Delta\sigma E_z(y, z)$. Here

$$div\,\mathbf{j} = \frac{\partial j_y}{\partial y} + \frac{\partial j_z}{\partial z} \neq 0, \qquad curl\,\mathbf{j} = \left(\frac{\partial j_z}{\partial y} - \frac{\partial j_y}{\partial z}\right)\mathbf{1}_x \neq 0. \tag{1.123}$$

In this case the electric excess current consists of potential and solenoidal parts.

Let us define the potential part, $\mathbf{j}_\mathrm{p}$, which causes the galvanic distortions. According to (1.115),

$$\left.\begin{aligned} j_{px}(M) &= 0 \\ j_{py}(M) &= -\frac{\partial}{\partial y}\iiint\limits_V G\,(M, M_v)\left(\frac{\partial j_y(M_v)}{\partial y} + \frac{\partial j_z(M_v)}{\partial z}\right) dV \\ j_{pz}(M) &= -\frac{\partial}{\partial z}\iiint\limits_V G\,(M, M_v)\left(\frac{\partial j_y(M_v)}{\partial y} + \frac{\partial j_z(M_v)}{\partial z}\right) dV \end{aligned}\right|_{M\in V.} \tag{1.124}$$

Next we define the equivalent excess magnetic current, $\mathbf{j}^m_\mathrm{s}$, which may cause the induction distortions. According to (1.116) and (1.121),

$$\left.\begin{aligned} & j^m_{sx}(M) \\ & = i\omega\mu_o \left\{ \frac{\partial}{\partial y} \iiint\limits_V G(M, M_v)\, j_z(M_v)\, dV - \frac{\partial}{\partial z} \iiint\limits_V G(M, M_v) j_y(M_v)\, dV \right\} \\ & j^m_{sy} = 0 \\ & j^m_{sz} = 0. \end{aligned} \right| \; {}_{M \in V.} \tag{1.125}$$

The linear magnetic current flows in the x-direction, that is, along the model strike, and does not depend on x. This current is equivalent to an infinitely long uniform solenoid embracing the inhomogeneous domain V. Its magnetic field is confined to V and is zero outside V (the solenoid does not liberate its magnetic field to outer space). It is obvious that the inductive magnetic field does not come up to the Earth's surface and we observe there only the galvanic effects.

Chapter 2
The Impedance Eigenstate Problem

2.1 The Classical Formulation of the Tensor Eigenstate Problem

Rotating the impedance tensor [**Z**], one may obtain a variety of different apparent-resistivity and impedance-phase curves, ρ_{xy}, ρ_{yx} and φ_{xy}, φ_{yx}, sometimes drastically conflicting in configuration. Such a great body of data is seemingly chaotic, but it can be systematized by the methods concerned with the eigenstate problem.

Solving the eigenstate problem, we focus all the information, contained in the components of the tensor, on its principal directions depending on geometry of the target geoelectric structures.

Recall the classical formulation of the tensor eigenstate problem. Let a real-valued symmetric tensor

$$[\mathbf{T}] = \begin{bmatrix} T_{xx} & T_{xy} \\ T_{yx} & T_{yy} \end{bmatrix}, \qquad T_{xy} = T_{yx} \tag{2.1}$$

transform a real-valued vector $\mathbf{V}(V_x,\ V_y)$ to the collinear vector $t\,\mathbf{V}(t\,V_x,\ t\ V_y)$:

$$[\mathbf{T}]\mathbf{V}{=}t\mathbf{V}, \tag{2.2}$$

where t is a scalar that characterizes the change in the vector modulus. The vector **V** satisfying (2.2) is the *eigenvector* of the tensor [**T**]. Its direction is the *principal direction* of the tensor [**T**]. The scalar factor t is the *principal value* or *eigenvalue* of the tensor [**T**].

If (2.2) is valid, then

$$\begin{aligned} (T_{xx} - t)\,V_x + T_{xy}\,V_y &= 0, \\ T_{yx}\,V_x + (T_{yy} - t)\,V_y &= 0\ . \end{aligned}$$

This uniform system of linear equations in $V_x,\ V_y$ can have nonzero solutions if its determinant is equal to zero:

M. Berdichevsky, V.I. Dmitriev, *Models and Methods of Magnetotellurics*,
DOI 10.1007/978-3-540-77814-1_2,

$$(T_{xx} - t)(T_{yy} - t) - T_{xy}T_{yx} = 0\,,$$

which gives the characteristic equation for the principal values t:

$$t^2 - (\,T_{xx} + T_{yy}\,)t + (\,T_{xx}\,T_{yy} - T_{xy}\,T_{yx}\,) = 0$$

and the equation for the principal directions:

$$\tan\alpha = \frac{V_y}{V_x} = \frac{t - T_{xx}}{T_{xy}} = \frac{T_{yx}}{t - T_{yy}} = \frac{t - T_{xx} + T_{yx}}{t + T_{xy} - T_{yy}}, \tag{2.4}$$

where α is an angle between the vector $\mathbf{V}$ and the x-axis.

It follows from (2.3) and (2.4) that any symmetric real-valued tensor $[\mathbf{T}]$ has two real principal values

$$\begin{aligned} t_1 &= \frac{\mathrm{tr}\,[\mathbf{T}]}{2} + \sqrt{\frac{(\mathrm{tr}\,[\mathbf{T}])^2}{4} - \det[\mathbf{T}]} = \frac{T_{xx} + T_{yy}}{2} + \sqrt{\frac{(T_{xx} + T_{yy})^2}{4} - (T_{xx}T_{yy} - T_{xy}T_{yx})}, \\ t_2 &= \frac{\mathrm{tr}\,[\mathbf{T}]}{2} - \sqrt{\frac{(\mathrm{tr}\,[\mathbf{T}])^2}{4} - \det[\mathbf{T}]} = \frac{T_{xx} + T_{yy}}{2} - \sqrt{\frac{(T_{xx} + T_{yy})^2}{4} - (T_{xx}T_{yy} - T_{xy}T_{yx})} \end{aligned} \tag{2.5}$$

and two orthogonal principal directions:

$$\begin{aligned} \alpha_1 &= \arctan\frac{\mathrm{t_1} - \mathrm{T_{xx}} + \mathrm{T_{yx}}}{\mathrm{t_1} + \mathrm{T_{xy}} - \mathrm{T_{yy}}}, \\ \alpha_2 &= \alpha_1 + \tfrac{\pi}{2} = \arctan\frac{t_2 - T_{xx} + T_{yx}}{t_2 + T_{xy} - T_{yy}}\,, \end{aligned} \tag{2.6}$$

where $\mathrm{tr}\,[\mathbf{T}] = T_{xx} + T_{yy}$ and $\det[\mathbf{T}] = T_{xx}T_{yy} - T_{xy}T_{yx}$.

From the solution of the eigenstate problem, we derive three independent parameters, t_1, t_2 and α_1, which fill all three degrees of freedom possessed by the matrix $[\mathbf{T}]$.

Rotating the symmetric tensor $[\mathbf{T}]$ through the angle α_1, we reduce it to its principal directions and get a diagonal tensor

$$[\mathbf{T}] = \begin{bmatrix} t_1 & 0 \\ 0 & t_2 \end{bmatrix}. \tag{2.7}$$

Thus, we convey all the information inherent in the four components $T_{xx}, T_{xy}, T_{yx}, T_{yy}$ of the tensor $[\mathbf{T}]$ to its principal values, t_1 and t_2 and principal directions, α_1, $\alpha_2 = \alpha_1 + \pi/2$.

On some alteration, this classical approach can be readily applied to the two-dimensional impedance tensor. Really, with (1.62), that is, with $skew_s = 0$ and

$skew_B = 0$, we can rotate the reference frame counterclockwise through the strike angle α determined by (1.58) and rearrange the tensor [**Z**] to the anti-diagonal tensor (1.54) with the longitudinal and transverse components on the secondary diagonal. What is more, following (1.16), we can rearrange the anti-diagonal tensor [**Z**] to the diagonal tensor [**Z**] with the longitudinal and transverse components on the principal diagonal.

Generally such a simple solution to the magnetotelluric eigenstate problem is unworkable. When it comes to the complex-valued impedance tensor [**Z**] characteristic of three-dimensional media, the conditions $skew_S = 0$, $skew_B = 0$ are violated and there is no real rotation angle that enables us to reduce the impedance tensor to the anti-diagonal (or diagonal) form. Clearly, in magnetotellurics we have to look for more general approaches that would be applicable in the case of asymmetric media. Swift (1967) was likely the first to suggest some basic ideas in this field.

Statement of the impedance eigenstate problem needs some extensions associated with the elliptic polarization of the magnetotelluric field. For the sake of integrity, it would be useful to give a brief review of the polarization definitions (Yee and Paulson, 1987).

2.2 Polarization of the Magnetotelluric Field

Following Yee and Paulson (1987), we consider the complex electric and magnetic fields

$$\mathbf{E}_\tau = \begin{bmatrix} E_x \\ E_y \end{bmatrix} = \begin{bmatrix} |E_x| e^{i\phi_x^E} \\ |E_y| e^{i\phi_y^E} \end{bmatrix}, \quad \mathbf{H}_\tau = \begin{bmatrix} H_x \\ H_y \end{bmatrix} = \begin{bmatrix} |H_x| e^{i\phi_x^H} \\ |H_y| e^{i\phi_y^H} \end{bmatrix}. \tag{2.8}$$

Their *polarization ratios* are**:**

$$\begin{aligned} P_{\mathrm{E}} &= \frac{E_y}{E_x} = \frac{|E_y|}{|E_x|} e^{i(\phi_y^E - \phi_x^E)} = \tan\theta^E e^{i\phi^E}, \\ P_{\mathrm{H}} &= \frac{H_y}{H_x} = \frac{|H_y|}{|H_x|} e^{i(\phi_y^H - \phi_x^H)} = \tan\theta^H e^{i\phi^H}, \end{aligned} \tag{2.9}$$

where

$$\begin{aligned} \tan\theta^E &= |P_{\mathrm{E}}| = \frac{|E_y|}{|E_x|}, \ \theta^E \in [0, \pi/2], \\ \tan\theta^H &= |P_{\mathrm{H}}| = \frac{|H_y|}{|H_x|}, \ \theta^H \in [0, \pi/2], \end{aligned}$$

and

$$\phi^E = \phi_y^E - \phi_x^E = \arg P_E,$$

$$\phi^H = \phi_y^H - \phi_x^H = \arg P_H\,.$$

In the t-domain

$$\mathbf{E}_\tau(t) = \begin{bmatrix} E_x(t) \\ E_y(t) \end{bmatrix} = \begin{bmatrix} |E_x| \cos(\omega t - \phi_x^E) \\ |E_y| \cos(\omega t - \phi_y^E) \end{bmatrix},$$
$$\mathbf{H}_\tau(t) = \begin{bmatrix} H_x(t) \\ H_y(t) \end{bmatrix} = \begin{bmatrix} |H_x| \cos(\omega t - \phi_x^H) \\ |H_y| \cos(\omega t - \phi_y^H) \end{bmatrix}. \tag{2.10}$$

Eliminating $\sin \omega t$ and $\cos \omega t$ from (2.10), we obtain the equations for the ellipses described by the endpoint of the vectors $\mathbf{E}_\tau(t)$, $\mathbf{H}_\tau(t)$:

$$\frac{E_x^2(t)}{|E_x|^2} + \frac{E_y^2(t)}{|E_y|^2} - 2\cos\phi^E \frac{E_x(t)\,E_y(t)}{|E_x|\,|E_y|} = \sin^2\phi^E,$$
$$\frac{H_x^2(t)}{|H_x|^2} + \frac{H_y^2(t)}{|H_y|^2} - 2\cos\phi^H \frac{H_x(t)\,H_y(t)}{|H_x|\,|H_y|} = \sin^2\phi^H. \tag{2.11}$$

These ellipses received the name *polarization ellipses.* Parameters of the polarization ellipses can be defined through the polarization ratios.

Let us begin with the polarization ellipse for the electric field (Fig. 2.1a). First find the angle α_E made by the major axis of the polarization ellipse with the x-axis. To this end, determine the time t_o, at which $E_\tau(t) = \sqrt{E_x^2(t) + E_y^2(t)}$ is maximum. From the conditions

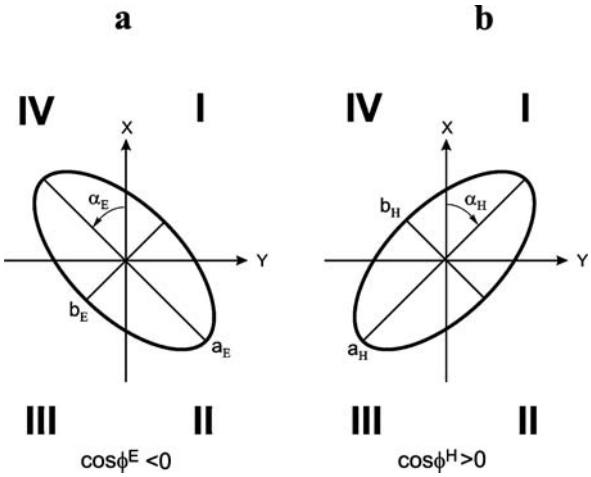

Fig. 2.1 Polarization ellipses of electric (**a**) and magnetic (**b**) eigenfields. **I**, **II**, **III**, **IV** – numbers of quadrants

$$\frac{dE_\tau(t)}{dt} = 0 \quad \text{with} \quad \frac{d^2 E_\tau(t)}{dt^2} < 0$$

we derive the following equation in t_o:

$$\tan 2\omega t_o = \frac{|E_x|^2 \sin 2\phi_x^E + |E_y|^2 \sin 2\phi_y^E}{|E_x|^2 \cos 2\phi_x^E + |E_y|^2 \cos 2\phi_y^E} \quad \text{with} \quad \tan\phi^E \tan(\omega t_o - \phi_x^E) > 0,$$

whence

$$\tan\alpha_E = \frac{|E_y|\cos(\omega t_o - \phi_y^E)}{|E_x|\cos(\omega t_o - \phi_x^E)} = \frac{|E_y|}{|E_x|}[1 + \tan\phi^E \tan(\omega t_o - \phi_x^E)]\cos\phi^E. \quad (2.12)$$

In accord with (2.9), (2.12) this equation becomes:

$$\tan 2\alpha_E = \frac{2\,\mathrm{Re}\,P_E}{1 - |P_E|^2} = \tan 2\theta^E \cos\phi^E, \quad (2.13)$$

where α_E is taken within quadrant I ($0 \le \alpha_E \le \pi/2$), if $\cos\phi^E \ge 0$ or within quadrant IV ($0 > \alpha_E \ge -\pi/2$), if $\cos\phi^E < 0$.

Next find the ratio ε_E between semiaxes of the polarization ellipse. This parameter is termed the field *ellipticity*. Substitution of t_o and $t_o + \pi/2\omega$ into $E_\tau(t)$ yields the major and minor semi-axes of the ellipse:

$$a_E = |E_x| \frac{\sqrt{1 + |P_E|^2 + 2\mathrm{Im}\,P_E} + \sqrt{1 + |P_E|^2 - 2\mathrm{Im}\,P_E}}{2},$$
$$b_E = |E_x| \frac{\sqrt{1 + |P_E|^2 + 2\mathrm{Im}\,P_E} - \sqrt{1 + |P_E|^2 - 2\mathrm{Im}\,P_E}}{2},$$

where the quantity b_E is defined with its sign: it is positive for $\mathrm{Im}\,P_E > 0$, that is, for $\sin\phi^E > 0$, and it is negative for $\mathrm{Im}\,P_E < 0$, that is, for $\sin\phi^E < 0$. Thus,

$$\varepsilon_E = \frac{b_E}{a_E} = \frac{\sqrt{1 + |P_E|^2 + 2\mathrm{Im}\,P_E} - \sqrt{1 + |P_E|^2 - 2\mathrm{Im}\,P_E}}{\sqrt{1 + |P_E|^2 + 2\mathrm{Im}\,P_E} + \sqrt{1 + |P_E|^2 - 2\mathrm{Im}\,P_E}} = \tan\gamma_E, \quad (2.14)$$

where

$$\gamma_E = \frac{1}{2}\arcsin(\sin 2\theta^E \sin\phi^E) \qquad -\pi/4 \le \gamma_E \le \pi/4$$

and

$$-1 \le \varepsilon_E \le 1.$$

Note that $|\varepsilon_E| = 0$ for the linear polarization, and $|\varepsilon_E| = 1$ for the circular polarization. What is the sense of the sign of ε_E? Let us define the angle velocity of the field rotation:

$$\Omega = \frac{d}{dt}\arctan\frac{E_y(t)}{E_x(t)} = \omega \sin\phi^E \frac{|E_x||E_y|}{|E_x|^2\cos^2(\omega t - \phi_x^E) + |E_y|^2\cos^2(\omega t - \phi_y^E)}.$$

This makes clear that the electric vector rotates clockwise if $\sin\phi^E > 0$, that is, for $\varepsilon_E > 0$, and counterclockwise if $\sin\phi^E < 0$, that is, for $\varepsilon_E < 0$.

With (2.14), we can present simple formulae for normalized semi-axes of polarization ellipse:

$$\begin{aligned}
\frac{a_E}{\sqrt{a_E^2 + b_E^2}} &= \frac{1}{\sqrt{1 + \dfrac{b_E^2}{a_E^2}}} = \frac{1}{\sqrt{1 + \tan^2\gamma_E}} = \cos\gamma_E, \\
\frac{b_E}{\sqrt{a_E^2 + b_E^2}} &= \frac{1}{\sqrt{1 + \dfrac{a_E^2}{b_E^2}}} = \frac{\tan\gamma_E}{\sqrt{1 + \tan^2\gamma_E}} = \sin\gamma_E.
\end{aligned} \tag{2.15}$$

It is obvious that the polarization state of the electric field is completely determined by its polarization ratio. The complex quantity $P_E = \tan\theta^E e^{i\phi^E}$ characterizes the entire class of electric fields with different $|E_x|$, $|E_y|$ and ϕ_x^E, ϕ_y^E, but with the same $\tan\theta^E = |E_y| / |E_x|$, $\phi^E = \phi_y^E - \phi_x^E$ and hence with the same elliptic parameters α_E, γ_E which define the orientation and shape of the polarization ellipse. According to (2.13), (2.14)

$$\begin{aligned}
\tan 2\alpha_E &= \tan 2\theta^E \cos\phi^E \\
-\pi/2 &\le \alpha_E \le \pi/2 \\
\varepsilon_E = \tan\gamma_E \qquad & \sin 2\gamma_E = \sin 2\theta^E \sin\phi^E \\
-1 \le \varepsilon \le 1 \qquad & -\pi/4 \le \gamma_E \le \pi/4.
\end{aligned} \tag{2.16}$$

Converting these relationships, we get

$$\begin{aligned}
\cos 2\theta^E &= \cos 2\gamma_E \cos 2\alpha_E \quad 0 \le \theta^E \le \pi/2 \\
\tan\phi^E &= \tan 2\gamma_E \csc 2\alpha_E \quad -\pi < \phi^E \le \pi.
\end{aligned} \tag{2.17}$$

Similar formulae are available for the polarization ellipse of the magnetic field (Fig. 2.1b).

The angle α_H between the major axis of the magnetic ellipse and the x-axis can be determined from the equation

$$\tan 2\alpha_H = \frac{2\mathrm{Re}\,P_H}{1 - |P_H|^2} = \tan 2\theta^H \cos\phi^H \tag{2.18}$$

where α_H is taken within quadrant I ($0 \le \alpha_H \le \pi/2$) if $\cos\phi^H \ge 0$ or within quadrant IV ($0 > \alpha_H \ge -\pi/2$) if $\cos\phi^H < 0$.

For the magnetic field ***ellipticity*** and normalized semi-axes of polarization ellipse we have

$$\varepsilon_H = \frac{b_H}{a_H} = \frac{\sqrt{1+|P_H|^2+2\mathrm{Im}\ P_H}-\sqrt{1+|P_H|^2-2\mathrm{Im}\ P_H}}{\sqrt{1+|P_H|^2+2\mathrm{Im}\ P_H}+\sqrt{1+|P_H|^2-2\mathrm{Im}\ P_H}} = \tan\gamma_H$$
$$\frac{a_H}{\sqrt{a_H^2+b_H^2}} = \cos\gamma_H \qquad \frac{b_H}{\sqrt{a_H^2+b_H^2}} = \sin\gamma_H, \tag{2.19}$$

where

$$\gamma_H = \frac{1}{2}\arcsin(\sin 2\theta^H \sin\phi^H) \qquad -\pi/4 \le \gamma_H \le \pi/4$$

and

$$-1 < \epsilon_H < 1.$$

Polarization ellipses offer a geometrical image of the magnetotelluric field. The major axis of the polarization ellipse gives preferential direction of the field, while the field ellipticity defines the measure of this preference and the sense of the field rotation.

Using polarization descriptors, we can readily define the spatial relationships between complex field vectors.

The complex electric fields, $\mathbf{E}_{\tau 1}$ and $\mathbf{E}_{\tau 2,}$ are said to be orthogonal provided that their scalar product is equal to 0:

$$\mathbf{E}_{\tau 1} \cdot \mathbf{E}_{\tau 2} = E_{x1}\bar{E}_{x2} + E_{y1}\bar{E}_{y2} = 0. \tag{2.20}$$

Here

$$P_{E_1}\bar{P}_{E_2} = -1 \tag{2.21}$$

and, according to (2.13) and (2.14),

$$\alpha_{E_1} - \alpha_{E_2} = \pm\frac{\pi}{2} \qquad \varepsilon_{E_1} = -\varepsilon_{E_2} \qquad \gamma_{E_1} = -\gamma_{E_2}. \tag{2.22}$$

So, the orthogonal electric fields have the similar polarization ellipses with perpendicular major axes and the opposite sense of field rotation.

The same holds good for the orthogonal magnetic fields, $\mathbf{H}_{\tau 1}$ and $\mathbf{H}_{\tau 2}$:

$$\mathbf{H}_{\tau 1} \cdot \mathbf{H}_{\tau 2} = H_{x1}\bar{H}_{x2} + H_{y1}\bar{H}_{y2} = 0, \tag{2.23}$$

whence

$$P_{H_1}\bar{P}_{H_2} = -1 \tag{2.24}$$

and, according to (2.18) and (2.19),

$$\alpha_{H_1} - \alpha_{H_2} = \pm\frac{\pi}{2} \qquad \varepsilon_{H_1} = -\varepsilon_{H_2} \qquad \gamma_{H_1} = -\gamma_{H_2}. \tag{2.25}$$

Relationships of this kind are exemplified in Fig. 2.2a. They will be referred to as the *EE orthogonality* and *HH orthogonality*.

Next we will consider a special event when the complex fields $\mathbf{E}_\tau$, $\mathbf{H}_\tau$ satisfy equation which is valid for orthogonality of real vectors:

$$E_x H_x + E_y H_y = 0. \tag{2.26}$$

Here

$$P_E P_H = -1 \tag{2.27}$$

and, according to (2.13), (2.14) and (2.18), (2.19),

$$\alpha_E - \alpha_H = \pm\frac{\pi}{2} \qquad \varepsilon_E = \varepsilon_H. \tag{2.28}$$

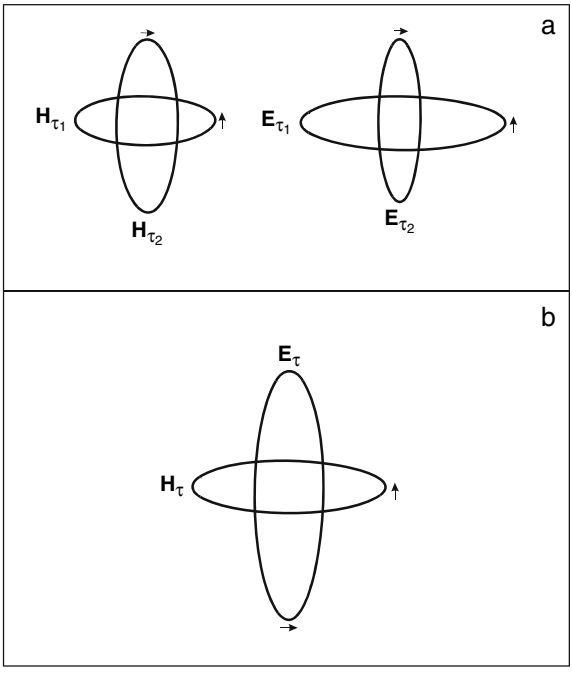

Fig. 2.2 Polarization ellipses of electric and magnetic eigenfields for *EE* and *HH* orthogonality (**a**) and *EH* quasi-orthogonality (**b**)

So, we have the similar polarization ellipses with perendicular major axes, but with the same sense of field rotation (Fig. 2.2b). Relationships of this kind will be referred to as the *EH quasi-orthogonality.*

With these definitions, we can enter into a discussion of basic approaches to the impedance eigenstate problem.

2.3 Basic Approaches to the Impedance Eigenstate Problem

The impedance eigenstate problem has been advanced by Sims and Bostick (1967), Eggers (1982), Spitz (1985), LaTorraca et al. (1986), Counil et al. (1986) and Yee and Paulson (1987). Entire gamut of different methods has been thoroughly reviewed by Yee and Paulson (1987), Groom and Bailey (1991) and Vozoff (1991).

In our book we will restrict ourselves to a close look at three most-used methods: (1) the Swift–Sims–Bostick method (the rotation approach), (2) the Swift–Eggers method (the modified classical approach), (3) the LaTorraca–Madden–Korringa method (the modified SVD approach). These methods determine the eigenstate of the three-dimensional impedance tensor so that the solution obtained satisfies one of the inherent properties of the two-dimensional impedance tensor.

Let us take a 2D-model with the strike along the x-axis. Here, according to (1.54),

$$[\mathbf{Z}] = \begin{bmatrix} 0 & Z^{\parallel} \\ -Z^{\perp} & 0 \end{bmatrix}, \tag{2.29}$$

whence

$$E_x = Z^{\parallel} H_y, \qquad E_y = -Z^{\perp} H_x. \tag{2.30}$$

It is natural to consider the longitudinal and transverse directions that run along and across the model strike as principal directions of $[\mathbf{Z}]$. In this context, the fields $\mathbf{E}_\tau$ and $\mathbf{H}_\tau$ linearly polarized along and across the model strike should be considered as eigenfields of $[\mathbf{Z}]$. The two-dimensional tensor $[\mathbf{Z}]$ has two pairs of the eigenfields:

$$\mathrm{TE-mode} \begin{cases} \mathbf{E}_{\tau 1} = \begin{bmatrix} E_{x1} \\ 0 \end{bmatrix} \\ \mathbf{H}_{\tau 1} = \begin{bmatrix} 0 \\ H_{y1} \end{bmatrix} \end{cases} \qquad \mathrm{TM-mode} \begin{cases} \mathbf{E}_{\tau 2} = \begin{bmatrix} 0 \\ E_{y2} \end{bmatrix} \\ \mathbf{H}_{\tau 2} = \begin{bmatrix} H_{x2} \\ 0 \end{bmatrix} \end{cases}. \tag{2.31}$$

In each pair, the electric eigenfield is the transform of the magnetic eigenfield:

$$\mathbf{E}_{\tau 1} = \zeta_1 \begin{bmatrix} 0 & 1 \\ -1 & 0 \end{bmatrix} \mathbf{H}_{\tau 1} \qquad \mathbf{E}_{\tau 2} = \zeta_2 \begin{bmatrix} 0 & 1 \\ -1 & 0 \end{bmatrix} \mathbf{H}_{\tau 2}, \tag{2.32}$$

where $\varsigma_1 = Z^{\parallel}$ and $\varsigma_2 = Z^{\perp}$ are the principal values (eigenvalues) of $[\mathbf{Z}]$.

These representations exhibit three inherent properties of the two-dimensional impedance tensor [**Z**]:

1. Tensor [**Z**], defined on its principal directions, has zero principal diagonal. By virtue of (2.29):

$$Z_{xx} = Z_{yy} = 0 \tag{2.33}$$

2. Eigenfields $\mathbf{E}_{\tau 1}$, $\mathbf{H}_{\tau 1}$ as well as eigenfields $\mathbf{E}_{\tau 2}$, $\mathbf{H}_{\tau 2}$ are quasi-orthogonal. At arbitrary orientation of the *x,y*-axes

$$\begin{aligned} E_{x1}H_{x1} + E_{y1}H_{y1} &= 0 \\ E_{x2}H_{x2} + E_{y2}H_{y2} &= 0, \end{aligned} \tag{2.34}$$

which is in agreement with (2.26). The tensor $\mathbf{E}_{\tau 2}$, $\mathbf{H}_{\tau 2}$ is characterized by the *EH* quasi-orthogonality of electric and magnetic eigenfields.

3. Eigenfields $\mathbf{E}_{\tau 1}$, $\mathbf{E}_{\tau 2}$ as well as eigenfields $\mathbf{H}_{\tau 1}$, $\mathbf{H}_{\tau 2}$ are orthogonal. At arbitrary orientation of the *x,y*-axes

$$\begin{aligned} E_{x1}\bar{E}_{x2} + E_{y1}\bar{E}_{y2} &= 0 \\ H_{x1}\bar{H}_{x2} + H_{y1}\bar{H}_{y2} &= 0, \end{aligned} \tag{2.35}$$

which is in agreement with (2.20) and (2.23). The tensor [**Z**] is characterized by the *EE* and *HH* orthogonality of electric and magnetic eigenfields.

The above properties of the two-dimensional impedance give a clue to generalization of the magnetotelluric eigenstate problem to the 3D model. Solving the 3D eigenstate problem, we attribute one of these properties to the three-dimensional impedance tensor. In the following we consider three methods of this kind. All these methods share the common property that in the case of a 2D medium they define the longitudinal and transverse directions as principal directions as well as the longitudinal and transverse impedances as principal impedances. In the general case of a 3D asymmetric medium they offer principal directions and principal impedances of an equivalent 2D tensor [**Z**].

2.4 The Swift–Sims–Bostick Method

This method has been proposed by Swift (1967) and advanced by Sims and Bostick (1967). The Swift–Sims–Bostick method (*SSB-method*) comes from (2.33) and reduces to the reference frame rotation that minimizes the principal diagonal components Z_{xx}, Z_{yy} of the impedance tensor [**Z**] obtained at the surface of a three-dimensional Earth. Sometimes the Swift–Sims–Bostick method (SSB method) is referred to as *rotation method*.

The parameter $M(\alpha)$ is introduced to characterize the relation between principal and secondary diagonal components, Z_{xx}, Z_{yy} and Z_{xy}, Z_{yx}, of the impedance tensor:

$$M(\alpha) = \frac{|\, Z_{xx}\,(\alpha)\,|^2 + |\, Z_{yy}\,(\alpha)\,|^2}{|\, Z_{xy}\,(\alpha)\,|^2 + |\, Z_{yx}\,(\alpha)\,|^2}. \tag{2.36}$$

Let us define the angle α, at which $M(\alpha)$ has a minimum. The condition

$$\frac{dM(\alpha)}{d\alpha} = 0 \text{ with } \frac{d^2 M(\alpha)}{d\alpha^2} > 0$$

results in the equation

$$\tan 4\alpha = \frac{2\,\mathrm{Re}\, Z_3 \bar{Z}_4}{|Z_4|^2 - |Z_3|^2} \tag{2.37}$$

with

$$2\mathrm{Re}\, Z_3 \bar{Z}_4 \sin 4\alpha + (|\, Z_4\,|^2 - |\, Z_3\,|^2)\cos 4\alpha < 0,$$

where $Z_3 = (Z_{xy} + Z_{yx})/2$ and $Z_4 = (Z_{xx} - Z_{yy})/2$.

This equation has two solutions, α_1 and $\alpha_2 = \alpha_1 + \pi/2$, which differ by $\pi/2$. Thus, we obtain two perpendicular directions, α_1 and α_2, with minimal principal diagonal, $Z_{xx}(\alpha_1)$, $Z_{yy}(\alpha_1)$ and $Z_{xx}(\alpha_2)$, $Z_{yy}(\alpha_2)$. These directions are considered as principal directions of the tensor $[\mathbf{Z}]$. The principal values of the tensor $[\mathbf{Z}]$ are obtained on the secondary diagonal as $\zeta_1 = Z_{xy}(\alpha_1) = -Z_{yx}(\alpha_2)$ and $\zeta_2 = -Z_{yx}(\alpha_1) = Z_{xy}(\alpha_2)$.

Thus, by the rotation method we derive five parameters:

$$|\zeta_1|\,,\ \xi_1 = \arg\zeta_1,\ \ |\zeta_2|\,,\ \xi_2 = \arg\zeta_2\,,\ \alpha_1, \tag{2.38}$$

which fill only five from eight degrees of freedom possessed by tensor $[\mathbf{Z}]$. So, the parameter space given by the rotation method is incomplete and this may result in ambiguity. Take for instance the tensor

$$[\mathbf{Z}] = \begin{bmatrix} Z_{xx} + \beta & Z_{xy} \\ Z_{yx} & Z_{yy} + \beta \end{bmatrix}$$

where β is an arbitrary quantity. To determine α_1 and calculate $Z_{xy}(\alpha_1)$, $Z_{yx}(\alpha_1)$ we use (2.37) and (1.27), but these equations contain only Z_1, Z_3, Z_4 which do not depend on β. Hence, we will receive the same principal directions and principal values for tensors $[\mathbf{Z}]$ with different β.

Let us consider the 2D and axially symmetric 3D-models. Here $\min M(\alpha) = 0$. So, the rotation method will give a tensor with zero principal diagonal and principal directions which coincide either with longitudinal and transverse directions or with tangential and radial directions.

Applying the rotation method to a real asymmetric medium, we look for direction, in which the tensor

$$[\mathbf{Z}] = \begin{bmatrix} Z_{xx}(\alpha) & Z_{xy}(\alpha) \\ Z_{yx}(\alpha) & Z_{yy}(\alpha) \end{bmatrix}$$

is best approximated by the tensor

$$[\tilde{\mathbf{Z}}] = \begin{bmatrix} 0 & Z_{xy}(\alpha) \\ Z_{yx}(\alpha) & 0 \end{bmatrix} = \begin{bmatrix} 0 & \zeta_1 \\ -\zeta_2 & 0 \end{bmatrix}.$$

The error of approximation can be evaluated using Euclidean norms of matrices $[\mathbf{Z} - \tilde{\mathbf{Z}}]$ and $[\mathbf{Z}]$:

$$\delta(\alpha) = \frac{||Z - \tilde{Z}||}{||Z||}$$

$$= \sqrt{\frac{| Z_{xx}(\alpha) |^2 + | Z_{yy}(\alpha) |^2}{| Z_{xx}(\alpha) |^2 + | Z_{xy}(\alpha) |^2 + | Z_{yx}(\alpha) |^2 + | Z_{yy}(\alpha) |^2}} = \sqrt{\frac{M(\alpha)}{1 + M(\alpha)}}. \tag{2.39}$$

So, the physical basis for this method is the approximation of a real asymmetric medium by the two-dimensional or axially symmetric medium. Such an approximation is justified if δ is sufficiently small (say, $\delta \leq 0.2$).

It is not unusual to receive large values for (for instance, $\delta > 0.5$). In that event we hardly can approximate the medium by two-dimensional or axisymmetric model. So, the physical basis for the rotation method is ruined and its application may lead to information losses.

To remove these limitations, we turn to the Swift–Eggers method or the LaTorraca–Madden–Korringa method. These methods are modifications of the standard methods of matrix algebra.

2.5 The Swift–Eggers Method

This method has been proposed by Swift (1967) and advanced by Eggers (1982). The Swift–Eggers method (*SE method*) can be considered as a modification of the classical approach shown in Sect. 2.1. Here we look for *EH* quasi-orthogonal magnetotelluric eigenfields, $\mathbf{E}_{\tau 1}$, $\mathbf{H}_{\tau 1}$ and $\mathbf{E}_{\tau 2}$, $\mathbf{H}_{\tau 2}$, which, according to (2.34), satisfy equation

$$E_{xm} H_{xm} + E_{ym} H_{ym} = 0, \qquad m = 1, 2. \tag{2.40}$$

Assume that

$$E_{x\,m} = \zeta_m H_{y\,m}, \qquad E_{y\,m} = -\zeta_m H_{x\,m}, \qquad m = 1, 2, \tag{2.41}$$

where ς_m is the complex principal value (eigenvalue, principal impedance) of the impedance tensor $[\mathbf{Z}]$.
Thus,

$$\mathbf{E}_{\tau m} = [\mathbf{Z}]\mathbf{H}_{\tau m} = \zeta_m \begin{bmatrix} 0 & 1 \\ -1 & 0 \end{bmatrix} \mathbf{H}_{\tau m}, \qquad m = 1, 2. \tag{2.42}$$

Rotating the magnetic eigenfield $\mathbf{H}_{\tau m}$ and the impedance $[\mathbf{Z}]$ through $\pm\pi/2$, we obtain the Adam formulation (1.16) of the eigenstate problem

$$[\overleftrightarrow{\mathbf{Z}}]\overleftrightarrow{\mathbf{H}}_{\tau m} = \zeta_m \overleftrightarrow{\mathbf{H}}_{\tau m}, \qquad m = 1, 2, \tag{2.43}$$

which coincides with the standard formulation (2.2). Here, with account for (1.1 6),

$$\overleftrightarrow{\mathbf{H}}_{\tau} = [\mathbf{R}(\pi/2)]\,\mathbf{H}_{\tau} = \begin{bmatrix} H_y \\ -H_x \end{bmatrix}$$

$$[\overleftrightarrow{\mathbf{Z}}] = [\mathbf{Z}][\mathbf{R}(-\pi/2)] = \begin{bmatrix} Z_{xy} & -Z_{xx} \\ Z_{yy} & -Z_{yx} \end{bmatrix}.$$

Writing (2.43) in full, we get

$$\begin{aligned} &Z_{xx} H_{x\,m} + (Z_{xy} - \zeta_m)\, H_{y\,m} = 0, \\ &(Z_{yx} + \zeta_m) H_{x\,m} + Z_{yy} H_{y\,m} = 0, \qquad m = 1, 2. \end{aligned} \tag{2.44}$$

Let the determinant of this uniform system be zero. Then

$$\zeta_m^2 - (Z_{xy} - Z_{yx})\zeta_m + (Z_{xx} Z_{yy} - Z_{xy} Z_{yx}) = 0, \qquad m = 1, 2. \tag{2.45}$$

Solving this characteristic equation, we find the complex principal values (eigenvalues) of the tensor $[\mathbf{Z}]$:

$$\begin{aligned} \zeta_1 &= \frac{Z_{xy} - Z_{yx} + \sqrt{(Z_{xy} - Z_{yx})^2 - 4(Z_{xx} Z_{yy} - Z_{xy} Z_{yx})}}{2} = \frac{1}{2}\left(\mathrm{I}_3 + \sqrt{\mathrm{I}_3^2 - 4\mathrm{I}_2}\right) \\ \zeta_2 &= \frac{Z_{xy} - Z_{yx} - \sqrt{(Z_{xy} - Z_{yx})^2 - 4(Z_{xx} Z_{yy} - Z_{xy} Z_{yx})}}{2} = \frac{1}{2}\left(\mathrm{I}_3 - \sqrt{\mathrm{I}_3^2 - 4\mathrm{I}_2}\right) \end{aligned} \tag{2.46}$$

expressed in terms of rotational invariants $\mathrm{I}_3 = \mathrm{tr}\left[\overleftrightarrow{\mathbf{Z}}\right] = Z_{xy} - Z_{yx}$ and $\mathrm{I}_2 = \det[\mathbf{Z}] = Z_{xx} Z_{yy} - Z_{xy} Z_{yx}$.

Moduli of principal values, $|\zeta_1|$ and $|\zeta_2|$, have a simple interpretation:

$$\sqrt{|E_{xm}|^2 + |E_{ym}|^2} = \sqrt{|\zeta_m H_{ym}|^2 + |\zeta_m H_{xm}|^2}$$
$$= |\zeta_m| \sqrt{|H_{xm}|^2 + |H_{ym}|^2}, \qquad m = 1, 2$$

whence

$$|\zeta_m| = \frac{\sqrt{|E_{xm}|^2 + |E_{ym}|^2}}{\sqrt{|H_{xm}|^2 + |H_{ym}|^2}}, \qquad m = 1,\ 2. \tag{2.47}$$

So, the moduli of principal impedances are the ratios between the Euclidean norms of the electric and magnetic eigenfields.

Next we should determine the principal directions of the tensor $[\mathbf{Z}]$. Here a special agreement is required. The point is that the electric and magnetic eigenfields, $\mathbf{E}_{\tau 1}$, $\mathbf{H}_{\tau 1}$ and $\mathbf{E}_{\tau 2}$, $\mathbf{H}_{\tau 2}$, are complex vectors. They can be characterized by directions of their real and imaginary parts or by orientation of their polarization ellipses. Let us define the principal directions of the impedance tensor as directions of the major axes of polarization ellipses for the electric eigenfields $\mathbf{E}_{\tau 1}$ and $\mathbf{E}_{\tau 2}$.

With (2.40) and (2.44), the polarization ratios for $\mathbf{E}_{\tau 1}$ and $\mathbf{E}_{\tau 2}$ are

$$P_{E_m} = \frac{E_{ym}}{E_{xm}} = -\frac{H_{xm}}{H_{ym}} = -\frac{\zeta_m - Z_{xy}}{Z_{xx}} = \frac{Z_{yy}}{\zeta_m + Z_{yx}} = -\frac{\zeta_m - Z_{xy} - Z_{yy}}{\zeta_m + Z_{xx} + Z_{yx}}, \qquad m = 1, 2. \tag{2.48}$$

Applying (2.13), we evaluate angles α_{E_1} and α_{E_2} made by major axes of the electric polarization ellipses with the x-axis:

$$\tan 2\alpha_{E_m} = \tan 2\theta^{E_m} \cos\phi^{E_m}, \qquad m = 1, 2, \tag{2.49}$$

where $\tan\theta^{E_m} = |P_{E_m}|$, $\phi^{E_m} = \arg P_{E_m}$. Note that the value of α_{E_m} is taken within quadrant I ($0 \le \alpha_{E_m} \le \pi/2$) if $\cos\phi^{E_m} \ge 0$ or within quadrant IV ($0 > \alpha_{E_m} \ge -\pi/2$) if $\cos\phi^{E_m} < 0$. The values of α_{E_1} and α_{E_2} indicate the directions of major axes of the electric polarization ellipses. These directions, determined modulo π, are considered as the principal directions of the magnetotelluric impedance tensor.

Finally we determine the ellipticity parameters ε_{E_1} and ε_{E_2}. In accord with (2.14),

$$\varepsilon_{E_m} = \tan\gamma_{E_m}, \qquad m = 1, 2 \tag{2.50}$$

where

$$\gamma_{E_m} = \frac{1}{2}\arcsin\left(\sin 2\theta^{E_m} \sin \phi^{E_m}\right) \qquad -\pi/4 \le \gamma_{E_m} \le \pi/4$$

and

$$-1 \le \varepsilon_{E_m} \le 1.$$

Thus, by the Swift–Eggers method we derive eight independent eigenstate parameters:

$$\begin{aligned} &|\varsigma_1|\,,\ \xi_1 = \arg\varsigma_1,\ \alpha_1 = \alpha_{E_1},\ \varepsilon_1 = \varepsilon_{E_1} \\ &|\varsigma_2|\,,\ \xi_2 = \arg\varsigma_2,\ \alpha_2 = \alpha_{E_2},\ \varepsilon_2 = \varepsilon_{E_2} \end{aligned} \tag{2.51}$$

which fill all eight degrees of freedom possessed by the matrix [**Z**].

There is a one-to-one correspondence between the impedance tensor and its principal values, principal directions and eigenfield ellipticities. Given ς_1, α_1, ε_1 and ς_2, α_2, ε_2, we can determine [**Z**]. The most simple are relationships between [**Z**] and ς_1, ς_2, P_{E_1}, P_{E_2}:

$$\begin{aligned} Z_{xx} &= \frac{\varsigma_2 - \varsigma_1}{P_{E_1} - P_{E_2}} & Z_{xy} &= \frac{P_{E_1}\varsigma_2 - P_{E_2}\varsigma_1}{P_{E_1} - P_{E_2}} \\ Z_{yx} &= \frac{P_{E_2}\varsigma_2 - P_{E_1}\varsigma_1}{P_{E_1} - P_{E_2}} & Z_{yy} &= \frac{P_{E_1}P_{E_2}(\varsigma_2 - \varsigma_1)}{P_{E_1} - P_{E_2}}\,. \end{aligned} \tag{2.52}$$

Here, with account for (2.9), (2.16) and (2.17),

$$P_{E_m} = \tan\theta_{E_m} e^{i\phi_m}, \qquad m = 1, 2,$$

where

$$\begin{aligned} \cos 2\theta^{E_m} &= \cos(2\arctan\varepsilon_{E_m})\cos 2\alpha_{E_m} \\ &\quad 0 \le \theta^{E_m} \le \pi/2 \\ \tan\phi^{E_m} &= \tan(2\arctan\varepsilon_{E_m})\csc 2\alpha_{E_m} \\ &\quad 0 \le \phi^{E_m} \le \pi \ \text{ if } \ 0 \le \varepsilon_{E_m} \le 1 \\ &\quad -\pi < \phi^{E_m} < 0 \quad \text{if } -1 \le \varepsilon_{E_m} < 0. \end{aligned}$$

Now we examine indications of the Swift–Eggers method in the models of different dimensionality.

In the 1D-model, we have $Z_{xx} = Z_{yy} = 0$ and $Z_{xy} = -Z_{yx} = Z$ where Z is the Tikhonov–Cagniard impedance. Here $\zeta_1 = \zeta_2 = Z$ and $P_{E_{1,2}} = 0/0$, $\alpha_{E_{1,2}} = 0/0$. The principal values of the tensor [**Z**] coincide with Tikhonov–Cagniard's

impedance, while the polarization ellipses and principal directions are indeterminate, since any magnetic field is transformed to a quasi-orthogonal electric field.

Take the 2D-model with the strike along the x-axis. Here $Z_{xx} = Z_{yy} = 0$ and $Z_{xy} = Z^{\parallel}$, $Z_{yx} = -Z^{\perp}$. With (2.46), (2.49), (2.50) we get $\zeta_1 = Z^{\parallel}$, $\zeta_2 = Z^{\perp}$ or $\zeta_1 = Z^{\parallel}$, $\zeta_2 = Z^{\perp}$ and $\alpha_1 = 0$, $\alpha_2 = \pi/2$ or $\alpha_1 = \pi/2$, $\alpha_2 = 0$ as well as $\varepsilon_{1,2} = 0$. The principal values of the tensor [**Z**] coincide with the longitudinal and the transverse impedances, while the principal directions are the longitudinal and transverse ones. The electric eigenfields are linearly polarized along the principal directions. At a single observation site, the Swift–Eggers method exposes the orientation of two-dimensional structures, though cannot distinguish between the longitudinal and transverse direction.

The similar situation is in the axially symmetric 3D-model. Here the tangential and radial impedances are the principal values of the tensor [**Z**], while the tangential and radial directions are its principal directions. The ellipticity of the electric eigenfields is zero. They are linearly polarized along principal directions.

Asymmetric 3D-structures manifest themselves in the elliptic polarization of the electric eigenfields ($\varepsilon_{1,2} \neq 0$) and in the violation of the perpendicularity of their ellipses ($|\alpha_1 - \alpha_2| \neq \pi/2$). A special case is a quasi-symmetric 3D-structure with $skew_S = 0$ and $skew_B \neq 0$. If $Z_{xx} + Z_{yy} = 0$, then it follows from (2.52) that $P_{E_1} P_{E_2} = -1$. Hence the electric eigenfields $\mathbf{E}_{\tau 1}$, $\mathbf{E}_{\tau 2}$ are quasi-orthogonal and $|\alpha_1 - \alpha_2| = \pi/2$.

Using the Swift–Eggers method, we can define three characeristic parameters which reveal the lateral inhomogeneities and indicate their dimensionality:

(1) the parameter of inhomogeneity

$$N = \frac{\zeta_1 - \zeta_2}{\zeta_1 + \zeta_2} \tag{2.53}$$

In the 1D-model we have $N = 0$. Departure of N from 0 is a measure of lateral inhomogeneity.

(2) the angular parameter of asymmetry (angular skew)

$$skew_{ang} = ||\alpha_1 - \alpha_2| - \pi/2| \,. \tag{2.54}$$

In the 2D-model as well as in the axially symmetric and quasi-symmetric 3D-models we have $skew_{ang} = 0$. Departure of $skew_{ang}$ from 0 is a measure of geoelectric asymmetry.

(3) the polarization parameter of asymmetry (polarization skew)

$$skew_{pol} = \frac{|\varepsilon_1| + |\varepsilon_2|}{2}. \tag{2.55}$$

In the 2D-model and axially symmetric 3D-model we have $skew_{pol} = 0$ indicating linear polarization of electric eigenfields. Departure of $skew_{pol}$ from 0 is a measure of geoelectric asymmetry.

It would be interesting to find relations between the principal values of the impedance tensor [**Z**] and scalar rotationally invariant impedances Z_{eff} and Z_{brd} introduced by (1.30). The effective impedance can be defined as the geometric mean of the principal impedances:

$$Z_{\text{eff}} = \sqrt{\zeta_1\,\zeta_2} = \sqrt{\det\,[\mathbf{Z}]} = \sqrt{Z_{xx}\,Z_{yy} - Z_{xy}\,Z_{yx}}. \tag{2.56}$$

The Berdichevsky impedance can be defined as the arithmetic mean of the principal impedances:

$$Z_{\text{brd}} = \frac{\zeta_1 + \zeta_2}{2} = \frac{Z_{xy} - Z_{yx}}{2}. \tag{2.57}$$

The principal impedances give rise to the *principal apparent resistivity* and *principal phase* curves:

$$\begin{aligned} \rho_1 &= \frac{|\,\zeta_1\,|^2}{\omega\,\mu_0} \qquad & \rho_2 &= \frac{|\,\zeta_2\,|^2}{\omega\,\mu_0} \\ \phi_1 &= \arg\zeta_1 = \xi_1 \qquad & \phi_2 &= \arg\zeta_2 = \xi_2\,. \end{aligned} \tag{2.58}$$

The $\rho_1,\ \rho_2$- and $\varphi_1,\ \varphi_2$-curves are oriented along the principal directions of the impedance tensor. Unfortunately, their orientation may vary with frequency. Therefore the principal MT-curves should be considered together with curves of $\alpha_1,\ \alpha_2$.

In parallel with principal MT-curves we can plot the effective MT-curves

$$\rho_{\text{eff}} = \frac{|\,Z_{\text{eff}}\,|^2}{\omega\mu_0} \qquad \varphi_{\text{eff}} = \arg Z_{\text{eff}} \tag{2.59}$$

and the Berdichevsky MT-curves

$$\rho_{\text{brd}} = \frac{|\,Z_{\text{brd}}\,|^2}{\omega\mu_0} \qquad \varphi_{\text{brd}} = \arg\,Z_{\text{brd}}\,. \tag{2.60}$$

2.6 The La Torraca–Madden–Korringa Method

The method offers a potent alternative to the Swift–Eggers method. It is based on the SVD (singular value decomposition) theorem of Lanczos (1961). The fundamental work in this area was done by LaTorraca et al. (1986) as well as by Yee and Paulson (1987). Applying the LaTorraca–Madden–Korringa method (*LMK method*), we look for *EE* and *HH* orthogonal magnetotelluric eigenfields $\mathbf{E}_{\tau 1},\ \mathbf{H}_{\tau 1}$ and $\mathbf{E}_{\tau 2},\ \mathbf{H}_{\tau 2}$, which, according to (2.20), (2.21) and (2.23), (2.24), satisfy equations

$$\begin{aligned}
&\mathbf{E}_{\tau m} = [\mathbf{Z}]\mathbf{H}_{\tau m}, \quad m = 1,\ 2 \\
&\mathbf{E}_{\tau 1} \cdot\ \mathbf{E}_{\tau 2} = E_{x1}\bar{E}_{x2} + E_{y1}\bar{E}_{y2} = 0 \qquad P_{E_1}\bar{P}_{E_2} = -1 \\
&\mathbf{H}_{\tau 1} \cdot\ \mathbf{H}_{\tau 2} = H_{x1}\bar{H}_{x2} + H_{y1}\bar{H}_{y2} = 0 \qquad P_{H_1}\bar{P}_{H_2} = -1\,.
\end{aligned} \tag{2.61}$$

Let us express these magnetotelluric eigenfields in terms of the polarization descriptors $\alpha_E,\ \alpha_H$ (α is an angle made by the major axis of polarization ellipse with the x-axis) and $\varepsilon_E,\ \varepsilon_H$($\varepsilon$ is a ratio between the minor, b, and major, a, semi-axes of polarization ellipse).

In conformity with (2.13), (2.18) and (2.23), (2.25),

$$\begin{aligned}
&\tan 2\alpha_{E_1} = \tan 2\theta^{E_1}\cos\phi^{E_1} \qquad &&\alpha_{E_2} = \alpha_{E_1} + \frac{\pi}{2} \\
&\tan 2\alpha_{H_1} = \tan 2\theta^{H_1}\cos\phi^{H_1} \qquad &&\alpha_{H_2} = \alpha_{H_1} + \frac{\pi}{2}\ ,
\end{aligned} \tag{2.62}$$

where $\tan\theta^{E_1} = \left|P_{E_1}\right|$, $\phi^{E_1} = \arg P_{E_1}$ and $\tan\theta^{H_1} = \left|P_{H_1}\right|$, $\phi^{H_1} = \arg P_{H_1}$. Here α_{E_1} is taken within quadrant I ($0 \le \alpha_{E_1} \le \pi/2$) if $\cos\phi^{E_1} \ge 0$ or within quadrant IV ($0 > \alpha_{E_1} \ge -\pi/2$) if $\cos\phi^{E_1} < 0$, while α_{H_1} is taken within quadrant I ($0 \le \alpha_{H_1} \le \pi/2$) or quadrant III ($\pi \le \alpha_{H_1} \le 3\pi/2$) if $\cos\phi^{H_1} \ge 0$, and within quadrant IV ($0 > \alpha_{H_1} \ge -\pi/2$) or quadrant II ($\pi > \alpha_{H_1} \ge \pi/2$) if $\cos\phi^{H_1} < 0$. So, we determine an acute angle α_{E_1} and have freedom in choosing either acute or blunt angle α_{H_1} to suit proper relationship between electric and magnetic eigenfields.

In the same vein, according to (2.14), (2.19) and (2.22), (2.25),

$$\begin{aligned}
&\varepsilon_{E_1} = \tan\gamma_{E_1} \quad \varepsilon_{E_2} = -\varepsilon_{E_1} \quad \gamma_{E_2} = -\gamma_{E_1} \\
&\varepsilon_{H_1} = \tan\gamma_{H_1} \quad \varepsilon_{H_2} = -\varepsilon_{H_1} \quad \gamma_{H_2} = -\gamma_{H_1}\ ,
\end{aligned} \tag{2.63}$$

where

$$\gamma_{E_1} = \frac{1}{2}\arcsin(\sin 2\theta^{E_1}\sin\phi^{E_1}) \qquad \gamma_{H_1} = \frac{1}{2}\arcsin(\sin 2\theta^{H_1}\sin\phi^{H_1})$$

with $-\pi/4 \le \gamma \le \pi/4$ and $-1 \le \epsilon \le 1$.

Using these definitions, we can introduce orthonormal basises $\mathbf{e}_1,\ \mathbf{e}_2$ and $\mathbf{h}_1,\ \mathbf{h}_2$ into the spaces of electric and magnetic fields. To this end, we normalize the eigenfields $\mathbf{E}_{\tau 1}, \mathbf{E}_{\tau 2}$ and $\mathbf{H}_{\tau 1}, \mathbf{H}_{\tau 2}$ to $\sqrt{a^2 + b^2}$ and multiply them by a phase factor $e^{-i\beta}$ such that their real and imaginary vectors coincide with major a and minor b semi-axes of corresponding polarization ellipse. With account for (2.15) and (2.19), we write

$$\mathbf{e}_1 = \frac{\mathbf{E}_{\tau 1} e^{-i\beta'_E}}{\sqrt{a_{E_1}^2 + b_{E_1}^2}} = \frac{a_{E_1}\mathbf{1}'_{a_E} + i b_{E_1}\mathbf{1}'_{b_E}}{\sqrt{a_{E_1}^2 + b_{E_1}^2}} = \mathbf{cos}\,\gamma_{E_1}\mathbf{1}'_{a_E} + i\mathbf{sin}\,\gamma_{E_1}\mathbf{1}'_{b_E}$$

$$\mathbf{h}_1 = \frac{\mathbf{H}_{\tau 1} e^{-i\beta'_H}}{\sqrt{a_{H_1}^2 + b_{H_1}^2}} = \frac{a_{H_1}\mathbf{1}'_{a_H} + i b_{H_1}\mathbf{1}'_{b_H}}{\sqrt{a_{H_1}^2 + b_{H_1}^2}} = \mathbf{cos}\,\gamma_{H_1}\mathbf{1}'_{a_H} + i\mathbf{sin}\gamma_{H_1}\mathbf{1}'_{b_H}$$

$$\mathbf{e}_2 = \frac{\mathbf{E}_{\tau 2} e^{-i\beta''_E}}{\sqrt{a_{E_2}^2 + b_{E_2}^2}} = \frac{a_{E_2}\mathbf{1}''_{a_E} + i b_{E_2}\mathbf{1}''_{b_E}}{\sqrt{a_{E_2}^2 + b_{E_2}^2}} = \mathbf{cos}\,\gamma_{E_2}\mathbf{1}''_{a_E} + i\mathbf{sin}\,\gamma_{E_2}\mathbf{1}''_{b_E} \tag{2.64}$$

$$\mathbf{h}_2 = \frac{\mathbf{H}_{\tau 2} e^{-i\beta''_H}}{\sqrt{a_{H_2}^2 + b_{H_2}^2}} = \frac{a_{H_2}\mathbf{1}''_{a_H} + i b_{H_2}\mathbf{1}''_{b_H}}{\sqrt{a_{H_2}^2 + b_{H_2}^2}} = \mathbf{cos}\,\gamma_{H_2}\mathbf{1}''_{a_H} + i\mathbf{sin}\gamma_{H_2}\mathbf{1}''_{b_H},$$

where $\mathbf{1}'_{a_E}$, $\mathbf{1}'_{a_H}$, $\mathbf{1}''_{a_E}$, $\mathbf{1}''_{a_H}$ and $\mathbf{1}'_{b_E}$, $\mathbf{1}'_{b_H}$, $\mathbf{1}''_{b_E}$, $\mathbf{1}''_{b_H}$ are unit vectors oriented along major and minor semi-axes.

The components of normalized eigenfields $\mathbf{e}_1$, $\mathbf{h}_1$ are

$$\begin{aligned} e_{1x} &= \cos\gamma_{E_1}\cos\alpha_{E_1} - i\sin\gamma_{E_1}\sin\alpha_{E_1} \\ e_{1y} &= \cos\gamma_{E_1}\sin\alpha_{E_1} + i\sin\gamma_{E_1}\cos\alpha_{E_1} \\ h_{1x} &= \cos\gamma_{H_1}\cos\alpha_{H_1} - i\sin\gamma_{H_1}\sin\alpha_{H_1} \\ h_{1y} &= \cos\gamma_{H_1}\sin\alpha_{H_1} + i\sin\gamma_{H_1}\cos\alpha_{H_1}\,. \end{aligned} \tag{2.65}$$

Taking into account (2.62) and (2.63), the components of normalized eigenfields $\mathbf{e}_2$, $\mathbf{h}_2$ can be written as

$$\begin{aligned} e_{2x} &= -\cos\gamma_{E_1}\sin\alpha_{E_1} + i\sin\gamma_{E_1}\cos\alpha_{E_1} \\ e_{2y} &= \cos\gamma_{E_1}\cos\alpha_{E_1} + i\sin\gamma_{E_1}\sin\alpha_{E_1} \\ h_{2x} &= -\cos\gamma_{H_1}\sin\alpha_{H_1} + i\sin\gamma_{H_1}\cos\alpha_{H_1} \\ h_{2y} &= \cos\gamma_{H_1}\cos\alpha_{H_1} + i\sin\gamma_{H_1}\sin\alpha_{H_1}\,. \end{aligned} \tag{2.66}$$

Equations (2.65) and (2.66) have π-ambiguity in α_{H_1}, which leads to π-ambiguity in phases of principal values of the impedance tensor. To remove this ambiguity, we assume that the Earth is everywhere passive and the real part of the complex Pointing vector calculated from $\mathbf{E}_{\tau 1}$ and $\mathbf{H}_{\tau 1}$ as well as from $\mathbf{e}_1$ and $\mathbf{h}_1$ cannot be directed upwards:

$$\mathrm{Re}\,(\mathbf{e}_1 \times \bar{\mathbf{h}}_1)_z \geq 0\,. \tag{2.67}$$

Substituting (2.65) into (2.67), we get

$$\sin(\alpha_{H_1} - \alpha_{E_1})\cos(\gamma_{H_1} - \gamma_{E_1}) \geq 0.$$

Since γ_{E_1} and γ_{H_1} are limited by $\pm\pi/4$, it is evident that $\cos(\gamma_{H_1} - \gamma_{E_1})$ is nonnegative by definition. Thus, the condition (2.67) is satisfied when $\sin(\alpha_{H_1} - \alpha_{E_1}) \geq 0$, that is, when orientation of the magnetic and electric polarization ellipses meets the condition

$$\alpha_{E_1} \leq \alpha_{H_1} \leq \alpha_{E_1} + \pi. \tag{2.68}$$

Let us consider properties of normalized eigenfields $\mathbf{e}_1$, $\mathbf{h}_1$ and $\mathbf{e}_2$, $\mathbf{h}_2$.
According to (2.64)

$$\begin{aligned} P_{e_m} &= \frac{e_{ym}}{e_{xm}} = \frac{E_{ym}}{E_{xm}} = P_{E_m}, \\ P_{h_m} &= \frac{h_{ym}}{h_{xm}} = \frac{H_{ym}}{H_{xm}} = P_{H_m}, \quad m = 1, 2. \end{aligned} \tag{2.69}$$

Vectors $\mathbf{e}_m$, $\mathbf{h}_m$ have the same polarization ratios as initial eigenfield vectors $\mathbf{E}_{\tau m}$, $\mathbf{H}_{\tau m}$. Hence all parameters characterizing polarization of the electric and magnetic eigenfields can be calculated from P_{e_m}, P_{h_m}.

What we have to stress is that vectors $\mathbf{e}_1$ and $\mathbf{e}_2$ as well as vectors $\mathbf{h}_1$ and $\mathbf{h}_2$ are orthonormal:

$$\mathbf{e}_m \cdot \mathbf{e}_n = \delta_{mn}, \qquad \mathbf{h}_m \cdot \mathbf{h}_n = \delta_{mn}, \tag{2.70}$$

where

$$\delta_{mn} = \begin{cases} 1 & m = n \\ 0 & m \neq n\,. \end{cases}$$

We represent normalized eigenfields $\mathbf{e}_1$, $\mathbf{e}_2$ and $\mathbf{h}_1$, $\mathbf{h}_2$ by matrices

$$[\mathbf{U}_e] = \begin{bmatrix} e_{1x} & e_{2x} \\ e_{1y} & e_{2y} \end{bmatrix}, \qquad [\mathbf{U}_h] = \begin{bmatrix} h_{1x} & h_{2x} \\ h_{1y} & h_{2y} \end{bmatrix} \tag{2.71}$$

forming orthonormal basises in the spaces of electric and magnetic fields. The conjugate matrices are

$$\overline{[\mathbf{U}_e]} = \begin{bmatrix} \bar{e}_{1x} & \bar{e}_{1y} \\ \bar{e}_{2x} & \bar{e}_{2y} \end{bmatrix}, \qquad \overline{[\mathbf{U}_h]} = \begin{bmatrix} \bar{h}_{1x} & \bar{h}_{1y} \\ \bar{h}_{2x} & \bar{h}_{2y} \end{bmatrix}. \tag{2.72}$$

By virtue of (2.70)

$$\overline{[\mathbf{U}_e]}\,[\mathbf{U}_e] = [\mathbf{U}_e]\overline{[\mathbf{U}_e]} = [\mathbf{I}]\,, \qquad \overline{[\mathbf{U}_h]}\,[\mathbf{U}_h] = [\mathbf{U}_h]\overline{[\mathbf{U}_h]} = [\mathbf{I}]\,, \tag{2.73}$$

where $[\mathbf{I}]$ is the identity matrix

$$[\mathbf{I}] = \begin{bmatrix} 1 & 0 \\ 0 & 1 \end{bmatrix}.$$

This implies that $[\mathbf{U}_e]$ and $[\mathbf{U}_h]$ are unitary matrices: their conjugate matrices coincide with their inverse matrices and they are commutative with their conjugate matrices.

Now we shall derive impedance equation for the normalized eigenfields. According to (2.64),

$$\mathbf{E}_{\tau 1} = \sqrt{a_{E_1}^2 + b_{E_1}^2}\, e^{i\beta'_E}\, \mathbf{e}_1 \qquad \mathbf{H}_{\tau 1} = \sqrt{a_{H_1}^2 + b_{H_1}^2}\, e^{i\beta'_H} \mathbf{h}_1$$

$$\mathbf{E}_{\tau 2} = \sqrt{a_{E_2}^2 + b_{E_2}^2}\, e^{i\beta''_E}\, \mathbf{e}_2 \qquad \mathbf{H}_{\tau 2} = \sqrt{a_{H_2}^2 + b_{H_2}^2}\, e^{i\beta''_H} \mathbf{h}_2\,.$$

Substituting these relations into the equation $\mathbf{E}_{\tau m} = [\mathbf{Z}]\,\mathbf{H}_{\tau m}$, $m = 1, 2$, we write

$$[\mathbf{Z}]\,\mathbf{h}_1 = \zeta_1 \mathbf{e}_1, \qquad [\mathbf{Z}]\,\mathbf{h}_2 = \zeta_2 \mathbf{e}_2, \tag{2.74}$$

where

$$\zeta_1 = \frac{\sqrt{a_{E_1}^2 + b_{E_1}^2}}{\sqrt{a_{H_1}^2 + b_{H_1}^2}} e^{i\,(\beta'_E - \beta'_H)}, \qquad \zeta_2 = \frac{\sqrt{a_{E_2}^2 + b_{E_2}^2}}{\sqrt{a_{H_2}^2 + b_{H_2}^2}} e^{i\,(\beta''_E - \beta''_H)}\,.$$

In matrix form

$$[\mathbf{Z}]\,[\mathbf{U}_h] = [\mathbf{U}_e]\,[\zeta]\,, \tag{2.75}$$

where $[\zeta]$ is a diagonal matrix:

$$[\zeta] = \begin{bmatrix} \zeta_1 & 0 \\ 0 & \zeta_2 \end{bmatrix}.$$

Multiplying (2.75) on the right by $\overline{[\mathbf{U}_h]}$, we get

$$[\mathbf{Z}] = [\mathbf{U}_e][\zeta]\,\overline{[\mathbf{U}_h]} \tag{2.76}$$

This decomposition of the impedance matrix differs from the standard singular value decomposition, SVD, in that the diagonal elements ζ_1 and ζ_2 of $[\zeta]$ are complex. Let us keep the standard SVD terminology and call these values the complex singular values. In the La Torraca–Madden–Korringa method the complex singular values, ζ_1 and ζ_2, are considered as principal values of the impedance tensor.

Matrix equation (2.76) has eight unknowns quantities (polarization parameters, α_{E_1}, γ_{E_1}, α_{H_1}, γ_{H_1}, and complex singular values, ζ_1 and ζ_2) against eight known quantities (complex components, Z_{xx}, Z_{xy}, Z_{yx}, Z_{yy}).

Moduli of complex singular values and polarization parameters are readily derived by standard SVD procedure. Introduce matrices

$$
\begin{aligned}
[\mathbf{C}_E] &= [\mathbf{Z}]\,\overline{[\mathbf{Z}]} = \begin{bmatrix} Z_{xx} & Z_{xy} \\ Z_{yx} & Z_{yy} \end{bmatrix} \begin{bmatrix} \bar{Z}_{xx} & \bar{Z}_{yx} \\ \bar{Z}_{xy} & \bar{Z}_{yy} \end{bmatrix} = \begin{bmatrix} |Z_{xx}|^2 + \left|Z_{xy}\right|^2 & Z_{xx}\bar{Z}_{yx} + Z_{xy}\bar{Z}_{yy} \\ \bar{Z}_{xx}Z_{yx} + \bar{Z}_{xy}Z_{yy} & \left|Z_{yx}\right|^2 + \left|Z_{yy}\right|^2 \end{bmatrix} \\
[\mathbf{C}_H] &= \overline{[\mathbf{Z}]}\,[\mathbf{Z}] = \begin{bmatrix} \bar{Z}_{xx} & \bar{Z}_{yx} \\ \bar{Z}_{xy} & \bar{Z}_{yy} \end{bmatrix} \begin{bmatrix} Z_{xx} & Z_{xy} \\ Z_{yx} & Z_{yy} \end{bmatrix} = \begin{bmatrix} |Z_{xx}|^2 + \left|Z_{yx}\right|^2 & \bar{Z}_{xx}Z_{xy} + \bar{Z}_{yx}Z_{yy} \\ Z_{xx}\bar{Z}_{xy} + Z_{yx}\bar{Z}_{yy} & \left|Z_{xy}\right|^2 + \left|Z_{yy}\right|^2 \end{bmatrix},
\end{aligned}
\tag{2.77}
$$

where $[\mathrm{Z}] = [\mathbf{U}_e][\zeta]\,\overline{[\mathbf{U}_h]}$ and $\overline{[\mathrm{Z}]} = [\mathbf{U}_h]\overline{[\zeta]}\,\overline{[\mathbf{U}_e]}$. Here

$$
\begin{aligned}
\operatorname{tr}[\mathbf{C}_E] = \operatorname{tr}[\mathbf{C}_H] &= |Z_{xx}|^2 + \left|Z_{xy}\right|^2 + \left|Z_{yx}\right|^2 + \left|Z_{yy}\right|^2 = \|\mathbf{Z}\|^2\,, \\
\det[\mathbf{C}_E] = \det[\mathbf{C}_H] &= \left|Z_{xx}Z_{yy} - Z_{xy}Z_{yx}\right|^2 = |\det[\mathbf{Z}]|^2\,,
\end{aligned}
\tag{2.78}
$$

where $\|\mathbf{Z}\|$ and $\det[\mathbf{Z}]$ are the Euclidean norm and determinant of the matrix $[\mathbf{Z}]$.

It is seen that $[\mathbf{C}_E]$ and $[\mathbf{C}_H]$ are Hermitian matrices: their principal diagonal elements are real, while the secondary diagonal elements are complex conjugate. The remarkable feature of Hermitian matrices is that their eigenvalues are real. In fact,

$$
\begin{aligned}
[\mathbf{C}_E] &= [\mathbf{U}_e][\zeta]\,\overline{[\mathbf{U}_h]}\,[\mathbf{U}_h]\overline{[\zeta]}\,\overline{[\mathbf{U}_e]} = [\mathbf{U}_e][\boldsymbol{\Sigma}]\,\overline{[\mathbf{U}_e]}, \\
[\mathbf{C}_H] &= [\mathbf{U}_h]\overline{[\zeta]}\,\overline{[\mathbf{U}_e]}\,[\mathbf{U}_e][\zeta]\,\overline{[\mathbf{U}_h]} = [\mathbf{U}_h][\boldsymbol{\Sigma}]\,\overline{[\mathbf{U}_h]},
\end{aligned}
$$

whence

$$
\begin{aligned}
[\mathbf{C}_E]\,[\mathbf{U}_e] &= [\mathbf{U}_e]\,[\boldsymbol{\Sigma}]\,, \\
[\mathbf{C}_H]\,[\mathbf{U}_h] &= [\mathbf{U}_h]\,[\mathbf{S}]\,,
\end{aligned}
\tag{2.79}
$$

where

$$
[\boldsymbol{\Sigma}] = \begin{bmatrix} |\zeta_1|^2 & 0 \\ 0 & |\zeta_2|^2 \end{bmatrix}.
$$

This matrix equation breaks down into four equations, which conform to classical eigenstate formulation (2.2):

$$\begin{aligned} [\mathbf{C}_E]\,\mathbf{e}_1 &= |\zeta_1|^2\,\mathbf{e}_1 \qquad & [\mathbf{C}_E]\,\mathbf{e}_2 &= |\zeta_2|^2\,\mathbf{e}_2 \\ [\mathbf{C}_H]\,\mathbf{h}_1 &= |\zeta_1|^2\,\mathbf{h}_1 \qquad & [\mathbf{C}_H]\,\mathbf{h}_2 &= |\zeta_2|^2\,\mathbf{h}_2\ . \end{aligned} \tag{2.80}$$

It is apparent that $|\zeta_1|^2$, $|\zeta_2|^2$ are eigenvalues of matrices $[\mathbf{C}_E]$, $[\mathbf{C}_H]$, while $\mathbf{e}_1$, $\mathbf{e}_2$ and $\mathbf{h}_1$, $\mathbf{h}_2$ are their eigenvectors.

In line with (2.5) and (2.78), we get

$$\begin{aligned} |\,\zeta_1|^2 &= \frac{\|\mathbf{Z}\|^2 + \sqrt{\|\mathbf{Z}\|^4 - 4\,|\det[\mathbf{Z}]\,|^2}}{2} = \frac{J_{11}^2 + \sqrt{J_{11}^4 - 4\,|\mathrm{I}_2|^2}}{2} \\ |\,\zeta_2|^2 &= \frac{\|\mathbf{Z}\|^2 - \sqrt{\|\mathbf{Z}\|^4 - 4\,|\det[\mathbf{Z}]\,|^2}}{2} = \frac{J_{11}^2 - \sqrt{J_{11}^4 - 4\,|\mathrm{I}_2|^2}}{2}\,, \end{aligned} \tag{2.81}$$

where ζ_1 and ζ_2 are the complex principal values of the impedance tensor $[\mathbf{Z}]$. Moduli of ζ_1 and ζ_2 are expressed in terms of rotational invariants $\mathrm{I}_2 = \det[\mathrm{Z}] = Z_{xx}Z_{yy} - Z_{xy}Z_{yx}$ and $J_{11} = \|\mathbf{Z}\| = \sqrt{|Z_{xx}|^2 + |Z_{xy}|^2 + |Z_{yx}|^2 + |Z_{yy}|^2}$. They are independent of the orientation of measurement axes. Note that $|\zeta_1| \geq |\zeta_2|$.

Similarly, in the line with (2.4) (2.69) and (2.77), we get

$$\begin{aligned} P_{E_1} &= \frac{|\zeta_1|^2 - |Z_{xx}|^2 - |Z_{xy}|^2}{Z_{xx}\bar{Z}_{yx} + Z_{xy}\bar{Z}_{yy}} = \frac{\bar{Z}_{xx}Z_{yx} + \bar{Z}_{xy}Z_{yy}}{|\zeta_1|^2 - |Z_{yx}|^2 - |Z_{yy}|^2} \\ &= \frac{|\zeta_1|^2 - |Z_{xx}|^2 - |Z_{xy}|^2 + \bar{Z}_{xx}Z_{yx} + \bar{Z}_{xy}Z_{yy}}{|\zeta_1|^2 - |Z_{yx}|^2 - |Z_{yy}|^2 + Z_{xx}\bar{Z}_{yx} + Z_{xy}\bar{Z}_{yy}}, \\ P_{H_1} &= \frac{|\zeta_1|^2 - |Z_{xx}|^2 - |Z_{yx}|^2}{\bar{Z}_{xx}Z_{xy} + \bar{Z}_{yx}Z_{yy}} = \frac{Z_{xx}\bar{Z}_{xy} + Z_{yx}\bar{Z}_{yy}}{|\zeta_1|^2 - |Z_{xy}|^2 - |Z_{yy}|^2} \\ &= \frac{|\zeta_1|^2 - |Z_{xx}|^2 - |Z_{yx}|^2 + Z_{xx}\bar{Z}_{xy} + Z_{yx}\bar{Z}_{yy}}{|\zeta_1|^2 - |Z_{xy}|^2 - |Z_{yy}|^2 + \bar{Z}_{xx}Z_{xy} + \bar{Z}_{yx}Z_{yy}}. \end{aligned} \tag{2.82}$$

Knowing P_{E_1} and P_{H_1}, we use (2.62), (2.63) and taking into account (2.68) derive principal directions, α_{E_1} and α_{H_1}, as well as ellipticities, ε_{E_1} and ε_{H_1}.

It remains to determine phases of the principal values. According to (2.74),

$$\begin{aligned} \xi_1 &= \arg \zeta_1 = \arg \frac{Z_{xx} h_{x1} + Z_{xy} h_{y1}}{e_{x1}} \\ \xi_2 &= \arg \zeta_2 = \arg \frac{Z_{xx} h_{x2} + Z_{xy} h_{y2}}{e_{x2}}, \end{aligned} \tag{2.83}$$

where the components of vectors $\mathbf{e}$, $\mathbf{h}$ are obtained by (2.65) and (2.66) with α, γ, known from (2.62), (2.63), (2.69). It is easy to show that ξ_1 and ξ_2 are rotationally invariant.

Thus, the La Torraca–Madden–Korringa method results in eight independent eigenstate parameters:

$$\begin{aligned} &|\zeta_1|, \ \xi_1 = \arg \zeta_1, \ \alpha_1 = \alpha_{E_1}, \ \varepsilon_1 = \varepsilon_{E_1} \\ &|\zeta_2|, \ \xi_2 = \arg \zeta_2, \ \alpha_2 = \alpha_{H_1}, \ \varepsilon_2 = \varepsilon_{H_1}, \end{aligned} \tag{2.84}$$

which fill all eight degrees of freedom possessed by the matrix $[\mathbf{Z}]$.

There is a one-to-one correspondence between the impedance tensor and its principal values, principal directions and eigenfield ellipticities. Given ζ_1, α_1, ε_1 and ζ_2, α_2, ε_2, we can determine $[\mathbf{Z}]$ using (2.76).

Let us examine indications of the La Torraca–Madden–Korringa method in models of different dimensionality.

In the 1D-model, we have $Z_{xx} = Z_{yy} = 0$ and $Z_{xy} = -Z_{yx} = Z$ where Z is the Tikhonov–Cagniard impedance. Here we get $|\zeta_1| = |\zeta_2| = |Z|$. All other definitions are not unique, since $P_{E_1} = 0/0$ and $P_{H_1} = 0/0$ (any orthogonal magnetic fields are transformed to orthogonal electric fields).

Turn to the 2D-model with the strike along the x-axis. Here $Z_{xx} = Z_{yy} = 0$ and $Z_{xy} = Z^{\parallel}$, $Z_{yx} = -Z^{\perp}$. With (2.62), (2.63) and (2.81), (2.83) we get $\zeta_1 = Z^{\parallel}$, $\zeta_2 = Z^{\perp}$ or $\zeta_1 = Z^{\perp}$, $\zeta_2 = Z^{\parallel}$ and $\alpha_1 = 0$, $\alpha_2 = \pi/2$ or $\alpha_1 = \pi/2$, $\alpha_2 = 0$ as well as $\varepsilon_{1,2} = 0$. The principal values of the tensor $[\mathbf{Z}]$ coincide with the longitudinal and the transverse impedances, while the principal directions are the longitudinal and transverse directions. The electric and magnetic eigenfields are linearly polarized along the principal directions. Note that 2D indications, given by the La Torraca–Madden–Korringa and Swift–Eggers methods, are the same. At a single observation site, both methods cannot distinguish between the longitudinal and transverse direction.

The similar situation is in the axially symmetric 3D-model. Here the principal values of the tensor $[\mathbf{Z}]$ coincide with the tangential and radial impedances, while the principal directions are the tangential and radial directions. The ellipticity of eigenfields is zero. So, the eigenfields are linearly polarized along principal directions.

In the asymmetric 3D-models, we observe the elliptic polarization of the electric and magnetic eigenfields ($\varepsilon \neq 0$) and the violation of the perpendicularity of

their ellipses ($\left|\alpha_{E_1} - \alpha_{H_1}\right| \neq \pi/2$). However, a quasi-symmetric 3D structure with $skew_S = 0$ and $skew_B \neq 0$ is a special case. If $Z_{xx} + Z_{yy} = 0$, then it follows from (2.82) that $P_{E_1}\bar{P}_{H_1} = -1$. Therefore the electric and magnetic eigenfields are orthogonal and $\left|\alpha_{E_1} - \alpha_{H_1}\right| = \pi/2$. Here the La Torraca–Madden–Korringa method displays the same effect of quasi-symmetry as the Swift–Eggers method.

Similar to the Swift–Eggers method, the La Torraca–Madden–Korringa method offers three characteristic parameters which reveal the lateral inhomogeneities and indicate their dimensionality. Using (2.84) and going back to (2.53), (2.54) and (2.55), we can specify the inhomogeneity parameter N, the angular parameter of asymmetry $skew_{ang}$, and the polarization parameter of asymmetry $skew_{pol}$.

Let us find relations between the principal values of the impedance tensor [**Z**] and scalar rotationally invariant impedances Z_{eff} and $\|\mathbf{Z}\|$ introduced by (1.30) and (1.33d). According to (2.76), (2.81), we get

$$\begin{aligned} Z_{\text{eff}} &= \sqrt{\det[\mathbf{Z}]} = \sqrt{\det[\mathbf{U}_e]\,\det[\mathbf{s}]\,\det\overline{[\mathbf{U}_h]}} \\ &= \sqrt{\det[\mathbf{s}]} = \sqrt{\zeta_1\zeta_2} = \sqrt{Z_{xx}Z_{yy} - Z_{xy}Z_{yx}}, \\ Z_{\text{rms}} &= \sqrt{\frac{|\zeta_1|^2 + |\zeta_2|^2}{2}} = \frac{1}{\sqrt{2}}\,\|\mathbf{Z}\| = \sqrt{\frac{|Z_{xx}|^2 + |Z_{xy}|^2 + |Z_{yx}|^2 + |Z_{yy}|^2}{2}}, \end{aligned} \tag{2.85}$$

where Z_{eff} and Z_{rms} are the effective and root-mean-square impedances.

Using rotationally invariant principal values ζ_1 and ζ_2 , we apply (2.58) and arrive at the principal apparent-resistivity and phase curves, ρ_1, ρ_2 and φ_1, φ_2, oriented along principal directions.

Furthermore, we can turn to (2.59) and plot the effective apparent-resistivity and impedance-phase curves ρ_{eff}, φ_{eff} as well as the root-mean-square apparent-resistivity curve

$$\rho_{\text{rms}} = \frac{Z_{\text{rms}}^2}{\omega\mu_{\text{o}}} \tag{2.86}$$

calculated from rotational invariant Z_{rms}.

2.7 Final Remarks on the Impedance Eigenstate Problem

We have considered three basic methods to solve the magnetotelluric eigenstate problem: (1) the Swift–Sims–Bostick, SSB method (the rotation approach), (2) the Swift–Eggers, SE method (the modified classical approach), (3) the LaTorraca–Madden–Korringa, LMK method (the modified SVD approach).

It is self-evident that the SE method and the LMK method are most informative, since, contrary to the rotation approach, they fill all eight degrees of freedom possessed by the matrix [**Z**] and provide a one-to-one correspondence between the impedance tensor [**Z**] and its eigenstate parameters.

Let us compare both modificatons.

1. The SE method does not impose any limitation on the medium under consideration. However, the LMK method assumes that the Earth is locally passive (it can only absorb the electromagnetic energy) and the real Pointing vector defined by the eigenfields everywhere points down. This limitation removing the π-ambiguity in phases of principal values of the impedance tensor is a weak point of the LMK method because nobody has proved that near-surface local inhomogeneities cannot emit the energy back into the air. Note that Yee and Paulson (1987) have proposed another modification of SVD approach with unitary matrices expressed in terms of polarization parameters θ, ϕ and this SVD version has no need of some limitations. But here we obtain the phases of principal impedances that are not rotationally invariant, and practical usefulness of this version is questionable.

2. The SE method provides the determination of the principal values ζ_1, ζ_2 in a wide class of geoelectric media including horizontally homogeneous medium. At the same time the LMK method in horizontally homogeneous medium delivers only $|\zeta_1|$, $|\zeta_2|$ ($\arg \varsigma_1$, $\arg \varsigma_2$ are undefined).

3. The principal values, ζ_1, ζ_2, found by the SE and LMK methods, coincide in the 1D-, 2D- and axisymmetric 3D-models, but differ in the asymmetric 3D-models. The LMK method is more sensitive to the geoelectric asymmetry than the SE method. Let ζ_m^{SE}, $m = 1, 2$ be the principal values obtained by the Swift–Eggers method. In virtue of (2.47)

$$\left|\zeta_m^{\mathrm{SE}}\right|_{m=1,2} = \frac{\sqrt{|E_{xm}|^2 + \left|E_{ym}\right|^2}}{\sqrt{|H_{xm}|^2 + \left|H_{ym}\right|^2}}, \tag{2.87}$$

where $\mathbf{E}_{\tau m}$ and $\mathbf{H}_{\tau m}$ are the quasi-orthogonal eigenfields envolved in the Swift–Eggers procedure. Take into account that $\mathbf{E}_{\tau\, m} = [\mathbf{Z}]\mathbf{H}_{\tau m}$ and expand the magnetic eigenfield with respect to basis $\mathbf{h}_1$, $\mathbf{h}_2$ formed by normalized magnetic eigenfields envolved in the La Torraca–Madden–Korringa procedure: $\mathbf{H}_{\tau m} = \hbar_{1\,m}\mathbf{h}_1 + \hbar_{2\,m}\mathbf{h}_2$. Then, according to (2.70), (2.77) and (2.80),

$$\begin{aligned}
|E_{xm}|^2 + \left|E_{ym}\right|^2 &= \bar{E}_{xm}E_{xm} + \bar{E}_{ym}E_{ym} = \overline{\mathbf{H}}_{\tau m}\overline{[\mathbf{Z}]}[\mathbf{Z}]\mathbf{H}_{\tau m} \\
&= \left(\bar{\hbar}_{1m}\overline{\mathbf{h}}_1 + \bar{\hbar}_{2m}\overline{\mathbf{h}}_2\right)[\mathbf{C}_H]\left(\hbar_{1m}\mathbf{h}_1 + \hbar_{2m}\mathbf{h}_2\right) \\
&= \left(\bar{\hbar}_{1m}\overline{\mathbf{h}}_1 + \bar{\hbar}_{2m}\overline{\mathbf{h}}_2\right)\left(\hbar_{1m}\left|\zeta_1^{\mathrm{LMK}}\right|^2\mathbf{h}_1 + \hbar_{2m}\left|\zeta_2^{\mathrm{LMK}}\right|^2\mathbf{h}_2\right) \\
&= |\hbar_{1m}|^2\left|\zeta_1^{\mathrm{LMK}}\right|^2 + |\hbar_{2m}|^2\left|\zeta_2^{\mathrm{LMK}}\right|^2, \\
|H_{xm}|^2 + \left|H_{ym}\right|^2 &= \bar{H}_{xm}H_{xm} + \bar{H}_{ym}H_{ym} \\
&= \left(\bar{\hbar}_{1m}\overline{\mathbf{h}}_1 + \bar{\hbar}_{2m}\overline{\mathbf{h}}_2\right)\left(\hbar_{1m}\mathbf{h}_1 + \hbar_{2m}\mathbf{h}_2\right) = |\hbar_{1m}|^2 + |\hbar_{2m}|^2,
\end{aligned} \tag{2.88}$$

where ζ_1^{LMK} and ζ_2^{LMK} are the impedance principal values, obtained by the La Torraca–Madden–Korringa procedure. Here $\left|\varsigma_1^{\mathrm{LMK}}\right| > \left|\zeta_2^{\mathrm{LMK}}\right|$. Substituting (2.88) in (2.87), we get

$$\underset{m=1,2}{\left|\zeta_m^{\mathrm{SE}}\right|} = \sqrt{\frac{|\hbar_{1m}|^2 \left|\zeta_1^{\mathrm{LMK}}\right|^2 + |\hbar_{2m}|^2 \left|\zeta_2^{\mathrm{LMK}}\right|^2}{|\hbar_{1m}|^2 + |\hbar_{2m}|^2}}, \tag{2.89}$$

whence

$$\left|\zeta_2^{\mathrm{LMK}}\right| < \underset{m=1,2}{\left|\zeta_m^{\mathrm{SE}}\right|} < \left|\zeta_1^{\mathrm{LMK}}\right|. \tag{2.90}$$

Clearly the LMK method has the advantage of higher sensitivity to three-dimensional asymmetric structures.

4. In the SE method, the asymmetry of the medium violates orthogonality of the electric eigenfields, while the electric and magnetic eigenfields are always quasi-orthogonal. And vice versa, in the LMK method the asymmetry of the medium violates orthogonality of the electric and magnetic eigenfields, while the electric eigenfields as well as the magnetic eigenfields are always orthogonal. In both methods the eigenfields respond to the geoelectric asymmetry, but in a different way.

5. The SE and LMK methods offer purely mathematical procedures and discussion about their physical meaning is a bit scholastic. Both methods complement each other. The magnetotelluric eigenstate analysis can help in revealing target geoelectric structures and establishing conditions that are most favorable for their study. This simple idea specifies the practical significance of the eigenstate problem. Just from this viewpoint we should judge the informativeness of different techniques devised for eigenstate analysis.

It would be instructive to test different eigenstate techniques using synthetic data computed for characteristic models.

Let us examine a three-layered superimposition model with a local Γ-shaped resistive inclusion in the first layer (conductive sediments) and a regional two-dimensional prismatic conductor in the second layer (resistive lithosphere). The model is presented in Fig. 2.3. Here we can also see the apparent-resistivity and impedance-phase curves obtained over the middle of the regional conductor in the absence of the local Γ-shaped inclusion. The eigenstate determinations were done by the Swift–Sims–Bostick, Swift–Eggers and La Torraca–Madden–Korringa methods at 14 sites located over the Γ-shaped inclusion and in its vicinity.

Figure 2.4 shows the principal values $\zeta_1 = |\zeta_1|\, e^{i\,\xi_1}$, $\zeta_2 = |\zeta_2|\, e^{i\,\xi_2}$ of the impedance tensor $[\mathbf{Z}]$ defined by the SSB, SE, and LMK methods at $T = 640$ s where the apparent-resistivity and impedance-phase curves distinctly reflect the influence of the regional conductor. In the model under consideration all three techniques yield closely related principal values: the difference in amplitudes and phases of ζ_1, ζ_2 at most observation sites does not exceed 5% and 3° and only at a few sites amounts up to 8–12% and 4–6°. But note that $|\zeta_1|$, $|\zeta_2|$ experience great

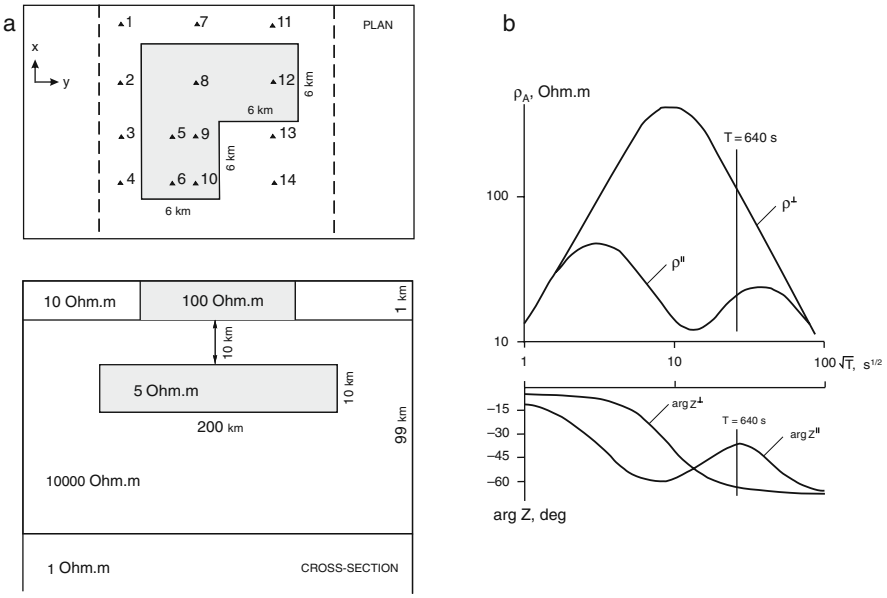

Fig. 2.3 A superimposition model with a Γ-shaped near-surface resistive inclusion and a 2D deep regional conductive prism; (**a)** the plan and cross-section of the model, 1, 2, 3,... observation sites, (**b)** the longitudinal and transverse apparent-resistivity and impedance-phase curves over the middle of the regional prism in the absence of the near-surface inclusion

scatter caused by local distorting influence of the near-surface Γ-shaped inclusion, while $\arg\zeta_1$, $\arg\zeta_2$ are close to $\arg\zeta^{\parallel}$, $\arg\zeta^{\perp}$ obtained in the absence of the near-surface inclusion.

Similarly, we compare the principal directions, α_1 and α_2, of the impedance tensor [**Z**] defined by all three methods. Here the more variegated pattern is observed (Fig. 2.5). Though the α-values obtained by different techniques are in good qualitative agreement, the difference between them is at some sites about 15–25°. The SE and LMK methods yield the best correlated α_1-values. The best correlated α_2-values are given by the SSB and LMK methods. Note that deviation of principal directions of the superimposition impedance tensor from principal directions of the regional two-dimensional impedance tensor ranges up to about 40°, but this scatter can be readily removed by averaging.

Distinction between the different eigenstate techniques vividly manifests itself in the inhomogeneity parameter N calculated by (2.53) as well as in the angular and elliptical parameters of asymmetry, $skew_{ang}$ and $skew_{pol}$, calculated by (2.54), (2.55). Figure 2.6 shows these parameters in comparison with the asymmetry parameter $skew_s$. Recall that deviation of N from zero reflects the lateral effects caused by 2D or 3D structures, while deviation of $skew_{ang}$, $skew_{pol}$ and $skew_s$ from zero points to the 3D asymmetry. In the model under consideration all eigenstate techniques give the same qualitative pattern for $|N|$, $skew_{ang}$ and $skew_{pol}$, but it is remarkable that the LMK method offers the maximum N-values being the most

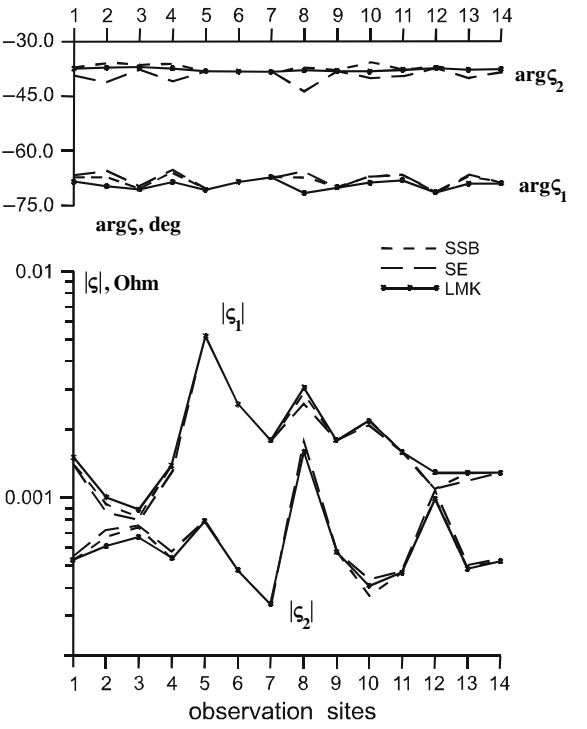

Fig. 2.4 Principal values of the impedance tensor in a superimposition model with a Γ-shaped near-surface resistive inclusion and a 2D deep regional conductive prism shown in Fig. 2.3; SSB – Swift–Sims–Bostick method, SE – Swift–Eggers method, LMK – La Torraca–Madden–Korringa method; $T = 640$ s

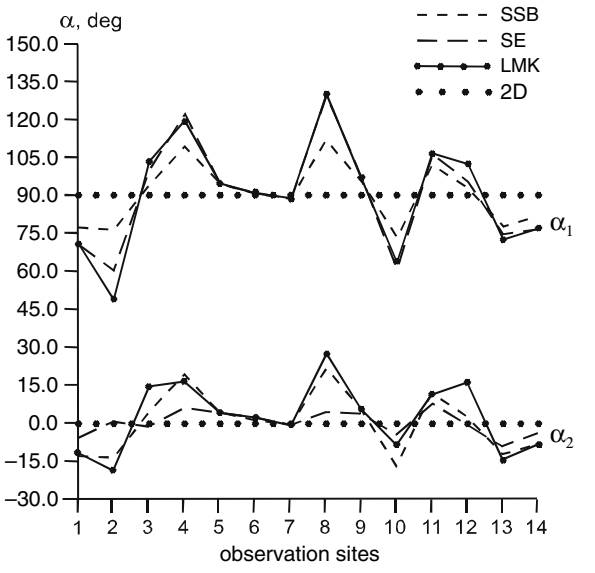

Fig. 2.5 Principal directions of the impedance tensor in a superimposition model with a Γ-shaped near-surface resistive inclusion and a 2D deep regional conductive prism shown in Fig. 2.3; SSB – Swift–Sims–Bostick method, SE – Swift–Eggers method, LMK – La Torraca–Madden–Korringa method, 2D–principal directions of the regional two-dimensional impedance in the absence of the near-surface inclusion; $T = 640$ s

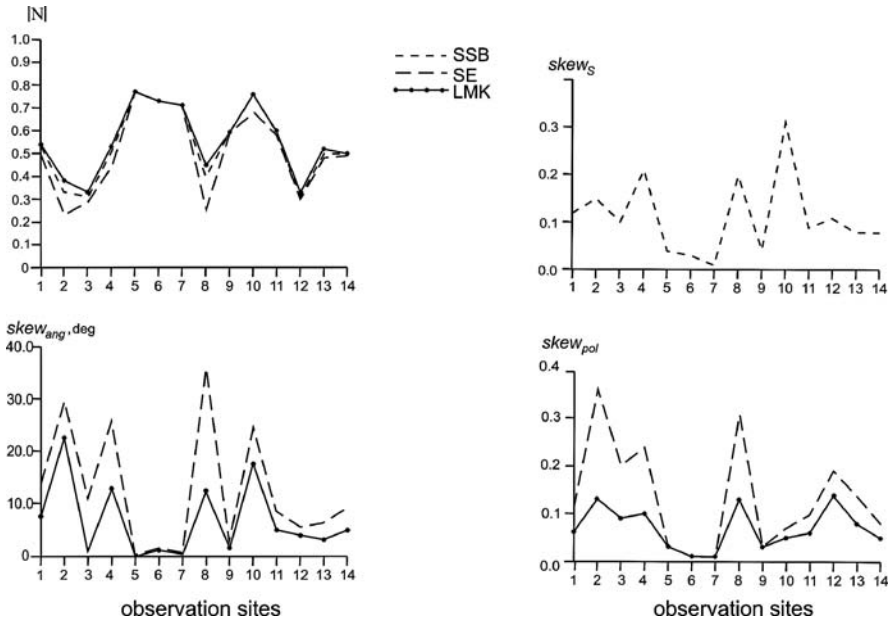

Fig. 2.6 Parameters of inhomogeneity N and asymmetry $skew_s$, $skew_{ang}$, $skew_{pol}$ in a superimposition model with a Γ-shaped near-surface resistive inclusion and a 2D deep regional conductive prism shown in Fig. 2.3; SSB – Swift–Sims–Bostick method, SE – Swift–Eggers method, LMK – La Torraca–Madden–Korringa method; T=640 s

sensitive to lateral effects, whereas the SE method offers the maximum $skew_{ang}$ and $skew_{pol}$, being the most sensitive to the structural asymmetry.

We see that in the presented model all three approaches to the magnetotelluric eigenstate analysis, based on the impedance rotation and the modifications of the classical formulation and SVD decomposition, provide closely related structural indications that differ only in sensitivity. What of these methods gives a better insight into the impedance eigenstate? We can say with confidence that (1) the Swift–Eggers and La Torraca–Madden–Korringa methods are preferable since they fill all eight degrees of freedom of magnetotelluric impedance tensor and so yield the most complete description of effects caused by three-dimensional inhomogeneities, (2) it would be helpful to combine these methods and gain the benefit from the most sensitive indications. And finally we have to stress that eigenstate indications may be dramatically distorted by near-surface small-scale inhomogeneities and in this case we should separate the local and regional effects.

Chapter 3
Separation of the Local and Regional Magnetotelluric Effects

3.1 Using the Local-Regional Decomposition

Applying the eigenstate techniques in a region with homogeneous superficial formations, we can identify the buried regional structures, define their dimensionality and strike, split the observed magnetotelluric field into the TM- and TE-modes, discern and analyze galvanic and induction responces. However the local superficial inhomogeneities may dramatically distort the eigenstate interpretation. A superimposition model exemplifying distortions of this kind was shown in Figs. 2.3, 2.4, 2.5, 2.6.

Separation of local and regional effects is a critical question of magnetotellurics. This question agitated scientists for a long time. A possibility to identify and remove the local near-surface distortions was examined in pioneering works of Bahr (1985) and Zhang, et al. (1987). The problem has been advanced in basic papers by Bahr (1988, 1991), Groom and Bailey (1989), Singer (1992), Smith (1995), Chave and Smith (1994), Chave and Jones (1997), McNeice and Jones (2001) and Caldwell et al. (2004). An excellent (though a bit outdated) review of developments in this field is available in Smith (1995).

Relation between local and regional effects can be described functionally with the local-regional decomposition (1.74), $[\mathbf{Z}^S] = [\mathbf{e}]\,[\mathbf{Z}^R]\,[\mathbf{h}]^{-1}$, involving the *regional impedance tensor* $[\mathbf{Z}^R]$, the *electric distortion tensor* $[\mathbf{e}]$ and *magnetic distortion tensor* $[\mathbf{h}] = [\mathbf{I}] + [\tilde{\mathbf{h}}]\,[\mathbf{Z}^R]$. However, the number of unknowns in this matrix decomposition is too large to get a resolvable system of equations (12 unknown complex values in $[\mathbf{e}]$, $[\mathbf{Z}^R]$, $[\mathbf{h}]$ against 4 known complex values in $[\mathbf{Z}^S]$). The local-regional decomposition needs some restrictions. There are three levels of restrictions.

1. First, we neglect magnetic anomalies caused by local superficial inhomogeneities and use the truncated low-frequency decomposition (1.75).
2. Second, we limit ourselves to the two-dimensional (or axisymmetric) regional structures.

M. Berdichevsky, V.I. Dmitriev, *Models and Methods of Magnetotellurics*,
DOI 10.1007/978-3-540-77814-1_3, © Springer-Verlag Berlin Heidelberg 2008

3. Third, we disregard the local induction in superficial inhomogeneities and apply the local-regional decomposition with real-valued tensor of electric distortion characterizd by local galvanic (static) effects.

These restrictions open the way to separation of local and regional effects.

Following is a cursory examination of the separation methods based on the superimposition models that contain local small-scale two- or three-dimensional inhomogeneities over a two- or three-dimensional large-scale regional structure. These methods are: (1) the Bahr method, (2) the Groom-Bailey method, (3) the Zhang-Roberts-Pedersen method, (4) the Chave-Smith method, and 5) the Caldwell-Bibby-Brown method.

3.2 The Bahr and Groom-Bailey Methods

Bahr (1988) suggested a method for separating local and regional effects in the superimposition model with local two-dimensional or three-dimensional near-surface inhomogeneities and regional two-dimensional background (*B method*). In this method we neglect the magnetic distortion and use the low-frequency truncated decomposition (1.75), $[\mathbf{Z}^S] = [\mathbf{e}]\,[\mathbf{Z}^R]$, where $[\mathbf{e}]$ is the real-valued tensor of electric distortion and $[\mathbf{Z}^R]$ is the two-dimensional regional impedance tensor with anti-diagonal matrix. A peculiarity of Bahr's method is that the characteristics of local and regional effects are given in an explicit form and their separation is performed analytically by means of simple formulae.

The basic assumptions in the Groom-Bailey method (Groom and Bailey, 1989) are the same as in the Bahr method, but separation of local and regional effect is performed numerically by solving an overdetermined system of equations with least squares fitting procedure.

We begin our consideration with the Bahr method.

3.2.1 The Bahr Method

Writing the basic equation (1.75) in the regional coordinate system (the x, y-axes are along and across the strike of the regional two-dimensional structure), we have

$$[\mathbf{Z}^S] = \begin{bmatrix} Z^S_{xx} & Z^S_{xy} \\ Z^S_{yx} & Z^S_{yy} \end{bmatrix} = \begin{bmatrix} e_{xx} & e_{xy} \\ e_{yx} & e_{yy} \end{bmatrix} \begin{bmatrix} 0 & \zeta^R_1 \\ -\zeta^R_2 & 0 \end{bmatrix} = \begin{bmatrix} -e_{xy}\zeta^R_2 & e_{xx}\zeta^R_1 \\ -e_{yy}\zeta^R_2 & e_{yx}\zeta^R_1 \end{bmatrix}, \quad (3.1)$$

where ζ^R_1 and ζ^R_2 are principal values of the regional impedance tensor (the longitudinal and transverse impedances) and e_{xx}, e_{xy}, e_{yx}, e_{yy} are components of the real-valued tensor of electric distortion. The columns of the superimposition tensor $[\mathbf{Z}^S]$ consist of in-phase or anti-phase components:

$$\begin{aligned}\arg\, Z^S_{xx} &= \begin{cases} \arg\, Z^S_{yx} & \text{for } e_{xy}e_{yy} > 0 \\ \arg\, Z^S_{yx} + \pi & \text{for } e_{xy}e_{yy} < 0 \end{cases} \\ \arg\, Z^S_{xy} &= \begin{cases} \arg\, Z^S_{yy} & \text{for } e_{xx}e_{yx} > 0 \\ \arg\, Z^S_{yy} + \pi & \text{for } e_{xx}e_{yx} < 0\,. \end{cases}\end{aligned} \tag{3.2}$$

Another peculiarity of the low-frequency truncated decomposition is that the tensor $[\mathbf{Z}^S]$ has zero $skew_B$ which can be accompanied with nonzero $skew_S$. In virtue of (1.61), (3.1)

$$skew_B = \frac{\sqrt{\left|\mathrm{Im}\left(Z^S_{xy}\,\bar{Z}^S_{yy} + Z^S_{xx}\,\bar{Z}^S_{yx}\right)\right|}}{\left|Z^S_{xy} - Z^S_{yx}\right|} = \frac{\sqrt{\left|\mathrm{Im}\left(e_{xx}e_{yx}\left|\zeta^R_1\right|^2 + e_{xy}e_{yy}\left|\zeta^R_2\right|^2\right)\right|}}{\left|e_{xx}\zeta^R_1 + e_{yy}\zeta^R_2\right|} = 0\,. \tag{3.3}$$

and

$$skew_S = \left|\frac{Z^S_{xx} + Z^S_{yy}}{Z^S_{xy} - Z^S_{yx}}\right| = \left|\frac{e_{xy}\zeta^R_2 - e_{yx}\zeta^R_1}{e_{xx}\zeta^R_1 + e_{yy}\zeta^R_2}\right|\,. \tag{3.4}$$

In general $e_{xy}\zeta^R_2 \neq e_{yx}\zeta^R_1$ and $skew_S \neq 0$.

We can say that the departure of $skew_S$ from 0 characterizes the local asymmetry, while $skew_B = 0$ indicates the regional two-dimensionality (or axially symmetric three-dimensionality). Condition $skew_B = 0$ defines the applicability of the Bahr method.

In an arbitrary coordinate system,

$$[\mathbf{Z}^S] = \begin{bmatrix} Z^S_{xx} & Z^S_{xy} \\ Z^S_{yx} & Z^S_{yy} \end{bmatrix} = \begin{bmatrix} \cos\alpha_R & -\sin\alpha_R \\ \sin\alpha_R & \cos\alpha_R \end{bmatrix} \begin{bmatrix} e_{xx} & e_{xy} \\ e_{yx} & e_{yy} \end{bmatrix} \begin{bmatrix} 0 & \zeta^R_1 \\ -\zeta^R_2 & 0 \end{bmatrix} \begin{bmatrix} \cos\alpha_R & \sin\alpha_R \\ -\sin\alpha_R & \cos\alpha_R \end{bmatrix},$$

where α_R is an angle between observation and regional coordinate systems, that is, a regional strike angle. This matrix equation contains nine real unknowns (a strike angle α_R, four real elements of the electric distortion tensor $[\mathbf{e}]$, and two complex principal values of the regional impedance tensor $[\mathbf{Z}^R]$) against eight degrees of freedom of the superimposition tensor $[\mathbf{Z}^S]$. So, we can count only on partial separation of local and regional effects.

Now we consider the separation technique in some detail. Let $skew_B = 0$. To determine the strike of the two-dimensional regional structure, we rotate the reference frame trough an angle α so that components $Z^S_{xx}(\alpha)$, $Z^S_{yx}(\alpha)$ and $Z^S_{xy}(\alpha)$, $Z^S_{yy}(\alpha)$ in columns of the tensor $[\mathbf{Z}^S(\alpha)]$ are in-phase or anti-phase. These phase conditions can be written in the form

$$\begin{aligned}\mathrm{Im}\left\{Z^S_{xx}(\alpha)\,\bar{Z}^S_{yx}(\alpha)\right\} &= 0 \\ \mathrm{Im}\left\{Z^S_{xy}(\alpha)\,\bar{Z}^S_{yy}(\alpha)\right\} &= 0\end{aligned} \tag{3.5}$$

where the bars denote the complex conjugation. With account for (1.27),

$$\begin{aligned}\mathrm{Im}\left\{\left(Z_2^S + Z_3^S \sin 2\alpha + Z_4^S \cos 2\alpha\right)\left(-\bar{Z}_1^S + \bar{Z}_3^S \cos 2\alpha - \bar{Z}_4^S \sin 2\alpha\right)\right\} = 0\\ \mathrm{Im}\left\{\left(Z_1^S + Z_3^S \cos 2\alpha - Z_4^S \sin 2\alpha\right)\left(\bar{Z}_2^S - \bar{Z}_3^S \sin 2\alpha - \bar{Z}_4^S \cos 2\alpha\right)\right\} = 0\,.\end{aligned}$$

Expanding and simplifying these equations, we obtain

$$A \sin 2\alpha - B \cos 2\alpha + C = 0, \qquad A \sin 2\alpha - B \cos 2\alpha - C = 0, \tag{3.6}$$

where

$$\begin{aligned}A &= \mathrm{Im}\left(Z_{xx}^S \bar{Z}_{yy}^S + Z_{xy}^S \bar{Z}_{yx}^S\right)\\ B &= \mathrm{Im}\left(Z_{yx}^S \bar{Z}_{xx}^S + Z_{xy}^S \bar{Z}_{yy}^S\right)\\ C &= \mathrm{Im}\left(Z_{xy}^S \bar{Z}_{yy}^S + Z_{xx}^S \bar{Z}_{yx}^S\right) = skew_B^2 \left|Z_{xy} - Z_{yx}\right|^2.\end{aligned}$$

Taking into account that $C = 0$ when $skew_B = 0$, we write

$$A \sin 2\alpha - B \cos 2\alpha = 0\,, \tag{3.7}$$

whence

$$\alpha = \frac{1}{2} \arctan \frac{B}{A} = \frac{1}{2} \arctan \frac{\mathrm{Im}\left(Z_{yx}^S \bar{Z}_{xx}^S + Z_{xy}^S \bar{Z}_{yy}^S\right)}{\mathrm{Im}\left(Z_{xx}^S \bar{Z}_{yy}^S + Z_{xy}^S \bar{Z}_{yx}^S\right)} = \begin{cases} \alpha_R \\ \alpha_R + \frac{\pi}{2}\,, \end{cases} \tag{3.8}$$

where α_R is a strike angle of the regional two-dimensional structure. Applying the Bahr method, we specify the principal directions, α_R and $\alpha_R + \pi/2$, of the regional impedance $[\mathbf{Z}^R]$.

Let $skew_B \neq 0$ because of measurement noises and asymmetry of regional structure. In that event

$$A \sin 2\alpha - B \cos 2\alpha + C \neq 0, \qquad A \sin 2\alpha - B \cos 2\alpha - C \neq 0\,.$$

Departure of these equations from 0 can be characterized by the quadratic deviation

$$\delta(\alpha) = (A \sin 2\alpha - B \cos 2\alpha + C)^2 + (A \sin 2\alpha - B \cos 2\alpha - C)^2\,. \tag{3.9}$$

At a minimum of $\delta(\alpha)$ we have the least disagreement between phases in columns of the tensor $[\mathbf{Z}^S]$. Solving the equation $d\,\delta(\alpha)/d\alpha = 0$ with $d^2\delta(\alpha)/d\alpha^2 > 0$, we find an angle $\alpha_R^{\min}$ which minimizes $\delta(\alpha)$. By virtue of (3.9)

$$\frac{d\,\delta(\alpha)}{d\alpha} = 8(A\sin 2\alpha - B\cos 2\alpha)(A\cos 2\alpha + B\sin 2\alpha) = 0,$$

$$\frac{d^2\delta(\alpha)}{d\alpha^2} = 16(A\cos 2\alpha + B\sin 2\alpha)^2 - 16(A\sin 2\alpha - B\cos 2\alpha)^2,$$

whence

$$A\sin 2\alpha_R^{\min} - B\cos 2\alpha_R^{\min} = 0, \tag{3.10}$$

which agrees with (3.7). Thus, the angle $\alpha_R^{\min}$ coincides with the regional strike angle, α_R, defined by (3.8). We see, that at $C \neq 0$ the (3.8) provides the best approximation to conditions (3.6), which determines the in-phase or anti-phase state in the columns of the superimposition tensor $[\mathbf{Z}^S]$.

Practical experience suggests that using the Bahr method we can get the reliable estimate of the strike angle α_R when $skew_B \leq 0.15$.

With known α_R, we evaluate phases of the principal values of $[\mathbf{Z}^R]$. To smooth noisy data, we use both components in columns of $[\mathbf{Z}^S]$. In accordance with (3.1)

$$\begin{aligned}
\xi_1^R &= \arg\zeta_1^R = \frac{1}{2}\left\{\arctan\frac{\mathrm{Im}Z_{xy}^S(\alpha_R)}{\mathrm{Re}Z_{xy}^S(\alpha_R)} + \arctan\frac{\mathrm{Im}Z_{yy}^S(\alpha_R)}{\mathrm{Re}Z_{yy}^S(\alpha_R)}\right\} \\
\xi_2^R &= \arg\zeta_2^R = \frac{1}{2}\left\{\arctan\frac{\mathrm{Im}Z_{xx}^S(\alpha_R)}{\mathrm{Re}Z_{xx}^S(\alpha_R)} + \arctan\frac{\mathrm{Im}Z_{yx}^S(\alpha_R)}{\mathrm{Re}Z_{yx}^S(\alpha_R)}\right\}.
\end{aligned} \tag{3.11}$$

Generally the phases ξ_1^R and ξ_2^R are taken in the fourth quadrant. Note that $\xi_1^R + \xi_2^R$ should be close to $\arg\det[\mathbf{Z}^S]$.

What about the moduli of the principal values of $[\mathbf{Z}^R]$? Let us introduce the vector components $\mathbf{e}^{(x)}(e_{xx},\ e_{yx})$, $\mathbf{e}^{(y)}(e_{xy},\ e_{yy})$ of the electric distortion tensor $[\mathbf{e}]$ (Fig. 3.1). Their direction is defined by angles β_x and β_y measured clockwise from the $x-$ axis and $y-$ axis respectively. Thus,

$$e^{(x)} = \left|\mathbf{e}^{(x)}\right| = \sqrt{e_{xx}^2 + e_{yx}^2}, \qquad e^{(y)} = \left|\mathbf{e}^{(y)}\right| = \sqrt{e_{xy}^2 + e_{yy}^2} \tag{3.12}$$

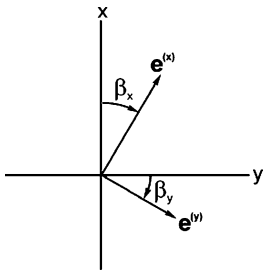

Fig. 3.1 Plotting the electric fields $\mathbf{e}^{(x)}$ and $\mathbf{e}^{(y)}$

and

$$\begin{aligned} &\beta_x = \arctan\frac{e_{yx}}{e_{xx}} && \beta_y = -\arctan\frac{e_{xy}}{e_{yy}} \\ &-\pi/2 < \beta_x < \pi/2 && -\pi/2 < \beta_y < \pi/2\,. \end{aligned} \tag{3.13}$$

Returning to (3.1), we get apparent amplitudes $\left|\tilde{\zeta}_1^R\right|$ and $\left|\tilde{\zeta}_2^R\right|$ of the principal regional impedances:

$$\left|\tilde{\zeta}_1^R\right| = e^{(y)}\left|\zeta_1^R\right| = \sqrt{\left|Z_{xy}^S\right|^2 + \left|Z_{yy}^S\right|^2} \qquad \left|\tilde{\zeta}_2^R\right| = e^{(x)}\left|\zeta_2^R\right| = \sqrt{\left|Z_{xx}^S\right|^2 + \left|Z_{yx}^S\right|^2}. \tag{3.14}$$

As is easy to see, moduli of the principal values of $[\mathbf{Z}^R]$ can be found in the inseparable conjunction with frequency-independent factors $e^{(x)}$ and $e^{(y)}$ that define intensity of static distortions of $\left|\zeta_1^R\right|$, $\left|\zeta_2^R\right|$ caused by near-surface local inhomogeneities.

To distinguish between longitudinal and transverse regional directions, $\alpha^{\parallel}$ and $\alpha^{\perp}$, and between longitudinal and transverse regional impedances, $Z^{\parallel}$ and $Z^{\perp}$, we have to use an additional geological or geophysical indication.

Along with characteristics of regional structure, the Bahr method may give some information on local structures. Let us show that the vector components $\mathbf{e}^{(x)}$ and $\mathbf{e}^{(y)}$ of the electric distortion tensor $[\mathbf{e}]$ coincide with electric fields that arise when a local inhomogeneity is excited by the unit electric fields linearly polarized in the x- and y-directions:

$$\mathbf{e}^{(x)} = \begin{bmatrix} e_{xx} & e_{xy} \\ e_{yx} & e_{yy} \end{bmatrix} \begin{bmatrix} 1 \\ 0 \end{bmatrix} = \begin{bmatrix} e_{xx} \\ e_{yx} \end{bmatrix}, \qquad \mathbf{e}^{(y)} = \begin{bmatrix} e_{xx} & e_{xy} \\ e_{yx} & e_{yy} \end{bmatrix} \begin{bmatrix} 0 \\ 1 \end{bmatrix} = \begin{bmatrix} e_{xy} \\ e_{yy} \end{bmatrix}. \tag{3.15}$$

Thus, the angles β_x, β_y indicate how a local inhomogeneity deflects the observed electric fields from the exciting field. In regional coordinates, according to (3.1) and (3.13),

$$\beta_x = \arctan\frac{e_{yx}}{e_{xx}} = \arctan\frac{Z_{yy}^S}{Z_{xy}^S}, \qquad \beta_y = -\arctan\frac{e_{xy}}{e_{yy}} = -\arctan\frac{Z_{xx}^S}{Z_{yx}^S}. \tag{3.16}$$

In practice, we take into account the phase inaccuracies and to avoid the complex angles use approximate formulae

$$\beta_x = \arctan \mathrm{Re}\frac{Z_{yy}^S}{Z_{xy}^S}, \qquad \beta_y = -\arctan \mathrm{Re}\frac{Z_{xx}^S}{Z_{yx}^S}. \tag{3.17}$$

Looking upon a map that represents the orientation of vectors $\mathbf{e}^{(x)}$ and $\mathbf{e}^{(y)}$, we may reveal the current concentration (current concentrates in a conductive body) or current flow around (currents flow around a resistive body) and thereby classify the near-surface structures by their conductivity.

The final findings of Bahr's method are:

$$\left|\tilde{\zeta}_1^R\right|,\ \xi_1^R = \arg\zeta_1^R,\ \left|\tilde{\zeta}_2^R\right|,\ \xi_2^R = \arg\zeta_2^R\ ,\ \alpha_R,\ \beta_x,\ \beta_y, \tag{3.18}$$

where the strike angle α_R is determined with $\pi/2$ ambiguity.

It should be particularly emphasized that the stability of these findings depends dramatically on difference in phase between the longitudinal and transverse regional impedances. In fact, with $\arg Z^{\parallel} = \arg Z^{\perp}$ we arrive at $\alpha_R = 0/0$ since $A = B = 0$ in (3.8). The phase difference must far exceed the measurement errors. A rotationally invariant measure of phase difference suggested by Bahr (1991) is

$$\begin{aligned}\mu &= \frac{\sqrt{\left|\mathrm{Im}\left(Z_{xy}^S \bar{Z}_{yy}^S + Z_{xx}^S \bar{Z}_{yx}^S + Z_{xx}^S \bar{Z}_{xy}^S + Z_{yx}^S \bar{Z}_{yy}^S\right)\right| + \left|\mathrm{Im}\left(Z_{xy}^S \bar{Z}_{yy}^S + Z_{xx}^S \bar{Z}_{yx}^S - Z_{xx}^S \bar{Z}_{xy}^S - Z_{yx}^S \bar{Z}_{yy}^S\right)\right|}}{\left|Z_{xy}^S - Z_{yx}^S\right|} \\ &= \frac{\sqrt{|J_{12} + J_{13}| + |J_{12} - J_{13}|}}{|2Z_{\mathrm{brd}}|}\ ,\end{aligned} \tag{3.19}$$

where Z_{brd}, J_{12} and J_{13} are invariants defined by (1.29), (1.34) and (1.35). We simplify this phase indicator taking into account that $skew_B = 0$ and hence $J_{12} = 0$. So, we write

$$\mu = \frac{\sqrt{2\,|J_{13}|}}{|2Z_{\mathrm{brd}}|} = \frac{\sqrt{2\left|\mathrm{Im}\left(Z_{xx}^S \bar{Z}_{xy}^S + Z_{yx}^S \bar{Z}_{yy}^S\right)\right|}}{\left|Z_{xy}^S - Z_{yx}^S\right|}\,. \tag{3.20}$$

If $\mu = 0$, phases of the longitudinal and transverse impedances coincide and (3.8) becomes indeterminate.

Parallel to μ we can derive another indicator which enables the direct estimating the phase difference. Let the tensors $[\mathbf{Z}^S]$ and $[\mathbf{Z}^S(\alpha_R)]$ be observed in an arbitrary and regional coordinate system respectively. In view of (1.29), (1.32), (3.1)

$$\begin{aligned}\det\left[\mathrm{Re}\ \mathbf{Z}^S\right] + \det\left[\mathrm{Im}\ \mathbf{Z}^S\right] &= \det\left[\mathrm{Re}\ \mathbf{Z}^S(\alpha_R)\right] + \det\left[\mathrm{Im}\ \mathbf{Z}^S(\alpha_R)\right] \\ &= \det\left[\mathbf{e}(\alpha_R)\right]\left(\mathrm{Re}\ Z^{\parallel}\mathrm{Re}\ Z^{\perp} + \mathrm{Im}\ Z^{\parallel}\mathrm{Im}\ Z^{\perp}\right) \\ &= \det\left[\mathbf{e}(\alpha_R)\right]\left|\ \det\left[\mathbf{Z}^R(\alpha_R)\right]\ \right|\left(\cos\arg\ Z^{\parallel}\cos\arg\ Z^{\perp}\right. \\ &\quad \left. + \sin\arg Z^{\parallel}\sin\arg\ Z^{\perp}\right) \\ &= \pm\left|\ \det\left[\mathbf{e}(\alpha_R)\right]\ \right|\left[\det\left[\mathbf{Z}^R(\alpha_R)\right]\ \right|\cos\Delta \\ &= \pm\left|\ \det\left[\mathbf{Z}^S(\alpha_R)\right]\right|\ \cos\Delta = \pm\left|\ \det\left[\mathbf{Z}^S\right]\ \right|\ \cos\Delta\end{aligned}$$

where $\Delta = \arg\ Z^{\parallel} - \arg\ Z^{\perp}$. Assuming that $-\pi/2 < \Delta < \pi/2$, we obtain

$$|\Delta| = \arccos\frac{\left|\ \det\left[\mathrm{Re}\ \mathrm{Z}^S\right] + \det\left[\mathrm{Im}\ \mathrm{Z}^S\right]\ \right|}{\left|\ \det\left[\mathrm{Z}^S\right]\ \right|}. \tag{3.21}$$

If impedance phases are measured with an accuracy of 2–3°, it would be enough to require that $|\Delta| > 15 \div 20°$.

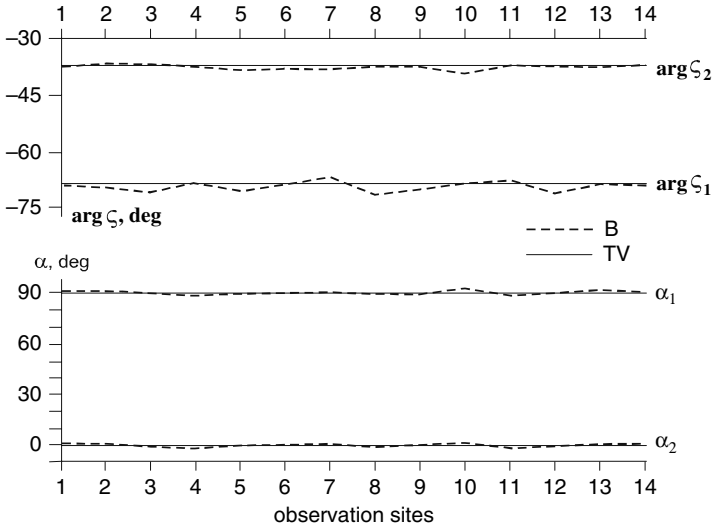

Fig. 3.2 Phases $\arg\zeta_1$, $\arg\zeta_2$ of the principal values of the regional two-dimensional impedance $[\mathbf{Z}^R]$ and its principal directions α_1, α_2 in a superimposition model with a Γ-shaped near-surface resistive inclusion and a 2D deep regional conductive prism shown in Fig. 2.3; B – Bahr method, TV – true value; $T = 640$ s

Now we would like to illustrate the potentialities of the Bahr method. Let us return to the three-layered (3D+2D)-superimposition model with a local Γ-shaped resistive inclusion in the sediments and a regional two-dimensional prismatic conductor in the resistive lithosphere (Fig. 2.3). At $T = 640$ s we have $skew_B < 0.1$ and $|\Delta| \approx 30^\circ$. These conditions favour the local-regional decomposition. Figure 3.2 displays the phases $\xi_1 = \arg\zeta_1$, $\xi_2 = \arg\zeta_2$ of the principal values of the regional two-dimensional impedance $[\mathbf{Z}^R]$ and its principal (transverse and longitudinal) directions, α_1 and α_2, deduced by the Bahr method. We see that $\arg\zeta$ and α are defined with an accuracy of 1–3° and 1–2° respectively. Figure 3.3 shows the chart of the unit electric fields $\mathbf{e}^{(y)}$ plotted by means of Bahr's method. We see here a typical picture of currents flowing around a near-surface resistive inclusion.

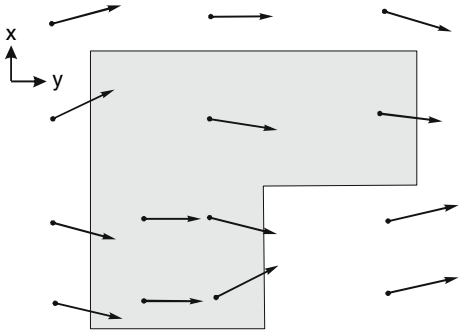

Fig. 3.3 Chart of the unit electric fields $\mathbf{e}^{(y)}$ in a superimposition model with a Γ-shaped near-surface resistive inclusion and a 2D deep regional conductive prism shown in Fig. 2.3; $T = 640$ s

In closing we will consider two special cases.

1. The (3D + 3D)-superimposition model contains a regional three-dimensional axisymmetric structure overlapped by the local near-surface three-dimensional inhomogeneity. In that case we have the same basic equation (3.1), so that the Bahr method can be applied to find the radial and tangential directions as well as phases of the radial and tangential principal impedances.
2. The horizontally layered one-dimensional medium contains only the local near-surface three-dimensional inhomogeneity. In this model, the low-frequency truncated decomposition takes the form

$$[\mathbf{Z}^S] = \begin{bmatrix} e_{xx} & e_{xy} \\ e_{yx} & e_{yy} \end{bmatrix} \begin{bmatrix} 0 & Z_{\mathrm{N}} \\ -Z_{\mathrm{N}} & 0 \end{bmatrix} = \begin{bmatrix} -e_{xy} Z_{\mathrm{N}} & e_{xx} Z_{\mathrm{N}} \\ -e_{yy} Z_{\mathrm{N}} & e_{yx} Z_{\mathrm{N}} \end{bmatrix}, \tag{3.22}$$

where Z_{N} is the normal (one-dimensional) impedance. Here, all the components of the impedance tensor $[\mathbf{Z}^S]$ are in-phase or anti-phase depending on the sign of components of the distortion tensor $[\mathbf{e}]$.

3.2.2 The Groom-Bailey Method

Another decomposition technique to separate local and regional effects has been suggested by Groom and Bailey (1989).

The basic assumptions in the Groom-Bailey method (*GB method*) are the same as in the Bahr method. The superimposition model containing a local two- or three-dimensional inhomogeneity over a two-dimensional regional structure is considered and the truncated low-frequency decomposition (3.1), $[\mathbf{Z}^S] = [\mathbf{e}]\,[\mathbf{Z}^R]$, with the real-valued electric distortion tensor $[\mathbf{e}]$ and anti-diagonal regional tensor $[\mathbf{Z}^R]$ is applied.

Using the regional coordinate system with x- and y-axes along and across the strike of the regional structure, we represent the distortion tensor $[\mathbf{e}]$ as the product of a real-valued scalar g and real-valued tensors $[\mathbf{T}]$, $[\mathbf{S}]$, $[\mathbf{A}]$:

$$[\mathbf{e}] = g\,[\mathbf{T}]\,[\mathbf{S}]\,[\mathbf{A}], \tag{3.23}$$

where

$$[\mathbf{T}] = N_T \begin{bmatrix} 1 & -t \\ t & 1 \end{bmatrix}, \qquad [\mathbf{S}] = N_S \begin{bmatrix} 1 & s \\ s & 1 \end{bmatrix}, \qquad [\mathbf{A}] = N_A \begin{bmatrix} 1+a & 0 \\ 0 & 1-a \end{bmatrix}.$$

and

$$N_T = \frac{1}{\sqrt{1+t^2}}, \qquad N_S = \frac{1}{\sqrt{1+s^2}}, \qquad N_A = \frac{1}{\sqrt{1+a^2}}.$$

Without going into detail we note that for all real-valued g, [**T**], [**S**] and [**A**] this decomposition is unique (Groom and Bailey, 1989). It has a simple physical interpretation. The factor g plays a part of the scaling parameter. The tensors [**T**], [**S**], [**A**] describe elementary distortions of the regional electric field $\mathbf{E}_\tau^R$.

Figure 3.4a shows a family of unit regional electric fields $\mathbf{E}_\tau^R$ linearly polarized in different directions. Here vectors 1,3 are oriented in the principal directios of the tensor $[\mathbf{Z}^R]$, i.e. along and across the strike of the regional structure, while vectors 2,4 bisect these principal directions.

The effect of the tensor [**T**] is shown in Fig. 3.4b. This tensor rotates all vectors through a clockwise angle $\beta_t = \arctan t$. It is said to be the *twist tensor*. The angle β_t is the *twist angle*.

The effect of the tensor [**S**] is shown in Fig. 3.4c. It looks like shear deformation. By analogy with the theory of deformation this tensor is said to be the *shear tensor*. It causes maximum angular changes in vectors 1,3 and does not change vectors 2,4. Vector 1 is deflected clockwise by an angle $\beta_s = \arctan s$, and vector 2 by the same angle, but counter-clockwise. The angle β_s is the *shear angle*.

The effect of the tensor [**A**] is shown in Fig. 3.4d. This tensor stretches the longitudinal and transverse components of electric vectors by different factors, creating a pattern of "anisotropy". It is said to be the *anisotropy tensor*.

Thus the factorization (3.23) reduces the distortions of regional electric field to scale change and shear, twist and anisotropy deformations.

Reverting to the truncated decomposition (1.75), we write

$$[\mathbf{Z}^S] = g\,[\mathbf{T}]\,[\mathbf{S}]\,[\mathbf{A}]\,[\mathbf{Z}^R] \tag{3.24}$$

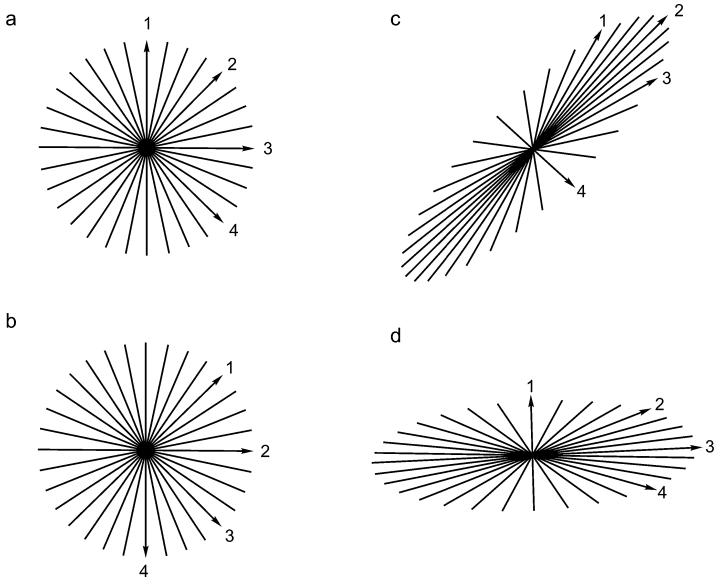

Fig. 3.4 Transformation of unit electric fields (**a**) by the twist (**b**), shear (**c**) and anisotropy (**d**) tensors

or

$$[\mathbf{Z}^S] = G\,[\tilde{\mathbf{T}}]\,[\tilde{\mathbf{S}}]\,[\tilde{\mathbf{A}}]\,[\mathbf{Z}^R] \tag{3.25}$$

where

$$G = g\frac{1}{\sqrt{(1+s^2)(1+t^2)(1+a^2)}}$$

and

$$[\tilde{\mathbf{T}}] = \begin{bmatrix} 1 & -t \\ t & 1 \end{bmatrix}, \qquad [\tilde{\mathbf{S}}] = \begin{bmatrix} 1 & s \\ s & 1 \end{bmatrix}, \qquad [\tilde{\mathbf{A}}] = \begin{bmatrix} 1+a & 0 \\ 0 & 1-a \end{bmatrix}.$$

$$[\mathbf{Z}^R] = \begin{bmatrix} 0 & \zeta_1^R \\ -\zeta_2^R & 0 \end{bmatrix}.$$

A peculiarity of decomposition (3.25) is that G and $[\tilde{\mathbf{A}}]$ cannot be determined separately from $[\mathbf{Z}^R]$. So, we actually deal with apparent regional impedance $[\tilde{\mathbf{Z}}^R]$ absorbing $G[\tilde{\mathbf{A}}]$:

$$[\tilde{\mathbf{Z}}^R] = G\,[\tilde{\mathbf{A}}]\,[\mathbf{Z}^R] = \begin{bmatrix} 0 & \tilde{\zeta}_1^R \\ -\tilde{\zeta}_2^R & 0 \end{bmatrix}, \tag{3.26}$$

where

$$\tilde{\zeta}_1^R = G(1+a)\zeta_1^R, \qquad \tilde{\zeta}_2^R = G(1-a)\zeta_2^R.$$

The principal impedance values $\tilde{\zeta}_1^R$ and $\tilde{\zeta}_2^R$ preserve the true phases, but their amplitudes differ from the true amplitudes by real-valued frequency-independent scalar factors $G(1+a)$ and $G(1-a)$, which characterize the static effect of near-surface local inhomogeneities.

Substituting (3.26) in (3.25), we get

$$[\mathbf{Z}^S] = [\tilde{\mathbf{T}}][\tilde{\mathbf{S}}]\,[\tilde{\mathbf{Z}}^R]. \tag{3.27}$$

Pass now from the regional coordinate system to a measurement coordinate system. At arbitrary orientation of the x, y-axes

$$[\mathbf{Z}^S] = [\mathbf{R}(\alpha_R)]^{-1}\,[\tilde{\mathbf{T}}]\,[\tilde{\mathbf{S}}]\,[\tilde{\mathbf{Z}}^R]\,[\mathbf{R}(\alpha_R)] \tag{3.28}$$

where α_R is the regional strike angle measured clockwise from the x-axis. This matrix equation enables the determination of regional strike angle, α_R, along with apparent regional impedance, $[\tilde{\mathbf{Z}}^R]$, and shear and twist parameters, t and s. On simple though cumbersome algebra we obtain

$$
\begin{aligned}
Z_1^S &= \sigma - st\delta \qquad\qquad Z_2^S = t\sigma + s\delta \\
Z_3^S &= (\delta - st\sigma)\cos 2\alpha_R - (t\delta + s\sigma)\sin 2\alpha_R \\
Z_4^S &= -(t\delta + s\sigma)\cos 2\alpha_R - (\delta - st\sigma)\sin 2\alpha_R ,
\end{aligned}
\tag{3.29}
$$

where

$$
\begin{aligned}
Z_1^S &= \frac{Z_{xy}^S - Z_{yx}^S}{2} \qquad Z_2^S = \frac{Z_{xx}^S + Z_{yy}^S}{2} \\
Z_3^S &= \frac{Z_{xy}^S + Z_{yx}^S}{2} \qquad Z_4^S = \frac{Z_{xx}^S - Z_{yy}^S}{2}
\end{aligned}
$$

and

$$
\delta = \frac{\tilde{\zeta}_1^R - \tilde{\zeta}_2^R}{2} \qquad \sigma = \frac{\tilde{\zeta}_1^R + \tilde{\zeta}_2^R}{2} .
$$

This is a system of eight equations formed by real and imaginary parts of (3.29) for seven unknowns: $t, s, \alpha_R, \operatorname{Re}\delta, \operatorname{Im}\delta, \operatorname{Re}\sigma, \operatorname{Im}\sigma$. The system is slightly overdetermined. It can be solved by a least squares fitting procedure with the $\pi/2$-ambiguity in the regional strike angle α_R.

The final findings of Groom-Bailey's method are:

$$
\left|\tilde{\xi}_1^R\right|, \ \xi_1^R = \arg\zeta_1^R, \ \left|\tilde{\zeta}_2^R\right|, \ \xi_2^R = \arg\zeta_2^R , \ \alpha_R, \ \beta_t, \ \beta_s . \tag{3.30}
$$

Similarly to the Bahr method, the Groom-Bailey method may give reasonable results if transverse and longitudinal regional impedances, ζ_1^R and ζ_2^R, have significantly different phases. The point is that at $\arg\zeta_1^R = \arg\zeta_2^R$ the system of equations (3.29) falls into two linearly dependent systems and becomes undetermined.

3.2.3 Final Remarks on the Bahr and Groom-Bailey Methods

Intuitively it seems that the Bahr and Groom-Bailey methods yield closely related characteristics of the local and regional structures. Let us examine the relationships between these two methods in more detail.

To begin with, we compare the deflection angles β_x and β_y, determined by Bahr's equations (3.16), with the twist and shear angles $\beta_t = \arctan t$ and $\beta_s = \arctan s$, determined by Groom-Bailey's equations (3.29). By virtue of (3.27)

$$
\begin{aligned}
[\mathbf{Z}^S] &= [\tilde{\mathbf{T}}][\tilde{\mathbf{S}}]\ [\tilde{\mathbf{Z}}^R] \\
&= \begin{bmatrix} 1 & -t \\ t & 1 \end{bmatrix} \begin{bmatrix} 1 & s \\ s & 1 \end{bmatrix} \begin{bmatrix} 0 & \tilde{\zeta}_1^R \\ -\tilde{\zeta}_2^R & 0 \end{bmatrix} = \begin{bmatrix} -(s-t)\,\tilde{\zeta}_2^R & (1-st)\,\tilde{\zeta}_1^R \\ -(1+st)\,\tilde{\zeta}_2^R & (s+t)\,\tilde{\zeta}_1^R \end{bmatrix},
\end{aligned}
\tag{3.31}
$$

whence

$$\begin{aligned}\tan\beta_x &= \frac{Z^S_{yy}}{Z^S_{xy}} = \frac{t+s}{1-st} = \frac{\tan\beta_t + \tan\beta_s}{1-\tan\beta_s\tan\beta_t} = \tan(\beta_t+\beta_s),\\ \tan\beta_y &= -\frac{Z^S_{xx}}{Z^S_{yx}} = \frac{t-s}{1+st} = \frac{\tan\beta_t - \tan\beta_s}{1+\tan\beta_s\tan\beta_t} = \tan(\beta_t-\beta_s),\end{aligned} \tag{3.32}$$

and hence

$$\begin{aligned}\beta_x &= \beta_t+\beta_s \qquad \beta_y = \beta_t-\beta_s,\\ \beta_t &= \frac{\beta_x+\beta_y}{2} \qquad \beta_s = \frac{\beta_x-\beta_y}{2}.\end{aligned} \tag{3.33}$$

Thus, we have simple arithmetic relations between $\beta_x,\ \beta_y$ and $\beta_t,\ \beta_s$.

Furthermore, it is easy to show that the Groom-Bailey decomposition

$$[\mathbf{e}] = g\frac{1}{\sqrt{1+t^2}}\frac{1}{\sqrt{1+s^2}}\frac{1}{\sqrt{1+a^2}}\begin{bmatrix}1 & -t\\ t & 1\end{bmatrix}\begin{bmatrix}1 & s\\ s & 1\end{bmatrix}\begin{bmatrix}1+a & 0\\ 0 & 1-a\end{bmatrix}$$

and the Bahr decomposition

$$[\mathbf{e}] = \begin{bmatrix}\cos\beta_x & -\sin\beta_y\\ \sin\beta_x & \cos\beta_y\end{bmatrix}\begin{bmatrix}e_x & 0\\ 0 & e_y\end{bmatrix}$$

are identical (Smith, 1995). Really, in view of (3.33),

$$\begin{aligned}[\mathbf{e}] &= \begin{bmatrix}\cos\beta_x & -\sin\beta_y\\ \sin\beta_x & \cos\beta_y\end{bmatrix}\begin{bmatrix}e_x & 0\\ 0 & e_y\end{bmatrix}\\ &= \begin{bmatrix}\cos\beta_t & -\sin\beta_t\\ \sin\beta_t & \cos\beta_t\end{bmatrix}\begin{bmatrix}\cos\beta_s & \sin\beta_s\\ \sin\beta_s & \cos\beta_s\end{bmatrix}\begin{bmatrix}e_x & 0\\ 0 & e_y\end{bmatrix}\\ &= e\cos\beta_t\cos\beta_s\begin{bmatrix}1 & -\tan\beta_t\\ \tan\beta_t & 1\end{bmatrix}\begin{bmatrix}1 & \tan\beta_s\\ \tan\beta_s & 1\end{bmatrix}\begin{bmatrix}1+a & 0\\ 0 & 1-a\end{bmatrix}\\ &= g\frac{1}{\sqrt{1+t^2}}\frac{1}{\sqrt{1+s^2}}\frac{1}{\sqrt{1+a^2}}\begin{bmatrix}1 & -t\\ t & 1\end{bmatrix}\begin{bmatrix}1 & s\\ s & 1\end{bmatrix}\begin{bmatrix}1+a & 0\\ 0 & 1-a\end{bmatrix},\end{aligned} \tag{3.34}$$

where

$$e = \frac{e_x+e_y}{2}, \qquad g = \sqrt{\frac{e_x^2+e_y^2}{2}}, \qquad a = \frac{e_x-e_y}{e_x+e_y}.$$

Thus, both the methods rest on the identical decompositions, but differ in parametrization and technology. Comparison between (3.18) and (3.30) suggests that the Bahr method with its analytical formulae and the Groom-Bailey method with its least squares fitting procedure offer the same information about local and regional structures (regional strike, phases and apparent amplitudes of principal regional impedances, deflection angles or twist and shear angles). The special merit of the Bahr method is that it suggests some auxiliary parameters ($skew_{\mathrm{B}}$, μ, Δ) that help to estimate the applicability of the truncated local-regional decomposition with a real-valued electric distortion tensor and a two-dimensional regional impedance. But the Groom-Bailey method has the advantage that due to the least squares fitting procedure it may provide better stability of the local-regional decomposition.

To illustrate the Bahr and Groom-Bailey methods numerically, we turn back to the superimposition model shown in Fig. 1.11. Here a local conductive body L in the form of vertical cylinder is superimposed upon a regional conductive two-dimensional prism R. Let ρ_1=100 Ohm·m, h_1= 0.1 km, ρ_L = 10 Ohm·m, a = 0.1 km, $\rho_2 = \infty$, h_2 = 100 km, ρ_R = 10 Ohm·m, h'_2 = 10 km, Δh = 10 km, v = 200 km, $\rho_3 = 0$. The problem was solved by the hybrid method given in Sect. 1.3.4. Calculations were carried out for the observation site O in the immediate neighborhood of the conductive cylinder (r = 0.11 km, $\theta = 45^{\mathrm{o}}$, $\alpha = 45^{\circ}$).

Figure 3.5 depicts the longitudinal and transverse apparent-resistivity and impedance-phase curves computed from the regional impedance in the absence of the local near-surface inhomogeneity. The effect of the buried conductive prism is clearly visible in longitudinal curves $\rho^{\parallel}$ and $\varphi^{\parallel}$. Special attention must be given to the phase curves. At $\sqrt{T} < 0.1\,\mathrm{s}^{1/2}$, $\sqrt{T} \approx 3\,\mathrm{s}^{1/2}$ and $\sqrt{T} > 100\,\mathrm{s}^{1/2}$ the phases of longitudinal and transverse impedances virtually coincide.

Consider some characteristic parameters, which define the applicability of the Bahr and Groom-Bailey decompositions. These parameters are: (1) Swift's $skew_{\mathrm{s}}$, (1.60), (2) Bahr's $skew_{\mathrm{B}}$, (1.61), (3) phase difference Δ (difference between longitudinal and transverse phases calculated directly from the superimposition impedance $[\mathbf{Z}^S]$), (3.21). Appart from these parameters, we also consider a model parameter q measuring the contribution of the local magnetic anomaly:

$$q = 0.5\,\|\mathbf{m}\| = 0.5\sqrt{|h_{xx} - 1|^2 + |h_{xy}|^2 + |h_{yx}|^2 + |h_{yy} - 1|^2}, \qquad (3.35)$$

where q is a calibrated Euclidean norm of difference $[\mathbf{m}] = [\mathbf{h}] - [\mathbf{I}]$ between the magnetic distortion matrix $[\mathbf{h}]$ and the identity matrix $[\mathbf{I}]$. Recall that local-regional Bahr's and Groom-Bailey's methods are applicable providing that $skew_B$ and q are sufficiently small, while Δ is sufficiently large.

Figure 3.6 shows all these parameters versus $\sqrt{\mathrm{T}}$. At high frequencies ($\sqrt{\mathrm{T}} < 0.1$ $\mathrm{s}^{1/2}$) the regional two-dimensional structure does not manifest itself, and the superimposition model acts as an axisymmetric model containing only a vertical near-surface cylinder. Here $skew_S$ and $skew_B$ come close to zero, while magnetic distortion is rather large ($q > 0.3$). However at intermediate frequencies

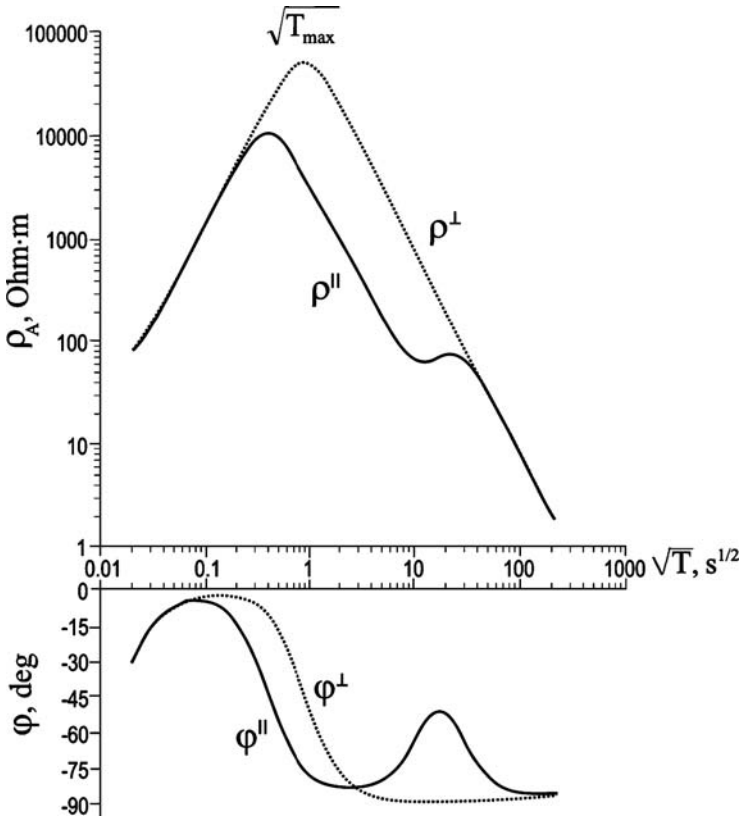

Fig. 3.5 Longitudinal and transverse apparent-resistivity and impedance-phase curves computed from the two-dimensional regional impedance; the superimposition model is shown in Fig. 1.11

(0.1 $s^{1/2} < \sqrt{T} < 10\ s^{1/2}$) the axial symmetry is violated by the regional structure, so that $skew_S$ ranges up to about 0.4. An increase in $skew_S$ is accompanied by an increase in $skew_B$ which reaches its peak at $\sqrt{T} = 0.5\ s^{1/2}$ and then tends to zero indicating the attenuation of local induction effects. Small values of $skew_B$ correlate with a drop in parameter q, which indicates the decay of local magnetic distortions. With small $skew_B$ and q we choose an area $5\ s^{1/2} < \sqrt{T} < 60\ s^{1/2}$, where the phase difference Δ varies from 7.5° to 35°. This area is most favorable for the local-regional decomposition. Coming back to Fig. 3.5, we see that the favorable area begins with $T \approx 25\,T_{max}$ where T_{max} is a period for the maximum of the $\rho^{\perp}-$ curve.

The Bahr and Groom-Bailey decompositions were carried out against random noises with standard deviation of 5% in the impedance amplitudes and 3° in the impedance phases.

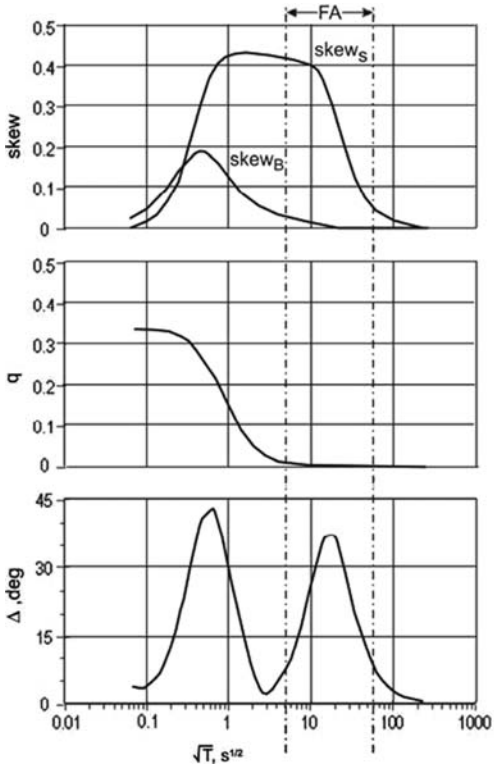

Fig. 3.6 Characteristic parameters $skew_S$, $skew_B$, Δ, q for the superimposition model shown in Fig. 1.11; FA – area favorable for LR-decomposition

Figures 3.7 and 3.8 present the regional strike angle α_R, the phases $\varphi^{\parallel}$ and $\varphi^{\perp}$ of the longitudinal and transverse regional impedances as well as the deflection angles β_x and β_y determined by Bahr's formulae. Within the favorable area FA the scatter in α_R varies from 10÷15° to 3÷6°, whereas outside the area FA it reaches 45° and even more. The scatter in $\varphi^{\perp}$ does not exceed 2÷3° (even outside the area FA), whereas the scatter in $\varphi^{\parallel}$ varies from 10÷15° to 2÷3°. The scatter in β_x and β_y is about 5÷10° within the area FA and increases to 15° outside this area.

Figures 3.9 and 3.10 presents the regional strike angle α, the phases $\varphi^{\parallel}$ and $\varphi^{\perp}$ of the longitudinal and transverse regional impedances as well as the twist and shear angles β_t and β_s determined by means of Groom-Bailey's least squares fitting procedure. Outside the favorable area FA the scatter in α_R ranges up to 30°, however within this area it drops to 5÷7°. The scatter in phases is about 3° for $\varphi^{\perp}$ and 3÷7° for $\varphi^{\parallel}$. The scatter in β_t and β_s is about 3–8° within the favorable area and increases to 25÷30° outside this area. Comparing the Bahr and Croom-Bailey decompositions, we see that Groom-Bailey's least squares fitting procedure provides more stable results that Bahr's analytical formulae.

It would be natural to combine the Bahr and Groom-Bailey techniques. It seems that the efficient separation of local and regional effects should consist of two stages. In the initial stage we have to choose frequencies favorable for local-regional

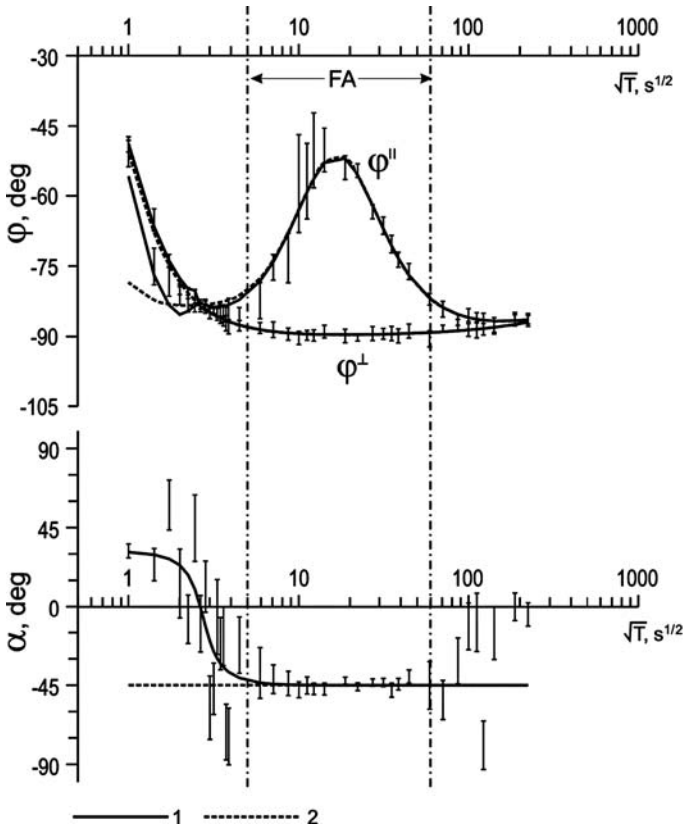

Fig. 3.7 The Bahr decomposition in the superimposition model shown in Fig. 1.11; α-regional strike, $\varphi^{\parallel}$ and $\varphi^{\perp}$- longitudinal and transverse phases of the two-dimensional regional impedance; vertical bars characterize the data scattering caused by measurement noise, FA – favorable area, 1-data for the noise-free impedance, 2-true data

decomposition. To this end we analyze $skew_S$ and $skew_B$ as well as phase parameter μ and phase difference Δ. In the later stage we take better advantage of Groom-Bailey's least squares fitting procedure and find regional strike angle α_R, regional impedance phases $\arg\zeta_1^R$, $\arg\zeta_2^R$ as well as twist and shear angles β_t, β_s. These latter can be converted to Bahr's deflection angles β_x, β_y which offer a clearer view of near-surface inhomogeneities. And finally the slight frequency dependence of α_R, $\arg\zeta_1^R$, $\arg\zeta_2^R$, and β_t, β_s may serve as a criterion for reliability of the local-regionall decomposition.

Following Jones and Groom (1993) and McNeice and Jones (2001), we can increase the noise-immunity of the Bahr-Groom-Bailey decomposition and separate the local and regional effects even in the case that the phase difference between the longitudinal and transverse regional impedances is rather small. On this way we apply the least squares statistic to a band of *n* frequencies and compose a system of

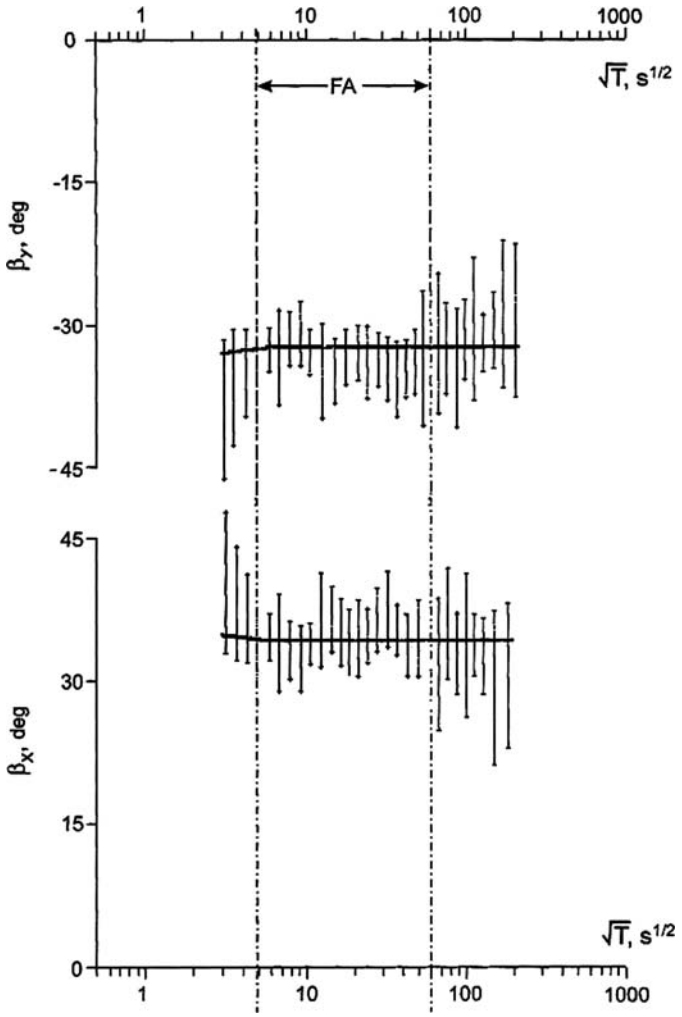

Fig. 3.8 The Bahr decomposition in the superimposition model shown in Fig. 1.11; β_x and β_y – deflection angles; vertical bars characterize the data scattering caused by measurement noise, FA – favorable area

$8n$ equations in $4n+3$ unknowns (real and imaginary parts of longitudinal and transverse regional impedances and frequency-independent α_R, β_t, β_s). Let $n = 5$. Thus, we have 40 equations in 23 unknowns. Solving this overdetermined system of equations, we considerably smooth out the scatter in the local and regional parameters. Another multi-frequency statistic has been suggested by Smith (1995). On this way we examine a sequence of tentative regional strikes, stepping in small increment to the strike angle, and select the best-fitting strike by weighted misfit minimization, taking into account the correlated measurements errors.

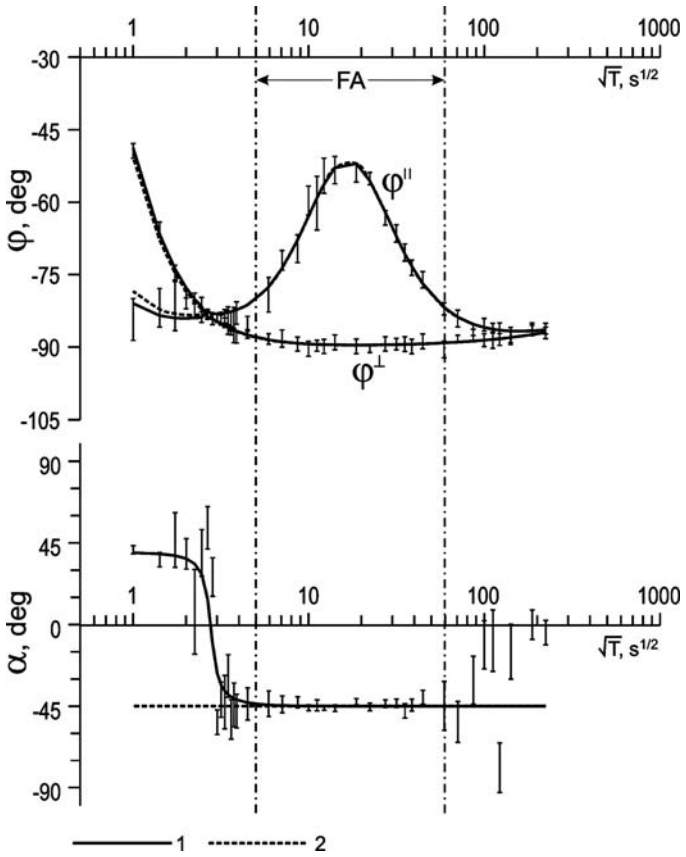

Fig. 3.9 The Groom-Bailey decomposition in the superimposition model shown in Fig. 1.11; α – regional strike, $\varphi^{\parallel}$ and $\varphi^{\perp}$ – longitudinal and transverse phases of the two-dimensional regional impedance; vertical bars characterize the data scattering caused by measurement noise, FA – favorable area, 1-data for the noise-free impedance, 2-true data

3.3 The Zhang-Roberts-Pedersen Method

Next we examine a special case that the (2D+2D)-superimposition model contains a two-dimensional local near-surface structure L over a two-dimensional regional structure R. The case has been investigated by Zhang et al. in their pioneering work (1987).

Let α_R and α_L be the angles of regional and local strike respectively (Fig. 3.11). In the regional coordinate system the *x,y*-axes are along and across the strike of the regional structure. In that event

$$[\mathbf{Z}^R] = \begin{bmatrix} 0 & \zeta_1^R \\ -\zeta_2^R & 0 \end{bmatrix},$$

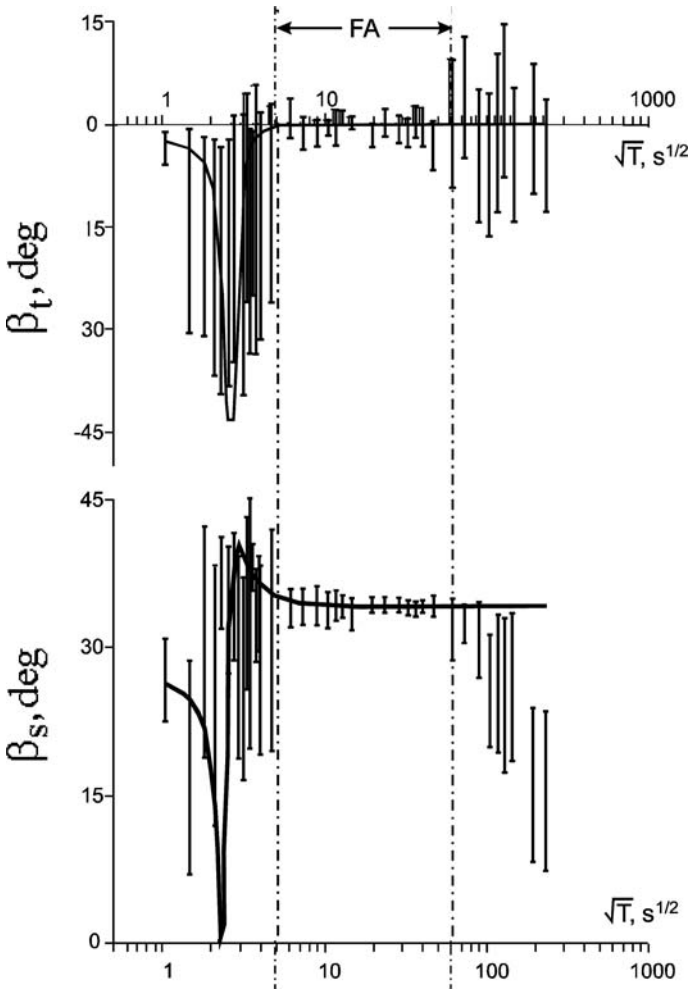

Fig. 3.10 The Groom-Bailey decomposition for the superimposition model shown in Fig. 1.11; β_t and β_s – twist-angle and shear-angle; vertical bars characterize the data scattering caused by measurement noise, FA – favorable area, 1-data for the noise-free local impedance, 2-true data

where ζ_1^R and ζ_2^R are principal values of the regional impedance tensor (the longitudinal and transverse impedances). Rotating the regional impedance $[\mathbf{Z}^R]$ trough the clockwise angle $\Delta\alpha = \alpha_L - \alpha_R$, we pass to the local coordinate system with the *x,y*-axes along and across the strike of the local structure. According to (1.27),

$$[\mathbf{Z}^R(\Delta\alpha)] = \begin{bmatrix} Z_3^R \sin 2\Delta\alpha & Z_1^R + Z_3^R \cos 2\Delta\alpha \\ -Z_1^R + Z_3^R \cos 2\Delta\alpha & -Z_3^R \sin 2\Delta\alpha \end{bmatrix}, \tag{3.36}$$

where

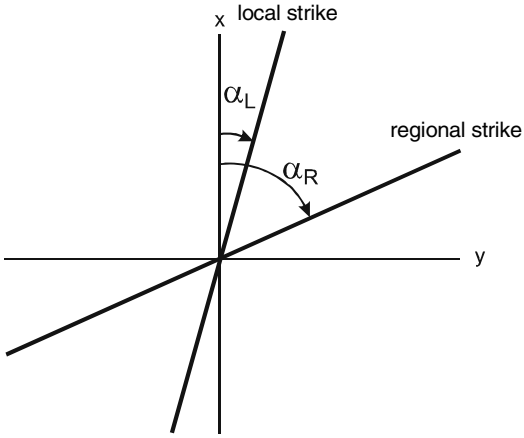

Fig. 3.11 Illustrating the Zhang-Roberts-Pedersen method

$$Z_1^R = \frac{\zeta_1^R + \zeta_2^R}{2}, \qquad Z_3^R = \frac{\zeta_1^R - \zeta_2^R}{2}.$$

It follows from the symmetry of a two-dimensional structure L that in the local coordinates the real-valued electric distortion tensor is diagonal:

$$[\mathbf{e}] = \begin{bmatrix} e_{xx} & 0 \\ 0 & e_{yy} \end{bmatrix} = \begin{bmatrix} e^{\parallel} & 0 \\ 0 & e^{\perp} \end{bmatrix}. \tag{3.37}$$

Here the positive longitudinal and transverse components, $e_{xx} = e^{\parallel}$ and $e_{yy} = e^{\perp}$, are aligned with and against the local strike. Thus, in the local coordinate system the superimposition impedance $[\mathbf{Z}^S]$ assumes the form

$$\begin{aligned}[\mathbf{Z}^S] &= \begin{bmatrix} Z_{xx}^S & Z_{xy}^S \\ Z_{yx}^S & Z_{yy}^S \end{bmatrix} = \begin{bmatrix} e^{\parallel} & 0 \\ 0 & e^{\perp} \end{bmatrix} \begin{bmatrix} Z_3^R \sin 2\Delta\alpha & Z_1^R + Z_3^R \cos 2\Delta\alpha \\ -Z_1^R + Z_3^R \cos 2\Delta\alpha & -Z_3^R \sin 2\Delta\alpha \end{bmatrix} \\ &= \begin{bmatrix} e^{\parallel} Z_3^R \sin 2\Delta\alpha & e^{\parallel}(Z_1^R + Z_3^R \cos 2\Delta\alpha) \\ -e^{\perp}(Z_1^R - Z_3^R \cos 2\Delta\alpha) & -e^{\perp} Z_3^R \sin 2\Delta\alpha \end{bmatrix}, \end{aligned} \tag{3.38}$$

where the diagonal components, Z_{xx}^S and Z_{yy}^Z, are anti-phase:

$$\arg Z_{xx}^S = \arg Z_{yy}^S + \pi\,. \tag{3.39}$$

A distinguishing feature of $[\mathbf{Z}^S]$ is that $skew_S = 0$, $skew_B = 0$ in the high frequency range (we observe only the local symmetrical effect) and $skew_S \neq 0$, $skew_B = 0$ in the low frequency range (we observe an asymmetrical superimposition of local and regional effects).

Now take a tensor $[\mathbf{Z}^S]$ measured on arbitrary axes *x, y*. Using the Bahr or Groom-Bailey decomposition, we determine the regional strike. To determine the local strike, we rotate $[\mathbf{Z}^S]$ trough a clockwise angle α so that components $Z_{xx}^S(\alpha)$ and $Z_{yy}^S(\alpha)$ satisfy (3.39). This condition can be written as

$$\mathrm{Im}\{Z^S_{xx}(\alpha)\,\bar{Z}^S_{yy}(\alpha)\} = 0, \qquad \mathrm{Re}\{Z^S_{xx}(\alpha)\,\bar{Z}^S_{yy}(\alpha)\} < 0 \tag{3.40}$$

or, with account for (1.27),

$$\begin{aligned}
&\mathrm{Im}\{(Z^S_2 + Z^S_3\sin 2\alpha + Z^S_4\cos 2\alpha)(\bar{Z}^S_2 - \bar{Z}^S_3\sin 2\alpha - \bar{Z}^S_4\cos 2\alpha)\}\\
&\quad = 2\mathrm{Im}(\bar{Z}^S_2 Z^S_3\sin 2\alpha + \bar{Z}^S_2 Z^S_4\cos 2\alpha) = 0,\\
&\mathrm{Re}\{(Z^S_2 + Z^S_3\sin 2\alpha + Z^S_4\cos 2\alpha)(\bar{Z}^S_2 - \bar{Z}^S_3\sin 2\alpha - \bar{Z}^S_4\cos 2\alpha)\} < 0,
\end{aligned}$$

where

$$Z^S_2 = \frac{Z^S_{xx} + Z^S_{yy}}{2}, \qquad Z^S_3 = \frac{Z^S_{xy} + Z^S_{yx}}{2}, \qquad Z^S_4 = \frac{Z^S_{xx} - Z^S_{yy}}{2}.$$

Hence

$$\begin{aligned}
\alpha &= \frac{1}{2}\arctan\frac{\mathrm{Im}Z^S_2\bar{Z}^S_4}{\mathrm{Im}\bar{Z}^S_2 Z^S_3}\\
&= \frac{1}{2}\arctan\frac{2\mathrm{Im}Z^S_{yy}\bar{Z}^S_{xx}}{\mathrm{Im}(Z_{xy} + Z_{yx})(\bar{Z}_{xx} + \bar{Z}_{yy})} = \begin{cases}\alpha_L\\ \alpha_L + \dfrac{\pi}{2}\end{cases}
\end{aligned} \tag{3.41}$$

with

$$\left|\frac{(Z^S_{xy} + Z^S_{yx})\sin 2\alpha + (Z^S_{xx} - Z^S_{yy})\cos 2\alpha}{Z^S_{xx} + Z^S_{yy}}\right| > 0.$$

Similarly to the Bahr method, we define the local superficial strike by the simple analytical formula. It is easy to verify that in the presence of measurement errors and model discrepancies this formula provides the best approximation to the condition (3.40), which defines the anti-phase state in the diagonal components of the superimposition tensor $[\mathbf{Z}^S]$.

The Zhang-Roberts-Pedersen method may considerably extend the useful working range of the Bahr-Groom-Bailey method. Combining both of these methods, we get not only the strike of a regional structure, but the strike of a near-surface local structure as well.

Moreover, we can take an advantage of the Zhang-Roberts-Pedersen method and estimate (at least roughly) the static effect of the superficial local structure and evaluate the principal regional impedances. Assume that a local structure is sufficiently long. Then considering L as a two-dimensional structure, we disregard the galvanic effect of the longitudinal current (electric charges hardly appear) and take $e^{\parallel} \approx 1$. Thus, we return to (3.38), we write

$$[\mathbf{Z}^S] = \begin{bmatrix} Z^S_{xx} & Z^S_{xy}\\ Z^S_{yx} & Z^S_{yy}\end{bmatrix} \approx \begin{bmatrix} Z^R_3\sin 2\Delta\alpha & Z^R_1 + Z^R_3\cos 2\Delta\alpha\\ -e^{\perp}(Z^R_1 - Z^R_3\cos 2\Delta\alpha) & -e^{\perp}Z^R_3\sin 2\Delta\alpha\end{bmatrix}, \tag{3.42}$$

from which

$$e^{\perp} \approx \left| \frac{Z^S_{yy}}{Z^S_{xx}} \right| \tag{3.43}$$

and

$$Z^R_1 \approx \frac{1}{2}\left\{ Z^S_{xy} - \frac{Z^S_{yx}}{e^{\perp}} \right\} \approx \frac{1}{2}\left\{ Z^S_{xy} - Z^S_{yx} \left| \frac{Z^S_{xx}}{Z^S_{yy}} \right| \right\}$$

$$Z^R_3 \approx \frac{1}{2\cos 2(\alpha_L - \alpha_R)}\left\{ Z^S_{xy} + \frac{Z^S_{yx}}{e^{\perp}} \right\} \approx \frac{1}{2\cos 2(\alpha_L - \alpha_R)}\left\{ Z^S_{xy} + Z^S_{yx} \left| \frac{Z^S_{xx}}{Z^S_{yy}} \right| \right\} \tag{3.44}$$

or

$$\zeta^R_1 = Z^R_1 + Z^R_3 \approx \frac{1}{2}\left\{ 1 + \frac{1}{\cos 2(\alpha_L - \alpha_R)} \right\} Z^S_{xy} - \frac{1}{2}\left\{ 1 - \frac{1}{\cos 2(\alpha_L - \alpha_R)} \right\} Z^S_{yx} \left| \frac{Z^S_{xx}}{Z^S_{yy}} \right|,$$

$$\zeta^R_2 = Z^R_1 - Z^R_3 \approx \frac{1}{2}\left\{ 1 - \frac{1}{\cos 2(\alpha_L - \alpha_R)} \right\} Z^S_{xy} - \frac{1}{2}\left\{ 1 + \frac{1}{\cos 2(\alpha_L - \alpha_R)} \right\} Z^S_{yx} \left| \frac{Z^S_{xx}}{Z^S_{yy}} \right|, \tag{3.45}$$

where Z^S_{xx}, Z^S_{xy}, Z^S_{yx}, Z^S_{yy} are components of the superimposition tensor $[\mathbf{Z}^S]$ expressed in local coordinates, and ζ^R_1, ζ^R_2 are principal values of the regional impedance.

Note that the findings of the Zhang-Roberts-Pedersen procedure are stable if the phase difference in the longitudinal and transverse regional impedances is rather large (say, 15–20°). In this point the Zhang-Roberts-Pedersen method is similar to the Bahr and Groom-Bailey methods.

3.4 The Chave-Smith Method

Chave and Smith (1994) considered not only the local electric distortions but the magnetic distortions as well and suggested a method based on the full local-regional decomposition (1.74). On this way we significantly extend the frequency range favorable for the local-regional decomposition. Recall, for instance, that in the case of a three-layered K-type medium we apply the truncated Bahr-Groom-Bailey decomposition beginning with T which far exceeds a period $T_{\max}$ for the maximum of the ρ_A-curve. With Chave-Smith's technique we can come down to T close to $T_{\max}$.

Return to the local-regional decomposition (3.25) underlying the Groom-Bailey method and rewrite it together with the magnetic distortion tensor [**h**]:

$$[\mathbf{Z}^S] = G\,[\tilde{\mathbf{T}}]\,[\tilde{\mathbf{S}}]\,[\tilde{\mathbf{A}}]\,[\mathbf{Z}^R]\,[\mathbf{h}]^{-1}, \tag{3.46}$$

where

$$G = g\frac{1}{\sqrt{(1+s^2)(1+t^2)(1+a^2)}}$$

and

$$[\tilde{\mathbf{T}}] = \begin{bmatrix} 1 & -t \\ t & 1 \end{bmatrix}, \qquad [\tilde{\mathbf{S}}] = \begin{bmatrix} 1 & s \\ s & 1 \end{bmatrix}, \qquad [\tilde{\mathbf{A}}] = \begin{bmatrix} 1+a & 0 \\ 0 & 1-a \end{bmatrix},$$

$$[\mathbf{Z}^R] = \begin{bmatrix} 0 & \zeta_1^R \\ -\zeta_2^R & 0 \end{bmatrix}, \qquad [\mathbf{h}] = [\mathbf{I}] + [\tilde{\mathbf{h}}]\,[\mathbf{Z}^R].$$

The incorporation of $[\mathbf{h}]$ into matrix equation (3.46) aggravates its indeterminacy. To get a resolvable system of equations giving the regional strike, we have to reduce the number of unknowns. To this end we expand $[\tilde{\mathbf{h}}]$ into the sum of diagonal and anti-diagonal tensors:

$$[\tilde{\mathbf{h}}] = \begin{bmatrix} \tilde{h}_{xx} & \tilde{h}_{xy} \\ \tilde{h}_{yx} & \tilde{h}_{yy} \end{bmatrix} = \begin{bmatrix} \tilde{h}_{xx} & 0 \\ 0 & \tilde{h}_{yy} \end{bmatrix} + \begin{bmatrix} 0 & \tilde{h}_{xy} \\ \tilde{h}_{yx} & 0 \end{bmatrix} = [\tilde{\mathbf{h}}]_D + [\tilde{\mathbf{h}}]_A\ ,$$

where

$$[\tilde{\mathbf{h}}]_D = \begin{bmatrix} \tilde{h}_{xx} & 0 \\ 0 & \tilde{h}_{yy} \end{bmatrix}, \qquad [\tilde{\mathbf{h}}]_A = \begin{bmatrix} 0 & \tilde{h}_{xy} \\ \tilde{h}_{yx} & 0 \end{bmatrix}.$$

Using this representation, we simplify the (3.46). On rather cumbersome algebra, we obtain:

$$\begin{aligned} [\mathbf{Z}^R]\,[\mathbf{h}]^{-1} &= [\mathbf{Z}^R]\,\{[\mathbf{I}] + [\tilde{\mathbf{h}}][\mathbf{Z}^R]\}^{-1} = \{(\,[\mathbf{I}] + [\tilde{\mathbf{h}}][\mathbf{Z}^R]\,)\,[\mathbf{Z}^R]^{-1}\} \\ &= \{(\,[\mathbf{I}] + [\tilde{\mathbf{h}}]_A[\mathbf{Z}^R]\,)\,[\mathbf{Z}^R]^{-1} + [\tilde{\mathbf{h}}]_D\}^{-1} = \left([\breve{\mathbf{Z}}^R]^{-1} + [\tilde{\mathbf{h}}]_D\right)^{-1} \\ &= \{(\,[\mathbf{I}] + [\tilde{\mathbf{h}}]_D[\breve{\mathbf{Z}}^R]\,)\,[\breve{\mathbf{Z}}^R]^{-1}\}^{-1} = [\breve{\mathbf{Z}}^R]\,(\,[\mathbf{I}] + [\tilde{\mathbf{h}}]_D[\breve{\mathbf{Z}}^R]\,)^{-1} \\ &= [\breve{\mathbf{Z}}^R]\,[\breve{\mathbf{h}}]^{-1}\ , \end{aligned} \tag{3.47}$$

where $[\breve{\mathbf{Z}}^R]$ is the transformed regional tensor with the anti-diagonal matrix:

$$\begin{aligned} [\breve{\mathbf{Z}}^R] &= [\mathbf{Z}^R]\,(\,[\mathbf{I}] + [\tilde{\mathbf{h}}]_A[\mathbf{Z}^R]\,)^{-1} \\ &= \begin{bmatrix} 0 & \zeta_1^R \\ -\zeta_2^R & 0 \end{bmatrix} \left(\begin{bmatrix} 1 & 0 \\ 0 & 1 \end{bmatrix} + \begin{bmatrix} 0 & \tilde{h}_{xy} \\ \tilde{h}_{yx} & 0 \end{bmatrix} \begin{bmatrix} 0 & \zeta_1^R \\ -\zeta_2^R & 0 \end{bmatrix} \right)^{-1} = \begin{bmatrix} 0 & \breve{\zeta}_1^R \\ -\breve{\zeta}_2^R & 0 \end{bmatrix}, \\ \breve{\zeta}_1^R &= \frac{\zeta_1^R}{1 + \tilde{h}_{yx}\zeta_1^R}\ , \quad \breve{\zeta}_2^R = \frac{\zeta_2^R}{1 - \tilde{h}_{xy}\zeta_2^R} \end{aligned} \tag{3.48}$$

and $[\breve{\mathbf{h}}]$ is the transformed magnetic distortion tensor whose matrix contains two unknown components on the secondary diagonal:

$$[\breve{\mathbf{h}}] = [\mathbf{I}] + [\tilde{\mathbf{h}}]_D[\breve{\mathbf{Z}}^R] = \begin{bmatrix} 1 & 0 \\ 0 & 1 \end{bmatrix} + \begin{bmatrix} \tilde{h}_{xx} & 0 \\ 0 & \tilde{h}_{yy} \end{bmatrix} \begin{bmatrix} 0 & \breve{\zeta}_1^R \\ -\breve{\zeta}_2^R & 0 \end{bmatrix} = \begin{bmatrix} 1 & \tilde{h}_{xx}\breve{\zeta}_1^R \\ -\tilde{h}_{yy}\breve{\zeta}_2^R & 1 \end{bmatrix}. \tag{3.49}$$

Substituting (3.47) into (3.46), we get

$$[\mathbf{Z}^S] = G\,[\tilde{\mathbf{T}}]\,[\tilde{\mathbf{S}}]\,[\tilde{\mathbf{A}}]\,[\breve{\mathbf{Z}}^R]\,[\breve{\mathbf{h}}]^{-1}. \tag{3.50}$$

This matrix equation holds the form of the initial equation (3.46), but it includes the transformed tensors $[\breve{\mathbf{Z}}^R]$ and $[\breve{\mathbf{h}}]$ instead of the regional impedance tensor $[\mathbf{Z}^R]$ and magnetic distortion tensor $[\mathbf{h}]$.

By analogy with (3.26) we introduce the apparent regional impedance $[\tilde{\mathbf{Z}}^R]$ absorbing the product $G\,[\tilde{\mathbf{A}}]$:

$$[\breve{\mathbf{Z}}^R] = G \begin{bmatrix} 1+a & 0 \\ 0 & 1-a \end{bmatrix} \begin{bmatrix} 0 & \breve{\zeta}_1^R \\ -\breve{\zeta}_2^R & 0 \end{bmatrix} = \begin{bmatrix} 0 & \tilde{\zeta}_1^R \\ -\tilde{\zeta}_2^R & 0 \end{bmatrix}, \tag{3.51}$$

where

$$\tilde{\zeta}_1^R = G\frac{(1+a)\zeta_1^R}{1+\tilde{h}_{yx}\zeta_1^R}, \qquad \tilde{\zeta}_2^R = G\frac{(1-a)\zeta_2^R}{1-\tilde{h}_{xy}\zeta_2^R}.$$

In this notation

$$[\mathbf{Z}^S] = [\tilde{\mathbf{T}}]\,[\tilde{\mathbf{S}}]\,[\tilde{\mathbf{Z}}^R]\,[\breve{\mathbf{h}}]^{-1}. \tag{3.52}$$

Here

$$[\breve{\mathbf{h}}] = [\mathbf{I}] + [\tilde{\mathbf{h}}]_D[\breve{\mathbf{Z}}^R] = [\mathbf{I}] + [\tilde{\mathbf{h}}]_D\frac{[\tilde{\mathbf{A}}]^{-1}}{G}G\,[\tilde{\mathbf{A}}][\breve{\mathbf{Z}}^R] = [\mathbf{I}] + [\hat{\mathbf{h}}]_D[\tilde{\mathbf{Z}}^R], \tag{3.53}$$

where $[\hat{\mathbf{h}}]_D$ is the diagonal tensor

$$[\hat{\mathbf{h}}]_D = [\tilde{\mathbf{h}}]_D\frac{[\tilde{\mathbf{A}}]^{-1}}{G} = \begin{bmatrix} \hat{h}_{xx} & 0 \\ 0 & \hat{h}_{yy} \end{bmatrix}$$

with components

$$\hat{h}_{xx} = \frac{\tilde{h}_{xx}}{G(1+a)}, \qquad \hat{h}_{yy} = \frac{\tilde{h}_{yy}}{G(1-a)}.$$

In an arbitrary coordinate system, we have the matrix equation:

$$[\mathbf{Z}^S] = [\mathbf{R}(\alpha_R)]^{-1}\,[\tilde{\mathbf{T}}]\,[\tilde{\mathbf{S}}]\,[\tilde{\mathbf{Z}}^R]\,[\breve{\mathbf{h}}]^{-1}[\mathbf{R}(\alpha_R)], \tag{3.54}$$

where α_R is the regional strike angle measured clockwise from the x-axis. In the full form

$$\begin{aligned}
Z_1^S &= \frac{(1-st)\tilde{\zeta}_1^R + (1+st)\tilde{\zeta}_2^R - \{\hat{h}_{yy}(s+t) - \hat{h}_{xx}(s-t)\}\tilde{\zeta}_1^R\tilde{\zeta}_2^R}{2(1+\hat{h}_{xx}\hat{h}_{yy}\tilde{\zeta}_1^R\tilde{\zeta}_2^R)},\\
Z_2^S &= \frac{(s+t)\tilde{\zeta}_1^R - (s-t)\tilde{\zeta}_2^R + \{\hat{h}_{yy}(1-st) + \hat{h}_{xx}(1+st)\}\tilde{\zeta}_1^R\tilde{\zeta}_2^R}{2(1+\hat{h}_{xx}\hat{h}_{yy}\tilde{\zeta}_1^R\tilde{\zeta}_2^R)},\\
Z_3^S &= \frac{(1-st)\tilde{\zeta}_1^R - (1+st)\tilde{\zeta}_2^R + \{\hat{h}_{yy}(s+t) + \hat{h}_{xx}(s-t)\}\tilde{\zeta}_1^R\tilde{\zeta}_2^R}{2(1+\hat{h}_{xx}\hat{h}_{yy}\tilde{\zeta}_1^R\tilde{\zeta}_2^R)}\cos 2\alpha_R\\
&\quad - \frac{(s+t)\tilde{\zeta}_1^R + (s-t)\tilde{\zeta}_2^R - \{\hat{h}_{yy}(1-st) - \hat{h}_{xx}(1+st)\}\tilde{\zeta}_1^R\tilde{\zeta}_2^R}{2(1+\hat{h}_{xx}\hat{h}_{yy}\tilde{\zeta}_1^R\tilde{\zeta}_2^R)}\sin 2\alpha_R\,,\\
Z_4^S &= -\frac{(s+t)\tilde{\zeta}_1^R + (s-t)\tilde{\zeta}_2^R - \{\hat{h}_{yy}(1-st) - \hat{h}_{xx}(1+st)\}\tilde{\zeta}_1^R\tilde{\zeta}_2^R}{2(1+\hat{h}_{xx}\hat{h}_{yy}\tilde{\zeta}_1^R\tilde{\zeta}_2^R)}\cos 2\alpha_R\\
&\quad - \frac{(1-st)\tilde{\zeta}_1^R - (1+st)\tilde{\zeta}_2^R - \{\hat{h}_{yy}(s+t) + \hat{h}_{xx}(s-t)\}\tilde{\zeta}_1^R\tilde{\zeta}_2^R}{2(1+\hat{h}_{xx}\hat{h}_{yy}\tilde{\zeta}_1^R\tilde{\zeta}_2^R)}\sin 2\alpha_R\,,
\end{aligned} \tag{3.55}$$

where

$$Z_1^S = \frac{Z_{xy}^S - Z_{yx}^S}{2} \qquad Z_2^S = \frac{Z_{xx}^S + Z_{yy}^S}{2}$$

$$Z_3^S = \frac{Z_{xy}^S + Z_{yx}^S}{2} \qquad Z_4^S = \frac{Z_{xx}^S - Z_{yy}^S}{2}\,.$$

On single frequency we have an underdetermined system of eight equations in nine unknowns: *t, s,* α_R, $\hat{h}_{xx}$, $\hat{h}_{yy}$ and $\mathrm{Re}\tilde{\zeta}_1^R$, $\mathrm{Im}\tilde{\zeta}_1^R$, $\mathrm{Re}\tilde{\zeta}_2^R$, $\mathrm{Im}\tilde{\zeta}_2^R$. It can be solved by least squares multifrequency fitting under the assumption that *t, s,* α_R, $\hat{h}_{xx}$, $\hat{h}_{yy}$ do not depend on frequency. Note that apparent regional impedances $\tilde{\zeta}_1^R$, $\tilde{\zeta}_2^R$ differ from the true regional impedances ζ_1^R, ζ_2^R not only in amplitude but in phase as well. So, we take into account the local magnetic anomalies, but restrict ourselves to determining the twist, shear, and regional strike.

3.5 The Caldwell-Bibby-Brown Method

The above techniques necessitate the two-dimensionality (or axial symmetry) of the regional background. Several approaches have been suggested to remove this constraint (Zhang et al., 1993; Utada and Munekane, 2000). The most intriguing approach was put forward by Caldwell et al. (2002a, b, 2004) and Bibby et al. (2005). Using the Caldwell-Bibby-Brown technique (*CBB method*), we analyze the phase tensor.

3.5.1 The Phase Tensor

Similar to the Bahr and Groom-Bailey methods, the Caldwell-Bibby-Brown method is based on the truncated low-frequency decomposition (1.75) neglecting the local magnetic distortions.

The idea of this elegant technique, which opens up fresh opportunities for separation of local and regional effects, is the following.

According to (1.75), $[\mathbf{Z}^S] = [\mathbf{e}]\,[\mathbf{Z}^R]$ where $[\mathbf{Z}^S]$ and $[\mathbf{Z}^R]$ are the superimposition and regional impedances, and $[\mathbf{e}]$ is the real-valued tensor of the local electric distortions. Applying this decomposition, we write

$$\begin{aligned}&[\mathbf{Z}^R] = [\mathrm{Re}\ \mathbf{Z}^R] + i\ [\mathrm{Im}\ \mathbf{Z}^R],\\ &[\mathbf{Z}^S] = [\mathrm{Re}\ \mathbf{Z}^S] + i[\mathrm{Im}\ \mathbf{Z}^S] = [\mathbf{e}]\ [\mathrm{Re}\ \mathbf{Z}^R] + i\ [\mathbf{e}][\mathrm{Im}\ \mathbf{Z}^R,\,]\end{aligned} \tag{3.56}$$

whence

$$[\mathrm{Re}\ \mathbf{Z}^S] = [\mathbf{e}]\ [\mathrm{Re}\ \mathbf{Z}^R], \qquad [\mathrm{Im}\ \mathbf{Z}^S] = [\mathbf{e}][\mathrm{Im}\ \mathbf{Z}^R]. \tag{3.57}$$

Let us introduce a real-valued tensor $[\mathbf{\Phi}]$ as the product of inverse of $[\mathrm{Re}\ \mathbf{Z}^S]$ by $[\mathrm{Im}\ \mathbf{Z}^S]$:

$$\begin{aligned}[\mathbf{\Phi}] = [\mathbf{\Phi}^S] &= [\mathrm{Re}\ \mathbf{Z}^S]^{-1}[\mathrm{Im}\ \mathbf{Z}^S] = [\mathrm{Re}\ \mathbf{Z}^R]^{-1}[\mathbf{e}]^{-1}[\mathbf{e}][\mathrm{Im}\ \mathbf{Z}^R]\\ &= [\mathrm{Re}\ \mathbf{Z}^R]^{-1}[\mathrm{Im}\ \mathbf{Z}^R] = [\mathbf{\Phi}^R] = \begin{bmatrix}\Phi_{xx} & \Phi_{xy}\\ \Phi_{yx} & \Phi_{yy}\end{bmatrix},\end{aligned} \tag{3.58}$$

where

$$\Phi_{xx} = \frac{\mathrm{Re}\ Z^S_{yy}\mathrm{Im}\ Z^S_{xx} - \mathrm{Re}\ Z^S_{xy}\mathrm{Im}\ Z^S_{yx}}{\mathrm{Re}\ Z^S_{xx}\mathrm{Re}\ Z^S_{yy} - \mathrm{Re}\ Z^S_{xy}\mathrm{Re}\ Z^S_{yx}} = \frac{\mathrm{Re}\ Z^R_{yy}\mathrm{Im}\ Z^R_{xx} - \mathrm{Re}\ Z^R_{xy}\mathrm{Im}\ Z^R_{yx}}{\mathrm{Re}\ Z^R_{xx}\mathrm{Re}\ Z^R_{yy} - \mathrm{Re}\ Z^R_{xy}\mathrm{Re}\ Z^R_{yx}},$$

$$\Phi_{xy} = \frac{\mathrm{Re}\, Z^S_{yy}\mathrm{Im}\, Z^S_{xy} - \mathrm{Re}\, Z^S_{xy}\mathrm{Im}\, Z^S_{yy}}{\mathrm{Re}\, Z^S_{xx}\mathrm{Re}\, Z^S_{yy} - \mathrm{Re}\, Z^S_{xy}\mathrm{Re}\, Z^S_{yx}} = \frac{\mathrm{Re}\, Z^R_{yy}\mathrm{Im}\, Z^R_{xy} - \mathrm{Re}\, Z^R_{xy}\mathrm{Im}\, Z^R_{yy}}{\mathrm{Re}\, Z^R_{xx}\mathrm{Re}\, Z^R_{yy} - \mathrm{Re}\, Z^R_{xy}\mathrm{Re}\, Z^R_{yx}},$$

$$\Phi_{yx} = \frac{\mathrm{Re}\, Z^S_{xx}\mathrm{Im}\, Z^S_{yx} - \mathrm{Re}\, Z^S_{yx}\mathrm{Im}\, Z^S_{xx}}{\mathrm{Re}\, Z^S_{xx}\mathrm{Re}\, Z^S_{yy} - \mathrm{Re}\, Z^S_{xy}\mathrm{Re}\, Z^S_{yx}} = \frac{\mathrm{Re}\, Z^R_{xx}\mathrm{Im}\, Z^R_{yx} - \mathrm{Re}\, Z^R_{yx}\mathrm{Im}\, Z^R_{xx}}{\mathrm{Re}\, Z^R_{xx}\mathrm{Re}\, Z^R_{yy} - \mathrm{Re}\, Z^R_{xy}\mathrm{Re}\, Z^R_{yx}},$$

$$\Phi_{yy} = \frac{\mathrm{Re}\, Z^S_{xx}\mathrm{Im}\, Z^S_{yy} - \mathrm{Re}\, Z^S_{yx}\mathrm{Im}\, Z^S_{xy}}{\mathrm{Re}\, Z^S_{xx}\mathrm{Re}\, Z^S_{yy} - \mathrm{Re}\, Z^S_{xy}\mathrm{Re}\, Z^S_{yx}} = \frac{\mathrm{Re}\, Z^R_{xx}\mathrm{Im}\, Z^R_{yy} - \mathrm{Re}\, Z^R_{yx}\mathrm{Im}\, Z^R_{xy}}{\mathrm{Re}\, Z^R_{xx}\mathrm{Re}\, Z^R_{yy} - \mathrm{Re}\, Z^R_{xy}\mathrm{Re}\, Z^R_{yx}}. \tag{3.59}$$

It is seen that $[\mathbf{\Phi}]$ is independent of local distortions. Without any assumptions of regional dimensionality we may derive the tensor $[\mathbf{\Phi}]$ immediately from the superimposition tensor $[\mathbf{Z}^S]$ as a true performance of the regional (one-dimensional, two-dimensional or three-dimensional) impedance $[\mathbf{Z}^R]$.

Rotating the tensor $[\mathbf{\Phi}]$ clockwise trough an angle α, we get

$$[\mathbf{\Phi}(\alpha)] = [\mathbf{R}(\alpha)]\,[\mathbf{\Phi}]\,[\mathbf{R}(\alpha)]^{-1}, \tag{3.60}$$

from which

$$\begin{aligned}
\Phi_{xx}(\alpha) &= \Phi_2 + \Phi_3 \sin 2\alpha + \Phi_4 \cos 2\alpha \\
\Phi_{xy}(\alpha) &= \Phi_1 + \Phi_3 \cos 2\alpha - \Phi_4 \sin 2\alpha \\
\Phi_{yx}(\alpha) &= -\Phi_1 + \Phi_3 \cos 2\alpha - \Phi_4 \sin 2\alpha \\
\Phi_{yy}(\alpha) &= \Phi_2 - \Phi_3 \sin 2\alpha - \Phi_4 \cos 2\alpha,
\end{aligned} \tag{3.61}$$

where

$$\begin{aligned}
\Phi_1 &= \frac{\Phi_{xy} - \Phi_{yx}}{2} \qquad \Phi_2 = \frac{\Phi_{xx} + \Phi_{yy}}{2}, \\
\Phi_3 &= \frac{\Phi_{xy} + \Phi_{yx}}{2} \qquad \Phi_4 = \frac{\Phi_{xx} - \Phi_{yy}}{2}.
\end{aligned} \tag{3.62}$$

The rotational invariants of the tensor $[\mathbf{\Phi}]$ are

$$\begin{aligned}
J_{14} &= \mathrm{tr}[\mathbf{\Phi}] = 2\Phi_2 = \Phi_{xx} + \Phi_{yy}, \\
J_{15} &= \det[\mathbf{\Phi}] = \Phi_{xx}\Phi_{yy} - \Phi_{xy}\Phi_{yx}, \\
J_{16} &= \Phi_{xy} - \Phi_{yx}, \\
J_{17} &= \|\mathbf{\Phi}\| = \sqrt{\Phi^2_{xx} + \Phi^2_{xy} + \Phi^2_{yx} + \Phi^2_{yy}}.
\end{aligned} \tag{3.63}$$

Take a model with a horizontally homogeneous (1D) medium containing local three-dimensional near-surface inhomogeneities. In this model, $Z^R_{xx} = Z^R_{yy} = 0$ and $Z^R_{xy} = -Z^R_{yx} = Z^R$, where Z^R is the regional one-dimensional impedance. Then, according to (3.60),

$$\Phi_{xx} = \frac{\text{Im } Z^R}{\text{Re } Z^R} = \tan\arg Z^R, \quad \Phi_{xy} = 0, \quad \Phi_{yx} = 0, \quad \Phi_{yy} = \frac{\text{Im } Z^R}{\text{Re } Z^R} = \tan\arg Z^R, \tag{3.64}$$

from which

$$[\mathbf{\Phi}] = \begin{bmatrix} \tan\arg Z^R & 0 \\ 0 & \tan\arg Z^R \end{bmatrix} = \tan\arg Z^R \begin{bmatrix} 1 & 0 \\ 0 & 1 \end{bmatrix}. \tag{3.65}$$

Here the tensor $[\mathbf{\Phi}]$ has a scalar matrix with the factor $\tan\arg Z^R$ characterizing the phase of the regional impedance.

Next examine a superimposition model with local three-dimensional near-surface inhomogeneities placed against a two-dimensional regional background. Let the x-axis run along the regional strike. Then

$$[\mathbf{Z}^R] = \begin{bmatrix} 0 & \zeta_1^R \\ -\zeta_2^R & 0 \end{bmatrix},$$

where ζ_1^R and ζ_2^R are principal values of the regional impedance tensor (the longitudinal and transverse impedances). By virtue of (3.60)

$$\Phi_{xx} = \frac{\text{Im } \zeta_2^R}{\text{Re } \zeta_2^R} = \tan\arg\zeta_2^R, \quad \Phi_{xy} = 0, \quad \Phi_{yx} = 0, \quad \Phi_{yy} = \frac{\text{Im } \zeta_1^R}{\text{Re } \zeta_1^R} = \tan\arg\zeta_1^R, \tag{3.66}$$

from which

$$[\mathbf{\Phi}] = \begin{bmatrix} \tan\arg\zeta_2^R & 0 \\ 0 & \tan\arg\zeta_1^R \end{bmatrix}. \tag{3.67}$$

Here the tensor $[\mathbf{\Phi}]$ has a diagonal matrix with the components $\tan\arg\zeta_2^R$ and $\tan\arg\zeta_1^R$ characterizing the phases of the transverse and longitudinal impedances. Evidently, the longitudinal and transverse directions are principal directions of the two-dimensional tensor $[\mathbf{\Phi}]$, while $\tan\arg\zeta_1^R$ and $\tan\arg\zeta_2^R$ are its principal values.

In accordance with (3.65) and (3.67), the tensor $[\mathbf{\Phi}]$ is given the name *phase tensor*.

Let us rotate the two-dimensional phase tensor $[\mathbf{\Phi}]$ clockwise through an angle α. According to (3.61),

$$\begin{aligned} \Phi_{xx} &= \Phi_2 + \Phi_4 \cos 2\alpha & \Phi_{xy} &= -\Phi_4 \sin 2\alpha \\ \Phi_{yx} &= -\Phi_4 \sin 2\alpha & \Phi_{yy} &= \Phi_2 - \Phi_4 \cos 2\alpha, \end{aligned}$$

from which

$$[\mathbf{\Phi}(\alpha)] = \begin{bmatrix} \Phi_2 + \Phi_4 \cos 2\alpha & -\Phi_4 \sin 2\alpha \\ -\Phi_4 \sin 2\alpha & \Phi_2 - \Phi_4 \cos 2\alpha \end{bmatrix}, \tag{3.68}$$

where

$$\Phi_2 = \frac{1}{2}(\tan \arg\zeta_1^R + \tan \arg\zeta_2^R) = \frac{\sin(\arg\zeta_1^R + \arg\zeta_2^R)}{2\cos \arg\zeta_1^R \cos \arg\zeta_2^R},$$
$$\Phi_4 = \frac{1}{2}(\tan \arg\zeta_1^R - \tan \arg\zeta_2^R) = \frac{\sin(\arg\zeta_1^R - \arg\zeta_2^R)}{2\cos \arg\zeta_1^R \cos \arg\zeta_2^R}.$$

In arbitrary coordinates, the two-dimensional phase tensor $[\mathbf{\Phi}]$ is symmetric. The similar properties of $[\mathbf{\Phi}]$ are observed in models with axially symmetric three-dimensional regional background. If the three-dimensional regional background is asymmetric, the symmetry of the phase tensor is violated.

3.5.2 Polar Diagrams of the Phase Tensor

The dependence of the components of the phase tensor upon the direction can be displayed by means of polar diagrams.

Let the phase tensor $[\mathbf{\Phi}]$ be defined on measurement axes x, y. Introduce new axes x', y' rotated through a clockwise angle α. In accordance with (3.61),

$$\begin{aligned} \varphi_{xx}(\alpha) &= |\arctan\Phi_{xx}(\alpha)| = |\arctan(\Phi_2 + \Phi_3 \sin 2\alpha + \Phi_4 \cos 2\alpha)|, \\ \varphi_{xy}(\alpha) &= \left|\arctan\Phi_{xy}(\alpha)\right| = |\arctan(\Phi_1 + \Phi_3 \cos 2\alpha - \Phi_4 \sin 2\alpha)|. \end{aligned} \tag{3.69}$$

Plotting these quantities on the x'-axis and changing α from 0 to 2π, we trace the polar diagrams of the phase tensor. They take the form of regular or irregular ovals with more or less narrow waist and may consist of four petals.

The φ_{xx}- and φ_{xy}-diagrams are exemplified in Fig. 3.12. They clearly indicate the dimensionality of regional structures.

In the event of horizontally homogeneous (1D) regional background, the φ_{xy}-diagram contracts to a point and vanishes, while the φ_{xx}-diagram is a circle of radius $\left|\arg Z^R\right|$ where Z^R is the regional one-dimensional impedance.

In the event of a two-dimensional or axially symmetric three-dimensional regional background, we have

$$\begin{aligned} \varphi_{xx} &= \left|\arctan(\Phi_{xx}\cos^2\alpha + \Phi_{yy}\sin^2\alpha)\right|, \\ \varphi_{xy} &= \left|\arctan\{(\Phi_{xx} - \Phi_{yy})\sin\alpha\cos\alpha\}\right|, \end{aligned} \tag{3.70}$$

where Φ_{xx}, Φ_{yy} are tangents of the phases of the longitudinal and transverse (or tangential and radial) regional impedances. The φ_{xx}-diagram assumes the form of

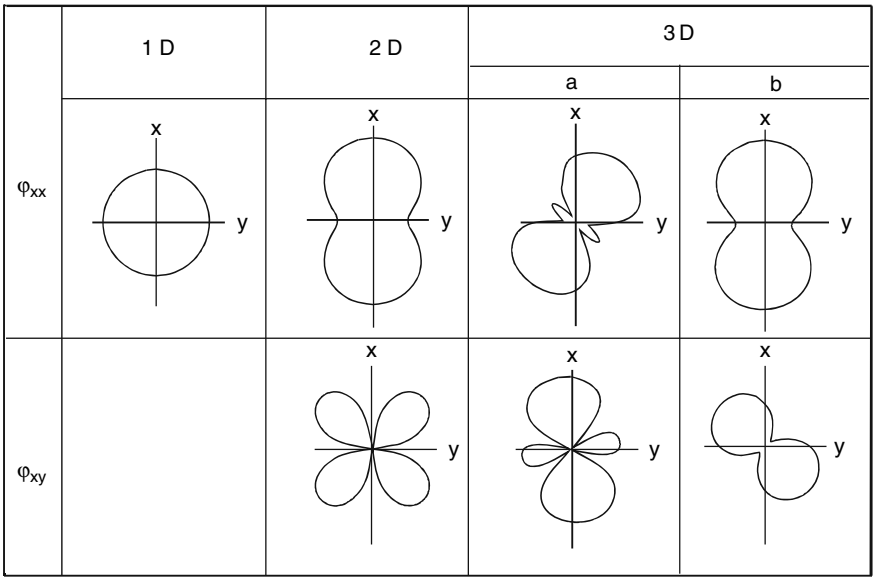

Fig. 3.12 Polar diagrams of the phase tensor;

1D: $Z = 4 - 2i$ $[\mathbf{\Phi} Z] = \begin{bmatrix} -0.5 & 0 \\ 0 & -0.5 \end{bmatrix}$,

2D: $[\mathbf{Z}] = \begin{bmatrix} 0 & 4-2i \\ -1+2i & 0 \end{bmatrix} \begin{matrix} skew_S = 0 \\ skew_B = 0 \end{matrix}$, $[\mathbf{\Phi}] = \begin{bmatrix} -2 & 0 \\ 0 & -0.5 \end{bmatrix}$ $skew_{CBB} = 0$,

3D,a: $[\mathbf{Z}] = \begin{bmatrix} -0.5-3i & 4-2i \\ -1+2i & 0.5+3i \end{bmatrix} \begin{matrix} skew_S = 0 \\ skew_B = 0.47 \end{matrix}$,

$[\mathbf{\Phi}] = \begin{bmatrix} -2.53 & -3.47 \\ -1.07 & -0.93 \end{bmatrix}$ $skew_{CBB} = 17.3^\circ$,

3D,b: $[\mathbf{Z}] = \begin{bmatrix} -0.5-3i & 4-2i \\ -1+2i & 0.1-i \end{bmatrix} \begin{matrix} skew_S = 0.63 \\ skew_B = 0.44 \end{matrix}$,

$[\mathbf{\Phi}] = \begin{bmatrix} -2.1 & 0.96 \\ -1.01 & -0.38 \end{bmatrix}$ $skew_{CBB} = 19.15^\circ$

a regular oval with a well-defined waist. Its maximal and minimal diameters are as large as doubled absolute value of the phases of the longitudinal and transverse (or tangential and radial) regional impedances. They are oriented in the longitudinal and transverse (or tangential and radial) directions. The φ_{xy}-diagram looks like a flower with four identical petals. The lines bisecting the angles between these petals are oriented in the longitudinal and transverse (or tangential and radial) directions.

In the event of asymmetric three-dimensional regional structures, the regular form of phase-tensor polar diagrams is violated. In the quasi-symmetric case ($skew_S = 0, skew_B \neq 0, skew_{CBB} \neq 0$) the 3D,a diagrams have petals of different

size. In the general case ($skew_S \neq 0$, $skew_B \neq 0$, $skew_{CBB} \neq 0$) the 3D,b diagrams look like a figure eight. It would be difficult to find any regularity in their relative positions.

To conclude, let us compare Fig. 3.12 with Fig. 1.7. The diagrams of φ_{xx} and $\arg Z_{xy}$ have similar form, while their orientations differ approximately by $\pi/2$.

3.5.3 The Phase-Tensor Eigenstate Problem

To solve the eigenstate problem, Caldwell and his workmates apply technique, which has its origin in the method of ellipses employed in the telluric current and dc-resistivity methods (Leonardon, 1948; Bibby, 1986).

Let us show the construction of the phase-tensor ellipse in some detail. The initial relation is

$$\mathbf{F}(\gamma) = [\mathbf{\Phi}]\ \mathbf{1}_\tau, \tag{3.71}$$

where the tensor $[\mathbf{\Phi}]$ transforms a circle, described by the horizontal unit vector $\mathbf{1}_\tau$, into the ellipse, described by the horizontal vector $\mathbf{F}$ which makes an angle γ with the x-axis. To find the equation of the phase-tensor ellipse, we apply the singular value decomposition of the phase tensor:

$$[\mathbf{\Phi}] = \begin{bmatrix} \cos(\alpha-\beta) & -\sin(\alpha-\beta) \\ \sin(\alpha-\beta) & \cos(\alpha-\beta) \end{bmatrix} \begin{bmatrix} \Psi_1 & 0 \\ 0 & \Psi_2 \end{bmatrix} \begin{bmatrix} \cos(\alpha+\beta) & \sin(\alpha+\beta) \\ -\sin(\alpha+\beta) & \cos(\alpha+\beta) \end{bmatrix}, \tag{3.72}$$

where Ψ_1 and Ψ_2 are the principal values of the phase tensor, $\Psi_1 \geq \Psi_2 > 0$. Solving the matrix equation (3.72), we get

$$\alpha = \frac{1}{2} \arctan \frac{\Phi_{xy} + \Phi_{yx}}{\Phi_{xx} - \Phi_{yy}}, \tag{3.73}$$

where $\alpha \in [0,\ \pi/2]$ when $\Phi_{xy} + \Phi_{yx} \geq 0$ and $\alpha \in (\pi/2,\ \pi)$ when $\Phi_{xy} + \Phi_{yx} < 0$,

$$\beta = \frac{1}{2} \arctan \frac{\Phi_{xy} - \Phi_{yx}}{\Phi_{xx} + \Phi_{yy}}, \tag{3.74}$$

where $\beta \in [0,\ \pi/2]$ when $\Phi_{xy} - \Phi_{yx} \geq 0$ and $\beta \in (\pi/2,\ \pi)$ when $\Phi_{xy} - \Phi_{yx} < 0$,

$$\begin{aligned} \Psi_1 &= \frac{1}{2} \left\{ \sqrt{\|\mathbf{\Phi}\|^2 + 2\,|\det[\mathbf{\Phi}]|} + \sqrt{\|\mathbf{\Phi}\|^2 - 2\,|\det[\mathbf{\Phi}]|} \right\}, \\ \Psi_2 &= \frac{1}{2} \left\{ \sqrt{\|\mathbf{\Phi}\|^2 + 2\,|\det[\mathbf{\Phi}]|} - \sqrt{\|\mathbf{\Phi}\|^2 - 2\,|\det[\mathbf{\Phi}]|} \right\}, \end{aligned} \tag{3.75}$$

where

$$\det[\mathbf{\Phi}] = \Phi_{xx}\Phi_{yy} - \Phi_{xy}\Phi_{yx},$$
$$\|\mathbf{\Phi}\| = \sqrt{\Phi_{xx}^2 + \Phi_{xy}^2 + \Phi_{yx}^2 + \Phi_{yy}^2}\,. \tag{3.76}$$

Substituting $[\mathbf{\Phi}]$ from (3.72) into (3.71), we obtain:

$$F^2 = \frac{\Psi_1^2\Psi_2^2}{\Psi_1^2\sin^2(\gamma-\alpha_1) + \Psi_2^2\cos^2(\gamma-\alpha_1)}, \tag{3.77}$$

where $\alpha_1 = \alpha - \beta$. This is the equation of an ellipse in polar coordinates F, γ. The major and minor semiaxes of the ellipse make the angles $\gamma = \alpha_1$ and $\gamma = \alpha_1 + \pi/2$ with the x-axis. They are equal to the principal values Ψ_1 and Ψ_2 of the phase tensor, which determine the principal phases $\varphi_1 = -\text{arctg}\Psi_1$ and $\varphi_2 = -\text{arctg}\Psi_2$ lying in the IV quadrant.

The phase-tensor ellipse can be constructed using (3.73), (3.74), and (3.75). It is defined by four independent parameters φ_1, φ_2, α, β that are free of distortions caused by near-surface inhomogeneities. These parameters characterize the regional background and fill all four degrees of freedom possessed by the matrix $[\mathbf{\Phi}]$.

The phase-tensor ellipses for a three-dimensional asymmetric and a two-dimensional regional backgrounds are exemplified in Fig. 3.13.

Let us consider the angles α and β, which control the orientation of the phase-tensor ellipse.

The angle α is defined by (3.73). It is curious that the Caldwell-Bibby-Brown formula (3.73), deduced for a three-dimensional asymmetric background, coincides with the basic Bahr formula (3.8), which yields the strike of the two-dimensional regional background. In fact, with due regard for (3.59),

$$\begin{aligned}\alpha &= \frac{1}{2}\arctan\frac{\Phi_{xy}+\Phi_{yx}}{\Phi_{xx}-\Phi_{yy}} \\ &= \frac{1}{2}\arctan\frac{\text{Re}\,Z_{yy}^S\text{Im}\,Z_{xy}^S - \text{Re}\,Z_{xy}^S\text{Im}\,Z_{yy}^S + \text{Re}\,Z_{xx}^S\text{Im}\,Z_{yx}^S - \text{Re}\,Z_{yx}^S\text{Im}\,Z_{xx}^S}{\text{Re}\,Z_{yy}^S\text{Im}\,Z_{xx}^S - \text{Re}\,Z_{xx}^S\text{Im}\,Z_{yy}^S + \text{Re}\,Z_{yx}^S\text{Im}\,Z_{xy}^S - \text{Re}\,Z_{xy}^S\text{Im}\,Z_{yx}^S} \\ &= \frac{1}{2}\arctan\frac{\text{Im}(Z_{yx}^S\bar{Z}_{xx}^S + Z_{xy}^S\bar{Z}_{yy}^S)}{\text{Im}(Z_{xx}^S\bar{Z}_{yy}^S + Z_{xy}^S\bar{Z}_{yx}^S)}\,.\end{aligned} \tag{3.78}$$

The angle β is defined by (3.74). This angular rotationally invariant parameter indicates the regional asymmetry. It is referred to as the *Caldwell-Bibby-Brown skew*:

$$skew_{CBB} = |\beta| = \frac{1}{2}\left|\arctan\frac{\Phi_{xy}-\Phi_{yx}}{\Phi_{xx}+\Phi_{yy}}\right|. \tag{3.79}$$

The Caldwell-Bibby-Brown $skew_{CBB}$ is taken in the range $[0,\ \pi/2]$. In models with 1D, 2D and axially symmetric 3D regional conductivity, $skew_{CBB} = 0$. Departure

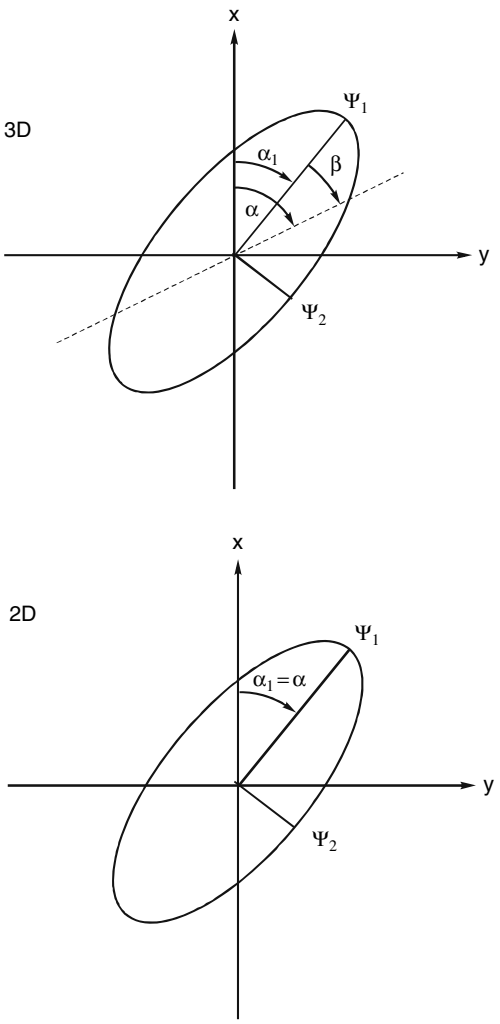

Fig. 3.13 Phase-tensor ellipses: 3D – three-dimensional regional background, 2D – two-dimensional regional background

of $skew_{CBB}$ from zero identifies the three-dimensional asymmetry of the regional background.

Note that the Caldwell-Bibby-Brown $skew_{CBB}$ given by (3.79) is connected with the Bahr $skew_B$ given by (1.61):

$$skew_{CBB} = \frac{1}{2}\arctan(M\, skew_B^2)\,, \tag{3.80}$$

where M is a scale factor

$$M = \frac{\left|Z_{xy}^S - Z_{yx}^S\right|^2}{(\Phi_{xx} + \Phi_{yy})(\mathrm{Re}\ Z_{xx}\mathrm{Re}\ Z_{yy} - \mathrm{Re}\ Z_{xy}\mathrm{Re}\ Z_{yx})}.$$

Let us come back to Fig. 3.13. In a model with the two-dimensional regional background, $skew_{CBB} = 0,\ skew_B = 0$ and $\alpha_1 = \alpha\,,\ \alpha_2 = \alpha + \pi/2$. So, applying the Cantwell-Bibby-Brown method, we determine the principal directions of the phase tensor that coincide with principal directions defined by Bahr's formula. Here the Cantwell-Bibby-Brown and Bahr methods give the identical results.

In the general case of the three-dimensonal asymmetric regional background, $skew_{CBB} \neq 0$ and $\alpha_1 = \alpha - \beta,\ \alpha_2 = \alpha - \beta + \pi/2$. Here we determine the principal directions of the phase tensor by the formula that is identical to Bahr's formula, but introduce a correction $\beta = skew_{CBB}$ for the regional background asymmetry. It is simply evident that such a correction makes sense if β considerably exceeds errors in the phase measurements With small β we can neglect the asymmetry and resort to the two-dimensional (or axially symmetric three-dimensional) approximation of the regional background.

Evidently, the Caldwell-Bibby-Brown method may be viewed as a three-dimensional generalization of the Bahr method.

Chapter 4
The Magnetovariational Response Functions

Along with the magnetotelluric response functions originating from linear relations between components of the electric and magnetic fields we can consider the magnetovariational response functions derived from linear relations between components of the magnetic field. This consideration may significantly enhance the capabilities of the magnetotellurics, since at low frequencies the magnetic field becomes free of near-surface distortions and shines a nondeceptive light on the deep geoelectric structures.

4.1 The Wiese–Parkinson Matrix

Return again to the model of inhomogeneous medium presented in Fig. 1.1. Recall that this layered model containing a bounded inhomogeneous domain V is excited by a plane elliptically polarized wave incident vertically on the Earth's surface. Proceeding from (1.12) and supplementing (1.13*c*,*d*) with an equation for vertical component of the magnetic field, we get

$$
\begin{aligned}
H_x &= H_x^{\mathrm{N}} + H_x^{\mathrm{A}} = H_{x\mathrm{o}}(1 + J_x^{H2}) + H_{y\mathrm{o}} J_x^{H1} && a \\
H_y &= H_y^{\mathrm{N}} + H_y^{\mathrm{A}} = H_{x\mathrm{o}} J_y^{H2} + H_{y\mathrm{o}}(1 + J_y^{H1}) && b \\
H_z &= H_z^{\mathrm{A}} = H_{x\mathrm{o}} J_z^{H2} + H_{y\mathrm{o}} J_z^{H1}, && c
\end{aligned}
\qquad (4.1)
$$

where $H_{x\mathrm{o}}$, $H_{y\mathrm{o}}$ are components of the normal magnetic field on the Earth's surface, and $\mathbf{J}^{H1}$, $\mathbf{J}^{H2}$ are convolutions of excess currents with the magnetic Green tensors. On eliminating $H_{x\mathrm{o}}$, $H_{y\mathrm{o}}$ from 4.1*a*,*b*) and substituting them in (4.1*c*), we obtain:

$$
H_z = W_{zx} H_x + W_{zy} H_y \qquad (4.2)
$$

M. Berdichevsky, V.I. Dmitriev, *Models and Methods of Magnetotellurics*,
DOI 10.1007/978-3-540-77814-1_4, © Springer-Verlag Berlin Heidelberg 2008

where

$$W_{zx} = \frac{J_z^{H2} + (J_y^{H1} J_z^{H2} - J_y^{H2} J_z^{H1})}{1 + J_x^{H2} + J_y^{H1} + (J_x^{H2} J_y^{H1} - J_x^{H1} J_y^{H2})},$$

$$W_{zy} = \frac{J_z^{H1} + (J_x^{H2} J_z^{H1} - J_x^{H1} J_z^{H2})}{1 + J_x^{H2} + J_y^{H1} + (J_x^{H2} J_y^{H1} - J_x^{H1} J_y^{H2})}.$$

This relation has been introduced in magnetotellurics by Parkinson (1959) and Wiese (1965). It is called the *Wiese–Parkinson relation*. The concept of the Wiese–Parkinson relation has been intensively advanced by Schmucker (1962, 1970, 1979), Jankovski (1972), and Vozoff (1972), as well as by Berdichevsky (1968), Lilley (1974), Rokityansky (1975), and Gregori and Lanzerotti (1980).

In matrix notation

$$H_z = [\mathbf{W}]\,\mathbf{H}_\tau, \tag{4.3}$$

where

$$[\mathbf{W}] = [W_{zx} \quad W_{zy}] \qquad \mathbf{H}_\tau = \begin{bmatrix} H_x \\ H_y \end{bmatrix}.$$

The matrix [**W**] came into play under the name of the *Wiese–Parkinson matrix* or the *tipper matrix* as it acts on the horizontal magnetic field and tips it into the vertical magnetic field (Vozoff, 1972).

The components W_{zx}, W_{zy} are determined from the vertical anomalous magnetic field. It is quite evident that they reflect the horizontal asymmetry of the excess currents of a galvanic and induction nature arising in the Earth due to lateral variations in the electric conductivity. It follows from Bio-Savart's law that the component W_{zx} defines a contribution of excess current flowing in the $y-$ direction, while the component W_{zy} defines a contribution of excess current flowing in the $x-$ direction. Let us agree to orient W_{zx}, W_{zy} to directions corresponding to their second subscript, that is, perpendicularly to the contributing current.

Note that the components W_{zx}, W_{zy} reflect not only the lateral conductivity variations but the vertical conductivity distribution as well. It follows directly from (4.2) where W_{zx}, W_{zy} depend on convolutions of excess currents with the magnetic Green tensor which is determined by normal conductivity distribution $\sigma_{\mathrm{N}}(z)$.

In the one-dimensional model the excess currents are absent. Here $W_{zx} = W_{zy} = 0$.

Consider a two-dimensional model with strike along the x-axis. Here $J_x^{H1} = J_x^{H2} = J_y^{H2} = J_z^{H2} = 0$, hence $W_{zx} = 0$. Thus,

$$[\mathbf{W}] = [0 \;\; W_{zy}], \qquad H_z = W_{zy} H_y, \tag{4.4}$$

where

$$W_{zy} = \frac{J_z^{H1}}{1 + J_y^{H1}}.$$

Clearly in this case the Wiese–Parkinson matrix contains only one component oriented across the strike.

The similar relation is characteristic of a three-dimensional axisymmetric model. In coordinates aligned with the radial and tangential directions, the Wiese–Parkinson matrix has only one component oriented radially.

In closing we follow Zhang et al. (1993) and Ritter and Banks (1998) and show that the Wiese–Parkinson matrix can be expressed in terms of the impedance tensor. On eliminating H_{xo}, H_{yo} from (1.13*a,b*) and substituting them in (4.1*c*), we obtain:

$$H_z = U_{zx} E_x + U_{zy} E_y,$$

where

$$U_{zx} = \frac{J_z^{H2} J_y^{E1} - J_z^{H1}(J_y^{E2} - Z_N)}{J_x^{E2} J_y^{E1} - (J_x^{E1} + Z_N)(J_y^{E2} - Z_N)}$$

$$U_{zy} = \frac{J_z^{H1} J_x^{E2} - J_z^{H2}(J_x^{E1} + Z_N)}{J_x^{E2} J_y^{E1} - (J_x^{E1} + Z_N)(J_y^{E2} - Z_N)}.$$

In matrix notation

$$H_z = [\mathbf{U}]\,\mathbf{E}_\tau = [\mathbf{U}]\,[\mathbf{Z}]\,\mathbf{H}_\tau = [\mathbf{W}]\,\mathbf{H}_\tau,$$

where

$$[\mathbf{U}] = \begin{bmatrix} U_{zx} & U_{zy} \end{bmatrix}$$

$$[\mathbf{W}] = [\mathbf{U}]\,[\mathbf{Z}] = \begin{bmatrix} U_{zx} & U_{zy} \end{bmatrix} \begin{bmatrix} Z_{xx} & Z_{xy} \\ Z_{yx} & Z_{yy} \end{bmatrix}$$

$$= \begin{bmatrix} U_{zx} Z_{xx} + U_{zy} Z_{yx} & U_{zx} Z_{xy} + U_{zy} Z_{yy} \end{bmatrix},$$

from which

$$\begin{aligned} W_{zx} &= U_{zx} Z_{xx} + U_{zy} Z_{yx} \\ W_{zy} &= U_{zx} Z_{xy} + U_{zy} Z_{yy}. \end{aligned} \tag{4.5}$$

There is good reason to believe that generally the impedance tensor [**Z**] reflects vertical and horizontal variations in the Earth's conductivity and that its components tend to zero as $\omega \to 0$. In view of (4.5) we can assume that the same properties are sha-red by the Wiese–Parkinson matrix [**W**].

In a two-dimensional model with strike along the $x-$ axis the relation (4.5) reduces to

$$\begin{aligned} W_{zx} &= 0 \\ W_{zy} &= U_{zx} Z_{xy}, \end{aligned} \tag{4.6}$$

where Z_{xy} is the longitudinal impedance. Let the anomalous magnetic field be caused by a near-surface body, whose dimensions are far less than the skin depth. Then we can ignore the induction effect and take U_{zx} as a real-valued factor. In that event W_{zy} and Z_{xy} are in-phase.

4.1.1 Rotation of the Wiese–Parkinson Matrix

How do the components of the Wiese–Parkinson matrix change as the x, y-axes rotate about the z-axis? Let α be a clockwise rotation angle. Then

$$H_z = [\mathbf{W}]\,\mathbf{H}_\tau = [\mathbf{W}][\mathbf{R}(\alpha)]^{-1}[\mathbf{R}(\alpha)]\mathbf{H}_\tau = [\mathbf{W}(\alpha)]\,\mathbf{H}_\tau(\alpha),$$

where

$$[\mathbf{W}(\alpha)] = [\mathbf{W}][\mathbf{R}(\alpha)]^{-1} \qquad \mathbf{H}_\tau(\alpha) = [\mathbf{R}(\alpha)]\,\mathbf{H}_\tau.$$

Thus,

$$\begin{aligned} W_{zx}(\alpha) &= -W_{zx}(\alpha \pm \pi) = \mp W_{zy}(\alpha \pm \pi/2) = W_{zx}\cos\alpha + W_{zy}\sin\alpha \\ W_{zy}(\alpha) &= -W_{zy}(\alpha \pm \pi) = \pm W_{zx}(\alpha \pm \pi/2) = -W_{zx}\sin\alpha + W_{zy}\cos\alpha\ . \end{aligned} \tag{4.7}$$

As is easy to see, in two-dimensional and axisymmetric three-dimensional models both the components, $W_{zx}(\alpha)$ and $W_{zy}(\alpha)$, are in-phase or anti-phase. Really, according to (4.4) and (4.7), we have

$$W_{zx}(\alpha) = W_{zy}(\alpha)\tan\alpha,$$

whence

$$\arg W_{zx}(\alpha) = \arg W_{zy}(\alpha) \quad \mod \pi. \tag{4.8}$$

Rotational invariants of the Wiese–Parkinson matrix are

$$W = \sqrt{W_{zx}^2 + W_{zy}^2} \qquad \|\mathbf{W}\| = \sqrt{|W_{zx}|^2 + |W_{zy}|^2}$$

$$\|\mathrm{Re}\ \mathbf{W}\| = \sqrt{(\mathrm{Re}\ W_{zx})^2 + (\mathrm{Re}\ W_{zy})^2} \qquad \|\mathrm{Im}\ \mathbf{W}\| = \sqrt{(\mathrm{Im}\ W_{zx})^2 + (\mathrm{Im}\ W_{zy})^2}$$

$$\begin{aligned} \mathrm{P}_1 &= \mathrm{Re}\ W_{zx}\mathrm{Im}\ W_{zy} - \mathrm{Re}\ W_{zy}\mathrm{Im}\ W_{zx} \\ \mathrm{P}_2 &= \mathrm{Re}\ W_{zx}\mathrm{Im}\ W_{zx} + \mathrm{Re}\ W_{zy}\mathrm{Im}\ W_{zy}. \end{aligned} \tag{4.9}$$

It comes to attention that in two-dimensional and three-dimensional axisymmetric models $\mathrm{P}_1 = 0$ and $\mathrm{P}_2 = \mathrm{Re}\ W_{zy}\mathrm{Im}\ W_{zy}$, where W_{zy} is a component oriented across the strike or radially. But note that in a quasistatic case when the Wiese–Parkinson matrix is real-valued we have $\mathrm{P}_1 = 0$ and $\mathrm{P}_2 = 0$ no matter what the structure of the medium.

With regard for (4.9), we introduce the *magnetovariational skew* (*Wiese–Parkinson skew*) as

$$skew_{mv} = \left|\frac{\mathrm{P}_1}{\mathrm{P}_2}\right| = \left|\frac{\mathrm{Re}\ W_{zx}\mathrm{Im}\ W_{zy} - \mathrm{Re}\ W_{zy}\mathrm{Im}\ W_{zx}}{\mathrm{Re}\ W_{zx}\mathrm{Im}\ W_{zx} + \mathrm{Re}\ W_{zy}\mathrm{Im}\ W_{zy}}\right|. \tag{4.10}$$

In 2D- and axially symmetric 3D-models we have $skew_{mv} = 0$. Departure of $skew_{mv}$ from 0 is a measure of geoelectric asymmetry. The important advantage of the magnetovariational $skew_{mv}$ over the magnetotelluric $sqew_s$ defined by (1.60) is that at low frequencies $skew_{mv}$ is not subject to near-surface distortions and reflects the asymmetry of deep zones of the Earth. But note that indications of $skew_{mv}$ are reliable in zones where magnetovariational anomalies are rather strong and the real and imaginary components [**W**] are sufficiently large.

4.1.2 Dispersion Relations in the Wiese–Parkinson Matrix

Marcuello, Queralt and Ledo demonstrated recently the two-dimensional and three-dimensional synthetic models, in which the real and imaginary components of the Wiese–Parkinson matrix meet the dispersion relations

$$\mathrm{Im}\ W_j(\omega_\mathrm{o}) = \frac{1}{\pi}\mathrm{pv}\int\limits_{-\infty}^{\infty} \frac{\mathrm{Re}\ W_j(\omega)}{\omega - \omega_\mathrm{o}}\, d\omega = \frac{2\omega_\mathrm{o}}{\pi}\mathrm{pv}\int\limits_{\mathrm{o}}^{\infty} \frac{\mathrm{Re}\ W_j(\omega)}{\omega^2 - \omega_\mathrm{o}^2}\, d\omega \tag{4.11}$$

$$\mathrm{Re}\ W_j(\omega_\mathrm{o}) = -\frac{1}{\pi}\mathrm{pv}\int\limits_{-\infty}^{\infty} \frac{\mathrm{Im}\ W_j(\omega)}{\omega - \omega_\mathrm{o}}\, d\omega = -\frac{2}{\pi}\mathrm{pv}\int\limits_{\mathrm{o}}^{\infty} \frac{\mathrm{Im}\ W_j(\omega)}{\omega^2 - \omega_\mathrm{o}^2}\omega\, d\omega \tag{4.12}$$

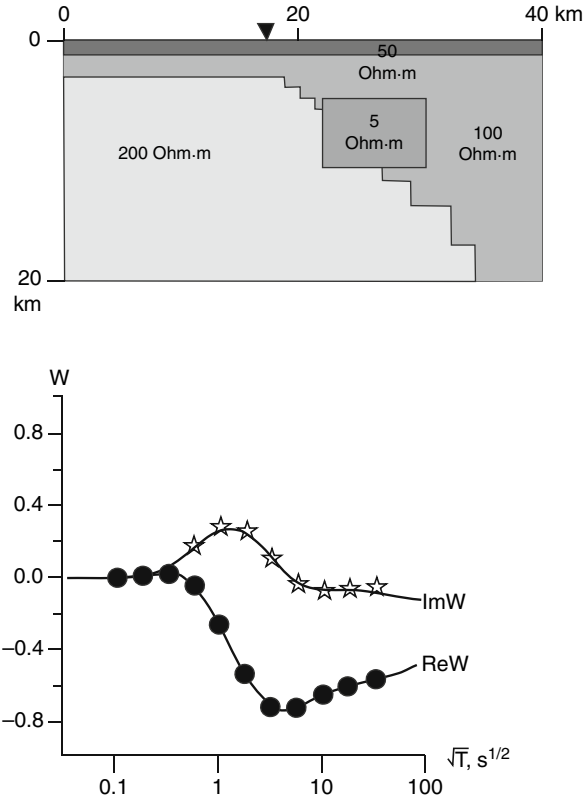

Fig. 4.1 Tipper dispersion relations in a two-dimensional model; *triangle* – observation site; ReW : *filled circles* and *solid line* – synthetic values of real tipper and their interpolation, ImW : *stars* and *solid line* – synthetic values of imaginary tipper and transform (4.11) of real tippers (Marcuello et al., 2005)

where $j = zx, zy$ and pv denotes a principal value of an integral in the Cauchy sense (Marcuello et al., 2002; Marcuello et al., 2005).

Figure 4.1 presents a two-dimensional model testifying to the adequacy of the dispersion relations between the real and imaginary components of the Wiese–Parkinson matrix. The transformation (4.11) of Re W is in good agreement with Im W. The similar agreement has been observed in a three-dimensional synthetic model, which contains an inclined conductive layer.

The consistency between the real and imaginary components of the Wiese–Parkinson matrix may suggest that they embody the same (or almost the same) information on the Earth conductivity.

In parallel with synthetic models, Marcuello, Queralt and Ledo applied the transformations (4.11) and (4.12) to magnetovariational data collected in the northern Iberian Peninsula. At many sites the field data met the dispersion relations, but there were sites, at which the dispersion relations were violated.

4.2 Vector Representation of the Wiese–Parkinson Matrix

The development of these graphical techniques was stimulated by pioneering works of Parkinson (1959), Wiese (1962, 1965), Schmucker (1962, 1970), Everett and Hyndman (1967), Jankovski (1972), Vozoff (1972), and Lilley (1974). The keystone idea was to represent the complex-valued Wiese–Parkinson matrix as a complex vector giving a pictorial image of the horizontal gradients of electric conductivity. Such a vector received the name *tipper vector* or *induction arrow*. Complex tipper (induction arrow) consists of real and imaginary tippers (real and imaginary induction arrows).

There exist two conventions concerning the real tipper direction. In the *Wiese convention*, the real tipper points away from the zone of higher conductivity. In the *Parkinson convention*, the real tipper points toward the zone of higher conductivity.

In our book we adopt the Wiese convention, which is popular in the Russian magnetotelluric school.

In the following we consider three types of tippers: the Wiese–Parkinson tipper, the Vozoff tipper, and the Schmucker tipper.

4.2.1 The Wiese–Parkinson Tipper Technique

Let us represent the Wiese–Parkinson matrix in the vector form

$$\mathbf{W} = W_{zx}\mathbf{1}_x + W_{zy}\mathbf{1}_y. \tag{4.13}$$

The vector $\mathbf{W}$ is given the name *Wiese–Parkinson tipper.*

The complex tipper $\mathbf{W}$ falls into the real and imaginary tippers:

$$\mathbf{W} = \mathrm{Re}\,\mathbf{W} + i\,\mathrm{Im}\,\mathbf{W}, \tag{4.14}$$

where

$$\begin{aligned} \mathrm{Re}\,\mathbf{W} &= \mathrm{Re}\,W_{\mathrm{zx}}\mathbf{1}_x + \mathrm{Re}\,W_{\mathrm{zy}}\mathbf{1}_y, \\ \mathrm{Im}\,\mathbf{W} &= \mathrm{Im}\,W_{\mathrm{zx}}\mathbf{1}_x + \mathrm{Im}\,W_{\mathrm{zy}}\mathbf{1}_y. \end{aligned} \tag{4.15}$$

Note that the rotational invariants P_1 and P_2 defined by (4.9) have meaning of the vector and scalar products of the real and imaginary tippers:

$$\mathrm{Re}\,\mathbf{W} \times \mathrm{Im}\,\mathbf{W} = \begin{vmatrix} \mathbf{1}_x & \mathbf{1}_y & \mathbf{1}_z \\ \mathrm{Re}\,W_{zx} & \mathrm{Re}\,W_{zy} & 0 \\ \mathrm{Im}\,W_{zx} & \mathrm{Im}\,W_{zy} & 0 \end{vmatrix} = (\mathrm{Re}\,W_{zx}\mathrm{Im}\,W_{zy} - \mathrm{Re}\,W_{zy}\mathrm{Im}\,W_{zx})\mathbf{1}_z = P_1\mathbf{1}_z$$

$$\mathrm{Re}\,\mathbf{W} \cdot \mathrm{Im}\,\mathbf{W} = \mathrm{Re}\,W_{zx}\mathrm{Im}\,W_{zx} + \mathrm{Re}\,W_{zy}\mathrm{Im}\,W_{zy} = P_2. \tag{4.16}$$

Thus, according to (4.10),

$$skew_{mv} = |\tan\alpha|\,, \tag{4.17}$$

where α is an angle between the real and imaginary tippers.

Turn again to the two-dimensional model with strike along the x-axis. According to (4.4)

$$\text{Re}\,\mathbf{W} = \text{Re}\,W_{zy}\mathbf{1}_y \qquad \text{Im}\,\mathbf{W} = \text{Im}\,W_{zy}\mathbf{1}_y. \tag{4.18}$$

Here the real and imaginary tippers are collinear, being perpendicular to the strike. Their vector product is equal to zero, $P_1 = 0$. Collinearity of the real and imaginary tippers is also observed in the axisymmetric three-dimensional model: vectors Re **W** and Im **W** are oriented toward the axis of symmetry or away from it. Asymmetry of the medium violates the collinearity of Re **W** and Im **W**.

Examples of real and imaginary Wiese–Parkinson tippers Re **W** and Im **W** for 2D and 3D-models are presented in Fig. 4.2.

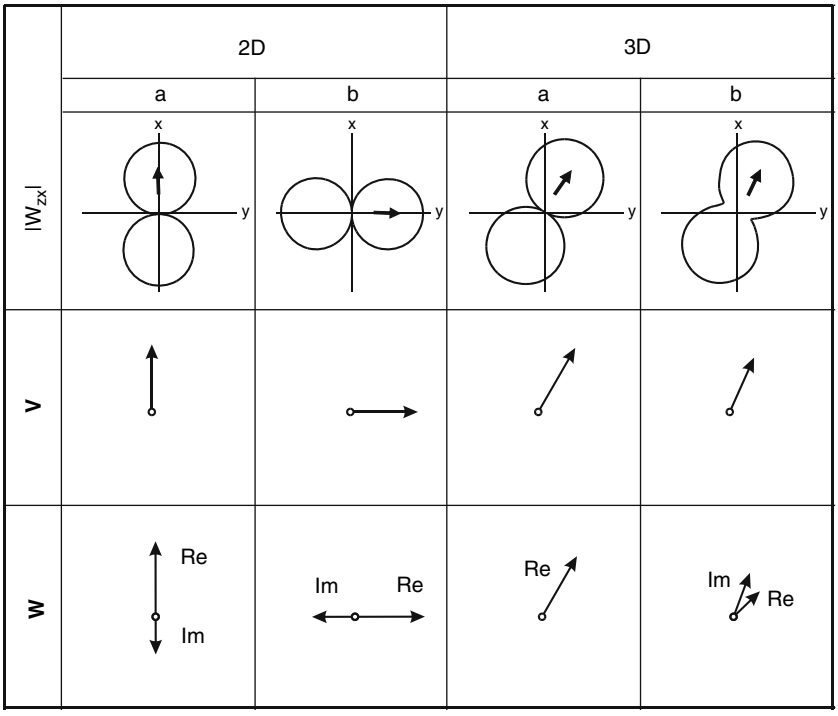

Fig. 4.2 The Wiese–Parkinson tippers **W**, Vozoff tippers **V** and polar diagrams of the Wiese–Parkinson matrix. 2 Da: $[\mathbf{W}] = [0.5e^{-i\pi/6}\ \ 0]$ 2Db: $[\mathbf{W}] = [0\ \ \ 0.5e^{-i\pi/6}\ ]$ 3 Da: $[\mathbf{W}] = [0.5\ \ 0.3]$ 3Db: $[\mathbf{W}] = [0.5e^{i\pi/3}\ \ 0.3e^{i\pi/6}]$

The real tippers show a remarkable property: over a wide range of sufficiently low frequencies they are directed away from zones of higher conductivity (current concentration) and towards zones of lower conductivity (current deconcentration). So, maps of real tippers may be most helpful in locating geoelectrical structures, their tracing, their classifying by conductivity. This property of real tippers is a direct consequence of the Bio-Savart law. Let us demonstrate this with a simple example (Fig. 4.3). Assume that the infinitely long rectilinear horizontal direct current flows along the x-axis trough an underground point C. At symmetrical surface points O_1 and O_2 we observe magnetic fields $\mathbf{H}^{(1)}$ and $\mathbf{H}^{(2)}$ with components

$$H_y^{(1)} = \frac{J\cos\alpha}{2\pi r}, \qquad H_z^{(1)} = -\frac{J\sin\alpha}{2\pi r}, \qquad H_y^{(2)} = \frac{J\cos\alpha}{2\pi r}, \qquad H_z^{(2)} = \frac{J\sin\alpha}{2\pi r},$$

where r is the distance between O_1, O_2 and C, while α is the angle made by $\mathbf{H}^{(1)}$, $\mathbf{H}^{(2)}$ with the Earth's surface. Thus, the tippers calculated from these magnetic fields are

$$\mathbf{W}^{(1)} = \frac{H_z^{(1)}}{H_y^{(1)}}\mathbf{1}_y = -\tan\alpha\mathbf{1}_y, \qquad \mathbf{W}^{(2)} = \frac{H_z^{(2)}}{H_y^{(2)}}\mathbf{1}_y = \tan\alpha\mathbf{1}_y.$$

Clearly they are directed away from the buried current.

The relations between the real and imaginer tippers can be illustrated by a simple two-dimensional model consisting of three layers: sediments (ρ_1'), resistive lithosphere ($\rho_2 = \infty$) and highly conductive mantle ($\rho_3 = 0$). The sediments contain a rectangular conductive inclusion ($\rho_1'' << \rho_1'$). The model is excited by the E-polarized field. Figure 4.4 presents the tippers Re $\mathbf{W}$ and Im $\mathbf{W}$ for different λ_1/h_1, where $\lambda_1 = 2\pi\sqrt{2\rho_1'/\omega\mu_o}$ is the wavelength in sediments. Within the S_1-interval ($\lambda_1/h_1 = 30,\ 45,\ 60$), the real and imaginary tippers point away from the conductive inclusion center. On the transition to the h-interval ($\lambda_1/h_1 = 100,\ 150$), the

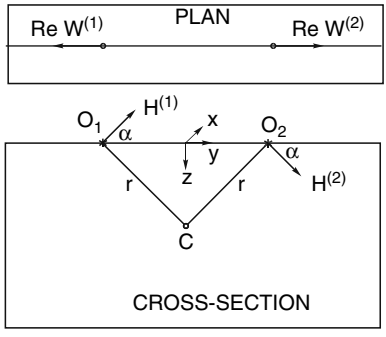

Fig. 4.3 Magnetic field of the infinitely long rectilinear direct current flowing through a buried point C

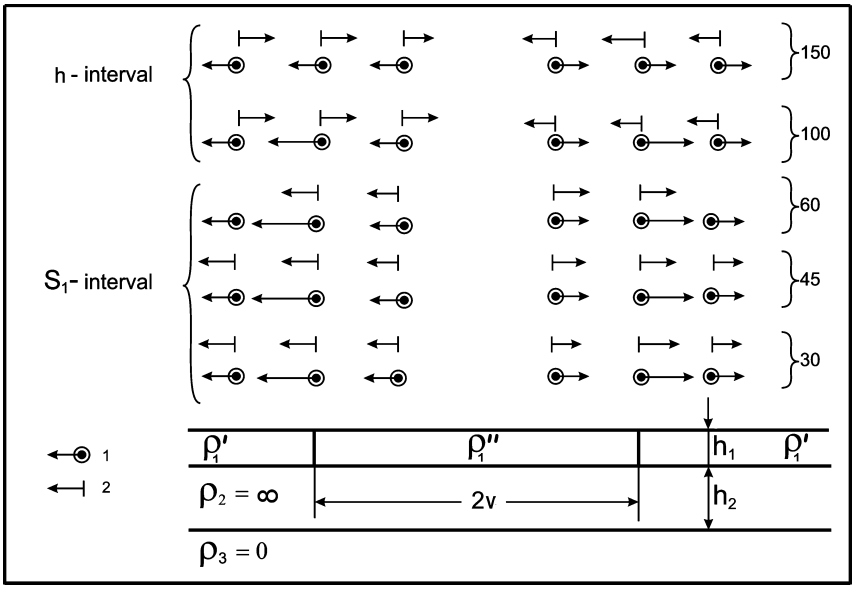

Fig. 4.4. The real and imaginary Wiese–Parkinson tippers over a near-surface rectangular inclusion of higher conductivity. Model parameters: $\rho''/\rho' = 1/16$, $v/h_1 = 8$, $h_2/h_1 = 21$. Calculated for $\lambda_1/h_1 = 30, 45, 60$ (S_1- interval), 100, 150 ($h-$ interval);1-real tipper, 2- imaginary tipper

real tippers preserve their orientation, whereas the imaginary tippers turn towards the center of conductive inclusion.

A spectacular practical example is given in Fig. 4.5. This map of the real Wiese–Parkinson tippers has been constructed for the Carpathian region in the early 1970s (Rokityansky, 1982). When crossing the mountains, we observe the reversal of Re **W** plotted for T =1000–1500 s. The induction arrows point away from the Carpathian arc. So, we can state with confidence that the Carpathian magnetovariational anomaly is formed by a narrow arc-shaped conductive zone in the deep roots of the mountains.

4.2.2 The Vozoff Tipper Technique

Another vector representation has been suggested by Vozoff (1972). It separates the amplitude and phase characteristics of the magnetovariational anomalies and offers a simple three-dimensional generalization of the longitudinal and transverse magnetic fields. We will describe this technique with some modifications proposed by Berdichevsky and Nguen Tkhan Van (1991).

Let us introduce the *tipper ratio* β as an amplitude characteristic of the magnetovariatonal anomaly:

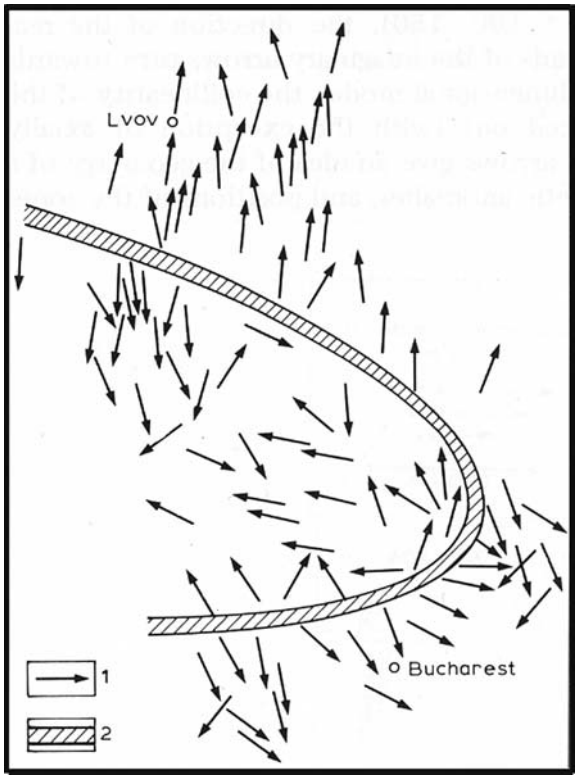

Fig. 4.5 Map of the Wiese tippers for the Carpathian region, periods 15–25 min; 1 – Wiese tipper, 2 – the Carpathian arc (Rokityansky, 1982)

$$\beta = \frac{|H_z|}{\sqrt{|H_x|^2 + |H_y|^2}} . \tag{4.19}$$

Consider a two-dimensional model and assume that horizontal magnetic field $\mathbf{H}_\tau$ is polarized linearly at a clockwise angle α to the x-axis which runs along the model strike. According to (4.4)

$$H_x = H_\tau \cos\alpha, \qquad H_y = H_\tau \sin\alpha, \qquad H_z = W_{zy} H_\tau \sin\alpha \ .$$

Thus,

$$\beta = \left| W_{zy} \sin\alpha \right| \ . \tag{4.20}$$

The tipper ratio has minimum $\beta_{\min} = 0$ for longitudinal magnetic field ($\mathbf{H}_\tau$ is polarized along the strike, $\alpha = 0$) and maximum $\beta_{\max} = \left| W_{zy} \right|$ for transverse magnetic field ($\mathbf{H}_\tau$ is polarized across the strike, $\alpha = \pi/2$).

These relations can be readily extended to a three-dimensional model. We will look for a *quasi-longitudinal magnetic field* $\mathbf{H}_\tau^{ql}$ and a *quasi-transverse magnetic*

field $\mathbf{H}_\tau^{q\,t}$ that provide a minimum and a maximum of β. Generally these fields are elliptically polarized.

In accordance with (4.2) and (4.9),

$$\beta = \frac{\left|W_{zx}H_x + W_{zy}H_y\right|}{\sqrt{|H_x|^2 + \left|H_y\right|^2}} = \sqrt{\frac{(W_{zx}H_x + W_{zy}H_y)(\bar{W}_{zx}\bar{H}_x + \bar{W}_{zy}\bar{H}_y)}{|H_x|^2 + \left|H_y\right|^2}} = \sqrt{\|\mathbf{W}\|^2 - \chi},$$

where

$$\chi = \frac{\left|\bar{W}_{zx}H_y - \bar{W}_{zy}H_x\right|^2}{|H_x|^2 + \left|H_y\right|^2} \geq 0\,.$$

Here the bar denotes the complex conjugation.

The quasi-longitudinal field $\mathbf{H}_\tau^{q\,l}$ corresponds to condition $\beta_{\min} = 0$. Thus, we have the equation

$$W_{zx}H_x^{q\,l} + W_{zy}H_y^{q\,l} = 0,$$

which gives the polarization ratio

$$P_H^{q\,l} = \frac{H_y^{q\,l}}{H_x^{q\,l}} = -\frac{W_{zx}}{W_{zy}}\,. \tag{4.21}$$

The quasi-transverse field $\mathbf{H}_\tau^{q\,t}$ corresponds to condition

$$\beta_{\max} = \beta\,\big|_{\chi=0} = \|\mathbf{W}\| = \sqrt{|W_{zx}|^2 + \left|W_{zy}\right|^2}\,. \tag{4.22}$$

Thus, we have the equation

$$\bar{W}_{zx}H_y^{q\,t} - \bar{W}_{zy}H_x^{q\,t} = 0,$$

which gives the polarization ratio

$$P_H^{q\,t} = \frac{H_y^{q\,t}}{H_x^{q\,t}} = \frac{\bar{W}_{zy}}{\bar{W}_{zx}}. \tag{4.23}$$

As is evident from (4.21) and (4.23),

$$P_H^{q\,l}\,\bar{P}_H^{q\,t} = -1. \tag{4.24}$$

The polarization ratios for the quasi-longitudinal and quasi-transverse magnetic fields comply with (2.24). This means that fields $\mathbf{H}_\tau^{q\,l}$ and $\mathbf{H}_\tau^{q\,t}$ are orthogonal.

The mayor axes of their polarization ellipses are oriented in the directions that can be regarded as quasi-longitudinal and quasi-transverse directions of the three-dimensional structure. The orthogonal quasi-longitudinal and quasi-transverse magnetic fields $\mathbf{H}_\tau^{q\,l}$ and $\mathbf{H}_\tau^{q\,t}$ are *tipper eigenfields*.

To determine the quasi-transverse direction, we find the clockwise angle $\alpha_H^{q\,t}$ between the x-axis and the major axis of the polarization ellipse of the quasi-transverse field $\mathbf{H}_\tau^{q\,t}$. By virtue of (2.18)

$$\tan 2\alpha_H^{q\,t} = \frac{2\mathrm{Re}\ P_H^{q\,t}}{1 - \left|P_H^{q\,t}\right|^2} = \tan 2\theta_H^{q\,t} \cos\phi_H^{q\,t}, \tag{4.25}$$

where $\tan\theta_H^{q\,t} = \left|P_H^{q\,t}\right|$, $\phi_H^{q\,t} = \arg P_H^{q\,t}$. Equation (4.25) defines $\alpha_H^{q\,t}$ modulo π. The angle $\alpha_H^{q\,t}$ is taken within quadrant I ($0 \le \alpha_H^{q\,t} \le \pi/2$) or III ($\pi \le \alpha_H^{q\,t} \le 3\pi/2$) if $\cos\phi_H^{q\,t} \ge 0$ and within quadrant II ($\pi/2 > \alpha_H^{q\,t} \ge \pi$) or IV ($3\pi/2 > \alpha_H^{q\,t} \ge 2\pi$) if $\cos\phi_H^{q\,t} < 0$. For the definiteness sake, we introduce the complementary condition

$$\left|\alpha_H^{qt} - \mathrm{arctg}\frac{\mathrm{Re}\ W_{zy}}{\mathrm{Re}\ W_{zx}}\right| < \frac{\pi}{2}, \tag{4.26}$$

which brings $\alpha_H^{q\,t}$ closer to direction of the real Wiese–Parkinson tipper Re $\mathbf{W}$.

By plotting $\|\mathbf{W}\|$ in the direction α_H^{qt}, we obtain the *Vozoff tipper*

$$\mathbf{V} = V_x\mathbf{1}_x + V_y\mathbf{1}_y, \tag{4.27}$$

where

$$V_x = \|\mathbf{W}\|\cos\alpha_H^{qt} \qquad V_y = \|\mathbf{W}\|\sin\alpha_H^{qt}.$$

The magnitude and direction of the Vozoff tipper fill two of four degrees of freedom for the complex-valued components W_{zx} and W_{zy} of the matrix [$\mathbf{W}$]. The tipper magnitude $\|\mathbf{W}\|$ characterizes the intensity of a magnetovariational anomaly, while the tipper direction $\alpha_H^{q\,t}$ helps in locating and identifying conductive and non-conductive structures. Over a wide range of sufficiently low frequencies the Vozoff tippers, similar to the real Wiese–Parkinson tippers, are directed away from the zones of higher conductivity and towards the zones of lower conductivity.

Two more parameters are the *tipper ellipticity,* ε_H^{qt}, and the *tipper phase,* φ_V. With these parameters we fill all the four degrees of freedom of the Wiese–Parkinson matrix.

The ellipticity ε_H^{qt} is estimated as a ratio between semi-axes of the polarization ellipse of the quasi-transverse magnetic field $\mathbf{H}_\tau^{qt}$. According to (2.19)

$$\varepsilon_H^{qt} = \frac{b_H^{qt}}{a_H^{qt}} = \frac{\sqrt{1 + \left|P_H^{qt}\right|^2 + 2\mathrm{Im}\ P_H^{qt}} - \sqrt{1 + \left|P_H^{qt}\right|^2 - 2\mathrm{Im}\ P_H^{qt}}}{\sqrt{1 + \left|P_H^{qt}\right|^2 + 2\mathrm{Im}\ P_H^{qt}} + \sqrt{1 + \left|P_H^{qt}\right|^2 - 2\mathrm{Im}\ P_H^{qt}}} = \tan\gamma_H^{qt}, \tag{4.28}$$

where

$$\chi_H^{qt} = \frac{1}{2}\arcsin(\sin 2\theta_H^{qt} \sin\phi_H^{qt}). \tag{4.29}$$

It is notable that

$$\mathrm{Im}\ P_H^{qt} = -\frac{\mathrm{Re}\ W_{zx}\mathrm{Im}\ W_{zy} - \mathrm{Re}\ W_{zy}\mathrm{Im}\ W_{zx}}{|W_{zx}|^2} = -\frac{P_1}{|W_{zx}|^2}, \tag{4.30}$$

where P_1 is the rotational invariant defined by (4.9). In the two-dimensional and axisymmetric three-dimensional models, $P_1 = 0$ and hence $\mathrm{Im}\ P_H^{qt} = 0$ and $\varepsilon_H^{qt} = 0$.

Now introduce the tipper phase φ_V. We can derive φ_V directly from the quasi-transverse field $\mathbf{H}_\tau^{qt}$:

$$\phi_V = \arg\frac{H_z^{qt}}{\sqrt{(H_x^{qt})^2 + (H_y^{qt})^2}}, \tag{4.31}$$

where $H_z^{qt} = W_{zx}H_x^{qt} + W_{zy}H_y^{qt}$. In view of (4.9) and (4.22)

$$\frac{H_z^{qt}}{\sqrt{(H_x^{qt})^2 + (H_y^{qt})^2}} = \frac{W_{zx} + W_{zy}\dfrac{H_y^{qt}}{H_x^{qt}}}{\sqrt{1 + \left(\dfrac{H_y^{qt}}{H_x^{qt}}\right)^2}} = \frac{W_{zx} + W_{zy}\dfrac{\bar{W}_{zy}}{\bar{W}_{zx}}}{\sqrt{1 + \left(\dfrac{\bar{W}_{zy}}{\bar{W}_{zx}}\right)^2}} = \frac{\|\mathbf{W}\|^2}{\bar{W}} = \frac{\|\mathbf{W}\|^2}{|W|^2}W,$$

whence

$$\varphi_V = \arg W = \arg\sqrt{W_{zx}^2 + W_{zy}^2}. \quad . \tag{4.32}$$

Here the phase φ_V is defined modulo π as argument of the rotational invariant W. It indicates the relations between the phase of excess electric currents generating the vertical magnetic field and the phase of the horizontal magnetic field. If φ_V is close to 0 or π, the in-phase (or anti-phase) active currents prevail. If φ_V is close to $\pm\,\pi/2$ the reactive currents prevail. This information could be helpful in geoelectric zoning and structural classification.

Note that with lowering frequency the Vozoff tipper $\mathbf{V}$ attenuates slower than the Wiese–Parkinson tipper Re $\mathbf{W}$. It seems that it provides the larger investigation depth.

The model examples of tippers **V** are shown in Fig. 4.2. In two-dimensional models the Vozoff tippers **V** and Wiese–Parkinson tippers Re **W** have the same direction, while in three-dimensional models the difference in their directions can be rather large. The advantage of the Vozoff tipper is the higher sensitivity to remote three-dimensional structures.

Figure 4.6 presents the Vozoff tippers **V** obtained along the regional profile crossing South Kamchatka (Berdichevsky and Nguen Tkhan Van, 1991). Here the ellipticity ε_H^{qt} varies from 0.15 to 0.3 indicating more or less strong three-dimensionalities. At the same time the tipper phase φ_V at periods 2500–10,000 s deviates rather slightly from 0° which evidences the dominating influence of the oceanic currents (coastal effect). On the Pacific coast this effect is much stronger than on the Sea-of-Okhotsk coast. The North-West and North-East orientation of

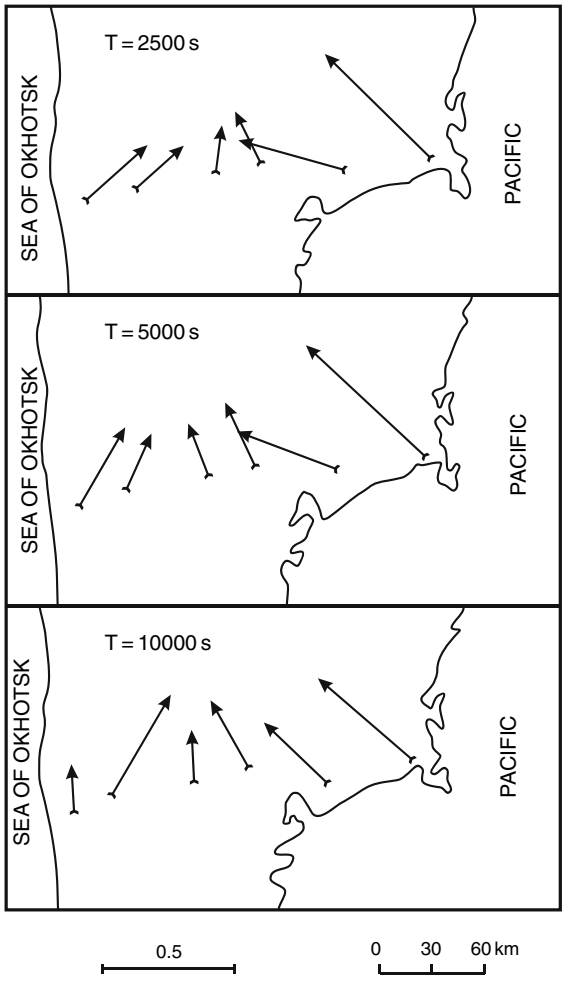

Fig. 4.6 The Vozoff tippers **V** obtained along profile crossing South Kamchatka (Berdichevsky and Nguen Tkhan Van, 1991)

the tippers can be explained by considerable impact of oceanic currents flowing around the Kamchatka peninsula on the south.

4.3 Polar Diagrams of the Wiese–Parkinson Matrix

This representation was originated by Berdichevsky (1968). Polar diagrams show the dependence of the components of the Wiese–Parkinson matrix upon orientation of the measurement axes. They characterize the dimensionality of geoelectric structures and outline their strike.

Plot a value $|W_{zx}(\alpha)|$ on the x-axis rotated clockwise through an angle α. As α goes from 0 to 2π, the resultant point describes a closed curve called the *polar diagram of the Wiese–Parkinson matrix.* Its equation is deduced from (4.7):

$$|W_{zx}(\alpha)| = \sqrt{|W_{zx}|^2 \cos^2\alpha + \left|W_{zy}\right|^2 \sin^2\alpha + 2\mathrm{Re}\; W_{zx}\bar{W}_{zy} \sin\alpha\cos\alpha}. \tag{4.33}$$

Find an angle α that provides extreme values of $|W_{zx}(\alpha)|$. From the extremum condition

$$\frac{d\,|W_{zx}(\alpha)|}{d\alpha} = 0$$

we derive

$$\tan 2\alpha = \frac{2\mathrm{Re}\; W_{zx}\,\bar{W}_{zy}}{|W_{zx}|^2 - \left|W_{zy}\right|^2}. \tag{4.34}$$

Solving this equation, we obtain two maxima and two minima of $|W_{zx}(\alpha)|$ that alternate in $\pi/2$. Obviously, the polar diagram may appear as a symmetric oval (with or without "waist") or as a figure-eight.

According to (4.33) and (4.34), the major and the minor semiaxes of the polar diagram of the Wiese–Parkinson matrix are

$$\begin{aligned} a_{WP} &= \sqrt{\frac{|W_{zx}|^2 + \left|W_{zy}\right|^2 + \sqrt{(|W_{zx}|^2 - \left|W_{zy}\right|^2)^2 + 4\mathrm{Re}^2 W_{zx}\bar{W}_{zy}}}{2}} \\ b_{WP} &= \sqrt{\frac{|W_{zx}|^2 + \left|W_{zy}\right|^2 - \sqrt{(|W_{zx}|^2 - \left|W_{zy}\right|^2)^2 + 4\mathrm{Re}^2 W_{zx}\bar{W}_{zy}}}{2}}, \end{aligned} \tag{4.35}$$

whence

$$a_{WP}^2 + b_{WP}^2 = |W_{zx}|^2 + \left|W_{zy}\right|^2 = \|\mathbf{W}\|^2. \tag{4.36}$$

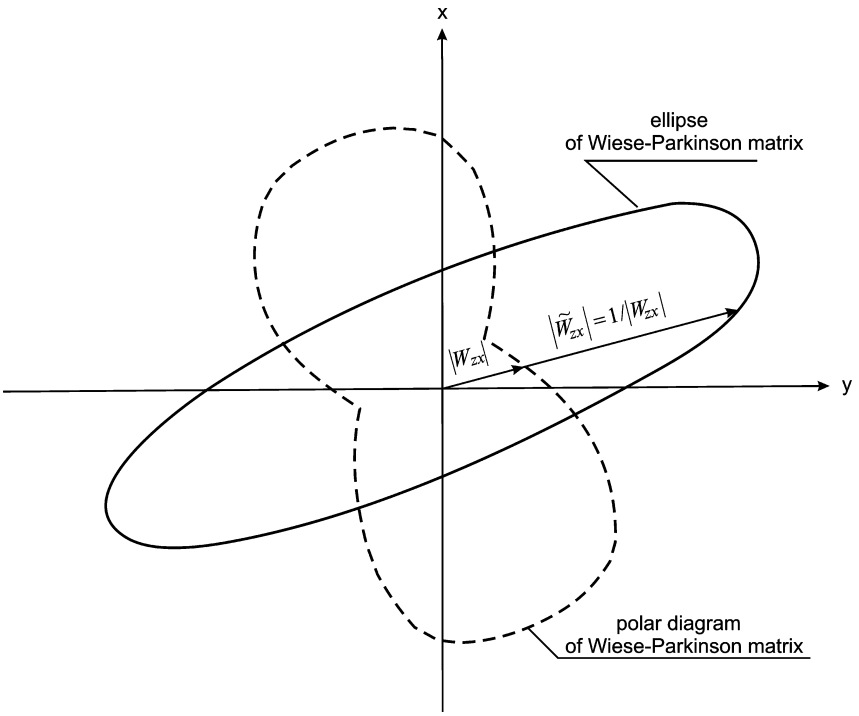

Fig. 4.7 The Wiese–Parkinson polar diagram and ellipse

It is notable that an inversion of the polar diagram of the Wiese–Parkinson matrix gives an ellipse (Fig. 4.7). Its equation is

$$\left|\tilde{W}_{zx}(\alpha)\right| = \frac{1}{\sqrt{|W_{zx}|^2 \cos^2\alpha + \left|W_{zy}\right|^2 \sin^2\alpha + 2\mathrm{Re}\, W_{zx}\bar{W}_{zy} \sin\alpha\cos\alpha}}, \quad (4.37)$$

where $\left|\tilde{W}_{zx}(\alpha)\right| = 1/|W_{zx}(\alpha)|$.

Let us compare equations (4.34) and (4.25). The directions of the major and the minor axes of the polar diagram of the Wiese–Parkinson matrix coincide with directions of the quasi-transverse and quasi-longitudinal magnetic fields defined by the Vozoff technique. Thus, with (4.26) we can choose the major semi-axis of polar diagram, which points away from zone of higher conductivity and toward zone of lower conductivity (the Wiese convention).

Examples of polar diagrams of the Wiese–Parkinson matrix for 2D and 3D-models are shown in Fig. 4.2. The polar-diagram major semi-axes which satisfy condition (4.26) are indicated by arrow. They are parallel to the Vozoff tippers V and point away from zone of higher conductivity.

In the two-dimensional model with the strike along the y-axis, we have $W_{zy} = 0$ (2D,a). Here

$$|W_{zx}(\alpha)| = |W_{zx} \cos\alpha| . \tag{4.38}$$

Similarly, in the two-dimensional model with the strike along the x-axis, we have $W_{zx} = 0$ (2D,b). Here

$$|W_{zx}(\alpha)| = \left|W_{zy} \sin\alpha\right| . \tag{4.39}$$

Thus, the two-dimensional polar diagrams are shaped as a figure-eight oriented perpendicularly to the strike. The diagram of the same shape is characteristic of any axisymmetric model. Here the figure-eight is oriented radially. It is remarkable that the figure-eight diagram is also characteristic of any real-valued Wiese–Parkinson matrix no matter what the structure of the medium (3D,a).

The polar diagrams in the form of an regular oval with more or less narrow waist characterizes a three-dimensional asymmetric model (3D,b).

We have considered three graphical representations of the Wiese–Parkinson matrix. The most efficient (most convenient, most informative) technique may be chosen depending on the conditions of survey, target structures and used period range.

4.4 Magnetic Tensors

Now we will consider the magnetic tensors, which define relation between the magnetic fields **H** at two sites: at an observation site and at a base (reference) site B. The concepts of the magnetic tensors came from the pioneering works of Schmucker (1970) and Berdichevsky (1968). The analysis of the magnetic tensors has been advanced by Varentsov (2004, 2005).

4.4.1 The Horizontal Magnetic Tensor

Coming back to the model of inhomogeneous medium presented in Fig. 1.1, we direct our attention to (1.13), and write

$$\begin{aligned} H_x(\mathbf{r}) &= H_x^{\mathrm{N}} + H_x^{\mathrm{A}}(\mathbf{r}) = H_{x\mathrm{o}}[1 + J_x^{H2}(\mathbf{r})] + H_{y\mathrm{o}} J_x^{H1}(\mathbf{r}), \\ H_y(\mathbf{r}) &= H_y^{\mathrm{N}} + H_y^{\mathrm{A}}(\mathbf{r}) = H_{x\mathrm{o}} J_y^{H2}(\mathbf{r}) + H_{y\mathrm{o}}[1 + J_y^{H1}(\mathbf{r})] , \end{aligned} \tag{4.40}$$

$$\begin{aligned} H_x(\mathbf{r}_{\mathrm{B}}) &= H_x^{\mathrm{N}} + H_x^{\mathrm{A}}(\mathbf{r}_{\mathrm{B}}) = H_{x\mathrm{o}}[1 + J_x^{H2}(\mathbf{r}_{\mathrm{B}})] + H_{y\mathrm{o}} J_x^{H1}(\mathbf{r}_{\mathrm{B}}), \\ H_y(\mathbf{r}_{\mathrm{B}}) &= H_y^{\mathrm{N}} + H_y^{\mathrm{A}}(\mathbf{r}_{\mathrm{B}}) = H_{x\mathrm{o}} J_y^{H2}(\mathbf{r}_{\mathrm{B}}) + H_{y\mathrm{o}}[1 + J_y^{H1}(\mathbf{r}_{\mathrm{B}})] . \end{aligned} \tag{4.41}$$

Eliminating $H_{x\mathrm{o}},\ H_{y\mathrm{o}}$ from (4.40) and (4.41), we get

$$\mathbf{H}_\tau(\mathbf{r}) = [\mathbf{M}(\mathbf{r}\,|\mathbf{r}_{\mathrm{B}})]\,\mathrm{H}_\tau(\mathbf{r}_{\mathrm{B}}), \tag{4.42}$$

where

$$\mathbf{H}_\tau(\mathbf{r}) = \begin{bmatrix} H_x(\mathbf{r}) \\ H_y(\mathbf{r}) \end{bmatrix} \qquad \mathbf{H}_\tau(\mathbf{r}_{\mathrm{B}}) = \begin{bmatrix} H_x(\mathbf{r}_{\mathrm{B}}) \\ H_y(\mathbf{r}_{\mathrm{B}}) \end{bmatrix} \tag{4.43}$$

and

$$\begin{aligned}[\mathbf{M}(\mathbf{r}\,|\mathbf{r}_{\mathrm{B}})] &= \begin{bmatrix} M_{xx}(\mathbf{r}\,|\mathbf{r}_{\mathrm{B}}) & M_{xy}(\mathbf{r}\,|\mathbf{r}_{\mathrm{B}}) \\ M_{yx}(\mathbf{r}\,|\mathbf{r}_{\mathrm{B}}) & M_{yy}(\mathbf{r}\,|\mathbf{r}_{\mathrm{B}}) \end{bmatrix} \\ &= \begin{bmatrix} [1 + J_x^{H2}(\mathbf{r})] & J_x^{H1}(\mathbf{r}) \\ J_y^{H2}(\mathbf{r}) & [1 + J_y^{H1}(\mathbf{r})] \end{bmatrix} \begin{bmatrix} [1 + J_x^{H2}(\mathbf{r}_{\mathrm{B}})] & J_x^{H1}(\mathbf{r}_{\mathrm{B}}) \\ J_y^{H2}(\mathbf{r}_{\mathrm{B}}) & [1 + J_y^{H1}(\mathbf{r}_{\mathrm{B}})] \end{bmatrix}^{-1}. \end{aligned} \tag{4.44}$$

Here $\mathbf{J}^{H1}$, $\mathbf{J}^{H2}$ are convolutions of the excess currents with the magnetic Green tensor defined by (1.12).

Let us cite some formulae that can be helpful in analyzing the horizontal magnetic tensor.

Rotating the horizontal magnetic tensor clockwise by an angle a (by the same angle at the observation and base sites), we get

$$[\mathbf{M}(\mathrm{a})] = [\mathbf{R}(\mathrm{a})][\mathbf{M}][\mathbf{R}(\mathrm{a})]^{-1}, \tag{4.45}$$

where

$$[\mathbf{R}(\mathrm{a})] = \begin{bmatrix} \cos\mathrm{a} & \sin\mathrm{a} \\ -\sin\mathrm{a} & \cos\mathrm{a} \end{bmatrix}, \qquad [\mathrm{R}(\mathrm{a})]^{-1} = \begin{bmatrix} \cos\mathrm{a} & -\sin\mathrm{a} \\ \sin\mathrm{a} & \cos\mathrm{a} \end{bmatrix}.$$

The *rotational invariants* are

$$\begin{aligned} \mathrm{tr}[\mathbf{M}] &= M_{xx} + M_{yy} \\ \det[\mathbf{M}] &= M_{xx}M_{yy} - M_{xy}M_{yx} \\ \mathrm{tr}[\overleftrightarrow{\mathbf{M}}] &= \mathrm{tr}[\mathbf{M}][\mathbf{R}(-\pi/2)] = M_{xy} - M_{yx} \\ \|\mathbf{M}\| &= \sqrt{|M_{xx}|^2 + |M_{xy}|^2 + |M_{yx}|^2 + |M_{yy}|^2}, \end{aligned} \tag{4.46}$$

where $[\overleftrightarrow{\mathbf{M}}] = [\mathbf{M}][\mathbf{R}(-\pi/2)]$.

The *horizontal magnetic tensor* $[\mathbf{M}]$ reflects variations in the geoelectric medium between the base and observation sites. We obtain the most clear image of these

variations if the base site is located in the normal magnetic field (in a horizontally homogeneous zone). Otherwise the effect of inhomogeneities situated at the base site will be transferred to the entire survey area and superimposed on the effects of inhomogeneities situated at the observation sites.

Let the base site be located in the horizontally homogeneous zone. Assume that the area under investigation contains a two-dimensional structure and the $x-$ axis runs along the strike of this structure. Then

$$[\mathbf{M}] = \begin{bmatrix} M^{\parallel} & 0 \\ 0 & M^{\perp} \end{bmatrix} = \begin{bmatrix} 1 & 0 \\ 0 & M^{\perp} \end{bmatrix}, \tag{4.47}$$

where $M^{\parallel} = H_x(\mathbf{r})/H_x(\mathbf{r}_B) = 1$ and $M^{\perp} = H_y(\mathbf{r})/H_y(\mathbf{r}_B)$. Here the necessary conditions for the two-dimensionality are observed:

$$skew_S^M = \left| \frac{M_{xy} - M_{yx}}{M_{xx} + M_{yy}} \right| = 0 \tag{4.48}$$

and

$$skew_B^M = \frac{\sqrt{\left|\mathrm{Im}\,(M_{xy}\bar{M}_{yy} + M_{xx}\bar{M}_{yx})\right|}}{\left|M_{xx} + M_{yy}\right|} = 0, \tag{4.49}$$

where $skew_S^M$ and $skew_B^M$ are magnetic asymmetry parameters (analogs of the Swift and Bahr parameters) and bars denote the complex conjugation.

If the base site is located in a quasi-homogeneous layered zone and conditions $skew_S^M \approx 0$ and $skew_B^M \approx 0$ are fulfilled at some observation sites, one can suppose that the medium under investigation is two-dimensional (quasi-two-dimensional) and determine its principal (longitudinal and transverse) directions from the equation

$$\tan 2\alpha = \mathrm{Re}\,\frac{M_{xy} + M_{yx}}{M_{yy} - M_{xx}}. \tag{4.50}$$

This is the simplest solution of the eigenstate problem. Its accuracy can be easily estimated comparing the longitudinal and transverse directions obtained at different sites.

Generally the eigenstate problem for the horizontal magnetic tensor [**M**] can be solved by one of the methods considered in Chap. 2.

Let us adopt the Swift–Eggers method. We will look for the collinear magnetic eigenfields $\mathbf{H}_{\tau m}(\mathbf{r})$ and $\mathbf{H}_{\tau m}(\mathbf{r}_\mathrm{B})$, $m = 1, 2$:

$$\mathbf{H}_{\tau m}(\mathbf{r}) = \mu_m \mathbf{H}_{\tau m}(\mathbf{r}_\mathrm{B}), \qquad m = 1, 2, \tag{4.51}$$

where μ_m is the complex principal value (eigenvalue) of the tensor $[\mathbf{M}(\mathbf{r}\,|\,\mathbf{r}_\mathrm{B})]$. In the x, $y-$ coordinates

$$H_{xm}(\mathbf{r}) = \mu_m H_{xm}(\mathbf{r}_\mathrm{B}) \qquad H_{ym}(\mathbf{r}) = \mu_m H_{ym}(\mathbf{r}_\mathrm{B}) \qquad m = 1, 2. \tag{4.52}$$

Substituting (4.52) in (4.42), we get

$$\begin{aligned} &(M_{xx} - \mu_m)H_{xm}(\mathbf{r}_\mathrm{B}) + M_{xy}H_{ym}(\mathbf{r}_\mathrm{B}) = 0 \\ &M_{yx}H_{xm}(\mathbf{r}_\mathrm{B}) + (M_{yy} - \mu_m)H_{ym}(\mathbf{r}_\mathrm{B}) = 0, \quad m = 1, 2. \end{aligned} \tag{4.53}$$

Assuming the determinant of this uniform system of linear equations to be zero, we obtain

$$\mu_m^2 - (M_{xx} + M_{yy})\mu_m + (M_{xx}M_{yy} - M_{xy}M_{yx}) = 0, \tag{4.54}$$

whence

$$\begin{aligned} \mu_1 &= \frac{(M_{xx} + M_{yy}) + \sqrt{(M_{xx} + M_{yy})^2 - 4(M_{xx}M_{yy} - M_{xy}M_{yx})}}{2}, \\ \mu_2 &= \frac{(M_{xx} + M_{yy}) - \sqrt{(M_{xx} + M_{yy})^2 - 4(M_{xx}M_{yy} - M_{xy}M_{yx})}}{2}. \end{aligned} \tag{4.55}$$

The principal directions of the tensor $[\mathbf{M}]$ are determined as directions of the major axes of the polarization ellipses of the magnetic eigenfields $\mathbf{H}_{\tau 1}(\mathbf{r})$ and $\mathbf{H}_{\tau 2}(\mathbf{r})$. With (4.52) and (4.53), the polarization ratios for $\mathbf{H}_{\tau 1}(\mathbf{r})$ and $\mathbf{H}_{\tau 2}(\mathbf{r})$ are

$$\begin{aligned} P_{H_m}(\mathbf{r}) &= \frac{H_{ym}(\mathbf{r})}{H_{xm}(\mathbf{r})} = \frac{H_{ym}(\mathbf{r}_\mathrm{B})}{H_{ym}(\mathbf{r}_\mathrm{B})} = \frac{\mu_m - M_{xx}}{M_{xy}} \\ &= \frac{M_{yx}}{\mu_m - M_{yy}} = \frac{\mu_m - M_{xx} + M_{yx}}{\mu_m + M_{xy} - M_{yy}}, \quad m = 1, 2. \end{aligned} \tag{4.56}$$

Substituting (4.56) into (2.18), we evaluate angles α_{H_1} and α_{H_2} made by major axes of the polarization ellipses with the x-axis:

$$\tan 2\alpha_{H_m} = \tan 2\theta^{H_m} \cos\phi^{H_m}, \qquad m = 1, 2 \tag{4.57}$$

where $\tan\theta^{H_m} = \left|P_{H_m}\right|$, $\phi^{H_m} = \arg P_{H_m}$. The values of α_{H_m} are taken within quadrant I ($0 \le \alpha_{H_m} \le \pi/2$) if $\cos\phi^{H_m} \ge 0$ or within quadrant IV ($0 > \alpha_{H_m} \ge -\pi/2$) if $\cos\phi^{H_m} < 0$.

Finally we determine the ellipticity parameters ε_{H_1} and ε_{H_2}. In accord with (2.19),

$$\varepsilon_{H_m} = \tan\gamma_{H_m}, \qquad m = 1, 2, \tag{4.58}$$

where

$$\gamma_{H_m} = \frac{1}{2}\arcsin(\sin 2\theta^{H_m} \sin \phi^{H_m}), \qquad -\phi/4 \le \gamma_{H_m} \le \pi/4$$

and

$$-1 \le \varepsilon_{H_m} \le 1.$$

Thus, by the Swift–Eggers method we derive eight independent eigenstate parameters:

$$\begin{aligned} &|\mu_1|, \ \arg \mu_1, \ \alpha_1 = \alpha_{H_1}, \ \varepsilon_1 = \varepsilon_{H_1} \\ &|\mu_2|, \ \arg \mu_2, \ \alpha_2 = \alpha_{H_2}, \ \varepsilon_2 = \varepsilon_{H_2}, \end{aligned} \tag{4.59}$$

which fill all eight degrees of freedom possessed by the matrix [**M**].

Take the 2D model with the strike along the x -axis. Here $M_{xy} = M_{yx} = 0$ and $M_{xx} = 1, \ M_{yy} = M^{\perp}$. Using (4.55) and (4.57), we get $\mu_1 = 1, \ \alpha_1 = 0$ and $\mu_2 = M^{\perp}, \ \alpha_2 = \pi/2$ or $\mu_1 = M^{\perp}, \ \alpha_1 = \pi/2$ and $\mu_2 = 1, \ \alpha_2 = 0$. With (4.58) we get $\varepsilon_{1,2} = 0$. The principal values of the magnetic tensor [**M**] coincide with its longitudinal and the transverse components, while the principal directions are the longitudinal and transverse ones. The magnetic eigenfields are linearly polarized along the principal directions. Measuring the horizontal magnetic field at observation and base sites, we define the dimensionality of structure, but cannot distinguish between the longitudinal and transverse direction.

Asymmetric 3D-structures manifest themselves in the elliptic polarization of the magnetic eigenfields ($\varepsilon_{1,2} \neq 0$) and in the violation of the perpendicularity of their ellipses ($|\alpha_1 - \alpha_2| \neq \pi/2$).

It is a simple matter to show that in the general case the scalar invariants det [**M**] and tr [**M**] of the tensor [**M**] can be expressed in terms of geometric and arithmetic means, μ_G and μ_A, of its principal values, μ_1 and μ_2:

$$\begin{aligned} \det[\mathbf{M}] &= M_{xx}M_{yy} - M_{xy}M_{yx} = \ \mu_1\mu_2 = \mu_G^2, \\ \mathrm{tr}[\mathbf{M}] &= \ M_{xx} + M_{yy} = \mu_1 + \mu_2 = 2\,\mu_A, \end{aligned} \tag{4.60}$$

where

$$\begin{aligned} \mu_G &= \sqrt{\mu_1\mu_2} = \sqrt{\det[\mathbf{M}]}\ , \\ \mu_A &= \frac{\mu_1 + \mu_2}{2} = \frac{1}{2}\mathrm{tr}[\mathbf{M}]. \end{aligned} \tag{4.61}$$

It seems that the geometric and arithmetic means μ_G and μ_A of the principal values of the tensor [**M**] can be taken as the invariant parameters characterizing the change in the intensity and phase of the horizontal magnetic field on the way from

the base site to the observation site. The most convenient is parameter μ_G because it is less subjected to distorting influence of inhomogeneity around the base site. Consider the "normal" base site B^{N} located in a horizontally homogeneous zone and an arbitrary "anomalous" base site B^{A} located in a horizontally inhomogeneous zone. According to (4.42),

$$\begin{aligned}\mathbf{H}_\tau(\mathbf{r}) &= [\mathbf{M}(\mathbf{r}\,|\mathbf{r}_{B^{\mathrm{A}}})]\,\mathbf{H}_\tau(\mathbf{r}_{B^{\mathrm{A}}}) \\ &= [\mathbf{M}(\mathbf{r}\,|\mathbf{r}_{B^{\mathrm{A}}})][\mathbf{M}(\mathbf{r}_{B^{\mathrm{A}}}\,|\mathbf{r}_{B^{\mathrm{N}}})]\mathbf{H}_\tau(\mathbf{r}_{B^{\mathrm{N}}}) = [\mathbf{M}(\mathbf{r}\,|\mathbf{r}_{B^{\mathrm{N}}})]\mathbf{H}_\tau(\mathbf{r}_{B^{\mathrm{N}}}),\end{aligned}$$

where

$$[\mathbf{M}(\mathbf{r}\,|\mathbf{r}_{B^{\mathrm{N}}})] = [\mathbf{M}(\mathbf{r}\,|\mathbf{r}_{B^{\mathrm{A}}})][\mathbf{M}(\mathbf{r}_{B^{\mathrm{A}}}\,|\mathbf{r}_{B^{\mathrm{N}}})],$$

whence

$$\det\,[\mathbf{M}(\mathbf{r}\,|\mathbf{r}_{B^{\mathrm{N}}})] = \det\,[\mathbf{M}(\mathbf{r}\,|\mathbf{r}_{B^{\mathrm{A}}})]\,\det\,[\mathbf{M}(\mathbf{r}_{B^{\mathrm{A}}}\,|\mathbf{r}_{B^{\mathrm{N}}})].$$

Thus,

$$\det\,[\mathbf{M}(\mathbf{r}\,|\mathbf{r}_{B^{\mathrm{A}}})] = \frac{1}{\det\,[\mathbf{M}(\mathbf{r}_{B^{\mathrm{A}}}\,|\mathbf{r}_{B^{\mathrm{N}}})]}\,\det\,[\mathbf{M}(\mathbf{r}\,|\mathbf{r}_{B^{\mathrm{N}}})]$$

and

$$\mu_G(\mathbf{r}\,|\mathbf{r}_{B^{\mathrm{A}}}) = \frac{1}{\mu_G(\mathbf{r}_{B^{\mathrm{A}}}\,|\mathbf{r}_{B^{\mathrm{N}}})}\,\mu_G(\mathbf{r}\,|\mathbf{r}_{B^{\mathrm{N}}}).$$

At a given frequency the values of $\mu_G(\mathbf{r}\,|\mathbf{r}_{B^{\mathrm{A}}})$ and $\mu_G(\mathbf{r}\,|\mathbf{r}_{B^{\mathrm{N}}})$ obtained with the anomalous and normal base sites B^{A} and B^{N} differ by the constant factor $1/\mu_G(\mathbf{r}_{B^{\mathrm{A}}}\,|\mathbf{r}_{B^{\mathrm{N}}})$. Hence, the ratio between parameters $\mu_G(\mathbf{r}_1\,|\mathbf{r}_{B^{\mathrm{A}}})$ and $\mu_G(\mathbf{r}_2\,|\mathbf{r}_{B^{\mathrm{A}}})$ determined at the observation sites $\mathrm{O}(\mathbf{r}_1)$ and $\mathrm{O}(\mathbf{r}_2)$ does not depend on position of the base site B^{A}:

$$\frac{\mu_G(\mathbf{r}_1\,|\mathbf{r}_{B^{\mathrm{A}}})}{\mu_G(\mathbf{r}_2\,|\mathbf{r}_{B^{\mathrm{A}}})} = \frac{\mu_G(\mathbf{r}_1\,|\mathbf{r}_{B^{\mathrm{N}}})}{\mu_G(\mathbf{r}_2\,|\mathbf{r}_{B^{\mathrm{N}}})}.$$

The relative variations of the geometric-mean parameter μ_G are invariant under position of the base site B^{A}. So, the parameter μ_G can give the most reliable image of configuration of geoelectric structures. By analogy with effective electric intensity D_{eff}, it referred to as the *effective magnetic intensity*

$$M_{\mathrm{eff}} = \sqrt{|\det\,[\mathbf{M}(\mathbf{r}|\mathbf{r}_B)]|}. \tag{4.62}$$

4.4.2 The Schmucker Tensor

Another tensor representation has been proposed by Schmucker in his classical monograph (Schmucker, 1970). It establishes the relation between the anomalous magnetic field $\mathbf{H}^{\mathrm{A}}$ at an observation site and the normal magnetic field $\mathbf{H}^{\mathrm{N}}_{\tau}$ at a base site B located in a horizontally homogeneous zone. From (4.1) we derive

$$\mathbf{H}^{\mathrm{A}}(\mathbf{r}) = [\mathbf{S}(\mathbf{r})|\mathbf{S}(\mathbf{r}_{\mathrm{B}})]\,\mathbf{H}^{\mathrm{N}}_{\tau}(\mathbf{r}_{\mathrm{B}}), \tag{4.63}$$

where

$$\mathbf{H}^{\mathrm{A}}(\mathbf{r}) = \begin{bmatrix} H^{\mathrm{A}}_{x}(\mathbf{r}) \\ H^{\mathrm{A}}_{y}(\mathbf{r}) \\ H^{\mathrm{A}}_{z}(\mathbf{r}) \end{bmatrix}, \qquad \mathbf{H}^{\mathrm{N}}_{\tau}(\mathbf{r}_{\mathrm{B}}) = \begin{bmatrix} H^{\mathrm{N}}_{x}(\mathbf{r}_{\mathrm{B}}) \\ H^{\mathrm{N}}_{y}(\mathbf{r}_{\mathrm{B}}) \end{bmatrix} \tag{4.64}$$

and

$$[\mathbf{S}(\mathbf{r}\,|\,\mathbf{r}_{\mathrm{B}})] = \begin{bmatrix} S_{xx}(\mathbf{r}\,|\,\mathbf{r}_{\mathrm{B}}) & S_{xy}(\mathbf{r}\,|\,\mathbf{r}_{\mathrm{B}}) \\ S_{yx}(\mathbf{r}\,|\,\mathbf{r}_{\mathrm{B}}) & S_{yy}(\mathbf{r}\,|\,\mathbf{r}_{\mathrm{B}}) \\ S_{zx}(\mathbf{r}\,|\,\mathbf{r}_{\mathrm{B}}) & S_{zy}(\mathbf{r}\,|\,\mathbf{r}_{\mathrm{B}}) \end{bmatrix} = \begin{bmatrix} J^{H2}_{x}(\mathbf{r}) & J^{H1}_{x}(\mathbf{r}) \\ J^{H2}_{y}(\mathbf{r}) & J^{H1}_{y}(\mathbf{r}) \\ J^{H2}_{z}(\mathbf{r}) & J^{H1}_{z}(\mathbf{r}) \end{bmatrix}. \tag{4.65}$$

Here $\mathbf{J}^{H1}$, $\mathbf{J}^{H2}$ are convolutions of the excess currents with the magnetic Green tensor defined by (1.12).

The tensor $[\mathbf{S}]$ is referred to as the *Schmucker tensor* or the *perturbation tensor*. It falls into the *horizontal Schmucker tensor*.

$$\begin{aligned} [\mathbf{S}_{\tau}(\mathbf{r}\,|\,\mathbf{r}_{\mathrm{B}})] &= \begin{bmatrix} S_{xx}(\mathbf{r}\,|\,\mathbf{r}_{\mathrm{B}}) & S_{xy}(\mathbf{r}\,|\,\mathbf{r}_{\mathrm{B}}) \\ S_{yx}(\mathbf{r}\,|\,\mathbf{r}_{\mathrm{B}}) & S_{yy}(\mathbf{r}\,|\,\mathbf{r}_{\mathrm{B}}) \end{bmatrix} = \begin{bmatrix} J^{H2}_{x}(\mathbf{r}) & J^{H1}_{x}(\mathbf{r}) \\ J^{H2}_{y}(\mathbf{r}) & J^{H1}_{y}(\mathbf{r}) \end{bmatrix}, \\ \mathbf{H}^{\mathrm{A}}_{\tau}(\mathbf{r}) &= [\mathbf{S}_{\tau}(\mathbf{r}\,|\,\mathbf{r}_{\mathrm{B}})]\,\mathbf{H}^{\mathrm{N}}_{\tau}(\mathbf{r}_{\mathrm{B}}), \end{aligned} \tag{4.66}$$

which is an analog of the magnetic tensor $[\mathbf{M}]$, and the *Schmucker matrix*

$$\begin{aligned} [\mathbf{S}_{z}(\mathbf{r}\,|\,\mathbf{r}_{\mathrm{B}})] &= \begin{bmatrix} S_{zx}(\mathbf{r}\,|\,\mathbf{r}_{\mathrm{B}}) & S_{zy}(\mathbf{r}\,|\,\mathbf{r}_{\mathrm{B}}) \end{bmatrix} = \begin{bmatrix} J^{H2}_{y}(\mathbf{r}) & J^{H1}_{y}(\mathbf{r}) \end{bmatrix}, \\ H^{\mathrm{A}}_{z}(\mathbf{r}) &= [\mathbf{S}_{z}(\mathbf{r}\,|\,\mathbf{r}_{\mathrm{B}})]\,\mathbf{H}^{\mathrm{N}}_{\tau}(\mathbf{r}_{\mathrm{B}}), \end{aligned} \tag{4.67}$$

which is an analog of the Wiese–Parkinson matrix $[\mathbf{W}]$.

Consider relationships between tensors $[\mathbf{S}_{\tau}]$ and $[\mathbf{M}]$ as well as between matrices $[\mathbf{S}_{z}]$ and $[\mathbf{W}]$. Inasmuch as the base site B is located in a horizontally homogeneous zone, it is evident that

$$\begin{aligned} [\mathbf{S}_{\tau}] &= [\mathbf{M}] - [\mathbf{I}] \\ [\mathbf{S}_{z}] &= [\mathbf{W}]\,[\mathbf{M}]\,, \end{aligned} \tag{4.68}$$

where

$$\begin{aligned} S_{xx} &= M_{xx} - 1 & \qquad S_{xy} &= M_{xy} \\ S_{yx} &= M_{yx} & \qquad S_{yy} &= M_{yy} - 1 \\ S_{zx} &= W_{zx}M_{xx} + W_{zy}M_{yx} & \qquad S_{zy} &= W_{zx}M_{xy} + W_{zy}M_{yy}. \end{aligned}$$

Using the horizontal Schmucker tensor $[\mathbf{S}_\tau]$, we can define the anomalous magnetic fields $\mathbf{p}$ and $\mathbf{q}$ that correspond to the unit normal magnetic fields $\mathbf{1}_x$ and $\mathbf{1}_y$ linearly polarized in the x- and y-directions. According to (4.66),

$$\mathbf{p} = S_{xx}\mathbf{1}_x + S_{yx}\mathbf{1}_y, \qquad \mathbf{q} = S_{xy}\mathbf{1}_x + S_{yy}\mathbf{1}_y \tag{4.69}$$

and

$$\begin{aligned} \operatorname{Re}\mathbf{p} &= \operatorname{Re}S_{xx}\mathbf{1}_x + \operatorname{Re}S_{yx}\mathbf{1}_y & \qquad \operatorname{Re}\mathbf{q} &= \operatorname{Re}S_{xy}\mathbf{1}_x + \operatorname{Re}S_{yy}\mathbf{1}_y \\ \operatorname{Im}\mathbf{p} &= \operatorname{Im}S_{xx}\mathbf{1}_x + \operatorname{Im}S_{yx}\mathbf{1}_y & \qquad \operatorname{Im}\mathbf{q} &= \operatorname{Im}S_{xy}\mathbf{1}_x + \operatorname{Im}S_{yy}\mathbf{1}_y. \end{aligned} \tag{4.70}$$

The vectors $\operatorname{Re}\mathbf{p}$, $\operatorname{Im}\mathbf{p}$ and $\operatorname{Re}\mathbf{q}$, $\operatorname{Im}\mathbf{q}$ are given the name real and imaginary *perturbation vectors* (*perturbation arrows*). They indicate intensity, phase and direction of the anomalous magnetic fields depending on polarization of the normal magnetic field. When rotated counterclockwise by $\pi/2$, they give an idea of the excess currents, which concentrate in zones of higher conductivity and flow around zones of lower conductivity.

Using the matrix $[\mathbf{S}_z]$, we can construct the real and imaginary *Schmucker tippers* (*Schmucker induction arrows*):

$$\operatorname{Re}\mathbf{S} = \operatorname{Re}S_{zx}\mathbf{1}_x + \operatorname{Re}S_{zy}\mathbf{1}_y, \qquad \operatorname{Im}\mathbf{S} = \operatorname{Im}S_{zx}\mathbf{1}_x + \operatorname{Im}S_{zy}\mathbf{1}_y. \tag{4.71}$$

A distinguishing feature of the Schmucker tippers is that they eliminate consideration of the horizontal components of the anomalous magnetic field and expose the pure effect of its vertical component.

Figure 4.8 shows, as an example, a map of the real Schmucker tippers $\operatorname{Re}\mathbf{S}$ for the Pacific coast of USA (Schmucker, 1970). All the arrows point away from the ocean and their magnitude decreases toward the continent. We observe here a typical coastal effect caused by the influence of oceanic currents flowing along the coast.

4.5 Magnetovariational Response Functions in the Superimposition Model

Let us consider the Wiese–Parkinson relation in the superimposition model containing local near-surface inhomogeneities against deep regional background.

Following Zhang et al. (1987, 1993), we assume that the vertical component of the anomalous magnetic field, H_z^{S}, observed in the superimposition model can be written as the sum

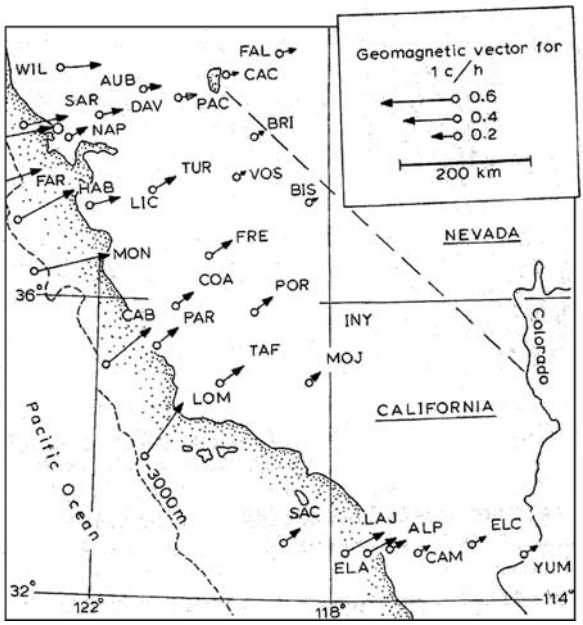

Fig. 4.8 Map of the Schmucker tippers for the Pacific coast of USA (Schmucker, 1970); reconstructed in the Wiese convention

$$H_z^S = H_z^R + H_z^L, \tag{4.72}$$

where H_z^R is caused by the regional inhomogeneity in the absence of local inhomogeneities and H_z^L is caused by local inhomogeneities in the presence of the regional inhomogeneity. Here, according to (1.68), (1.69) and (4.3),

$$H_z^R = [\mathbf{W}^R]\,\mathbf{H}_\tau^R \qquad H_z^L = [\tilde{\mathbf{h}}_z]\,\mathbf{E}_\tau^R = [\tilde{\mathbf{h}}_z]\,[\mathbf{Z}^R]\,\mathbf{H}_\tau^R, \tag{4.73}$$

where $\mathbf{E}_\tau^R$ and $\mathbf{H}_\tau^R$ are horizontal components of the regional magnetotelluric field, $[\mathbf{Z}^R]$ and $[\mathbf{W}^R]$ are the regional impedance tensor and the regional Wiese–Parkinson matrix, and $[\tilde{\mathbf{h}}_z] = [\tilde{h}_{zx}\ \ \tilde{h}_{zy}]$ is the distortion matrix.

Substituting (4.73) in (4.72) and taking into account (1.68) and (1.70), we get

$$H_z^S = \{[\mathbf{W}^R] + [\tilde{\mathbf{h}}_z]\,[\mathbf{Z}^R]\}\,\mathbf{H}_\tau^R = \{[\mathbf{W}^R] + [\tilde{\mathbf{h}}_z]\,[\mathbf{Z}^R]\}[\mathbf{h}]^{-1}\mathbf{H}_\tau^S = [\mathbf{W}^S]\,\mathbf{H}_\tau^S, \tag{4.74}$$

where, with regard for (1.70), (1.74),

$$\begin{aligned}
[\mathbf{h}] &= [\mathbf{I}] + [\tilde{\mathbf{h}}][\mathbf{Z}^R] \\
[\mathbf{W}^S] &= \{[\mathbf{W}^R] + [\tilde{\mathbf{h}}_z]\,[\mathbf{Z}^R]\}[\mathbf{h}]^{-1} \\
&= [\mathbf{W}^R]\,\{[\mathbf{I}] + [\tilde{\mathbf{h}}]\,[\mathbf{Z}^R]\}^{-1} + [\tilde{\mathbf{h}}_z]\,[\mathbf{e}]^{-1}[\mathbf{Z}^S] = [\widehat{\mathbf{W}}^R] + [\widehat{\mathbf{W}}^L].
\end{aligned} \tag{4.75}$$

Here $[\widehat{\mathbf{W}}^R]$ and $[\widehat{\mathbf{W}}^L]$ are the regional and local Wiese–Parkinson matrices distorted by local anomalies of the horizontal magnetic field:

$$[\widehat{\mathbf{W}}^R] = [\mathbf{W}^R]\,[\mathbf{h}]^{-1} = [\mathbf{W}^R]\{[\mathbf{I}] + [\tilde{\mathbf{h}}]\,[\mathbf{Z}^R]\}^{-1}, \tag{4.76}$$

$$[\widehat{\mathbf{W}}^L] = [\tilde{\mathbf{h}}_z]\,[\mathbf{e}]^{-1}[\mathbf{Z}^S]. \tag{4.77}$$

Decomposition (4.75) has been suggested in the excellent paper by Zhang et al. (1993). It reveals three significant properties of the Wiese–Parkinson matrix that manifest themselves in the superimposition model:

1. The regional and local Wiese–Parkinson matrices $[\widehat{\mathbf{W}}^R]$ and $[\widehat{\mathbf{W}}^L]$ involve the impedances $[\mathbf{Z}^R]$ and $[\mathbf{Z}^S]$ and it is just this that can explain why the tipper reflects not only the horizontal conductivity contrasts but the vertical contrasts as well.

2. Let the local near-surface inhomogeneities be much smaller than the induction scale length defined by the skin-depth. Then their electromagnetic excitation can be described in the direct-current approximation, so that the distortion matrices $[\mathbf{e}]$, $[\tilde{\mathbf{h}}]$, $[\tilde{\mathbf{h}}_z]$ are real-valued and frequency-independent. Hence, in the low-frequency range, the local Wiese–Parkinson matrix assumes the form

$$[\widehat{\mathbf{W}}^L] = [\widehat{\mathbf{t}}][\mathbf{Z}^S], \tag{4.78}$$

where $[\widehat{\mathbf{t}}] = [\tilde{\mathbf{h}}_z]\,[\mathbf{e}]^{-1} = [\widehat{t}_{zx}\ \widehat{t}_{zy}]$. Thus,

$$\begin{aligned} \widehat{W}^L_{zy} &= \widehat{t}_{zx} Z^S_{xx} + \widehat{t}_{zy} Z^S_{yx} \\ \widehat{W}^L_{zy} &= \widehat{t}_{zx} Z^S_{xy} + \widehat{t}_{zy} Z^S_{yy}\,. \end{aligned} \tag{4.79}$$

As is seen, the components of the local Wiese–Parkinson matrix are linear combinations of the impedance tensor components. The coefficients $\widehat{t}_{zx}$, $\widehat{t}_{zy}$ of these combinations are real and frequency-independent, so that W^L_{zx}, W^L_{zy} reflect the frequency dependence of Z^S_{xx}, Z^S_{yx} and Z^S_{xy}, Z^S_{yy}, while the phases of $\widehat{W}^L_{zx}$ and $\widehat{W}^L_{zy}$ mix the phases of Z^S_{xx}, Z^S_{yx} and Z^S_{xy}, Z^S_{yy}.

3. Let us assume that $[\mathbf{Z}^R]$ and $[\mathbf{Z}^S]$ in (4.76) and (4.77) go down with lowering frequency. In this case the distorting effects of local near-surface inhomogeneities attenuate at large periods, so that $[[\widehat{\mathbf{W}}^L] \cong 0$ and the Wiese–Parkinson matrix $[\mathbf{W}^S] \cong [\mathbf{W}^R]$ carries undistorted information on deep regional structures.

Below we consider three methods which separate the local and regional effect in the magnrtovariational response functions. The main difficulty on this

way is that a number of unknown parameters in the decomposition (4.75) is vastly larger than a number of known parameters determined from the field observation.

4.5.1 The Zhang–Pedersen–Mareschal–Chouteau Method

Zhang and his workmates (Zhang et al., 1993) assume that the local and regional effects in the Wiese–Parkinson matrix are uncorrelated. Then they apply (4.75) and (4.78), and define the local and regional Wiese–Parkinson matrices $[\widehat{\mathbf{W}}^L]$ and $[\widehat{\mathbf{W}}^R] = [\mathbf{W}^S] - [\widehat{\mathbf{W}}^L]$ using the observed impedance tensor $[\mathbf{Z}^S]$ and the least-squares estimates of $[\widehat{\mathbf{t}}]$ obtained through minimizing the misfit

$$q = \left\| \tilde{W}^S_{zx} - \widehat{t}_{zx}\tilde{Z}^S_{xx} - \widehat{t}_{zy}\tilde{Z}^S_{yx} \right\|^2 + \left\| \tilde{W}^S_{zy} - \widehat{t}_{zx}\tilde{Z}^S_{xy} - \widehat{t}_{zy}\tilde{Z}^S_{yy} \right\|^2, \tag{4.80}$$

where letters with tilde denote realizations normalized to the standard deviations of W^S_{zx} and W^S_{zy}. The accuracy of such decomposition depends on to what extent the assumption that the local and regional effects are uncorrelated is true.

4.5.2 The Ritter–Banks Method

Another approach has been suggested by Ritter and Banks (1998). This approach rests on the decomposition

$$\begin{aligned} H^S_z = H^R_z + H^L_z = \left\{[\mathbf{W}^R] + [\tilde{\mathbf{h}}_z][\mathbf{Z}^R]\right\}\mathbf{H}^R_\tau = [\mathbf{W}^S]\mathbf{H}^R_\tau, \\ [\mathbf{W}^S] = [\mathbf{W}^R] + [\mathbf{W}^L], \end{aligned} \tag{4.81}$$

following from (4.72) and (4.73). Here $[\mathbf{W}^R] = [\widehat{\mathbf{W}}^R][\mathbf{h}]$ and $[\mathbf{W}^L] = [\tilde{\mathbf{h}}_z][\mathbf{Z}^R] = [\widehat{\mathbf{W}}^{\mathbf{L}}][\mathbf{h}]$ are the regional and local Wiese–Parkinson matrices defined at low frequencies when the distortion matrix $[\tilde{\mathbf{h}}_z]$ is real-valued and frequency-independent. Thus, along with (4.79) we have the linear relations between components of the local Wiese–Parkinson matrix and the regional impedance tensor:

$$\begin{aligned} W^L_{zx} = \tilde{h}_{zx}Z^R_{xx} + \tilde{h}_{zy}Z^R_{yx}, \\ W^L_{zy} = \tilde{h}_{zx}Z^R_{xy} + \tilde{h}_{zy}Z^R_{yy}. \end{aligned} \tag{4.82}$$

In the Ritter–Banks method we examine a model that contains a two-dimensional local inhomogeneity against a two-dimensional regional background. The regional and local strike angles are α_R and α_L counted clockwise from the x-axis. This is the same (2D+2D)-superimposition model as in the Zhang–Roberts–Pedersen method described in Sect. 3.3. According to (4.81),

$$[\mathbf{W}^S] = [W^S_{zx} \;\; W^S_{zy}] = \left[[\mathbf{W}^S(\alpha_R)]\,[\mathbf{R}(\alpha_R)] + [\tilde{\mathbf{h}}_z(\alpha_L)]\,[\mathbf{R}(\alpha_L - \alpha_R)][\mathbf{Z}^R(\alpha_R)]\,[\mathbf{R}(\alpha_R)]\right] \tag{4.83}$$

where $[\mathbf{R}(\alpha)]$ is the rotation matrix:

$$[\mathbf{R}(\alpha)] = \begin{bmatrix} \cos\alpha & \sin\alpha \\ -\sin\alpha & \cos\alpha \end{bmatrix},$$

$[\mathbf{Z}^R(\alpha_R)]$ is the regional impedance tensor:

$$[\mathbf{Z}^R(\alpha_R)] = \begin{bmatrix} 0 & Z^{\parallel} \\ -Z^{\perp} & 0 \end{bmatrix},$$

$\left[\mathbf{W}^S(\alpha_R)\right]$ and $\left[\tilde{\mathbf{h}}_z(\alpha_L)\right]$ are the Wiese–Parkinson matrix and the magnetic distortion tensor in the regional and local coordinates:

$$\left[\mathbf{W}^S(\alpha_R)\right] = \left[0 \;\; W^S_{zy}(\alpha_R)\right], \qquad \left[\tilde{\mathbf{h}}_z(\alpha_L)\right] = \left[\tilde{h}_{zx}(\alpha_L)\; 0\right].$$

Test of (4.83) is performed simultaneously on the set of observation sites. It reduces to hypothetical event analysis. By varying the horizontal magnetic field polarization and monitoring the vertical magnetic field predicted for different events, we can find the regional strike and the phase of the regional impedance.

4.5.3 The Berdichevsky–Kuznetsov Method

The (2D+2D)-superimposition problem can be greatly simplified if magnetic areal observations are carried out synchronously with a base site located in the area with the normal magnetic field and the strikes of two-dimensional structures are known from tippers analysis.

Following Zhang et al. (1987, 1993) and Ritter and Banks (1998), we consider the 3D superimposition model which contains two 2D structures of different strike.

Examine the horizontally-layered model, in which two-dimensional horizontal conductive prisms P' and P'' with strike angles α' and α'' are located at different depths. The prisms are separated by thick highly resistive strata so that the galvanic connection between them is virtually absent. At low frequencies the induction connection is also absent. With these assumptions, we assume that each of the prisms manifests itself as an independent body and the total magnetovariational effect of both prisms is a sum of their partial effects. The model is excited by a plane electromagnetic wave incident vertically on the Earth's surface.

Let the magnetic field be measured simultaneously at two sites: at an arbitrary observation site and at a base (reference) site B selected in the area with the normal magnetic field. Assume that the observations result in four magnetovariational response functions:

1) the Schmucker matrix

$$[\mathbf{S}_z] = \begin{bmatrix} S_{zx} & S_{zy} \end{bmatrix} \qquad H_z(\mathbf{r}) = H_z^{\mathrm{A}}(\mathbf{r}) = [\mathbf{S}_z]\,\mathbf{H}_\tau^{\mathrm{N}}(\mathbf{r}_{\mathrm{B}}), \tag{4.84}$$

2) the horizontal Schmucker tensor

$$[\mathbf{S}_z] = \begin{bmatrix} S_{xx} & S_{xy} \\ S_{yx} & S_{yy} \end{bmatrix} \qquad \mathbf{H}_\tau^{\mathrm{A}}(\mathbf{r}) = [\mathbf{S}_\tau]\mathbf{H}_\tau^{\mathrm{N}}(\mathbf{r}_{\mathrm{B}}), \tag{4.85}$$

3) the Wiese–Parkinson matrix (the tipper)

$$[\mathbf{W}] = \begin{bmatrix} W_{zx} & W_{zy} \end{bmatrix} \qquad H_z(\mathbf{r}) = H_z^{\mathrm{A}}(\mathbf{r}) = [\mathbf{W}]\,\mathbf{H}_\tau(\mathbf{r}), \tag{4.86}$$

4) the horizontal magnetic tensor

$$[\mathbf{M}] = \begin{bmatrix} M_{xx} & M_{xy} \\ M_{yx} & M_{yy} \end{bmatrix} \qquad \mathbf{H}_\tau(\mathbf{r}) = \mathbf{H}_\tau^{\mathrm{N}}(\mathbf{r}_{\mathrm{B}}) + \mathbf{H}_\tau^{\mathrm{A}}(\mathbf{r}) = [\mathbf{M}]\,\mathbf{H}_\tau^{\mathrm{N}}(\mathbf{r}_{\mathrm{B}}). \tag{4.87}$$

Here the superscripts N and A indicate the normal and anomalous magnetic fields.

The problem is to find the matrices $\left[\mathbf{S}_z'\right]$, $\left[\mathbf{S}_\tau'\right]$, $\left[\mathbf{W}'\right]$, $\left[\mathbf{M}'\right]$ that define the effect of the prism P' in the absence of the prism P'' and the matrices $\left[\mathbf{S}_z''\right]$, $\left[\mathbf{S}_\tau''\right]$, $\left[\mathbf{W}''\right]$, $\left[\mathbf{M}''\right]$ that define the effect of the prism P'' in the absence of the prism P'. These matrices are said to be partial.

Introduce arbitrary measurement coordinates x, y as well as the coordinates x', y' and x'', y'' tied with prisms P' and P'' : the x' - axis is oriented along the strike of the prism P' and the x'' - axis is oriented along the strike of the prism P''. Azimuths of the prism strike, α' and α'', are measured clockwise from the x -axis.

In the coordinates x', y'we have

$$\left[\mathbf{S}_z'\right] = \begin{bmatrix} 0 & S_{zy}' \end{bmatrix} \qquad \left[\mathbf{S}_\tau'\right] = \begin{bmatrix} 0 & 0 \\ 0 & S_{yy}' \end{bmatrix}. \tag{4.88}$$

In the coordinates x'', y'' we have

$$\left[\mathbf{S}_z''\right] = \begin{bmatrix} 0 & S_{zy}'' \end{bmatrix} \qquad \left[\mathbf{S}_\tau''\right] = \begin{bmatrix} 0 & 0 \\ 0 & S_{yy}'' \end{bmatrix}. \tag{4.89}$$

In the measurement coordinates x, y we have:

$$
\begin{aligned}
\left[\tilde{\mathbf{S}}'_z\right] &= \left[\mathbf{S}'_z\right]\left[\mathbf{R}(\alpha')\right] = S'_{zy}\left[-\sin\alpha'\ \cos\alpha'\right] \\
\left[\tilde{\mathbf{S}}'_\tau\right] &= \left[\mathbf{R}(-\alpha')\right]\left[\mathbf{S}'_\tau\right]\left[\mathbf{R}(\alpha')\right] = S'_{yy}\begin{bmatrix} \sin^2\alpha' & -\sin\alpha'\cos\alpha' \\ -\sin\alpha'\cos\alpha' & \cos^2\alpha' \end{bmatrix} \\
\left[\tilde{\mathbf{S}}''_z\right] &= \left[\mathbf{S}''_z\right]\left[\mathbf{R}(\alpha'')\right] = S''_{zy}\left[-\sin\alpha''\ \cos\alpha''\right] \\
\left[\tilde{\mathbf{S}}''_\tau\right] &= \left[\mathbf{R}(-\alpha'')\right]\left[\mathbf{S}''_\tau\right]\left[\mathbf{R}(\alpha'')\right] = S''_{yy}\begin{bmatrix} \sin^2\alpha'' & -\sin\alpha''\cos\alpha'' \\ -\sin\alpha''\cos\alpha'' & \cos^2\alpha'' \end{bmatrix},
\end{aligned}
\tag{4.90}
$$

where $[\mathbf{R}(\alpha)]$ is the rotation matrix

$$
[\mathbf{R}(\alpha)] = \begin{bmatrix} \cos\alpha & \sin\alpha \\ -\sin\alpha & \cos\alpha \end{bmatrix}.
$$

Represent the total effect of both prisms as a sum of their partial effects:

$$
H_z^{\mathrm{A}} = H_z^{\mathrm{A}'} + H_z^{\mathrm{A}''}, \qquad \mathbf{H}_\tau^{\mathrm{A}} = \mathbf{H}_\tau^{\mathrm{A}'} + \mathbf{H}_\tau^{\mathrm{A}''}. \tag{4.91}
$$

Substituting (4.84), (4.85) into (4.91), we get

$$
\begin{aligned}
[\mathbf{S}_z]\,\mathbf{H}_\tau^{\mathrm{N}} &= \left[\tilde{\mathbf{S}}'_z\right]\mathbf{H}_\tau^{\mathrm{N}} + \left[\tilde{\mathbf{S}}''_z\right]\mathbf{H}_\tau^{\mathrm{N}} = \left\{\left[\tilde{\mathbf{S}}'_z\right] + \left[\tilde{\mathbf{S}}''_z\right]\right\}\mathbf{H}_\tau^{\mathrm{N}} \\
[\mathbf{S}_\tau]\,\mathbf{H}_\tau^{\mathrm{N}} &= \left[\tilde{\mathbf{S}}'_\tau\right]\mathbf{H}_\tau^{\mathrm{N}} + \left[\tilde{\mathbf{S}}''_\tau\right]\mathbf{H}_\tau^{\mathrm{N}} = \left\{\left[\tilde{\mathbf{S}}'_\tau\right] + \left[\tilde{\mathbf{S}}''_\tau\right]\right\}\mathbf{H}_\tau^{\mathrm{N}},
\end{aligned}
\tag{4.92}
$$

whence

$$
\begin{aligned}
[\mathbf{S}_z] &= \left[\tilde{\mathbf{S}}'_z\right] + \left[\tilde{\mathbf{S}}''_z\right] \\
[\mathbf{S}_\tau] &= \left[\tilde{\mathbf{S}}'_\tau\right] + \left[\tilde{\mathbf{S}}''_\tau\right].
\end{aligned}
\tag{4.93}
$$

Thus, we decompose the measured matrices $[\mathrm{S_z}]$, $[\mathrm{S}_\tau]$ reflecting both the prisms into the partial matrices $\left[\tilde{\mathrm{S}}'_{\mathrm{z}}\right]$, $\left[\tilde{\mathrm{S}}'_\tau\right]$ and $\left[\tilde{\mathrm{S}}''_{\mathrm{z}}\right]$, $\left[\tilde{\mathrm{S}}''_\tau\right]$ reflecting each prism separately.

There exist linear relations between components of the measured and partial matrices. According to (4.90) and (4.93),

$$
\begin{aligned}
S_{zx} &= -S'_{zy}\sin\alpha' - S''_{zy}\sin\alpha'' \\
S_{zy} &= S'_{zy}\cos\alpha' + S''_{zy}\cos\alpha''
\end{aligned}
\tag{4.94}
$$

and

$$
\begin{aligned}
S_{xx} &= S'_{yy}\sin^2\alpha' + S''_{yy}\sin^2\alpha'' \\
S_{xy} &= S_{yx} = -S'_{yy}\sin\alpha'\cos\alpha' - S''_{yy}\sin\alpha''\cos\alpha'' \\
S_{yy} &= S'_{yy}\cos^2\alpha' + S''_{yy}\cos^2\alpha''.
\end{aligned}
\tag{4.95}
$$

These relations form the equations for $S'_{zy},\ S''_{zy}$ and $S'_{yy},\ S''_{yy}$.

With $\alpha' \neq \alpha''$ the solution of the equations system (4.94) is given by

$$
S'_{zy} = \frac{S_{zx}\cos\alpha'' + S_{zy}\sin\alpha''}{\sin(\alpha'' - \alpha')}, \qquad S''_{zy} = -\frac{S_{zx}\cos\alpha' + S_{zy}\sin\alpha'}{\sin(\alpha'' - \alpha')}. \tag{4.96}
$$

The equations system (4.95) is overdetermined and compatible. Its solution can be given by

$$
\begin{aligned}
S'_{yy} &= \frac{\mathrm{tr}\,[\mathbf{S}_\tau]}{2} + \sqrt{\frac{\{\mathrm{tr}\,[\mathbf{S}_\tau]\}^2}{4} - \frac{\det[\mathbf{S}_\tau]}{\sin^2(\alpha'' - \alpha')}} \\
S''_{yy} &= \frac{\mathrm{tr}\,[\mathbf{S}_\tau]}{2} - \sqrt{\frac{\{\mathrm{tr}\,[\mathbf{S}_\tau]\}^2}{4} - \frac{\det[\mathbf{S}_\tau]}{\sin^2(\alpha'' - \alpha')}},
\end{aligned}
\tag{4.97}
$$

where $\mathrm{tr}\,[\mathbf{S}_\tau]$ and $\det[\mathbf{S}_\tau]$ are the trace and determinant of the matrix $[\mathbf{S}_\tau]$:

$$
\mathrm{tr}\,[\mathbf{S}_\tau] = S_{xx} + S_{yy} \qquad \det\,[\mathbf{S}_\tau] = S_{xx}S_{yy} - S_{xy}S_{yx}.
$$

Using (4.96) and (4.97), we determine the partial matrices $\left[\tilde{\mathbf{S}}'_z\right], \left[\tilde{\mathbf{S}}'_\tau\right]$ and $\left[\tilde{\mathbf{S}}''_z\right], \left[\tilde{\mathbf{S}}''_\tau\right]$:

$$
\begin{aligned}
&\left[\tilde{\mathbf{S}}'_z\right] = \left[\, -S'_{zy}\sin\alpha' \;\; S'_{zy}\cos\alpha' \,\right], \qquad \left[\tilde{\mathbf{S}}'_\tau\right] = \begin{bmatrix} S'_{yy}\sin^2\alpha' & -S'_{yy}\sin\alpha'\cos\alpha' \\ -S'_{yy}\sin\alpha'\cos\alpha' & S'_{yy}\cos^2\alpha' \end{bmatrix}, \\
&\left[\tilde{\mathbf{S}}''_z\right] = \left[\, -S''_{zy}\sin\alpha'' \;\; S''_{zy}\cos\alpha'' \,\right], \qquad \left[\tilde{\mathbf{S}}''_\tau\right] = \begin{bmatrix} S''_{yy}\sin^2\alpha'' & -S''_{yy}\sin\alpha''\cos\alpha'' \\ -S''_{yy}\sin\alpha''\cos\alpha'' & S''_{yy}\cos^2\alpha'' \end{bmatrix}.
\end{aligned}
\tag{4.98}
$$

The decomposition of the matrices $[\mathbf{M}]$ and $[\mathbf{W}]$ is easily derived from the decomposition of the matrices $[\mathbf{S}_\tau]$ and $[\mathbf{S}_z]$. By virtue of (4.84), (4.85), (4.86), and (4.87)

$$
[\mathbf{M}] = [\mathbf{S}_\tau] + [\mathbf{I}], \qquad [\mathbf{W}] = [\mathbf{S}_z]\,[\mathbf{M}]^{-1}, \tag{4.99}
$$

where $[\mathbf{I}]$ is the identity matrix:

$$[\mathbf{I}] = \begin{bmatrix} 1 & 0 \\ 0 & 1 \end{bmatrix}.$$

Thus, in the measurement coordinates

$$\left[\tilde{\mathbf{M}}'\right] = \left[\tilde{\mathbf{S}}'_{\tau}\right] + [\mathbf{I}], \qquad \left[\tilde{\mathbf{M}}''\right] = \left[\tilde{\mathbf{S}}''_{\tau}\right] + [\mathbf{I}] \tag{4.100}$$

and

$$\left[\tilde{\mathbf{W}}'\right] = \left[\tilde{\mathbf{S}}'_{z}\right]\left[\tilde{\mathbf{M}}'\right]^{-1}, \qquad \left[\tilde{\mathbf{W}}''\right] = \left[\tilde{\mathbf{S}}''_{z}\right]\left[\tilde{\mathbf{M}}''\right]^{-1}, \tag{4.101}$$

whence

$$\begin{aligned} \left[\tilde{\mathbf{M}}'\right] &= \begin{bmatrix} 1 + S'_{yy}\sin^2\alpha' & -S'_{yy}\sin\alpha'\cos\alpha' \\ -S'_{yy}\sin\alpha'\cos\alpha' & 1 + S'_{yy}\cos^2\alpha' \end{bmatrix} \\ \left[\tilde{\mathbf{M}}''\right] &= \begin{bmatrix} 1 + S''_{yy}\sin^2\alpha'' & -S''_{yy}\sin\alpha''\cos\alpha'' \\ -S''_{yy}\sin\alpha''\cos\alpha'' & 1 + S''_{yy}\cos^2\alpha'' \end{bmatrix} \end{aligned} \tag{4.102}$$

and

$$\begin{aligned} \left[\tilde{\mathbf{W}}'\right] &= \frac{S'_{zy}}{1 + S'_{yy}}\left[-\sin\alpha' \quad \cos\alpha'\right] \\ \left[\tilde{\mathbf{W}}''\right] &= \frac{S''_{zy}}{1 + S''_{yy}}\left[-\sin\alpha'' \quad \cos\alpha''\right]. \end{aligned} \tag{4.103}$$

Applying this approach to the superimposition problem, we can decompose a three-dimensional magnetovariational anomaly into two independent two-dimensional anomalies and reduce 3D inversion to two self-contained 2D inversions.

Figure 4.9 presents an example of such a decomposition. Consider a three-dimensional superimposition model consisting of the sedimentary cover ($\rho_1 = 10\,\text{Ohm}\cdot\text{m}$, $h_1 = 0.1\,\text{km}$, $\rho_2 = 100\,\text{Ohm}\cdot\text{m}$, $h_2 = 0.9\,\text{km}$), the resistive lithosphere ($\rho_3 = 1000\,\text{Ohm}\cdot\text{m}$, $h_3 = 99\,\text{km}$) and the conductive mantle ($\rho_4 = 20\,\text{Ohm}\cdot\text{m}$). The lithosphere contains the crustal two-dimensional conductive prism CP of 6 Ohm·m resistivity, its thickness, width and azimuth being 3 km, 100 km and 135° respectively, and the mantle two-dimensional conductive prism MP of 5 Ohm·m resistivity, its thickness, width and azimuth being 50 km, 300 km and 0° respectively. Azimuths of the crustal and mantle prisms are determined from the pseudo-topographies of the 3D tipper invariants $\|\mathbf{W}\| = \sqrt{|W_{zx}|^2 + |W_{zy}|^2}$, plotted on periods of 1 and 10,000 s. Decomposing 3D invariant $\|\mathbf{W}\|$ into two 2D invariants $\|\mathbf{W}'\|$ and $\|\mathbf{W}''\|$, we separate partial two-dimensional effects of the crustal and mantle prisms, CP and MP, with reasonable accuracy.

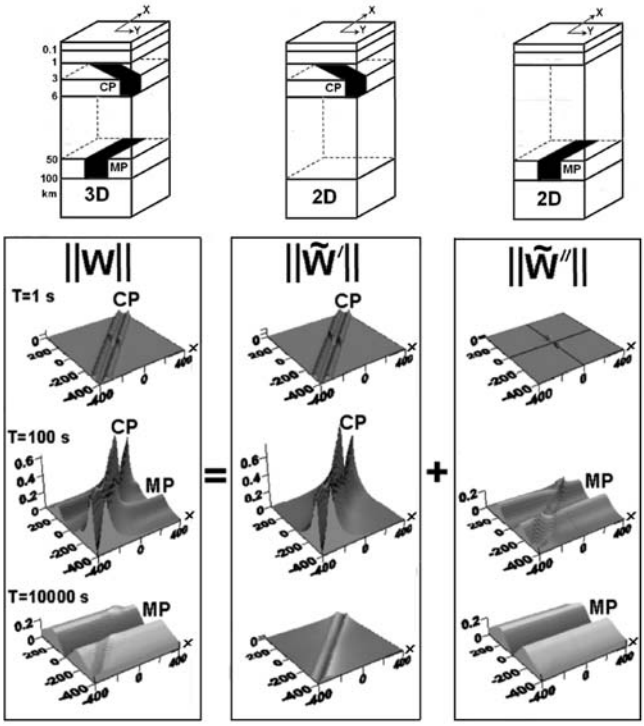

Fig. 4.9 Decomposition of the 3D tipper invariant $\|\mathbf{W}\| = \sqrt{|W_{zx}|^2 + |W_{zy}|^2}$ into the 2D tipper invariants $\|\tilde{\mathbf{W}}'\| = \sqrt{|\tilde{W}'_{zx}|^2 + |\tilde{W}'_{zy}|^2}$ and $\|\tilde{\mathbf{W}}''\| = \sqrt{|\tilde{W}''_{zx}|^2 + |\tilde{W}''_{zy}|^2}$ reflecting partial effects of the crustal prism CP and mantle prism MP

4.6 Magnetic Perturbation Ellipses

The Schmucker perturbation vectors **p** and **q** are defined by (4.69) and (4.70) as transforms of the unit normal magnetic fields $\mathbf{1}_x$ and $\mathbf{1}_y$ polarized at the base site in the x- and y-directions. Now we will show that vectors **p** and **q** can be incorporated into ellipses, which give better image of geoelectric structures perturbing the magnetic field.

Let us begin with real vectors Re **p** and Re **q**. Turn to (4.66) and introduce the following notations:

$$\begin{aligned} H_x^{\mathrm{A}}(\mathbf{r}) &= U, \qquad H_y^{\mathrm{A}}(\mathbf{r}) = V, \\ H_x^{\mathrm{N}}(\mathbf{r}_{\mathrm{B}}) &= X, \qquad H_y^{\mathrm{N}}(\mathbf{r}_{\mathrm{B}}) = Y, \\ a &= \mathrm{Re}\, S_{xx}(\mathbf{r}|\,\mathbf{r}_{\mathrm{B}}), \qquad b = \mathrm{Re}\, S_{xy}(\mathbf{r}|\,\mathbf{r}_{\mathrm{B}}), \\ c &= \mathrm{Re}\, S_{yx}(\mathbf{r}|\,\mathbf{r}_{\mathrm{B}}), \qquad d = \mathrm{Re}\, S_{yy}(\mathbf{r}|\,\mathbf{r}_{\mathrm{B}}), \end{aligned} \tag{4.104}$$

where X, Y and U, V take the real values.

In these notations the horizontal Schmucker tensor $[\mathbf{S}_\tau]$ transforms the XY plane into the UV plane:

$$\begin{aligned} U &= aX + bY \\ V &= cX + dY. \end{aligned} \tag{4.105}$$

It is easy to prove that a circle $X^2 + Y^2 = 1$ given in the XY plane (at base site) is transformed into an ellipse

$$(c^2 + d^2)U^2 - 2(bd + ac)UV + (a^2 + b^2)V^2 = (ad - bc)^2 \tag{4.106}$$

centered at the origin of the plane UV at observation site. This ellipse is referred to as the *real perturbation ellipse*. It is an analog of the Doll telluric ellipse applied in the telluric current prospecting (Leonardon, 1948; Berdichevsky, 1965).

The transformation of the unit circle into a perturbation ellipse is shown in Fig. 4.10. The perturbation vectors Re **p** and Re **q** are transforms of the conjugate radii $\mathbf{1}_x$ and $\mathbf{1}_y$ of the unit circle. Evidently the vectors Re **p** and Re **q** are conjugate radii of the perturbation ellipse. It is seen from presented example that perturbation ellipse reflects the field anisotropy much better than perturbation vectors.

In canonical form, the perturbation ellipse equation (4.106) is

$$\frac{(U')^2}{A^2} + \frac{(V')^2}{B^2} = 1, \tag{4.107}$$

where

$$\begin{aligned} A &= \sqrt{\frac{a^2 + b^2 + c^2 + d^2}{2} + \sqrt{\frac{(a^2 + b^2 + c^2 + d^2)^2}{4} - (ad - bc)^2}} \\ B &= \sqrt{\frac{a^2 + b^2 + c^2 + d^2}{2} - \sqrt{\frac{(a^2 + b^2 + c^2 + d^2)^2}{4} - (ad - bc)^2}} \end{aligned} \tag{4.108}$$

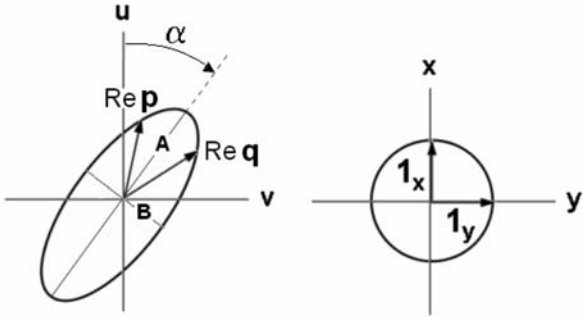

Fig. 4.10 The Schmucker perturbation vectors Re **p** and Re **q** are conjugate radii of the magnetic perturbation ellipse

are the major and minor semi-axes of the ellipse. Here

$$AB = ad - bc = \det\left[\mathrm{Re}\,\mathbf{S}_\tau(\mathbf{r}|\,\mathbf{r}_\mathrm{B})\right]. \tag{4.109}$$

The slope of the major axis is

$$\begin{aligned}\tan\alpha &= \frac{2(ac+bd)}{a^2+b^2-c^2-d^2+\sqrt{(a^2+b^2+c^2+d^2)^2-4(ad-bc)^2}}\\ &= \frac{a^2+b^2-c^2-d^2-\sqrt{(a^2+b^2+c^2+d^2)^2-4(ad-bc)^2}}{-2(ac+bd)}\\ &= \frac{a^2+b^2-c^2-d^2+2(ac+bd)-\sqrt{(a^2+b^2+c^2+d^2)^2-4(ad-bc)^2}}{a^2+b^2-c^2-d^2-2(ac+bd)+\sqrt{(a^2+b^2+c^2+d^2)^2-4(ad-bc)^2}}.\end{aligned} \tag{4.110}$$

Similarly we construct the perturbation ellipse for the Schmucker tensor $[\mathrm{Im}\,\mathbf{S}_\tau]$. Substituting

$$a = \mathrm{Im}\,S_{xx}(\mathbf{r}|\,\mathbf{r}_\mathrm{B}), \qquad b = \mathrm{Im}\,S_{xy}(\mathbf{r}|\,\mathbf{r}_\mathrm{B}),$$

$$c = \mathrm{Im}\,S_{yx}(\mathbf{r}|\,\mathbf{r}_\mathrm{B}), \qquad d = \mathrm{Im}\,S_{yy}(\mathbf{r}|\,\mathbf{r}_\mathrm{B})$$

into (4.108) and (4.110), we get the semi-axes and the slope of the major axis of the *imaginary perturbation ellipse* associated with the imaginary perturbation vectors $\mathrm{Im}\,\mathbf{p}$ and $\mathrm{Im}\,\mathbf{q}$.

The same technique can be used for constructing the real and imaginary ellipses of the horizontal magnetic tensor $[\mathbf{M}]$.

Chapter 5
The Recent Developments

5.1 Advancement of the Plane-Wave Model

We have examined the plane-wave model of the inhomogeneous Earth that offers basic invariant magnetotelluric and magnetovariational response functions: the impedance tensor [**Z**] and phase tensor $[\mathbf{\Phi}]$, the Doll and magnetic tensors [**D**] and [**M**], the Schmucker perturbation tensor [**S**], the Wiese–Parkinson and Vozoff tipper vectors **W** and **V**.

The condition of existence of these invariant response functions is that the normal magnetic field allows for the plane-wave (one-dimensional) approximation. This actually is the case if the horizontal components of the normal magnetic field change slowly along the Earth's surface and its vertical component is close to zero.

Unfortunately, the question on physical feasibility of the plane-wave model with its one-dimensional normal magnetic field is poorly studied theoretically. Up to now we content ourselves with empirical estimates derived from the practical magnetotelluric experience. There are good grounds to believe that at middle and low latitudes (far away from the polar field sources) the magnetotelluric and magnetovariational response functions in a broad range of frequencies (from 10^3 to 10^{-4} Hz) yield to stable determination and give geologically meaningful information on the structure of the Earth's interior. The more complicated situation is encountered in the polar zones with their dramatic electromagnetic disturbances caused by events in the ionosphere and magnetosphere.

Concluding the analysis of magnetotelluric and magnetovariational response functions, we would like to consider a generalized model taking into account a source effect which may manifest itself in considerable departure of the normal magnetic field from the plane wave (specifically, with noticeable vertical magnetic component).

The model to be examined is presented in Fig. 5.1. It consists of the horizontally homogeneous Earth of normal conductivity $\sigma_N(z)$ and a bounded three-dimensional inhomogeneous domain V of conductivity $\sigma(x, y.z) = \sigma_N(z) + \Delta\sigma(x, y, z)$, where $\Delta\sigma(x, y, z)$ is an excess conductivity that varies arbitrarily in x, y, z. The Earth comes in contact with the nonconducting air, $\sigma_{air} = 0$. The field is excited by

M. Berdichevsky, V.I. Dmitriev, *Models and Methods of Magnetotellurics*,
DOI 10.1007/978-3-540-77814-1_5, © Springer-Verlag Berlin Heidelberg 2008

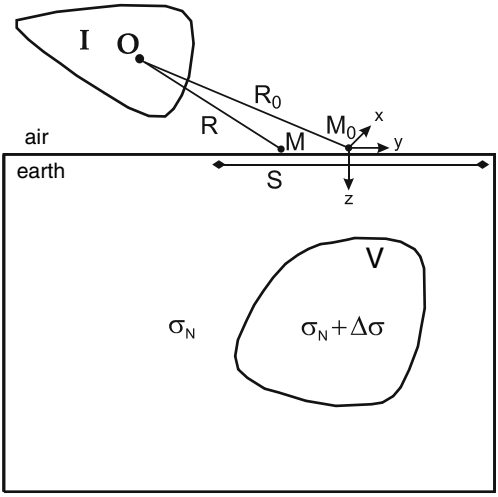

Fig. 5.1 Illustrating the determination of the generalized impedance tensor

primary currents of density $\mathbf{j}^p$ closed in a source domain I located above the Earth. The centre of the domain I is at a point O, its maximum radius is r_i.

The electromagnetic field meets here the Maxwell equations

$$curl\,\mathbf{H} = \sigma\mathbf{E} + \mathbf{j}^p, \qquad curl\,\mathbf{E} = i\omega\mu_o\mathbf{H}, z \in [-\infty, \infty]. \tag{5.1}$$

For the normal field excited in the horizontally layered Earth in the absence of the inhomogeneous domain V we have

$$curl\,\mathbf{H}^N = \sigma_N\mathbf{E}^N, \qquad curl\,\mathbf{E}^N = i\omega\mu_o\mathbf{H}^N, z \geq 0. \tag{5.2}$$

5.1.1 Analysis of the Normal Magnetotelluric Field

A remarkable feature of the model is that the normal current flows parallel to the boundary between the conducting Earth and the nonconducting air and the normal electric field in the Earth has no vertical component (Berdichevsky and Zhdanov, 1984; Zhdanov and Keller, 1994):

$$E_z^N \equiv 0, \qquad z \geq 0. \tag{5.3}$$

In order to model the normal field, we introduce the following limitations:

- The magnetotelluric observations are performed on the Earth's surface in the domain S : $\sqrt{x^2 + y^2} \leq r_s$. Its centre M_o coincides with the origin of the coordinate system, r_s is its maximum radius;

- The distance between the source domain I and the observation domain S is much larger than maximum radii r_{i} and r_{s} of these domains. Implying that the normal field rather slowly varies along the Earth's surface, we assume that

$$\left|\frac{\partial H_z^{\mathrm{N}}}{\partial y}\right| \ll \left|\frac{\partial H_y^{\mathrm{N}}}{\partial z}\right|, \qquad \left|\frac{\partial H_z^{\mathrm{N}}}{\partial x}\right| \ll \left|\frac{\partial H_x^{\mathrm{N}}}{\partial z}\right|. \tag{5.4}$$

Under these conditions, we write the Maxwell equations (5.2) in the form

$$\begin{aligned}
&\frac{\partial H_y^{\mathrm{N}}}{\partial z} = -\sigma_{\mathrm{N}} E_x^{\mathrm{N}}, \quad \frac{\partial H_x^{\mathrm{N}}}{\partial z} = \sigma_{\mathrm{N}} E_y^{\mathrm{N}}, \quad \frac{\partial H_y^{\mathrm{N}}}{\partial x} - \frac{\partial H_x^{\mathrm{N}}}{\partial y} = 0, \\
&\frac{\partial E_y^{\mathrm{N}}}{\partial z} = -i\omega\mu_{\mathrm{o}} H_x^{\mathrm{N}}, \quad \frac{\partial E_x^{\mathrm{N}}}{\partial z} = i\omega\mu_{\mathrm{o}} H_y^{\mathrm{N}}, \quad \frac{\partial E_y^{\mathrm{N}}}{\partial x} - \frac{\partial E_x^{\mathrm{N}}}{\partial y} = i\omega\mu_{\mathrm{o}} H_z^{\mathrm{N}}.
\end{aligned} \tag{5.5}$$

Such a field can be expressed in terms of a scalar function $U(x, y, z)$:

$$\begin{aligned}
&E_x^{\mathrm{N}} = -\frac{1}{\sigma_{\mathrm{N}}}\frac{\partial^2 U}{\partial y \partial z}, \qquad E_y^{\mathrm{N}} = \frac{1}{\sigma_{\mathrm{N}}}\frac{\partial^2 U}{\partial x \partial z}, \qquad E_z^{\mathrm{N}} = 0, \\
&H_x^{\mathrm{N}} = \frac{\partial U}{\partial x}, \qquad H_y^{\mathrm{N}} = \frac{\partial U}{\partial y}, \qquad H_z^{\mathrm{N}} = \frac{1}{i\omega\mu_{\mathrm{o}}\sigma_{\mathrm{N}}}\frac{\partial}{\partial z}\left(\frac{\partial^2 U}{\partial x^2} + \frac{\partial^2 U}{\partial y^2}\right).
\end{aligned} \tag{5.6}$$

It is easy to verify that the function $U(x, y, z)$ meets the one-dimensional equation

$$\frac{\partial}{\partial z}\left(\frac{1}{\sigma_{\mathrm{N}}}\frac{\partial U}{\partial z}\right) + i\omega\mu_{\mathrm{o}} U = 0 \tag{5.7}$$

with boundary condition $U|_{z=0} = U_{\mathrm{o}}(x, y)$ at the Earth's surface and continuity conditions for U and $\frac{1}{\sigma_{\mathrm{N}}}\frac{\partial U}{\partial z}$ at the boundaries between layers.

Proceeding from (5.7), we represent the function U as

$$\mathrm{U}(x, y, z) = \mathrm{U}_{\mathrm{o}}(x, y)\, \nu(z), \tag{5.8}$$

where $\nu(z)$ is the solution of the one-dimensional problem

$$\frac{\mathrm{d}}{\mathrm{dz}}\left(\frac{1}{\sigma_{\mathrm{N}}}\frac{\mathrm{d}\nu}{\mathrm{dz}}\right) + \mathrm{i}\omega\mu_{\mathrm{o}}\nu = 0, \qquad z \geq 0 \tag{5.9}$$

with boundary conditions $\nu|_{z=0} = 1$ at the Earth's surface, continuity conditions for $\nu(z)$ and $\frac{1}{\sigma_{\mathrm{N}}}\frac{d\nu}{dz}$ at the boundaries between layers and condition $\nu \to 0$ at $z \to \infty$.

This problem coincides with the magnetotelluric problem on the horizontally uniform magnetic field in a horizontally layered medium (Berdichevsky and Dmitriev, 2002). Thus, we can introduce the normal one-dimensional impedance Z_{N} satisfying the Riccati equation

$$\frac{\partial Z_{\mathrm{N}}}{\partial z} - \sigma_{\mathrm{N}} Z_{\mathrm{N}}^2 = \mathrm{i}\omega\mu_{\mathrm{o}} \tag{5.10}$$

and express Z_{N} as

$$Z_{\mathrm{N}} = -\frac{1}{\sigma_{\mathrm{N}}\nu}\frac{d\nu}{dz}. \tag{5.11}$$

Summing up (5.6), (5.8) and (5.11), we write

$$\begin{aligned}
&E_x^{\mathrm{N}} = \nu(z) Z_{\mathrm{N}}(z)\frac{\partial U_{\mathrm{o}}(x,\,y)}{\partial y}, \qquad E_y^{\mathrm{N}} = -\nu(z) Z_{\mathrm{N}}(z)\frac{\partial U_{\mathrm{o}}(x,\,y)}{\partial x}, \qquad E_z^{\mathrm{N}} = 0,\\
&H_x^{\mathrm{N}} = \nu(z)\frac{\partial U_{\mathrm{o}}(x,\,y)}{\partial x}, \qquad H_y^{\mathrm{N}} = \nu(z)\frac{\partial U_{\mathrm{o}}(x,\,y)}{\partial y},\\
&H_z^{\mathrm{N}} = -\frac{\nu(z) Z_{\mathrm{N}}(z)}{i\omega\mu_{\mathrm{o}}}\left(\frac{\partial^2 U_{\mathrm{o}}(x,\,y)}{\partial x^2} + \frac{\partial^2 U_{\mathrm{o}}(x,\,y)}{\partial y^2}\right).
\end{aligned} \tag{5.12}$$

Thus, determination of the normal field reduces to differentiating $U_{\mathrm{o}}(x,\,y)$.

Next we come back to Fig. 5.1 and assume that $R_{\mathrm{o}} >> r_{\mathrm{i}}$, $R_{\mathrm{o}} >> r_{\mathrm{s}}$, where $R_{\mathrm{o}} = \sqrt{x_{\mathrm{o}}^2 + y_{\mathrm{o}}^2 + z_{\mathrm{o}}^2}$ is a distance between the centre $\mathrm{O}(x_{\mathrm{o}},\, y_{\mathrm{o}},\, z_{\mathrm{o}})$ of the source domain I and the centre $\mathrm{M}_{\mathrm{o}}(0,\,0,\,0)$ of the observation domain S, while r_{i} and r_{s} are maximum radii of the domains I and S. Then we define $U_{\mathrm{o}}(x,\,y)$ as

$$U_{\mathrm{o}}(x,\,y) \approx U_{\mathrm{o}}(R), \qquad R \approx R_{\mathrm{o}}, \tag{5.13}$$

where $R = \sqrt{(x - x_{\mathrm{o}})^2 + (y - y_{\mathrm{o}})^2 + z_{\mathrm{o}}^2}$ is a distance between the observation site $\mathrm{M}(x,\,y,\,z = 0)$ and the centre $\mathrm{O}(x_{\mathrm{o}},\, y_{\mathrm{o}},\, z_{\mathrm{o}})$ of the source domain I. So, we obtain:

$$\begin{aligned}
&\frac{\partial U_{\mathrm{o}}(x,\,y)}{\partial x} \approx \frac{dU_{\mathrm{o}}(R)}{dR}\frac{\partial R}{\partial x} = (x - x_{\mathrm{o}})\frac{1}{R}\frac{dU_{\mathrm{o}}(R)}{dR} \approx (x - x_{\mathrm{o}})\frac{1}{R}\frac{dU_{\mathrm{o}}(R)}{dR}\bigg|_{R=R_{\mathrm{o}}} = C_{\mathrm{o}}(x - x_{\mathrm{o}}),\\
&\frac{\partial U_{\mathrm{o}}(x,\,y)}{\partial y} = \frac{dU_{\mathrm{o}}(R)}{dR}\frac{\partial R}{\partial y} = (y - y_{\mathrm{o}})\frac{1}{R}\frac{dU_{\mathrm{o}}(R)}{dR} \approx (y - y_{\mathrm{o}})\frac{1}{R}\frac{dU_{\mathrm{o}}(R)}{dR}\bigg|_{R=R_{\mathrm{o}}} = C_{\mathrm{o}}(y - y_{\mathrm{o}}),\\
&\frac{\partial^2 U_{\mathrm{o}}(x,\,y)}{\partial x^2} + \frac{\partial^2 U_{\mathrm{o}}(x,\,y)}{\partial y^2} \approx \frac{1}{R}\frac{dU_{\mathrm{o}}(R)}{dR}\bigg|_{R=R_{\mathrm{o}}} = C_{\mathrm{o}},
\end{aligned} \tag{5.14}$$

where

$$C_{\mathrm{o}} = \frac{1}{R}\frac{dU_{\mathrm{o}}(R)}{dR}\bigg|_{R=R_{\mathrm{o}}}.$$

Substituting (5.14) into (5.12), we get

$$E_x^{\mathrm{N}} = C_{\mathrm{o}}(y-y_{\mathrm{o}})\,\nu(z)\,Z_{\mathrm{N}}(z), \qquad E_y^{\mathrm{N}} = -C_{\mathrm{o}}(x-x_{\mathrm{o}})\,\nu(z)\,Z_{\mathrm{N}}(z), \qquad E_z^{\mathrm{N}} = 0,$$
$$H_x^{\mathrm{N}} = C_{\mathrm{o}}(x-x_{\mathrm{o}})\,\nu(z), \qquad H_y^{\mathrm{N}} = C_{\mathrm{o}}(y-y_{\mathrm{o}})\,\nu(z), \qquad H_z^{\mathrm{N}} = -\frac{C_{\mathrm{o}}}{i\omega\mu_{\mathrm{o}}}\,\nu(z)\,Z_{\mathrm{N}}(z). \tag{5.15}$$

It is evident that the normal field defined by (5.15) can be considered as a field of remote magnetic dipole located at the centre O of the source domain I. This field is the superposition of three independent modes.

Determine the normal magnetic field at the origin of coordinates (at the centre $\mathrm{M_o}$ of the observation domain S. In virtue of (5.15)

$$\begin{aligned} H_x^{\mathrm{N}}(x=0,\,y=0,\,z=0) &= -C_{\mathrm{o}}x_{\mathrm{o}} = H_{x\mathrm{o}}^{\mathrm{N}},\\ H_y^{\mathrm{N}}(x=0,\,y=0,\,z=0) &= -C_{\mathrm{o}}y_{\mathrm{o}} = H_{y\mathrm{o}}^{\mathrm{N}},\\ H_z^{\mathrm{N}}(x=0,\,y=0,\,z=0) &= -\frac{C_{\mathrm{o}}}{i\omega\mu_{\mathrm{o}}}Z_{\mathrm{N}}(0) = H_{z\mathrm{o}}^{\mathrm{N}}. \end{aligned} \tag{5.16}$$

Plugging (5.16) into (5.15), we get

$$\begin{aligned} E_x^{\mathrm{N}} &= H_{y\mathrm{o}}^{\mathrm{N}}\,\nu(z)Z_{\mathrm{N}}(z) - H_{z\mathrm{o}}^{\mathrm{N}}\frac{i\omega\mu_{\mathrm{o}}y\nu(z)Z_{\mathrm{N}}(z)}{Z_{\mathrm{N}}(0)},\\ E_y^{\mathrm{N}} &= -H_{x\mathrm{o}}^{\mathrm{N}}\,\nu(z)Z_{\mathrm{N}}(z) + H_{z\mathrm{o}}^{\mathrm{N}}\frac{i\omega\mu_{\mathrm{o}}x\nu(z)Z_{\mathrm{N}}(z)}{Z_{\mathrm{N}}(0)},\\ E_z^{\mathrm{N}} &= 0. \end{aligned}$$

and

$$H_x^{\mathrm{N}} = H_{x\mathrm{o}}^{\mathrm{N}}\,\nu(z) - H_{z\mathrm{o}}^{\mathrm{N}}\frac{i\omega\mu_{\mathrm{o}}x\nu(z)}{Z_{\mathrm{N}}(0)}, \qquad H_y^{\mathrm{N}} = H_{y\mathrm{o}}^{\mathrm{N}}\,\nu(z) - H_{z\mathrm{o}}^{\mathrm{N}}\frac{i\omega\mu_{\mathrm{o}}y\nu(z)}{Z_{\mathrm{N}}(0)},$$
$$H_z^{\mathrm{N}} = H_{z\mathrm{o}}^{\mathrm{N}}\,\nu(z)\frac{Z_{\mathrm{N}}(z)}{Z_{\mathrm{N}}(0)}.$$

Grouping the field components that have the same factor $H_{x\mathrm{o}}^{\mathrm{N}},\ H_{y\mathrm{o}}^{\mathrm{N}},\ H_{z\mathrm{o}}^{\mathrm{N}}$, we obtain three independent modes: two plane-wave modes with polarization in the orthogonal directions:

$$H_{xo}^{\mathrm{N}}\begin{cases}\tilde{\mathbf{E}}^{\mathrm{N}(1)}=\{0,\ -\nu(z)Z_{\mathrm{N}}(z),\ 0\}\\ \tilde{\mathbf{H}}^{\mathrm{N}(1)}=\{\nu(z),\ 0,\ 0\}\end{cases}\qquad H_{\mathrm{yo}}^{\mathrm{N}}\begin{cases}\tilde{\mathbf{E}}^{\mathrm{N}(2)}=\{\nu(z)Z_{\mathrm{N}}(z),\ 0,\ 0\}\\ \tilde{\mathbf{H}}^{\mathrm{N}(2)}=\{0,\ \nu(z),\ 0\}\end{cases}\tag{5.17}$$

and a source-effect mode with the vertical magnetic component and linear variations of the horizontal components along the Earth's surface:

$$H_{zo}^{\mathrm{N}}\begin{cases}\tilde{\mathbf{E}}^{\mathrm{N}(3)}=\{-\dfrac{i\omega\mu_{\mathrm{o}}y\nu(z)Z_{\mathrm{N}}(z)}{2Z_{\mathrm{N}}(0)},\ \dfrac{i\omega\mu_{\mathrm{o}}x\nu(z)Z_{\mathrm{N}}(z)}{2Z_{\mathrm{N}}(0)},\ 0\}\\ \tilde{\mathbf{H}}^{\mathrm{N}(3)}=\{-\dfrac{i\omega\mu_{\mathrm{o}}x\nu(z)}{2Z_{\mathrm{N}}(0)},\ -\dfrac{i\omega\mu_{\mathrm{o}}y\nu(z)}{2Z_{\mathrm{N}}(0)},\ \dfrac{\nu(z)Z_{\mathrm{N}}(z)}{Z_{\mathrm{N}}(0)}\}.\end{cases}\tag{5.18}$$

Modes $\left\{\tilde{\mathbf{E}}^{\mathrm{N}(1)},\tilde{\mathbf{H}}^{\mathrm{N}(1)}\right\}$, $\left\{\tilde{\mathbf{E}}^{\mathrm{N}(2)},\tilde{\mathbf{H}}^{\mathrm{N}(2)}\right\}$ and $\left\{\tilde{\mathbf{E}}^{\mathrm{N}(3)},\tilde{\mathbf{H}}^{\mathrm{N}(3)}\right\}$ contain normalized fields that satisfy the conditions:

$$\begin{aligned}&\tilde{\mathbf{E}}^{\mathrm{N}(1)}(x=0,\ y=0,\ z=0)=\{0,\ -Z_{\mathrm{N}}(0),\ 0\},\quad &&\tilde{\mathbf{H}}^{\mathrm{N}(1)}(x=0,\ y=0,\ z=0)=\{1,\ 0,\ 0\},\\ &\tilde{\mathbf{E}}^{\mathrm{N}(2)}(x=0,\ y=0,\ z=0)=\{Z_{\mathrm{N}}(0),\ 0,\ 0\},\quad &&\tilde{\mathbf{H}}^{\mathrm{N}(2)}(x=0,\ y=0,\ z=0)=\{0,\ 1,\ 0\},\\ &\tilde{\mathbf{E}}^{\mathrm{N}(3)}(x=0,\ y=0,\ z=0)=\{0,\ 0,\ 0\},\quad &&\tilde{\mathbf{H}}^{\mathrm{N}(3)}(x=0,\ y=0,\ z=0)=\{0,\ 0,\ 1\}.\end{aligned}$$

An arbitrary normal field is the superposition of all three modes:

$$\begin{aligned}\mathbf{E}^{\mathrm{N}}&=H_{xo}^{\mathrm{N}}\tilde{\mathbf{E}}^{\mathrm{N}(1)}+H_{\mathrm{yo}}^{\mathrm{N}}\tilde{\mathbf{E}}^{\mathrm{N}(2)}+H_{zo}^{\mathrm{N}}\tilde{\mathbf{E}}^{\mathrm{N}(3)},\\ \mathbf{H}^{\mathrm{N}}&=H_{xo}^{\mathrm{N}}\tilde{\mathbf{H}}^{\mathrm{N}(1)}+H_{\mathrm{yo}}^{\mathrm{N}}\tilde{\mathbf{H}}^{\mathrm{N}(2)}+H_{zo}^{\mathrm{N}}\tilde{\mathbf{H}}^{\mathrm{N}(3)},\end{aligned}\tag{5.19}$$

where H_{xo}^{N}, $H_{\mathrm{yo}}^{\mathrm{N}}$, H_{zo}^{N} are values of the normal magnetic fields at the origin of the coordinates:

$$\mathbf{H}^{\mathrm{N}}(x=0,\ y=0,\ z=0)=\{H_{xo}^{\mathrm{N}},\ H_{\mathrm{yo}}^{\mathrm{N}},\ H_{zo}^{\mathrm{N}}\}.\tag{5.20}$$

In the general case when all three modes are available on the Earth's surface we get

$$Z_{\mathrm{N}}(0)=\frac{E_x^{\mathrm{N}}(z=0)}{H_y^{\mathrm{N}}(z=0)}=-\frac{E_y^{\mathrm{N}}(z=0)}{H_x^{\mathrm{N}}(z=0)}\tag{5.21}$$

and

$$Z_{\mathrm{N}}(0)=-i\omega\mu_{\mathrm{o}}\frac{H_z^{\mathrm{N}}(z=0)}{\dfrac{\partial H_x^{\mathrm{N}}(z=0)}{\partial x}+\dfrac{\partial H_y^{\mathrm{N}}(z=0)}{\partial y}}.\tag{5.22}$$

Thus, the normal magnetotelluric field varying linearly with the distance from its source allows for determining the one-dimensional normal impedance Z_N by magnetotelluric and magnetovariational relationships (5.21) and (5.22). This is in good agreement with the known definitions (1.2) and (1.3), suggested by Dmitriev and Berdichevsky (1979) and Weidelt (1978) that are at the heart of one-dimensional Tikhonov–Cagniard's magnetotellurics.

Now estimate a distance at which we can neglect the source effect and approximate the normal field by a plane-wave. To this end we define the amplitude ratio β^N between vertical and horizontal components of the normal magnetic field at the centre M_o of the observation domain. With a glance to (5.16),

$$\beta^N = \frac{\left|H_{zo}^N\right|}{\sqrt{\left|H_{xo}^N\right|^2 + \left|H_{yo}^N\right|^2}} = \frac{|Z_N(0)|}{\omega\mu_o\sqrt{x_o^2 + y_o^2}} = \frac{1}{r_o}\sqrt{\frac{\rho_N}{\omega\mu_o}} = \frac{h_{\text{eff}}}{r_o} \tag{5.23}$$

where ρ_N is the normal apparent resistivity of the Earth:

$$\rho_N = |Z_N(0)|^2 / \omega\mu_o,$$

h_{eff} is the effective penetration depth determined by the normal impedance or the normal apparent resistivity:

$$h_{\text{eff}} = \frac{|Z_N(0)|}{\omega\mu_o} = \sqrt{\frac{\rho_N}{\omega\mu_o}} \tag{5.24}$$

and r_o is the distance between the centre M_o of the observation domain and the projection of the centre O of the source domain on the Earth's surface:

$$r_o = \sqrt{x_o^2 + y_o^2}.$$

Let us disregard the vertical component of the normal magnetic field if β^N does not exceed 0.05. Assume that the lithosphere thickness is about 100 km. Then $h_{\text{eff}} \leq$ 100 km and the condition $\beta^N \leq 0.05$ for polar magnetic perturbations is observed at distances $r_o \geq 2000$ km, that is, at the middle and low latitudes.

5.1.2 MT and MV Response Functions in the Absence of the Source Effect

We have divided the normal field $\{\tilde{\mathbf{E}}^N, \tilde{\mathbf{H}}^N\}$ into two plane-wave modes $\{\tilde{\mathbf{E}}^{N(m)}, \tilde{\mathbf{H}}^{N(m)}\}$, $m = 1, 2$ defined by (5.17) and a source-effect mode $\{\tilde{\mathbf{E}}^{N(3)}, \tilde{\mathbf{H}}^{N(3)}\}$ defined by (5.18). If the vertical component of the normal magnetic field

is sufficiently small, we can disregard the source-effect mode and restrict ourselves to analysis of the plane-wave modes. On this way we go back to the magnetotelluric and magnetovariational response functions discussed in Chaps. 1 and 4. For the sake of integrity we can consider these functions in the terms of the generalized model examined in the present Section.

Within the inhomogeneous domain V each plane-wave mode generates the excess current $\mathbf{j}^{ex(m)}$, $m = 1, 2$ that excites the anomalous field $\{\tilde{\mathbf{E}}^{\mathrm{A}(m)}, \tilde{\mathbf{H}}^{\mathrm{A}(m)}\}$, $m = 1, 2$. Summing the normal and anomalous fields, we get

$$\begin{aligned} \tilde{\mathbf{E}}^{(m)} &= \tilde{\mathbf{E}}^{\mathrm{N}(m)} + \tilde{\mathbf{E}}^{\mathrm{A}(m)} \\ \tilde{\mathbf{H}}^{(m)} &= \tilde{\mathbf{H}}^{\mathrm{N}(m)} + \tilde{\mathbf{H}}^{\mathrm{A}(m)} \qquad m = 1, 2. \end{aligned} \tag{5.25}$$

The total field on the Earth's surface is

$$\begin{aligned} \mathbf{E} &= H_{x\mathrm{o}}^{\mathrm{N}} \tilde{\mathbf{E}}^{(1)} + H_{y\mathrm{o}}^{\mathrm{N}} \tilde{\mathbf{E}}^{(2)}, \\ \mathbf{H} &= H_{x\mathrm{o}}^{\mathrm{N}} \tilde{\mathbf{H}}^{(1)} + H_{y\mathrm{o}}^{\mathrm{N}} \tilde{\mathbf{H}}^{(2)}, \end{aligned} \tag{5.26}$$

where

$$\mathbf{E} = \mathbf{E}(x, y, z = 0), \ \tilde{\mathbf{E}}^{(1)} = \tilde{\mathbf{E}}^{(1)}(x, y, z = 0), \ \tilde{\mathbf{E}}^{(2)} = \tilde{\mathbf{E}}^{(2)}(x, y, z = 0),$$
$$\mathbf{H} = \mathbf{H}(x, y, z = 0), \ \tilde{\mathbf{H}}^{(1)} = \tilde{\mathbf{H}}^{(1)}(x, y, z = 0), \ \tilde{\mathbf{H}}^{(2)} = \tilde{\mathbf{H}}^{(2)}(x, y, z = 0) \ .$$

In the full form

$$\begin{aligned} E_x &= H_{x\mathrm{o}}^{\mathrm{N}} \tilde{E}_x^{(1)} + H_{y\mathrm{o}}^{\mathrm{N}} \tilde{E}_x^{(2)} \\ E_y &= H_{x\mathrm{o}}^{\mathrm{N}} \tilde{E}_y^{(1)} + H_{y\mathrm{o}}^{\mathrm{N}} \tilde{E}_y^{(2)} \end{aligned} \tag{5.27}$$

and

$$\begin{aligned} H_x &= H_{x\mathrm{o}}^{\mathrm{N}} \tilde{H}_x^{(1)} + H_{y\mathrm{o}}^{\mathrm{N}} \tilde{H}_x^{(2)} \qquad a \\ H_y &= H_{x\mathrm{o}}^{\mathrm{N}} \tilde{H}_y^{(1)} + H_{y\mathrm{o}}^{\mathrm{N}} \tilde{H}_y^{(2)} \qquad b \\ H_z &= H_{x\mathrm{o}}^{\mathrm{N}} \tilde{H}_z^{(1)} + H_{y\mathrm{o}}^{\mathrm{N}} \tilde{H}_z^{(2)} \, . \qquad c \end{aligned} \tag{5.28}$$

From (5.28*a,b*) we find

$$\begin{aligned} H_{x\mathrm{o}}^{\mathrm{N}} &= \frac{H_x \tilde{H}_y^{(2)} - H_y \tilde{H}_x^{(2)}}{\tilde{H}_x^{(1)} \tilde{H}_y^{(2)} - \tilde{H}_y^{(1)} \tilde{H}_x^{(2)}}, \\ H_{y\mathrm{o}}^{\mathrm{N}} &= \frac{-H_x \tilde{H}_y^{(1)} + H_y \tilde{H}_x^{(1)}}{\tilde{H}_x^{(1)} \tilde{H}_y^{(2)} - \tilde{H}_y^{(1)} \tilde{H}_x^{(2)}} \, . \end{aligned} \tag{5.29}$$

By substituting (5.29) in (5.27) and (5.28*c*) we get the impedance relations

$$\begin{aligned} E_x &= Z_{xx} H_x + Z_{xy} H_y, \\ E_y &= Z_{yx} H_x + Z_{yy} H_y, \end{aligned} \tag{5.30}$$

where

$$\begin{aligned} Z_{xx} &= \frac{\tilde{E}_x^{(1)} \tilde{H}_y^{(2)} - \tilde{E}_x^{(2)} \tilde{H}_y^{(1)}}{\tilde{H}_x^{(1)} \tilde{H}_y^{(2)} - \tilde{H}_y^{(1)} \tilde{H}_x^{(2)}}, \qquad Z_{xy} = \frac{\tilde{E}_x^{(2)} \tilde{H}_x^{(1)} - \tilde{E}_x^{(1)} \tilde{H}_x^{(2)}}{\tilde{H}_x^{(1)} \tilde{H}_y^{(2)} - \tilde{H}_y^{(1)} \tilde{H}_x^{(2)}}, \\ Z_{yx} &= \frac{\tilde{E}_y^{(1)} \tilde{H}_y^{(2)} - \tilde{E}_y^{(2)} \tilde{H}_y^{(1)}}{\tilde{H}_x^{(1)} \tilde{H}_y^{(2)} - \tilde{H}_y^{(1)} \tilde{H}_x^{(2)}}, \qquad Z_{yy} = \frac{\tilde{E}_y^{(2)} \tilde{H}_x^{(1)} - \tilde{E}_y^{(1)} \tilde{H}_x^{(2)}}{\tilde{H}_x^{(1)} \tilde{H}_y^{(2)} - \tilde{H}_y^{(1)} \tilde{H}_x^{(2)}}, \end{aligned} \tag{5.31}$$

and the Wiese–Parkinson relation

$$H_z = W_{zx} H_x + W_{zy} H_y, \tag{5.32}$$

where

$$W_{zx} = \frac{\tilde{H}_z^{(1)} \tilde{H}_y^{(2)} - \tilde{H}_z^{(2)} \tilde{H}_y^{(1)}}{\tilde{H}_x^{(1)} \tilde{H}_y^{(2)} - \tilde{H}_y^{(1)} \tilde{H}_x^{(2)}}, \qquad W_{zx} = \frac{\tilde{H}_z^{(2)} \tilde{H}_x^{(1)} - \tilde{H}_z^{(1)} \tilde{H}_x^{(2)}}{\tilde{H}_x^{(1)} \tilde{H}_y^{(2)} - \tilde{H}_y^{(1)} \tilde{H}_x^{(2)}} \, . W_{zy} \tag{5.33}$$

5.1.3 The Source Effect

Now we have to find out how these determinations change due to the source effect that generates the normal field with the vertical magnetic component. Considering all three modes of the normal field (two plane-wave modes and the source-effect mode), we get

$$\begin{aligned} \tilde{\mathbf{E}}^{(m)} &= \tilde{\mathbf{E}}^{\mathrm{N}(m)} + \tilde{\mathbf{E}}^{\mathrm{A}(m)}, \\ \tilde{\mathbf{H}}^{(m)} &= \tilde{\mathbf{H}}^{\mathrm{N}(m)} + \tilde{\mathbf{H}}^{\mathrm{A}(m)}, \qquad m = 1,\ 2,\ 3. \end{aligned} \tag{5.34}$$

The total field on the Earth's surface is

$$\begin{aligned} \mathbf{E} &= H_{x\mathrm{o}}^{\mathrm{N}} \tilde{\mathbf{E}}^{(1)} + H_{y\mathrm{o}}^{\mathrm{N}} \tilde{\mathbf{E}}^{(2)} + H_{z\mathrm{o}}^{\mathrm{N}} \tilde{\mathbf{E}}^{(3)}, \\ \mathbf{H} &= H_{x\mathrm{o}}^{\mathrm{N}} \tilde{\mathbf{H}}^{(1)} + H_{y\mathrm{o}}^{\mathrm{N}} \tilde{\mathbf{H}}^{(2)} + H_{z\mathrm{o}}^{\mathrm{N}} \tilde{\mathbf{H}}^{(3)}, \end{aligned} \tag{5.35}$$

where

$$\begin{aligned}
&\mathbf{E} = \mathbf{E}(x,\, y,\, z = 0), && \tilde{\mathbf{E}}^{(1)} = \tilde{\mathbf{E}}^{(1)}(x,\, y,\, z = 0),\\
&\tilde{\mathbf{E}}^{(2)} = \tilde{\mathbf{E}}^{(2)}(x,\, y,\, z = 0), && \tilde{\mathbf{E}}^{(3)} = \tilde{\mathbf{E}}^{(3)}(x,\, y,\, z = 0)\,,\\
&\mathbf{H} = \mathbf{H}(x,\, y,\, z = 0), && \tilde{\mathbf{H}}^{(1)} = \tilde{\mathbf{H}}^{(1)}(x,\, y,\, z = 0),\\
&\tilde{\mathbf{H}}^{(2)} = \tilde{\mathbf{H}}^{(2)}(x,\, y,\, z = 0), && \tilde{\mathbf{H}}^{(3)} = \tilde{\mathbf{H}}^{(3)}(x,\, y,\, z = 0).
\end{aligned}$$

In full form

$$\begin{aligned}
E_x &= H^{\mathrm{N}}_{x\mathrm{o}} E^{(1)}_x + H^{\mathrm{N}}_{y\mathrm{o}} E^{(2)}_x + H^{\mathrm{N}}_{z\mathrm{o}} E^{(3)}_x,\\
E_y &= H^{\mathrm{N}}_{x\mathrm{o}} E^{(1)}_y + H^{\mathrm{N}}_{y\mathrm{o}} E^{(2)}_y + H^{\mathrm{N}}_{z\mathrm{o}} E^{(3)}_y,\\
E_z &= 0\,.
\end{aligned} \tag{5.36}$$

and

$$\begin{aligned}
H_x &= H^{\mathrm{N}}_{x\mathrm{o}} \tilde{H}^{(1)}_x + H^{\mathrm{N}}_{y\mathrm{o}} \tilde{H}^{(2)}_x + H^{\mathrm{N}}_{z\mathrm{o}} \tilde{H}^{(3)}_x,\\
H_y &= H^{\mathrm{N}}_{x\mathrm{o}} \tilde{H}^{(1)}_y + H^{\mathrm{N}}_{y\mathrm{o}} \tilde{H}^{(2)}_y + H^{\mathrm{N}}_{z\mathrm{o}} \tilde{H}^{(3)}_y,\\
H_z &= H^{\mathrm{N}}_{x\mathrm{o}} \tilde{H}^{(1)}_z + H^{\mathrm{N}}_{y\mathrm{o}} \tilde{H}^{(2)}_z + H^{\mathrm{N}}_{z\mathrm{o}} \tilde{H}^{(3)}_z\,.
\end{aligned} \tag{5.37}$$

Clearly we have three independent constants, $H^N_{x\mathrm{o}}$, $H^N_{y\mathrm{o}}$ and $H^N_{z\mathrm{o}}$ (three degrees of freedom), that can be determined from (5.37):

$$\begin{aligned}
H^N_{x\mathrm{o}} &= \frac{1}{Q}\begin{vmatrix} H_x & H_y & H_z\\ \tilde{H}^{(2)}_x & \tilde{H}^{(2)}_y & \tilde{H}^{(2)}_z\\ \tilde{H}^{(3)}_x & \tilde{H}^{(3)}_y & \tilde{H}^{(3)}_z \end{vmatrix}, \qquad H^N_{y\mathrm{o}} = \frac{1}{Q}\begin{vmatrix} H_x & H_y & H_z\\ \tilde{H}^{(3)}_x & \tilde{H}^{(3)}_y & \tilde{H}^{(3)}_z\\ \tilde{H}^{(1)}_x & \tilde{H}^{(1)}_y & \tilde{H}^{(1)}_z \end{vmatrix},\\
H^N_{z\mathrm{o}} &= \frac{1}{Q}\begin{vmatrix} H_x & H_y & H_z\\ \tilde{H}^{(1)}_x & \tilde{H}^{(1)}_y & \tilde{H}^{(1)}_z\\ \tilde{H}^{(2)}_x & \tilde{H}^{(2)}_y & \tilde{H}^{(2)}_z \end{vmatrix},
\end{aligned} \tag{5.38}$$

where

$$Q = \begin{vmatrix} \tilde{H}^{(1)}_x & \tilde{H}^{(1)}_y & \tilde{H}^{(1)}_z\\ \tilde{H}^{(2)}_x & \tilde{H}^{(2)}_y & \tilde{H}^{(2)}_z\\ \tilde{H}^{(3)}_x & \tilde{H}^{(3)}_y & \tilde{H}^{(3)}_z \end{vmatrix}.$$

Substituting (5.38) into (5.36) we obtain

$$\begin{aligned}
E_x &= Z'_{xx} H_x + Z'_{xy} H_y + Z'_{xz} H_z,\\
E_y &= Z'_{yx} H_x + Z'_{yy} H_y + Z'_{yz} H_z,\\
E_z &= 0\,,
\end{aligned} \tag{5.39}$$

where

$$Z'_{xx} = \frac{1}{Q}\begin{vmatrix} \tilde{E}_x^{(1)} & \tilde{E}_x^{(2)} & \tilde{E}_x^{(3)} \\ \tilde{H}_y^{(1)} & \tilde{H}_y^{(2)} & \tilde{H}_y^{(3)} \\ \tilde{H}_z^{(1)} & \tilde{H}_z^{(2)} & \tilde{H}_z^{(3)} \end{vmatrix}, \qquad Z'_{yx} = \frac{1}{Q}\begin{vmatrix} \tilde{E}_y^{(1)} & \tilde{E}_y^{(2)} & \tilde{E}_y^{(3)} \\ \tilde{H}_y^{(1)} & \tilde{H}_y^{(2)} & \tilde{H}_y^{(3)} \\ \tilde{H}_z^{(1)} & \tilde{H}_z^{(2)} & \tilde{H}_z^{(3)} \end{vmatrix},$$

$$Z'_{xy} = \frac{1}{Q}\begin{vmatrix} \tilde{E}_x^{(1)} & \tilde{E}_x^{(2)} & \tilde{E}_x^{(3)} \\ \tilde{H}_z^{(1)} & \tilde{H}_z^{(2)} & \tilde{H}_z^{(3)} \\ \tilde{H}_x^{(1)} & \tilde{H}_x^{(2)} & \tilde{H}_x^{(3)} \end{vmatrix}, \qquad Z'_{yy} = \frac{1}{Q}\begin{vmatrix} \tilde{E}_y^{(1)} & \tilde{E}_y^{(2)} & \tilde{E}_y^{(3)} \\ \tilde{H}_z^{(1)} & \tilde{H}_z^{(2)} & \tilde{H}_z^{(3)} \\ \tilde{H}_x^{(1)} & \tilde{H}_x^{(2)} & \tilde{H}_x^{(3)} \end{vmatrix},$$

$$Z'_{xz} = \frac{1}{Q}\begin{vmatrix} \tilde{E}_x^{(1)} & \tilde{E}_x^{(2)} & \tilde{E}_x^{(3)} \\ \tilde{H}_x^{(1)} & \tilde{H}_x^{(2)} & \tilde{H}_x^{(3)} \\ \tilde{H}_y^{(1)} & \tilde{H}_y^{(2)} & \tilde{H}_y^{(3)} \end{vmatrix}, \qquad Z'_{yz} = \frac{1}{Q}\begin{vmatrix} \tilde{E}_y^{(1)} & \tilde{E}_y^{(2)} & \tilde{E}_y^{(3)} \\ \tilde{H}_x^{(1)} & \tilde{H}_x^{(2)} & \tilde{H}_x^{(3)} \\ \tilde{H}_y^{(1)} & \tilde{H}_y^{(2)} & \tilde{H}_y^{(3)} \end{vmatrix}.$$

In the matrix form

$$\mathbf{E} = [\mathbf{Z}']\mathbf{H}, \tag{5.40}$$

where

$$\mathbf{E} = \begin{bmatrix} E_x \\ E_y \end{bmatrix}, \qquad [\mathbf{Z}'] = \begin{bmatrix} Z'_{xx} & Z'_{xy} & Z'_{xz} \\ Z'_{yx} & Z'_{yy} & Z'_{yz} \end{bmatrix}, \qquad \mathbf{H} = \begin{bmatrix} H_x \\ H_y \\ H_z \end{bmatrix}.$$

Taking the source effect into account, we can determine the *generalized impedance tensor* $\left[\mathbf{Z}'\right]$ with matrix of the order 2×3 and can't determine the Wiese–Parkinson matrix (all three components of the magnetic field become independent, which manifests itself in the dramatic multiple-coherence drop). But it is significant that Varentsov and his workmates in their experiments on the Baltic shield get around this problem by selecting time intervals with rather large coherence (Varentsov et al., 2003a, b), while Vanyan and his workmates reconstruct a plane-wave normal field by averaging geomagnetic disturbances over a long period of time (Vanyan et al., 2002b).

Going toward the strong source effect, the sophisticated situations may arise that need examination, theoretical comprehension and special technological solutions. The recent promising results obtained by Schmucker and by Semenov et al. in combining the gradient and tipper soundings (Schmucker, 2003, 2004; Semenov et al., in press) may be very helpful in this area.

5.1.4 Final Remarks on the Generalized Impedance Tensor

For many years the magnetotelluric theory defines the impedance of the Earth at two model levels: (1) the scalar impedance of the horizontally homogeneous medium excited by a field with linearly varying horizontal components (the Tikhonov–Cagniard impedance), and (2) the tensor impedance of the horizontally inhomogeneous medium excited by a plane wave. The generalized model includes both the levels and supplements them with a third level, namely, with the tensor impedance of the horizontally inhomogeneous medium excited by a electromagnetic field with linearly varying horizontal components and a vertical magnetic component. Application of this model can considerably extend the capabilities of magnetotellurics in zones that are unfavorable for plane-wave approximation of the normal field, say, in the auroral zones.

Let the normal field consist of three independent modes (two plane-wave modes and a source-field mode with vertical magnetic component). Hence, we determine 6 components of the generalized impedance tensor. The question is how to solve the inverse problem using all six components. We can suggest two different approaches to this problem.

1. Immediate inversion of the generalized impedance tensor. Given a resistivity model, determine electromagnetic fields excited by each mode of the normal field and calculate the components of the generalized impedance tensor. Solution of the inverse problem reduces to the regularized iterative minimization of the misfits of the generalized impedance tensor.

2. Solution of the inverse problem consists of three stages: (1) synthesis of the plane-wave magnetotelluric fields from the generalized impedance tensors, (2) reconstruction of the basic impedance tensor, [**Z**], and the tipper matrix, [**W**], (3) inversion of [**Z**] and [**W**] using standard methods.

5.2 Synthesis of the Magnetotelluric Field

A common set of magnetotelluric and magnetovariational data usually consists of the impedance and tipper matrices obtained on the network of autonomous field stations. We can pave the new ways to the qualitative and quantitative interpretation of MT and MV data by converting autonomous impedances and tippers into the synthetic magnetic field and computing the horizontal magnetic tensors that are slightly subjected to the low-frequency distortions caused by the near-surface local inhomogeneities and provide sufficiently high sensitivity to the regional structures (Barashkov, 1986; Dmitriev and Kruglov, 1995, 1996; Dmitriev and Mershchikova, 2002).

We will consider the following conversions:

1. Synthesis of the synchronous magnetic field from the impedance tensors.
2. Synthesis of the synchronous magnetic field from the Wiese–Parkinson matrices.
3. Synthesis of the synchronous magnetic field from the generalized impedance tensors.

The synthetic field is determined in the air as a field excited by a plane wave vertically incident on the Earth's surface at which the impedance relation (1.14) and the Wiese–Parkinson relation (4.2) are satisfied.

We begin with analysis of relations between components of the anomalous magnetotelluric field in the air.

5.2.1 Anomalous Magnetotelluric Field in the Air

Examine a three-dimensional model where the horizontally homogeneous layered Earth includes a bounded inhomogeneous domain of arbitrary geometry. The air is supposed to be nonconductive. Following the traditional geoelectric representation, we ignore the displacement currents and assume that inhomogeneities of the Earth cause the anomalous field $\mathbf{E}^{\mathrm{A}}(E_x^{\mathrm{A}},\ E_y^{\mathrm{A}},\ 0), \mathbf{H}^{\mathrm{A}}(H_x^{\mathrm{A}},\ H_y^{\mathrm{A}},\ H_z^{\mathrm{A}})$ in the air, which meets the Laplace equation and consists solely of the TE-mode (Schmucker, 1971a; Berdichevsky and Jakovlev, 1984).

The anomalous electromagnetic field in the air can be expressed in terms of its components at the Earth's surface. Let $\mathbf{E}^{\mathrm{A}}$, $\mathbf{H}^{\mathrm{A}}$ be known at the Earth's surface $z = 0$. Then we have the boundary-value problems for $\mathbf{E}^{\mathrm{A}}$, $\mathbf{H}^{\mathrm{A}}$ in the air:

$$\begin{aligned}
&\Delta\mathbf{E}^{\mathrm{A}}(x, y, z) = 0 \quad \text{at} \quad -\infty<x,\ y<\infty \qquad z<0\\
&\mathbf{E}^{\mathrm{A}}(x, y, z = 0) = \mathbf{E}_{\mathrm{o}}^{\mathrm{A}}(x, y) \qquad\qquad \mathbf{E}_{\mathrm{o}}^{\mathrm{A}}(x, y) \to 0 \ \text{ as } \ \sqrt{x^2 + y^2} \to \infty\\
&\mathbf{E}^{\mathrm{A}}(x, y, z) \to 0 \ \text{ as } \ \sqrt{x^2 + y^2 + z^2} \to \infty
\end{aligned} \tag{5.41}$$

and

$$\begin{aligned}
&\Delta\mathbf{H}^{\mathrm{A}}(x, y, z) = 0 \quad \text{at} \quad -\infty<x,\ y<\infty \qquad z<0\\
&\mathbf{H}^{\mathrm{A}}(x, y, z = 0) = \mathbf{H}_{\mathrm{o}}^{\mathrm{A}}(x, y) \qquad\qquad \mathbf{H}_{\mathrm{o}}^{\mathrm{A}}(x, y) \to 0 \ \text{ as } \ \sqrt{x^2 + y^2} \to \infty\\
&\mathbf{H}^{\mathrm{A}}(x, y, z) \to 0 \ \text{ as } \ \sqrt{x^2 + y^2 + z^2} \to \infty,
\end{aligned} \tag{5.42}$$

where $\mathbf{E}^{\mathrm{A}}(x, y, z)$, $\mathbf{H}^{\mathrm{A}}(x, y, z)$ and $\mathbf{E}_{\mathrm{o}}^{\mathrm{A}}(x, y)$, $\mathbf{H}_{\mathrm{o}}^{\mathrm{A}}(x, y)$ are the anomalous electric and magnetic fields in the air and at the Earth's surface. Solutions of these problems are given by the Poisson integrals for the half-space $z \le 0$ (Tikhonov and Samarsky, 1999):

$$\begin{aligned}
\mathbf{E}^{\mathrm{A}}(x, y, z) &= -\frac{1}{2\pi}\frac{\partial}{\partial z}\int\limits_{-\infty}^{\infty}\int\limits_{-\infty}^{\infty}\mathbf{E}_{\mathrm{o}}^{\mathrm{A}}(x_{\mathrm{o}}, y_{\mathrm{o}})\frac{dx_{\mathrm{o}}\,dy_{\mathrm{o}}}{\sqrt{(x - x_{\mathrm{o}})^2 + (y - y_{\mathrm{o}})^2 + z^2}}\ ,\\
\mathbf{H}^{\mathrm{A}}(x, y, z) &= -\frac{1}{2\pi}\frac{\partial}{\partial z}\int\limits_{-\infty}^{\infty}\int\limits_{-\infty}^{\infty}\mathbf{H}_{\mathrm{o}}^{\mathrm{A}}(x_{\mathrm{o}}, y_{\mathrm{o}})\frac{dx_{\mathrm{o}}\,dy_{\mathrm{o}}}{\sqrt{(x - x_{\mathrm{o}})^2 + (y - y_{\mathrm{o}})^2 + z^2}}.
\end{aligned} \tag{5.43}$$

The integral relations of this kind can be considered as three-dimensional magnetotelluric analogues of the Kertz formulae (Berdichevsky and Jakovlev, 1984; Berdichevsky and Zhdanov, 1984). The integrals are taken in the sense of their principal values.

In the scalar form

$$E_x^{\mathrm{A}}(x,y,z) = -\frac{1}{2\pi}\frac{\partial}{\partial z}\int_{-\infty}^{\infty}\int_{-\infty}^{\infty} E_{ox}^{\mathrm{A}}(x_o,y_o)\frac{dx_o\,dy_o}{\sqrt{(x-x_o)^2+(y-y_o)^2+z^2}} \quad a$$

$$E_y^{\mathrm{A}}(x,y,z) = -\frac{1}{2\pi}\frac{\partial}{\partial z}\int_{-\infty}^{\infty}\int_{-\infty}^{\infty} E_{oy}^{\mathrm{A}}(x_o,y_o)\frac{dx_o\,dy_o}{\sqrt{(x-x_o)^2+(y-y_o)^2+z^2}} \quad b \tag{5.44}$$

and

$$H_x^{\mathrm{A}}(x,y,z) = -\frac{1}{2\pi}\frac{\partial}{\partial z}\int_{-\infty}^{\infty}\int_{-\infty}^{\infty} H_{ox}^{\mathrm{A}}(x_o,y_o)\frac{dx_o\,dy_o}{\sqrt{(x-x_o)^2+(y-y_o)^2+z^2}} \quad a$$

$$H_y^{\mathrm{A}}(x,y,z) = -\frac{1}{2\pi}\frac{\partial}{\partial z}\int_{-\infty}^{\infty}\int_{-\infty}^{\infty} H_{oy}^{\mathrm{A}}(x_o,y_o)\frac{dx_o\,dy_o}{\sqrt{(x-x_o)^2+(y-y_o)^2+z^2}} \quad b$$

$$H_z^{\mathrm{A}}(x,y,z) = -\frac{1}{2\pi}\frac{\partial}{\partial z}\int_{-\infty}^{\infty}\int_{-\infty}^{\infty} H_{oz}^{\mathrm{A}}(x_o,y_o)\frac{dx_o\,dy_o}{\sqrt{(x-x_o)^2+(y-y_o)^2+z^2}}. \quad c \tag{5.45}$$

These formulae make it possible to extend the anomalous field from the Earth's surface to any higher level in the air and weaken in this way the influence of near-surface inhomogeneities.

From (5.45) we can easily derive the integral relations between vertical and horizontal components of the anomalous magnetic field. Note that in the nonconducting air $curl\,\mathbf{H}^{\mathrm{A}} = 0$.Hence

$$\frac{\partial H_x^{\mathrm{A}}}{\partial z} = \frac{\partial H_z^{\mathrm{A}}}{\partial x}, \qquad \frac{\partial H_y^{\mathrm{A}}}{\partial z} = \frac{\partial H_z^{\mathrm{A}}}{\partial y}. \tag{5.46}$$

Substituting (5.45*c*) in (5.46) and taking into account that $H_{x,y}^{\mathrm{A}} \to 0$ as $z \to -\infty$, we obtain

$$H_x^{\mathrm{A}}(x,y,z) = -\frac{1}{2\pi}\frac{\partial}{\partial x}\int_{-\infty}^{\infty}\int_{-\infty}^{\infty} H_{oz}^{\mathrm{A}}(x_o,y_o)\frac{dx_o\,dy_o}{\sqrt{(x-x_o)^2+(y-y_o)^2+z^2}}$$

$$H_y^{\mathrm{A}}(x,y,z) = -\frac{1}{2\pi}\frac{\partial}{\partial y}\int_{-\infty}^{\infty}\int_{-\infty}^{\infty} H_{oz}^{\mathrm{A}}(x_o,y_o)\frac{dx_o\,dy_o}{\sqrt{(x-x_o)^2+(y-y_o)^2+z^2}}. \tag{5.47}$$

On the other hand, substituting (5.45a,b) in

$$div\mathbf{H}^{\mathrm{A}} = \frac{\partial H_x^{\mathrm{A}}}{\partial x} + \frac{\partial H_y^{\mathrm{A}}}{\partial y} + \frac{\partial H_z^{\mathrm{A}}}{\partial z} = 0$$

and taking into account that $H_z^{\mathrm{A}} \to 0$ as $z \to -\infty$, we obtain

$$H_z^{\mathrm{A}}(x, y, z) = \frac{1}{2\pi}\frac{\partial}{\partial x}\int_{-\infty}^{\infty}\int_{-\infty}^{\infty} H_{ox}^{\mathrm{A}}(x_{\mathrm{o}}, y_{\mathrm{o}})\frac{dx_{\mathrm{o}}dy_{\mathrm{o}}}{\sqrt{(x-x_{\mathrm{o}})^2+(y-y_{\mathrm{o}})^2+z^2}}$$
$$+ \frac{1}{2\pi}\frac{\partial}{\partial y}\int_{-\infty}^{\infty}\int_{-\infty}^{\infty} H_{oy}^{\mathrm{A}}(x_{\mathrm{o}}, y_{\mathrm{o}})\frac{dx_{\mathrm{o}}dy_{\mathrm{o}}}{\sqrt{(x-x_{\mathrm{o}})^2+(y-y_{\mathrm{o}})^2+z^2}}. \tag{5.48}$$

Now we derive the integral relations between anomalous electric and magnetic fields, $\mathbf{E}^{\mathrm{A}}$ and $\mathbf{H}^{\mathrm{A}}$. Using Maxwell's equation $curl\mathbf{E}^{\mathrm{A}} = i\omega\mu_{\mathrm{o}}\mathbf{H}^{\mathrm{A}}$ and taking into account that $E_z^{\mathrm{A}} = 0$ in the TE-mode, we write

$$\frac{\partial E_x^{\mathrm{A}}}{\partial z} = i\omega\mu_{\mathrm{o}}H_y^{\mathrm{A}}, \qquad \frac{\partial E_y^{\mathrm{A}}}{\partial z} = -i\omega\mu_{\mathrm{o}}H_x^{\mathrm{A}}. \tag{5.49}$$

Substituting (5.45*a,b*) in (5.49), we get

$$E_x^{\mathrm{A}}(x, y, z) = -\frac{i\omega\mu_{\mathrm{o}}}{2\pi}\int_{-\infty}^{\infty}\int_{-\infty}^{\infty} H_{oy}^{\mathrm{A}}(x_{\mathrm{o}}, y_{\mathrm{o}})\frac{dx_{\mathrm{o}}dy_{\mathrm{o}}}{\sqrt{(x-x_{\mathrm{o}})^2+(y-y_{\mathrm{o}})^2+z^2}}$$
$$E_y^{\mathrm{A}}(x, y, z) = \frac{i\omega\mu_{\mathrm{o}}}{2\pi}\int_{-\infty}^{\infty}\int_{-\infty}^{\infty} H_{ox}^{\mathrm{A}}(x_{\mathrm{o}}, y_{\mathrm{o}})\frac{dx_{\mathrm{o}}dy_{\mathrm{o}}}{\sqrt{(x-x_{\mathrm{o}})^2+(y-y_{\mathrm{o}})^2+z^2}}. \tag{5.50}$$

The integral operators in (5.50) can be inverted. Substituting (5.44*a,b*) in (5.49), we get

$$H_x^{\mathrm{A}}(x, y, z) = \frac{i}{2\pi\omega\mu_{\mathrm{o}}}\frac{\partial^2}{\partial z^2}\int_{-\infty}^{\infty}\int_{-\infty}^{\infty} E_{oy}^{\mathrm{A}}(x_{\mathrm{o}}, y_{\mathrm{o}})\frac{dx_{\mathrm{o}}dy_{\mathrm{o}}}{\sqrt{(x-x_{\mathrm{o}})^2+(y-y_{\mathrm{o}})^2+z^2}}$$
$$H_y^{\mathrm{A}}(x, y, z) = -\frac{i}{2\pi\omega\mu_{\mathrm{o}}}\frac{\partial^2}{\partial z^2}\int_{-\infty}^{\infty}\int_{-\infty}^{\infty} E_{ox}^{\mathrm{A}}(x_{\mathrm{o}}, y_{\mathrm{o}})\frac{dx_{\mathrm{o}}dy_{\mathrm{o}}}{\sqrt{(x-x_{\mathrm{o}})^2+(y-y_{\mathrm{o}})^2+z^2}}. \tag{5.51}$$

Alternatively, substituting (5.44a,b) in

$$\frac{\partial E_y^{\mathrm{A}}}{\partial x} - \frac{\partial E_x^{\mathrm{A}}}{\partial y} = i\omega\mu_{\mathrm{o}}H_z^{\mathrm{A}} \tag{5.52}$$

and taking into account (5.46), we get

$$H_x^{\mathrm{A}}(x,y,z)=\frac{i}{2\pi\omega\mu_{\mathrm{o}}}\frac{\partial^2}{\partial x^2}\int\limits_{-\infty}^{\infty}\int\limits_{-\infty}^{\infty}E_{oy}^{\mathrm{A}}(x_{\mathrm{o}},y_{\mathrm{o}})\frac{dx_{\mathrm{o}}dy_{\mathrm{o}}}{\sqrt{(x-x_{\mathrm{o}})^2+(y-y_{\mathrm{o}})^2+z^2}}$$
$$-\frac{i}{2\pi\omega\mu_{\mathrm{o}}}\frac{\partial^2}{\partial x\partial y}\int\limits_{-\infty}^{\infty}\int\limits_{-\infty}^{\infty}E_{ox}^{\mathrm{A}}(x_{\mathrm{o}},y_{\mathrm{o}})\frac{dx_{\mathrm{o}}dy_{\mathrm{o}}}{\sqrt{(x-x_{\mathrm{o}})^2+(y-y_{\mathrm{o}})^2+z^2}},\tag{5.53}$$

$$H_y^{\mathrm{A}}(x,y,z)=\frac{i}{2\pi\omega\mu_{\mathrm{o}}}\frac{\partial^2}{\partial x\partial y}\int\limits_{-\infty}^{\infty}\int\limits_{-\infty}^{\infty}E_{oy}^{\mathrm{A}}(x_{\mathrm{o}},y_{\mathrm{o}})\frac{dx_{\mathrm{o}}dy_{\mathrm{o}}}{\sqrt{(x-x_{\mathrm{o}})^2+(y-y_{\mathrm{o}})^2+z^2}}$$
$$-\frac{i}{2\pi\omega\mu_{\mathrm{o}}}\frac{\partial^2}{\partial y^2}\int\limits_{-\infty}^{\infty}\int\limits_{-\infty}^{\infty}E_{ox}^{\mathrm{A}}(x_{\mathrm{o}},y_{\mathrm{o}})\frac{dx_{\mathrm{o}}dy_{\mathrm{o}}}{\sqrt{(x-x_{\mathrm{o}})^2+(y-y_{\mathrm{o}})^2+z^2}},\tag{5.54}$$

$$H_z^{\mathrm{A}}(x,y,z)=\frac{i}{2\pi\omega\mu_{\mathrm{o}}}\frac{\partial^2}{\partial y\partial z}\int\limits_{-\infty}^{\infty}\int\limits_{-\infty}^{\infty}E_{ox}^{\mathrm{A}}(x_{\mathrm{o}},y_{\mathrm{o}})\frac{dx_{\mathrm{o}}dy_{\mathrm{o}}}{\sqrt{(x-x_{\mathrm{o}})^2+(y-y_{\mathrm{o}})^2+z^2}}$$
$$-\frac{i}{2\pi\omega\mu_{\mathrm{o}}}\frac{\partial^2}{\partial x\partial z}\int\limits_{-\infty}^{\infty}\int\limits_{-\infty}^{\infty}E_{oy}^{\mathrm{A}}(x_{\mathrm{o}},y_{\mathrm{o}})\frac{dx_{\mathrm{o}}dy_{\mathrm{o}}}{\sqrt{(x-x_{\mathrm{o}})^2+(y-y_{\mathrm{o}})^2+z^2}}.\tag{5.55}$$

In the case of two-dimensional structures the formulae are simplified. Let the x-axis run along the strike. Consider the TE-mode of the anomalous field in the air. For $z\le 0$ we have

$$H_y^{\mathrm{A}}(y,z)=-\frac{1}{\pi}\int\limits_{-\infty}^{\infty}H_{oz}^{\mathrm{A}}(y_{\mathrm{o}})\frac{(y_{\mathrm{o}}-y)dy_{\mathrm{o}}}{(y-y_{\mathrm{o}})^2+z^2}\qquad a$$
$$H_z^{\mathrm{A}}(y,z)=\frac{1}{\pi}\int\limits_{-\infty}^{\infty}H_{oy}^{A}(y_{\mathrm{o}})\frac{(y_{\mathrm{o}}-y)dy_{\mathrm{o}}}{(y-y_{\mathrm{o}})^2+z^2}\qquad b\tag{5.56}$$

and

$$E_x^{\mathrm{A}}(y,z)=-\frac{i\omega\mu_{\mathrm{o}}}{\pi}\int\limits_{-\infty}^{\infty}H_{oy}^{\mathrm{A}}(y_{\mathrm{o}})\ln\frac{1}{\sqrt{(y-y_{\mathrm{o}})^2+z^2}}dy_{\mathrm{o}}\qquad a$$
$$H_y^{\mathrm{A}}(y,z)=\frac{i}{\pi\omega\mu_{\mathrm{o}}}\int\limits_{-\infty}^{\infty}E_{ox}^{\mathrm{A}}(y_{\mathrm{o}})\frac{(y_{\mathrm{o}}-y)^2-z^2}{\left((y-y_{\mathrm{o}})^2+z^2\right)^2}dy_{\mathrm{o}}.\qquad b\tag{5.57}$$

Here (5.56) and (5.57) are two-dimensional counterparts of (5.47), (5.48) and (5.50), (5.51). These formulae can be supplemented by the formula

$$E^{\mathrm{A}}_{\mathrm{o}x}(y) = -i\omega\mu_{\mathrm{o}} \int_{-\infty}^{y} H^{\mathrm{A}}_{\mathrm{o}z}(y_{\mathrm{o}})\, dy_{\mathrm{o}}, \tag{5.58}$$

which follows directly from Maxwell's equation $\partial E^{\mathrm{A}}_{\mathrm{o}x}/\partial y = -i\omega\mu_{\mathrm{o}} H^{\mathrm{A}}_{\mathrm{o}z}$.

We have derived the integral relations that enable us to synthesize the synchronous magnetotelluric field from the magnetotelluric and magnetovariational response functions measured on the Earth's surface.

5.2.2 *Synthesis of the Magnetic Field from the Impedance Tensors*

Let the impedance tensor $[\mathbf{Z}(x, y)]$ be measured on the Earth's surface. Synthesis of the magnetic field $\mathbf{H}_{\mathrm{o}}(x, y)$ from the $[\mathbf{Z}(x, y)]$ reduces to the solution of the system of the integral equations of the second kind.

For the sake of convenience we express the linear relations between horizontal components of the magnetic and electric fields, $\mathbf{H}_{\mathrm{o}}(x, y)$ and $\mathbf{E}_{\mathrm{o}}(x, y)$, in terms of the admittance tensor $[\mathbf{Y}] = [\mathbf{Z}]^{-1}$. Proceeding from (1.19), we write:

$$\begin{aligned} H_{\mathrm{o}x} - Y_{xx}E_{\mathrm{o}x} - Y_{xy}E_{\mathrm{o}y} &= 0, \\ H_{\mathrm{o}y} - Y_{yx}E_{\mathrm{o}x} - Y_{yy}E_{\mathrm{o}y} &= 0, \end{aligned} \tag{5.59}$$

where

$$Y_{xx} = \frac{Z_{yy}}{Z_{xx}Z_{yy} - Z_{xy}Z_{yx}}, \qquad Y_{xy} = -\frac{Z_{xy}}{Z_{xx}Z_{yy} - Z_{xy}Z_{yx}},$$

$$Y_{yx} = -\frac{Z_{yx}}{Z_{xx}Z_{yy} - Z_{xy}Z_{yx}}, \qquad Y_{yy} = \frac{Z_{xx}}{Z_{xx}Z_{yy} - Z_{xy}Z_{yx}}.$$

Separating the normal and anomalous fields, we get

$$\begin{aligned} &H^{\mathrm{A}}_{\mathrm{o}x}(x, y) - Y_{xx}(x, y)E^{\mathrm{A}}_{\mathrm{o}x}(x, y) - Y_{xy}(x, y)E^{\mathrm{A}}_{\mathrm{o}y}(x, y) \\ &\qquad = -H^{\mathrm{N}}_{\mathrm{o}x} + Y_{xx}(x, y)E^{\mathrm{N}}_{\mathrm{o}x} + Y_{xy}(x, y)E^{\mathrm{N}}_{\mathrm{o}y} \\ &H^{\mathrm{A}}_{\mathrm{o}y}(x, y) - Y_{yx}(x, y)E^{\mathrm{A}}_{\mathrm{o}x}(x, y) - Y_{yy}(x, y)E^{\mathrm{A}}_{\mathrm{o}y}(x, y) \\ &\qquad = -H^{\mathrm{N}}_{\mathrm{o}y} + Y_{yx}(x, y)E^{\mathrm{N}}_{\mathrm{o}x} + Y_{yy}(x, y)E^{\mathrm{N}}_{\mathrm{o}y}. \end{aligned} \tag{5.60}$$

On substituting (5.50) into (5.60), we write

$$H^{\mathrm{A}}_{ox}(x,y)+\frac{i\omega\mu_{\mathrm{o}}}{2\pi}\int\limits_{-\infty}^{\infty}\int\limits_{-\infty}^{\infty}\frac{Y_{xx}(x,y)H^{\mathrm{A}}_{oy}(x_{\mathrm{o}},y_{\mathrm{o}})-Y_{xy}(x,y)H^{\mathrm{A}}_{ox}(x_{\mathrm{o}},y_{\mathrm{o}})}{\sqrt{(x-x_{\mathrm{o}})^2+(y-y_{\mathrm{o}})^2}}dx_{\mathrm{o}}dy_{\mathrm{o}}=F_x(x,y)$$
$$H^{\mathrm{A}}_{oy}(x,y)+\frac{i\omega\mu_{\mathrm{o}}}{2\pi}\int\limits_{-\infty}^{\infty}\int\limits_{-\infty}^{\infty}\frac{Y_{yx}(x,y)H^{\mathrm{A}}_{oy}(x_{\mathrm{o}},y_{\mathrm{o}})-Y_{yy}(x,y)H^{\mathrm{A}}_{ox}(x_{\mathrm{o}},y_{\mathrm{o}})}{\sqrt{(x-x_{\mathrm{o}})^2+(y-y_{\mathrm{o}})^2}}dx_{\mathrm{o}}dy_{\mathrm{o}}=F_y(x,y),\tag{5.61}$$

where

$$\begin{aligned}F_x(x,y)&=-H^{\mathrm{N}}_{ox}+Y_{xx}(x,y)E^{\mathrm{N}}_{ox}+Y_{xy}(x,y)E^{\mathrm{N}}_{oy}\\&=Y_{xx}(x,y)Z_{\mathrm{N}}H^{\mathrm{N}}_{oy}-\{Y_{xy}(x,y)Z_{\mathrm{N}}+1\}H^{\mathrm{N}}_{ox},\\F_y(x,y)&=-H^{\mathrm{N}}_{oy}+Y_{yx}(x,y)E^{\mathrm{N}}_{ox}+Y_{yy}(x,y)E^{\mathrm{N}}_{oy}\\&=\{Y_{yx}(x,y)Z_{\mathrm{N}}-1\}H^{\mathrm{N}}_{oy}-Y_{yy}(x,y)Z_{\mathrm{N}}H^{\mathrm{N}}_{ox}\end{aligned}$$

and

$$Z_{\mathrm{N}}=\frac{E^{\mathrm{N}}_{ox}}{H^{\mathrm{N}}_{oy}}=-\frac{E^{\mathrm{N}}_{oy}}{H^{\mathrm{N}}_{ox}}.$$

The integral equations (5.61) let us determine the horizontal components, H^{A}_{ox} and H^{A}_{oy}, of the anomalous magnetic field $\mathbf{H}^{\mathrm{A}}_{\mathrm{o}}$ at the Earth's surface from the measured admittance tensor $[\mathbf{Y}]$ and given normal impedance Z_{N} and normal magnetic field $\mathbf{H}^{\mathrm{N}}_{\mathrm{o}}$. It is advantageous to take $\mathbf{H}^{\mathrm{N}}_{\mathrm{o}}$ as a field linearly polarized in the direction, which ensures a maximum sensitivity of $\mathbf{H}^{\mathrm{A}}_{\mathrm{o}}$ to target structures. In regions with elongated structures we merely direct the normal magnetic field against the prevailing strike. Let the target structures be elongated along the $x-$axis. Then, the normal magnetic field reflecting the distribution of the longitudinal excess currents is chosen as $\mathbf{H}^{\mathrm{N}}_{\mathrm{o}}=H^{\mathrm{N}}_{oy}1_y$. In that event

$$\begin{aligned}F_x&=Y_{xx}(x,y)Z_{\mathrm{N}}H^{\mathrm{N}}_{oy},\\F_y&=\{Y_{yx}(x,y)Z_{\mathrm{N}}-1\}H^{\mathrm{N}}_{oy},\end{aligned}\tag{5.62}$$

where $Y_{xx}(x,y)\,Z_{\mathrm{N}}\to 0$ and $Y_{yx}(x,y)\,Z_{\mathrm{N}}\to 1$ as $\sqrt{x^2+y^2}\to\infty$.

Introduce normalized anomalous fields

$$\widehat{H}^{\mathrm{A}}_{ox}(x,y)=\frac{H^{\mathrm{A}}_{ox}(x,y)}{H^{\mathrm{N}}_{oy}},\qquad\widehat{H}^{\mathrm{A}}_{oy}(x,y)=\frac{H^{\mathrm{A}}_{oy}(x,y)}{H^{\mathrm{N}}_{oy}}.\tag{5.63}$$

On substituting (5.62) and (5.63) into (5.61), the system of the integral equations for horizontal components of the anomalous magnetic field assumes the form

$$\widehat{H}^{\mathrm{A}}_{ox}(x,y)+\frac{i\omega\mu_{\mathrm{o}}}{2\pi}\int\limits_{-\infty}^{\infty}\int\limits_{-\infty}^{\infty}\frac{Y_{xx}(x,y)\widehat{H}^{\mathrm{A}}_{oy}(x_{\mathrm{o}},y_{\mathrm{o}})-Y_{xy}(x,y)\widehat{H}^{\mathrm{A}}_{ox}(x_{\mathrm{o}},y_{\mathrm{o}})}{\sqrt{(x-x_{\mathrm{o}})^2+(y-y_{\mathrm{o}})^2}}dx_{\mathrm{o}}\,dy_{\mathrm{o}}=Y_{xx}(x,y)Z_{\mathrm{N}},$$

$$\widehat{H}^{\mathrm{A}}_{oy}(x,y)+\frac{i\omega\mu_{\mathrm{o}}}{2\pi}\int\limits_{-\infty}^{\infty}\int\limits_{-\infty}^{\infty}l\frac{Y_{yx}(x,y)\widehat{H}^{\mathrm{A}}_{oy}(x_{\mathrm{o}},y_{\mathrm{o}})-Y_{yy}(x,y)\widehat{H}^{\mathrm{A}}_{ox}(x_{\mathrm{o}},y_{\mathrm{o}})}{\sqrt{(x-x_{\mathrm{o}})^2+(y-y_{\mathrm{o}})^2}}dx_{\mathrm{o}}\,dy_{\mathrm{o}}$$
$$=Y_{yx}(x,y)Z_{\mathrm{N}}-1. \tag{5.64}$$

To determine $\widehat{H}^{\mathrm{A}}_{ox}(x,y)$ and $\widehat{H}^{\mathrm{A}}_{oy}(x,y)$ from this system of integral equations, it suffices to know the admittance (impedance) tensor. Having determined the horizontal components of the normalized anomalous magnetic field, we can compute its vertical component. By virtue of (5.48)

$$\widehat{H}^{\mathrm{A}}_{oz}(x,y)=\frac{1}{2\pi}\frac{\partial}{\partial x}\int\limits_{-\infty}^{\infty}\int\limits_{-\infty}^{\infty}\widehat{H}^{\mathrm{A}}_{ox}(x_{\mathrm{o}},y_{\mathrm{o}})\frac{dx_{\mathrm{o}}\,dy_{\mathrm{o}}}{\sqrt{(x-x_{\mathrm{o}})^2+(y-y_{\mathrm{o}})^2+z^2}}$$
$$+\frac{1}{2\pi}\frac{\partial}{\partial y}\int\limits_{-\infty}^{\infty}\int\limits_{-\infty}^{\infty}\widehat{H}^{\mathrm{A}}_{oy}(x_{\mathrm{o}},y_{\mathrm{o}})\frac{dx_{\mathrm{o}}\,dy_{\mathrm{o}}}{\sqrt{(x-x_{\mathrm{o}})^2+(y-y_{\mathrm{o}})^2+z^2}}, \tag{5.65}$$

where

$$\widehat{H}^{\mathrm{A}}_{oz}(x,y)=\frac{H^{\mathrm{A}}_{oz}(x,y)}{H^{\mathrm{N}}_{oy}}\ .$$

Note that the anomalous magnetic field derived from (5.64) is readily transformed in the anomalous electric field. Using (5.50), we get

$$\widehat{E}^{\mathrm{A}}_{ox}(x,y)=-\frac{i\omega\mu_{\mathrm{o}}}{2\pi}\int\limits_{-\infty}^{\infty}\int\limits_{-\infty}^{\infty}\widehat{H}^{\mathrm{A}}_{oy}(x_{\mathrm{o}},y_{\mathrm{o}})\frac{dx_{\mathrm{o}}\,dy_{\mathrm{o}}}{\sqrt{(x-x_{\mathrm{o}})^2+(y-y_{\mathrm{o}})^2+z^2}}$$
$$\widehat{E}^{\mathrm{A}}_{oy}(x,y)=\frac{i\omega\mu_{\mathrm{o}}}{2\pi}\int\limits_{-\infty}^{\infty}\int\limits_{-\infty}^{\infty}\widehat{H}^{\mathrm{A}}_{ox}(x_{\mathrm{o}},y_{\mathrm{o}})\frac{dx_{\mathrm{o}}\,dy_{\mathrm{o}}}{\sqrt{(x-x_{\mathrm{o}})^2+(y-y_{\mathrm{o}})^2+z^2}}, \tag{5.66}$$

where

$$\widehat{E}^{\mathrm{A}}_{ox}(x,y)=\frac{E^{\mathrm{A}}_{ox}(x,y)}{H^{N}_{oy}}\qquad \widehat{E}^{\mathrm{A}}_{oy}(x,y)=\frac{E^{\mathrm{A}}_{oy}(x,y)}{H^{N}_{oy}}.$$

To complete this consideration, we present the two-dimensional analogues of (5.64), (5.65) and (5.66). Let x be the strike of the 2D model. Then, according to (5.56b), (5.58) and (5.64), we have the integral equation for $\widehat{H}^{\mathrm{A}}_{oy}(y)$

$$\widehat{H}^{\mathrm{A}}_{oy}(y) + \frac{i\omega\mu_o}{\pi} Y_{yx}(y) \int\limits_{-\infty}^{\infty} \widehat{H}^{\mathrm{A}}_{oy}(y_0) \ln \frac{1}{|y_o - y|} dy_o = Y_{yx}(y) Z_N - 1 \tag{5.67}$$

and the formulae to compute $\widehat{H}^{\mathrm{A}}_{oz}(y)$ and $\widehat{E}^{\mathrm{A}}_{ox}(y)$:

$$\widehat{H}^{\mathrm{A}}_{oz}(y) = \frac{1}{\pi} \int\limits_{-\infty}^{\infty} \widehat{H}^{\mathrm{A}}_{oy}(y_o) \frac{dy_o}{y_o - y} \tag{5.68}$$

$$\widehat{E}^{\mathrm{A}}_{ox}(y) = \begin{cases} \dfrac{i\omega\mu_o}{\pi} \displaystyle\int\limits_{-\infty}^{\infty} \widehat{H}^{\mathrm{A}}_{oy}(y_o) \ln \frac{1}{|y_o - y|} dy_o \\ -i\omega\mu_o \displaystyle\int\limits_{-\infty}^{y} \widehat{H}^{\mathrm{A}}_{oz}(y_o)\, dy_o. \end{cases} \tag{5.69}$$

5.2.3 Synthesis of the Magnetic Field from the Tippers

Now we will show that the magnetic field can be synthesized not only from the impedance tensors, but from the tippers as well.

Let the Wiese–Parkinson matrix $[\mathbf{W}(x, y)]$ be given on the Earth's surface. Reasoning from (4.2), we assume that

$$H_{oz} - W_{zx} H_{ox} - W_{zy} H_{oy} = 0. \tag{5.70}$$

Separating the normal and anomalous fields, we get

$$\begin{aligned} H^{\mathrm{A}}_{oz}(x, y) - W_{zx}(x, y) H^{\mathrm{A}}_{ox}(x, y) - W_{zy}(x, y) H^{\mathrm{A}}_{oy}(x, y) \\ = W_{zx}(x, y) H^{\mathrm{N}}_{ox} + W_{zy}(x, y) H^{\mathrm{N}}_{oy}. \end{aligned} \tag{5.71}$$

The normal magnetic field is $\mathbf{H}^{\mathrm{N}}_o = H^{\mathrm{N}}_{oy} 1_y$. Then, with a glance to (5.47), we have

$$\begin{aligned} H^{\mathrm{A}}_{oz}(x, y) + \frac{W_{zx}(x, y)}{2\pi} \frac{\partial}{\partial x} \int\limits_{-\infty}^{\infty} \int\limits_{-\infty}^{\infty} H^{\mathrm{A}}_{oz}(x_o, y_o) \frac{dx_o\, dy_o}{\sqrt{(x - x_o)^2 + (y - y_o)^2 + z^2}} \\ + \frac{W_{zy}(x, y)}{2\pi} \frac{\partial}{\partial y} \int\limits_{-\infty}^{\infty} \int\limits_{-\infty}^{\infty} H^{\mathrm{A}}_{oz}(x_o, y_o) \frac{dx_o\, dy_o}{\sqrt{(x - x_o)^2 + (y - y_o)^2 + z^2}} = W_{zy}(x, y) H^{\mathrm{N}}_{oy}\,. \end{aligned} \tag{5.72}$$

For the normalized anomalous magnetic field, $\widehat{H}^{\mathrm{A}}_{\mathrm{oz}}(x, y) = H^{\mathrm{A}}_{\mathrm{oz}}(x, y)/H^{\mathrm{N}}_{\mathrm{oy}}$, we obtain

$$\widehat{H}^{\mathrm{A}}_{\mathrm{oz}}(x, y) + \int_{-\infty}^{\infty}\int_{-\infty}^{\infty} K(x, y, x_{\mathrm{o}}, y_{\mathrm{o}})\, \widehat{H}^{\mathrm{A}}_{\mathrm{oz}}(x_{\mathrm{o}}, y_{\mathrm{o}})\, dx_{\mathrm{o}}\, dy_{\mathrm{o}} = W_{zy}(x, y), \tag{5.73}$$

where

$$\begin{aligned} K(x, y, x_{\mathrm{o}}, y_{\mathrm{o}}) = {} & \frac{W_{zx}(x, y)}{2\pi}\frac{\partial}{\partial x}\frac{1}{\sqrt{(x - x_{\mathrm{o}})^2 + (y - y_{\mathrm{o}})^2}} \\ & + \frac{W_{zy}(x, y)}{2\pi}\frac{\partial}{\partial y}\frac{1}{\sqrt{(x - x_{\mathrm{o}})^2 + (y - y_{\mathrm{o}})^2}} \\ & + \frac{(x_{\mathrm{o}} - x)W_{zx}(x, y) + (y_{\mathrm{o}} - y)W_{zy}(x, y)}{2\pi[(x - x_{\mathrm{o}})^2 + (y - y_{\mathrm{o}})^2]^{3/2}}\ . \end{aligned}$$

With $\sqrt{x_{\mathrm{o}}^2 + y_{\mathrm{o}}^2} \to \infty$, the kernel $K(x, y, x_{\mathrm{o}}, y_{\mathrm{o}})$ decreases sufficiently fast, and this allows us to integrate $\widehat{H}^{\mathrm{A}}_{\mathrm{oz}}(x_{\mathrm{o}}, y_{\mathrm{o}})$ within relatively small area. Note also that $K(x, y, x_{\mathrm{o}}, y_{\mathrm{o}})$ has a singularity at $\sqrt{(x - x_{\mathrm{o}})^2 + (y - y_{\mathrm{o}})^2} \to 0$. So, in the vicinity of this point, the integral should be taken as its principal value in the Cauchy sense. Here we have to take into account that

$$\begin{aligned} & \int_{-\infty}^{\infty}\int_{-\infty}^{\infty} K(x, y, x_{\mathrm{o}}, y_{\mathrm{o}})\ dx_0 dy_0 \\ & \quad = -\frac{W_{zx}(x, y)}{2\pi}\int_{-\infty}^{\infty}\int_{-\infty}^{\infty}\frac{\partial}{\partial x_{\mathrm{o}}}\frac{1}{\sqrt{(x - x_{\mathrm{o}})^2 + (y - y_{\mathrm{o}})^2}} dx_{\mathrm{o}} dy_{\mathrm{o}} \\ & \qquad - \frac{W_{zy}(x, y)}{2\pi}\int_{-\infty}^{\infty}\int_{-\infty}^{\infty}\frac{\partial}{\partial y_{\mathrm{o}}}\frac{1}{\sqrt{(x - x_{\mathrm{o}})^2 + (y - y_{\mathrm{o}})^2}} dx_{\mathrm{o}} dy_{\mathrm{o}} = 0. \end{aligned}$$

Using this property of $K(x, y, x_{\mathrm{o}}, y_{\mathrm{o}})$, we rewrite integral equation (5.73) in the form

$$\widehat{H}^{\mathrm{A}}_{\mathrm{oz}}(x, y) + \int_{-\infty}^{\infty}\int_{-\infty}^{\infty} K(x, y, x_{\mathrm{o}}, y_{\mathrm{o}})[\, \widehat{H}^{\mathrm{A}}_{\mathrm{oz}}(x_{\mathrm{o}}, y_{\mathrm{o}}) - \widehat{H}^{\mathrm{A}}_{\mathrm{oz}}(x, y)]\, dx_{\mathrm{o}}\, dy_{\mathrm{o}} = W_{zy}(x, y). \tag{5.74}$$

It is simply evident now that the singularity is of little importance, since $\tilde{H}^{\mathrm{A}}_{\mathrm{oz}}(x_{\mathrm{o}}, y_{\mathrm{o}}) - \tilde{H}^{\mathrm{A}}_{\mathrm{oz}}(x, y) \to 0$ as $\sqrt{(x - x_{\mathrm{o}})^2 + (y - y_{\mathrm{o}})^2} \to 0$.

Solving integral equation (5.74), we determine the normalized vertical component of the anomalous magnetic field on the Earth's surface. With a knowledge of $\tilde{H}^{\mathrm{A}}_{\mathrm{oz}}(x, y)$, we use (5.47) and compute the normalized horizontal com-ponents of the anomalous magnetic field

$$\begin{aligned}
\widehat{H}^{\mathrm{A}}_{\mathrm{ox}}(x, y) &= \frac{1}{2\pi}\frac{\partial}{\partial x}\int\limits_{-\infty}^{\infty}\int\limits_{-\infty}^{\infty}\widehat{H}^{\mathrm{A}}_{\mathrm{oz}}(x_{\mathrm{o}}, y_{\mathrm{o}})\frac{dx_{\mathrm{o}}\,dy_{\mathrm{o}}}{\sqrt{(x-x_{\mathrm{o}})^2+(y-y_{\mathrm{o}})^2+z^2}} \\
\widehat{H}^{\mathrm{A}}_{\mathrm{oy}}(x, y) &= \frac{1}{2\pi}\frac{\partial}{\partial y}\int\limits_{-\infty}^{\infty}\int\limits_{-\infty}^{\infty}\widehat{H}^{\mathrm{A}}_{\mathrm{oz}}(x_{\mathrm{o}}, y_{\mathrm{o}})\frac{dx_{\mathrm{o}}\,dy_{\mathrm{o}}}{\sqrt{(x-x_{\mathrm{o}})^2+(y-y_{\mathrm{o}})^2+z^2}}\,.
\end{aligned} \tag{5.75}$$

And what is more, we can substitute (5.75) in (5.66) and calculate the normalized components of the anomalous electric field, $\widehat{E}^{\mathrm{A}}_{\mathrm{ox}}(x, y)$ and $\widehat{E}^{\mathrm{A}}_{\mathrm{oy}}(x, y)$.

Equations obtained are readily reduced to the two-dimensional case. Let x be the strike of the model. Then (5.73) assumes the form

$$\widehat{H}^{\mathrm{A}}_{\mathrm{oz}}(y) + \int\limits_{-\infty}^{\infty} L(y, y_{\mathrm{o}})\,\widehat{H}_{\mathrm{oz}}(y_{\mathrm{o}})\,dy_{\mathrm{o}} = W_{zy}(y), \tag{5.76}$$

where the kernel $L(y, y_{\mathrm{o}})$ is

$$L(y, y_{\mathrm{o}}) = \frac{W_{zy}(y)}{2\pi}\int\limits_{-\infty}^{\infty}\frac{\partial}{\partial y}\frac{1}{\sqrt{(x-x_{\mathrm{o}})^2+(y-y_{\mathrm{o}})^2}}dx_{\mathrm{o}} = \frac{W_{zy}(y)}{\pi\,(y-y_{\mathrm{o}})}\,, \tag{5.77}$$

from which

$$\widehat{H}^{\mathrm{A}}_{\mathrm{oz}}(y) + \frac{W_{zy}(y)}{\pi}\int\limits_{-\infty}^{\infty}\frac{\widehat{H}^{\mathrm{A}}_{\mathrm{oz}}(y_{\mathrm{o}})\,dy_{\mathrm{o}}}{y-y_{\mathrm{o}}} = W_{zy}(y). \tag{5.78}$$

Note that the equation for $\widehat{H}^{\mathrm{A}}_{\mathrm{oz}}(y)$ can be translated into the equation for $\widehat{H}^{\mathrm{A}}_{\mathrm{oy}}(y)$. Substituting $\widehat{H}^{\mathrm{A}}_{\mathrm{oz}} = W_{zy}(\widehat{H}^{\mathrm{A}}_{\mathrm{oy}} + 1)$ in (5.78), we get

$$\widehat{H}^{\mathrm{A}}_{\mathrm{oy}}(y) + \frac{1}{\pi}\int\limits_{-\infty}^{\infty}\frac{W_{zy}(y_{\mathrm{o}})\,\widehat{H}^{\mathrm{A}}_{\mathrm{oy}}(y_{\mathrm{o}})}{y-y_{\mathrm{o}}}dy_{\mathrm{o}} = -\frac{1}{\pi}\int\limits_{-\infty}^{\infty}\frac{W_{zy}(y_{\mathrm{o}})\,dy_{\mathrm{o}}}{y-y_{\mathrm{o}}}. \tag{5.79}$$

On inverting the Hilbert transformation, we write the equation for $\widehat{H}^{\mathrm{A}}_{\mathrm{oy}}(y)$ in a form suggested by Vanyan et al. (1998):

$$W_{zy}(y)\widehat{H}^{\mathrm{A}}_{\mathrm{o}y}(y)+\frac{1}{\pi}\int\limits_{-\infty}^{\infty}\frac{\widehat{H}^{\mathrm{A}}_{\mathrm{o}y}(y_{\mathrm{o}})}{y-y_{\mathrm{o}}}dy_{\mathrm{o}}=-W_{zy}(y). \tag{5.80}$$

In the closing stage of the synthesis, it is a simple matter to apply (5.69) and translate the anomalous magnetic field into the anomalous electric field.

Summing up, we arrive at a conclusion that the Wiese–Parkinson matrices given at all points of the Earth's surface carry complete information on magnetotelluric anomalies. Using this information with a knowledge of the normal field and the normal impedance, we can reconstruct the magnetotelluric field and the impedances. Thus, considering a two-dimensional model and taking into account (5.58), we have (Vanyan et al.,1997):

$$E_{\mathrm{o}x}(y)=E^{\mathrm{N}}_{\mathrm{o}x}-i\omega\mu_{\mathrm{o}}\int\limits_{-\infty}^{y}H^{\mathrm{A}}_{\mathrm{o}z}(y_{\mathrm{o}})\,dy_{\mathrm{o}}, \tag{5.81}$$

whence

$$Z^{\parallel}(y)=\frac{E_{\mathrm{o}x}(y)}{H_{\mathrm{o}y}(y)}=\frac{1}{\widehat{H}^{\mathrm{A}}_{\mathrm{o}y}(y)+1}\{Z_{\mathrm{N}}-i\omega\mu_{\mathrm{o}}\int\limits_{-\infty}^{y}\widehat{H}^{\mathrm{A}}_{\mathrm{o}z}(y_{\mathrm{o}})\,dy_{\mathrm{o}}\}\,. \tag{5.82}$$

5.2.4 Synthesis of the Magnetic Field from the Generalized Impedance Tensors

Let the normal field in the generalized impedance model contain three independent modes: two plane-wave modes with polarization in the orthogonal directions and the source-effect mode with vertical magnetic component. In that model we have the generalized impedance tensor

$$[\mathbf{Z}']=\begin{bmatrix}Z'_{xx} & Z'_{xy} & Z'_{xz}\\ Z'_{yx} & Z'_{yy} & Z'_{yz}\end{bmatrix},$$

which transforms the magnetic field $\mathbf{H}(H_x, H_y, H_z)$ into the electric field $\mathbf{E}(E_x, E_y)$:

$$E_x=Z'_{xx}H_x+Z'_{xy}H_y+Z'_{xz}H_z,$$

$$E_y=Z'_{yx}H_x+Z'_{yy}H_y+Z'_{yz}H_z\,.$$

Separating the normal and anomalous fields, we get

$$
\begin{aligned}
&E^{\mathrm{A}}_{\mathrm{o}x}(x,y) - Z'_{xx}(x,y)H^{\mathrm{A}}_{\mathrm{o}x}(x,y) - Z'_{xy}(x,y)H^{\mathrm{A}}_{\mathrm{o}y}(x,y) - Z'_{xz}(x,y)H^{\mathrm{A}}_{\mathrm{o}z}(x,y)\\
&= -E^{\mathrm{N}}_{\mathrm{o}x}(x,y) + Z'_{xx}(x,y)H^{\mathrm{N}}_{\mathrm{o}x}(x,y) + Z'_{xy}(x,y)H^{\mathrm{N}}_{\mathrm{o}y}(x,y) + Z'_{xz}(x,y)H^{\mathrm{N}}_{\mathrm{o}z}(x,y)\\
&E^{\mathrm{A}}_{\mathrm{o}y}(x,y) - Z'_{yx}(x,y)H^{\mathrm{A}}_{\mathrm{o}x}(x,y) - Z'_{yy}(x,y)H^{\mathrm{A}}_{\mathrm{o}y}(x,y) - Z'_{yz}(x,y)H^{\mathrm{A}}_{\mathrm{o}z}(x,y)\\
&= -E^{\mathrm{N}}_{\mathrm{o}x}(x,y) + Z'_{yx}(x,y)H^{\mathrm{N}}_{\mathrm{o}x}(x,y) + Z'_{yy}(x,y)H^{\mathrm{N}}_{\mathrm{o}y}(x,y) + Z'_{yz}(x,y)H^{\mathrm{N}}_{\mathrm{o}z}(x,y)\,.
\end{aligned}
\tag{5.83}
$$

Substituting (5.48), (5.50) in (5.83), we obtain a system of integral equations for horizontal components of the anomalous magnetic field:

$$
\begin{aligned}
&Z'_{xx}(x,y)H^{\mathrm{A}}_{\mathrm{o}x}(x,y) + Z'_{xy}(x,y)H^{\mathrm{A}}_{\mathrm{o}y}(x,y)\\
&- \frac{Z'_{xz}(x,y)}{2\pi}\frac{\partial}{\partial x}\int\limits_{-\infty}^{\infty}\int\limits_{-\infty}^{\infty} H^{\mathrm{A}}_{\mathrm{o}x}(x_{\mathrm{o}},y_{\mathrm{o}})\frac{dx_{\mathrm{o}}dy_{\mathrm{o}}}{\sqrt{(x-x_{\mathrm{o}})^2+(y-y_{\mathrm{o}})^2+z^2}}\\
&+ \frac{Z'_{xz}(x,y)}{2\pi}\frac{\partial}{\partial y}\int\limits_{-\infty}^{\infty}\int\limits_{-\infty}^{\infty} H^{\mathrm{A}}_{\mathrm{o}y}(x_{\mathrm{o}},y_{\mathrm{o}})\frac{dx_{\mathrm{o}}dy_{\mathrm{o}}}{\sqrt{(x-x_{\mathrm{o}})^2+(y-y_{\mathrm{o}})^2+z^2}}\\
&- \frac{i\omega\mu_{\mathrm{o}}}{2\pi}\int\limits_{-\infty}^{\infty}\int\limits_{-\infty}^{\infty} H^{\mathrm{A}}_{\mathrm{o}y}(x_{\mathrm{o}},y_{\mathrm{o}})\frac{dx_{\mathrm{o}}dy_{\mathrm{o}}}{\sqrt{(x-x_{\mathrm{o}})^2+(y-y_{\mathrm{o}})^2+z^2}}\\
&= E^{\mathrm{N}}_{\mathrm{o}x}(x,y) - Z'_{xx}(x,y)H^{\mathrm{N}}_{\mathrm{o}x}(x,y) - Z'_{xy}(x,y)H^{\mathrm{N}}_{\mathrm{o}y}(x,y) - Z'_{xz}(x,y)H^{\mathrm{N}}_{\mathrm{o}z}(x,y)\,,
\end{aligned}
\tag{5.84}
$$

and

$$
\begin{aligned}
&Z'_{yx}(x,y)H^{\mathrm{A}}_{\mathrm{o}x}(x,y) + Z'_{yy}(x,y)H^{\mathrm{A}}_{\mathrm{o}y}(x,y)\\
&- \frac{Z'_{yz}(x,y)}{2\pi}\frac{\partial}{\partial x}\int\limits_{-\infty}^{\infty}\int\limits_{-\infty}^{\infty} H^{\mathrm{A}}_{\mathrm{o}x}(x_{\mathrm{o}},y_{\mathrm{o}})\frac{dx_{\mathrm{o}}dy_{\mathrm{o}}}{\sqrt{(x-x_{\mathrm{o}})^2+(y-y_{\mathrm{o}})^2+z^2}}\\
&+ \frac{Z'_{yz}(x,y)}{2\pi}\frac{\partial}{\partial y}\int\limits_{-\infty}^{\infty}\int\limits_{-\infty}^{\infty} H^{\mathrm{A}}_{\mathrm{o}y}(x_{\mathrm{o}},y_{\mathrm{o}})\frac{dx_{\mathrm{o}}dy_{\mathrm{o}}}{\sqrt{(x-x_{\mathrm{o}})^2+(y-y_{\mathrm{o}})^2+z^2}}\\
&+ \frac{i\omega\mu_{\mathrm{o}}}{2\pi}\int\limits_{-\infty}^{\infty}\int\limits_{-\infty}^{\infty} H^{\mathrm{A}}_{\mathrm{o}x}(x_{\mathrm{o}},y_{\mathrm{o}})\frac{dx_{\mathrm{o}}dy_{\mathrm{o}}}{\sqrt{(x-x_{\mathrm{o}})^2+(y-y_{\mathrm{o}})^2+z^2}}\\
&= E^{\mathrm{N}}_{\mathrm{o}y}(x,y) - Z'_{yx}(x,y)H^{\mathrm{N}}_{\mathrm{o}x}(x,y) - Z'_{yy}(x,y)H^{\mathrm{N}}_{\mathrm{o}y}(x,y) - Z'_{yz}(x,y)H^{\mathrm{N}}_{\mathrm{o}z}(x,y)\,.
\end{aligned}
\tag{5.85}
$$

In these equations we can choose any polarization of the normal magnetotelluric field. For instance, we can take the normal field as a horizontally polarized uniform field and in this way eliminate the source effect.

Let the Earth's inhomogeneities be elongated in the x-direction. To provide the high sensitivity of the magnetic field to geoelectric structures, we set $\mathbf{E}_{\mathrm{o}}^{\mathrm{N}} = E_{\mathrm{ox}}^{\mathrm{N}} 1_x$, $\mathbf{H}_{\mathrm{o}}^{\mathrm{N}} = H_{\mathrm{oy}}^{\mathrm{N}} 1_y$. Then, we get a system of integral equations for normalized horizontal components of the anomalous magnetic field:

$$
\begin{aligned}
&Z'_{xx}(x,y)\widehat{H}^{\mathrm{A}}_{\mathrm{ox}}(x,y) + Z'_{xy}(x,y)\widehat{H}^{\mathrm{A}}_{\mathrm{oy}}(x,y) \\
&+ \frac{Z'_{xz}(x,y)}{2\pi}\frac{\partial}{\partial x}\int\limits_{-\infty}^{\infty}\int\limits_{-\infty}^{\infty}\widehat{H}^{\mathrm{A}}_{\mathrm{ox}}(x_{\mathrm{o}},y_{\mathrm{o}})\frac{dx_{\mathrm{o}}\,dy_{\mathrm{o}}}{\sqrt{(x-x_{\mathrm{o}})^2+(y-y_{\mathrm{o}})^2+z^2}} \\
&+ \frac{Z'_{xz}(x,y)}{2\pi}\frac{\partial}{\partial y}\int\limits_{-\infty}^{\infty}\int\limits_{-\infty}^{\infty}\widehat{H}^{\mathrm{A}}_{\mathrm{oy}}(x_{\mathrm{o}},y_{\mathrm{o}})\frac{dx_{\mathrm{o}}\,dy_{\mathrm{o}}}{\sqrt{(x-x_{\mathrm{o}})^2+(y-y_{\mathrm{o}})^2+z^2}} \\
&+ \frac{i\omega\mu_{\mathrm{o}}}{2\pi}\int\limits_{-\infty}^{\infty}\int\limits_{-\infty}^{\infty}\widehat{H}^{\mathrm{A}}_{\mathrm{oy}}(x_{\mathrm{o}},y_{\mathrm{o}})\frac{dx_{\mathrm{o}}\,dy_{\mathrm{o}}}{\sqrt{(x-x_{\mathrm{o}})^2+(y-y_{\mathrm{o}})^2+z^2}} = Z_{\mathrm{N}} - Z'_{xy}(x,y)
\end{aligned}
\tag{5.86}
$$

and

$$
\begin{aligned}
&Z'_{yx}(x,y)\widehat{H}^{\mathrm{A}}_{\mathrm{ox}}(x,y) + Z'_{yy}(x,y)\widehat{H}^{\mathrm{A}}_{\mathrm{oy}}(x,y) \\
&+ \frac{Z'_{yz}(x,y)}{2\pi}\frac{\partial}{\partial x}\int\limits_{-\infty}^{\infty}\int\limits_{-\infty}^{\infty}\widehat{H}^{\mathrm{A}}_{\mathrm{ox}}(x_{\mathrm{o}},y_{\mathrm{o}})\frac{dx_{\mathrm{o}}\,dy_{\mathrm{o}}}{\sqrt{(x-x_{\mathrm{o}})^2+(y-y_{\mathrm{o}})^2+z^2}} \\
&+ \frac{Z'_{yz}(x,y)}{2\pi}\frac{\partial}{\partial y}\int\limits_{-\infty}^{\infty}\int\limits_{-\infty}^{\infty}\widehat{H}^{\mathrm{A}}_{\mathrm{oy}}(x_{\mathrm{o}},y_{\mathrm{o}})\frac{dx_{\mathrm{o}}\,dy_{\mathrm{o}}}{\sqrt{(x-x_{\mathrm{o}})^2+(y-y_{\mathrm{o}})^2+z^2}} \\
&+ \frac{i\omega\mu_{\mathrm{o}}}{2\pi}\int\limits_{-\infty}^{\infty}\int\limits_{-\infty}^{\infty}\widehat{H}^{\mathrm{A}}_{\mathrm{ox}}(x_{\mathrm{o}},y_{\mathrm{o}})\frac{dx_{\mathrm{o}}\,dy_{\mathrm{o}}}{\sqrt{(x-x_{\mathrm{o}})^2+(y-y_{\mathrm{o}})^2+z^2}} = -Z'_{yy}(x,y),
\end{aligned}
\tag{5.87}
$$

where Z_{N} is the normal impedance and $\widehat{H}^{\mathrm{A}}_{ox} = H^{\mathrm{A}}_{ox}/H^{\mathrm{N}}_{oy}$, $\widehat{H}^{\mathrm{A}}_{oy} = H^{\mathrm{A}}_{oy}/H^{\mathrm{N}}_{oy}$. Solving these integral equations and using (5.48), (5.50), we find the magnetotelluric field excited by the plane wave of given polarization. Calculating the magnetotelluric fields for two different polarizations, we can compute the impedance and tipper matrices relating to the plane-wave excitation of the medium under investigation.

5.2.5 *Model Experiments on the Synthesis of the Magnetic Field*

Let us consider numerical experiments on the synthesis of the magnetic field from a given impedance or tipper (Fig. 5.2). The model consists of the homogeneous upper layer of resistivity ρ_1 resting on a resistive basement of resistivity ρ_2, which

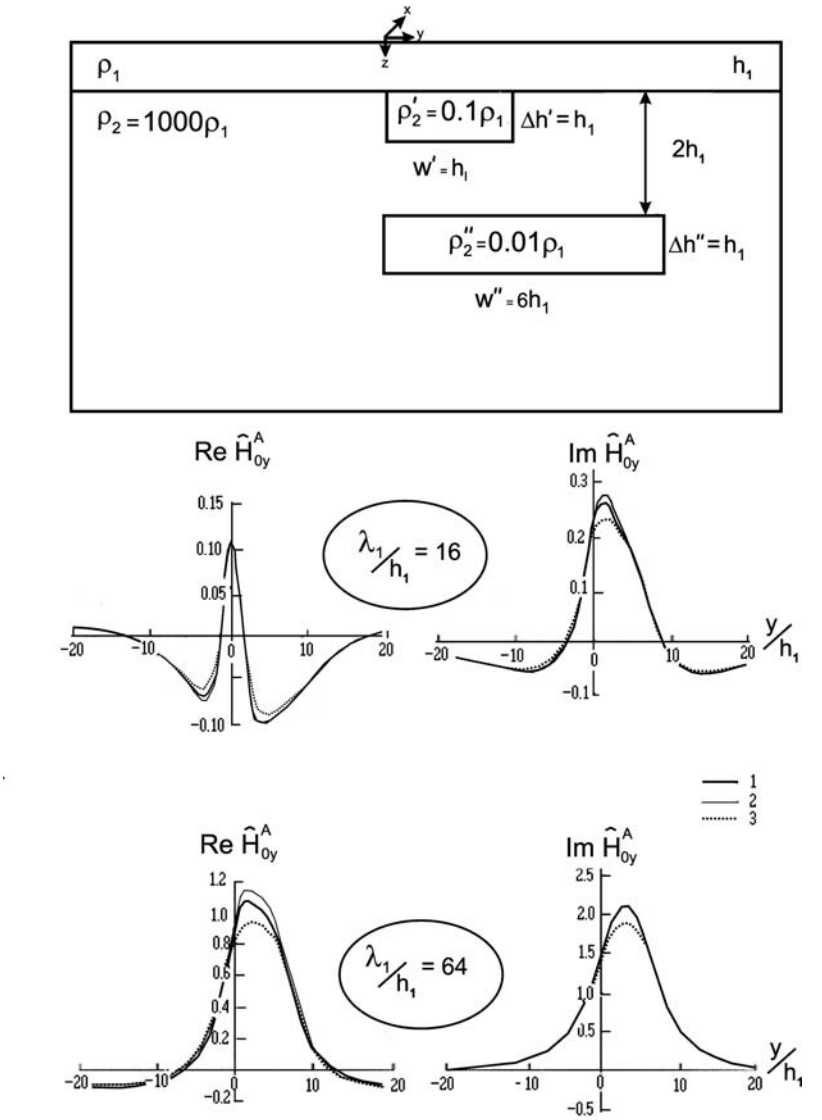

Fig. 5.2 Model experiments on the synthesis of the magnetic field; 1 – initial magnetic field, 2 – magnetic field synthesized from the longitudinal impedances, 3 – magnetic field synthesized from the tippers

contains two two-dimensional conductive prisms of resistivities ρ_2', ρ_2'' and widths w', w'' with strike along the x-axis. The anomalous magnetic field $\widehat{H}_{oy}^{A}$ computed for this model (thick line) is compared with synthetic anomalous magnetic field derived from the longitudinal impedance Z_{xy} (thin line) and the tipper W_{zy} (dotted

line). The initial and synthetic fields are seen to be in reasonable good agreement. This result is characteristic of rather wide frequency range, from $\lambda_1/h_1 = 16$ to $\lambda_1/h_1 = 64$, where $\lambda_1 = 2\pi\sqrt{2\rho_1/\omega\mu_o}$ is the wave-length in the upper layer. But note that such a good agreement is possible if Z_{xy} and W_{zy} are given on sufficiently long profile. In our case, with depth and width of the lower conductive zone being $3h_1$ and $6h_1$, good accuracy of the magnetic field reconstruction is attained when the impedance and tipper are specified at distances of up to $\pm 25h_1$.

Part II
Basic Models of the Distortion Theory

Chapter 6
Two Classic Models of the Distortion Theory

In the subsequent chapters we will consider how the near-surface and deep inhomogeneities distort the magnetotelluric and magnetovariational response functions observed on the Earth's surface. We are going to examine a number of models with a view to find the characteristic evidences of two-dimensional and three-dimensional galvanic and induction distortions and look for ways of their recognition. All models to be examined are excited by a plane monochromatic wave vertically incident on the Earth's surface. We have to analise the informativeness of MT- and MV-soundings and provide the background necessary for qualitative interpretation of experimental data and identification of objective geoelectric structures.

As a preliminary we would like to review two, now classic, models put forward by Obukhov (1962), d'Erceville and Kunetz (1962) and Rankin (1962) at dawn of magnetotellurics. A special feature of these two-dimensional models is that they offer analytical solutions for the TM-mode.

6.1 The Vertical-Interface Model

We start with a vertical-interface model shown in Fig. 6.1. Meaningful analysis of this model can be found in works by Weaver (1963, 1994), Berdichevsky (1968), Jones and Price (1970) and Fischer et al. (1992). The model consists of the nonconductive air and the conductive Earth that includes two quarter-spaces of different resistivities, ρ' and ρ'', divided by the infinite vertical interface $y = 0$, $0 \le z \le \infty$. The problem for the TM-mode has been solved independently by Obukhov (1962) and d'Erceville and Kunetz (1962). Following these pioneering works, we write

$$H_x(y,z) = \begin{cases} \dot{H}_x^{\mathrm{N}}(z) + \dot{H}_x^{\mathrm{A}}(y,z) & y \le 0,\ z \ge 0 \\ \ddot{H}_x^{\mathrm{N}}(z) + \ddot{H}_x^{\mathrm{A}}(y,z) & y \ge 0,\ z \ge 0, \end{cases} \tag{6.1}$$

where $\dot{H}_x^{\mathrm{N}}$, $\dot{H}_x^{\mathrm{A}}$ and $\ddot{H}_x^{\mathrm{N}}$, $\ddot{H}_x^{\mathrm{A}}$ are the normal and anomalous magnetic fields within the left and right quarter-spaces.

M. Berdichevsky, V.I. Dmitriev, *Models and Methods of Magnetotellurics*,
DOI 10.1007/978-3-540-77814-1_6, © Springer-Verlag Berlin Heidelberg 2008

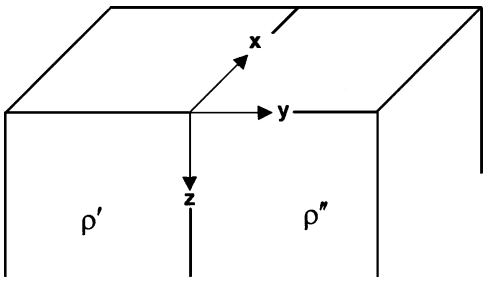

Fig. 6.1 The vertical-interface model

The normal fields are defined as

$$\dot{H}_x^{\mathrm{N}} = H_{x\mathrm{o}} e^{ik'z}, \qquad \ddot{H}_x^{\mathrm{N}} = H_{x\mathrm{o}} e^{ik''z}. \tag{6.2}$$

Here $k' = \sqrt{i\omega\mu_{\mathrm{o}}/\rho'}$, $k'' = \sqrt{i\omega\mu_{\mathrm{o}}/\rho''}$, $\mathrm{Im}\, k > 0$ and $H_{x\mathrm{o}} = \dot{H}_x^{\mathrm{N}}(0) = \ddot{H}_x^{\mathrm{N}}(0) = 2\,H^p(0)$, where $H^p(0)$ is the primary magnetic field on the Earth's surface $z = 0$.

The anomalous fields meet the equations

$$\frac{\partial^2 \dot{H}_x^{\mathrm{A}}}{\partial z^2} + \frac{\partial^2 \dot{H}_x^{\mathrm{A}}}{\partial y^2} + (k')^2 \dot{H}_x^{\mathrm{A}} = 0, \qquad \frac{\partial^2 \ddot{H}_x^{\mathrm{A}}}{\partial z^2} + \frac{\partial^2 \ddot{H}_x^{\mathrm{A}}}{\partial y^2} + (k'')^2 \ddot{H}_x^{\mathrm{A}} = 0 \tag{6.3}$$

with the boundary conditions $\dot{H}_x^{\mathrm{A}}(0) = \ddot{H}_x^{\mathrm{A}}(0) = 0$ on the Earth's surface and the conditions $\dot{H}_x^{\mathrm{A}}(z > 0) \underset{y \to -\infty}{\to} 0$, $\ddot{H}_x^{\mathrm{A}}(z > 0) \underset{y \to \infty}{\to} 0$ at infinity.

Solving these equations by the method of separation of variables, we get

$$\dot{H}_x^{\mathrm{A}} = \int_0^\infty a'_m e^{\eta' y} \sin m z \, dm, \qquad \ddot{H}_x^{\mathrm{A}} = \int_0^\infty a''_m e^{-\eta'' y} \sin m z \, dm, \tag{6.4}$$

where

$$\eta' = \sqrt{m^2 - (k')^2}, \qquad \eta'' = \sqrt{m^2 - (k'')^2}, \qquad \mathrm{Re}\, \eta > 0.$$

The constants a'_m and a''_m can be defined from the boundary conditions at the vertical interface $y = 0$. It follows from the continuity of H_x and $E_z = -\rho\, \partial H_x / \partial y$ that

$$\left.\begin{aligned} \dot{H}_x^{\mathrm{N}} - \ddot{H}_x^{\mathrm{N}} &= \ddot{H}_x^{\mathrm{A}} - \dot{H}_x^{\mathrm{A}} \\ \rho' \frac{\partial \dot{H}_x^{\mathrm{A}}}{\partial \mathrm{y}} &= \rho'' \frac{\partial \ddot{H}_x^{\mathrm{A}}}{\partial \mathrm{y}} \end{aligned}\right|_{y=0}. \tag{6.5}$$

With account for (6.2),

$$\dot{H}_x^{\mathrm{N}} - \ddot{H}_x^{\mathrm{N}} = H_{xo}(e^{ik'z} - e^{ik''z}) = \int_0^\infty b_m \sin mz\, dm, \tag{6.6}$$

where

$$b_m = \frac{2mH_{xo}}{\pi} \frac{(k'')^2 - (k')^2}{(\eta'\eta'')^2}. \tag{6.7}$$

Substituting (6.4) and (6.6) in (6.5) and equating the terms with the same subscript, we obtain

$$a_m'' - a_m' = b_m, \qquad \rho' a_m' \eta' + \rho'' a_m'' \eta'' = 0, \tag{6.8}$$

whence

$$\begin{aligned} a_m' &= 2H_{xo} \frac{(k')^2 - (k'')^2}{\pi} \frac{m}{(\eta'\eta'')^2 (1 + \eta'\rho'/\eta''\rho'')}, \\ a_m'' &= -2H_{xo} \frac{(k')^2 - (k'')^2}{\pi} \frac{\rho'}{\rho''} \frac{m}{\eta' (\eta'')^3 (1 + \eta'\rho'/\eta''\rho'')}. \end{aligned} \tag{6.9}$$

Returning to (6.1) and (6.4), we write

$$H_x = \begin{cases} \dot{H}_x^{\mathrm{N}} + 2H_{xo} \dfrac{(k')^2 - (k'')^2}{\pi} \displaystyle\int_0^\infty \frac{me^{\eta' y} \sin mz\, dm}{(\eta'\eta'')^2 (1 + \eta'\rho'/\eta''\rho'')} & y \le 0 \\ \ddot{H}_x^{\mathrm{N}} - 2H_{xo} \dfrac{(k')^2 - (k'')^2}{\pi} \dfrac{\rho'}{\rho''} \displaystyle\int_0^\infty \frac{me^{-\eta'' y} \sin mz\, dm}{\eta' (\eta'')^3 (1 + \eta'\rho'/\eta''\rho'')} & y \ge 0. \end{cases} \tag{6.10}$$

Differentiation of the magnetic field H_x with respect to z gives the electric field E_y. On the Earth surface ($z = 0$):

$$E_y = \rho \frac{\partial H_x}{\partial z} = \begin{cases} \dot{E}_y^{\mathrm{N}} + 2H_{xo} \dfrac{(k')^2 - (k'')^2}{\pi} \rho' \displaystyle\int_0^\infty \frac{m^2 e^{\eta' y}\, dm}{(\eta'\eta'')^2 (1 + \eta'\rho'/\eta''\rho'')} & y \le 0 \\ \ddot{E}_y^{\mathrm{N}} - 2H_{xo} \dfrac{(k')^2 - (k'')^2}{\pi} \rho' \displaystyle\int_0^\infty \frac{m^2 e^{-\eta'' y}\, dm}{\eta' (\eta'')^3 (1 + \eta'\rho'/\eta''\rho'')} & y \ge 0, \end{cases} \tag{6.11}$$

where $\dot{E}_y^{\mathrm{N}}$, $\ddot{E}_y^{\mathrm{N}}$ are the normal electric fields within the left and right quarter-spaces.

The transverse impedance assumes the form:

$$Z^{\perp} = -\frac{E_y}{H_{xo}} = \begin{cases} \dot{Z}_N + 2\dfrac{(k'')^2 - (k')^2}{\pi}\rho' \int\limits_0^{\infty} \dfrac{m^2 e^{\eta' y}\, dm}{(\eta'\eta'')^2 (1 + \eta'\rho'/\eta''\rho'')} & y \le 0 \\ \ddot{Z}_N - 2\dfrac{(k'')^2 - (k')^2}{\pi}\ \rho' \int\limits_0^{\infty} \dfrac{m^2 e^{-\eta'' y}\, dm}{\eta' (\eta'')^3 (1 + \eta'\rho'/\eta''\rho'')} & y \ge 0, \end{cases} \tag{6.12}$$

where

$$\dot{Z}_N = -\dot{E}_y^N / H_{xo} = \sqrt{-i\omega\mu_o\rho'},$$

$$\ddot{Z}_N = -\ddot{E}_y^N / H_{xo} = \sqrt{-i\omega\mu_o\rho''},$$

$$\dot{Z}_N / \ddot{Z}_N = \dot{E}_y^N / \ddot{E}_y^N = \sqrt{\rho'/\rho''},$$

are the normal impedances for the left and right quarter-spaces. Here the transverse impedance consists of the normal impedance Z_N and a distortion term that at great distances from the vertical interface decays exponentially as $e^{-\mathrm{Im}\, k|y|} = e^{-|y|/\sqrt{2}h_{\mathrm{eff}}}$, where h_{eff} is the *effective penetration depth*

$$h_{\mathrm{eff}} = \frac{|Z_N|}{\omega\mu_o} = \sqrt{\frac{\rho}{\omega\mu_o}},$$

which can be used as a scale parameter of the magnetotelluric anomaly.

We have obtained rather simple analytical expression for the TM-mode. It would be interesting to supplement this result with numerical solution for the TE-mode. The TE-problem was solved using the finite element method (Wannamaker et al., 1987).

Figures 6.2 and 6.3 present the transverse and longitudinal apparent-resistivity and impedance-phase curves, $\rho^{\perp}/\rho'$, $\varphi^{\perp}$ and $\rho^{\parallel}/\rho'$, $\varphi^{\parallel}$ observed at a site over the left quarter-space. The dimensionless quantities $h'_{\mathrm{eff}}/|y|$ are plotted as abscissas. Here h'_{eff} is the effective penetration depth and $|y|$ is a distance from the vertical interface. With increasing h'_{eff} (lowering frequency) and with decreasing $|y|$ (going toward the vertical interface), the apparent resistivity departs from ρ', while the impedance phase departs from -45°. When $\rho'' > \rho'$, the transverse resistivities, $\rho^{\perp}$, quickly descend and the transverse phases, $\varphi^{\perp}$, have deep minima, while the longitudinal resistivities, $\rho^{\parallel}$, slowly ascend and the longitudinal phases, $\varphi^{\parallel}$, have flattened maxima. And vice versa, when $\rho'' < \rho'$, the longitudinal resistivities, $\rho^{\parallel}$, quickly descend and the longitudinall phases, $\varphi^{\parallel}$, have deep minima, while the transverse resistivities, $\rho^{\perp}$, slowly ascend and the transverse phases, $\varphi^{\perp}$,have flattened maxima. We see that the transverse and longitudinal curves conflict with each other. They come apart, so that descending of one curve corresponds to ascending of another curve. This effect will be called the *divergence effect*. Distortions of the transverse curves are of a galvanic nature, whereas the distortions of the longitudinal curves are of a

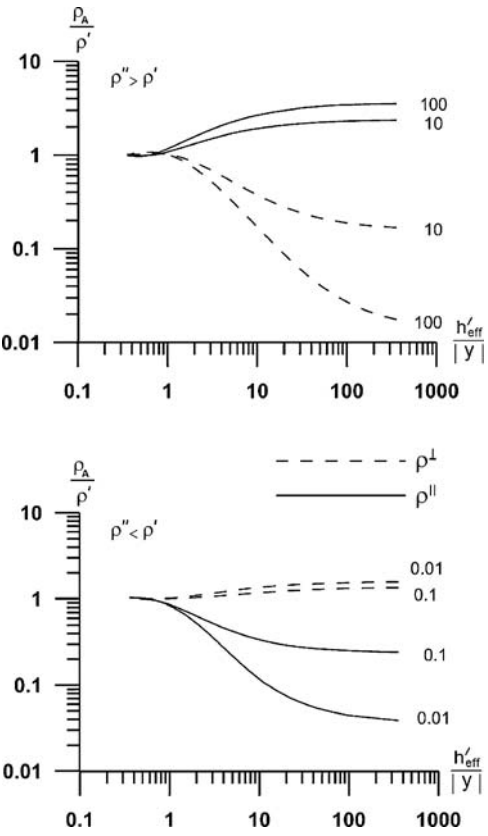

Fig. 6.2 Longitudinal and transverse apparent-resistivity curves in the vertical-interface model. Observation site is located over the left quarter-space. Curve parameter: ρ''/ρ'

induction nature. But it is remarkable that in spite of the different physical nature, both effects vanish at closely related distances. Distortions of the apparent resistivities $\rho^{\perp}$, $\rho^{\parallel}$ attenuate at $|y| \approx 1.25\, h'_{\text{eff}}$. Distortions of the phases $\varphi^{\perp}$, $\varphi^{\parallel}$ run to greater distances and attenuate at $|y| \approx 3\, h'_{\text{eff}}$.

To gain a better insight into the physical nature of these distortions, we turn to Figures 6.4 and 6.5, which show the $E_x(y)$, $H_y(y)$ and $E_y(y)$-profiles related to the TE- and TM-modes. The fields E_x, E_y, H_y vary from the left normal fields $\dot{E}_x^{\text{N}}$, $\dot{E}_y^{\text{N}}$, $\dot{H}_y^{\text{N}}$ to the right normal fields $\ddot{E}_x^{\text{N}}$, $\ddot{E}_y^{\text{N}}$, $\ddot{H}_y^{\text{N}}$. They are normalized to the right normal field. Note that $\dot{E}_x^{\text{N}} \neq \ddot{E}_x^{\text{N}}$, $\dot{E}_y^{\text{N}} \neq \ddot{E}_y^{\text{N}}$, $\dot{H}_y^{\text{N}} = \ddot{H}_y^{\text{N}}$.

The smooth monotonous transition from $\dot{E}_x^{\text{N}} = \ddot{E}_x^{\text{N}} \sqrt{\rho'_1/\rho''_1}$ to $\ddot{E}_x^{\text{N}}$ is accounted for by the mutual induction of the longitudinal excess currents. It consists of two zones. Within the left ("conductive") quarter-space we have a zone of the current concentration. Within the right ("resistive") quarter-space we have a zone of the current deconcentration. The concentration and deconcentration zones manifest themselves in the maximum and minimum of the transverse magnetic field H_y. At high frequencies, both the zones and the corresponding magnetic anomalies narrow in the

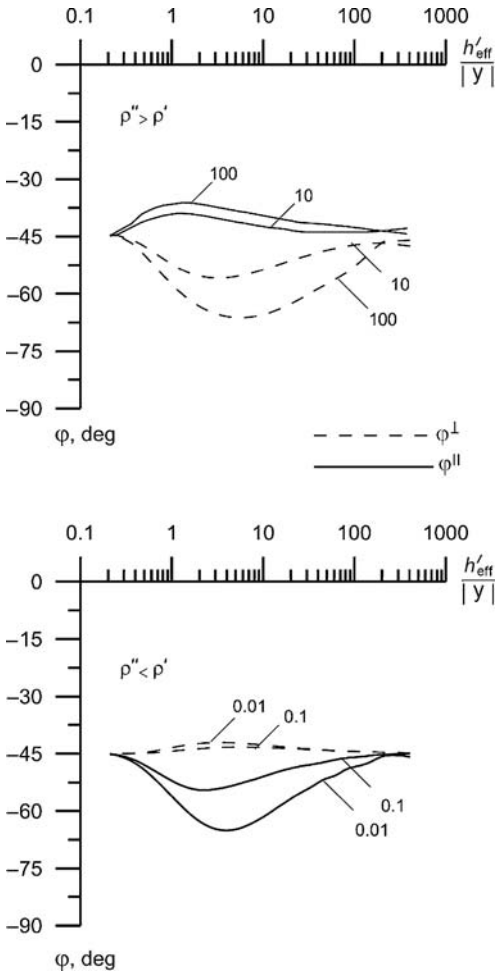

Fig. 6.3 Longitudinal and transverse impedance-phase curves in the vertical-interface model. Observation site is located over the left quarter-space. Curve parameter: ρ''/ρ'

vicinity of the vertical interface. With lowering frequency, the anomalies of E_x and H_y flatten out. This effect can be considered as the *horizontal skin effect.*

The transverse electric field E_y varies also from the left normal field $\dot{E}_y^{\mathrm{N}} = \ddot{E}_y^{\mathrm{N}}\sqrt{\rho'/\rho''}$ to the right normal field $\ddot{E}_y^{\mathrm{N}}$, but now it has a jump at the vertical interface due to surface excess charges. The characteristic feature of the transverse electric field is that its jump is preceded in the left quarter-space by almost a tenfold drop in E_y, which is getting steeper when frequency increases. This effect is associated with rearrangement of the transverse current due to different skin depths in the left and right quarter-spaces. It bears the name of the *current rearrangement effect.*

Next we consider the frequency responses of the real and imaginary parts of the tipper W_{zy} at a site over the left quarter-space (Fig. 6.6). It is remarkable that the $\mathrm{Re}W_{zy}$, $\mathrm{Im}W_{zy}$-curves for $\rho''/\rho' = 10$ and $\rho''/\rho' = 0.1$ are aproximately

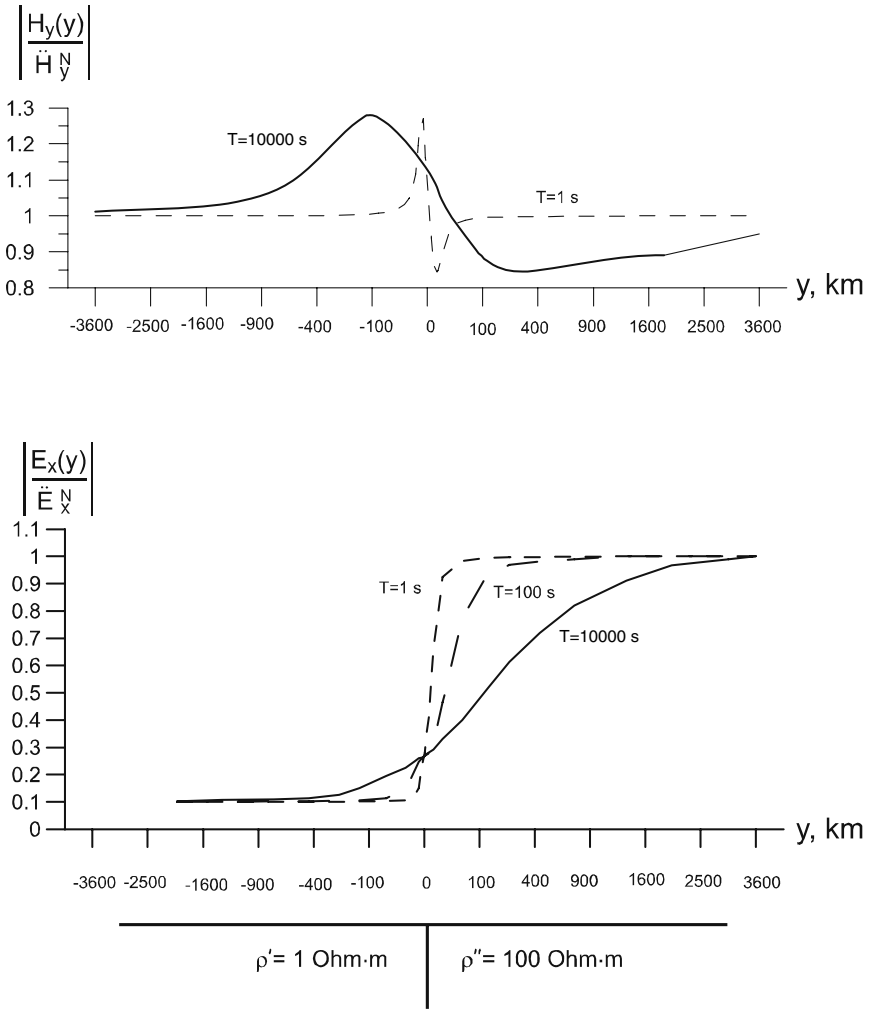

Fig. 6.4 The electric and magnetic field profiles in the vertical-interface model (TE-mode). Model parameters: $\rho' = 1\,\text{Ohm} \cdot \text{m}$, $\rho'' = 100\,\text{Ohm} \cdot \text{m}$. Profile parameter: period T=1, 100, 10000 s

symmetric. Note that $\text{Re}W_{zy}$, $\text{Im}W_{zy}$ are positive for $\rho''/\rho' = 10$ and negative for $\rho''/\rho' = 0.1$. So, the real and imaginary induction arrows plotted by $\text{Re}W_{zy}$, $\text{Im}W_{zy}$ are directed from the quarter-space of lower resistivity to the quarter-space of higher resistivity. But it is significant that at low frequencies the imaginary arrows vanish, while the real arrows achieve their maximum.

In closing we take a brief look at the $W_{zy}-$profiles shown in Fig. 6.7. The $\text{Re}W_{zy}$-profiles contain a nearly symmetric maximum just over the vertical interface. Its width is of the order 3 $(h'_{\text{eff}} + h''_{\text{eff}})$. The $\text{Im}W_{zy}-$profiles contain two maxima separated by a deep spike minimum at the vertical interface. The total width of this

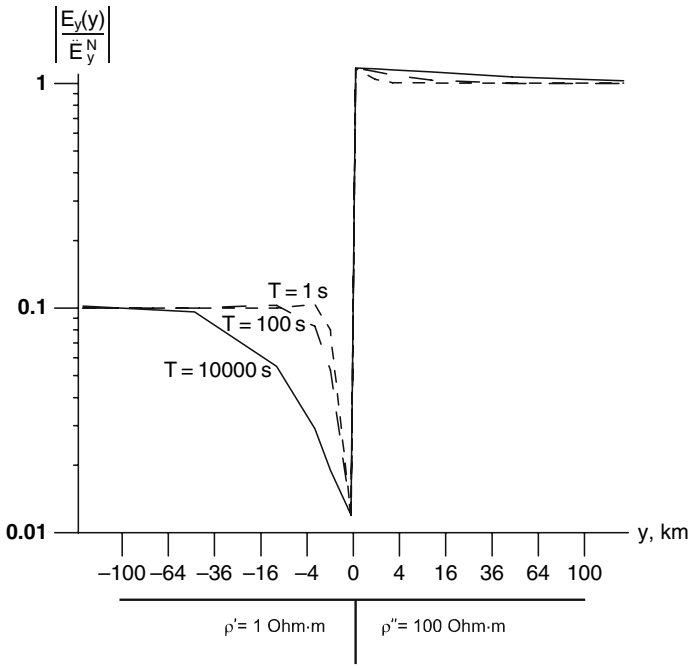

Fig. 6.5 The electric field profiles in the vertical-interface model (TM-mode) Model parameters: $\rho' = 1$ Ohm $\cdot$ m, $\rho'' = 100$ Ohm $\cdot$ m. Profile parameter: period T=1, 100, 10000 s

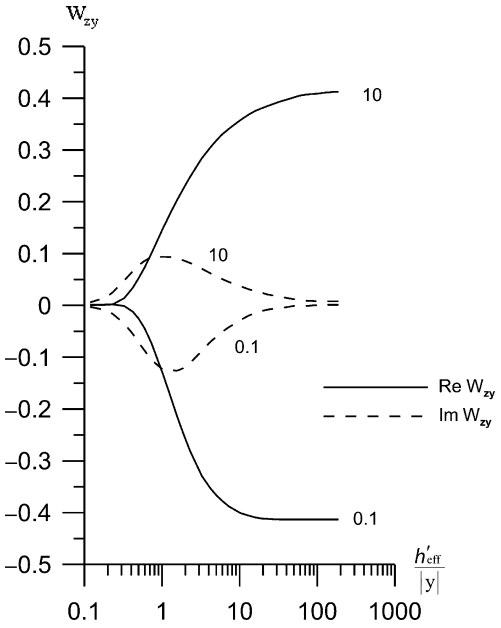

Fig. 6.6 The tipper W_{zy} over the left quarter-space. Curve parameter: ρ''/ρ'

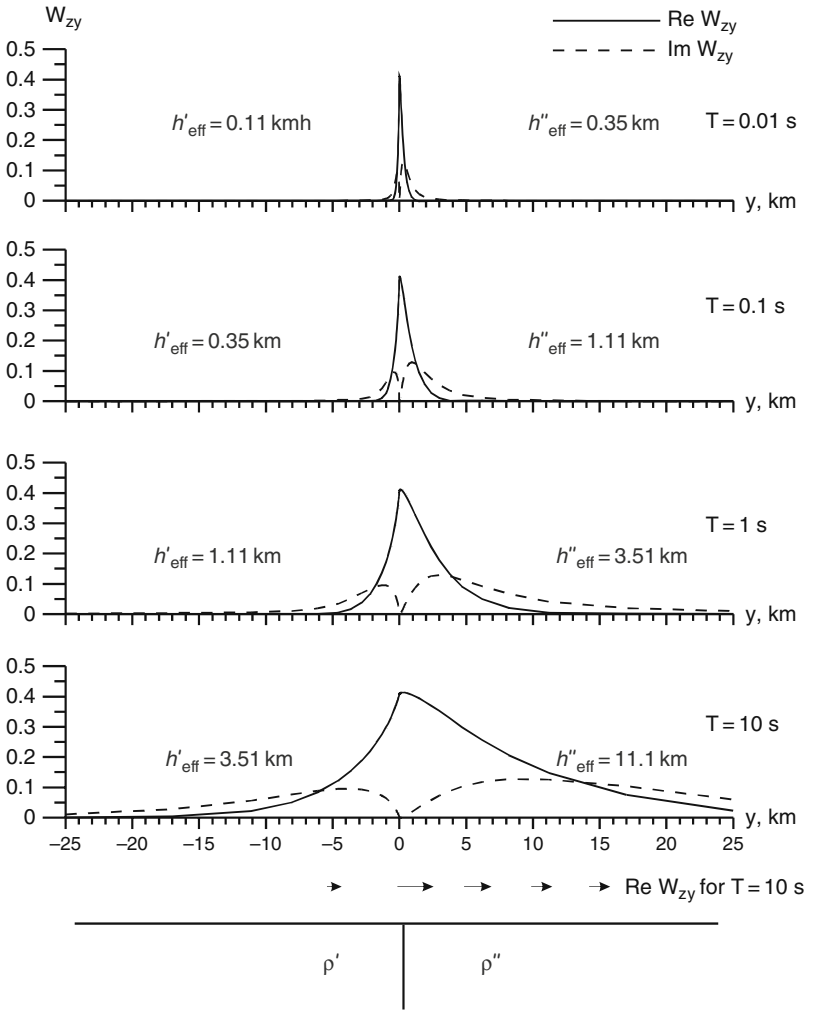

Fig. 6.7 Profiles of the tipper W_{zy} in the vertical-interface model. Model parameters: $\rho' = 10$ Ohm·m, $\rho'' = 100$ Ohm · m

anomaly is about 5 $(h'_{\text{eff}} + h''_{\text{eff}})$. The real inductive arrows are shown at the bottom of Fig. 6.7. They radiate from left to right, that is, from lower to higher resistivity.

6.2 The Dike Model

This two-dimensional model has been advanced by Rankin (1962). It can give an idea of local magnetotelluric anomalies. The model consists of the nonconductive air and the conductive Earth of resistivity ρ' that includes a dike of width $2v$ and

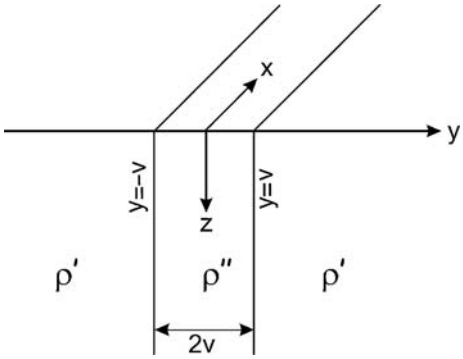

Fig. 6.8 The dike model

resistivity ρ'' bounded by the infinite vertical interfaces, $y = -v,\ 0 \le z \le \infty$ and $y = v,\ 0 \le z \le \infty$ (Fig. 6.8).

Let us begin with solution for the TM-mode. By analogy with (6.1), we write

$$H_x(y,z) = \begin{cases} \dot{H}_x^{\mathrm{N}}(z) + \dot{H}_x^{\mathrm{A}}(y,z) & |y| \ge v,\ z \ge 0 \\ \ddot{H}_x^{\mathrm{N}}(z) + \ddot{H}_x^{\mathrm{A}}(y,z) & |y| \le v,\ z \ge 0, \end{cases} \tag{6.13}$$

where $\dot{H}_x^{\mathrm{N}}$, $\dot{H}_x^{\mathrm{A}}$ and $\ddot{H}_x^{\mathrm{N}}$, $\ddot{H}_x^{\mathrm{A}}$ are the normal and anomalous magnetic fields outside and inside the dike.

Solving equations (6.3) and taking into account the symmetry conditions, we get

$$H_x^{\mathrm{A}} = \begin{cases} \dot{H}_{\mathrm{x}}^{\mathrm{A}} = \int\limits_0^\infty a'_m e^{-\eta'|y|} \sin mz\, dm & |y| \ge v \\ \ddot{H}_x^{\mathrm{A}} = \int\limits_0^\infty a''_m \cosh \eta'' y \sin mz\, dm & |y| \le v, \end{cases} \tag{6.14}$$

where

$$\eta' = \sqrt{m^2 - (k')^2}, \qquad \eta'' = \sqrt{m^2 - (k'')^2}, \qquad \mathrm{Re}\ \eta > 0.$$

The constants a'_m and a''_m are defined from the boundary conditions at the vertical interfaces $y = \pm v$. Similarly to (6.5),

$$\left.\begin{array}{c} \dot{H}_x^{\mathrm{N}} - \ddot{H}_x^{\mathrm{N}} = \ddot{H}_x^{\mathrm{A}} - \dot{H}_x^{\mathrm{A}} \\ \rho' \frac{\partial \dot{H}_x^{\mathrm{A}}}{\partial y} = \rho'' \frac{\partial \ddot{H}_x^{\mathrm{A}}}{\partial y} \end{array}\right|_{|y|=v}, \tag{6.15}$$

where, according to (6.6) and (6.7),

$$\dot{H}_x^{\mathrm{N}} - \ddot{H}_x^{\mathrm{N}} = H_{x\mathrm{o}}(e^{ik'z} - e^{ik''z}) = \int_0^\infty b_m \sin mz \, dm$$

and

$$b_m = \frac{2mH_{x\mathrm{o}}}{\pi} \frac{(k'')^2 - (k')^2}{(\eta'\eta'')^2} .$$

Substituting (6.14) and (6.6) in (6.15) and equating the terms with the same subscript, we obtain

$$a_m'' \cos\ \mathrm{h}\eta''v - a_m' e^{-\eta' v} = b_m, \qquad \rho' a_m' \eta' e^{-\eta' v} + \rho'' a_m'' \eta'' \sin\ \mathrm{h}\eta'' v = 0, \quad (6.16)$$

whence

$$\begin{aligned} a_m' &= \frac{2mH_{x\mathrm{o}}}{\pi} \frac{(k')^2 - (k'')^2}{(\eta')^3\eta''} \frac{\rho''}{\rho'} \frac{e^{\eta' w} \sin\ \mathrm{h}\eta'' v}{\cos\ \mathrm{h}\eta'' v + \dfrac{\rho''\eta''}{\rho'\eta'} \sin\ \mathrm{h}\eta'' v} \\ a_m'' &= -\frac{2mH_{x\mathrm{o}}}{\pi} \frac{(k')^2 - (k'')^2}{(\eta'\eta'')^2} \frac{1}{\cos\ \mathrm{h}\eta'' v + \dfrac{\rho''\eta''}{\rho'\eta'} \sin\ \mathrm{h}\eta'' v} . \end{aligned} \quad (6.17)$$

Then, with a glance to (6.13) and (6.14),

$$H_x = \begin{cases} \dot{H}_x^{\mathrm{N}} + 2H_{x\mathrm{o}} \dfrac{(k')^2 - (k'')^2}{\pi} \dfrac{\rho''}{\rho'} \displaystyle\int_0^\infty \frac{m \sin\ \mathrm{h}\eta'' v}{(\eta')^3\eta''} \frac{e^{-\eta'(|y|-v)} \sin mz \, dm}{\cos\ \mathrm{h}\eta'' v + \dfrac{\rho''\eta''}{\rho'\eta'} \sin\ \mathrm{h}\eta'' v} & |y| \geq v \\ \ddot{H}_x^{\mathrm{N}} - 2H_{x\mathrm{o}} \dfrac{(k')^2 - (k'')^2}{\pi} \displaystyle\int_0^\infty \frac{m}{(\eta'\eta'')^2} \frac{\cos\ \mathrm{h}\eta'' y \ \sin mz \, dm}{\cos\ \mathrm{h}\eta'' v + \dfrac{\rho''\eta''}{\rho'\eta'} \sin\ \mathrm{h}\eta'' v} & |y| \leq v \end{cases} \quad (6.18)$$

and

$$E_y\big|_{z=0} = \begin{cases} \dot{E}_y^{\mathrm{N}} + 2H_{x\mathrm{o}} \dfrac{(k')^2 - (k'')^2}{\pi} \rho'' \displaystyle\int_0^\infty \frac{m^2 \sin\ \mathrm{h}\eta'' v}{(\eta')^3\eta''} \frac{e^{-\eta'(|y|-v)} \, dm}{\cos\ \mathrm{h}\eta'' v + \dfrac{\rho''\eta''}{\rho'\eta'} \sin\ \mathrm{h}\eta'' v} & |y| \geq v \\ \ddot{E}_y^{\mathrm{N}} - 2H_{x\mathrm{o}} \dfrac{(k')^2 - (k'')^2}{\pi} \rho'' \displaystyle\int_0^\infty \frac{m^2}{(\eta'\eta'')^2} \frac{\cos\ \mathrm{h}\eta'' y \ dm}{\cos\ \mathrm{h}\eta'' v + \dfrac{\rho''\eta''}{\rho'\eta'} \sin\ \mathrm{h}\eta'' v} & |y| \leq v . \end{cases} \quad (6.19)$$

The transverse impedance assumes the form:

$$Z^{\perp} = \begin{cases} \dot{Z}_{\mathrm{N}} + 2\dfrac{(k'')^2 - (k')^2}{\pi}\rho'' \int\limits_0^{\infty} \dfrac{m^2 \sin\ \mathrm{h}\eta'' v}{(\eta')^3 \eta''} \dfrac{e^{-\eta'(|y|-v)}\, dm}{\cos\ \mathrm{h}\eta'' v + \dfrac{\rho''\eta''}{\rho'\eta'} \sin\ \mathrm{h}\eta'' v} & |y| \geq v \\ \ddot{Z}_{\mathrm{N}} - 2\dfrac{(k'')^2 - (k')^2}{\pi}\rho'' \int\limits_0^{\infty} \dfrac{m^2}{(\eta'\eta'')^2} \dfrac{\cos\ \mathrm{h}\eta'' y\ dm}{\cos\ \mathrm{h}\eta'' v + \dfrac{\rho''\eta''}{\rho'\eta'} \sin\ \mathrm{h}\eta'' v} & |y| \leq v\,. \end{cases} \tag{6.20}$$

Here, similar to the vertical-interface model, the transverse impedance consists of the normal impedances $\dot{Z}_{\mathrm{N}}$, $\ddot{Z}_{\mathrm{N}}$ and distortion terms. At great distances from the dike, $|y| >> v$, the distortion terms decay exponentially as $e^{-\mathrm{Im}\, k'\, \Delta y} = e^{-\Delta y/\sqrt{2} h'_{\mathrm{eff}}}$, where $\Delta y = |y| - v$ is the distance from the dike edge and h'_{eff} is the effective penetration depth.

Again, as in the vertical-interface model, we supplement the analytical solution with numerical solution using the finite element method (Wannamaker et al., 1987).

We consider a dike 1 km wide in the half-space of resistivity $\rho' = 10$ Ohm·m. The dike of restivity $\rho'' = 100$ Ohm·m is said to be "resistive" and the dike of resistivity $\rho'' = 1$ Ohm·m is said to be "conductive".

Figures 6.9 demonstrates the apparent-resistivity, impedance-phase and tipper curves obtained on the left of the dike. The observation site is located at the distance $\Delta y = |y| - v = 100$ m from the dike. Let us compare the apparent-resistivty and impedance-phase curves with locally normal curves of $\dot{\rho}_{\mathrm{n}} = \left|\dot{Z}_{\mathrm{N}}\right|^2 \Big/ \omega\mu_{\mathrm{o}} = \rho'$ and $\dot{\varphi}_{\mathrm{n}} = \arg \dot{Z}_{\mathrm{N}} = -45^{\mathrm{o}}$ characterizing the homogeneous vicinity of the dike. Look at the apparent-resistivity curves. At high frequencies the longitudinal $\rho^{\parallel}-$curves and the transverse $\rho^{\perp}-$curves coincide with the locally normal $\dot{\rho}_{\mathrm{n}}$-curve. The induction and galvanic effects of the dike become evident at frequencies, on which the effective penetration depth exceeds the distance to the dike, $h'_{\mathrm{eff}} > 100$ m. With lowering frequency these effects attenuate and the apparent-resistivity curves merge again with the locally normal $\dot{\rho}_{\mathrm{n}}$-curve. The resistive dike manifests itself in the bell-type $\rho^{\parallel}-$curve and the bowl-type $\rho^{\perp}-$curve, whereas the conductive dike manifests itself in the bowl-type $\rho^{\parallel}-$curve and the bell-type $\rho^{\perp}-$curve. Similar divergence effects are characteristic of the phase curves, $\varphi^{\parallel}$ and $\varphi^{\perp}$. We can say that in the vicinity of the dike the magnetotelluic sounding reflects the horizontal resistivity distribution. Come now to the tipper curves. It is notable that the conductive dike causes more intensive magnetovariational anomaly than the resistive one. Note also that the $\mathrm{Re}W_{zy}-$curve is bell-type on the left of the resistive dike, while it is bowl-type on the left of the conductive dike. At the same time, $\mathrm{Im}W_{zy}$ varies in sign, and with lowering frequency it may go from one quadrant to another.

Next examine the magnetotelluric response functions, obtained over the middle of the resistive and conductive dikes (Fig. 6.10). Compare the apparent-resistivty and impedance-phase curves with locally normal curves of $\ddot{\rho}_{\mathrm{n}} = \left|\ddot{Z}_{\mathrm{N}}\right|^2 \Big/ \omega\mu_{\mathrm{o}} = \rho''$,

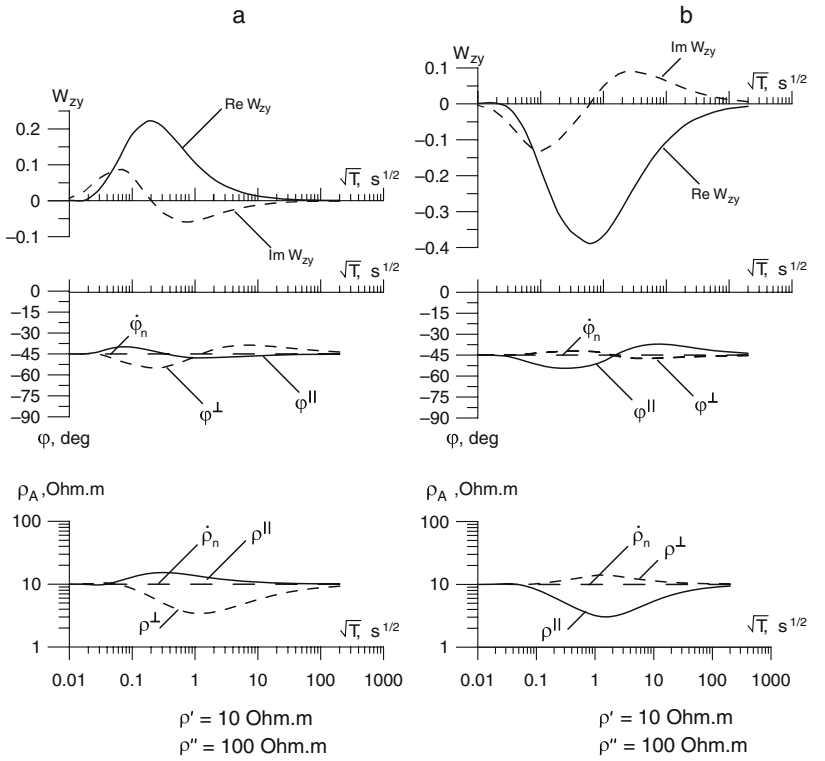

Fig. 6.9 Curves for the apparent resistivity, impedance phase and tipper, obtained on the left of the dike. The observation site is located at the distance 100 m from the dike; a – resistive dike, $v = 0.5$ km, $\rho' = 10$ Ohm · m, $\rho'' = 100$ Ohm · m ; b – conductive dike, $v = 0.5$ km, $\rho' = 10$ Ohm · m, $\rho'' = 1$ Ohm · m

$\ddot{\varphi}_n = \arg\ddot{Z}_N = -45^o$and $\dot{\rho}_n = \left|\dot{Z}_N\right|^2 \Big/ \omega\mu_o = \rho'$, $\dot{\varphi}_n = \arg\dot{Z}_N = -45^o$. Let us begin with a high-frequency range where the effective penetration depth is less than the half-width of the dike, $h''_{\text{eff}} < 0.5$ km. Here the $\rho^{\parallel}-$curves and $\rho^{\perp}-$curves are undistorted, they coincide with the locally normal $\ddot{\rho}_n$-curve characterizing the dike. With lowering frequency we observe the strong divergence effect. The curves for $\rho^{\parallel}$ and $\rho^{\perp}$ depart up and down from the $\ddot{\rho}_n$-curve. Here the the longitudinal resistivities $\rho^{\parallel}$ smooth the effect of the dike, while the transverse resistivities $\rho^{\perp}$ exxagerate the effect of the dike. With $h''_{\text{eff}} > 75$ km, the longitudinal $\rho^{\parallel}-$curves approach the locally normal $\dot{\rho}_n$-curve characterizing the surrounding medium.

The E_x- and H_y-profiles (the TE-mode) and the E_y-profiles (the TM-mode) are shown in Figs. 6.11 and 6.12. The electric and magnetic fields are normalized to their values at infinity, $E_x(\infty) = \dot{E}^N_x$, $E_y(\infty) = \dot{E}^N_y$, $H_y(\infty) = \dot{H}^N_y$.

Anomalies of E_x and H_y are of the induction nature. The resistive dike manifests itself in the maximum of E_x and the minimum of H_y. The conductive dike manifests

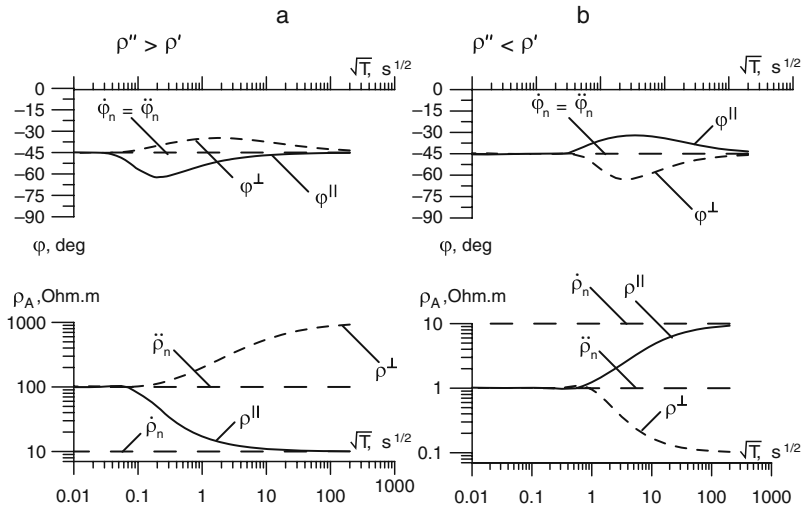

Fig. 6.10 Curves for the apparent resistivity and impedance phase, obtained in the middle of the dike ($y = 0$); a – resistive dike, $v = 0.5$ km, $\rho' = 10$ Ohm·m, $\rho'' = 100$ Ohm·m ; b – conductive dike, $v = 0.5$ km, $\rho' = 10$ Ohm · m, $\rho'' = 1$ Ohm · m

itself in the minimum of E_x and the maximum of H_y. Outside the dike these anomalies quickly attenuate. Give your attention to the side maxima and minima of H_y bordering the resistive and conductive dike at high frequencies ($T = 0.01$ s for the resistive dike and $T = 1$ s for the conductive dike). These extrema reflect the horizontall skin effect at the dike edges. With lowering frequency the anomalies of E_x and H_y diminish. They die out provided $h''_{\text{eff}} >> 2v$ ($T = 100$ s in the case of the resistive dike and $T = 10000$ s in the case of the conductive dike). We see that resolving power of E_x and H_y decreases with depth.

Anomalies of E_y are of the galvanic nature. They have a jump on the dike edges and produce strongly pronounced maxima (over the resistive dike) and minima (over the conductive dike). These extrema are fringed by the side minima and maxima of E_y associated with rearrangement of the transverse currents due to different skin depth in the dike and in the ambient medium. With lowering frequency the side extrema vanish, while the central extrema take the rectangular form.

In closing consider the W_{zy}-profiles given in Fig. 6.13. The resistive and conductive dikes manifest themselves in zigzag anomalies of $\text{Re}W_{zy}$ and $\text{Im}W_{zy}$ with maximum and minimum over the dike edges. The resistive dike makes a zigzag with left maximum and right minimum, whereas the conductive dike makes a zigzag with right maximum and left minimum. The width of anomalies is of the order of $10h'_{\text{eff}}$. With lowering frequency the anomalies decay, faster for the resistive dike and slower for the conductive dike. At the bottom of Fig. 6.13 the real inductive arrows are shown. They converge to the resistive dike and diverge outward from the conductive dike.

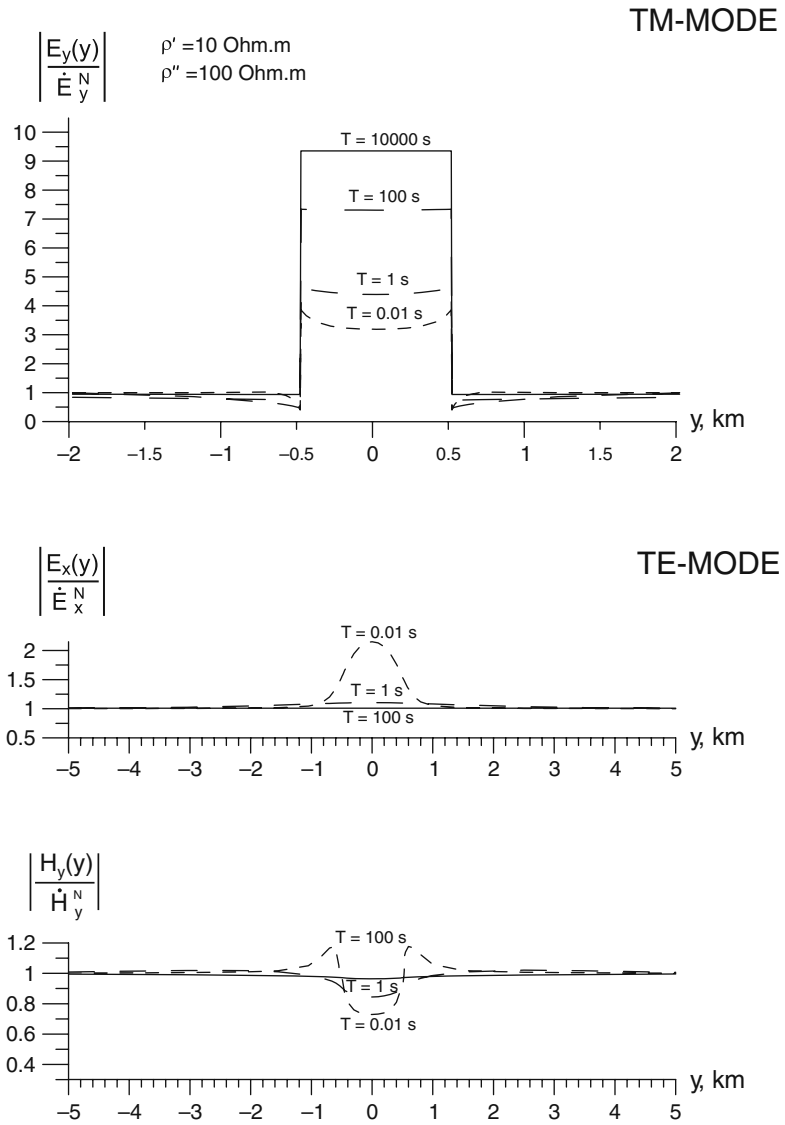

Fig. 6.11 Profiles of the electromagnetic field in the model with the resistive dike; $v = 0.5\,\text{km}$, $\rho' = 10\ \text{Ohm} \cdot \text{m}$, $\rho'' = 100\ \text{Ohm} \cdot \text{m}$

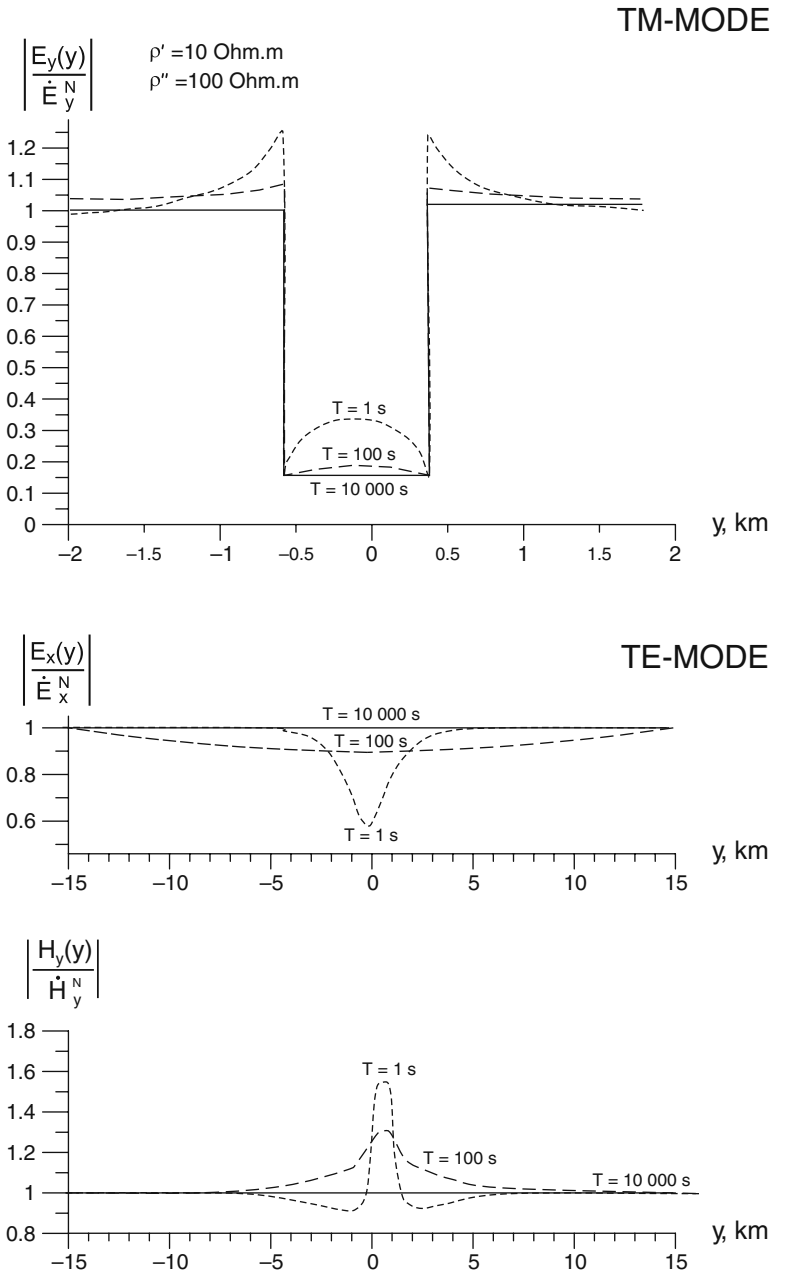

Fig. 6.12 Profiles of the electromagnetic field in the model with the conductive dike; $v = 0.5\,\text{km}$, $\rho' = 10\ \text{Ohm} \cdot \text{m}$, $\rho'' = 1\ \text{Ohm} \cdot \text{m}$

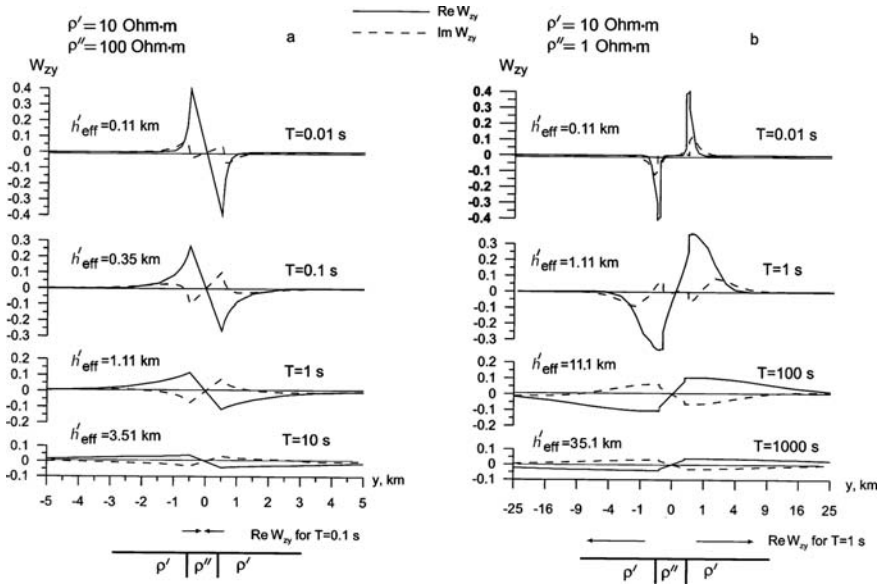

Fig. 6.13 Profiles of the tipper in the dike model; a – resistive dike, $v = 0.5\,\text{km}$, $\rho' = 10\ \text{Ohm} \cdot \text{m}$, $\rho'' = 100\ \text{Ohm} \cdot \text{m}$; b – conductive dike, $v = 0.5\,\text{km}$, $\rho' = 10\ \text{Ohm} \cdot \text{m}$, $\rho'' = 1\ \text{Ohm} \cdot \text{m}$

Chapter 7
Models of the Near-Surface Distortions

We will consider three kinds of near-surface effects distorting the magnetotelluric field: (1) effects of small-scale inclusions located at shallow depth or even outcropped, (2) effects, caused by variations in the conductance of sediments underlaid with resistive basement, and (3) effects caused by structures in the basement topography. Our concern is to gain a more penetrating insight into physical mechanisms of distorting effects.

7.1 Distortions Caused by Small-Scale Near-Surface Inclusions

This kind of distortions will be referred to as ρ-*effect*. Let us examine two-dimensional and three-dimensional ρ-effects.

7.1.1 The Two-Dimensional ρ-Effect of the Semicylinder and Prism

A model of the two-dimensional ρ-effect that provides simple analytic solution is presented in Fig. 7.1. The model consists of three layers: the sediments (ρ_1', h_1), the resistive lithosphere ($\rho_2 >> \rho_1',\ h_2 >> h_1$), and the conductive mantle (ρ_3). The sediments contain an outcropped inclusion in the form of an infinitely long horizontal semicylinder (ρ_1'', $a << h_1$). Assume that at the periods under consideration the effective penetration depth h_{eff} is many times larger than the semicylinder radius a. So, considering the anomalous field, caused by the inclusion, we can neglect the induction effects and reduce the problem to the direct-current statement demonstrating the galvanic effects in the TM-mode.

Introduce a cylindrical coordinate system r, θ, x with x being the axis of the semicylinder. Ignoring influence of lithosphere and mantle, we determine the scalar potential of the electric field in the Earth as

M. Berdichevsky, V.I. Dmitriev, *Models and Methods of Magnetotellurics*,
DOI 10.1007/978-3-540-77814-1_7,

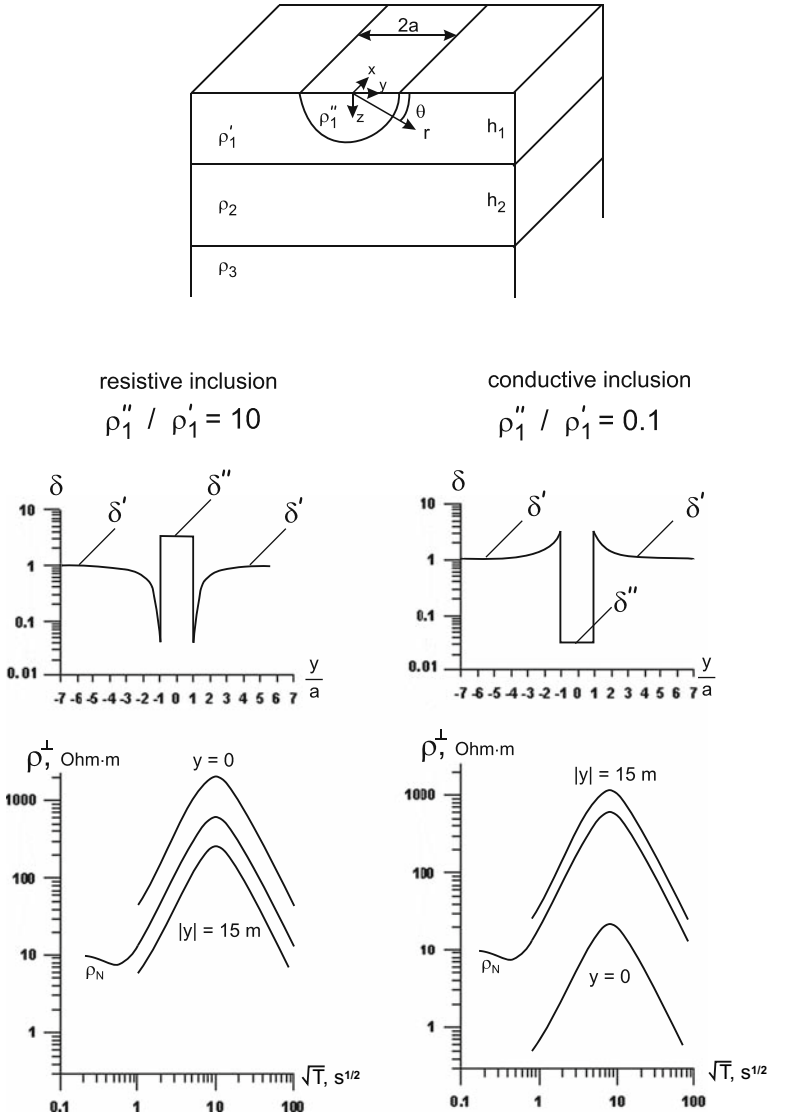

Fig. 7.1 Two-dimensional ρ-effect of the outcropped small-scale semicylinder; model parameters: $\rho_1' = 10$ Ohm·m, $h_1 = 1$ km, $\rho_2 = 100000$ Ohm·m, $h_2 = 124$ km, $\rho_3 = 0$, $a = 10$ m; conductive semicylinder $\rho_1'' = 1$ Ohm·m, resistive semicylinder $\rho_1'' = 100$ Ohm·m

$$U(r,\theta,\omega)=\begin{cases}E_y^{\mathrm{N}}(\omega)\left\{-r\cos\theta+\dfrac{\rho_1'-\rho_1''}{\rho_1'+\rho_1''}\dfrac{a^2\cos\theta}{r}\right\} & \text{for} \quad r\geq a\\ -E_y^{\mathrm{N}}(\omega)\dfrac{2\rho_1''}{\rho_1'+\rho_1''}r\cos\theta & \text{for} \quad r\leq a,\end{cases} \tag{7.1}$$

where $E_y^{\mathrm{N}}(\omega)$ is the normal electric field on the Earth's surface $z=0$ (Smythe, 1950). The function U satisfies the boundary conditions

$$\left.\frac{\partial U}{\partial\theta}\right|_{\theta=+0,\pi-0}=0 \qquad U|_{r=a+0}=U|_{r=a-0} \qquad \left.\frac{1}{\rho_1'}\frac{\partial U}{\partial r}\right|_{r=a+0}=\left.\frac{1}{\rho_1''}\frac{\partial U}{\partial r}\right|_{r=a-0}.$$

On differentiating U, we get the electric field along the y-axis:

$$\begin{aligned}E_y(y,\omega)=E_y(y,z=0,\omega)&=-\left.\frac{\partial U(r,\theta,\omega)}{\partial r}\right|_{\theta=0}\\ &=\begin{cases}\left\{1+\dfrac{\rho_1'-\rho_1''}{\rho_1'+\rho_1''}\dfrac{a^2}{y^2}\right\}E_y^{\mathrm{N}}(\omega) & \text{for} \quad |y|\geq a\\ \dfrac{2\rho_1''}{\rho_1'+\rho_1''}E_y^{\mathrm{N}}(\omega) & \text{for} \quad |y|\leq a,\end{cases}\end{aligned} \tag{7.2}$$

whence

$$Z^{\perp}(y,\omega)=-\frac{E_y(y,\omega)}{H_x^{\mathrm{N}}}=\begin{cases}\left\{1+\dfrac{\rho_1'-\rho_1''}{\rho_1'+\rho_1''}\dfrac{a^2}{y^2}\right\}Z_{\mathrm{N}}(\omega) & \text{for} \quad |y|\geq a\\ \dfrac{2\rho_2''}{\rho_1'+\rho_1''}Z_{\mathrm{N}}(\omega) & \text{for} \quad |y|\leq a,\end{cases} \tag{7.3}$$

where H_x^{N} is the normal magnetic field on the Earth's surface and $Z_{\mathrm{N}}=-E_y^{\mathrm{N}}/H_x^{\mathrm{N}}$ is the normal impedance.

Thus,

$$\rho^{\perp}(y,\omega)=\frac{\left|Z^{\perp}(y,\omega)\right|^2}{\omega\mu_{\mathrm{o}}}=\begin{cases}\left\{1+\dfrac{\rho_1'-\rho_1''}{\rho_1'+\rho_1''}\dfrac{a^2}{y^2}\right\}^2\rho_{\mathrm{N}}(\omega)=\delta'\rho_{\mathrm{N}}(\omega) & \text{for} \quad |y|\geq a\\ \left\{\dfrac{2\rho_1''}{\rho_1'+\rho''}\right\}^2\rho_{\mathrm{N}}(\omega)=\delta''\rho_{\mathrm{N}}(\omega) & \text{for} \quad |y|\leq a,\end{cases} \tag{7.4}$$

where $\rho_{\mathrm{N}}=|Z_{\mathrm{N}}|^2/\omega\mu_0$ is the normal apparent resistivity and δ',δ'' are the real frequency-independent distortion factors

$$\delta'=\left\{1+\frac{\dfrac{\rho_1'}{\rho_1''}-1}{\dfrac{\rho_1'}{\rho_1''}+1}\frac{a^2}{y^2}\right\},\ \delta''=\left\{\frac{2}{\dfrac{\rho_1'}{\rho_1''}+1}\right\}^2. \tag{7.5}$$

In the traditional log − representation

$$\log \rho^{\perp}(y, \omega) = \log \rho_{N}(\omega) + \begin{cases} \log \delta' & \text{for} \quad |y| \geq a \\ \log \delta'' & \text{for} \quad |y| \leq a. \end{cases} \tag{7.6}$$

So, the MTS-distortion defined in accordance to (1.101) is

$$\Delta\rho^{\perp} = \log \rho^{\perp} - \log \rho_{N} = \log \delta.$$

It is evident that electric charges accumulated at the inclusion surface produce the galvanic anomaly, which manifests itself in the vertical *static shift* of the transverse apparent-resistivity curves. The magnitude $\log \delta$ of the static shift is defined by ρ_1'/ρ_1''. This effect goes under the name of ρ–*effect*. Beginning with a critical frequency that depends on the inclusion size, the ρ−effect shifts the low-frequency branches of the $\rho^{\perp}$−curves up or down. It does not change the shape of shifted $\rho^{\perp}$− curves and does not affect the corresponding impedance-phase curves.

Let us consider a model with $\rho_1' = 10$ Ohm·m, $h_1 = 1$km, $\rho_2 = 10^5$ Ohm·m, $h_2 = 124$ km, $\rho_3 = 0$, and $a = 10$ m, $\rho_1'' = 100$ Ohm·m ("resistive" inclusion) or 1 Ohm·m ("conductive" inclusion). The semicylinder radius a is several orders less than the effective penetration depth h_{eff} required for the sufficiently complete information on $\rho_N(z)$. Look at the graphs of δ and the apparent-resistivity curves of $\rho^{\perp}$ presented in Fig. 7.1. In the vicinity of the resistive inclusion we see a drastic fall of δ' caused by deconcentration of currents flowing under the inclusion. Here $\delta' < 1$ and the $\rho^{\perp}$–curve with its ascending and descending branches is shifted downward. Over the resistive inclusion $\delta'' > 1$ and the $\rho^{\perp}$−curve with its ascending and descending branches is shifted upward. But note that δ'' does not exceed 4 even if ρ_1'' is infinitely large. Exactly the converse situation is characteristic of the conductive inclusion. In its vicinity we have a rise of δ' caused by concentration of currents flowing into the inclusion. Here $\delta' > 1$ and the $\rho^{\perp}$−curve with its ascending and descending branches is shifted upward, but δ' does not exceed 4 even if ρ_1'' is infinitesimal. Over the conductive inclusions we see a drastic fall of δ'' and the $\rho^{\perp}$−curve with its ascending and descending branches is shifted profoundly downward.

Similar effect is observed in a model with a prismatic outcropped conductive inclusion (Fig. 7.2). The computations have been performed using the finite-element method (Wannamaker et al., 1987). Look upon the apparent-resistivity and impedance-phase curves obtained over the middle of the inclusion ($y = 0$). The $\rho^{\perp}$-curve with its ascending and descending branches is shifted downward more than by one decade. But in form it is almost identical to the normal ρ_N-curve. This static effect does not affect the $\varphi^{\perp}$-curve, whose ascending and descending branches merge with the normal φ_N-curve.

The immediate interpretation of the $\rho^{\perp}$-curve distorted by the ρ −effect would yield dramatic errors in the sediments conductance and depth to the conductive mantle. Fortunately the distorted TM-mode is accompanied by the TE-mode that is hardly distorted: the ascending and descending branches of the curves for $\rho^{\parallel}$, $\varphi^{\parallel}$ merge with the normal ρ_N- and φ_N-curves.

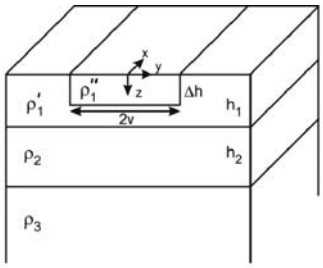

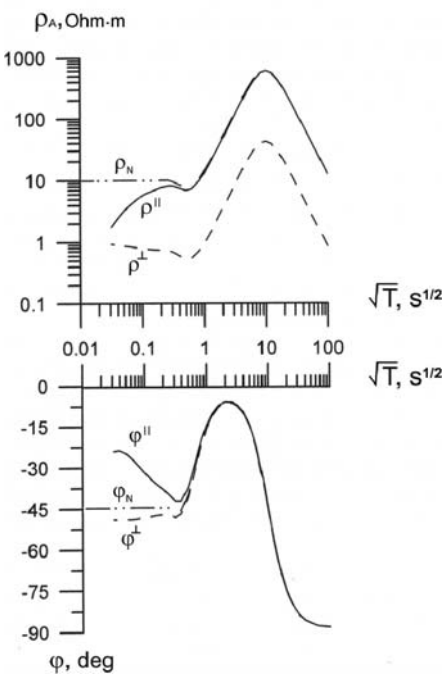

Fig. 7.2 Two-dimensional ρ-effect of the outcropped small-scale conductive prism; model parameters: $\rho_1' =$ 10 Ohm·m, $h_1 = 1$ km, $\rho_1'' =$ 1 Ohm·m, $\Delta h = 10$ m, $v =$ 20 m, $\rho_2 = 100000$ Ohm·m, $h_2 = 124$ km, $\rho_3 = 0$. The observation site is located in the middle of the prism ($y = 0$)

7.1.2 The Three-Dimensional ρ-Effect of the Hemisphere

Let us take the same layered model as in the previous subsection and replace the semicylinder by a small hemisphere (Fig. 7.3). Assuming that the effective penetration depth is many times larger than the hemisphere radius a, we neglect the induction effects as well as the influence of the lithosphere and mantle and solve the problem in direct-current approximation.

Introduce a spherical coordinate system r, θ, φ with origin at the centre of the hemisphere (θ is polar distance counted off from the $z-$ axis and φ is longitude counted off from the $yz-$ plane). Following (Groom and Bailey, 1991), we define the scalar potential of the electric field in the Earth as

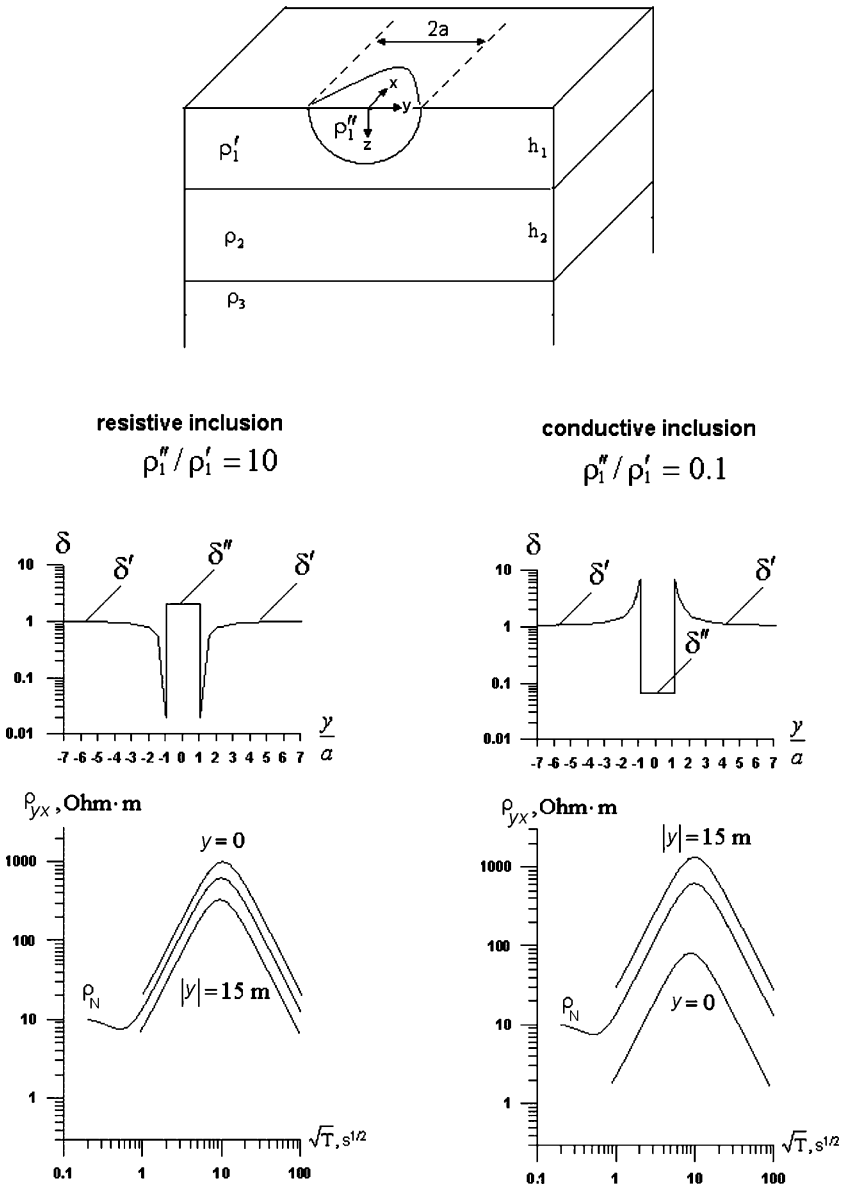

Fig. 7.3 Three-dimensional ρ-effect of the outcropped small-scale hemisphere; observation sites are located on the central y-profile; model parameters: $\rho_1' = 10$ Ohm·m, $h_1 = 1$ km, $\rho_2 = 100000$ Ohm·m, $h_2 = 124$ km, $\rho_3 = 0$, $a = 10$ m; conductive hemisphere $\rho_1'' = 1$ Ohm·m, resistive hemisphere $\rho_1'' = 100$ Ohm·m

$$U(r,\theta,\varphi,\omega)=\begin{cases}E_y^{\mathrm{N}}(\omega)\left\{-r+\dfrac{\rho_1'-\rho_1''}{\rho_1'+2\rho_1''}\dfrac{a^3}{r^2}\right\}\sin\theta\cos\varphi & \text{for} \quad r\geq a\\ -E_y^{\mathrm{N}}(\omega)\dfrac{3\rho_1''}{\rho_1'+2\rho_1''}r\sin\theta\cos\varphi & \text{for} \quad r\leq a,\end{cases} \tag{7.7}$$

where $E_y^{\mathrm{N}}(\omega)=E_y^{\mathrm{N}}(x,y,z=0,\omega)$ is the normal electric field on the Earth's surface. The function U satisfies the boundary conditions

$$\left.\frac{\partial U}{\partial\theta}\right|_{\theta=\pi/2-0}=0 \qquad U|_{r=a+0}=U|_{r=a-0} \qquad \left.\frac{1}{\rho_1'}\frac{\partial U}{\partial r}\right|_{r=a+0}=\left.\frac{1}{\rho_1''}\frac{\partial U}{\partial r}\right|_{r=a-0}.$$

On differentiating U, we get the electric field along the y-axis:

$$\begin{aligned}E_y(y,\omega)&=E_y(x,y,z=0,\omega)\big|_{x=0}=-\left.\frac{\partial U(r,\theta,\varphi,\omega)}{\partial r}\right|_{\substack{\theta=\pi/2\\ \varphi=0}}\\ &=\begin{cases}\left\{1+2\dfrac{\rho_1'-\rho_1''}{\rho_1'+2\rho_1''}\dfrac{a^3}{|y|^3}\right\}E_y^{\mathrm{N}}(\omega) & \text{for} \quad |y|\geq a\\ \dfrac{3\rho_1''}{\rho_1'+2\rho_1''}E_y^{\mathrm{N}}(\omega) & \text{for} \quad |y|\leq a.\end{cases}\end{aligned} \tag{7.8}$$

The corresponding magnetic field can be determined by the Bio-Savart law (integrating excess currents inside and outside the hemisphere). The estimation shows that at $a<<h_1$ the magnetic effect of the hemisphere is negligibly small within the S_1- and h-intervals. So, we can write $H_x(x,y,z=0,\omega)=H_x^{\mathrm{N}}$, where H_x^{N} is the normal magnetic field at the Earth surface. On simplest mathematics we get

$$Z_{yx}(y,\omega)=-\frac{E_y(y,\omega)}{H_x^{\mathrm{N}}}=\begin{cases}\left\{1+2\dfrac{\rho_1'-\rho_1''}{\rho_1'+2\rho_1''}\dfrac{a^3}{|y|^3}\right\}Z_{\mathrm{N}}(\omega) & \text{for} \quad |y|\geq a\\ \dfrac{3\rho_1''}{\rho_1'+2\rho_1''}Z_{\mathrm{N}}(\omega) & \text{for} \quad |y|\leq a\end{cases} \tag{7.9}$$

and

$$\begin{aligned}\rho_{yx}(y,\omega)&=\frac{\left|Z_{yx}(y,\omega)\right|^2}{\omega\mu_{\mathrm{o}}}\\ &=\begin{cases}\left\{1+2\dfrac{\rho_1'-\rho_1''}{\rho_1'+2\rho_1''}\dfrac{a^3}{|y|^3}\right\}^2\rho_{\mathrm{N}}(\omega)=\delta'\rho_{\mathrm{N}}(\omega) & \text{for} \quad y\geq a\\ \left\{\dfrac{3\rho_1''}{\rho_1'+2\rho_1''}\right\}^2\rho_{\mathrm{N}}(\omega)=\delta''\rho_{\mathrm{N}}(\omega) & \text{for} \quad y\leq a,\end{cases}\end{aligned} \tag{7.10}$$

where $\rho_{\mathrm{N}}=|Z_{\mathrm{N}}|^2/\omega\mu_{\mathrm{o}}$ is the normal apparent resistivity and δ',δ'' are the real frequency-independent distortion factors

$$\delta' = \left\{ 1 + 2\frac{\dfrac{\rho_1'}{\rho_1''} - 1}{\dfrac{\rho_1'}{\rho_1''} + 2}\frac{a^3}{|y|^3} \right\}^2 \qquad \delta'' = \left\{ \frac{3}{\dfrac{\rho_1'}{\rho_1''} + 2} \right\}^2 \tag{7.11}$$

which, according to (7.6), characterize the magnitude of the static shift.

Let us compare the static shifts observed in the 3D-model with a hemisphere and in the 2D-model with a semicylinder of the same relative resistivity. Reasoning from (7.5) and (7.11), we can show that

$$\frac{\log \delta''(3D)}{\log \delta''(2D)} = \frac{\log\left\{ \dfrac{3}{\dfrac{\rho_1'}{\rho_1''} + 2} \right\}}{\log\left\{ \dfrac{2}{\dfrac{\rho_1'}{\rho_1''} + 1} \right\}} < 1, \tag{7.12}$$

which is valid for resistive and conductive inclusions, $\rho_1'' > \rho_1'$ and $\rho_1'' < \rho_1'$. Thus, the three-dimensional $\rho-$effect is less expressive than two-dimensional one. This can be accounted for by the redistribution of currents that flow around a 3D resistive inclusion and inflow from each side into a 3D conductive inclusion. The three-dimensional $\rho-$effect is exemplified in Fig. 7.3. We see here the same pattern as in Fig. 7.1, but the static shift over the near-surface inclusion is noticeably reduced.

In models under consideration the total conductance S_1 of the upper layer varies but little. Now we have to examine models with significant variations in the sediments conductance.

7.2 Two-Dimensional Conductance Models

The distortions caused by variations in the sediments conductance will be referred to as *S-effect*. Let us begin our analysis with the two-dimensional S-effect.

7.2.1 The Tikhonov-Dmitriev Basic Model

We will examine several models that are essential for understanding the nature of the near-surface distortions caused by variations in the conductance S_1 of the sediments underlaid with resistive basement.

Here we consider a pioneering model devised by Tikhonov and Dmitriev (1969). This two-dimensional model consists of three layers (Fig. 7.4). The upper layer of uniform resistivity $\rho_1 = const$ simulates the sediments. It contains an infinitely

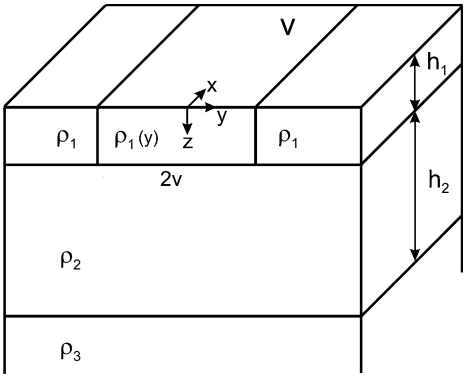

Fig. 7.4 The Tikhonov-Dmitriev two-dimensional basic model

long inhomogeneous domain V of width $2v$ and arbitrarily varying resistivity $\rho_1(y)$. The underlying homogeneous layer of high resistivity, $\rho_2 >> \rho_1$, and great thickness, $h_2 >> h_1$, is identified with the consolidated crust and mantle. The perfectly conductive bottom layer $\rho_3 = 0$, relates to the asthenosphere. The air is supposed to be a perfect insulator. So, we have

$$\rho_1 = \begin{cases} \rho_1 = const & |y| \geq v \\ \rho_1(y) & |y| \leq v \end{cases} \qquad S_1 = \begin{cases} S_1 = const & |y| \geq v \\ S_1(y) & |y| \leq v \end{cases} \tag{7.13}$$

$$\rho_2 >> \rho_1 \quad h_2 >> h_1 \quad R_2 >> R_1 \quad \rho_3 = 0,$$

where $S_1 = h_1/\rho_1$ is the longitudinal conductance of the upper layer, and $R_1 = h_1\rho_1$, $R_2 = h_2\rho_2$ are the transverse resistances of the upper and intermediate layers.

With $|y| \to \infty$ the electric and magnetic fields tend to the normal fields $\mathbf{E}^{\mathrm{N}}, \mathbf{H}^{\mathrm{N}}$.

The normal impedance of the model is defined by (1.43):

$$Z_{\mathrm{N}} = \frac{E_{\mathrm{x}}^{\mathrm{N}}}{H_{\mathrm{y}}^{\mathrm{N}}} = -\frac{E_{\mathrm{y}}^{\mathrm{N}}}{H_{\mathrm{x}}^{\mathrm{N}}} = -\frac{\omega\mu_{\mathrm{o}}}{k_1} \tan\ \mathrm{h} \left\{ ik_1h_1 + \tan\ \mathrm{h}^{-1} \frac{k_1}{k_2} \tan\ \mathrm{h}\ ik_2h_2 \right\}, \tag{7.14}$$

where $k_1 = \sqrt{i\omega\mu_{\mathrm{o}}/\rho_1}$ and $k_2 = \sqrt{i\omega\mu_{\mathrm{o}}/\rho_2}$. The model is characterized by the bell-like normal apparent-resistivity curve, $\rho_{\mathrm{N}} = |Z_{\mathrm{N}}|^2 / \omega\mu_{\mathrm{o}}$, consisting of the ascending and descending branches (Fig. 1.4). The ascending branch corresponds to the S_1-interval carrying information on the conductance $S_1 = h_1/\rho_1$ of the upper layer. Here the impedance phase comes to 0. The descending branch corresponds to the h-interval carrying information on the depth $h = h_1 + h_2$ of the perfectly conductive basement. Here the impedance phase comes to $-\pi/2$.

The problem on the layered medium with inhomogeneous upper layer can be solved in the *generalized thin-sheet approximation* first introduced by Dmitriev (1969). An independent analysis of such a generalization can be found in the review given by Ranganayaki and Madden (1980).

Let us recall the original idea of the *thin-sheet approximation* suggested by Sheinmann (1947) and Price (1949). In this approach an inhomogeneous horizontal

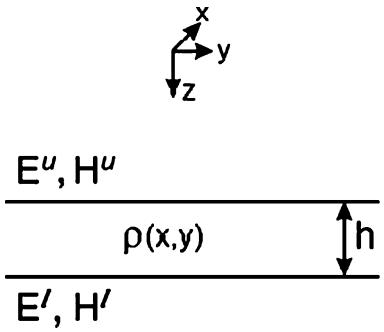

Fig. 7.5 Illustrating the generalized thin-sheet approximation

layer is approximated by a plane with variable conductance $S(x, y)$. This plane is called the *S−plane*. The Price-Sheinmann boundary conditions for the *S−plane* are (Berdichevsky and Zhdanov, 1984)

$$\begin{aligned} E_x^l - E_x^u &= 0 \qquad H_x^l - H_x^u = SE_y^u \\ E_y^l - E_y^u &= 0 \qquad H_y^l - H_y^u = -SE_x^u, \end{aligned} \tag{7.15}$$

where superscripts l and u denote the lower and upper sides of the layer.

The Dmitriev generalization introduces into consideration the thickness of the layer. Figure 7.5 displays a horizontal layer with constant thickness h and variable resistivity $\rho(x, y)$. Expanding the horizontal components of the electromagnetic field in a Taylor series and keeping the first two terms, we write

$$E_{\mathrm{x,y}}^l = E_{\mathrm{x,y}}^u + h\frac{\partial E_{\mathrm{x,y}}^u}{\partial z} \qquad H_{\mathrm{x,y}}^l = H_{\mathrm{x,y}}^u + h\frac{\partial H_{\mathrm{x,y}}^u}{\partial z}.$$

Using the Maxwell equations and substituting the horizontal derivatives for the vertical derivatives, we get

$$\begin{aligned} E_{\mathrm{x}}^l - E_{\mathrm{x}}^u &= i\omega\mu_{\mathrm{o}} h H_{\mathrm{y}}^u + \frac{\partial}{\partial x}\left[R\left(\frac{\partial H_{\mathrm{y}}^u}{\partial x} - \frac{\partial H_{\mathrm{x}}^u}{\partial y}\right)\right] \\ E_{\mathrm{y}}^l - E_{\mathrm{y}}^u &= -i\omega\mu_{\mathrm{o}} h H_{\mathrm{x}}^u + \frac{\partial}{\partial y}\left[R\left(\frac{\partial H_{\mathrm{y}}^u}{\partial x} - \frac{\partial H_{\mathrm{x}}^u}{\partial y}\right)\right] \\ H_{\mathrm{x}}^l - H_{\mathrm{x}}^u &= SE_{\mathrm{y}}^u + \frac{h}{i\omega\mu_{\mathrm{o}}}\left(\frac{\partial^2 E_{\mathrm{y}}^u}{\partial x^2} - \frac{\partial^2 E_{\mathrm{x}}^u}{\partial x \partial y}\right) \\ H_{\mathrm{y}}^l - H_{\mathrm{y}}^u &= -SE_{\mathrm{x}}^u + \frac{h}{i\omega\mu_{\mathrm{o}}}\left(\frac{\partial^2 E_{\mathrm{y}}^u}{\partial x \partial y} - \frac{\partial^2 E_{\mathrm{x}}^u}{\partial y^2}\right), \end{aligned} \tag{7.16}$$

where $S = h/\rho$ and $R = h_\rho$ are the *longitudinal conductance* and the *transverse resistance* of the layer.

These boundary conditions differ from those given by Sheinman (1947) and Price (1949) in the terms proportional to h. They account for the finite thickness of the layer.

Using (7.16), we solve the problem for TM- and TE-modes. It will be remembered that the *TM-mode* is associated with *H-polarized wave* (the field **H** is polarized in the strike direction). This mode gives the transverse MT-curves (telluric current flows across the structures). The *TE-mode* is associated with *E-polarized wave* (the field **E** is polarized in the strike direction). This mode gives the longitudinal MT-curves (telluric current flows along the structures). The main difference between these modes is that in a two-dimensional medium the TM-mode charges the structures, and its anomalies are of the galvanic nature, while the TE-mode does not charges the structures, and its anomalies are of the induction nature.

In the model under consideration the TM-mode is represented by the components $E_y(y, z)$, $E_z(y, z)$, $H_x(y, z)$. On the Earth's surface $E_z(y, +0) = 0$ and $H_x(y, 0) = H_x^N = const$. On the surface of the perfectly conductive basement $E_y(y, h) = 0$. By virtue of (7.16)

$$\begin{aligned} E_y(y,0) &= E_y(y,h_1) + i\omega\mu_o h_1 H_x^N && a \\ E_y(y,h_1) &= i\omega\mu_o h_2 H_x(y,h_1) + R_2 \frac{d^2 H_x(y,h_1)}{dy^2} && b \\ H_x(y,h_1) &= H_x^N + S_1(y) E_y(y,0). && c \end{aligned} \tag{7.17}$$

Eliminating $E_y(y, h_1)$ and $H_x(y, h_1)$ from these relations, we get the equation for the transverse impedance at the Earth's surface, $z = 0$:

$$R_2 \frac{d^2}{dy^2} S_1(y) Z^{\perp}(y) - [1 - i\omega\mu_o S_1(y) h_2] Z^{\perp}(y) = i\omega\mu_o h, \tag{7.18}$$

where $Z^{\perp}(y) = -E_y(y, 0)/H_x^N$ and $h = h_1 + h_2$. This differential equation can be easily reduced to the integral equation

$$Z^{\perp}(y) = \frac{S_1}{S_1(y)} Z_N + \frac{1}{S_1(y)} \int_{-v}^{v} G(y - y') Z^{\perp}(y') [S_1(y') - S_1] dy', \tag{7.19}$$

where Z_N is the normal impedance defined in the approximation (1.44) as

$$Z_N = -\frac{i\omega\mu_o h}{1 - i\omega\mu_o S_1 h_2}$$

and $G(y - y')$ is the Green function of the equation (7.18):

$$G(y - y') = \frac{fg}{2} e^{-g|y-y'|/f} \tag{7.20}$$

with

$$f = \frac{1}{\sqrt{1 - i\omega\mu_o S_1 h_2}} \quad \mathrm{Re}\, f > 0$$
$$g = \frac{1}{\sqrt{S_1 R_2}} = \sqrt{\frac{\rho_1}{h_1 h_2 \rho_2}}. \tag{7.21}$$

The parameters f and g have a simple physical meaning.

According to (1.48) and (1.49),

$$f \approx \frac{1}{\sqrt{1 - i\dfrac{T_{\max}}{T}}} \approx \frac{1}{\sqrt{1 + \dfrac{J_1}{J_3}}} \approx \sqrt{1 - \frac{J_1}{J}}, \tag{7.22}$$

where $T_{\max}$ is a period relating to the maximum of the normal apparent-resistivity curve ρ_N, J is the total current induced in the normal model, J_1 and J_3 are the currents induced in the upper layer and at the surface of the perfectly conductive basement (Berdichevsky and Dmitriev, 2002). It is seen that f reflects the distribution of the currents induced in the layered Earth. Due to the skin effect it varies from rather small complex values within the S_1-interval to 1 within the h-interval. This parameter will be referred to as the *induction parameter.*

The parameter g characterizes the galvanic coupling between the upper layer and the basement. It can be considered as a measure of transparency of the resistive intermediate layer or, in other words, as a measure of percolation of the excess currents through the intermediate layer. The smaller the longitudinal conductance S_1 of the upper layer and the smaller the transverse resistance R_2 of the intermediate layer, the larger the parameter g and the larger the exchange of excess currents between the upper layer and the basement. This parameter is referred to as *galvanic parameter* (Berdichevsky and Dmitriev, 1976).

Figure 7.6 shows the normalized amplitude of the Green function calculated for $h_2/h_1 = 49$ and $\rho_2/\rho_1 = 1000, 100$ with $\lambda_1/h_1 = 25, 50$ (S_1-interval) and $\lambda_1/h_1 = 100$ (h-interval). Here $\lambda_1 = 2\pi\sqrt{2\rho_1/\omega\mu_o}$ is the wavelength in the upper layer of the normal model. The Green function plays the role of a spatial filter. The degree of filter locality depends on ρ_2/ρ_1 and λ_1/h_1. The lower ρ_2/ρ_1 and the less λ_1/h_1, the narrower the filter pass-band. In the S_1-interval ($\lambda_1/h_1 = 25$, $|f| = 0.4$) the degree of filter locality is much higher than in the h-interval ($\lambda_1/h_1 = 100$, $|f| = 0.97$).

It would be interesting to make some asymptotic estimates.

Let $\rho_2/\rho_1 \to \infty$ and $g \to 0$. Here the galvanic coupling between the upper layer and the conductive basement is violated (no leakage through the intermediate layer) and the Green function tends to zero. Consequently, the contribution of the integral term becomes negligibly small. Thus, with account for (7.19) and (7.20),

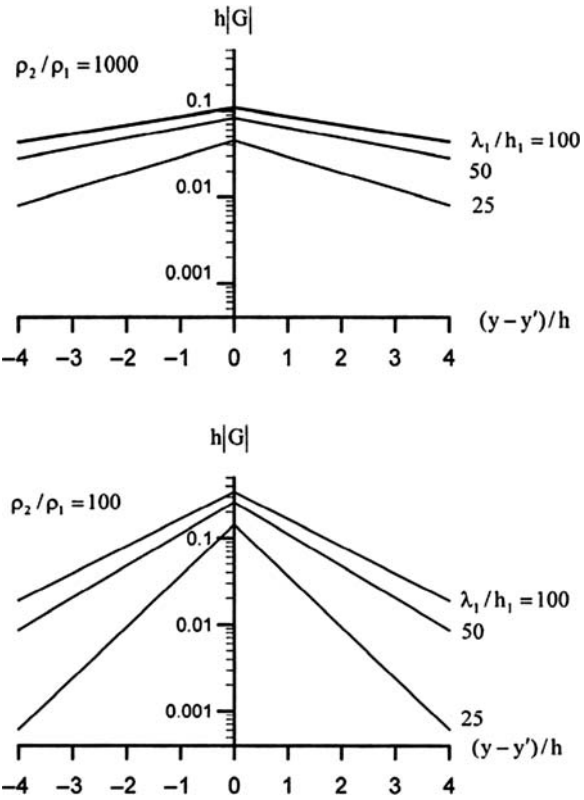

Fig. 7.6 The Green function in the Tikhonov-Dmitriev model, the TM-mode; model parameters: $h_2/h_1 = 49$, $\rho_2/\rho_1 = 100, 1000$, $\rho_3 = 0$; curve parameter: λ_1/h_1

$$Z^{\perp}(y) = \frac{S_1}{S_1(y)} Z_{\mathrm{N}} = \begin{cases} \dfrac{1}{S_1(y)} = Z_{\mathrm{n}} & \text{in the } S_1\text{-interval} \\ -i\dfrac{S_1}{S_1(y)}\omega\mu_{\mathrm{o}}h = \dfrac{S_1}{S_1(y)}Z_{\mathrm{n}} & \text{in the } h\text{-interval.} \end{cases} \tag{7.23}$$

In such approximation the transverse impedance $Z^{\perp}(y)$ is defined as the product of the normal impedance Z_{N} by the frequency-independent real factor $S_1/S_1(y)$. In the S_1-interval the transverse impedance $Z^{\perp}(y)$ coincides with the locally normal impedance $Z_{\mathrm{n}}(y) = 1/S_1(y)$. But in the h-interval it differs from $Z_{\mathrm{n}}(y) = -i\omega\mu_{\mathrm{o}}h$ by the factor proportional to $1/S_1(y)$. The low-frequency values of $Z^{\perp}(y)$ reflect variations in $S_1(y)$. They are statically distorted. This galvanic distortion was given the title *S-effect*.

The *S*-effect manifests itself in the vertical *static shift* of the low-frequency descending branch of the transverse apparent resistivity curve. According to (7.23),

$$\rho^{\perp}(y) = \frac{\left|Z^{\perp}(y)\right|^2}{\omega\mu_{\mathrm{o}}} = \left\{\frac{S_1}{S_1(y)}\right\}^2 \rho_{\mathrm{N}} =$$

$$= \begin{cases} \dfrac{1}{\omega\mu_o S_1^2(y)} = \rho_n & \text{in the } S_1\text{-interval} \\ \omega\mu_o \left\{ \dfrac{S_1}{S_1(y)} \right\}^2 h^2 = \delta\rho_n & \text{in the } h\text{-interval,} \end{cases} \tag{7.24}$$

where δ is the real frequency-independent *distortion factor*

$$\delta = \left\{ \frac{S_1}{S_1(y)} \right\}^2 .$$

The apparent-resistivity distortion defined in accordance to (1.101) is

$$\Delta\rho^{\perp} = \log\rho^{\perp} - \log\rho_n = \begin{cases} 0 & \text{in the } S_1\text{-interval} \\ \log\delta = 2\log\dfrac{S_1}{S_1(y)} & \text{in the } h\text{-interval.} \end{cases} \tag{7.25}$$

Here the ascending branch of the $\rho^{\perp}$-curve is undistorted, whereas its descending branch is distorted (even dramatically distorted) being displaced from the locally normal ρ_n-curve by the frequency-independent distance $\log\delta$ (downward when $S_1(y) > S_1$ and upward when $S_1(y) < S_1$).

Take a look at the transverse phase curve. According to (7.23) and (1.102)

$$\varphi^{\perp}(y) \approx \begin{cases} 0 & \text{in the } S_1\text{-interval} \\ -\dfrac{\pi}{2} & \text{in the } h\text{-interval} \end{cases} \tag{7.26}$$

and

$$\Delta\varphi^{\perp} = \varphi^{\perp} - \varphi_n = \begin{cases} 0 & \text{in the } S_1\text{-interval} \\ 0 & \text{in the } h\text{-interval.} \end{cases} \tag{7.27}$$

Here the ascending and descending branches of the $\varphi^{\perp}$-curve are undistorted: they merge with the locally normal φ_n-curve.

The one-dimensional inversion of the amplitude $\rho^{\perp}(y)$-curves distorted by the $S-$effect allows for determining the conductance $S_1(y)$ of the upper layer but, instead of the depth h to the conductive basement, it yields an *apparent depth*

$$h_A(y) = \frac{S_1}{S_1(y)} h \tag{7.28}$$

that may differ markedly from h. Errors in determining h cannot be avoided even by the integrated one-dimensional inversion of the amplitude and phase curves. So, in studying the relief of a highly conductive mantle at a depth of about 100 km we may obtain a surface with strange zigzags caused by inhomogeneitis in sediments at a depth of several tens or hundreds of meters. Looking through old journals, we find numerous examples of such a naïve interpretation.

Intuition suggests that with decreasing ρ_2/ρ_1 and hence with increasing g the $S-$effect attenuates. Indeed the less is ρ_2 and the larger is ρ_1, the better is galvanic coupling between the upper layer and conductive basement and the more intensive is vertical redistribution of currents normalizing the electromagnetic field. This heuristic consideration can be easily confirmed with asymptotic estimate. In the h-interval

$$G(y-y') = \frac{g}{2} e^{-g|y-y'|}.$$

If the galvanic parameter g is sufficiently large, then the Green function $G(y-y')$ assumes the form of the delta-like function $\tilde{\delta}(y-y')$. Hence, with accordance to (7.19),

$$\begin{aligned} Z^{\perp}(y) &= -i\omega\mu_o \frac{S_1}{S_1(y)} h + \frac{1}{S_1(y)} \int_{-v}^{v} [S_1(y') - S_1] Z^{\perp}(y') \tilde{\delta}(y-y') dy' \\ &\approx -i\omega\mu_o \frac{S_1}{S_1(y)} h + \left[1 - \frac{S_1}{S_1(y)} \right] Z^{\perp}(y) \end{aligned}$$

whence

$$Z^{\perp}(y) \approx Z_n(y) = -i\omega\mu_o h, \quad \rho^{\perp}(y) \approx \rho_n(y) = \omega\mu_o h^2. \tag{7.29}$$

Clearly, in the case of sufficiently large g the $S-$effect vanishes. Galvanic leakage from the upper layer may kill the $S-$effect.

How does the $S-$effect attenuate with distance from the inhomogeneity? Letting $|y| >> v$, we can write (7.19) as

$$Z^{\perp}(y) \approx Z_N + \frac{fg}{2S_1} e^{-g\mathrm{Re}\ \frac{1}{f}(|y|-v)} e^{-ig\mathrm{Im}\ \frac{1}{f}(|y|-v)} \int_{-v}^{v} Z^{\perp}(y')[S_1(y') - S_1] dy'. \tag{7.30}$$

Outside the inhomogeneity the anomalous field, characterized by the integral term, decays exponentially as $e^{-(|y|-v)/d}$, where

$$d = \frac{1}{g\mathrm{Re}\ \dfrac{1}{f}} = \frac{\sqrt{S_1 R_2}}{\mathrm{Re}\ \sqrt{1 - i\omega\mu_o S_1 h_2}}. \tag{7.31}$$

Parameter d allows to estimate the distance, at which the $S-$effect attenuates and the distorted transverse impedance readjusts to the normalcy. This parameter is referred to as *adjustment distance* (Ranganayaki and Madden, 1980; Singer and Fainberg, 1985; Singer, 1992). The influence of the inhomogeneity can be neglected if

$$|y| - v >> d. \tag{7.32}$$

In the $h-$interval $\omega\mu_o S_1 h_2 << 1$. Here the adjustment distance is the inverse of the galvanic parameter:

$$d = \sqrt{S_1 R_2} = \frac{1}{g} \tag{7.33}$$

Considering a model with continuous change of the conductance S_1, we assume that intensity of the S-effect depends on relation between generation of excess current in the upper layer and its leakage into the underlying intermediate layer. To gain a better insight into this mechanism, we examine a two-dimensional model suggested by Kuznetsov (2005). Letting

$$S_1(y) = S_1 + S_o \cos ly \quad l = \frac{2\pi}{L} \quad S_o < S_1, \tag{7.34}$$

we turn to the initial equation (7.18) and write for the h-interval:

$$R_2 \frac{d^2}{dy^2} S_1(y) Z^{\perp}(y) - Z^{\perp}(y) = i\omega\mu_o h, \tag{7.35}$$

where $Z^{\perp}(y)$ is represented as a Fourier decomposition

$$Z^{\perp}(y) = \sum_o^{\infty} a_n \cos nly. \tag{7.36}$$

Substituting (7.36) in (7.35) and taking into account that

$$\cos ly \cos nly = \frac{1}{2}[\cos(1+n)ly + \cos(1-n)ly],$$

we have

$$\begin{aligned} R_2 \frac{d^2}{dy^2} \left[S_1 \sum_o^{\infty} a_n \cos nly + \frac{1}{2} S_o \sum_o^{\infty} a_n [\cos(1+n)ly + \cos(1-n)ly] \right] \\ - \sum_o^{\infty} a_n \cos nly = i\omega\mu_o h, \end{aligned} \tag{7.37}$$

from which

$$\begin{aligned} l^2 R_2 \left[S_1 \sum_o^{\infty} a_n n^2 \cos nly + \frac{1}{2} S_o \sum_o^{\infty} a_n [(1+n)^2 \cos(1+n)ly \right. \\ \left. + (1-n)^2 \cos(1-n)ly] \right] + \sum_o^{\infty} a_n \cos nly + i\omega\mu_o h = \sum_o^{\infty} b_n \cos nly = 0. \end{aligned} \tag{7.38}$$

Equating the coefficients of this Fourier decomposition to zero, we obtain a system of the linear algebraic equations in $a_o, a_1 \ldots a_{n+1}$:

$$\begin{aligned} b_o &= a_o + i\omega\mu_o h = 0 \\ b_1 &= (1 + l^2 S_1 R_2)a_1 + \frac{1}{2} l^2 S_o R_2 (a_o + a_2) = 0 \\ b_n &= (1 + n^2 l^2 S_1 R_2)a_n + \frac{n^2}{2} l^2 S_o R_2 (a_{n-1} + a_{n+1}) = 0. \end{aligned} \tag{7.39}$$

It is not difficult to show that a_n is proportional to S_o^n. Thus, at the sufficiently small amplitude $S_o << S_1$ we can restrict ourselves to the first and second terms of the impedance decomposition (7.36). By virtue of (7.39)

$$a_o = -i\omega\mu_o h \; a_1 = \frac{l^2 S_o R_2}{1 + l^2 S_1 R_2} i\omega\mu_o h, \tag{7.40}$$

whence

$$Z^{\perp}(y) = a_o + a_1 \cos ly = -i\omega\mu_o h \left[1 - \frac{l^2 S_o R_2}{1 + l^2 S_1 R_2} \cos ly \right]. \tag{7.41}$$

Here the transverse impedance $Z^{\perp}(y)$ is subjected to the S–effect. It reflects the variations in the conductance $S_1(y)$ of the upper layer and delivers the oscillating apparent depth $h_A(y)$ to the conductive bottom:

$$h_A(y) = h \left[1 - \frac{l^2 S_o R_2}{1 + l^2 S_1 R_2} \cos ly \right] = h - h_o \cos ly, \tag{7.42}$$

where

$$h_o = h \frac{l^2 S_o R_2}{1 + l^2 S_1 R_2}.$$

To estimate the intensity of the $S-$effect, we correlate the relative amplitudes

$$\widehat{h} = \frac{h_o}{h} = \frac{l^2 S_o R_2}{1 + l^2 S_1 R_2}, \quad \widehat{S} = \frac{S_o}{S_1}. \tag{7.43}$$

The measure of the $S-$effect intensity can be introduced in the form

$$Q = \frac{\widehat{h}}{\widehat{S}} = \frac{1}{1 + 1/l^2 S_1 R_2} = \frac{1}{1 + L^2/4\pi^2 d^2}, \tag{7.44}$$

where $d = \sqrt{S_1 R_2}$ is the adjustment distance. The oscillation period L has a meaning of the width of the structures. This critical parameter defines the intensity of the $S-$effect. As $L << 2\pi d$, we have the narrow structures with barely perceptible leakage of the excess current. Hence we observe here the strong S-effect with $\widehat{h} \approx \widehat{S}$ and $Q \approx 1$. As $L >> 2\pi d$, we have the wide structures and the excess current in the upper layer is barely perceptible due to the strong leakage. Hence we observe here the weak $S-$effect with $\widehat{h} << \widehat{S}$ and $Q \approx 0$.

Figure 7.7 presents the $L-$dependence of Q. The strong $S-$effect with Q exceeding 0.9 shows itself at $L \leq 2d$. The weak $S-$effect with $Q \leq 0.1$ is observed at $L \geq 20d$. Let $\rho_1 = 10$ Ohm·m, $h_1 = 1$ km (sediments) and $\rho_2 = 10^4$ Ohm·m, $h_2 = 100$ km (lithosphere). In this typical geoelectric situation we have the adjustment distance $d = 316$ km and the strong $S-$effect is to be expected over the regional structures (elevations, depressions) even 500–600 km wide.

Next we examine the TE-mode. It is represented by the components $E_x(y, z)$, $H_y(y, z)$, $H_z(y, z)$. On the surface of the perfectly conductive basement $E_x(y, h) = 0$. By virtue of (7.16)

$$\begin{aligned} E_x(y, 0) &= E_x(y, h_1) - i\omega\mu_o h_1 H_y(y, 0) \\ E_x(y, h_1) &= -i\omega\mu_o h_2 H_y(y, h_1) \\ H_y(y, 0) &= H_y(y, h_1) + S_1(y) E_x(y, 0) + \frac{h_1}{i\omega\mu_o} \frac{d^2 E_x(y, 0)}{dy^2}. \end{aligned} \tag{7.45}$$

Eliminating $E_x(y, h_1)$ and $H_y(y, h_1)$ from these equations, we get the differential relation between the electric and magnetic fields on the Earth's surface $z = 0$:

$$h_1 h_2 \frac{d^2 E_x(y)}{dy^2} - [1 - i\omega\mu_o S_1(y) h_2] E_x(y) = i\omega\mu_o h H_y(y), \tag{7.46}$$

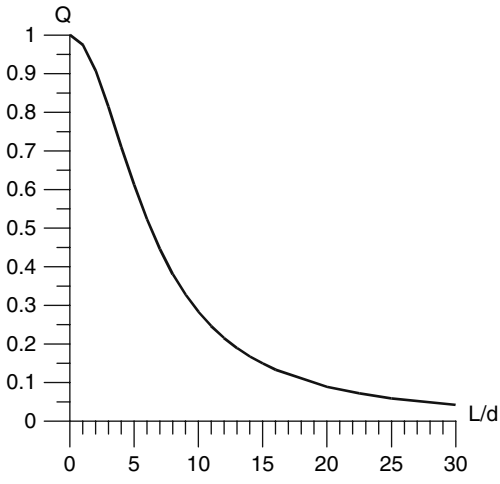

Fig. 7.7 Intensity of the S-effect in relation to the width of the structure L and adjustment distance d

where $E_x(y) \to E_x^{\mathrm{N}}$ and $H_y(y) \to H_y^{\mathrm{N}}$ as $|y| \to \infty$. This relation can be used as the boundary condition for the problem on the electric field in the air. On applying the Green theorem to the region $z \le 0$, the problem is reduced to the integral equation for $E_x(y) = E_x(y, 0)$:

$$E_x(y) = E_x^{\mathrm{N}} + i\omega\mu_{\mathrm{o}} \int_{-v}^{v} G(y - y')E_x(y')[S_1(y') - S_1]dy', \tag{7.47}$$

where the Green function

$$G(y - y') = \frac{h_2}{\pi} \int_0^{\infty} \frac{\cos m(y - y')dm}{h_1 h_2 m^2 + hm + 1/f^2} \tag{7.48}$$

involves the induction parameter f defined by (7.21).

Now we turn to the magnetic field. From (7.46), (7.47) and (7.48) we can easily derive formulas for the magnetic field on the Earth surface, $H_y(y) = H_y(y, 0)$ and $H_z(y) = H_z(y, 0)$:

$$\begin{aligned} H_y(y) &= H_y^{\mathrm{N}} + \int_{-v}^{v} \tilde{G}(y - y')E_x(y')[S_1(y') - S_1]dy' \quad a \\ H_z(y) &= \int_{-v}^{v} G(y - y')\frac{d}{dy'}\{E_x(y')[S_1(y') - S_1]\}dy', \quad b \end{aligned} \tag{7.49}$$

where $\tilde{G}(y - y')$ is a function obtained by differentiating the Green function G:

$$\tilde{G}(y - y') = \frac{h_2}{\pi} \int_0^{\infty} \frac{m \cos m(y - y')dm}{h_1 h_2\ m^2 + hm + 1/f^2}. \tag{7.50}$$

The normalized amplitude of the Green function G is plotted in Fig. 7.8. Calculations were done for $h_2/h_1 = 49$ with $\lambda_1/h_1 = 25, 50$ (S_1-interval) and $\lambda_1/h_1 = 100$ (h-interval). The Green function plays the role of a spatial filter. The filter pass-band at a level of 0.1 max $|G|$ is about $2h_{eff} = 2Z_{\mathrm{N}}/\omega\mu_{\mathrm{o}}$. It increases monotonously with lowering frequency. So, if at high frequencies we observe the induction effect of currents flowing in the vicinity of the observation site, then at low frequencies the remote zones begin to affect. The same regularities are characteristic of the function $\tilde{G}$ that governs the horizontal magnetic field. Once again we see that the magnetotelluric sounding is developing not only in the vertical direction, but in the horizontal direction as well. In passing to the h-interval, the induction effects begin to attenuate. Really, the contribution of the integral terms in (7.47) and (7.49a) becomes negligibly small as $\omega \to 0$ and the magnetotelluric field comes to the normalcy.

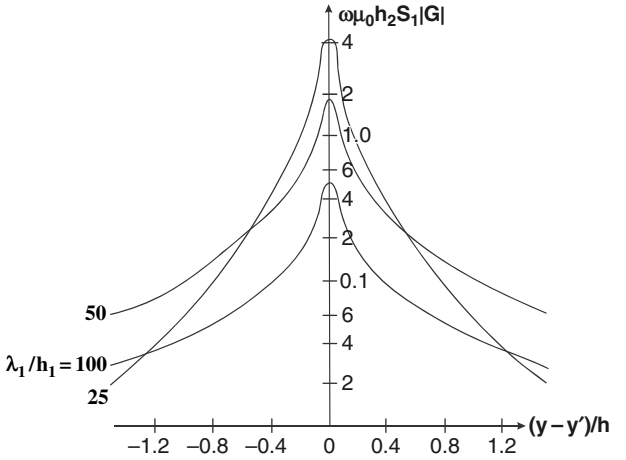

Fig. 7.8 The Green function in the Tikhonov-Dmitriev model, the TE-mode; model parameters: $h_2/h_1 = 49$, $\rho_2 = \infty$, $\rho_3 = 0$; curve parameter: λ_1/h_1

Summing up, we define the longitudinal impedance

$$Z^{\parallel}(y) \approx \begin{cases} q(y,\omega)Z_{\mathrm{n}}(y) = \dfrac{q(y,\omega)}{S_1(y)} & \text{in the } S_1\text{-interval} \\ \underset{q(y,\omega)\to 1 \text{ as } \omega\to 0}{q(y,\omega)Z_{\mathrm{n}}(y) = -iq(y,\omega)\omega\mu_0 h} & \text{in the } h\text{-interval,} \end{cases} \tag{7.51}$$

where $q(y, \omega)$ is a frequency-dependent complex factor accounting for distortions caused by the inductive interaction between near-surface excess currents.

The longitudinal apparent resistivities and phases assume the form

$$\rho^{\parallel}(y) \approx \begin{cases} \delta(y,\omega)\rho_{\mathrm{n}}(y) = \dfrac{\delta(y,\omega)}{\omega\mu_{\mathrm{o}}S_1^2(y)} & \text{in the } S_1\text{-interval} \\ \underset{|q(y,\omega)|\to 1 \text{ as } \omega\to 0}{\delta(y,\omega)\rho_{\mathrm{n}}(y) = \delta(y,\omega)\omega\mu_{\mathrm{o}}h^2} & \text{in the } h\text{-interval} \end{cases} \tag{7.52}$$

$$\varphi^{\parallel}(y) \approx \begin{cases} \varphi_{\mathrm{n}}(y) + \arg q(y,\omega) & \text{in the } S_1\text{-interval} \\ \underset{\arg q(y,\omega)\to 0 \text{ as } \omega\to 0}{\varphi_{\mathrm{n}}(y) + \arg q(y,\omega)} & \text{in the } h\text{-interval,} \end{cases} \tag{7.53}$$

where $\delta(y, \omega) = |q(y, \omega)|^2$.

Thus, the induction effects are most pronounced within the S_1-interval. They may tangibly affect the ascending branches of the apparent-resistivity and phase curves, and their one-dimensional inversion may give false geoelectric structures. But within the h-interval the induction effects die out and the one-dimensional

inversion of the descending branches of the apparent-resistivity and phase curves may yield a real depth to the conductive basement.

Next consider the anomalies of the vertical magnetic field. In the integral relation (7.49b) the Green function affects the derivative of the excess current. It is evident that the intensity of H_z−anomalies depends on how fast E_x and S_1 change. Physically it means that H_z reflects the asymmetry of the excess current. The maximum anomalies of H_z are observed above discontinuities of S_1, say, above the vertical interfaces. Anomalies of H_z like anomalies of E_x and H_y appear within the S_1-interval and disappear in the h-interval. This specifies the shape of the frequency responses of the tipper. The mechanism of attenuation of the near-surface magnetic anomalies is easy to understand: it follows from (1.49) that with lowering frequency the current in the upper inhomogeneous layer decays ($J_1/J_3 \to 0$).

In conclusion, we will derive two useful estimates.

1. At what frequency do the induction effects attenuate? To get an answer, it would be enough to define the boundary of the h-interval. From (1.48) we can derive the following rough estimate:

$$T >> 2\pi\mu_o h_2 \max S_1, \quad \omega << \frac{1}{\mu_o h_2 \max S_1}. \tag{7.54}$$

2. How far do the induction effects extend? Turn to (7.48) and (7.50) and represent the functions $G(y-y')$ and $\tilde{G}(y-y')$ as

$$\begin{aligned} G(u) &= \frac{h_2}{\pi h_{\text{eff}}} \int_0^\infty \frac{\cos\tilde{m}ud\tilde{m}}{\tilde{h}_1\tilde{h}_2\tilde{m}^2 + \tilde{h}\tilde{m} + 1/f^2} \\ \tilde{G}(u) &= \frac{h_2}{\pi h_{\text{eff}}^2} \int_0^\infty \frac{\tilde{m}\cos\tilde{m}ud\tilde{m}}{\tilde{h}_1\tilde{h}_2\tilde{m}^2 + \tilde{h}\tilde{m} + 1/f^2}, \end{aligned} \tag{7.55}$$

where

$$u = \left|y - y'\right| / h_{\text{eff}}, \tilde{m} = mh_{\text{eff}}, \tilde{h}_1 = h_1/h_{\text{eff}}, \tilde{h}_2 = h_2/h_{\text{eff}}, \tilde{h} = h/h_{\text{eff}},$$

and $h_{\text{eff}} = |Z_N|/\omega\mu_o$ is the effective penetration depth defined by the normal impedance. Successively integrating (7.55) by parts, we obtain the asymptotic decompositions of the functions $G(u)$ and $\tilde{G}(u)$ for $u \to \infty$. Let $|y| - v >> h_{\text{eff}}$. Keeping the first terms in decompositions of $G(u)$ and $\tilde{G}(u)$, we write

$$G(u) = \frac{h_2 h f^4}{\pi h_{\text{eff}}^2}\frac{1}{u^2} + O\left(\frac{1}{u^4}\right), \quad \tilde{G}(u) = -\frac{h_2 f^2}{\pi h_{\text{eff}}^2}\frac{1}{u^2} + O\left(\frac{1}{u^4}\right). \tag{7.56}$$

Substitute (7.56) in (7.47) and (7.49). Taking into account (1.44) and (7.20), we obtain the components of the anomalous electromagnetic field far away from the edge of the inclusion:

$$
\begin{aligned}
E_x^{\mathrm{A}}(y) &= E_x(y) - E_x^{\mathrm{N}} = \frac{i\omega\mu_{\mathrm{o}} h_2 h f^4}{\pi(|y|-v)^2}\int_{-v}^{v} E_x(y')[S_1(y') - S_1]dy' \\
&= -Z_{\mathrm{N}}\frac{h_2 f^2}{\pi(|y|-v)^2}\int_{-v}^{v} E_x(y')[S_1(y') - S_1]dy', \\
H_y^{\mathrm{A}}(y) &= -\frac{h_2 f^2}{\pi(|y|-v)^2}\int_{-v}^{v} E_x(y')[S_1(y') - S_1]dy', \\
H_z(y) &= -\frac{2h_2 h f^4}{\pi(|y|-v)^3}\int_{-v}^{v} E_x(y')[S_1(y') - S_1]dy' \\
&= -\frac{Z_{\mathrm{N}}}{i\omega\mu_{\mathrm{o}}}\frac{2h_2 f^2}{\pi(|y|-v)^3}\int_{-v}^{v} E_x(y')[S_1(y') - S_1]dy',
\end{aligned}
\tag{7.57}
$$

whence

$$
\begin{aligned}
\frac{E_x^{\mathrm{A}}(y)}{H_y^{\mathrm{A}}(y)} &= Z_{\mathrm{N}} \quad a \\
-i\omega\mu_{\mathrm{o}}\frac{H_z}{\frac{dH_y^{\mathrm{A}}}{dy}} &= Z_{\mathrm{N}}. \quad b
\end{aligned}
\tag{7.58}
$$

Equation (7.58a) means that the Leontovich condition (Leontovich, 1948) is satisfied in the far zone $|y| - v >> h_{\mathrm{eff}}$. The ratio between E_x^{A} and H_y^{A} equals the normal impedance Z_{N} no matter how strong the magnetotelluric anomalies are. Here the longitudinal impedance $Z^{\parallel}$, defined by magnetotelluric ratio E_x/H_y, coincides with the normal impedance Z_{N}:

$$
Z^{\parallel}(y) = \frac{E_x(y)}{H_y(y)} = \frac{E_x^{\mathrm{N}}(y) + E_x^{\mathrm{A}}(y)}{H_y^{\mathrm{N}}(y) + H_y^{\mathrm{A}}(y)} = \frac{Z_{\mathrm{N}} H_y^{\mathrm{N}}(y) + Z_{\mathrm{N}} H_y^{\mathrm{A}}(y)}{H_y^{\mathrm{N}}(y) + H_y^{\mathrm{A}}(y)} = Z_{\mathrm{N}}. \tag{7.59}
$$

Equation (7.58b) suggests that along with estimation (7.59), we can estimate Z_{N} using the magnetovariational ratio (1.3). Taking into account that $\partial H_y^{\mathrm{N}} \big/ \partial \mathrm{y} = 0$, we write

$$
-i\omega\mu_{\mathrm{o}}\frac{H_z}{\frac{dH_y^{A}}{dy}} = -i\omega\mu_{\mathrm{o}}\frac{H_z}{\frac{dH_y^{N}}{dy} + \frac{dH_y^{A}}{dy}} = -i\omega\mu_{\mathrm{o}}\frac{H_z}{\frac{dH_y}{dy}} = Z_{\mathrm{N}}. \tag{7.60}
$$

Note that (7.60) is valid for a field with quadratic spatial variation of H_y, while (7.59) is valid for a field with linear spatial variation of H_y (Weidelt, 1978; Dmitriev

and Berdichevsky, 1979; Berdichevsky and Dmitriev, 2002). Intending to determine the normal impedance Z_N, one can use the magnetovariational ratio at lesser distances from inhomogeneity than the magnetotelluric ratio (Fiskina et al., 1986).

As an example, we will consider in greater detail the 2D-models with sediments consisting of two and three homogeneous segments.

7.2.2 The Two-Segment Model

Figure 7.9 presents a model where the upper layer consists of two homogeneous segments of resistivities ρ_1' and ρ_1''. Here

$$\rho_1 = \begin{cases} \rho_1' & y \le 0 \\ \rho_1'' & y \ge 0 \end{cases} \qquad S_1 = \begin{cases} S_1' & y \le 0 \\ S_1'' & y \ge 0 \end{cases} \tag{7.61}$$
$$\rho_2 >> \rho_1 \quad h_2 >> h_1 \quad R_2 >> R_1 \quad \rho_3 = 0,$$

where $S_1' = h_1/\rho_1'$, $S_1'' = h_1/\rho_1''$ are the conductances of the left and right segments of the upper layer and $R_1 = h_1\rho_1$, $R_2 = h_2\rho_2$ are the resistances of the upper and intermediate layers.

The two-segment model was examined by Ranganayaki and Madden (1980), Dawson et al. (1982), Dawson (1983), Berdichevsky and Jakovlev (1989), Barashkov and Jakovlev (1989), Weaver (1994).

The model under consideration admits of a simple analytical solution for the TM-mode.

Return to (7.18). It falls into two equations with constant coefficients:

$$\frac{d^2}{dy^2}Z^{\perp}(y) - \frac{(g')^2}{(f')^2}Z^{\perp}(y) = -\frac{(g')^2}{(f')^2}\dot{Z}_N \qquad y \le 0$$
$$\frac{d^2}{dy^2}Z^{\perp}(y) - \frac{(g'')^2}{(f'')^2}Z^{\perp}(y) = -\frac{(g'')^2}{(f'')^2}\ddot{Z}_N \quad y \ge 0, \tag{7.62}$$

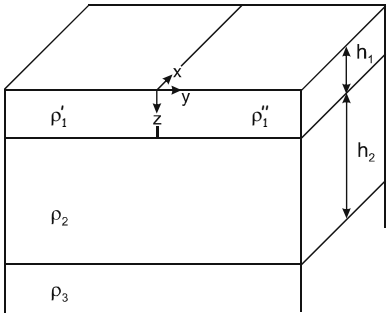

Fig. 7.9 The two-segment model

where g', $g''$and f', f'' are galvanic and induction parameters and $\dot{Z}_N, \ddot{Z}_N$ are normal impedances in the left and right segments. By virtue of (7.21)

$$\dot{Z}_N = -\frac{i\omega\mu_o h}{1 - i\omega\mu_o S_1' h_2}, \ddot{Z}_N = -\frac{i\omega\mu_o h}{1 - i\omega\mu_o S_1'' h_2}.$$

Here $Z^{\perp}(y) \underset{y\to-\infty}{\to} \dot{Z}_N$ and $Z^{\perp}(y) \underset{y\to\infty}{\to} \ddot{Z}_N$.

Solutions of these equations are

$$Z^{\perp}(y) = \begin{cases} \dot{Z}_N + Ae^{g'y/f'} & y \le 0 \\ \ddot{Z}_N + Be^{-g''y/f''} & y \ge 0. \end{cases} \tag{7.63}$$

Note that behavior of $Z^{\perp}$ within each segment is governed by local values of galvanic and induction parameters, g and f.

The coefficients A and B are determined from the conditions that $S_1 Z^{\perp}$ and $S_1 dZ^{\perp}/dy$ are continuous at the boundary between the segments:

$$\begin{aligned} S_1' Z^{\perp}\big|_{y=0} &= S_1'' Z^{\perp}\big|_{y=0} & a \\ S_1' \frac{dZ^{\perp}}{dy}\bigg|_{y=0} &= S_1'' \frac{dZ^{\perp}}{dy}\bigg|_{y=0.} & b \end{aligned} \tag{7.64}$$

Condition (7.64*a*) provides the continuity of the horizontal component j_y of the current density at the Earth's surface:

$$S_1 Z^{\perp} = -\frac{h_1}{\rho_1}\frac{E_y(z=0)}{H_x^N} = \frac{h_1}{H_x^N} j_y(z=+0),$$

while condition (7.64*b*) implies the continuity of the vertical component j_z of the current density at the floor of the upper layer. By virtue of (7.17*c*)

$$S_1 \frac{dZ^{\perp}}{dy} = -\frac{1}{H_x^N}\frac{dH_x(z=h_1)}{dy} = -\frac{j_z(z=h_1)}{H_x^N}.$$

Substitution of (7.63) into (7.64) gives a system of linear equations for unknowns A and B:

$$\begin{aligned} S_1' A - S_1'' B &= S_1''\ddot{Z}_N - S_1'\dot{Z}_N \\ S_1' \frac{g'}{f'} A + S_1'' \frac{g''}{f''} B &= 0, \end{aligned} \tag{7.65}$$

from which

$$Z^{\perp}(y) = \begin{cases} \dot{Z}_{\mathrm{N}} \left\{ 1 - \left(1 - \sqrt{\dfrac{S_1''}{S_1'}} \dfrac{f''}{f'} \right) e^{\frac{g'}{f'} y} \right\} & y \le 0 \\ \ddot{Z}_{\mathrm{N}} \left\{ 1 - \left(1 - \sqrt{\dfrac{S_1'}{S_1''}} \dfrac{f'}{f''} \right) e^{-\frac{g''}{f''} y} \right\} & y \ge 0 \end{cases} \tag{7.66}$$

and

$$\rho^{\perp}(y) = \frac{\left| Z^{\perp}(y) \right|^2}{\omega \mu_{\mathrm{o}}} = \begin{cases} \dot{\rho}_{\mathrm{n}} \left| 1 - \left(1 - \sqrt{\dfrac{S_1''}{S_1'}} \dfrac{f''}{f'} \right) e^{\frac{g'}{f'} y} \right|^2 & y \le 0 \\ \ddot{\rho}_{\mathrm{n}} \left| 1 - \left(1 - \sqrt{\dfrac{S_1'}{S_1''}} \dfrac{f'}{f''} \right) e^{-\frac{g''}{f''} y} \right|^2 & y \ge 0, \end{cases} \tag{7.67}$$

where $\dot{\rho}_{\mathrm{n}}$ and $\ddot{\rho}_{\mathrm{n}}$ are locally normal apparent resistivities for the left and right segments:

$$\dot{\rho}_n = \frac{\left| \dot{Z}_N \right|^2}{\omega \mu_{\mathrm{o}}} = \frac{\omega \mu_{\mathrm{o}} h^2}{\left| 1 - i \omega \mu_{\mathrm{o}} S_1' h_2 \right|^2} \quad \ddot{\rho}_n = \frac{\left| \ddot{Z}_N \right|^2}{\omega \mu_{\mathrm{o}}} = \frac{\omega \mu_{\mathrm{o}} h^2}{\left| 1 - i \omega \mu_{\mathrm{o}} S_1'' h_2 \right|^2}.$$

One can readily see that within the S_1-interval (at the ascending branch of the $\rho^{\perp}$-curves) the distortions of the transverse impedance and apparent resistivity are small if not negligibly small. Let $\omega \mu_{\mathrm{o}} S_1' h_2 >> 1$ and $\omega \mu_{\mathrm{o}} S_1'' h_2 >> 1$. Then

$$\sqrt{\frac{S_1'}{S_1''}} \frac{f'}{f''} \approx 1,$$

whence

$$Z^{\perp}(y) \approx \begin{cases} \dot{Z}_{\mathrm{N}} = \dfrac{1}{S_1'} & y \le 0 \\ \ddot{Z}_{\mathrm{N}} = \dfrac{1}{S_1''} & y \ge 0 \end{cases} \qquad \rho^{\perp}(y) \approx \begin{cases} \dot{\rho}_{\mathrm{n}} = \dfrac{1}{\omega \mu_{\mathrm{o}} (S_1')^2} & y \le 0 \\ \ddot{\rho}_{\mathrm{n}} = \dfrac{1}{\omega \mu_{\mathrm{o}} (S_1'')^2} & y \ge 0. \end{cases} \tag{7.68}$$

But within the h-interval (at the descending branch of the $\rho^{\perp}$-curves) the distortions become stronger. Given the large difference between S_1' and S_1'', we observe the dramatic S-effect, which manifests itself in the static shift of the descending branches of the apparent-resistivity curves and scarcely affects the phase curves. If $\omega \mu_{\mathrm{o}} S_1' h_2 << 1$ and $\omega \mu_{\mathrm{o}} S_1'' h_2 << 1$, then $f' \approx f'' \approx 1$. Replacing the galvanic parameters g', g'' by adjustments distances $d' = 1/g'$, $d'' = 1/g''$, we write

$$Z^{\perp}(y) \approx \begin{cases} \dot{Z}_{\mathrm{N}} \left\{ 1 - \left(1 - \sqrt{\dfrac{S_1''}{S_1'}} \right) e^{y/d'} \right\} & y \le 0 \\ \ddot{Z}_{\mathrm{N}} \left\{ 1 - \left(1 - \sqrt{\dfrac{S_1'}{S_1''}} \right) e^{-y/d''} \right\} & y \ge 0 \end{cases}$$

$$\rho^{\perp}(y) \approx \begin{cases} \dot{\rho}_{\mathrm{n}} \left| 1 - \left(1 - \sqrt{\dfrac{S_1''}{S_1'}} \right) e^{y/d'} \right|^2 & y \le 0 \\ \ddot{\rho}_{\mathrm{n}} \left| 1 - \left(1 - \sqrt{\dfrac{S_1'}{S_1''}} \right) e^{-y/d''} \right|^2 & y \ge 0, \end{cases} \tag{7.69}$$

where $\dot{Z}_{\mathrm{N}} = \ddot{Z}_{\mathrm{N}} = -i\omega\mu_{\mathrm{o}} h$ and $\dot{\rho}_{\mathrm{n}} = \ddot{\rho}_{\mathrm{n}} = \omega\mu_{\mathrm{o}} h^2$.

The S-effect is most pronounced at the boundary between the left and right segments:

$$Z^{\perp}(0) \approx \begin{cases} \dot{Z}_{\mathrm{N}} \sqrt{\dfrac{S_1''}{S_1'}} & y = -0 \\ \ddot{Z}_{\mathrm{N}} \sqrt{\dfrac{S_1'}{S_1''}} & y = +0 \end{cases} \qquad \rho^{\perp}(0) \approx \begin{cases} \dot{\rho}_{\mathrm{n}} \dfrac{S_1''}{S_1'} & y = -0 \\ \ddot{\rho}_{\mathrm{n}} \dfrac{S_1'}{S_1''} & y = +0. \end{cases} \tag{7.70}$$

With distance from the conductance discontinuity the S-effect exponentially attenuates and the transverse apparent resistivity comes to the normalcy. Table 7.1 presents the distances y, at which $\rho^{\perp}$ takes its locally normal value, $\dot{\rho}_{\mathrm{n}}$ or $\ddot{\rho}_{\mathrm{n}}$, with an accuracy of 5%. For $2 \le S_1'/S_1'' \le 1000$ these critical distances chage from $2.4d$ to $3.7d$ at the left conductive segment and from $2.8d$ to $7.1d$ at the right resistive segment. Take, for instance, the sediments conductance and the lithosphere resistance characteristic of platform regions: $S_1 \sim 250\,S$ and $R_2 \sim 10^9$ Ohm $\cdot$ m^2. Here the adjustment distance d is of order 500 km. Thus, the S-effect caused by variations in the sediments conductance can cover a vast geological province.

As an example we consider a 2D-model with parameters $\rho_1' = 10$ Ohm·m, $\rho_1'' = 100$ Ohm·m, $h_1 = 1$km, $\rho_2 = 10^5$ Ohm·m, $h_2 = 99$km, $\rho_3 = 0$. Calculations have been performed using analytical solution (7.69) and with the finite element method (Wannamaker et al., 1987).

Table 7.1 Distances at which $\rho^{\perp} \approx \rho_{\mathrm{n}}$ with an accuracy of 5%

S_1'/S_1''	2	5	10	50	100	1000
$\lvert y\rvert/d'$ $y < 0$	2.4	3.0	3.3	3.5	3.6	3.7
y/d'' $y > 0$	2.8	3.9	4.5	5.5	5.9	7.1

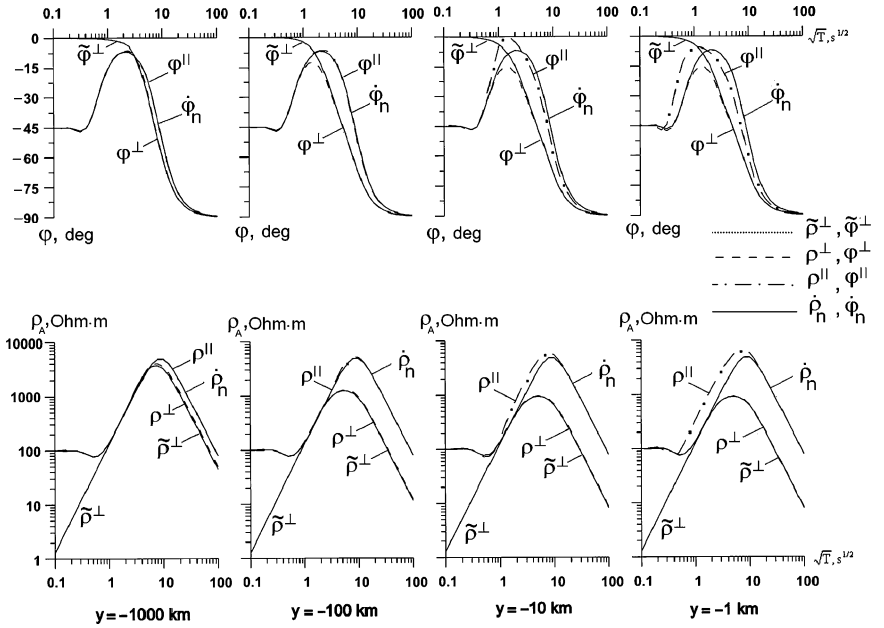

Fig. 7.10 Longitudinal and transverse apparent-resistivity and impedance-phase curves over the left conductive segment in the model shown in Fig. 7.9; y-distance to the boundary between segments; $\tilde{\rho}^{\perp}$, $\tilde{\varphi}^{\perp}$-analytical solution, $\rho^{\perp}$, $\varphi^{\perp}$ and $\rho^{\parallel}$, $\varphi^{\parallel}$-numerical solution by means of the finite element method, $\dot{\rho}_n$, $\dot{\varphi}_n$- locally normal solution. Model parameters: $\rho_1' = 10$ Ohm·m, $\rho_1'' = 100$ Ohm·m, $h_1 = 1$ km, $\rho_2 = 10^5$ Ohm·m, $h_2 = 99$ km, $\rho_3 = 0$

Figures 7.10 and 7.11 show the apparent-resistivity and impedance-phase curves obtained over the left and right segments at different distances from the conductance discontinuity.

First of all note that within the S_1- and h-intervals the transverse $\rho^{\perp}$-curves plotted from the analytical and numerical solutions agree fairly well. The ascending branches of the $\rho^{\perp}$-curves are not distorted. They coincide with ascending branches of the locally normal ρ_n-curves. However, the descending branches of the $\rho^{\perp}$-curves are distorted by the S-effect. They are shifted from the locally normal ρ_n-curves, down over the left conductive segment and up over the right resistive segment. The maximum S-effect is observed at the boundary between the segments. With distance from the conductance discontinuity the S-effect monotonously decreases. It vanishes at $y \approx -3000$ km over the left segment ($d' = 1000$ km) and at $y \approx 1200$ km over the right segment ($d'' = 316$ km). These estimates are in a good agreement with Table 7.1. Now have a look at the transverse phase curves. In passing to the h-interval the $\varphi^{\perp}$-curves, plotted from the analytical and numerical solutions, merge together and with lowering frequency they approach the locally normal φ_n-curves. A remarkable property of the S-effect is that the drastically shifted branches of the $\rho^{\perp}$-curves correspond to the slightly distorted branches of the $\varphi^{\perp}$-curves.

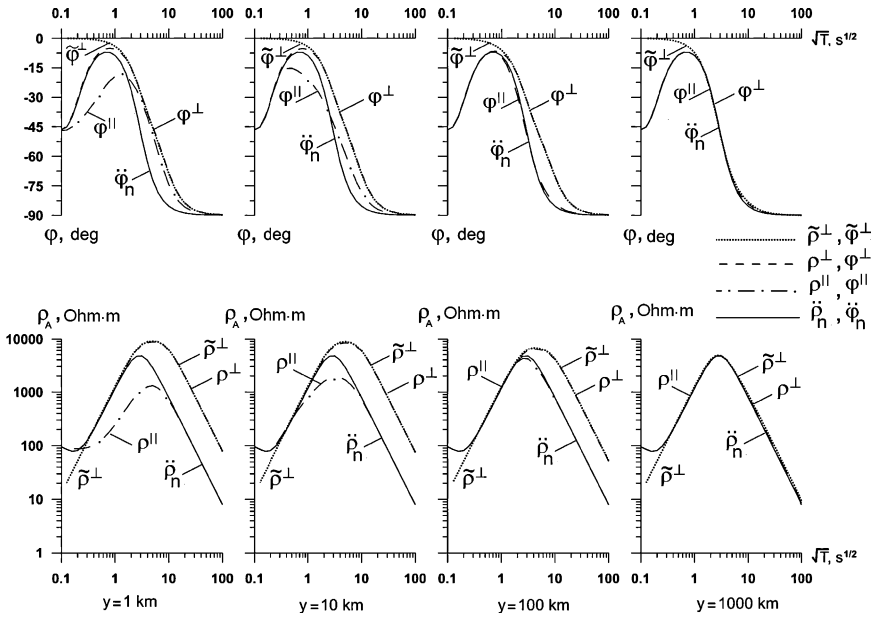

Fig. 7.11 Longitudinal and transverse apparent-resistivity and impedance-phase curves over the right resistive segment in the model shown in Fig. 7.9; y-distance to the boundary between segments; $\tilde{\rho}^{\perp}$, $\tilde{\varphi}^{\perp}$-analytical solution, $\rho^{\perp}$, $\varphi^{\perp}$ and $\rho^{\parallel}$, $\varphi^{\parallel}$-numerical solution by means of the finite element method, $\ddot{\rho}_n$, $\ddot{\varphi}_n$- locally normal solution. Model parameters: $\rho_1' = 10\,\Omega\text{m}$, $\rho_1'' = 100\,\Omega\text{m}$, $h_1 = 1$ km, $\rho_2 = 10^5\,\Omega\text{m}$, $h_2 = 99$ km, $\rho_3 = 0$

Quite different relations are characteristic of the longitudinal magnetotelluric curves, distorted by the induction effects. These distortions are clearly seen near the boundary between the left and right segments. The ascending branches of the $\rho^{\parallel}$- and $\varphi^{\parallel}$-curves are deformed. Within the conductive segment they are affected by the resistive segment and become steeper ($y = -1$km, -10 km). Within the resistive segment they are affected by the conductive segment and flatten out ($y = 1$km, $y = 10$ km). The induction effects vanish at $|y| \geq 100$ km, which corresponds to the condition

$$|y| \geq \max h_{\text{eff}} = h = h_1 + h_2. \tag{7.71}$$

Figure 7.12 displays the tipper curves. With distance from the boundary between the segments the tippers rather quickly diminish. The large tippers are observed in the region $|y| \leq 10$ km. Within the h-interval ($T \geq 1000$ s) tippers decay. Note that $\text{Re}\,W_{zy}$ is positive throughout all frequencies under examination, while $\text{Im}\,W_{zy}$ changes the sign. With lowering frequency the tipper phases, $\varphi_W = \arg W_{zy}$, go from the Ith quadrant to the IVth quadrant and merge with the longitudinal impedance

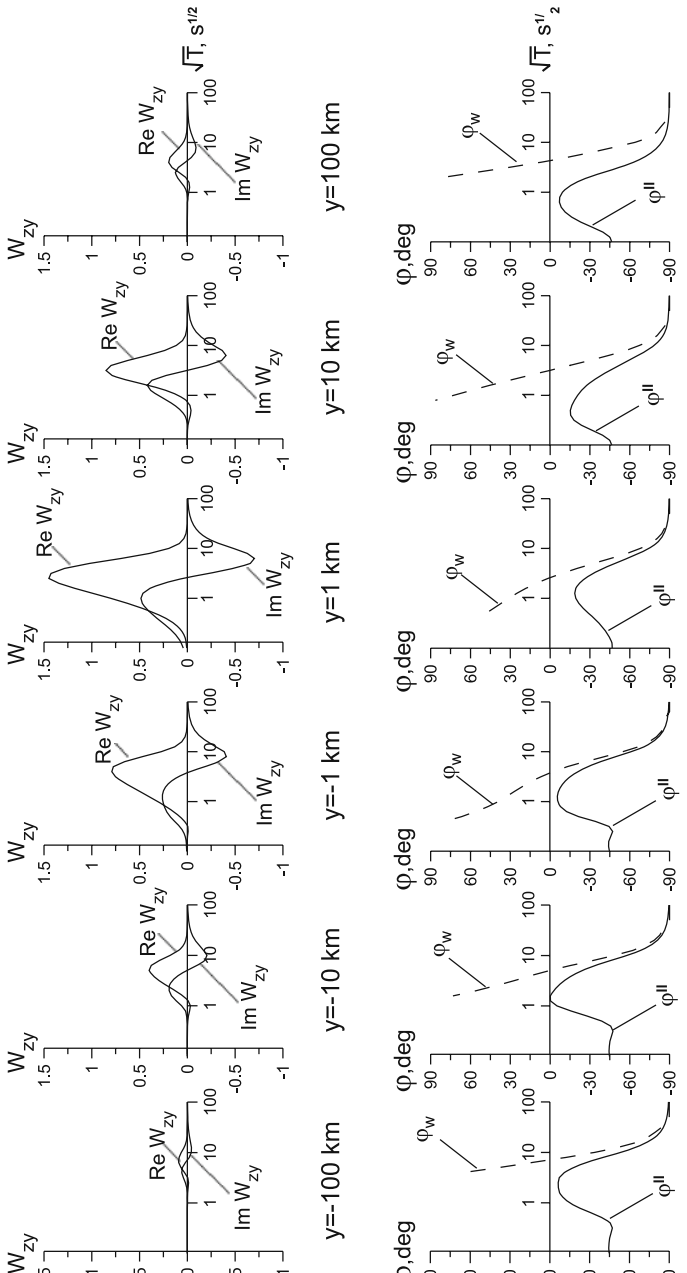

Fig. 7.12 Tipper curves in the two-segment model shown in Fig. 7.9; y-distance to the boundary between segments; $\mathrm{Re}\,W_{zy}$, $\mathrm{Im}\,W_{zy}$ – real and imaginary tippers, φ_w-phase of W_{zy}, $\varphi^{\|}$- phase of $Z^{\|}$. Model parameters: $\rho'_1 = 10\,\Omega\mathrm{m}$, $\rho''_1 = 100\,\Omega\mathrm{m}$, $h_1 = 1\,\mathrm{km}$, $\rho_2 = 10^5\,\Omega\mathrm{m}$, $h_2 = 99\,\mathrm{km}$, $\rho_3 = 0$

phases, $\varphi^{\parallel}$. This relation between the tipper and the longitudinal impedance is in agreement with decomposition (4.79) suggested in (Zhang et al., 1993).

Next we will consider the electric and magnetic profiles related to the TE- and TM-modes.

Figure 7.13 shows E_x- and H_y-profiles crossing the two-segment model. The fields E_x, H_y are components of the TE-mode. They are normalized to the right normal fields $\ddot{E}_x^{\mathrm{N}}$, $\ddot{H}_y^{\mathrm{N}} = \dot{H}_y^{\mathrm{N}}$. At high frequencies the longitudinal electric field E_x rises steeply up from $0.1\,\ddot{E}_x^{\mathrm{N}}$ ($T = 1$ s) and from $0.22\,\ddot{E}_x^{\mathrm{N}}$ ($T = 15$ s) to $\ddot{E}_x^{\mathrm{N}}$. With lowering frequency this sharp transition monotonously flattens ($T = 40 \div 100$ s). Areas of observable changes in E_x spread up to 400 km from the boundary between the segments of different resistivity. The electric anomaly is accompanied by the well-defined maxima and minima of the transverse magnetic field H_y. These extrema reflect the concentration and deconcentration of the electric currents at the segment boundary. The higher frequency, the narrower the concentration and deconcentration zones and the sharper the magnetic extrema. Here we again see the horizontal skin effect. It clearly manifests itself in the range covered T = $1 \div 40$ s and embraces the areas of about 400 km wide. At $T > 250$ s the skin effect attenuates.

Figure 7.14 shows the E_y-profile (the TM-mode). The transverse electric field E_y is normalized to the normal field $\ddot{E}_y^{\mathrm{N}}$. It has a jump on the boundary between the left (conductive) and right (resistive) segments. Over the left segment we see a fall of E_y, which is accounted for by rearrangement of the transverse current due to different skin depths in the left and right segments and by current leakage (the current meets the resistive segment and flows under it – let us recall an old geophysical joke "the current is not a fool"). The effect of skin-depth difference is characteristic of high frequencies ($T = 0.15$ s). Its distortion zone does not exceed 1 km. At low frequencies the under-flow effect dominates ($T = 15$ s, 1500 s). We can estimate its remote action by the adjustment distance d. Over the left segment it is observed at distances numbered in the hundreds and even thousands of km ($d' - 3d'$). The distortion of the high-frequency field E_y over the right segment is rather weak ($T = 0.15$ s). But with lowering frequency ($T = 15$ s, 1500 s), we notice a pronounced anomaly of E_y, which attenuates due to leakage of excess current into the underlying medium. Here the distortion zone numbers in the hundreds of km ($1.5\,d''$).

Finally, we consider the W_{zy}-profiles (Fig. 7.15). Here $\mathrm{Re}W_{zy}$ is positive everywhere, while $\mathrm{Im}W_{zy}$ changes the sign with frequency. The $\mathrm{Re}W_{zy}$-profiles have a nearly symmetric maximum, whose form slightly depends on frequency. The highest maximum of $\mathrm{Re}W_{zy}$ is observed in the S_1-interval ($T = 10$ s). The $\mathrm{Im}W_{zy}$-profiles show maxima or minima which alternate with frequency. In the h –interval ($T = 1000$ s) tippers vanish. The real inductive arrows are shown at the bottom of Fig. 7.15. They radiate from left to right, that is, from higher to lower conductivities.

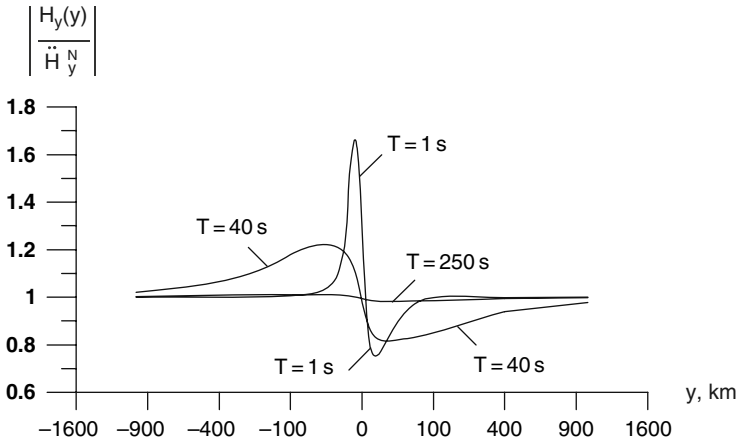

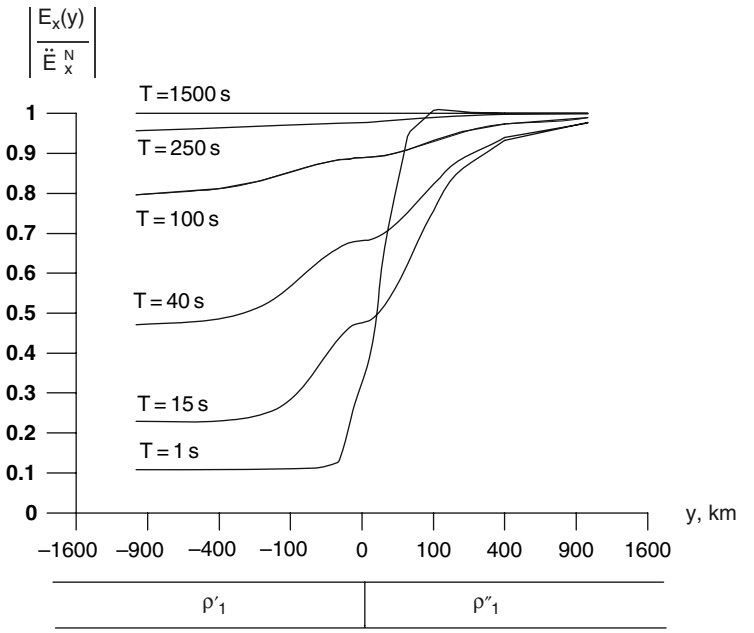

Fig. 7.13 Electric and magnetic field profiles (TE-mode) in the two-segment model shown in Fig. 7.9; y-distance to the boundary between segments. Model parameters: $\rho_1' = 10\,\Omega\text{m}$, $\rho_1'' = 100\,\Omega\text{m}$, $h_1 = 1\,\text{km}$, $\rho_2 = 10^5\,\Omega\text{m}$, $h_2 = 99\,\text{km}$, $\rho_3 = 0$. Profile parameter: period $T = 1$–1500 s

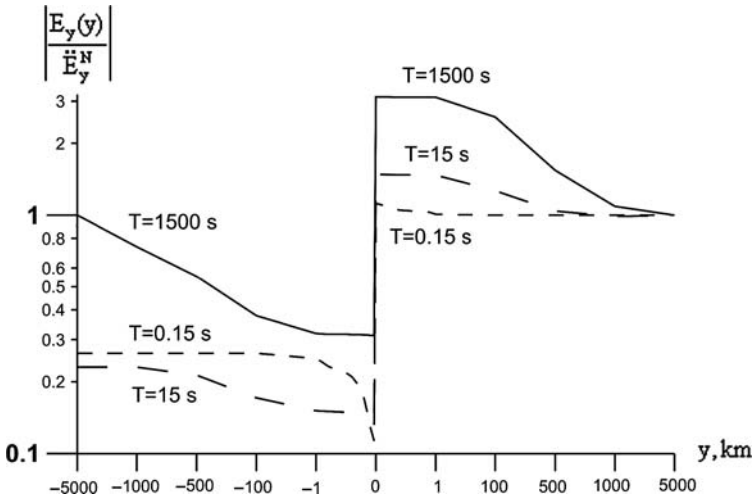

Fig. 7.14 Electric field profiles (TM-mode) in the two-segment model shown in Fig. 7.9; y-distance to the boundary between segments. Model parameters: $\rho_1' = 10\,\Omega\text{m}$, $\rho_1'' = 100\,\Omega\text{m}$, $h_1 = 1\,\text{km}$, $\rho_2 = 10^5\,\Omega\text{m}$, $h_2 = 99\,\text{km}$, $\rho_3 = 0$. Profile parameter: period $T = 0.15 - 1500\,\text{s}$

7.2.3 The Three-Segment Model

Now we consider a model where the upper layer consists of three segments (Berdichevsky and Jakovlev, 1989; Weaver, 1994). The model is shown in Fig. 7.16. Here the central segment of resistivity ρ_1'' and width $2v$ is bordered by the left and right segments of resistivity ρ_1'. In this model

$$\rho_1 = \begin{cases} \rho_1' & y \le -v \\ \rho_1'' & -v \le y \le v \\ \rho_1' & y \ge v \end{cases} \qquad S_1 = \begin{cases} S_1' & y \le -v \\ S_1'' & -v \le y \le v \\ S_1' & y \ge v \end{cases} \tag{7.72}$$

$$\rho_2 >> \rho_1 \qquad h_2 >> h_1 \qquad R_2 >> R_1 \qquad \rho_3 = 0,$$

where $S_1' = h_1/\rho_1'$, $S_1'' = h_1/\rho_1''$ are the longitudinal conductances of the side and central segments of the upper layer and $R_1 = h_1\rho_1$, $R_2 = h_2\rho_2$ are the transverse resistances of the upper and intermediate layers.

Now (7.18) falls in the following two equations with constant coefficients:

$$\begin{aligned} \frac{d^2}{dy^2}Z^{\perp}(y) - \frac{(g')^2}{(f')^2}Z^{\perp}(y) &= -\frac{(g')^2}{(f')^2}\dot{Z}_{\text{N}} \quad |y| \ge v \\ \frac{d^2}{dy^2}Z^{\perp}(y) - \frac{(g'')^2}{(f'')^2}Z^{\perp}(y) &= -\frac{(g'')^2}{(f'')^2}\ddot{Z}_{\text{N}} \quad |y| \le v, \end{aligned} \tag{7.73}$$

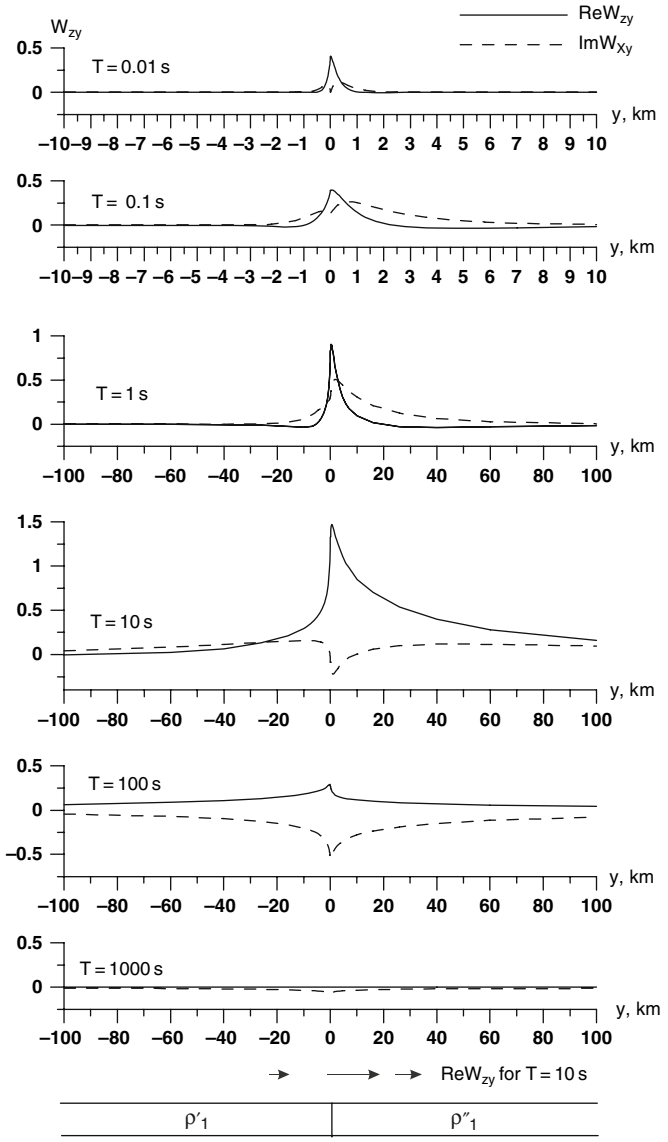

Fig. 7.15 Tipper profiles in the two-segment model from Fig. 7.9; y-distance to the boundary between segments. At the bottom – real inductive arrows. Model parameters: $\rho_1' = 10\,\Omega\text{m}$, $\rho_1'' = 100\,\Omega\text{m}$, $h_1 = 1\,\text{km}$, $\rho_2 = 10^5\,\Omega\text{m}$, $h_2 = 99\,\text{km}$, $\rho_3 = 0$. Profile parameter: period $T = 0.01 - 1000\,\text{s}$

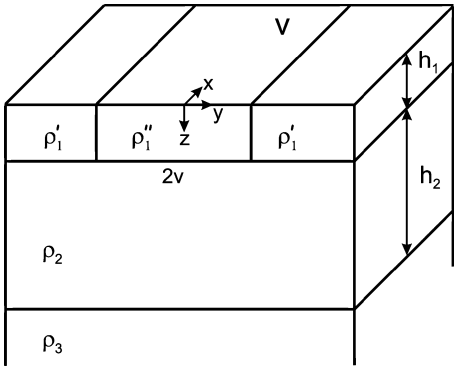

Fig. 7.16 The three-segment model

where notations g', f' and g'', f'' are the same as in (7.62), and $\dot{Z}_N, \ddot{Z}_N$ are normal impedances for the side segments and the central segment.

Solutions of these equations are

$$Z^{\perp}(y) = \begin{cases} \dot{Z}_N + Ae^{-g'|y|/f'} & |y| \geq v \\ \ddot{Z}_N + B\cos\,\mathrm{h}\dfrac{g''}{f''}y & |y| \leq v. \end{cases} \tag{7.74}$$

The coefficients A and B are determined by satisfying conditions (7.64) at the edges of the central segment, $|y| = v$. Thus, we obtain

$$Z^{\perp}(y) = \begin{cases} \dot{Z}_N \left[1 - \dfrac{1}{\gamma} \dfrac{\gamma^2 - \eta^2}{\gamma + \eta \cot\,\mathrm{h}\dfrac{g''}{f''}v} e^{-g'(|y|-v)/f'} \right] & |y| \geq v \\ \ddot{Z}_N \left[1 + \dfrac{1}{\eta \sin\,\mathrm{h}\dfrac{g''}{f''}v} \dfrac{\gamma^2 - \eta^2}{\gamma + \eta \cot\,\mathrm{h}\dfrac{g''}{f''}v} \cos\,\mathrm{h}\dfrac{g''}{f''}y \right] & |y| \leq v, \end{cases} \tag{7.75}$$

where

$$\gamma = \sqrt{\frac{S_1'}{S_1''}} \quad \eta = \frac{f'}{f''} = \sqrt{\frac{1 - i\omega\mu_o S''_1 h_2}{1 - i\omega\mu_o S'_1 h_2}}.$$

The transverse apparent resistivities are

$$\rho^{\perp}(y)=\frac{\left|Z^{\perp}(y)\right|^2}{\omega\mu_o}=\begin{cases}\dot{\rho}_n\left|1-\dfrac{1}{\gamma}\dfrac{\gamma^2-\eta^2}{\gamma+\eta\cot\ h\dfrac{g''}{f''}v}e^{-g'(|y|-v)/f'}\right|^2 & |y|\geq v\\ \ddot{\rho}_n\left|1+\dfrac{1}{\eta\sin\ h\dfrac{g''}{f''}v}\dfrac{\gamma^2-\eta^2}{\gamma+\eta\cot\ h\dfrac{g''}{f''}v}\cos\ h\dfrac{g''}{f''}y\right|^2 & |y|\leq v,\end{cases}\tag{7.76}$$

where $\dot{\rho}_n$ and $\ddot{\rho}_n$ are locally normal apparent resistivities in the side segments and the central segment.

Once again we see that variations in the conductance S_1 of the upper layer may dramatically distort the descending branches of the apparent-resistivity curves (S-effect) but leaves almost undistorted their ascending branches. Let $\omega\mu_o S_1' h_2 >> 1$ and $\omega\mu_o S_1'' h_2 >> 1$. Then in the S_1-interval (within the ascending branch of the $\rho^{\perp}$-curves), we have $\eta\approx\gamma$, whence

$$\begin{aligned}Z^{\perp}(y)&\approx\begin{cases}\dot{Z}_N=\dfrac{1}{S_1'} & |y|\geq v\\ \ddot{Z}_N=\dfrac{1}{S_1''} & |y|\leq v\end{cases}\\ \rho^{\perp}(y)=\frac{\left|Z^{\perp}(y)\right|^2}{\omega\mu_o}&\approx\begin{cases}\dot{\rho}_n=\dfrac{1}{\omega\mu_o(S_1')^2} & |y|\geq v\\ \ddot{\rho}_n=\dfrac{1}{\omega\mu_o(S_1'')^2} & |y|\leq v.\end{cases}\end{aligned}\tag{7.77}$$

In this approximation, the transverse impedance and apparent resistivity do not depart from their locally normal values.

Now pass on to the h-interval. Let $\omega\mu_o S_1' h_2 << 1$ and $\omega\mu_o S_1'' h_2 << 1$. Then, within the descending branch of the $\rho^{\perp}$-curves, we have $f'\approx f''\approx 1$ and $\eta\approx 1$, whence

$$Z^{\perp}(y)\approx\begin{cases}\dot{Z}_N\left[1-\dfrac{1-\dfrac{S_1''}{S_1'}}{1+\sqrt{\dfrac{S_1''}{S_1'}}\cot\ h\dfrac{v}{d''}}e^{-(|y|-v)/d'}\right] & |y|\geq v\\ \ddot{Z}_N\left[1-\dfrac{1}{\sin\ h\dfrac{v}{d''}}\dfrac{1-\dfrac{S_1'}{S_1''}}{\sqrt{\dfrac{S_1'}{S_1''}}+\cot\ h\dfrac{v}{d''}}\cos\ h\dfrac{y}{d''}\right] & |y|\leq v\end{cases}\tag{7.78}$$

and

$$\rho^{\perp}(y) \approx \begin{cases} \dot{\rho}_{\mathrm{n}} \left| 1 - \dfrac{1 - \dfrac{S_1''}{S_1'}}{1 + \sqrt{\dfrac{S_1''}{S_1'}} \operatorname{cot\ h} \dfrac{w}{d''}} e^{-(|y|-v)/d'} \right|^2 & |y| \geq v \\ \ddot{\rho}_{\mathrm{n}} \left| 1 - \dfrac{1}{\sin\ \mathrm{h} \dfrac{v}{d''}} \dfrac{1 - \dfrac{S_1'}{S_1''}}{\sqrt{\dfrac{S_1'}{S_1''}} + \operatorname{cot\ h} \dfrac{v}{d''}} \cos\ \mathrm{h} \dfrac{y}{d''} \right|^2 & |y| \leq v, \end{cases} \tag{7.79}$$

where $d' = 1/g'$, $d'' = 1/g''$ are adjustment distances for side and central segments and $\dot{Z}_{\mathrm{N}} = \ddot{Z}_{\mathrm{N}} = -i\omega\mu_{\mathrm{o}} h$, $\dot{\rho}_{\mathrm{n}} = \ddot{\rho}_{\mathrm{n}} = \omega\mu_{\mathrm{o}} h^2$.

These equations clearly demonstrate the key features of the S-effect in the three-segment model.

The most pronounced S-effect is observed at the edges of the central segment:

$$Z^{\perp}(\pm v) \approx \begin{cases} \dot{Z}_{\mathrm{N}} \left[1 - \dfrac{1 - \dfrac{S_1''}{S_1'}}{1 + \sqrt{\dfrac{S_1''}{S_1'}} \operatorname{cot\ h} \dfrac{v}{d''}} \right] & |y| = v + 0 \\ \ddot{Z}_{\mathrm{N}} \left[1 - \dfrac{\left(1 - \dfrac{S_1'}{S_1''}\right) \operatorname{cot\ h} \dfrac{v}{d''}}{\sqrt{\dfrac{S_1'}{S_1''}} + \operatorname{cot\ h} \dfrac{v}{d''}} \right] & |y| = v - 0 \end{cases} \tag{7.80}$$

and

$$\rho^{\perp}(\pm v) \approx \begin{cases} \dot{\rho}_{\mathrm{n}} \left| 1 - \dfrac{1 - \dfrac{S_1''}{S_1'}}{1 + \sqrt{\dfrac{S_1''}{S_1'}} \operatorname{cot\ h} \dfrac{v}{d''}} \right|^2 & |y| = v + 0 \\ \ddot{\rho}_{\mathrm{n}} \left| 1 - \dfrac{\left(1 - \dfrac{S_1'}{S_1''}\right) \operatorname{cot\ h} \dfrac{v}{d''}}{\sqrt{\dfrac{S_1'}{S_1''}} + \operatorname{cot\ h} \dfrac{v}{d''}} \right|^2 & |y| = v - 0. \end{cases} \tag{7.81}$$

If $v \geq 3d''$, we set $\coth(v/d'') \approx 1$ and receive the same estimates (7.70) for the S-effect as in the two-segment model:

$$Z^{\perp}(\pm v) \approx \begin{cases} \dot{Z}_{\mathrm{N}} \sqrt{\dfrac{S_1''}{S_1'}} & |y| = v + 0 \\ \ddot{Z}_{\mathrm{N}} \sqrt{\dfrac{S_1'}{S_1''}} & |y| = v - 0 \end{cases} \qquad \rho^{\perp}(\pm v) \approx \begin{cases} \dot{\rho}_{\mathrm{n}} \dfrac{S_1''}{S_1'} & |y| = v + 0 \\ \ddot{\rho}_{\mathrm{n}} \dfrac{S_1'}{S_1''} & |y| = v - 0. \end{cases} \tag{7.82}$$

Moving away from the central segment, the S-effect exponentially attenuates. We can turn to Table 7.1 and estimate a distance, at which $\rho^{\perp}$ approaches its locally normal value $\dot{\rho}_{\mathrm{n}}$ with an accuracy of 5%. It is a question of several adjustment distances.

It would be interesting to estimate the width $w = 2v$ of the central segment, at whose middle ($y = 0$) the transverse apparent resistivity $\rho^{\perp}$ is close to its locally normal value $\ddot{\rho}_{\mathrm{n}}$. Figure 7.17 shows the dependence of $\rho^{\perp}(0)/\ddot{\rho}_{\mathrm{N}}$ on w for models with and $S_1''/S_1' = 0.01$, $d'' = 100\,\mathrm{km}$ and $S_1''/S_1' = 100$, $d'' = 1000\,\mathrm{km}$. The

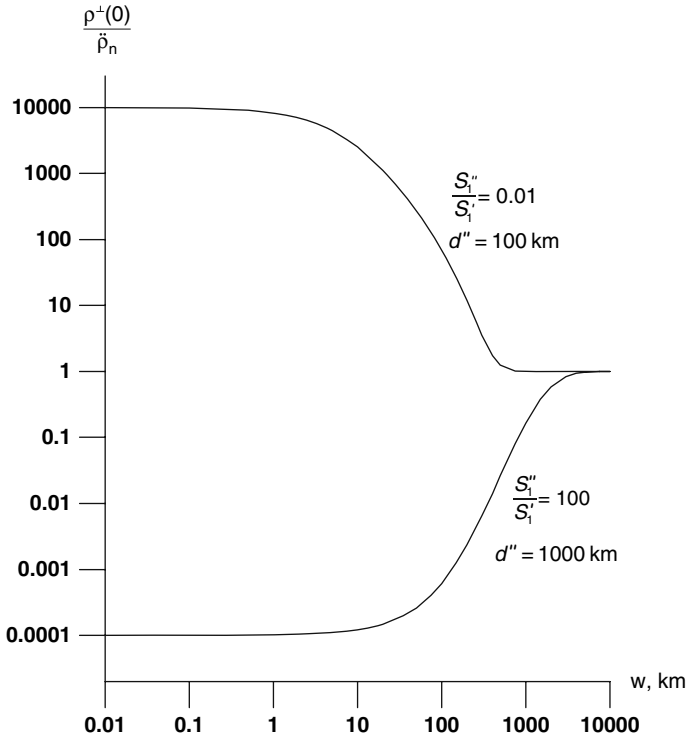

Fig. 7.17 The w-dependence of the normalized transverse apparent resistivity $\rho^{\perp}(0)/\ddot{\rho}_{\mathrm{n}}$ obtained in the middle of the central segment of the model shown in Fig. 7.16

calculations were done by (7.79). We see that at $w < 0.01d''$ the entire central segment is embraced with strong S-effect (no visible current leakage from the upper layer). With widening the central segment, the S-effect weakens due to current leakage through the upper layer bottom. At $w \sim 5 \div 7.5\ d''$ the S-effect in the middle of the central segment virtually vanishes. It is a question of distances that may number in the hundreds and thousands of km.

Let us consider the magnetotelluric and magnetovariational curves calculated for the three-segment model using analytical solutions (7.75), (7.76) and with the finite element method (Wannamaker et al.,1987).

Figsures 7.18 and 7.19 display the transverse and longitudinal apparent-resistivity and impedance-phase curves obtained in the model with the resistive central segment 20 km wide.

Once again we see that within the S_1- and h-intervals the $\rho^{\perp}$-curves plotted from the analytical and finite-element solutions agree fairly well. Ascending branches of the $\rho^{\perp}$-curves are not distorted. They coincide with ascending branches of the locally normal $\dot{\rho}_n$-curves. However, descending branches of the $\rho^{\perp}$-curves are distorted by the S-effect. Over the side segments they are shifted down reflecting the current leakage (the current penetrates into the intermediate layer and flows under the resistive central segment). These distortions are noticeable even at great distances from the central segment ($y = -1010$ km, $\Delta y = |y| - v = 1000$ km, adjustment distance $d' \approx 1000$ km). When coming closer to the central segment, the distortion increases. In the immediate neighborhood of the central segment ($y = -11$ km, $\Delta y = 1$ km), the transverse apparent resistivity $\rho^{\perp}$ is 4 times less than $\dot{\rho}_n$. Over the central segment, the ascending branches of the $\rho^{\perp}$-curves elongate and their descending branches shift up reflecting the drop in S_1. Here $\rho^{\perp}$ is 2000 times greater than $\dot{\rho}_n$.

It is quite another matter with the $\rho^{\parallel}$-curves. Over the side segments the longitudinal $\rho^{\parallel}$-curves are slightly distorted. Induction effect caused by the resistive insertion is noticeable only in the immediate neighborhood of the central segment ($y = -11$ km, $\Delta y = 1$ km). Here the ascending branch of the $\rho^{\parallel}$-curve shifts to the left and becomes less sloping. In going to the central segment, we observe a remarkable strong distortion reflecting the inductive influence of excess currents concentrated at both sides of the resistive central segment. Here the $\rho^{\parallel}$ -curves acquire a well-defined false minimum that could be mistaken as an evidence of a deep conductive layer underlying the central segment. This effect is known as the *effect of false conductive layer*.

Now we turn to the phase curves. Note that the descending branches of the transverse $\varphi^{\perp}$-curves plotted from the analytical and finite-element solutions merge together. Over the side segments the ascending and descending branches of the $\varphi^{\perp}$-curves come close to the normal $\dot{\varphi}_n$-curves (slight phase distortions). But in the region of the maximum of the $\varphi^{\perp}$-curves we observe a considerable discrepancy between $\varphi^{\perp}$ and $\dot{\varphi}_n$. At the same time the longitudinal $\varphi^{\parallel}$-curves are almost everywhere in close agreement with the normal $\dot{\varphi}_n$-curves. Only in the immediate neighborhood of the central segment ($\Delta y = 1$km) we have the $\varphi^{\parallel}$-curve, whose ascending branch is strongly shifted to the left. Somewhat different relations are

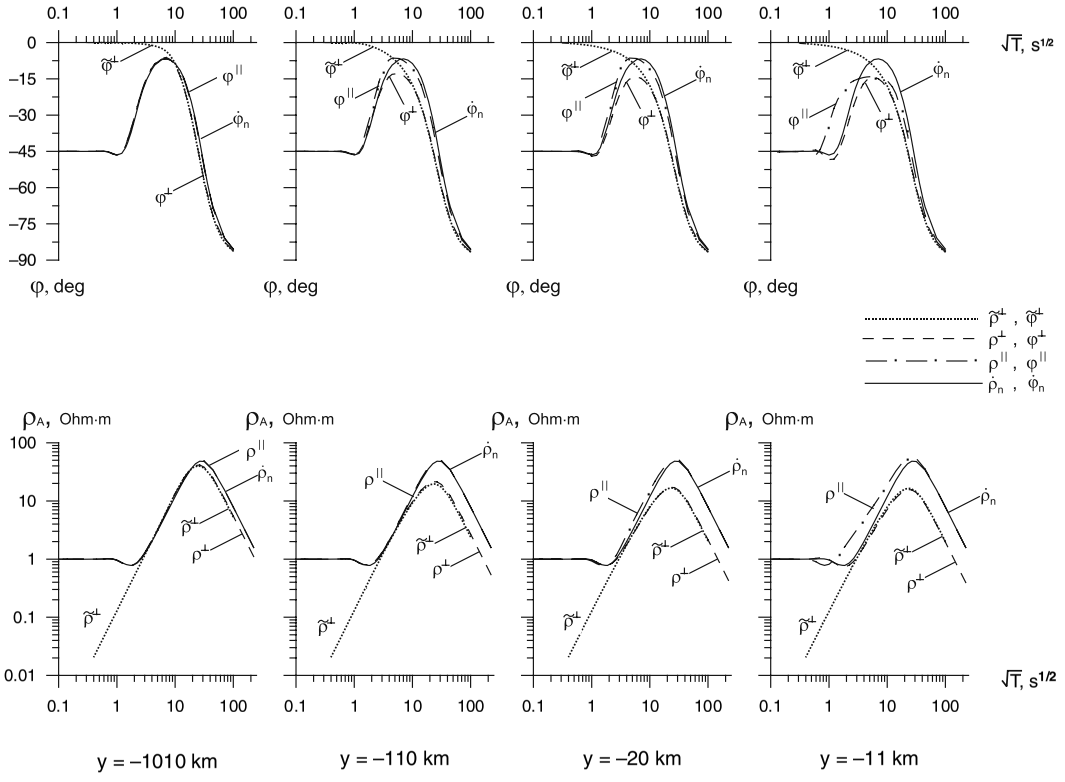

Fig. 7.18 Longitudinal and transverse apparent-resistivity and impedance-phase curves over the left conductive segment in the model shown in Fig. 7.16; y-distance to the centre of the model; $\tilde{\rho}^{\perp}$, $\tilde{\varphi}^{\perp}$-analytical solution, $\rho^{\perp}$, $\varphi^{\perp}$ and $\rho^{\parallel}$, $\varphi^{\parallel}$–solution by the finite elements method, $\dot{\rho}_n$, $\dot{\varphi}_n$ - locally normal solution. Model parameters: $\rho_1' = 1\,\Omega\text{m}$, $h_1 = 1\,\text{km}$, $\rho_1'' = 100\,\Omega\text{m}$, $v = 10\,\text{km}$, $\rho_2 = 10000\,\Omega\text{m}$, $h_2 = 99\,\text{km}$, $\rho_3 = 0$

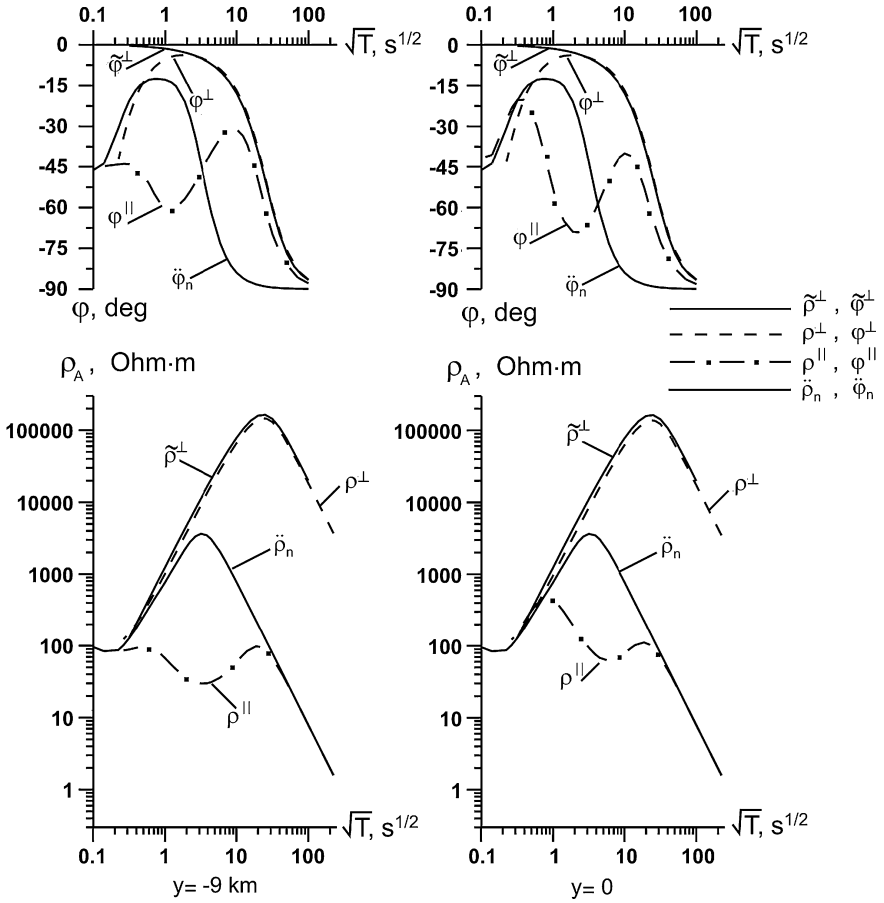

Fig. 7.19 Longitudinal and transverse apparent-resistivity and impedance-phase curves over the resistive central segment in the model shown in Fig. 7.16; y-distance to the centre of the model; $\tilde{\rho}^{\perp}$, $\tilde{\varphi}^{\perp}$-analytical solution, $\rho^{\perp}$, $\varphi^{\perp}$ and $\rho^{\parallel}$, $\varphi^{\parallel}$-solution by the finite elements method, $\ddot{\rho}_n$, $\ddot{\varphi}_n$-locally normal solution. Model parameters: $\rho_1' = 1$ Ohm·m, $h_1 = 1$km, $\rho_1'' = 100$ Ohm·m, $v = 10$ km, $\rho_2 = 10000$ Ohm·m, $h_2 = 99$ km, $\rho_3 = 0$

characteristic of the central segments. Here the ascending branch of the $\varphi^{\perp}$-curves is slightly distorted, whereas their descending branch shifts drastically to the right. And the $\varphi^{\parallel}$-curves have a pronounced minimum (effect of false conductive layer), while their descending branch is shifted to the right and comes close to the $\varphi^{\perp}$-curve.

Figure 7.20 displays the tipper curves, which are antisymmetric with respect to the midpoint of the central segment. At all frequencies the real tippers are positive in the left part of the model and negative in its right part. At the same time the imaginary tipper change their sign with frequency. The large tippers are observed over the edges of the central segment ($|\Delta y| \leq 3$km). They rather quickly attenuate with distance from the central segment. Within the h-interval ($T \geq 8000$ s) the real and imaginary tippers decay. With lowering frequency the tipper phases, $\varphi_w =$

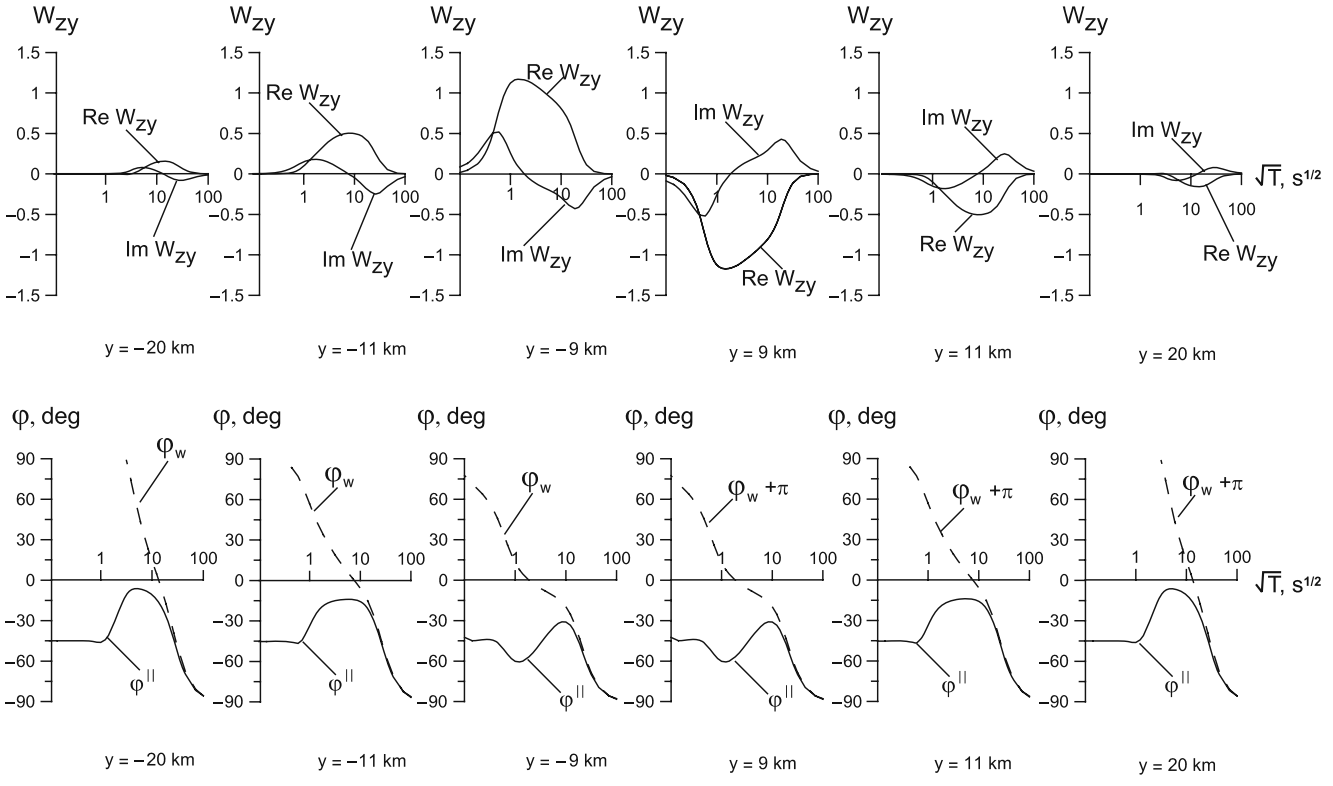

Fig. 7.20 Tipper curves in the three-segment model shown in Fig. 7.16 with resistive central segment; y-distance to the centre of the model; $\mathrm{Re}\,W_{zy}$, $\mathrm{Im}\,W_{zy}$ – real and imaginary tippers, φ_w-phase of W_{zy}, $\varphi^{\parallel}$-phase of $Z^{\parallel}$. Model parameters: $\rho_1' = 1\,\Omega\mathrm{m}$, $h_1 = 1\,\mathrm{km}$, $\rho_1'' = 100\,\Omega\mathrm{m}$, $v = 10\,\mathrm{km}$, $\rho_2 = 10000\,\Omega\mathrm{m}$, $h_2 = 99\,\mathrm{km}$, $\rho_3 = 0$

arg W_{zy} or $\varphi_w = \arg W_{zy} + \pi$, pass from the Ith quadrant to the IVth quadrant and merge with the longitudinal impedance phases, $\varphi^{\parallel}$. This is in accordance with (4.6), predicted in (Zhang et al., 1993).

Next we consider the model with the conductive central segment 20 km wide. We observe here the same effects as in the model with the resistive central segment.

The transverse and longitudinal apparent-resistivity and impedance-phase curves obtained in this model are shown in Figs. 7.21 and 7.22. The $\rho^{\perp}$- and $\varphi^{\perp}$-curves (finite-element solution) are consistent with $\tilde{\rho}^{\perp}$- and $\tilde{\varphi}^{\perp}$-curves (analytical solution). Their distortion is rather weak within the resistive side segments bordering the conductive central segment. Here the $\rho^{\perp}$- and $\varphi^{\perp}$-curves are close to the normal ones. At the same time the $\rho^{\parallel}$- and $\varphi^{\parallel}$-curves are distorted by the induction effect smoothing their ascending branches. This effect vanishes at distances of the order of the effective penetration depth (100 km). Going to the central segment, we observe

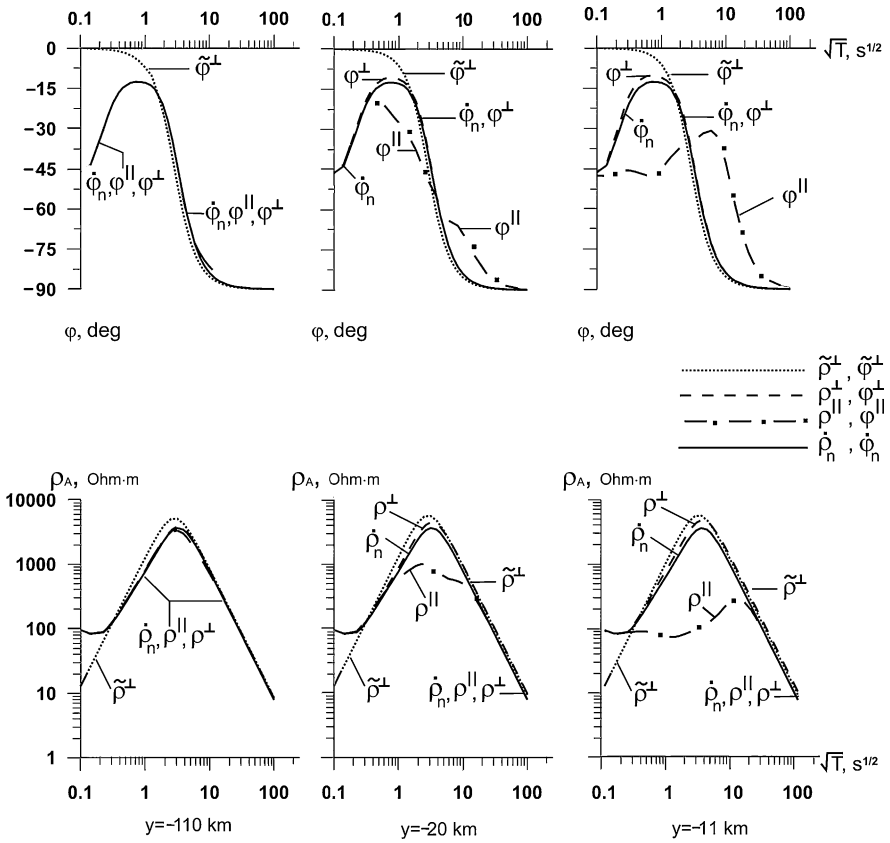

Fig. 7.21 Longitudinal and transverse apparent-resistivity and impedance-phase curves over the left resistive segment in the model shown in Fig. 7.16; y-distance to the centre of the model; $\tilde{\rho}^{\perp}, \tilde{\varphi}^{\perp}$-analytical solution, $\rho^{\perp}, \varphi^{\perp}$ and $\rho^{\parallel}, \varphi^{\parallel}$-numerical solution by the finite elements method, $\dot{\rho}_n, \dot{\varphi}_n$ – locally normal solution. Model parameters: $\rho_1' = 1$ Ohm·m, $h_1 = 1$ km, $\rho_1'' = 1$ Ohm·m, $v = 10$ km, $\rho_2 = 10000$ Ohm·m, $h_2 = 99$ km, $\rho_3 = 0$

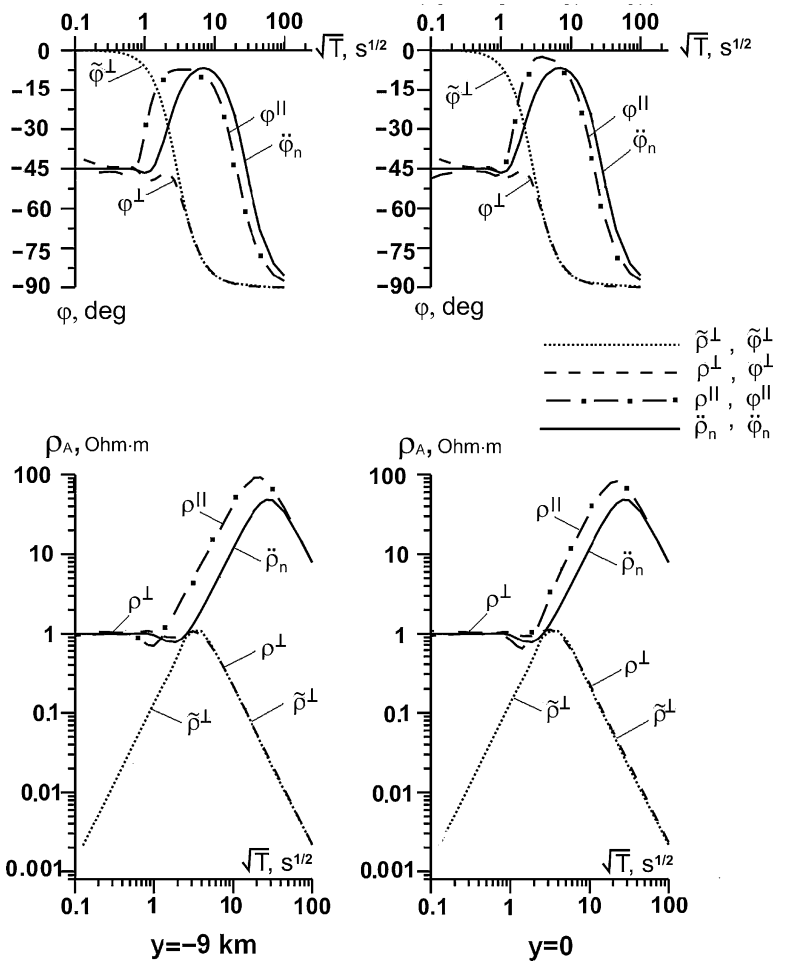

Fig. 7.22 Longitudinal and transverse apparent-resistivity and impedance-phase curves over the central conductive segment in the model from Fig. 7.16; y-distance to the centre of the model; $\tilde{\rho}^{\perp}$, $\tilde{\varphi}^{\perp}$-analytical solution, $\rho^{\perp}$, $\varphi^{\perp}$ and $\rho^{\parallel}$, $\varphi^{\parallel}$-numerical solution by the finite elements method, $\ddot{\rho}_n$, $\ddot{\varphi}_n$-locally normal solution. Model parameters: $\rho_1' = 100$ Ohm·m, $h_1 = 1$ km, $\rho_1'' = 100$ Ohm·m, $v = 10$ km, $\rho_2 = 10000$ Ohm·m, $h_2 = 99$ km, $\rho_3 = 0$

the strong S-effect that dramatically distorts the $\rho^{\perp}$-curves. These curves have no ascending branch and their descending branch is shifted deeply down. Here the $\rho^{\parallel}$- and $\varphi^{\parallel}$- curves are much less distorted.

Figure 7.23 presents the tipper curves. Here over the side segments bordering the conductive central segment we observe rather large tippers at distances $\Delta y = |y| - v$ about 30 km. Comparing Fig. 7.23 with Fig. 7.20, we see that conductive structures cause more vigorous magnetovariational anomalies than resistive structures. Note also that in this model low-frequency tippers show the same property as in the model with the resistive central segment: the tipper phases, $\varphi_W = \arg W_{zy}$ or

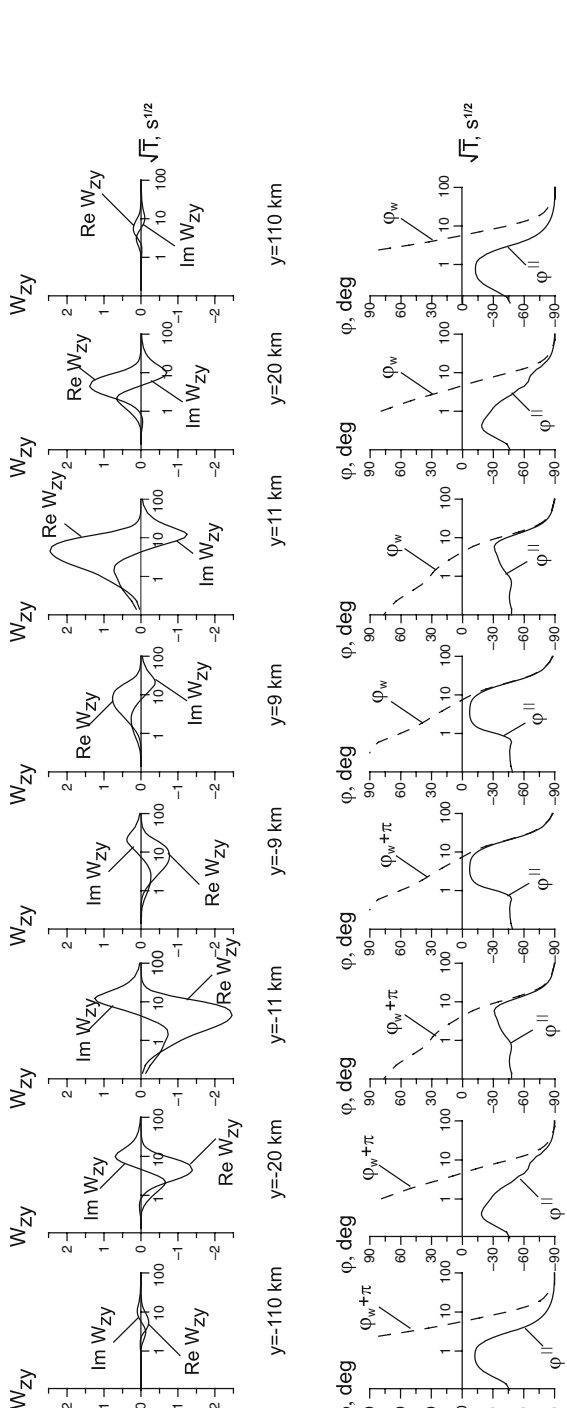

Fig. 7.23 Tipper curves in the three-segment model from Fig. 7.16 with conductive central segment; y-distance to the centre of the model; $\mathrm{Re}\,W_{zy}$, $\mathrm{Im}\,W_{zy}$ – real and imaginary tippers, φ_w-phase of W_{zy}, $\varphi^{\|}$- phase of $Z^{\|}$. Model parameters: $\rho_1' = 100$ Ohm·m, $h_1 = 1$ km, $\rho_1'' = 1$ Ohm·m, $v = 10$ km, $\rho_2 = 10000$ Ohm·m, $h_2 = 99$ km, $\rho_3 = 0$

$\varphi_w = \arg W_{zy} + \pi$, pass from the Ith quadrant to the IVth quadrant and merge with the longitudinal impedance phases, $\varphi^{\parallel}$.

In closing consider the field and tipper profiles.

Figure 7.24 presents the electric and magnetic profiles in a model with the resistive central segment. The fields E_x, H_y (TE-mode) and E_y (TM-mode) are normalized to the normal fields $\dot{E}_x^{\mathrm{N}}, \dot{E}_y^{\mathrm{N}}, \dot{H}_y^{\mathrm{N}}$. The inductive TE-anomalies envelope the central segment and rather quickly attenuate with distance. At the distances

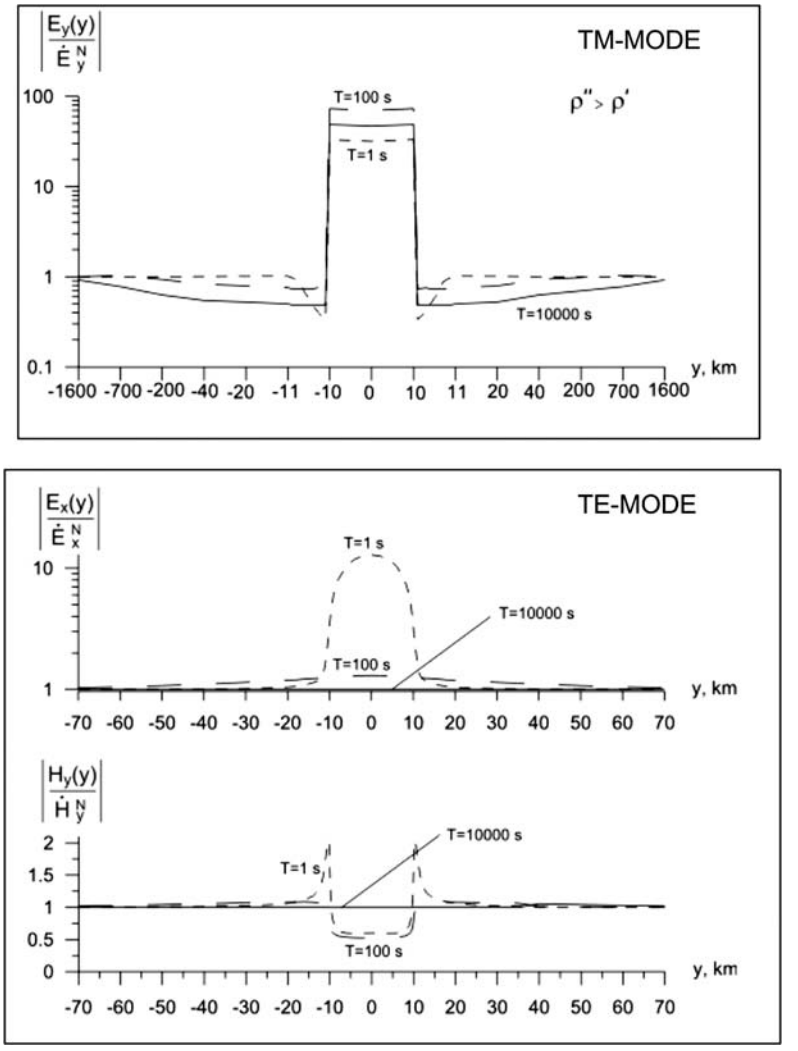

Fig. 7.24 Electromagnetic field profiles in the three-segment model with resistive central segment shown in Fig. 7.16; y-distance to the centre of the model. Model parameters: $\rho_1' = 1\,\Omega\mathrm{m}$, $h_1 = 1\,\mathrm{km}$, $\rho_1'' = 100\,\Omega\mathrm{m}$, $v = 10\,\mathrm{km}$, $\rho_2 = 10000\,\Omega\mathrm{m}$, $h_2 = 99\,\mathrm{km}$, $\rho_3 = 0$ Profile parameter: period $T = 1$–10000 s

$\Delta y = |y| - v = 30$ km they virtually vanish. Let us take a look at their frequency dependence. On a period $T = 1$s we observe a bell-like maximum of E_x and a bowl-like minimum of H_y fringed with sharp side maxima. The minimum of H_y is caused by current deficiency within the central resistive segment, while the side maxima reflect the concentration of longitudinal currents in the neighborhood of the central segment (horizontal skin effect). Such events are characterized by the condition $h''_{\text{eff}} << 2v$ (the effective depth penetration is much less than the width of central segment). At low frequencies, when $h''_{\text{eff}} >> 2v$, these anomalies flatten ($T = 100$s) and vanish ($T = 10000$ s). This effect is referred to as *inductive flattening*. Quite different picture is exhibited by the galvanic TM-anomaly. Over the central segment we have a box-like maximum of E_y whose amplitude slightly depends on frequency. Outside the central segment two types of galvanic anomalies are observed. At high frequency ($T = 1$s) we have sharp side minima of E_y associated with rearrangement of transverse currents due to different skin depth in the central segment and in the bordering side segments. With lowering frequency these minima vanish and we see a slow decrease of E_y caused by current leakage (transverse currents penetrate into the underlying medium and flow under the resistive segment). In the h-interval ($T = 10000$ s) this effect extends to distances about 1000 km.

The electric and magnetic profiles in a model with the conductive central segment are presented in Fig. 7.25. First consider the inductive TE-anomalies. The central segment manifests itself in a bowl-like minimum of E_x ($T = 1s$, $h''_{\text{eff}} << 2v$). At the low frequencies this minimum flattens and vanishes ($T = 100 - 10000\ s$, $h''_{\text{eff}} >> 2v$). A decrease in E_x is accompanied with an increase in H_y. Note that at high frequencies the horizontal skin effect makes itself evident within the central segment: the excess longitudinal currents are concentrated at its boundaries causing the sharp side maxima of H_y ($T = 1$s). At the low frequencies the excess currents are distributed uniformly and the anomaly of H_y assumes the form of a bell-like maximum ($T = 100$ s). At $T = 10000\ s$ this maximum decays. The anomalies of E_x and H_y attenuate rather quickly with distance. At the distances $\Delta y = |y| - v >> 100$ km they virtually vanish. Coming to the galvanic TM-anomalies, we observe an abrupt drop in E_y over the central segment (current rearrangement effect, which shows up in sharp side minima). Note also that within the central segment $\left|E_y/\dot{E}_y^{\text{N}}\right| << \left|E_x/\dot{E}_x^{\text{N}}\right|$ for $T \geq 100$ s. If the normal field is isometric ($\dot{E}_x^{\text{N}} = \dot{E}_y^{\text{N}}$), then $\left|E_y\right| << |E_x|$. The low-frequency electric field is quasilinearly polarized along the conductive central segment, which serves as a current channel. This effect looks like a *channeling effect*.

Figure 7.26 displays the W_{zy}-profiles. We see here the same zigzag anomalies of $\text{Re}W_{zy}$ and $\text{Im}W_{zy}$ as in the dike model (compare Fig. 7.26 with Fig. 6.13). Note that the real and imaginary tippers are intensive in the S_1-interval and they quickly decay in going to the h-interval.

7.2.4 The Screening Effect

In closing we consider a case that highly resistive intermediate layer inhibits the current rearrangement and impairs or even blocks the access to information on the

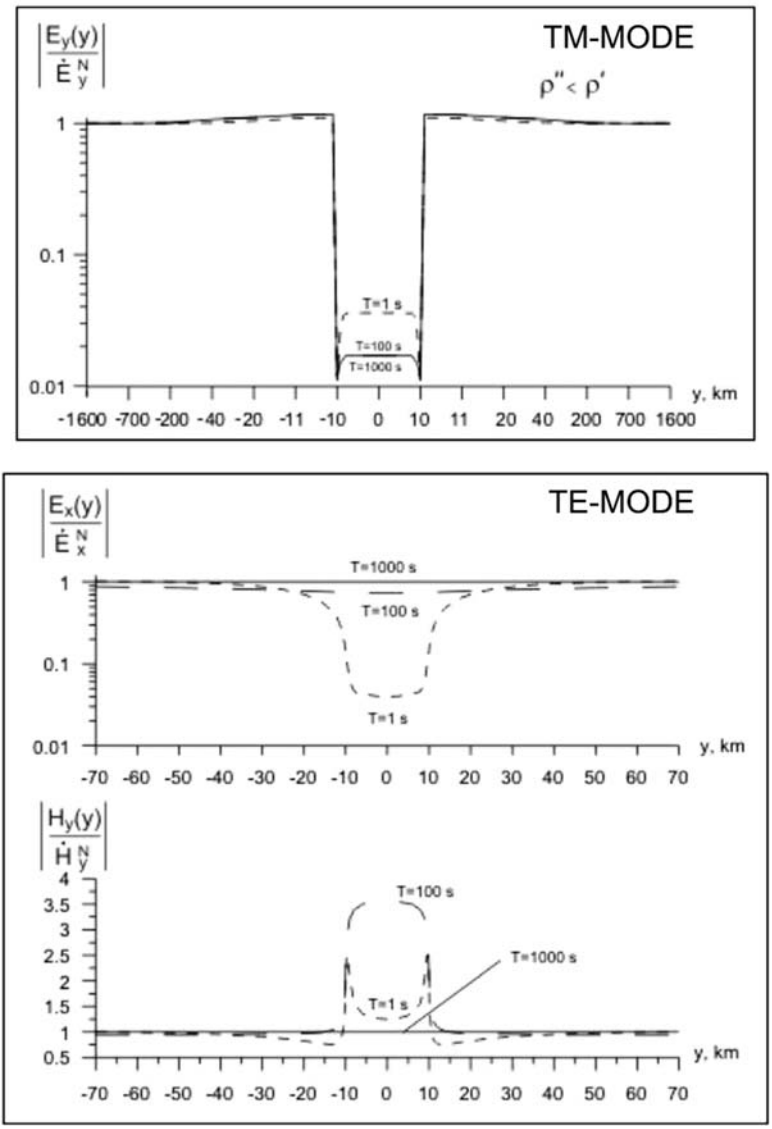

Fig. 7.25 Electromagnetic field profiles in the three-segment model with conductive central segment shown in Fig. 7.16; y-distance to the centre of the model. Model parameters: $\rho_1' = 100$ Ohm·m, $h_1 = 1$ km, $\rho_1'' = 1$ Ohm·m, $v = 10$ km, $\rho_2 = 10000$ Ohm·m, $h_2 = 99$ km, $\rho_3 = 0$ Profile parameter: period $T = 1 - 1000$ s

conductance of underlying sedimentary strata. This galvanic effect is referred to as the *screening or shielding effect.*

A model of the galvanic-screening effect is shown in Fig. 7.27. Here the sedimentary strata consists of three layers: the upper conductive layer (ρ_1, h_1), the highly resistive intermediate layer $\rho_2 >> \rho_1, h_2$) and the lower inhomogeneous

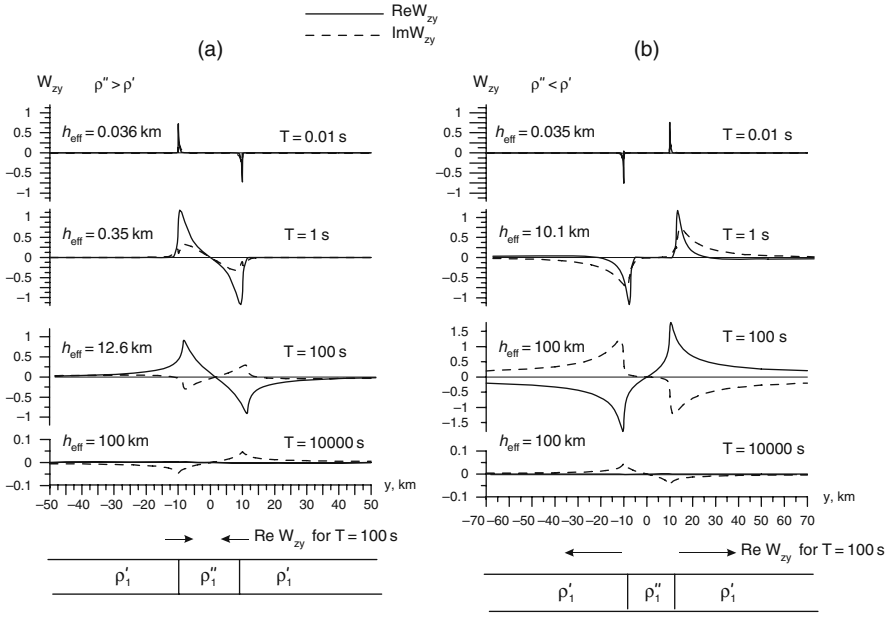

Fig. 7.26 Tipper profiles in the three-segment model shown in Fig. 7.16; y-distance to the centre of the model. At the bottom – real inductive arrows. Model parameters: a – in the model with resistive central segment $\rho_1' = 1$ Ohm·m, $\rho_1'' = 100$ Ohm·m, $v = 10$ km, $h_1 = 1$, $\rho_2 = 10000$ Ohm·m, $h_2 = 99$ km, $\rho_3 = 0$; b – in the model with conductive central segment $\rho_1' = 100$ Ohm·m, $\rho_1'' = 1$ Ohm·m, $v = 10$ km, $h_1 = 1$ km, $\rho_2 = 10000$ Ohm·m, $h_2 = 99$km, $\rho_3 = 0$. Profile parameter: period $T = 0.01 - 10000$ s

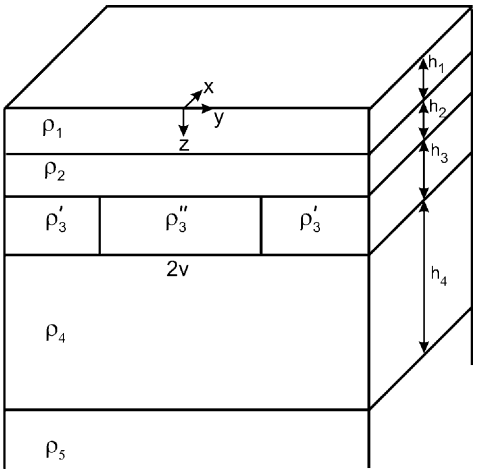

Fig. 7.27 Three-segment model with a higly resistive screening layer

three-segment layer (ρ_3, h_3) with the side segments of resistivity ρ_3' and the central segment of resistivity ρ_3'' and width $2v$. The sediments rest on the highly resistive lithosphere ($\rho_4 >> \rho_1$, $h_4 >> h_1+h_2+h_3$) underlaid with highly conductive mantle ($\rho_5 = 0$).

Let us begin with analytical solution of the problem for the TM-mode. Following (Berdichevsky and Jakovlev,1990), we ignore the influence of the conductive mantle and set $\rho_4 \to \infty$, $h_4 \to \infty$. Then, using Dmitriev's thin-sheet approximation (7.16) and taking into account that on the surface of the perfect insulator $H_x = 0$, we write

$$
\begin{aligned}
&E_y(y,0) = E_y(y,h_1) + i\omega\mu_o h_1 H_x^N \\
&E_y(y,h_1) = E_y(y,h_{12}) + i\omega\mu_o h_2 H_x(y,h_1) + R_2 \frac{d^2 H_x(y,h_1)}{dy^2} \\
&H_x(y,h_1) = H_x^N + S_1 E_y(y,0) \\
&H_x(y,h_{12}) = H_x(y,h_1) + S_2 E_y(y,h_1) \\
&H_x(y,h_{12}) = -S_3(y) E_y(y,h_{12}),
\end{aligned}
$$

where $h_{12} = h_1 + h_2$ and $S_1 = h_1/\rho_1$, $S_2 = h_2/\rho_2$, $S_3(y) = h_3/\rho_3(y)$, $R_2 = h_2\rho_2$. Eliminating $E_y(y,h_1)$, $E_y(y,h_{12})$ and $H_x(y,h_1)$, $H_x(y,h_{12})$ from these equations, we get the equation for the transverse impedance at the Earth's surface, $z = 0$:

$$
\begin{aligned}
&S_1 R_2 \frac{d^2 S_3(y) Z^{\perp}(y)}{dy^2} - [S(y) - i\omega\mu_o S_1 h_2 S_3(y)] Z^{\perp}(y) \\
&= -\{1 - i\omega\mu_o [h_1 S_2 + h_{12} S_3(y)]\},
\end{aligned}
\tag{7.83}
$$

where $Z^{\perp}(y) = -E_y(y)/H_x^N$ and $S(y) = S_1 + S_2 + S_3(y)$. With $\omega\mu_o S_1 h_2 << 1$ and $\omega\mu_o[h_1 S_2 + h_{12} S_3(y)] << 1$ we are in the S-interval. Here (7.83) reduces to the equation

$$
S_1 R_2 \frac{d^2 S_3(y) Z^{\perp}(y)}{dy^2} - S(y) Z^{\perp}(y) = -1, \tag{7.84}
$$

which falls into two equations with constant coefficients:

$$
\begin{aligned}
&S_1 R_2 S_3' \frac{d^2 Z^{\perp}(y)}{dy^2} - S' Z^{\perp}(y) = -1 \qquad |y| \geq v \\
&S_1 R_2 S_3'' \frac{d^2 Z^{\perp}(y)}{dy^2} - S'' Z^{\perp}(y) = -1 \quad |y| \leq v,
\end{aligned}
\tag{7.85}
$$

where $S_3' = h_3/\rho_3'$, $S_3'' = h_3/\rho_3''$ and $S' = S_1 + S_2 + S_3'$, $S'' = S_1 + S_2 + S_3''$.

General solutions of equations (7.85) are

$$
Z^{\perp}(y) = \begin{cases} \dot{Z}_N + A e^{-\bar{g}'|y|} & |y| \geq v \\ \ddot{Z}_N + B \cos\ \mathrm{h}\bar{g}'' y & |y| \leq v, \end{cases} \tag{7.86}
$$

where $\bar{g}'$, $\bar{g}''$ are the generalized galvanic parameters of the ρ_3'- and ρ_3''-segments:

$$\bar{g}' = \sqrt{\frac{S'}{S_1 R_2 S_s'}} = \sqrt{\frac{S'}{S_3'}}\, g \quad \bar{g}'' = \sqrt{\frac{S''}{S_1 R_2 S_3''}} = \sqrt{\frac{S''}{S_3''}}\, g$$
$$g = \frac{1}{\sqrt{S_1 R_2}} \tag{7.87}$$

and $\dot{Z}_N, \ddot{Z}_N$ are the normal impedances:

$$\dot{Z}_N = \frac{1}{S'}, \quad \ddot{Z}_N = \frac{1}{S''}. \tag{7.88}$$

The generalized adjustment distances are

$$\bar{d}' = \frac{1}{\bar{g}'} = \sqrt{\frac{S_3'}{S'}} d, \quad \bar{d}'' = \frac{1}{\bar{g}''} = \sqrt{\frac{S_3''}{S''}} d, \quad d = \sqrt{S_1 R_2}. \tag{7.89}$$

They differ from the standard adjustment distance d by factor depending on ratio between S_3 and S. The less the conductance S_3 of sediments covered with highly resistive layer, the less the generalized adjustment distance.

The coefficients A and B are determined from the conditions that $Z^{\perp}$ and $dZ^{\perp}/dy$ are continuous at $|y| = v$. It is easy to show that these conditions provide continuity of current densities j_y and j_z within the first and second layers.

On simple mathematics we obtain

$$Z^{\perp}(y) = \begin{cases} \dfrac{1}{S'} \left[1 - \dfrac{\Delta S_3}{S'' + q' \cot \mathrm{h} \dfrac{v}{\bar{d}''}} e^{-(|y|-v)/\bar{d}'} \right] & |y| \geq v \\ \dfrac{1}{S''} \left[1 + \dfrac{1}{\sin \mathrm{h} \dfrac{v}{\bar{d}''}} \dfrac{\Delta S_3}{q'' + S' \cot \mathrm{h} \dfrac{v}{\bar{d}''}} \cos \mathrm{h} \dfrac{y}{\bar{d}''} \right] & |y| \leq v, \end{cases} \tag{7.90}$$

where

$$\Delta S_3 = S_3'' - S_3', \quad q' = \sqrt{\frac{S' S'' S_3''}{S_3'}}, \quad q'' = \sqrt{\frac{S' S'' S_3'}{S_3''}}.$$

These representations give a good account of the screening effect. The central segment manifests itself due to current penetrating through the shielding layer ρ_2. The conductive penetrability of the layer ρ_2 is characterized by the generalized galvanic parameters $\bar{g}'$ and $\bar{g}''$, which define the generalized adjustment distances $\bar{d}'$ and $\bar{d}''$. The most indicative is the relation between $\bar{d}''$ and the half-width v of central segment. According to (7.90),

$$\begin{aligned} Z^{\perp}(0) &\approx \frac{1}{S''} \quad \text{weak} \quad \text{screening} \\ \bar{d}'' << v & \\ Z^{\perp}(y) &\approx \frac{1}{S'} \quad \text{strong} \quad \text{screening.} \\ \bar{d}'' >> v & \end{aligned} \tag{7.91}$$

The screening effect is exemplified in Fig. 7.28. Here the apparent-resistivity curves obtained over the middle of the central conductive segment ($y = 0$) are shown. They have been computed by the finite-element method (Wannamaker et al., 1987). The resistivity ρ_2 of the shielding layer takes the value from 1000 to 125000 Ohm·m. Let us consider the transverse $\rho^{\perp}-$ curves. They depend heavily

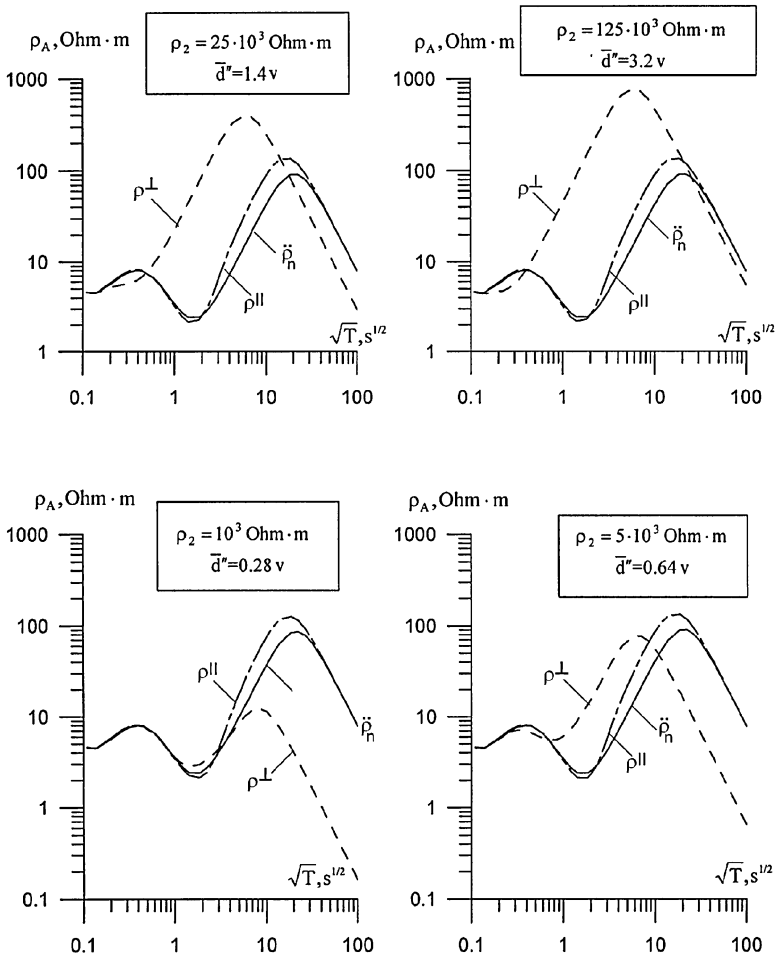

Fig. 7.28 The screening effect in the model shown in Fig. 7.27. Model parameters: $\rho_1 = 5$ Ohm·m, $h_1 = 0.2$ km, $\rho_2 = 1000, 5000, 25000, 125000$ Ohm·m, $h_2 = 0.3$ km, $\rho_3' = 100$ Ohm·m, $\rho_3'' = 1$ Ohm·m $h_3 = 0.3$ km, $v = 15$ km, $\rho_4 = 10000$ Ohm·m, $\rho_5 = 0$

on ρ_2. In the case that $\rho_2 = 1000\,\text{Ohm·m}$ and $\bar{d}''/v = 0.28$ the conductive central segment is hardly screened: the $\rho^{\perp}-$curve has a well-defined minimum reflecting the conductive segment of the layer ρ_3 and its ascending branch is close to the locally normal $\ddot{\rho}_n-$curve (descending branch of the $\rho^{\perp}-$curve is shifted down because of the $S-$effect). But with $\rho_2 = 5000\,\text{Ohm·m}$ and $\bar{d}''/v = 0.64$ the minimum of the $\rho^{\perp}-$curve flattens and with $\rho_2 \geq 25000$ Ohm·m and $\bar{d}''/v \geq 1.4$ vanishes at all. Here we observe the strong screening of the conductive central segment. This effect does not affect the longitudinal $\rho^{\parallel}-$curves, which are close to the locally normal $\ddot{\rho}_n-$curve but have steeper ascending branch due to inductive influence of resistive side segments.

7.3 Three-Dimensional Conductance Models

Let us consider several thin-sheet models, which admit analytic representations of the three-dimensional S-effect.

7.3.1 The Dmitriev-Barashkov Basic Model

The three-dimensional model of the S-effect, suggested by Dmitriev and Barashkov (Barashkov, 1983; Barashkov and Dmitriev, 1987), is shown in Fig. 7.29. Here

$$\begin{array}{ll} \rho_1(x,y) \to \rho_1 = const, & S_1(x,y) \to S_1 = const \\ \sqrt{x^2+y^2}\to\infty & \sqrt{x^2+y^2}\to\infty \\ \rho_2 >> \rho_1 \quad h_2 >> h_1, & R_2 >> R_1 \quad \rho_3 = 0, \end{array} \tag{7.92}$$

where $S_1(x,y) = h_1/\rho_1(x,y)$, $R_1 = h_1\rho_1$, $R_2 = h_2\rho_2$. The function $\rho_1(x,y)$ is twice differentiable.

Here we briefly run through cumbersome mathematics. The problem is solved in thin-sheet S-approximation and involves two polarizations of the normal electromagnetic field:

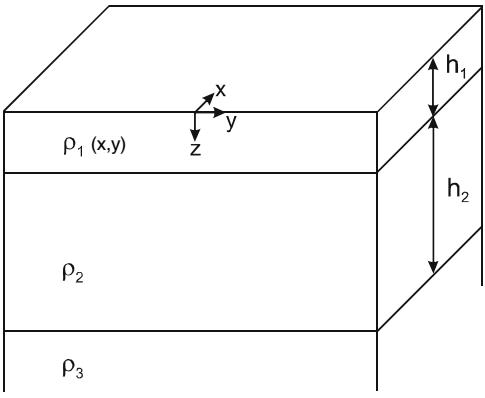

Fig. 7.29 The Dmitriev-Barashkov basic model

$$\mathbf{E}^{\mathrm{N}(1)} = \left\{E_x^{\mathrm{N}}, 0, 0\right\}, \mathbf{H}^{\mathrm{N}(1)} = \left\{0, H_y^{\mathrm{N}}, 0\right\}$$
$$\mathbf{E}^{\mathrm{N}(2)} = \left\{0, E_y^{\mathrm{N}}, 0\right\}, \mathbf{H}^{\mathrm{N}(2)} = \left\{H_x^{\mathrm{N}}, 0, 0\right\}.$$

The low-frequency asymptotics of the impedance tensor, obtained for sufficiently slow S_1-variations, assumes the form

$$[\mathbf{Z}(x, y, \omega)] = [\mathbf{e}][\mathbf{Z}_{\mathrm{N}}(\omega)], \tag{7.93}$$

where $[\mathbf{Z}_{\mathrm{N}}(\omega)]$ is the normal one-dimensional low-frequency impedance tensor determining the depth h to the conductive basement:

$$[\mathbf{Z}_{\mathrm{N}}(\omega)] = \begin{bmatrix} 0 & Z_{\mathrm{N}}(\omega) \\ -Z_{\mathrm{N}}(\omega) & 0 \end{bmatrix}, \quad Z_{\mathrm{N}}(\omega) = -i\omega\mu_{\mathrm{o}}h \tag{7.94}$$

and $[\mathbf{e}]$ is the real-valued frequency-independent electric distortion matrix determining the S-effect:

$$[\mathbf{e}(x, y)] = \begin{bmatrix} 1 - \dfrac{\partial u(x, y)}{\partial x} & -\dfrac{\partial v(x, y)}{\partial x} \\ -\dfrac{\partial u(x, y)}{\partial y} & 1 - \dfrac{\partial v(x, y)}{\partial y} \end{bmatrix}. \tag{7.95}$$

Here $u(x, y)$, $v(x, y)$ are scalar potentials of the normalized anomalous electric fields in the first ($m = 1$) and the second ($m = 2$) polarizations of the normal field:

$$\frac{\mathbf{E}^{\mathrm{A}(1)}}{E_x^{\mathrm{N}}} = -\mathrm{grad}\, u, \quad \frac{\mathbf{E}^{\mathrm{A}(2)}}{E_y^{\mathrm{N}}} = -\mathrm{grad}\, v. \tag{7.96}$$

The functions $u(x, y)$, $v(x, y)$ are derived from the equations

$$\begin{aligned} &\frac{\partial}{\partial x}\left(\frac{1}{g^2(x, y)}\frac{\partial u(x, y)}{\partial x}\right) + \frac{\partial}{\partial y}\left(\frac{1}{g^2(x, y)}\frac{\partial u(x, y)}{\partial y}\right) - u(x, y) = \frac{\partial}{\partial x}\frac{1}{g^2(x, y)}\ a \\ &\frac{\partial}{\partial x}\left(\frac{1}{g^2(x, y)}\frac{\partial v(x, y)}{\partial x}\right) + \frac{\partial}{\partial y}\left(\frac{1}{g^2(x, y)}\frac{\partial v(x, y)}{\partial y}\right) - v(x, y) = \frac{\partial}{\partial y}\frac{1}{g^2(x, y)}, b \end{aligned} \tag{7.97}$$

where $g(x, y) = 1/\sqrt{S_1(x, y)R_2}$ is the local galvanic parameter.

It is seen that the three-dimensional $S-$effect depends on distribution of galvanic parameter $g(x, y)$ and its gradients. We observe here the same mechanisms as in above-examined two-dimensional models of the $S-$effect.

An important point is that the transition from Dmitriev-Barashkov's model to the two-dimensional Tikhonov-Dmitriev model can be accomplished by simple elongating of three-dimensional structures. Let S_1, v, g be functions of y. Then, according to (7.96) and (7.97),

$$\frac{d^2}{dy^2}\left\{\frac{1}{g^2(y)}\left(\frac{dv(y)}{dy}-1\right)\right\}-\frac{dv(y)}{dy}=0,$$

whence on some substitutions we obtain

$$R^2\frac{d^2}{dy^2}S_1(y)Z^{\perp}(y)-Z^{\perp}(y)=i\omega\mu_o h,\quad Z^{\perp}=-\frac{E_y}{H_x^N},$$

which coincides with low-frequency asymptotics of Tikhonov-Dmitriev's equation (7.18).

Evidently the Dmitriev-Barashkov model can be considered as a three-dimensional generalization of the two-dimensional Tikhonov-Dmitriev model.

7.3.2 The Singer-Fainberg Model

Now we review another three-dimensional generalization of the Tikhonov-Dmitriev model suggested by Singer and Fainberg (1985) and Fainberg and Singer (1987). The Singer-Fainberg model gains a better insight into the physical mechanism of anomalies caused by the S_1-variations and allows for estimating their long-range action.

The model is shown in Fig. 7.30. It has the same normal background as in the Tikhonov-Dmitriev model, but its upper layer contains a closed anomalous domain V bounded by arbitrary cylindrical surface:

$$\rho_1=\begin{cases}\rho_1=const & \text{outside } V\\ \rho_1(x,y) & \text{inside } V\end{cases}\qquad S_1=\begin{cases}S_1=const & \text{outside } V\\ S_1(x,y) & \text{inside } V\end{cases}\qquad(7.98)$$

$$\rho_2>>\rho_1\qquad h_2>>h_1\qquad R_2>>R_1\qquad \rho_3=0,$$

where $S_1=h_1/\rho_1$ is the conductance of the upper layer, and $R_1=h_1\rho_1$, $R_2=h_2\rho_2$ are the resistances of the upper and intermediate layers.

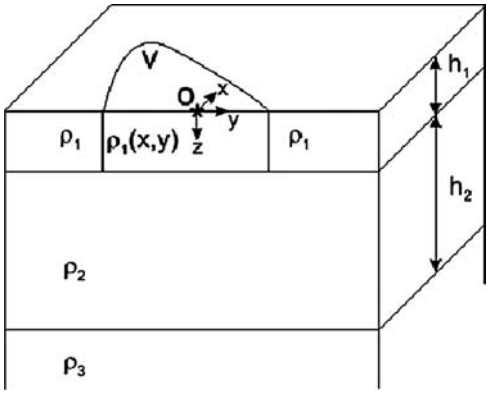

Fig. 7.30 The Singer-Fainberg model

The problem is solved in the Price-Sheinmann thin-sheet approximation.

On the Earth's surface the electric and magnetic fields $\mathbf{E}_\tau(E_x, E_y)$ and $\mathbf{H}(H_x, H_y, H_z)$ are determined from the integral equation

$$\mathbf{E}_\tau(\mathbf{r}) = \mathbf{E}_\tau^{\mathrm{N}} + \mathbf{E}_\tau^{\mathrm{A}}(\mathbf{r}) = \mathbf{E}_\tau^{\mathrm{N}} + \iint\limits_V [\mathbf{G}^E(\mathbf{r}|\mathbf{r}_\mathrm{s})]\Delta S_1(\mathbf{r}_\mathrm{s})\mathbf{E}_\tau(\mathbf{r}_\mathrm{s})ds \tag{7.99a}$$

and the integral relation

$$\mathbf{H}(\mathbf{r}) = \mathbf{H}_\tau^{\mathrm{N}} + \mathbf{H}_\tau^{\mathrm{A}}(\mathbf{r}) = \mathbf{H}_\tau^{\mathrm{N}} + \iint\limits_V [\mathbf{G}^H(\mathbf{r}|\mathbf{r}_\mathrm{s})]\Delta S_1(\mathbf{r}_\mathrm{s})\mathbf{E}_\tau(\mathbf{r}_\mathrm{s})ds, \tag{7.99b}$$

where $\mathbf{E}_\tau^{\mathrm{N}}(E_x^{\mathrm{N}}, E_y^{\mathrm{N}})$, $\mathbf{H}_\tau^{\mathrm{N}}(H_x^{\mathrm{N}}, H_y^{\mathrm{N}})$ and $\mathbf{E}_\tau^{\mathrm{A}}(E_x^{\mathrm{A}}, E_y^{\mathrm{A}})$, $\mathbf{H}_\tau^{\mathrm{A}}(H_x^{\mathrm{A}}, H_y^{\mathrm{A}})$ are the normal and anomalous electric and magnetic fields, $\Delta S_1(\mathbf{r}_\mathrm{s}) = S_1(\mathbf{r}_\mathrm{s}) - S_1$ is the excessive conductance, $[\mathbf{G}^E]$ and $[\mathbf{G}^H]$ are the electric and magnetic Green tensors for the horizontally layered normal background.

Let the distance to the anomalous domain V be much greater than its maximum diameter. Turn to (7.99a) and (7.99b) and represent the anomalous electromagnetic field $\mathbf{E}^{\mathrm{A}}, \mathbf{H}^{\mathrm{A}}$ observed far avay from the domain V as the field of an equivalent electric dipole located at a point O in the middle of V. Taking the Green tensors outside the integrals, we use cylindrical coordinates r, φ, z with the origin at the equivalent dipole, and write

$$\begin{aligned} \mathbf{E}_\tau^{\mathrm{A}} &= [\mathbf{G}^E] \iint\limits_V \Delta S_1(\mathbf{r}_\mathrm{s})\mathbf{E}_\tau(\mathbf{r}_\mathrm{s})ds = [\mathbf{G}^E]\mathbf{P} \\ \mathbf{H}_\tau^{\mathrm{A}} &= [\mathbf{G}^H] \iint\limits_V \Delta S_1(\mathbf{r}_\mathrm{s})\mathbf{E}_\tau(\mathbf{r}_\mathrm{s})ds = [\mathbf{G}^H]\mathbf{P}, \end{aligned} \tag{7.100}$$

where

$$\mathbf{P} = \iint\limits_V \Delta S_1(\mathbf{r}_\mathrm{s})\mathbf{E}_\tau(\mathbf{r}_\mathrm{s})ds \tag{7.101}$$

is the moment of the equivalent electric dipole. Note that $\mathbf{E}_\tau$ and $\mathbf{P}$ tend to zero as $\omega \to 0$.

Using cylindrical coordinates r, φ, z with the origin at the point O, we write

$$\begin{aligned} &E_r^{\mathrm{A}} = \frac{P_r}{S_1}\left\{\frac{Q_1(r)}{r} + \frac{dQ_4(r)}{dr}\right\}, \qquad E_\varphi^{\mathrm{A}} = \frac{P_\varphi}{S_1}\left\{\frac{dQ_1(r)}{dr} + \frac{Q_4(r)}{r}\right\}, \\ &H_r^{\mathrm{A}} = P_\varphi \frac{dQ_3(r)}{dr}, H_\varphi^A = -P_r\frac{Q_3(r)}{r}, \quad H_z^{\mathrm{A}} = -P_\varphi\left\{\frac{1}{r}\frac{d}{dr}r\frac{dQ_2(r)}{dr} - \frac{Q_2(r)}{r^2}\right\}, \end{aligned} \tag{7.102}$$

where $P_r = \mathbf{P}\cdot\mathbf{1}_r$, $P_\varphi = \mathbf{P}\cdot\mathbf{1}_\varphi$, $\mathbf{1}_r = \mathbf{r}/r$, $\mathbf{1}_\varphi = \mathbf{1}_r \times \mathbf{1}_z$, $\mathbf{P} = P_r\mathbf{1}_r + P_\varphi\mathbf{1}_\varphi$.

Functions Q_1, Q_2, Q_3, Q_4 are defined by

$$Q_l(r) = \frac{1}{2\pi}\int_0^\infty q_l(m)J_1(mr)dm, l = 1, 2, 3, 4, \tag{7.103}$$

where J_1 is the first order Bessel function, and

$$q_1(m) = \left(1 - i\omega\mu_o S_1 \frac{\bar{Z}^{TE}}{m\bar{Z}^{TE} - i\omega\mu_o}\right)^{-1}, q_2(m) = \frac{\bar{Z}^{TE}}{m\bar{Z}^{TE} - i\omega\mu_o(1 + S_1\bar{Z}^{TE})},$$
$$q_3(m) = \frac{m\bar{Z}^{TE}}{m\bar{Z}^{TE} - i\omega\mu_o(1 + S_1\bar{Z}^{TE})}, \quad q_4(m) = \frac{1}{1 + S_1\bar{Z}^{TM}}. \tag{7.104}$$

The spectral TE- and TM-impedances $\bar{Z}^{TE}$ and $\bar{Z}^{TM}$ of the two-layered horizontally homogeneous medium underlying the inhomogeneous S_1- plane are computed as

$$\bar{Z}^{TE} = -\frac{i\omega\mu_o}{\eta_2}\tanh\eta_2 h_2, \bar{Z}^{TM} = \eta_2\rho_2\tanh\eta_2 h_2, \eta_2 = \sqrt{m^2 - i\omega\mu_o/\rho_2}. \tag{7.105}$$

They relate to the TE- and TM-modes which reflect the induction and galvanic effects respectively.

As is seen from (7.102), (7.103) and (7.104), the Green tensor $[\mathbf{G}^E]$ governing the anomaly of the electric field involves both impedances, "inductive" $\bar{Z}^{TE}$ and "galvanic" $\bar{Z}^{TM}$, while the Green tensor $[\mathbf{G}^H]$ governing the anomaly of the magnetic field involves only the "inductive" impedance $\bar{Z}^{TE}$. This defines essentially different character of electric and magnetic anomalies. With lowering frequency the inductive impedance $\bar{Z}^{TE}$ tends to zero:

$$\bar{Z}^{TE}_{\omega\to 0} \to 0, \tag{7.106}$$

whereas the galvanic impedance $\bar{Z}^{TM}$ takes on a static value:

$$\bar{Z}^{TM}_{\omega\to 0} \to m\rho_2\tanh mh_2. \tag{7.107}$$

Substituting (7.106), (7.107) into (7.102), (7.103) and (7.104), we have

$$\begin{aligned}
&\frac{E^{\mathrm{A}}_r}{P_r}_{\omega\to 0} \to \frac{1}{2\pi S_1}\left\{\frac{1}{r^2} + \frac{d}{dr}\int_0^\infty \frac{J_1(mr)}{1 + mS_1\rho_2\tanh mh_2}dm\right\}\\
&\frac{E^{\mathrm{A}}_\varphi}{P_\varphi}_{\omega\to 0} \to \frac{1}{2\pi S_1}\left\{-\frac{1}{r^2} + \frac{1}{r}\int_0^\infty \frac{J_1(mr)}{1 + mS_1\rho_2\tanh mh_2}dm\right\}\\
&H^{\mathrm{A}}_{r\,\omega\to 0} \to 0, \quad H^{\mathrm{A}}_{\varphi\,\omega\to 0} \to 0, \quad H^{\mathrm{A}}_{z\,\omega\to 0} \to 0.
\end{aligned} \tag{7.108}$$

This mathematics sheds light on the physical mechanisms of the magnetotelluric anomalies caused by near-surface three-dimensional inhomogeneities. Anomalies of electric field include the induction and galvanic parts. At low frequency they lose the inductive part and become static. Anomalies of the magnetic field are of the inductive nature. At low frequency they vanish. The remarkable property of the magnetic field is that with lowering frequency it gets free of near-surface distortions.

At what distance from inhomogeneity can we determine the true normal impedance? Singer and Fainberg answer this question, using two criteria: $r >> \lambda_o$ and $r >> \lambda_L$. Combining these criteria, they write

$$r >> \max(\lambda_o, \lambda_L). \tag{7.109}$$

Parameter λ_o is an effective penetration depth $\bar{h}_{\text{eff}}$ derived from the Tikhonov-Cagniard impedance $\bar{Z}$ of the two-layered horizontally homogeneous medium underlying the inhomogeneous S_1- plane:

$$\lambda_o = \bar{h}_{\text{eff}} = \left|\bar{Z}\right| / \omega\mu_o, \tag{7.110}$$

where

$$\bar{Z} = \sqrt{-i\omega\mu_o\rho_2}\,\tan\,\mathrm{h}\sqrt{-i\omega\mu_o/\rho_2}h_2.$$

Parameter λ_L is a generalized adjustment distance

$$\lambda_L = \frac{f}{|g|} = \sqrt{\frac{S_1 R_2}{|1 - i\omega\mu_o S_1 h_2|}}, \tag{7.111}$$

where g and f are the galvanic and induction parameters defined by (7.21). Note that Singer and Fainberg prefer to write λ_L as

$$\lambda_L = \sqrt{\frac{R_2}{\left|S_1^{-1} + \underline{Z}\right|}}, \tag{7.112}$$

where $\underline{Z} = -i\omega\mu_o h_2$ is the low-frequency asymptotics of $\bar{Z}$. The advantage of (7.112) is that it allows to generalize the estimation of λ_L to the multilayered mantle.

Let us come back to (7.102), (7.103), (7.104) and (7.105). Assuming that $r >> \lambda_o$, we reduce Q_1, Q_2, Q_3, Q_4 to the far-zone asymptotics and write

$$\begin{aligned} E_r^A &= \frac{1}{2\pi i\omega\mu_o} P_r Z_N^2 \left\{ \frac{1}{r^3} + \frac{1}{S_1 Z_N \lambda_o \lambda_L^2} \sqrt{\frac{\pi}{2r/\lambda_L}} \left(1 + \frac{1}{2r/\lambda_L}\right) e^{-r/\lambda_L} \right\} \\ E_\varphi^A &= -\frac{1}{2\pi i\omega\mu_o} P_\varphi Z_N^2 \left\{ \frac{2}{r^3} + \frac{1}{r S_1 Z_N \lambda_o \lambda_L} \sqrt{\frac{\pi}{2r/\lambda_L}} e^{-r/\lambda_L} \right\} \end{aligned} \tag{7.113}$$

and

$$
\begin{aligned}
H_r^{\mathrm{A}} &= -\frac{P_\varphi Z_{\mathrm{N}}}{\pi i \omega \mu_{\mathrm{o}} r^3} \\
H_\varphi^{\mathrm{A}} &= -\frac{P_r Z_{\mathrm{N}}}{2\pi i \omega \mu_{\mathrm{o}} r^3} \\
H_z^{\mathrm{A}} &= \frac{3 P_\varphi Z_{\mathrm{N}}^2}{2\pi \omega^2 \mu_{\mathrm{o}}^2 r^4},
\end{aligned}
\tag{7.114}
$$

where Z_{N} is the normal Tikhonov-Cagniard impedance on the Earth's surface.

Now evaluate the ratio between vertical component of the anomalous magnetic field and two-dimensional divergence of its horizontal components. By virtue of (7.114)

$$
-i\omega\mu_{\mathrm{o}} \frac{H_z^{\mathrm{A}}}{div \mathbf{H}_\tau^{\mathrm{A}}} = -i\omega\mu_{\mathrm{o}} \frac{H_z^{\mathrm{A}}}{\frac{1}{r}\left\{\frac{\partial}{\partial r}\left[r H_r^{\mathrm{A}}\right] + \frac{\partial}{\partial \varphi}\left[H_\varphi^{\mathrm{A}}\right]\right\}} = Z_{\mathrm{N}},
$$

whence

$$
-i\omega\mu_{\mathrm{o}} \frac{H_z}{div \mathbf{H}_\tau} = -i\omega\mu_{\mathrm{o}} \frac{H_z^{\mathrm{N}} + H_z^{\mathrm{A}}}{div \mathbf{H}_\tau^{\mathrm{N}} + div \mathbf{H}_\tau^{\mathrm{A}}} = -i\omega\mu_0 \frac{H_z^{\mathrm{A}}}{div \mathbf{H}_\tau^{\mathrm{A}}} = Z_{\mathrm{N}}, \tag{7.115}
$$

where $H_z^{\mathrm{N}} = 0$ and $div \mathbf{H}_\tau^{\mathrm{N}} = 0$. So, the condition $r >> \lambda_0$ defines a zone, in which we can estimate Z_{N}, using the magnetovariational ratio (1.3).

Next evaluate the ratio between orthogonal components of the anomalous electric and magnetic fields. By virtue of (7.113) and (7.114)

$$
\begin{aligned}
\frac{E_\varphi^{\mathrm{A}}(\mathbf{r})}{H_r^{\mathrm{A}}(\mathbf{r})} &= Z_{\mathrm{N}} \left\{1 + \frac{r^2}{2 S_1 Z_{\mathrm{N}} \bar{h}_{\mathrm{eff}} \lambda_L} \sqrt{\frac{\pi}{2r/\lambda_L}} e^{-r/\lambda_L}\right\} \\
\frac{E_r^{\mathrm{A}}(\mathbf{r})}{H_\varphi^{\mathrm{A}}(\mathbf{r})} &= -Z_{\mathrm{N}} \left\{1 + \frac{r^3}{S_1 Z_{\mathrm{N}} \bar{h}_{\mathrm{eff}} \lambda_L^2} \sqrt{\frac{\pi}{2r/\lambda_L}} \left(1 + \frac{1}{2r/\lambda_L}\right) e^{-r/\lambda_L}\right\}.
\end{aligned}
\tag{7.116}
$$

Assume that along with condition $r >> \lambda_{\mathrm{o}}$ the condition $r >> \lambda_L$ is observed. Disregarding the second term in the braces, we get

$$
\frac{E_\varphi^{\mathrm{A}}(\mathbf{r})}{H_r^{\mathrm{A}}(\mathbf{r})} = -\frac{E_r^{\mathrm{A}}(\mathbf{r})}{H_\varphi^{\mathrm{A}}(\mathbf{r})} = Z_{\mathrm{N}}, \tag{7.117}
$$

whence

$$\frac{E_\varphi(\mathbf{r})}{H_r(\mathbf{r})} = \frac{E_\varphi^{\mathrm{N}}(\mathbf{r}) + E_\varphi^{\mathrm{A}}(\mathbf{r})}{H_r^{\mathrm{N}}(\mathbf{r}) + H_r^{\mathrm{A}}(\mathbf{r})} = \frac{Z_{\mathrm{N}} H_\varphi^{\mathrm{N}}(\mathbf{r}) + Z_{\mathrm{N}} H_\varphi^{\mathrm{A}}(\mathbf{r})}{H_\varphi^{\mathrm{N}}(\mathbf{r}) + H_\varphi^{\mathrm{A}}(\mathbf{r})} = Z_{\mathrm{N}}$$
$$\frac{E_r(\mathbf{r})}{H_\varphi(\mathbf{r})} = \frac{E_r^{\mathrm{N}}(\mathbf{r}) + E_r^{\mathrm{A}}(\mathbf{r})}{H_\varphi^{\mathrm{N}}(\mathbf{r}) + H_\varphi^{\mathrm{A}}(\mathbf{r})} = -\frac{Z_{\mathrm{N}} H_r^{\mathrm{N}}(\mathbf{r}) + Z_{\mathrm{N}} H_r^{\mathrm{A}}(\mathbf{r})}{H_r^{\mathrm{N}}(\mathbf{r}) + H_r^{\mathrm{A}}(\mathbf{r})} = -Z_{\mathrm{N}}. \tag{7.118}$$

So, the condition $r >> \max\{\lambda_o, \lambda_L\}$ defines a zone, in which we can estimate Z_{N}, using the magnetovariational and magnetotelluric ratios.

Singer and Fainberg believe that these rough estimates can be applied even to large-scale inhomogeneities. In that event one has to estimate the distance $r_{\min}$ from the nearest edge of the inhomogeneous area.

7.3.3 The Berdichevsky-Dmitriev Model

Let us recall this simple model that gives an analytic image of galvanic distortions caused by three-dimensional sedimentary structures (Berdichevsky and Dmitriev, 1976). The model is shown in Fig. 7.31. It consists from sediments (ρ_1', h_1), the resistive lithosphere ($\rho_2 = \infty, h_2 >> h_1$), and the conductive mantle ($\rho_3 = 0$). The sediments contain an inclusion in the form of elliptic cylinder of resistivity ρ_1'' with diameters $2a$, $2b$ along x, y. In the Price-Sheinmann thin-sheet S-approximation we have

$$S_1 = \begin{cases} S_1' = h_1/\rho_1' & \text{outside the inclusion} \\ S_1'' = h_1/\rho_1'' & \text{inside the inclusion.} \end{cases} \tag{7.119}$$

To get an analytic solution to this three-dimensional problem, we ignore the current leakage through the ρ_2-layer and use the hybrid quasistatic method based on the LR-decomposition. The mathematcs is performed in three stages as shown in Sect. 1.3.4.

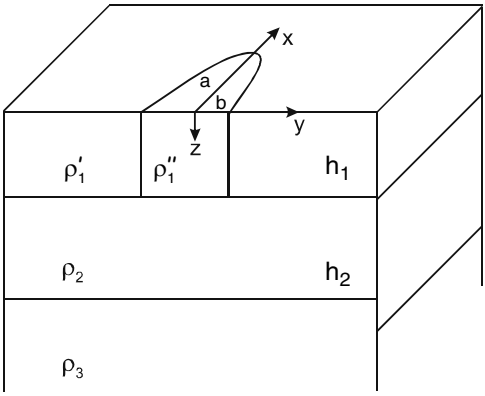

Fig. 7.31 The Berdichevsky-Dmitriev model

In the first stage, the normal impedance of the one-dimensional background is derived in the absence of the inclusion:

$$[\mathbf{Z}_{\mathrm{N}}] = \begin{bmatrix} 0 & Z_{\mathrm{N}} \\ -Z_{\mathrm{N}} & 0 \end{bmatrix}, \tag{7.120}$$

where

$$Z_{\mathrm{N}} = \frac{-i\omega\mu_{\mathrm{o}}h}{1 - i\omega\mu_{\mathrm{o}}S_1'h_2}, \quad h = h_1 + h_2.$$

In the second stage, we find the electric and magnetic distortion tensors [**e**] and [**h**].

The tensor [**e**] is derived from the well-known problem on infinitely long elliptical cylinder in the uniform static field (Smythe, 1950). Restricting our consideration to measurements along the y-axis, we get

$$[\mathbf{e}] = \begin{bmatrix} e_{xx} & 0 \\ 0 & e_{yy} \end{bmatrix} \tag{7.121}$$

where

$$\begin{aligned}
e_{\substack{xx \\ |y|>b}} &= \frac{\left(a^2S_1' - b^2S_1''\right)\sqrt{a^2 - b^2 + y^2} + ab\left(S_1'' - S_1'\right)|y|}{(a-b)\left(aS_1' + bS_1''\right)\sqrt{a^2 - b^2 + y^2}} = 1 + f\left(y, \frac{S_1''}{S_1'}\right) \\
e_{\substack{xx \\ |y|<b}} &= S_1'\frac{a+b}{aS_1' + bS_1''} \\
e_{\substack{yy \\ |y|>b}} &= \frac{\left(a^2S_1'' - b^2S_1'\right)\sqrt{a^2 - b^2 + y^2} + ab\left(S_1' - S_1''\right)|y|}{(a-b)\left(aS_1'' + bS_1'\right)\sqrt{a^2 - b^2 + y^2}} = 1 + f\left(y, \frac{S_1'}{S_1''}\right) \\
e_{\substack{yy \\ |y|<b}} &= S_1'\frac{a+b}{aS_1'' + bS_1'}
\end{aligned} \tag{7.122}$$

and

$$f(y, \eta) = \frac{ab(1-\eta)}{(a-b)(a+b\eta)}\left\{1 - \frac{|y|}{\sqrt{a^2 - b^2 + y^2}}\right\}, \eta = \frac{S_1'}{S_1''} \text{ or } \frac{S_1''}{S_1'}.$$

The tensor [**h**] is determined by (1.85). With a knowledge of $[\mathbf{Z}_{\mathrm{N}}]$ and [**e**] we have

$$[\mathbf{h}] = \begin{bmatrix} h_{xx} & 0 \\ 0 & h_{yy} \end{bmatrix}, \tag{7.123}$$

where

$$h_{xx} = 1 + \frac{1}{2}(S_1 e_{yy} - S_1')Z_{\mathrm{N}}$$
$$h_{yy} = 1 + \frac{1}{2}(S_1 e_{xx} - S_1')Z_{\mathrm{N}},$$
$$S_1 = \begin{cases} S_1' & \text{for} \quad |y| < b \\ S_1'' & \text{for} \quad |y| > b. \end{cases} \tag{7.124}$$

At the last stage, we substitute (7.120), (7.121), (7.123) into (1.74) and determine

$$[\mathbf{Z}] = \begin{bmatrix} 0 & Z_{xy} \\ Z_{yx} & 0 \end{bmatrix}, \tag{7.125}$$

where

$$Z_{xy} = \frac{e_{xx}}{\frac{1}{Z_{\mathrm{N}}} + \frac{1}{2}(S_1 e_{xx} - S_1')}$$
$$Z_{yx} = -\frac{e_{yy}}{\frac{1}{Z_{\mathrm{N}}} + \frac{1}{2}(S_1 e_{yy} - S_1')}. \tag{7.126}$$

Finally,

$$\rho_{xy} = \frac{\left|Z_{xy}\right|^2}{\omega\mu_{\mathrm{o}}} \quad \rho_{yx} = \frac{\left|Z_{yx}\right|^2}{\omega\mu_{\mathrm{o}}}, \tag{7.127}$$

where

$$\rho_{xy}\left(\frac{S_1''}{S_1'}\right) = \rho_{yx}\left(\frac{S_1'}{S_1''}\right) \quad \text{for} \quad |y| > b$$
$$\rho_{xy}\left(\frac{a}{b}\right) = \rho_{yx}\left(\frac{b}{a}\right) \qquad \text{for} \quad |y| < b.$$

Let us consider the apparent resistivities ρ_{xy} and ρ_{yx} outside the inclusion ($|y| > b$). According to (7.120), (7.125) and (7.127),

$$\underset{|y|>b}{\rho_{xy}} = \begin{cases} \delta_{xy}^{S}\dot{\rho}_{\mathrm{n}}^{S} & \text{in the } S_1 - \text{interval} \\ \delta_{xy}^{h}\dot{\rho}_{\mathrm{n}}^{h} & \text{in the } h - \text{interval} \end{cases}$$
$$\underset{|y|>b}{\rho_{yx}} = \begin{cases} \delta_{yx}^{S}\dot{\rho}_{\mathrm{n}}^{S} & \text{in the } S_1 - \text{interval} \\ \delta_{yx}^{h}\dot{\rho}_{\mathrm{n}}^{h} & \text{in the } h - \text{interval}, \end{cases} \tag{7.128}$$

where the locally normal apparent resistivities $\dot{\rho}_{\mathrm{n}}^{S}$, $\dot{\rho}_{\mathrm{n}}^{h}$ in the S_1- and $h-$ intervals are

$$\dot{\rho}_{\mathrm{n}}^{S} = \frac{1}{\omega\mu_{\mathrm{o}}(S_1')^2}, \quad \dot{\rho}_{\mathrm{n}}^{h} = \omega\mu_{\mathrm{o}}h^2$$

and the 3D-distortion factors are

$$\delta_{xy}^{S} = \left\{1 + \frac{f(y, S_1''/S_1')}{2 + f(y, S_1''/S_1')}\right\}^2 \quad \delta_{xy}^{h} = \left\{1 + f(y, S_1''/S_1')\right\}^2$$

$$\delta_{yx}^{S} = \left\{1 + \frac{f(y, S_1'/S_1'')}{2 + f(y, S_1'/S_1'')}\right\}^2 \quad \delta_{yx}^{h} = \left\{1 + f(y, S_1'/S_1'')\right\}^2.$$

Letting $S_1'' < S_1'$, it is easy to show that $\delta_{xy}^{S} > 1$, $\delta_{xy}^{h} > 1$ and $\delta_{yx}^{S} < 1$, $\delta_{yx}^{h} < 1$. So, $\rho_{xy} > \dot{\rho}_{\mathrm{n}}$, $\rho_{yx} < \dot{\rho}_{\mathrm{n}}$ and $\rho_{xy} > \rho_{yx}$. These relations are characteristic of the lateral *flow-around effect* observed in the vicinity of a resistive inclusion where zones of the current concentration and deconcentration appear (Fig. 7.32). In the concentration zones the apparent resistivities increase, while in the deconcentration zones they decrease.

Letting $S_1'' > S_1'$, we have $\delta_{xy}^{S} < 1$, $\delta_{xy}^{h} < 1$ and $\delta_{yx}^{S} > 1$, $\delta_{yx}^{h} > 1$. So, $\rho_{xy} < \dot{\rho}_{\mathrm{n}}$, $\rho_{yx} > \dot{\rho}_{\mathrm{n}}$ and $\rho_{xy} < \rho_{yx}$. These relations are characteristic of the lateral *current-gathering effect* observed in the vicinity of a conductive inclusion. Zones of the current concentration and deconcentration, in which the apparent resistivities increase and decrease, are displayed in Fig. 7.33.

Figure 7.34 presents the apparent-resistivity curves, ρ_{xy} and ρ_{yx}, distorted by the flow-around and current-gathering effects. The observation site $x = 0$, $y = 1.5\,\mathrm{b}$ is located outside a resistive ($S_1''/S_1' = 1/16$) or conductive ($S_1''/S_1' = 16$) inclusion. The $\rho_{\mathrm{A}}-$curves are plotted in the log-log scale with ordinates $\rho_{\mathrm{A}}/\rho_1'$ and abscissas λ_1'/h_1, where λ_1' is the wavelength in the medium of resistivity ρ_1'. The curves of ρ_{xy} and ρ_{yx} are similar in form. They replicate the bell-type normal curve of $\dot{\rho}_{\mathrm{n}}$, but

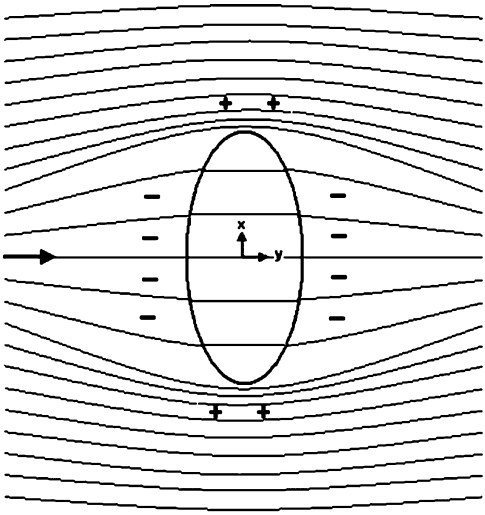

Fig. 7.32 Flow-around effect in the vicinity of a resistive inclusion

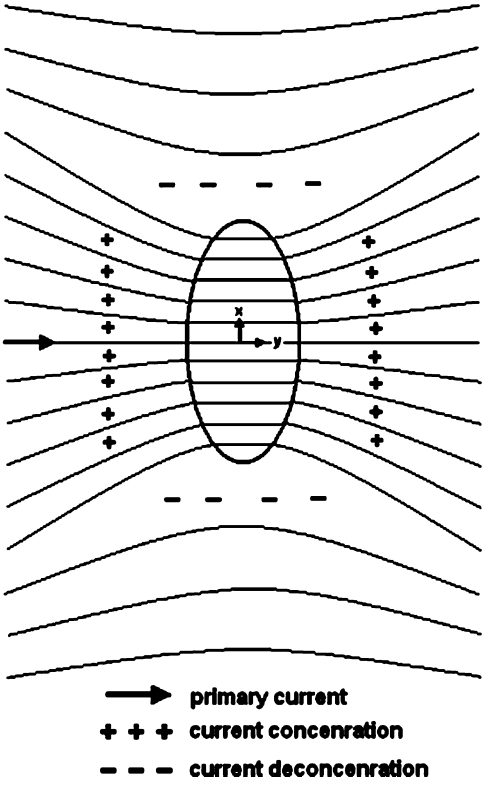

Fig. 7.33 Current-gathering effect in a conductive inclusion

are shifted up or down (with small horizontal displacement). In the case of resistive inclusion with $S_1''/S_1' = 1/16$ the ρ_{xy}-curves are shifted up, while the ρ_{yx}-curves are shifted down (the flow-around effect). In the case of conductive inclusion with $S_1''/S_1' = 16$ the ρ_{xy}-curves are shifted down, while the ρ_{yx}-curves are shifted up (the current-gathering effect). The magnitude of the static shift depends on a/b. Consider, for instance, the ρ_{yx}-curve in the vicinity of the resistive inclusion. Its shift reflecting the flow-around effect dramatically increases when a/b changes from 0.2 to 5 and then decreases and vanishes when a/b changes from 5 to ∞. This reminds the behavior of a prudent pedestrian who turns around a short barrier but climbs over a long barrier.

Asymptotic estimates derived from (7.122) show that galvanic distortions caused by the flow-around and current-gathering effects attenuate at the distances

$$y >> \sqrt{\frac{ab(a+b)(1-\eta)}{2(a+b\eta)}}, \quad \eta = \begin{cases} \dfrac{S_1''}{S_1'} & \text{for} \quad \rho_{xy} \\ \\ \dfrac{S_1'}{S_1''} & \text{for} \quad \rho_{yx}. \end{cases} \tag{7.129}$$

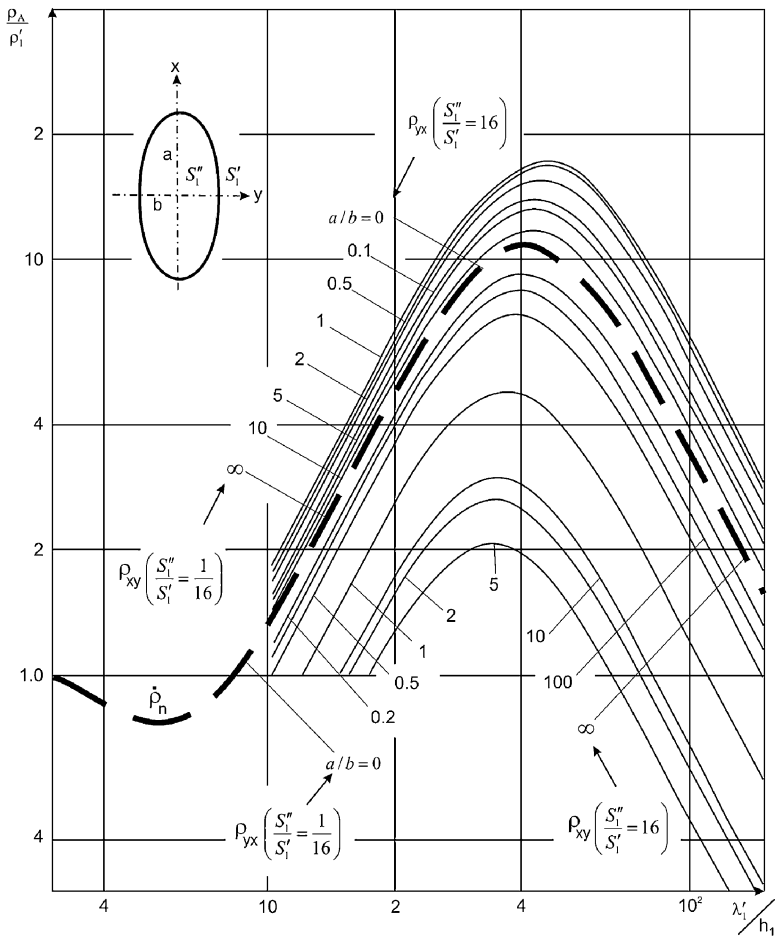

Fig. 7.34 Apparent-resistivity curves ρ_{xy} and ρ_{yx} distorted by the flow-around and current-gathering effects in the vicinity of a resistive ($S_1''/S_1' = 1/16$) or conductive ($S_1''/S_1' = 16$) inclusion, $\rho_{xy}(S_1''/S_1') = \rho_{yx}(S_1'/S_1'')$. The observation is carried out at the site $x = 0$, $y = 1.5b$. Curve parameter: a/b, model parameters: $\rho_2/\rho_1 = \infty$, $\rho_3/\rho_1 = 0$, $h_2/h_1 = 20$

The distortions can be somewhat suppressed using the Berdichevsky scalar impedance. Figure 7.35 demonstrates the apparent-resistivity curves $\rho_{\text{brd}} = |Z_{\text{brd}}|^2/\omega\mu_0$, where $Z_{\text{brd}} = (Z_{xy} - Z_{yx})/2$. Note that $\rho_{\text{brd}}(\rho_1''/\rho_1') = \rho_{\text{brd}}(\rho_1'/\rho_1'')$. Given $\rho_1''/\rho_1' = 1/16$ or 16, the curves of ρ_{brd} calculated for a/b from 0.1 to 1 approach the normal curve $\dot{\rho}_{\text{n}}$.

Figure 7.36 presents the apparent-resistivity curves of ρ_{xy} and ρ_{yx} obtained over the inclusion ($|y| < b$). Here the fields $\mathbf{E}_\tau$ and $\mathbf{H}_\tau$ are uniform, so that the impedance tensor does not depend on the position of the observer. At $a/b \to \infty$ we have a two-dimensional resistive or conductive inclusion directed along the x-axis. The

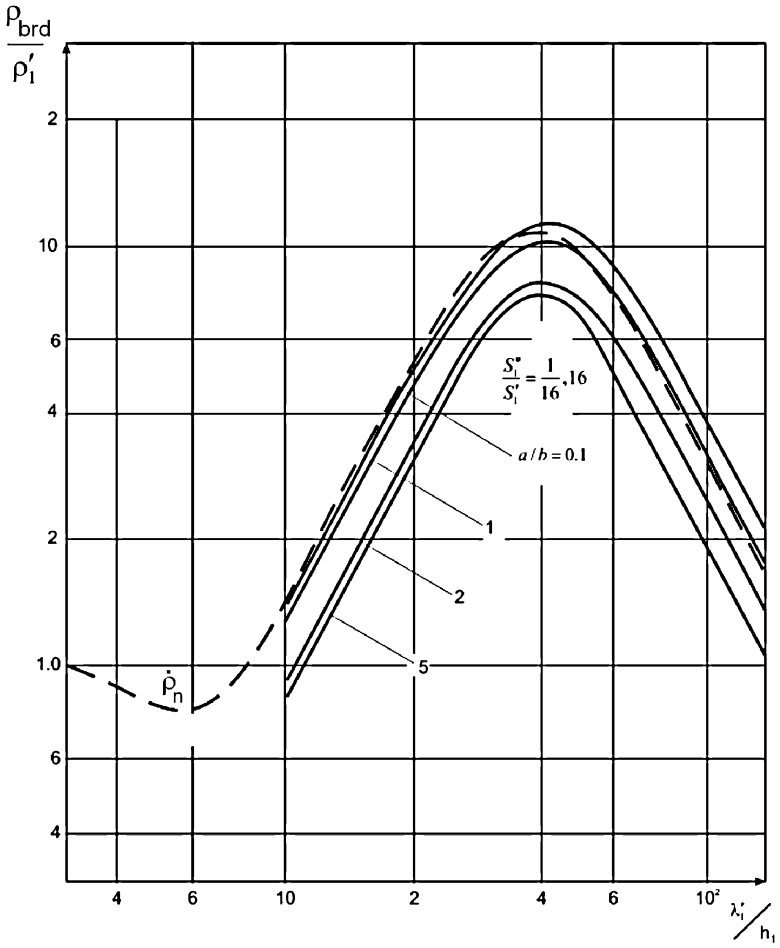

Fig. 7.35 Apparent-resistivity curves ρ_{brd} observed in the vicinity of a resistive ($S_1''/S_1' = 1/16$) or conductive ($S_1''/S_1' = 16$) inclusion, $\rho_{brd}(S_1''/S_1') = \rho_{brd}(S_1'/S_1'')$. The observation is carried out at the site $x = 0$, $y = 1.5b$. Model parameters: $\rho_2/\rho_1 = \infty$, $\rho_3/\rho_1 = 0$, $h_2/h_1 = 20$. Curve parameter: a/b

inclusion is connected with the limit curves $\rho_{yx} = \rho^{\perp}$ and $\rho_{xy} = \rho^{\parallel}$, which refer to the $H-$ and $E-$polarized fields respectively. In the case of a resistive inclusion ($S_1''/S_1' = 1/16$) the ascending branch of the transverse ρ_{yx}-curve merges with the S_1-line, while its descending branch lies far above the h-line. At the same time the ascending branch of the longitudinal ρ_{xy}-curve lies far below the S_1-line, while its descending branch merges with the h-line. In the case of a conductive inclusion ($S_1''/S_1' = 16$) the transverse ρ_{yx}-curve has no ascending branch, while its descending branch lies far below the h-line. At the same time the ascending branch of the longitudinal ρ_{xy}-curve lies above the S_1-line, while its descending branch merges with the h-line. With decreasing a/b, the lateral flow-around and current-gathering

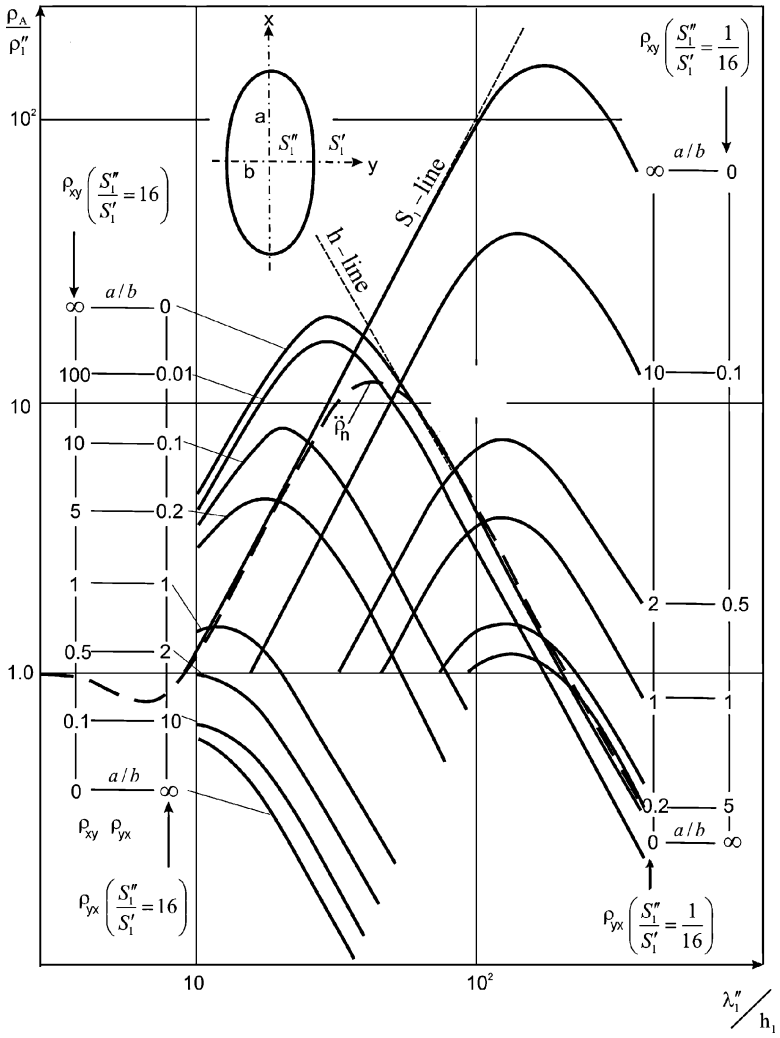

Fig. 7.36 Apparent-resistivity curves ρ_{xy} and ρ_{yx} distorted by the flow-around and current-gathering effects over a resistive ($S_1''/S_1' = 1/16$) or conductive ($S_1''/S_1' = 16$) inclusion, $\rho_{xy}(S_1''/S_1') = \rho_{yx}(S_1'/S_1'')$. The observation is carried out at the site $x = 0$, $|y| < b$. Model parameters: $\rho_2/\rho_1 = \infty$, $\rho_3/\rho_1 = 0$, $h_2/h_1 = 20$. Curve parameter: a/b, $\rho_{xy}(a/b) = \rho_{yx}(b/a)$

effects appear. They manifest themselves clearly in the fact that the ascending branches of the trasverse ρ_{yx}-curves recede from the S_1-line, while their descending branches approach the h-line. We see that the flow-around and current-gathering effects distort the ascending branches of the transverse apparent-resistivity curves, but reduce the $S-$effect distorting their descending branches. At the same time the ascending branches of the longitudinal ρ_{xy}-curves approach the S_1-line, while their descending branches recede from the h-line. The flow-around and current-gathering

effects reduce the distortion of the ascending branches of the longitudinal apparent-resistivity curves, but distort their descending branches.

In our consideration the inclusion *elongation* $e = a/b, a > b$ (aspect ratio) can be used as a parameter that controls an accuracy of the two-dimensional approximation of the three-dimensional inclusions. Considering an inclusion elongated in the $x-$ direction, we introduce the following decompositions of the apparent resistivities observed over the inclusion:

$$\begin{aligned}\rho_{xy}(3D) &= \begin{cases} p^S_{xy}\rho^S_{xy}(2D) & \text{in the } S_1\text{-interval} \\ p^h_{xy}\rho^h_{xy}(2D) & \text{in the } h\text{-interval} \end{cases} \\ \rho_{yx}(3D) &= \begin{cases} p^S_{yx}\rho^S_{yx}(2D) & \text{in the } S_1\text{-interval} \\ p^h_{yx}\rho^h_{\mathrm{yx}}(2D) & \text{in the } h\text{-interval.} \end{cases}\end{aligned} \tag{7.130}$$

Here $\rho^S_{xy}(2D)$, $\rho^h_{xy}(2D)$, $\rho^S_{yx}(2D)$, $\rho^h_{yx}(2D)$ are the two-dimensional apparent resistivities, obtained at $e \to \infty$, and p^S_{xy}, p^h_{xy}, p^S_{yx}, p^h_{yx} are the factors characterizing their three-dimensional distortions. According to (7.122) and (7.126),

$$\begin{aligned}\rho^S_{xy}(2D) &= \frac{4}{\omega\mu_o(S_1' + S_1'')^2} \qquad \rho^h_{xy}(2D) = \omega\mu_o h^2 \\ \rho^S_{yx}(2D) &= \frac{1}{\omega\mu_o(S_1'')^2} \qquad\quad \rho^h_{yx}(2D) = \omega\mu_o h^2\left(\frac{S_1'}{S_1''}\right)^2\end{aligned} \tag{7.131}$$

and

$$\begin{aligned}p^S_{xy} &= \frac{(e+1)^2}{\left(e + \dfrac{2}{1 + S_1'/S_1''}\right)^2} \qquad p^h_{xy} = \frac{(e+1)^2}{(e + S_1''/S_1')^2} \\ p^S_{yx} &= \frac{(e+1)^2}{\left(e + \dfrac{1 + S_1'/S_1''}{2}\right)^2} \qquad p^h_{yx} = \frac{(e+1)^2}{(e + S_1'/S_1'')^2}.\end{aligned} \tag{7.132}$$

The factors p^S_{xy}, p^h_{xy}, p^S_{yx}, p^h_{yx} tend to 1, as the elongation e tends to ∞ (the elliptic cylinder degenerates into a two-dimensional prism). Naturally the departure of p^S_{xy}, p^h_{xy}, p^S_{yx}, p^h_{yx} from 1 is a measure of the inclusion three-dimensionality. Assume that the elliptic inclusion can be considered as quasi-two-dimensional, provided $0.9 \le p^S_{xy}, p^h_{xy}, p^S_{yx}, p^h_{yx} \le 1.1$, that is, if the longitudinal and transverse apparent resistivities, ρ_{xy} and ρ_{yx}, differ from the two-dimensional apparent resistivities $\rho^S_{xy}(2D)$, $\rho^h_{xy}(2D)$ and $\rho^S_{yx}(2D)$, $\rho^h_{yx}(2D)$ at most by 10%. Thus, in view of (7.132), we can derive the simple estimates for the quasi-two-dimensionality of resistive and conductive elliptic inclusions (Table 7.2). The most favorable estimates

Table 7.2 Conditions of the quasi-two-dimensionality of elliptic inclusion

$m = S_1''/S_1'$	The S_1- interval		The $h-$ interval	
	Longitudinal ρ_{xy} - curve	Transverse ρ_{yx} - curve	Longitudinal ρ_{xy} - curve	Transverse ρ_{yx} - curve
Resistive inclusion				
$m < 1$				
* * *				
$m = 0.5$	$e = 6$	$e = 8.55$	$e = 9.5$	$e = 18$
$m = 0.1$	$e = 16$	$e = 80.1$	$e = 17.9$	$e = 170$
$m = 0.01$	$e = 19.6$	$e = 939$	$e = 19.8$	$e = 1880$
$m = 0$	$e = 20$	$e = \infty$	$e = 20$	$e = \infty$
Conductive inclusion				
$m > 1$				
* * *				
$m = 2$	$e = 5.33$	$e = 4.27$	$e = 18$	$e = 9.5$
$m = 10$	$e = 14.5$	$e = 8.45$	$e = 170$	$e = 17.9$
$m = 100$	$e = 17.6$	$e = 9.39$	$e = 1880$	$e = 19.8$
$m = \infty$	$e = 18$	$e = 9.5$	$e = \infty$	$e = 20$

are for the longitudinal $\rho_{xy}-$curves, observed over a resistive inclusion (e does not exceed 20 in the S_1- and $h-$intervals), and for the transverse $\rho_{yx}-$curves, observed over a conductive inclusion (e does not exceed 9.5 in the S_1-interval and 20 in the $h-$ interval). At the same time the longitudinal $\rho_{xy}-$curves, observed over a conductive inclusion, and the transverse $\rho_{yx}-$curves, observed over a resistive inclusion, call for elongations e which range up to 100 or even 1000. The different robustness of the longitudinal and transverse apparent-resistivity curves to the 3D effects generated by the resistive and conductive elliptical inclusions is accounted for by difference in current around-flow and current gathering mechanisms.

7.3.4 The Golubtsova Model

The elliptic-cylinder model exposes the galvanic mechanism of the three-dimensional near-surface distortions. In addition to this analytic model, it would be useful to consider a similar numerical model that reflects both the mechanisms, galvanic and induction. Let us examine the model consisting of sediments (ρ_1', h_1), the resistive lithosphere ($\rho_2 >> \rho_1', h_2 >> h_1$), and the conductive mantle ($\rho_3 << \rho_2$). The sediments contain a regional conductive inclusion in the form of a round cylinder of the radius a with resistivity $\rho_1''(r)$, which decreases monotonically from $\rho_1''(a) = \rho_1'$ at the inclusion edge to $\rho_1''(0) = \min \rho_1''$ at its centre. The calculations were performed by Debabov's program in the Price-Sheinmann thin-sheet S-approximation (Debabov, 1980; Golubtsova, 1981). So, we have a conductance model with $S_1' = h_1/\rho_1'$ and $S_1''(r) = h_1/\rho_1''(r)$, where $S_1''(a) = S_1'$ and $S_1''(0) = \max S_1''$. Figure 7.37 shows the field profiles, which pass through the

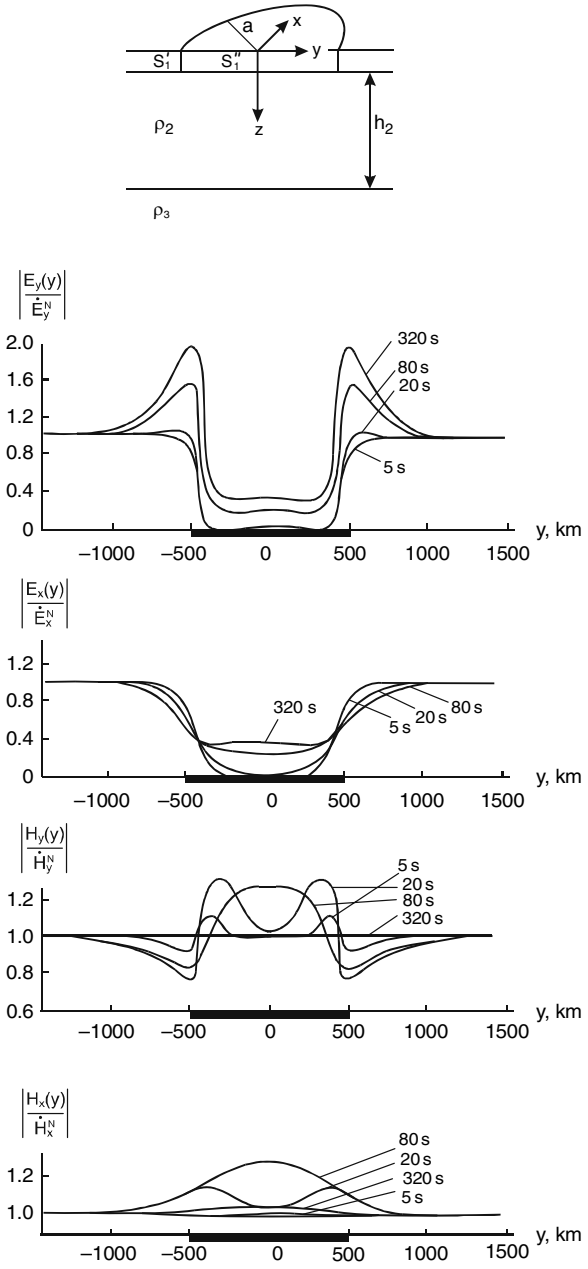

Fig. 7.37 Electromagnetic field profiles in a model with the axially symmetric conductive inclusion in the upper layer. The profiles pass through the inclusion centre in the $y-$direction. Models parameters: $S_1' = 10$S, max $S_1'' = 1000$S, $a = 500$ km, $\rho_2 = 10^4$ Ohm·m, $h_2 = 225$ km, $\rho_3 = 1$ Ohm·m (Golubtsova, 1981)

inclusion centre in the $y-$direction. The electric and magnetic fields are normalized to the normal fields $\dot{E}_x^{\mathrm{N}}, \dot{E}_y^{\mathrm{N}}, \dot{H}_x^{\mathrm{N}}, \dot{H}_y^{N}$. The components E_y, H_x correspond to the primary electric field polarized along the profile. The components E_x, H_y, H_z correspond to the primary electric field polarized across the profile. Both the components of the electric field, E_x and E_y, have a vast minimum over the conductive inclusion. At low frequencies ($T = 80-320$ s) the inclusion borders with zones of increased E_y and decreased E_x. This exhibits the current-gathering effect entailing the concentration and deconcentration zones in the vicinity of a conductive inclusion (Fig. 7.32). But at high frequencies ($T = 5-20$ s) the horizontal skin effect comes into play inside the conductive inclusion. It concentrates the current at the inclusion sides and, hence, counteracts the current-gathering effect. The side maxima of E_y vanish, and flanges of the central minimum of E_x become steeper (the current-gathering effect attenuates). The same mechanism shows up in the magnetic field. At low frequencies ($T = 80$ s) both the horizontal components of the magnetic field, H_x and H_y, have a vast maximum caused by current gathering inside the conductive inclusion. At high frequencies ($T = 5 - 20$ s) the current-gathering effect attenuates, and we observe the side maxima of H_y, which reflect the horizontal skin effect. It is remarkable that high-frequency observations carried out at the edge of a vast isometric conductive structure may admit the two-dimensional interpretation inasmuch as they are slightly distorted by the current-gathering effect.

7.4 Models of Structures in the Basement Topography

To complete analysis of near-surface distortions, we examine two models of buried topographic structures violating the horizontal homogeneity of sediments.

7.4.1 The Horst Model

The cross-section of this two-dimensional model is shown in Fig. 7.38. The upper layer (ρ_1) simulates the conductive sedimentary strata underlaid by the resistive lithosphere (ρ_2) resting on the highly conductive mantle (ρ_3). The model is a counterpart of the three-segment conductance model with a resistive central segment (Fig. 7.16). Let us compare these two models.

Figure 7.39 presents the longitudinal and transverse apparent-resistivity and impedance-phase curves obtained outside and over the horst 20 km wide. The conductive clearance between the roof of the horst and the Earth's surface canalizes the transverse current and conspicuously changes the behavior of the transverse curves, $\rho^{\perp}$ and $\varphi^{\perp}$, outside the horst. Distortions of the curves $\rho^{\perp}$ and $\varphi^{\perp}$ attenuate rather quickly with distance (due to diminution of the current leakage trough the upper-layer bottom). In the immediate vicinity of the horst the $\rho^{\perp}$-curves are shifted upwards (due to the near-surface current concentration). Over the horst we have the curves $\rho^{\perp}$ and $\varphi^{\perp}$, which look much as they do in the three-segment

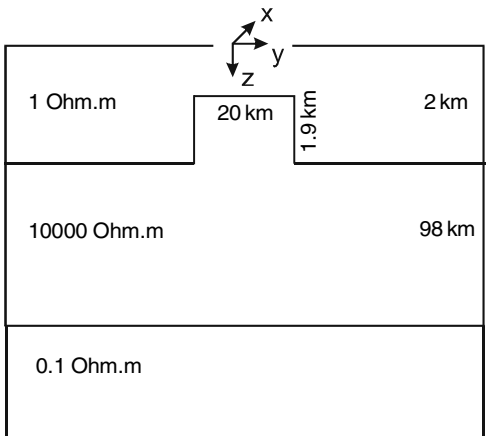

Fig. 7.38 Model of the two-dimensional horst

conductance model (Figures 7.18, 7.19). Their ascending branches are close to the locally normal curves $\ddot{\rho}_n$, while their descending branches are drastically shifted upwards (the $S-$effect). As for the longitudinal curves, $\rho^{\parallel}$ and $\varphi^{\parallel}$, they are little different from those in the three-segment conductance model and they have a false minimum caused by the inductive influence of excess currents concentrated at both sides of the horst (the effect of false conductive layer).

Figure 7.40 displays the tipper curves reflecting pictorially the horst structure. They are much like those in the three-segment model (Fig. 7.20).

Figure 7.41 demonstrates the field profiles, which pass across the horst in the $y-$direction. The electric and magnetic fields are normalized to the normal fields $\dot{E}_x^N, \dot{E}_y^N, \dot{H}_y^N$ observed at $|y| \to \infty$. In many respects the field profiles replicate those in the three-segment model (Fig. 7.24), but it is notable that in the horst model we get the box-like E_y- profiles without side minima, so that the transverse electric field more adequately reflects the structure of the medium than in the three-segment model.

Now we come to the two-dimensional approximation of the three-dimensional horst. What is the condition of quasi-two-dimensionality, which allows for the two-dimensional interpretation of the response functions obtained over a three-dimensional horst and in its vicinity? Reasoning from the Berdichevsky-Dmitriev model (Sect. 7.3.3), we can suppose that the quasi-two-dimensionality condition in the middle part of the elongated horst depends on its elongation (aspect ratio) and conductivity contrast. It seems that the same is valid for the horst vicinity if a distance to the horst is far less than its half-length. It can be also presumed that with increasing frequency, the two-dimensional approximation becomes more accurate (due to skin effect, which extinguishes the influence of the far ends of a horst).

Consider a three-dimensional horst shown in Fig. 7.42. Let us examine a set of models with fixed parameters $\rho_1 = 10\,\text{Ohm·m}, h_1 = 1\,\text{km}, \Delta h = 0.7$ km, $\rho_2 = 10^3$ Ohm·m, $h_2 = 99$ km, $\rho_3 = 10$ Ohm·m and variable parameters $v = 7.5$ km,

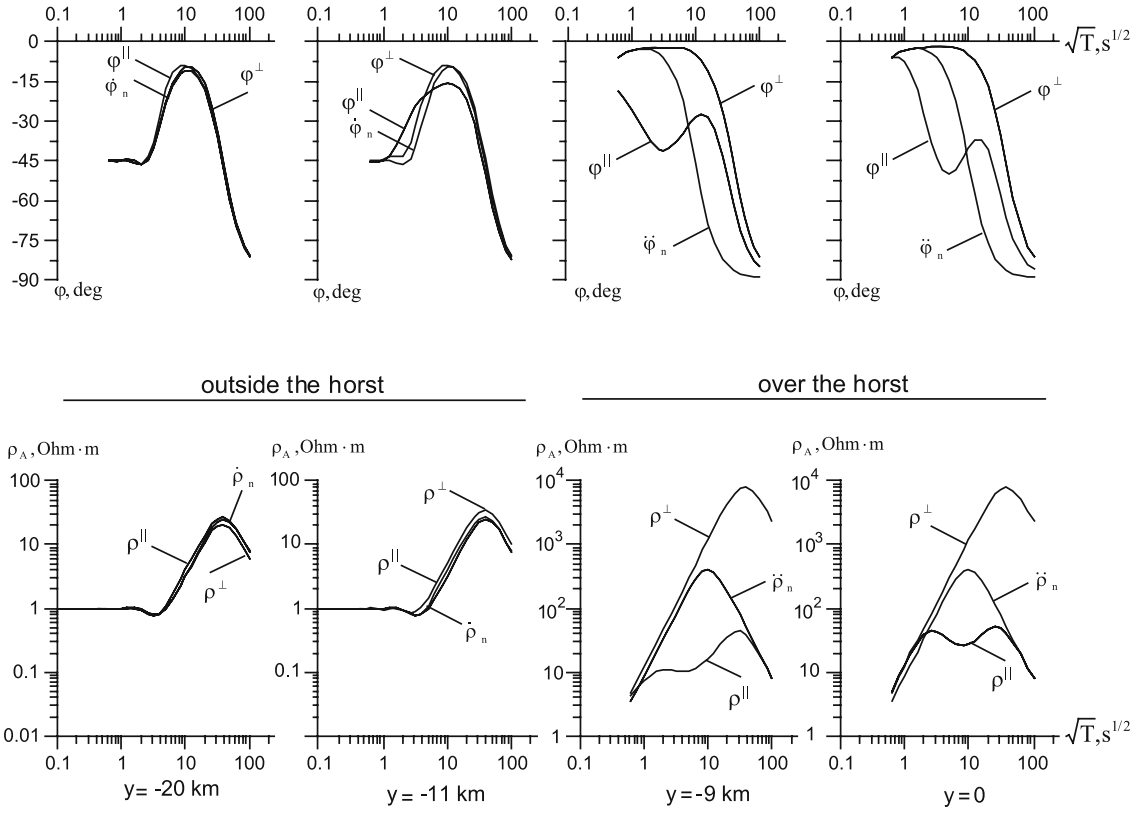

Fig. 7.39 Longitudinal and transverse apparent-resistivity and impedance-phase curves, $\rho^{\parallel}$, $\varphi^{\parallel}$ and $\rho^{\perp}$, $\varphi^{\perp}$, outside and over the horst in the model shown in Fig. 7.38; $\dot{\rho}_n$, $\dot{\varphi}_n$ and $\ddot{\rho}_n$, $\ddot{\varphi}_n$ - locally normal curves; *y*-distance to the centre of the model

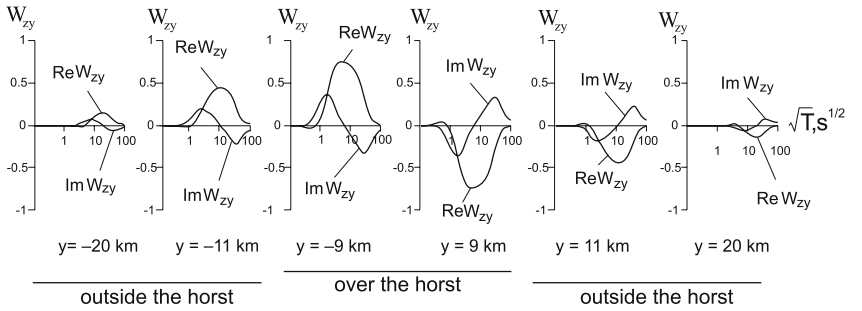

Fig. 7.40 Tipper curves, $\mathrm{Re}W_{zy}$ and $\mathrm{Im}W_{zy}$, outside and over the horst in the model shown in Fig. 7.38; y-distance to the centre of the model

$l = 15, 75, 150, 300$ km; $v = 15$km, $l = 30, 150, 300, 600$ km; $v = 30$ km, $l = 60, 300, 600, 1200$ km, where $2v$ and l are the width and length of the horst. Straightforward computation testifies that on this parametrical set the horst elongation $e = l/2v$ may be well used as a stable indicator of quasi-two-dimensionality. By way of example consider a horst 60 km wide and 60 km long ($e = 1$). Figure 7.43 demonstrates the three-dimensional and two-dimensional ($e = \infty$) apparent-resistivity, impedance-phase and tipper curves, obtained along a central profile running in the $y-$direction.

The apparent resistivity ρ_{xy}, ρ_{yx} and phase $\varphi_{xy}, \varphi_{yx}$ curves observed over the horst ($y = 0$, $y = 22.5$ km) show up rather strong flow-around effect. Here, at low frequencies, we get ρ_{xy} (3D) $>> \rho^{\parallel}$(2D), φ_{xy}(3D) $>> \varphi^{\parallel}$(2D) and ρ_{yx}(3D) $<< \rho^{\perp}$(2D), φ_{yx}(3D) $<< \varphi^{\perp}$(2D). The flow-around effect also manifests itself in the tipper curves $\mathrm{Re}W_{zy}$(3D) and $\mathrm{Im}W_{zy}$(3D), measured outside the horst ($y = 37.5$ km). But it quickly attenuates as the horst elongation e increases. Figure 7.44 demonstrates the apparent resistivity, impedance-phase and tipper curves for a horst 60 km wide and 600 km long ($e = 10$). Here the curves for ρ_{xy}(3D), ρ_{yx}(3D) and φ_{xy}(3D), φ_{yx}(3D) virtually merge with the two-dimensional curves for $\rho^{\parallel}$(2D), $\rho^{\perp}$(2D) and $\varphi^{\parallel}$(2D), $\varphi^{\perp}$(2D), while the curves for $\mathrm{Re}W_{zy}$(3D), $\mathrm{Im}W_{zy}$(3D) are sufficiently close to the curves for $\mathrm{Re}W_{zy}$(2D), $\mathrm{Im}W_{zy}$(2D). It seems that the condition $e \geq 10$ provides the quasi-two-dimensionality of the horst 60 km wide. The same condition is found for the horsts 15 and 30 km wide. It should be recognized that this condition is valid not only over the horst, but in its visinity $|y| - v \leq 0.5l$ as well.

Now compare the quasi-two-dimensionality condition, obtained in the horst model, with conditions, obtained in the elliptic-cylinder model with equivalent contrast of conductances: $m = S_1''/S_1' = (h_1 - \Delta h)/h_1 = 0.3$. Using estimates given by (7.132) for the 10%-difference between ρ_{A}(3D) and ρ_{A}(2D), we get $e^S_{xy} \geq 10.3, e^S_{yx} \geq 21.2$ in the S_1-interval and $e^h_{xy} \geq 13.7, e^h_{yx} \geq 43.3$ in the $h-$interval. Consider the quasi-two-dimensionality conditions for the horst and elliptic-cylinder. They are almost the same for the longitudinal $\rho_{xy}-$curves ($e \geq 10$ against $e^S_{xy} \geq 10.3, e^h_{xy} \geq 13.7$) and considerably differ for the transverse

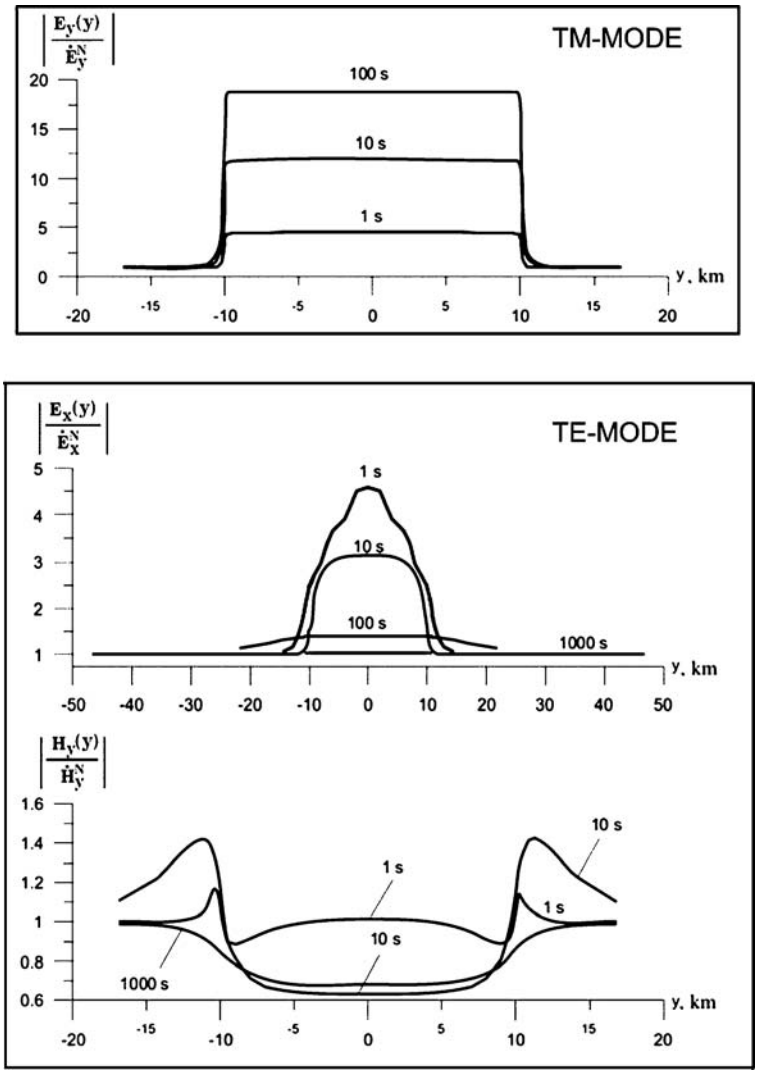

Fig. 7.41 Electromagnetic field profiles outside and over the horst in the model shown in Fig. 7.38; y-distance to the centre of the model. Profile parameter: period $T = 1$–1000 s

ρ_{yx}−curves ($e \geq 10$ against $e^S_{yx} \geq 21.2$, $e^h_{yx} \geq 43.3$). The latter is accounted for by a great role of the transverse currents flowing through the conductive clearance between the roof of the horst and the Earth's surface. When narrowing the clearance (or filling it with a resistive layer), we intensify the flow-around effect and bring the quasi-two-dimensionality condition for the horst close to the quasi-two-dimensionality condition for the elliptic cylinder.

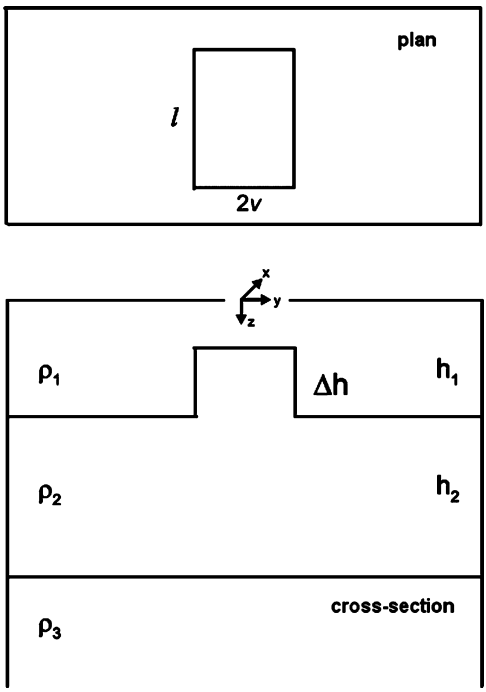

Fig. 7.42 Model of a three-dimensional horst

7.4.2 The Graben Model

A two-dimensional model of the graben is shown in Fig. 7.45. Similar to the horst model, the upper layer (ρ_1) simulates the conductive sedimentary strata underlaid by the resistive lithosphere (ρ_2) resting on the highly conductive mantle (ρ_3). The graben model is a counterpart of the three-segment conductance model with a conductive central segment (Fig. 7.16). Let us compare these two models.

Figure 7.46 presents the longitudinal and transverse apparent-resistivity and impedance-phase curves, $\rho^{\parallel}$, $\rho^{\perp}$ and $\varphi^{\parallel}$, $\varphi^{\perp}$, observed outside and over the graben. They closely resemble the curves for $\rho^{\parallel}$, $\rho^{\perp}$ and $\varphi^{\parallel}$, $\varphi^{\perp}$ obtained in the three-segment model (Figs. 7.21 and 7.22). Outside the graben the $\rho^{\perp}-$ and $\varphi^{\perp}-$curves are hardly distorted, while the $\rho^{\parallel}-$ and $\varphi^{\parallel}-$curves experience the strong effect of false conductive layer, which however quickly attenuates with distance. Over the graben the $\rho^{\perp}-$ and $\varphi^{\perp}-$curves are drastically distorted by the strong $S-$effect (the descending branches of the $\rho^{\perp}-$curves are displaced from the locally normal $\ddot{\rho}_n$-curve almost by two decades), while the $\rho^{\parallel}-$ and $\varphi^{\parallel}-$curves are distorted rather slightly.

The tipper curves are shown in Fig. 7.47. They are much like those in the three-segment model (Fig. 7.23).

Figure 7.48 shows the field profiles, which pass across the graben in the $y-$ direction.The electric and magnetic fields are normalized to the normal fields $\dot{E}_x^{\mathrm{N}}, \dot{E}_y^{\mathrm{N}}, \dot{H}_y^{N}$ observed at $|y| \to \infty$. The field profiles are not too different from

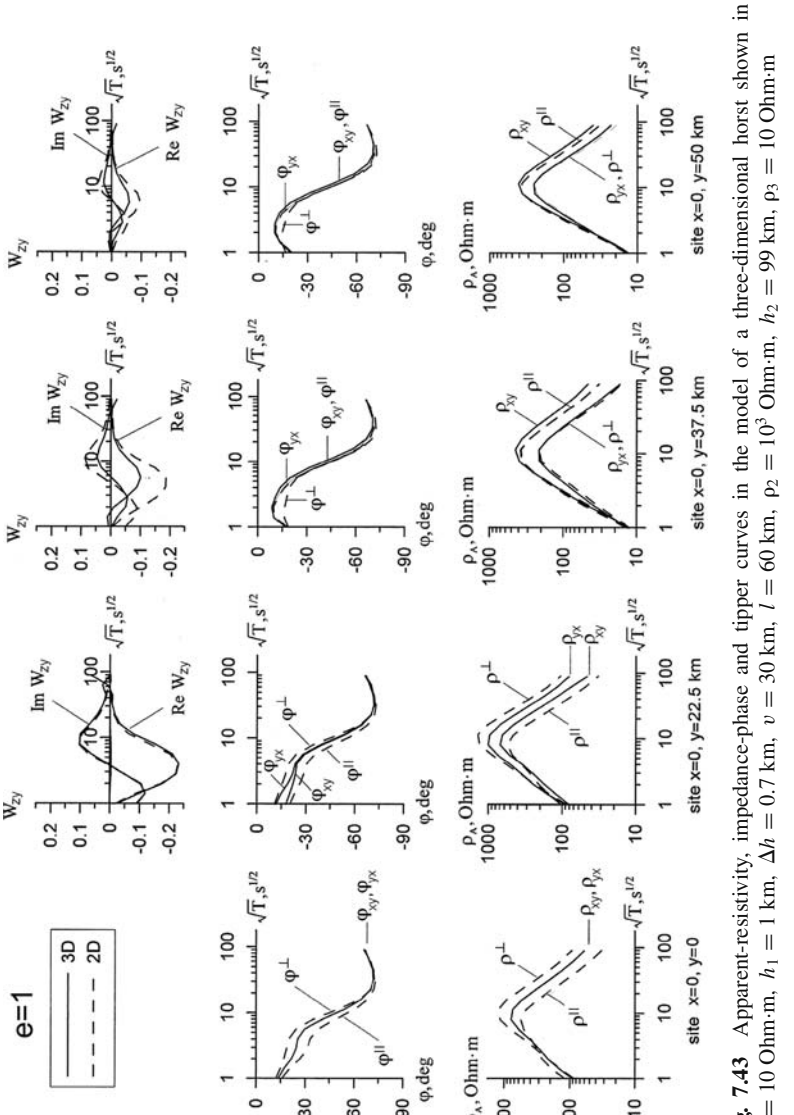

Fig. 7.43 Apparent-resistivity, impedance-phase and tipper curves in the model of a three-dimensional horst shown in Fig. 7.42. Model parameters: $\rho_1 = 10$ Ohm·m, $h_1 = 1$ km, $\Delta h = 0.7$ km, $v = 30$ km, $l = 60$ km, $\rho_2 = 10^3$ Ohm·m, $h_2 = 99$ km, $\rho_3 = 10$ Ohm·m

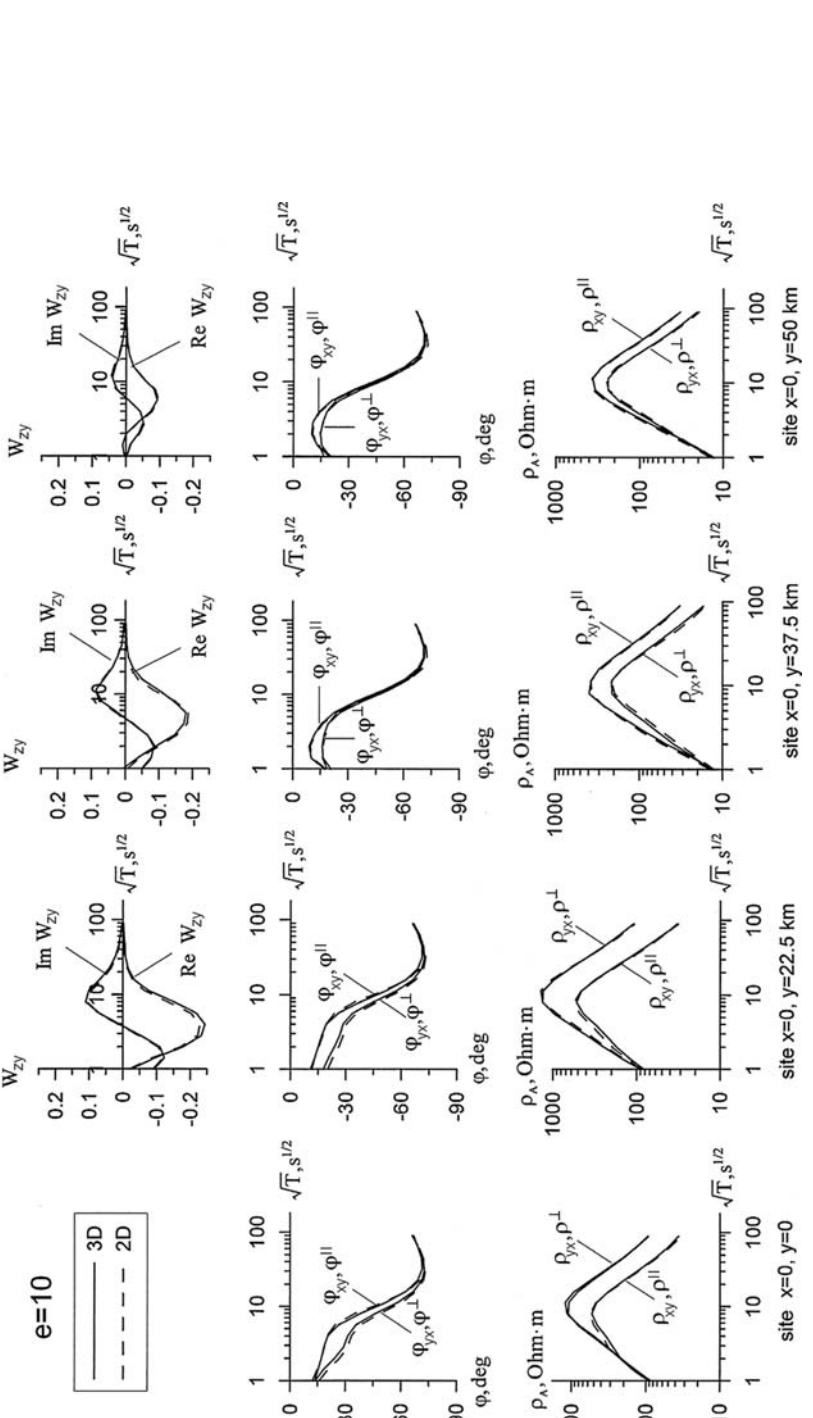

Fig. 7.44 Apparent-resistivity, impedance-phase and tipper curves in the model of a three-dimensional horst shown in Fig. 7.42. Model parameters: $\rho_1 = 10$ Ohm·m, $h_1 = 1$ km, $\Delta h = 0.7$ km, $v = 30$ km, $l = 600$ km, $\rho_2 = 10^3$ Ohm·m, $h_2 = 99$ km, $\rho_3 = 10$ Ohm·m

those in the three-segment model (Fig. 7.25). Over the graben we observe an abrupt drop in E_y, though without side minima associated with the current rearrangement effect. Here $\left|E_y/\dot{E}_y^{\mathrm{N}}\right| << \left|E_x/\dot{E}_x^{\mathrm{N}}\right|$ at $T \geq 100\,\mathrm{s}$. It means that with an isotropic normal field ($\dot{E}_x^{\mathrm{N}} = \dot{E}_y^{\mathrm{N}}$) the low frequency electric field is polarized quasi-linearly along the graben (the channeling effect). Another characteristic feature of the model is a strong horizontal skin effect, which concentrates longitudinal currents at the graben boundaries. It becomes distinctly apparent in side maxima of H_y ($T = 1, 10\,\mathrm{s}$).

Finally we examine conditions favorable to the two-dimensional approximation of the three-dimensional graben shown in Fig. 7.49. Let us consider a set of three-dimensional models with fixed parameters $\rho_1 = 10$ Ohm·m, $h_1 = 0.3$ km, $\Delta h = 1.7$ km, $\rho_2 = 10^3$ Ohm·m, $h_2 = 99.7$ km, $\rho_3 = 10$ Ohm·m and variable parameters $v = 15$ km, $l = 30, 150, 300$ km; $v = 30$ km, $l = 60, 300, 600$ km. As in the case of the horst, we use the elongation $e = l/2v$ as an indicator of quasi-two-dimensionality. Figure 7.50 demonstrates the three-dimensional and two-dimensional ($l = \infty$) apparent-resistivity, impedance-phase and tipper curves along a central $y-$profile going across a graben 60 km wide and 60 km long ($e = 1$). It is remarkable that the transverse curves for $\rho_{yx}(3D)$, $\varphi_{yx}(3D)$, observed over the graben edge ($y = 29, 31$ km) and outside the graben ($y = 40$ km) are close to the curves for $\rho_{yx}(2D)$, $\varphi_{yx}(2D)$ and can be treated as quasi-two-dimensional. At the same time the longitudinal curves for $\rho_{xy}(3D)$, $\varphi_{xy}(3D)$ and the tipper curves for $\mathrm{Re}W_{zy}(3D)$, $\mathrm{Im}W_{zy}(3D)$ differ noticeably from the curves for $\rho_{xy}(2D)$, $\varphi_{xy}(2D)$ and $\mathrm{Re}W_{zy}(2D)$, $\mathrm{Im}W_{zy}(2D)$. One can arrive to conclusion that the TM-mode is more robust to the current-gathering effect than the TE-mode.

The current-gathering effect rather quickly attenuates as the graben elongation e increases. Figure 7.51 demonstrates the apparent-resistivity, impedance-phase and tipper curves for a graben 60 km wide and 600 km long ($e = 10$). Now the three-dimensional curves for $\rho_{xy}(3D)$, $\rho_{yx}(3D)$, $\varphi_{xy}(3D)$, $\varphi_{yx}(3D)$ and

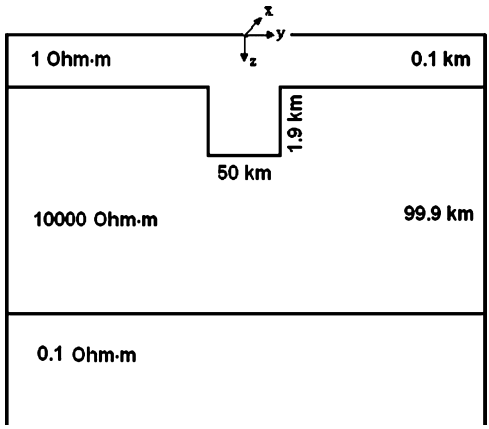

Fig. 7.45 Model of the two-dimensional graben

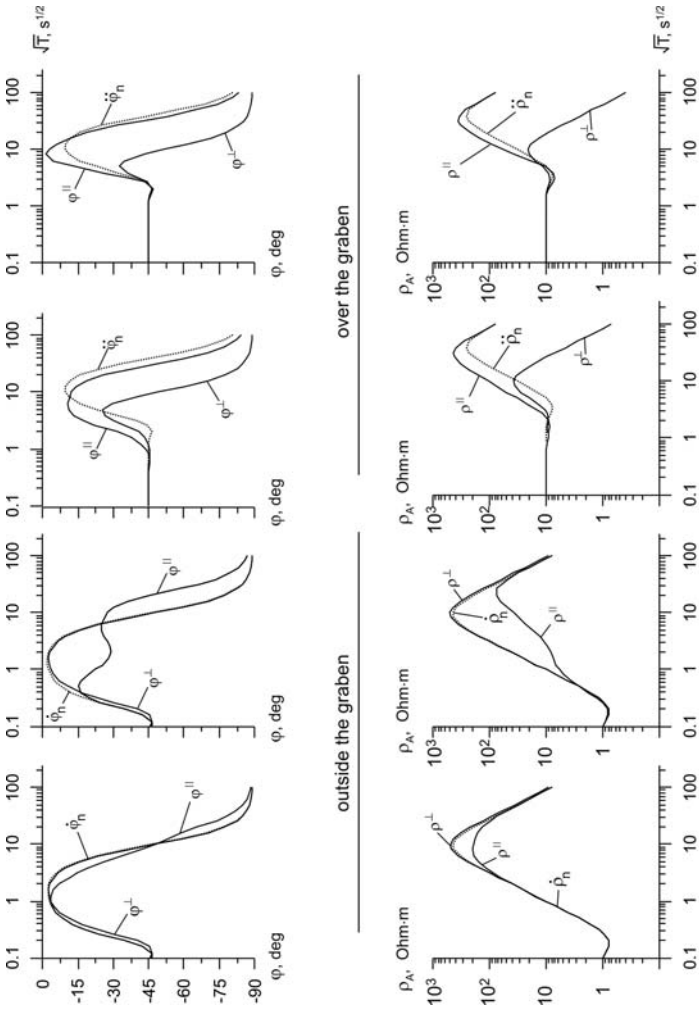

Fig. 7.46 Longitudinal and transverse apparent-resistivity and impedance-phase curves, $\rho^{\parallel}$, $\varphi^{\parallel}$ and $\rho^{\perp}$, $\varphi^{\perp}$, outside and over the graben in the model shown in Fig. 7.45; $\dot{\rho}_n, \dot{\varphi}_n$ and $\ddot{\rho}_n, \ddot{\varphi}_n$ - locally normal curves; y-distance to the centre of the model

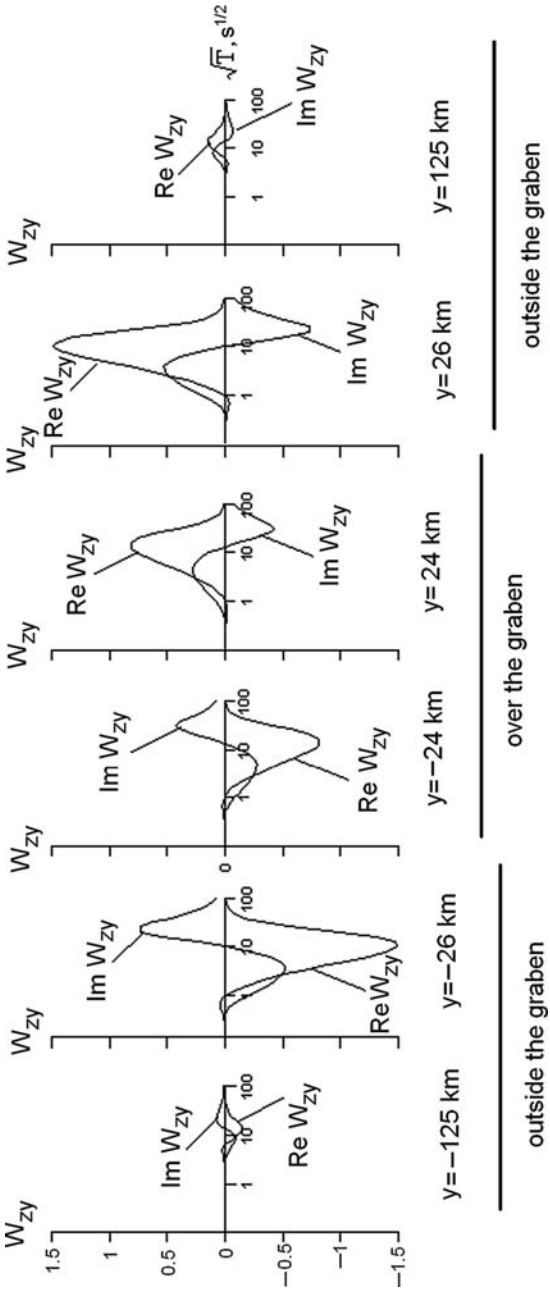

Fig. 7.47 Tipper curves, ReW_{zy} and IMW_{zy}, outside and over the graben in the model shown in Fig. 7.45; y-distance to the centre of the model

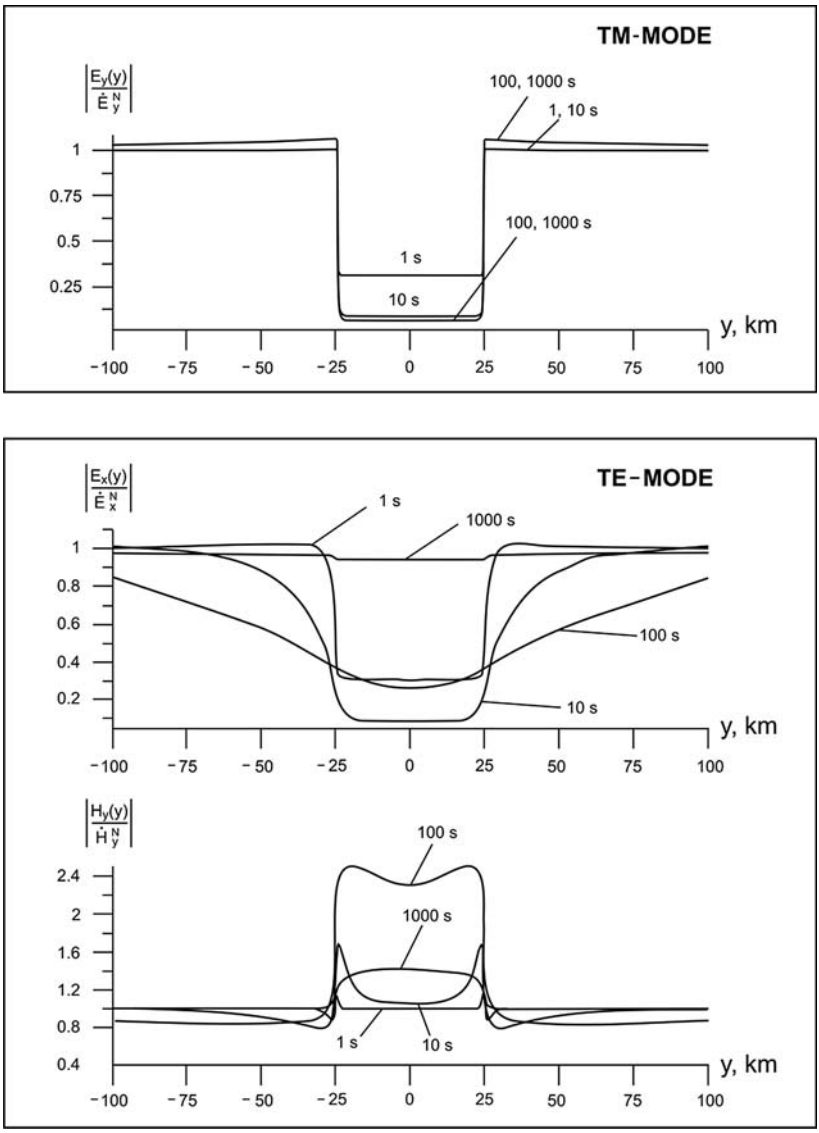

Fig. 7.48 Electromagnetic field profiles outside and over the graben in the model shown in Fig. 7.38; *y*-distance to the centre of the model. Profile parameter: period $T = 1$–1000 s

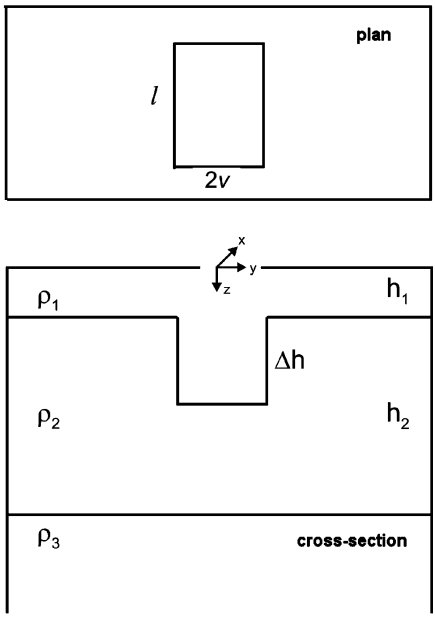

Fig. 7.49 Model of a three-dimensional graben

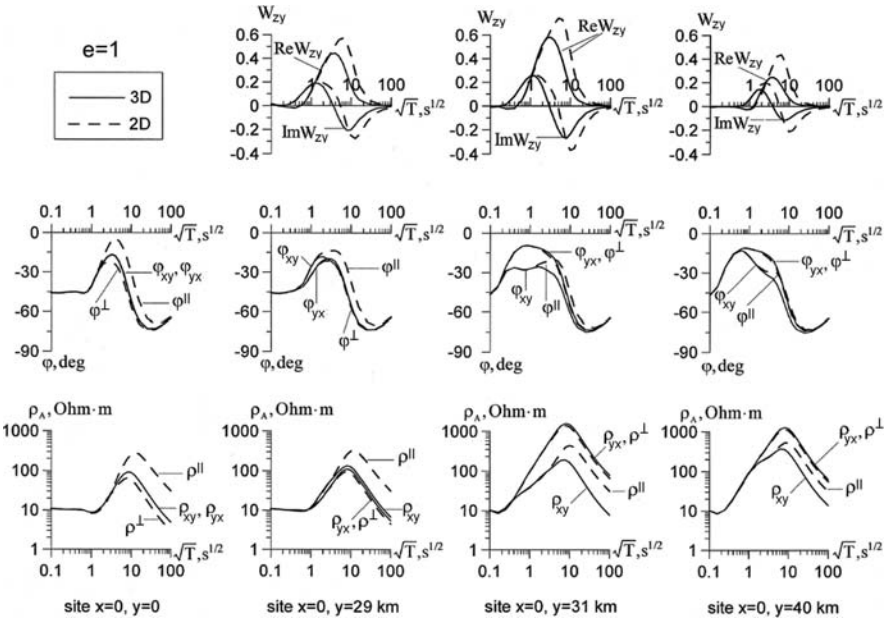

Fig. 7.50 Apparent-resistivity, impedance-phase and tipper curves in the model of a three-dimensional graben shown in Fig. 7.49. Model parameters: $\rho_1 = 10$ Ohm·m, $h_1 = 0.3$ km, $\Delta h = 1.7$ km, $v = 30$ km, $l = 60$ km $\rho_2 = 10^3$ Ohm·m, $h_2 = 99.7$ km, $\rho_3 = 10$ Ohm·m

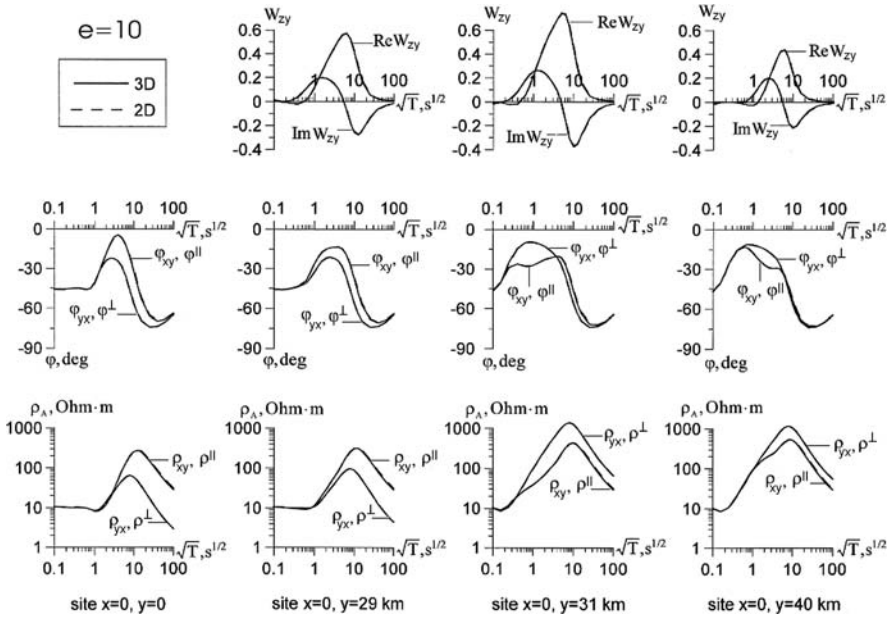

Fig. 7.51 Apparent-resistivity, impedance-phase and tipper curves in the model of a three-dimensional graben shown in Fig. 7.49. Model parameters: $\rho_1 = 10$ Ohm·m, $h_1 = 0.3$ km, $\Delta h = 1.7$ km, $v = 30$ km, $l = 600$ km, $\rho_2 = 10^3$ Ohm·m, $h_2 = 99.7$ km, $\rho_3 = 10$ Ohm·m

$\mathrm{Re}W_{zy}(3D)$, $\mathrm{Im}W_{zy}(3D)$ virtually merge with the two-dimensional curves for $\rho^{\parallel}(2D)$, $\rho^{\perp}(2D)$,$\varphi^{\parallel}(2D)$, $\varphi^{\perp}(2D)$ and $\mathrm{Re}W_{zy}(2D)$, $\mathrm{Im}W_{zy}(2D)$. Thus, the condition $e \geq 10$ confidently provides quasi-two-dimensionality of the graben 60 km wide. The same condition is found for the graben 30 km wide.

Let us compare the condition $e \geq 10$ with conditions obtained in the elliptic-cylinder model with equivalent contrast of conductances: $m = S_1''/S_1' = (h_1 + \Delta h)/h_1 = 6.7$. Using estimates given by (7.132) for 10%-difference between $\rho_A(3D)$ and $\rho_A(2D)$, we get $e_{xy}^S \geq 13.1$, $e_{yx}^S \geq 8$ in the S_1-interval and $e_{xy}^h \geq 107.3$, $e_{yx}^h \geq 16.8$ in the $h-$interval. We see that the quasi-two-dimensionality in the graben model may be provided by considerably smaller elongation than in the elliptic-cylinder model. This can be accounted for by dominating role of the currents flowing into the graben from above.

Chapter 8
Models of Deep Geoelectric Structures

In the preceding chapter, we studied the near-surface magnetotelluric anomalies caused by geoelectric inhomogeneities in the sediments. Now we turn our attention to the deep geoelectric inhomogeneities located in the consolidated Earth's crust and the upper mantle.

Figure 8.1 shows generalized resistivity-depth profiles for stable (SR) and active (AR) regions, compiled from geothermal and geoelectric data as well as from laboratory measurements (Vanyan, 1997). In stable regions, the resistivity decreases monotonically from $10^4 \div 10^5$ Ohm·m near the Earth's surface to 10 Ohm·m at depths of the order of 400 km. This global resistivity decay is conditioned by the gradual warm-up of the Earth's interior and its phase changes. The total resistance of the lithosphere is about 10^9 Ohm·m^2 in stable regions and 3×10^8 Ohm·m^2 in active regions (Kuvshinov, 2004). Two local minima of resistivity can be recognized against this background in active regions, one in the crust (C), and the other in the upper mantle (A). The resistivity minimum in the Earth's crust is explained by the fluidization ($\rho = 10 \div 250$ Ohm·m) or the graphitization ($\rho = 0.1 \div 100$ Ohm·m) of crystalline rocks. The resistivity minimum in the upper mantle is caused by asthenospheric partial melting ($\rho = 10 \div 50$ Ohm·m) and hydrogen diffusity. Studying the deep conductive anomalies, C and A, we can obtain an unique information on the fluid regime, petrophysics, reology, thermodynamics and geodynamics of the Earth's interior.

Keeping this in mind, we examine models of three kinds: (1) models of crustal conductive zones, (2) models of asthenosphere conductive zones, (3) models of deep conductive faults.

8.1 Models of Crustal Conductive Zones

Figure 8.2 demonstrates the one-dimensional apparent-resistivity curves calculated for crustal conductive layers located at a depth of 20 km, their conductance being two–four times greater than the sediments conductance. Under these conditions, the crustal conductors display themselves in vast minima or bendings of the

M. Berdichevsky, V.I. Dmitriev, *Models and Methods of Magnetotellurics*,
DOI 10.1007/978-3-540-77814-1_8,

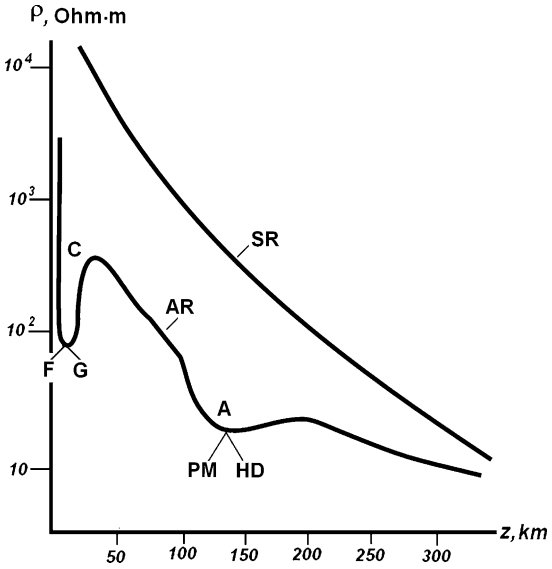

Fig. 8.1 Geoelectric resistivity-depth profiles in a tectonically stable and a tectonically active region. SR – stable ("cold") region, AR – active ("hot") region; C – zone of decreased resistivity in the crust, F – fluidization, $\rho = 10 \div 250$ Ohm·m, G – graphitization, $\rho = 0.1 \div 100$ Ohm·m; A – asthenospheric zone of decreased resistivity, PM – partial melting, HD – hydrogen diffusity, $\rho = 10 \div 50$ Ohm·m (Vanyan, 1977)

apparent-resistivity curves near the line $h = 25$ km. How do they display themselves in two-dimensional and three-dimensional models?

A two-dimensional model of the crustal conductive zone is shown in Fig. 8.3. The upper layer (ρ_1) simulates the conductive sedimentary strata underlaid with the resistive lithosphere (ρ_2) resting on the highly conductive mantle (ρ_3). The lithosphere consists of three layers (ρ_2', ρ_2'', ρ_3''), the ρ_2''−layer contains a conductive infinitely long prism of resistivity ρ_c, its half-width is v. The prism runs in the x−direction.

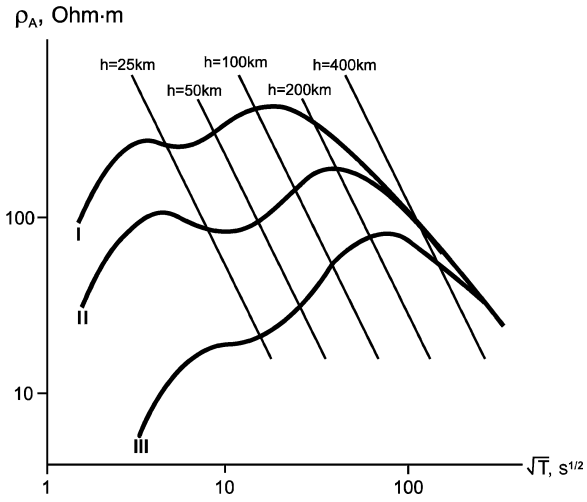

Fig. 8.2 One-dimensional apparent-resistivity curves over the crustal conductive layer at a depth of 20 km; h-lines for 25, 50, 100, 200, and 400 km are shown. I – sediments conductance 50 S, crustal conductive layer conductance 100 S; II – sediments conductance 100 S, crustal conductive layer conductance 400 S; III – sediments conductance 500 S, crustal conductive layer conductance 1000 S (Vanyan and Shilovsky, 1983)

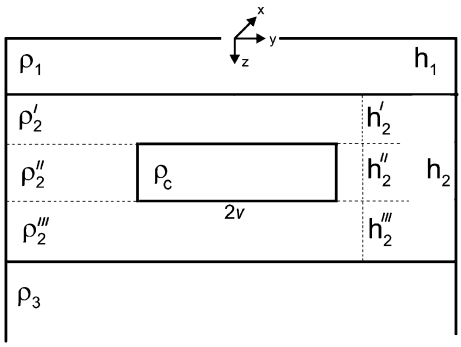

Fig. 8.3 Model of a two-dimensional crustal conductive zone: ρ_1- conductive sediments, ρ_2- resistive lithosphere, ρ_c- crustal conductive zone, ρ_3- conductive mantle

8.1.1 Magnetotelluric Anomaly Caused by Crustal Conductive Zone

To gain a better insight into physical mechanisms of magnetotelluric anomaly caused by the crustal conductive zone, we start our consideration with the field profiles passing across the prism in the $y-$direction. The electric and magnetic fields are normalized to the normal fields $\dot{E}_x^{\mathrm{N}}, \dot{E}_y^{\mathrm{N}}, \dot{H}_y^{\mathrm{N}}$ obtained at $|y| \to \infty$.

Figure 8.4 presents the E_y-profile, which vividly displays the peculiarities of the TM-mode in a model with the wide conductive zone ($\upsilon = 500$ km). We recognize here three effects conditioned by shunting action of the conductive prism:

– The current selects a path of the least resistance and flows from the resistive ρ_2-layer into the conductive ρ_1-layer. The near-surface current concentration arising in regions M_1 and M_3 manifests itself in side maxima of E_y developed on low frequencies ($T = 1000 \div 10000$ s).

– The near-surface current flows from the conductive ρ_1-layer into the conductive prism. In region M_2, the near-surface current deconcentration evolves. It manifests itself in a vast central minimum of E_y developed over wide frequency range ($T = 100 \div 10000$ s).

– The deep current flows from the conductive ρ_3-layer into the conductive prism. This effect decreases the near-surface current deconcentration. In region M_2, we observe a gentle maximum of E_y superimposed on the central minimum of E_y ($T = 10000$ s).

Quite different pattern is displayed by the TE-mode. Figure 8.5 presents the E_x- and H_y-profiles. The crusal conductive zone is reflected in the wide bowl-shaped minimum of E_x ($T = 100$ s). With lowering frequency this minimum flattens out. It practically vanishes at $T \geq 10000$ s, where effective penetration depth h_{eff} is much greater than prism width 2υ ($h_{\mathrm{eff}} >> 2\upsilon$). The H_y-profile has more complicated appearance. Here the crustal conductive zone is reflected in the gentle central maximum caused by excess current filling the prism and in rather sharp side maxima and minima, which arise due to the horizontal skin effect at the edges of the prism ($T = 100$ s). At lower frequencies the central maximum increases, while the side extrema flatten out ($T = 1000$ s). But

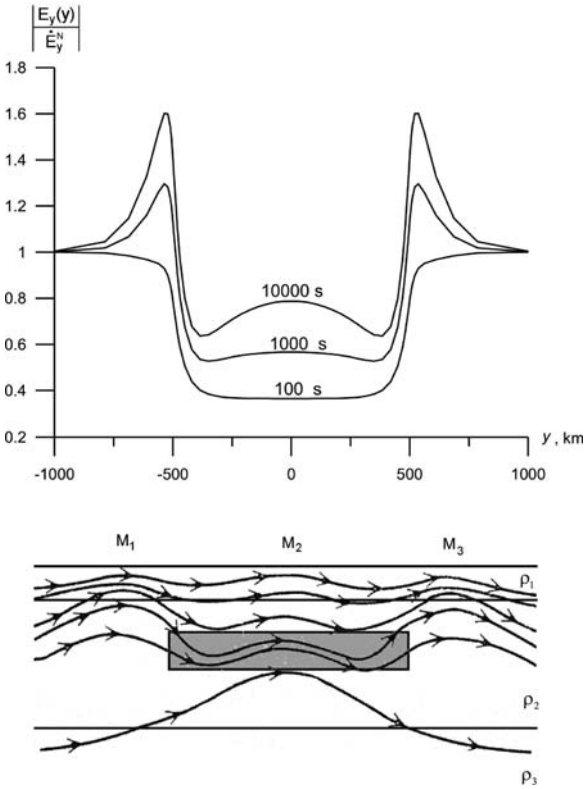

Fig. 8.4 Electric profiles (TM-mode) passing across the conductive zone shown in Fig. 8.3. Model parameters: $\rho_1 = 10\,\Omega\text{m}$, $h_1 = 1\,\text{km}$, $\rho_2' = \rho_2'' = 1000\,\Omega\text{m}$, $h_2' = 19\,\text{km}$, $h_2'' = 15\,\text{km}$ $\rho_c = 10\,\Omega\text{m}$, $v = 500\,\text{km}$, $\rho_2''' = 500\,\Omega\text{m}$, $h_2''' = 65\,\text{km}$, $\rho_3 = 10\,\Omega\text{m}$. Profile parameter: period $T = 100, 1000, 10000\,\text{s}$

with further lowering frequency when most of current is induced in the homogeneous conductive mantle the magnetic anomaly almost completely decays ($T = 10000\,\text{s}$).

8.1.2 Magnetotelluric and Magnetovariational Response Functions in the Model of Crustal Conductive Zone

Now examine the apparent-resistivity and impedance-phase curves observed in the two-dimensional model from Fig. 8.3.

Figure 8.6 shows the transverse and longitudinal curves $\rho^{\perp}$, $\varphi^{\perp}$ and $\rho^{\parallel}$, $\varphi^{\parallel}$ together with the locally normal curves $\dot{\rho}_n$, $\dot{\varphi}_n$ (outside the prism) and $\ddot{\rho}_n$, $\ddot{\varphi}_n$ (over the prism). They have been obtained at the different distances y from the epicentre of the crustal conductive zone. The low-frequency branches of the transverse curves $\rho^{\perp}$, $\varphi^{\perp}$ observed over the central part of the prism are distorted ($y = 0 \div 250\text{km}$). They are shifted down with respect to the locally normal curves $\ddot{\rho}_n$, $\ddot{\varphi}_n$. This galvanic effect is accounted for by the transverse-current redistribution due to the shunting action of the crustal conductive zone. Inasmuch as its intensity depends on the prism conductance $S_c = \Delta h/\rho_c$, it is termed the *deep S-effect*. Outside the

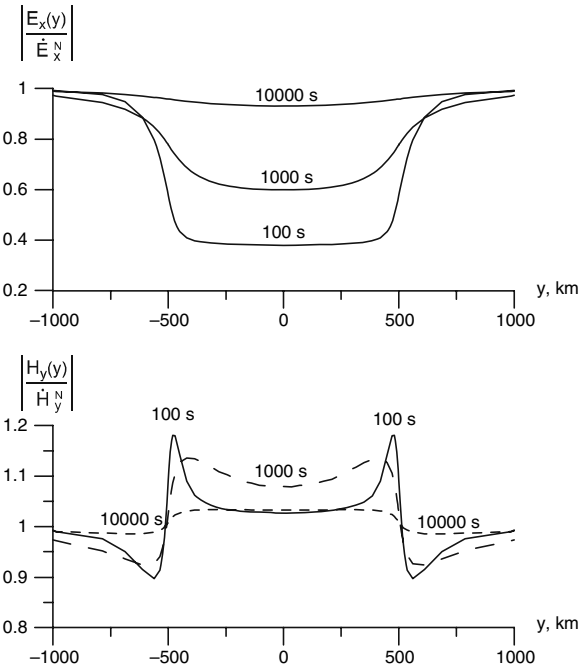

Fig. 8.5 Electromagnetic profiles (TE-mode) passing across the conductive zone shown in Fig 8.3. Model parameters: $\rho_1 = 10$ Ohm·m, $h_1 = 1$ km, $\rho'_2 = \rho''_2 = 1000$ Ohm·m, $h'_2 = 19$ km, $h''_2 = 15$ km, $\rho_c = 10$ Ohm·m, $v = 500$ km, $\rho'''_2 = 500$ Ohm·m, $h'''_2 = 65$ km, $\rho_3 = 10$ Ohm·m. Profile parameter: period T = 100, 1000, 10000 s

prism ($y = 501 \div 700$ km) the deep S-effect shifts the low-frequency branches of the transverse curves $\rho^{\perp}$, $\varphi^{\perp}$ up. It quickly attenuates with distance and vanishes at $y \geq 800$ km. The formal one-dimensional inversion of the MT-curves distorted by the deep S-effect yields a false elevation and false side depressions of the conductive mantle.

Not so dramatic are the induction effects. The longitudinal curves $\rho^{\parallel}$, $\varphi^{\parallel}$ are essentially distorted only near the edges of the conductive prism ($y = 499 \div 501$ km). Here we observe the $\rho^{\parallel}$- and $\varphi^{\parallel}$-curves with flattened descending branches. Away from the conductive prism ($y = 600$, 700km) and over its central part ($y = 0 \div 250$ km) the longitudinal curves $\rho^{\parallel}$, $\varphi^{\parallel}$ merge with the locally normal curves ρ_n, φ_n and allow for the one-dimensional inversion.

How does the dimension of the crustal conductive zone affect the apparent-resistivity and impedance-phase curves? Figure 8.7 shows the apparent-resistivity curves in the model where half-width v of the prism varies from 25 to 850 km. The observation site is located at the epicentre of the crustal conductive zone ($y = 0$). The conductive prism with $v = 25$ km is almost completely screened in the TM-mode (the bell-shaped $\rho^{\perp}$-curve shows no evidence of crustal conductor). But in the TE-mode we see the $\rho^{\parallel}$-curve, which has a gentle displaced minimum revealing the presence of the conductive prism. Let us increase the prism half-width. In the case $v = 100$ km, the $\rho^{\perp}$-curve has a small knee reflecting the crustal conductor, while the $\rho^{\parallel}$-curve practically merges with the locally normal curve $\ddot{\rho}_n$. The case $v = 150$ km is of special interest. Here the prism half-width v is more than threefold adjustment

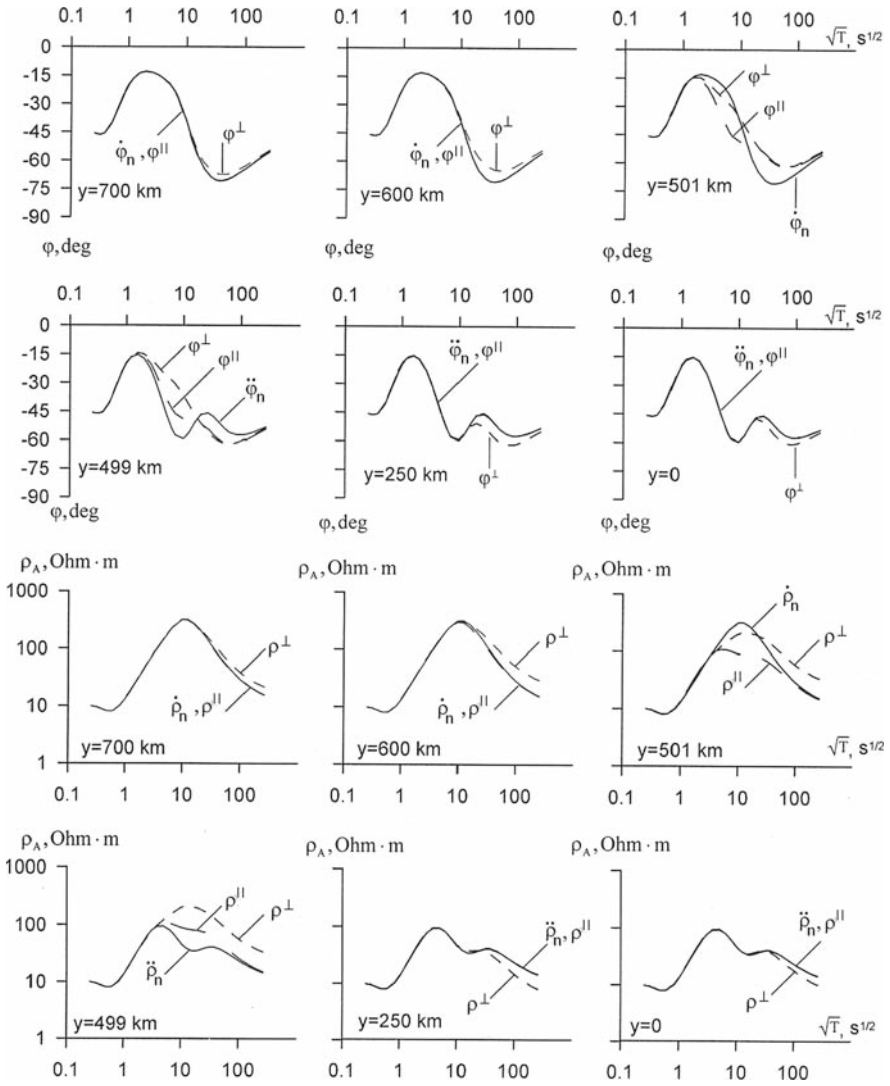

Fig. 8.6 Transverse and longitudinal magnetotelluric curves obtained at different distance y from the epicenter of the conductive zone shown in Fig. 8.3. Model parameters: $\rho_1 = 10\,\Omega\text{hm}\cdot\text{m}$, $h_1 = 1\,\text{km}$, $\rho_2' = \rho_2'' = 1000\,\Omega\text{hm}\cdot\text{m}$, $h_2' = 19\,\text{km}$, $h_2'' = 15\,\text{km}$, $\rho_c = 10\ \Omega\text{hm}\cdot\text{m}$, $v = 500\,\text{km}$, $\rho_2''' = 500\,\Omega\text{hm}\cdot\text{m}$, $h_2''' = 65\,\text{km}$, $\rho_3 = 10\ \Omega\text{hm}\cdot\text{m}$

distance $d = \sqrt{h_1 h_2' \rho_2'/\rho_1} = 43.6\,\text{km}$ calculated from parameters of the ρ_1-layer and the $\rho_2'-$layer, which separates the ρ_1-layer from the conductve prism. In this condition, the $\rho^{\perp}$-curve shows the descending branch, which consists of two parts. The first part is undistorted, it merges with the locally normal $\ddot{\rho}_n-$curve and marks a depth to the conductive prism. The second part lies beneath the $\ddot{\rho}_n-$curve, it is

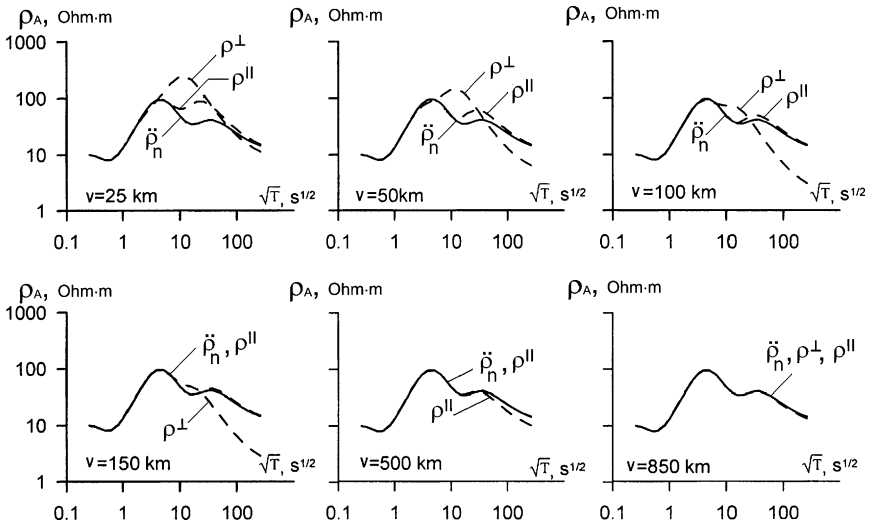

Fig. 8.7 Transverse and longitudinal magnetotelluric curves obtained at the epicentre of the conductive zones of different half-width v. The mode is shown in Fig. 8.3. Model parameters: $\rho_1 = 10\,\Omega\text{m}$, $h_1 = 1\,\text{km}$, $\rho_2' = \rho_2'' = 1000\,\Omega\text{m}$, $h_2' = 19\,\text{km}$, $h_2'' = 15\,\text{km}$, $\rho_c = 10\ \Omega\text{m}$, $\rho_2''' = 500\,\Omega\text{m}$, $h_2''' = 65\,\text{km}$, $\rho_3 = 10\,\Omega\text{m}$

distorted by the deep *S*-effect. With further increasing v, the deep *S*-effect attenuates, the $\rho^{\perp}$-curve is normalized, and at $v = 850\,\text{km}$ both the curves, $\rho^{\perp}$ and $\rho^{\parallel}$, coincide with the locally normal curve $\ddot{\rho}_n$. Note that in the model under consideration the $\rho^{\parallel}$-curve allows for the one-dimensional inversion if the half-width v of the conductive prism is 5 times larger than its depth $h_1 + h_2'$ (see Fig. 8.3), whereas the one-dimensional inversion of the $\rho^{\perp}$-curve is justified if the half-width v is 42.5 times larger than the depth $h_1 + h_2'$. This is pay for the screening effect and the deep *S*-effect.

Let us discuss these effects at greater length. It would be instructive to answer two questions: (1) how does the galvanic-screening effect depend on resistivity ρ_2' of the layer overlying the crustal conductive zone? (2) how does the deep *S*-effect depend on resistivity ρ_2''' of the layer underlying the crustal conductive zone?

Figure 8.8 shows the transverse apparent-resistivity $\rho^{\perp}$-curves in the model from Fig. 8.3 with half-width of the conductive prism $v = 500\,\text{km}$ and resistivity ρ_2' of the overlying layer varying from 1000 Ohm·m to 100000 Ohm·m. The observation site is located at the epicentre of the crustal conductive zone ($y = 0$). The screening effect of the overlying layer with resistivity $\rho_2' = 1000\,\Omega\text{m}$ is rather slight. Here, in a wide range of high and medium frequencies, the $\rho^{\perp}$-curve merges with the locally normal $\ddot{\rho}_n$-curve. It has a distinct minimum reflecting the conductive prism. With increasing ρ_2' this minimum is smoothed and at $\rho_2' = 100000\,\Omega\text{m}$ we get the bell-shaped $\rho^{\perp}$-curve with no evidence of crustal conductor (complete screening). Intuition suggests that the screening effect can be roughly estimated by means of adjustment distance $d = \sqrt{S_1 R_2'}$, where $S_1 = h_1/\rho_1$ and $R_2' = h_2'\rho_2'$. When

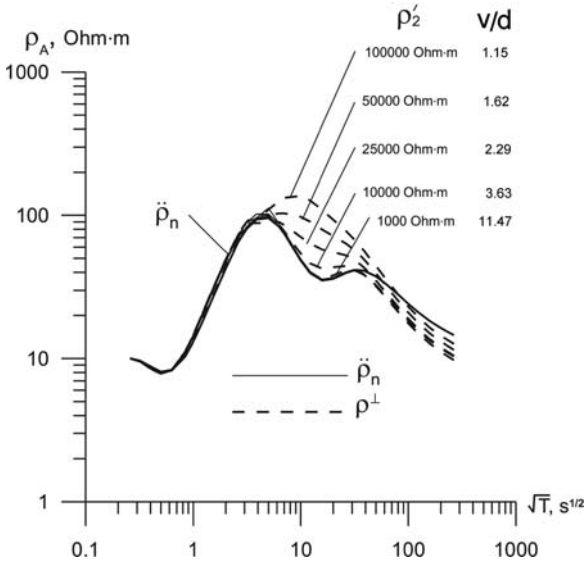

Fig. 8.8 The screening effect in relation to the resistivity ρ'_2 of the layer overlapping the crustal conductive zone shown in Fig. 8.3. The observation site is located at the zone epicentre. Model parameters: $\rho_1 = 10$ Ohm·m, $h_1 = 1$ km, $\rho'_2 = 1000$ Ohm·m, $h'_2 = 19$ km, $h''_2 = 15$ km, $\rho_c = 10$ Ohm·m, $v = 500$ km, $\rho'''_2 = 500$ Ohm·m, $h'''_2 = 65$ km, $\rho_3 = 10$ Ohm·m

resistivity ρ'_2 changes from 1000 Ohm·m to 100000 Ohm·m, the ratio v/d runs from 11.47 to 1.15. Reasoning from Fig. 8.8, we establish three levels of screening: (1) slight screening: $v/d \geq 10$, (2) moderate screening: $v/d \approx 2 \div 3.5$ and (3) strong screening: $v/d \leq 1$.

Figure 8.9 presents the transverse apparent-resistivity $\rho^{\perp}$-curves in the model from Fig. 8.3 with half-width of the conductive prism $v = 500$ km and resistivity ρ'''_2 of the underlying layer varying from 250 Ohm·m to 32000 Ohm·m. The observation

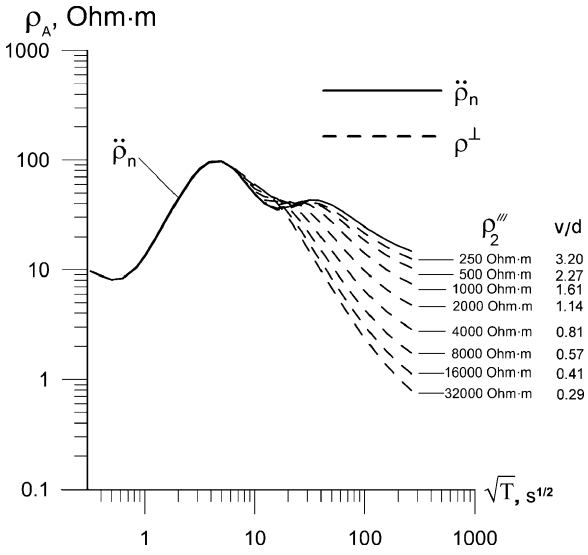

Fig. 8.9 The deep *S*-effect in relation to the resistivity ρ'''_2 of the layer underlying the crustal conductive zone. The model is shown in Fig. 8.3. The observation site is located at the zone epicentre Model parameters: $\rho_1 = 10$ Ohm·m, $h_1 = 1$ km, $\rho'_2 = \rho''_2 = 1000$ Ohm·m, $h'_2 = 19$ km, $h''_2 = 15$ km, $\rho_c = 10$ Ohm·m, $v = 500$ km, $h'''_2 = 65$ km, $\rho_3 = 10$ Ohm·m

site is located at the epicentre of the crustal conductive zone ($y = 0$). The deep S-effect observed in the model with resistivity $\rho_2''' = 250$ Ohm·m is rather slight. Here the $\rho^{\perp}$-curve is close to the locally normal $\ddot{\rho}_n$-curve. But with increasing ρ_2''' its minimum reflecting the conductive prism is smoothed and its descending mantle branch shifts down. At $\rho_2''' = 32000$ Ohm·m we observe strong deep S-effect. Here the minimum on the $\rho^{\perp}$-curve disappears, while vertical displacement of the descending branch is about one decade. Using adjustment distance $d = \sqrt{S_c R_2'''}$ with $S_c = h_2''/\rho_c$ and $R_2''' = h_2''' \rho_2'''$, we can roughly estimate the deep S-effect. Reasoning from Fig. 8.9, we establish three levels of deep S-effect (1) slight deep S-effect: $v/d \geq 3$, (2) moderate deep S-effect : $v/d \approx 1.5 \div 2.5$ and (3) strong deep S-effect: $v/d \leq 1$.

More precise estimates of the deep S-effect based on analytical solutions can be found in (Berdichevsky and Jakovlev, 1991; Singer, 1992).

The W_{zy}-profiles are shown in Fig. 8.10. In the period range from 50 to 10000 s the real tippers Re W_{zy} do not change their sign with frequency. But the imaginary tippers Im W_{zy} do change their sign with frequency. Note that Re W_{zy} and Im W_{zy} are of the same sign on high frequencies ($T = 50$–100 s) and of opposite sign on low frequencies ($T = 1000$–10000 s). The maxima and minima of ReW_{zy} and ImW_{zy} are observed over the left and right edges of the deep conductive prism. It is evident that at all frequencies under consideration the real induction arrows point away from

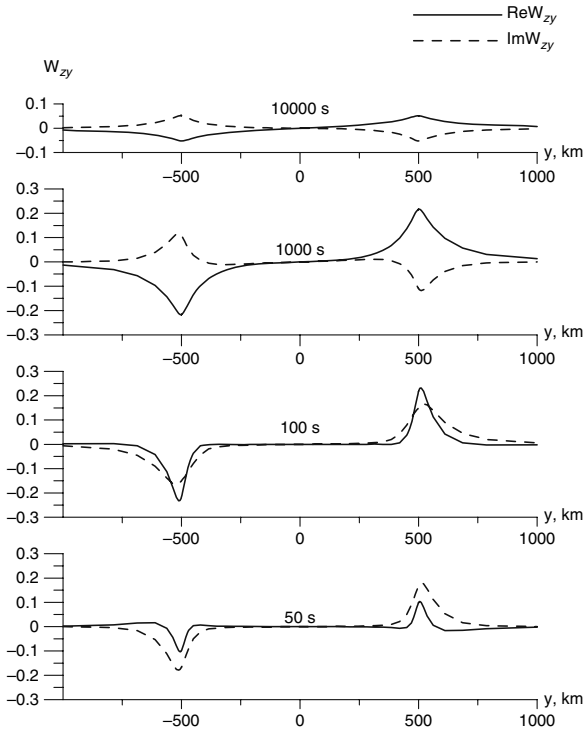

Fig. 8.10 Tipper profiles passing across the crustal conductive zone. The model is shown in Fig. 8.3. Model parameters: $\rho_1 = 10$ Ohm·m, $h_1 = 1$ km, $\rho_2' = \rho_2'' = 1000$ Ohm·m, $h_2' = 19$ km, $h_2'' = 15$ km, $\rho_c = 10$ Ohm·m, $v = 500$ km, $\rho_2''' = 500$ Ohm·m, $h_2''' = 65$ km, $\rho_3 = 10$ Ohm·m

the epicentre of the crustal conductive zone, while the imaginary induction arrows reverse their direction in the transition from the high frequencies to the low ones.

How are the real and imaginary tippers influenced by dimension of a crustal conductive zone and its resistivity? Fig. 8.11 presents curves for Re W_{zy} and Im W_{zy} measured over the right edge of the conductive prism with half-width $v = 25, 500$ km and $\rho_c = 10, 25, 50$ Ohm·m. It is seen that narrowing the prism from 1000 km to 50 km and increasing its resistivity from 10 to 50 Ohm·m we substantially diminish the real and imaginary tippers, but they still are measurable.

8.1.3 Electromagnetic Excitation of Crustal Conductors

Two physical mechanisms, galvanic and inductive, may be implicated in the electromagnetic excitation of the three-dimensional crustal conductors.

The galvanic mechanism is associated with electric currents that percolate from sediments and concentrate within the crustal conductive zone. The resistive crustal layers underlying the sediments hamper the current redistribution and screen the conductive zone. Intensity of the galvanic excitation can be estimated by the adjustment distance $d = \sqrt{S_{sed} R_{crust}}$, where S_{sed} is the sediments conductance and R_{crust}

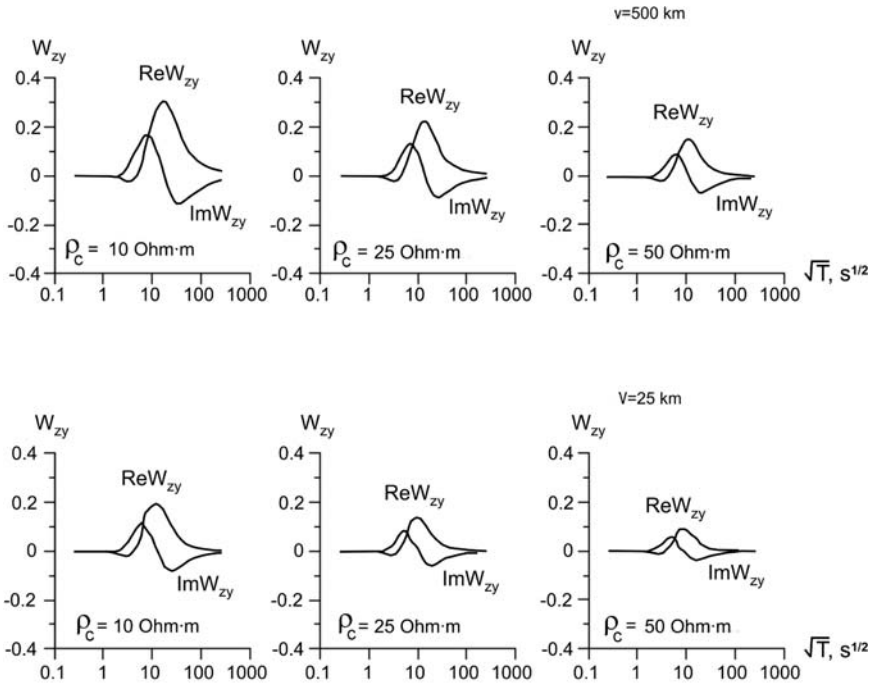

Fig. 8.11 Real and imaginary tippers over the right edge of wide ($v = 500$ km) and narrow ($v = 25$ km) crustal conductive zone of resistivity $\rho_c = 10$, 25, 50 Ohm·m. The model is shown in Fig. 8.3. Model parameters: $\rho_1 = 10$ Ohm·m, $h_1 = 1$ km, $\rho'_2 = \rho''_2 = 1000$ Ohm·m, $h'_2 = 19$ km, $h''_2 = 15$ km, $\rho'''_2 = 500$ Ohm·m, $h'''_2 = 65$ km, $\rho_3 = 10$ Ohm·m

is the resistance of the crustal layers between the sediments and the conductive zone. Reasoning from model estimates, we believe that a three-dimensional conductive zone with maximum horizontal diameter $D_{\max}$ manifests itself rather notably if $D_{\max} > 3d$. Let $S_{\text{sed}} = 100\,S$ and $R_{\text{crust}} = 10^7\,\text{Ohm}\cdot\text{m}^2$ (conductive zone is overlaid with a crustal layer of resistivity 1000 Ohm·m and thickness 10 km). Then $d = 31.6$ km. Here the crustal conductor with horizontal diameter $D_{\max} = 100$ km is expected to be quite detectable. But it is of no use to hope that such a conductor can be excited galvanically if the resistance of upper layer exceeds $10^8 \div 5 \cdot 10^8\,\text{Ohm}\cdot\text{m}^2$.

The inductive mechanism is associated with local induction in the crustal conductors. This mode seems to have the advantage that the buried three-dimensional conductors may be excited and detected, no matter how resistive the surroundings are (Berdichevsky et al., 1984, 1992; Vanyan et al., 1986, 1988, 1991; Egorov, 1987). Let us estimate the intensity of local induction in the real crustal conductors (fluidized, graphitized). Following (Kaufman, 1994), consider a conductive sphere with a radius a and resistivity ρ placed in the homogeneous non-conductive space with a uniform magnetic field $\mathbf{H}_o$ directed along the horizontal x-axis (Fig. 8.12). Examine the anomalous magnetic field $\mathbf{H}^A$ arising due to local induction in the sphere. Over the sphere, at its epicentre ($x = 0,\ y = 0,\ |z| = a + h$), we have

$$\mathbf{H}^A = \frac{1}{2} D \mathbf{H}_o \frac{a^3}{(a+h)^3}, \tag{8.1}$$

from which

$$\left| \frac{H^A}{H_o} \right| = \frac{1}{2} |D| \frac{a^3}{(a+h)^3}, \tag{8.2}$$

where

$$D = \frac{3 \coth p(1-i)}{p(1-i)} + \frac{3}{2p^2 i} - 1. \tag{8.3}$$

Here h is a distance between the observation site and the surface of the sphere, while p is the *induction-factor* defined as the ratio between the radius a of the sphere and the skin-depth $\delta = \sqrt{2\rho/\omega\mu_o}$:

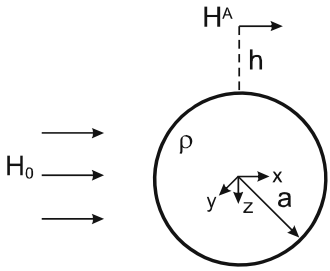

Fig. 8.12 Coducting sphere of resistivity ρ in a uniform magnetic field $\mathbf{H}_o$; $\mathbf{H}^A$- magnetic field of the currents induced within the sphere

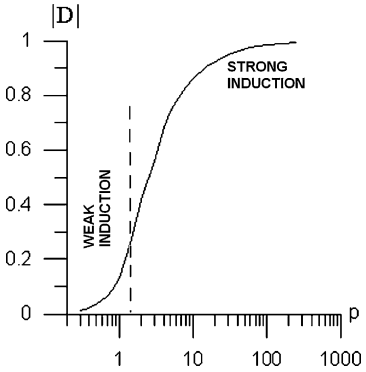

Fig. 8.13 The p-dependence of $|D|$

$$p = a/\delta. \tag{8.4}$$

The parameter D defines the moment $\mathbf{M} = 2\pi a^3 D\mathbf{H}_o$ of an equivalent magnetic dipole situated at the centre of the sphere. It characterizes the intensity of local induction. The p-dependence of $|D|$ is shown in Fig. 8.13. We distinguish here two ranges: (1) $p < 1.5$, weak local induction, and (2) $p \gg 1.5$, strong local induction. The point is which of these ranges the fluidized and graphitized crustal conductors fall into.

Conductive zones of the fluid nature usually occur at a depth of about 15–25 km. Their thickness amounts to 15–20 km, while their resistivity may reach 10–15 Ohm·m. To test intensity of local induction, we consider a cubic conductor $20 \times 20 \times 20$ km with resistivity 10 Ohm·m and the upper face at a depth 15 km. Assume that observations cover a period range from 25 to 3000 s. For rough estimation, take an equivalent sphere with $a = 10$ km and $h = 15$ km. Now calculate the anomalous magnetic field $\left|H^A/H_o\right|$ appearing due to local induction within the conductor. According to (8.2), (8.3) and (8.4), we get for $T \geq 25$ s: $\delta \geq 7.96$ km, $p \leq 1.25$, $|D| \leq 0.2$, $\left|H^A/H_o\right| \leq 0.006$. This is a case of weak local induction: the induced magnetic field is negligibly small against the inducing magnetic field.

Next test the intensity of local induction in conductive zones of the graphite nature. Their resistivity reaches 1 Ohm·m (and even less). They usually occur at a depth of about 3–15 km and their thickness does not exceed 3–4 km. Consider a cubic conductor $4 \times 4 \times 4$ km with resistivity 1 Ohm·m and the upper face at a depth 3 km. Assume that it manifests itself at periods from 10 to 1000 s. Taking the equivalent conductive sphere with $\rho = 1$ Ohm·m and $a = 2$ km, $h = 3$ km, we get for $T \geq 10$ s : $\delta \geq 1.59$, $p \leq 1.26$, $|D| \leq 0.2$, $\left|H^A/H_o\right| \leq 0.0064$. Once again we meet a case of weak local induction within a crustal conductor.

Clearly these rough estimations are preliminary. Satisfactory analysis can be performed by modeling specific three-dimensional structures. The distinguishing feature of the weak local induction is that magnetotelluric anomalies decay when we increase the resistivity of the host medium which contain conductive bodies.

8.1.4 On the Quasi-Two-Dimensionality of Crustal Conductors

At what elongation, that is, at what ratio between the longitudinal and transverse sizes can a crustal conducitve zone be considered as a quasi-two-dimensional one and described by a two-dimensional model?

To begin with we recall rough criteria of quasi-two-dimensionality derived from the well-known problem on a conductive ellipsoid of revolution (Svetov, 1960, 1973; Kaufman, 1974). The ellipsoid of resistivity ρ_i is placed in the infinite homogeneous space of resistivity ρ_e with the uniform electric field directed along the ellipsoid maximum diameter. If the electromagnetic wave length λ inside and outside the ellipsoid is many times its maximum diameter, we can use the direct-current approximation and get the condition of quasi-two-dimensionality of the magnetic anomaly excited by a longitudinal electric field in a simple form dependent on the resistivity contrast ρ_e/ρ_i:

$$e = \frac{a}{b} \geq 4 \sqrt[1.7]{\frac{\rho_e}{\rho_i}} \qquad \lambda >> a, \tag{8.5}$$

where a and b are maximum and minimum ellipsoid diameters. Taking $\rho_e = 1000\,\Omega\text{m}$ and $\rho_i = 10\,\Omega\text{m}$, we conclude that the ellipsoid can be approximated by an infinitely long cylinder if its elongation e is over 60. Unfortinately, such an estimate may go beyond the scope of real large-scale geological structures. Another condition of quasi-two-dimensionality can be suggested for high frequencies. If the wave length λ outside the conductive ellipsoid is less than its maximum diameter ($\lambda < a$), the skin effect extinguishes the influence of the far ends and at the middle part of the ellipsoid the electromagnetic anomaly excited by the transverse electric field is quasi-two-dimensional.

To get more specific estimate, we consider the three-layered Earth including conductive sediments ρ_1, resistive lithosphere ρ_2 with a conductive right prism ρ_2' of length l, width $2v$, thickness Δh, and a conductive mantle ρ_3 (Fig. 8.14). Let us test a set of models with fixed parameters $\rho_1 = 10\ \Omega\text{m}$, $h_1 = 1\,\text{km}$, $\Delta h = 15\,\text{km}$, $h_2 = 99\,\text{km}$, $h_2' = 14\,\text{km}$, $\rho_2' = 10\,\Omega\text{m}$, $\rho_3 = 10\,\Omega\text{m}$ and variable parameters $\rho_2 = 1000$, $10000\,\Omega\text{m}$, $v = 7.5\,\text{km}$, $l = 15$, 75, 105, 150, 225, 300, 375 km; $v = 15\,\text{km}$, $l = 30$, 150, 300, 450, 600 km; $v = 30\,\text{km}$, $l = 60$, 180, 300, 600, 900 km, where v and l are half-width and length of the conductive prism.

Take the model containing the conductive cube with $l = 15\,\text{km}$, $v = 7.5\,\text{km}$, $\Delta h = 15\,\text{km}$, which manifests itself in the period range $T \geq 25\,\text{s}$. To define its induction-factor p, we use the equivalent sphere. According to (8.4), $p \leq 0.94$. This indicates rather weak local induction in the model under consideration. It seems that the same is true for the entire model set.

By way of example inspect a three-dimensional model with parameters $\rho_2 = 10^3\,\Omega\text{m}$, $v = 30\,\text{km}$, $l = 60\,\text{km}$ (elongation $e = 1$) together with its two-dimensional counterpart ($l = \infty$). Figure 8.15 presents the 3D and 2D apparent-resistivity, impedance-phase and tipper curves obtained on a central profile going in the $y-$direction. At all sites the curves ρ_{xy}(3D), ρ_{yx}(3D) and φ_{xy}(3D), φ_{yx}(3D)

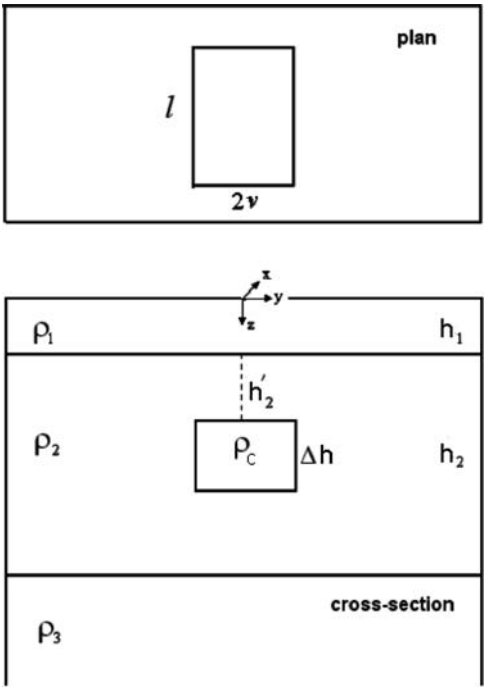

Fig. 8.14 Model of a three-dimensional crustal conductive zone

are close to the transverse curves $\rho^{\perp}$(2D) and $\varphi^{\perp}$(2D), while the tippers Re W_{zy}(3D), Im W_{zy}(3D) do not exceed 0.05. Due to rather strong galvanic screening and negligible local induction we observe here only slight evidences of the conductive prism. The transverse ρ_{yx}(3D)-curve obtained over the prism ($x = 0$, $y = 0$) has the ascending branch with gentle bending, while its descending branch is shifted somewhat down due to the deep *S*-effect. But with increasing the prism elongation the screening effect attenuates (longitudinal current penetrates into the prism) and the curves ρ_{xy}(3D), φ_{xy}(3D) come close to the two-humped longitudinal curves $\rho^{\parallel}$(2D), $\varphi^{\parallel}$(2D), while the tippers Re W_{zy}(3D), Im W_{zy}(3D) grow. At $v = 30$ km, $l = 600$ km ($e = 10$) the curves Re W_{zy}(3D), Im W_{zy}(3D) practically merge with the curves Re W_{zy}(2D), Im W_{zy}(2D) and this opens up the way to the two-dimensional interpretation of the tippers. Finally at $v = 30$ km, $l = 900$ km ($e = 15$) the curves ρ_{yx}(3D), ρ_{xy}(3D) and φ_{yx}(3D), φ_{xy}(3D) virtually coincide with the curves $\rho^{\perp}$(2D), $\rho^{\parallel}$(2D) and $\varphi^{\perp}$(2D), $\varphi^{\parallel}$(2D) so that the apparent-resistivities and impedance-phases also become quasi-two-dimensional (Fig. 8.16).

Testing the entire model set, we have got the results that are summarized in Table 8.1. Note that conditions of the quasi-two-dimensionality depend on the crustal conductor width *2v*: the wider the conductor, the less its elongation that provides quasi-two-dimensionality. Note also that when raizing the lithosphere resistivity we aggrevate the screening effect and increase the crustal-conductor elongation that provides quasi-two-dimensionality. This clearly confirms the galvanic nature

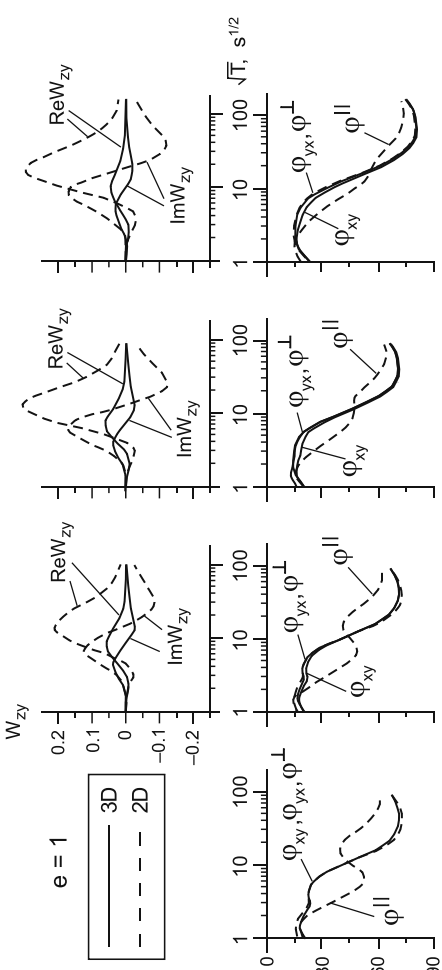

Fig. 8.15 Apparent-resistivity, impedance-phase and tipper curves in the model of a three-dimensional crustal conductive zone shown in Fig. 8.14. Model parameters $\rho_1 = 10\,\Omega\text{m}$, $h_1 = 1\,\text{km}$, $\rho_2 = 1000\,\Omega\text{m}$, $h'_2 = 14\,\text{km}$, $\Delta h = 15\,\text{km}$, $v = 30\,\text{km}$, $l = 60\,\text{km}$, $\rho_c = 10\,\Omega\text{m}$, $h_2 = 99\,\text{km}$, $\rho_3 = 10\,\Omega\text{m}$

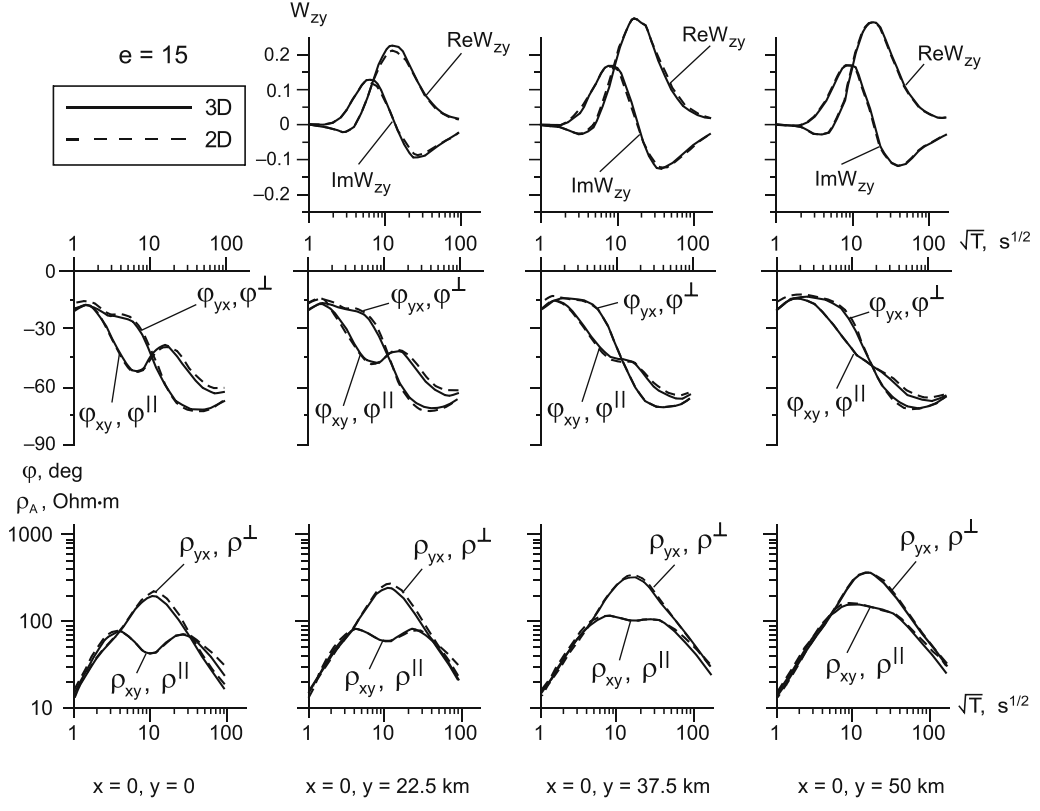

Fig. 8.16 Apparent-resistivity, impedance-phase and tipper curves in the model of a three-dimensional crustal conductive zone shown in Fig. 8.14. Model parameters: $\rho_1 = 10$ Ohm·m, $h_1 = 1$ km, $\rho_2 = 1000$ Ohm·m, $h'_2 = 14$ km, $\Delta h = 15$ km, $v = 30$ km, $l = 900$ km, $\rho_c = 10$ Ohm·m, $h_2 = 99$ km, $\rho_3 = 10$ Ohm·m

Table 8.1 Elongations of crustal conductor providing the tipper quasi-two-dimensionality (W-2D) and the apparent-resistivity and impedance-phase quasi-two-dimensionality (ρ, φ-2D)

Lithosphere resistivity	Conductor width (km)	Conductor elongation	
		W-2D	ρ,φ-2D
1000 Ohm·m	15	20	25
	30	15	20
	60	10	15
10000 Ohm·m	15	30	50
	30	25	35
	60	20	25

of low-frequency magnetelluric anomalies. And finally we have to emphasize that the quasi-two-dimensionality conditions inferred are valid not only over the crustal conductor, but in its visinity as well, $|y| - v << 0.5\,l$.

8.1.5 Are Deep Crustal Conductors Isotropic or Anisotropic?

One of the significant problems of modern deep magnetotellurics is recognition of anisotropy in the crustal and mantle conductive zones (Bahr and Duba, 2000; Bahr and Simpson, 2002; Wannamaker, 2005). The difficulty is that isotropic and anisotropic bounded deep conductors located in or under a highly resistive medium may manifest themselves in the equivalent magnetotelluric and magnetovariational response functions, which cannot distinguish between isotropy and anisotropy and admit both the interpretations.

It is generally agreed that a stable difference between the principal values of the impedance tensors observed over a large area with 2D indications counts in favor of anisotropy. Is such an evidence reliable?

Let us consider two typical examples of crustal conductors and define conditions, at which equivalency between isotropy and anisotropy is the case.

Figure 8.17 presents the two-dimensional layered models ICC (isotropic crustal conductor) and ACC-I (anisotropic crustal conductor). They simulate the conductive sediments and the resistive lithosphere underlaid with the conductive mantle. In the Earth's crust, at a depth of 20–35 km, the model ICC contains the isotropic crustal conductor in the form of the two-dimensional homogeneous prism of resistivity of 10 Ohm·m and width of 44 km. In the model ACC-I we have the same prism composed of alternating vertical layers of resistivities of 5 and 1000 Ohm·m. The strike of vertical layers coincides with the prism strike. The prism can be considered as an anisotropic (macroanisotropic) crustal conductor with the diagonal resistivity tensor

$$\left[\boldsymbol{\rho}_{\text{ACC - I}}\right] = \begin{bmatrix} \rho_{xx} & 0 & 0 \\ 0 & \rho_{yy} & 0 \\ 0 & 0 & \rho_{zz} \end{bmatrix}.$$

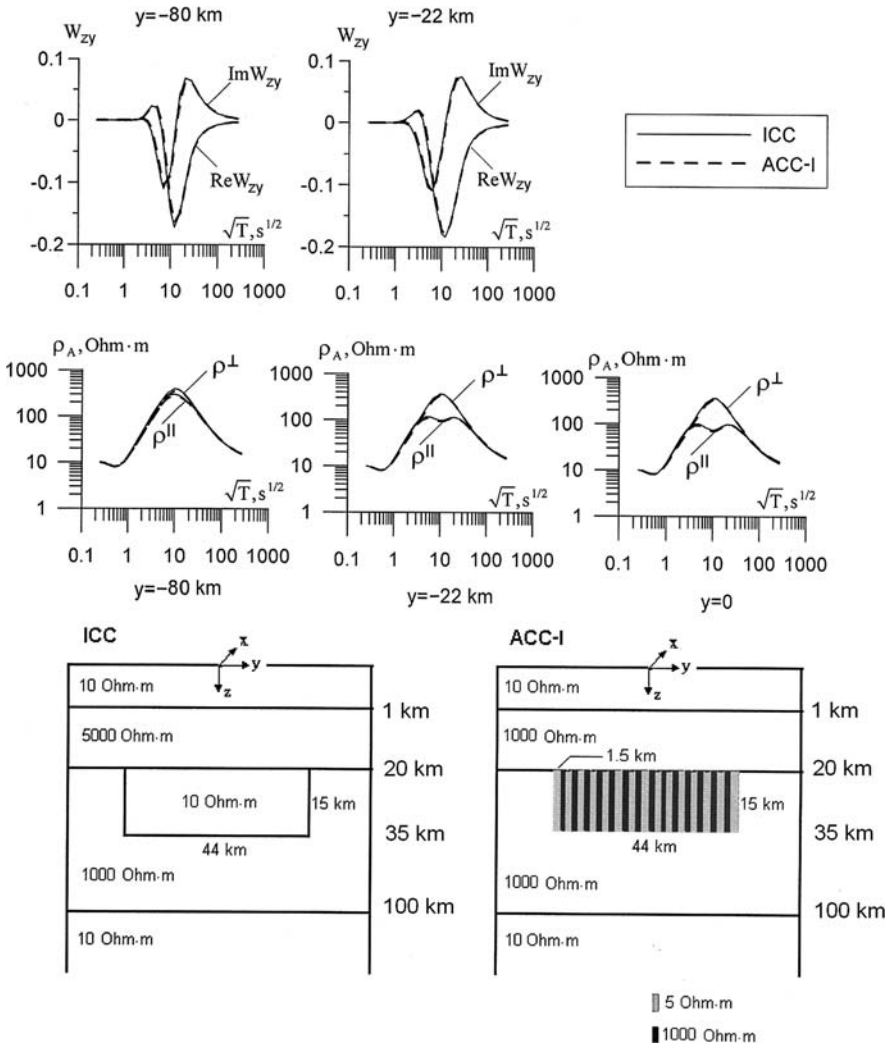

Fig. 8.17 Two-dimensional models of the crustal conductive zones. The model ICC contains an isotropic crustal conductor, the model ACC-I contains an anisotropic crustal conductor with alternating vertical dykes

From Kirchhoff's laws, we have: $\rho_{xx} \approx 10$ Ohm·m, $\rho_{yy} \approx 500$ Ohm·m, and $\rho_{zz} \approx 10$ Ohm·m. The apparent-resistivity and tipper curves have been computed for different distances from the model centre ($y = 0$, -22, -80 km). The calculations performed by the finite-element method (Wannamaker et al., 1987) show that the apparent–resistivity and tipper curves generated in the models ICC and ACC-I are so close to each other that it would be impossible to distinguish between them.

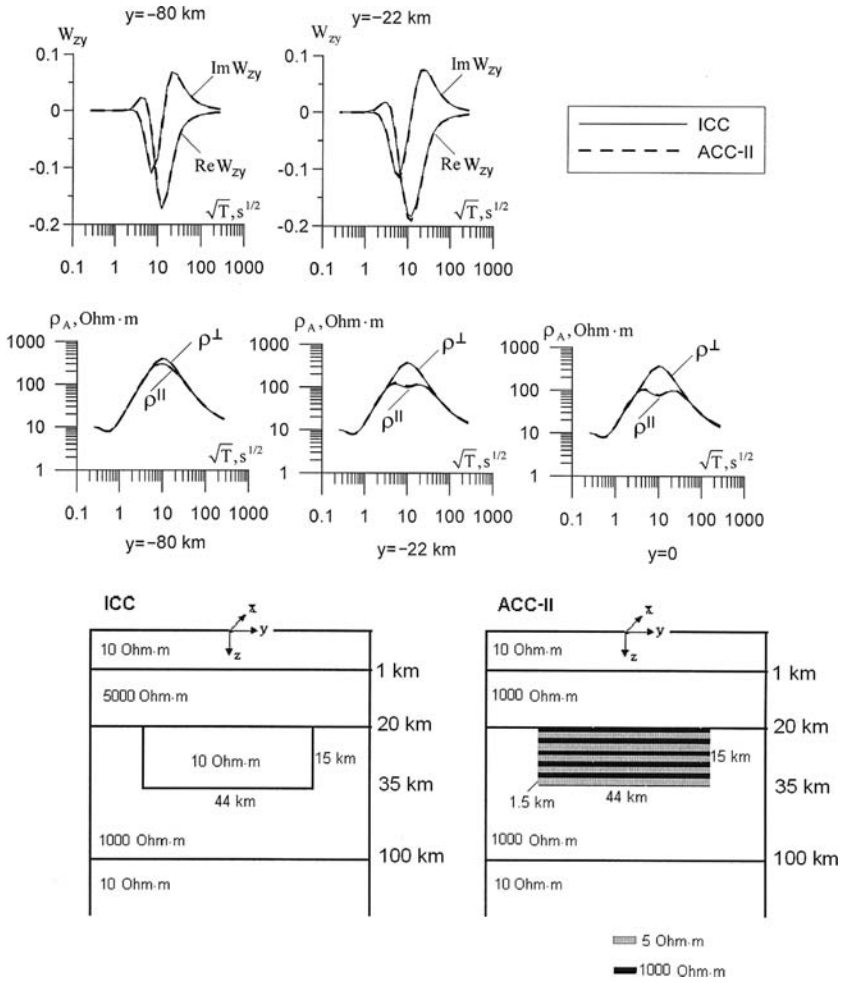

Fig. 8.18 Two-dimensional models of the crustal conductor. The model ICC contains an isotropic crustal conductor, the model ACC-II contains an anisotropic crustal conductor with alternating horizontal layers of higher and lower resistivity

A similar relation is observed in Fig. 8.18. We have here the same model ICC with the isotropic crustal conductor in the form of the two-dimensional prism of resistivity of 10 Ohm·m and the model ACC-II with the prism composed of alternating horizontal layers of resistivities of 5 and 1000 Ohm·m. The prism can be considered as an anisotropic (macroanisotropic) conductor with the diagonal resistivity tensor.

$$\left[\boldsymbol{\rho}_{\text{ACC - II}}\right] = \begin{bmatrix} \rho_{xx} & 0 & 0 \\ 0 & \rho_{yy} & 0 \\ 0 & 0 & \rho_{zz} \end{bmatrix}.$$

From Kirchhoff's laws, we have: $\rho_{xx} \approx 10$ Ohm·m, $\rho_{yy} \approx 10$ Ohm·m, and $\rho_{zz} \approx 500$ Ohm·m. The apparent-resistivity and tipper curves computed for different distances from the model centre ($y = 0,\ -22,\ -80$ km) are also closely related to each other and cannot distinguish between isotropy and anisotropy.

The isotropy-anisotropy equivalence has simple physical interpretation. The TE-mode is associated with longitudinal currents. It provides the anisotropic-isotropic equivalence since these currents penetrate into the anisotropic and isotropic conductors in a similar way and their integral effect is almost the same. The TM-mode reflects the behavior of the transverse currents, which penetrate into the anisotropic and isotropic conductors in a different way and hence may detect the difference between anisotropy and isotropy. But the TM-mode is subjected to galvanic screening and its informativeness depends on the screening-effect intensity. We suggest a straightforward rough criterion for the anisotropy-isotropy equivalence: the deep isotropic and anisotropic conductors are equivalent provided that $w < 2d$, where w is the width of the conductor and $d = \sqrt{S_{sed} R_{crust}}$ is the adjustment distance determined by the sedimentary conductance S_{sed} and resistance R_{crust} of crustal strata separating the conductor from the sediments. In the equivalent models ICC and ACC-I as well as ICC and ACC-II (see Figs. 8.17 and 8.18), we have $d = 43.6 - 97.5$ km and $w = 44$ km. Here $w << 2d$. Widening the crustal conductor or decreasing the resistance of the overlying strata, we arrive at models with transverse apparent-resistivity curves which distinguish between the isotropy and anisotropy. In models with a moderate resistance of the upper crust, say $R_{crust} \approx 10^7$ Ohm·m^2, typical for active regions, the difference between the isotropic and anisotropic crustal conductors, 100–150 km wide, may be seen. Under these conditions, the studies of anisotropic crustal conductors make undoubted practical sense.

8.2 Models of Asthenosphere Conductive Zones

Figure 8.19 presents the apparent-resistivity curves calculated for a one-dimensional model with the sediments of conductance 150 S and the asthenosphere of conductance from 0 to 20000 S. The horizontal asthenospheric layer occurs at a depth of 90 km. It shows up rather vividly when its conductance exceeds 2000–3000 S. In that event the apparent-resistivity curves have a steep descending branch close to the line $h = 100$ km.

Seen below are several models illustrating the magnetotelluric anomalies caused by asthenosphere conductive zones.

8.2.1 The Dmitriev-Mershchikova Cosine-Relief Model

Giving credit to simple analytical solutions, we begin with a two-dimensional model suggested by Dmitriev and Mershchikova (1974). This three-layered model is shown

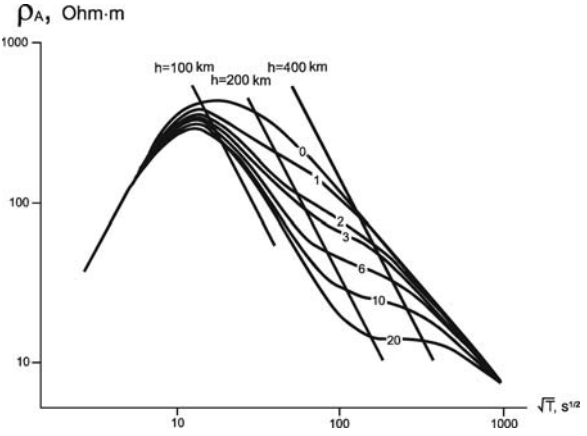

Fig. 8.19 One-dimensional apparent-resistivity curves over the asthenospheric conductive layer at a depth of 90 km. The sediments conductance 150 S; curve parameter – asthenosphere conductance in 1000 S; h-lines for 100, 200, and 400 km are shown. From (Vanyan and Shilovsky, 1983)

in Fig. 8.20. Here the layers ρ_1 and ρ_2 simulate the conductive sediments and resistive lithosphere, while the highly conductive basement, $\rho_3 = 0$, is identified with asthenosphere. The asthenosphere surface has the cosine relief with the period L and amplitude h_o counted off from the mean depth $h_1 + h_2$. The local depth to the asthenosphere is defined as

$$h(y) = h_1 + h_2(y) = h_1 + h_2 - h_o \cos ly, \tag{8.6}$$

where $l = 2\pi/L$.

First we consider the TM-mode. It is clear that the transverse impedance $Z^{\perp}(y)$ is an even periodic function with the period L that can be represented by a Fourier decomposition

$$Z^{\perp}(y) = -\frac{E_y(y)}{H_x(y)} = \bar{Z} + \sum_{1}^{\infty} a_n \cos nly, \tag{8.7}$$

where $\bar{Z}$ is a normal impedance obtained at $h_o = 0$. Substituting $Z^{\perp}(y)$ into equation (7.35) valid for the mantle descending branch of the apparent-resistivity curves (the h-interval), we get

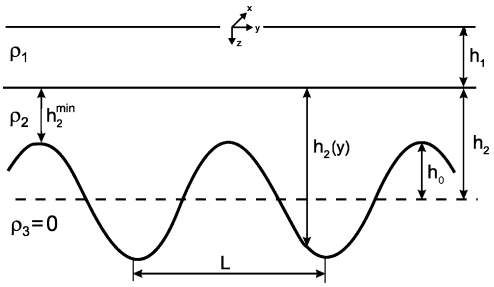

Fig. 8.20 Two-dimensional model with the cosine relief of the asthenosphere surface

$$S_1 R_2(y)\frac{d^2}{dy^2}\sum_1^\infty a_n \cos nly - \sum_1^\infty a_n \cos nly + i\omega\mu_o h(y) = \bar{Z}, \tag{8.8}$$

where $S_1 = h_1/\rho_1$ and $R_2(y) = h_2(y)\rho_2$. On differentiation, we write

$$l^2 S_1 \rho_2 \left[\frac{1}{2} h_o \sum_1^\infty a_n n^2 \{\cos(1+n)ly + \cos(1-n)ly\} - h_2 \sum_1^\infty a_n n^2 \cos nly\right] - \sum_1^\infty a_n \cos nly - i\omega\,\mu_o h_o \cos ly = \bar{Z} - i\omega\,\mu_o(h_1 + h_2). \tag{8.9}$$

Fourier coefficients a_n are found by minimizing the misfit of (8.9). The arithmetic shows that we can restrict ourselves to series with 7 terms. In the case that $h_o \le 0.3\,h_2$ and $L \ge 4\,h_o$, the low-frequency transverse impedance is approximated by formula

$$\left|Z^\perp(y)\right| \approx \omega\mu_o h^\perp(y)$$

where

$$h^\perp(y) = h_1 + h_2 - \alpha^\perp h_o \cos\frac{2\pi}{L} y. \tag{8.10}$$

Here $\alpha^\perp$ is a distortion factor dependent on the *galvanic ratio* $\beta^\perp = L/d_{\min}$, where $d_{\min}$ is the minimum adjustment distance:

$$\begin{aligned} \alpha^\perp &= e^{-3/(\beta^\perp)^{1.4}} \\ d_{\min} &= \sqrt{S_1 R_2^{\min}}, \qquad R_2^{\min} = h_2^{\min}\rho_2. \end{aligned} \tag{8.11}$$

A similar approximation can be proposed for the TE-mode. Let us consider the low-frequency longitudinal impedance. Reducing (7.46) to the h-interval, we get

$$h_1 h_2(y)\frac{d^2 E_x(y)}{dy^2} - E_x(y) = i\omega\mu_o h(y) H_y(y). \tag{8.12}$$

Obviously $E_x(y)$ and $H_y(y)$ are even periodic functions with the period L. They can be represented by the Fourier decompositions

$$\begin{aligned} E_x(y) &= \bar{E}_x + \sum_1^\infty b_n e^{nlz}\cos nly\Big|_{z=0} = \bar{E}_x + \sum_1^\infty b_n \cos nly \\ H_y(y) &= \frac{1}{i\omega\mu_o}\frac{\partial E_x(y,z)}{\partial z}\Big|_{z=0} = \bar{H}_y + \frac{l}{i\omega\mu_o}\sum_1^\infty b_n n \cos nly, \end{aligned} \tag{8.13}$$

where $\bar{E}_x = \bar{Z}\bar{H}_y$ and $\bar{H}_y$ are normal fields obtained for $h_o = 0$.

Substitution of (8.13) into (8.12) gives

$$l^2 h_1(h_2 - h_o \cos ly) \sum_1^\infty b_n n^2 \cos nly + l\{(h_1 + h_2) - h_o \cos ly\} \sum_1^\infty b_n n \cos nly$$

$$+ \sum_1^\infty b_n \cos nly - i\omega\mu_o h_o \bar{H}_y \cos ly \; = \; - \bar{Z}\bar{H}_y - i\omega\mu_o(h_1 + h_2)\bar{H}_y. \tag{8.14}$$

Fourier coefficients b_n are found by minimizing the misfit of (8.14). Restricting ourselves to series with 6 terms, we determine the low-frequency longitudinal impedance as

$$Z^{\parallel}(y) = \frac{E_x(y)}{H_y(y)} = \frac{\bar{Z}\bar{H}_y + \sum_1^6 b_n \cos nly}{\bar{H}_y + \frac{l}{i\omega\mu_o} \sum_1^6 b_n n \cos nly}. \tag{8.15}$$

In the case that $h_o \le 0.3\, h_2$ and $L \ge 4\, h_o$, the low-frequency longitudinal impedance is approximated by formula

$$\left|Z^{\parallel}(y)\right| \approx \omega\, \mu_o h^{\parallel}(y), \tag{8.16}$$

where

$$h^{\parallel}(y) = h_1 + h_2 - \alpha^{\parallel} h_o \cos \frac{2\pi}{L} y.$$

Here $\alpha^{\parallel}$ is a distortion factor dependent on the *inductive ratio* $\beta^{\parallel}$:

$$\alpha^{\parallel} = e^{-0.7/(\beta^{\parallel})^{1.2}}, \qquad \beta^{\parallel} = \frac{L}{h_1 + h_2^{\min}}. \tag{8.17}$$

Note that $\alpha^{\perp} < 1$ and $\alpha^{\parallel} < 1$. Returning to (8.10) and (8.16), we see that the magnetotelluric sounding smoothes out the asthenosphere topography. Instead of the true amplitude h_o, we get a reduced amplitude $h_o^{\perp} = a^{\perp} h_o$ due to the galvanic screening effect in the TM-mode and a reduced amplitude $h_o^{\parallel} = a^{\parallel} h_o$ due to the induction-flattening effect in the TE-mode. According to (8.11), departure of $\alpha^{\perp}$ from 1 does not exceed 0.1 provided that $L > 12\, d_{\min}$. According to (8.17), departure of $\alpha^{\parallel}$ from 1 does not exceed 0.1 provided that $L > 5\,(h_1 + h_2^{\min})$.

The TM- and TE-mechanisms of the electromagnetic distortions caused by the asthenosphere relief is shown in Fig. 8.21. We see here the conductive redistribution of the transverse currents (TM-mode) and the mutual induction of the longitudinal currents (TE-mode).

What is relation between these two effects? Consider some typical examples. Let $\rho_1 = 10\,\text{Ohm·m}$, $h_1 = 1\,\text{km}$, $\rho_2 = 10000\ \text{Ohm·m}$, $h_2^{\min} = 50\,\text{km}$, $d_{\min} = 227\,\text{km}$. The

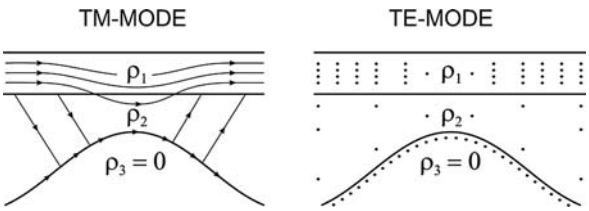

Fig. 8.21 TM- and TE-mechanisms of the electromagnetic distortions caused by the asthenosphere relief

distortion factors $\alpha^{\perp}$, $\alpha^{\parallel}$ along with galvanic and inductive ratios $\beta^{\perp}$, $\beta^{\parallel}$ calculated for different periods L are presented in Table 8.2. We see that in the TM-mode the asthenosphere topography is severely screened over a wide range of periods L up to 500 km ($\alpha^{\perp} \leq 0.38$, $\beta^{\perp} \leq 2.23$), whereas in the TE-mode the asthenosphere topography manifests itself quite distinctly even at $L = 100$ km ($\alpha^{\parallel} = 0.73$, $\beta^{\parallel} = 1.96$). One can say that the TE-mode may be more sensitive to the asthenosphere topography than the TM-mode.

8.2.2 Magnetotelluric Anomalies Caused by the Asthenosphere Uplift

Now we turn to more realistic model discribing a single two-dimensional uplift of the asthenosphere (Fig. 8.22). Here the layers ρ_1,ρ_2 and ρ_3 simulate the conductive sediments, the resistive lithosphere, and the conductive asthenosphere, while v and Δh are the half-width of the uplift and its amplitude.

Let us begin with a model of the uplift. Its parameters are: $\rho_1 = 10$ Ohm·m, $h_1 = 1$ km, $\rho_2 = 10000$ Ohm·m, $h_2 = 99$ km, $\rho_3 = 10$ Ohm·m, $v = 250$ km, $h_2' = 50$ km.

Figure 8.23 presents the field profiles, which pass across the asthenosphere uplift in the $y-$direction. The electric and magnetic fields, normalized to the normal fields $\dot{E}_x^{\mathrm{N}}, \dot{E}_y^{\mathrm{N}}, \dot{H}_y^{\mathrm{N}}$ given at $|y| \to \infty$, are calculated for periods relating to the descending branch of the apparent-resistivity curves. The asthenosphere uplift manifests itself in minima of the electric fields. Once again we see the distinction between the TM- and TE-modes. In the TM-mode we have the transverse field E_y with

Table 8.2 Distortion factors $a^{\perp}$, $a^{\parallel}$ in relation to the period L

L, km	100	200	300	500	1000	2000
TM-mode						
$\beta^{\perp}$	0.45	0.9	1.34	2.23	4.46	8.93
$a^{\perp}$	0.0001	0.03	0.14	0.38	0.69	0.87
TE-mode						
$\beta^{\parallel}$	1.96	3.92	5.88	9.8	19.6	39.2
$a^{\parallel}$	0.73	0.87	0.92	0.96	0.98	0.99

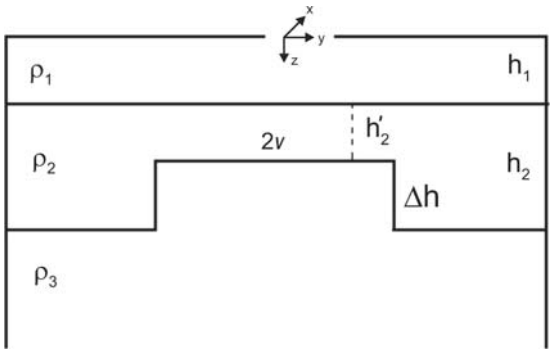

Fig. 8.22 Two-dimensional model of the asthenosphere uplift

well-defined minima observed over the entire h-interval ($T = 100$–100000 s), while in the TE-mode the minima of the longitudinal field E_x disappear with lowering frequency (low-frequency flattening). At the same time the H_y-profile shows the gentle central maximum, caused by excess current filling the uplift, and rather sharp side maxima and minima, which arise due to the horizontal skin effect at the edges of the uplift ($T = 100$ s). At lower frequencies the central maximum increases, while the side extrema flatten out ($T = 1000$ s). But with further lowering frequency when the most of current is induced in the homogeneous conductive mantle the magnetic anomaly almost completely decays ($T = 100000$ s).

Now examine the apparent-resistivity and impedance-phase curves observed in the two-dimensional model of the asthenosphere uplift. Figure 8.24 shows the transverse and longitudinal curves $\rho^{\perp}$, $\varphi^{\perp}$ and $\rho^{\parallel}$, $\varphi^{\parallel}$ together with the locally normal curves $\dot{\rho}_n$, $\dot{\varphi}_n$ outside the uplift and $\ddot{\rho}_n$, $\ddot{\varphi}_n$ over the uplift. They have been obtained in the model from Fig. 8.22 at the different distances y from the epicentre of the uplift.

Consider the apparent-resistivity and impedance-phase curves observed over the central part of the uplift ($y = 0 \div 125$ km). Here the descending mantle branches of the transverse curves $\rho^{\perp}$, $\varphi^{\perp}$ are distorted by moderate screening effect. They are shifted somewhat upward with respect to the locally normal curves $\ddot{\rho}_n$, $\ddot{\varphi}_n$. At the same time the descending mantle branches of the longitudinal curves $\rho^{\parallel}$, $\varphi^{\parallel}$ are virtually undistorted. They merge with the locally normal curves $\ddot{\rho}_n$, $\ddot{\varphi}_n$.

Coming to the apparent-resistivity and impedance-phase curves observed outside the uplift ($y = 251 \div 300$ km), we see that their descending mantle branches are shifted somewhat downward with respect to the locally normal curves $\dot{\rho}_n$, $\dot{\varphi}_n$. These distortions are accounted for by galvanic and induction effects of the conductive uplift. At $y = 500$ km both the effects attenuate. Here the curves $\rho^{\perp}$, $\varphi^{\perp}$ and $\rho^{\parallel}$, $\varphi^{\parallel}$ merge with the locally normal curves $\dot{\rho}_n$, $\dot{\varphi}_n$.

It would be instructive to find out how the distortions of the apparent-resistivity curves depend on the dimension of the uplift. Figure 8.25 shows the curves $\rho^{\perp}$, $\rho^{\parallel}$ in the model from Fig. 8.22 with half-width v of the uplift varying from 5 km to 750 km. The observation site is located over the epicentre of the uplift ($y = 0$). By analogy with (8.11) and (8.17), we estimate the intensity of the distortions

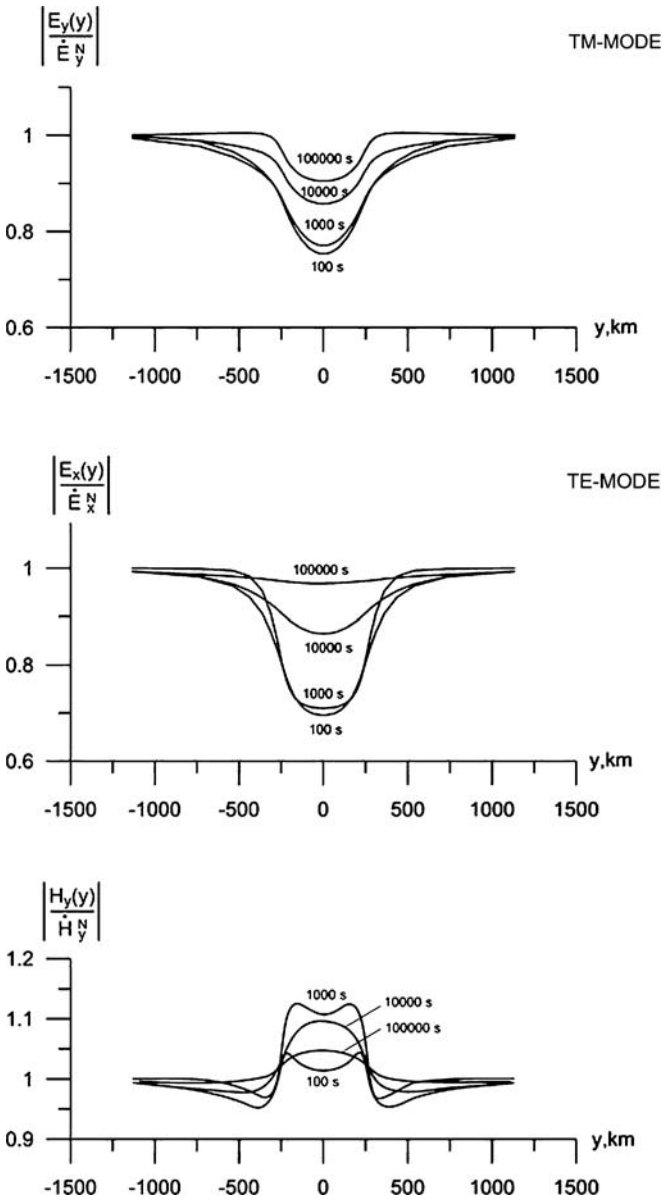

Fig. 8.23 The E_y−profiles and E_x, H_y−profiles passing across the regional asthenosphere uplift ($v = 250$ km). For the model from Fig. 8.22 with parameters $\rho_1 = 10$ Ohm·m, $h_1 = 1$ km, $\rho_2 = 10000$ Ohm·m, $h_2 = 99$ km, $h'_2 = 49$ km, $\Delta h = 50$ km, $\rho_3 = 10$ Ohm·m. Period $T = 100,\ 1000,\ 10000$ s, 100000 s

in terms of the galvanic ratio $\beta^{\perp} = v/d$ and inductive ratio $\beta^{\parallel} = v/h$, where $d = \sqrt{h_1(h_1 + h'_2)\rho_2/\rho_1} = 223.6$ km is the adjustment distance over the uplift and

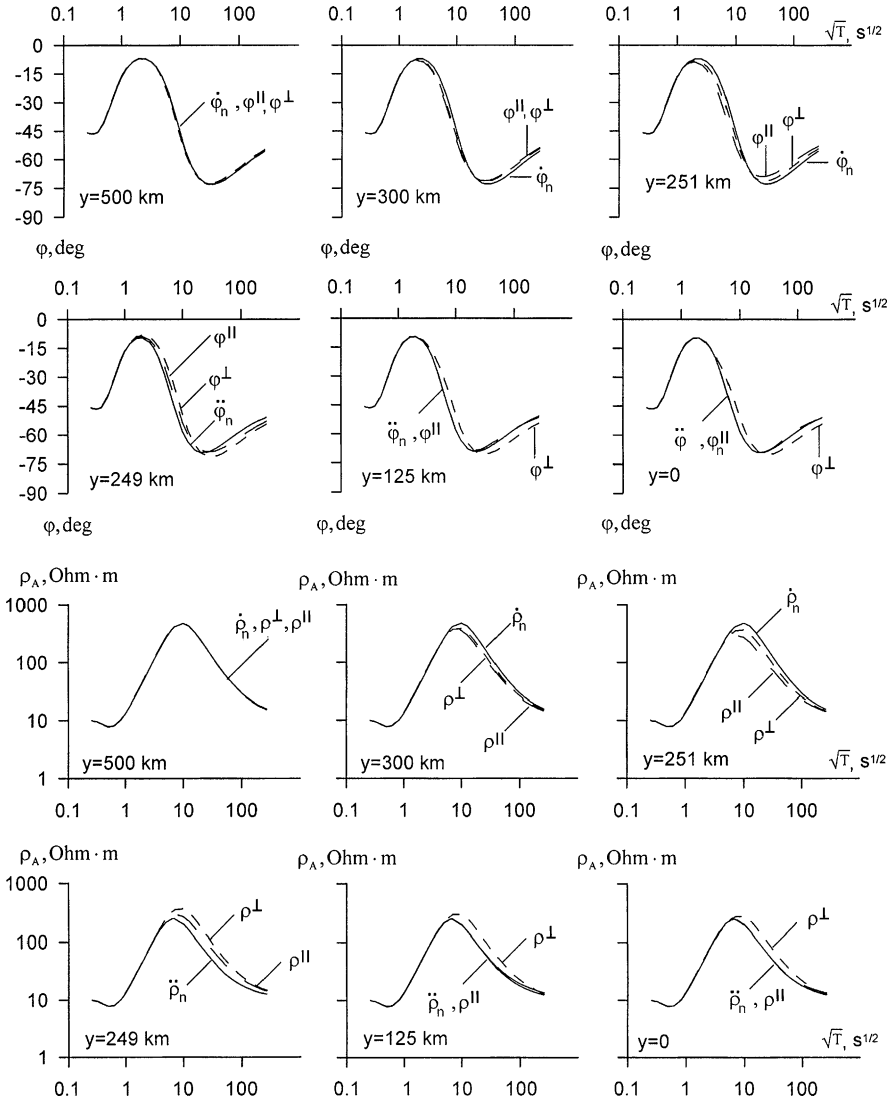

Fig. 8.24 The transverse and longitudinal magnetotelluric curves $\rho^{\perp}$, $\varphi^{\perp}$ and $\rho^{\parallel}$, $\varphi^{\parallel}$ obtained at different distance y from the epicentre of the regional asthenosphere uplift (v=250 km); $\dot{\rho}_n$, $\dot{\varphi}_n$ and $\ddot{\rho}_n$, $\ddot{\varphi}_n$ – locally normal curves outside and over the asthenosphere uplift. For the model from Fig. 8.22 with parameters $\rho_1 = 10$ Ohm·m, $h_1 = 1$ km, $\rho_2 = 10000$ Ohm·m, $h_2 = 99$ km, $h'_2 = 49$ km, $\Delta h = 50$ km, $\rho_3 = 10$ Ohm·m

$h = h_1 + h'_2 = 50$ km is the depth to the uplift. The uplift with $v = 5$ km is hardly distinguishable because of screening and low-frequency flattening. Here the curves $\rho^{\perp}$ and $\rho^{\parallel}$ are close to the locally normal $\dot{\rho}_n$-curve characterizing the uplift surroundings. These distortions are marked by small values of the galvanic and induc-

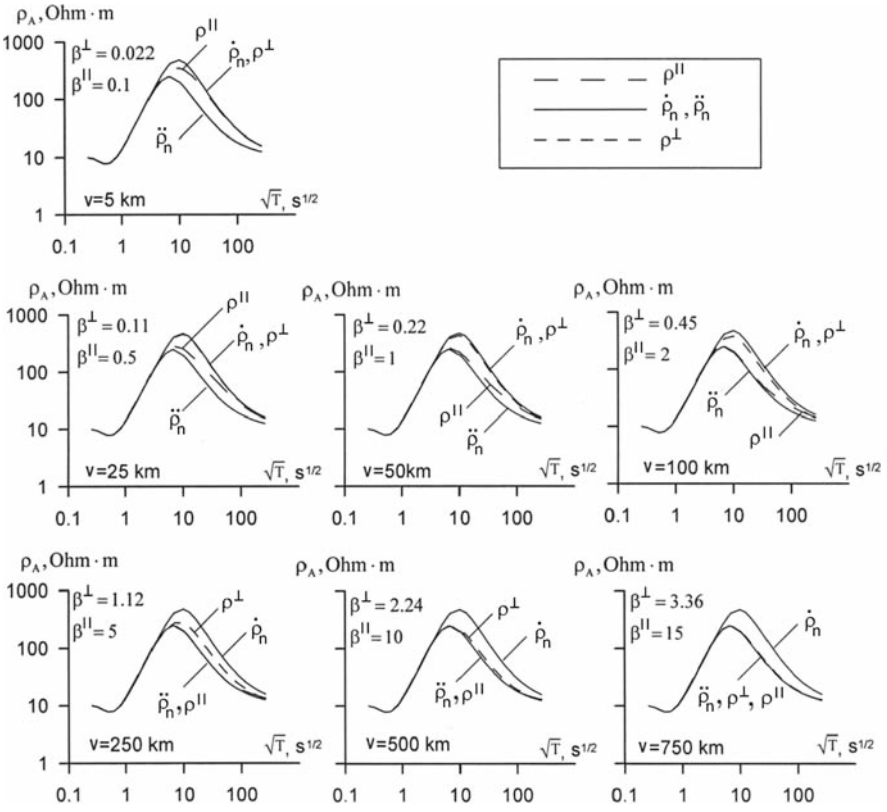

Fig. 8.25 The transverse and longitudinal apparent-resistivity curves $\rho^{\perp}$, $\rho^{\parallel}$ in relation to the width of the asthenosphere uplift. The observation site is located at the epicentre of the uplift. The uplift half-width $v = 5$, 25, 50, 100, 250, 500, 750 km; $\dot{\rho}_n$, $\dot{\varphi}_n$ and $\ddot{\rho}_n$, $\ddot{\varphi}_n$ – locally normal curves outside and over the asthenosphere uplift. For the model from Fig. 8.22 with parameters $\rho_1 = 10$ Ohm·m, $h_1 = 1$ km, $\rho_2 = 10000$ Ohm·m, $h_2 = 99$ km, $h'_2 = 49$ km, $\Delta h = 50$ km, $\rho_3 = 10$ Ohm·m

tive ratios ($\beta^{\perp} = 0.022$, $\beta^{\parallel} = 0.1$). With widening the uplift, the curves $\rho^{\perp}$, $\rho^{\parallel}$ depart from the $\dot{\rho}_n$-curve and approach the $\ddot{\rho}_n$-curve characterizing the uplift. At $v = 100$ km, the $\rho^{\parallel}$-curve almost merges with the $\ddot{\rho}_n$-curve ($\beta^{\parallel} = 2$) and comes to the normalcy, while the $\rho^{\perp}$-curve remains close to $\dot{\rho}_n$-curve and shows no evidence of the uplift ($\beta^{\perp} = 0.45$). But at $v = 500$ km, the $\rho^{\perp}$-curve almost merges with the $\ddot{\rho}_n$-curve and also comes to the normalcy ($\beta^{\perp} = 2.24$). Using these estimates, we can say that in model under consideration the $\rho^{\parallel}$-curves allow for the one-dimensional inversion if $\beta^{\parallel} \geq 2$, whereas the one-dimensional inversion of the $\rho^{\perp}$-curves is justified if $\beta^{\perp} \geq 2 \div 2.5$.

The next question is how the distortions of the apparent-resistivity curves depend on the lithosphere resistivity. Figure 8.26 shows the curves in the model from Fig. 8.22 with the lithosphere resistivity $\rho_2 = 1000$, 10000, 100000 Ohm·m and the half-width of the asthenosphere uplift $v = 100$, 250 km. The obser-

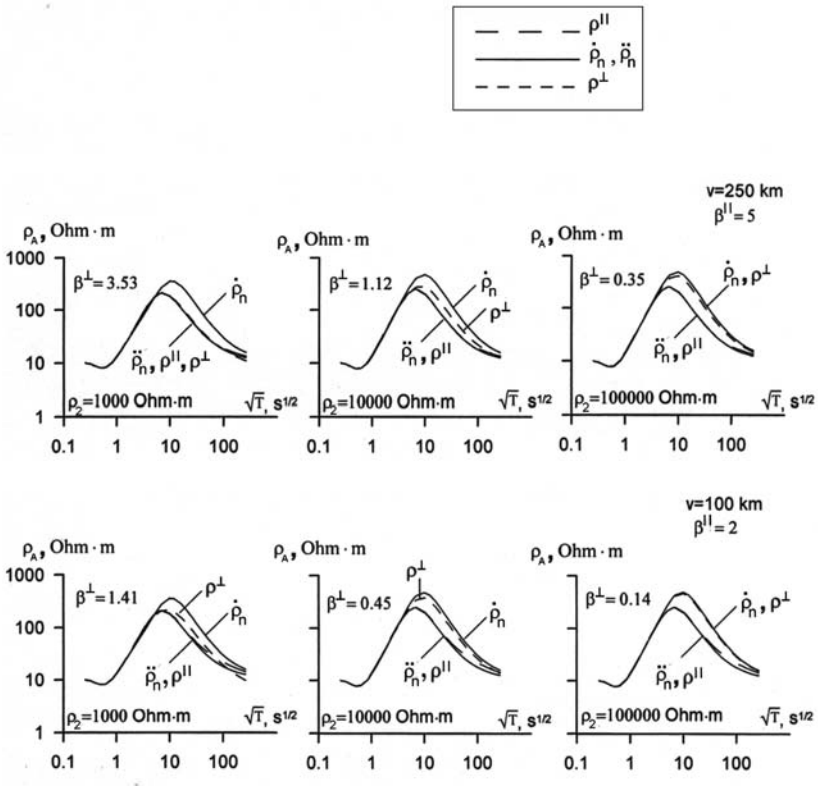

Fig. 8.26 The transverse and longitudinal apparent-resistivity curves $\rho^{\perp}$, $\rho^{\parallel}$ in relation to the width of the asthenosphere uplift and the lithosphere resistivity. The observation site is located at the epicentre of the uplift. The uplift half-width $v = 100,\ 250$ km; the lithosphere resistivity $\rho_2 = 1000,\ 10000,\ 100000$ Ohm·m; $\dot{\rho}_n$, $\dot{\varphi}_n$ and $\ddot{\rho}_n$, $\ddot{\varphi}_n$ – locally normal curves outside and over the asthenosphere uplift. For the model from Fig. 8.22 with parameters $\rho_1 = 10$ Ohm·m, $h_1 = 1$ km, $h_2 = 99$ km, $h'_2 = 49$ km, $\Delta h = 50$ km, $\rho_3 = 10$ Ohm·m

vation site is located at the epicentre of the uplift ($y = 0$). Here the transverse $\rho^{\perp}$-curve at $v = 250$ km and $\rho_2 = 1000$ Ohm·m is practically undistorted ($\beta^{\perp} = 3.53$). It merges with the locally normal $\ddot{\rho}_n$-curve characterizing the uplift. But with increasing ρ_2 and decreasing v the screening effect comes into play. At $v = 250$ km, $\rho_2 = 10000$ Ohm·m ($\beta^{\perp} = 1.12$) and $v = 100$ km, $\rho_2 = 1000$ Ohm·m ($\beta^{\perp} = 1.41$) the $\rho^{\perp}$-curve departs from the $\ddot{\rho}_n$-curve and approaches the locally normal $\dot{\rho}_n$-curve which characterises the uplift surroundings. At $v = 250$ km, $\rho_2 = 100000$ Ohm·m ($\beta^{\perp} = 0.35$) and $v = 100$ km, $\rho_2 = 100000$ Ohm·m ($\beta^{\perp} = 0.14$) the $\rho^{\perp}$-curve merges with the $\dot{\rho}_n$-curve so that the asthenosphere uplift is actually screened. Quite different are the longitudinal $\rho^{\parallel}$-curves. At $\rho_2 \geq 1000$ Ohm·m and $v \geq 100$ km ($\beta^{\parallel} \geq 2$) they merge with the locally normal $\ddot{\rho}_n$-curve. In a model with the uplift whose half-width is

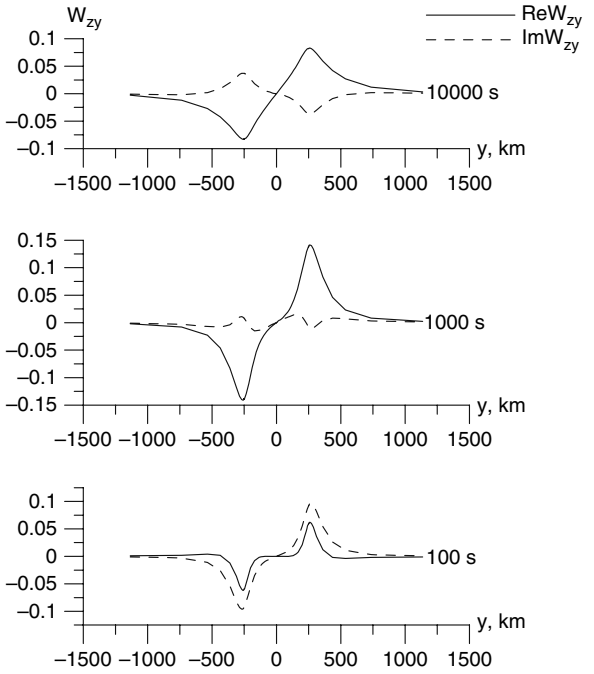

Fig. 8.27 The W_{zy}- profiles passing across the regional asthenosphere uplift ($v = 250$ km). For the model from Fig. 8.22 with parameters $\rho_1 = 10$ Ohm·m, $h_1 = 1$ km, $\rho_2 = 10000$ Ohm·m, $h_2 = 99$ km, $h'_2 = 49$ km, $\Delta h = 50$ km, $\rho_3 = 10$ Ohm·m. Period $T = 100$, 1000, 10000 s

twice its depth, the $\rho^{\parallel}$-curves measured at the epicentre of the uplift are slightly distorted and allow for one-dimensional interpretation.

The W_{zy}-profiles are shown in Fig. 8.27. In the period range from 100 s to 10000 s the real tippers Re W_{zy} do not change their sign with frequency, while the imaginary tippers ImW_{zy} do change. Note that ReW_{zy} and Im W_{zy} are of the same sign on high frequencies ($T = 100$ s) and of opposite sign on low frequencies ($T =$ 1000–10000 s). The minima and maxima of ReW_{zy} and ImW_{zy} are observed over the left and right edges of the asthenosphere uplift. It is evident that at all frequencies under consideration the real induction arrows point away from the uplift epicentre, while the imaginary induction arrows reverse their direction in the transition from the high frequencies to the low ones.

Figure 8.28 presents curves for ReW_{zy} and ImW_{zy} measured over the right edge of the uplift with half-width $v = 50,\ 250$ km and $\rho_3 = 10, 25, 50$ Ohm·m. It is seen that narrowing the uplift from 500 km to 100 km and increasing its resistivity from 10 Ohm·m to 50 Ohm·m we substantially diminish the real and imaginary tippers, but they still are measurable.

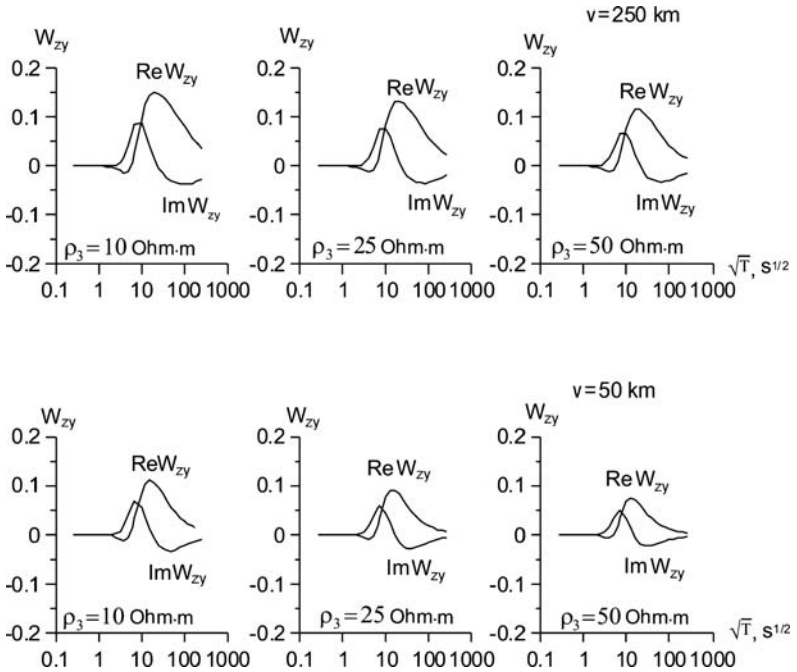

Fig. 8.28 Real and imaginary tippers over the right edge of regional asthenosphere uplift ($v = 50$, 250 km) of resistivity $\rho_3 = 10$, 25, 50 Ohm·m. For the model from Fig. 8.22 with parameters $\rho_1 = 10$ Ohm·m, $h_1 = 1$ km, $\rho_2 = 100000$ Ohm·m, $h_2 = 99$ km, $h'_2 = 49$ km, $\Delta h = 50$ km, $\rho_3 = 10$ Ohm·m

8.2.3 May Asthenospheric Structures be Excited Inductively?

Optimism in this field was supported by the papers, in which the astenospheric structures were treated as perfect conductors and the inductive mechanism of electromagnetic excitation played a considerable role (Vanyan et al.,1986, 1988, 1991; Egorov, 1987; Berdichevsky et al., 1992). In that simplified consideration, the asthenospheric conductors were manifested by noticeable magnetotelluric anomalies (in spite of the highly resistive lithosphere that screens the galvanic effects). Naturally the question arises: to what extent do these models approach the reality?

Examine the above model of the asthenosphere uplift. Let the uplift assume the form of a $100 \times 100 \times 100$ km cubic block with resistivity $\rho = 50$ Ohm·m and the upper face at a depth $h = 50$ km. For rough estimation, we use an equivalent sphere with $a = 50$ km and $a + h = 100$ km (see Fig. 8.12). Suppose that the asthenosphere uplift manifests itself in the period range $T = 100 - 2500\,s$ and calculate the anomalous magnetic field $\left|H^{\mathrm{A}}/H_{\mathrm{o}}\right|$ appearing due to local induction within the uplift. According to (8.2), (8.3) and (8.4), we get $\delta \geq 61.6$ km, $p \leq 0.81$, $|D| \leq 0.09$, $\left|H^{\mathrm{A}}/H_{\mathrm{o}}\right| \leq 0.0056$. This is a case of weak local induction: the induced magnetic field is negligibly small against the inducing magnetic field. When studying

such an asthenosphere uplift, we most likely can count only on the galvanic mechanism of electromagnetic excitation. It seems that we have to revise inferences from the papers cited above.

8.2.4 On the Quasi-Two-Dimensionality of Asthenospheric Structures

Consider three-layered models including conductive sediments ρ_1 and resistive lithosphere ρ_2 underlaid with conductive asthenosphere ρ_3 (Fig. 8.29). The asthenosphere surface has a three-dimensional rectangular uplift of length l, width $2v$ and amplitude Δh.

Let us test a set of these models at fixed parameters $\rho_1 = 10$ Ohm·m, $h_1 = 1$ km, $h_2 = 99$ km, $h'_2 = 49$ km, $\Delta h = 50$ km, $\rho_3 = 10$ Ohm·m and variable parameters $\rho_2 = 1000, 10000$ Ohm·m; $2v = 30$ km, $l = 30, 150, 300, 360, 450, 600, 750$ km; $2v = 60$ km, $l = 60, 180, 300, 600, 900, 1200, 1500, 3000$ km.

Figure 8.30 exemplifies the apparent-resistivity, impedance-phase and tipper curves obtained in the three-dimensional model of the asthenosphere uplift with $\rho_2 = 10000$ Ohm·m, $v = 30$ km, $l = 60$ km (elongation $e = 1$) and its

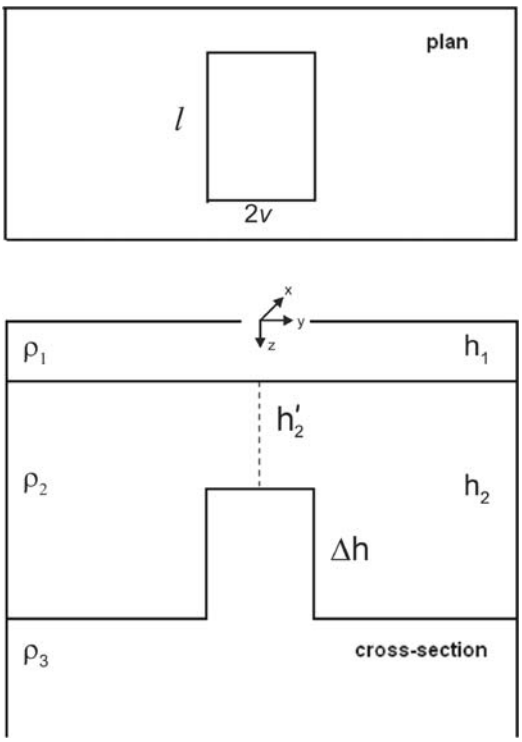

Fig. 8.29 A model with the three-dimensional asthenosphere uplift

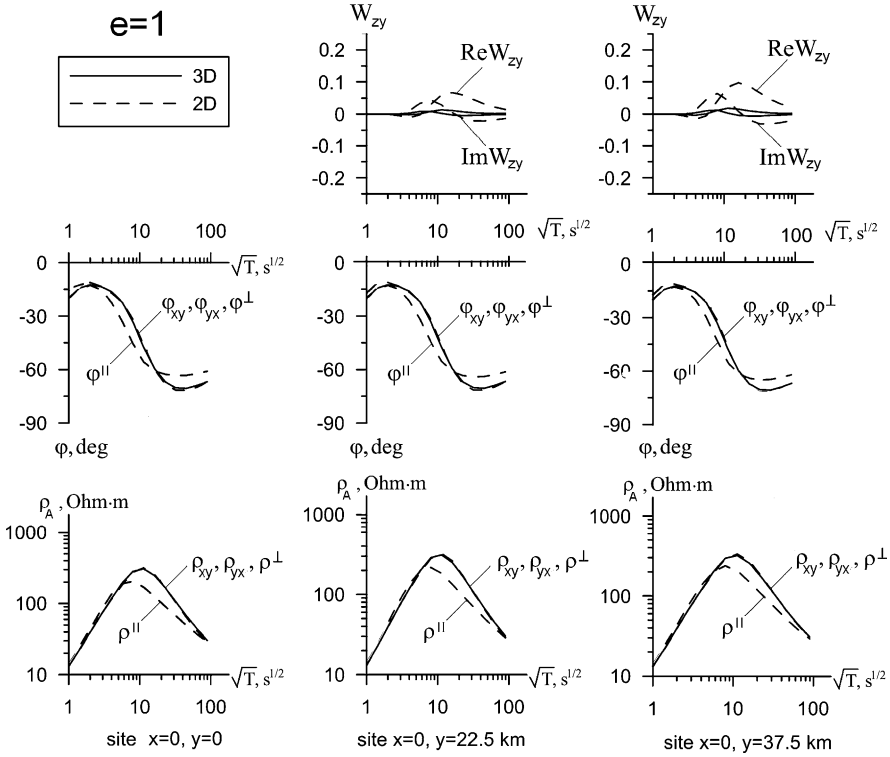

Fig. 8.30 The apparent-resistivity, impedance-phase and tipper curves in the model of the asthenosphere uplift from Fig. 8.29 with parameters $\rho_1 = 10$ Ohm·m, $h_1 = 1$km, $\rho_2 = 10000$ Ohm·m, $h_2' = 49$ km, $\Delta h = 50$ km, $v = 30$ km, $l = 60$ km, $\rho_3 = 10$ Ohm·m. Elongation of the three-dimensional uplift $e = l/2\,v = 1$

two-dimensional counterpart ($l = \infty$). The observation sites are located on a central profile going in the $y-$ direction. At all sites the curves ρ_{xy}(3D), ρ_{yx}(3D) and φ_{xy}(3D), φ_{yx}(3D) are close to the transverse curves $\rho^{\perp}$(2D) and $\varphi^{\perp}$(2D), while the tippers $\mathrm{Re}W_{zy}$(3D), $\mathrm{Im}W_{zy}$(3D) do not exceed 0.02. Here the resistive lithosphere heavily screens the asthenosphere uplift.

With elongating the uplift, the screening effect attenuates and the curves ρ_{xy}(3D), φ_{xy}(3D) come close to the longitudinal curves $\rho^{\parallel}$(2D), $\varphi^{\parallel}$(2D), while the tippers $\mathrm{Re}W_{zy}$(3D), $\mathrm{Im}W_{zy}$(3D) increase. At $v = 30$ km, $l = 600$ km ($e = 10$) the curves $\mathrm{Re}W_{zy}$(3D), $\mathrm{Im}W_{zy}$(3D) come close to the curves $\mathrm{Re}W_{zy}$(2D), $\mathrm{Im}W_{zy}$(2D) and yield to the two-dimensional interpretation. Finally at $v = 30$ km, $l = 900$ ($e = 15$) the curves ρ_{xy}(3D), ρ_{yx}(3D) and φ_{xy}(3D), φ_{yx}(3D) merge with the curves $\rho^{\parallel}$(2D), $\rho^{\perp}$(2D) and $\varphi^{\parallel}$(2D), $\varphi^{\perp}$(2D), and also admit the two-dimensional interpretation (Fig. 8.31).

The results of this test are summarized in Table 8.3. We observe here the same regularities as in Table 8.1 which presents results obtained in the model of a crustal

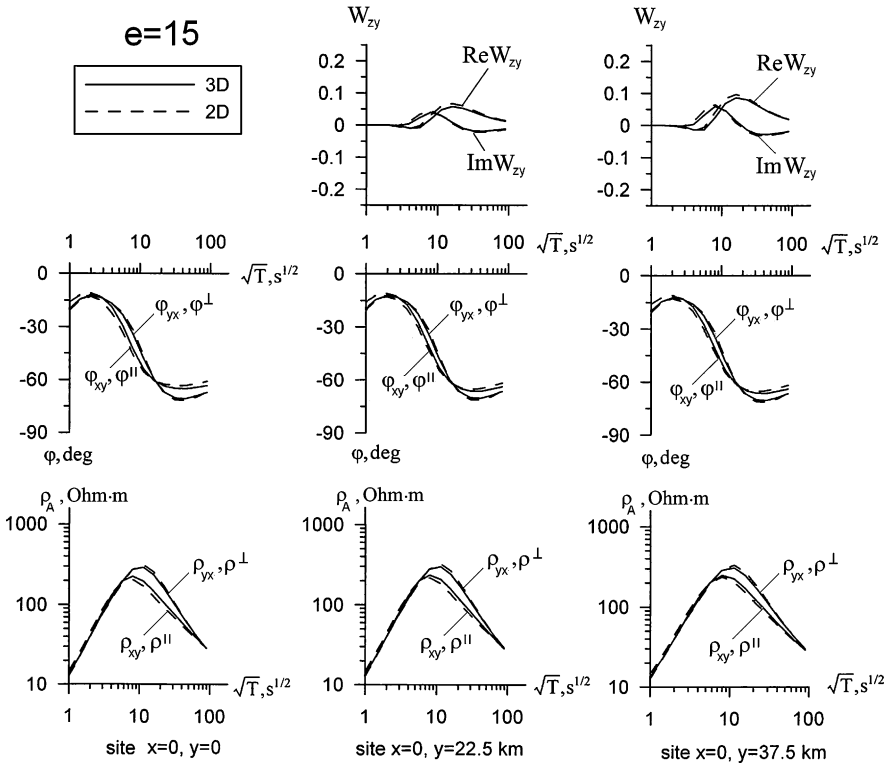

Fig. 8.31 The apparent-resistivity, impedance-phase and tipper curves in the model of the asthenosphere uplift from Fig. 8.29 with parameters $\rho_1 = 10$ Ohm·m, $h_1 = 1$km, $\rho_2 = 10000$ Ohm·m, $h_2' = 49$ km, $\Delta h = 50$ km, $v = 30$ km, $l = 900$ km, $\rho_3 = 10$ Ohm·m. Elongation of the three-dimensional uplift $e = l/2v = 15$

conductor. The conditions of quasi-two-dimensionality of the asthenosphere uplift depend on its width $2v$. The wider the uplift, the less its elongation that provides quasi-two-dimensionality. Note also that the higher the lithosphere resistivity, the stronger the galvanic screening and the larger the uplift elongation that provides

Table 8.3 Elongations of asthenosphere uplift providing the tipper quasi-two-dimensionality (W-2D) and the apparent-resistivity and the impedance- phase quasi-two-dimensionality (ρ, φ-2D)

Lithosphere resistivity (Ohm·m)	Uplift width (km)	Uplift elongation	
		W-2D	ρ, φ -2D
1000	30	10	15
	60	7	10
10000	60	10	15

quasi-two-dimensionality. This clearly suggests that in the models under consideration the local induction is weak and magnetelluric anomalies are of galvanic nature.

8.2.5 Are Asthenospheric Structures Isotropic or Anisotropic?

In studying the upper mantle, we may face the anisotropy-isotropy equivalence. Asthenospheric conductive zones located under the highly resistive lithosphere can manifest themselves in the equivalent response functions, which do not distinguish between isotropy and anisotropy and admit both the interpretations.

Let us consider two examples concerning the asthenosphere uplift.

Figure 8.32 shows the two-dimensional models IAU-I (isotropic asthenosphere uplift) and AAU-I (anisotropic asthenosphere uplift). The model IAU-I contains the isotropic asthenosphere uplift of resistivity of 9.1 Ohm·m, width of 200 km and amplitude of 50 km. In the model AAU-I we have the same uplift composed of alternating vertical dykes of resistivities of 5 and 50 Ohm·m (the strike of vertical dykes coincides with the uplift strike). The uplift can be considered as an anisotropic (macroanisitropic) conductor with the diagonal resistivity tensor

$$\left[\boldsymbol{\rho}_{\text{AAU - I}}\right] = \begin{bmatrix} \rho_{xx} & 0 & 0 \\ 0 & \rho_{yy} & 0 \\ 0 & 0 & \rho_{zz} \end{bmatrix}.$$

where $\rho_{xx} \approx 9.1$ Ohm·m, $\rho_{yy} = 27.5$ Ohm·m, and $\rho_{zz} \approx 9.1$ Ohm·m.

The calculations performed by the finite-element method (Wannamaker et al., 1986) show that the apparent–resistivity and tipper curves obtained in the models IAU-I and AAU-I are close to each other. The models demonstrate the anisotropy-isotropy equivalence.

Next consider Fig. 8.33, which presents the two-dimensional models IAU-II (isotropic asthenosphere uplift) and AAU-II (anisotropic asthenosphere uplift). The model IAU-II contains the isotropic asthenosphere uplift of resistivity of 10 Ohm·m, width of 200 km and amplitude of 50 km. In the model AAU-II we have the same uplift composed of alternating horizontal layers of resistivities of 5 and 1000 Ohm·m. The uplift can be considered as an anisotropic (macroanisotropic) conductor with the diagonal resistivity tensor

$$\left[\boldsymbol{\rho}_{\text{AAU - II}}\right] = \begin{bmatrix} \rho_{xx} & 0 & 0 \\ 0 & \rho_{yy} & 0 \\ 0 & 0 & \rho_{zz} \end{bmatrix}.$$

where $\rho_{xx} \approx 10$ Ohm·m, $\rho_{yy} \approx 10$ Ohm·m, and $\rho_{zz} \approx 500$ Ohm·m.

The apparent-resistivity and tipper curves obtained in the models IAU-II and AAU-II are also close to each other (anisotropy-isotropy equivalence).

In closing, consider Fig. 8.34, which presents the two-dimensional models IA-I (isotropic asthenolith) and AA-I (anisotropic asthenolith) with the lithosphere resistance of $1.5 \cdot 10^9$ Ohm·m^2. The model IA-I contains the deep-seated extended isotropic asthenolith of resistivity of 18.2 Ohm·m, width of 500 km and amplitude of 100 km. In the model AA-I we have the same asthenolith composed of alternating vertical layers of resistivities of 10 and 100 Ohm·m (the strike of vertical layers coincides with the asthenolith strike). Here

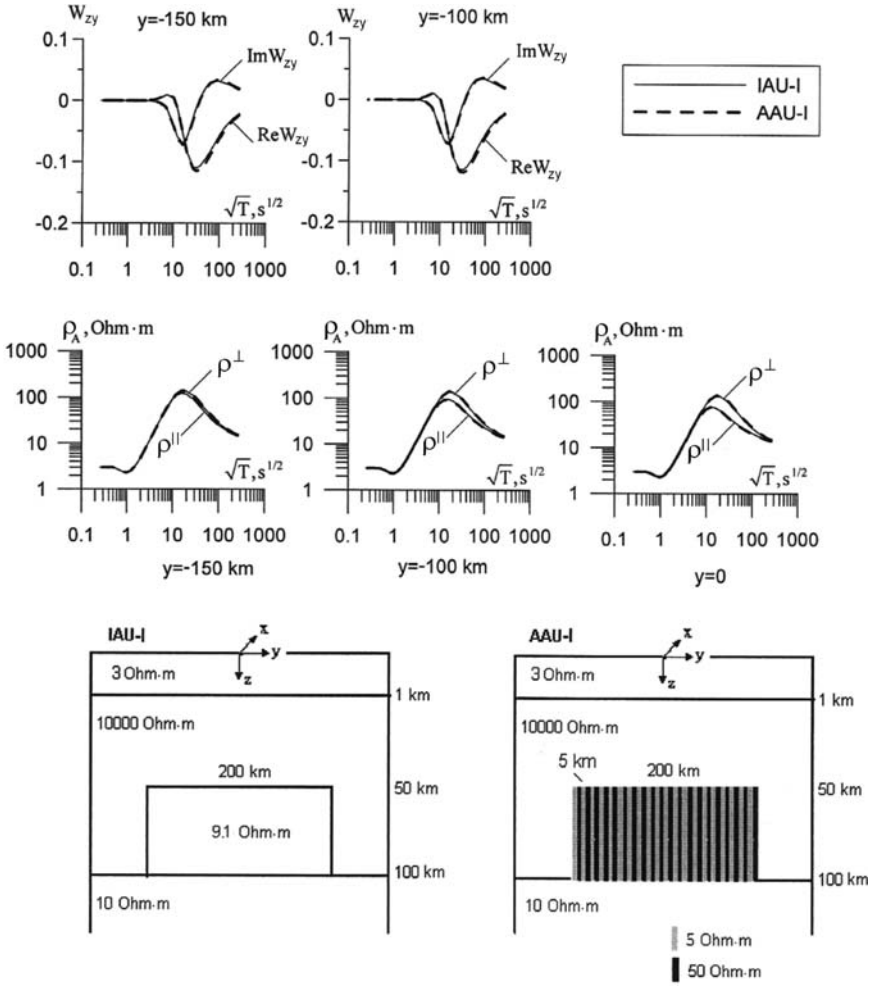

Fig. 8.32 Two-dimensional models of the asthenosphere uplift. The model IAU-I contains an isotropic asthenosphere uplift, the model AAU-I contains an anisotropic asthenosphere uplift with alternating vertical dykes

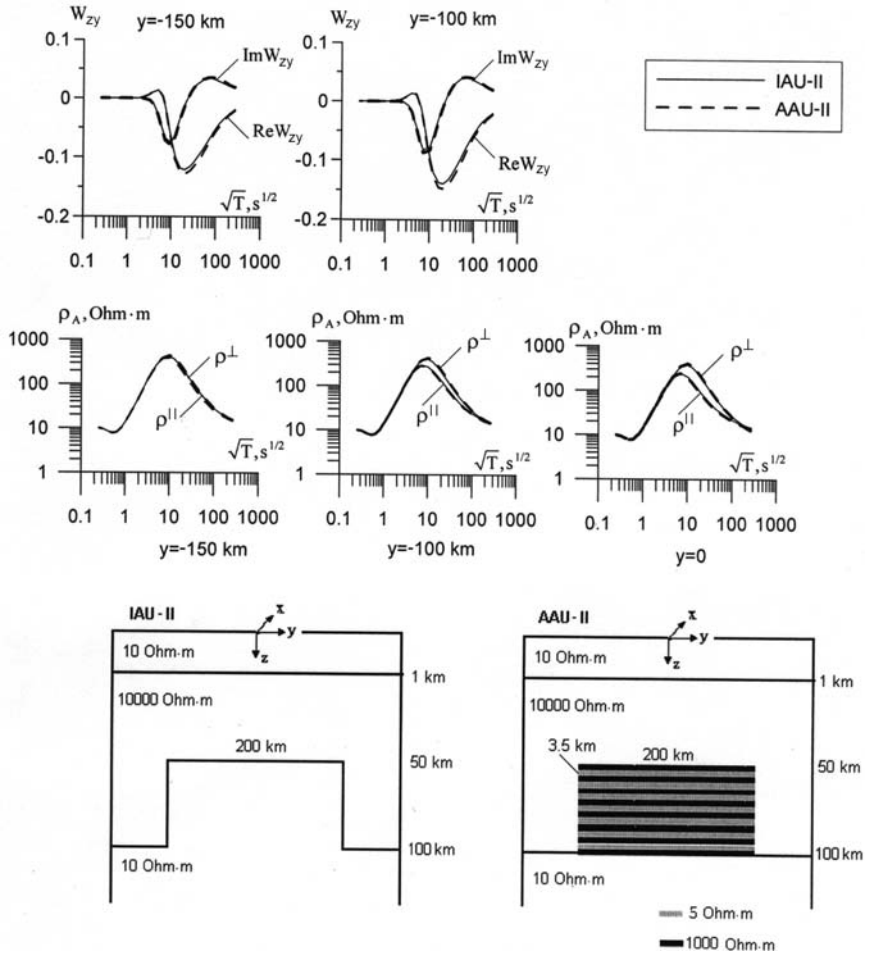

Fig. 8.33 Two-dimensional models of the asthenosphere uplift. The model IAU-II contains an isotropic asthenosphere uplift, the model AAU-II contains an anisotropic asthenosphere uplift with alternating horizontal layers of higher and lower resistivity

$$\left[\boldsymbol{\rho}_{\text{AA-I}}\right] = \begin{bmatrix} \rho_{xx} & 0 & 0 \\ 0 & \rho_{yy} & 0 \\ 0 & 0 & \rho_{zz} \end{bmatrix},$$

where $\rho_{xx} \approx 18.2$ Ohm·m, $\rho_{yy} = 55$ Ohm·m, and $\rho_{zz} \approx 18.2$ Ohm·m.

We see that the apparent–resistivity and tipper curves obtained in the models IA-I and AA-I are close to each other (anisotropy-isotropy equivalence). But with decreasing the lithosphere resistance, the equivalence between isotropy and anisotropy in the asthenolith disappears. Figure 8.35 shows the models IA-II and AA-II with the lithosphere resistance of $1.5 \cdot 10^8$ Ohm·m^2. Here the transverse

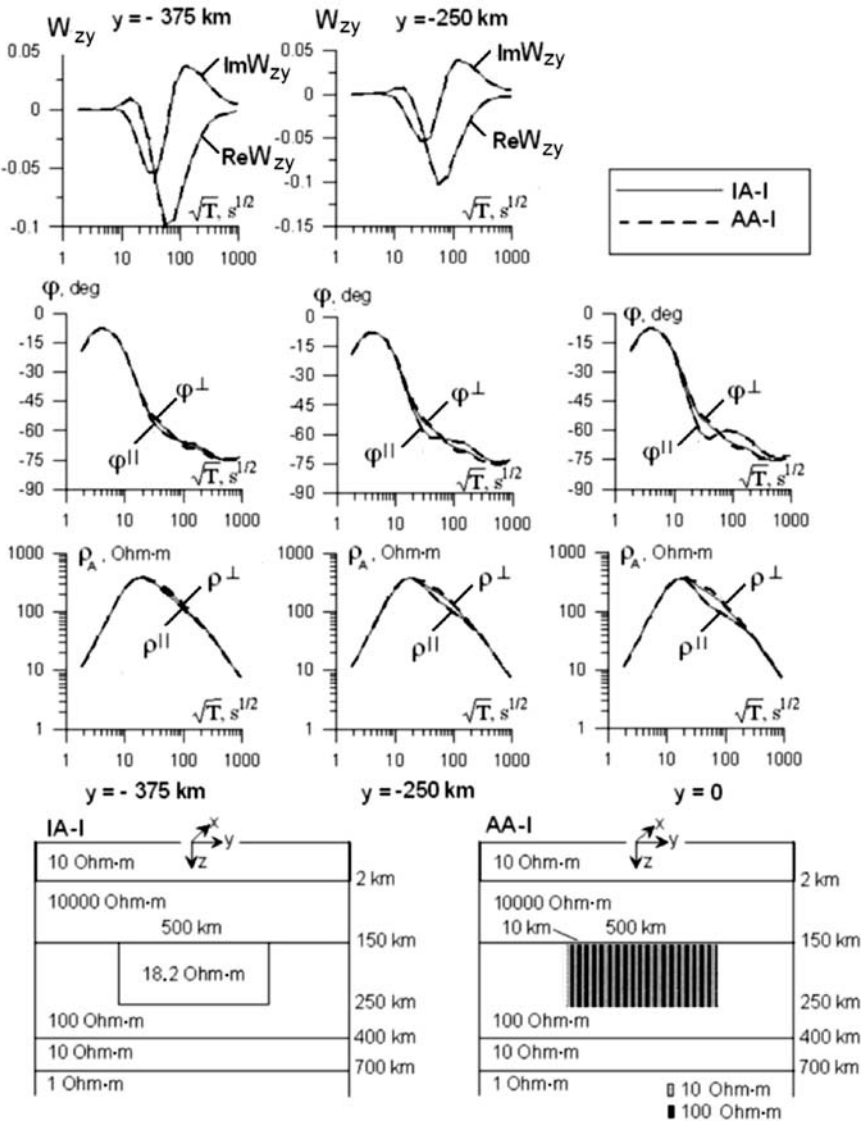

Fig. 8.34 Two-dimensional models of the asthenolith. The model IA-I contains an isotropic asthenolith, the model AA-I contains an anisotropic asthenolith with alternating vertical layers of higher and lower resistivity. The lithosphere resistance $1.5 \cdot 10^9$ Ohm·m^2

apparent resistivity and impedance-phase curves obtained over the asthenoliths ($y = 0$) noticeably differ from each other.

We would like to stress again that the main factor that conditions the equivalence between isotropy and anisotropy is the lithosphere resistance defining the screening effect. The least favorable for studying the anisotropic asthenosphere are the

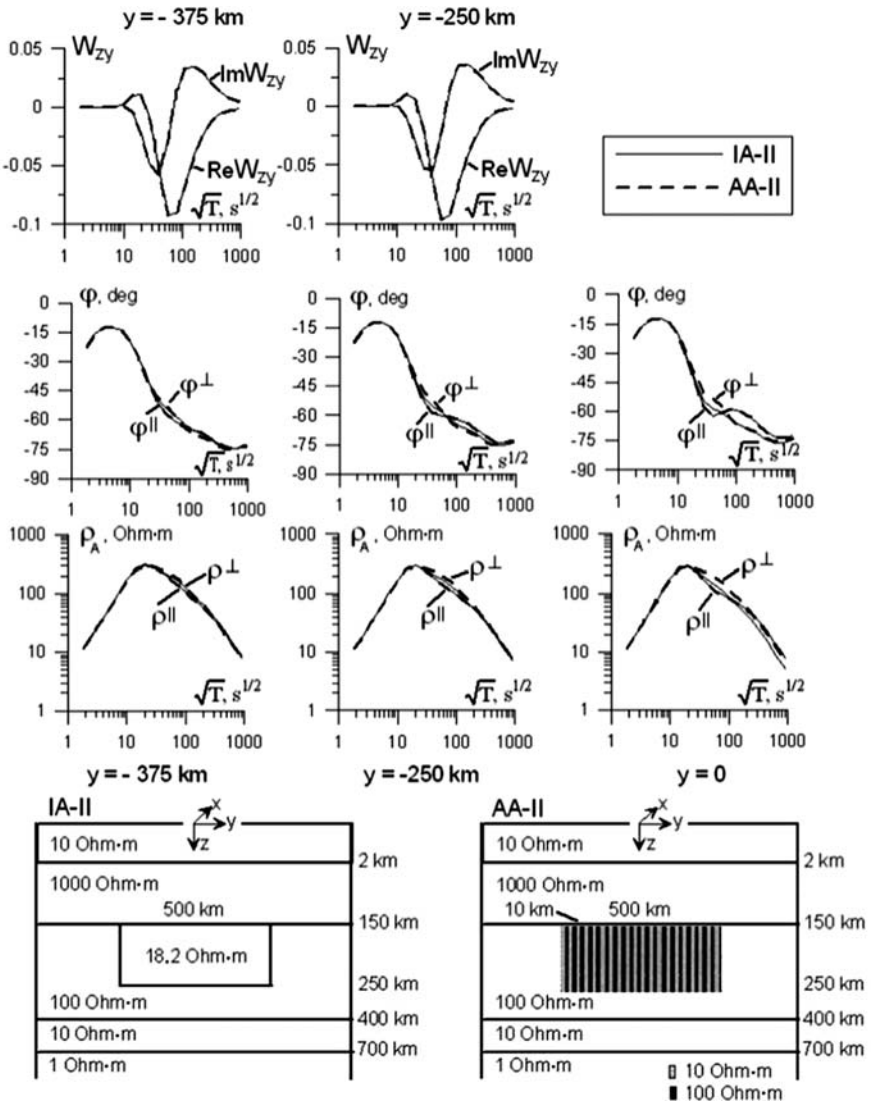

Fig. 8.35 Two-dimensional models of the asthenolith. The model IA-II contains an isotropic asthenolith, the model AA-II contains an anisotropic asthenolith with alternating vertical layers of higher and lower resistivity. The lithosphere resistance $1.5 \cdot 10^8$ Ohm·m^2

stable regions where the lithosphere resistance ranges up to $10^9 \div 5 \cdot 10^9$ Ohm·m^2 and the TM-mode is characterized by the strong screening effect ($w < 2d$ where w is the asthenosphere width, $d = \sqrt{S_{sed} R_{lit}}$ is the adjustment distance, S_{sed} is the sedimentary conductance and R_{lit} is the resistance of lithospheric strata separating an asthenospheric conductor from the sediments). Here the anisotropy-isotropy equivalence may exist even at distances of about 300–500 km. Widening

the asthenospheric conductor, we get models which expose considerable difference between isotropy and anisotropy at the distances of about 1000÷1500 km stretching over the whole tectonic province. But in active regions (especially with deep conductive faults) the lithosphere resistance drops to $10^8 \div 5 \cdot 10^8$ Ohm·m^2 and the screening effect is not so dramatic (especially if sedimentary conductance is small). Here, in all likelihood, we can differentiate between the anisotropic and isotropic asthenospheric conductors even at distances of order of 300÷500 km and obtain unique information on the state of the Earth's interior.

Summing up, we can say that studying the crustal and mantle conductive zones we run the risk of wrong interpretation. But note that for the final conclusions, it would be necessary to consider a set of models, in which the anisotropy strike does not coincide with the strike of deep conductors.

Chapter 9
Models of Deep Faults

The deep fluidized or graphitized faults form conductive channels, which cross the highly resistive lithosphere and provide the vertical redistribution of excess currents. This physical mechanism normalizes the magnetotelluric field distorted by near-surface inhomogeneities and increases its sensitivity to crustal and mantle conductive zones (Berdichevsky et al., 1993, 1994). It is evident that the deep fluidized faults define to a large part the efficiency of deep magnetotellurics.

9.1 Near-Surface Inhomogeneity in the Presence of Conductive Faults

This two-dimensional model is shown in Fig. 9.1. It consists of the three-segment sediments (ρ_1', ρ_1'', ρ_1'), the resistive lithosphere (ρ_2) and the mantle highly conductive zone ($\rho_3 = 0$). The central sedimentary segment of width 2ν and resistivity ρ_1'' is bordered by conductive vertical channels of width q and resistivity ρ_f which simulate faults connecting sediments with mantle. Here

$$\rho_1 = \begin{cases} \rho_1' & y \geq \nu \\ \rho_1'' & -\nu \leq y \leq \nu \\ \rho_1' & y \leq -\nu \end{cases} \quad \rho_2 = \begin{cases} \rho_2 & y \geq \nu + q \\ \rho_f & \nu + q \geq y \geq \nu \\ \rho_2 & -\nu \leq y \leq \nu \\ \rho_f & -\nu - q \leq y \leq -\nu \\ \rho_2 & y \leq -\nu - q \end{cases} \quad \rho_3 = 0 \quad h_2 \gg h_1. \tag{9.1}$$

The attractive feature of the problem is that it admits of an analytical solution for the TM-mode. Using the Dmitriev thin-sheet approximation, we turn to (7.17) and take into account that the lithosphere has the variable resistivity. Then, eliminating $E_y(y, h_1)$, $H_x(y, h_1)$ from (7.17) and assuming that $H_x(y, 0) = H_x^N = const$, we get the equation for the transverse impedance $Z^{\perp}(y) = -E_y(y, 0)/H_x^N$:

$$h_2 \frac{d}{dy} \rho_2(y) \frac{d}{dy} S_1(y) Z^{\perp}(y) - [1 - i\omega\mu_o S_1(y) h_2] Z^{\perp}(y) = i\omega\mu_o h\,, \tag{9.2}$$

M. Berdichevsky, V.I. Dmitriev, *Models and Methods of Magnetotellurics*,
DOI 10.1007/978-3-540-77814-1_9, © Springer-Verlag Berlin Heidelberg 2008

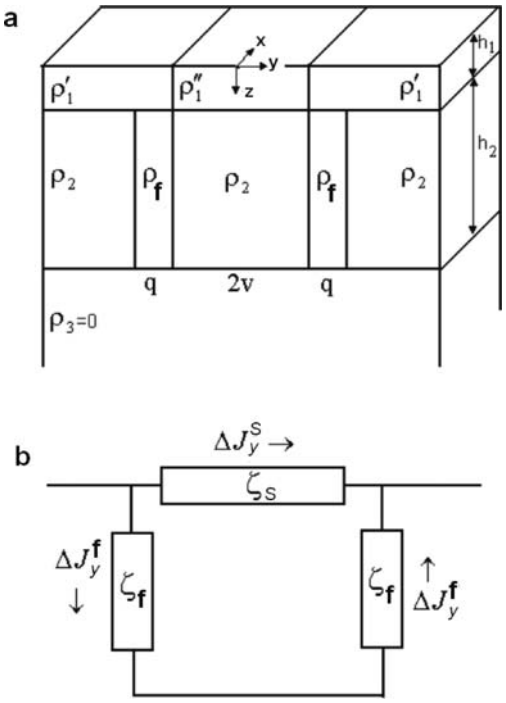

Fig. 9.1 The two-dimensional model with conductive faults bordering the central sedimentary segment (a) and its equivalent electric circuit (b)

where $S_1(y) = h_1/\rho_1(y)$ and $h = h_1 + h_2$. With regard to (9.1), this equation falls into three independent equations with constant coefficients:

$$\begin{aligned}
&\frac{d^2Z^{\perp}(y)}{dx^2} - \left(\frac{g_1'}{f'}\right)^2 Z^{\perp}(y) = -\left(\frac{g_1'}{f'}\right)^2 \dot{Z}_N \quad y \geq v+q \\
&\frac{d^2Z^{\perp}(y)}{dx^2} - \left(\frac{g_2'}{f'}\right)^2 Z^{\perp}(y) = -\left(\frac{g_2'}{f'}\right)^2 \dot{Z}_N \quad v+q \geq y \geq v \\
&\frac{d^2Z^{\perp}(y)}{dx^2} - \left(\frac{g''}{f''}\right)^2 Z^{\perp}(y) = -\left(\frac{g''}{f''}\right)^2 \ddot{Z}_N \quad 0 \leq y \leq v\,,
\end{aligned} \tag{9.3}$$

where $g_1,\ g_2,\ g_3$ are galvanic parameters:

$$g_1' = \frac{1}{\sqrt{S_1' R_2'}} \qquad g_2' = \frac{1}{\sqrt{S_1' R_2''}} \qquad g'' = \frac{1}{\sqrt{S_1'' R_2'}}$$

$$S_1' = h_1/\rho_1' \qquad S_1'' = h_1/\rho_1'' \qquad R_2' = h_2\rho_2 \qquad R_2'' = h_2\rho_f\,,$$

$f',\ f''$ are induction parameters:

$$f' = \frac{1}{\sqrt{1 - i\omega\mu_o S_1' h_2}}, \qquad f'' = \frac{1}{\sqrt{1 - i\omega\mu_o S_1'' h_2}},$$

and $\dot{Z}_N$, $\ddot{Z}_N$ are normal impedances of side and central segments defined in the thin-sheet approximation:

$$\dot{Z}_N = -\frac{i\omega\mu_o h}{1 - i\omega\mu_o S_1' h_2}, \qquad \ddot{Z}_N = -\frac{i\omega\mu_o h}{1 - i\omega\mu_o S_1'' h_2}.$$

Solutions of these equations are

$$Z^{\perp}(y) = \begin{cases} \dot{Z}_N + Ae^{-g_1' y/f'} & y \geq v + q \\ \dot{Z}_N + Be^{-g_2' y/f'} + Ce^{g_2' y/f'} & v + q \geq y \geq v \\ \ddot{Z}_N + D\cos\,\mathrm{h}\dfrac{g''}{f''} y & 0 \leq y \leq v. \end{cases} \tag{9.4}$$

Constants A, B, C, D are found from conditions that $S_1(y)Z^{\perp}(y)$ and $\rho_2(y)\frac{dS_1(y)Z^{\perp}(y)}{dy}$ are continuous at $y = v$ and $y = v + q$.

The first condition ensures the horizontal component of the current density j_y to be continuous at the Earth's surface:

$$S_1(y)Z^{\perp}(y) = -\frac{h_1}{\rho_1(y)}\frac{E_y(y,0)}{H_x^N} = -\frac{h_1}{H_x^N} j_y(y,0).$$

The second condition ensures the vertical component of the electric field E_z to be continuous at the floor of sediments:

$$\begin{aligned} \rho_2(y)\frac{dS_1(y)Z^{\perp}(y)}{dy} &= -\frac{\rho_2(y)}{H_x^N}\frac{dS_1(y)E_y(y,0)}{dy} = \frac{\rho_2(y)}{H_x^N}\frac{d\left[H_x^N - H_x(y,h_1)\right]}{dy} \\ &= -\frac{\rho_2(y)}{H_x^N}\frac{dH_x(y,h_1)}{dy} = \frac{E_z(y,h_1)}{H_x^N}. \end{aligned}$$

On cumbersome mathematics we get

$$\begin{aligned} A &= \dot{Z}_N(1+k)\left(\eta^2 - \gamma^2\right) e^{\left[g_1'(w+q) - g_2' q\right]/f'} \left[\gamma^2\left(1 + ke^{-2g_2' q/f'}\right) + \eta\frac{g''}{g_2'}\left(1 - ke^{-2g_2' q/f'}\right)\coth\frac{g''}{f''}v\right]^{-1} \\ B &= \dot{Z}_N\left(\eta^2 - \gamma^2\right) e^{g_2' w/f'} \left[\gamma^2\left(1 + ke^{-2g_2' q/f'}\right) + \eta\frac{g''}{g_2'}\left(1 - ke^{-2g_2' q/f'}\right)\coth\frac{g''}{f''}v\right]^{-1} \\ C &= \dot{Z}_N\left(\eta^2 - \gamma^2\right) e^{-g_2'(w+2q)/f'} \left[\gamma^2\left(1 + ke^{-2g_2' q/f'}\right) + \eta\frac{g''}{g_2'}\left(1 - ke^{-2g_2' q/f'}\right)\coth\frac{g''}{f''}v\right]^{-1} \\ D &= \ddot{Z}_N\frac{g''\left(\eta^2 - \gamma^2\right)}{\eta\, g_2'\sinh\dfrac{g''}{f''}v}\left(ke^{-2g_2' q/f'} - 1\right)\left[\gamma^2\left(1 + ke^{-2g_2' q/f'}\right) + \eta\frac{g''}{g_2'}\left(1 - ke^{-2g_2' q/f'}\right)\coth\frac{g''}{f''}v\right]^{-1}, \end{aligned} \tag{9.5}$$

where

$$k = \frac{\sqrt{\rho_f} - \sqrt{\rho_2}}{\sqrt{\rho_f} + \sqrt{\rho_2}}, \qquad \gamma = \sqrt{\frac{S_1'}{S_1''}}, \qquad \eta = \frac{f''}{f'} = \frac{\sqrt{1 - i\omega\mu_o S_1' h_2}}{\sqrt{1 - i\omega\mu_o S_1'' h_2}}.$$

In the absence of faults ($\rho_f = \rho_2$), we return to the three-segment model examined in Sect. 7.2.3. This model contains a near-surface inhomogeneity, which distorts the transverse impedance in the low-frequency range.

Consider the transverse impedance $Z^\perp$ in a model with conductive faults.

Let us begin with the S_1 – interval relating to the ascending branch of the apparent-resistivity curve $\rho^\perp = \left|Z^\perp\right|^2 \Big/ \omega\mu_o$. Here $\omega\mu_o S_1 h_2 \gg 1$. Then $f \approx \sqrt{-i\omega\mu_o S_1 h_2}$, whence $\eta \approx \gamma$. Hence the coefficients A, B, C and D defined by (9.5) are close to zero, from which

$$Z^\perp(y) \approx \begin{cases} \dot{Z}_N = \dfrac{1}{S_1'} & |y| \geq v + q \\ \ddot{Z}_N = \dfrac{1}{S_1''} & |y| \leq v\,. \end{cases} \tag{9.6}$$

Here we arrive at the same representation (7.77) inferred in Sect. 7.2.3 for the three-segment model without conductive faults. In the S_1 – interval the transverse impedance is not distorted.

Now we pass on to the h – interval relating to the descending branch of the apparent-resistivity curve $\rho^\perp = \left|Z^\perp\right|^2 \Big/ \omega\mu_o$. Here $\omega\mu_o S_1 h_2 \ll 1$. Then $f \approx 1$, whence $\eta \approx 1$. Thus,

$$\begin{aligned}
A &\approx \dot{Z}_N(1+k)(1-\gamma^2)e^{[g_1'(w+q)-g_2'q]/f'}\left[\gamma^2\left(1+ke^{-2g_2'q/f'}\right)+\frac{g''}{g_2'}\left(1-ke^{-2g_2'q/f'}\right)\coth\frac{g''}{f''}v\right]^{-1} \\
B &\approx \dot{Z}_N\left(1-\gamma^2\right)e^{g_2'w/f'}\left[\gamma^2\left(1+ke^{-2g_2'q/f'}\right)+\frac{g''}{g_2'}\left(1-ke^{-2g_2'q/f'}\right)\coth\frac{g''}{f''}v\right]^{-1} \\
C &\approx \dot{Z}_N\left(1-\gamma^2\right)e^{-g_2'(w+2q)/f'}\left[\gamma^2\left(1+ke^{-2g_2'q/f'}\right)+\frac{g''}{g_2'}\left(1-ke^{-2g_2'q/f'}\right)\coth\frac{g''}{f''}v\right]^{-1} \\
D &\approx \ddot{Z}_N\frac{g''(1-\gamma^2)}{g_2'\sin\mathrm{h}\dfrac{g''}{f''}v}\left(ke^{-2g_2'q/f'}-1\right)\left[\gamma^2\left(1+ke^{-2g_2'q/f'}\right)+\frac{g''}{g_2'}\left(1-ke^{-2g_2'q/f'}\right)\coth\frac{g''}{f''}v\right]^{-1}.
\end{aligned} \tag{9.7}$$

The normalizing role of the faults is seen from two asymptotic estimates.

Let $\rho_2 \to \infty$, $\rho_f \to \infty$. In this model the lithosphere is of infinitely high resistivity and the faults are absent. Then $A = B = C = 0$ and $D = \gamma^2 - 1$, whence

$$Z^\perp(y) \approx \begin{cases} Z_N = -i\omega\mu_o h & |y| \geq v \\ \gamma^2 Z_N = -i\omega\mu_o \gamma^2 h & |y| \leq v. \end{cases} \tag{9.8}$$

The model without faults exhibits the strong S – effect: the transverse impedance $Z^{\perp}$ observed over the central segment differs from the locally normal impedance Z_{n} by the distortion factor $\alpha^{\perp} = \gamma^2 = S_1'/S_1''$.

Let $\rho_2 \to \infty$, $\rho_{\mathrm{f}} \to 0$. In this model the faults are of infinitesimal resistivity. Then $A = 0$, $D = 0$, whence

$$Z^{\perp}(y) \approx \begin{cases} Z_{\mathrm{N}} = -i\omega\mu_{\mathrm{o}}h & |y| \geq v + q \\ Z_{\mathrm{N}} = -i\omega\mu_{\mathrm{o}}h & |y| \leq v \end{cases} \tag{9.9}$$

Here the S – effect is suppressed and the transverse impedance $Z^{\perp}$ comes to the normalcy: excess current arising in the inhomogeneous sediments is released through the conductive faults.

Clearly the intensity of the S – effect depends on the fault resistivity. Consider this mechanism from the physical point of view.

The impact of a thin fault crossing highly resistive lithosphere can be defined by two integral parameters: by the resistance $\zeta_{\mathrm{f}} = \rho_{\mathrm{f}} h_2/q = R_2''/q$ of the fault in the vertical direction and by the resistance $\zeta_s = 2\rho_1'' v/h_1 = 2v/S_1''$ of the sedimentary central segment in the horizontal direction. Let us return to (9.7) and find asymptotics of coefficients A and D at $q \to 0$ and $\rho_2 \to \infty$. Using Taylor-series expansion of exponential and hyperbolic functions, we write

$$\begin{aligned} A &\approx -i\omega\mu_{\mathrm{o}}h \left(1 - \frac{S_1'}{S_1''}\right) \frac{1}{\dfrac{S_1'}{S_1''} + \dfrac{1}{P}(F+1)}, \\ D &\approx -i\omega\mu_{\mathrm{o}}h \left(\frac{S_1'}{S_1''} - 1\right) \frac{1}{P\dfrac{S_1'}{S_1''} + F + 1}, \end{aligned} \tag{9.10}$$

where

$$P = \frac{v}{\sqrt{S_1' R_2'}}, \qquad F = \frac{\zeta_s}{2\zeta_f} = \frac{vq}{S_1'' R_2''}.$$

These asymptotic formulae are valid for small q and great ρ_2. They have simple physical interpretation. We believe that vertical redistribution of excess current includes two mechanisms: (1) slow percolation through the highly resistive lithosphere; the intensity of this mechanism is determined by parameter P (the greater is P, the more intensive is the percolation), and (2) abrupt flow through the conductive faults; the intensity of this mechanism is determined by parameter F (the greater is F, the more intensive is the abrupt flow). In (9.10) these two mechanisms are expressed separately.

The fault effect is dominant when $P S_1'/S_1'' \ll F+1$ with $S_1' > S_1''$ or when $P \ll F+1$ with $S_1' < S_1''$. Let one of these conditions be satisfied. Then, ignoring the percolation effect, we get

$$A = 0 \qquad D = -i\omega\mu_o h \left(\frac{S_1'}{S_1''} - 1\right) \frac{1}{F+1}, \tag{9.11}$$

whence

$$Z^{\perp}(y) \approx \begin{cases} -i\omega\mu_o h & |y| \geq v+q \\ -i\omega\mu_o \alpha^{\perp} h & |y| \leq v\,, \end{cases} \tag{9.12}$$

where $\alpha^{\perp}$ is a distortion factor which defines the intensity of the S – effect (magnitude of the static shift of the apparent-resistivity descending branch):

$$\alpha^{\perp} = \frac{F + S_1'/S_1''}{F+1}.$$

Here the S – effect enhances when the fault resistivity increases:

$$\underset{F\to 0}{\alpha^{\perp}} \to \frac{S_1'}{S_1''}$$

and the S – effect vanishes when the fault resistivity decreases:

$$\underset{F\to \infty}{\alpha^{\perp}} \to 1.$$

In this approximation the action of faults reduces to the simple shunting. An equivalent electric circuit is shown in Fig. 9.1. The sedimentary central segment with resistance ζ_s is shunted by faults with resistance $2\zeta_{\mathrm{f}}$. Determine the excess current ΔJ_y filling the central segments in the absence of the faults ($\rho_2 = \rho_{\mathrm{f}} = \infty$). In the model without leakage, we have the constant current $J_y = E_y S_1 = const$. Therefore $J_y(-\nu \leq y \leq \nu) = E_y(-\nu \leq y \leq \nu) S_1'' = E_y^{\mathrm{N}} S_1'$, where E_y^{N} is the normal electric field. At the same time, the normal current in the central segment is $J_y^{\mathrm{N}} = E_y^{\mathrm{N}} S_1''$. So, $\Delta J_y = J_y - J_y^N = E_y^{\mathrm{N}}(S_1' - S_1'')$. Now introduce the faults and establish relations between excess currents ΔJ_y^s and ΔJ_y^f flowing in sediments and faults respefctively. From Kirchhoff's laws

$$\Delta J_y^s + \Delta J_y^f = \Delta J_y = E_y^{\mathrm{N}}(S_1' - S_1'')$$
$$\frac{\Delta J_y^s}{\Delta J_y^f} = \frac{2\zeta_f}{\zeta_s} = \frac{1}{F}$$

whence

$$\Delta J_y^s = E_y^{\mathrm{N}} \frac{S_1' - S_1''}{F+1}.$$

Summing J_y^{N} and ΔJ_y^s, we obtain the total current J_y^s flowing in sediments:

$$J_y^s = J_y^{\mathrm{N}} + \Delta J_y^s = E_y^{\mathrm{N}} \frac{S_1' - S_1''}{1+F}.$$

Consequently,

$$E_y(-v \le y \le v) = \frac{J_y^s}{S_1''} = E_y^{\mathrm{N}} \frac{F + S_1'/S_1''}{F+1},$$

whence

$$Z^{\perp}(-v \le y \le v) = -\frac{E_y(-v \le y \le v)}{H_x} = -i\omega\mu_0\alpha^{\perp}h\,, \qquad \alpha^{\perp} = \frac{F + S_1'/S_1''}{F+1},$$

which coincides with (9.12).

Using (9.12), we can suggest a simple criterion of slight S – effect. Let us believe that the S – effect is slight if deviation of $\alpha^{\perp}$ from 1 does not exceed 0.2. This condition is fulfilled if $F \ge 5S_1'/S_1'' - 6$ when $S_1'/S_1'' \ge 1.2$ or if $F \ge 4 - 5S_1'/S_1''$ when $S_1'/S_1'' \le 0.8$.

As an pictorial example we consider the apparent-resistivity curves in the model from Fig. 9.1. Let us take fixed parameters $\rho_1' = 10\,\Omega\mathrm{hm}\cdot\mathrm{m}$, $h_1 = 1\,\mathrm{km}$, $\rho_1'' = 200\,\Omega\mathrm{hm}\cdot\mathrm{m}$, $v = 10\,\mathrm{km}$, $\rho_2 = 10000\,\Omega\mathrm{hm}\cdot\mathrm{m}$, $h_2 = 20$ km, $\rho_3 = 0$ and variable parameters $q = 0 \div 1\,\mathrm{km}$, $\rho_{\mathrm{f}} = 1 \div 3\ \Omega\mathrm{hm}\cdot\mathrm{m}$. Here $S_1'/S_1'' = 20$. Figure 9.2

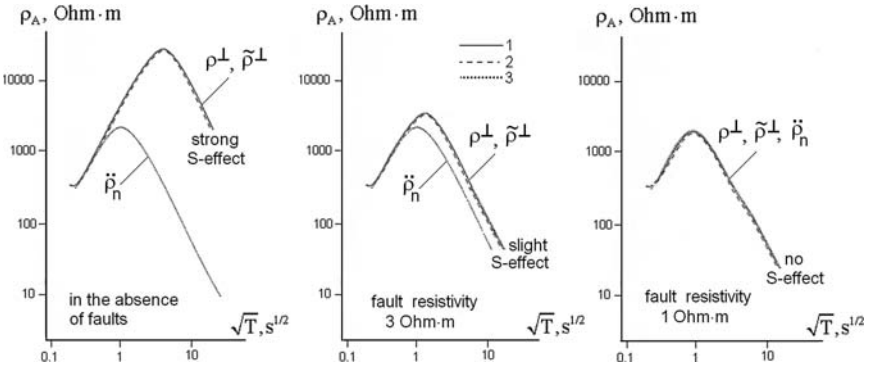

Fig. 9.2 Transverse apparent-resistivity $\rho^{\perp}$ – curves in the model shown in Fig. 9.1. Observation site is located at the centre of the model ($y = 0$). Model parameters: $\rho_1' = 10\ \Omega\mathrm{hm}\cdot\mathrm{m}$, $h_1 = 1\,\mathrm{km}$, $\rho_1'' = 200\ \Omega\mathrm{hm}\cdot\mathrm{m}$, $v = 10\,\mathrm{km}$, $\rho_2 = 10000\ \Omega\mathrm{hm}\cdot\mathrm{m}$, $h_2 = 20\,\mathrm{km}$, $\mathrm{q} = 0, 1\,\mathrm{km}$, $\rho_f = 1, 3\ \Omega\mathrm{hm}\cdot\mathrm{m}$, $\rho_3 = 0$; 1 – transverse $\rho^{\perp}$ – curve computed by means of the finite element method, 2 – transverse $\rho^{\perp}$ – curve computed from analytical solution (9.4), 3 – locally normal $\ddot{\rho}_{\mathrm{n}}$ – curve

shows the transverse $\rho^{\perp}$ – curves obtained at the centre of the model ($y = 0$) from analytical solution (9.4) and finite element solution (Wannamaker et al. 1987). Note that both the solutions virtually coincide. In the absence of faults (q = 0) we observe the strong *S* – effect: the descending branch of the $\rho^{\perp}$ – curve is dramatically shifted upward with respect to the locally normal $\ddot{\rho}_n$ – curve, its static shift being about two decades. But with conductive faults the situation essentially changes. In the case $\rho_f = 3\,\text{Ohm} \cdot \text{m}$ the static shift considerably diminishes, while in the case ρ_f = 1 Ohm·m the $\rho^{\perp}$ – curve practically merges with locally normal $\ddot{\rho}_n$ – curve.

9.2 Deep Inhomogeneity in the Presence of Conductive Faults

In the previous section we saw that the deep faults normalize the apparent-resistivity curves distorted by near-surface *S*-inhomogeneity. Now we will show that the deep faults increase the sensitivity of the apparent-resistivity curves to deep conductive zones.

Figure 9.3 presents a two-dimensional model consisting of five layers. Here the homogeneous conductive sediments (ρ_1) and resistive lithosphere (ρ_2, ρ_3, ρ_4) rest on the conductive mantle (ρ_5). The lithosphere contains a conductive crustal zone (ρ_3'') of width 2ν bordering by vertical conductive channels (faults) of resistivity ρ_f and width q that connect sediments with conductive mantle.

The $\rho^{\perp}$ – curves obtained over the midpoint of the conductive zone ($y = 0$) are shown in Fig. 9.4. The calculations have been performed for fixed parameters $\rho_1 = 10\,\text{Ohm} \cdot \text{m}$, $h_1 = 1\,\text{km}$, $\rho_2 = 100000\ \text{Ohm} \cdot \text{m}$, $h_2 = 19\,\text{km}$, $\rho_3' = 1000\ \text{Ohm} \cdot \text{m}$, $\rho_3'' = 10\,\text{Ohm} \cdot \text{m}$, $h_3 = 15\,\text{km}$, $\rho_4 = 1000\,\text{Ohm} \cdot \text{m}$, $h_4 = 65\,\text{km}$, $\rho_5 = 10\,\text{Ohm} \cdot \text{m}$ and variable parameters $q = 0, 5$ km, $\nu = 25, 100, 250, 500$ km; $\rho_f = 1, 5, 10\ \text{Ohm} \cdot \text{m}$. Note that in the model under consideration the lithosphere resistance is about $10^9\ \text{Ohm}\cdot\text{m}^2$ which is typical for stable regions. In the absence of faults ($q = 0$) the conductive zone is strongly screened by highly resistive layers of the llithosphere. Thus, at $\nu = 25, 100$ km the transverse $\rho^{\perp}$ – curves practically coincide with the locally normal $\dot{\rho}_n$ – curve connected with a normal background.

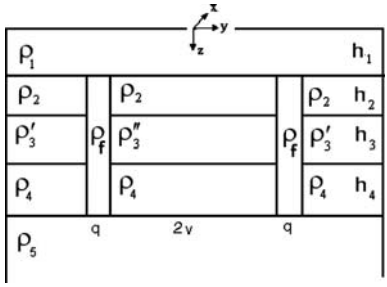

Fig. 9.3 The two-dimensional model with conductive faults bordering the deep conductive zone

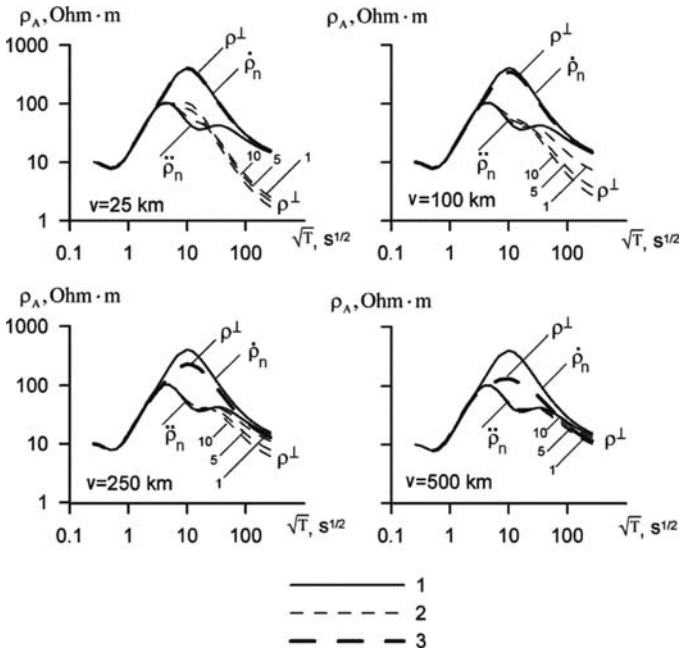

Fig. 9.4 Transverse apparent-resistivity $\rho^{\perp}$ – curves observed at the epicentre of the deep conductive zone ($y = 0$) in the model from Fig. 9.3 with fixed parameters $\rho_1 = 10\,\text{Ohm} \cdot \text{m}$, $h_1 = 1\,\text{km}$, $\rho_2 = 100000\,\text{Ohm} \cdot \text{m}$, $h_2 = 19\,\text{km}$, $\rho'_3 = 1000\,\text{Ohm} \cdot \text{m}$, $\rho'_3 = 10\,\text{Ohm} \cdot \text{m}$, $h_3 = 15\,\text{km}$, $\rho_4 = 1000\,\text{Ohm} \cdot \text{m}$, $h_4 = 65\,\text{km}$, $\rho_5 = 10\,\text{Ohm} \cdot \text{m}$ and variable parameters $v = 25, 100, 250, 500\,\text{km}$; $\rho_f = 1,\ 5,\ 10\,\text{Ohm} \cdot \text{m}$; 1 – locally normal curves $\dot{\rho}_n$, $\ddot{\rho}_n$, 2 – transverse $\rho^{\perp}$ – curves in the presence of conductive faults ($q = 5\,\text{km}$), curve parameter: ρ_f, $\text{Ohm} \cdot \text{m}$, 3 – transverse $\rho^{\perp}$ – curve in the absence of conductive faults ($q = 0$)

When widening the conductive zone ($v = 250,\ 500\,\text{km}$), the $\rho^{\perp}$ – curves slightly flatten still preserving their bell-like shape without distinct evidences of a conductive zone. The different pattern is observed when conductive faults are present. Even relatively narrow conductive zone ($w = 25,\ 100\,\text{km}$) manifests itself in the $\rho^{\perp}$ – curves with a descending branch, which enables one to estimate a depth to this zone. Here the deep S – effect is clearly observable (at low-frequencies the descending branch of the $\rho^{\perp}$ – curves is shifted downwards with respect to the locally normal $\ddot{\rho}_n$ – curve connected with a central segment of the model). When widening the conductive zone ($v = 250,\ 500\,\text{km}$), the deep S – effect attenuates and the low-frequency branches of the $\rho^{\perp}$ – curves approach the locally normal $\ddot{\rho}_n$ – curve. The lower the fault resistivity, the weaker the deep S – effect and the closer the $\rho^{\perp}$ – curve to the normalcy. In the case $v = 250\,\text{km}$, $\rho_f = 1\,\text{Ohm} \cdot \text{m}$ or $v = 500\,\text{km}$, $\rho_f = 5\,\text{Ohm} \cdot \text{m}$ the $\rho^{\perp}$ – curve virtually comes to the normalcy and provides the reliable 1D inversion.

The calculations show that highly resistive layers of the continental lithosphere ($10000 \div 100000\,\text{Ohm} \cdot \text{m}$) forbid the galvanic access to the deep conductive zones (the screening effect). If the net of deep conductive faults crossing the continental

lithosphere had not been sufficiently dense, the regional palette of the magnetotelluric data would been consisted of the uniform bell-type apparent-resistivity curves with verticall scattering of their mantle branches due to the near-surface S – effect. It can be said without exaggeration that in many regions magnetotellurics owes its information on crustal and mantle conductivity to the deep conductive faults crossing the resistive lithosphere.

9.3 Current Channeling in Conductive Faults

The notion of the current channeling (conductive channeling) has been introduced into magnetotellurics by Weidelt (1977). He used the thin sheet approximation and examined a plane-wave model consisting of the upper inhomogeneous layer (ρ_1) and the homogeneous two-layered substratum ($\rho_2 = 1000$ Ohm·m, $h_2 = 250$ km, $\rho_3 = 50$ Ohm·m). The upper layer contains the homogeneous background of conductance $S_n = 500\,S$ and a highly conductive cranked channel of conductance $S = 4000\,S$. Figure 9.5 shows how the total and anomalous currents flow in the upper layer. It is seen that the density of the anomalous current is significantly enhanced within the conductive channel. This concentration effect received the name *current channeling*. The current channeling is defined as concentration of induced current in highly conductive elongated structures. The main idea in this definition is that currents induced in a large remote area flow via conductive channels into domain under investigation and generate here an anomalous magnetic field which has little in common with the normal magnetic field representative for that domain (Weidelt, 1977). The early works on the current channeling effect had been reviewed by Jones (1983). The Simpson and Bahr monograph (2005) provides a present look on this effect.

It is generally taken that the current channeling effect is of a three-dimensional nature and requires a three-dimensional treatment. But here we would like to note

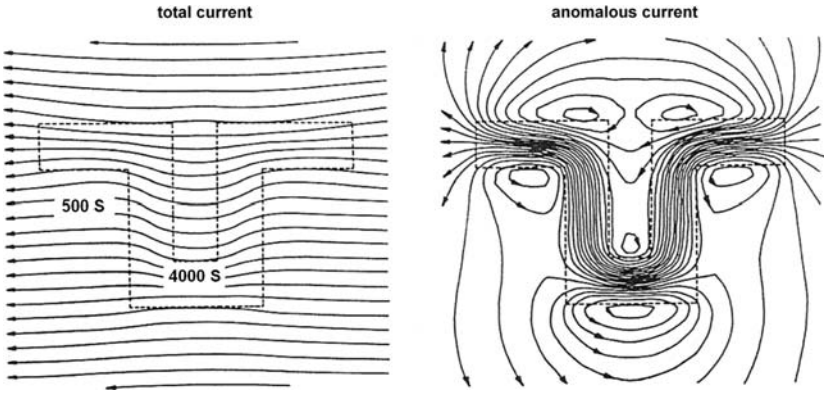

Fig. 9.5 The Weidelt model of current channeling: systems of total and anomalous currents in the layer with a cranked conductive inclusion, $T = 1800$ s

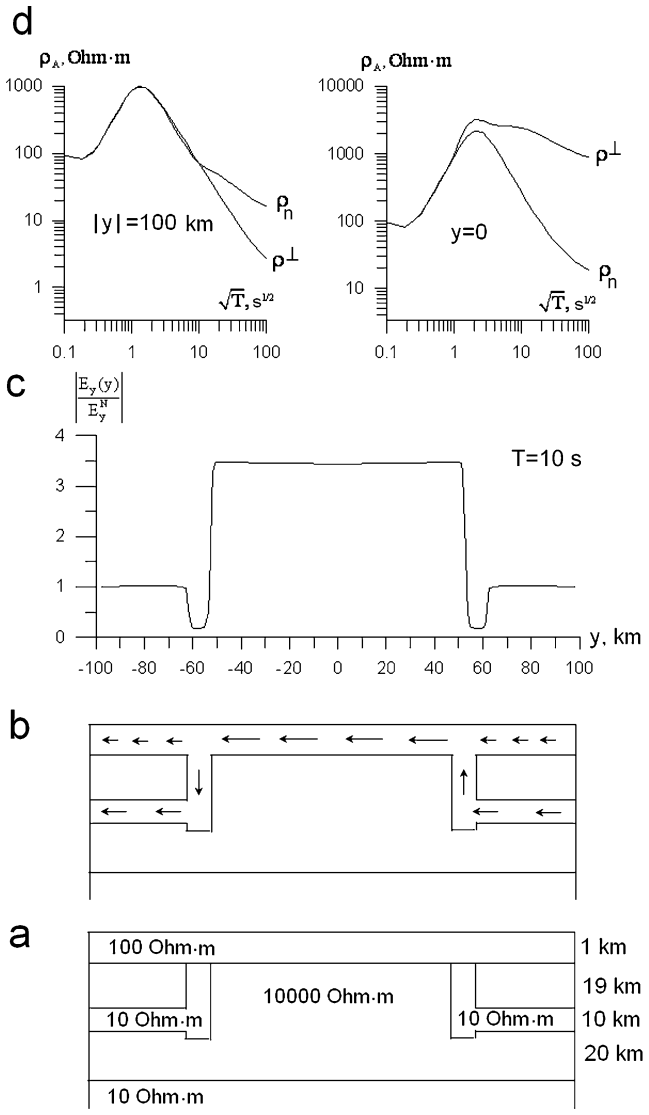

Fig. 9.6 Current channeling in the conductive faults: (a) model cross-section, (b) current channeling, (c) profile of the transverse electric field $E_y(y)$ normalized to the normal field E_y^{N}, (d) transverse apparent-resistivity curves $\rho^{\perp}$ and locally normal apparent-resistivity curves ρ_{n} over central block ($y = 0$) and side blocks ($|y| = 100$ km)

that two-dimensional models with deep conductive faults demonstrate effects, which can be reasonably considered as current channeling.

An example of such a model is given in Fig. 9.6. The two-dimensional model consists of the central resistive block bordered by the deep conductive faults, which

connect the conductive upper layer (sediments) with deep (crustal) conductive layers localized within the side resistive blocks (Fig. 9.6a). The crustal layers, the faults and the sediments form a closed conductive circuit. The transverse currents, which at low frequencies are induced in the crustal conductive layers, are channeled through the conductive faults and concentrate within sediments (Fig. 9.6b). This channeling effect clearly manifests itself over the central segment. Here at low frequencies the transverse electric field dramatically increases (Fig. 9.6c) and a descending branch of the transverse apparent-resistivity $\rho^{\perp}$ – curves lies far above the locally normal apparent-resistivity ρ_n – curve (Fig. 9.6d).

Part III
Interpretation of Magnetotelluric and Magnetovariational Data

Chapter 10
Statement of Inverse Problem

The inverse problem in magnetotellurics using the plane-wave approximation of the source field consists in the determination of the geoelectric structure of the Earth from a dependence of the magnetotelluric and magnetovariational response functions on observation coordinates $x,\ y,\ z = 0$ and frequency ω of the electromagnetic field. Magnetotelluric and magnevariational inversions usually reduce to solution of the operator equations for the impedance tensor and tipper:

$$\begin{aligned} [\mathbf{Z}\{x, y, z = 0, \omega, \sigma(x, y, z)\}] &= [\tilde{\mathbf{Z}}] \quad a \\ \mathbf{W}\{x, y, z = 0, \omega, \sigma(x, y, z)\} &= \tilde{\mathbf{W}}, \quad b \end{aligned} \tag{10.1}$$

where $[\mathbf{Z}]$ and $\mathbf{W}$ are operators of the forward problem that calculate the impedance tensor and tipper from a given electrical conductivity $\sigma(x, y, z)$, both the operators depend parametrically on x, y, ω; $[\tilde{\mathbf{Z}}]$ and $\tilde{\mathbf{W}}$ are the impedance tensor and tipper determined on the set of surface points (x, y) and frequencies ω with errors δ_Z and δ_W.

The electrical conductivity $\sigma(x, y, z)$ is found from the conditions

$$\begin{aligned} \left\| [\tilde{\mathbf{Z}}] - [\mathbf{Z}\{x, y, z = 0, \omega, \sigma(x, y, z)\}] \right\| &\le \delta_Z \quad a \\ \left\| \tilde{\mathbf{W}} - \mathbf{W}\{x, y, z = 0, \omega, \sigma(x, y, z)\} \right\| &\le \delta_W. \quad b \end{aligned} \tag{10.2}$$

Inverse problem (10.1) includes *MT inversion* (10.1*a*) and *MV inversion* (10.1*b*). It is solved in the class of piecewise-homogeneous or piecewise-continuous models excited by a plane wave vertically incident on the Earth's surface, $z = 0$. Inversions (10.1*a*) and (10.1*b*) should be mutually consistent. They result in approximate conductivity distributions $\tilde{\sigma}(x, y, z)$ such that misfits of the impedance tensor and tipper do not exceed errors, δ_Z and δ_W, in the initial data. The distributions $\tilde{\sigma}(x, y, z)$ generate a set Σ_δ of equivalent solutions of the inverse problem (10.1).

Magnetovariational inversion (10.1*b*), (10.2*b*) can be extended by inversion of the horizontal magnetic tensor:

M. Berdichevsky, V.I. Dmitriev, *Models and Methods of Magnetotellurics*,
DOI 10.1007/978-3-540-77814-1_10, © Springer-Verlag Berlin Heidelberg 2008

$$[\mathbf{M}\{x, y, z = 0, \omega, \sigma(x, y, z)\}] = [\tilde{\mathbf{M}}] \qquad c \qquad (10.1)$$

$$\left\| [\tilde{\mathbf{M}}] - [\mathbf{M}\{x, y, z = 0, \omega, \sigma(x, y, z)\}] \right\| \leq \delta_M, \qquad c \qquad (10.2)$$

where $[\mathbf{M}]$ is operator of the forward problem that calculates the magnetic tensor from a given electrical conductivity $\sigma(x, y, z)$, it depends parametrically on x, y, ω; $[\tilde{\mathbf{M}}]$ is the magnetic tensor determined on the set of surface points (x, y) and frequencies ω with errors δ_M.

Errors in the initial data δ_Z, δ_W, δ_M include the measurement and model errors. The *measurement errors* are commonly random. They arise due to instrumental noises, external interferences, and inaccuracies in the calculation of $[\tilde{\mathbf{Z}}]$, $\tilde{\mathbf{W}}$, $[\tilde{\mathbf{M}}]$. Improvement in instrumentation and field data processing methods decreases these errors. Presently, due to progress in MT technologies, measurement errors are, as a rule, fairly small (the problems may be encountered in zones of intense industrial disturbances). The main difficulty is connected with *model errors* that arise due to the inevitable deviation of numerical simulations from real geoelectric structures and real MT fields. As an example, we can cite the errors arising in 2D inversion of data obtained above 3D structures or the errors typical of polar zones, where the magnetic field of ionospheric currents has a vertical component contradicting the plane-wave approximation. Model errors are systematic. They are usually larger than measurement errors. To estimate the model errors, we need a tentative mathematical modeling.

Strategy and informativeness of the inverse problems depend on the dimensionality of models.

The simplest inverse problem is 1D inversion carried out in the class of one-dimensional models. It applies the mathematics of zero horizontal derivatives. Such a mathematics provides the local determination of the electrical conductivity along vertical profiles passing through observation points. The 1D inversion evidently ignores distortions produced by lateral geoelectric inhomogeneities. It is justified if horizontal variations in the conductivity are fairly small. Otherwise, it can miss real structures and give birth to false structures (artefacts).

The transition to 2D and 3D inversions carried out in the classes of two- and three-dimensional models enables the more or less adequate regard for the horizontal geoelectric inhomogeneities, but calls for horizontal derivatives. This mathematics substantially complicates the inverse problem.

10.1 On Multi-Dimensional Inverse Problem

Consider three distinguishing features of the multi-dimensional inverse problem.

10.1.1 Normal Background

In solving the multi-dimensional inverse problem, we face the contradiction between a finite area of MT and MV observations and a mathematical statement

colling for conditions at infinity. In forward problem, this contradiction can be easily removed through the embedding the observation area into the reasonably constructed infinite horizontally homogeneous layered medium considered as a *normal background*. In the inverse problem, the normal background of the medium under consideration is unknown and it should be chosen as a mathematical abstraction consistent with observation data obtained at the boundary of the observation area and a priori geological and geophysical information.

Note that using the homogeneous half-space as a normal background, we run the risk of false structures at the periphery of the observation area. With the help of these structures the computer tries compensate the contradictions between the real geolectric medium and homogeneous half-space.

We believe that in the general three-dimensional case a normal background consistent with the real medium can be introduced by the extrapolation of scalar invariants of the measured impedance tensors, for example, the invariant Z_{brd} (the Berdichevsky impedance) or Z_{eff} (the effective impedance). The idea is to adjust the normal background to a mean value of the impedance invariants obtained at the boundary of the observation area. This techique will be referred to as the *adjustment method*. Let values of the impedance tensor $[\mathbf{Z}]$ be determined in an observation area S_0 bounded by a contour C_0 and let $[\mathbf{Z}^{(l)}],\ l = 1, 2...L$ be specified at L points of C_0 (Fig. 10.1). The average value of the invariant Z_{brd} on the contour C_0, i.e., on the boundary of the observation area, is found as

$$\bar{Z}_{\text{brd}} = ant \log \frac{1}{L} \sum_{l=1}^{L} \log Z_{\text{brd}}^{(l)} = ant \log \frac{1}{L} \sum_{l=1}^{L} \log \frac{Z_{xy}^{(l)} - Z_{yx}^{(l)}}{2}. \tag{10.3}$$

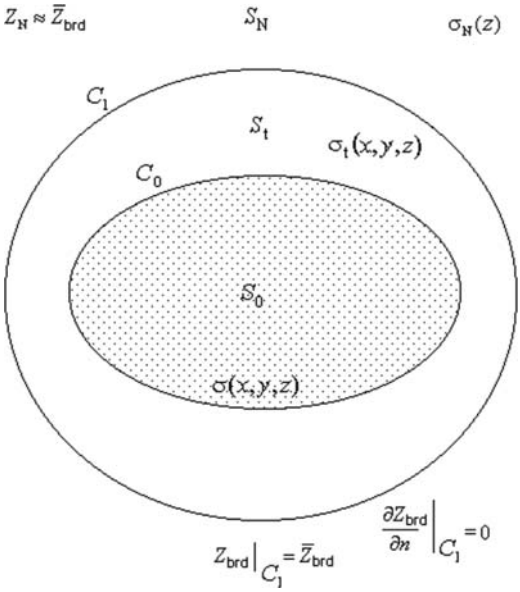

Fig. 10.1 Introduction of a normal background into the 3D interpretation model

Using the spline approximation, the values Z_{brd} are extrapolated in such a way that the condition $Z_{\text{brd}} = \bar{Z}_{\text{brd}}$ is valid on a new boundary contour C_1 and the derivative of Z_{brd} along the normal to C_1 vanishes. Given these conditions, we assume that the impedance $\bar{Z}_{\text{brd}}$ is close to the normal impedance Z_{N} of a horizontally layered medium in the infinite normalized area S_{N} external with respect to C_1 and determine its normal conductivity $\sigma_{\text{N}}(z)$ by the one-dimensional inversion of the impedances $\bar{Z}_{\text{brd}}$. At the last stage we perform the one-dimensional inversion of the impedances Z_{brd} extrapolated in the transition zone S_{t} and find gently varying transition conductivities $\sigma_{\text{t}}(x, y, z)$ between the observation area S_0 and the normalized area S_{N}. So, we get a model, in which a normal background and a transition zone embrace the observation area:

$$\sigma(M) = \begin{cases} \sigma(x,\ y,\ z) & M \in S_0 \\ \sigma_{\text{t}}(x,\ y,\ z) & M \in S_{\text{t}} \\ \sigma_{\text{N}}(z) & M \in S_{\text{N}}. \end{cases} \tag{10.4}$$

The conductivity σ_{t} in the transition zone can be corrected at the stage of the three-dimensional inversion.

Likewise, the normal background is introduced using the effective impedances Z_{eff}.

To test this algorithm, we should make sure that an expansion of the transition zone S_{t} has no significant effect on the results of MT and MV inversions in the central part of the observation area S_0.

The adjustment method based on the averaging and extrapolation of Z_{brd}, Z_{eff} or $Z^{\parallel}$, $Z^{\perp}$ can be applied in a 2D approximation of elongated structures. Let observations be carried out along a transverse profile P_0 from $y = -c_0$ to $y = c_0$ (Fig. 10.2). The average of the invariant Z_{brd} at the edges of the profile is determined as

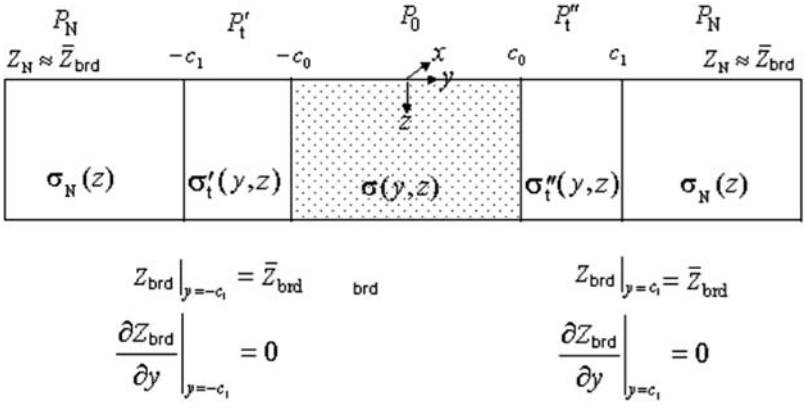

Fig. 10.2 Introduction of a normal background into the 2D interpretation model

$$\begin{aligned}\bar{Z}_{\text{brd}} &= ant\log\frac{1}{2}\{Z_{\text{brd}}(y=-c_0)+Z_{\text{brd}}(y=c_0)\}\\ &= ant\log\frac{Z^{\parallel}(-c_0)+Z^{\perp}(-c_0)+Z^{\parallel}(c_0)+Z^{\perp}(c_0)}{4}.\end{aligned}\tag{10.5}$$

Using a spline or linear extrapolation, the values of Z_{brd} are taken beyond the observation profile P_0 in such a way that the conditions $Z_{\text{brd}} = \bar{Z}_{\text{brd}}$ and $\partial Z_{\text{brd}}/\partial y = 0$ be valid at the points $y = -c_1$ and $y = c_1$. The extrapolation frames the profile $P_0(-c_0 \le y \le c_0)$ by the transition zones $P_{\text{t}}'(-c_1<y<-c_0)$, $P_{\text{t}}''(c_0<y<c_1)$ and the infinite normalized profiles $P_{\text{N}}(y \le -c_1)$, $P_{\text{N}}(y \ge c_1)$ with the normal impedance $Z_{\text{N}} \approx \bar{Z}_{\text{brd}}$. On the one-dimensional inversion of the normal impedance $Z_{\text{N}} \approx \bar{Z}_{\text{brd}}$ we get a model with a symmetric normal background:

$$\sigma(y,z) = \begin{cases}\sigma_{\text{N}}(z) & y \le -c_1\\ \sigma_{\text{t}}'(y,z) & -c_1<y<-c_0\\ \sigma(y,z) & -c_0 \le y \le c_0\\ \sigma_{\text{t}}''(y,z) & c_0<y<c_1\\ \sigma_{\text{N}}(z) & y \ge c_1.\end{cases}\tag{10.6}$$

Alternatively, we can determine a symmetric normal background by separate extrapollation of the longitudinal or transverse impedances, $Z^{\parallel}$ or $Z^{\perp}$.

Introduction of a two-dimensional symmetric homogeneous background is quite understandable, if the impedance values measured at the edges of the observation profile P_0 do not greatly differ from each other. In the regions with strongly pronounced asymmetry (for instance, on the ocean coast or at foothills), geophysicists give usually preference to an asymmetric background characterized by the different normal impedances $\dot{Z}_{\text{N}}$, $\ddot{Z}_{\text{N}}$ and the different normal conductivities $\dot{\sigma}_{\text{N}}(z)$, $\ddot{\sigma}_{\text{N}}(z)$ which provide the best adjustment to the real geoelectric structures bordering the observation profile. Evidently this approach is tolerable provided that a sufficient information on the areas adjacent to edges of the profile is available.

Note that any two-dimensional asymmetric model by means of mirror-image can be reduced to a symmetric model with a homogeneous background.

10.1.2 On Detailedness of the Multi-Dimensional Inversion

Compared to the one-dimensional inversion, the two-dimensional and three-dimensional inversions are less stable since they require a much greater number of free parameters for constructing adequate models. Solution of the two-dimensional or three-dimensional inverse problem is meaningful provided it is sought within a sufficiently narrow set of plausible models forming an interpretation model. But here we come up against the *paradox of instability*. The more restricted the interpretation model, the more stable the inverse problem and the poorer the detailedness of its solution. On the other hand, the more stable the inverse problem, the higher

its resolution. The resolution of the inverse problem and the detailedness of its solution are antagonistic. The inverse problem should be solved with optimum relation between stability, resolution and detailedness (Berdichevsky and Dmitriev, 2002). We have to fit the solution detailedness to the inversion resolution and smooth or schematize models of the geoelectric medium (to diminish a number of parameters). This complies with the diffusive nature of the low-frequency magnetotelluric field that can offer only a smoothed integral image of the geoelectric medium. Existing in the Earth buried sharp conductivity contrasts can be introduced into the interpretation model using a priori information or hypotheses. Thus, the most complete interpretation is performed by a compromise between *smoothing inversion* and *contrasting inversions*. An interpretation model with a small number of layers and structures is preferable. The additional layers and structures should be introduced providing the magnetotelluric and magnetovariational indications demand their presence.

10.1.3 On Redundancy of Observation Data

Solving a 1D inverse problem, we determine a conductivity distribution $\sigma(z)$ from the scalar complex-valued Tikhonov–Cagniard impedance Z, i.e., from two scalar response functions $|Z|$ and $\arg Z$, which have different resolving power and can nicely complement each other.

When increasing the interpretation dimensionality, we significantly extent the number of response functions derived from observation data. The two-dimensional and three-dimensional inverse problems are *multicriterion problems*. Magnetotelluric inversion aimed at determining the conductivity distribution involves complex-valued matrices of the impedance tensor (2×2), the phase tensor (2×2), the horizontal magnetic tensor (2×2), the tipper (1×2). Summing up, we say that a scalar real function defining a two-dimensional or three-dimensional distribution of the electrical conductivity is going to be derived from 28 scalar real functions. These functions have different sensitivity to parameters of the interpretation model and different immunity to galvanic distortions that ruin information on buried geoelectric structures. How can we cope with such a great body of observation data which have quite divergent properties? On joint simultaneous inversion they can bother each other impairing the inversion accuracy. The challenge is to devise the interpretation scenarios combining the inversions of different response functions in the most efficient way.

10.2 Inverse Problem as a Sequence of Forward Problems

Solving inverse problem (10.1), (10.2), we compare the observed response functions with model response functions derived from hypothetical conductivity distributions $\sigma(x, y, z)$ and sequentially minimize the model misfit by means of the iterative procedure. So, the inverse problem reduces to a sequence of the forward

problems. Let us construct the operators of the forward problem, $[\mathbf{Z}\{x, y, z = 0, \omega, \sigma(x, y, z)\}]$ and $\mathbf{W}\{x, y, z = 0, \omega, \sigma(x, y, z)\}$, that at each iteration step calculate the impedance tensor and tipper from a given conductivity $\sigma(x, y, z)$. Obviously, these operators depend on the dimensionality of the model.

10.2.1 Forward Problem in the Class of 1D-Models

Let us consider a 1D-model in which the electrical conductivity $\sigma(z)$ is a piecewise-constant function of depth z:

$$\sigma(z) = \sigma_m \quad \text{for} \quad z_{m-1} < z < z_m,\ m \in [1, M],\ z_o = 0,\ z_M = \infty,\ h_m = z_m - z_{m-1}, \tag{10.7}$$

where σ_m and h_m are the conductivity and thickness of the mth layer, respectively. At a depth $z = z_{M-1}$, the model rests on an infinite homogeneous basement having a conductivity $\sigma_M = const$. The scalar impedance Z of this model can be found directly from the Riccati equation:

$$\frac{dZ(z, \omega)}{dz} - \sigma(z)Z^2(z, \omega) = i\omega\mu_o, \qquad z \in [0, z_{M-1}], \tag{10.8}$$

where $Z(z, \omega)$ satisfies the boundary condition

$$Z(z_{M-1}, \omega) = (1 - i)\sqrt{\frac{\omega\mu_o}{2\sigma_M}}$$

and is continuous at boundaries between layers.

10.2.2 Forward Problem in the Class of 2D-Models

Let a 2D-model striking along the x-axis contain an anomalous doman $|y| \le l$ where the conductivity is a piecewise-constant function of the horizontal coordinate y and depth z and let this domain be bordered by infinite normal background $y < -l$ and $y > l$ where the conductivity depends solely on the depth z:

$$\sigma = \begin{cases} \sigma_N(z) & y < -l \\ \sigma(y, z) & -l \le y \le l \\ \sigma_N(z) & y > l. \end{cases} \tag{10.9}$$

The electromagnetic field in a 2D-model can be divided into two independent modes: the induction TE-mode with the components E_x, H_y, H_z and the galvanic TM-mode with the components E_y, E_z, H_x. The TE-mode gives the longitudinal impedance $Z^{\parallel}$ and the tipper W_{zy}, which reflect the induction effects of geoelectric structures (induction anomalies), whereas the TM-mode gives the transverse impedance $Z^{\perp}$, reflecting the galvanic effects of geoelectric structures (galvanic

anomalies). Thus, we have three independent formulations of the inverse problem, separating induction and galvanic anomalies of different physical origin.

1. MT inversion (TE-mode): the conductivity $\sigma(y, z)$ is found from the longitudinal impedance $\tilde{Z}^{\parallel}$. To determine the operator $Z^{\parallel}\{y, z = 0, \omega, \sigma(y, z)\}$, the longitudinal impedance is written in the form

$$Z^{\parallel}(y, z = 0, \omega) = \frac{E_x(y, z = 0, \omega)}{H_y(y, z = 0, \omega)} = i\omega\mu_o \left. \frac{E_x(y, z, \omega)}{\dfrac{\partial E_x(y, z, \omega)}{\partial z}} \right|_{z=0}, \tag{10.10}$$

where $E_x(y, z, \omega)$ is obtained from the Helmholtz equations

$$\begin{aligned} &\frac{\partial^2 E_x(y, z, \omega)}{\partial y^2} + \frac{\partial^2 E_x(y, z, \omega)}{\partial z^2} + i\omega\mu_o \sigma_N(z) E_x(y, z, \omega) = 0, \qquad |y| > l, \\ &\frac{\partial^2 E_x(y, z, \omega)}{\partial y^2} + \frac{\partial^2 E_x(y, z, \omega)}{\partial z^2} + i\omega\mu_o \sigma(y, z) E_x(y, z, \omega) = 0 \qquad |y| \le l \end{aligned} \tag{10.11}$$

with the conditions at infinity

$$E_x(y, z, \omega) \underset{|y|\to\infty}{\to} E_x^N(z, \omega), \qquad E_x(y, z, \omega) \underset{z\to\infty}{\to} 0 \tag{10.12}$$

and the boundary conditions

$$[E_x(y, z, \omega)]_S = 0, \qquad \left[\frac{\partial E_x(y, z, \omega)}{\partial n}\right]_S = 0. \tag{10.13}$$

Here, $E_x^N(z, \omega)$ is the normal electric field, and n is the normal to the boundary S between blocks or layers of different conductivities. The square brackets in (10.13) indicate a jump of a function at the boundary S. The anomalous electric field $E_x^A(y, z) = E_x(y, z) - E_x^N(z)$ satisfies in the air the radiation condition.

For the longitudinal impedance we have

$$Z^{\parallel}(y, z, \omega) \underset{|y|\to\infty}{\to} Z_N(z, \omega) = \frac{E_x^N(z, \omega)}{H_y^N(z, \omega)}, \tag{10.14}$$

where $Z_N(z, \omega)$ and $H_y^N(z, \omega)$, are the normal (one-dimensional) impedance and the normal magnetic field.

2. MV inversion (TE-mode): the conductivity $\sigma(y, z)$ is found from the tipper $\tilde{W}_{zy}$. To determine the operator $W_{zy}\{y, z = 0, \omega, \sigma(y, z)\}$, the tipper is written in the form

$$W_{zy}(y, z = 0, \omega) = \frac{H_z(y, z = 0, \omega)}{H_y(y, z = 0, \omega)} = - \left. \frac{\dfrac{\partial E_x(y, z, \omega)}{\partial y}}{\dfrac{\partial E_x(y, z, \omega)}{\partial z}} \right|_{z=0}, \tag{10.15}$$

where $E_x(y, z, \omega)$ is obtained from Helmholtz equations (10.11) with conditions at infinity (10.12) and boundary conditions (10.13). According to (10.12) and (10.15),

$$W_{zy}(y, z, \omega) \underset{|y|\to\infty}{\to} 0, \tag{10.16}$$

i.e., the tipper vanishes as the distance from the anomalous zone tends to infinity.

3. MT inversion (TM-mode): the conductivity $\sigma(y, z)$ is found from the transverse impedance $\tilde{Z}^{\perp}$. To determine the operator $Z^{\perp}\{y, z = 0, \omega, \sigma(y, z)\}$, we write the transverse impedance as

$$Z^{\perp}(y, z = 0, \omega) = -\frac{E_y(y, z = 0, \omega)}{H_x(y, z = 0, \omega)} = -\frac{1}{\sigma(y, z)} \frac{\left.\dfrac{\partial H_x(y, z, \omega)}{\partial z}\right|_{z=0}}{H_x(y, z = 0, \omega)}, \tag{10.17}$$

where $H_x(y, z, \omega)$ is obtained from the equations

$$\begin{aligned} &\frac{1}{\sigma_{\mathrm{N}}(z)} \frac{\partial^2 H_x(y, z, \omega)}{\partial y^2} + \frac{\partial}{\partial z}\left\{\frac{1}{\sigma_{\mathrm{N}}(z)} \frac{\partial H_x(y, z, \omega)}{\partial z}\right\} + i\omega\mu_{\mathrm{o}} H_x(y, z, \omega) = 0 \quad |y| > l \\ &\frac{\partial}{\partial y}\left\{\frac{1}{\sigma(y, z)} \frac{\partial H_x(y, z, \omega)}{\partial y}\right\} + \frac{\partial}{\partial z}\left\{\frac{1}{\sigma(y, z)} \frac{\partial H_x(y, z, \omega)}{\partial z}\right\} + i\omega\mu_{\mathrm{o}} H_x(y, z, \omega) = 0 \quad |y| \le l \end{aligned} \tag{10.18}$$

with the conditions at infinity

$$H_x(y, z, \omega) \underset{|y|\to\infty}{\to} H_x^{\mathrm{N}}(z, \omega), \qquad H_x(y, z, \omega) \underset{z\to\infty}{\to} 0 \tag{10.19}$$

and the boundary conditions

$$[H_x(y, z, \omega)]_S = 0, \quad \left[\frac{1}{\sigma(y, z)} \frac{\partial H_x(y, z, \omega)}{\partial n}\right]_S = 0 \quad H_x(y, z = 0, \omega) = H_x^{\mathrm{N}}(\omega) \tag{10.20}$$

where $H_x^{\mathrm{N}}(z, \omega)$ is the normal magnetic field.

According to (10.17) and (10.19), we have

$$Z^{\perp}(y, z, \omega) \underset{|y|\to\infty}{\to} Z_{\mathrm{N}}(z, \omega) = -\frac{E_y^{\mathrm{N}}(z, \omega)}{H_x^{\mathrm{N}}(z, \omega)}, \tag{10.21}$$

where $Z_{\mathrm{N}}(z, \omega)$ and $E_y^{\mathrm{N}}(z, \omega)$ are the normal (one-dimensional) impedance and the normal electric field.

10.2.3 Forward Problem in the Class of 3D-Models

Now, we consider MT and MV inversions in the class of 3D-models. Let a homogeneously layered Earth with the normal conductivity $\sigma_N(z)$ depending on depth z contain a bounded anomalous domain V in which the conductivity $\sigma(x, y, z)$ is an arbitrary piecewise-continuous function of the horizontal coordinates x, y and the depth z. This model admits two independent formulations of the inverse problem that separate MT and MV inversions with their different sensitivities to near-surface distortions.

1. MT inversion: conductivity $\sigma(x, y, z)$ is found from the impedance tensor $[\tilde{\mathbf{Z}}]$. To determine the operator $[\mathbf{Z}\{x, y, z = 0, \omega, \sigma(x, y, z)\}]$, we use integral equations.

Recall that the electromagnetic field in a 3D model satisfies the integral relations

$$\begin{aligned}\mathbf{E}(\mathbf{r}) &= \mathbf{E}^{\mathrm{N}}(\mathbf{r}) + \iiint_V \Delta\sigma(\mathbf{r}_{\mathrm{v}})[\mathbf{G}^E(\mathbf{r}\,|\mathbf{r}_v)]\mathbf{E}(\mathbf{r}_v)dV \qquad a\\ \mathbf{H}(\mathbf{r}) &= \mathbf{H}^{\mathrm{N}}(\mathbf{r}) + \iiint_V \Delta\sigma(\mathbf{r}_{\mathrm{v}})[\mathbf{G}^H(\mathbf{r}\,|\mathbf{r}_v)]\mathbf{E}(\mathbf{r}_v)dV, \quad b\end{aligned} \tag{10.22}$$

where $\mathbf{E}^{\mathrm{N}}$, $\mathbf{H}^{\mathrm{N}}$ are the normal electric and magnetic fields, $[\mathbf{G}^E]$, $[\mathbf{G}^H]$ are the electric and magnetic Green tensors, $\Delta\sigma = \sigma - \sigma_{\mathrm{N}}$ is the excess (anomalous) conductivity, $M(\mathbf{r})$ is an arbitrary point in the Earth or on its surface, and $M_v(\mathbf{r}_v)$ is a point in the anomalous domain V.

An integral equation for the electric field inside the anomalous region is readily derived from (10.22a). Assume that $M(\mathbf{r}) \in V$. Then

$$\mathbf{E}(\mathbf{r}'_v) - \iiint_V \Delta\sigma(\mathbf{r}_{\mathrm{v}})[\mathbf{G}^E(\mathbf{r}'_v\,|\mathbf{r}_v)]\mathbf{E}(\mathbf{r}_v)\,dV = \mathbf{E}^{\mathrm{N}}(\mathbf{r}'_v)\,. \tag{10.23}$$

Solving integral equation (10.23) and determining the electric field inside V, we substitute $\mathbf{E}(\mathbf{r}_v)$ into (10.22) and find the electric and magnetic fields on the Earth's surface. The special convenience of this approach is that the electric and magnetic Green tensors are calculated only once for a given normal conductivity $\sigma_{\mathrm{N}}(z)$. When the conductivity $\sigma(\mathbf{r}_v)$ changes in the iterative inversion procedure, kernels of integrals in (10.22) are simply obtained through the multiplication of the known Green tensors by the excess conductivity $\Delta\sigma(\mathbf{r}_v)$. This substantially shortens the computational time because kernels of integrals need not be calculated anew whenever the model of the medium changes.

The electric and magnetic fields are found for two different polarizations of the normal field:

$$\begin{aligned}\mathbf{E}^{\mathbf{N}(1)} &= \{E_x^{\mathrm{N}(1)}, 0, 0\} \quad \mathbf{H}^{\mathbf{N}(1)} = \{0, H_y^{\mathrm{N}(1)}, 0\}\\ \mathbf{E}^{\mathbf{N}(2)} &= \{0, E_y^{\mathrm{N}(2)}, 0\} \quad \mathbf{H}^{\mathbf{N}(2)} = \{H_x^{\mathrm{N}(2)}, 0, 0\}\,.\end{aligned}$$

The resulting electromagnetic fields on the Earth's surface $\mathbf{E}^{(1)} = \{E_x^{(1)}, E_y^{(1)}, 0\}$, $\mathbf{H}^{(1)} = \{H_x^{(1)}, H_y^{(1)}, H_z^{(1)}\}$ and $\mathbf{E}^{(2)} = \{E_x^{(2)}, E_y^{(2)}, 0\}$, $\mathbf{H}^{(2)} = \{H_x^{(2)}, H_y^{(2)}, H_z^{(2)}\}$ provide the system of linear equations for the impedance tensor components:

$$\begin{cases} Z_{xx}H_x^{(1)} + Z_{xy}H_y^{(1)} = E_x^{(1)} \\ Z_{xx}H_x^{(2)} + Z_{xy}H_y^{(2)} = E_x^{(2)} \end{cases} \qquad \begin{cases} Z_{yx}H_x^{(1)} + Z_{yy}H_y^{(1)} = E_y^{(1)} \\ Z_{yx}H_x^{(2)} + Z_{yy}H_y^{(2)} = E_y^{(2)}, \end{cases} \tag{10.24}$$

whence

$$Z_{xx} = \frac{E_x^{(1)}H_y^{(2)} - E_x^{(2)}H_y^{(1)}}{H_x^{(1)}H_y^{(2)} - H_x^{(2)}H_y^{(1)}} \qquad Z_{xy} = \frac{E_x^{(2)}H_x^{(1)} - E_x^{(1)}H_x^{(2)}}{H_x^{(1)}H_y^{(2)} - H_x^{(2)}H_y^{(1)}}$$

$$Z_{yx} = \frac{E_y^{(1)}H_y^{(2)} - E_y^{(2)}H_y^{(1)}}{H_x^{(1)}H_y^{(2)} - H_x^{(2)}H_y^{(1)}} \qquad Z_{yy} = \frac{E_y^{(2)}H_x^{(1)} - E_y^{(1)}H_x^{(2)}}{H_x^{(1)}H_y^{(2)} - H_x^{(2)}H_y^{(1)}}. \tag{10.25}$$

2. MV inversion: conductivity $\sigma(x,\ y,\ z)$ is found from the tipper $\tilde{\mathbf{W}}$. To determine the operator $\mathbf{W}\{x, y, z = 0, \omega, \sigma(x, y, z)\}$, we use the magnetic fields $\mathbf{H}^{(1)} = \{H_x^{(1)}, H_y^{(1)}, H_z^{(1)}\}$ and $\mathbf{H}^{(2)} = \{H_x^{(2)}, H_y^{(2)}, H_z^{(2)}\}$, obtained on the Earth's surface for two different polarizations of the normal field, and solve the system of linear equations

$$\begin{cases} W_{zx}H_x^{(1)} + W_{zy}H_y^{(1)} = H_z^{(1)} \\ W_{zx}H_x^{(2)} + W_{zy}H_y^{(2)} = H_z^{(2)}, \end{cases} \tag{10.26}$$

which yields the tipper components

$$W_{zx} = \frac{H_z^{(1)}H_y^{(2)} - H_z^{(2)}H_y^{(1)}}{H_x^{(1)}H_y^{(2)} - H_x^{(2)}H_y^{(1)}}, \qquad W_{zy} = \frac{H_z^{(2)}H_x^{(1)} - H_z^{(1)}H_x^{(2)}}{H_x^{(1)}H_y^{(2)} - H_x^{(2)}H_y^{(1)}}. \tag{10.27}$$

10.3 Three Questions of Hadamard

Solving an inverse problem, one should answer three questions of Hadamard:

1. Does the solution of this problem exist?
2. Is it unique?
3. Is it stable with respect to small errors in initial data?

These questions determine the correctness of the inverse problem. If its solution exists and if it is unique and stable, the problem is well-posed (posed correctly). But if one of these conditions is violated, the problem is regarded as ill-posed (posed incorrectly), and it calls for special consideration. We will show that inverse problems of magnetotellurics are ill-posed.

10.3.1 On the Existence of Solution to the Inverse Problem

At first glance, this question appears to be simple, because the impedance tensor $[\tilde{\mathbf{Z}}]$ and the tipper $\tilde{\mathbf{W}}$ measured on the Earth's surface should correspond to the really existing distribution of conductivity in the inhomogeneous Earth. However, the experimental values of the impedance tensor and the tipper are inaccurate, and they may conflict with mathematical models.

Let $[\tilde{\mathbf{Z}}]$ and $\tilde{\mathbf{W}}$ contain measurement and model errors δ_Z and δ_W. It is evident that the real distribution of conductivity in the Earth and the real MT and MV response functions do not belong to the chosen model class on which the inverse problem is defined. Such an inverse problem does not have a rigorous solution. To remove this contradiction, the notion of quasi-solution is introduced: a conductivity distribution $\sigma(x, y, z)$ is said to be a *quasi-solution* of the inverse problem (10.1) if the conditions (10.2) are satisfied, i.e., if the misfits of the impedance tensor and the tipper do not exceed errors in the initial data, δ_Z and δ_W. The inverse problem (10.1) has a set of quasi-solutions. From this set we have to select a quasi-solution that provides (at a given level of abstraction) the best approximation to the real geoelectric structure. This conductivity distribution $\hat{\sigma}(x, y, z)$ is called the *exact model solution*. When solving the inverse problem, we endeavour to find the exact model solution.

Using the notion of the exact model solution, we can formalize the definition of measurement and model errors. Let $[\hat{\mathbf{Z}}]$ and $\hat{\mathbf{W}}$ be the impedance tensor and the tipper obtained from a model that belongs to the chosen model class and has the conductivity $\bar{\sigma}(x, y, z)$. Then, measurement errors are determined as

$$\delta_Z^{ms} = \| [\hat{\mathbf{Z}}] - [\hat{\mathbf{Z}}] \|, \qquad \delta_W^{ms} = \| \hat{\mathbf{W}} - \hat{\mathbf{W}} \| \tag{10.28}$$

and model errors are determined as

$$\begin{aligned} \delta_Z^{md} &= \| [\hat{\mathbf{Z}}] - [\hat{\mathbf{Z}}\{x, y, z = 0, \omega, \sigma(x, y, z)\}] \| \\ \delta_W^{md} &= \| \hat{\mathbf{W}} - \hat{\mathbf{W}}\{x, y, z = 0, \omega, \sigma(x, y, z)\} \| . \end{aligned} \tag{10.29}$$

Setting $\delta_Z = \delta_Z^{ms} + \delta_Z^{md}$ and $\delta_W = \delta_W^{ms} + \delta_W^{md}$ and applying the triangle rule, we reduce (10.28), (10.29) to the initial condition (10.2).

10.3.2 On the Uniqueness of Solution to the Inverse Problem

We proceed from the following heuristic statement. The inverse problem has a unique solution if it is defined on a given model class and the impedance tensor and the tipper belonging to this class are exactly determined on the entire Earth's surface in the entire frequency range. This statement was proven in four partial cases.

I. Tikhonov (1965) proved the uniqueness theorem for 1D MT inversion in the class of piecewise-analytical functions $\sigma(z)$. In our book we present a simplified proof of the Tikhonov theorem for the case of a homogeneously layered model.

Let $\sigma(z)$ be a piecewise-constant function of the depth z:

$$\sigma(z) = \sigma_m$$

at $z_{m-1}<z<z_m$, $m \in [1, M]$, $z_o = 0$, $z_M = \infty$, $h_m = z_m - z_{m-1}$, where σ_m and h_m are the conductivity and thickness of the mth layer and z_m is the depth of its lower boundary. At the depth $z = z_{M-1}$, the model rests on an infinite homogeneous basement of conductivity $\sigma_M = const$. The admittance $Y(z, \omega)$ in this homogeneously layered model satisfies the Riccati equation

$$\frac{dY(z, \omega)}{dz} + i\omega\mu_o Y^2(z, \omega) = -\sigma(z), \qquad z \in [0, z_{M-1}], \ \omega \in [0.\infty] \tag{10.30}$$

with the boundary conditions

$$[Y(z, \omega)]_S = 0, \qquad Y(z_{M-1}, \omega) = (1 + i)\sqrt{\frac{\sigma_M}{2\omega\mu_o}}.$$

Using (10.30), we can easily derive a recurrent formula expressing $Y_{m-1} = Y(z_{m-1}, \omega)$ through $Y_m = Y(z_m, \omega)$:

$$Y_{m-1} = \beta_m \frac{(\beta_m + Y_m) - (\beta_m - Y_m)e^{2ik_m h_m}}{(\beta_m + Y_m) + (\beta_m - Y_m)e^{2ik_m h_m}}, \tag{10.31}$$

where k_m is the wavenumber of the mth layer:

$$k_m = (1 + i)\sqrt{\frac{\omega\mu_o\sigma_m}{2}}$$

and

$$\beta_m = \frac{k_m}{\omega\mu_o} = (1 + i)\sqrt{\frac{\sigma_m}{2\omega\mu_o}}.$$

Inverse of (10.31) yields a formula determining Y_m through Y_{m-1} (converting the admittance from the upper boundary of the mth layer to its lower boundary):

$$Y_m = \beta_m \frac{(\beta_m + Y_{m-1}) - (\beta_m - Y_{m-1})e^{2ik_m h_m}}{(\beta_m + Y_{m-1}) + (\beta_m - Y_{m-1})e^{2ik_m h_m}}. \tag{10.32}$$

Let the admittance $Y_o = Y(0, \omega)$ be known at the Earth's surface, while the conductivity $\sigma(z)$ be known in the interval $0 < z < z_m$. Then, the successive application of (10.32) provides the admittance $Y_m = Y(z_m, \omega)$ at a depth z_m.

Now, we prove the theorem of uniqueness, which is formulated as follows. If $Y^{(1)}(z, \omega)$ and $Y^{(2)}(z, \omega)$ are the solutions of problem (10.30) for $\sigma^{(1)}(z)$ and $\sigma^{(2)}(z)$, then $Y_o^{(1)}(\omega) \equiv Y_o^{(2)}(\omega)$ implies that $\sigma^{(1)}(z) \equiv \sigma^{(2)}(z)$. This theorem is proven ad absurdum. Assume that

$$\begin{aligned} &Y_o^{(1)}(\omega) \equiv Y_o^{(2)}(\omega) && a \\ &\sigma^{(1)}(z) \equiv \sigma^{(2)}(z) \text{ at } 0 < z < z_{m-1} && b \\ &\sigma^{(1)}(z) \neq \sigma^{(2)}(z) \text{ at } z > z_{m-1}. && c \end{aligned} \tag{10.33}$$

Then, applying (10.32) to (10.33*a*) and (10.33*b*) and extending $Y_0^{(1)}$ and $Y_0^{(2)}$ to the depth z_{m-1}, we obtain $Y_{m-1}^{(1)}(\omega) \equiv Y_{m-1}^{(2)}(\omega)$. Let us determine the high-frequency asymptotics of $Y_{m-1}(\omega)$. According to (10.31),

$$Y_{m-1}(\omega) \underset{\omega \to \infty}{\sim} \beta_m = (1 + i)\sqrt{\frac{\sigma_m}{2\omega\mu_o}}. \tag{10.34}$$

Thus, the identity $Y_{m-1}^{(1)}(\omega) \equiv Y_{m-1}^{(2)}(\omega)$ leads to $\sigma_m^{(1)} = \sigma_m^{(2)}$, which contradicts the assumption (10.33*c*). Successively increasing m, we reach the model basement and obtain $\sigma^{(1)}(z) \equiv \sigma^{(2)}(z)$, $z \geq 0$. The theorem of uniqueness is proven.

II. The next step was made by Weidelt (1978), who proved the uniqueness theorem for a 2D model excited by an *E*-polarized field. In this model, the electrical conductivity $\sigma(y, z)$ is supposed to be an analytical function. It has been shown that simultaneous observations of horizontal components of the electric and magnetic fields, carried out in the entire frequency range $0 < \omega < \infty$ along an y-profile of a finite length, provide the unique determination of $\sigma(y, z)$.

The Weidelt theorem was generalized by Gusarov (1981), who considered a 2D *E*-polarized model with the piecewise-analytical conductivity $\sigma(y, z)$. The Gusarov theorem states that the piecewise-analytical function $\sigma(y, z)$ is uniquely determined by the longitudinal impedance $Z^{\parallel} = Z_{xy}$ specified in the entire frequency range $0 < \omega < \infty$ on an infinite y-profile $-\infty < y < \infty$.

All these proofs have their basis in the skin effect. Due to the skin effect, there always exists a high frequency such that the field or impedance can be approximated by a high-frequency asymptotics depending on a local conductivity. Comparison of high-frequency asymptotics for various geoelectric structures suggests that different distributions of conductivity σ correspond to different fields and different impedances. Unfortunately, the realization of this simple idea encounters significant mathematical difficulties due to complexity of the determination of the field high-frequency asymptotics in heterogeneous media.

Resorting to intuition, the above proofs of uniqueness can be extended to the general 3D case of MT inversions. It appears evident that the ω− dependence of the impedance tensor ensures determination of the vertical variations in the conductivity, whereas its *x, y*-dependence characterizes the horizontal variations in the conductivity. Intuition suggests that measurements of the MT impedance made in a wide frequency range along sufficiently long profiles or over a sufficiently large area can provide information which enables the reconstruction of the geoelectric structure of the region studied.

III. The uniqueness of the MV inversion for a long time was open to question. It seemed that the tipper characterizes horizontal heterogeneities of the medium, but cannot provide information on its normal layered structure because $W_{zx} = W_{zy} = 0$ in a horizontally homogeneous model. However, if the medium is horizontally inhomogeneous, the manetovariational sounding can be considered as a common frequency sounding using the magnetic field of a local buried source. The latter is formed by any geoelectric inhomogeneity $\Delta\sigma(x, y, z)$ filled with excess electric current. It is evident that this current and its magnetic field depend not only on the structure of the inhomogeneity, $\Delta\sigma(x, y, z)$, but also on the normal structure, $\sigma_N(z)$. Thus, the solution $\sigma(x, y, z) = \sigma_N(z) + \Delta\sigma(x, y, z)$ of the magnetovariational inverse problem exists and we should find out whether it is unique.

The theorem of uniqueness for the MV inversion was proven by Dmitriev (Berdichevsky et al., 2000; Dmitriev, 2005). Let us consider a model shown in Fig. 10.3. In this model, a homogeneously layered Earth with the normal conductivity

$$\sigma_N(z) = \begin{cases} \sigma(z) & 0 \le z \le D \\ \sigma_D & D \le z \end{cases}$$

contains a 2D inhomogeneous domain S of conductivity $\sigma(y, z) = \sigma_N(z) + \Delta\sigma(y, z)$, where $\Delta\sigma(y, z)$ is the excess conductivity. The inhomogeneity is striking along the x-axis, and the maximum diameter of its cross-section is d. The functions $\sigma_N(z)$ and

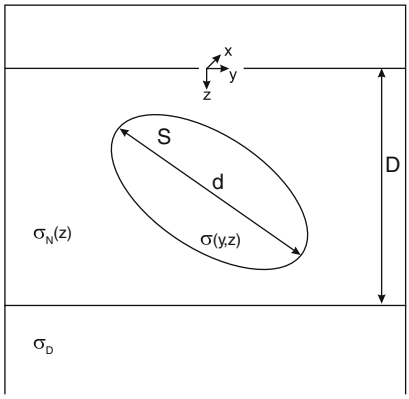

Fig. 10.3 A layered model with a 2D inhomogeneous bounded domain S

$\Delta\sigma(y, z)$ are piecewise-analytical. An infinite homogeneous basement of conductivity $\sigma_D = const$ occurs at a depth D. The model is excited by the plane E-polarized electromagnetic wave incident vertically on the Earth's surface $z = 0$.

The Dmitriev theorem states that the piecewise-analytical distribution of conductivity

$$\sigma(M) = \begin{cases} \sigma_{\mathrm{N}}(z) & M \notin S \\ \sigma_{\mathrm{N}}(z) + \Delta\sigma(y, z) & M \in S \end{cases}$$

is uniquely determined by exact values of the tipper

$$W_{zy}(y) = \frac{H_z(y, z = 0)}{H_y(y, z = 0)}, \qquad -\infty < y < \infty, \qquad 0 \le \omega < \infty,$$

given on the Earth's surface $z = 0$ at all points of the y-axis from $-\infty$ to ∞ in the entire range of frequencies ω from 0 to ∞.

The uniqueness theorem is proven in two stages. First we derive the asymptotics of the tipper $W_{zy}(y)$ at a great distance from the inhomogeneity S and show that it determines the normal conductivity $\sigma_{\mathrm{N}}(z)$. Then, with the known conductivity $\sigma_{\mathrm{N}}(z)$, we prove that the tipper uniquely determines the longitudinal impedance of the inhomogeneous medium.

The anomalous magnetic field $\mathbf{H}^{\mathrm{A}}$ on the Earth's surface can be represented as a field produced in a horizontally homogeneous layered medium by excess current of density j_x distributed in the domain S. Normalizing $\mathbf{H}^{\mathrm{A}}$, we write:

$$\begin{aligned} \widehat{H}^{\mathrm{A}}_{\mathrm{oy}}(y) &= \frac{H^{\mathrm{A}}_y(y, z = 0)}{H^{\mathrm{N}}_y(z = 0)} = \int\limits_S j_x(M_{\mathrm{o}}) h_y(y, M_{\mathrm{o}})\, dS \\ \widehat{H}^{\mathrm{A}}_{\mathrm{oz}}(y) &= \frac{H^{\mathrm{A}}_z(y, z = 0)}{H^{\mathrm{N}}_y(z = 0)} = \int\limits_S j_x(M_{\mathrm{o}}) h_z(y, M_{\mathrm{o}})\, dS, \end{aligned} \tag{10.35}$$

where $h_y(y, M_{\mathrm{o}})$, $h_z(y, M_{\mathrm{o}})$ are magnetic fields produced at the surface of a horizontally homogeneous medium by an infinitely long linear current of the unit density flowing at the point $M_{\mathrm{o}}(y_{\mathrm{o}}, z_{\mathrm{o}}) \in S$ in the x -direction. The functions $h_y(y, M_{\mathrm{o}})$ and $h_z(y, M_{\mathrm{o}})$ assume the form (Dmitriev, 1969; Berdichevsky and Zhdanov, 1984)

$$\begin{aligned} h_y(y, M_{\mathrm{o}}) &= \frac{i}{\omega\mu_{\mathrm{o}}} \lim_{z \to 0} \int\limits_0^\infty \cos\lambda(y - y_{\mathrm{o}})\, e^{\lambda z}\, U(\lambda, z = 0, z_{\mathrm{o}})\lambda\, d\lambda \\ h_z(y, M_{\mathrm{o}}) &= -\frac{i}{\omega\mu_{\mathrm{o}}} \lim_{z \to 0} \int\limits_0^\infty \sin\lambda(y - y_{\mathrm{o}})\, e^{\lambda z}\, U(\lambda, z = 0, z_{\mathrm{o}})\lambda\, d\lambda, \end{aligned} \tag{10.36}$$

where the factor $e^{\lambda z}$ relates to the upper half-space $z \le 0$ and the function $U(\lambda, z, z_{\mathrm{o}})$ is the solution of the boundary problem

$$\frac{d^2U(\lambda, z, z_o)}{dz^2} - \eta^2(\lambda, z)U(\lambda, z, z_o) = -\delta(z - z_o) \qquad z, z_o \in [0, D]$$
$$\eta(\lambda, z) = \sqrt{\lambda^2 - i\omega\mu_o\sigma_N(z)} \qquad \mathrm{Re}\,\eta > 0 \tag{10.37}$$

with conditions

$$\frac{d\,U(\lambda, z, z_o)}{dz} + \lambda\, U(\lambda, z, z_o) = 0 \qquad z = 0$$
$$\frac{d\,U(\lambda, z, z_o)}{dz} - \eta_D(\lambda)U(\lambda, z, z_o) = 0 \qquad z = D$$
$$\eta_D(\lambda) = \sqrt{\lambda^2 - i\omega\mu_o\sigma_D} \qquad \mathrm{Re}\,\eta_D > 0.$$

Let us turn to (10.36) and find the asymptotics of the functions $h_y(y, M_o)$ and $h_z(y, M_o)$ at $|y - y_o| \to \infty$. Given large $|y - y_o|$, harmonics of low spatial frequencies λ make the major contribution to $h_y(y, M_o)$, $h_z(y, M_o)$. Expanding $U(\lambda, z = 0, z_o)$ in powers of small λ, we get

$$U(\lambda, z = 0, z_o) = U(\lambda = 0, z = 0, z_o) + \lambda \left.\frac{dU(\lambda, z = 0, z_o)}{d\lambda}\right|_{\lambda=0} + \ldots,$$

whence, upon the substitution into (10.36) and integration, we obtain

$$h_y(y, M_o) = \frac{i}{\omega\mu_o}\frac{U(\lambda = 0, z = 0, z_o)}{(y - y_o)^2} + O\left(\frac{1}{(y - y_o)^4}\right)$$
$$h_z(y, M_o) = \frac{2i}{\omega\mu_o}\frac{1}{(y - y_o)^3}\left.\frac{d\,U(\lambda, z = 0, z_o)}{d\lambda}\right|_{\lambda=0} + O\left(\frac{1}{(y - y_o)^5}\right). \tag{10.38}$$

In order to write the relations between $\widehat{H}^{A}_{0y}$ and $\widehat{H}^{A}_{0z}$ in the form containing the MT impedance, we introduce the functions

$$V_y(z) = U(\lambda = 0, z, z_o), \qquad V_z(z) = \left.\frac{d\,U(\lambda, z, z_o)}{d\lambda}\right|_{\lambda=0}. \tag{10.39}$$

The function $V_y(z)$ is the solution of problem (10.37) at $\lambda = 0$. The problem for the function $V_z(z)$ is solved by differentiating (10.37) with respect to λ and setting $\lambda = 0$. Then,

$$\frac{d^2V_z(z)}{dz^2} + i\omega\mu_o\,\sigma(z)V_z(z) = 0 \qquad z \in [0, D]$$
$$\left.\frac{dV_z(z)}{dz}\right|_{z=+0} = -V_y(0)$$
$$\left.\frac{dV_z(z)}{dz}\right|_{z=D} - \sqrt{-i\omega\mu_o\,\sigma_D}V_z(D) = 0. \tag{10.40}$$

In this notation,

$$h_y(y, M_o) = \frac{i}{\omega\mu_o}\frac{V_y(0)}{(y-y_o)^2} + O\left(\frac{1}{(y-y_o)^4}\right)$$
$$h_z(y, M_o) = \frac{2i}{\omega\mu_o}\frac{V_z(0)}{(y-y_o)^3} + O\left(\frac{1}{(y-y_o)^5}\right). \tag{10.41}$$

Now return to (10.35) and determine the anomalous magnetic field at the great distances from the inhomogeneity. Let $|y - y_o| >> d$. Then,

$$\widehat{H}^A_{oy}(y) = \frac{i}{\omega\mu_o}V_y(0)\int_S \frac{j_x(M_o)}{(y-y_o)^2}\,dS = \frac{i}{\omega\mu_o}\frac{V_y(0)}{(y-y_S)^2}\int_S j_x(M_o)\,dS = \frac{i}{\omega\mu_o}\frac{V_y(0)}{(y-y_S)^2}J_x$$
$$\widehat{H}^A_{oz}(y) = \frac{2i}{\omega\mu_o}V_z(0)\int_S \frac{j_x(M_o)}{(y-y_o)^3}\,dS = \frac{2i}{\omega\mu_o}\frac{V_z(0)}{(y-y_S)^3}\int_S j_x(M_o)\,dS = \frac{2i}{\omega\mu_o}\frac{V_z(0)}{(y-y_S)^3}J_x, \tag{10.42}$$

where

$$J_x = \int_S j_x(M_o)\,dS$$

is the total excess current in the inhomogeneity and y_S is the coordinate of the central point of its cross-section S. Thus, with regard for (10.40), we have

$$\frac{\widehat{H}^A_{oz}(y)}{\widehat{H}^A_{oy}(y)} = \frac{2}{(y-y_S)}\frac{V_z(0)}{V_y(0)} = -\frac{2}{(y-y_S)}\frac{V_z(0)}{\left.\dfrac{dV_z(z)}{dz}\right|_{z=0}} \tag{10.43}$$

It is easy to show that the ratio $\widehat{H}^A_{0z} / \widehat{H}^A_{0y}$ can be expressed through the normal impedance of the Earth. Let us introduce the function

$$Z(z) = \mathrm{i}\omega\mu_o\frac{V_z(z)}{\dfrac{dV_z(z)}{dz}}. \tag{10.44}$$

It is seen from (10.40) that $Z(z)$ satisfies the Riccati equation

$$\frac{dZ(z)}{dz} - \sigma_N(z)\,Z^2(z) = \mathrm{i}\omega\mu_o \tag{10.45}$$

with the boundary condition

$$Z(D) = \sqrt{\frac{-i\omega\mu_o}{\sigma_D}}.$$

We obtained the known problem (1.40) for the impedance of a 1D medium with the conductivity $\sigma_{\text{N}}(z)$, $0 \le z \le D$ and $\sigma_D = const$, $z > D$. The function $Z(z)$ in the model under consideration evidently represents the normal impedance $Z_{\text{N}}(z)$. Setting $Z(z) = Z_{\text{N}}(z)$ and taking into account (10.43), (10.44) and (10.45), we find the far-zone asymptotics

$$Z_{\text{N}}(0) = -\frac{i\omega\mu_{\text{o}}(y - y_S)}{2}\frac{\widehat{H}^{\text{A}}_{\text{oz}}(y)}{\widehat{H}^{\text{A}}_{\text{oy}}(y)}\bigg|_{|y-y_S|>>d} = -\frac{i\omega\mu_{\text{o}}(y - y_S)}{2}\frac{H^{\text{A}}_{\text{oz}}(y)}{H^{\text{A}}_{\text{oy}}(y)}\bigg|_{|y-y_S|>>d} \tag{10.46}$$

that coincides with the known expression for a remote infinitely long linear current (Vanyan, 1965). The normal impedance $Z_{\text{N}}(0)$ is connected with the ratio of the components $\widehat{H}^{\text{A}}_{0z}$ and $\widehat{H}^{\text{A}}_{0y}$ of the anomalous magnetic field, which can be determined from values of the tipper W_{zy} known at all points of the y-axis from $-\infty$ to ∞. To find $\widehat{H}^{\text{A}}_{0y}$, we solve the integral equation (5.80)

$$W_{zy}(y)\widehat{H}^{A}_{\text{oy}}(y) + \frac{1}{\pi}\int\limits_{-\infty}^{\infty}\frac{\widehat{H}^{A}_{\text{oy}}(y_{\text{o}})}{y - y_{\text{o}}}dy_{\text{o}} = -W_{zy}(y).$$

Then we compute

$$\widehat{H}^{\text{A}}_{\text{oz}} = W_{zy}(1 + \widehat{H}^{\text{A}}_{\text{oy}}) \tag{10.47}.$$

Knowing W_{zy}, we synthesize the normalized anomalous magnetic field $\widehat{H}^{\text{A}}_{0y}$, $\widehat{H}^{\text{A}}_{0z}$ and calculate the normal impedance Z_{N} from the far-zone asymptotics. With known $\widehat{H}^{\text{A}}_{0y}$, $\widehat{H}^{\text{A}}_{0z}$ and Z_{N}, we integrate the second Maxwell equation (the Faraday law) and continue the longitudinal impedance $Z^{\parallel}$ to the entire y-axis:

$$Z^{\parallel}(y) = \frac{E_x(y)}{H_y(y)} = \frac{1}{1 + \widehat{H}^{\text{A}}_{\text{oy}}}\left\{Z_{\text{N}} - i\omega\mu_{\text{o}}\int\limits_{-\infty}^{\text{y}}\widehat{H}^{\text{A}}_{\text{oz}}(y)\,dy\right\}. \tag{10.48}$$

Thus, we find $Z^{\parallel}$ from W_{zy}. A one-to-one correspondence exists between $Z^{\parallel}$ and W_{zy}. Therefore, we can apply the Gusarov theorem (1981), stating that inversion of $Z^{\parallel}$ has a unique solution, and extend this result to inversion of W_{zy}. The uniqueness theorem for 2D MT inversion (the TE-mode) gives rise to that for 2D MV inversion. Moreover these two theorems can be supplemented by the uniqueness theorem for the horizontal magnetic field.

IV. Return to a 2D model shown in Fig. 10.3. Let the longitudinal impedance $Z^{\parallel}(y) = Z^{\parallel}(y, z = 0) = E_x(y, z = 0)/H_y(y, z = 0)$ be known at all points of the y-axis from $-\infty$ to ∞ in the entire range of frequencies ω from 0 to ∞.

The electric field $E_x(y, z)$ in the air is a solution of the problem

$$\frac{\partial^2 E_x(y,z)}{\partial y^2} + \frac{\partial^2 E_x(y,z)}{\partial z^2} + k_o^2 E_x(y,z) = 0 \qquad -\infty < y < \infty \qquad 0 \geq z > -\infty \tag{10.49}$$

with boundary condition on the Earth's surface

$$E_x(y, z=0) = Z^{\parallel}(y)\, H_y(y, z=0) = \frac{Z^{\parallel}(y)}{i\omega\mu_o} \left.\frac{\partial E_x(y,z)}{\partial z}\right|_{z=0}$$

and absorption condition in the air

$$\left\{E_x(y,z) - E_o e^{ik_o z}\right\} \to 0 \quad \text{as} \quad \sqrt{y^2+z^2} \to \infty,$$

were k_o is the air wavenumber, $\mathrm{Im}\, k_o > 0$, and E_o is the amplitude of the incident wave. It is well known that a problem of this kind has a unique solution continuously depending on the coefficient $Z^{\parallel}(y)$ in the boundary condition. Consequently, to the different impedances $Z^{\parallel}_{(1)}(y)$ and $Z^{\parallel}_{(2)}(y)$, the different electric fields $E_x^{(1)}(y, z)$ and $E_x^{(2)}(y, z)$ correspond.

Does it mean that to different impedances there correspond different magnetic fields on the Earth's surface?

Let us give the proof by contradiction. The boundary problem for the electric field can be rewritten as

$$\begin{aligned} &\frac{\partial^2 E_x(y,\ z)}{\partial y^2} + \frac{\partial^2 E_x(y,\ z)}{\partial z^2} + k_o^2 E_x(y,\ z) = 0 \quad -\infty < y < \infty, 0 \geq z > -\infty \\ &\left.\frac{\partial E_x(y,\ z)}{\partial z}\right|_{z=0} = i\omega\mu_o\, H_y(y,\ z=0) \\ &\left\{E_x(y,\ z) - E_o e^{ik_o z}\right\} \to 0 \quad \text{as} \quad \sqrt{y^2+z^2} \to \infty. \end{aligned} \tag{10.50}$$

Solution of this problem exists and is unique. Hence, to identical magnetic fields $H_y^{(1)}(y, z = 0) \equiv H_y^{(2)}(y, z = 0)$ identical electric fields $E_x^{(1)}(y, z) \equiv E_x^{(2)}(y, z)$ correspond.

Assume that to the different impedances $Z^{\parallel}_{(1)}(y,\ \omega)$ and $Z^{\parallel}_{(2)}(y,\ \omega)$, the identical magnetic fields $H_y^{(1)}(y, z = 0) \equiv H_y^{(2)}(y, z = 0)$ correspond. But it follows from (10.50) follows that in this case the identical electric fields $E_x^{(1)}(y, z) \equiv E_x^{(2)}(y, z)$ also correspond to the different impedances $Z^{\parallel}_{(1)}(y,\ \omega)$ and $Z^{\parallel}_{(2)}(y,\ \omega)$, which contradicts the statement derived from (10.49). So, we say that to different impedances $Z^{\parallel}_{(1)}(y,\ \omega)$ and $Z^{\parallel}_{(2)}(y,\ \omega)$ different magnetic fields $H_y^{(1)}(y, z = 0)$ and $H_y^{(2)}(y, z = 0)$ correspond. And taking into account the Gusarov uniqueness theorem for the longitudinal impedance $Z^{\parallel}(y, \omega)$, we state that to different conductivity distributions $\sigma^{(1)}(y, z)$ and $\sigma^{(2)}(y, z)$ there correspond different magnetic fields $H_y^{(1)}(y, z = 0)$

and $H_y^{(2)}(y, z = 0)$ on the Earth's surface. The uniqueness theorem for the magnetic field $H_y(y, z = 0)$ is proved.

Both the methods, MT and MV soundings, have a common mathematical basis. The 2D conductivity distribution is uniquely determined from exact values of TE impedances as well as from exact values of tippers or transverse horizontal magnetic fields given on the infinitely long transverse profile in the entire frequency range.

10.3.3 On the Instability of the Inverse Problem

Inverse problems of magnetotellurics are unstable. The set Σ_δ, characterized by small misfits of the impedance tensor and tipper, can contain equivalent solutions that strongly differ from one another and from the exact model solution.

We illustrate this property of the inverse problem by the example of the 1D inversion. The analysis is based on the theorem of stability of the *S*-distribution proven by Dmitriev in (Berdichevsky and Dmitriev, 1991, 2002).

Recall that the *S-distribution* stands for a function

$$S(z) = \int_0^z \sigma(z)\, dz \tag{10.51}$$

determining the conductance of the Earth on the interval $[0, z]$ The conductivity σ is connected with the conductance S through the differential relation $\sigma(z) = dS(z)/dz$.

The theorem of stability of the *S*-distribution consists of two statements.

1. The admittance $Y(\omega) = Y(z = 0, \omega)$ measured at the Earth's surface depends continuously on $S(z)$. Thus, the condition

$$\left\| S^{(1)}(\omega) - S^{(2)}(\omega) \right\|_C \le \varepsilon \tag{10.52}$$

implies that

$$\left\| Y^{(1)}(\omega) - Y^{(2)}(\omega) \right\|_{L_2} \le \delta(\varepsilon), \tag{10.53}$$

where $\delta \to 0$ at $\varepsilon \to 0$.

2. The conductance $S(z)$ is stably determined from the admittance $Y(\omega) = Y(z = 0,\ \omega)$ measured at the Earth's surface. Thus,

$$\left\| S^{(1)}(\omega) - S^{(2)}(\omega) \right\|_C \to 0 \tag{10.54}$$

if

$$\left\| Y^{(1)}(\omega) - Y^{(2)}(\omega) \right\|_{L_2} \to 0. \tag{10.55}$$

Take the set of conductivity distributions obtained from the inversion of 1D admittance:

$$\sigma_\delta \in \Sigma_\delta = \{\sigma(z) : \left\| \tilde{Y}(\omega) - Y[\omega, \sigma(z)] \right\|_{L_2} \le \delta_Y\}, \tag{10.56}$$

where $\tilde{Y}(\omega)$ is the measured admittance, $Y[\omega, \sigma(z)]$ is the operator calculating the admittance from a given distribution $\sigma(z)$, and δ_Y is the error in the admittance. The theorem of stability of the S-distribution implies that, for any $\sigma_\delta^{(1)}(z)$ and $\sigma_\delta^{(2)}(z)$ from the set Σ_δ, the following condition is valid:

$$\left\| \int_0^z \sigma_\delta^{(1)}(z)dz - \int_0^z \sigma_\delta^{(2)}(z)dz \right\|_C \le \varepsilon(\delta_Y), \tag{10.57}$$

where $\varepsilon \to 0$ as $\delta_Y \to 0$. If $\sigma_\delta^{(1)}(z)$ and $\sigma_\delta^{(2)}(z)$ meet condition (10.57), they are equivalent, i.e., they are characterized by closely related S-distributions and cannot be resolved by MT observations performed with an error δ_Y. Such $\sigma-$ distributions are called *S-equivalent distributions*. We say that Σ_δ is the set of S-equivalent distributions of the conductivity. In the framework of one-dimensional magnetotellurics, we can formulate the following generalized principle of S-equivalence: the conductance S characterizes the whole set Σ_δ of equivalent solutions of the inverse problem. To specify the entire set Σ_δ it is sufficient to know its S-distribution.

Differentiating the conductance $S(z)$, one intends to find the conductivity $\sigma(z)$. However, the immediate numerical differentiation of $S(z)$ is an unstable operation generating a scatter in the distribution $\sigma(z)$. The determination of $\sigma(z)$ from $Y(\omega)$ is evidently an ill-posed problem. It is easy to show, that there exist essentially different distributions $\sigma^{(1)}(z)$ and $\sigma^{(2)}(z)$ corresponding to close distributions $S^{(1)}(z)$ and $S^{(2)}(z)$, and thereby to close distributions $Y^{(1)}(\omega)$ and $Y^{(2)}(\omega)$.

As an example, consider a model with an infinite homogeneous basement at a depth h. Let

$$\sigma^{(1)}(z) - \sigma^{(2)}(z) = \begin{cases} 0 & \text{for} \quad z \notin [z',\, z' + \Delta h] \\ c/\sqrt{\Delta h} & \text{for} \quad z \in [z',\, z' + \Delta h], \end{cases} \tag{10.58}$$

where $z' + \Delta h < h$, while c and Δh are arbitrary positive constants. Then

$$\begin{aligned} S^{(1)}(z) - S^{(2)}(z) &= \int_0^z [\sigma^{(1)}(z) - \sigma^{(2)}(z)]dz \\ &= \begin{cases} 0 & \text{for} \quad 0 \le z \le z' \\ \dfrac{c(z - z')}{\sqrt{\Delta h}} & \text{for} \quad z' \le z \le z' + \Delta h \\ c\sqrt{\Delta h} & \text{for} \quad z' + \Delta h \le z \le h. \end{cases} \end{aligned} \tag{10.59}$$

The norms of deviations (10.58) and (10.59) are determined as

$$N_\sigma = \left\|\sigma^{(1)}(z) - \sigma^{(2)}(z)\right\|_{L_2} = \left\{\int_0^h [\sigma^{(1)}(z) - \sigma^{(2)}(z)]^2 dz\right\}^{1/2} = c$$

$$N_S = \left\|S^{(1)}(z) - S^{(2)}(z)\right\|_{L_3} = \left\{\int_0^h [S^{(1)}(z) - S^{(2)}(z)]^2 dz\right\}^{1/2} \tag{10.60}$$

$$= c\sqrt{\Delta h(h - z' - 2\Delta h/3)}.$$

Choosing large c and small Δh, the deviation N_σ can always be done arbitrarily large, and the deviation N_S arbitrarily small. Consequently, arbitrarily differing conductivities can correspond to close conductances and close admittances.

Let the medium contain a thin layer, whose conductance S_o is much smaller than the conductance S of the overlying layers. The conductivity of the layer can vary within wide limits constrained by the condition $S_o << S$, but these variations scarcely affect the admittance measured on the Earth's surface.

The one-dimensional inverse problem is unstable. Evidently, we have every reason to extend this conclusion to the two-dimensional and three-dimensional inverse problems. Compare, for example, a 2D or 3D-model with a slowly varying boundary between two deep layers and a model in which this boundary rapidly fluctuates around its slow variation. Their MT and MV response functions observed on the Earth's surface will virtually coincide, although these models are largely different.

Inverse problems of magnetotellurics are unstable. An arbitrarily small error in initial MT and MV data can lead to an arbitrarily large error in the inversion of these data, i.e., in the conductivity distribution. Using the terminology of Hadamard, we state that the inverse problems of magnetotellurics are ill-posed. An immediate solution of an ill-posed (unstable) problem is generally meaningless, because it can yield results far from reality.

10.4 In the Light of the Theory of Ill-Posed Problems. . .

The cornerstone of the MT and MV data interpretation is the theory of ill-posed problems. Its basic principles were formulated by Tikhonov (1963). Presently, methods of this theory have been developed rather comprehensively and are widely used in practice (Tikhonov and Arsenin, 1977; Lavrentyev et al., 1980; Glasko, 1984; Tikhonov and Goncharsky, 1987; Zhdanov, 2002) The Russian mathematical school headed by Tikhonov gave rise to a new doctrine of physical experiment encompassing various fields of science and technology.

Following (Berdichevsky and Dmitriev, 1991, 2002; Zhdanov, 2002), we consider inverse problems of magnetotellurics in light of Tikhonov's theory of regularization, which provides a basis for developing the strategy of MT and MV inversions.

10.4.1 Conditionally Well-Posed Formulation of the Inverse Problem

The interpretation of an unstable MT or MV inverse problem is meaningful if a priori geological-geophysical information on the region under consideration is used and certain restraints on its geoelectric structure are imposed. This is a way for transforming an unstable problem into a stable one. In the absence of a priori information restricting the scope of search, we can obtain only one of equivalent models or, at best, a model with a significantly smoothed distribution of conductivity leveling out contrasts of sought-for structures.

Thus, the transformation of an unstable problem into a stable one is accomplished by restricting the scope of search. Before searching, we have to decide where we are searching and what we are searching for (Goltsman, 1971). Otherwise, our interpretation will remind a Russian fairy tale whose hero was told: "Go there no one knows where and bring somewhat no one knows what".

Considering a set Σ_δ of equivalent solutions, we choose a *compact subset* Σ_δ^C containing the exact model solution and consisting of solutions that are sufficiently close to the exact model solution (recall that a functional set is compact if any sequence of functions in this set contains a subsequence converging to a function also belonging to this set – the necessary condition of compactness of a set is its boundedness). The theory of regularization is based on the Tikhonov theorem on the stability of an inverse problem defined on compact subset (Tikhonov and Arsenin, 1977; Berdichevsky and Dmitriev, 2002). This theorem is formulated as follows: if the error δ in the initial information tends to zero, the solution of the inverse problem on a compact subset Σ_δ^C converges to the exact model solution. An ill-posed inverse problem that has an unique solution and is stable on the compact subset Σ_δ^C is called *conditionally well-posed problem* (or well-posed after Tikhonov), and the subset Σ_δ^C is called a *correctness set*. Thus, the inverse problem, which is ill-posed after Hadamard, becomes well-posed after Tikhonov.

The compact subset Σ_δ^C (the correctness set) is chosen on a basis of a priori geological and geophysical information and constraints obtained directly from the qualitative analysis of the observation data and hypotheses tests that help to localize and identify geoelectric structures.

What we want to stress is that a new geoelectric model is evolved from previous geological and geophysical models. The solution of an MT or MV inverse problem is efficient if magnetotellurics gives a new information as compared to what was known before MT and MV observations.

In defining the correctness set, i.e., in imposing restraints on the geoelectric structure of the medium, one should keep in mind that the condition $\delta \to 0$ is unrealizable in practice, because any initial information obtained by processing field measurements is never free from errors. Therefore, we should speak of the practical stability of a conditionally well-posed problem. The problem with real errors δ is regarded as practically stable if the correctness set consists of plausible solutions which are sufficiently close to the exact model solution.

Here arises a paradoxical situation. The narrower the correctness set is, the more stable will be the inverse problem. The more stable is the inverse problem, the higher is its resolution, but the poorer is the detailedness of its solutions. The resolution of the inverse problem and the detailedness of its solutions appear to be antagonistic. We call this situation the *paradox of instability*. Desiring to improve the detailedness of an inversion, we extend the correctness set. But as a consequence, the resolution is decreased and the practical stability deteriorates. Thus, the details of the inversion may be lost in errors. It is clear that in solving an inverse problem, it is vital to find the optimal relation between detailedness and resolution. The detailedness of an inversion must be correlated with the resolution.

The correctness set, in which the solution to the inverse problem is sought for, forms an *interpretation model*. The latter should incorporate ideas (hypotheses) on the Earth's stratification and local and regional structures disturbing this stratification.

The interpretation models of magnetotellurics are divided into two classes: (1) *quasi-homogeneous layered models*, (2) *locally inhomogeneous layered models* (Fig. 10.4).

A quasi-homogeneous layered model consists of a finite number of infinite or pinching-out layers. In this model class, the electrical conductivities of layers and their boundaries slowly vary in horizontal directions (easy dipping, gentle folding). A very important feature of the quasi-homogeneous layered models is the presence of high-resistivity layers playing the role of galvanic screens. The screening effect characterized by the galvanic parameter of the model determines the intensity of near-surface galvanic anomalies and the sensitivity of the magnetotelluric sounding to deep conductive structures.

A locally inhomogeneous layered model consists of a finite number of layers with breaks and sharp variations of their conductivity and boundaries. It may include

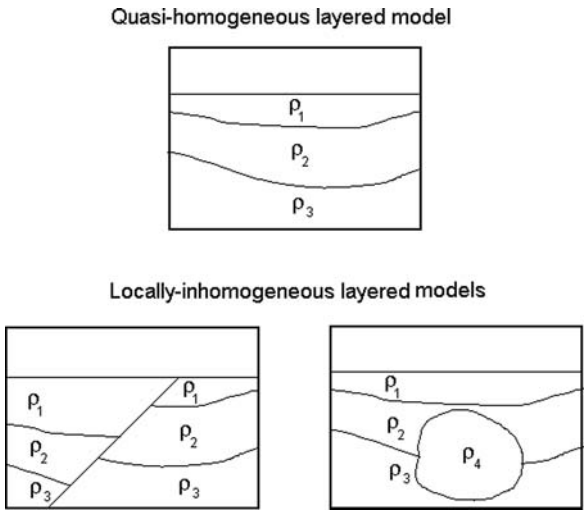

Fig. 10.4 Quasi-homogeneous and locally-inhomogeneous layered models

discontinuities, displacements, subductions, intersections, bounded inclusions and channels of more or less complicated geometry.

The interpretation model should meet the following two requirements: (1) it should be simple (being determined by a small number of free parameters that ensure the practical stability of the inverse problem), and (2) it should be informative (reflecting main properties of the geoelectric medium and containing target layers and structures). These conditions are opposite: the simpler is the model, the less informative it is. Here the paradox of instability manifests itself. Thus, we have to choose an optimal model, that is, it should be reasonably informative yet sufficiently simple. The detailedness of an inversion should be provided by the resolution of the inverse problem.This is a crucial point of the interpretation, predetermining not only the strategy for inversion, but also, to some degree, its result. At this stage of interpretation, the factors such as intuition of a researcher, his professional skill and academic experience, his understanding of the actual geological situation and goals of the MT survey, his adherence to traditions and willingness to deviate from these traditions – all plays a role.

Constructing an interpretation model, a researcher is limited by a priori information and by results of qualitative analysis of field measurements as well as by hypotheses tests. Just in this sense we say that the interpretation of MT and MV data is effective under the condition of sufficiently reasonable constrains. The statement "the better we know the medium under consideration, the better we can determine its geoelectric structure" seems paradoxical. But it actually means that, solving the inverse problem, we improve and widen our knowledge of the Earth's structure, and therefore, the better is this structure known, the more meaningful and detailed are the new results.

The amount of a priori information required for constructing an optimal interpretation model depends on the complexity of the medium and on the goals of the interpretation. Whereas rather detailed a priori information on tectonics and geodynamics are required in rift or subduction zones, only very general ideas on the Earth's stratification are sufficient for stable platforms with gentle folding.

Moreover, we can reject a priori information at the preliminary stage of interpretation and perform the smoothing Occam inversion. This simple transformation provides a gross geoelectric regionalization helpful for the identification of zones of interest for further interpretation.

Tikhonov's theory of ill-posed problems offers two basic approaches to the interpretation of MT and MV data: (1) *optimization method*, and (2) *regularization method* (Berdichevsky and Dmitriev, 1991, 2002). We briefly describe these approaches.

10.4.2 Optimization Method

This approach is effective in studying simple media, described by a small number of parameters. Return to inverse problem (10.1) and assume that available a priori information constrains a sufficiently narrow compact set M of admissible solutions

including the exact model solution. Let values of the impedance tensor $[\tilde{\mathbf{Z}}]$ and the tipper $\tilde{\mathbf{W}}$ be known from observations. Then we can determine the approximate solutions $\tilde{\sigma}^Z(x, y, z)$ and $\tilde{\sigma}^W(x, y, z)$ of problem (10.1) by minimizing the *misfit functionals*:

$$\begin{aligned} \mathrm{I}^Z\{\tilde{\sigma}^Z\} &= \left\|[\tilde{\mathbf{Z}}] - [\mathbf{Z}\{x, y, z = 0, \omega, \tilde{\sigma}^Z(x, y, z)\}]\right\| \\ &= \inf_{\sigma \in M} \left\|[\tilde{\mathbf{Z}}] - [\mathbf{Z}\{x, y, z = 0, \omega, \sigma(x, y, z)\}]\right\| \\ \mathrm{I}^W\{\tilde{\sigma}^W\} &= \left\|\tilde{\mathbf{W}} - \mathbf{W}\{x, y, z = 0, \omega, \tilde{\sigma}^W(x, y, z)\}\right\| \\ &= \inf_{\sigma \in M} \left\|\tilde{\mathbf{W}} - \mathbf{W}\{x, y, z = 0, \omega, \sigma(x, y, z)\}\right\| . \end{aligned} \tag{10.61}$$

The misfit minimization procedure is usually iterative. A starting model is constructed through the parametrization of the interpretation model. Solving the forward problem for the starting model, we calculate the misfits between model and experimental values of the impedance tensor and the tipper.Then a new model, decreasing the misfits, is chosen. The iterations are performed until the misfits approach the level of errors in the initial values of $[\tilde{\mathbf{Z}}]$ and $\tilde{\mathbf{W}}$. If the misfits cannot be decreased to the level of errors in the initial data, this implies that the compact set M is overly narrow. In this case, we test successively widening compacta (e.g., we increase the density of subdivision of the model). A compactum on which the equation misfit is equal to the error in initial data is regarded as an optimal compact set. However, an overly wide compactum makes the problem unstable and can yield a solution that differs strongly from the exact model solution. This limits the practicality of the optimization method.

It is obvious that separate inversions of the impedance and the tipper make sense if solutions $\tilde{\sigma}^Z(x, y, z)$ and $\tilde{\sigma}^W(x, y, z)$ are close to each other. Otherwise magnetotelluric and magnetovariational inversions call for correlation. We can, for instance, carry out the magnetotelluric and magnetovariational inversions in parallel, minimizing the functional of total misfit

$$\begin{aligned} \mathrm{I}\{\sigma(x, y, z)\} = g_Z \left\|[\tilde{\mathbf{Z}}] - [\mathbf{Z}\{x, y, z = 0, \omega, \sigma(x, y, z)\}]\right\|^2 \\ + g_W \left\|\tilde{\mathbf{W}} - \mathbf{W}\{x, y, z = 0, \omega, \sigma(x, y, z)\}\right\|^2 \end{aligned} \tag{10.62}$$

and controlling the contributions of magnetotelluric and magnetovariational inversions by means of weights, g_Z and g_W. Alternatively, we can accomplish successive partial inversions, minimizing the functionals of magnetotelluric and magnetovariational misfits

$$\begin{aligned} \mathrm{I}^Z\{\sigma(x, y, z)\} &= \left\|[\tilde{\mathbf{Z}}] - [\mathbf{Z}\{x, y, z = 0, \omega, \sigma(x, y, z)\}]\right\|^2 \\ \mathrm{I}^W\{\sigma(x, y, z)\} &= \left\|\tilde{\mathbf{W}} - \mathbf{W}\{x, y, z = 0, \omega, \sigma(x, y, z)\}\right\|^2 . \end{aligned} \tag{10.63}$$

Adopting this strategy, we start with magnetovariational inversions, which is free from distorting effects of local near-surface inhomogeneities, and then proceed to magnetotelluric inversion with a starting model, constructed from the results of magnetovariational inversion.

10.4.3 Regularization Method

Regularization of solutions substantially widens the possibilities of interpretation. Given a sufficient amount of a priori information, this approach provides maximum geoelectric information consistent with the accuracy of field observations and modeling. The main peculiarity of the *regularization method* is that criterion for choosing an approximate solution is included directly in the algorithm of inversion. When solving the inverse problem, the compactum M narrows around the exact model solution. The regularization method admits the introduction of any type of a priori information with control of its influence on the solution of the inverse problem. What is more, the regularization method enables one to focus the inversion on the target layers and structures.

This approach is based on the *regularization principle*: the criterion for the selection of solution should be such that the inferred approximate solution tends to the exact model solution of the inverse problem, when the errors in the initial information tend to zero. The regularization principle for MT (1.1*a*) and MV (1.1*b*) inversions takes the form

$$\begin{aligned} \lim_{\delta_Z \to 0} \hat{\sigma}^Z(x, y, z) &= \hat{\sigma}^Z(x, y, z), \\ \lim_{\delta_W \to 0} \hat{\sigma}^W(x, y, z) &= \hat{\sigma}^W(x, y, z), \end{aligned} \tag{10.64}$$

where $\hat{\sigma}^Z$, $\hat{\sigma}^W$ and $\hat{\sigma}^Z$, $\hat{\sigma}^W$ are approximate and exact model solutions of MT and MV problems, and δ_Z, δ_W are errors in the initial data.

The regularization principle is implemented with the help of a *regularizing operator*. The regularizing operator R of an inverse problem is referred to as a set of analytical and numerical operations that allows one to obtain an approximate solution satisfying the regularization principle. In inverse problems of geophysics, it is advantageous to use a regularizing operator R depending on a numerical parameter $\alpha > 0$, which is called the *regularization parameter*. As the error δ in the initial data tends to zero, the regularization parameter α should also tend to zero:

$$\begin{aligned} &\lim_{\delta_Z \to 0} \alpha \to 0 \qquad \text{MT inversion} \\ &\lim_{\delta_W \to 0} \alpha \to 0 \qquad \text{MV inversion} \end{aligned} \tag{10.65}$$

and the regularizing operator, when applied to the approximate response function, should yield the exact model solution.

$$\begin{aligned} &\lim_{\delta_Z \to 0} R_\alpha[\tilde{\mathbf{Z}}] = \bar{\sigma}^Z(x.y, z) \quad \text{MT inversion} \\ &\lim_{\delta_W \to 0} R_\alpha \tilde{\mathbf{W}} = \bar{\sigma}^W(x, y, z) \quad \text{MV inversion} \end{aligned} \tag{10.66}$$

The magnetotelluric and magnetovariational inversions reduce to constructing the regularizing operator R_α and determining the regularization parameter α consistent with the accuracy of observations. The approximation solution obtained in this way is stable with respect to errors in the initial data. It is called a *regularized solution*.

Variational methods of constructing the regularizing operator are most widespread in geophysics. A *stabilizing functional* (*stabilizer*), providing a criterion for the selection of admissible solutions, plays a key role in this approach. The stabilizer is usually written in the form

$$\Omega\{\sigma(x, y, z)\} \le C, \tag{10.67}$$

where C is a positive constant. The functional $\Omega\{\sigma(x, y, z)\}$ determines a compact set of functions $\sigma(x, y, z) \in \Sigma_C$. The smaller the value of C, the narrower the set Σ_C. Introducing (10.67), inverse problem (1.1) is formulated as a variational problem for a conditional extremum:

$$\begin{cases} \inf \Omega\{\sigma(x, y, z)\} \\ \left\| [\tilde{\mathbf{Z}}] - [\mathbf{Z}\{x, y, z = 0, \omega, \sigma(x, y, z)\}] \right\| \le \delta_Z \qquad a \\ \left\| \tilde{\mathbf{W}} - \mathbf{W}\{x, y, z = 0, \omega, \sigma(x, y, z)\} \right\| \le \delta_W. \qquad b \end{cases} \tag{10.68}$$

So, we find a minimum compactum Σ_C consisting of functions $\sigma(x, y, z)$ that satisfy conditions (10.68*a*) and (10.68*b*). The set Σ of approximate solutions to such an inverse problem is the intersection of the compactum Σ_C with the sets Σ_{δ_Z} and Σ_{δ_W} of equivalent solutions of MT and MV inverse problems:

$$\Sigma = \Sigma_C \cap \Sigma_{\delta_Z} \cap \Sigma_{\delta_W}. \tag{10.69}$$

It is convenient to replace the conditional-extremum problem by the unconditional-extremum problem:

$$\inf \Phi_\alpha\{\sigma(x, y, z)\}, \tag{10.70}$$

where Φ_α is the *Tikhonov regularizing functional*,

$$\Phi_\alpha\{\sigma(x, y, z)\} = \mathrm{I}\{\sigma(x, y, z)\} + \alpha\Omega\{\sigma(x, y, z)\}, \tag{10.71}$$

consisting of the misfit functional $I(\sigma)$ and the stabilizing functional $\Omega(\sigma)$. The solution of this inverse problem reduces to the minimization of $\Phi_\alpha(\sigma)$, that is, to the minimization of $I(\sigma)$ and $\Omega(\sigma)$. Whereas the initial problem (10.1) is unstable, the solution obtained by minimizing the functional Φ_α is stable with respect to small variations in $[\tilde{\mathbf{Z}}]$ and $\tilde{\mathbf{W}}$. The point is that the functional $\Omega(\sigma)$ narrows the class of possible solutions and stabilizes the problem. It is given the name the stabilizer.

The structure of the misfit functional $I(\sigma)$ depends on the inversion strategy. It can be a functional (10.62) of total misfit, when carrying out the magnetotelluric and magnetovariational inversions in parallel, or fuctionals (10.63) of partiall misfits, when accomplishing successive inversions.

The structure of the stabilizing functional $\Omega(\sigma)$ depends on a priori restraints imposed on the inverse problem. It can be, for example, the requirement of smoothness of $\sigma(x, y, z)$ satisfied by minimizing the functional

$$\Omega(\sigma) = \iiint\limits_V \left\{ \left(\frac{\partial \sigma}{\partial x}\right)^2 + \left(\frac{\partial \sigma}{\partial y}\right)^2 + \left(\frac{\partial \sigma}{\partial z}\right)^2 \right\} dxdydz \tag{10.72}$$

or the requirement of closeness of $\sigma(x, y, z)$ to a hypothetical model $\sigma_0(x, y, z)$ satisfied by minimizing the functional

$$\Omega(\sigma) = \iiint\limits_V \{\sigma(x, y, z) - \sigma_0(x, y, z)\}^2 dxdydz. \tag{10.73}$$

The weight of the stabilizing functional, i.e., the degree of its effect on the solution of an inverse problem, is controlled by the regularization parameter α (Fig. 10.5). At large α, the minimization of $\Phi_\alpha(\sigma)$ leads to the dominating minimization of $\Omega(\sigma)$, i.e., oversmoothes the solution or retains it near the a priori

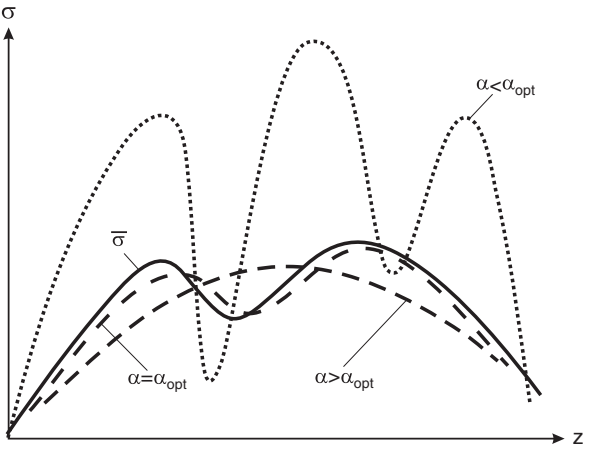

Fig. 10.5 Dependence of the solution of an inverse problem on the regularization parameter α; $\bar{\sigma}$ is an exact model solution

hypothetical model, ignoring results of observations. At small α, the minimization of $\Phi_\alpha(\sigma)$ leads to the dominating minimization of $I(\sigma)$, i.e., the stabilizing effect of $\Omega(\sigma)$ is suppressed and an unstable incorrect solution is obtained. An optimum value of α providing a sufficiently small misfit and ensuring sufficiently strong stabilization of the solution is to be found.

The regularization parameter α should be consistent with the error δ in the initial information. The optimum value of α can be chosen by testing a monotonically decreasing sequence $\alpha_1 > \alpha_2 > \ldots > \alpha_n$. For each α, variational problem (10.70) is solved and the iterative sequence of solutions characterized by their misfit is determined. The parameter $\alpha = \alpha_{opt}$, at which the misfit attains the error δ in the initial data, is regarded as an optimum parameter. The optimum parameter of regularization provides a conductivity distribution fitting best the exact model solution. This simple technique is applicable if the error δ is well known. However, we commonly have a more or less gross estimate:

$$\delta_{\min} \leq \delta \leq \delta_{\max}. \tag{10.74}$$

In this case, solutions consistent with various values of δ from interval (10.74) are tested. Close solutions selected from the resulting set are averaged, providing an approximation to the exact model solution.

If we know next to nothing of measurement and model errors, the parameter α_{opt} cannot be chosen by the knowledge of solution misfits. In this case, a quasi-optimal value of the regularization parameter is determined. For example, α_{opt} can be defined as a value α at which the solution of the problem significantly deviates from requirements of the stabilizer (smoothness or closeness to the hypothetical model) but yet remains sufficiently stable. This heuristic method for the determination of α_{opt} was proposed by Hansen (1998). It is based on the so-called L-representation. A monotonically decreasing sequence of regularization parameters $\alpha_1 > \alpha_2 > \ldots > \alpha_n$ is tested and the misfit I_α and the stabilizer Ω_α are determined for various α and a fixed minimum of Tikhonov's functional Φ_α. Figure 10.6 presents the curve of Ω_α versus I_α on a log–log scale. This curve has typically the L-shaped form, with a fairly distinct bend separating a nearly horizontal branch with large I_α and small Ω_α from a nearly vertical branch with small I_α and large Ω_α. The exact model solution is best approximated by assuming that the central point of the bend, characterized by the largest curvature, defines the quasi-optimal parameter of regularization, α_{opt}.

10.4.4 A Few Words About the Backus–Gilbert Method

A description of the Backus–Gilbert method usually begins with the following statements (Backus and Gilbert, 1968). The number of observations is always finite, but the characteristics of the medium cannot be represented a priori by a finite number of parameters. If the space of the observation data is finite-dimensional but the space of

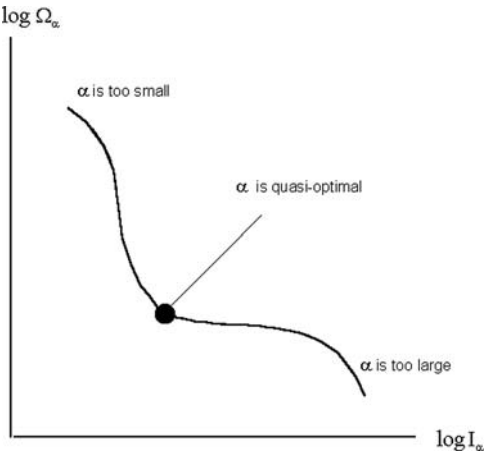

Fig. 10.6 The L-representation

the Earth's parameters is infinite-dimensional, the inverse problem is indeterminate, that is, it has an infinite number of solutions. Indeterminacy (to be more precise, underdeterminancy) of the inverse problem holds even for ideally accurate initial data. However, if it is not possible to obtain an exact solution to the problem, it is possible to find a smoothed (locally averaged) characteristic of the medium which for a given set of observed quantities is determined uniquely and provides the best approximation to the parameters of the desired model. Thus, emphasis is placed on the construction of an optimal smoothing operator having the properties of a spatial filter.

The theory of Backus and Gilbert is sometimes opposed to the Tikhonov theory of ill-posed problems. It is said that the Backus–Gilbert method is designed for underdetermined problems with limited number of sufficiently accurate initial data, whereas the Tikhonov method is presented to problems that may have a unique solution but they are unstable because of inaccuracy in the initial data. Is such a demarcation justified? With interpolation and extrapolation, a set of discrete samplings can be represented as a continuous function approximating the true field characteristic, and then an underdetermined problem reduces to a problem that is unstable due to errors of approximation. It seems that the theory of Backus and Gilbert may by considered as an integral part of the general theory of ill-posed problems.

10.4.5 Probabilistic Statement of the Inverse Problem

The inverse problem (10.1), (10.2) can be stated in probabilistic terms (Goltsman, 1971; Kovtun, 1980; Tarantola and Valette, 1982; Yanovskaja and Porokhova, 1983; Glasko, 1984; Tarantola, 1987; Backus, 1988; Spichak, 1999, 2005). It seems that the probabilistic approach involving the powerful methods of the probability theory and statistics may give a simple and convenient tools for solving inverse problems of magnetotellurics and analyzing solutions obtained.

Which of approaches – deterministic or probabilistic – is the more general? The question sounds a bit scholastic, inasmuch as the two approaches have a common philosophy. The point is that in the probabilistic formulation the inverse problem remains unstable and still needs the regularization, which directly does not follow from probabilistic formalism. Obviously, the principle definitions for the probabilistic inverse problem should be derived from the general theory of regularization.

Let us come back to operator equations (10.1). In a general form we can write

$$\mathrm{F}\{x, y, z = 0, \omega, \sigma(x, y, z)\} = \tilde{\mathrm{F}}, \tag{10.75}$$

where F is an operator of the forward problem, which depends parametrically on x, y, ω and calculates the tensor or vector response function F from a given electrical conductivity $\sigma(x, y, z)$, and $\tilde{\mathrm{F}}$ is this response function determined on the sets of observation points $M(x, y)$ and frequencies ω with error δ.

We will begin with the principle of regularization, which in the deterministic terms is expressed by (10.64). These equations can be readily rewritten in probabilistic terms. Concerning (10.75), we write

$$\lim_{\delta \to 0} P\{\|\tilde{\sigma} - \bar{\sigma}\| > \varepsilon\} = 0, \tag{10.76}$$

where P is the probability that the error of the solution (the deviation of approximate solutions $\tilde{\sigma}$ from the exact model solution $\bar{\sigma}$) is larger than an arbitrarily small positive number ε. Equation (10.76) expresses the stochastic principle of regularization. An inversion operator constructed on the basis of this principle is called a *stochastically regularizing operator.*

To exemplify the construction of the stochastically regularizing operator, we consider the *method of maximum likelihood* (Goltsman, 1971; Kovtun, 1980; Yanovskaja and Porokhova, 1983).

Following Goltsman (1971), we introduce the *likelihood function* as:

$$l(\sigma) = \ln p(\sigma) p_{\sigma}(\tilde{\mathrm{F}}), \tag{10.77}$$

where $p(\sigma)$ is the density of the a priori (unconditional) probability of the solution σ and $p_{\sigma}(\tilde{\mathrm{F}})$ is the density of the a posteriori (conditional) probability of a response function $\tilde{\mathrm{F}}$ for the given conductivity distribution σ. It is reasonable to think that if a solution σ comes into being , the probability of this event is fairly great. We can go a bit further and suppose that the most probable event characterized by the maximum likelihood is the advent of a solution σ that is close to the exact model solution $\bar{\sigma}$. This heuristic consideration says that the approximate solution to the problem (10.75) can be found from the condition for the maximum likelihood function

$$l(\tilde{\sigma}) = \sup_{\sigma \in \Sigma_{\delta}} l(\sigma) \tag{10.78}$$

One cannot say that we know the statistics of errors δ in the initial data well. However, we can restrict ourselves to considering the measurement errors and accept the normal (Gaussian) probability distribution for the function $\tilde{\mathrm{F}}$:

$$p_\sigma(\tilde{\mathrm{F}}) = \frac{1}{s_\mathrm{F}\sqrt{2\pi}} \exp\left\langle -\frac{\left\|\tilde{\mathrm{F}} - \mathrm{F}\{\sigma\}\right\|^2}{2s_\mathrm{F}^2} \right\rangle, \tag{10.79}$$

where s_F is the root-mean-square (standard) deviation of $\tilde{\mathrm{F}}$.

The situation with statistical description of the Earth's conductivitiy,σ, is even worse. Here our information is very limited, and depending on a priori data, we can rely on more or less reasonable hypotheses. Let us show some examples.

1. If a priori information about the medium is rather scanty, then all we can do is to assume that σ is distributed uniformly over an infinite space Σ_δ. But then, the inverse problem is unstable and its statement (no matter, deterministic or probabilistic) makes no sense.

2. Let a priori information available allow us to assume that σ belongs to a compact set $M \in \Sigma_\delta$, and that it is distributed in this set with uniform density

$$p(\sigma) = \begin{cases} const \neq 0 & \sigma \in M \\ 0 & \sigma \notin M. \end{cases} \tag{10.80}$$

Then

$$\ell(\sigma) = \ln \frac{const}{s_\mathrm{F}\sqrt{2\pi}} - \frac{\left\|\tilde{\mathrm{F}} - \mathrm{F}\{\sigma\}\right\|^2}{2s_\mathrm{F}^2}. \tag{10.81}$$

In this case, the condition for maximum likelihood (10.78) reduces to equation

$$\left\|\tilde{\mathbf{F}} - \mathbf{F}(\tilde{\sigma})\right\| = \inf_{\sigma \in M} \left\|\tilde{\mathbf{F}} - \mathbf{F}(\sigma)\right\|. \tag{10.82}$$

implying the minimization of the misfit functional

$$\mathrm{I} = \left\|\tilde{\mathrm{F}} - \mathrm{F}\{\sigma\}\right\|^2 \tag{10.83}$$

as in the optimization method. The problem is conditionally correct and can be solved directly by the optimization method, using (10.62) or (10.63).

3. Now, let us suppose that the existing a priori information is sufficient for constructing a hypothetical conductivity distribution σ_0, which belongs to a compact set $M \subset \Sigma_\delta$. The requirement for the desired solution σ is that it must be close to σ_0 (in probabilistic sense !). We will express this requirement in terms of the normal distribution

$$p(\sigma) = \frac{1}{s_\sigma\sqrt{2\pi}} \exp\left\langle -\frac{\|\sigma - \sigma_0\|^2}{2s_\sigma^2} \right\rangle, \tag{10.84}$$

where s_σ is the root-mean-square (standard) deviation of σ. Introduce a parameter α, which is equal to the ratio of variances D for the $\tilde{F}$ and σ:

$$\alpha = \frac{D_{\tilde{F}}}{D_\sigma} = \frac{s^2_{\tilde{F}}}{s^2_\sigma}. \tag{10.85}$$

Then

$$\ell(\sigma) = \ln \frac{1}{2\pi s_{\tilde{F}} s_\sigma} - \frac{1}{2s^2_{\tilde{F}}} \Phi_\alpha(\sigma), \tag{10.86}$$

where

$$\Phi_\alpha(\sigma) = \left\| \tilde{\mathrm{F}} - \mathrm{F}\{\sigma\} \right\|^2 + \alpha \left\| \sigma - \sigma_0 \right\|^2. \tag{10.87}$$

In this case the condition for maximum likelihood (10.78) reduces to equation

$$\Phi_\alpha(\tilde{\sigma}) = \inf_{\sigma \in M} \Phi_\alpha(\sigma) \tag{10.88}$$

implying the minimization of Tikhonov's functional $\Phi_\alpha(\sigma)$ as in the regularization method. Here the functional $\Phi_\alpha(\sigma)$ consists of the misfit functional I and the stabilizing functional Ω with the regularization parameter α:

$$\Phi_\alpha(\alpha) = \mathrm{I} + \alpha\Omega$$
$$\mathrm{I} = \left\| \tilde{\mathrm{F}} - \mathrm{F}\{\sigma\} \right\|^2 \qquad \Omega = \left\| \sigma - \sigma_0 \right\|^2 \qquad \alpha = s^2_{\tilde{F}} / s^2_\sigma.$$

The problem is conditionally correct and can be solved directly by the regularization method, using (10.71).

We see that the maximum likelihood method leads to the same algorithms as in the deterministic approach. A similar conclusion can be made for the *Bayesian inversion* based on the Bayes theorem of hypotheses (Zhdanov, 2002). If we limit our consideration to the inversion of MT and MV data, the advantage of probabilistic approaches is not obvious. However, these approaches using the powerful methods of the modern probability theory and statistics do give a simple and convenient tool for analyzing a solution obtained.

10.5 Comparison Criteria

To compare magnetotelluric and magnetovariational response functions and determine their misfits, we use some special criteria taking into account the pequliarities of the inverse problems of magnetotellurics. The comparison criteria must be constructed so that the contributions of data with a similar amount of information will be the same. The point is that periods, T, as well as apparent resistivities, ρ_A, and moduli of impedances, $|Z|$, can vary over several orders of magnitude. By virtue of the principle of similitude, the ranges with similar relative variations of these values

carry similar amounts of information. Therefore, for a uniform comparison, it is best to represent T and ρ_A, $|Z|$ in bilogarithmic coordinates $\ln T$ and $\ln \rho_A$, $\ln |Z|$. At the same time, phases of impedances, $\arg Z$, as well as real and imaginary parts of the tipper, Re W and Im W, should be represented in a space with logarithmic abscissas $\ln T$ and arithmetic ordinates $\arg Z$ and Re W, Im W.

Let us begin with the one-dimensional inversion. Consider the Tikhonov–Cagniard impedance in bilogarithmic representation:

$$\ln Z(\ln T) = \ln |Z(\ln T)|\, e^{i \arg Z(\ln T)} = \ln |Z(\ln T)| + i \arg Z(\ln T). \tag{10.89}$$

Assume that this function determining a relationship between $\ln Z$ and $\ln T$ belongs to the metric function R – norm. Thus, we introduce the R – norm for the impedance $Z(T)$:

$$\|Z(T)\|_R^2 = \|\ln Z(\ln T)\|_{L_2}^2 = \|\ln |Z(\ln T)|\|_{L_2}^2 + \|\arg Z(\ln T)\|_{L_2.}^2 \tag{10.90}$$

Compare impedances $\tilde{Z}(T)$ and $Z(T)$ obtained from the field measurements and model computations. In the R – norm, the distance between these impedances, determining the impedance misfit, is expressed as

$$\begin{aligned}
&\left\| \tilde{Z}(T) - Z(T) \right\|_R^2 \\
&= \left\| \ln \left| \tilde{Z}(\ln T) \right| - \ln |Z(\ln T)| \right\|_{L_2}^2 + \left\| \arg \tilde{Z}(\ln T) - \arg Z(\ln T) \right\|_{L_2}^2 \\
&= \int_{T_{\min}}^{T_{\max}} \left\{ \left[\ln \frac{\left| \tilde{Z}(\ln T) \right|}{|Z(\ln T)|} \right]^2 + \left[\arg \tilde{Z}(\ln T) - \arg Z(\ln T) \right]^2 \right\} \frac{dT}{T},
\end{aligned} \tag{10.91}$$

where $T_{\min}$ and $T_{\max}$ are minimal and maximal periods bounding the observation interval. This equation defines the impedance metric in the R – norm.

In practice, the impedance is measured over a finite number of periods $T_1,\ T_2, \ldots T_{M-1},\ T_M$, where $T_1 = T_{\min}$, $T_M = T_{\max}$. On integrating (10.91) by trapezoid rule, we get

$$\begin{aligned}
\left\| \tilde{Z}(T) - Z(T) \right\|_R^2 = {} & \frac{1}{2} \left\{ \left[\ln \left| \frac{\tilde{Z}(\ln T_1)}{Z(\ln T_1)} \right| \right]^2 + [\arg \tilde{Z}(\ln T_1) - \arg Z(\ln T_1)]^2 \right\} \ln \frac{T_2}{T_1} \\
& + \frac{1}{2} \sum_{m=2}^{M-1} \left\{ \left[\ln \left| \frac{\tilde{Z}(\ln T_m)}{Z(\ln T_m)} \right| \right]^2 + [\arg \tilde{Z}(\ln T_m) - \arg Z(\ln T_m)]^2 \right\} \ln \frac{T_{m+1}}{T_{m-1}} \\
& + \frac{1}{2} \left\{ \left[\ln \left| \frac{\tilde{Z}(\ln T_M)}{Z(\ln T_M)} \right| \right]^2 + [\arg \tilde{Z}(\ln T_M) - \arg Z(\ln T_M)]^2 \right\} \ln \frac{T_M}{T_{M-1}}.
\end{aligned} \tag{10.92}$$

Let the impedances $\tilde{Z}(T)$ and $Z(T)$ be obtained on a logarithmic uniform grid

$$T_m = \gamma^{m-1} T_{\min}\,,\ \ \gamma > 1,\ \ m \in [1,\ M]. \tag{10.93}$$

Then,

$$\begin{aligned}\left\|\tilde{Z}(T) - Z(T)\right\|_R^2 = {} & \frac{1}{2}\ln\gamma\left\{\left[\ln\left|\frac{\tilde{Z}(\ln T_1)}{Z(\ln T_1)}\right|\right]^2 + [\arg\tilde{Z}(\ln T_1) - \arg Z(\ln T_1)]^2\right\} \\ & + \ln\gamma\sum_{m=2}^{M-1}\left\{\left[\ln\left|\frac{\tilde{Z}(\ln T_m)}{Z(\ln T_m)}\right|\right]^2 + [\arg\tilde{Z}(\ln T_m) - \arg Z(\ln T_m)]^2\right\} \\ & + \frac{1}{2}\ln\gamma\left\{\left[\ln\left|\frac{\tilde{Z}(\ln T_M)}{Z(\ln T_M)}\right|\right]^2 + [\arg\tilde{Z}(\ln T_M) - \arg Z(\ln T_M)]^2\right\},\end{aligned} \tag{10.94}$$

where $\ln\gamma$ is a distance between adjacent measurements.

Similarly, we can define R – norm for the admittance:

$$\|Y(T)\|_R^2 = \|\ln Y(\ln T)\|_{L_2}^2 = \|\ln|Y(\ln T)|\|_{L_2}^2 + \|\arg Y(\ln T)\|_{L_2}^2.\,. \tag{10.95}$$

The admittance metric (misfit) is defined as

$$\begin{aligned}&\left\|\tilde{Y}(T) - Y(T)\right\|_R^2 \\ &= \left\|\ln\left|\tilde{Y}(\ln T)\right| - \ln|Y(\ln T)|\right\|_{L_2}^2 + \left\|\arg\tilde{Y}(\ln T) - \arg Y(\ln T)\right\|_{L_2}^2 \\ &= \int_{T_{\min}}^{T_{\max}}\left\{\left[\ln\left|\frac{\tilde{Y}(\ln T)}{Y(\ln T)}\right|\right]^2 + \left[\arg\tilde{Y}(\ln T) - \arg Y(\ln T)\right]^2\right\}\frac{dT}{T},\end{aligned} \tag{10.96}$$

where $\tilde{Y}(T)$ and $Y(T)$ are admittances obtained from the field measurements and model computations. In discrete representation we write

$$\begin{aligned}\left\|\tilde{Y}(T) - Y(T)\right\|_R^2 = {} & \frac{1}{2}\left\{\left[\ln\left|\frac{\tilde{Y}(\ln T_1)}{Y(\ln T_1)}\right|\right]^2 + [\arg\tilde{Y}(\ln T_1) - \arg Y(\ln T_1)]^2\right\}\ln\frac{T_2}{T_1} \\ & + \frac{1}{2}\sum_{m=2}^{M-1}\left\{\left[\ln\left|\frac{\tilde{Y}(\ln T_m)}{Y(\ln T_m)}\right|\right]^2 + [\arg\tilde{Y}(\ln T_m) - \arg Y(\ln T_m)]^2\right\}\ln\frac{T_{m+1}}{T_{m-1}} \\ & + \frac{1}{2}\left\{\left[\ln\left|\frac{\tilde{Y}(\ln T_M)}{Y(\ln T_M)}\right|\right]^2 + [\arg\tilde{Y}(\ln T_M) - \arg Y(\ln T_M)]^2\right\}\ln\frac{T_M}{T_{M-1}},\end{aligned} \tag{10.97}$$

where $T_1 = T_{\min}$ and $T_M = T_{\max}$. On a logarithmic uniform grid (10.93), we have

$$\left\|\tilde{Y}(T)-Y(T)\right\|_R^2=\frac{1}{2}\ln\gamma\left\{\left[\ln\left|\frac{\tilde{Y}(\ln T_1)}{Y(\ln T_1)}\right|\right]^2+[\arg\tilde{Y}(\ln T_1)-\arg Y(\ln T_1)]^2\right\}$$
$$+\ln\gamma\sum_{m=2}^{M-1}\left\{\left[\ln\left|\frac{\tilde{Y}(\ln T_m)}{Y(\ln T_m)}\right|\right]^2+[\arg\tilde{Y}(\ln T_m)-\arg Y(\ln T_m)]^2\right\}$$
$$+\frac{1}{2}\ln\gamma\left\{\left[\ln\left|\frac{\tilde{Y}(\ln T_M)}{Y(\ln T_M)}\right|\right]^2+[\arg\tilde{Y}(\ln T_M)-\arg Y(\ln T_M)]^2\right\}. \tag{10.98}$$

Note that in the function space R the impedance and admittance metrics coincide:

$$\left\|\tilde{Z}(T)-Z(T)\right\|_R^2=\left\|\tilde{Y}(T)-Y(T)\right\|_R^2. \tag{10.99}$$

Let us supplement the impedance and impedance metrics with the apparent-resistivity metrics. By analogy with (10.91) and (10.92), we get

$$\|\tilde{\rho}_{\mathrm{A}}(T)-\rho_{\mathrm{A}}(T)\|_R^2=\int_{T_{\min}}^{T_{\max}}\left[\ln\frac{\tilde{\rho}_{\mathrm{A}}(\ln T)}{\rho_{\mathrm{A}}(\ln T)}\right]^2\frac{dT}{T}$$
$$+\frac{1}{2}\left\{\left[\ln\frac{\tilde{\rho}_{\mathrm{A}}(\ln T_1)}{\rho_{\mathrm{A}}(\ln T_1)}\right]^2\ln\frac{T_2}{T_1}+\sum_{m=2}^{M-1}\left[\ln\frac{\tilde{\rho}_{\mathrm{A}}(\ln T_m)}{\rho_{\mathrm{A}}(\ln T_m)}\right]^2\ln\frac{T_{m+1}}{T_{m-1}}+\frac{1}{2}\left[\ln\frac{\tilde{\rho}_{\mathrm{A}}(\ln T_M)}{\rho_{\mathrm{A}}(\ln T_M)}\right]^2\ln\frac{T_M}{T_{M-1}}\right\}, \tag{10.100}$$

where $\tilde{\rho}_{\mathrm{A}}$ and ρ_{A} are apparent resistivities obtained from the field measurements and model computations and $T_1=T_{\min}$, $T_M=T_{\max}$. On a logarithmic uniform grid (10.93), the apparent-resistivity misfit takes the form

$$\|\tilde{\rho}_{\mathrm{A}}(T)-\rho_{\mathrm{A}}(T)\|_R^2=\ln\gamma\left\{\frac{1}{2}\left[\ln\frac{\tilde{\rho}_{\mathrm{A}}(\ln T_1)}{\rho_{\mathrm{A}}(\ln T_1)}\right]^2+\sum_{m=2}^{M-1}\left[\ln\frac{\tilde{\rho}_{\mathrm{A}}(\ln T_m)}{\rho_{\mathrm{A}}(\ln T_m)}\right]^2+\frac{1}{2}\left[\ln\frac{\tilde{\rho}_{\mathrm{A}}(\ln T_M)}{\rho_{\mathrm{A}}(\ln T_M)}\right]^2\right\}. \tag{10.101}$$

When $\tilde{\rho}_{\mathrm{A}}$ comes close to ρ_{A}, we have

$$\left[\ln\frac{\tilde{\rho}_{\mathrm{A}}}{\rho_{\mathrm{A}}}\right]^2=\left[\ln(1+\frac{\tilde{\rho}_{\mathrm{A}}-\rho_{\mathrm{A}}}{\rho_{\mathrm{A}}})\right]^2\approx\left[\frac{\tilde{\rho}_{\mathrm{A}}-\rho_{\mathrm{A}}}{\rho_{\mathrm{A}}}\right]^2. \tag{10.102}$$

Using such an approximation, we consider the apparent-resistivity misfit as a quadratic sum of partial relative misfits with a factor $\ln\gamma$. The similar approximation is valid for logarithmic misfit of the impedance or admittance.

Going over to the general case of the three-dimensional inversion, we introduce coordinates x, y of the observation sites and define the impedance and admittance tensors, $[\mathbf{Z}]$ and $[\mathbf{Y}]$, the tipper, $\mathbf{W}$, and the apparent resistivity, ρ_{A}, in the function space R.

We have

$$\begin{aligned}
\ln Z(x, y, \ln T) &= \ln |Z(x, y, \ln T)|\, e^{i \arg Z(x, y, \ln T)} = \ln |Z(x, y, \ln T)| + i \arg Z(x, y, \ln T) \\
\ln Y(x, y, \ln T) &= \ln |Y(x, y, \ln T)|\, e^{i \arg Y(x, y, \ln T)} = \ln |Y(x, y, \ln T)| + i \arg Y(x, y, \ln T) \\
W(x, y, \ln T) &= \operatorname{Re} W(x, y, \ln T) + i \operatorname{Im} W(x, y, \ln T) \\
&\quad \ln \rho_{\mathrm{A}}(x, y, \ln T),
\end{aligned} \tag{10.103}$$

where Z is a component of the tensor $[\mathbf{Z}]$ (for instance, Z_{xy}) or its scalar invariant (for instance, $Z_{\mathrm{eff}} = \sqrt{Z_{xx} Z_{yy} - Z_{xy} Z_{yx}}$), Y is a component of the tensor $[\mathbf{Y}]$ (for instance, Y_{xy}) or its scalar invariant that reduces to the Tikhonov–Cagnard admittance in the 1D-model (for instance, $Y_{\mathrm{eff}} = \sqrt{Y_{xx} Y_{yy} - Y_{xy} Y_{yx}}$), W is a component of the tipper $\mathbf{W}$ (for instance, W_{zx}) or its scalar invariant (for instance, $W = \sqrt{W_{zx}^2 + W_{zy}^2}$), ρ_{A} is a component of the apparent resistivity (for instance, ρ_{xy}) or one of its scalar invariant (for instance, $\rho_{\mathrm{eff}} = |Z_{\mathrm{eff}}|^2 / \omega \mu_{\mathrm{o}}$).

The impedance, admittance, tipper and apparent-resistivities metrics (misfits) are defined as

$$\begin{aligned}
&\left\| \tilde{Z}(x, y, T) - Z(x, y, T) \right\|_R^2 \\
&= \int_X \int_Y \int_{T_{\min}}^{T_{\max}} \left\{ \left[\ln \frac{\left| \tilde{Z}(x, y, \ln T) \right|}{|Z(x, y, \ln T)|} \right]^2 + [\arg \tilde{Z}(x, y, \ln T) - \arg Z(x, y, \ln T)]^2 \right\} \frac{dT}{T} dy dx
\end{aligned} \tag{10.104}$$

$$\begin{aligned}
&\left\| \tilde{Y}(x, y, T) - Y(x, y, T) \right\|_R^2 \\
&= \int_X \int_Y \int_{T_{\min}}^{T_{\max}} \left\{ \left[\ln \frac{\left| \tilde{Y}(x, y, \ln T) \right|}{|Y(x, y, \ln T)|} \right]^2 + [\arg \tilde{Y}(x, y, \ln T) - \arg Y(x, y, \ln T)]^2 \right\} \frac{dT}{T} dy dx
\end{aligned} \tag{10.105}$$

$$\begin{aligned}
&\left\| \tilde{W}(x, y, T) - W(x, y, T) \right\|_R^2 \\
&= \int_X \int_Y \int_{T_{\min}}^{T_{\max}} [\operatorname{Re} \tilde{W}(x, y, \ln T) - \operatorname{Re} W(x, y, \ln T)]^2 \frac{dT}{T} dy dx \\
&\quad + \int_X \int_Y \int_{T_{\min}}^{T_{\max}} [\operatorname{Im} \tilde{W}(x, y, \ln T) - \operatorname{Im} W(x, y, \ln T)]^2 \frac{dT}{T} dy dx
\end{aligned} \tag{10.106}$$

$$\|\tilde{\rho}_{\mathrm{A}}(x, y, T) - \rho_{\mathrm{A}}(x, y, T)\|_R^2 = \int_X \int_Y \int_{T_{\min}}^{T_{\max}} \left[\ln \frac{\tilde{\rho}_{\mathrm{A}}(x, y, \ln T)}{\rho_{\mathrm{A}}(x, y, \ln T)}\right]^2 \frac{dT}{T} dy dx. \quad (10.107)$$

These misfits are readily written in the discrete form. As an example, consider the apparent-resistivity misfit

$$\begin{aligned}\|\tilde{\rho}_{\mathrm{A}}(x, y, T) - \rho_{\mathrm{A}}(x, y, T)\|_R^2 = {} & \frac{1}{2} \sum_{k=1}^{K} \sum_{l=1}^{L} \left[\ln \frac{\tilde{\rho}_{\mathrm{A}}(x_k, y_l, \ln T_1)}{\rho_{\mathrm{A}}(x_k, y_l, \ln T_1)}\right]^2 \ln \frac{T_2}{T_1} \\ & + \frac{1}{2} \sum_{k=1}^{K} \sum_{l=1}^{L} \sum_{m=2}^{M-1} \left[\ln \frac{\tilde{\rho}_{\mathrm{A}}(x_k, y_l, \ln T_m)}{\rho_{\mathrm{A}}(x_k, y_l, \ln T_m)}\right]^2 \ln \frac{T_{m+1}}{T_{m-1}} \\ & + \frac{1}{2} \sum_{k=1}^{K} \sum_{l=1}^{L} \left[\ln \frac{\tilde{\rho}_{\mathrm{A}}(x_k, y_l, \ln T_M)}{\rho_{\mathrm{A}}(x_k, y_l, \ln T_M)}\right]^2 \ln \frac{T_M}{T_{M-1}},\end{aligned} \quad (10.108)$$

where $k \in [1, K]$, $l \in [1, L]$, $m \in [2, M-1]$, $T_1 = T_{\min}$, $T_M = T_{\max}$.

It is self-evident that since the misfits of magnetotelluric and magnetovariational response functions are expressed in the metric of the function space R, the inaccuracies δ of the initial data (measurement and model errors) must be expressed in the same metric. Take, for instance, the apparent-resistivity misfit specified in the space R by (10.107), (10.108). We will compare this misfit with an error δ_ρ of the same structure. Following (10.102), we determine δ_ρ by relative deviations of apparent resistivities:

$$\begin{aligned}\delta_\rho^2 = {} & \int_X \int_Y \int_{T_{\min}}^{T_{\max}} \left[\frac{\Delta\rho_{\mathrm{A}}(x, y, \ln T)}{\rho_{\mathrm{A}}(x, y, \ln T)}\right]^2 \frac{dT}{T} dy dx \\ = {} & \frac{1}{2} \sum_{k=1}^{K} \sum_{l=1}^{L} \left[\frac{\Delta\rho_{\mathrm{A}}(x_k, y_l, \ln T_1)}{\rho_{\mathrm{A}}(x_k, y_l, \ln T_1)}\right]^2 \ln \frac{T_2}{T_1} \\ & + \frac{1}{2} \sum_{k=1}^{K} \sum_{l=1}^{L} \sum_{m=2}^{M-1} \left[\frac{\Delta\rho_{\mathrm{A}}(x_k, y_l, \ln T_m)}{\rho_{\mathrm{A}}(x_k, y_l, \ln T_m)}\right]^2 \ln \frac{T_{m+1}}{T_{m-1}} \\ & + \frac{1}{2} \sum_{k=1}^{K} \sum_{l=1}^{L} \left[\frac{\Delta\rho_{\mathrm{A}}(x_k, y_l, \ln T_M)}{\rho_{\mathrm{A}}(x_k, y_l, \ln T_M)}\right]^2 \ln \frac{T_M}{T_{M-1}},\end{aligned} \quad (10.109)$$

where $k \in [1, K]$, $l \in [1, L]$, $m \in [2, M-1]$, $T_1 = T_{\min}$, $T_M = T_{\max}$.

Next we turn to comparison of geoelectric media. These criteria must stress the influence of those characteristics of the medium that reflect best of all the objective structures and contribute most significantly to the response functions. In this respect, the electrical conductivity is at premium. Magnetotellurics has enhanced sensitivity

to conductors. It is directed for the most part to studies of conductive zones (ore deposits, hydrothermas, reservoirs, fluid-saturated layers and faults, fractured areas, dehydration areas, graphitization and melting areas). Within these zones, the electric conductivity may increase up to several orders.There is good reason to believe that geoelectric media considered in MT and MV studies should be compared just by their conductivity $\sigma(x, y, z)$.

In comparing distributions of $\sigma^{(1)}(x, y, z)$ and $\sigma^{(2)}(x, y, z)$ we use the L_2 – norm

$$\left\|\sigma^{(1)}(x, y, z) - \sigma^{(2)}(x, y, z)\right\|_{L_2}^2 = \iiint\limits_V p(z)\left\{\sigma^{(1)}(x, y, z) - \sigma^{(2)}(x, y, z)\right\}^2 dV, \tag{10.110}$$

where $p(z)$ is a weight function that decreases monotonically with depth (reflecting the decrease of sounding resolution).

In the case of peacewise constant distributions of $\sigma^{(1)}(x, y, z)$ and $\sigma^{(2)}(x, y, z)$, we can introduce a D – norm summing the conductivity deviations over the homogeneous blocks:

$$\left\|\sigma^{(1)}(x, y, z) - \sigma^{(2)}(x, y, z)\right\|_D^2 = \sum_{l=1}^{L}\sum_{m=1}^{M}\sum_{n=1}^{N} p_n\left\{\sigma_{lmn}^{(1)} - \sigma_{lmn}^{(2)}\right\}^2, \tag{10.111}$$

where indices l, m, n define the distribution of the blocks in x, y, z, and p_n is a monotonically decreasing factor that reflects the decrease of sounding resolution with depth.

Chapter 11
The Interpretation Model

Interpretation of the magnetotelluric and magnetovariational data starts with constructing an *interpretation model*. It is composed on the basis of a priory geological and geophysical information and plausible hypotheses. And great consideration is given to the analysis of magnetotelluric and magnetovariational response functions and their rough tentative inversions. Summing up different evidences (lithologic, petrophysical, tectonic, geodynamic, seismic, geothermic, geoelectric), we create reasonable qualitative image of the medium under consideration and constrain a model class, within which the solution of the inverse problem is sought for. The interpretation model should take into account the aim and the area of the search, that is, designate the target objects, which we are going to find, and characterize (at least presumably) the host medium, in which these objects are to be found. Just at this stage of interpretation we form the correctness set (a set of geophysically meaningful solutions) and transform the ill-posed unstable inverse problem into a conditionally well-posed stable one. Just at this stage of interpretation we compose an optimal grid for the inversion of field data, choose the normal background and starting values of resistivities (conductivities), suggest the strategy of solution of the inverse problem.

To get the trustworthy and sufficiently complete magnetotelluric indications necessary for constructing the adequate interpretation model we examine and remove the static distortions of the apparent resistivities caused by near-surface inhomogeneities.

11.1 Analyzing the Static Distortions

The static distortions caused by near-surface inhomogeneities extend over the whole low-frequencies range and severely plague the interpretation of the apparent-resistiviy curves, generating false geoelectric structures.

In Part II of our book we considered a few models illustrating two kinds of the static distortions: the $S-$effect caused by variations in the conductance S of the upper layer underlaid with resistive bedding and the $\rho-$effect caused by small

M. Berdichevsky, V.I. Dmitriev, *Models and Methods of Magnetotellurics*,
DOI 10.1007/978-3-540-77814-1_11, © Springer-Verlag Berlin Heidelberg 2008

surface inhomogeneities of higher or lower resistivity ρ. Now we are going to review the current state of the art in this field and consider some techniques for correcting the apparent-resistivity curves distorted by static effects.

Static effects are observed in the period range $T > T_s$, where the skin-depth is much larger than the dimensions of the inhomogeneity. At these periods the local induction dies out and galvanic anomalous field caused by charges becomes quasi-static. Anomalies of this kind manifest themselves in the vertical shift of the bilogarithmic apparent-resistivity curves. The shape of the shifted curves and corresponding section of the phase curves remain unchanged. The initial period T_s depends on the dimensions and position of the causative inhomogeneity (Berdichevsky and Dmitriev, 1976; Jones, 1988; Vozoff, 1991; Singer, 1992; Weaver, 1994; Zhdanov and Keller, 1994; Berdichevsky and Dmitriev, 2002).

11.1.1 Recognising the Static Distortions

To recognize and evaluate the static shift of the apparent-resistivity curves ρ_A, we need some references. It would be natural to measure the static shift of ρ_A-curve from the locally normal ρ_n-curve calculated for the observation site. Unfortunately such estimation is possible only in theory. In practice, we can correlate adjacent ρ_A-curves or use some references derived from frequency, transient or magnetovariatonal soundings.

Let us start with the *S*-effect. Figure 11.1 shows a two-dimensional model composed of an inhomogeneous upper layer (sediments) underlaid with a horizontally homogeneous layered substratum (the crust and upper mantle). The sediments contain several 20 km wide sections with stepwise twofold increase in the resistivity. The sediments conductance varies from 100 to 2.5 S. The substratum consists of a thick resistive strata (the lithosphere) and a highly conductive basement (the asthenosphere). The resistive lithosphere includes a crustal conductive layer.

The transverse apparent-resistivity curves obtained in this model are presented in Fig. 11.2. They have two maxima which are separated by a distinct minimum reflecting the crustal conductive layer. As the upper-layer conductance decreases from 100 S at site 1 to 2.5 S at site 6, the $\rho^{\perp}$-curves with their ascending and descending branches move conformally upwards, holding the same two-humped shape. But note that the ascending branches which carry information on the upper-layer conductance merge with the locally normal ρ_n-curves. These branches are slightly distorted. Their one-dimensional inversion gives adequate values of *S*. At the same time the descending branches carrying information on the conductive basement are dramatically distorted. They are shifted from the locally normal ρ_n-curves. The vertical shift amounts up to 2.5 decades. It is easy to imagine what a crazy substratum would be obtained by one-dimensional inversion of these branches.

Let us estimate the intensity of the *S*-effect. Figure 11.3 shows the correlation between apparent resistivities $\rho^{\perp}(\sqrt{T} = 100\,\mathrm{s}^{1/2})$ and $\rho^{\perp}(\sqrt{T} = 1\,\mathrm{s}^{1/2})$ related

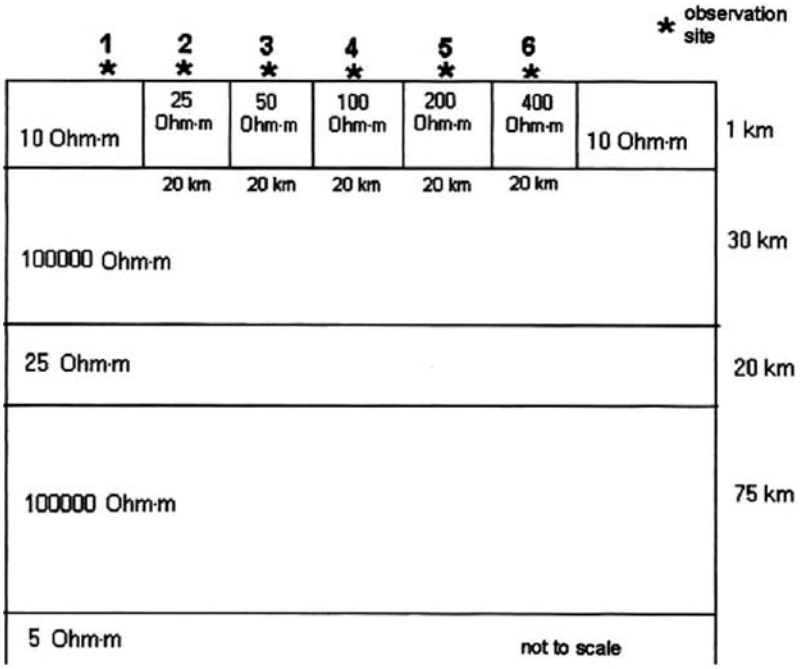

Fig. 11.1 Two-dimensional model of the *S*-effect

to descending and ascending branches of the $\rho^{\perp}$-curves. The graph is plotted to bilogarithmic scale. It is approximated by a straight line with inclination close to 45°. Thus, a relationship between $\rho^{\perp}(\sqrt{T} = 100\,\mathrm{s}^{1/2})$ and $\rho^{\perp}(\sqrt{T} = 1\,\mathrm{s}^{1/2})$ can be represented as

$$\begin{aligned} \rho^{\perp}(\sqrt{T} = 100\,\mathrm{s}^{1/2}) &\approx C\rho^{\perp}(\sqrt{T} = 1\,\mathrm{s}^{1/2}) \\ \log\rho^{\perp}(\sqrt{T} = 100\,\mathrm{s}^{1/2}) &\approx \log C + \log\rho^{\perp}(\sqrt{T} = 1\,\mathrm{s}^{1/2}), \end{aligned} \tag{11.1}$$

where C is a constant. This relation indicates a strong $S-$ effect (due to high resistivity of the substratum underlying the inhomogeneous upper layer). It is easy to verify that a decrease in the substratum resistivity weakens the $S-$effect and this manifests itself in diminishing the regression inclination.

The transverse phase curves are exhibited in Fig. 11.4. Their high-frequency ascending and low-frequency descending branches are close to the locally-normal φ_{n}-curves being slightly distorted. However, in the middle-frequency range they depart from the locally normal φ_n-curves and this distortion amounts up to 50°.

It is important to find the initial period T_{s} of the static shift (a period separating the distorted descending branch of the $\rho^{\perp}$-curves from their undistorted ascending branch). A good indicator can be given by the phase curves. Have a look at

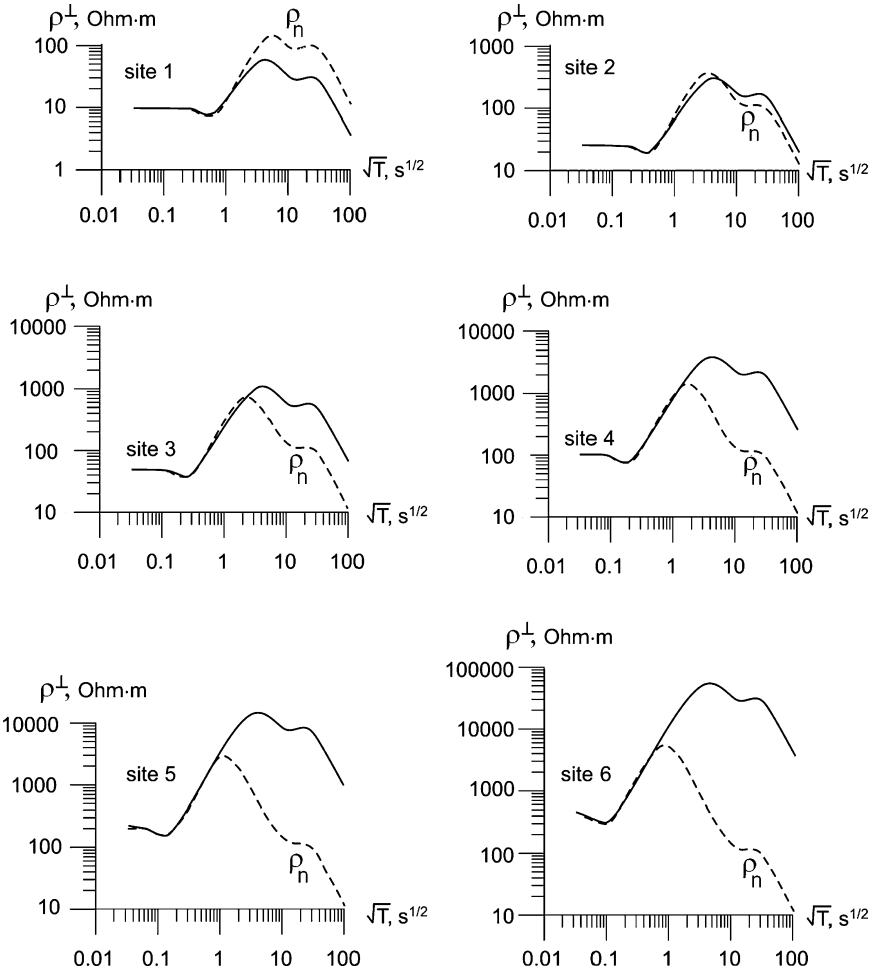

Fig. 11.2 Transverse apparent-resistivity curves in the model of the *S*-effect from Fig. 11.1

Fig. 11.5. The adjacent $\varphi^{\perp}$-curves diverge within a range of the slightly distorted high-frequency branches of the $\rho^{\perp}$-curves, but they come together within a range of the statically shifted low-frequency branches of these curves. So, the initial period T_s of the *S*-effect can be evaluated as a boundary between zones with diverged and converged phase curves. Using this indication in the case under consideration, we get $T_s \approx 9$ s.

Now consider the $\rho-$ effect. The case is illustrated in Fig. 11.6. Here the upper layer contains a two-dimensional small outcropped inclusion, 10 m thick and 120 m wide, consisting of conductive and resistive sections, while the host medium is the same as in the previous model given in Fig. 11.1. The transverse $\rho^{\perp}$-curves are presented in Fig. 11.7. They show the conspicuous static shift, though variations

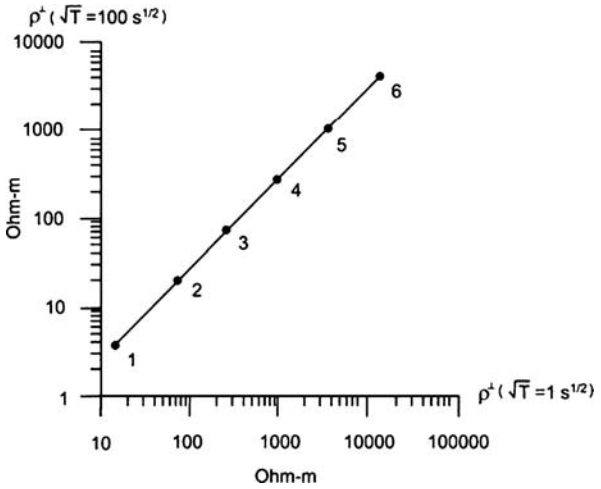

Fig. 11.3 Correlation between the apparent resistivites $\rho^{\perp}(\sqrt{T} = 100\,s^{1/2})$ and $\rho^{\perp}(\sqrt{T} = 1\,s^{1/2})$ related to descending and ascending branches of the $\rho^{\perp}$-curves obtained in the model of the *S*-effect shown in Fig. 11.1; 1, 2, 3. . .- observation sites

in the sediments conductance S_1 do not exceed 10%. The peculiarity of this case is that not only the descending low-frequency branches of the $\rho^{\perp}$-curves, but their ascending high-frequency branches also are shifted vertically from the locally normal ρ_n-curves. One can see that the $\rho^{\perp}$-curves suffer the static distortion over the entire frequency range including the ascending and descending branches, which carry information on the upper layer and substratum. Note that within this frequency range the $\varphi^{\perp}$-curves are not distorted being closely related to the locally normal φ_n-curves (Fig. 11.8). Using the phase indication, that is, marking a boundary between zones with diverged and converged phase curves, we evaluate the initial period of the ρ-effect as $T_s \approx 0.25$ s (Fig. 11.9). Let us give a glance at Fig. 11.10 correlating the descending and ascending branches of the $\rho^{\perp}$-curves. The graph can be approximated by a straight line with inclination close to 45°. Remarkable as it is, the ρ− effect demonstrates the same relations between descending and ascending branches of the $\rho^{\perp}$-curves as the strong *S*− effect.

The above definitions of the *S*− and ρ − effects retain their meaning in the three-dimensional situation. An example of the ρ − effect caused by a three-dimensional outcropped inhomogeneity with random lognormal distribution of resistivities is given in Figs. 11.11 and 11.12. Here the apparent-resistivity curves, ρ_{xy} and ρ_{yx}, with their high-frequency ascending branch and low-frequency two-humped descending branch are conformally scattered about the normal ρ_N-curve. Their static shift embraces 2.5 decades, whereas the corresponding phase curves, φ_{xy} and φ_{yx}, merge with normal φ_N-curve. Correlating the descending and ascending branches of the $\rho_{xy}-$ and $\rho_{yx}-$ curves, we get a graph with inclination close to 45°, which indicates the strong static shift (Fig. 11.13).

Behind the *S*− and ρ− effects are the same physical mechanisms. However, they operate in different frequency intervals and on different spatial scales – so, these

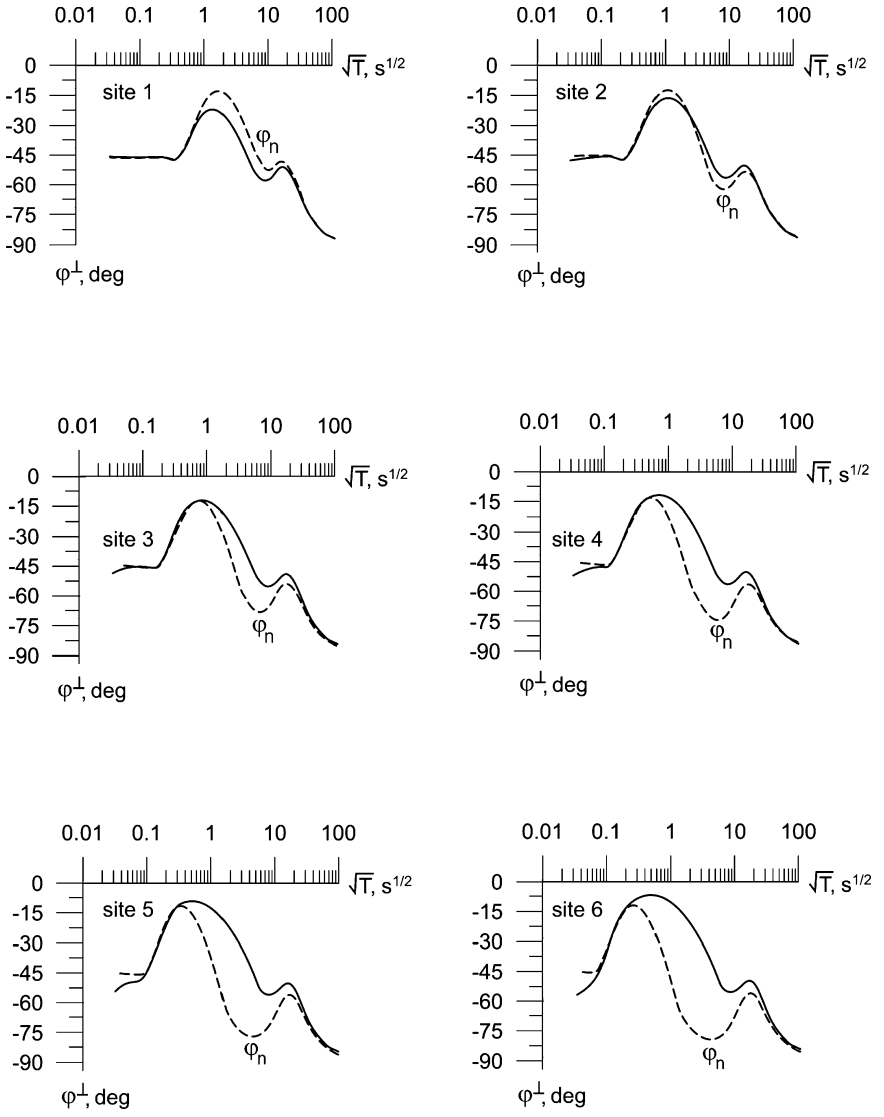

Fig. 11.4 Transverse impedance-phase curves in the model of the *S*-effect shown in Fig. 11.1

effects may differ in manifestation and hence in the correction technique. Consider, for instance, apparent-resistivity curves in a three-layered model with $\rho_2 \gg \rho_1$ and $\rho_3 \ll \rho_2$. When correcting the $S-$ effect, we have to correct only the descending branch of the ρ_A- curves reflecting the depth $h_1 + h_2$. But in the case of the $\rho-$ effect, both the ascending and descending branches of the ρ_A-curves reflecting the conductance S_1 and the depth $h_1 + h_2$ should be corrected. How can we recognize the $S-$ and $\rho-$effects in data? Considering ρ_A-curves, we can hardly tell

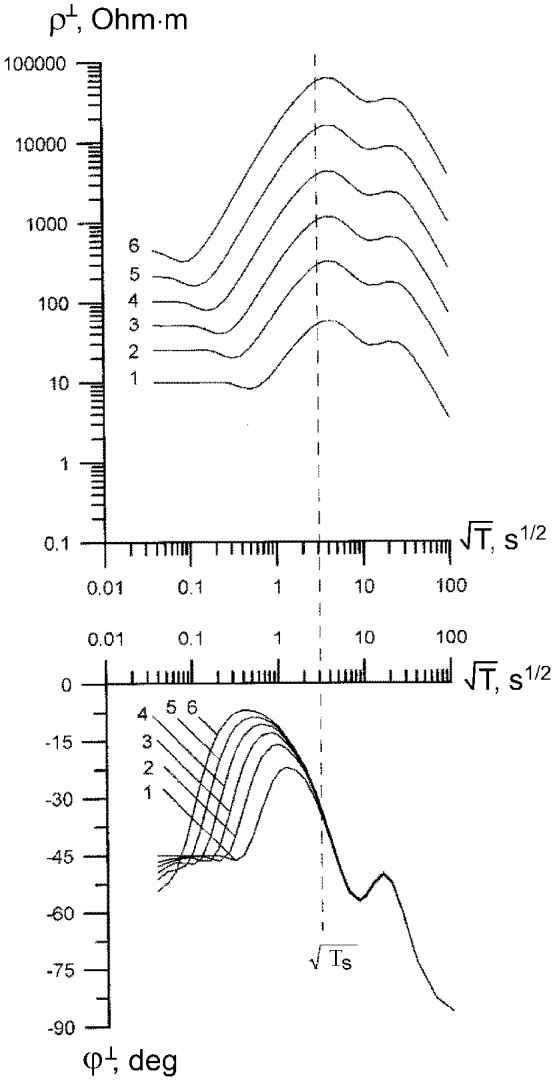

Fig. 11.5 Combined graph of the transverse apparent-resistivity and impedance-phase curves obtained in the model of the *S*-effect shown in Fig. 11.1

the $S-$effect from the $\rho-$effect. The impedance-phase curves are more indicative, since they help to estimate the initial period T_S as a period where adjacent phase curves merge together. So, we can suggest a simple rule for static shift correction. The ρ_A- curves should be corrected for the static shift at periods with coincident phases at the adjacent sites. Other evidences may be found by correlating apparent resistivities $\rho_A-$with sediments conductance S_{sed} determined from frequency and transient soundings or resistivity logging. If, for instance, the ρ_A- values from the low-frequency descending branch of apparent-resistiviry curves correlate with the $S_{sed}-$values, then we can suppose that they are distorted by the $S-$effect. And

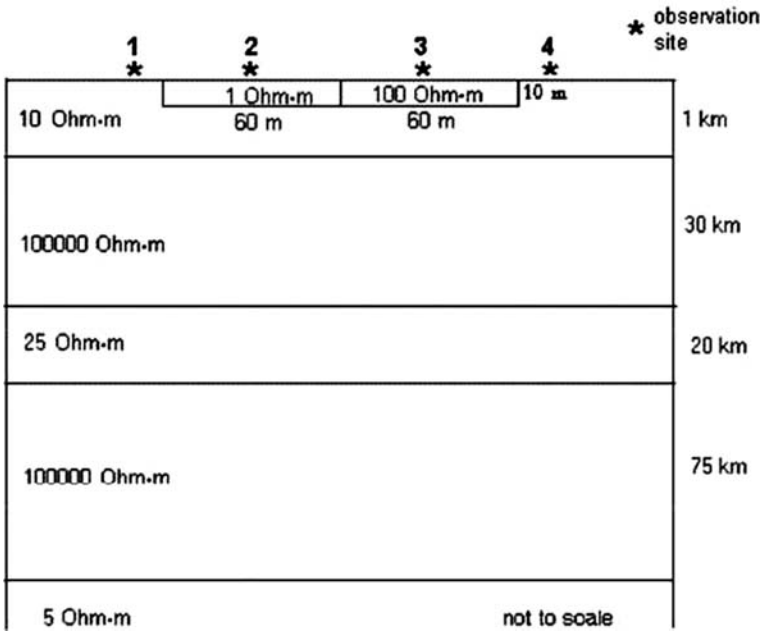

Fig. 11.6 Two-dimensional model of the ρ-effect

conversely, if the ρ_A-values from the high-frequency ascending branch of apparent-resistivity curves do not correlate with the $S_{sed}-$values, then we can suppose that they are distorted by the ρ−effect.

Success of magnetotelluric soundings depends dramatically on the reliability of the static-shift corrections. There is no standard universal remedy for static shift, so the best result can be attained by combining different correction techniques. Modern magnitotellurics offers a variety of methods for the static-shift correction (Larsen, 1977; Bostick, 1984; Jones, 1988; Kaufman, 1988; Berdichevsky et al., 1989b; Pellerin and Hohmann, 1990; Vozoff, 1991; Singer, 1992). These methods use statistical averaging, filtering, fitting to a given reference, and mathematical modeling.

11.1.2 Averaging Apparent Resistivities

A simple statistics for suppressing the ρ−effect has been suggested in (Berdichevsky et al., 1980). Following this paper, we consider the magnitude of the static shift as a random variable with lognormal distribution. Returning to the model shown in Figs. 11.11 and 11.12, we write

$$\rho_{xy}^{(i)} = \delta_{xy}^{(i)}\rho_N \qquad \rho_{yx}^{(i)} = \delta_{yx}^{(i)}\rho_N \qquad i = 1, 2, \ldots 22 \tag{11.2}$$

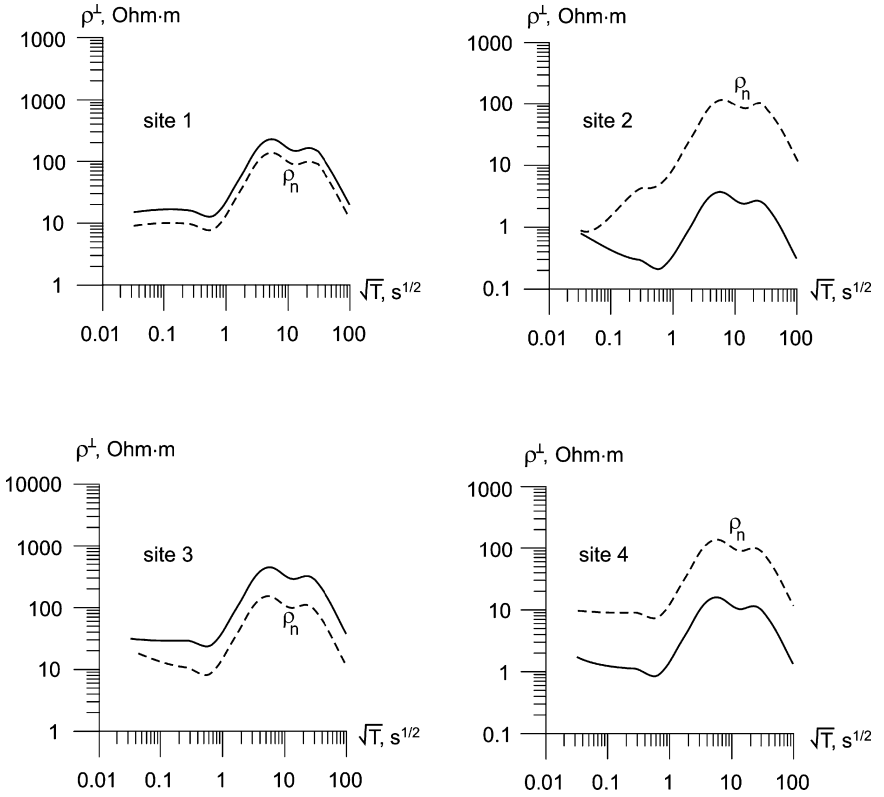

Fig. 11.7 Transverse apparent-resistivity curves in the model of the ρ-effect shown in Fig. 11.6

and

$$\log \rho_{xy}^{(i)} = \log \delta_{xy}^{(i)} + \log \rho_{\mathrm{N}} \quad \log\ \rho_{yx}^{(i)} = \log \delta_{yx}^{(i)} + \log \rho_{\mathrm{N}} \quad i = 1, 2, \ldots 22, \tag{11.3}$$

where $\delta_{xy}^{(i)}$, $\delta_{yx}^{(i)}$ are the real frequency-independent distortion factors in the three-dimensional model of the ρ−effect and i is the site number. Averaging of $\log \rho_{xy}^{(i)}$ and $\log \rho_{yx}^{(i)}$ gives

$$\log \hat{\rho}_{xy} = \frac{1}{22} \sum_{i=1}^{22} \log \rho_{xy}^{(i)} = \frac{1}{22} \sum_{i=1}^{22} \log \delta_{xy}^{(i)} + \log \rho_{\mathrm{N}} = \log \hat{\delta}_{xy} + \log \rho_{\mathrm{N}} \approx \log \rho_{\mathrm{N}}$$

$$\log \hat{\rho}_{yx} = \frac{1}{22} \sum_{i=1}^{22} \log \rho_{yx}^{(i)} = \frac{1}{22} \sum_{i=1}^{22} \log \delta_{yx}^{(i)} + \log \rho_{\mathrm{N}} = \log \hat{\delta}_{yx} + \log \rho_{\mathrm{N}} \approx \log \rho_{\mathrm{N}} \tag{11.4}$$

or

$$\hat{\rho}_{xy} = \hat{\delta}_{xy} \rho_{\mathrm{N}} \qquad \hat{\rho}_{yx} = \hat{\delta}_{yx} \rho_{\mathrm{N}}, \tag{11.5}$$

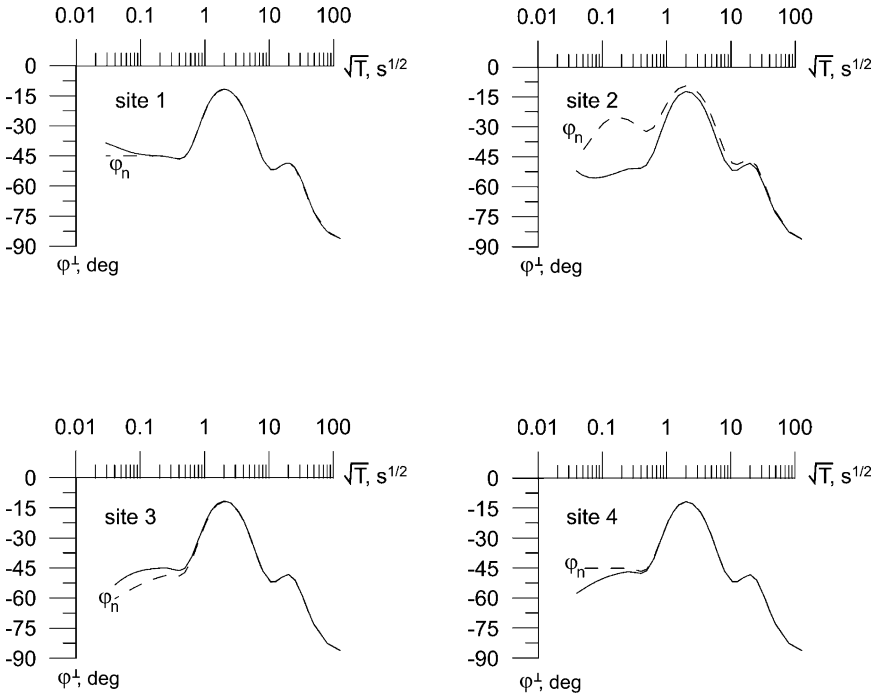

Fig. 11.8 Transverse impedance-phase curves in the model of the ρ -effect shown in Fig. 11.6

where

$$\hat{\rho}_{xy} = \left\{ \prod_{i=1}^{22} \rho_{xy}^{(i)} \right\}^{1/22} \qquad \hat{\delta}_{xy} = \left\{ \prod_{i=1}^{22} \delta_{xy}^{(i)} \right\}^{1/22} \approx 1$$
$$\hat{\rho}_{yx} = \left\{ \prod_{i=1}^{22} \rho_{yx}^{(i)} \right\}^{1/22} \qquad \hat{\delta}_{yx} = \left\{ \prod_{i=1}^{22} \delta_{yx}^{(i)} \right\}^{1/22} \approx 1. \tag{11.6}$$

Figure 11.14 presents the apparent-resistivity curves $\hat{\rho}_{xy}$ and $\hat{\rho}_{yx}$ averaged over 22 sites on the local near-surface inhomogeneity. They are close to the normal ρ_N-curve characterizing the regional background (departure of $\hat{\rho}_{xy}$, $\hat{\rho}_{yx}$ from ρ_N does not exceed 12%). We can say that the averaging removes the geoelectric noise caused by the ρ− effect.

The potentials of statistical suppression of the ρ−effect were clearly demonstrated in the Baikal region (Berdichevsky et al., 1980). Here the apparent-resistivity curves suffer severe local distortions due to near-surface intrusions and permafrost lenses. The area under investigation is divided into vast zones I, II, III,. . . with conformal ρ_{eff}− curves (Fig. 11.15a). Within each zone, the strong static shift covers 1, 2 or even 3 decades (Fig. 11.15b). The immediate inversion of all these chaotically

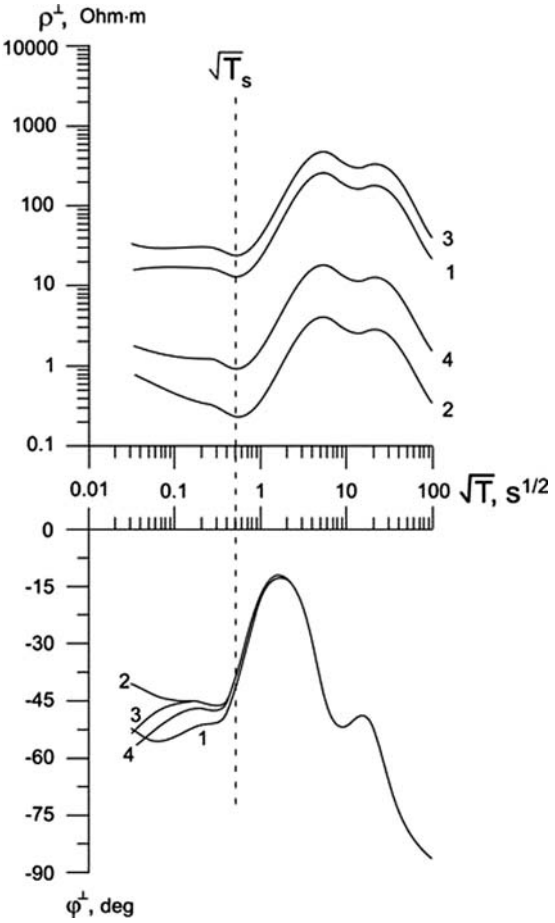

Fig. 11.9 Combined graph of the transverse apparent-resistivity and impedance-phase curves obtained in the model of the ρ-effect shown in Fig. 11.6

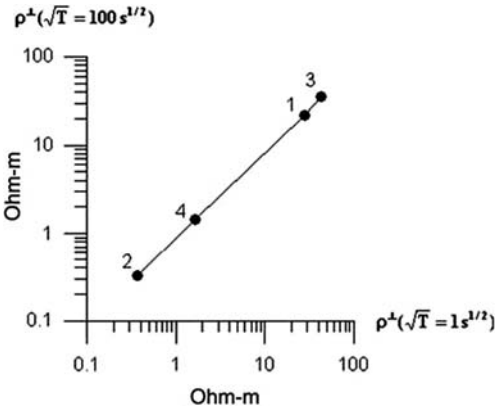

Fig. 11.10 Correlation between the apparent resistivites $\rho^{\perp}(\sqrt{T} = 100\,s^{1/2})$ and $\rho^{\perp}(\sqrt{T} = 1\,s^{1/2})$ related to descending and ascending branches of the $\rho^{\perp}$-curves obtained in the model of the ρ-effect shown in Fig. 11.6; 1, 2, 3, 4 - observation sites

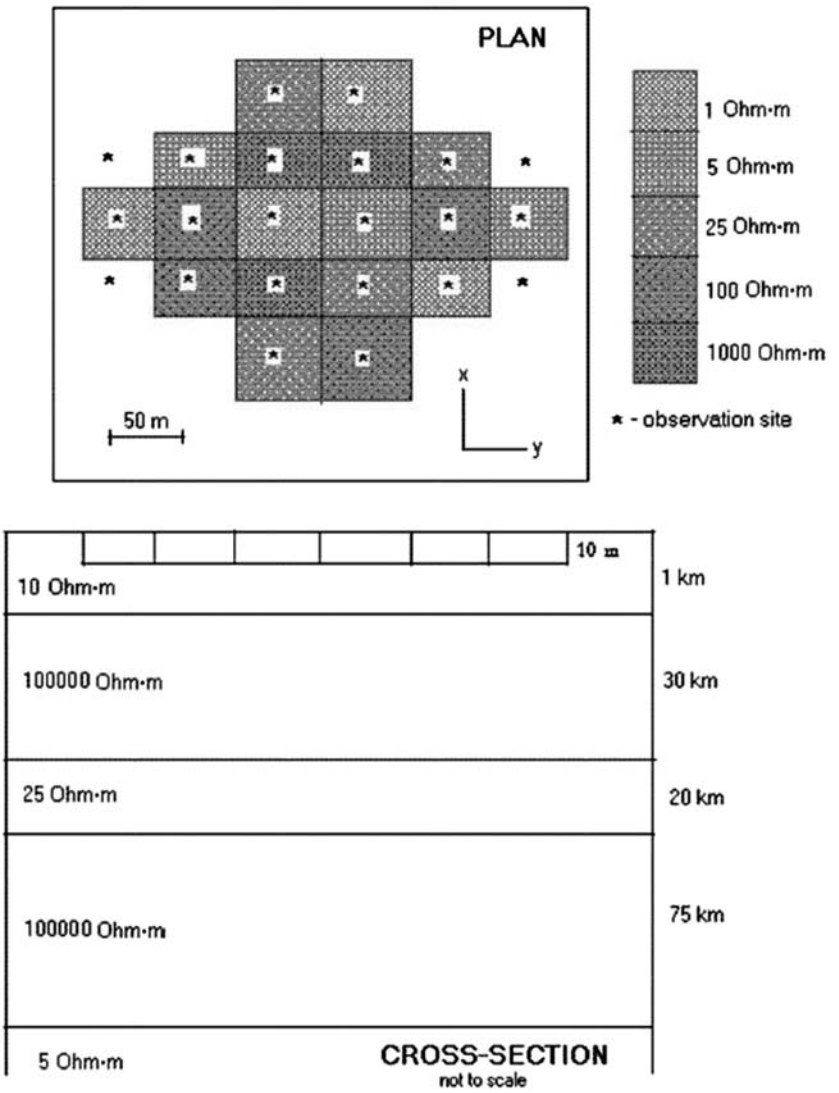

Fig. 11.11 Three-dimensional model of the ρ-effect

scattered MT data is senseless. But in each zone we can average conformal apparent-resistivity curves and get

$$\hat{\rho}_{\text{eff}} = ant \log \left\{ \frac{1}{N} \sum \log \rho_{\text{eff}} \right\}. \tag{11.7}$$

Typical histograms of $\log \rho_{\text{eff}}/\hat{\rho}_{\text{eff}}$ obtained in zones I and III are shown in Fig. 11.16. It is indicative that statistical distributions of $\log \rho_{\text{eff}}$ are fairly well

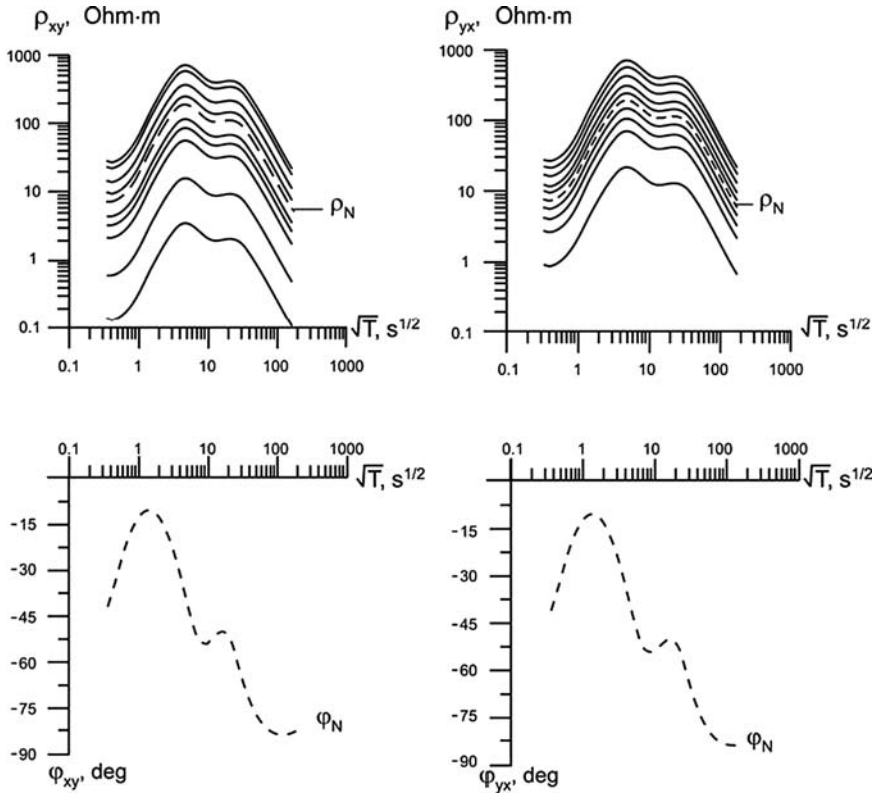

Fig. 11.12 Combined graph of the apparent-resistivity and impedance-phase curves obtained in the model of the ρ-effect shown in Fig. 11.11

approximated by the log-normal low (solid line).When averaging $\log \rho_{\text{eff}}$ over each zone, we get a visibly consistent and geophysically meaningful pattern. The result of the trial one-dimensional inversion of the average $\hat{\rho}_{\text{eff}}$ – curves is presented in Fig. 11.17. On the Siberian platform we find a deep conductive layer with resistivity of 100–200 Ohm·m at a depth from 25 to 40 km. Approaching the Baikal rift, the crustal layer rises and its resistivity diminishes. In the Trans-Baikal zone the depth to the conductor reaches 15 km, whereas the resistivity reduces to 10–15 Ohm·m. So, even at this rough level, we gain an insight into geoelectric structure of the Baikal rift.

11.1.3 Filtering Apparent Resistivities

Generally the spatial spectrum of magnetotelluric responces functions (impedances, apparent resistivities) consists of high frequencies characterizing the non-interpretable geoelectric noise produced by small-scale near-surface

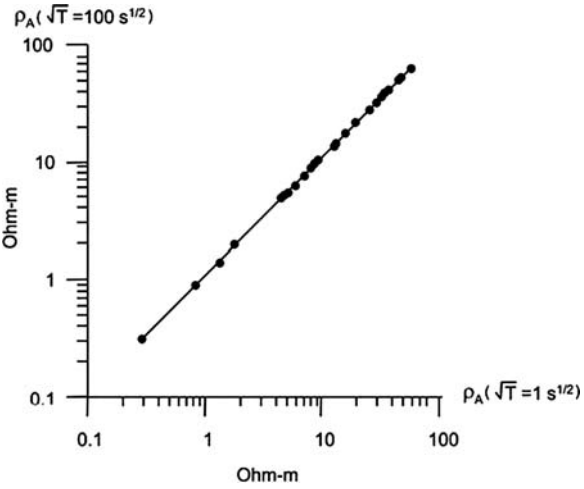

Fig. 11.13 Correlation between the apparent resistivites $\rho_A(\sqrt{T}=100\,s^{1/2})$ and $\rho_A(\sqrt{T}=1\,s^{1/2})$ related to descending and ascending branches of the ρ_A-curves obtained in the model of the ρ-effect shown in Fig. 11.1

inhomogeneities and low frequencies corresponding to the large-scale buried structures of different orders that are the target of MT-survey. In this context, the suppression of the noise reduces to the low-frequency filtration.

A simplest low-frequency filter can be constructed using a low-order polynomials (Kaufman, 1988). As an example, take a filter that smoothes the spatial variations of the effective apparent resistivities:

$$\rho_{\text{eff}}(x) = a_0 + a_1 x + a_2 x^2 \tag{11.8}$$

or

$$\rho_{\text{eff}}(x, y) = a_0 + a_1 x + a_2 y + a_3 x^2 + a_4 xy + a_5 y^2, \tag{11.9}$$

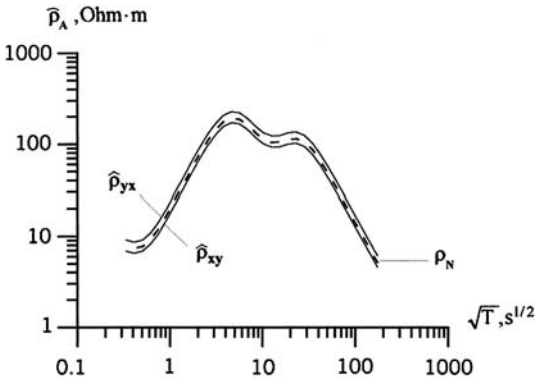

Fig. 11.14 Averaging the ρ_A-curves obtained in the model of the ρ-effect shown in Fig. 11.11

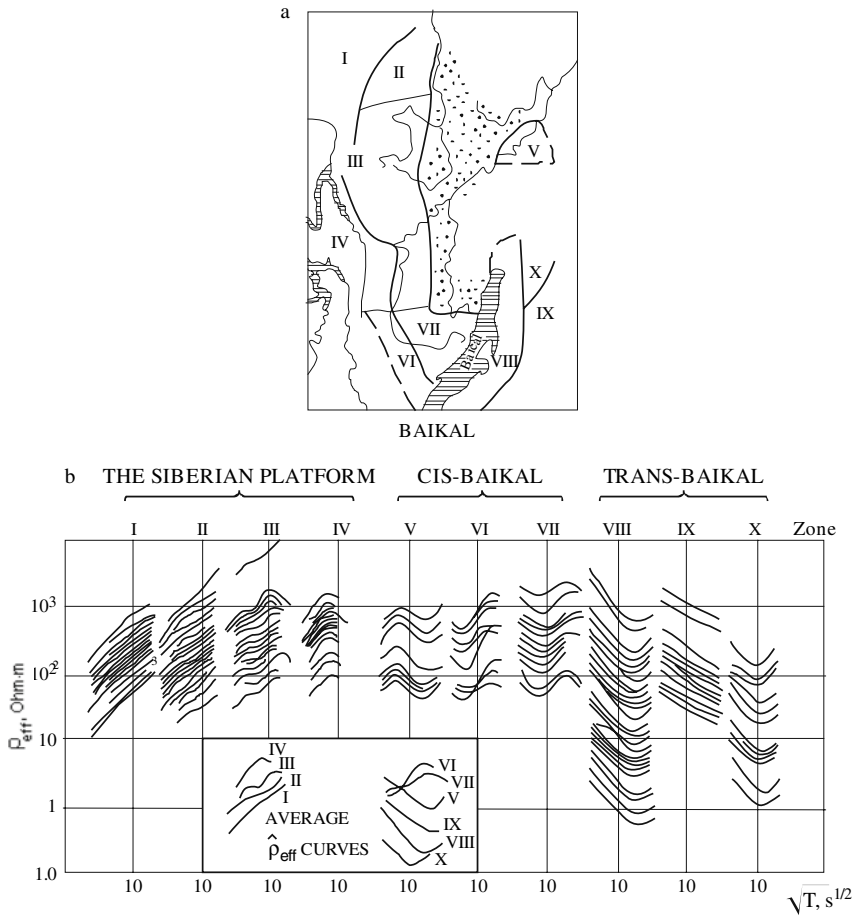

Fig. 11.15 Averaging the conformal ρ_{eff}-curves observed in the Baikal region; a – zones of the conformal ρ_{eff}-curves, b –conformal ρ_{eff}-curves and their averaging (Berdichevsky et al., 1980, 1989b)

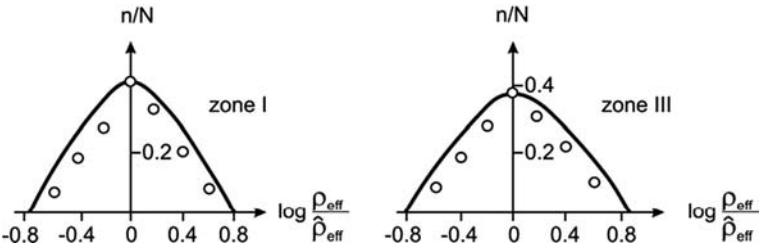

Fig. 11.16 Histograms of the apparent resistivities distorted by the ρ-effect (Berdichevsky et al., 1980)

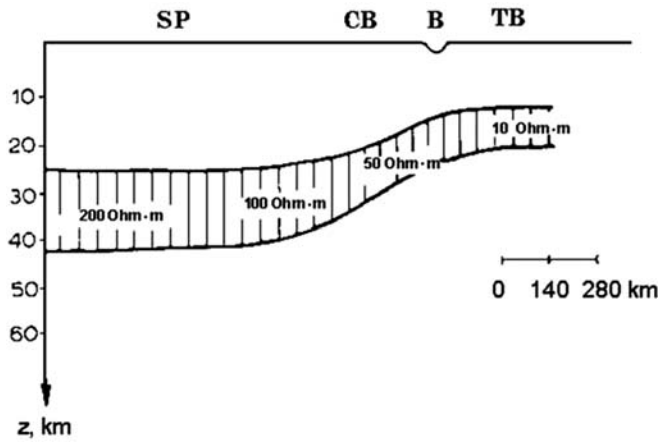

Fig. 11.17 Trial geoelectric model of the Baikal rift; one-dmensional inversion of the averaged ρ_{eff}-curves (Berdichevsky et al., 1980)

where coefficients $a_0, a_1, a_2 \ldots$ of polynomial approximation are determined by the least squares method. Note that an optimum order of the polynomial is chosen in accordance with supposed dimensions of target structures.

Consider now a filtering technique known as Electro-Magnetic Array Profiling, *EMAP* (Bostick, 1984; Torres-Verdin and Bostick, 1992). The typical EMAP array is shown in Fig. 11.18. It consists of the magnetic base station and the measurement electric dipoles, which are continuously aligned along the profile oriented across the structural strike (the employment of a continuous array helps to avoid aliasing). The

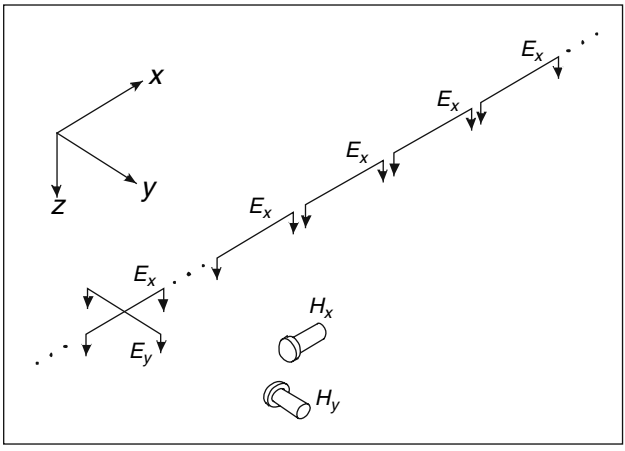

Fig. 11.18 The typical EMAP array (Torres-Verdin and Bostick, 1992)

impedances are defined from the magnetic field H_y measured at a base station and the filtered electric fields E_x^{flt} measured on the profile.

The low-frequency spatial filtering is performed by means of the Hanning transformation (Bernard and Rader, 1969):

$$\begin{aligned} E_{\text{x}}^{\text{flt}}(x_0) &= \int\limits_{x_0-W/2}^{x_0+W/2} E_{\text{x}}(x)\, H(x-x_0)\, dx = \frac{1}{2\pi} \int\limits_{-\infty}^{\infty} e_{\text{x}}(k_{\text{x}})\, h(k_{\text{x}})\, e^{-ik_{\text{x}}x_0} dk_{\text{x}} \\ &= \frac{1}{2\pi} \int\limits_{-\infty}^{\infty} e_{\text{x}}^{\text{flt}}(k_{\text{x}})\, e^{-ik_{\text{x}}x_0} dk_{\text{x}}, \end{aligned} \tag{11.10}$$

where $H(x)$ is the Hanning window of width W:

$$H(x) = \begin{cases} \dfrac{1}{W}\left(1+\cos\dfrac{2\pi x}{W}\right) & |x| \le \dfrac{W}{2} \\ 0 & |x| > \dfrac{W}{2}\ , \end{cases}$$

$h(k_{\text{x}})$ is its frequency response as a function of the spatial frequency k_{x}:

$$\begin{aligned} h(k_{\text{x}}) &= \int\limits_{-\infty}^{\infty} H(x) e^{ik_{\text{x}}x} dx = \frac{1}{W} \int\limits_{-W/2}^{W/2} \left(1+\cos\frac{2\pi x}{W}\right) e^{ik_{\text{x}}x} dx \\ &= \frac{\sin\dfrac{Wk_{\text{x}}}{2}}{\dfrac{Wk_{\text{x}}}{2}} \left(1 - \frac{\dfrac{1}{2}}{1+\dfrac{2\pi}{Wk_{\text{x}}}} - \frac{\dfrac{1}{2}}{1-\dfrac{2\pi}{Wk_{\text{x}}}}\right) = \frac{\sin\dfrac{Wk_{\text{x}}}{2}}{\dfrac{Wk_{\text{x}}}{2}} \frac{\dfrac{4\pi^2}{W^2k_{\text{x}}^2}}{\dfrac{4\pi^2}{W^2k_{\text{x}}^2}-1}, \end{aligned}$$

$e_{\text{x}}(k_{\text{x}})$ is the spatial spectrum of the observed electric field $E(x)$:

$$e_{\text{x}}(k_{\text{x}}) = \int\limits_{-\infty}^{\infty} E_{\mathbf{x}}(x) e^{ik_{\text{x}}x} dx,$$

and $e_x^{\text{flt}}(k_{\text{x}})$ is the spatial spectrum of the filtered electric field $E_{\text{x}}^{\text{flt}}(x)$:

$$e_{\text{x}}^{\text{flt}}(k_{\text{x}}) = h(k_{\text{x}}) \mathrm{e}_{\text{x}}(k_{\text{x}})\,.$$

Figure 11.19 presents the filter using the Hanning windows. Its 3 dB cutoff point with $h \approx 0.7$ is located at $Wk_{\text{x}} \approx 4.52$. With increasing Wk_{x} the amplitude falls as $1/(Wk_{\text{x}})^3$. At $Wk_{\text{x}} \approx 10.36$ we have 20 dB attenuation with $h = 0.1$.

The critical question is how to choose the optimum window width W. Bostick (1984) believes that W should be proportional to the effective penetration depth h_{eff}:

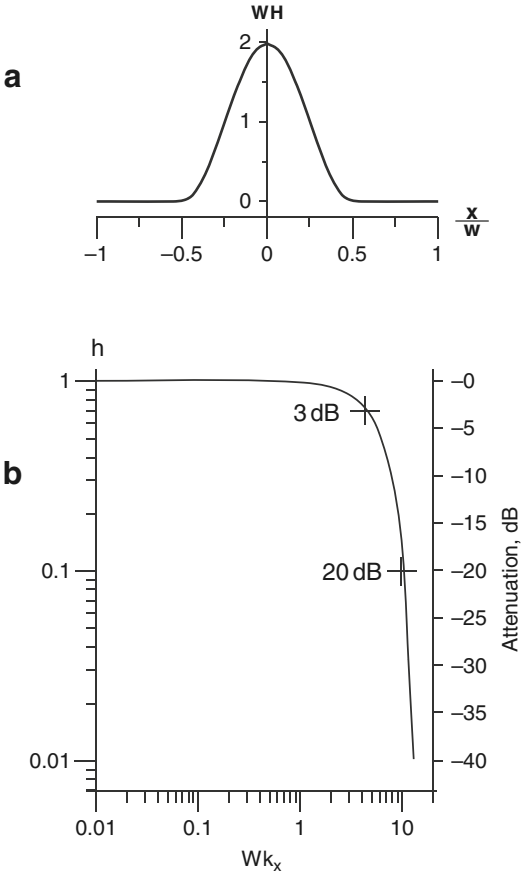

Fig. 11.19 The EMAP filter using the Hunning window (Torres-Verdin and Bostick, 1992)

$$W = Ch_{\text{eff}} \qquad 1 \le C \le 4\,,$$

where $h_{\text{eff}} = \left|Z_{\text{xy}}\right| / \omega\mu_{\text{o}}$. It is strange, because we have to take into account the scale of near-surface local inhomogeneities rather than the induction in the layered host medium. Wouldn't it be more reasonable to take $W \gg \Delta x$, where Δx is the characteristic dimension of static anomalies producing the geoelectric noise?

Next we consider an areal filtering technique applied by Berdichevsky and Nechaeva (1975) and Berdichevsky et al. (1989b). In the simplest case, the two-dimensional filtration of apparent resistivities ρ_{A} can be performed discretely by means of a rectangular window $W_{\text{x}} \times W_{\text{y}}$ formed by two box-functions, $B_{\text{x}}(x)$ and $B_{\text{y}}(y)$:

$$\rho_{\text{A}}^{\text{flt}}(x_{\text{o}}, y_{\text{o}}) = \frac{1}{N} \sum_{\text{i}} \sum_{\text{j}} \rho_{\text{A}}(x_{\text{i}}, y_{\text{j}})\, B_{\text{x}}(x_{\text{i}} - x_{\text{o}})\, B_{\text{y}}(y_{\text{j}} - y_{\text{o}}), \tag{11.11}$$

where

$$B_x(x) = \begin{cases} 1 & |x| \le \dfrac{W_x}{2} \\ 0 & |x| \ge \dfrac{W_x}{2} \end{cases} \qquad B_y(y) = \begin{cases} 1 & |y| \le \dfrac{W_y}{2} \\ 0 & |y| \ge \dfrac{W_y}{2}, \end{cases}$$

N is a total number of observation sites located inside the window and x_o, y_o is its middle point (Fig. 11.20). The filter provides a fair smoothing of the geoelectric noise on condition that lengths W_x and W_y are more than twice the autocorrelation radius of local anomalies of apparent resistivities. To filter ρ_A-curves, we represent MT-data as a set of apparent-resistivity maps for various periods. Each map is smoothed using a sliding window (11.11). The apparent resistivities from smoothed maps are synthesized, thereby yielding filtered ρ_A^{flt}-curves that reflect the regional structures.

By way of example, we will show the filtration of the apparent-resistivity curves, ρ_{xy} and ρ_{yx}, obtained in southwest Jakutiya. High geoelectric noise caused by permafrost lenses is observed in this province. Dimensions of lenses vary from 0.5–1 km to 10–20 km. The dimension $W = W_x = W_y$ of the sliding window have been determined from an analysis of the normalized autocorrelation functions of apparent resistivities calculated along several profiles crossing the region under investigation. The autocorrelation function *R(t)* along the profile AB is demonstrated in Fig. 11.21. It consists of a wide maximum related to local anomalies and a subhorizontal oscillating branch associated with regional structures. A radius of autocorrelation of local anomalies has been taken to be equal to a distance $t = 42$ km, at which $R(t) = 0$. Estimates for other profiles are about the same. Doubling the radius of autocorrelation, we have constructed a filter with square window 84×84 km. Figure 11.22 presents the filtration of the ρ_{xy}-resistivity map for $T = 225$ s. The initial map exhibits a mosaic of apparent resistivities that veils the effects of regional structures. Upon filtering we have got a smoothed map with fairly visible large-scale structures – Botuobian elevation (maximum of ρ_{xy}) and Iggiattian depression (minimum of ρ_{xy}). The filtered apparent-resistivity curves are exemplified in Fig. 11.23.

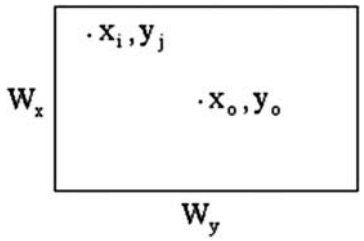

Fig. 11.20 Rectangular window for the two-dimensional filtration

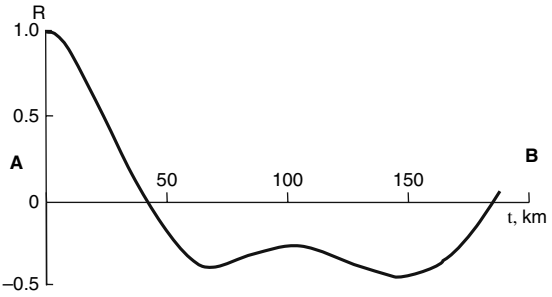

Fig. 11.21 Autocorrelation function of ρ_{xy} values along the profile AB

One can see that low-frequency branches of the filtered curves come closer together reflecting regular, large-scale variations in apparent resistivities.

Let us consider an example of another filtering technique employed by company North-West Ltd (Russia) for suppressing geoelectric noise along single profiles. Figure 11.24 presents a set of graphs showing spatial variations of $|Z_{xy}|$ at different periods T. The strong ρ-effect with sharp outliers replicated at all T from 14 to 1000 s is in evidence here. These static distortions are suppressed by smoothing a graph obtained for T = 14 s. To this end we remove the most dramatic outliers and use an exponential low-frequency filter

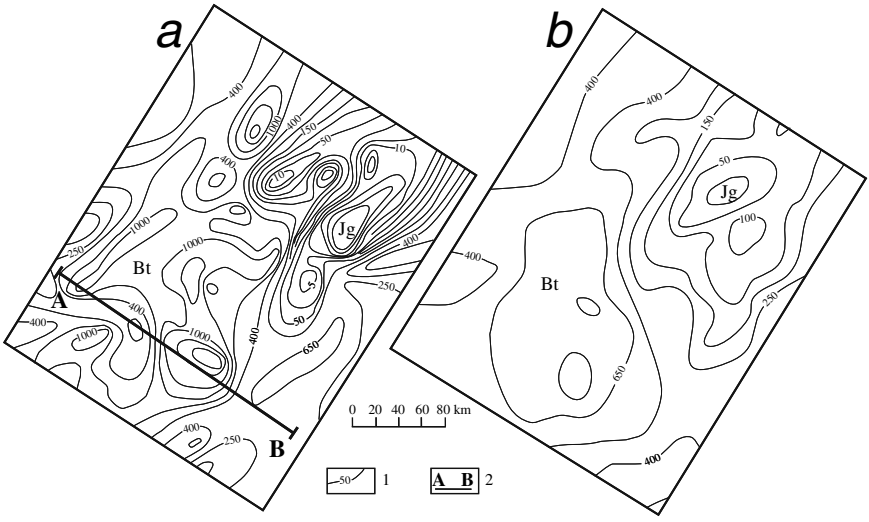

Fig. 11.22 Filtering the apparent-resistivity map: 1 – contour of ρ_{xy} values in Ohm·m, 2 – correlation profile

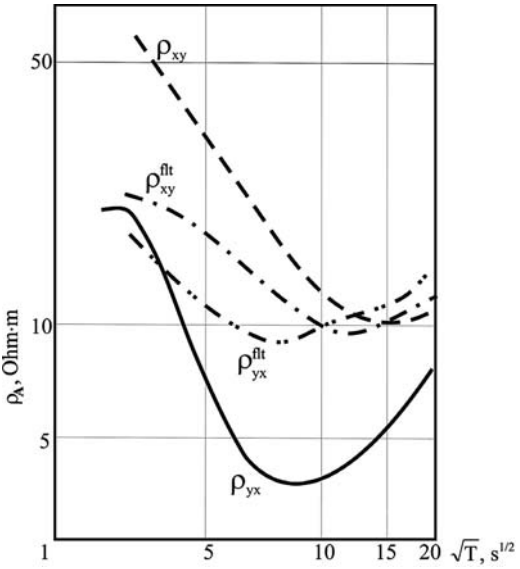

Fig. 11.23 Apparent-resistivity curves filtered by the rectangular window

$$\left|Z_{xy}^{\text{flt}}(T=14\,\text{s})\right|_i = \frac{\sum\limits_{j=1}^{n}\left|Z_{xy}(T=14\,\text{s})\right|_j e^{-\left\{\frac{|x_i-x_j|}{\tau}\right\}^q}}{\sum\limits_{j=1}^{n} e^{-\left\{\frac{|x_i-x_j|}{\tau}\right\}^q}}, \tag{11.12}$$

where τ and q are the filter half-width and steepness. The low-frequency filtration of $\left|Z_{xy}(T=14\,\text{s})\right|$ with τ =7.5 km and q =1 results in $\left|Z_{xy}^{\text{flt}}(T=14\,\text{s})\right|$. Now we can calculate correction factors

$$K_i = \frac{\left|Z_{xy}^{\text{flt}}(T=14\text{s})\right|_i}{\left|Z_{xy}(T=14\text{s})\right|_i}$$

and obtain smoothed values $\left|Z_{xy}^{\text{flt}}(T)\right|_i = K_i \left|Z_{xy}(T)\right|_i$ for all $T>14$ s. In this way we construct graphs of $\left|Z_{xy}^{\text{flt}}\right|$. The apparent-resistivity curves of $\rho_{xy}^{\text{flt}} = \left|Z_{xy}^{\text{flt}}\right|^2/\omega\mu_0$ are shown in Fig. 11.25.

11.1.4 Fitting Apparent Resistivities to Reference Level

It is simply evident that averaging and filtering of the apparent-resistivity curves entail the information losses. In order to avoid these losses, we can use techniques based on fitting the shifted apparent-resistivity curves to some reference level.

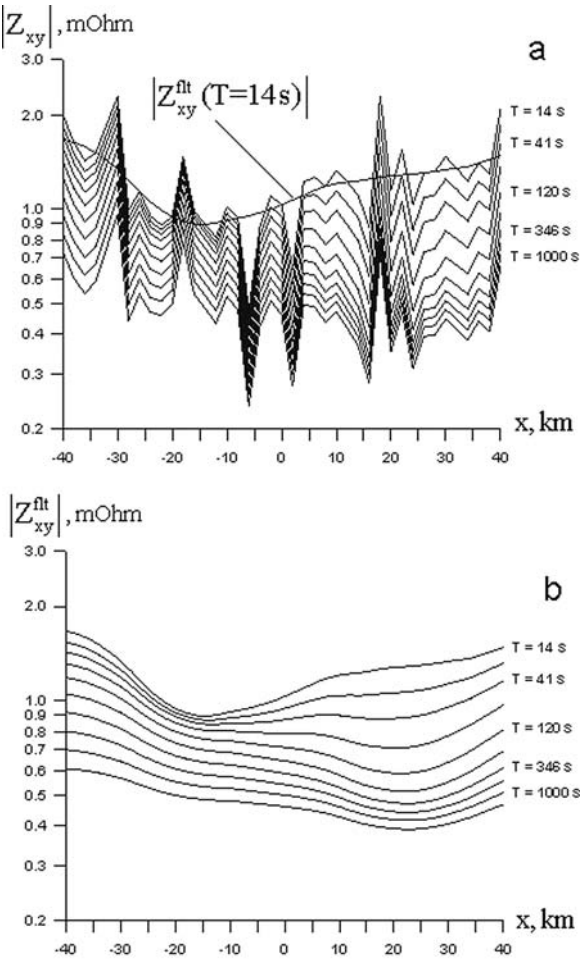

Fig. 11.24 North-West filtering technique: a – filtering a graph obtained at T= 14 s, b – multiplying the graphs, obtained at $T > 14$ s, by correction factors

The most beneficial are techniques relying on extraneous references. We will consider two techniques of that kind: (1) using transient electromagnetic sounding (TEM-Sounding, TEMS), and (2) using global magnetovariational sounding (GMV-Soundig, GMVS).

It seems that Andrieux and Wightman (1984) were the first who tried to eliminate the ρ−effect by applying TEMS. The idea was widely discussed in the literature. This approach can be efficient if near-surface local inhomogeneities are embedded in a host one-dimensional medium.

Sternberg et al.(1988) use a TEMS-system consisting of a square transmitter loop and recording central loop. There is good reason to believe that the observed magnetic field is hardly distorted by small surficial bodies. In order to compare TEM- and MT-data, the skin-depths in the frequency- and time-domains are equated. This yields the relation $T = 5.15$t between magnetotelluric period T and transient

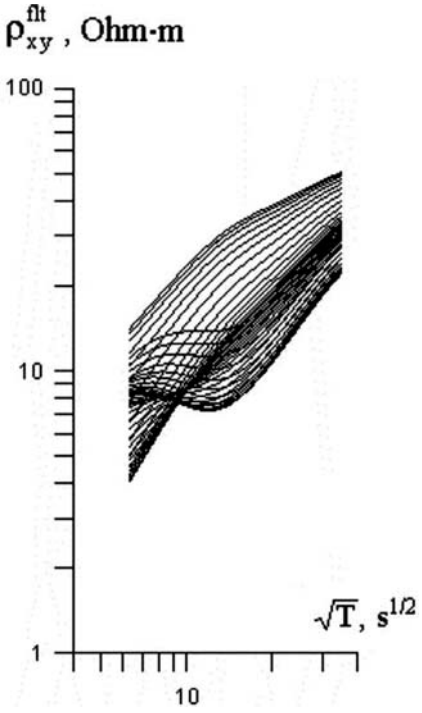

Fig. 11.25 Apparent-resistivity curves filtered by the North-West technique

time *t*. One-dimensional modeling shows that in the absence of sharp resistivity contrasts the transient apparent-resistivity curves $\rho_{TEM}(5.15t)$and the undistorted magnetotelluric apparent-resistivity curves $\rho_{MT}(T)$ are almost similar. As long as we avoid comparing the steep parts of the ρ_{TEM}- and ρ_{MT}-curves, the transient apparent-resistivity curves offer rather reliable reference for correcting magnetotelluric apparent-resistivity curves distorted by the static shift. A practical example of such a correction is given in Fig. 11.26. Here the transient ρ_{TEM}-curve offers a resistivity-depth profile that is in line with well-log data. At the same time the magnetotelluric ρ_{MT}-curve is displaced to the left from the transient ρ_{TEM}-curve, and its inversion differs severely from well-log data. Correcting this distortion, the ρ_{MT}-curve is shifted to the right so that its high-frequency branch fits the ρ_{TEM}-curve. Now the inversion of the static-shift corrected ρ_{MT}-curve is in reasonably good agreement with the well-log resistivities.

Another shift-correction technique involving TEM-soundings has been suggested by Pellerin and Hohmann (1990). To improve the accuracy in comparing MT- and TEM-data, the apparent-resistivity ρ_{TEM}-curve is converted to the apparent-resistivity ρ_{MT}-curve. The correction scheme is simple. The one-dimensional TEM-inversion gives a resistivity-depth profile, from which a reference ρ_{MT}-curve is calculated. Then the distorted ρ_{MT}-curve is matched with the reference ρ_{MT}-curve. Here, contrary to Sternberg et al. (1988), we compare data of the same kind and do not place restrictions on the resistivity contrasts. The technique is

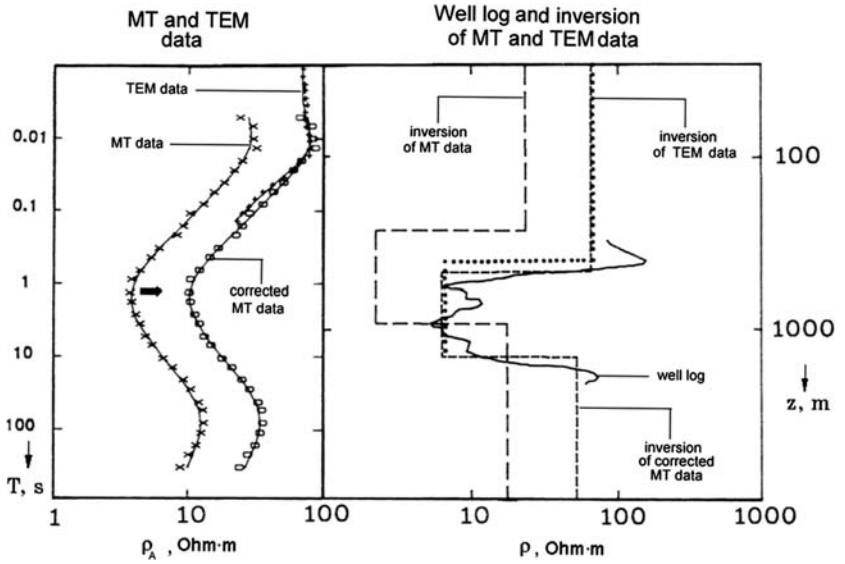

Fig. 11.26 Static-shift correction using TEM data as a reference (Sternberg et al., 1988)

exemplified in Fig. 11.27. Here the discrepancy between the observed phase curves, φ_{xy} and φ_{yx}, is within the accuracy of the measurement, whereas the conformal apparent-resistivity curves, ρ_{xy} and ρ_{yx}, are shifted from each other by one-half decade. But the ρ_{xy}-curve fits rather well the ρ_{MT}-curve computed from the TEM-data and hence can be considered as undistorted. At the same time the ρ_{yx}-curve

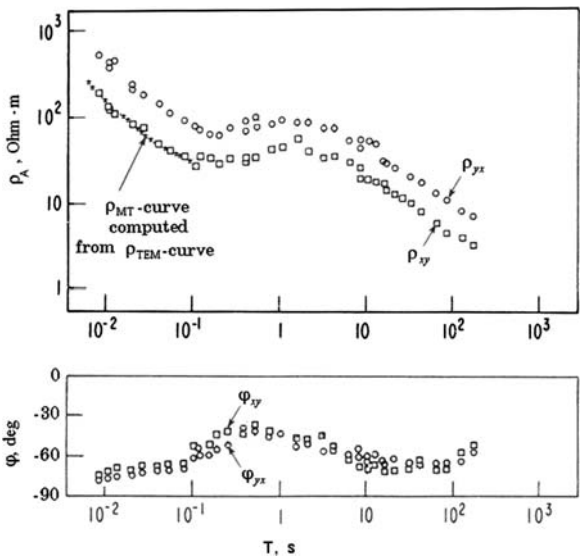

Fig. 11.27 Static-shift correction using TEM data as a reference (Pellerin and Hohmann, 1990)

is evidently distorted and should be shifted downwards to match the ρ_{xy}- curve. After correction we have two closely related ρ_{xy}- and ρ_{yx}-curves typical of a one-dimensional model.

Lastly we consider a correction technique involving global magnetovariational sounding, GMVS (Larsen, 1977; Rokityansky, 1982; Berdichevsky et al., 1989a, b; Vanyan, 1997; Berdichevsky and Dmitriev, 2002). The technique is used to correct apparent-resistivity curves distorted by the ρ- and *S*-effects. Here the reference is given by the *standard aparent-resistivity curve* ρ_{st} reproduced from GMVS and large magnetotelluric statistics collected in different geological provinces. The ρ_{st}-curve defines an average planetary distribution of the Earth's conductivity that can be adopted as a normal geoelectric model of our planet. Figure 11.28 shows the standard ρ_{st}-curve suggested by Fainberg in his pioneering works (1983a, b). It is composed of GMVS data and magnetotelluric extension that can be formed by slightly distorted MT-curves obtained in different geological provinces. We will use the ρ_{st}-curve edited by Vanyan with regard to further generalizations of GMVS and MT data (Vanyan, 1997; Berdichevsky et al., 1989a, b). Coordinates of this ρ_{st}-curve are set out in Table 11.1. Figure 11.29 presents two examples of how corrections are performed. Let a long-period apparent–resistivity curve ρ_{xy} be distorted by the ρ-effect that persists throughout the entire MT recording range. Its low-frequency descending branch lies much below the ρ_{st}-curve. To remove the ρ-effect, the ρ_{xy}-curve should be shifted upward so that its low-frequency descending branch fits the ρ_{st}-curve. In the case of the *S*-effect, the correction procedure becomes more intricate. We have to take into account that the high-frequency ascending branch of the ρ_{xy}-curve reflecting the upper layer conductance is slightly distorted and does not need any correction. So only the low-frequency branch of

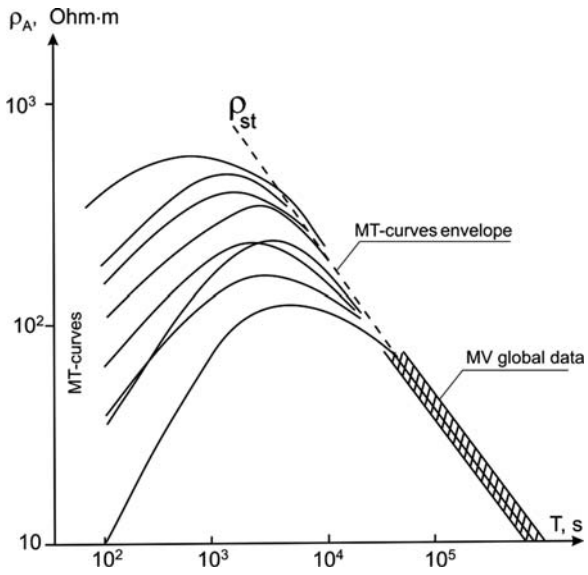

Fig. 11.28 Constructing the standard apparent-resistivity curve ρ_{st}

Table 11.1 Standard apparent resistivities

ρ_{st}, Ohm·m	28000	10000	3500	1600	700	260	120	52
$\sqrt{T}$, $s^{1/2}$	1	2	5	10	20	50	100	200

the ρ_{xy}-curve including its bowl-type and bell-type elements is shifted upward to fit the ρ_{st}-curve. Then the intact and shifted parts of the ρ_{xy}-curve are smoothly interpolated.

Unfortunately, this attractive method should be applied with some reservation. The most reliable results can be obtained in stable geological provinces (or at least far away from anomalous zones such as rifts, subductions, plumes, volcanoes) where the mantle's conductivity at depth of about 300–500 km hardly experiences gross changes in horizontal directions. Note also that the distortions of low-frequency

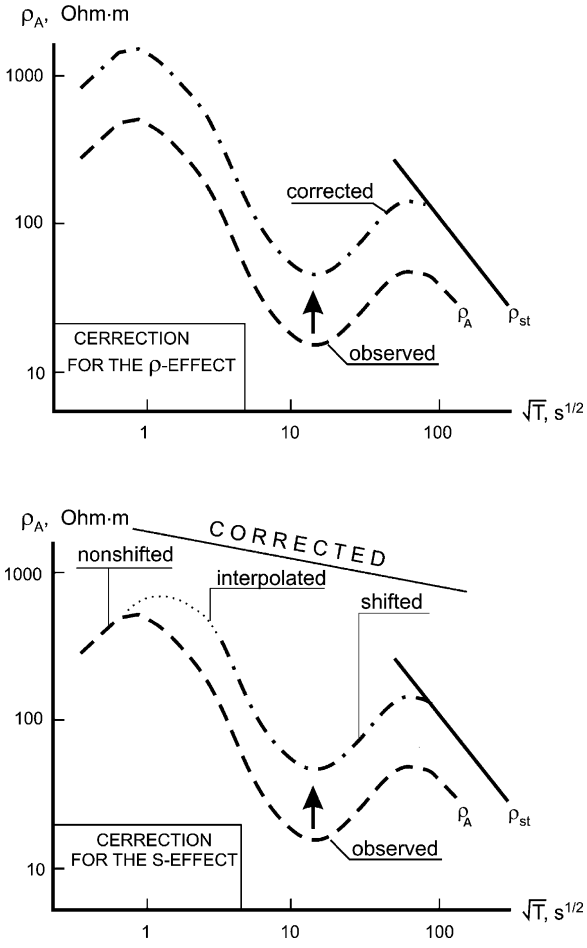

Fig. 11.29 Static-shift correction using the standard apparent-resistivity curve ρ_{st} as a reference

branches of the apparent-resistivity curves caused by bounded conductive zones in deep layers of the Earth's crust (the deep *S*-effect) may severely spoil the static-shift corrections.

Let us mention one more fitting technique which can be useful for qualitative analysis of the apparent-resistivity curves. It is based on the vertical translation of the ρ_A−curves to the $\bar{S}$− line, where $\bar{S}$ is a mean conductance of the upper conductive layer underlaid with a resistive substratum (Feldman et al., 1988; Berdichevsky et al., 1988; Dmitriev-Berdichevsky, 1988). This approach is exemplified in Fig. 12.54.

11.1.5 Modeling the Distortions

Let some electromagnetic soundings (with direct or alternating current) give sufficiently complete information on conductance *S* of the upper layer underlaid with highly resistive rocks. Then we can construct a thin-sheet model reflecting the horizontal variations in *S* and compute corrections for the distortions caused by the *S*-effect. This idea has been realized by Fainberg et al. (1995) in the *dynamic-correction method.* A distinguishing feature of this method is that corrections can be applied in a wide frequency range (including transition from undistorted branch of the apparent-resistivity curves to their statically shifted branch).

We will illustrate the principle of the dynamic corrections by the example of magnetotelluric sounding aimed at studying deep conductive zones in the lithosphere or asthenosphere (Berdichevsky, 1996). Assume that the inhomogeneous sediments rest on the highly resistive layers of the crystalline Earth's crust. Following (1.75), we represent the measured impedance tensor

$$[\mathbf{Z}] = \begin{bmatrix} \mathrm{Z}_{xx} & \mathrm{Z}_{xy} \\ \mathrm{Z}_{yx} & \mathrm{Z}_{yy} \end{bmatrix}$$

as

$$[\mathbf{Z}] = [\mathbf{e}]\,[\mathbf{Z}^R], \tag{11.13}$$

where

$$[\mathbf{e}] = \begin{bmatrix} \mathrm{e}_{xx} & \mathrm{e}_{xy} \\ \mathrm{e}_{yx} & \mathrm{e}_{yy} \end{bmatrix}$$

is the electric-distortion tensor, and

$$[\mathbf{Z}^R] = \begin{bmatrix} \mathrm{Z}^{\mathrm{R}}_{xx} & Z^R_{xy} \\ Z^R_{yx} & Z^R_{yy} \end{bmatrix}$$

is the regional three-dimensional impedance tensor in the absence of sediments inhomogeneities. In order to determine the distortion tensor [**e**], we examine a two-layered model with the inhomogeneous upper layer of given conductance $S(x, y)$ and the homogeneous basement of high resisistivity ρ_B. The model is excited by a plane wave. Solving the problem in the low-frequency thin-sheet approximation, we get the model impedance

$$[\mathbf{Z}^m] = \begin{bmatrix} Z^m_{xx} & Z^m_{xy} \\ Z^m_{yx} & Z^m_{yy} \end{bmatrix}$$

that, similar to (11.13), can be presented as

$$[\mathbf{Z}^m] = [\mathbf{e}^m]\,[\mathbf{Z}^m_N], \tag{11.14}$$

where $[\mathbf{e}^m]$is the tensor of the electric distortion:

$$[\mathbf{e}^m] = \begin{bmatrix} \mathrm{e}^m_{xx} & \mathrm{e}^m_{xy} \\ \mathrm{e}^m_{yx} & \mathrm{e}^m_{yy} \end{bmatrix}$$

and $[\mathbf{Z}^m_N]$ is the normal impedance defined by the normal conductance S_{N}:

$$[\mathbf{Z}^m_{\mathrm{N}}] = \begin{bmatrix} 0 & Z^m_{\mathrm{N}} \\ -Z^m_{\mathrm{N}} & 0 \end{bmatrix} \qquad Z^m_{\mathrm{N}} = \frac{1}{S_{\mathrm{N}} + \dfrac{1}{\sqrt{-i\omega\mu_{\mathrm{o}}\rho_B}}}\,.$$

In such an approximation we determine the tensor of the electric distortion as

$$[\mathbf{e}^m] = [\mathbf{Z}^m]\,[\mathbf{Z}^m_N]^{-1}. \tag{11.15}$$

Let the $S-$ effect weakly depend on the structure of the highly resistive lithosphere. Then

$$[\mathbf{e}] \approx [\mathbf{e}^m], \tag{11.16}$$

and

$$[\mathbf{Z}^R] = [\mathbf{e}]^{-1}[\mathbf{Z}] \approx [\mathbf{e}^m]^{-1}[\mathbf{Z}] = [\mathbf{Z}^m_{\mathrm{N}}][\mathbf{Z}^m]^{-1}[\mathbf{Z}]\,. \tag{11.17}$$

Thus, we compute the regional impedance tensor, which is supposed to be free of near-surface distortions caused by the *S*-effect. Now we can solve the eigenstate problem (say, by the Swift-Eggers method) and define the principal

apparent-resistivity and principal phase curves related to the principal directions of the regional impedance tensor.

Note that accuracy of dynamic corrections depends on the choice of the normal conductance S_N and the basement resistivity ρ_B. So, it would be reasonable to test the distortion matrix $[\mathbf{e}^m]$ obtained at different S_N and ρ_B.

11.1.6 Saving the Static Shift Troubles

Can we dispose of static distortions? We manage to do this for the geoelectric noise caused by the $\rho-$ effect. Making good use of the averaging and filtering techniques, we smooth the local random distortions and pave the way for meaningful geophysical interpretation. Certainly, on this way we lose some information, but it can be possible to improve the MT-inversion by involving local TEMS- references.

In the case of static distortions caused by the *S*-effect we have a more complicated situation. The scale of these distortions depends on dimensions of causing geoelectric structures as well as on the galvanic transparency of resistive rocks underlying the inhomogeneous upper layer. We can observe the local *S*-effects (stretching over hundreds of meters) and the regional *S*-effects (extending for hundreds of kilometers). It is evident that the averaging and filtering techniques are efficient only for local *S*-effects. To eliminate the regional *S*-effect, we should use reference given by the standard apparent-resistivity curve ρ_{st} or apply the dynamic corrections (that is, to solve the two-dimensional or three-dimensional problem for given distribution of the upper layer conductance). Both approaches are associated with uncertainties that are difficult to control and we not always manage to estimate the reliability of shift-corrected apparent-resistivity curves. It is the *S*-effect that deserves the notorious title of the main villain of the magnetotelluric piece.

Can we dispose of the *S*-effect? It would be possible, if we remove the inversion uncertainties caused by near-surface galvanic anomalies of the electric field. We see two different pragmatic approaches to this problem.

1. Development of a new interpretation strategy in which the magnetic field is a primary source of information on the Earth's conductivity. The remarkable property of the magnetic field is that with lowering frequency the anomalies caused by near-surface inhomogeneities attenuate and the anomalies caused by deep inhomogeneities come to light. So the magnetic field can scan the Earth illuminating successively deeper and deeper areas independently of near-surface inhomogeneities. On this way we employ the MVS-MTS complex with MVS, which plays the role of a basic method, and MTS, which controls and supplements the MVS data.

2. Interpretation of magnetotelluric and magnetovariational response functions in the hypotheses test mode. Hypotheses are made on the basis of modern geological and geophysical ideas (with all their controversies and viewpoints variety). On this way we construct several starting models that correspond to the different hypotheses and give unambiguous references for correcting the apparent-resitivity curves. The most credible is a hypothesis that shows minimal model misfit.

In our book we will give special prominence to both approaches.

11.2 Stratifying the Geoelectric Background

At this stage we perform some rough one-dimensional estimates stratifying the geoelectric background. Two appropriate techniques can be used: the Occam inversion provided by smoothing stabilizer (Constable et al., 1987; Parker, 1994) or the Zohdy transformation, suggested originally for the resistivity method (Zohdy, 1989; Andreeva et al., 1991; Hobbs and Dumitresku, 1997; Berdichevsky and Dmitriev, 2002). We shall restrict our consideration to Zohdy's transformation. The key advantage of this approach is that it yields immediately the stable $S-$distribution. So, we get a firm and pictorial basis for geoelectric stratification.

Magnetotelluric modification of Zohdy's transformation has its origin in the Molochnov-Viet transformation (Berdichevsky and Dmitriev, 2002), which translates the apparent-resistivity curve $\rho_A(\sqrt{T})$into a resistivity-depth profile $\rho(z)$:

$$\rho(\sqrt{T}) = \begin{cases} \rho_A(\sqrt{T})\left[1 + \frac{1}{2}\frac{d\log\rho_A(\sqrt{T})}{d\log\sqrt{T}}\right]^2 & \text{for } \frac{d\log\rho_A(\sqrt{T})}{d\log\sqrt{T}} \le 0 \\ \rho_A(\sqrt{T})\left[1 - \frac{1}{2}\frac{d\log\rho_A(\sqrt{T})}{d\log\sqrt{T}}\right]^{-2} & \text{for } \frac{d\log\rho_A(\sqrt{T})}{d\log\sqrt{T}} \ge 0 \end{cases}$$

$$z(\sqrt{T}) = h_{\text{eff}}(\sqrt{T}) = \sqrt{\frac{\rho_A(\sqrt{T})T}{2\pi\mu_o}} \quad . \tag{11.18}$$

Simplicity of the Molochnov-Viet transformation is achieved at the cost of a severe sacrifice in its accuracy. An apparent-resistivity curve calculated from $\rho(z)$ may dramatically differ from the initial curve $\rho_A(\sqrt{T})$. We can reduce this difference by means of iterative procedure involving *Zohdy corrections*.

Let $\rho_A(\sqrt{T})$ be given on a sufficiently dense grid T_m, $m \in [0, M]$:

$$\rho_A(\sqrt{T_m}) = \rho_A^{(m)}.$$

At nth iteration we have

$$\begin{aligned} \rho^{(m,n)} &= \rho^{(n)}(\sqrt{T_m}) = \rho^{(n)}(z^{(m)}) \\ z^{(m)} &= z(\sqrt{T_m}) = \sqrt{\frac{\rho_A(\sqrt{T}_m)T_m}{2\pi\mu_o}} \\ \rho_A^{(m,n)} &= \rho_A^{(n)}(\sqrt{T_m}) \end{aligned} \tag{11.19}$$

and

$$\rho_{\mathrm{A}}^{(m,n)} = P\,\rho^{(m,n)}, \tag{11.20}$$

where P is an operator transforming resistivity-depth profile into apparent-resistivity curve. Multiplying $\rho^{(m,n)}$ by Zohdy's correction factor $Z^{(m,n)}$, we get

$$\rho^{(m,n+1)} = Z^{(m,n)}\rho^{(m,n)}, \tag{11.21}$$

where

$$Z^{(m,n)} = \frac{\rho_{\mathrm{A}}^{(m)}}{\rho_{\mathrm{A}}^{(m,n)}}.$$

We illustrate Zohdy's corrections by a simple example. Let the resistivity-depth profile $\rho^{(m,1)}$ is given by (11.18). Correcting $\rho^{(m,1)}$, we obtain the second iteration

$$\rho^{(m,2)} = Z^{(m,1)}\rho^{(m,1)},$$

where, according to (11.20) and (11.21),

$$Z^{(m,1)} = \frac{\rho_{\mathrm{A}}^{(m)}}{\rho_{\mathrm{A}}^{(m,1)}} \qquad \rho_{\mathrm{A}}^{(m,1)} = P\,\rho^{(m,1)}.$$

If $\rho_{\mathrm{A}}^{(m,1)} > \rho_{\mathrm{A}}^{(m)}$, the value for $\rho^{(m,1)}$ is overstated but it is reduced by Zohdy's factor. And vice versa, if $\rho_{\mathrm{A}}^{(m,1)} < \rho_{\mathrm{A}}^{(m)}$, the value for $\rho^{(m,1)}$ is understated but it is enhancved by Zohdy's factor. It seems that we arrive at the second iteration with diminished misfit of resistivity profile $\rho^{(m,2)}$. This heuristic consideration suggests that Zohdy's multiplications decrease the misfit of transformation.

Iterations are continued until the misfit

$$\Im^{(n)} = \frac{100\,\%}{M}\sum_{m=1}^{M}\left|\ln\frac{\rho_{\mathrm{A}}^{(m,n)}}{\rho_{\mathrm{A}}^{(m)}}\right| \tag{11.22}$$

becomes reasonably small. Though lacking theoretical support, this simple approach works rather well in practice. It is typical that on 25–50 iterations we reach a misfit of the order of 2–3%.

Figure 11.30 shows the five-layer test model. Parameters of the model are: $\rho_1 = 10\,\Omega\mathrm{hm}\cdot\mathrm{m}$, $h_1 = 1\,\mathrm{km}$, $\rho_2 = 100\,\Omega\mathrm{hm}\cdot\mathrm{m}$, $h_2 = 2\,\mathrm{km}$, $\rho_3 = 10\ \Omega\mathrm{hm}\cdot\mathrm{m}$, $h_3 = 3\,\mathrm{km}$, $\rho_4 = 1\,\Omega\mathrm{hm}\cdot\mathrm{m}$, $h_4 = 4.2\,\mathrm{km}$, $\rho_5 = 60\,\Omega\mathrm{hm}\cdot\mathrm{m}$. The original ρ_{A}-curve has pronounced maximum and minimum corresponding to the second and third layers. Its starting transformation made by the Molochnov-Viet scheme yields a smoothed resistivity distribution $\rho(z)$ with a misfit of 96% for its ρ_{A}-response. The Zohdy

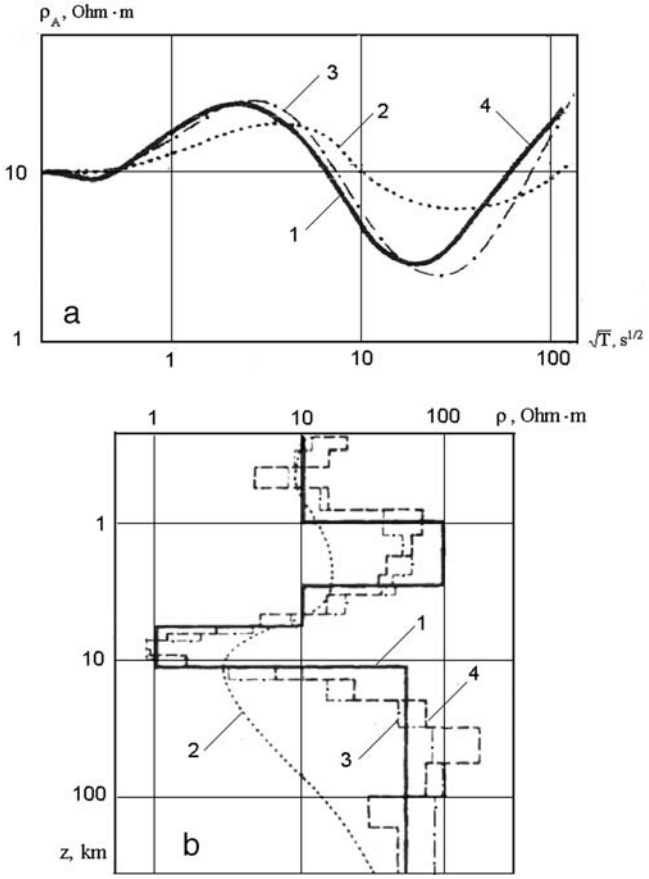

Fig. 11.30 Zohdy transformation of an apparent resistivity curve; a – apparent resistivity curves: 1 – original data, 2 – result of the differential Molochnov-Viet transformation, misfit in apparent resistivity 96%, 3 – result of Zohdy transformation, 12 iterations, misfit in apparent resistivity 16%, 4 – result of Zohdy transformation, 39 iterations, misfit in apparent resistivity 1% b – resistivity profiles: 1,2,3,4 are the same as above

iterative corrections reduce the ρ_A-response misfit to 16 % (12 iterations) and 1 % (39 iterations). Now the resistivity distributions $\rho(z)$come near to the original one, though conspicuously differ in details. But note that the conductance distribution $S(z)$ obtained by 39 iterations virtually merges with original one (Fig. 11.31). It is determined stably and characterizes the whole variety of equivalent solutions of the one-dimensional inverse problem (Berdichevsky and Dmitriev, 2002).

Let us gain the benefit from $S(z)$ and stratify (at least roughly) the lithosphere in the Tungus syneclise. Figure 11.32 shows a set of the S-distributions obtained along the river Podkamennaya Tunguska. Here the main indicator of the geoelectric stratification is the rate of vertical changes of the conductance $S(z)$. Fast and moderate changes correspond to conductive layers, while slow changes relate to resistive

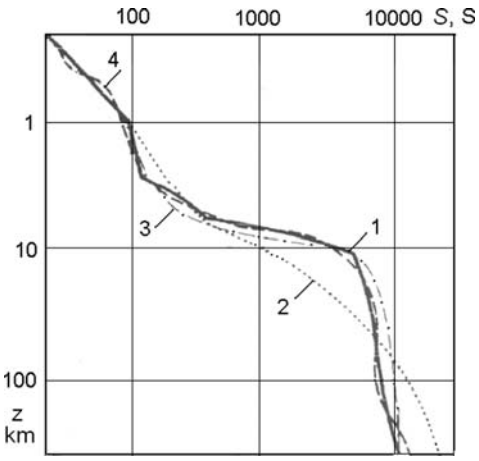

Fig. 11.31 *S*-distribution obtained by Zohdy transformation shown in Fig. 11.30; 1 – original data, 2 – result of the differential Molochnov-Viet transformation, misfit in apparent resistivity 96%, 3 – result of Zohdy's transformation, 12 iterations, misfit in apparent resistivity 16%, 4 – result of Zohdy's transformation, 39 iterations, misfit in apparent resistivity 1%

layers. The boundaries between conductive and resistive layers are reflected in the maxima of curvature of $S(z)$. Let us correlate the *S*-distributions at sites 1–11. In most cases they present a five-layer strata. Connecting the curvature maxima, we outline the conductive layer in the lower crust (25–50 km) underlaid with the resistive mantle (50–100 km) and the mantle conductor (>100 km). Note that in some places the smoothness of boundaries is violated (may be, because of three-dimensional distortions). Of course, the accuracy of these results leaves much to be desired and they need further consideration. But "exploration problems sometimes require a simple 'yes' or 'no' answer to the question such as 'Does a buried conductor exist here?'" (Vozoff, 1991).

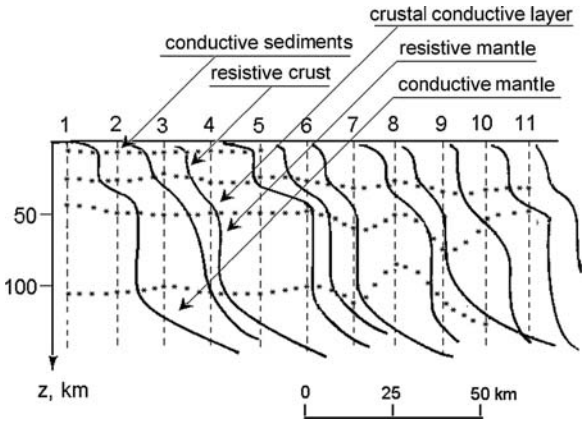

Fig. 11.32 Correlating the vertical *S*-distributions along the river Podkamennaya Tunguska

11.3 Identifying the Geoelectric Structures

We can localize the geoelectric structures and define their dimensionality using the magnetovariational and magnetotelluric formalized tests. Note that these tests establish only necessary conditions of one- and two-dimensionality. For the final conclusion we analyze the spatial distribution of the necessary conditions and examine trial three-dimensional models.

11.3.1 The Magnetovariational Test

The initial invariant parameters for the magnetovariational test are derived from (4.9) and (4.10). We use two parameters:

1. The magnetovariational innhomogeneity parameter determined as

$$N_{mv} = \|\mathbf{W}\| = \sqrt{|W_{zx}|^2 + |W_{zy}|^2}.$$

2. The magnetovariational asymmetry parameter determined as

$$skew_{mv} = \left| \frac{\text{Re } W_{zx} \text{ Im } W_{zy} - \text{Re } W_{zy} \text{ Im } W_{zx}}{\text{Re } W_{zx} \text{ Im } W_{zx} + \text{Re } W_{zy} \text{ Im } W_{zy}} \right|.$$

Parameters N_{mv} and $skew_{mv}$ are estimated with respect to threshold values δ that characterize the level of measurements errors. If N_{mv} and $skew_{mv}$ are beneath δ, they are considered to be zero. Testing N_{mv}, we assume that $\delta = 0.03$–0.05. Testing $skew_{mv}$, we take $\delta = 0.1$–0.2, which, according to (4.17), corresponds to angle of 6–11° or 169–174° between the real and imaginary tippers. Note that in zones with small $\|\text{Re } \mathbf{W}\| = \sqrt{(\text{Re } W_{zx})^2 + (\text{Re } W_{zy})^2}$, $\|\text{Im } \mathbf{W}\| = \sqrt{(\text{Im } W_{zx})^2 + (\text{Im } W_{zy})^2}$ the asymmetry parameter $skew_{mv}$ is calculated unstably. Its evaluation makes sense if $\|\text{Re } \mathbf{W}\| \geq 0.07 - 0.1$ and $\|\text{Im}\mathbf{W}\| \geq 0.07 - 0.1$.

The flow chart for the magnetovariational dimensionality test is shown in Fig. 11.33. Applying this test, we can differentiate three types of structures approximating the geoelectric medium: (1) one-dimensional structures, (2) two-dimensional structures or axisymmetric three-dimensional structures, (3) asymmetric three-dimensional structures.

The starting point is the inhomogeneity parameter N_{mv}. Inspecting N_{mv}, we outline the horizontally homogeneous one-dimensional (quasi-one-dimensional) areas with $N_{mv} \leq \delta$ and the horizontally inhomogeneous areas with $N_{mv} \gg \delta$. The horizontally inhomogeneous areas are the subject for further study. They manifest themselves in anomalies observed over the edges of inhomogeneities. Testing $skew_{mv}$, we can divide these areas into zones with $skew_{mv} \leq \delta$, corresponding to two-dimensional (elongated) or axisymmetric three-dimensional (isometric) structures,

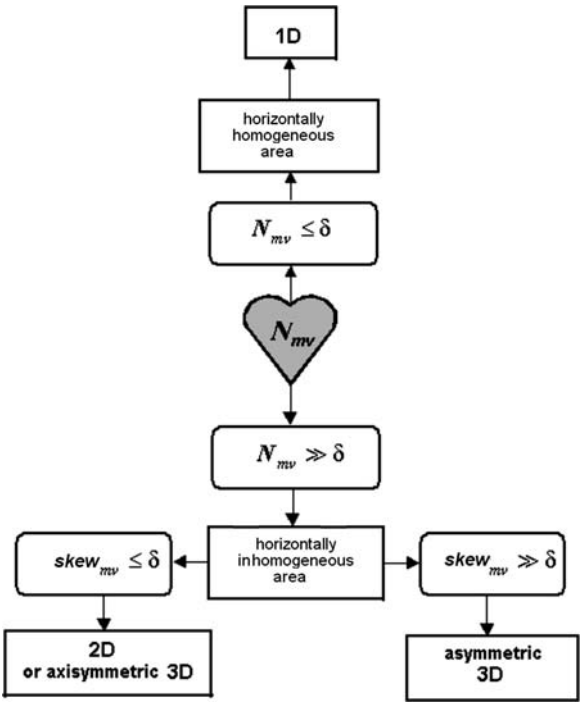

Fig. 11.33 Flow chart for the magnetovariational dimensionality test

and zones with $skew_{mv} >> \delta$, corresponding to three-dimensional asymmetric structures. What we would like to stress is that at low frequencies the magnetovariational parameters become free from near-surface effects and reflect more and more deep structures. So, applying the magnetovariational test on different frequencies, we can plot the maps, pseudo-sections and pseudo-topographies of N_{mv} and $skew_{mv}$, and see how the detected structures change with depth.

11.3.2 The Magnetotelluric Test

The magnetotelluric test came from the pioneering works of Bahr (1991) and Weaver et al. (2000). The *Bahr test* and *Weaver-Agarval-Lilley test* (WAL test) have been analysed and advanced in (Weaver, 2003; Weaver et al., 2003; Marti et al., 2005). These tests examine five invariant parameters derived from the impedance and phase tensors and provide complete dimensionality classification. Note that the Weaver-Agarval-Lilley test presents the impedance tensor as a sum of three matrices associated with 1D, 2D and 3D regional structures respectively and seems to be somewhat sophisticated.

In our book we consider a simplified magnetotelluric test applied in (Berdichevsky and Dmitriev, 2002). This test rests on the same logic scheme as in (Weaver et al., 2000; 2003), but operates with customary parameters *N* and *skew*

reflecting the geoelectric inhomogeneity and asymmetry (Swift, 1967; Bahr, 1988; Caldwell et al., 2004; Berdichevsky and Dmitriev, 2002).

Using the Berdichevsky-Dmitriev magnetotelluric test on sufficiently low frequencies, we ignore the magnetic anomalies caused by near-surface inhomogeneities. So, following Bahr (1988) and Caldwell et al. (2004), we proceed from the truncated decomposition (1.75), $[\mathbf{Z}] = [\mathbf{e}][\mathbf{Z}^R]$, where $[\mathbf{e}]$ is the real-valued tensor of local electric distortion and $[\mathbf{Z}^R]$is the regional impedance tensor.

The initial invariant parameters in the Berdichevsky-Dmitriev test are:

1. The inhomogeneity parameter determined by (2.46) and (2.53):

$$N_{mt} = \frac{\zeta_1 - \zeta_2}{\zeta_1 + \zeta_2} = \sqrt{1 - 4\frac{Z_{xx}Z_{yy} - Z_{xy}Z_{yx}}{(Z_{xy} - Z_{yx})^2}},$$

where ζ_1, ζ_2 are principal impedances derived from the Swift-Eggers decomposition.

2. The Swift asymmetry parameter determined by (1.60):

$$skew_S = \left|\frac{Z_{xx} + Z_{xy}}{Z_{xy} - Z_{yx}}\right|.$$

Its analog is the angle asymmetry parameter determined by (2.54):

$$skew_{ang} = A = ||\alpha_1 - \alpha_2| - \pi/2|\,,$$

where angles α_1, α_2 define the principal directions derived from the Swift-Eggers decomposition.

3. The Bahr phase-sensitive asymmetry parameter determined by (1.61):

$$skew_B = \frac{\sqrt{\left|\mathrm{Im}(Z_{xy}\bar{Z}_{yy} + Z_{xx}\bar{Z}_{yx})\right|}}{\left|Z_{xy} - Z_{yx}\right|},$$

where the bars denote the complex conjugation. Its analog is the Caldwell-Bibby-Brown asymmetry parameter $skew_{CBB}$, determined by (3.80) from the phase tensor:

$$skew_{CBB} = \frac{1}{2}\arctan\left|\frac{\Phi_{xy} - \Phi_{yx}}{\Phi_{xx} + \Phi_{yy}}\right| = \frac{1}{2}\arctan(M\,skew_B^2),$$

where scale factor M is

$$M = \frac{\left|Z_{xy} - Z_{yx}\right|^2}{\left|(\Phi_{xx} + \Phi_{yy})(\mathrm{Re}Z_{xx}\mathrm{Re}Z_{yy} - \mathrm{Re}Z_{xy}\mathrm{Re}Z_{yx})\right|}.$$

All the parameters are estimated with respect to threshold values δ that characterize the level of measurements errors. In the magnetotelluric test, we usually take

δ between 0.05 and 0.15 for $|N_{mt}|$, $\mathrm{Im}N_{mt}$, $skew_S$, $skew_B$ and between 2°and 5° for $skew_{ang}$, $skew_{CBB}$.

The flow chart for the magnetotelluric test is shown in Fig. 11.34. With the help of this test we can outline horizontally homogeneous (quasi-one-dimensional) areas and horizontally inhomogeneous areas with two-dimensional (elongated) or axisymmetric (isometric) structures and asymmetric three-dimensional structures. What's more, it is possible to single out the two-dimensional and axisymmetric structures with in-phase principal impedances ($\arg \zeta_1 = \arg \zeta_2$), which are unfavorable for the Bahr and Groom-Bailey decompositions.

Applying the magnetotelluric test, we use the profiles, maps, pseudo-sections as well as pseudo-topographies of $|N_{mt}|$, $\mathrm{Im}N_{mt}$ and $skew_S$, $skew_B$, $skew_{CBB}$ and discern the local (near-surface) and regional (deep) structures.

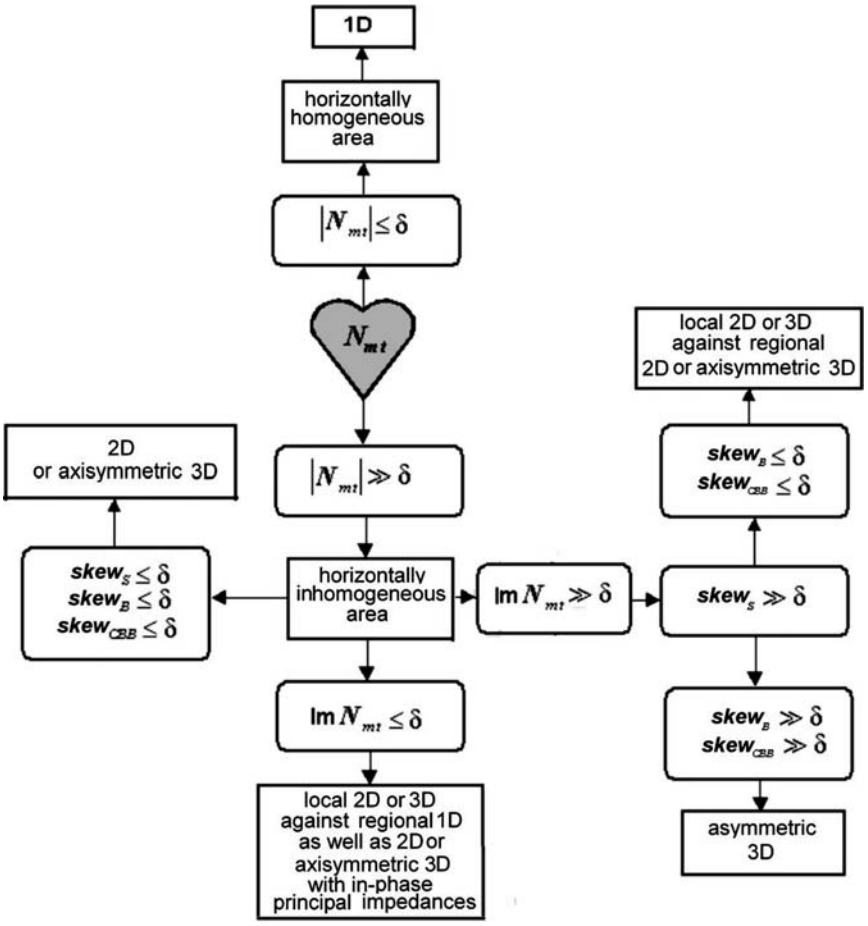

Fig. 11.34 Flow chart for the magnetotelluric dimensionality test

The starting point in Berdichevsky-Dmitriev test is the inhomogeneity parameter N_{mt}. Here we outline the horizontally homogeneous (quasi-one-dimensional) areas with $|N_{mt}| \leq \delta$ and recognize the two-dimensional and three-dimensional areas with $|N_{mt}| >> \delta$, which are the subject for further study. Testing *skew* and $\mathrm{Im}N_{mt}$, we divide these areas into zones of four types: (1) zones with two-dimensional (elongated) or axisymmetric (isometric) three-dimensional structures ($skew_S \leq \delta$, $skew_B \leq \delta$, $skew_{CBB} \leq \delta$), (2) zones with local two-dimensional (elongated) or three-dimensional structures and regional one-dimensional (quasi-one-dimesional) structures as well as two-dimensional or axisymmetric structures with in-phase principal impedances ($\mathrm{Im}N_{mt} \leq \delta$), (3) zones with local two-dimensional or three-dimensional structures and regional two-dimensional (elongated) or axisymmetric (isometric) three-dimensional structures ($\mathrm{Im}N_{mt} >> \delta$, $skew_S >> \delta$, $skew_B \leq \delta$, $skew_{CBB} \leq \delta$), (4) zones with asymmetric three-dimensional structures ($\mathrm{Im}N_{mt} >> \delta$, $skew_S >> \delta$, $skew_B >> \delta$, $skew_{CBB} >> \delta$).

Summing up the magnetovariational and magnetotelluric tests, we classify the target structures and apply the Zhang-Roberts-Pedersen, Bahr, Groom-Bailey, Chave-Smith, Ritter-Banks techniques to determine the strike of the regional two-dimensional background.

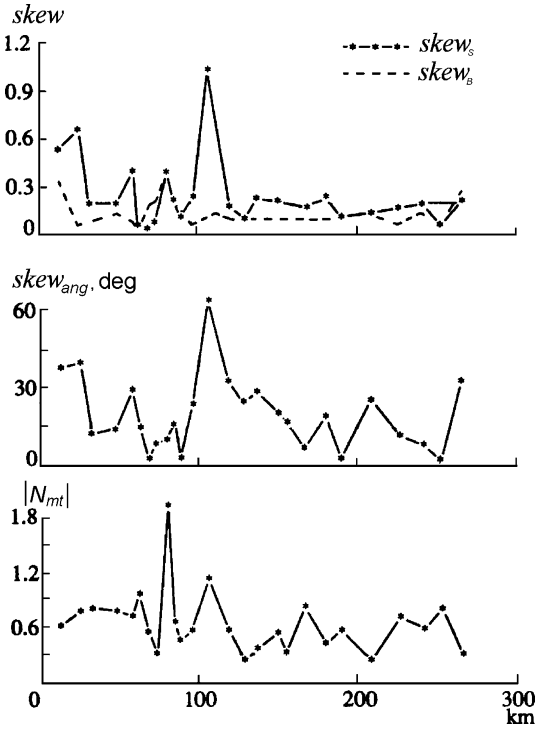

Fig. 11.35 Magnetotelluric parameters $|N_{mt}|$, $sqew_{ang}$,$skew_B$, $skew_S$ along a profile crossing the Kirghiz Tien Shan

11.3.3 Determining the Strike of the Regional Two-Dimensional Background

By way of example, let us consider the magnetotelluric parameters N_{mt}, $skew_{ang}$, $skew_S$, and $skew_B$ obtained on a submeridional profile crossing the Kirghiz Tien Shan (Fig. 11.35). The values of $|N_{mt}|$ almost everywhere exceed 0.3, indicating a strong lateral inhomogeneity. But in some parts of the profile, large values of $skew_S$ ($>>0.2$) correlate with relatively small values of $skew_B$ (< 0.1–0.15), revealing a superposition of local 3D structures and regional 2D background. Note that almost all anomalies of $skew_S \geq 0.3$ are reflected in $skew_{ang} \geq 15^\circ$. Figure 11.36 presents the impedance principal directions PD_{SE} defined by the Swift-Eggers decomposition and the strike of the regional 2D background specified by the Bahr decomposition. The directions PD_{SE} vary chaotically, evidencing a random noise caused by local 3D inhomogeneities, whereas the regional strike gravitates to latitudinal direction with rather small deviations.

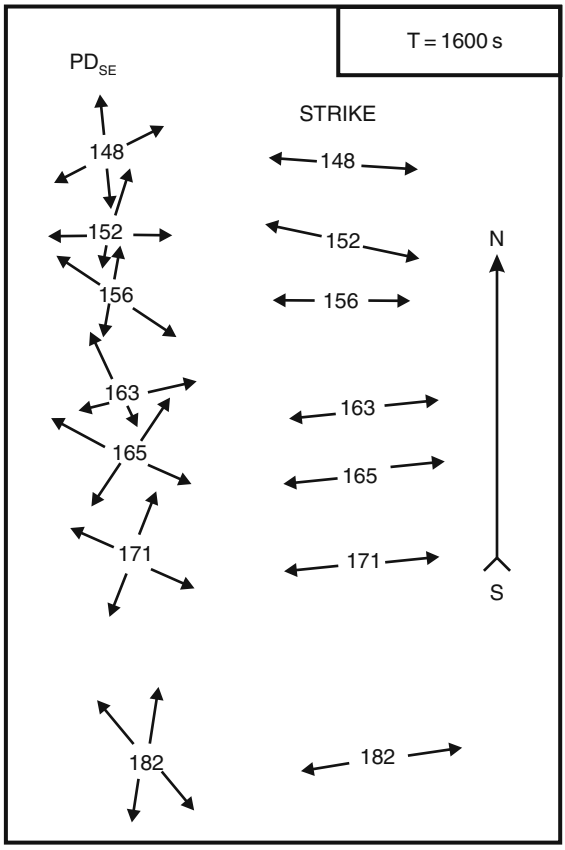

Fig. 11.36 Impedance principal directions along a profile crossing the Kirghiz Tien Shan; PD_{SE}– defined by Swift-Eggers method, STRIKE – defined by Bahr method

11.4 Visualizing the Geoelectric Structures

The magnetovariational and magnetotelluric tests may give a good indication of dimensionality of geoelectric structures, their position and strike. We detail these indications by visualizing the geoelectric structures. This can be done in several ways – for instance: (1) plotting tipper vectors (induction arrows), (2) constructing impedance and tipper polar diagrams, (3) drawing the profiles, maps, pseudo-sections and pseudo-topographies of magnetotelluric and magnetovariational response functions.

11.4.1 Plotting Tipper Vectors

We will start with tipper vectors. Recall that in the Wiese convention the real tippers diverge from conductive structures and converge to resistive structures. In the 2D model they are perpendicular to the structure strike. Considering tippers, we classify structures by their conductivity and trace their geometry.

Let us return to the model from Fig. 2.3. This superimposition model contains a Γ-shaped resistive inclusion in the upper layer and a 2D deep regional conductive prism in the intermediate layer. Figure 11.37 presents the Wiese-Parkinson and Vozoff tippers, Re **W** and **V**, calculated for period $T = 160$ s. One can see that arrows Re **W** and **V** converge to the middle of the Γ-shaped resistive inclusion, the **V**-arrows giving somewhat more distinct pattern than the Re **W**-arrows.

Next we consider two instructive experimental examples.

Figure 11.38 presents a map of the Kirghiz Tien Shan with real Wiese-Parkinson tippers Re **W** plotted for $T = 1600$ s (Trapeznikov et al., 1997). Southern regions of the Kirghiz Tien Shan exhibit small chaotically oriented induction arrows. But

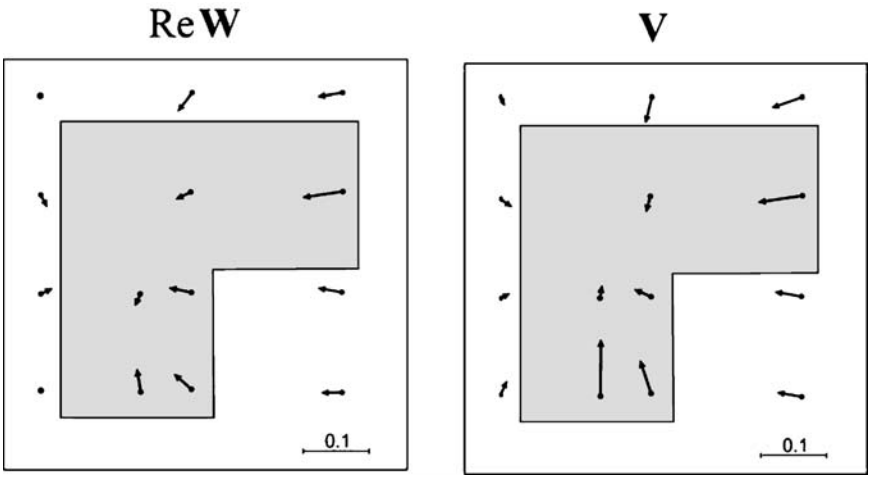

Fig. 11.37 Real Wiese-Parkinson tippers Re **W** and Vozoff tippers **V** over a near-surface Γ-shaped resistive inclusion in the superimposition model shown in Fig. 2.3

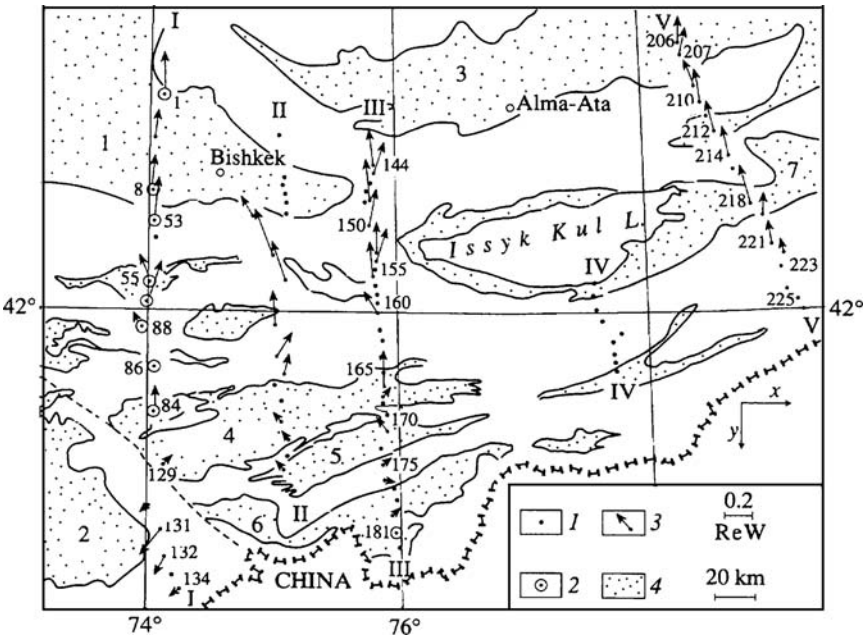

Fig. 11.38 Real Wiese-Parkinson tippers Re **W** along profiles I-I, II-II, III-III, IV-IV, V-V crossing the Kirghiz Tien Shan, T=1600 s (Trapeznikov et al., 1997) 1- MTS, 2- long-period deep MTS, 3- Re **W**, 4- sedimentary basins: Chu (1), Fergana (2), Ili (3), Naryn (4), Atbashi (5), Susamyr (6), Issyk Kul (7)

moving north, we meet a vast area with large induction arrows which are directed toward the northwest, north and northeast. We can believe that such anomaly is caused by a deep conductive layer whose resistivity increases from the south to the north.

Figure 11.39 shows a map of the south-west of the East European platform with real Wiese-Parkinson tippers Re **W** plotted for $T = 300$ s (Jankovski et al., 2004). We see a striking correlation between the iduction arrows and configuration of the crystalline basement depth isolines. The vectors Re **W** are directed toward the basement uplift, being transverse to the depth isolines. Here the induction arrows reflect the topography of the crystalline basement.

One more example of the real Wiese-Parkinson tippers Re **W** taken from the audiomagnetotellurics surveys in Jakutia is shown in Fig. 11.40. We see here the induction arrows plotted for $T = 0.001$ s. They run out of an isometric conductive zone that coincides with the known diamond pipe filled with loose volcanic formations.

11.4.2 Constructing Impedance and Tipper Polar Diagrams

The typical polar diagrams of the impedance tensor, phase tensor, and tipper were shown in Figs. 1.7, 1.8, 3.12, 4.2. Now we consider the polar diagrams of the

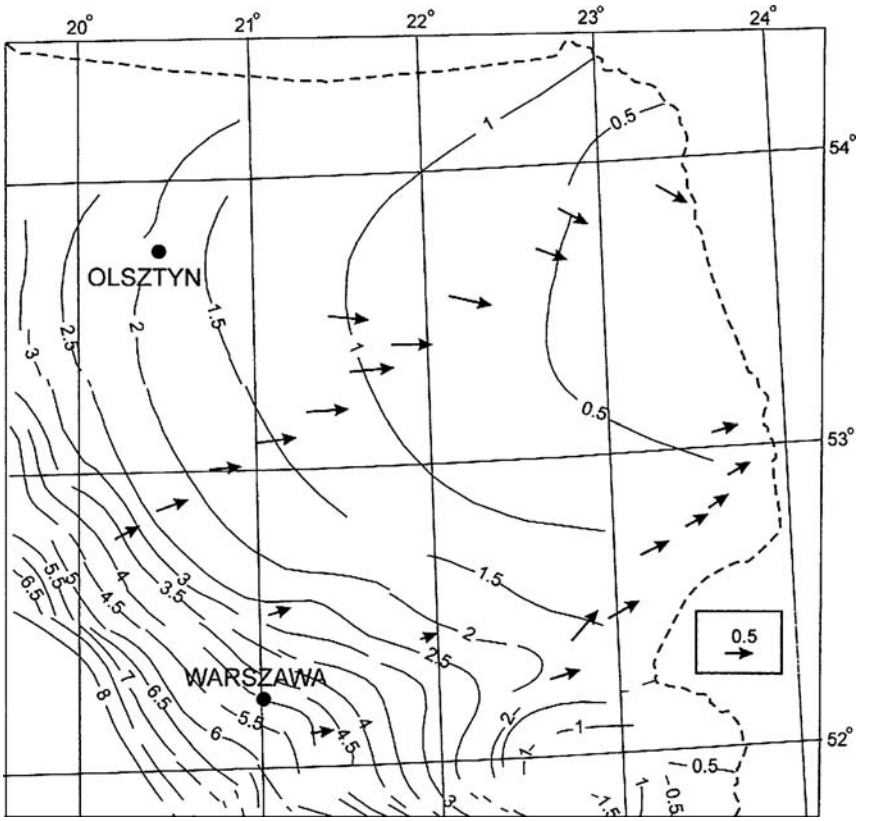

Fig. 11.39 Real Wiese-Parkinson tippers Re **W** at the south-west periphery of the East European platform, T=300 s (Jankovski et al., 2004)

impedance and phase tensors synthesized for the superimposition model from Fig. 2.3. The model contains a near-surface local resistive Γ-shaped inclusion and a deep regional conductive two-dimensional prism. The calculations have been performed at $T = 640$ s.

The amplitude diagrams of $|Z_{xx}|$ and $|Z_{xy}|$ shown in Figs. 11.41a,b expose a distorting effect of the near-surface resistive inclusion. The behavior of the $|Z_{xx}|$-diagrams is difficult to interpret: the variations in their shape and orientation seem to be rather chaotical. But the $|Z_{xy}|$-diagrams look like regular ovals with a more or less narrow waist, and their major diameters follow the direction of the current flowing around the resistive inclusion. So, they can give an idea of the inclusion resistivity and its geometry. The phase diagrams of $|\arg Z_{xy}|$ are worthy of special attention (Fig. 11.41c). They are free from the distorting effect of the near-surface inclusion. These diagrams everywhere appear as identical regular ovals elongated across the strike of the deep regional prism. The directions of the minimum diameter determine the strike of the prism, and the maximum and minimum half-diameters yield the phase of the transverse and longitudinal regional impedances $|\arg Z^{\perp}|$ and $|\arg Z^{\parallel}|$. Uncertainties of these determination do not exceed 5°.

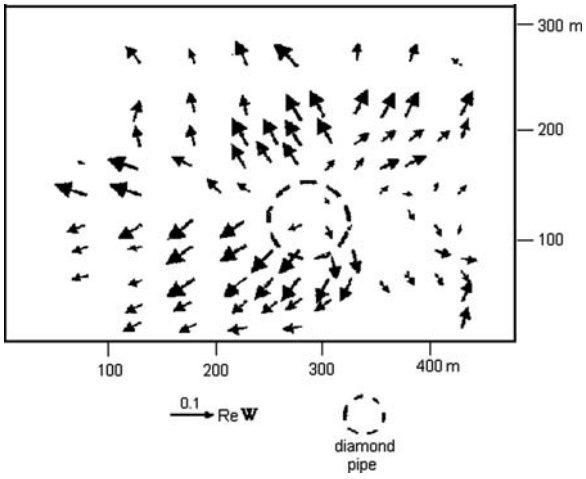

Fig. 11.40 Real Wiese-Parkinson tippers Re **W** over the diamond pipe (Jakutia), T=0.001 s

Figures 11.41d,e present the polar diagrams of the E- and H-polarized impedances. They show dramatic influence of the near-surface resistive inclusion. The Z_E- diagrams are the most intriguing. Their orientation changes rather sharply following the direction of the current flowing around the resistive inclusion. Here the flow-around effect is more pronounced than in the $|Z_{xy}|$-diagrams.

Polar diagrams of the phase tensor are shown in Fig. 11.41f,g. The great majority of the φ_{xx}-diagrams have the shape of regular ovals elongated along the strike of the deep regional prism. Being analogues of the $|\arg Z_{xy}|$-diagrams, they are similar in shape but are oriented at a right angle. The directions of the maximum diameter of the φ_{xx}- diagrams determine the strike of the prism, and the minimum and maximum half-diameters yield the phases of the transverse and longitudinal regional impedances $|\arg Z^{\perp}|$ and $|\arg Z^{\parallel}|$. Uncertainties of these determinations may reach 10–12°. Almost all the φ_{xy}- diagrams appear as four-petal flowers, and the bisectors between the petals are directed along and across the strike of the regional prism. However at two sites we observe rather large deviation from this pattern specific to the 2D-model. Comparing between (Fig. 11.41f,g) and (Fig. 11.41c), we can see that the phase diagrams of the impedance tensor are less distorted by the near-surface inclusion and better approximate the deep two-dimensional prism than the diagrams of the phase tensor. This can be explained by the fact that the phase tensor is defined without taking into account the near-surface magnetic anomalies.

It seems that the combined analysis of impedance polar diagrams can be usefull in separating the local and regional effects. The analysis is most effective with the E- polarized impedance diagrams, characterizing the near-surface structure, and the phase diagrams of the impedance tensor, throwing light on the deep structure.

This analysis can be supplemented by the analysis the tipper diagrams, which expose the near-surface structure on high frequencies and the deep structure on the low frequencies. The tipper diagrams have the form of figure-eight, their waist defines the departure from the two-dimensionality and they can bring an arrow, which points away from the conductive zone.

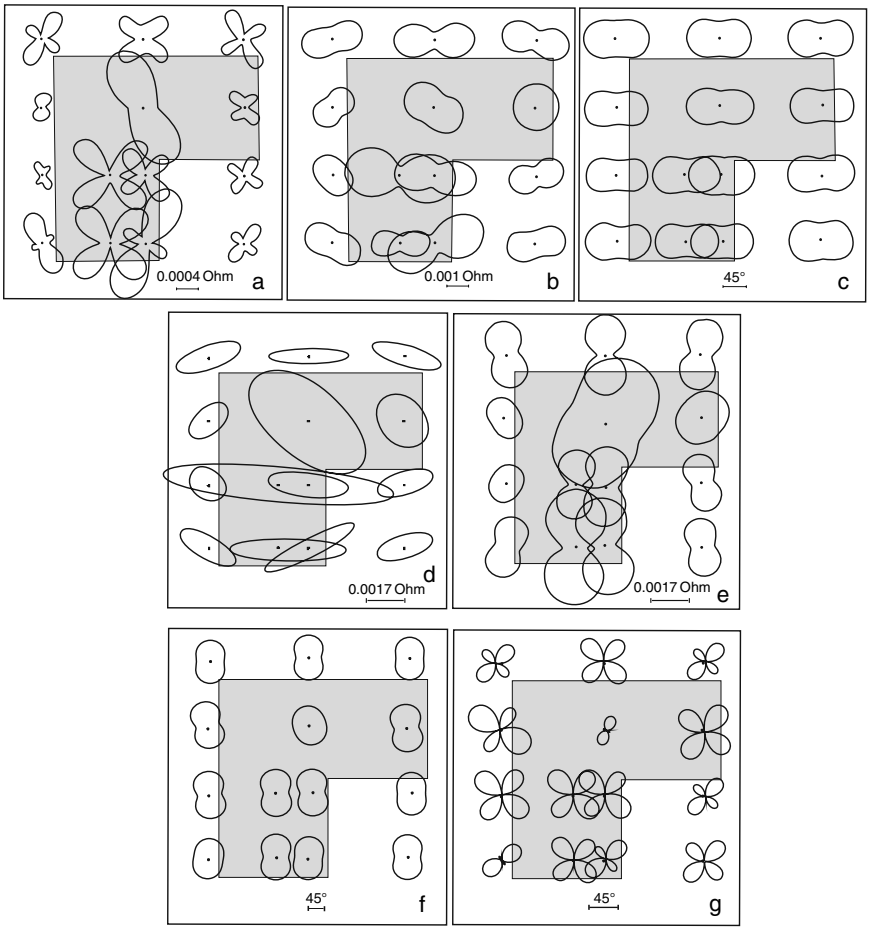

Fig. 11.41 Polar diagram of the impedance tensor and phase tensor in the superimposition model shown in Fig. 2.3; the model contains a near-surface local resistive Γ-shaped inclusion and a deep regional conductive 2D prism. Impedance tensor: a – diagram of $|Z_{xx}|$, b - diagram of $|Z_{xy}|$, c - diagram of $|\arg Z_{xy}|$; Polarized impedances: d – diagram of *E*-polarized impedance, e - diagram of *H*-polarized impedance; Phase tensor: f – diagram of φ_{xx}, g - diagram of φ_{xy}

Figure 11.42 exemplifies relationships between magnetotelluric and magnetovariational low-frequency polar diagrams plotted along the same profile as in Figs. 11.36. No regularity can be seen in the behavior of the diagrams of $|Z_{xy}|$ and$|Z_{xx}|$. Their shape and orientation vary chaotically. This should be ascribed to a strong effect of local near-surface 3D inhomogeneities, producing random noise. The diagrams of $|\arg Z_{xy}|$ are more stable with respect to near-surface distortions. At many sites they are elongated in the submeridional direction, reflecting the sublatitudinal strike of the regional 2D structures. The most informative are the tipper diagrams. All of them are oriented in the submeridional direction, their waist

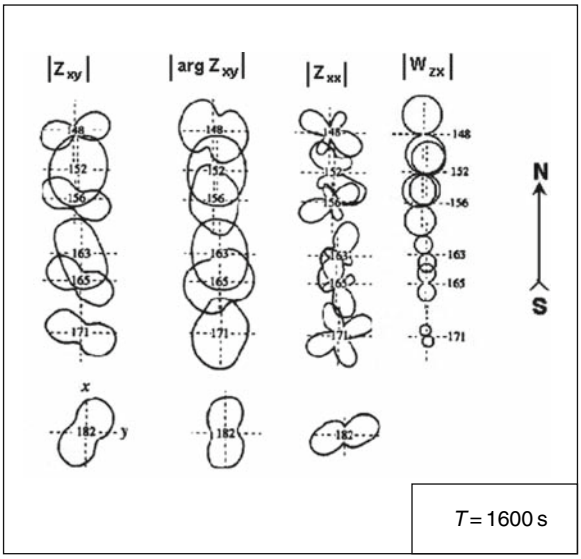

Fig. 11.42 Polar diagrams of the impedance tensor and Wiese-Parkinson matrix along a profile crossing the Kirghiz Tien Shan

being rather narrow. This confidently indicates the regional two-dimensional background with the sublatitudinal strike.

11.4.3 Drawing the Profiles, Maps, Pseudo-Sections and Pseudo-Topographies of MT and MV Response Functions

More detailed information on the shape and position of geoelectric structures can be obtained from the profiles, maps, pseudo-sections and pseudo-topographies of magnetotelluric and magnetovariational response functions. We will consider several examples demonstrating the informativeness of these graphical representations.

Figure 11.43 presents the electric (telluric) and magnetic effective intensities, $D_{\text{eff}} = \sqrt{|D_{xx}D_{yy} - D_{xy}D_{yx}|}$ and $M_{\text{eff}} = \sqrt{|M_{xx}M_{yy} - M_{xy}M_{yx}|}$, along a profile crossing the East Urals and the Tobol'sk tectonic zone. The thickness of the sandy-argillaceous Cenozoic and Mezozoic strata increases from 600 m near the Urals to 2000 m in the vicinity of Tobol'sk. Some small-scale structures are seen against this background. Here D_{eff} and M_{eff} are in rather good agreement with each other. They evidently reflect the regional Mezozoic topography. To downsinking of the bottom of the Mezozoic sediments there corresponds a decrease in D_{eff} and an increase in M_{eff}. Such a correlation is typical for regions with quiet tectonics and gentle geoelectric variations in the absence of high resistive screening layers.

Quite different picture is observed in regions, where the sediments contain high resistive screening layer. Here the electric intensity D_{eff} reflects the topography of this layer, while the magnetic intensity M_{eff} can reflect the crystalline basement topography.

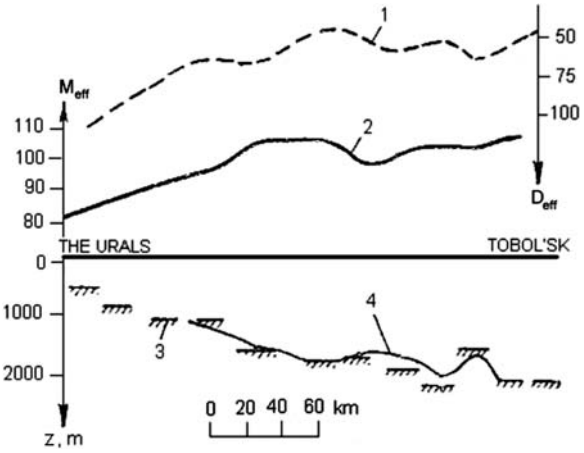

Fig. 11.43 Electric and magnetic effective intensities D_{eff} and M_{eff} along the profile Urals-Tobol'sk; 1 – D_{eff} (conventional units), 2 – M_{eff} (conventional units), 3 – Mezozoic bottom from MTS-data, 4 – Mezozoic bottom from seismic data

Consider an example of such relations taken from the MT-surveys on the Siberian platform. The terrigenous sediments in the region under consideration contain trappean intrusions (Upper Cambrian) and salt-bearing strata (Lower Cambrian). Figure 11.44 presents a map (**a**) for the depth of reflecting horizon in the Lower Cambrian and for the sediments conductance S. The contours on the seismic horizon outline two deep structures: the Sokolov depression (SD) and the Romanov uplift (RU). At the same time the conductance contours show a submeridional uplift at the place where the reflection seismics gives the Sokolov depression. Explanation to this contradiction is that the S-map reflects topograthy of near-surface trappean intrusions. Let us compare the map A with a map (**b**) for the telluric and magnetic effective intensities, D_{eff} and M_{eff}. The S– and D_{eff}−maps look similar. A submeridional maximum of D_{eff} outlined in the vicinity of the village Sokolov corresponds to the minimum of S elongated approximately in the same direction. By and large the seismic map and the M_{eff}–map are also similar. The minimum of M_{eff} outlined in the vicinity of the village Romanov corresponds (with some displacement) to the Romanov uplift. Summing up, we can say that D_{eff}–map characterizes (at least qualitatively) the trappean intrusions, while the M_{eff}–map provides a rough idea of the basement topography.

Next we will show a synthetic example. Let us turn again to the superimposition model from Fig. 2.3 containing a near-surface local resistive Γ-shaped inclusion and a deep regional conductive two-dimensional prism. Figure 11.45 shows the contour maps of the apparent resistivities

$$\rho_{\text{eff}} = \frac{|Z_{\text{eff}}|^2}{\omega\mu_o} = \frac{\left|Z_{xx}Z_{yy} - Z_{xy}Z_{yx}\right|}{\omega\mu_o}, \qquad \rho_{\text{brd}} = \frac{|Z_{\text{brd}}|^2}{\omega\mu_o} = \frac{\left|Z_{xy} - Z_{yx}\right|^2}{4\omega\mu_o},$$

$$\rho_{\text{rms}} = \frac{Z_{\text{rms}}^2}{\omega\mu_o} = \frac{|Z_{xx}|^2 + \left|Z_{xy}\right|^2 + \left|Z_{yx}\right|^2 + \left|Z_{yy}\right|^2}{2\omega\mu_o}$$

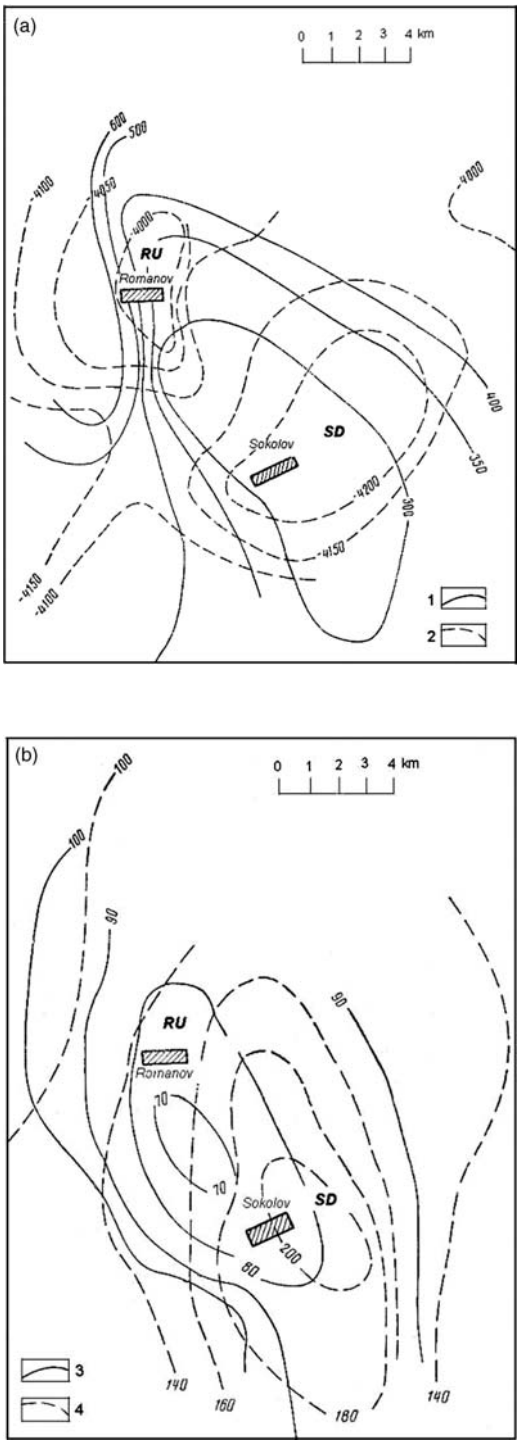

Fig. 11.44 Mapping the electric and magnetic effective intensities D_{eff} and M_{eff} in the Siberian platform. (**a**) map of the sediments conductance in comparison with structural map of the reflecting horizon in the Lower Cambrian, 1 – contours of conductance (S), 2 – structural contours on reflecting horizon (m). (**b**) map of magnetic effective intensity M_{eff} and electric effective intensity D_{eff}, 3 – contours of M_{eff} (conventional units), 4 – contours of D_{eff} (conventional units)

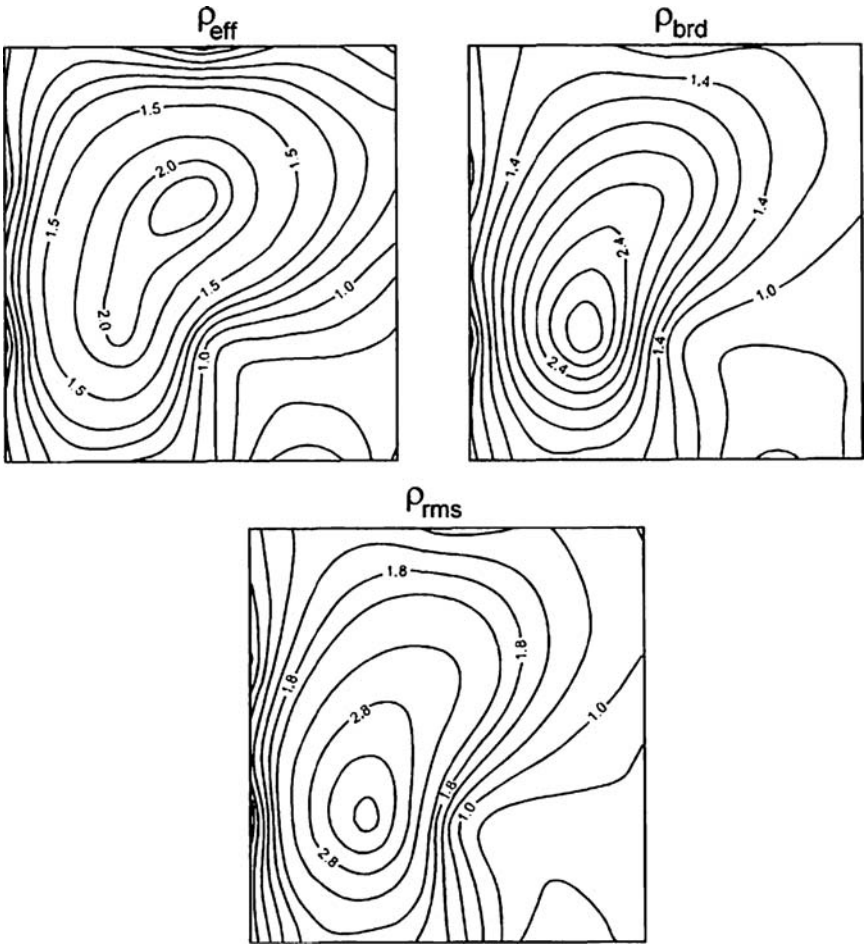

Fig. 11.45 Maps of apparent resistivities ρ_{eff}, ρ_{brd}, ρ_{rms} in the model shown in Fig. 2.3. The model contains a near-surface resistive Γ-shaped inclusion

plotted at $T = 640$ s. All three maps exhibit more or less smoothed Γ-shaped maximum reflecting the inclusion shape. Note that over the entire range of low frequencies relating to the S_1- and h-intervals the form of the contour lines is hardly changed. Note also that the most adequate inclusion shape is given by ρ_{eff}, whereas ρ_{rms} gives the largest amplitude of the Γ-shaped maximum.

Next we will consider the pseudo-sections and pseudo-topograpfies of the magnetotelluric and magnetovariational response functions that can give the most pictorial image of geoelectric structures.

Figure 11.46 provides a synthetic example of pseudo-sections of apparent resistivity and impedance phase. A two-dimensional model consists of a conductive layer, $\rho_1 = 10\,\Omega\text{m}$, and a resistive layer, $\rho_2 = 10000\,\Omega\text{m}$, resting on

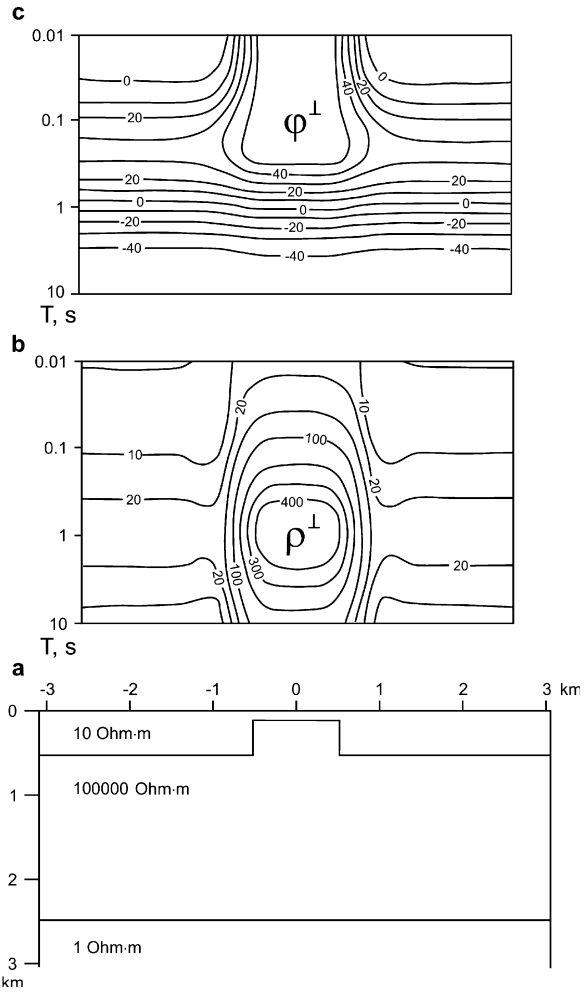

Fig. 11.46 Pseudo-sections of the transverse apparent restivity $\rho^{\perp}$ and impedance phase $\varphi^{\perp}$ in a model with the horst in the upper layer; (**a**) the model cross-section, (**b**) pseudo-section of $\rho^{\perp}$, (**c**) pseudo-section of $\varphi^{\perp}$

a conductive basement, $\rho_3 = 1\,\text{Ohm} \cdot \text{m}$. The surface of the ρ_2– layer forms a rectangular ledge imitating a horst. The pseudo-sections of the transverse apparent resistivities, $\rho^{\perp}$, and transverse impedance phases, $\varphi^{\perp}$, are oriented across the horst. Both of these cross-sections demonstrate intensive anomalies reflecting the horst. But anomaly of $\rho^{\perp}$ has a false deep root in the lower part of the pseudo-section. This root is caused by the static shift of the low-frequency branches of transverse $\rho^{\perp}$-curves (the *S*– effect). At the same time, the anomaly of $\varphi^{\perp}$ is closed within the upper part of the pseudo-section related to the ρ_1- layer and does not violate the horizontal layering of the underlying medium. So, comparing the amplitude and phase pseudo-sections, we can get a good image of the horst and outline the area with strong static distortions of the $\rho^{\perp}$ – curves.

A prominent example of the pseudo-sections of the effective apparent resistivity and impedance phase, ρ_{eff} and φ_{eff}, is given in (Ranganayaki, 1984). Figure 11.47

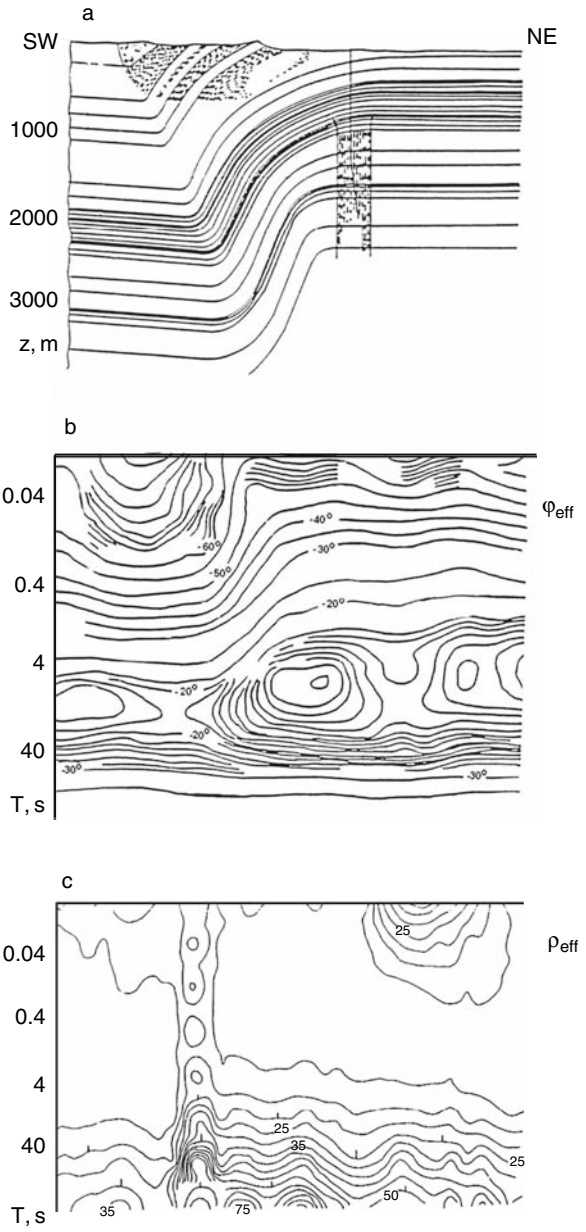

Fig. 11.47 Geologic cros-section of The Women's Pocket Anticline and pseudo-sections of effective impedance phase φ_{eff} and apparent resistivity ρ_{eff}; (**a**) geologic cross-section, (**b**) pseudo-section of φ_{eff}, (**c**) pseudo-section of ρ_{eff} (Ranganayaki, 1984)

presents the geologic cross-section of the steep anticlinal fold (The Woman's Pocket fold in Golden Valley County, Montana) as well as ρ_{eff} and φ_{eff} pseudo-sections plotted along the same profile. It is rather instructive to see how closely the φ_{eff} pseudosection resembles the geologic cross-section. Moving from the SW side of the fold to its NE side, we observe a sharp decrease in φ_{eff} ($T = 0.04 - 4$ s), which

shows that the fold involves a steep uprise of resistive layers. But at $T > 40$ s the phase contours become horizontal, which suggests that the basement of the fold is flat-layered. The ρ_{eff} pseudo-section is less indicative. At $T > 40$ s the NE side of the fold is marked by higher values of ρ_{eff} reflecting an uprise of resistive layers. There is no evidence of the flat-layered basement. A characteristic feature of the ρ_{eff} pseudo-section is that the near-surface inhomogeneity generates the vertical static anomaly that runs between the two sides of the fold through the entire ρ_{eff} pseudo-section (the ρ-effect) and spoils information on the fold.

Now we consider several examples of the pseudo-topography. This pictorial technique is a three-dimensional generalization of the pseudo-sections. We present pseudo-topographies plotted from synthetic data.

An initial three-dimensional model is shown in Fig. 11.48. In this seven-layer model, the first, second and third layers imitate sediments, whereas the fourth, fifth, and sixth layers are identified with the high-resistivity lithosphere. A conductive mantle serves as the base of the model. The first sedimentary layer contains a

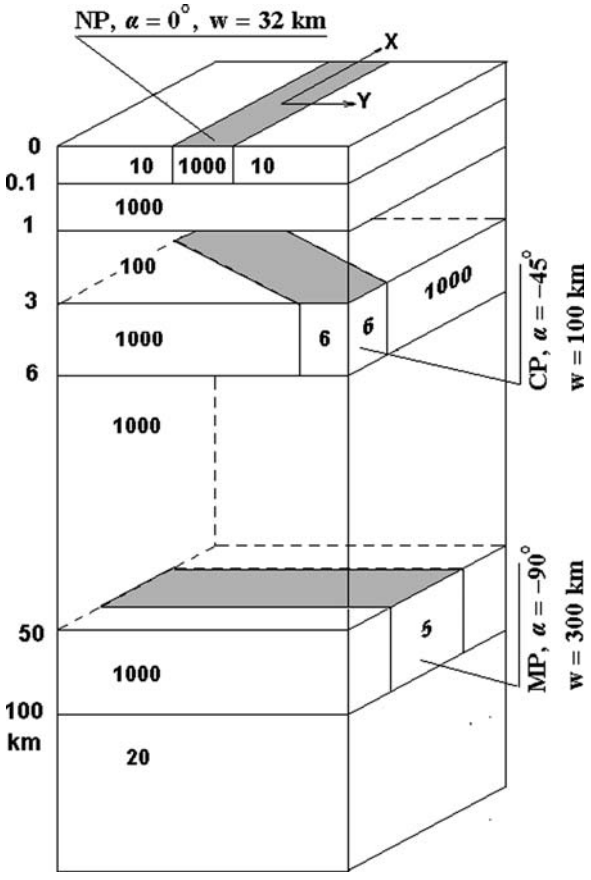

Fig. 11.48 Three-dimensional synthetic model containing a near-surface (NP), crustal (CP), and mantle (MP) 2-D prisms; α is the prism strike azimuth, w is the prism width, and the numbers in the frontal and lateral faces of the model are resistivities of the layers and prisms in Ohm·m

high-resistivity inclusion in the form of an infinitely long rectangular prism NP (near-surface prism) 32 km wide striking at an azimuth 0° measured from the *x*-axis. The fourth (crustal) layer contains a conductive inclusion in the form of an infinitely long rectangular prism CP (crustal prism) 100 km wide striking at an azimuth of –45°. The prism contacts the sedimentary cover. The conductive mantle has an uplift in the form of an infinitely long rectangular prism MP (mantle prism) with a width of 300 km, a height of 50 km, and a strike azimuth of –90°.

The forward problem was solved with the help of the standard Mackie program (Mackie et al., 1994). Based on this solution, the following magnetovariational and magnetotelluric response functions were calculated:

1. The Wiese–Parkinson matrix [**W**] interrelating horizontal and vertical components of the magnetic field:

$$H_z = [\mathbf{W}]\,\mathbf{H}_\tau, \quad [\mathbf{W}] = [W_{zx}\ W_{zy}], \qquad \mathbf{H}_\tau = \begin{bmatrix} H_x \\ H_y \end{bmatrix}.$$

The pseudo-topography of the invariant $\|\mathbf{W}\| = \sqrt{|W_{zx}|^2 + |W_{zy}|^2}$ is constructed. At the surface of a horizontally homogeneous Earth, we have $\|\mathbf{W}\| = 0$.

2. The magnetic tensor [**M**] relating horizontal components of the magnetic field to horizontal components of the normal magnetic field:

$$\mathbf{H}_\tau = [\mathbf{M}]\,\mathbf{H}_\tau^{\mathrm{N}}, \quad \mathbf{H}_\tau = \begin{bmatrix} H_x \\ H_y \end{bmatrix}, \quad [\mathbf{M}] = \begin{bmatrix} M_{xx} & M_{xy} \\ M_{yx} & M_{yy} \end{bmatrix}, \qquad \mathbf{H}_\tau^{\mathrm{N}} = \begin{bmatrix} H_x^{\mathrm{N}} \\ H_y^{\mathrm{N}} \end{bmatrix}.$$

The pseudo-topography of the invariant

$$\|\mathbf{M}\| = \sqrt{\frac{|M_{xx}|^2 + |M_{xy}|^2 + |M_{yx}|^2 + |M_{yy}|^2}{2}}$$

is constructed. At the surface of a horizontally homogeneous Earth, we have $\|\mathbf{M}\| = 1$.

3. The impedance tensor [**Z**] relating horizontal components of the electric field to horizontal components of the magnetic field:

$$\mathbf{E}_\tau = [\mathbf{Z}]\,\mathbf{H}_\tau, \qquad \mathbf{E}_\tau = \begin{bmatrix} E_x \\ E_y \end{bmatrix}, \qquad [\mathbf{Z}] = \begin{bmatrix} Z_{xx} & Z_{xy} \\ Z_{yx} & Z_{yy} \end{bmatrix}, \qquad \mathbf{H}_\tau = \begin{bmatrix} H_x \\ H_y \end{bmatrix}.$$

The invariant $Z_{\mathrm{brd}} = (Z_{xy} - Z_{yx})/2$ is calculated and the pseudo-topographies of the apparent resistivity $\rho_{\mathrm{brd}} = |Z_{\mathrm{brd}}|^2/\omega\mu_{\mathrm{o}}$ and the phase $\varphi_{\mathrm{brd}} = -\arg Z_{\mathrm{brd}}$ are constructed. We have $\rho_{\mathrm{brd}} = \rho$ and $\varphi_{\mathrm{brd}} = 45^\circ$ at the surface of a homogeneous Earth having a resistivity of $\rho = const$.

4. The phase tensor [Φ] obtained by the transformation of the impedance tensor:

$$[\Phi] = [\mathrm{Re}\ \mathbf{Z}]^{-1}[\mathrm{Im}\ \mathrm{Z}] = \begin{bmatrix} \Phi_{xx} & \Phi_{xy} \\ \Phi_{yx} & \Phi_{yy} \end{bmatrix}.$$

The pseudo-topography of the apparent phase

$$\varphi_{\mathrm{A}} = -\arctan \frac{\Phi_{xx} + \Phi_{yy}}{2}$$

is constructed. At the surface of a horizontally homogeneous Earth, we have

$$\varphi_{\mathrm{A}} = -\arg Z, \text{ where } Z \text{ is the 1D Tikhonov–Cagniard impedance.}$$

Figure 11.49 shows the pseudo-topography of Wiese–Parkinson matrix invariant $\|\mathbf{W}\|$ constructed in the range of periods from 0.16 to 10000 s. The near-surface, crustal, and mantle prisms are clearly recognizable here as edge maxima of $\|\mathbf{W}\|$ delineating the prisms. With increasing period, these maxima become smoother and broaden because the resolution of the Wiese–Parkinson matrix drops with depth. Examining the pseudo-topography of the invariant $\|\mathbf{W}\|$, we can identify periods at which the effects of various prisms are superimposed on each other and periods at which each prism is seen as a separate body unaffected (or almost unaffected) by the other prisms (the effects of the prisms are not superimposed). Thus, the period $T = 0.16$ s demonstrates the pure effect of the near-surface prism, while, at longer periods, the effects of the crustal ($T = 40$ s) and mantle ($T = 10000$ s) prisms are predominant. At these periods, we can change projections of the near-surface, crustal, and mantle prisms and find their azimuths (0, –45°, and –90°). Moreover, each of these prisms can admit a trial 2D inversion performed in a more or less narrow interval of periods around 0.16, 40, or 10000 s excluding the presence of other prisms. It is evident that the pseudo-topography of the invariant $\|\mathbf{W}\|$ of the Wiese–Parkinson matrix provides a good basis for the choice of adequate interpretation model.

We arrive at the same conclusion, examining the pseudo-topography of the invariant $\|\mathbf{M}\|$ of the magnetic tensor [**M**] shown in Fig. 11.50. The pseudo-topography of $\|\mathbf{M}\|$ is constructed in the same range of periods from 0.16 to 10000 s. The high resistivity near-surface prism is observed at the period $T = 0.16$ s as a 2D "graben" framed by maxima that arise due to the external skin effect in the conductive medium surrounding the prism (at high frequencies, the longitudinal electric current concentrates near the vertical faces of the high resistivity prism). With decreasing frequency, the effect of the near-surface prism decays, giving room to the effect of the conductive crustal prism ($T = 1$ and 6.3 s) which manifests itself as 2D "horst" with side maxima arising due to the internal skin effect. The effect of the crustal prism prevails at the period $T = 40$ s, so that this prism can be regarded as a separate body almost free from the influence of the near-surface and mantle prisms. The further decrease in frequency reveals the mantle prism resolved in the form of a flat maximum. The effects of the mantle and crustal prisms are superimposed at $T = 250$ s. At $T = 10000$ s, the effect of the mantle prism becomes predominant, while the effect of the crustal prism is nearly unrecognizable. In the vicinity of the

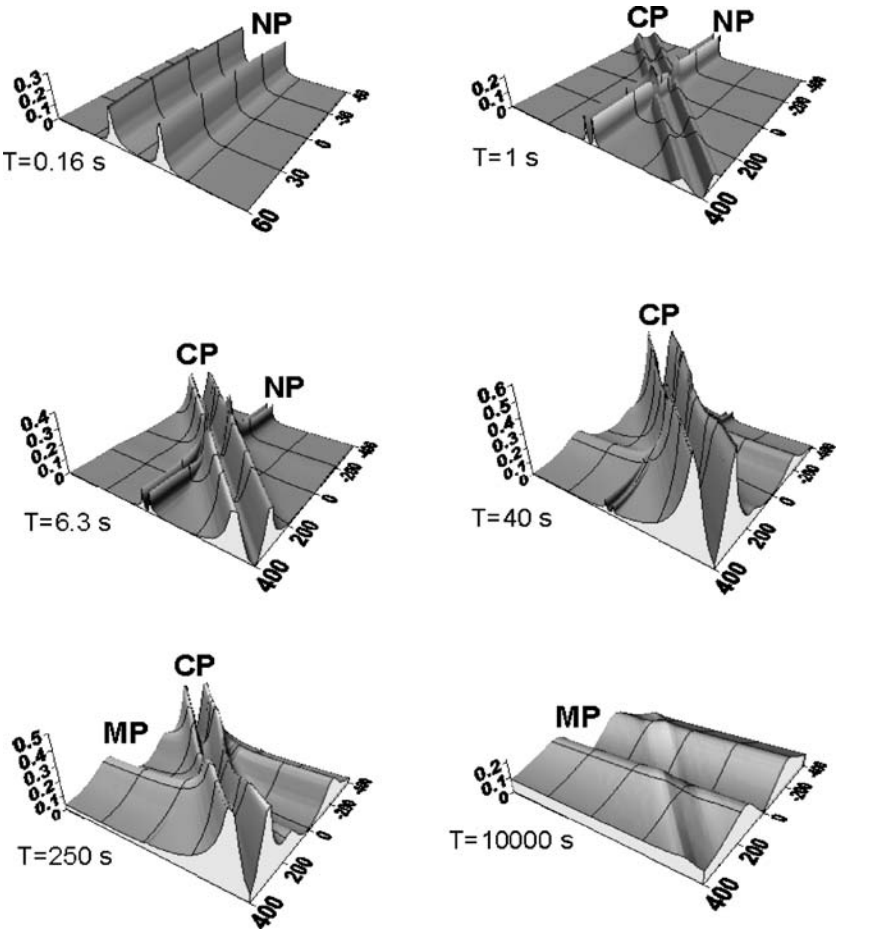

Fig. 11.49 Pseudo-topographies of the invariant $\|\mathbf{W}\|$ of the Wiese–Parkinson matrix: NP, CP, and MP are, respectively, the near-surface, crustal, and mantle prisms. The horizontal scale of distances is given in kilometers

periods $T = 0.16$, 40, and 10000 s, we can determine azimuths of all three prisms and perform a trial 2D inversion for each prism ignoring the presence of other prisms.

Now come back to the initial model and introduce chaotically distributed small-scale heterogeneities into the first sedimentary layer. Figure 11.51 presents the pseudo-topography of the invariant $\|\mathbf{W}\|$ of the Wiese-Parkinson matrix and the invariant $\|\mathbf{M}\|$ of the magnetic tensor constructed for this contaminated model. At $T = 1$ s, the effects of the near-surface and crustal prisms are lost in the geoelectric noise produced by the local heterogeneities of the sedimentary cover. However, already at $T = 6.3$ s, the effect of the crustal prism becomes noticeable and, at the period $T = 40$ s, it exceeds significantly the level of geoelectric noise. With the further decrease in frequency, the near-surface geoelectric noise disappears, and the

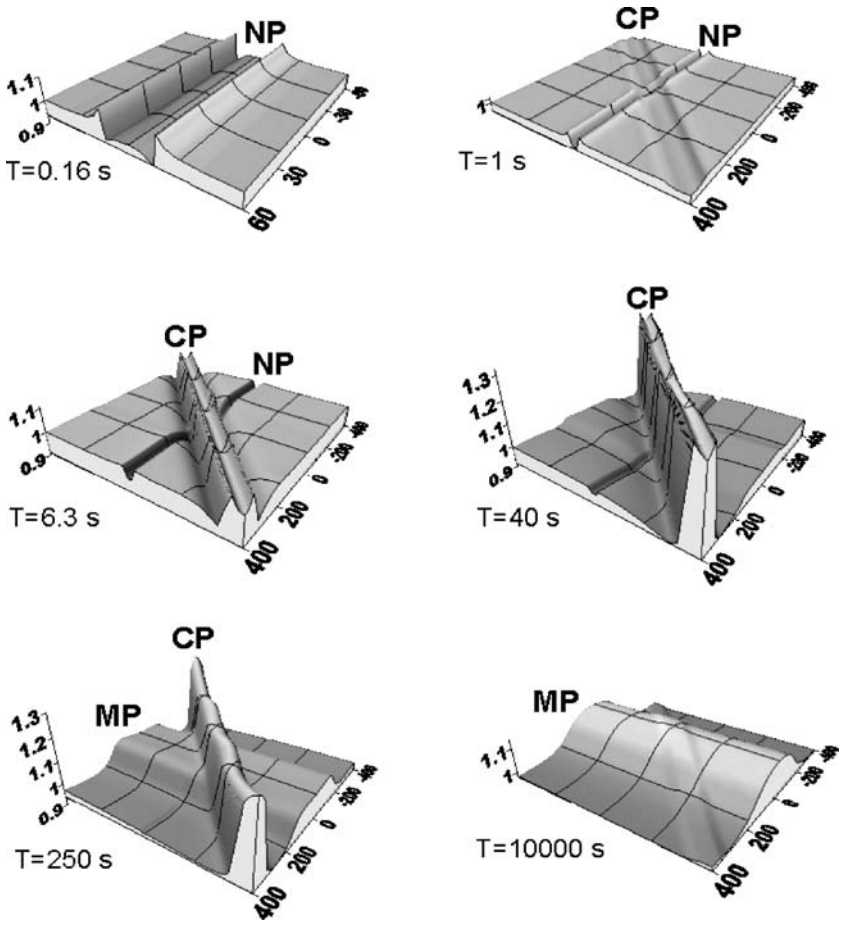

Fig. 11.50 Pseudo-topographies of the invariant $\|\mathbf{M}\|$ of the magnetic tensor: NP, CP, and MP are, respectively, the near-surface, crustal, and mantle prisms. The horizontal scale of distances is given in kilometers

effects of the crustal and mantle prisms in the interval of periods 250–10000 s are actually undistorted.

Summing up, we can say that the magnetovariational response functions, [**W**] and [**M**], resolve both the horizontal and vertical variations in the Earth's conductivity and are immune to the local near-surface galvanic distortions. There is every reason to believe that magnetovariational functions specified in a wide frequency range contain sufficiently complete parametric information on the geoelectric medium and this information can be obtained without troubles caused by the static shift.

Next we consider the pseudo-topographies of the magnetotelluric response functions.

Figure 11.52 presents the pseudo-topographies of the apparent resistivity ρ_{brd} constructed in the range of periods from 0.16 to 10000 s. At the period $T = 0.16$ s,

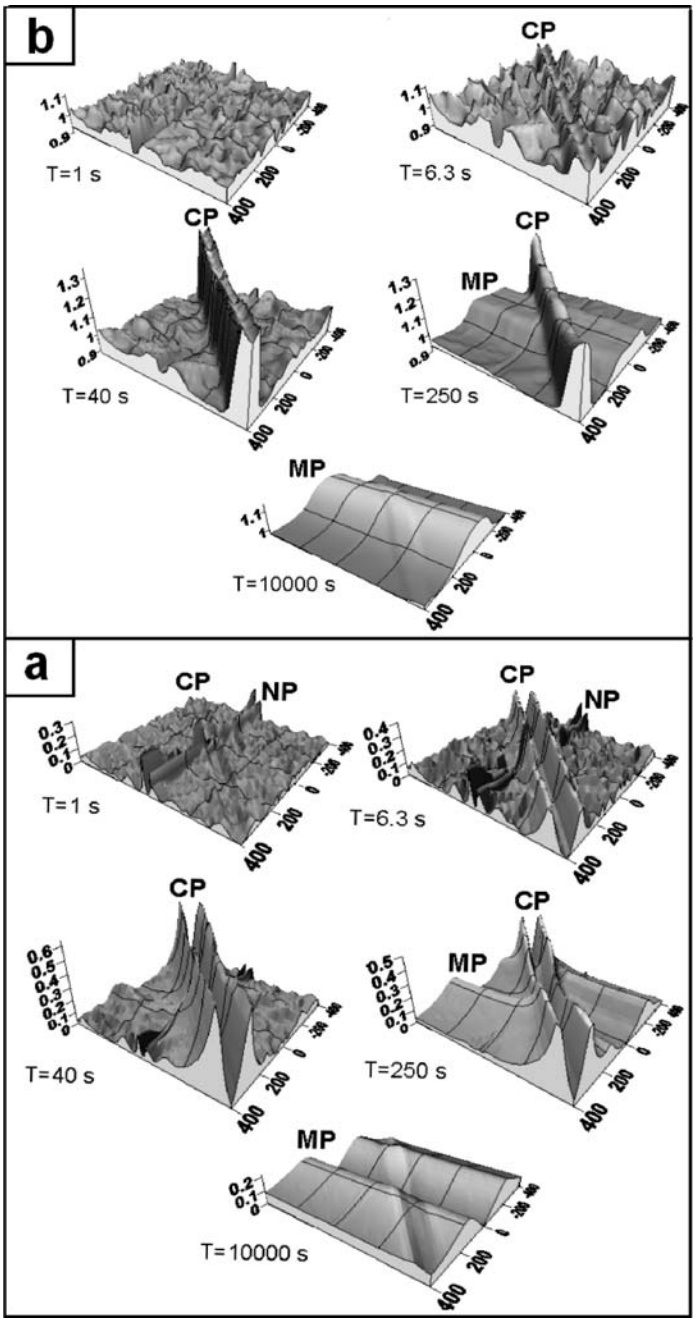

Fig. 11.51 Pseudo-topographies of the invariants $\|\mathbf{W}\|$ and $\|\mathbf{M}\|$ in the presence of strong near-surface noise: a - the invariant $\|\mathbf{W}\|$ of the Wiese–Parkinson matrix, b - the invariant $\|\mathbf{M}\|$ of the magnetic tensor, CP and MP are the crustal and mantle prisms, respectively. The horizontal scale of distances is given in kilometers

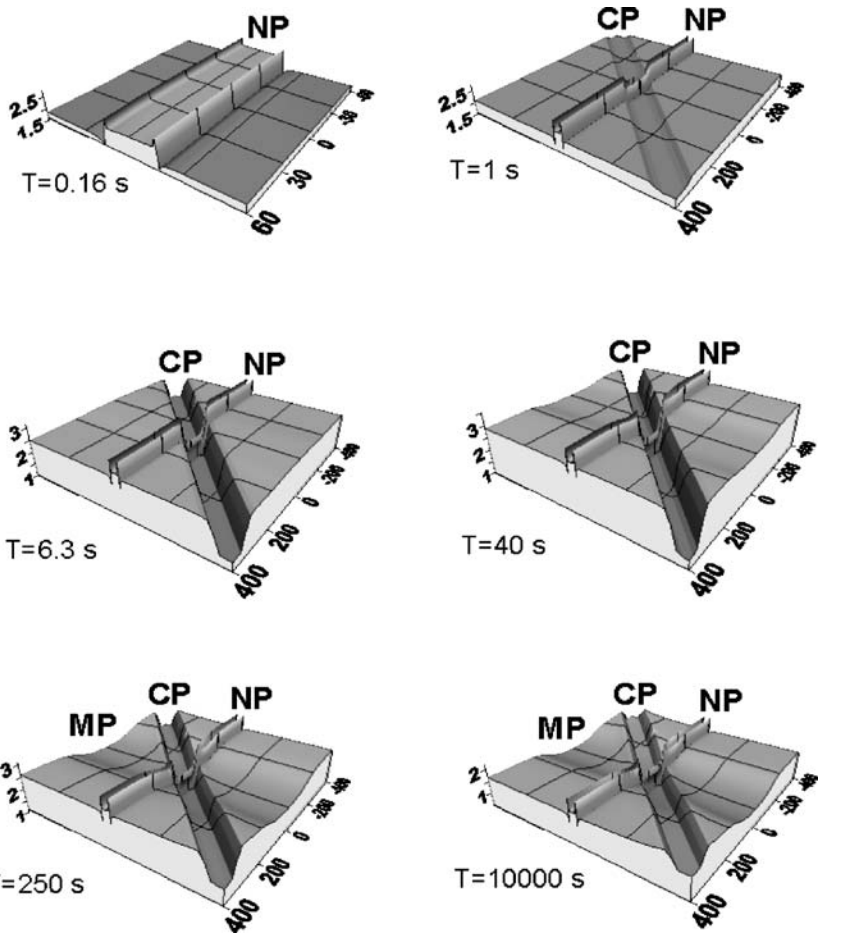

Fig. 11.52 Pseudo-topographies of the apparent resistivity ρ_{brd}: NP, CP, and MP are the near-surface, crustal, and mantle prisms, respectively. The horizontal scale of distances is given in kilometers, and the vertical scale of resistivities is given in logarithmic units of Ohm·m

we see the pure effect of the high-resistivity near-surface prism represented as a 2D "horst" framed by external minima and internal maxima arising due to the redistribution of the transverse current. With decreasing frequency, this effect does not attenuate but is superimposed on the effect of the conductive crustal prism resolved as a 2D "graben" (T = 1, 6.3, and 40 s). Here we see the joint action of two effects: the "horst" with an azimuth of 0°, reflecting the near-surface prism, and the "graben" with an azimuth of –45°, reflecting the crustal prism. With a further decrease in frequency, both effects are superimposed on the effect of the conductive mantle prism resolved as a gentle 2D "valley" striking at an azimuth of –90°

(T = 250 and 10000 s). Here the mantle-prism image bears evidences of the crustal prism and even of the near-surfase prism.

The pseudo-topography of the phase φ_{brd} is shown in Fig. 11.53. At $T = 0.16$ s, the high-resistivity near-surface prism is imaged as a 2D "horst" with an azimuth of 0°. When lowering frequency, this effect attenuates rather rapidly, giving place to the effect of the conductive crustal prism imaged as a 2D "horst" with an azimuth of –45° (T=1 and 6.3 s). As the frequency is further decreased, the effect of the near-surface prism virtually vanishes and we can see the superimposition of the crustal and mantle effects (T = 40 and 250 s). Here the conductive mantle prism is imaged as a gently sloping uplift striking at –90°. Both the effects are weakly expressed at the period $T = 10000$ s where the impedance phase reflects the homogeneous mantle underlying the mantle prism (at depths much greater than 100 km). To sum up, we

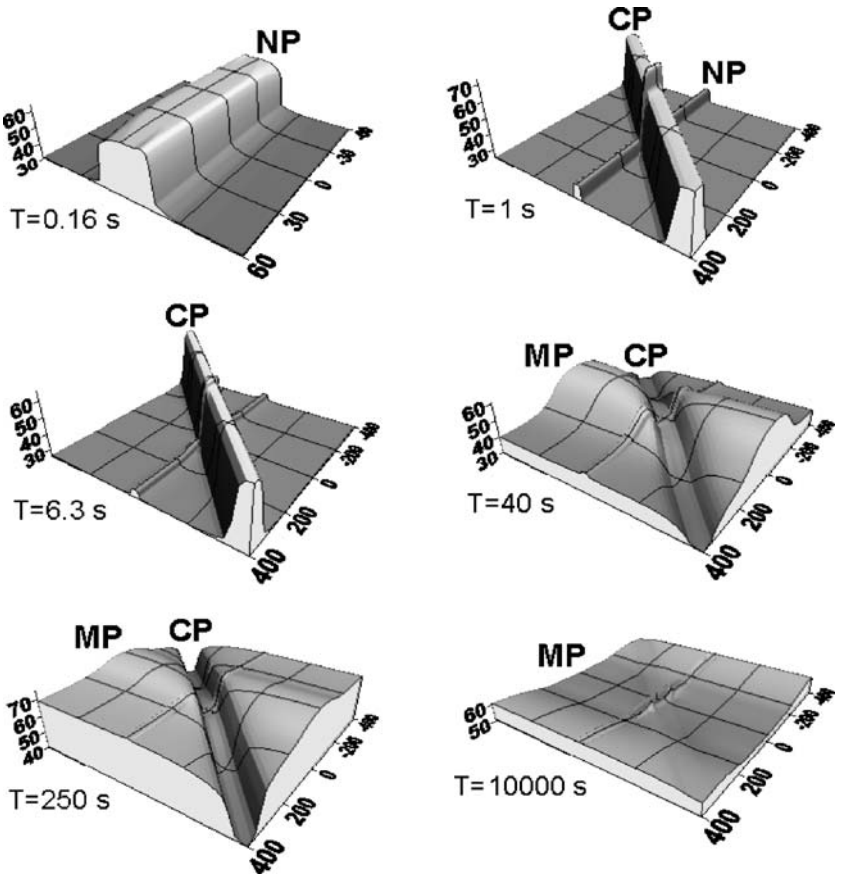

Fig. 11.53 Pseudo-topographies of the impedance phase φ_{brd}: NP, CP, and MP are, respectively, the near-surface, crustal, and mantle prisms. The horizontal scale of distances is given in kilometers, and the vertical scale of phases is given in degrees

note that (1) the phase φ_{brd} is much less subjected to near-surface distortions than the apparent resistivity ρ_{brd}, (2) in the model under consideration, the phase immunity to near-surface distortions is quite comparable with the immunity of the magnetovariational invariants $\|\mathbf{W}\|$ and $\|\mathbf{M}\|$, and (3) the resolution of the phase φ_{brd} leads in depth the resolution of the apparent resistivity ρ_{brd} and the magnetovariational invariants $\|\mathbf{W}\|$ and $\|\mathbf{M}\|$: whereas ρ_{brd}, $\|\mathbf{W}\|$ and $\|\mathbf{M}\|$ reliably detect the mantle prism in the range of periods 250–10000 s, the phase φ_{brd} reveals the mantle prism in the interval 40–250 s.

The pseudo-topography of the apparent phase φ_A determined from the phase tensor $[\mathbf{\Phi}]$ is displayed in Fig. 11.54. Comparing the pseudo-topographies of φ_A and φ_{brd}, we see that in the model under consideration the phase φ_A has approximately the same immunity to near-surface distortions as the phase φ_{brd}. In both pseudo-topographies, the effect of the near-surface prism virtually vanishes at the period $T = 6.3$ s, and the effect of the crustal prism decays at a period of about 10000 s.

Finally, we consider pseudo-topographies of the apparent resistivity ρ_{brd} and phase φ_{brd} determined in the model with the first sedimentary layer containing chaotically distributed small-scale heterogeneities. The pseudo-topography of ρ_{brd} is shown in Fig. 11.55. We see that the geoelectric noise produced by local heterogeneities fills all levels of the pseudo-topography, from $T = 1$ s to $T = 10000$ s. In this "forest" the near-surface, crustal and mantle prisms are lost. The pseudotopography of φ_{brd} shown in Fig. 11.56 is much more informative. Here, the levels $T = 1, 6.3$, and 40 s are filled with smoothed geoelectric noise which does not cover the crustal prism. And the levels $T = 250$ and 10000 s are almost free of the noise. Against this background, the effects of the crustal and mantle prisms can be identified quite reliably.

It seems that the pseudo-topography technique can prove helpful for constructing the interpretation model. The main advantage of this technique is that the topography of magnetotelluric and magnetovariational invariants is constructed without any restrictions and can give a fairly comprehensive idea of the resolution of different response functions, mutual position and shape of geoelectric structures, the superposition of their effects, the thickness and height of the "forest" produced by geoelectric noise.

11.5 Mapping the Sediments Conductance

The sediments conductance S is a traditional geoelectric parameter widely used in all methods of the electric and electromagnetic soundings with direct and alternating current. This parameter readily determined from the apparent-resistivity curves can give a qualitative information on the topography of the crystalline basement and variations in the thickness and resistivity of the sedimentary layers. Maps of S may provide the geolectric zoning of vast areas. They are helpful in recognizing local and regional structures as well as in analyzing the informativeness of the magnetotelluric and magnetovariational response functions.

Determining the sediments conductance by magnetotelluric sounding, we usually take the $\rho_{eff} -$ curves and apply a simplified technique which is valid for the 1D

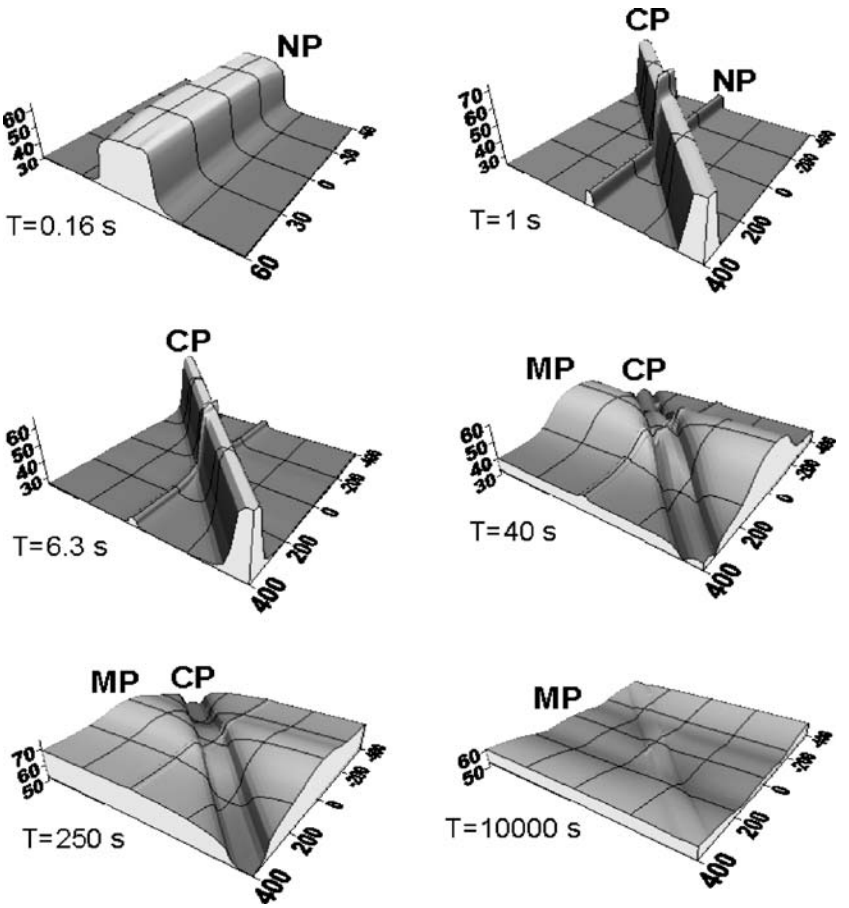

Fig. 11.54 Pseudo-topographies of the aparent phase φ_A: NP, CP, and MP are, respectively, the near-surface, crustal, and mantle prisms. The horizontal scale of distances is given in kilometers, and the vertical scale of phases is given in degrees

model (Berdichevsky and Dmitriev, 2002). Here some inaccuracies are possible due to distorting influence of geoelectric inhomogeneities.

The geophysical literature offers several approaches providing more adequate determination of the sediments conductance (Schmucker, 1971b; Vasseur and Weidelt, 1973; Obukhov et al., 1983; Berdichevsky and Zhdanov, 1984; Singer and Fainberg, 1997). We restrict our consideration to the Singer-Fainberg method as well as the Obukhov method which reduce the conductance determination to more or less simple arithmetic.

11.5.1 The Singer-Fainberg Method

The basic model in this method consists of an inhomogeneous thin layer resting on the one-dimensional resistive substratum that can contain conductive layers at a

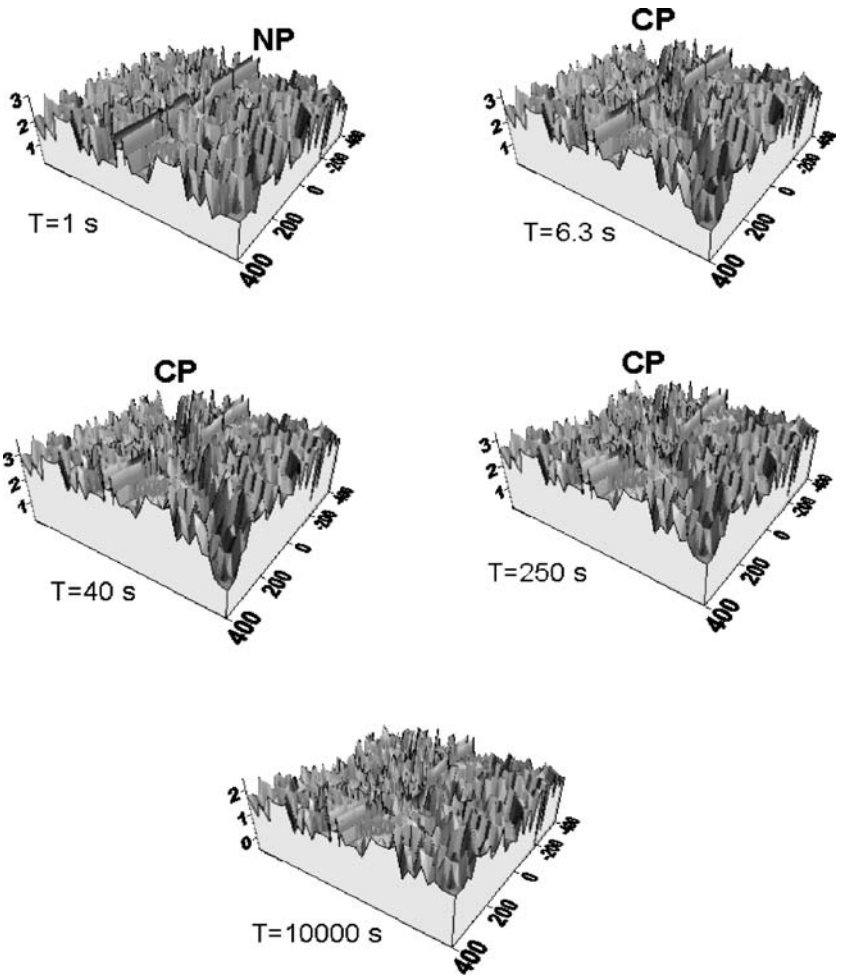

Fig. 11.55 Pseudo-topographies of the apparent resistivity ρ_{brd} in the presence of strong near-surface noise: NP and CP are, respectively, the near-surface and crustal prisms. The horizontal scale of distances is given in kilometers, and the vertical scale of resistivities is given in logarithmic units of Ohm·m

sufficiently large depth (Singer and Fainberg, 1997). The upper layer $\{\rho_1(x, y),\ h_1\}$ is characterized by conductance $S_1(x, y) = h_1/\rho_1(x, y)$. Applying the Price-Sheinmann boundary conditions (7.15) valid within the S_1- interval, we write

$$\begin{aligned} H_x(x, y, h_1) - H_x(x, y, 0) &= S_1(x, y)E_y(x, y, 0) \\ H_y(x, y, h_1) - H_y(x, y, 0) &= -S_1(x, y)E_x(x, y, 0) \\ E_x(x, y, h_1) &= E_x(x, y, 0) \\ E_y(x, y, h_1) &= E_y(x, y, 0), \end{aligned} \tag{11.23}$$

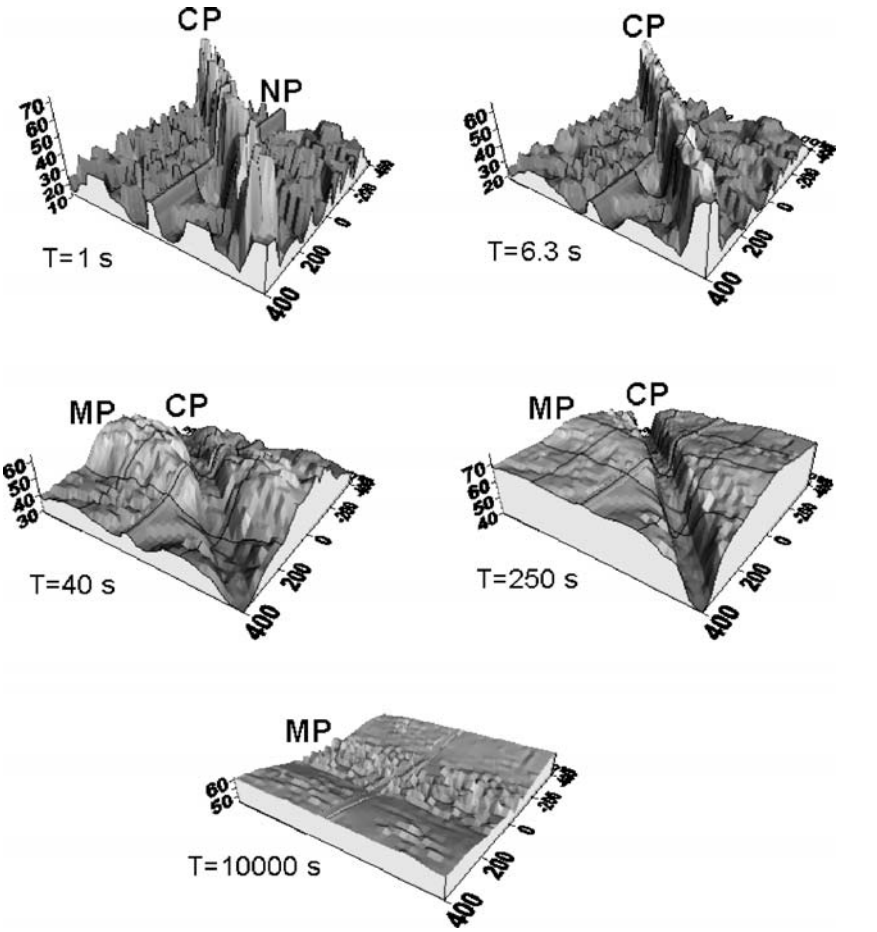

Fig. 11.56 Pseudo-topographies of the impedance phase φ_{brd} in the presence of strong near-surface noise: NP, CP, and MP are, respectively, the near-surface, crustal, and mantle prisms. The horizontal scale of distances is given in kilometers, and the vertical scale of phases is given in degrees

whence

$$S_1(x, y) = \begin{cases} \dfrac{H_x(x, y, h_1) - H_x(x, y, 0)}{E_y(x, y, 0)} \\ -\dfrac{H_y(x, y, h_1) - H_y(x, y, 0)}{E_x(x, y, 0)}. \end{cases} \tag{11.24}$$

Let the electromagnetic field $\mathbf{E}_\tau(E_x, E_y)\big|_{z=0}$, $\mathbf{H}_\tau(H_x, H_y)\big|_{z=0}$ be known on the Earth's surface. Then with the given underlying substratum we can transform

$\mathbf{E}_\tau(E_x, E_y)\big|_{z=h_1} = \mathbf{E}_\tau(E_x, E_y)\big|_{z=0}$ into $\mathbf{H}_\tau(H_x, H_y)\big|_{z=h_1}$ and find S_1 from (11.24). The problem is easily converted to the spectral domain. The Fourier spectra for the electromagnetic field are

$$\begin{aligned}\mathbf{e}_\tau(e_x, e_y)\big|_{z=h_1} &= \int_{-\infty}^{\infty}\int_{-\infty}^{\infty} \mathbf{E}_\tau(E_x, E_y)\big|_{z=h_1} e^{i(k_x x + k_y y)} dx\, dy \\ \mathbf{h}_\tau(h_x, h_y)\big|_{z=h_1} &= \int_{-\infty}^{\infty}\int_{-\infty}^{\infty} \mathbf{H}_\tau(H_x, H_y)\big|_{z=h_1} e^{i(k_x x + k_y y)} dx\, dy,\end{aligned} \tag{11.25}$$

where k_x, k_y are the spatial frequencies. Note that there exists the linear relation between **h** and **e** (Berdichevsky and Dmitriev, 2002):

$$\mathbf{h} = \left[\overleftrightarrow{\mathbf{Y}}\right]\mathbf{e} \qquad \left[\overleftrightarrow{\mathbf{Y}}\right] = \begin{bmatrix} \overleftrightarrow{Y}_{xx} & \overleftrightarrow{Y}_{xy} \\ \overleftrightarrow{Y}_{yx} & \overleftrightarrow{Y}_{yy} \end{bmatrix}, \tag{11.26}$$

where $\left[\ddot{\mathbf{Y}}\right]$ is the spectral admittance tensor. Its components are

$$\begin{aligned} \overleftrightarrow{Y}_{xx} &= -\frac{k_x k_y}{k_x^2 + k_y^2}\left(Y_\eta^{TM} - Y_\eta^{TE}\right) \qquad \overleftrightarrow{Y}_{xy} = -Y_\eta^{TM} + \frac{k_x^2}{k_x^2 + k_y^2}\left(Y_\eta^{TM} - Y_\eta^{TE}\right) \\ \overleftrightarrow{Y}_{xy} &= Y_\eta^{TM} - \frac{k_y^2}{k_x^2 + k_y^2}\left(Y_\eta^{TM} - Y_\eta^{TE}\right) \qquad \overleftrightarrow{Y}_{yy} = \frac{k_x k_y}{k_x^2 + k_y^2}\left(Y_\eta^{TM} - Y_\eta^{TE}\right), \end{aligned} \tag{11.27}$$

where Y_η^{TM} and Y_η^{TE} are the spectral admittances in the TM- and TM-modes defined from the Riccati equations:

$$\begin{aligned} &\frac{dY_\eta^{TM}}{dz} - \rho\left(k_x^2 + k_y^2 - \frac{i\omega\mu_o}{\rho}\right)\left(Y_\eta^{TM}\right)^2 = -\frac{1}{\rho} && z \ge h_1 \\ &\frac{dY_\eta^{TE}}{dz} + i\omega\mu_o\left(Y_\eta^{TE}\right)^2 = -\frac{i}{\omega\mu_o}\left(k_x^2 + k_y^2 - \frac{i\omega\mu_o}{\rho}\right) && z \ge h_1. \end{aligned} \tag{11.28}$$

Thus, defining the spectum $\mathbf{e}_\tau(e_x, e_y)\big|_{z=h_1}$ of the known electric field $\mathbf{E}_\tau(E_x, E_y)\big|_{z=h_1}$ and determining the spectral admittance tensor $\left[\ddot{\mathbf{Y}}\right]$, we can calculate the spectrum $\mathbf{h}_\tau(h_x, h_y)\big|_{z=h_1}$ and compute the magnetic field

$$\begin{aligned}\mathbf{H}_\tau(H_x, H_y)\big|_{z=h_1} &= \frac{1}{4\pi^2}\int\limits_{-\infty}^{\infty}\int\limits_{-\infty}^{\infty}\mathbf{h}_\tau(h_x, h_y)\big|_{z=h_1} e^{-i(k_x x+k_y y)}dk_x\,dk_y \\ &= \frac{1}{4\pi^2}\int\limits_{-\infty}^{\infty}\int\limits_{-\infty}^{\infty}\left[\overleftrightarrow{\mathbf{Y}}\right]\mathbf{e}_\tau(e_x, e_y)\Big|_{z=h_1} e^{-i(k_x x+k_y y)}dk_x\,dk_y,\end{aligned} \tag{11.29}$$

which opens the way to evaluating $S_1(x, y)$ by (11.24). At practical computation we apply the Fourier-Bessel transformation and reduce the double Fourier integral to the more convenient Hankel integral, which provides the better accuracy and robustness. The calculations are performed on the frequencies related to the ascending branch of the apparent-resisrivity curves.

A model example of mapping $S_1(x, y)$ is shown in Fig. 11.57. The subsurface layer with background conductance of 10 S contains a large-scale $\Gamma-$ shaped anomaly with conductance of 100 S and a small-scale square anomaly with conductance of 15 S. It is underlaid with a 20 Ohm·m homogeneous basement. The calculation has been performed for the period of 0.1 s. We see that the Singer-Fainberg method gives sharply defined images of the $S-$ anomalies with distortions below 10%. This is much better than in the maps of the apparent resistivity shown in Fig. 11.45.

11.5.2 The Obukhov Method

The idea of this method is derived from the same model as in the Singer-Fainberg method (Obukhov et al., 1983). Ignoring the basement conductivity ($\rho_2 \to \infty,\ h_2 \to \infty$), we assume that a thin horizontal $S_1(x, y)-$ layer is located in the free space. Such simplification is justified on the frequencies related to the S_1- interval.

Let us represent the magnetic field $\mathbf{H}_\tau$ as a sum of the external field $\mathbf{H}_\tau^{\text{ext}}$ created by primary currents above the $S_1(x, y)-$ layer and the internal magnetic field $\mathbf{H}_\tau^{\text{int}}$ created by currents induced within the $S_1(x, y)-$ layer:

$$\mathbf{H}_\tau = \mathbf{H}_\tau^{\text{ext}} + \mathbf{H}_\tau^{\text{int}}. \tag{11.30}$$

Applying the Price-Sheinmann conditions (7.15), we write for the internal magnetic field $\mathbf{H}^{\text{int}}$:

$$\begin{aligned}H_x^{\text{int}}(x, y, h_1) - H_x^{\text{int}}(x, y, 0) &= S_1(x, y)E_y^-(x, y, 0) \\ H_y^{\text{int}}(x, y, h_1) - H_y^{\text{int}}(x, y, 0) &= -S_1(x, y)E_x^-(x, y, 0).\end{aligned} \tag{11.31}$$

It follows from the Bio-Savart law that the horizontal components of $\mathbf{H}^{\text{int}}(x, y, h_1)$ and $\mathbf{H}^{\text{int}}(x, y, 0)$ are antisymmetric, that is, they have the same moduli and the opposite phases, $H_x^{\text{int}}(x, y, h_1) = -H_x^{\text{int}}(x, y, 0)$ and $H_y^{\text{int}}(x, y, h_1) = -H_y^{\text{int}}(x, y, 0)$. So, on the Earth's surface

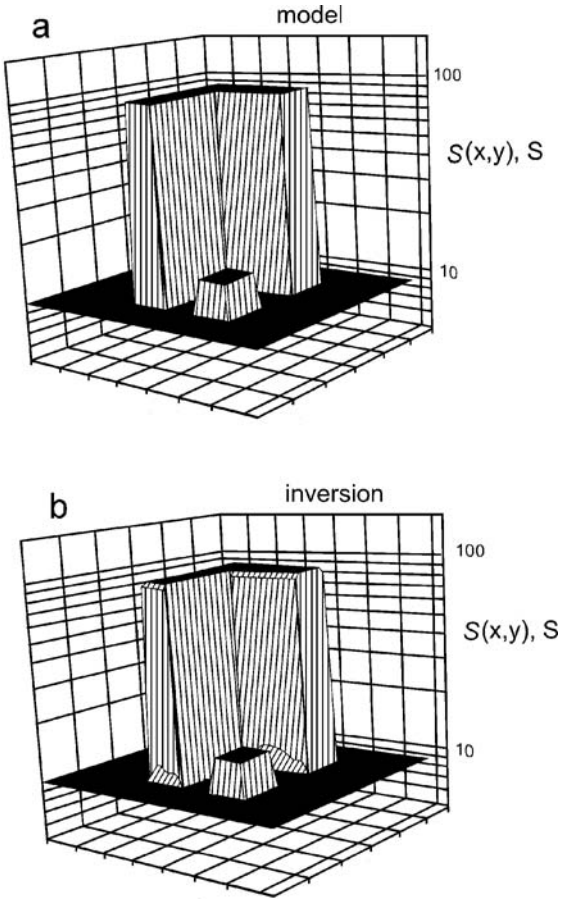

Fig. 11.57 Mapping upper-layer conductance S by the Singer-Fainberg method; (**a**) an initial model of the S - anomaly, (**b**) the conductance S evaluated by the Singer-Fainberg inversion (Singer and Fainberg, 1997)

$$
\begin{aligned}
H_x^{\text{int}}(x, y, 0) &= -\frac{1}{2} S_1(x, y) E_y(x, y, 0) \\
H_y^{\text{int}}(x, y, 0) &= \frac{1}{2} S_1(x, y) E_x(x, y, 0).
\end{aligned}
\tag{11.32}
$$

In the vector form

$$
\begin{aligned}
&\mathbf{H}_\tau^{\text{int}}(x, y) = \frac{1}{2} S_1(x, y)\ [\mathbf{R}(-\pi/2]\ \mathbf{E}_\tau(x, y) = \left[\boldsymbol{\Sigma}(x, y)\right] \mathbf{H}_\tau(x, y) \qquad a \\
&\mathbf{H}_\tau^{\text{ext}}(x, y) = \mathbf{H}_\tau(x, y) - \mathbf{H}_\tau^{\text{int}}(x, y) = \left\{[\mathbf{I}] - \left[\boldsymbol{\Sigma}(x, y)\right]\right\} \mathbf{H}_\tau(x, y), \qquad b
\end{aligned}
\tag{11.33}
$$

where

$$[\mathbf{I}] = \begin{bmatrix} 1 & 0 \\ 0 & 1 \end{bmatrix} \qquad [\mathbf{R}(-\pi/2] = \begin{bmatrix} 0 & -1 \\ 1 & 0 \end{bmatrix} \qquad [\mathbf{Z}(x, y)] = \begin{bmatrix} Z_{xx} & Z_{xy} \\ Z_{yx} & Z_{yy} \end{bmatrix}$$
$$\left[\boldsymbol{\Sigma}(x, y)\right] = \frac{1}{2} S_1(x, y)\,[\mathbf{R}(-\pi/2]\,[\mathbf{Z}(x, y)]$$

and

$$\mathbf{H}_\tau^{\text{int}}(x, y) = \mathbf{H}_\tau^{\text{int}}(x, y, 0) \qquad \mathbf{H}_\tau^{\text{ext}}(x, y) = \mathbf{H}_\tau^{\text{ext}}(x, y, 0),$$
$$\mathbf{H}_\tau(x, y) = \mathbf{H}_\tau(x, y, 0) \qquad \mathbf{E}_\tau(x, y) = \mathbf{E}_\tau(x, y, 0).$$

Now we gain the benefit from the magnetic tensor $[\mathbf{M}(x, y|\, x_{\text{B}}, y_{\text{B}})]$ defining the relation between the horizontal magnetic fields $\mathbf{H}_\tau(x, y)$ and $\mathbf{H}_\tau(x_{\text{B}}, y_{\text{B}})$ at two sites: at a site $\text{O}(x, y)$ and at a base site $\text{B}(x_{\text{B}}, y_{\text{B}})$. Substituting $[\mathbf{M}(x, y|\, x_{\text{B}}, y_{\text{B}})]\mathbf{H}_\tau(x_{\text{B}}, y_{\text{B}})$ for $\mathbf{H}_\tau(x, y)$, we rewrite (11.33) in the form

$$\begin{aligned} \mathbf{H}_\tau^{\text{int}}(x, y) &= \left[\boldsymbol{\Sigma}(x, y)\right][\mathbf{M}(x, y|\, x_{\text{B}}, y_{\text{B}})]\mathbf{H}_\tau(x_{\text{B}}, y_{\text{B}}) && a \\ \mathbf{H}_\tau^{\text{ext}}(x, y) &= \left\{[\mathbf{I}] - \left[\boldsymbol{\Sigma}(x, y)\right]\right\}[\mathbf{M}(x, y|\, x_{\text{B}}, y_{\text{B}})]\mathbf{H}_\tau(x_{\text{B}}, y_{\text{B}}). && b \end{aligned} \tag{11.34}$$

Let the sediments conductance $S_1(x_{\text{B}}, y_{\text{B}})$ be given at the base site (say, from the TEM-sounding). Then we can turn to (11.33*b*) and determine the external magnetic field $\mathbf{H}_\tau^{\text{ext}}(x_{\text{B}}, y_{\text{B}})$ at the base site. Taking into account that $\mathbf{H}_\tau^{\text{ext}}$ is uniform in the model excited by a plane wave, we get by virtue of (11.33*b*):

$$\mathbf{H}_\tau^{\text{ext}} = \left\{[\mathbf{I}] - \left[\boldsymbol{\Sigma}(x_{\text{B}}, y_{\text{B}})\right]\right\}\mathbf{H}_\tau(x_{\text{B}}, y_{\text{B}}). \tag{11.35}$$

Using (11.35), we obtain the internal magnetic field $\mathbf{H}_\tau^{\text{int}}(x, y)$ at any of observation sites:

$$\mathbf{H}_\tau^{\text{int}}(x, y) = \mathbf{H}_\tau(x, y) - \mathbf{H}_\tau^{\text{ext}} = \{[\mathbf{M}(x, y|\, x_{\text{B}}, y_{\text{B}})] - [\mathbf{I}] + \left[\boldsymbol{\Sigma}(x_{\text{B}}, y_{\text{B}})\right]\}\mathbf{H}_\tau(x_{\text{B}}, y_{\text{B}}). \tag{11.36}$$

Finally we exclude $\mathbf{H}_\tau(x_{\text{B}}, y_{\text{B}})$ from (11.33*b*) and (11.36), and derive a redundant matrix equation that gives unknown $S_1(x, y)$ with known $[\mathbf{Z}]$, $[\mathbf{M}(x, y|\, x_{\text{B}}, y_{\text{B}})]$ and $S_1(x_{\text{B}}, y_{\text{B}})$:

$$\left[\boldsymbol{\Sigma}(x, y)\right][\mathbf{M}(x, y|\, x_{\text{B}}, y_{\text{B}})] = [\mathbf{M}(x, y|\, x_{\text{B}}, y_{\text{B}})] - [\mathbf{I}] + \left[\boldsymbol{\Sigma}(x_{\text{B}}, y_{\text{B}})\right]. \tag{11.37}$$

Solving this equation, we obtain

$$S_1(x, y) = \frac{S_1'(x, y) + S_1''(x, y)}{2}, \tag{11.38}$$

where

$$S_1'(x,\ y) = 2\left|\frac{1 - M_{yy}(x_B, y_B \,|\, x, y) + [M_{xy}(x_B, y_B \,|\, x, y)\ Z_{xx}(x_B, y_B) + M_{yy}(x_B, y_B \,|\, x, y)\ Z_{xy}(x_B, y_B)]S(x_B, y_B)/2}{Z_{xy}(x, y)}\right|$$

$$S_1''(x,\ y) = 2\left|\frac{1 - M_{xx}(x_B, y_B \,|\, x, y) - [M_{xx}(x_B, y_B \,|\, x, y)\ Z_{yx}(x_B, y_B) + M_{yx}(x_B, y_B \,|\, x, y)\ Z_{yy}(x_B, y_B)]S(x_B, y_B)/2}{Z_{yx}(x, y)}\right|.$$

Here

$$\delta = 2\frac{S_1' - S_1''}{S_1' + S_1''}$$

characterizes the measurement and model errors.

The above technique is a part of more general approach which is referred to as the *Obukhov* Z^{int}*– transformation*. Let us recall this interesting approach which can be usefull in indentifying the geoelectric structures.

On the surface of the 1D model, the internal magnetic field $\mathbf{H}_\tau^{\text{int}} = \mathbf{H}_\tau/2$. In view of this, we can introduce an "internal" 1D impedanse Z^{int} as

$$Z^{\text{int}} = \frac{E_x}{H_y^{\text{int}}} = -\frac{E_y}{H_x^{\text{int}}} = 2Z \tag{11.39}$$

and an "internal" apparent resistivity ρ^{int} as

$$\rho^{\text{int}} = \frac{\left|Z^{\text{int}}\right|^2}{4\omega\mu_o} = \frac{|Z|^2}{\omega\mu_o} = \rho_A. \tag{11.40}$$

In the 1D model, the impedance Z^{int} and apparent resistivity ρ^{int} coincide respectively with the doubled Tikhonov-Cagniard impedance Z and the Tikhonov-Cagniard apparent resistivity ρ_A.

Similarly we can introduce an "internal"-impedance tensor in the 2D and 3D models. To this end, we turn to (1.13) and replace H_x, H_y for H_x^{int}, H_y^{int}:

$$\begin{aligned}
E_x &= E_x^N + E_x^A = H_{x\,o}J_x^{E2} + H_{y\,o}(Z_N + J_x^{E\,1}) && a\\
E_y &= E_y^N + E_y^A = H_{x\,o}(-Z_N + J_y^{E2}) + H_{y\,o}J_y^{E1} && b\\
H_x^{\text{int}} &= 0.5H_x^N + H_x^A = H_{x\,o}(0.5 + J_x^{H2}) + H_{y\,o}J_x^{H\,1} && c\\
H_y^{\text{int}} &= 0.5H_y^N + H_y^A = H_{x\,o}J_y^{H\,2} + H_{y\,o}(0.5 + J_y^{H\ 1}). && d
\end{aligned} \tag{11.41}$$

Eliminating H_{xo}, H_{yo} from (11.41 *c,d*) and substituting these values in (11.41 *a,b*), we establish

$$E_x = Z_{xx}^{\text{int}} H_x^{\text{int}} + Z_{xy}^{\text{int}} H_y^{\text{int}}$$
$$E_y = Z_{yx}^{\text{int}} H_x^{\text{int}} + Z_{yy}^{\text{int}} H_y^{\text{int}},$$

where

$$Z_{xx}^{\text{int}} = \frac{0.5J_x^{\text{E2}} - Z_{\text{N}} J_y^{\text{H2}} + (J_x^{\text{E2}} J_y^{\text{H1}} - J_x^{\text{E1}} J_y^{\text{H2}})}{0.25 + 0.5(J_x^{\text{H2}} + J_y^{\text{H1}}) + (J_x^{\text{H2}} J_y^{\text{H1}} - J_x^{\text{H1}} J_y^{\text{H2}})}$$
$$Z_{xy}^{\text{int}} = \frac{Z_{\text{N}}(0.5 + J_x^{\text{H2}}) + 0.5J_x^{\text{E1}} + (J_x^{\text{E1}} J_x^{\text{H2}} - J_x^{\text{E2}} J_x^{\text{H1}})}{0.25 + 0.5(J_x^{\text{H2}} + J_y^{\text{H1}}) + (J_x^{\text{H2}} J_y^{\text{H1}} - J_x^{\text{H1}} J_y^{\text{H2}})}$$
$$Z_{yx}^{\text{int}} = \frac{0.5J_y^{\text{E2}} - Z_{\text{N}}(0.5 + J_y^{\text{H1}}) + (J_y^{\text{E2}} J_y^{\text{H1}} - J_y^{\text{E1}} J_y^{\text{H2}})}{0.25 + 0.5(J_x^{\text{H2}} + J_y^{\text{H1}}) + (J_x^{\text{H2}} J_y^{\text{H1}} - J_x^{\text{H1}} J_y^{\text{H2}})}$$
$$Z_{yy}^{\text{int}} = \frac{0.5J_y^{\text{E1}} + Z_{\text{N}} J_x^{\text{H1}} + (J_y^{\text{E1}} J_x^{\text{H2}} - J_y^{\text{E2}} J_x^{\text{H1}})}{0.25 + 0.5(J_x^{\text{H2}} + J_y^{\text{H1}}) + (J_x^{\text{H2}} J_y^{\text{H1}} - J_x^{\text{H1}} J_y^{\text{H2}})}.$$

Thus, we have the complex-valued tensor $\left[\mathbf{Z}^{\text{int}}\right]$ that transforms the horizontal internal magnetic field $\mathbf{H}_\tau^{\text{int}}$ into the horizontal electric field $\mathbf{E}_\tau$:

$$\mathbf{E}_\tau = \left[\mathbf{Z}^{\text{int}}\right] \mathbf{H}_\tau^{\text{int}}. \tag{11.43}$$

With a knowledge of magnetic tensor [**M**], it is possible to establish relations between the impedance tensors $\left[\mathbf{Z}^{\text{int}}\right]$ and [**Z**]. Let us menage to locate the base site within an undistorbed area where $\mathbf{H}(x_{\text{B}}, y_{\text{B}}) = \mathbf{H}^{\text{N}} = 2\mathbf{H}_\tau^{\text{ext}}$. Then at any observation site

$$\begin{aligned}\mathbf{H}_\tau^{\text{int}}(x, y) &= \mathbf{H}_\tau(x, y) - 0.5\,[\mathbf{M}(x_{\text{B}}, y_{\text{B}}\,|x, y)\,]\,\mathbf{H}_\tau(x, y) \\ &= ([\mathbf{I}] - 0.5\,[\mathbf{M}(x_{\text{B}}, y_{\text{B}}\,|x, y)\,])\,\mathbf{H}_\tau(x, y).\end{aligned} \tag{11.44}$$

So, in view of (11.43)

$$\begin{aligned}\mathbf{E}_\tau(x, y) &= \left[\mathbf{Z}^{\text{int}}(x, y)\right] \mathbf{H}_\tau^{\text{int}}(x, y) \\ &= \left[\mathbf{Z}^{\text{int}}(x, y)\right] ([\mathbf{I}] - 0.5\,[\mathbf{M}(x_{\text{B}}, y_{\text{B}}\,|x, y)\,])\,\mathbf{H}_\tau(x, y) \\ &= [\mathbf{Z}(x, y)]\,\mathbf{H}_\tau(x, y),\end{aligned} \tag{11.45}$$

whence

$$[\mathbf{Z}(x, y)] = \left[\mathbf{Z}^{\text{int}}(x, y)\right] ([\mathbf{I}] - 0.5\,[\mathbf{M}(x_{\text{B}}, y_{\text{B}}\,|x, y)\,]) \tag{11.46}$$

and

$$\left[\mathbf{Z}^{\text{int}}(x, y)\right] = [\mathbf{Z}(x, y)]\,([\mathbf{I}] - 0.5\,[\mathbf{M}(x_{\text{B}}, y_{\text{B}}\,|x, y)\,])^{-1}. \tag{11.47}$$

The internal apparent resistivities are:

$$\rho_{xy}^{\text{int}}(x, y) = \frac{\left|Z_{xy}^{\text{int}}(x, y)\right|^2}{\omega\mu_o} \qquad \rho_{yx}^{\text{int}}(x, y) = \frac{\left|Z_{yx}^{\text{int}}(x, y)\right|^2}{\omega\mu_o}. \tag{11.48}$$

where

$$Z_{xy}^{\text{int}}(x, y) = \frac{0.5Z_{xx}(x, y)M_{xy}(x_B, y_B\,|x, y) + Z_{xy}(x, y)\{1 - 0.5M_{xx}(x_B, y_B\,|x, y)\}}{1 - 0.5\text{tr}\,[\mathbf{M}_{xx}(x_B, y_B\,|x, y)] + 0.25\,\det\,[\mathbf{M}_{xx}(x_B, y_B\,|x, y)]}$$

$$Z_{yx}^{\text{int}}(x, y) = \frac{0.5Z_{yy}(x, y)M_{yx}(x_B, y_B\,|x, y) + Z_{yx}(x, y)\{1 - 0.5M_{yy}(x_B, y_B\,|x, y)\}}{1 - 0.5\text{tr}\,[\mathbf{M}_{xx}(x_B, y_B\,|x, y)] + 0.25\,\det\,[\mathbf{M}_{xx}(x_B, y_B\,|x, y)]}.$$

Within the S_1- interval

$$\left[\mathbf{Z}^{\text{int}}\right] \approx \begin{bmatrix} 0 & Z_{xy}^{\text{int}} \\ Z_{yx}^{\text{int}} & 0 \end{bmatrix} \qquad Z_{xy}^{\text{int}} \approx -Z_{yx}^{\text{int}} \approx \frac{1}{S_1} \qquad \rho_{xy}^{\text{int}} \approx \rho_{yx}^{\text{int}} \approx \frac{1}{\omega\mu_o S_1^2}. \tag{11.49}$$

The remarkable property of the internal apparent resistivities is that they are robust to the induction effects as well as to some galvanic effects (for instance, to flow-around and current-gathering effects). It is believed that in these cases the electric and internal magnetic fields are proportional to the same factor characterizing the intensity of the magnetotelluric anomaly.

Figure 11.58 shows the longitudinal apparent-resistivity $\rho^{\parallel}-$ curve, obtained over the middle of the resistive central segment in the two-dimensional three-segment model. This curve has a broad minimum caused by the inductive

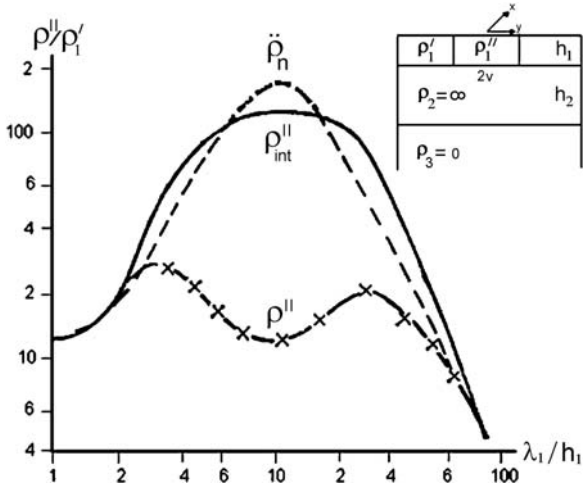

Fig. 11.58 The Obukhov transformation in the two-dimensional three-segment model; the apparent-resistivity curves are obtained at the midpoint of the resistive central segment: $\rho^{\parallel}$ - longitudinal apparent resistivity, $\rho_{\text{int}}^{\parallel}$-internal longitudinal apparent resistivity, $\ddot{\rho}_n$ - locally normal apparent resistivity

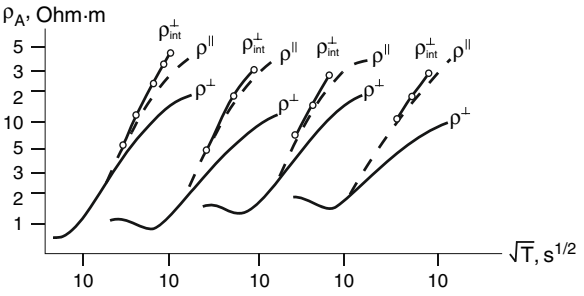

Fig. 11.59 The Obukhov transformation of the apparent-resistivity curves in the Ciskopetdag foredeep: $\rho^{\parallel}$ - longitudinal apparent resistivity, $\rho^{\perp}$ - transverse apparent resistivity, $\rho^{\perp}_{\text{int}}$-internal transverse apparent resistivity

influence of excess currents concentrated at both sides of the resistive segment (effect of false conductive layer). On the $Z^{\text{int}}-$ transformation, we get the $\rho^{\parallel}_{\text{int}}-$ curve, which assumes the bell-like form and approaches the locally normal $\ddot{\rho}_n-$ curve.

Convincing example of Obukhov's transformation is given in Fig. 11.59. We see the transverse and longitudinal apparent-resistivity curves obtained across and along the Ciskopetdag foredeep. Note that the transverse $\rho^{\perp}-$ curves have a gently inclined ascending branch and they flatten as we approach the Kopetdag. This is a manifestation of the regional flow-around effect (the transverse current flows around the resistive mountain ridge). The Obukhov transformation straightens the ascending branches of the $\rho^{\perp}_{\text{int}}-$ curves and they approach the slightly distorted longitudinal $\rho^{\parallel}-$ curves.

Chapter 12
Inversion Strategy

The past decade witnessed the striking technological and methodological advances in exploration and academic magnetotellurics. Field equipments ensuring a stable determination of magnetotelluric and magnetovariational response functions have been worked out. Effective programs have been developed for 1D, 2D and even 3D inversions of impedances and tippers. Magnetovariational sounding, for many years considered as an assistant in localizing and identifying the geoelectric structures, has been put in the forefront of the modern magnetotellurics. It became a powerful tool for resolving and studying the horizontal and vertical conductivity distribution without static shift problem. New approaches to the analysis and interpretation widening the informativeness of geoelectrics have been proposed. Field investigations have been conducted in many tectonic provinces of the world providing basically new information on the Earth's crust and upper mantle that essentially supplements the results obtained by seismics.

All these results need to be systemized and generalized. The development of a modern philosophy of the magnetotelluric interpretation is a challenge of current research. Nowadays we already have some works responding to this challenge. On the geophysical bookshelves we find monographs considering the methods of regularized solution of inverse problems based on the ideas of Tikhonov (Zhdanov, 2002; Berdichevsky and Dmitriev, 2002) and examining the technological and geological aspects of magnetotellurics (Simpson and Bahr, 2005).

In the present monograph, we would like to focus our attention on the strategy of the integrated multicriterion inversion of the magnetelluric and magnetovariational response functions.

12.1 The Smoothing and Contrasting Inversions

In general, we can consider two types of conductivity distributions $\sigma(x, y, z)$: (1) a smooth distribution $\sigma(x, y, z)$ that is continuous with its gradient, (2) a contrasty distribution $\sigma(x, y, z)$ that has discontinuities. Let an inhomogeneous body, smooth or contrasty, be buried into the homogeneous Earth. It manifests itself at the Earth's

M. Berdichevsky, V.I. Dmitriev, *Models and Methods of Magnetotellurics*,
DOI 10.1007/978-3-540-77814-1_12, © Springer-Verlag Berlin Heidelberg 2008

surface in a smoothed diffusive magnetotelluric anomaly with extent that can considerably exceed the body dimensions. The resolution of the magnetotelluric and magnetovariational soundings is such that we cannot distinguish the smooth body from the contrasty one. In view of errors in the initial data, both $\sigma-$ distributions are equivalent. To decide between the smooth and contrasty $\sigma-$ distributions, we need a priori information or some hypotheses.

In regions with sufficiently slow horizontal variations in the conductivity and thickness of the geoelectric layers, we can take a quasi-homogeneous layered interpretation model and regularize the magnetotelluric and magnetovariational inversions by smoothing the solution obtained. This traditional form of Tikhonov's regularization is named the *smoothing inversion* or *Occam inversion* (after William of Occam, English philosopher, 1285–1349, whose maxim says that assumptions introduced to explain a thing must not be multiplied beyond necessity).

The Occam inversion is implemented on the large grids and its stability is ensured by the smoothing stabilizer. The simplest form of the smoothing stabilizer is

$$\Omega(\sigma) = \iiint\limits_V \left\{ g_1 \left[\left(\frac{\partial \sigma}{\partial x} \right)^2 + \left(\frac{\partial \sigma}{\partial y} \right)^2 \right] + g_2 \left(\frac{\partial \sigma}{\partial z} \right)^2 \right\} dxdydz, \qquad (12.1)$$

where $\sigma = \sigma(x, y, x)$ is a solution of the inverse problem and g_1, g_2 are weights controlling the horizontal and vertical smoothing. Requirements of the smoothness of $\sigma(x, y, z)$ can be readily supplemented with requirement of the closeness of $\sigma(x, y, z)$ to the hypothetical model $\sigma_0(x, y, z)$. In this case we can construct the stabilizing functional as

$$\Omega(\sigma) = \iiint\limits_V \left\{ g_1 \left[\left(\frac{\partial \sigma}{\partial x} \right)^2 + \left(\frac{\partial \sigma}{\partial y} \right)^2 \right] + g_2 \left(\frac{\partial \sigma}{\partial z} \right)^2 + g_3 (\sigma - \sigma_0)^2 \right\} dxdydz, \qquad (12.2)$$

where a weight g_3 is chosen so small that requirement of the closeness of σ to σ_0 does not dominate over requirements of the smoothness of σ.

The mathematical programs OCCAM, REBOCC and NLCG based on the smoothing inversion are widely used in exploration magnetotellurics (Constable et al., 1987; DeGroot-Hedlin and Constable, 1990; Siripunvaraporn and Egbert, 2000; Rodi and Mackie, 2001). They have proved to be quite efficient in studying the regional structure of the sedimentary basins in areas with gentle tectonics.

Unfortunately, there is a limit to what can be done with smoothing inversion. Magnetotellurics is of frequent use in areas where we look for sharp geoelectric contrasts between different geological formations (for instance, in areas with ore-bearing bodies or fluidized layers and faults). When smoothing, we get blurred images and lose significant information (smear or even miss the real structures). In that events we have to take a locally inhomogeneous interpretation model characterized by a contrasty $\sigma-$distribution and regularize the magnetotelluric and magnetovariational inversions by keeping the solution close to a hypothetical

contrasty model σ_0. This form of Tikhonov's regularization is named the *contrasting inversion*. It has been realized in programs INV2D, II2DC and IGF-MT2D developed by Varentsov and Novozhynsky (Varentsov, 2002; Novozhynski and Pushkarev, 2001).

The contrasty interpretation model usually consists of reasonably small number of homogeneous blocks with fixed geometry of their boundaries. The density of blocky partition is larger in zones with expected structures and less in empty zones. Position of the blocks and their shape are chosen using a priori information, qualitative magnetotelluric and magnetovariational indications, tentative smoothing inversions, and hypotheses. Stability of the contrasting inversion is ensured by the blocky stabilizer

$$\Omega(\sigma) = \sum_{l=1}^{L} g_l \left\{ \sigma^{(l)} - \sigma_0^{(l)} \right\}^2, \tag{12.3}$$

where g_l is a weight controlling the contribution of the lth block.

The smoothing and contrasting inversions operate at different levels of automation.

The smoothing inversion is best suited to automatic operation. Let the geoelectric survey be carried out in a region with supposedly gentle tectonics. If analysis of magnetotelluric impedances shows sufficiently small values for the parameters of inhomogeneity, the smoothing inversion calls for stratifying the geoelectric medium, defining the normal background, correlating the $S-$distribution, analyzing the model misfits and estimating the inversion accuracy. So, the smoothing inversion enables rather fast interpretation of the large amounts of field data and is particularly attractive in the commercial magnetotelluric surveys.

On the contrary, the contrasting inversion calls for intensive contacts between the geophysicist and the computer. The point is that results of the inversion may depend on the partition of the blocky model and in the course of inversion we have to follow the misfit minimization and improve the shape and position of the blocks associated with target structures. Besides, we have to take into account the properties of the different response functions and on this basis to divide the interpretation into a succession of interrelated partial inversions focused upon different target structures. Moreover, we can accomplish some tentative inversions intended for the hypotheses testing and correct the interpretation model. The contrasting inversion helps to obtain rather complete and meaningful description of the intricately built medium, but it is time-consuming. Its application is usually limited by regional studies and deep academic investigations.

In closing, let us mention two recent developments that may extend the capabilities of the smoothing and contrasting inversions: (1) Zhdanov suggested a focusing stabilizers that exposes the sharp conductivity variations against a smoothed background (Zhdanov, 2002), (2) Varentsov constructed a scanning windows that superimposes smoothed conductivity variations upon a piecewise homogeneous blocky background (Varentsov, 2002).

12.2 The Hypotheses Test Mode

We consistently stress that the interpretation efficiency considerably depends on the amount of a priori geological and geophysical information. However the requirements imposed upon a priori information can be reduced when the inverse problem is considered as a problem of hypotheses testing.

Let us entertain a hypothesis that the upper mantle contains a conductive zone (asthenosphere) originated from partial melting. The blocky interpretation model for this inverse problem should include some conductive blocks corresponding to the supposed asthenosphere. To execute the inversion, we introduce a stabilizer determining the deviation of the solution from the tested hypothesis. By minimizing Tikhonov's functional and computing the model misfit, we can answer the question whether the tested hypothesis is consistent with the observation data. Moreover, when changing the conductivity and the position of the "asthenosphere" blocks and controlling these changes by the model misfit, we correct the tested hypothesis.

A similar approach can be applied to compare the alternative hypotheses. Let one of hypotheses provide the misfit that does not exceed the uncertainty in the field data and is far less than the misfits of the other hypotheses. Then this hypothesis is taken as the most credible. But if different hypotheses are characterized by the misfits of the same order, then we conclude that all these hypotheses are equivalent. It means that we dramatically need an additional information to choose the most credible one.

12.3 Quasi-One-Dimensional MT Inversion

This approach can be used in investigating quasi-homogeneous layered media (vertical conductivity distribution is piecewise constant, while conductivity and thickness of the layers change slowly in horizontal directions). The quasi-one-dimensional inversion is efficient in regions with gentle sedimentary tectonics, say, on the vast platform. Here the magnetovariational anomalies can be rather weak so that magnetovariational soundings are hardly applicable and we restrict ourselves to magnetotelluric soundings.

The concept of the quasi-one-dimensional inversion is simple (Dmitriev, 1987; Barashkov and Dmitriev, 1990; Oldenburg and Ellis, 1993). We look for a 3D conductivity distribution such that the magnetotelluric response function (impedance or apparent resistivity) at each observation site is close to the locally normal response function and admits the one-dimensional inversion. The quasi-one-dimensional inversion is controlled by the misfit of the 3D model obtained by synthesizing the one-dimensional inversions.

12.3.1 Synthesizing the One-Dimensional Inversions

By way of example, consider a quasi-homogeneous layered medium and take apparent-resistivity curves $\tilde{\rho}_{\mathrm{brd}}(x_m,\ y_m, T)$ measured at sites O_m, $m = 1, 2, \ldots M$.

The inversion of all these curves is performed in the class of 1D layered models. With regularized optimization, we get

$$\Phi_\alpha[\tilde{\sigma}_m(z)] = \inf_\sigma \Phi_\alpha[\sigma_m(z)] \qquad m = 1, 2, ...M, \tag{12.4}$$

where $\tilde{\sigma}_m(z) = \tilde{\sigma}(x_m, y_m, z)$ is an approximate solution of the 1D inverse problem, α is a regularization parameter, and $\Phi_\alpha[\sigma_m(z)]$ is Tikhonov's functional involving the misfit functional I and stabilizing functional Ω:

$$\Phi_\alpha[\sigma_m(z)] = \mathrm{I}[\sigma_m(z)] + \alpha\Omega[\sigma_m(z)] \qquad m = 1, 2, ...M. \tag{12.5}$$

The misfit functional assumes the form

$$\mathrm{I}[\sigma_\mathrm{m}(\mathrm{z})] = \left\| \tilde{\rho}_\mathrm{brd}(x_m, y_m, T) - \rho_\mathrm{A}^{1D}[x_m, y_m, T, \sigma_m(z)] \right\|_R^2 \qquad m = 1, 2, ...M, \tag{12.6}$$

where $\rho_\mathrm{A}^{1D}[x_m, y_m, T, \sigma_m(z)]$ is an operator of the local one-dimensional direct problem that calculates the apparent resistivity ρ_A for a period T and a given electrical conductivity $\sigma_m(z)$.

The stabilizing functional $\Omega[\sigma_m(z)]$ provides the proximity of the solution $\tilde{\sigma}_m(z)$, obtained at a site O_m, to the solution $\tilde{\sigma}_{m-1}(z)$, obtained at a neighboring site O_{m-1}:

$$\Omega[\sigma_m(z)] = \|\sigma_m(z) - \tilde{\sigma}_{m-1}(z)\|_{L_2}^2 \qquad m = 1, 2, ...M. \tag{12.7}$$

In this way we ensure the slow horizontal changes in $\sigma(x, y, z)$ within the area under consideration. The initial normal conductivity distribution $\tilde{\sigma}_1(z) = \sigma_\mathrm{N}(z)$ is taken at the site O_1 that belongs to the boundary C_1 of the normalized area S_N (Fig. 10.1). It can also be taken at any site O_m, where a priori information (for instance, well-log data) provides the reliable determination of $\tilde{\sigma}_m(z)$.

Having solved the 1D inverse problems for all sites O_m, we find a set of one-dimensional approximate solutions $\tilde{\sigma}_m(z)$, $m = 1, 2, \ldots M$. Next we synthesize $\tilde{\sigma}_m(z) = \tilde{\sigma}(x_m, y_m, z)$ and accomplish their spline-approximation in x, y with a minimum norm of horizontal derivatives of conductivity. So we construct a smoothed quasi-one-dimensional solution $\tilde{\sigma}(x, y, z)$ of the three-dimensional inverse problem. An operator of such quasi-one-dimensional inversion is designated as σ^{q1D}:

$$\tilde{\sigma}(x, y, z) = \sigma^{q1D}\{\tilde{\rho}_\mathrm{brd}(x_m, y_m, T)\} \qquad m = 1, 2, ...M. \tag{12.8}$$

The misfit of the quasi-one-dimensional inversion is

$$\mathrm{I}[\tilde{\sigma}(x, y, z)] = \sum_{m=1}^{M} \left\| \rho_\mathrm{brd}^{3D}[x_m, y_m, T, \tilde{\sigma}(x, y, z)] - \tilde{\rho}_\mathrm{brd}(x_m, y_m, T) \right\|_R^2, \tag{12.9}$$

where $\rho_{\text{brd}}^{3D}[x_m, y_m, T, \tilde{\sigma}(x, y, z)]$ is an operator of the three-dimensional direct problem that calculates the apparent resistivity ρ_{brd} for a period T and a given electric conductivity $\tilde{\sigma}(x, y, z)$.

12.3.2 Using the S–Method

The foregoing technique of one-dimensional successive inversions is convenient if the number of geoelectric layers does not change within the area under consideration. But in the case that the sedimentary strata contain pinching-out layers, we have to solve the 1D problems with the maximum number of layers. Evidently this impairs the solution stability, because false thin layers may appear. In that event we can take advantage of the $S-$method which allows the Earth stratification to be made at the last stage of the inversion (Dmitriev, 1987).

The $S-$method consists in solving an unstable nonlinear 1D inverse problem in two steps.

The first step reduces to determining conductance distributions

$$S_m(z) = S(x_m, y_m, z) = \int_0^z \sigma_m(z)dz \qquad m = 1, 2, ...M \tag{12.10}$$

from $\tilde{\rho}_{\text{brd}}(x_m, y_m, T)$. This is a stable nonlinear problem (recall the Dmitriev theorem of stability of the $S-$distribution). The second step is that of determining $\sigma_m(z)$ from $S_m(z)$. This is an unstable linear problem. Thus, instead of solving a single complicated problem, we successively solve two simpler problems.

The conductance distributions, $S_m(z)$, are evaluated by minimizing the Tikhonov functional

$$\Phi_\alpha[S_m(z)] = \text{I}[S_m(z)] + \alpha\Omega[S_m(z)], \;\; S_m(z) = \int_0^z \sigma_m(z)dz \qquad m = 1, 2, ...M, \tag{12.11}$$

where the misfit functional is

$$\text{I}[S_{\text{m}}(\text{z})] = \left\| \tilde{\rho}_{\text{brd}}(x_m, y_m, T) - \rho_{\text{A}}^{1D}[x_m, y_m, T, \sigma_m(z)] \right\|_R^2 \qquad m = 1, 2, ...M$$

and the stabilizing functional is

$$\Omega[S_m(z)] = \left\| S_m(z) - \tilde{S}_{m-1}(z) \right\|_{L_2}^2 \qquad m = 1, 2, ...M.$$

Here $\sigma_m(z)$ is a piecewise-constant function digitized on a large number of steps. When integrating unstable $\sigma_m(z)$, we get stable $\tilde{S}_m(z)$. This stage in the 1D

solution is called the *S-transformation*. The obtained $\tilde{S}_m(z), m = 1, 2, \ldots M$ can be smoothed in *x,y* by a spline with a minimum norm of horizontal derivatives of the conductance.

At the second step we determine $\sigma_m(z)$ from $\tilde{S}_m(z), m = 1, 2, \ldots M$. A minimization problem for $\sigma_m(z)$ is

$$\inf\{\Phi_\alpha(\sigma_m(z)\} = \inf\{\mathrm{I}[\sigma_m(z)] + \alpha\Omega[\sigma_m(z)]\} \qquad m = 1, 2, \ldots M, \tag{12.12}$$

where

$$\mathrm{I}[\sigma_m(z)] = \left\| \tilde{S}_m(z) - \int_0^z \sigma_m(z)dz \right\|^2_{L_2}$$
$$\Omega[\sigma_m(z)] = \| p(z)[\sigma_m(z) - \sigma_0(z)]\|^2_{L_2}.$$

Here α is the regularization parameter, $\sigma_0(z)$ is the hypothetical model constructed on the basis of a priori information, $p(z)$ is a weighting factor that decreases monotonically with depth.

The Euler equation for (12.11) can be reduced to the Volterra integral equation of the second kind:

$$\alpha p(z)[\sigma_m(z) - \sigma_0(z)] + \int_0^z (z - \zeta)\sigma_m(\zeta)d\zeta = \int_0^z \tilde{S}_m(\zeta)\, d\zeta \qquad z \in [0,\ z_{\max}]. \tag{12.13}$$

On simple rearrangement, we write

$$\alpha p(z)\Delta\sigma_m(z) + \int_0^z (z - \zeta)\Delta\sigma_m(\zeta)d\zeta = f_m(z) \qquad z \in [0,\ z_{\max}], \tag{12.14}$$

where

$$\Delta\sigma_m(z) = \sigma_m(z) - \sigma_0(z)$$
$$f_m(z) = \int_0^z \tilde{S}_m(\zeta)\, d\zeta - \int_0^z (z - \zeta)\sigma_0(\zeta)d\zeta = \int_0^z [\tilde{S}_m(\zeta) - S_0(\zeta)]\, d\zeta$$
$$S_0(z) = \int_0^z \sigma_0(\zeta)d\zeta\,.$$

Solving this equation for a given α, we find $\Delta\sigma_m(z)|_\alpha$ and calculate $\sigma_m(z)|_\alpha = \sigma_0(z) + \Delta\sigma_m(z)|_\alpha$. So, we find a set of approximate one-dimensional solutions

$\tilde{\sigma}_m(z) = \tilde{\sigma}_m(z)|_{\alpha_{opt}}$ $m = 1, 2, \ldots M$, obtained for the optimal regularization parameter $\alpha = \alpha_{opt}$.

Synthesizing $\tilde{\sigma}_m(z)$ and accomplishing their spline-approximation in *x,y*, we construct a smoothed quasi-one-dimensional solution $\tilde{\sigma}(x, y, z)$ of the three-dimensional inverse problem with misfit calculated by (12.9).

The simple alternative to the minimization problem (12.11) is to determine conductivity profiles $\tilde{\sigma}_m(z)$ by numerical differentiation of smoothed conductance distributions $\tilde{S}_m(z)$:

$$\tilde{\sigma}_m(z) = \frac{d\,\tilde{S}_m(z)}{d\,z} \qquad m = 1, 2, \ldots M, \tag{12.15}$$

where $\tilde{S}_m(z)$ is spline-approximated in z. Moreover, we can use a simple graphics and approximate $\tilde{S}_m(z)$ by a broken line corresponding to a piesewise-constant $\tilde{\sigma}_m(z)$. However, while we gain in simplicity, we lose in detailedness.

An example of *S*-transformation taken from a survey in the Tungus syneclise is shown in Fig. 12.1. The initial $\tilde{\rho}_A-$ curve was inverted on different large grids with different started models (from 60 to 100 layers). Though values obtained for $\tilde{\sigma}(z)$ are rather whimsical and can dramatically diverge, the corresponding apparent-resistivity curves are close to the $\tilde{\rho}_A-$ curve (Fig. 12.1a) and the *S*-profiles calculated from $\tilde{\sigma}(z)-$ distributions faithfully copy each other (Fig. 12.1b). The mean *S*-profile presented in Fig. 12.1c consists of 6 quasi-linear segments approximated by a broken line which presents the piecewise-constant $\tilde{\sigma}(z)$-distribution. The "breaks" are so sharp that the approximation can be done even manually. The thickness of a layer is determined from the abscissas of the breaks, while the ratio of thickness to conductance difference gives the layer resistivity. Finally we get a six-layer resistivity profile in which a conductive asthenosphere can be recognized at a depth of about 70 km (Fig. 12.1d). Such a simple visualization permits us not only to solve the inverse problem, but also to evaluate visually the accuracy of the solution in a given model class. For example, in Fig. 12.1c, it can clearly be seen that the depth to the asthenosphere has been determined with an uncertainty of about ± 5 km.

The advantages of the *S*-method in comparison with other methods of solving the one-dimensional inverse magnetotelluric problem seem to be indisputable. First, we obtain the integral characteristics of the entire set of equivalent solutions. Second, the way in which a priori information is introduced is simplified. Third, the potentialities of the qualitative interpretation are expanded. Really, the linear parts of the *S*-distribution correspond to homogeneous layers and the breaks, that is, the rapid changes in the slope of the *S*-profile mark the boundaries between these layers. On the other hand, if the *S*-distribution has a significant curvature, this is the evidence for the presence of gradient layer. Thus, even at the first stage we obtain an indicative geoelectric pattern. We can separate homogeneous layers from gradient layers, evaluate their mean electric conductivity and assign the plausible position of their boundaries.

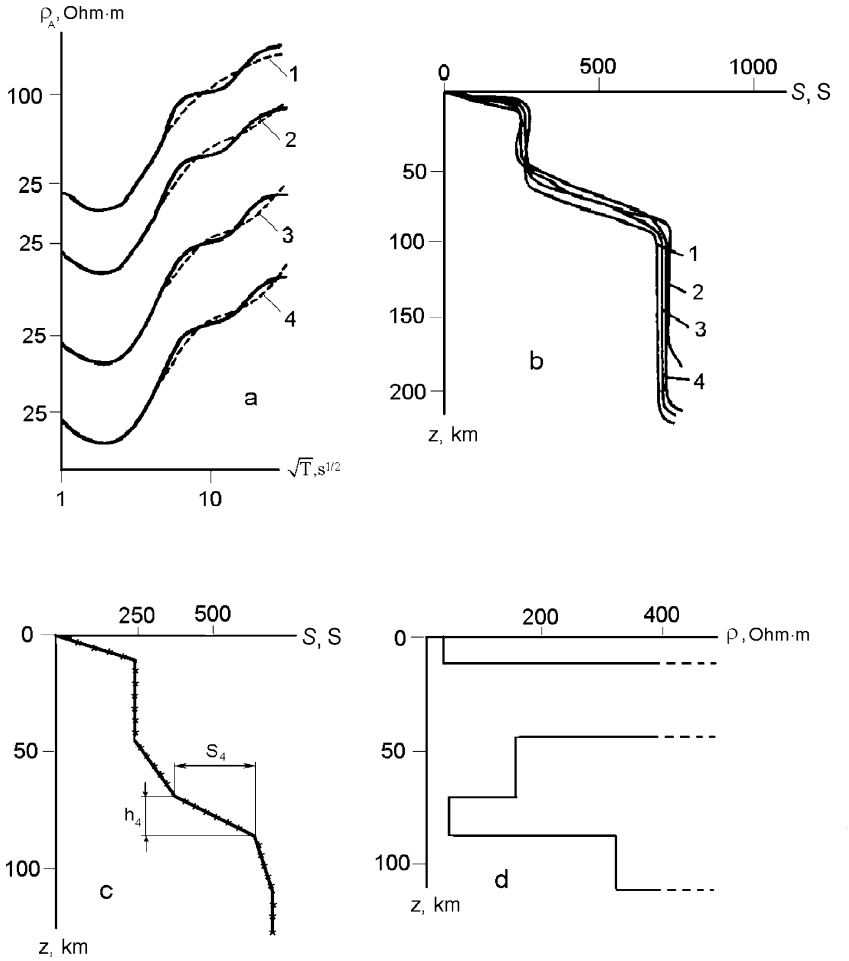

Fig. 12.1 Interpretation of a ρ_A—curve using the *S*-method. (**a**) Approximation of a ρ_A— curve (*solid line*) with curves computed from various equivalent solutions (*dashed line*); 1 – initial approximation is a homogeneous medium, 100 layers; 2 – initial approximation is a homogeneous medium, 60 layers; 3 – initial approximation is an alternating sequence of conductive and resistive layers, 100 layers; 4 – initial approximation is an alternating sequence of conductive and resistive layers, 60 layers. (**b**) The *S*-distributions. (**c**) Approximation of the average *S*-distribution by a broken line and determination of resistivity of the fourth layer, $\rho_4 = h_4/S_4$. (**d**) Six-layer geoelectric strata determined from the average *S*-profile

12.3.3 Correcting Quasi-One-Dimensional Inversion

If the misfit (12.9) is too large, the quasi-one-dimensional solution $\tilde{\sigma}(x, y, z)$ can be improved by using a convergent iterative procedure.

At the first iteration, we follow (Barashkov and Dmitriev, 1990; Oldenburg and Ellis, 1993) and write

$$\tilde{\sigma}^{(1)}(x, y, z) = \sigma^{q1D}\{\tilde{\rho}_{\text{brd}}(x_m, y_m, T) - \rho^{3D}_{\text{brd}}[x_m, y_m, T, \tilde{\sigma}(x, y, z)] + \rho^{1D}_{\text{A}}[x_m, y_m, T, \tilde{\sigma}_m(z)]\} \quad m = 1, 2, \ldots M, \tag{12.16}$$

where σ^{q1D}, ρ^{3D}_{brd}, and ρ^{1D}_{A} are operators of the quasi-one-dimensional inversion, three-dimensional inversion, and local one-dimensional inversion respectively.

At the second iteration

$$\tilde{\sigma}^{(2)}(x, y, z) = \sigma^{q1D}\{\tilde{\rho}_{\text{brd}}(x_m, y_m, T) - \rho^{3D}_{\text{brd}}[x_m, y_m, T, \tilde{\sigma}^{(1)}(x, y, z)] + \rho^{1D}_{\text{A}}[x_m, y_m, T, \tilde{\sigma}^{(1)}_m(z)]\} \quad m = 1, 2, \ldots M. \tag{12.17}$$

At the kth iteration

$$\tilde{\sigma}^{(k)}(x, y, z) = \sigma^{q1D}\{\tilde{\rho}_{\text{brd}}(x_m, y_m, T) - \rho^{3D}_{\text{brd}}[x_m, y_m, T, \tilde{\sigma}^{(k-1)}(x, y, z)] + \rho^{1D}_{\text{A}}[x_m, y_m, T, \tilde{\sigma}^{(k-1)}_m(z)]\} \quad m = 1, 2, \ldots M. \tag{12.18}$$

Its misfit is

$$\text{I}[\tilde{\sigma}^{(k)}(x, y, z)] = \sum_{m=1}^{M} \left\| \rho^{3D}_{\text{brd}}[x_m, y_m, T, \tilde{\sigma}^{(k)}(x, y, z)] - \tilde{\rho}_{\text{brd}}(x_m, y_m, T) \right\|^2_R . \tag{12.19}$$

Each iteration brings ρ^{3D}_{brd} closer to $\tilde{\rho}_{\text{brd}}$. Hence, $\tilde{\sigma}(x, y, z)$ approaches $\sigma^{q1D}\{\rho^{1D}_{\text{A}}\}$. It means that we near a solution where apparent resistivities at each observation site coincide with their locally normal values.

The quasi-one-dimensional inversion can be considered as an analog of the smoothing inversion. Both the methods define models with a smooth conductivity distribution. The difference is that in the smoothing inversion stabilizer (12.1) is minimized over the entire inhomogeneity domain (integral smoothing), while in the quasi-one-dimensional inversion we use stabilizer (12.7) and minimize the difference between conductivities at neighboring sites (local smoothing).

Convergence of this iterative procedure for sufficiently slow horizontal change in $\sigma(x, y, z)$ has been proved by Barashkov (1983). In actual practice, we usually observe rather fast convergence of iterative procedure (3–5 iterations).

From the practical standpoint, the quasi-one-dimensional inversion is very convenient, since the multi-dimensional direct problem is solved only several times. Figure 12.2 presents examples of quasi-one-dimensional inversion of the transverse apparent-resistivity $\rho^{\perp}-$ curves calculated for a model with a two-dimensional graben and horst. Here the second and the third iterations approximate fairly well the topograhy of a resistive basement.

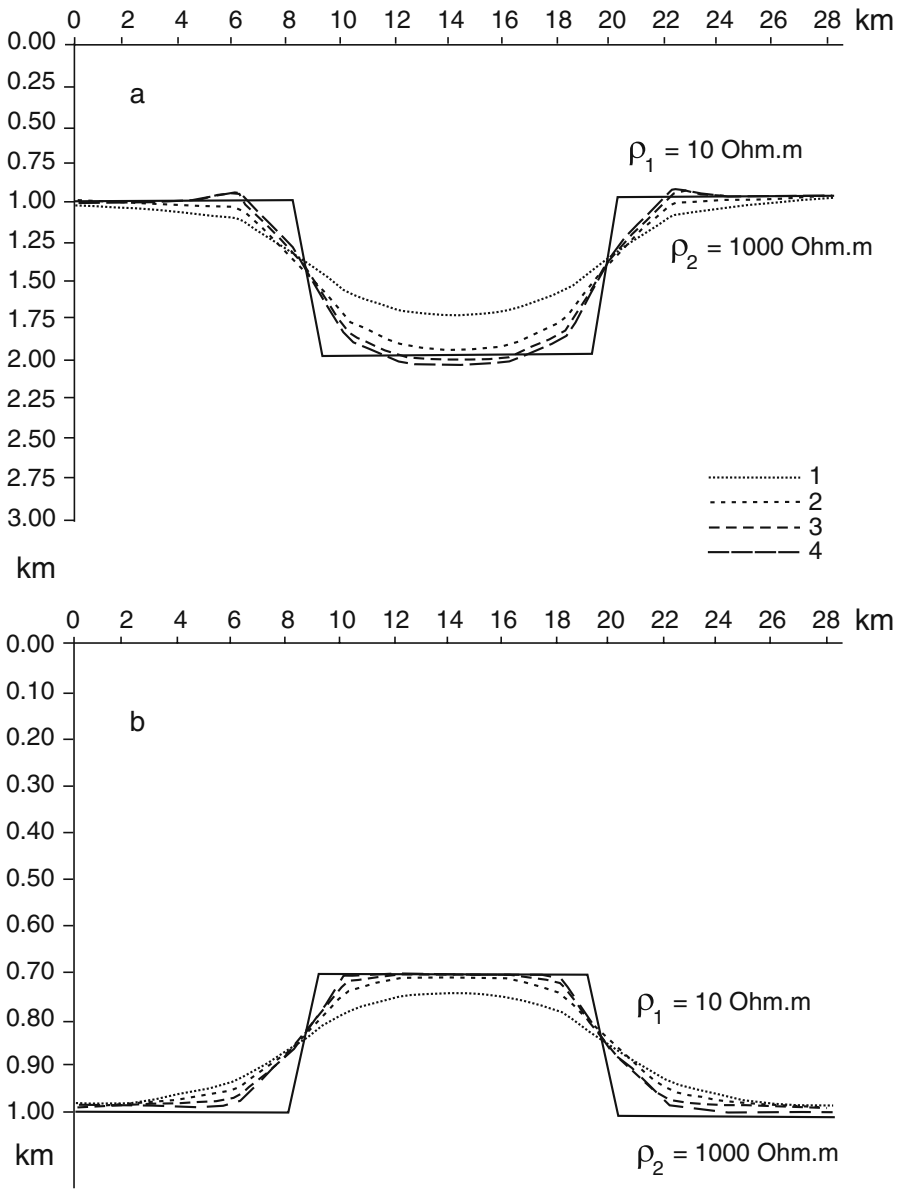

Fig. 12.2 Quasi-one-dimensional interpretation of the transverse $\rho^{\perp}$-curves over a graben (**a**) and a horst (**b**); 1,2,3,4-numbers of iteration

12.4 Two-Dimensional Bimodal MV-MT Inversion

This approach is widely used in investigating locally inhomogeneous layered media that have well-defined extended strike and allow for two-dimensional approximation.

The condition of *quasi-two-dimensionality* of the structures under study can be established by means of magnetovariational and magnetotelluric tests (Sect. 11.3.1, 11.3.2) and with a priori 3D modelling. A convincing a posteriori evidence of quasi-two-dimensionality is that the two-dimensional inversions of different magnetovariational and magnetotelluric response functions (tippers, magnetic tensors, impedance tensors) agree with each other.

The two-dimensional magnetotelluric field consists of the TM- and TE-modes. The TM-mode is related to the H-polarized wave generating the transverse MT-curves (telluric current flows across the structures, its magnetic field is directed along the structures and does not depend on the Earth's conductivity). The TE-mode is related to the E-polarized wave generating the longitudinal MT-curves together with the tippers and horizontal magnetic tensor (telluric current flows along the structures, its magnetic field is directed across the structures). The main difference between these modes is that the TM-mode charges the structures, and its anomalies are of galvanic nature, but the TE-mode does not charge the structures, and its anomalies are of inductive nature.

The TM- and TE-modes offer different sensitivity to near-surface and deep conductivity and provide different accuracy of 2D-approximation of real 3D structures. These properties of the TM- and TE-modes dictate the philosophy and practical strategy of the two-dimensional interpretation of MT-data collected in the regions with elongated structures.

The problems of two-dimensional interpretation of magnetotelluric and magnetotevariational soundings have been discussed in many papers and monographs (Svetov, 1973; Kaufman, 1974; Berdichevsky and Dmitriev, 1976, 2002; Jupp and Vozoff, 1977; Kaufman and Keller 1981; Veselovsky and Yudin, 1988; Park et al., 1983, 1991; Wannamaker et al., 1984; Berdichevsky and Zhdanov, 1984; Park, 1985; Mackie et al., 1988; Wannamaker et al., 1989a, 1991; Berdichevsky et al. 1992b, 1995, 1998, 2003; Weaver, 1994; Zhdanov and Keller, 1994; Gupta and Jones, 1995; Banks et al., 1996; Zhdanov, 2002; Mehanee and Zhdanov, 2002; Ledo et al., 2002; Ledo, 2006). The discussion exhibits a wide range of various and sometimes conflicting viewpoints, from "the TM-impedance functions are emphasized because theory and experiment show that they are more robust to three-dimensional effects. . ." (Wannamaker et al., 1989) and "Two-dimensional modeling should emphasize the TM-mode impedance. . . because it is more immune to finite strike effects." (Wannamaker, 1999) to ". . .inverting both the TE- and TM-modes results in models that fit the TM locally without resolving large-scale structure evinced only by the TE-mode." (Banks et al., 1996) and ". . . the most comprehensive and reliable information on the Earth's conductivity can be derived by means of bimodal inversion, that is using both the TM- and TE-modes." (Berdichevsky et al., 1998).

In our book we will present some approaches to the two-dimensional MT and MV interpretation that are characteristic of the Russian magnetotelluric school.

Discussing the strategy of two-dimensional interpretation of MT- and MV-data, we have to address Part II of our book and answer three questions. In decreasing order of importance, these questions are: (1) what field mode is more sensitive to the near-surface and deep structures which are the targets of magnetotellurics? (2) what field mode is more robust to the 3D-effects caused by real geological bodies? (3) what field mode is more susceptible to the static distortions caused by near-surface inhomogeneities?

12.4.1 Sensitivity of the TM- and TE-Modes to the Target Structures

This point is crucial in determining the magnetotelluric informativeness. We know that the TM-mode may be more sensitive to near-surface structures and fluid-saturated faults as well as the lithosphere resistance (porosity, fissuring), whereas the TE-mode may be more sensitive to deep conductive (fluidized, graphitized, partially melted) zones.

Consider the basic lithosphere model consisting of the upper conductive layer (the sediments), the intermediate resistive layers (the consolidated crust and upper mantle), and the conductive basement (the asthenosphere).

We will start with examining the sensitivity of TM- and TE-modes to near-surface structures. In Fig. 12.3, the sediments with thickness of 1 km contain a two-dimensional horst-like resistive elevation with amplitude of 0.7 km and width of 1 km. The horst is clearly marked by the transverse apparent resistivities $\rho^{\perp}$ for periods 0.1–10000 s covering the S_1- and $h-$ intervals and by the transfer phases $\varphi^{\perp}$ for periods 0.1–1 s relating to the very beginning of the S_1- interval. But it is dramatically smoothed in corresponding graphs of the longitudinal apparent resistivity $\rho^{\parallel}$ and the phase $\varphi^{\parallel}$, while the real and imaginary tippers, $\mathrm{Re}\,\mathbf{W}$ and $\mathrm{Im}\,\mathbf{W}$, are close to the detection threshold. The narrow horst is readily detected using the TM-mode, but it may be missed when using the TE-mode.

Next we examine the sensitivity of TM- and TE-modes to deep structures. Consider a model that contains a two-dimensional prominent asthenosphere elevation with amplitude of 75 km and width of 150 km.

Figure 12.4 displaces a case typical for stable regions. Here the lithosphere resistance is about $3{\cdot}10^9$ Ohm·m^2. The asthenosphere elevation is indiscernible in the transverse apparent resistivities $\rho^{\perp}$ and phases $\varphi^{\perp}$ for periods 100–10000 s (the $h-$ interval), but it reveals itself markedly in the corresponding graphs of the longitudinal apparent resistivities $\rho^{\parallel}$ and phases $\varphi^{\parallel}$ and generates the real and imaginary tippers, $\mathrm{Re}\,\mathbf{W}$ and $\mathrm{Im}\,\mathbf{W}$, that considerably exceed the detection threshold. Clearly the asthenosphere elevation can be indicated with confidence using the TE-mode, but it may be missed when using the TM-mode (the screening effect).

Figure 12.5 displays a case typical for active regions. Here the lithosphere resistance is reduced to $2.5{\cdot}10^8$ Ohm·m^2. This visibly affects the TM-mode: the

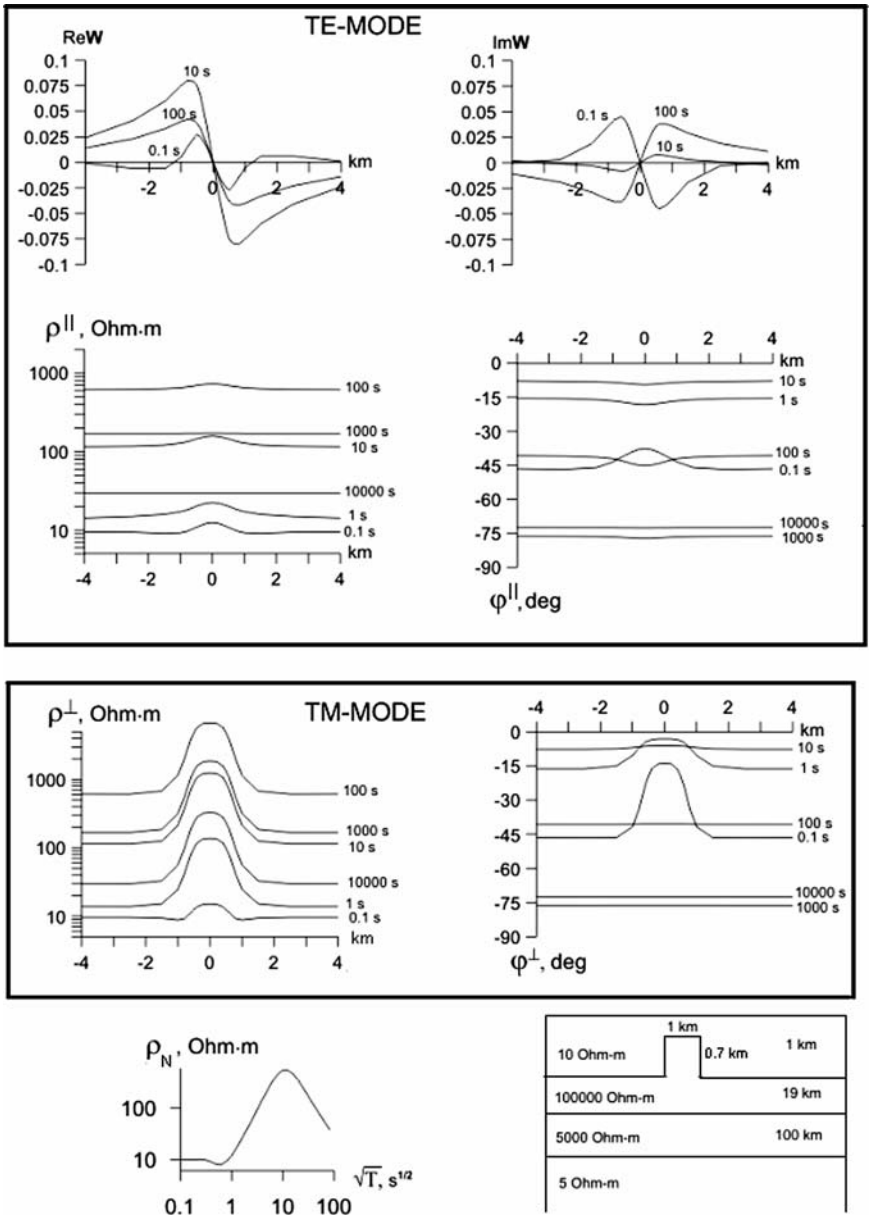

Fig. 12.3 Illustrating the sensitivity of the TM- and TE-modes to near-surface structures. The normal ρ_N-curve is shown on the lower left. At the top: apparent-resistivity, impedance-phase and tipper profiles; profile parameter: period T

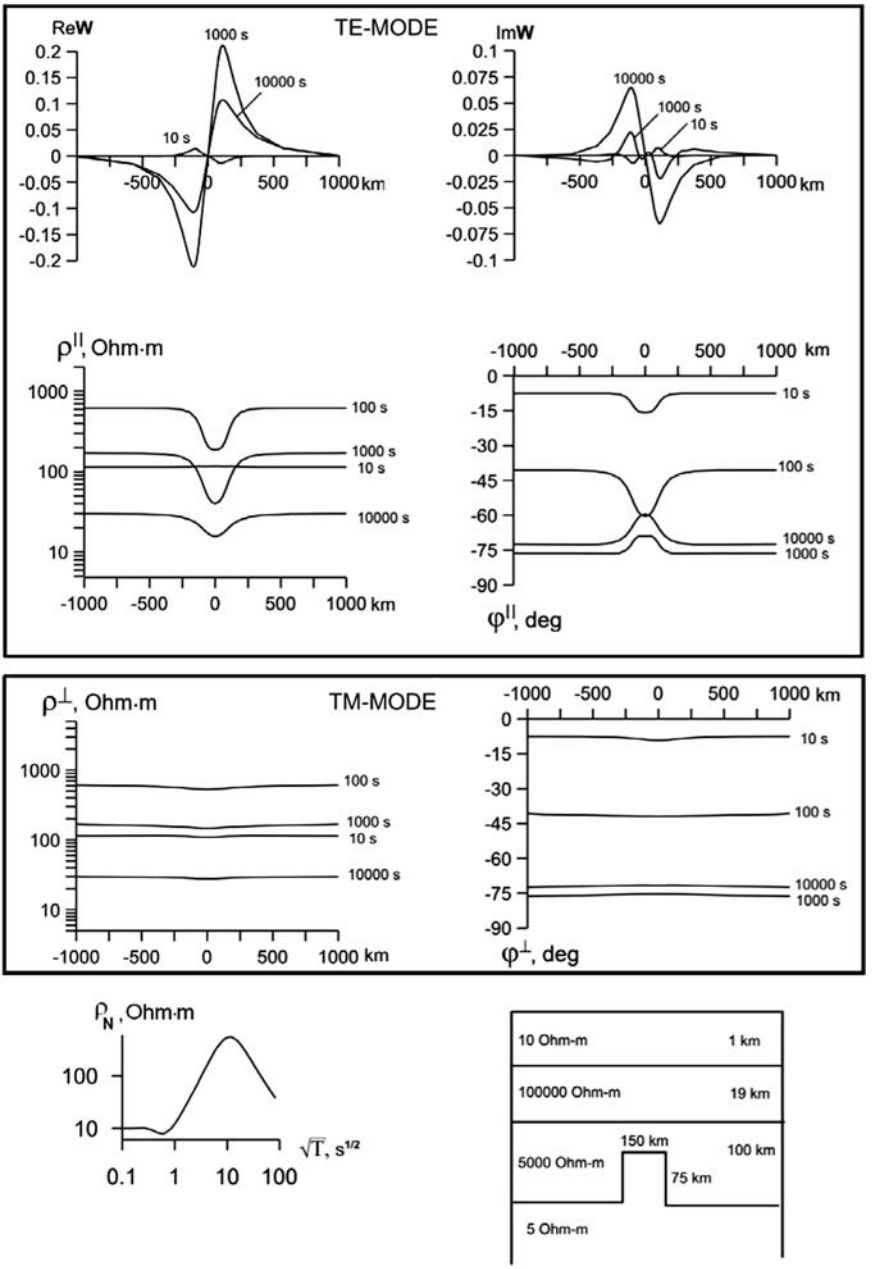

Fig. 12.4 Illustrating the sensitivity of the TM- and TE-modes to deep structures (a case typical of stable regions). The normal ρ_N-curve is shown on the lower left. At the top: apparent-resistivity, impedance-phase and tipper profiles; profile parameter: period T

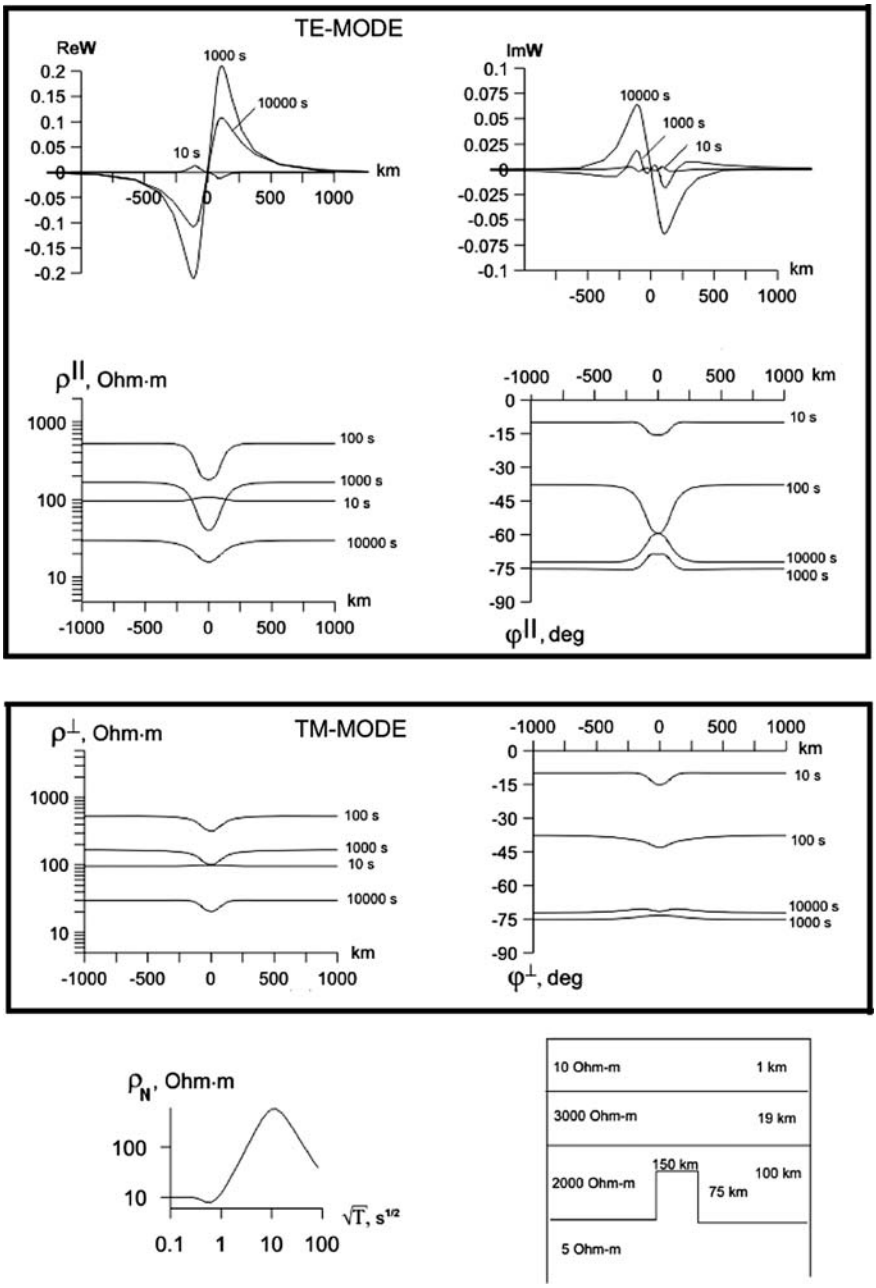

Fig. 12.5 Illustrating the sensitivity of the TM- and TE-modes to deep structures (a case typical of active regions). The normal ρ_N-curve is shown on the lower left. At the top: apparent-resistivity, impedance-phase and tipper profiles; profile parameter: period T

screening effect abates and the discernible $\rho^{\perp}$- and $\varphi^{\perp}$-anomalies caused by the asthenosphere elevation come into play. At the same time the $\rho^{\parallel}-$, $\varphi^{\parallel}-$ and $W-$ anomalies are hardly changed. The TM-mode is more sensitive to the lithosphere resistance than the TE-mode.

Another remarkable property of the TM-mode is that it may indicate the presence of conductive subvertical channels (fluid-saturated faults) crossing the resistive litosphere. Let us revert to the model with the asthenosphere elevation shown in Fig. 12.4 and introduce into it two two-dimensional vertical conductive channels which intersect the lithosphere and connect the asthenosphere elevation with the sediments. This model is shown in Fig. 12.6. Comparing Fig. 12.6 with Fig. 12.4, we see, that the current channeling slightly affects the TE-mode, but it abates the screening effect in the TM-mode so that the discernible $\rho^{\perp}$ - and $\varphi^{\perp}$-anomalies occur reflecting the asthenosphere elevation.

12.4.2 Robustness of the TM- and TE-Modes to the 3D-Effects

The two-dimensional model is a convenient mathematical abstraction that separates the magnetotelluric field into two modes of different physical nature: the TM-mode associated with galvanic anomalies and the TE-mode associated with induction anomalies. The question naturally arises: which of these modes is more robust to the 3D effects caused by real geological bodies.?

Summing up the analysis carried out in Part II of our book and taking into account the estimates suggested in (Svetov, 1973; Kaufman, 1974; Berdichevsky and Dmitriev, 1976; Veselovsky and Yudin, 1988; Berdichevsky et al., 1995), we can say that the TM-mode is more robust to 3D effects caused by conductive bodies (that is, by current gathering), while the TE-mode is more robust to 3D effects caused by resistive bodies (that is, by current around-flow).

Let us exemplify this statement by two characteristic models that have given a keen insight into the problem being a subject of rather long discussion.

Figure 12.7 presents a famous model of conductive sedimentary basin suggested by Wannamaker et al. (1984). The model has a layered background and Fig. 12.7 contains an elongated rectangular prism of resistivity $\rho = 2\,\mathrm{Ohm}\cdot\mathrm{m}$ located in the first layer of resistivity 400 Ohm·m. The prism's length and width are $l = 35$km and $w = 15$km, its elongation (aspect ratio) is $e = l/w = 2.3$. The apparent-resistivity curves have been computed for the central site O. In the left side of Fig. 12.8, we show the three-dimensional longitudinal and transverse apparent-resistivty curves of $\rho^{\parallel}_{3D}$ and $\rho^{\perp}_{3D}$ oriented along and across the strike of the prism (in x and y directions). For comparison, the two-dimensional longitudinal and transverse apparent-resistivty curves of $\rho^{\parallel}_{2D}$ and $\rho^{\perp}_{2D}$ are shown too. They correspond to the TM- and TE-modes generated in a 2D-model containing the prism with $l \to \infty$. The locally normal one-dimensional curve ρ_n is displayed as well. In the period range from 0.01 to 1 s, the three-dimensional curves of $\rho^{\parallel}_{3D}$ and $\rho^{\perp}_{3D}$ virtually coincide with the normal ρ_n- curve. These high-frequency branches of the ρ_A- curves admit the 1D-inversion determining a depth to the conductive prism. With lowering frequency,

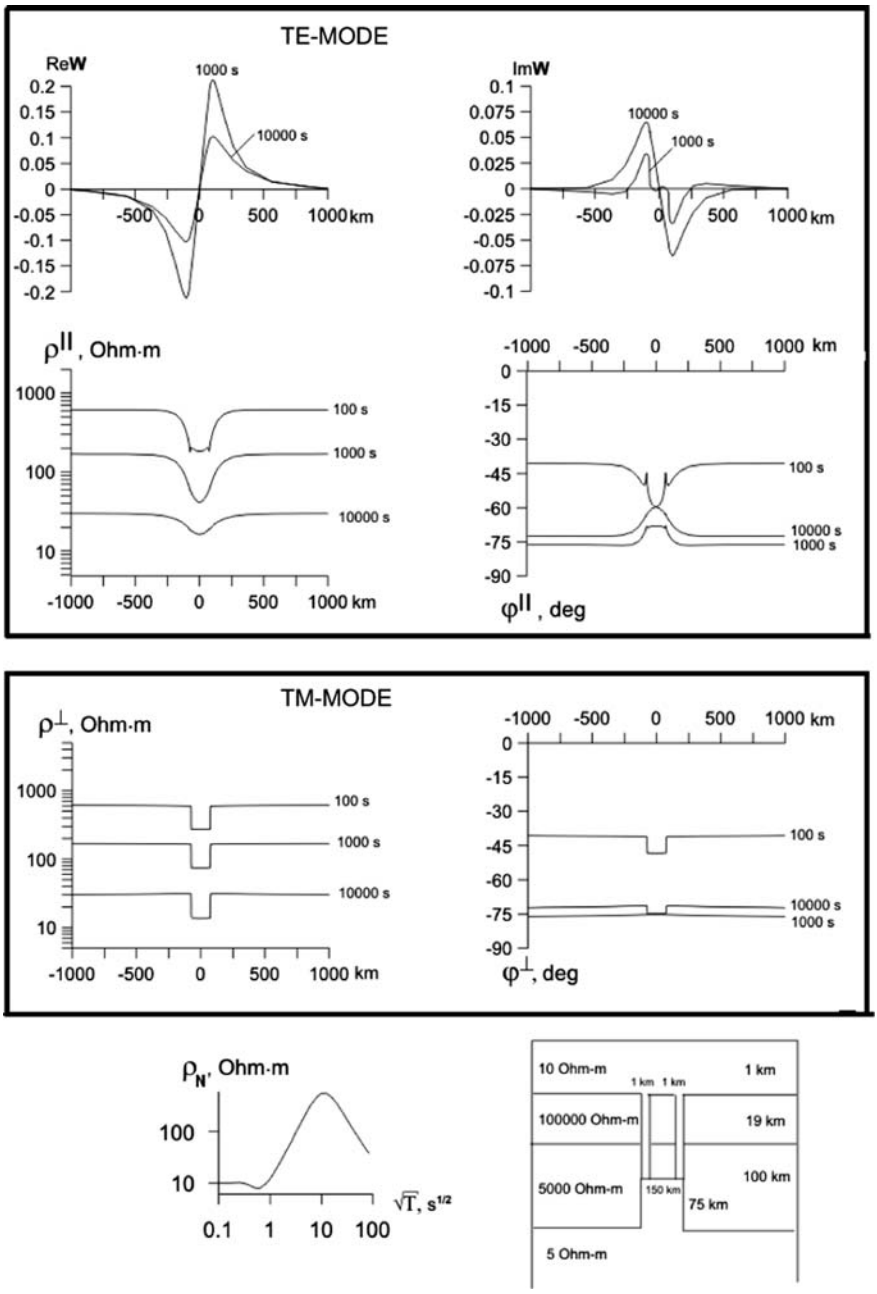

Fig. 12.6 Illustrating the sensitivity of the TM- and TE-modes to deep structures in the presence of conductive faults. The normal ρ_N-curve is shown on the lower left. At the top: apparent-resistivity, impedance-phase and tipper profiles; profile parameter: period T

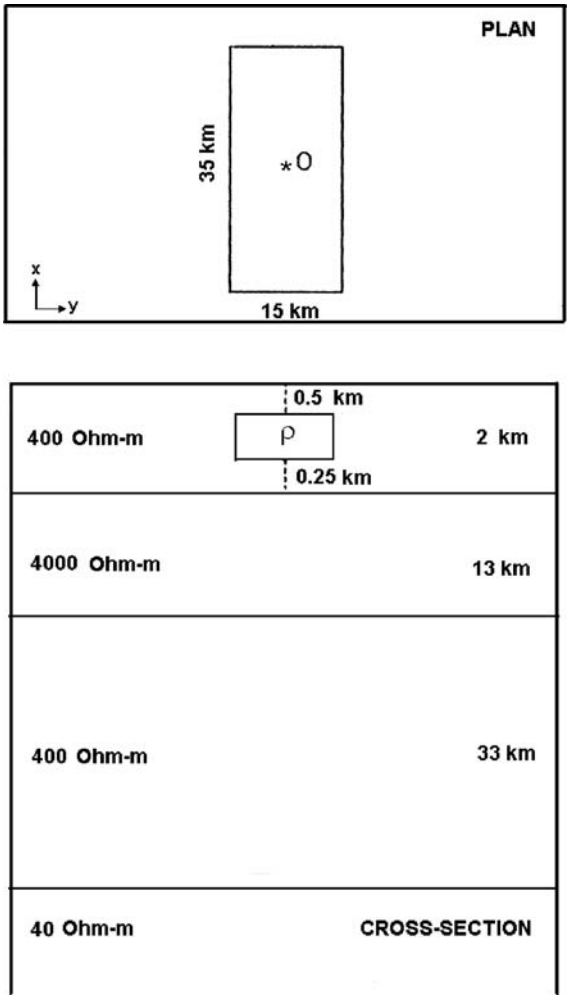

Fig. 12.7 Model with an elongated prismatic inclusion, O – sounding site (Wannamaker et al., 1984)

the difference between the three-dimensional $\rho_A -$ curves and the normal $\rho_n -$ curve drastically increases up to several orders. These distortions originate from the current gathering effect. But note that the transverse $\rho^{\perp}_{3D}$-curve is close to the two-dimensional $\rho^{\perp}_{2D}$-curve and its 2D-inversion is quite acceptable. At the same time the longitudinal $\rho^{\parallel}_{3D}$-curve departs dramatically from the two-dimensional $\rho^{\parallel}_{2D}$-curve, and its 2D-inversion will introduce a spurious conductor in place of the resistive crust.

It is quite evident that in the model with conductive prism the TM-impedance is more robust to 3D-effects than the TE-impedance. But can we expand this remarkable property of the TM-mode to the general case?

Let us replace the prism of 2 Ohm·m resistivity by a prism of the same geometry but of 40000 Ohm·m resistivity. Now we simulate a resistive mountain root rather

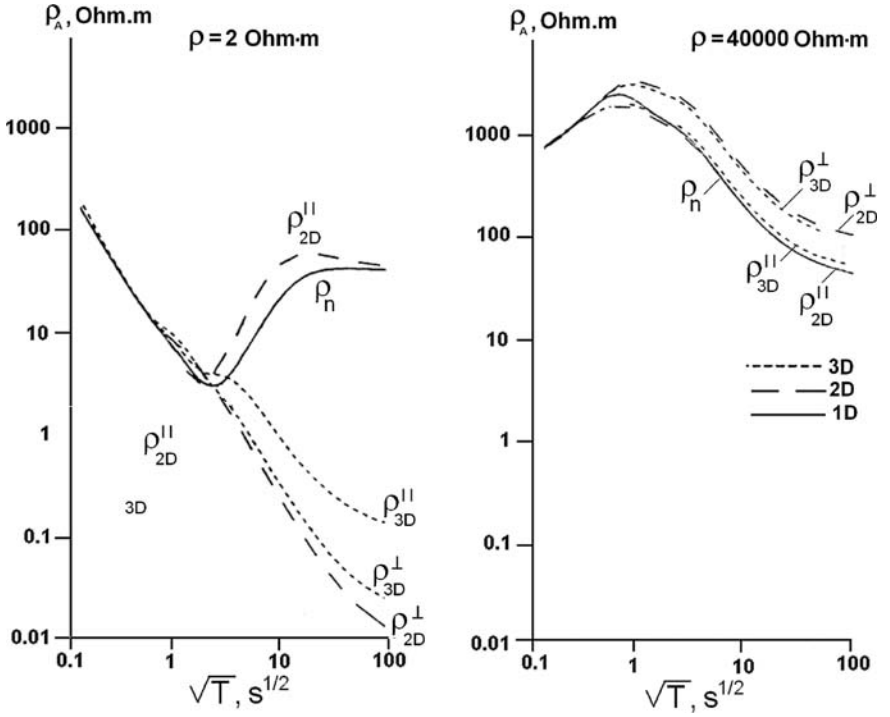

Fig. 12.8 Apparent resistivity curves in model shown in Fig. 12.7; ρ -prism resistivity. Solid lines: locally normal 1D-curves. Dashed lines – long dash: longitudinal and transverse 2D-curves, short dash: longitudinal and transverse 3D-curves

than a conductive basin, and observe currents flowing around instead of currents gathering. The ρ_A- curves are displayed in the right side of Fig. 12.8. We see that the relationship between the three-dimensional and two-dimensional curves changes radically. In fact, in the model with resistive prism, both of the three-dimensional curves are close to their two-dimensional counterparts. What's more, the longitudinal curve of $\rho^{\parallel}_{3D}$ is close not only to the curve of $\rho^{\parallel}_{2D}$ but even to the locally normal curve of ρ_n. The longitudinal 3D-response corresponding to the TE-mode is almost undistorted! It admits not only 2D-inversion, but even 1D-inversion.

In a model with the resistive prism the around-flow effect consists of three elements: over-flow (currents flow over the prism), under-flow (currents flow under the prism) and side-flow (currents flow along the sides of the prism). Here the over- and under-flow effects prevail, and this is why the curve of $\rho^{\perp}_{3D}$ is close to the curve of $\rho^{\perp}_{2D}$. It would be instructive to consider a model with prevalent side-flow effect. Figure 12.9 presents a model, in which the sediments include a three-dimensional horst-like elevation approaching the Earth's surface. The length and width of the horst are $l = 12$ km and $w = 2$ km, the clearance between the roof of the horst and the Earth's surface being 10 m. The horst elongation is $e = l/w = 6$. One can expect that in this model the side-flow effect will dominate, and the agreement between

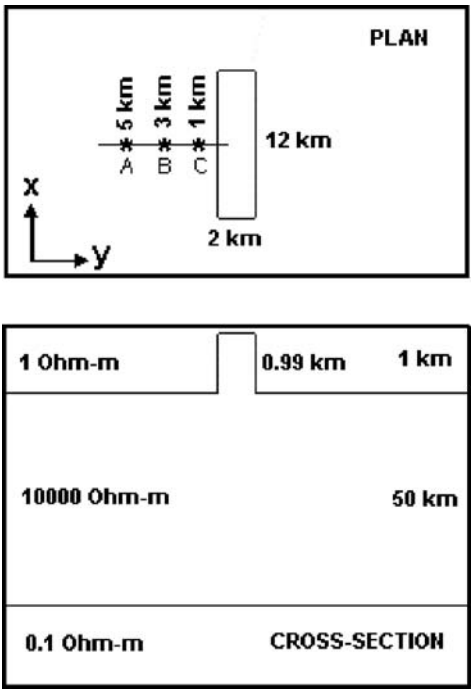

Fig. 12.9 Model with a three-dimensional horst-like resistive elevation in the sediments; A,B,C -sounding sites and their distance to elevation edge

$\rho^{\perp}_{3D}$- and $\rho^{\perp}_{2D}$-curves will be violated. Figure 12.10 shows the three-dimensional transverse and longitudinal curves of $\rho^{\perp}_{3D}$ and $\rho^{\parallel}_{3D}$ obtained along the central profile at different distances from the horst edge (5, 3 and 1 km, sites A,B and C respectively). Also shown are the two-dimensional curves of $\rho^{\perp}_{2D}$ and $\rho^{\parallel}_{2D}$ corresponding to the model with the infinitely long horst, and the locally normal curves of ρ_n corresponding to the model without a horst. It is notable that at all sites the longitudinal curves of $\rho^{\parallel}_{3D}$ practically coincide with the $\rho^{\parallel}_{2D}$- and ρ_n-curves. Clearly, they allow for two-dimensional and even one-dimensional inversion. At the same time the transverse $\rho^{\perp}_{3D}$-curves drop below the $\rho^{\perp}_{2D}$-curves, and this fall drastically increases in the immediate vicinity of the horst. At site C (1 km from the horst) the $\rho^{\perp}_{2D}$-curve tips over, and the degree of its distortion is almost the same as in the case of longitudinal $\rho^{\parallel}_{3D}$-curve in the model with a conductive prism. Going to the impedance phases, we note that fall of the $\rho^{\perp}_{3D}$-curves is accompanied by severe deformation of $\varphi^{\perp}_{3D}$-curves. These properties of the around-flow effect indicate its galvanic-inductive nature (intensity of current around-flow is governed by horizontal skin-effect in the conductive medium surrounding a resistive body). Needless to say that the formal two-dimensional inversion of the transverse curves of $\rho^{\perp}_{3D}$ and $\varphi^{\perp}_{3D}$ will introduce a spurious conductor.

The around-flow effect is observed quite often in foothills. Figure 12.11 presents the longitudinal ($\rho^{\parallel}$) and transverse ($\rho^{\perp}$) apparent-resistivity curves measured along a profile crossing the Precaucasian foredeep (Berdichevsky and Dmitriev, 1976).

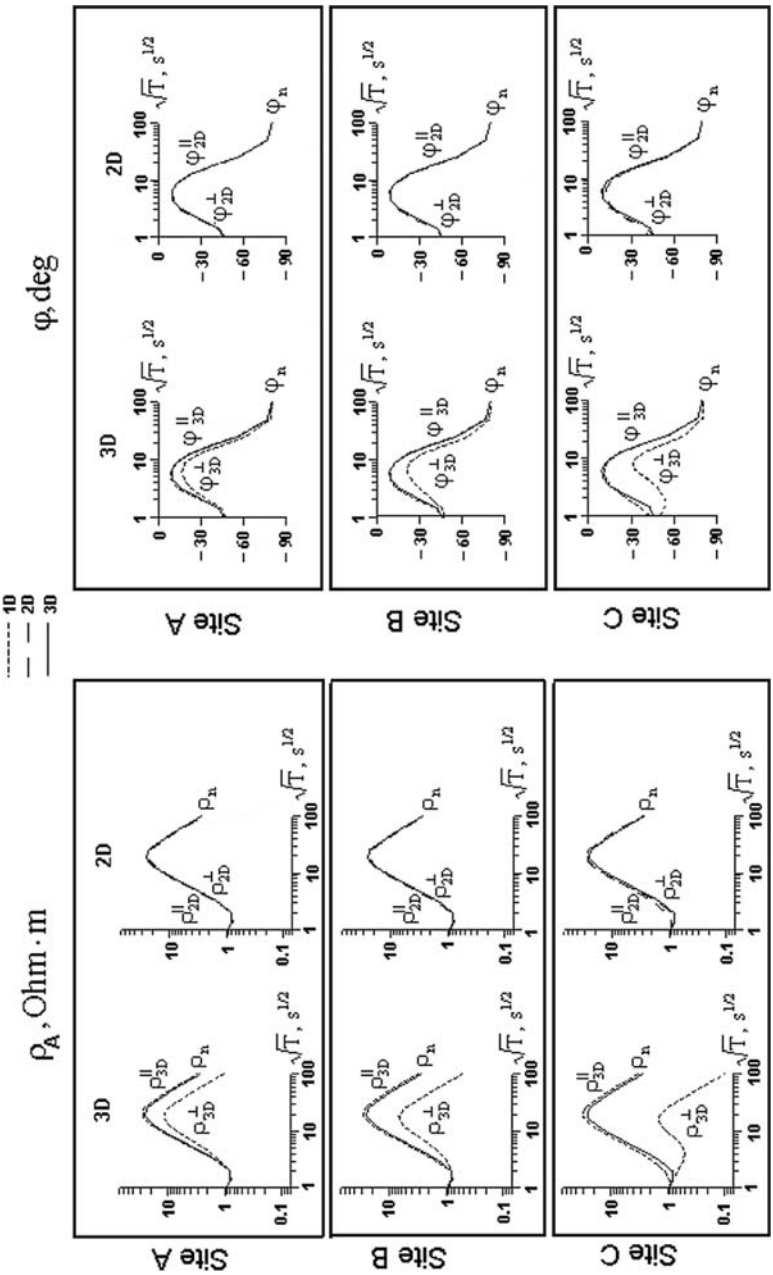

Fig. 12.10 Apparent resistivity and phase curves in model shown in Fig. 12.9. Solid lines: locally normal1D-curves. *Dashed lines – long dash:* longitudinal and transverse 2D-curves, short dash: longitudinal and transverse 3D-curves

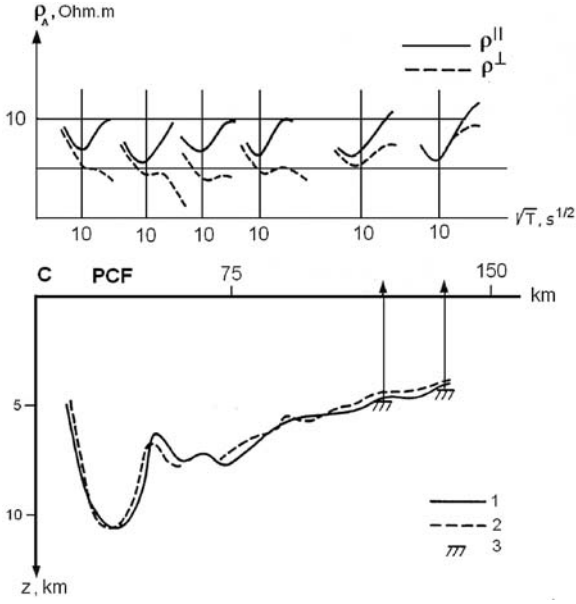

Fig. 12.11 Top: longitudinal ($\rho^{\parallel}$) and transverse ($\rho^{\perp}$) apparent-resistivity curves along a profile crossing the Precaucasian foredeep. Bottom: geophysical cross-section; C –the Caucasian ridge, PCF- the Precaucasian foredeep; surface of the Paleozoic basement from $\rho^{\parallel}$-curves (1), from seismics (2), from drilling (3)

The longitudinal $\rho^{\parallel}$-curves are bowl-type throughout the entire profile, 150 km long. Their 1D-interpretation yields the Paleozoic basement topography that is in close agreement with seismics and drillings. At the same time the transverse $\rho^{\perp}$-curves change their shape, from the bowl-type at the distance of 120–150 km from mountains to a falling type in the vicinity of mountains. Small wonder that 1D- and even 2D-interpretation of the transverse $\rho^{\perp}$-curves would give incongruous (say, crazy) results that have nothing in common with seismic data and general geological ideas of the region's structure. Suffice it to say that with TM-inversion, the resistivity of sediments falls to 0.1 Ohm·m, while the solid high-ohmic lithosphere wedges out and the conductive "asthenosphere" appears at the depth of about 8–10 km. It seems that this remarkable situation is the same as in model with a three-dimensional horst shown in Figs.12.9 and 12.10. The resemblance in behavior of experimental and model MT-curves is striking. It is evident that within the Precaucasian foredeep, we meet an intensive 3D-effect connected with currents flowing around the high-ohmic Caucasian Ridge. The flow-around effect dramatically distorts the transverse $\rho^{\perp}$-curves (the TM-mode) and scarcely affects the longitudinal $\rho^{\parallel}$-curves (the TE-mode). So, one cannot agree with the statements like "2D-interpretation of the TM-mode is more accurate than the TE-mode in the presence of 3D-bodies" (Park, 1996) or "2D-modelling should concentrate on the impedance in the TM-mode because of its low sensitivity to the effect of finite strike" (Wannamaker, 1999). In fact, the TM-impedance is more robust to 3D-effects caused by conductive structures (that is, by current gathering), but the TE-impedance may be more robust (even considerably more robust!) to 3D-effects caused by resistive structures (that is, by current around-flow).

Can we predict (at least roughly) the effect of finite strike of elongated structures? It wouldn't be dramatically wrong if we assume that the conductive structure (say, graben) in the TM-field and the resistive structure (say, horst or ridge) in the TE-field allow for the two-dimensional approximation provided their elongation exceeds 5–10. But conditions of the two-dimensional approximation of elongated structures dramatically change when we consider the conductive structures in the TE-field and the resistive structures in the TM-field. The question is about elongations that range up to 15–25 (and even more) depending on geoelectric situation. Such elongated structures, if they exist, are a rarity in nature. We believe that any two-dimensional inversion may need a posteriori estimation if not correction of model errors caused by 2D approximation.

12.4.3 Susceptibility of the TM- and TE-Modes to Near-surface Galvanic Distortions

In the abstract two-dimensional model, only the TM-mode suffers from the near-surface galvanic distortions which manifest themselves in static shift of apparent-resistivity curves. But in actual practice, we may deal with superposition of large-scale elongated structures and small-scale three-dimensional near-surface inhomogeneities of more or less complicated form. In that events, both the field modes, TM and TE, are distorted and hence not only the transverse but also the longitudinal apparent-resistivity curves suffer from static shift. Fortunately, the experience suggests that in many cases (even in mountains) the longitudinal $\rho^{\parallel}-$ curves are less disturbed than the transverse $\rho^{\perp}-$ curves (Kovtun, 1989; Moroz, 1991; Dyakonova et al., 1986; Alperovich et al., 1980; Berdichevsky and Dmitriev, 2002). This is typical for regions with a predominance of elongated inhomogeneities with a common strike in the absence of pronounced local 3D-inhomogeneities.

Let us show three indicative examples.

In Fig. 12.12 we see the longitudinal and transverse apparent-resistivity curves, $\rho^{\parallel}$ and $\rho^{\perp}$, obtained in the vicinity of the Urals (Dyakonova et al., 1986). Here the longitudinal $\rho^{\parallel}$-curves experience far lesser static shift than the transverse $\rho^{\perp}$-curves. The descending mantle branches of the longitudinal curves are close to each other. They gravitate to the standard curve of ρ_{st}. At the same time, the corresponding transverse curves cross the ρ_{st}-curve and their mantle branches are shifted upward by decade and a half.

The longitudinal and transverse apparent-resistivity curves, $\rho^{\parallel}$ and $\rho^{\perp}$, obtained on the Kola Peninsula (Djakonova et al., 1986) are presented in Fig. 12.13. Here almost the same pattern is observed. The longitudinal curves seem to be slightly distorted. Their left descending branches merge together, reflecting a conductive layer in the lower part of the Earth's crust. The mantle branches of these curves are arranged about the standard curve of ρ_{st}, though with a slightly different slope. Compare the longitudinal curves with transverse ones. The transverse curves cross the ρ_{st} –curve. They are drastically shifted upward (up to decade).

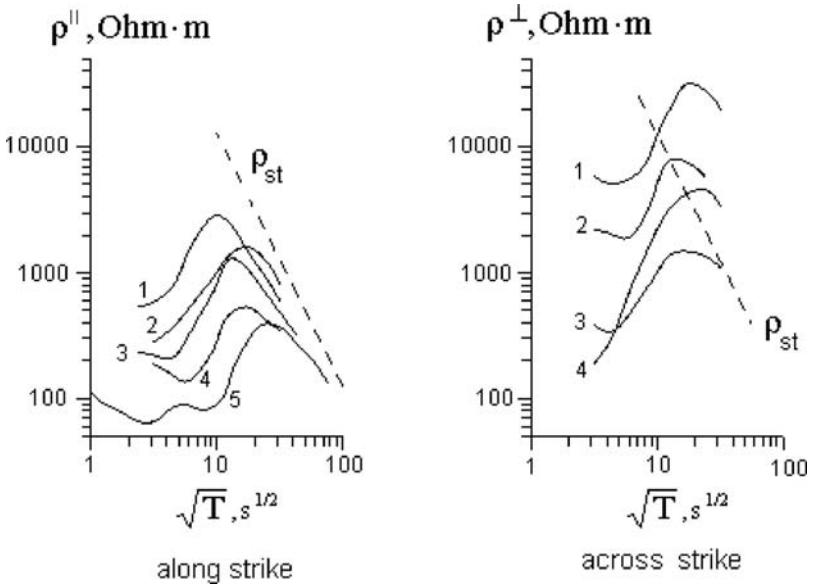

Fig. 12.12 Longitudinal and transverse apparent-resistivity curves characteristic of the Urals, ρ_{st} – the standard apparent-resistivity curve

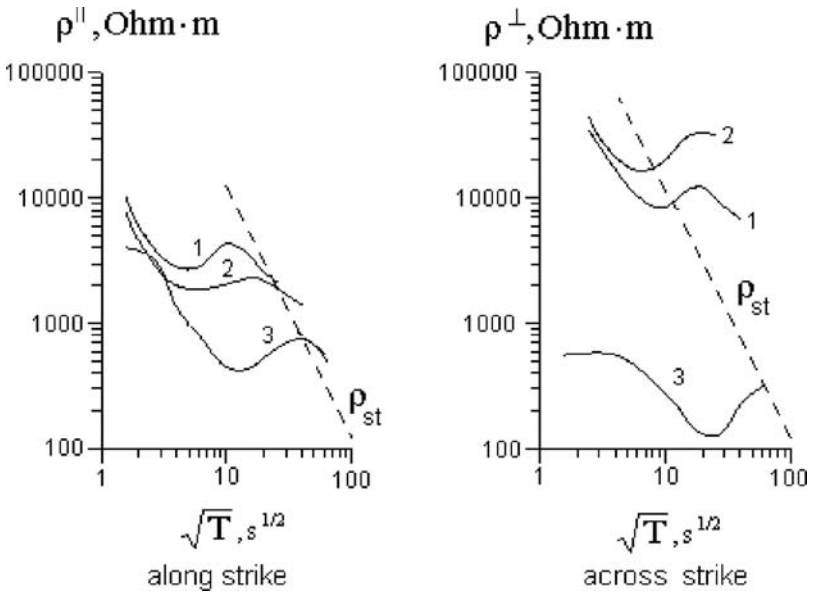

Fig. 12.13 Longitudinal and transverse apparent-resistivity curves characteristic of the Kola Peninsula, ρ_{st} – the standard apparent-resistivity curve

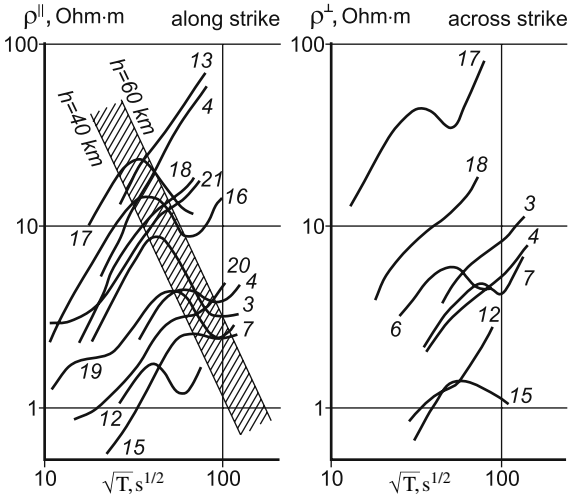

Fig. 12.14 Longitudinal and transverse apparent-resistivity curves characteristic of the Kamchatka Peninsula

No less indicative are the apparent-resistivity curves obtained on the Kamchatka peninsula (Fig. 12.14). At many sites, the descending branches of the longitudinal $\rho^{\parallel}$-curves lie between the *h*-lines 40 and 60 km detecting the elevation of the partially melted asthenosphere in the region of contemporary volcanism. At the same time, the transverse $\rho^{\perp}$-curves exhibit the vertical scattering that ranges up to two decades and is hard of interpretation.

The last example is drawn from the magnetotelluric soundings carried out in the mountains of the Kirghiz Tien Shan (Trapeznikov et al., 1997). The longitudinal and transverse apparent-resistivity curves, $\rho^{\parallel}$ and $\rho^{\perp}$, are presented in Fig. 12.15. The

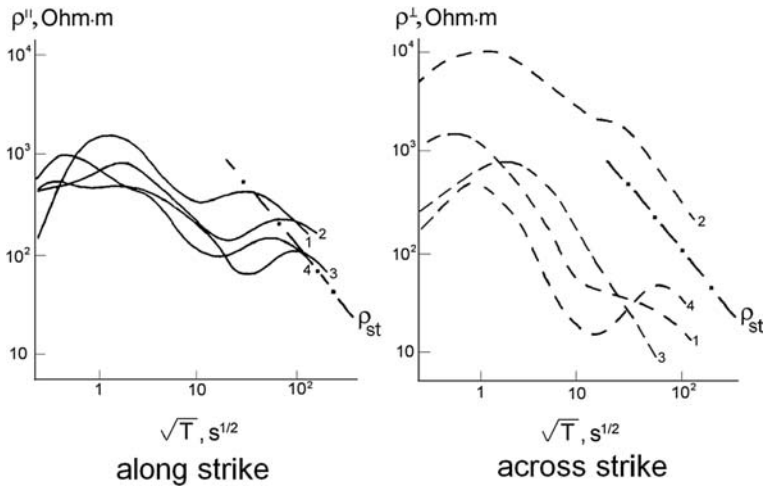

Fig. 12.15 Longitudinal and transverse apparent-resistivity curves characteristic of the Kirghiz Tien Shan, ρ_{st} – the standard apparent-resistivity curve

longitudinal curves exhibit distinctive minima and clearly outlined descending mantle branches, which are close to the standard ρ_{st}-curve (small static shift !). It seems that these curves are weakly distorted and may be used for rough 1D-estimates. One can presume that minima of the $\rho^{\parallel}$-curves are caused by a crustal conductive layer. It lies at a depth of about 20–30 km, and its conductance increases from 200–300 S in the north (MTS-1) to 1000–1500 S in the south (MTS-4). These estimates are in accordance with a model constructed from the tipper inversion (Fig. 5). Quite different pattern is given by the transverse curves. The crustal conductor is clearly evidenced only by the $\rho^{\perp}-$ curve from MTS-4, carried out near a deep fault. But with distance from the fault the crustal conductor is screened and the apparen-resistivity minimum degenerates into gentle bendings (MTS-1, MTS-2). What is more, the mantle branches of the $\rho^{\perp}-$ curves are significantly displaced upward and downward from the standard ρ_{st}-curve (large static shift).

Beyond question, in the above examples the longitudinal $\rho^{\parallel}-$ curves are less susceptible to near-surface galvanic distortions than the transverse $\rho^{\perp}-$ curves.

12.4.4 Informational Complementarity of the TM- and TE-Modes

We have examined the main properties of the TM- and TE-modes in the presence of elongated target structures. The results of this consideration are summarized in Table 12.1, which shows the susceptibility of the TM- and TE-modes to near-surface static distortions and their accuracy in the 2D-approximation of elongated structures as well as their sensitivity to near-surface and deep structures, the lithosphere resistance and conductive faults.

The TM-mode ($\rho^{\perp}$, $\varphi^{\perp}$) provides the better accuracy in the 2D-approximation of conductive structures and the better sensitivity to near-surface structures as well as to the lithosphere resistance and deep faults, but it suffers from the screening effect and may miss the deep structures (for instance, conductive zones in the high-resistive lithosphere).

The TE-mode ($\mathrm{Re}\,\mathbf{W}$, $\mathrm{Im}\,\mathbf{W}$, $\rho^{\parallel}$, $\varphi^{\parallel}$) ensures the better accuracy in the 2D-approximation of resistive structures and the better sensitivity to deep structures, but it is open to large errors in the 2D-approximation of conductive structures. Also, if the transverse apparent-resistivity curves in the TM-mode suffer dramatically from the static shift, the TE-mode may change the situation for the better (the tipper and longitudinal impedance-phase curves do not experience static distortions, while the longitudinal apparent-resistivity curves under favorable conditions are slightly distorted).

The TM- and TE-modes nicely complement each other: gaps left by one mode are filled by another mode. In this sense we say that the TM- and TE-modes satisfy the principle of *informational complementarity*.

The complementarity principle forms a sound basis for the 2D-interpretation strategy.

The sensitivity to the target structures is of critical importance. Consider, for instance, a magnetotelluric survey designed to studying conductive zones in deep

Table 12.1 Two-dimensional inversion: properties of the TE- and TM-MODES

MODE	response function	near-surface static distortions		accuracy of 2D approximation		sensitivity			
		ρ – effect	S – effect;	conductive structure	resistive structure	near-surface structure	deep structure	lithosphere resistance	conductive fault
TE-mode induction anomalies	Re W	absent !	absent !	worse	better !	worse	better !	worse	worse
	Im W	absent !	absent !	worse	better !	worse	better !	worse	worse
	$\rho^{\parallel}$	reduced susceptibility !		worse	better !	worse	better !	worse	worse
	$\varphi^{\parallel}$	absent !	absent on low frequency !	worse	better !	worse	better !	worse	worse
TM-mode galvanic anomalies	$\rho^{\perp}$	strong	strong on low frequency	better !	worse	better !	worse	better !	better !
	$\varphi^{\perp}$	absent !	absent on low frequency !	better !	worse	better !	worse	better !	better !

layers of the resistiive lithosphere. Due to severe galvanic screening, the sensitivity of the TM-mode is too poor for this task. So, the TE-mode with its higher sensitivity to buried conductors is the only contributor of useful information. The situation is paradoxical. We have to abandon the TM-mode with its high accuracy of 2D-approximation, and instead to harness the less-accurate TE-mode. But there is no way to the necessary information except by using the TE-mode with all troubles arising from the 2D-approximation errors and the 3D-static effects that cannot be reproduced by two-dimensional modeling. It is better to get rough (maybe even qualitative) information than no information. Thus, we have to use the TE-mode and try to control the errors of its two-dimensional inversion by means of a posteriori 3D-estimates.

In closing, we state that in the general case the most comprehensive and reliable information on the Earth's conductivity can be derived by means of bimodal inversion, using the TE- and TM-modes (tippers, magnetic tensors, longitudinal and transverse MT-curves).

12.5 Two Approaches to Multicriterion Inverse Problem

Solution to an inverse problem, constrained by the interpretation model, is chosen using criteria of the minimal misfits. These criteria ensure the agreement between the solution and the observation data. The number of criteria is determined by the number of the response functions in use (real and imaginary or amplitude and face functions). If the inversion envolves a few response functions, the problem is multicriterion.

The two-dimensional integrated interpretation of magnetovariational and magnetotelluric data belongs to the class of multicriterion problems. The electric conductivity of the Earth can be usually inferred from the TE-mode with the response functions $\mathrm{Re}W$ and $\mathrm{Im}W$, $\rho^{\parallel}$ and $\varphi^{\parallel}$ (real and imaginary tippers, longitudinal apparent resistivities and phases of longitudinal impedances) and the TM-mode with the response functions $\rho^{\perp}$and $\varphi^{\perp}$ (transverse apparent resistivities and phases of transverse impedances). These functions differ in the sensitivity to target geoelectric structures, in the robustness to 3D effects, in the susceptibility to near-surface static distortions. The TE-mode is more sensitive to deep structures and less sensitive to the resistance of the lithosphere, whereas the TM-mode is less sensitive to deep structures and more sensitive to the resistance of the lithosphere. On the other hand, the apparent resistivities may suffer from the near-surface static distortions, whereas the low-frequency tippers and impedance phases are immune to these troubles. An algorithm of the 2D bimodal inversion should be constructed so that the different response functions support and complement each other. When inverting the different response functions, one should give priority to the most reliable elements of the solution and suppress the least reliable ones.

The following two approaches are possible in solving multicriterion inverse problems: (1) *parallel inversion* of all response functions taking part in the interpretation, and (2) *successive partial inversion* of each of the response functions.

The parallel inversion summarizes all inversion criteria related to various response functions. In solving a 2D inverse problem, the parallel inversion of M response functions reduces to the minimization of the Tikhonov's functional Φ_α containing the total misfit. For instanse,

$$\inf_{\mathbf{p}} \Phi_\alpha \{\sigma(y,z)\} = \inf_{\mathbf{p}} \left\{ \sum_{m=1}^{M} g_m \mathrm{I}_m \{\sigma(y,z)\} + \alpha\Omega\{\sigma(y,z)\} \right\}, \tag{12.20}$$

where

$$\mathrm{I}_m \{\sigma(y,z)\} = \left\| \tilde{F}_m - F_m \{y, z=0,\ \omega, \sigma(y,z)\} \right\|_R^2$$
$$\Omega\{\sigma(y,z)\} = \|\sigma(y,z) - \sigma_0(y,z)\|_{L_2}^2 .$$

Here $\mathbf{p}$ is the vector of the sought-for parameters, $\tilde{F}_m$ is the mth response function, F_m is an operator of the forward problem that calculates the mth response function for a given electric conductivity $\sigma(y,z)$, I_m is the misfit of the mth response function, g_m is a weight representing the significance of the mth response function, $\sigma_0(y,z)$ is a hypothetical model.

At first glance, the parallel inversion seems to be the most attractive because it incorporates simultaneously all response functions in use and considerably simplifies the work of the geophysicist. One can even say that the parallel inversion opens the way to the automatic inversion. Let us consider the situation more attentively.

If various response functions F_m have the same sensitivity to all parameters $\mathbf{p}(p_1,\ p_2, \ldots)$ of the geoelectric medium and the same immunity to near-surface distortions, their parallel inversion is not very advantageous because one, the most reliably determined (the least susceptible to geoelectric noise), response function is sufficient for a comprehensive inversion.

The use of several response functions can extend the inversion potentials if these functions differ significantly in their sensitivity to various parameters of the geoelectric medium and in their immunity to near-surface distortions. However, in this case their joint inversion may become conflicting. Really the different functions can bother each other, because they impose different constraints on the geoelectric medium and demand different criteria for mimimizing the model misfit. Moreover such a joint inversion increases the risk of falling into a local minimum.

True enough, it is possible that in some cases a fortunate choice of weights allows one to construct a self-consistent meaningful model with a sufficiently small overall misfit. However, the adequate selection of such weights is itself a complex problem that is hard to solve rationally.

Apparently, the SPI method (successive partial inversions) is the best approach to the solution of a multicriterion inverse problem.

Let a response function F_m be the most sensitive to the vector of parameters $\mathbf{p}^{(m)}$. Then, the partial mth inversion in the multicriterion two-dimensonal problem calls for the minimization of the following Tikhonov's functional on the set of the parameters $\mathbf{p}^{(m)}$, with the parameters $\mathbf{p} - \mathbf{p}^{(m)}$ being fixed:

$$\inf_{\mathbf{p}^{(m)}} \Phi_{\alpha}^{(m)} \{\sigma(y,z)\} = \inf_{\mathbf{p}^{(m)}} \{ \mathrm{I}_m\{\sigma(y,z)\} + \alpha\Omega_m \{\sigma(y,z)\}\}, \tag{12.21}$$

where

$$\mathrm{I}_m\{\sigma(y,z)\} = \left\| \tilde{F}_m - F_m\{y, z=0,\ \omega, \sigma(y,z)\} \right\|_R^2$$
$$\Omega_m\{\sigma(y,z)\} = \left\| \sigma(y,z) - \sigma^{(m-1)}(y,z) \right\|_{L_2}^2$$

and $\sigma^{(m-1)}(y,z)$ is a model obtained by the $(m-1)$th inversion.

Step-by-step examination of the different response functions F_m, $m = 1, 2, \ldots M$ reduces the solution of the multicriterion problem to a sequence of partial inversions. Each partial inversion can be aimed to solving some specific problem and focused on some specific structures.

Partial inversions comprehensively incorporate specific features of the response functions, their informativeness, and their confidence intervals. They admit the information exchange between various response functions, enable a convenient interactive dialog, and are easily tested. And finally they decrease the number of sought-for parameters and hence improve the stability of the inverse problem. We believe that this direction of research is most promising for further development of methods designed for the integrated interpretation of MVS and MTS data.

Magnetotelluric soundings carried out in various geological provinces showed the proficiency of the SPI method (Trapeznikov et al., 1997; Berdichevsky et al., 1998, 1999; Pous et al., 2001; Vanyan et al., 2002a, b). Below, we briefly describe some model experiments elucidating the potentials of successive partial inversions with MV priority.

Figure 12.16 displays a 2D model schematically illustrating geoelectric structure of the Kirghiz Tien Shan (Trapeznikov et al., 1997). The model will be referred to as the TS model. It includes (1) inhomogeneous sediments (resistivity varies from 10 to 100 Ohm·m), (2) an inhomogeneous resistive crust (resistivity varies from 10^4 in the south to 10^5 Ohm·m in the north), (3) a deep crustal layer with resistivity increasing monotonically from 10 Ohm·m in the south to 300 Ohm·m in the north, (4) conductive zones A, B, and C branching from the crustal conductive layer, (5) a poorly conductive mantle underlaid by a conductive asthenosphere at a depth of 150 km.

The forward problem has been solved with the finite element method (Wannamaker et al., 1987). Gaussian white noise has been introduced into the response functions: it has standard deviations of 5% for apparent resistivities $\rho^{\parallel}$, $\rho^{\perp}$ and tippers Re W_{zy}, Im W_{zy} and 2.5° for phases $\varphi^{\parallel}$, $\varphi^{\perp}$. To imitate the static shift caused by small 3D near-surface inhomogeneities, the apparent resistivities were multiplied by random real numbers uniformly distributed in the interval from 0.5 to 2.

It is interesting to estimate a frequency range within which the tipper becomes virtually free of near-surface effects. Figure 12.17 demonstrates frequency responses of Re W_{zy} and Im W_{zy} calculated for TS model and for the same model but with a homogeneous upper layer of a resistivity of 10 Ohm·m. Except for a few

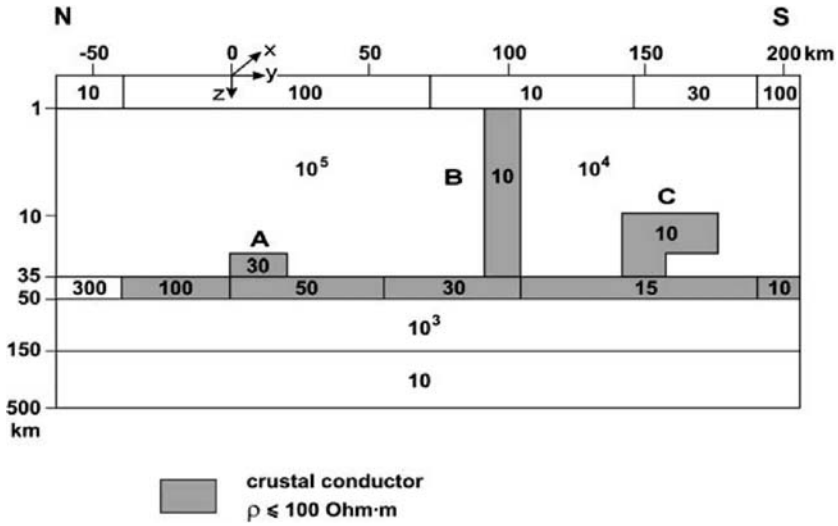

Fig. 12.16 The two-dimensional TS model; resistivity values in Ohm·m are shown within blocks; blocks of lower crustal resistivities are shaded; A, B, and C are local conductive zones in the crust

sites (y = 45 km for Re W_{zy} and $y = -45$, 55, 100 km for Im W_{zy}), the Re W_{zy} and Im W_{zy} curves obtained for models with inhomogeneous and homogeneous upper layers merge together at periods of order 100 s and even less. These periods relate to the low-frequency range, in which the near-surface MV anomalies attenuate and effects of deep conductive zones come to the forefront.

The integrated interpretation of the synthetic data obtained in the TS model has been performed by the method of partial inversions.

Constructing the interpretation model, we assumed that the following a priori information was available: (1) the sedimentary cover is inhomogeneous, with an average thickness of 1 km, (2) the consolidated crust is inhomogeneous and can contain local conductive zones, its resistivity can experience regional variations, and an inhomogeneous conductive layer can exist near or within the seismic waveguide (35–50 km), (3) the upper mantle consists of homogeneous layers, and its resistivity at depths below 200 km can amount to 20 Ohm·m, (4) the profile under observation is bordered on north and south by vast asymmetric media which slowly vary with distance.

To detail these assumptions, we performed a trial inversion of the tippers using a smoothing program capable of revealing crustal conductive zones. We applied the REBOCC program (Siripunvaraporn and Egbert, 2000) and take a homogeneous half-space with a resistivity of 100 Ohm·m as an initial approximation. Figure 12.18 presents this trial model TS-1, resulting from the inversion of Re W_{zy} and Im W_{sy}. It shows clear evidences of three local crustal conductors A, B, and C ($\rho < 30$ Ohm·m) but fails to stratify the crust and upper mantle.

The a priori information complemented with data on local crustal conductors provides the construction of a blocky interpretation model. On this way, we tested

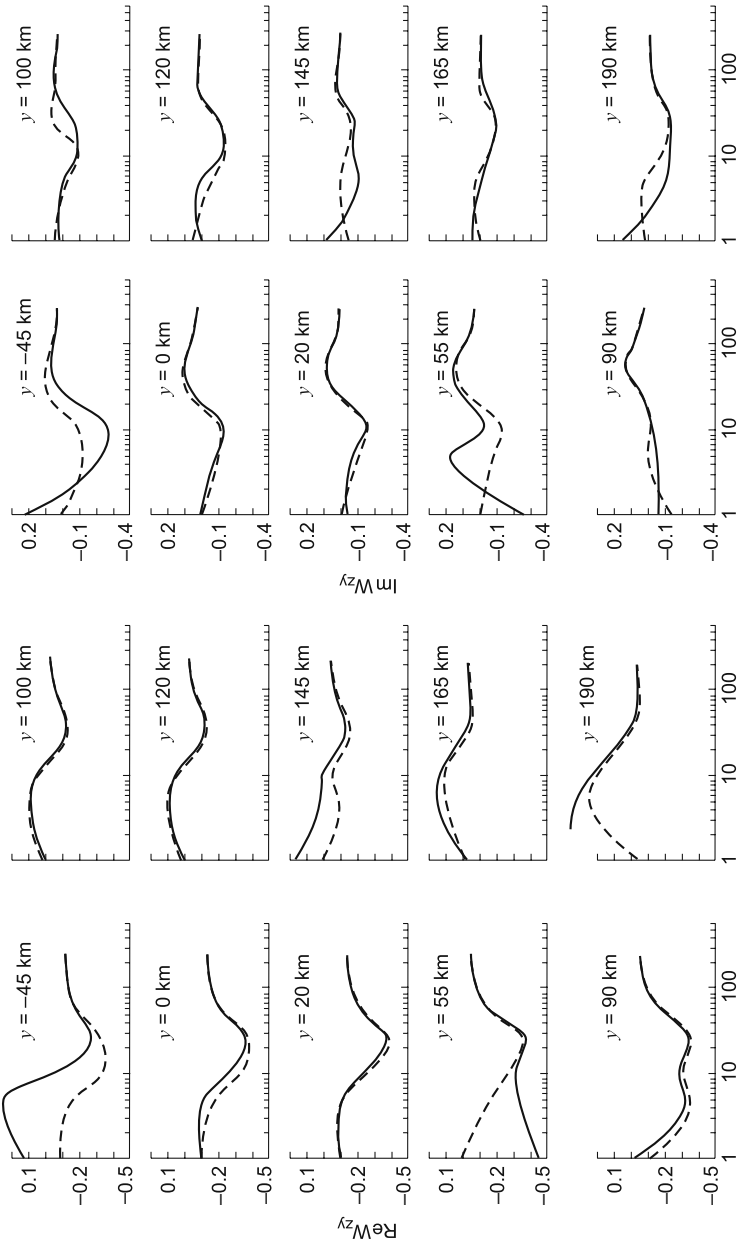

Fig. 12.17 Frequency responses of tippers Re W_{zy} and Im W_{zy}. Solid and broken lines are related to the TS model with inhomogeneous and homogeneous upper layer, respectively

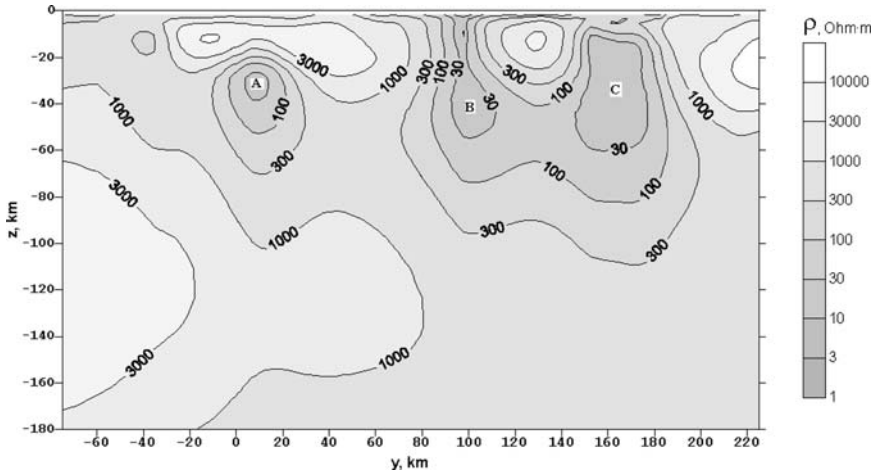

Fig. 12.18 Model TS-1; inversion of tippers Re W_{zy} and Im W_{zy} has been performed using the smoothing REBOCC program; A, B, and C are conductive zones in the crust (cf. Fig. 12.16)

three hypotheses concerning the position of the crustal conductive layer: (1) a conductive layer overlies the seismic waveguide (25–35 km), (2) a conductive layer coincides with the seismic waveguide (35–50 km), (3) a conductive layer underlies the seismic waveguide (50–70 km). The interpretation model has been constructed in line with the second hypothesis, which resulted in the minimum model misfit. It consists of 70 blocks of a fixed geometry (Fig. 12.19). The partition density depends on the position and size of supposed structures and is highest within the sedimentary cover, local crustal conductors, and crustal conductive layer. The model allows for

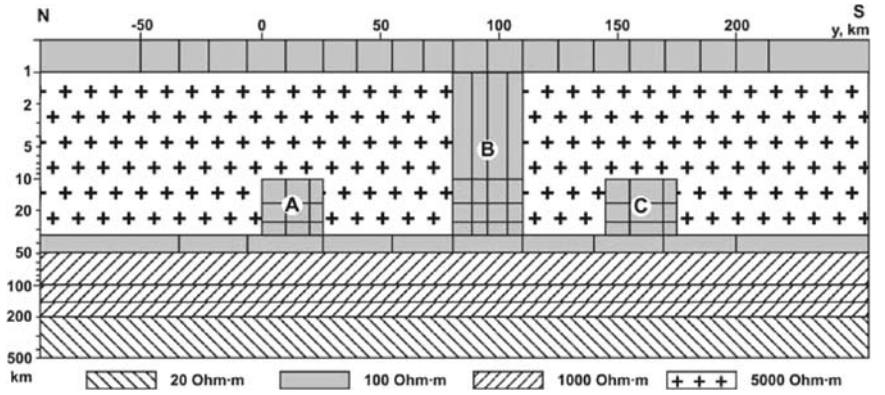

Fig. 12.19 The two-dimensional blocky interpretation model; starting resistivities are shown within blocks

the symmetric or asymmetric bordering background that is composed of horizontally homogeneous layers.

Partial inversions of the synthetic data have been carried out in the class of blocky media with the use of the II2DC program (Varentsov, 2002) in the following succession: (1) Re W_{zy} and Im W_{zy} inversion → (2) $\varphi^{\parallel}$ inversion → (3) $\rho^{\perp}$ and $\varphi^{\perp}$ inversion. All the inversions were conducted automatically.

Below, we consider each inversion separately.

1. Inversion of the real and imaginary tippers, Re W_{zy} and Im W_{zy}. Starting resistivities for this inversion are shown in Fig. 12.19. The tipper inversion results in the model presented in Fig. 12.20. It is referred to as the TS-2 model. The model agrees well with the initial TS model. The divergence between the tippers calculated from both models in the period range from 1 to 10000 s is generally no more than 0.02 (Fig. 12.21). Using the MV data alone, we have successfully reconstructed the most significant elements of the initial model, including the inhomogeneous sedimentary cover, the local crustal conductors A, B, and C, and the inhomogeneous crustal conductive layer whose resistivity varies from 234 Ohm·m in the north to 16 Ohm·m in the south (from 300 to 10 Ohm·m in the initial model). Also resolved was the contrast between the nonconductive and conductive mantle (1667 Ohm·m/109 Ohm·m in the TS-2 model against 1000 Ohm·m /10 Ohm·m in the initial TS model). We see that the MV response functions measured on a 200 km profile enable not only to detect the local conductive zones but to stratify the medium as well (with an accuracy sufficient for obtaining some petrophysical estimates).

2. Inversion of the longitudinal-impedance phases, $\varphi^{\parallel}$. At this stage, without going beyond the TE-mode, we control the tipper inversion and gain additional constraints on the stratification of the medium. The point is that the longitudinal apparent-resistivity $\rho^{\parallel}$ – curves are distorted by static shift caused by near-surface 3-D inhomogeneities. We avoided this difficulty by restricting ourselves to the

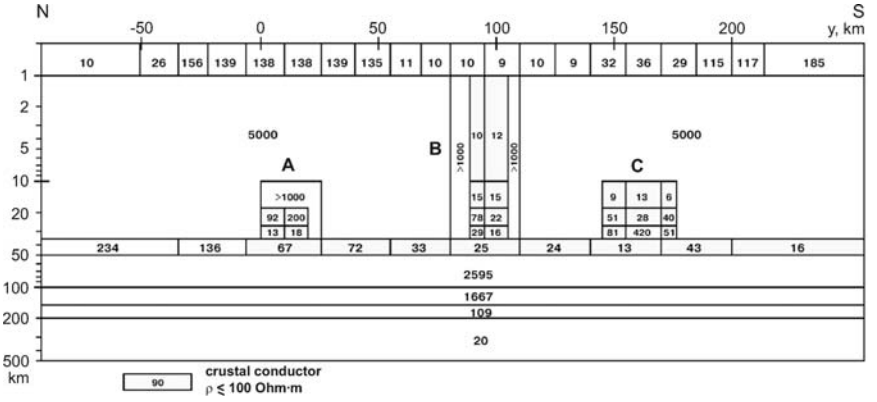

Fig. 12.20 Model TS-2; inversion of the tippers Re W_{zy} and Im W_{zy} has been performed using the blocky II2DC program; resistivity values in Ohm·m are shown within blocks; blocks of lower crustal resistivity are shaded (cf. Fig. 12.16)

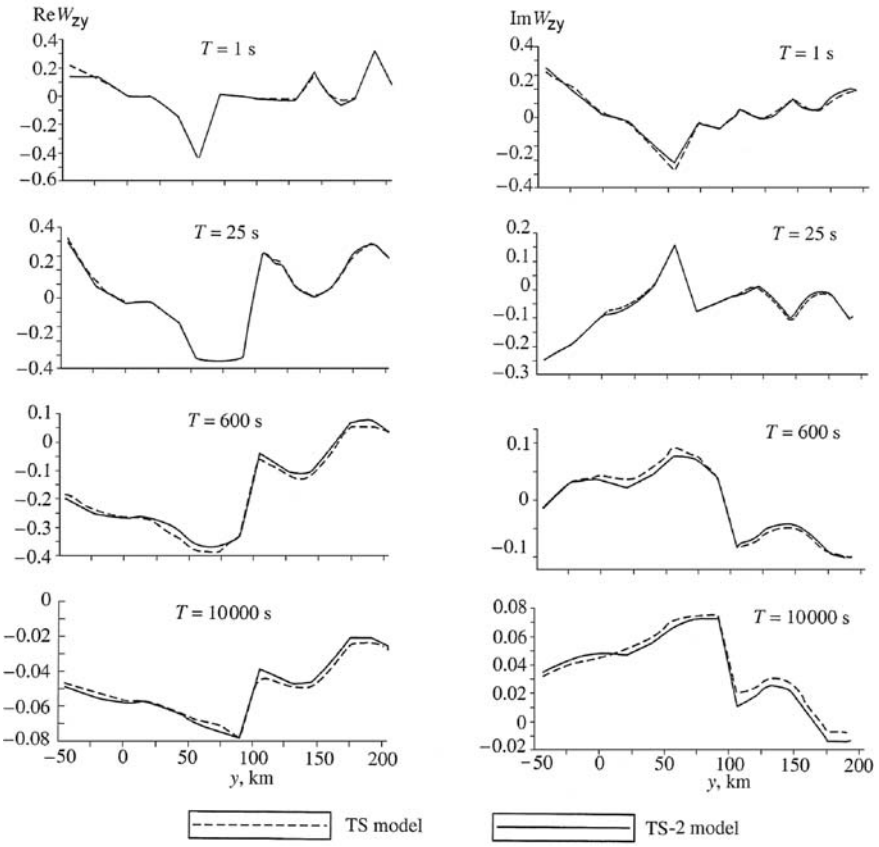

Fig. 12.21 Comparison of tippers Re W_{zy}, Im W_{zy} from the TS-2 and TS models

inversion of the undistorted $\varphi^{\parallel}-$ curves. If $\rho^{\parallel}-$ and $\varphi^{\parallel}-$ curves meet the dispersion relations, the disregard of the $\rho^{\parallel}-$ curves does not lead to a loss of information. We interpreted the $\varphi^{\parallel}-$ curves using the starting model TS-2, obtained from the tipper inversion. Inversion of $\varphi^{\parallel}$ was performed with fixed resistivities of the sedimentary cover. It resulted in the model, which is referred to as the TS-3 model. The model is shown in Fig. 12.22. The divergences between the phases from the TS-3 model and initial TS model do not exceed 2.5° (Fig. 12.23). Comparing the TS-3 and TS-2 models, we see that the phase inversion agrees reasonably well with the tipper inversion. Two points are of particular interest: (1) the edge resistivities of the inhomogeneous crustal layer (343 and 10 Ohm·m) became closer to their true values (300 and 10 Ohm·m), and (2) the contrast between the nonconductive and conductive mantle became sharper (3801 Ohm·m /15 Ohm·m in the TS-3 model against 1000 Ohm·m /10 Ohm·m in the initial TS model). Thus, the phase inversion visibly improved the accuracy of the stratification.

3. Inversion of the transverse apparent resistivity and impedance-phase, $\rho^{\perp}$ and $\varphi^{\perp}$. At this stage we pass on to the TM-mode, which is sensitive to galvanic effects.

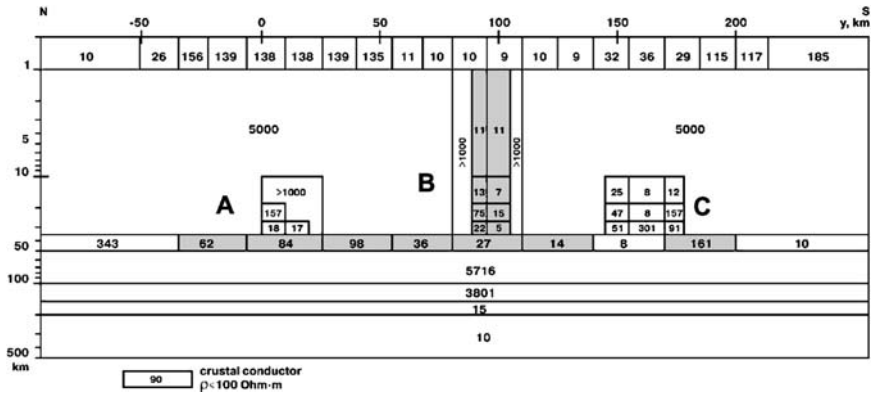

Fig. 12.22 Model TS-3; inversion of the impedance phases $\varphi^{\parallel}$ has been performed using the blocky II2DC program; resistivity values in Ohm·m are shown within blocks; blocks of lower crustal resistivities are shaded (cf. Fig. 12.16)

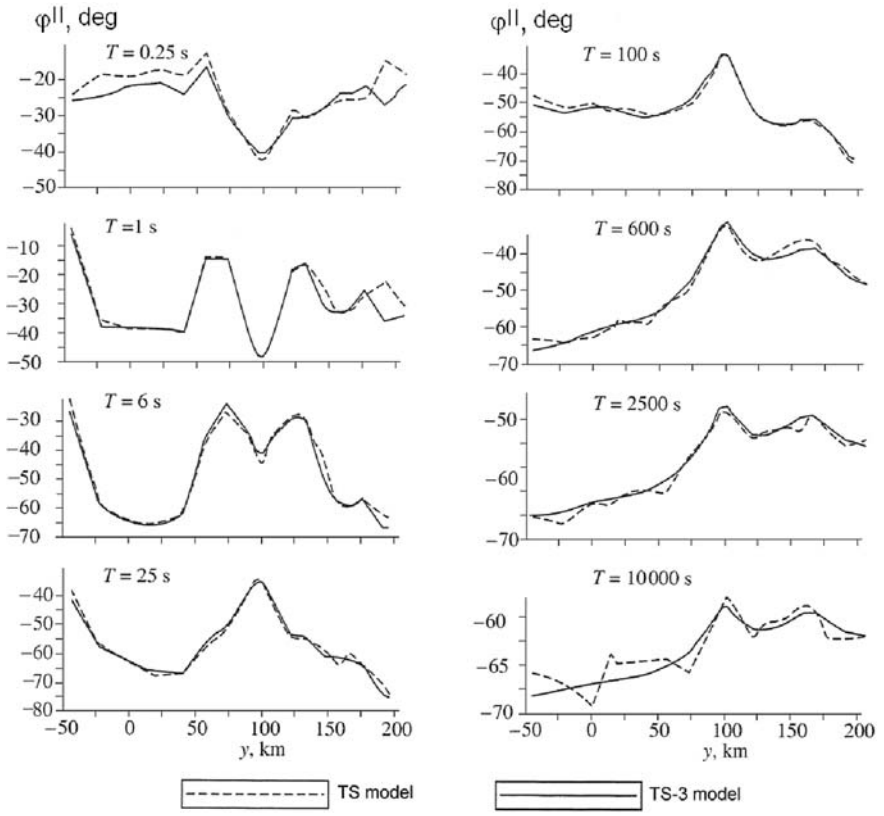

Fig. 12.23 Comparison of impedance phases $\varphi^{\parallel}$ from the TS-3 and TS models

Its inversion is focused on estimating the resistivity of the upper crust. The TS-3 model, obtained from the $\varphi^{\parallel}-$ inversion, was used as a starting model. Here we fixed all resistivities except for crustal blocks that contact the sedimentary cover. The $\rho^{\perp}-$ and $\varphi^{\perp}-$ inversion resulted in the TS-4 model, shown in Fig. 12.24. It confirms the galvanic connection between the vertical conductive zone B and sediments, and reveals the asymmetry of the highly resistive upper crust whose resistivity changes from 283 000 Ohm·m in the north to 13 000 Ohm·m in the south (in the initial TS model, from 100 000 Ohm·m in the north to 10 000 Ohm·m in the south).

The TS-4 model is the final model obtained from the successively applied automatic partial inversions. Its agreement with the initial TS model is evident. All of the essential TS structures are well resolved in the TS-4 model. Misfits between these models at the overwhelming majority of sites do not exceed 0.02 in tippers and 2.5° in phases. The transverse apparent-resistivity misfits are shown in Fig. 12.25. The TS-4 and TS models yield similar regional variation in $\rho^{\perp}$ with a local scatter caused by geoelectric noise. Note that irregular alternation of cells with higher and lower resitivity within zones B and C as well as within the crustal condutive layer can be readily smoothed without increasing the model misfits.

Next we consider the case when the a priory information on the media bordering the profile is rather scanty. In that event we have to apply the adjustment method suggested in Sect. 10.1.1. Figure 12.26 presents the longitudinal $\rho^{\parallel}-$ curves obtained at the edges of profile, $y = -50$ km and $y = 200$ km, as well as the average $\bar{\rho}^{\parallel}-$ curve that is taken as a curve for the normal apparent resistivity ρ_N. One-dimensional inversion of this curve yields a normal background which is introduced symmetrically into the interpretation model from Fig. 12.19 at a distance of 300 km from each edge of the profile. Repeating the partial inversions in the same succession as in case of an asymmetrical normal background, we obtain a final model TS-5 shown in Fig. 12.27. All of the essential TS structures are clearly seen in this model. The only essential difference between models constructed with asymmetric and symmetric

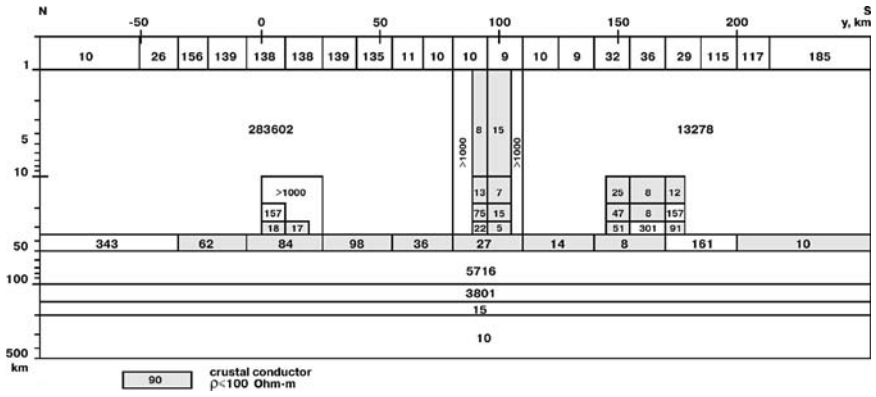

Fig. 12.24 Model TS-4; inversion of the apparent resistivities $\rho^{\perp}$ ad impedance phases $\varphi^{\perp}$ has been performed using the blocky II2DC program; resistivity values in Ohm·m are shown within blocks; blocks of lower crustal resistivities are shaded (cf. Fig. 12.16)

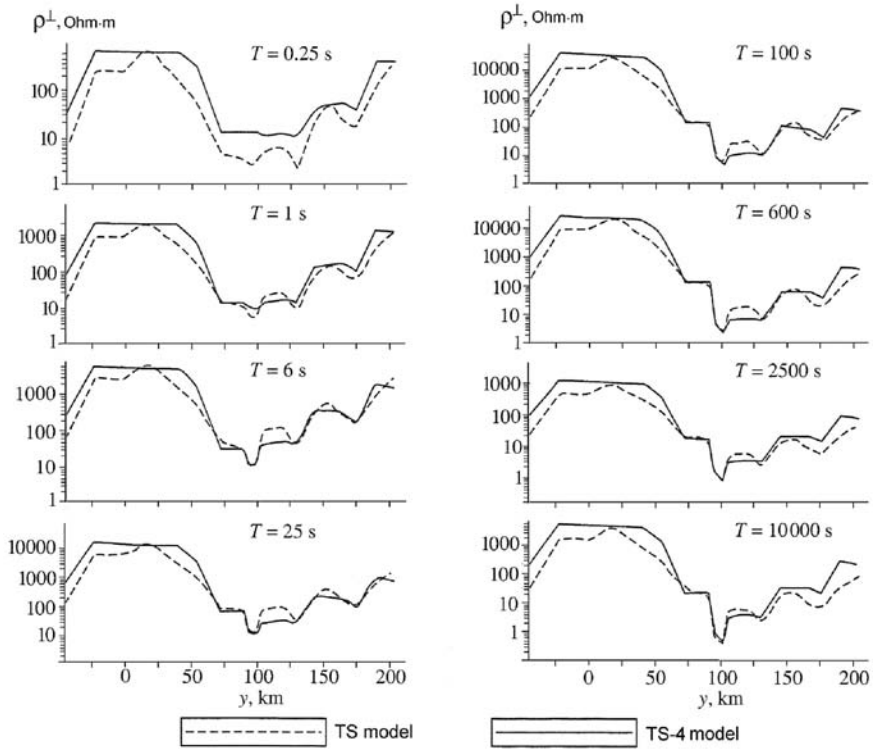

Fig. 12.25 Comparison of impedance apparent resistivities $\rho^{\perp}$ from the TS-4 and TS models

backgrounds is that in the case of the symmetric background the horizontal changes of resistivity in the upper crust and crustal conductive layer are less strong.

In closing, we turn back to the starting model with asymmetrical normal background and perform the parallel inversion of all response functions (Re W_{zy}, Im W_{zy},

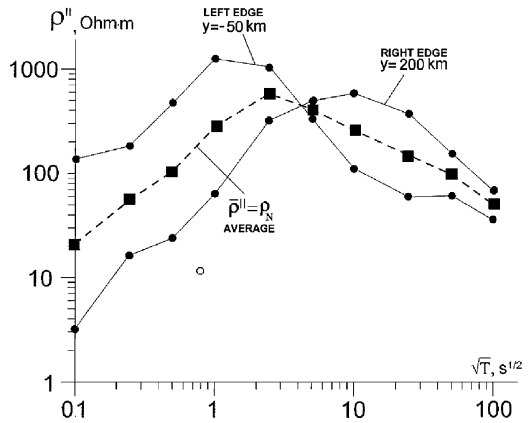

Fig. 12.26 Averaging the longitudinal apparent-resistivty curves $\rho^{\parallel}$ obtained at the edges of profile

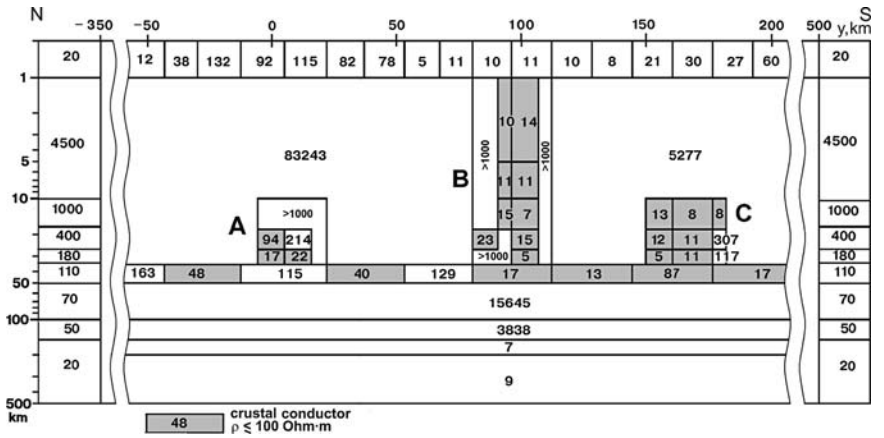

Fig. 12.27 Model TS-5; partial inversions have been performed using the blocky II2DC program with a symmetric normal background; resistivity values in Ohm·m are shown within blocks; blocks of lower crustal resistivities are shaded (cf. Figs.12.27 and 12.24)

$\varphi^{\parallel}$, $\rho^{\perp}$ and $\varphi^{\perp}$) used in constructing the TS-4 model. Figure 12.28 displays the TS-6 model obtained by parallel inversion. In this model: (1) resistivity contrasts in the sedimentary cover are significantly smoothed, (2) the resistivity contrast in the upper, highly resistive crust is also significantly smoothed, (3) the conductive zones A and C are resolved with some degree of certainty, while the central through-the-crust conductive zone B is completely destroyed, (4) the contrast between the two edge resistivities in the crustal conducting layer is much lower, and (5) the monotonic decrease of the mantle resistivity is disturbed (a highly resistive layer appears in the conductive mantle). We see that the parallel inversion of all response functions in use impairs the information on the Earth's interior.

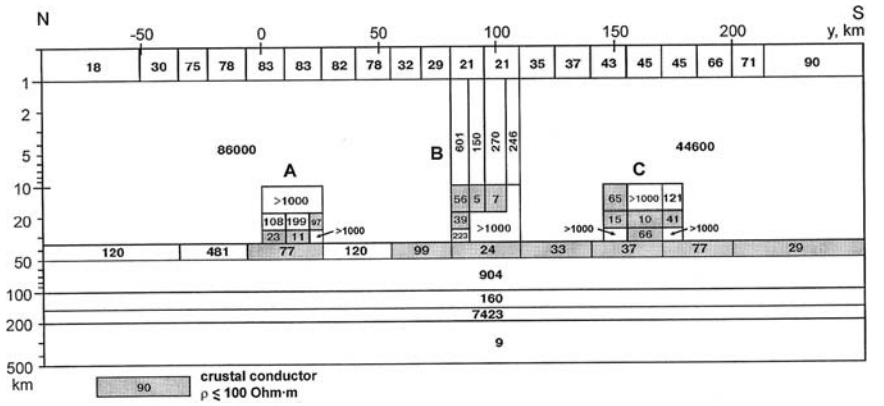

Fig. 12.28 Model TS-6; the parallel inversion of Re W_{zy}, Im W_{zy}, $\varphi^{\parallel}$, $\rho^{\perp}$, and $\varphi^{\perp}$ has been performed using the blocky II2DC program with an asymmetric normal background; resistivity values in Ohm·m are shown within blocks; blocks of lower crustal resistivities are shaded (cf. Figs.12.16 and 12.24)

Of course, the parallel inversion is the simplest approach to a multicriterion problem, and apparently this is the reason why it is popular among geophysicists fascinated by the possibility of automatic inversions eliminating the necessity of comprehensive analysis. The technique of successive partial inversions undoubtedly complicates the work, and this is a possible reason for the objections raised in discussions. However, our experiments on the integrated interpretation of MV and MT data indicate that the game, albeit more difficult, is worth the candle.

In the last sections of our book we would like to look upon two case histories illustrating the interpretation of magnetotelluric and magnetovariational data by means of hypotheses testing and succession of partial inversions.

12.6 Geoelctric Model of the Baikal Rift

Magnetotelluric studies in the Baikal rift zone have been conducted for many years, beginning in 1960s (the Eastern Geophysical Trust, Institute of the Earth's Crust, and the University of Moscow). These pioneering works, initiated by V. Pospeev (Pospeev, 1976), deeply influenced the development of geoelectrics in our country. During three decades, nearly 1000 MT-soundings were carried out within the rift zone and adjacent areas. Unfortunately, the data obtained are nonuniform in their quality. A considerable part of this vast territory was studied at the dawn of magnetotellurics, in the 1960s and 1970s, when observations were made with analog medium-frequency instrumentation and were processed manually, by rough (visual or approximate) methods. Interpretation of these data is usually reduced to one-dimensional inversion of effective apparent-resistivity curves, thereby ignoring the distortions caused by near-surface inhomogeneities. Authentic magnetotelluric measurements using digital broadband instrumentation as well as efficient methods of spectral analysis and geoelectric noise suppression were started in the late 1970s, but by that time the research activities had been shifted from the Baikal rift into Trans-Baikal areas and further to the east. It was not until 20 years later that an attempt was made to analyze and generalize these obsolete results obtained in the Baikal rift zone, to select the most reliable data and construct a meaningful geoelectric model of this province, typical of continental rifting (Berdichevsky et al., 1999; Berdichevsky and Dmitriev, 2002). It has been shown that magnetotellurics may play a decisive role in choosing between the competing conceptions for the deep structure of the Baikal rift. Let us consider this instructive two-dimensional interpretation accomplished as a sequence of partial inversions of apparent-resistivity curves in the hypothesis test mode.

12.6.1 Two Concepts of the Baikal Rift Zone

Two different concepts of the Baikal rift zone are discussed in the literature:

1. The mantle-diapir concept. Figure 12.29a presents a schematic cross-section of the Baikal rift zone along a profile transecting the middle part of Lake Baikal.

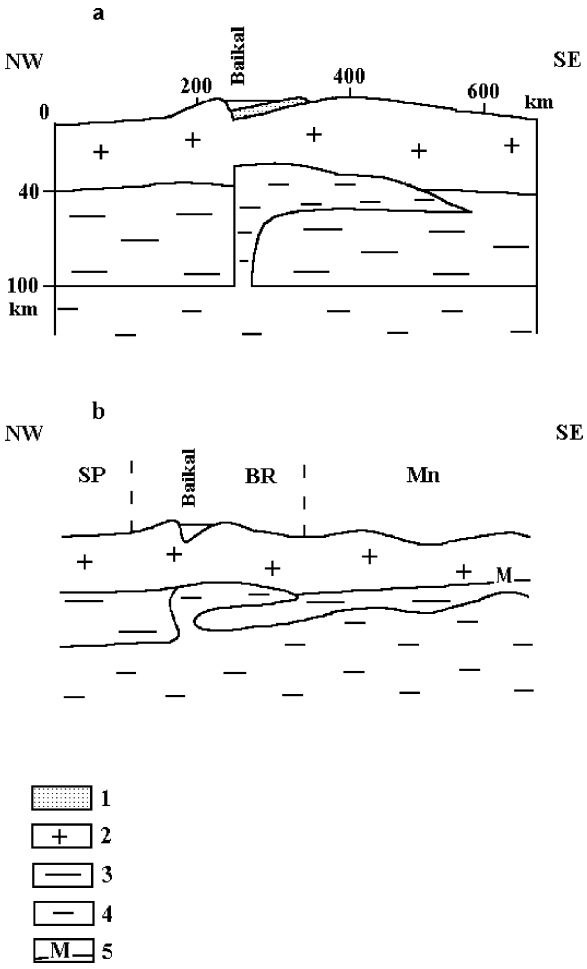

Fig. 12.29 Mantle-diapir model of the Baikal rift zone; (**a**) after Krylov et al. (1975, 1981) and Puzyrev (1997), (**b**) after Grachev (1996); SP -Siberian plate, BR-Baikal rift, Mn – Mongolia; 1 – sediments, 2 – the Earth's crust, 3 – normal mantle, 4 – anomalous mantle, 5 – M-discontinuity

This model proposed by Puzyrev and Krylov has been constructed on the basis of deep seismic soundings and seismological data (Krylov et al., 1975, 1981; Puzyrev, 1997). Here, the subhorizontal surface of the low-velocity asthenosphere is recognized at a depth of about 100 km. A subvertical slitlike channel (associated with a fault separating the Siberian Platform from the Baikal region) branches off from asthenospheric layer. A subhorizontal low-velocity zone, the so-called anomalous mantle, is contiguous to this channel. The anomalous low-velocity mantle has the shape of a "visor" adjoining the Moho surface. The average thickness of this zone is about 20 km. It is distinctly separated from the subhorizontal asthenosphere and extends in a northeasterly direction for a distance greater than 1500 km. On a transverse section of the Baikal Rift zone, the anomalous mantle gradually thins out to the southeast.

The Puzyrev-Krylov model was substantially developed by Grachev in his study of continental rifting dynamics (Grachev, 1996). Grachev stresses the asymmetry of the Baikal Rift, which manifests itself in a rise of the low-velocity asthenosphere on the transition from platform to folded zone (Fig. 12.29b). The formation of the anomalous mantle, with its subvertical stem and subhorizontal apophysis, is interpreted in terms of a mantle diapir, that is, as intrusion of magma into the continental lithosphere, typical of the prerifting regime.

2. The asthenospheric-upwarp concept. This alternative concept, conceived by Zorin and his colleagues, is based on gravimetry, deep seismic soundings, and teleseismic observations (Zorin, 1971; Gao et al., 1994). In developing this concept, they passed through several versions. The earliest version of the model is illustrated in Fig. 12.30a. Here, the rift zone mantle includes a vast, compact region of lower density, reaching and even crossing the Moho. It is considered to be an

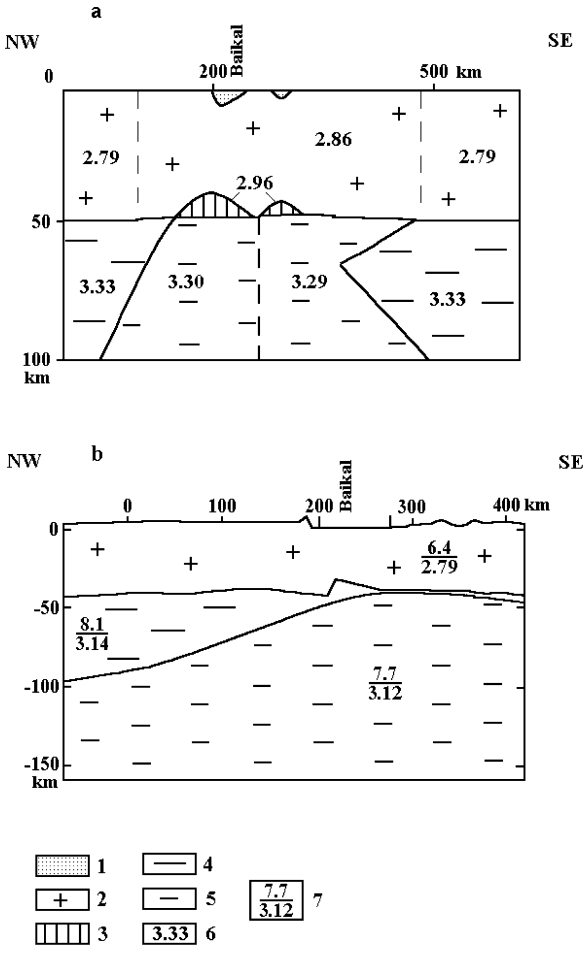

Fig. 12.30 Asthenospheric-upwarp model of the Baikal rift zone; (**a**) early version, after Zorin (1971), (**b**) – recent version, after Gao et al. (1994); 1 – sediments, 2 – The Earth's crust, 3 – basic and ultrabasic intrusion, 4 – normal mantle, 5 – anomalous mantle, 6 – density, g/sm^3, 7 – numerator-velocity of *P*-wave, km/s, denominator-density, g/sm^3

asthenospheric upwarp with deep roots. The upwarp symmetry is disturbed by a small, narrow nose wedging out to the southeast. In a more recent version, this nose is absent, but instead, the asthenospheric upwarp is markedly asymmetric, being characterized by significant reductions in density and velocity (Fig. 12.30b).

Tectonically, these two models are essentially different. In the Puzyrev-Krylov-Grachev model, the anomalous mantle recognized immediately beneath the Moho occurs as a stratal apophysis isolated from the main asthenosphere, while in the Zorin model, it is represented by a massive, uniform plumelike body integrated with a deep mantle.

The two concepts in question say nothing about the Earth's crust in the Baikal rift zone. In this respect, we should note two facts: (1) Within the Baikal rift zone, it has been established with considerable reliability that the crust contains a waveguide with its top at depths of 12–15 km, and (2) The lithosphere in the Baikal region is dissected by numerous deep faults. Two major faults (Obruchevsky and Barguzin)\ bound the Baikal graben. The Main Mongolo-Okhotsky fault separates the folded systems of the eastern Trans-Baikal region.

12.6.2 Synthesis of Apparen-Resitivity Curves

Nowadays, we have at our disposal a lot of effective apparent-resistivity curves, ρ_{eff}, and some quasi-longitudinal and quasi-transverse apparent-resistivity curves, $\rho^{\parallel}$ and $\rho^{\perp}$, oriented along ($Az = 45^{\circ} \pm 15^{\circ}$) and across ($Az = 135^{\circ} \pm 15^{\circ}$) the Baikal graben. The ρ_A-curves are most often limited by periods of 10–30 min. In recent years, some reference MT soundings have been carried out, ranging to several hours.

Figure 12.31 displays a map of the Baikal region outlining five zones with different types of the apparent-resistivity curves. Zone I is situated on the Siberian platform. Zone II relates to the Cis-Baikal trough, and zone III is associated with the

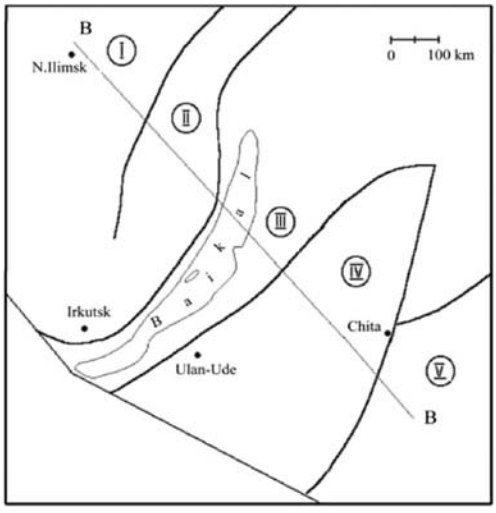

Fig. 12.31 Map of types of apparent-resistivity curves; I, II, III, IV, V – numbers of zones, within which the ρ_A – curves are of the same type

western Trans-Baikal. Zones IV and V represent the folded systems of the southeastern Trans-Baikal. Each zone contains about 8–10 short-period MT soundings and 1–3 long-period reference MT soundings. Within each zone, the apparent-resistivity curves are similar in form but dramatically suffer from the static shift caused by near-surface trappean intrusions. The distorted ρ_A-curves have been corrected by averaging and synthesized by vertical translation (the average long-period ρ_A-curves are vertically shifted to the average short-period ρ_A-curves). Given a representative statistics of short-period magnetotelluric soundings, this noise abatement procedure may combine separate fragments of MT soundings and construct continuous noise-suppressed ρ_A-curves that cover the entire interval of periods – from a few seconds to a few hours.

The synthesized average curves of apparent resistivity obtained in the various zones are plotted in Fig. 12.32. We believe that the uncertainty for the synthesized apparent resistivity does not exceed 10% at high frequencies and 20% at

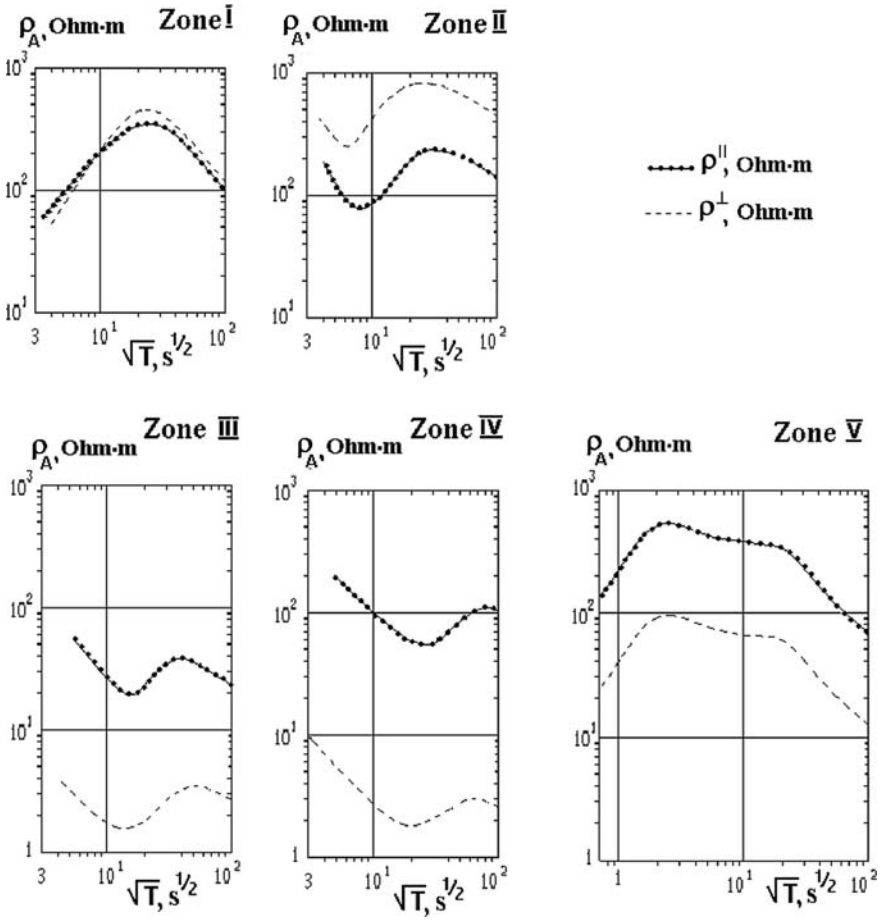

Fig. 12.32 The synthesized apparent-resistivty curves in I, II, III, IV, V zones

low frequencies. On the Siberian Platform, zone I, we have bell-shaped ρ_A-curves. Approaching the Baikal graben (zones II, III), we get the $\rho^{\parallel}$- and $\rho^{\perp}$-curves with deep minimum in a period range of 100–500 s. This minimum is most pronounced in the western Trans-Baikal (zone IV). In the southeastern Trans-Baikal it degenerates into the flattened descending branch (zone V). The rough estimates allow us to associate the minima of apparent resistivities with an inhomogeneous crustal conductive layer at a depth of 15–30 km.

12.6.3 Interpretation Model

Generalizing the reliable geological and geophysical data, we distinguish the following properties of the Baikal rift zone that control the structure of the interpretation model: (1) The Baikal rift is a linear structure trending northeast, (2) The Baikal rift zone is dissected by deep faults striking mostly northeast, (3) The crust of the Baikal rift zone includes an inhomogeneous conductive layer, which may correlate with the seismic waveguide, and (4) The upper mantle of the Baikal rift zone is laterally heterogeneous and may contain such structures as a mantle diapir or asthenosphere upwarp.

Constructing the interpretation model, we assume that the Baikal rift zone admits the inversion of apparent-resistivity curves in the class of two-dimensional structures with a northeast strike. Evidently, a two-dimensional interpretation model should incorporate the following elements: (1) a heterogeneous surface layer (sediments) whose conductance varies in accordance with the known electric-prospecting data, (2) a high-resistivity upper crust with a conductive layer, (3) vertical conductive channels simulating deep faults, and (4) a heterogeneous upper mantle with conductive inclusions.

12.6.4 Bimodal Inversion in the Hypotheses Test Mode

The strategy of bimodal interpretation depends on the sensitivity of the TM- and TE- modes to the target structures.

The TE-mode is the main source of information about deep structure in areas with a monolithic upper lithosphere, where the TM-mode is hardly informative due to the screening effect of the high-resistivity lithospheric layers. The situation is different in areas with fault-block tectonics. Conductive (fluid-saturated, graphitized) faults favor the vertical redistribution of telluric currents induced in various layers of the crust and upper mantle and thus increase the sensitivity of the TM-mode to deep structures. Under these conditions, the TM-mode can play an important (perhaps, even leading) role in the interpretation of MT soundings aimed to studies of the Earth's crust and upper mantle.

One of the most objectionable problems in the bimodal interpretation of MT soundings is the correction of longitudinal $\rho^{\parallel}$-curves distorted by the regional *S*-effect. Some crude estimates can be performed by ignoring the lateral variations in

the deep electric conductivity and reducing the $\rho^{\parallel}$-curves to the standard (normal) ρ_{st}-curve constructed from global magnetovariational sounding and representative statistics of MT data. However, such a normalization procedure is hardly applicable in a rift zone where strong lateral inhomogeneity of the upper mantle can be expected. Here we should pose the inverse problem as a problem of hypotheses testing and to compensate static shift by reducing the $\rho^{\parallel}$-curves to the reference longitudinal curves defined from a two-dimensional model corresponding to the hypothesis being tested.

The two-dimensional interpretation of the longitudinal and transverse curves, $\rho^{\parallel}$ and $\rho^{\perp}$, obtained in the Baikal region was carried out in the hypotheses test mode. The two-level algorithm consisting of sequence of the TE and TM partial inversions was used. We will consider the application of this algorithm in greater detail.

Level I (TE inversion). At this level, we construct a starting model consistent with the hypothesis tested, and correct the longitudinal $\rho^{\parallel}$-curves, reducing them to the reference $\rho^{\parallel}$ -curves calculated from the starting model. Inversion of corrected $\rho^{\parallel}$-curves yields information about the crustal conductive layer.

Level 2 (TM inversion). At this level, the model derived from the TE inversion of the corrected longitudinal $\rho^{\parallel}$-curves is taken as a starting model. Inversion of the transverse $\rho^{\perp}$-curves yields information about faults and allows us to edit crustal and mantle structures.

The model resulting from the TM inversion may be taken as a starting model for the repeated TE inversion. Consecutive transitions from one level to another continue until we attain a sufficiently small model misfit.

Let us turn to MT soundings in the Baikal region. The INV2D program suggested by Golubev and Varentsov (1994) has been used for their bimodal inversion. The program approximates the inhomogeneous Earth by a piecewise-uniform medium consisting of 40 blocks with fixed (20 blocks) and free (20 blocks) resistivities. The free resistivities are fitted through minimization of the Tikhonov functional involving a misfit functional and stabilizer that ensures proximity of inversion to the starting model. The geometry of blocks is chosen in such a way that the misfit minimization could lead to the formation of structures consistent with a hypotheses being tested.

12.6.5 Test of the Mantle-Diapir Hypothesis

The two-dimensional starting model corresponding to the mantle-diapir hypothesis is shown in Fig. 12.33. It includes the following elements: (1) inhomogeneous sedimentary cover differentiated by using a priori geoelectric data, (2) a homogeneous lithosphere with a resistivity 10^4 Ohm·m, (3) an asymmetric asthenosphere with a resistivity varying from 100–200 to 20–30 Ohm·m, (4) a mantle diapir with an apophysis of 100 Ohm·m resistivity, (5) a low-resistivity mantle (5 Ohm·m).

Let us take the starting model as a reference for correcting the longitudinal $\rho^{\parallel}$-curves. Comparing the experimental curves of $\rho^{\parallel}$ with the theoretical curves of $\rho^{\parallel}_{sm}$ calculated from starting model, we see that $\rho^{\parallel}$-curves are close to $\rho^{\parallel}_{sm}$-curves

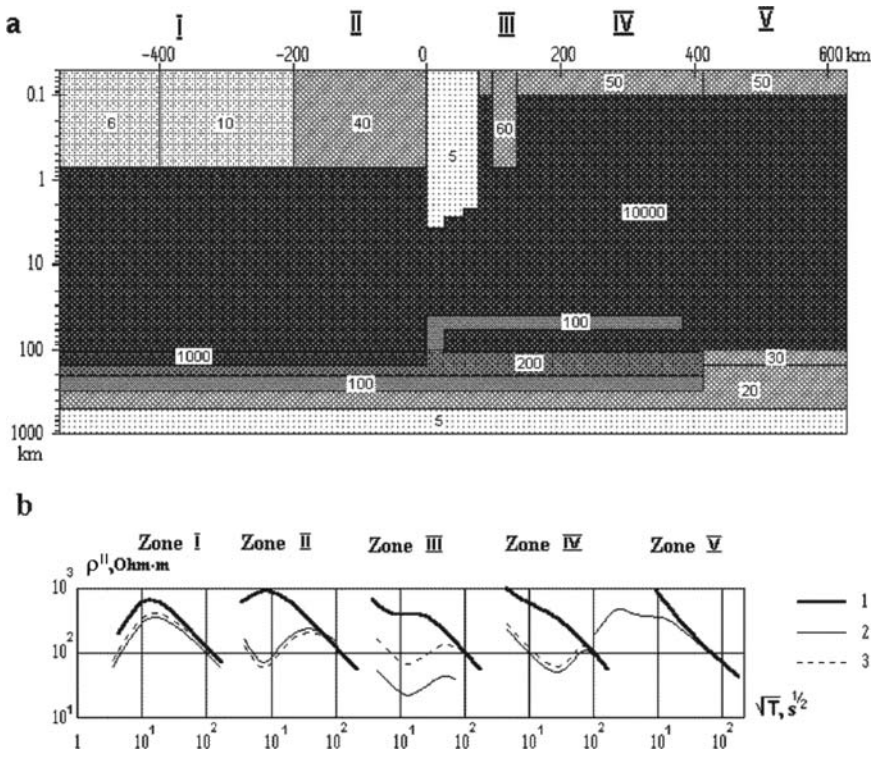

Fig. 12.33 Interpretation of ρ_A-curves in the mantle-diapir model class. (**a**) starting model; Roman numerals – numbers of zones, Arabic numerals – values of resistivity in Ohm·m; (**b**) correction of longitudinal $\rho^{\parallel}$-curves, 1 – theoretical $\rho^{\parallel}$-curve calculated from starting model, 2 – experimental synthetic $\rho^{\parallel}$-curve, 3 – corrected $\rho^{\parallel}$-curve

in all zones, except for zone IV (Barguzin synclinorium), thereby confirming the validity of the starting model. The $\rho^{\parallel}$-curves are corrected through their vertical translaton that fits the low-frequency branches to the model $\rho^{\parallel}_{sm}$-curves. The shift is generally small which indicates a weak regional *S*-effect.

The TE inversion of corrected $\rho^{\parallel}$-curves is illustrated in Fig. 12.34. It optimizes the resistivities of the crust. The initial structure of the sedimentary cover and upper mantle was fixed during the entire cycle of iterations. The inversion clearly reveals a continuous conductive layer in the middle crust whose resistivity decreases from 200 Ohm·m in the platform area I, II to 30–15 Ohm·m in the rift zone III, IV and 60 Ohm·m in the southeastern Trans-Baikal region V, VI (Fig. 12.31). The accuracy of inversion is rather high. The general *rms* misfit does not exceeds 12%.

Going to the TM inversion, we insert narrow near-surface conductive zones in the sedimentary cover to simulate the static shift of the transverse $\rho^{\perp}$-curves. The TM inversion optimizes the resistivities of the upper crust, crustal conductive layer and upper mantle. The result of 25 iterations is presented in Fig. 12.35. The crustal conductive layer changes insignificantly. Considerable variations are observed in the

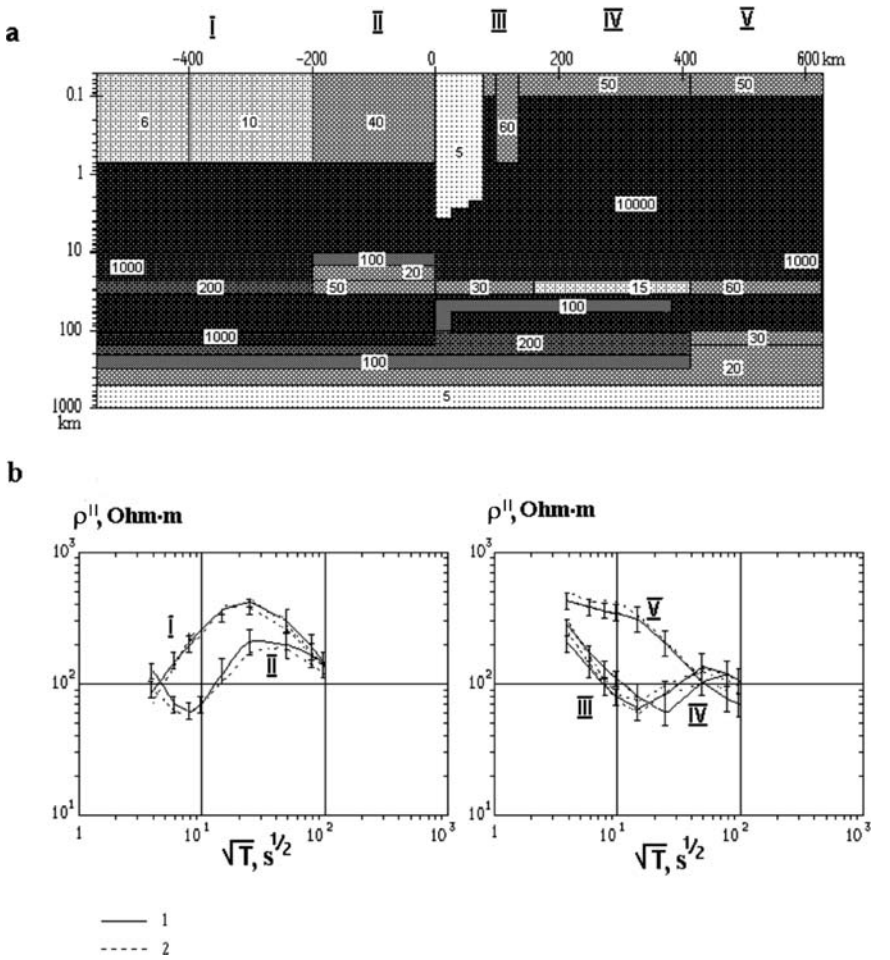

Fig. 12.34 Interpretation of ρ_A-curves in the mantle-diapir model class. (**a**) TE-inversion; Roman numerals – numbers of zones, Arabic numerals -values of resistivity in Ohm·m; (**b**) relation between experimental (1) and model (2) $\rho^{\|}$-curves

upper crust and lower lithosphere of the western (I, II, III) and southeastern (V, VI) zones: resistivities increase to 10000 Ohm·m in I, II, III zones and decrease to 1000 and 500 Ohm·m in V, VI zones. At the same time, the mantle resistivity under the platform (I, II, III) increases to 100 Ohm·m at depths of 300–500 km. The iterations provide accurate inversion within zones I, II, III and VI, where the *rms* misfit does not exceed 16%. However, the model and experimental apparent-resistivity curves diverge dramatically in zones IV and V, in the vicinity of the Baikal rift, where misfits of their low-frequency branches amount to 90%, considerably exceeding the errors of apprent-resistivity synthesis.

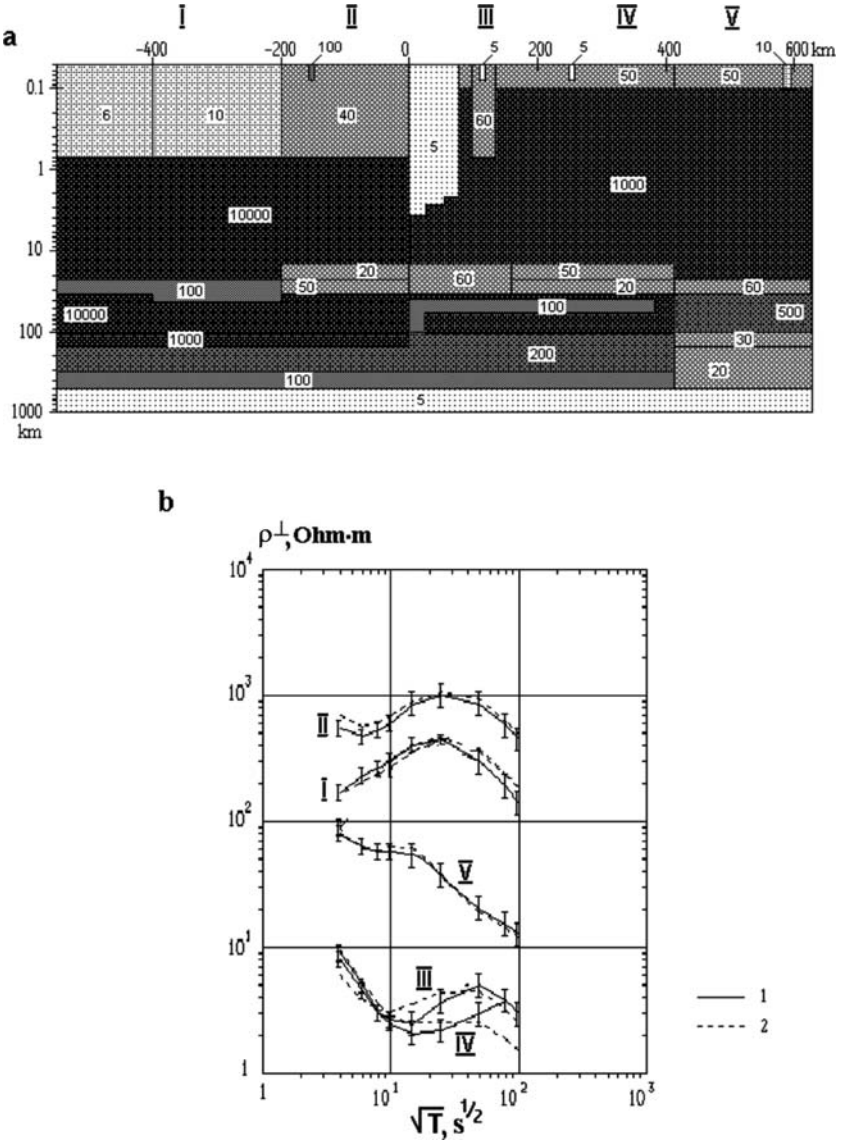

Fig. 12.35 Interpretation of ρ_{λ}-curves in the mantle-diapir model class without conductive faults. (**a**) TM-inversion; Roman numerals – numbers of zones, Arabic numerals -values of resistivity in Ohm·m; (**b**) relation between experimental (1) and model (2) $\rho^{\perp}$-curves

Convergence of the TM inversion is significantly improved if vertical conductive channels crossing the high-resistivity lithosphere are introduced into the starting model. Figure 12.36 shows the result of such inversion. Here, we have a model with three vertical conductive channels associated with the Obruchevsky, Barguzin,

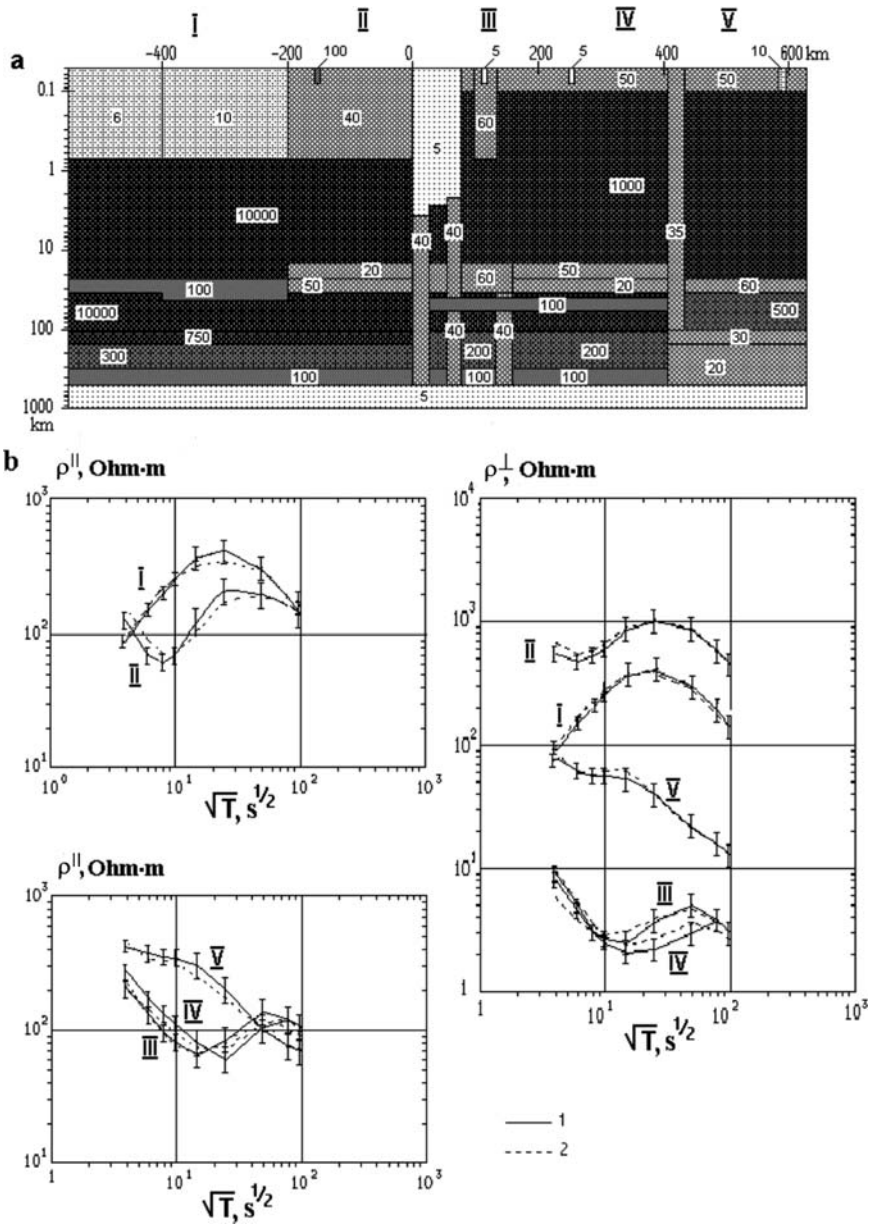

Fig. 12.36 Interpretation of ρ_A-curves in the mantle-diapir model class with conductive faults. (**a**) TE- and TM-inversion; Roman numerals – numbers of zones, Arabic numerals -values of resistivity in Ohm·m; (**b**) relation between experimental (1) and model (2) $\rho^{\parallel}$- and $\rho^{\perp}$- curves

and Main Mongolo-Okhotsky faults. These channels connect the sediments with the conductive mantle. Although the starting resistivities of the crust and upper mantle in this model remain unchanged, the experimental and model $\rho^{\perp}$-curves converge, and misfits of their low-frequency branches do not exceed 20%. At the same time, the $\rho^{\parallel}$-curves are weakly affected by the conductive faults, and the misfits of these curves remain as small as during the TE inversion in the absence of the faults.

The inferred model, whose misfits do not exceed the assumed uncertainty of the apparent-resistivity synthesis, may be considered a final result of the bimodal interpretation of MT soundings in the class of mantle diapir models. In assessing the adequacy of this result, two questions should be answered: (1) Is the asthenosphere asymmetry reliably diagnosed? and (2) Is the anomalous mantle reliably outlined? Analysis of the model shows that we can answer both questions in the positive. By smoothing the asthenosphere asymmetry and excluding the anomalous mantle, we conspicuously increase the model misfits. In the course of several model tests we conclude that the resistivity of the anomalous mantle is about 50–100 Ohm·m. Assuming that the decrease of mantle velocity is caused by partial melting, such resistivity values indicate that the concentration of the liquid phase does not exceed a few percent. This estimate is consistent with seismic estimates by Krylov (1981).

What is the geological nature of the vertical conductive channels? Evidently, in the upper and middle crust they may be interpreted as fluid-saturated fault zones. But one might suppose that in the lower crust and upper mantle these channels are associated with deep roots of the faults, characterized by vertical fracturing that conveys mantle fluids.

Summing up, we can say that the mantle diapir hypothesis is fairly consistent with the MT data.

12.6.6 Test of the Asthenosphere-Upwarp Hypothesis

Figure 12.37 shows starting models that correspond to the early and recent versions of the asthenospheric-upwarp hypothesis (cf. Figure 12.30). The main elements of these models are: (1) inhomogeneous sediments which are differentiated using a priori geoelectric data, (2) a homogeneous lithosphere with a resistivity of 10^4 Ohm·m, (3) an asthenospheric upwarp with a resistivity 100 Ohm·m and with its roof at a depth of 50 km.

Experimental longitudinal and transverse curves of $\rho^{\parallel}$ and $\rho^{\perp}$ were interpreted using the same algorithm as above. The latter includes: (1) correction of longitudinal $\rho^{\parallel}$curves through their vertical translation, bringing their low-frequency branches into coincidence with the model curves of ρ_{sm} calculated from starting model, (2) inversion of corrected the $\rho^{\parallel}$-curves, and (3) inversion of the $\rho^{\perp}$-curves.

The final results of TM inversion are presented in Fig. 12.38 (the early version of the hypothesis) and Fig. 12.39 (the recent version of the hypothesis). Both hypotheses give low-frequency TM inversion misfits that go far beyond a 20% confidence boundary. Evidently, the models with asthenospheric upwarp that comes in contact with the Moho are in conflict with the MT data.

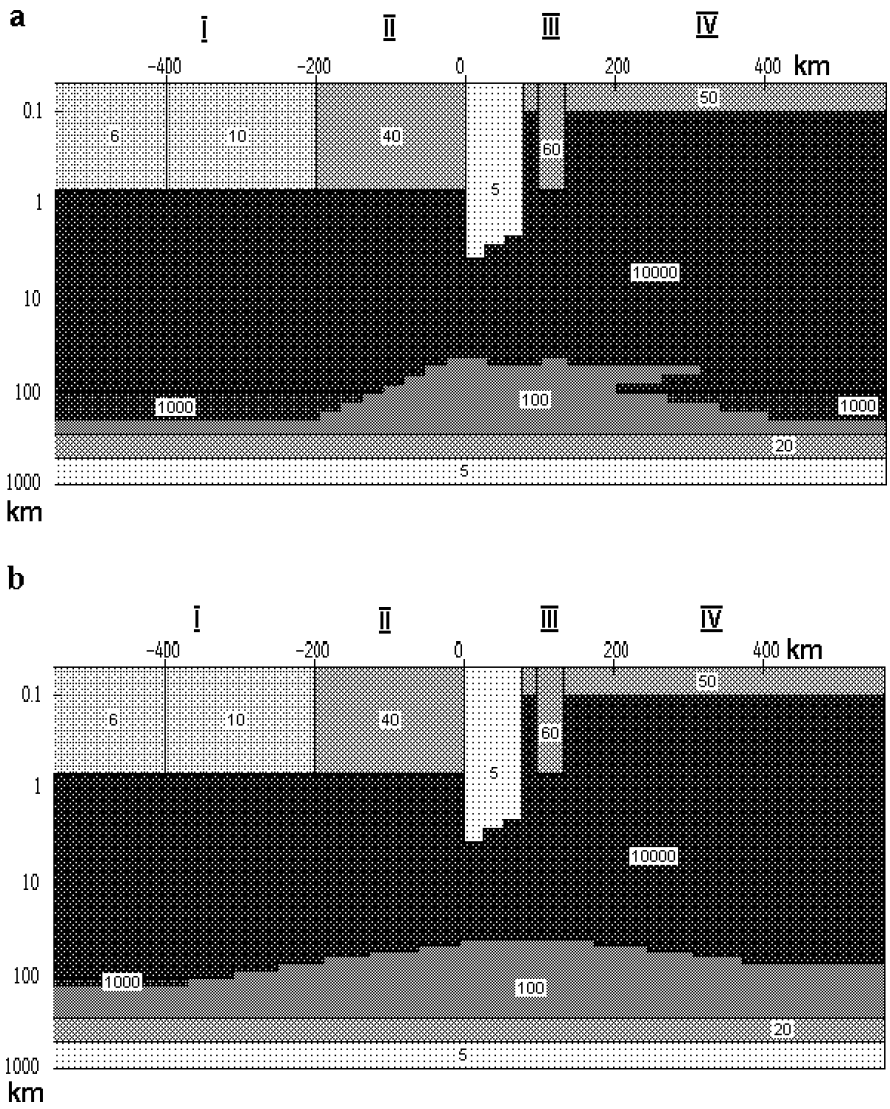

Fig. 12.37 Starting models for interpretation of ρ_A -curves in asthenospheric-upwarp model class; (**a**) early version, (**b**) recent version; Roman numerals – numbers of zones, Arabic numerals -values of resistivity, Ohm. m

12.6.7 Final Remarks on the Geoelectric Model of the Baikal Rift Zone

The interpretation of MT soundings in the hypothesis test mode has two important features to be stressed: (1) The starting model, constructed in compliance with a hypothesis being tested, allows for obtaining certain reference levels needed for

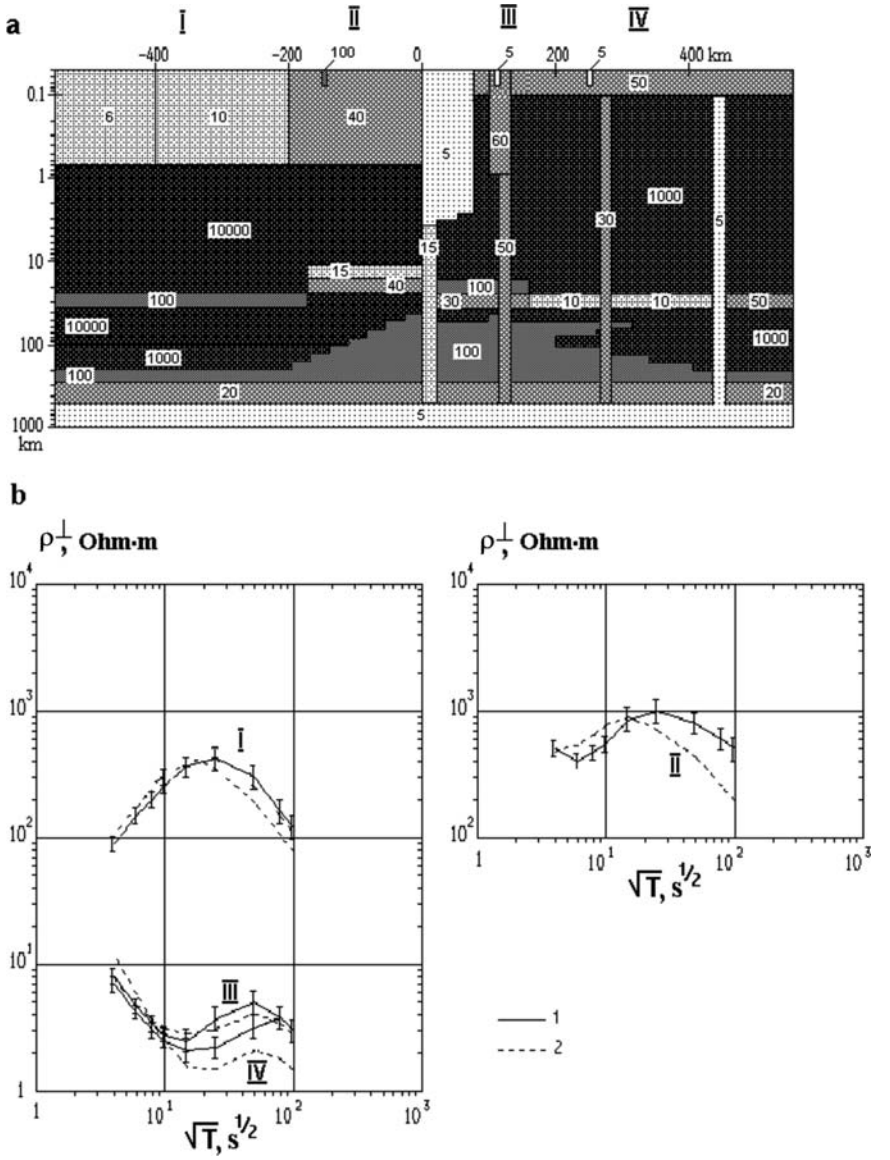

Fig. 12.38 Interpretation of $\rho^{\perp}$-curves in asthenospheric-upwarp model class, the early version. (**a**) TM-inversion, Roman numerals – numbers of zones, Arabic numerals – values of resistivity in Ohm·m, (**b**) relation between experimental (1) and model (2) $\rho^{\perp}$-curves

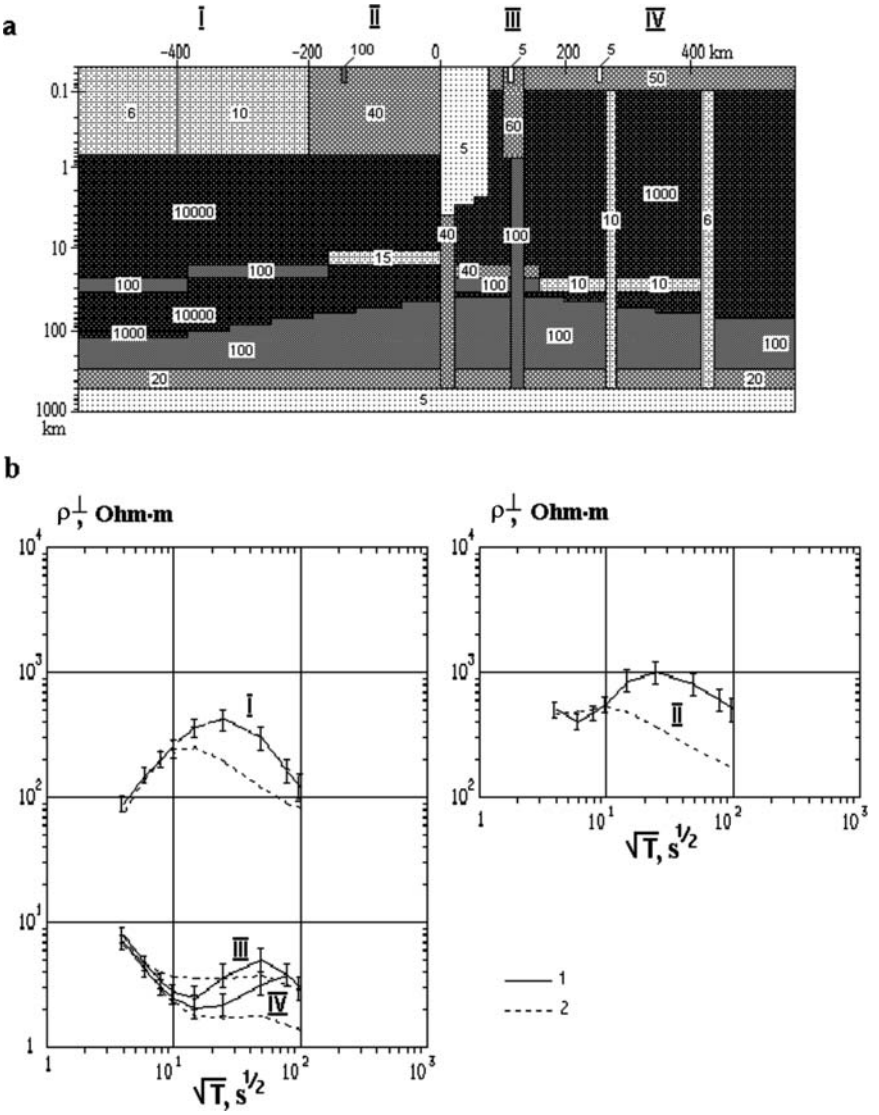

Fig. 12.39 Interpretation of $\rho^{\perp}$-curves in asthenospheric-upwarp model class, the recent version. (**a**) TM-inversion, Roman numerals – numbers of zones, Arabic numerals – values of resistivity in Ohm·m, (**b**) relation between experimental (1) and model (2) $\rho^{\perp}$-curves

confident correction of static shifts, (2) The interpretation is conducted in a narrow model class bounded by the limits of a hypothesis being tested. So, the inversion stability is enhanced, but its resolution is decreased.

These features were clearly demonstrated in the course of interpreting the MT soundings conducted in the Baikal rift zone. We avoided the uncertainties that come about from corrections of static shifts. We obtained rather reliable evidence in favor of the mantle diapir model. However, we missed many details in the structure of the Baikal rift. Their examination requires other approaches and a better quality of field data (wide frequency range of MT-variations, integrated MV and MT studies, robust processing techniques, considerably denser observations). But what we have to stress is that magnetotellurics due to its unique possibilities settled the long-term discussion about the deep structure of the Baikal rift.

12.7 Geoelectric Model of the Cascadia Subduction Zone

In 1978, on the initiative of Vanyan, a global geoelectric project was organized under the auspices of the International Association of Geomagnetism and Aeronomy (IAGA) with the aim of studying deep electric conductivity characterizing melting processes in the asthenosphere. Work on this project, named ELAS (ELectrical conductivity of the ASthenosphere), was conducted throughout the world, and the objectives of the projects were extended. It had included investigations of the conductivity in the lithosphere and asthenosphere (Electrical conductivity of the Lithosphere and ASthenosphere). The ELAS project brought geoelectrics to the forefront of modern geodynamics.

One of the most important events in the history of the ELAS project was the EMSLAB experiment (ElectroMagnetic Study of the Lithosphere and Asthenosphere Beneath the Juan de Fuca plate) conducted from 1985 to 1988 by US, Canadian, and Mexican geophysicists on the Pacific coast of North America in the Cascadia subduction zone (where the Juan de Fuca microplate subducts under the northwestern continental margin).

Figure 12.40 shows the network of the EMSLAB observations (Wannamaker et al., 1989a). Almost the entire Juan de Fuca plate and adjacent part of the Pacific orogenic belt were covered by MV soundings with a spacing of 50–100 km. MT soundings were performed mainly on an E–W profile near the town of Lincoln. This profile was named the Lincoln line. Spacings of MT and MV soundings on the Lincoln line were about 5 km (39 MTS sites) in a period range of 0.01–500 s and 10 km (15 deep MTS sites) in a period range of 50–10000 s.

Researchers involved in the EMSLAB experiment had hoped to obtain new information on the state and structure of the crust and upper mantle in the Cascadia subduction zone.

The first geoelectric models of the Cascadia subduction zone were constructed either by means of the Backus–Gilbert smoothing method (Jiracek et al., 1989) or manually, by the trial-and-error approach (Wannamaker et al., 1989b; Vanyan et al., 1988). These models were vulnerable to criticism, but they showed that

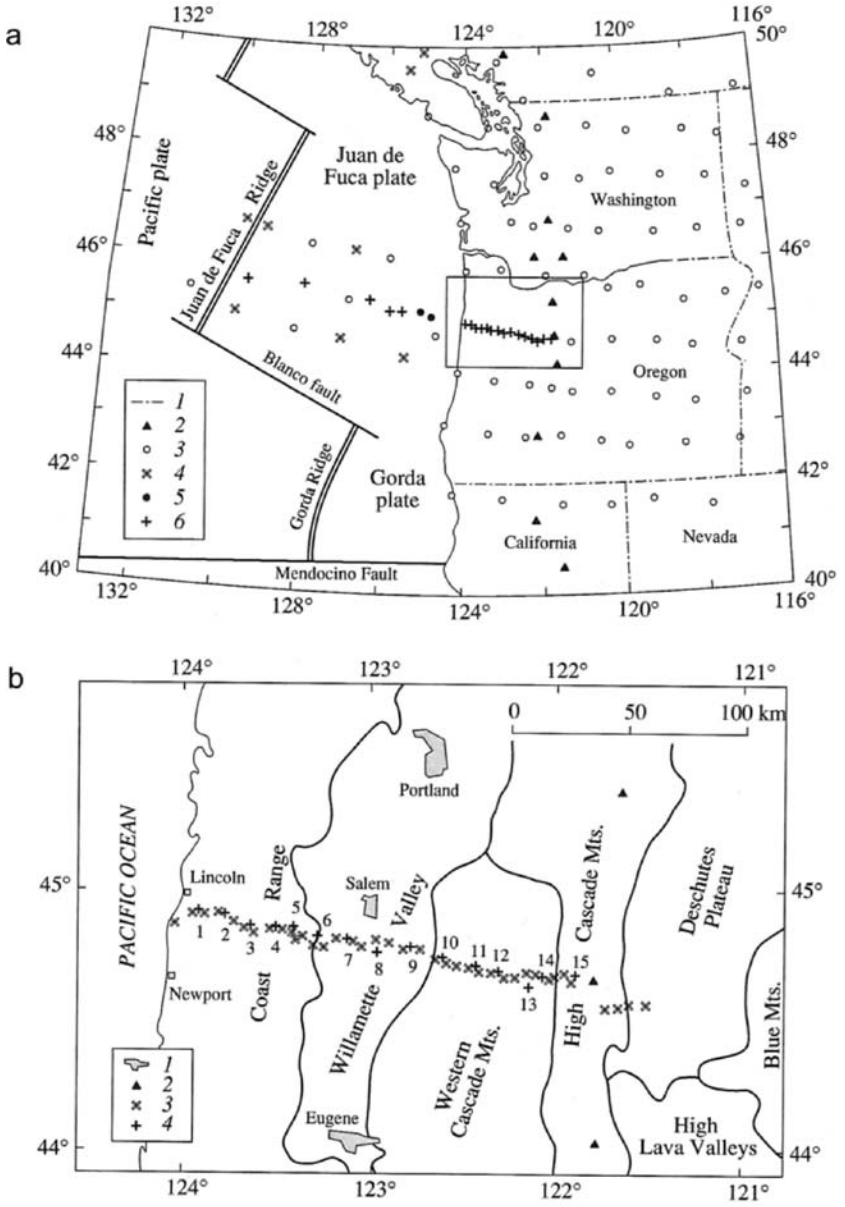

Fig. 12.40 Electromagnetic sounding network in the EMSLAB experiment. (**a**) General scheme: (1) state boundaries, (2) volcano, (3) MV sounding, (4) MT sounding, (5) MV sounding on the Lincoln line, (6) MT sounding on the Lincoln line. (**b**) Schematic map showing continental MT sounding sites: (1) towns, (2) volcano, (3) MT sounding, (4) deep MT sounding (Wannamaker et al., 1989a)

magnetotellurics can serve as a productive tool for studying the subduction zone. Presently, we recall these results with an understanding of the important role that they played in the history of deep geoelectric studies.

The 1990s were marked by a rapid development of computational geoelectrics (Zhdanov and Spichak, 1992; Mackie and Madden, 1993; Varentsov, 1999; Siripunvaraporn and Egbert, 2000; Novozhynski and Pushkarev, 2001). The creation of computational programs that enable the automatized inversion of the MT and MV response functions in complex media opened the way toward the improvement of the EMSLAB results (Zhdanov and Spichak, 1992; Berdichevsky et al., 1992a; Varentsov et al., 1996). This discussion set the stage for revising ideas of the Cascadia subduction zone. Let us follow (Pushkarev, 2002; Pushkarev et al., 2002; Vanyan et al., 2002a) and consider a new model of the Cascadia subduction zone constructed in the hypoteses test mode with the priority of MV soundings.

12.7.1 Brief Geological Description of the Cascadia Subduction Zone

The region under study is a part of the Pacific orogenic belt, characterized by intense Tertiary and Quaternary volcanism. The main geological structures of the region originate from the subduction and accompanying volcanism (Khain and Lomize, 1995). They extend S–N for up to 300–500 km. The S–N (x) and W–E (y) directions can be regarded as the major tectonic directions, defining the longitudinal ($||$) and transverse ($\perp$) components of the impedance tensor.

The Juan de Fuca spreading ridge, giving rise to the Juan de Fuca plate, is located at a short distance from the coast (about 500 km). Moving eastward, we cross the following structures: (1) the abyssal basin of the Juan de Fuca plate, (2) the continental slope composed of compacted sediments of the accretionary prism, (3) the shelf covered by loose sediments, (4) the Coast Range consisting of volcanic–sedimentary rocks, (5) the gently dipping Willamette Valley filled with a thick sequence of sediments and basaltic intrusions, (6) the Western (older) and (7) the High (younger) Cascade mountains composed of volcanic and volcanic–sedimentary rocks typical of present-day active volcanic arcs, and (8) the lava-covered Deschutes Plateau.

The oceanic crust within the abyssal basin of the Juan de Fuca plate has a structure typical of the Pacific. It comprises three layers: (1) a sedimentary layer 1–2 km thick, (2) a 1.5–2 km thick layer of basalts (pillow lavas) and basaltic flows with dolerite dikes, and (3) a layer of fully crystalline igneous rocks (gabbro and ultramafic varieties) 3–4 km thick.

The Cascade Range includes high peaks and sharply defined mountain crests. The highest peaks are volcanic cones developed on the ancient basement. The mountain structures are composed of Oligocene–Pliocene volcanic rocks represented by lava flows and significant amounts of breccias, tuffs, and mudflow deposits. The structure of the Cascade Range is complicated by the emplacement of intrusive massifs.

The more easterly plateau is also dominated by volcanic rocks with prevailing Pliocene and Pleistocene lavas.

12.7.2 Geophysical Investigations in the Cascadia Subduction Zone

Figure 12.41 presents a schematic map of the Cascadia subduction zone, reflecting the main features of contemporary tectonic processes: crustal seismicity, volcanism, and formation of the accretionary complex.

Earthquake sources concentrate in the northern and southern parts of the subduction zone, within the states of Washington and California, where the Benioff zone is traced quite reliably. According to seismological evidence, the oceanic plate subducts at a low angle in these areas, with its dip gradually increasing to 45°. At the same time, the central part of the subduction relating to the state of Oregon is aseismic. Here, the oceanic plate also starts subducting at a low angle, but seismic tomography data indicate that, at depths of about 40–80 km, it is sharply curved and then descends at an angle of about 70°.

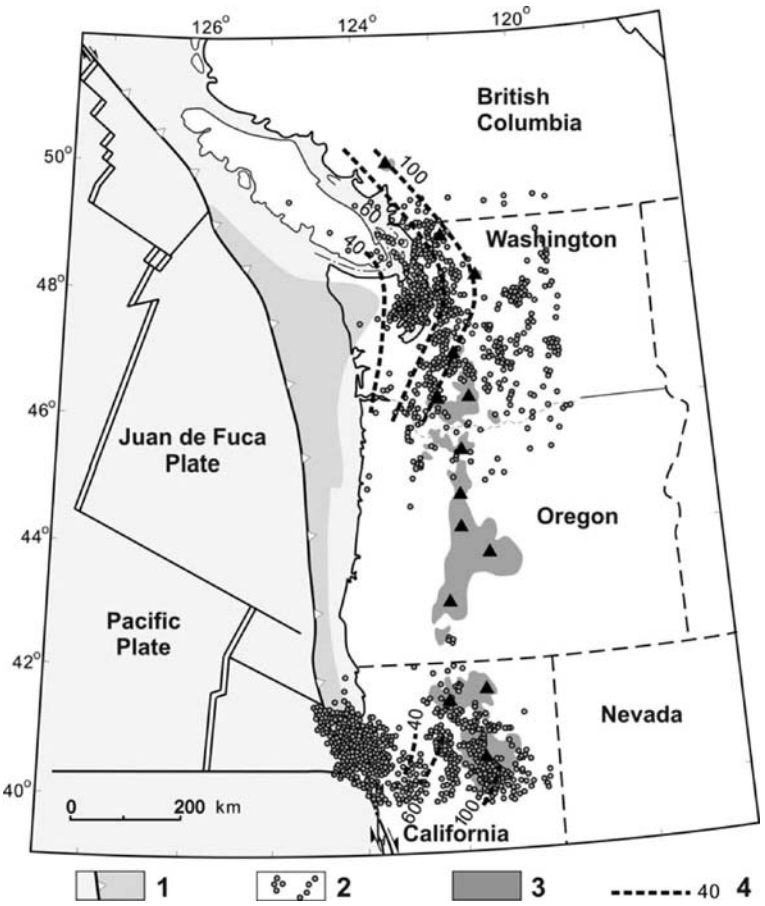

Fig. 12.41 Evidences of recent tectonic processes: (1) accretionary complex, (2) crustal seismicity, (3) Quaternary volcanic rocks, (4) depth to the Benioff zone in km (Romanyuk et al., 2001b)

Let us consider the most comprehensive seismic model of the central Cascadia subduction zone developed by Trehu et al. (1994). It is based on reflection data and natural seismicity observations. Figure 12.42 shows the velocity section along an E–W profile near the Lincoln line. The downgoing slab with velocities increasing from 6.5 to 8 km/s is clearly recognizable. The continental part of the seismic section is characterized by a more or less gently dipping bedding, with a monotonic increase in the velocities from 5 km/s at depths of 1–2 km to 7 km/s at depths of about 20 km. No P-wave velocity inversion was discovered within the crust.

According to seismic refraction data, the near-surface P-wave velocities range from 2.9 to 5.2 km/s. The upper and middle crust at depths of 3–30 km is characterized by velocities of 6.1–6.5 km/s. Beneath the High Cascades, the lower crust at a depth of 45 km has a velocity of about 7 km/s. The Moho is fixed at a depth of 45 km. Importantly, a low-velocity layer was identified, although not very reliably, in the middle crust.

Gravity data were used by Romanyuk et al. (2001a) to construct a two-dimensional density stratification model of the Cascadia subduction zone along a profile crossing central Oregon (Fig. 12.43). The oceanic crust has densities of 1.90–2.45 g/cm3 (sediments), 2.79 g/cm3 (basalts and dolerites), and 3 g/cm3 (gabbros and ultramafic rocks). The oceanic mantle to a depth of 40 km has a density of 3.33–3.35 g/cm3 (lithosphere). In a depth range of 40–140 km, its density is reduced to 3.3 g/cm3 (asthenosphere). The densities of the oceanic lithosphere and asthenosphere increase as they subduct under the continent.

Next examine the data of numerous measurements of the heat flow and temperature gradient. Near the Coast Range and the Willamette Valley, the heat flow amounts to 40 mW/m^2 and the temperature gradient is about 30°C/km. These values increase in the Western Cascades and they reach 105 mW/m^2 and 65°C/km in the High Cascades. Here we encounter a lot of hot springs. The Cascades heat flow maximum is attributed to the influence of an extensive magma chamber at depths of

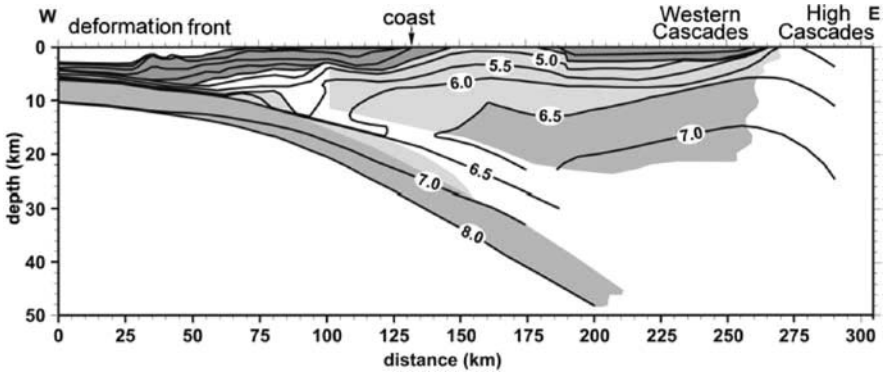

Fig. 12.42 Deep seismic section along an E–W profile close to the Lincoln line. Numbers indicate P-wave velocities in km/s (Trehu et al., 1994)

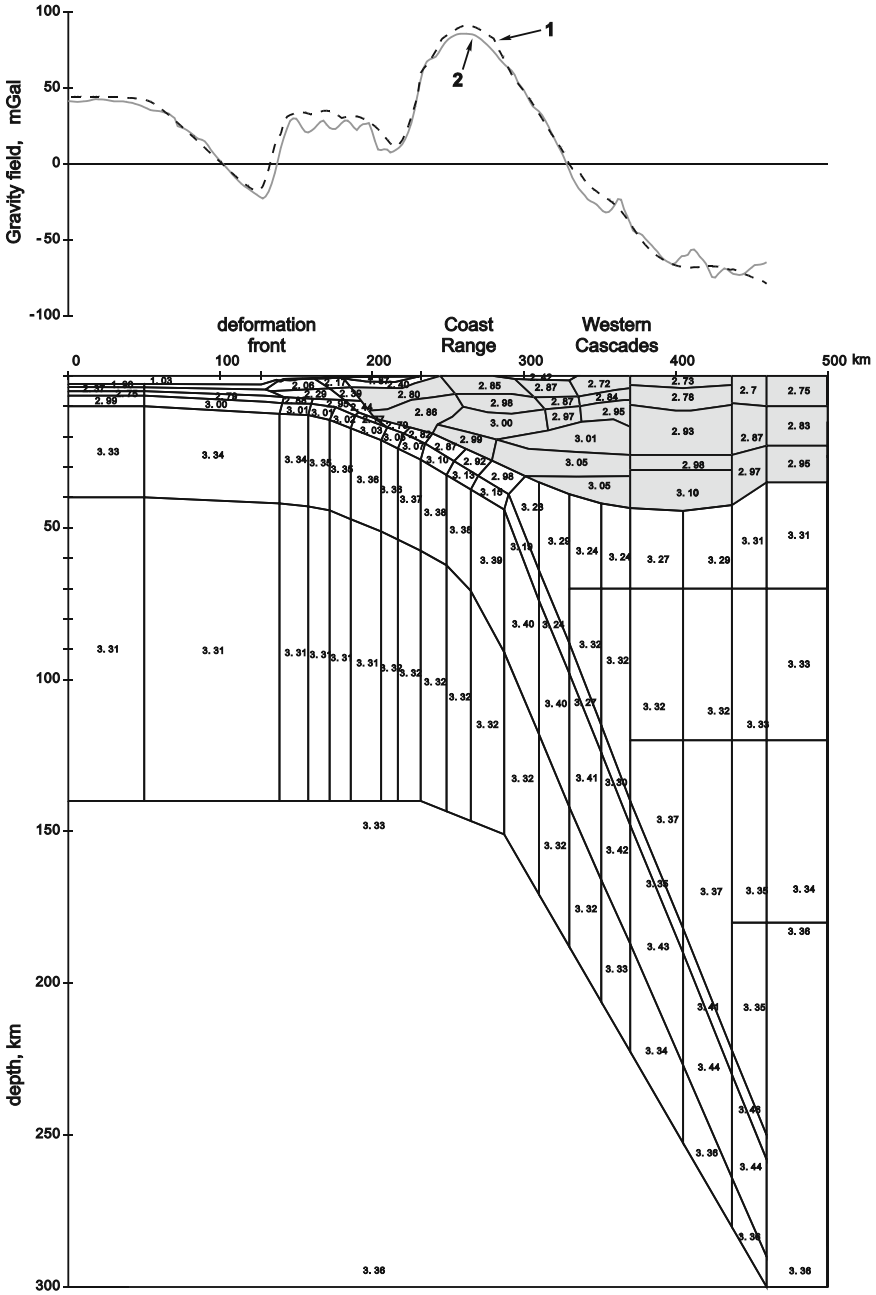

Fig. 12.43 Density model along the E–W profile crossing central Oregon; (1) model, (2) observations. Numbers indicate densities in g/cm^3 (Romanyuk et al., 2001a)

about 10–20 km. Ingebritsen et al. (1989) believe that heat rises from great depths through a relatively narrow zone.

Figure 12.44 shows a predictive geothermal and petrological model Cascadia, generalizing current ideas of the subduction zone and its fluid regime (Romanyuk et al., 2001b). The prediction is based on the existing estimates of the heat flow and depths of the Curie isotherm (∼500°C) as well as petrological analysis of magmas, and some other data. The continental crust above the downgoing Juan de Fuca plate in the near-shore area is characterized by lower temperatures. A subvertical zone of higher temperatures reaching the melting point of wet peridotite (∼900°C) has been outlined beneath the High Cascades. The release of fluids in the upper part of the subducting plate can be associated with several mechanisms. First, free water of micropores and microfractures is released under the action of increasing lithostatic pressure at depths of up to 30 km. Then, at depths of 30–50 km, where the temperature exceeds 400°C, dehydration of minerals such as talc, serpentine, and chlorite starts. Finally, basalt is transformed into eclogite at depths greater than 75 km, and amphibolite exsolution can take place at depths exceeding 90 km. All these processes are accompanied by release of fluids. Supposedly, fluids released at shallow depths migrate through the contact zone between the subducting and continental plates. At greater depths, fluids can be absorbed by mantle peridotites (serpentinization) at lower temperatures and disturb phase equilibria at higher temperatures, giving rise to wet melting. Melts migrate upward to the Earth's surface, resulting in the formation of a volcanic arc.

In conclusion, we note the results of sea-floor frequency sounding on the Pacific Plate (Vanyan, 1997). The upper part of the oceanic crust consisting of sediments and basaltic pillow lavas is characterized by a higher porosity and has a resistivity of 3–10 Ohm·m. Below, the resistivity markedly increases, reaching at least 10 000 Ohm·m.

Such is the a priori geological and geophysical information on the basis of which we will interpret geoelectric data obtained on the Lincoln line.

12.7.3 MT and MV Soundings on the Ocean Coast

The resistivity contrast on the ocean coast, reaching three and even four orders of magnitude, causes a strong MT anomaly referred to as the *coast effect*. This anomaly has galvanic and inductive components.

The galvanic anomalies arise when the electric current flows perpendicular to the shoreline (the TM-mode). The shoreward oceanic electric current divides into two branches.

One part of the current flows into the continental sedimentary cover. Sediments capture the oceanic current and channel it far from the coast, with slow leakage into the crystalline basement and deep conductive zones. This phenomenon can be referred to as a *continental-trap effect*. The size of the continental trap is of the order of several adjustment distances $\sqrt{S_1 R_2}$, where $S_1 = h_1/\rho_1$ is the average

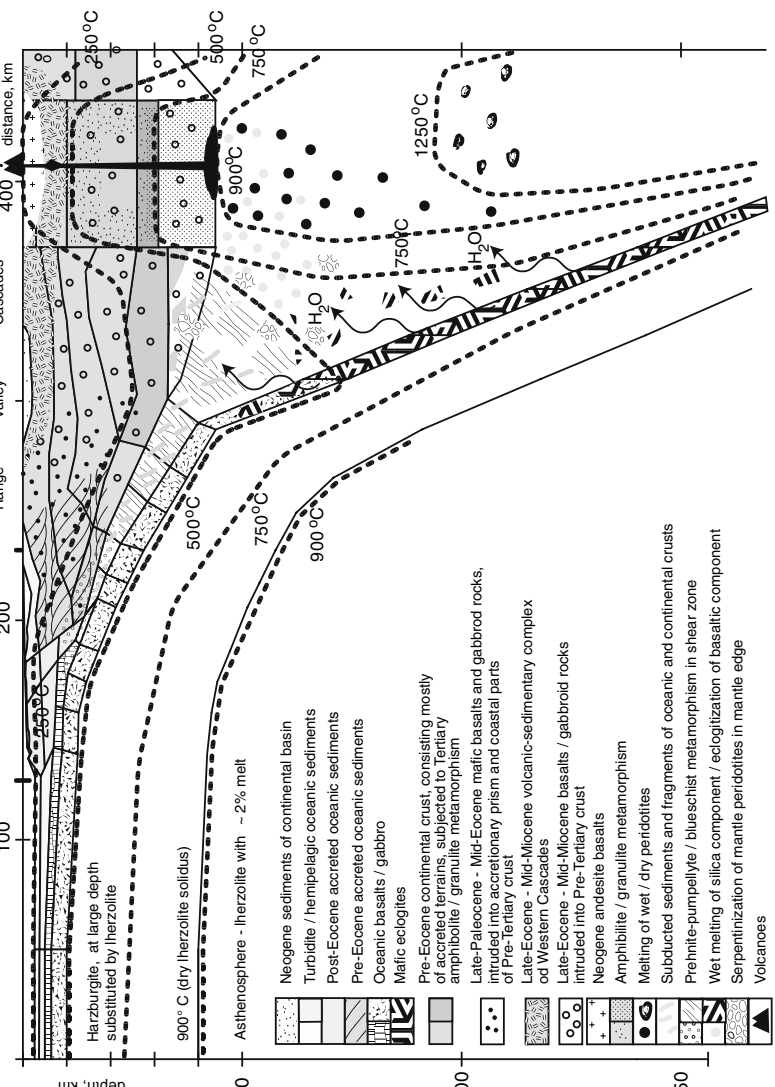

Fig. 12.44 Predictive geothermal and petrological model CASCADIA along the E–W profile crossing central Oregon (Romanyuk et al., 2001b)

conductance of the sedimentary cover and $R_2 = h_2\rho_2$ is the average resistance of the high-resistivity crust that separates the sedimentary cover from the deep conductive zone.

Another part of the oceanic electric current bypasses the continental trap. The current leaks into the ocean floor and is distributed among continental deep conductive zones.

The proportion of the currents flowing into the sedimentary cover to the current penetrating into deep conductors defines the degree of low-frequency distortions of the transverse MT-curves and their sensitivity to crustal and mantle conductivity anomalies.

The inductive anomalies arise as the electric current flows parallel to the coast (the TE-mode). They are caused by the inductive interaction between oceanic and continental longitudinal electric currents. At high frequencies the longitudinal excessive currents concentrate in the near-coast zone. Inductive distortions of longitudinal MT-curves are observed near the shore and they decay at distances of the same order as a depth to the well-conducting mantle. In the near-coast zone, the asymmetry of longitudinal electric currents generates the vertical component of the magnetic field, which can exceed its horizontal component.

By way of illustration, we turn to the work of Berdichevsky et al. (1992) and consider two-dimensional models A and S (Fig. 12.45). Geologically, these models are substantially different. Model A imitates an active tectonic zone. Its continental part involves a thick conductor, encompassing the lower crust and upper mantle. In the same depth range, model S contains only a thin crustal conductor, characteristic of stable tectonic zones.

Let us examine the behavior of the transverse and longitudinal apparent-resistivity curves of $\rho_A^{\perp}$, $\rho_S^{\perp}$ and $\rho_A^{\parallel}$, $\rho_S^{\parallel}$ calculated for models A and S. Relationships observed on the oceanic profile are rather simple. In the near-coast zone, the $\rho^{\perp}$-curves are thrown down reflecting the current leakage from the ocean to the continental crustal and mantle conductors. The leakage effects slowly attenuate with distance from the continent. Even at distances about 1000 km, the low-frequency resistivities $\rho_A^{\perp}$, $\rho_S^{\perp}$ differ dramatically from the normal apparent-resistivity ρ_{n}^{o}. The induction effects distorting the longitudinal apparent-resistivity curves are far more local. They are visible in the near-coast zone, but they vanish at distances of about 50 km and the resistivities $\rho_A^{\parallel}$, $\rho_S^{\parallel}$ virtually merge with the normal apparent-resistivity ρ_n^o. Somewhat different relationships are observed on the continental profile. Near the coast, the ascending branches of the transverse $\rho^{\perp}$-curves coincide with the normal apparent-resistivity curve of ρ_n^c. However, with decreasing frequency, the $\rho^{\perp}$-curves depart from the ρ_n^c-curve: their ascending branches lengthen, and the descending branches shift upward by 2.5 decades. No evidence of a crustal or crust–mantle conductive layer is available there. With distance from the ocean, the shape of the $\rho^{\perp}$-curves slowly changes: gentle inflections and minima reflecting a deep conductive layer appear and the descending branches shift downward. Finally, at a distance of about 700 km (six adjustment distances), the $\rho^{\perp}$-curves merge with the normal curve of ρ_n^c. The behavior of the transverse apparent resistivity curves $\rho^{\perp}$ can be accounted for by the continental trap effect. The situation

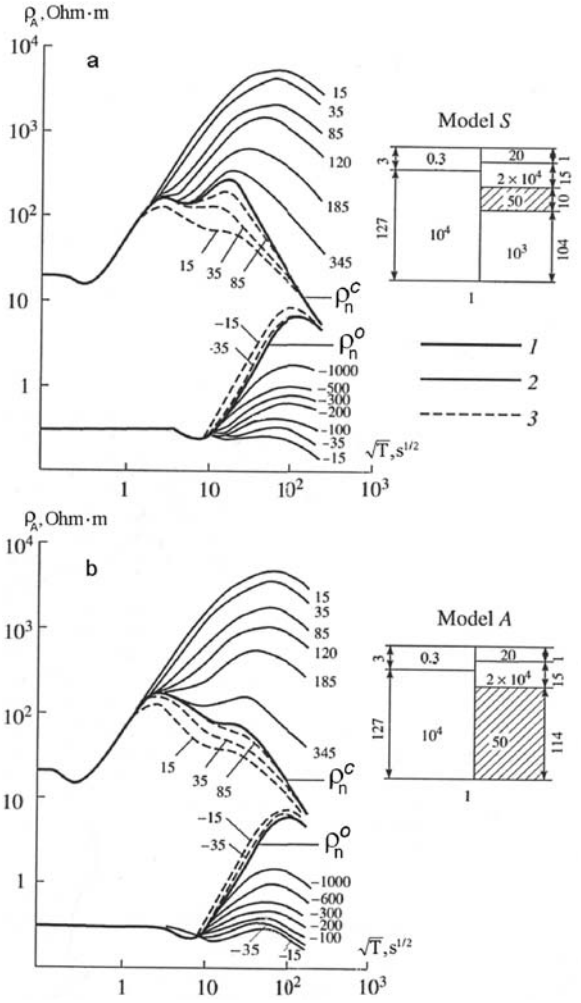

Fig. 12.45 Apparent-resistivity curves in models of the stable (S) and active (A) tectonic zones; 1 – locally normal curves ρ_n^c (continent) and ρ_n^o (ocean), 2 – transverse $\rho^{\perp}$-curves, 3 – longitudinal $\rho^{\parallel}$-curves. Parameter of the curves is the distance to the coast in km. Resistivities (Ohm·m) and thicknesses (km) of layers are shown in the model sections: a – model *S,* b – model *A*

with the longitudinal curves $\rho^{\parallel}$ is quite different. Their behavior is governed by the inductive effect. Even in the near-coast zone, they have distinct inflections and minima indicating the presence of a crustal or crust–mantle conductive layer. At a distance of about 100 km from the coast, the $\rho^{\parallel}$-curves merge with the normal curve ρ_n^c.

In closing, we can compare the resolution of the TM- and TE-modes. It is seen from Fig. 12.46 that at a distance of 15 km and even of 85 km from the coast the transverse curves of $\rho_A^{\perp}$ and $\rho_S^{\perp}$ obtained in models A and S practically coincide (they differ by no more than 3–5% throughout the period range considered). So, using the TM-mode in an 85 km wide alongshore zone, it is impossible to distinguish a crustal conductor 10 km thick from a crust-mantle conductor 114 km

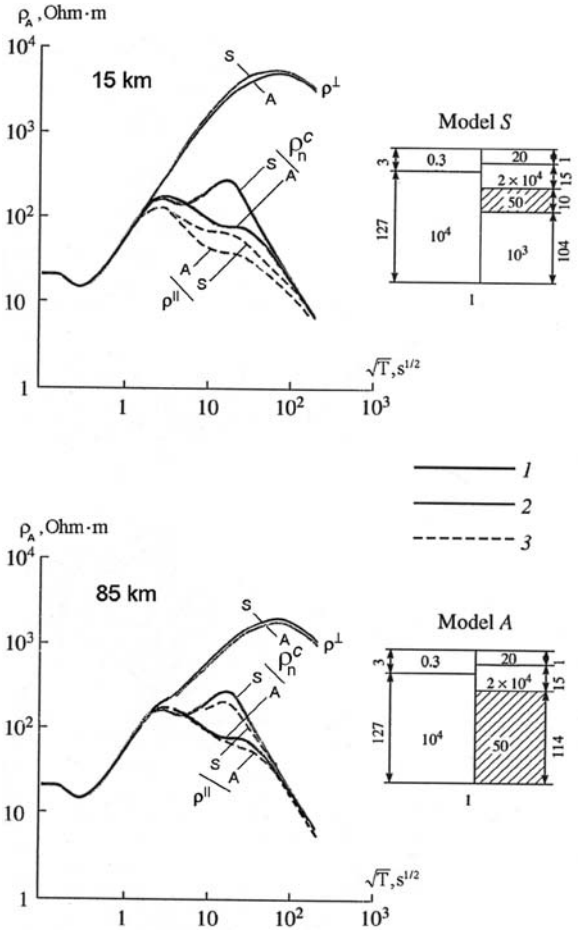

Fig. 12.46 Illustrating the resolution of the apparent-resistivity curves in models *S* and *A* at distances of 15 and 85 km from the coast: 1 – locally normal curves (ρ_n^c), 2 – transverse curve ($\rho^{\perp}$), 3 – longitudinal curve ($\rho^{\parallel}$)

thick. In the same zone, the TE-mode clearly distinguishes between crustal and crust-mantle conductors.

Next we will examine the behavior of the tipper. Figure 12.47 shows the curves of $|W_{zy}|$. The coast effect produces an extensive W_{zy}-anomaly extending for about 100 km in the ocean and 300 km on the continent. Note rather high resolution of tippers: at periods of 100 and 1000 s, the difference between models A and S displays itself quite distinctly even in the near-coast zone.

Evidently, the TE-mode (longitudinal apparent resistivities and tippers) is more sensitive to deep conductive zones compared to the TM-mode (transverse apparent resistivities). This statement, derived from the analysis of simplest models, needs more detailed elaboration taking into account the structure of the subduction zone. Figure 12.48 presents a blocky model of the subduction zone involving the following components: (1) ocean, (2) continental sediments, (3) oc – oceanic crust, (4) oa – oceanic asthenosphere, (5) sp – subducting plate, (6) cc – continental

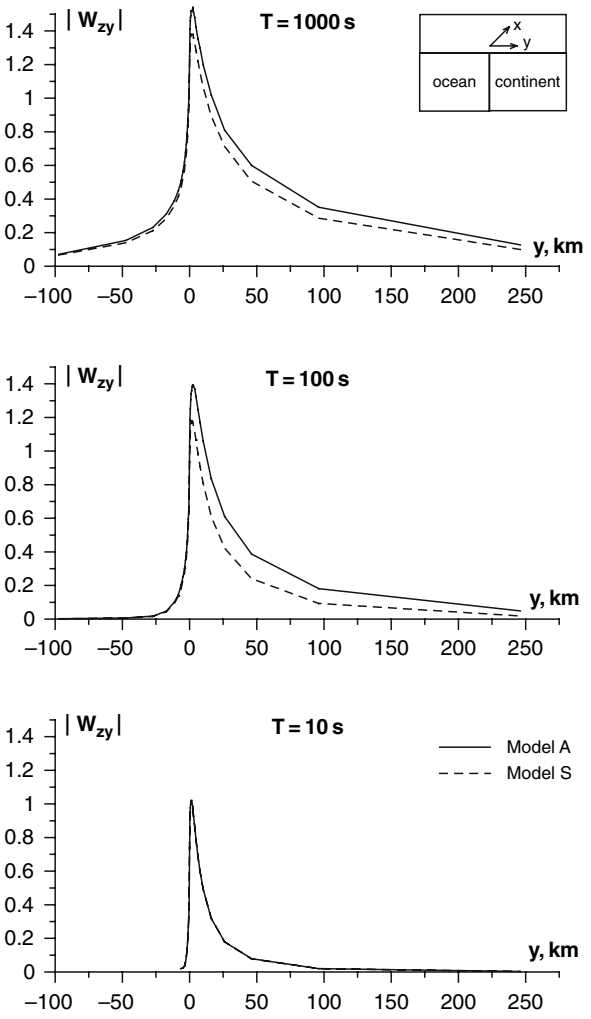

Fig. 12.47 Tipper curves in the models of stable (*S*) and active (*A*) tectonic zones. Parameters of the models *S* and *A* are the same as in Fig. 12.45

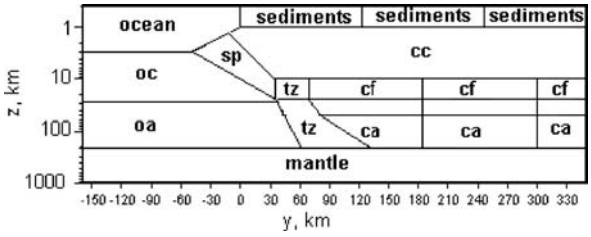

Fig. 12.48 Exploratory blocky model of the subduction zone

crust, (7) tz – transition zone, (8) cf – crustal fluidized layer, (9) ca – continental asthenosphere, (10) mantle. Varying the resistivities of blocks sp, cc, tz, cfl, and ca, we construct a set of models representing different geodynamical situations and enabling the estimation of the sensitivity of the TE- and TM-modes to the subducting plate, continental crustal conductors, and continental asthenosphere. The initial model has a continental section, in which subducting plate, crustal conductors and asthenosphere are absent. It is successively complicated by introducing the following components into the continental section: (1) a crustal conductive layer (either of infinite extent or 300 km wide), (2) a downsinking conductive plate either connected or unconnected with the crustal conductive layer, and (3) a conductive asthenosphere (either of infinite extent or 300 km wide) connected or unconnected with the oceanic asthenoshere. Analysis of these models leads to the following evident conclusions that are valid for the continental profile crossing 200 km wide alongshore zone:

1) the resistance of the continental upper crust can be estimated by the TM-mode,
2) the crustal conductive layer of infinite and finite extent is best expressed by the TE-mode,
3) the conductive junction of the plate with the crustal conductive layer is best resolved by the TM-mode,
4) the conductive continental asthenosphere is best resolved y the TE-mode; even a well-defined asthenosphere 300 km wide may be overlooked by the TM-mode,
5) the conductive junction of the continental asthenosphere with the oceanic asthtenosphe is poorly reflected in both modes,
6) the difference between continental conductors of infinite and finite extent is better resolved by the TM-mode.

These conclusions agree with the results of trial inversions of synthetic data obtained for the examined models. Interpretation has been performed with the programs Inv2D-FG (Golubev and Varentsov, 1994) and IGF-MT2D (Novozhynski and Pushkarev, 2001), which provide a regularized solution of the magnetotelluric and magnetovariational inverse problems in the class of piecewise-uniform (blocky) media. The inversion of the TE-mode (longitudinal apparent resistivities, longitudinal impedance phases, tipper components) successfully reconstructed the continental cross-sections with crustal and astenospheric conductors. The inversion of the TM-mode (transverse apparent resistivities and transverse impedance phases) was less efficient (crustal and astenospheric conductors are defined with gaps and distortions). However, the TM-mode determined more reliably the resistivity of the continental upper crust and fixed the junction of the subducting plate with the crustal conductive layer.

12.7.4 On the Regional Near-surface Distortions

Now we have to give due consideration to regional near-surface heterogeneities crossed by the Lincoln line and elucidate their influence on magnetotelluric and magnetovariational response functions.

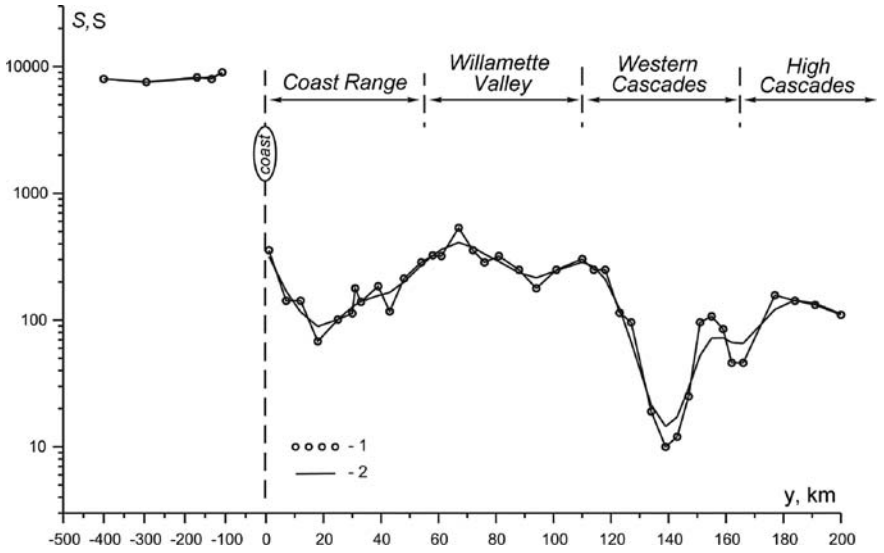

Fig. 12.49 Conductance S of the upper layer along the Lincoln line: 1-observations, 2-spline approximation

Figure 12.49 plots the conductance S of the upper layer along the Lincoln line. The plot is based on bathymetric data and MT soundings from oceanic and continental segments of the profile. The conductance S in the deep ocean is of the order of 10000 S. The Coast Range, composed of Early Tertiary sediments and volcanic rocks, is characterized by a conductance of about 100–150 S. The volcanic–sedimentary complex of the western part of the Western Cascades and the thick sequence of Tertiary deposits filling the Willamette Valley are characterized by conductances reaching 250–300 S. In the eastern part of the Western Cascades, where these deposits wedge out, the conductance drops to 10 S. Beneath the High Cascades and the backarc plateau, the S values once again increase, reflecting the development of volcanic–sedimentary rocks underlying Late Tertiary and Quaternary volcanic formations.

Figure 12.50 presents a map of the conductance S of the upper layer encompassing the Juan de Fuca Ridge and plate with adjacent continental areas. In constructing this map, the data on sediments thickness and their average resistivities have been used. The Juan de Fuca Ridge (I) and the abyssal basin of the Juan de Fuca plate (II) are clearly seen in this map. The following structures of submeridional strike are outlined on the continent: the Coast Range (III), the Willamette Valley (IV) and the Puget Sound lowland (V), the Western Cascades (VI) and the High Cascades (VII). This map has been incorporated into a less detailed map covering the entire northwestern United States (1280 km $\times$ 1280 km) and superimposed on a uniform background of $S = 10000$ S. Estimates indicate that, in modeling the magnetotelluric field in the central part of this map, the influence of its edges can be neglected.

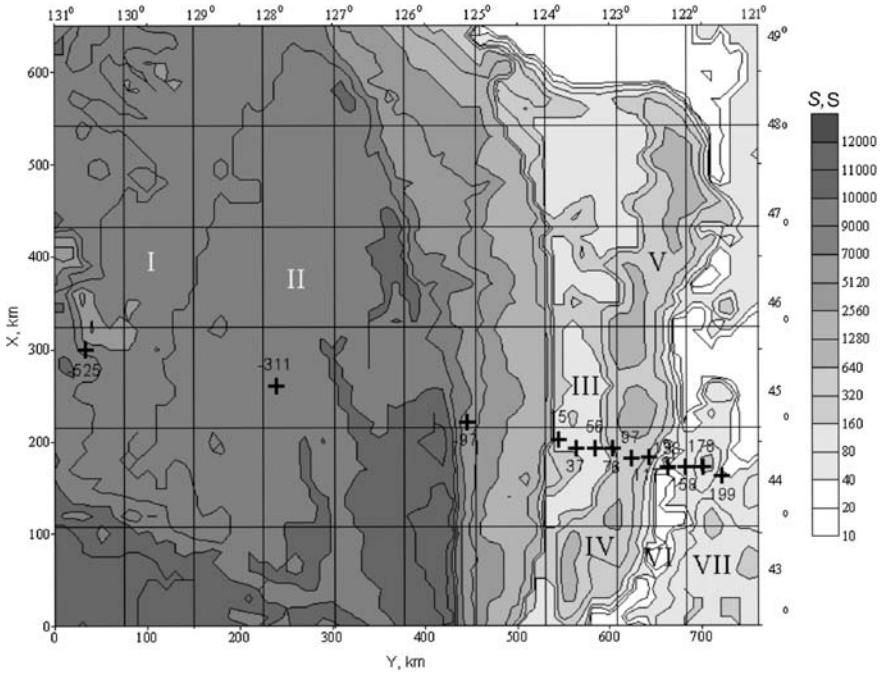

Fig. 12.50 Map showing the conductance S of the upper layer. Stations on the Lincoln line are indicated by crosses with distances from the coast in km

The three-dimensional magnetotelluric field on the Lincoln line was calculated in the approximation of an inhomogeneous thin layer $S(x, y)$ underlain with a horizontally homogeneous layered medium. The latter has been taken as the average continental background in the model of the Cascadia subduction zone suggested by Varentsov et al. (1996). The calculations were performed with the SLPROG program (Singer and Fainberg, 1985). Figure 12.51 shows the 3D curves of apparent resistivities, impedance phase and tippers obtained along the Lincoln line at different distance r from the coast. They are compared with corresponding locally normal 1D curves as well as with the 2D curves calculated for a two-dimensional model, in which the *S(r)* values specified on the Lincoln line were continued northward and southward. In the Coast Range and Willamette Valley zone ($r = 15$–76 km), the 3D and 2D curves fall close together, and in many cases they virtually coincide (the marked static shift of the longitudinal and transverse apparent-resistivity curves, ρ_{xy} and ρ_{yx}, is observed only not far from the shore). Somewhat different relations are characteristic of the Cascades and Deshutes Plateau zone ($r = 117$–178 km). Here the agreement between the 3D and 2D curves is preserved as a whole, but the static shift of the transverse curves ρ_{yx} reaches half-decade and at some sites the high-frequency branches of the 3D and 2D phase curves demonstrate some discrepancies. A common peculiarity of the Lincoln line is that almost without exception the 3D and 2D longitudinal apparent-resistivity and impedancee-phase curves, ρ_{xy}

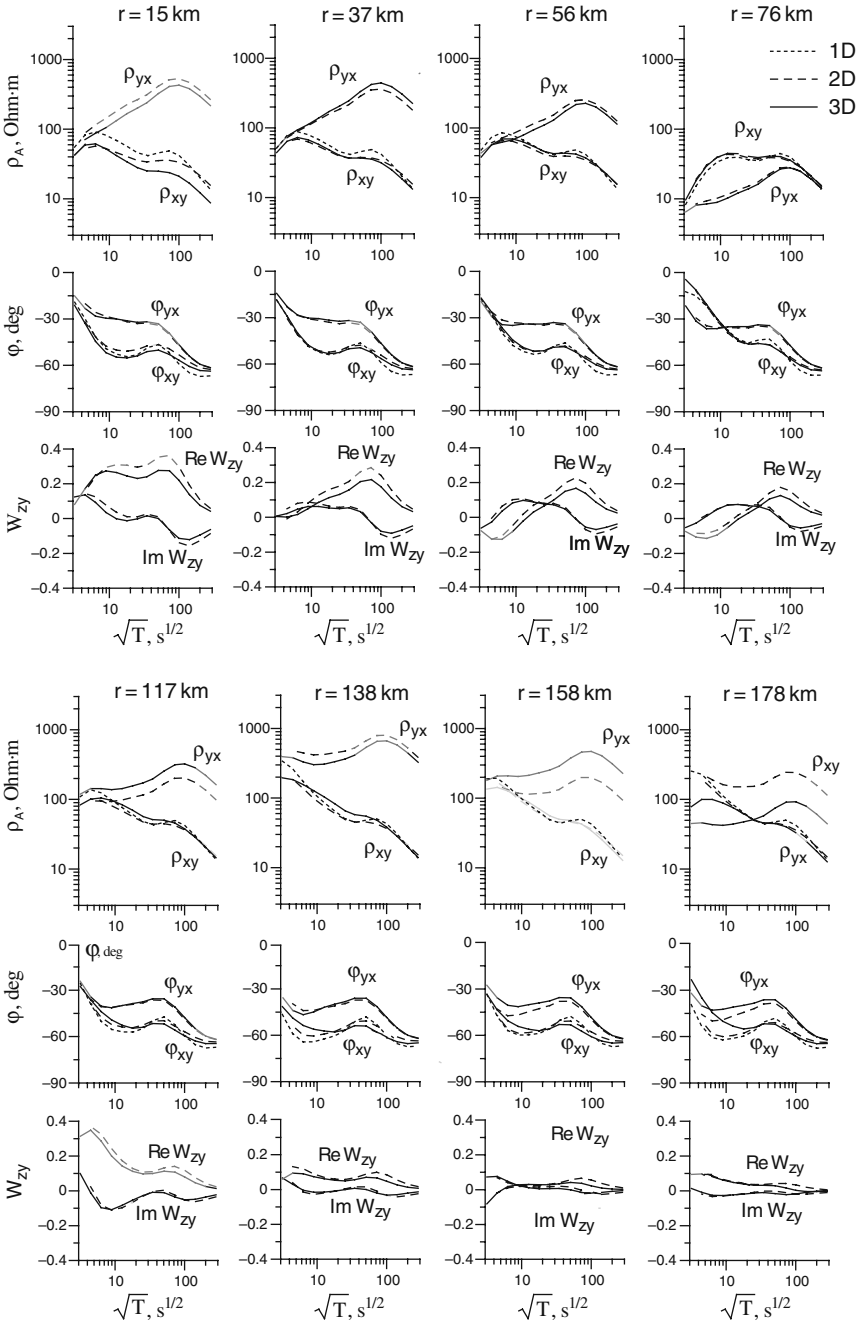

Fig. 12.51 Three-dimensional (3D) curves of ρ_{xy}, ρ_{yx}, φ_{xy}, φ_{yx}, Re W_{zy}, Im W_{zy} along Lincoln line, r is a distance from the coast. The corresponding 2D curves calculated for a two-dimensional model and locally normal 1D curves calculated for a one-dimensional model are also shown

and φ_{xy}, agree closely with the 1D locally normal curves ρ_n and φ_n. Summing up, we can assume that the regional structure of near-surface rocks in the vicinity of the Lincoln line is favorable for a 2D interpretation of MT and MV soundings. This important result is consistent with the estimates obtained by Zhdanov and Spichak (1992) and Spichak (1999).

12.7.5 Models EMSLAB-I and EMSLAB-II

Two models are of special interest in the discussion about the geoelectric structure of the Cascadia subduction zone: the EMSLAB-I model (Wannamaker et al., 1989b) and the EMSLAB-II model (Varentsov et al., 1996).

The EMSLAB-I model is shown in Fig. 12.52. This two-dimensional model has been constructed by the trial-and-error method with a high priority to the TM-mode, which, as the authors of the model believe, is tolerant to 3D deviations from the two-dimensionality. This model minimizes the misfit of the curves of $\rho^{\perp}$, $\varphi^{\perp}$ and virtually ignores the misfit of the curves of $\rho^{\parallel}$, $\varphi^{\parallel}$. The most interesting elements in the EMSLAB-I model are (1) the upper conductive part of the oceanic plate subducting under the Coast Range, (2) a subhorizontal conductive layer in the continental crust thickening under the High Cascades, and (3) a well-developed conductive asthenosphere under the ocean. The question of whether the downgoing plate is connected with the crustal conductor is left open. No continental asthenosphere is present in this model, although the shape of the experimental curves of $\rho^{\parallel}$, $\varphi^{\parallel}$ indicates a

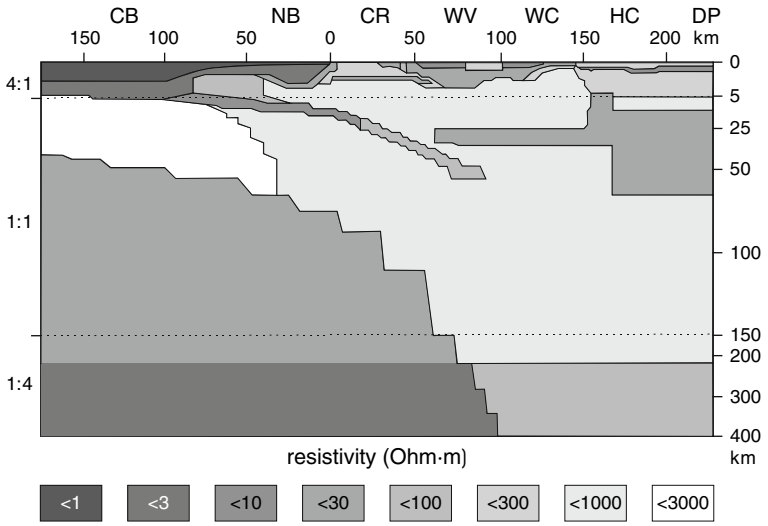

Fig. 12.52 The EMSLAB I model: CB – Cascadia Basin, NB – Newport Basin, CR – Coast Range, WV – Willamette Valley, WC – Western Cascades, HC – High Cascades, DP – Deschutes Plateau (Wannamaker et al., 1989b)

low resistivity in the upper mantle. The absence of gross discrepancies between the observational and model values of Re W_{zy}, Im W_{zy} is regarded as evidence of reliability of the model.

Unfortunately, the EMSLAB-I model is vulnerable to criticism. A resistive (cold) continental mantle contradicts the modern geodynamic concepts of the Cascadia subduction zone (compare EMSLAB-I model with the predictive model CASCADIA shown in Fig. 12.43). It is natural to think that the EMSLAB-I model does not show the continental asthenosphere because of a low sensitivity of TM-mode to mantle conductors. The point is that in the Cascadia subduction zone, only bimodal inversion using both modes (TE + TM) can provide a key to studying the asthenosphere (Berdichevsky et al., 1992).

Experiments on the bimodal interpretation of MT and MV data from the Cascadia subduction zone resulted in the EMSLAB-II model (Fig. 12.53). This two-dimensional model has been constructed with the INV2D-FG program designed for automated inversion (Varentsov et al., 1996). The program enabled the optimization of resistivities in 20 blocks with a fixed geometry. The following response functions were used in the course of bimodal inversions of MT and MV data: (1) $\varphi^{\perp}$ and Re W_{zy}(maximum weight), (2) $\varphi^{\parallel}$ and $\rho^{\perp}$ (normal weight), and (3) $\rho^{\parallel}$(minimum weight). The EMSLAB-II model has much in common with the EMSLAB-I model: the same oceanic asthenosphere, the same downgoing plate, and the same crustal conductive layer. However, the plate is connected with the crustal conductor, and the continental mantle contains a conductive asthenosphere (!) separated from the oceanic asthenosphere. Thus, a new evidence for partial melting in the continental mantle has been obtained.

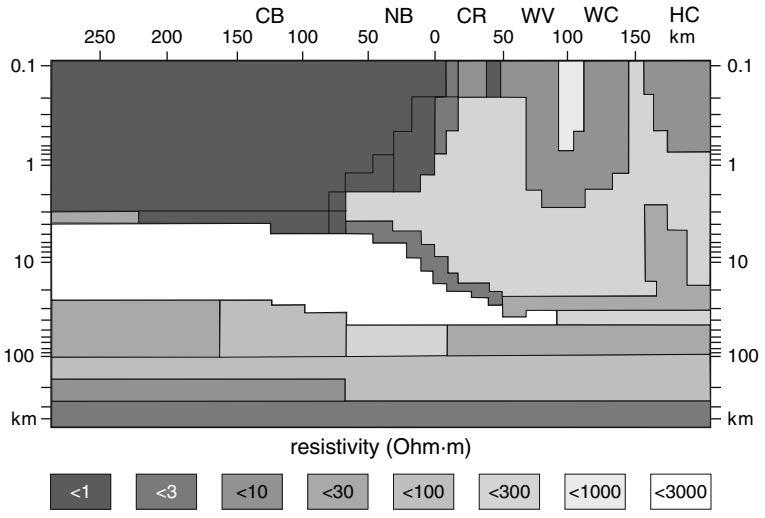

Fig. 12.53 The EMSLAB II model. Notation is the same as in Fig. 12.52 (Varentsov et al., 1996)

The main drawback of the EMSLAB-II model is its schematism caused by the limitations of the INV2D-FG program. Nowadays we have at our disposal more effective programs for two-dimensional automated inversion of MT and MV data. They include the smoothing program REBOCC, implementing Occam's razor (Siripunvaraporn and Egbert, 2000), and the programs IGF-MT2D (Novozhynski and Pushkarev, 2001) and II2DC (Varentsov, 1999), which provide the optimization of models containing 512 and more blocks of a fixed geometry. Advances in computing magnetotellurics open up new avenues for the interpretation of EMSLAB data.

12.7.6 Analysis of Observations on the Lincoln Line

Figure 12.54 shows the transverse apparent-resistivity curves obtained on the continental part of the Lincoln line. The curves consist of two ascending branches separated by an inflection or a minimum. The low-frequency ascending branches of these curves have identical slopes and occupy nearly two decades. To get a better insight into the behavior of apparent resistivities, we normalize the $\rho^{\perp}$-curves by shifting them vertically so that their left-hand ascending branches fit best the line of the average conductance $S = 50$ S of the upper layer. The normalized $\rho^{\perp}$-curves demonstrate a simple regular relation: the greater the distance from the coast, the deeper the central minimum of these curves and the lower their right-hand branch. Comparing Fig. 12.54 with Fig. 12.45, we find a striking similarity between the normalized $\rho^{\perp}$-curves obtained on the Lincoln line and the theoretical $\rho^{\perp}$-curves calculated for the models A and S. It seems evident that the continental trap effect is observed on the Lincoln line and that precisely this effect rather than the influence of lithospheric and asthenospheric structures governs the transverse $\rho^{\perp}$-curves at various distances from the coast.

The longitudinal apparent resistivity curves obtained in the same period range are shown in Fig. 12.55. With distance from the coast, the $\rho^{\parallel}$-curves change in shape, showing bell- and bowl-type branches. In many cases the $\rho^{\parallel}$-curves have gently ascending or descending low-frequency branches lying at various levels. One might assume that the longitudinal $\rho^{\parallel}$-curves reflect variations in the geoelectric structure of the lithosphere and asthenosphere but are distorted by static shifts and occasionally by 3D effects.

Note that the transverse curves of $\rho^{\perp}$ and $\varphi^{\perp}$ satisfy the dispersion relations at all sites of the Lincoln line. However, the longitudinal curves of $\rho^{\parallel}$ and $\varphi^{\parallel}$ episodically violate the dispersion relations (sites 3, 4, 10, and 13), as is seen in Fig. 12.56.

Now we turn to the analysis of the inhomogeneity parameter N (in Swift-Eggers determination) and asymmetry parameters $skew_S$ and $skew_B$, which help to identify geoelectric structures and determine their dimensionality. The pseudo-sections of these parameters are presented in Fig. 12.57. At high frequencies ($T << 1$ s), the inhomogeneity parameter N fluctuates at the level of 0.1, indicating the acceptability of one-dimensional estimates of the resistivity for near-surface rocks. With lowering frequency, we notice an influence of deeper inhomogeneities. At $T = 1$s, the

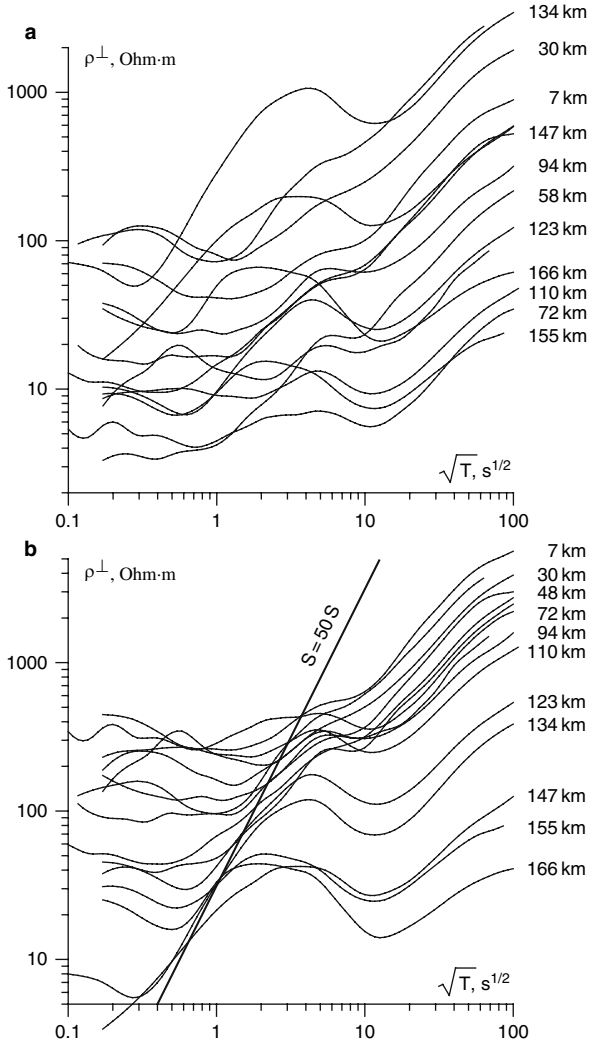

Fig. 12.54 Transverse apparent resistivity $\rho^{\perp}$- curves along the continental part of the Lincoln line: (**a**) observed curves, (**b**) normalized curves. The parameter of the curves is the distance to the coast

parameter N varies from 0.1–0.2 in the Willamette Valley and High Cascades to 0.4 in the Coast Range and Western Cascades. At low frequentcy (T>100 s), N increases to 0.4 in the Willamette Valley and to 0.5–0.8 in the Coast Range and Cascades. Large values of N, are associated, as a rule, with large values of $skew_S$ (0.3–0.5) and small values of $skew_B$(0.1–0.15). Thus, following Bahr, we can regard the deep regional background of the Cascadia subduction zone as a two-dimensional. Deep three-dimensional effects make itself evident only in the Willamette Valley and in

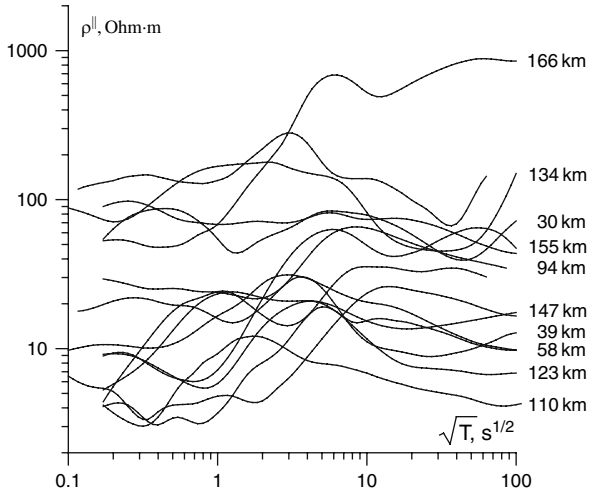

Fig. 12.55 Longitudinal apparent resistivity $\rho^{\parallel}$- curves along the continental part of the Lincoln line. The parameter of the curves is the distance to the coast

the High Cascades, where low-frequency values of $skew_B$ exceed 0.3. The azimuth of the strike of the regional two-dimensional structures determined from the Bahr decomposition varies from 0° to 10°. This agrees with orientation of tipper polar diagrams and induction arrows at many points on the Lincoln line. As an illustration, Fig. 12.58 shows the tipper polar diagrams for $T = 2500$ s and real induction arrows for $T = 6400$ s. Within the Coast Range,the tipper diagrams are figures-of-eight with their major axis oriented transversally or subtransversaly to the shoreline.

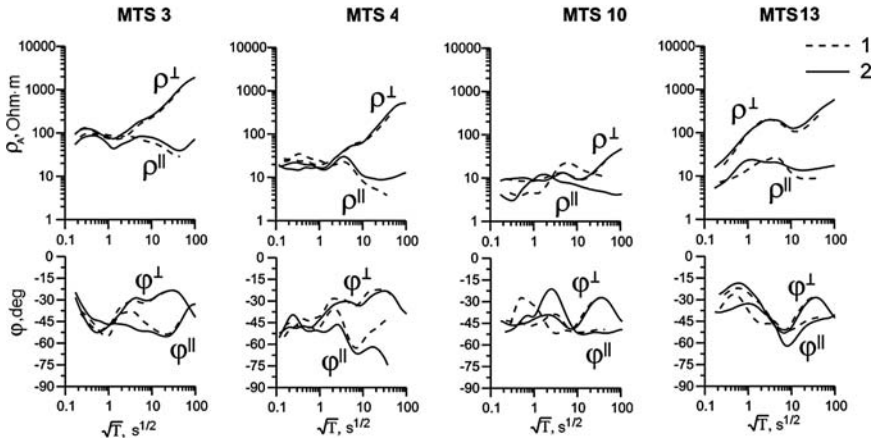

Fig. 12.56 Dispersion relations between apparent-resistivity ρ_A- curves and phase φ- curves: 1- observations, 2- dispersion transformation

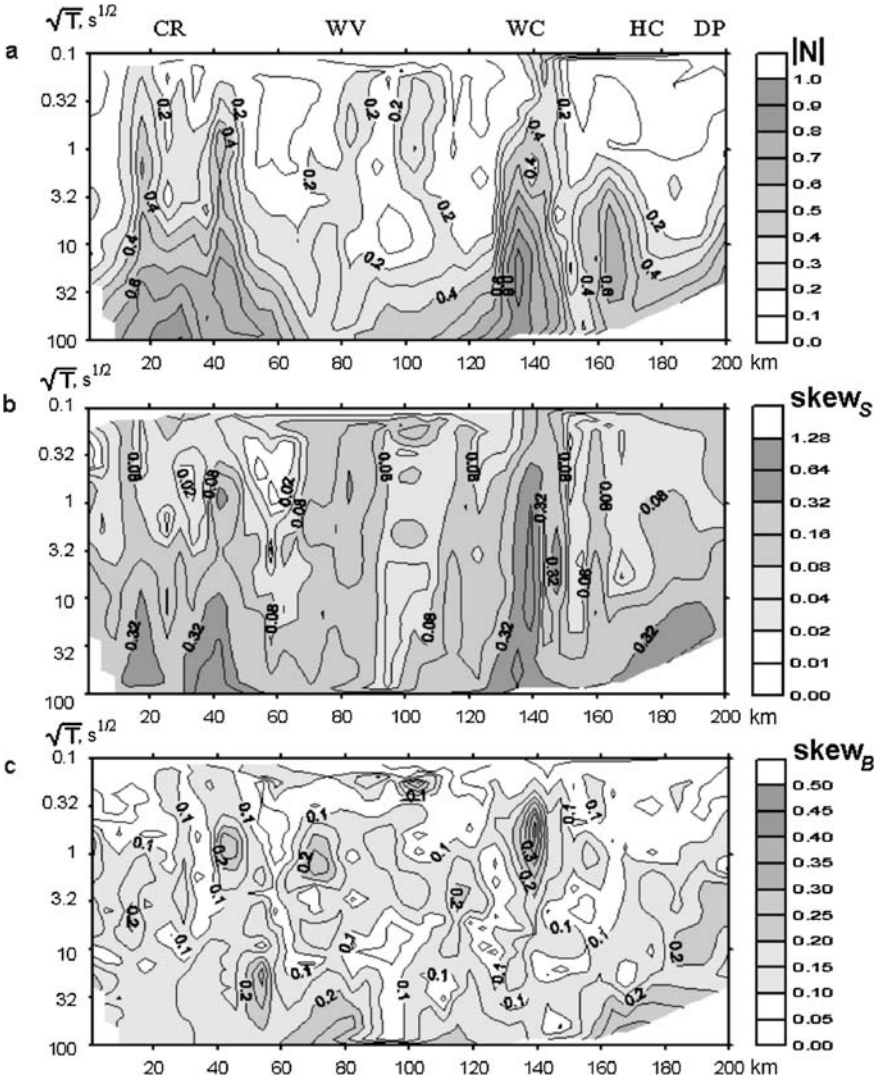

Fig. 12.57 Pseudo-sections of the magnetotelluric parameters of (**a**) inhomgeneity parameter *N*, (**b**) asymmetry parameter $skew_s$, and (**c**) asymmetry parameter $skew_B$: CR – Coast Range, WV – Willamette Valley, WC – Western Cascades, HC – High Cascades, DP – Deschutes Plateau

Much the same diagrams (though with some exceptions) are typical of the Willamette Valley. Within the High Cascades, magnetic diagrams degenerate into ovals but retain a transverse orientation. The real induction arrows point eastward, here and there with small deviations. It seems that in the EMSLAB experiment we can seek a solution to the inverse geoelectric problem within a class of two-dimensional media with meridional strike.

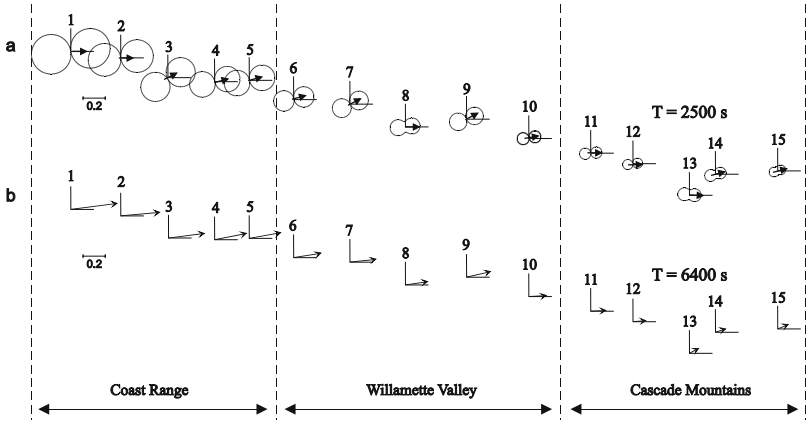

Fig. 12.58 Magnetic polar diagrams and real induction arrows along the continental part of the Lincoln line: a – tipper polar diagrams at the period $T = 2500$ s, b – real induction arrows at the period $T = 6400$ s

12.7.7 A New Geolectric Model of Cascadia: EMSLAB-III

The interpretation of data obtained on the Lincoln line is performed in the hypotheses test mode by the method of partial inversions. It consists of three stages.

At the first stage, we carry out the one-dimensional inversion of short-period curves of the effective apparent resistivity and impedance phase, ρ_{eff} and φ_{eff}, and construct an approximate geoelectric section of the volcanic–sedimentary cover to a depth of 3.5 km (Fig. 12.59). This section, consistent with the near-surface part of the EMSLAB-I model (Wannamaker et al., 1989b), is incorporated into the starting two-dimensional interpretation model.

At the second stage, we use the REBOCC program realizing the Occam razor and conduct experiments with a smoothed two-dimensional inversion. Under the complex conditions of the Cascadia subduction zone, the joint inversion of the TE and TM-modes yields intricately alternating low- and high-resistivity spots with a poor misfit minimization. The real structures of the subduction zone can hardly be recognized in these queer spots. The most interesting result is obtained from the partial inversions of the TE-mode (tippers and phases of the longitudinal impedance). It is shown in Fig. 12.60. Here the vast western and eastern conductive zones are distinctly outlined. They are separated by a rather narrow T-shaped high-resistivity zone that relates to the downgoing oceanic plate. In this simple pattern, the western and eastern conductors are identified as an oceanic asthenosphere with its top fixed at a depth of about 30–40 km and as a crust–mantle area of dehydration and partial melting in the depth range of 10–20 to 60–70 km. It is noteworthy that the upper boundary of the eastern conductor resembles the relief of the crustal conductive layer in the models EMSLAB-I and EMSLAB-II.

At the third, final, stage we apply the method of partial inversions and construct a new geoelectric model of the Cascadia subduction zone called the EMSLAB-III

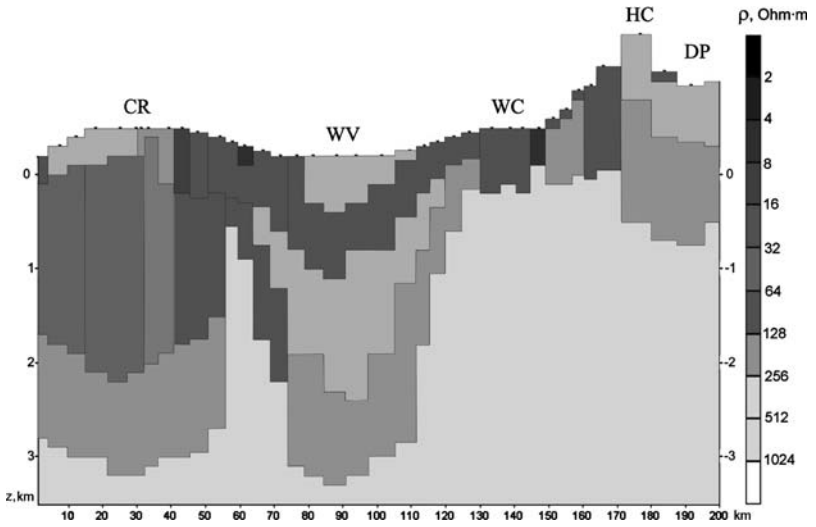

Fig. 12.59 Resistivity section of the volcanic–sedimentary strata derived from short-period MT-curves ($T = 0.01–100$ s). Notation is the same as in Fig. 12.57

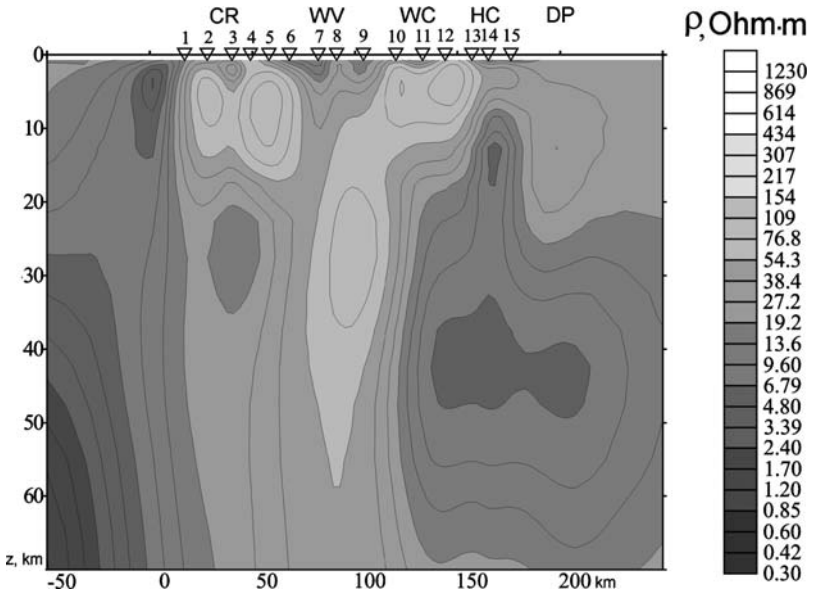

Fig. 12.60 Two-dimensional smoothing REBOCC inversion of the TE-mode (Re W_{zy}, Im W_{zy}, $\varphi^{\parallel}$). Notation is the same as in Fig. 12.57

model. Long-period MV and MT curves ($T = 1 - 10000$ s) are interpreted with the programs IGF-MT2D (Novozhynski and Pushkarev, 2001) and II2DC (Varentsov, 2002), implementing the misfit minimization in the class of blocky media with a fixed geometry of blocks. The interpretation is conducted in the hypotheses test mode. We examine three hypotheses of the Cascadia subduction zone which involve (1) dehydration in the continental crust (EMSLAB-I model, Fig. 12.52), (2) dehydration in the continental crust and development of a continental partially melted asthenosphere (EMSLAB-II model, Fig. 12.53), and (3) dehydration in the continental crust and development of a continental asthenosphere with a subvertical magmatic zone of ascending melting (predictive CASCADIA model, Fig. 12.44).

The two-dimensional interpretation model (START model) is shown in Fig. 12.61 with starting values of resistivities. The oceanic water resistivity is taken as 0.3 Ohm·m. The seafloor topography and thicknesses of bottom sediments, as well as sediments of the accretionary prism and shelf, are specified from the bathymetric and sedimentary thickness maps. The depth to the oceanic asthensphere is defined as 37 km in conformity with the models CASCADIA, EMSLAB-I, and EMSLAB-II. The surface of the subducting oceanic plate is reconstructed from seismic data (Trehu et al., 1994) and seismic tomography imagery (Weaver and Michaelson, 1985; Rasmussen and Humphries, 1988). The structure of the continental volcanic–sedimentary cover is determined from the 1D inversion of short-period MT curves. The downgoing plate as well as continental crust and mantle are divided into uniform, resistive blocks (10^3–10^4 Ohm·m) whose distribution allows a free choice of crustal and mantle structures consistent with the three hypotheses under the question. The hypothesis that best fits observations is selected automatically in the process of resistivity optimization and misfit minimization.

Let us use an interpretation scheme in which the magnetovariational inversion plays a leading role, whereas the magnetotelluric inversion serves to check and edit the MV results. The main advantage of this scheme is that, with lowering frequency, the magnetovariational tipper becomes free from the distorting effects of near-surface heterogeneities. It is clear that, in this way, we substantially improve the reliability of geoelectric information burdened with galvanic distortions of apparent resistivities.

Magnetovariational and magnetotelluric data obtained at 15 stations on the Lincoln line ($T = 1$–10000 s) are successively interpreted on three levels (Fig. 12.62). Here, we follow the same algorithm of partial inversions as in Section 12.6 describing the experiments on integrated interpretation of synthetic MV and MT data.

Level I. Inversion of Re W_{zy} and Im W_{zy}(TE-mode). The START model was taken as the starting model. The MV inversion yields the TP model shown in Fig. 12.63. The model misfits are given in Table 12.2, where $\delta\mathrm{Re}\ W_{zy}$ and $\delta\mathrm{Im}\ W_{zy}$ are the misfits of the real and imaginary tippers (rms deviations of the model values from the observed values), while $\Delta\mathrm{Re}\ W_{zy} = \left|\max \mathrm{Re}\ W_{zy} - \min \mathrm{Re}\ W_{zy}\right|$ and $\Delta\,\mathrm{Im}\ W_{zy} = \left|\max \mathrm{Im}\ W_{zy} - \min \mathrm{Im}\ W_{zy}\right|$ characterize the maximum variation in

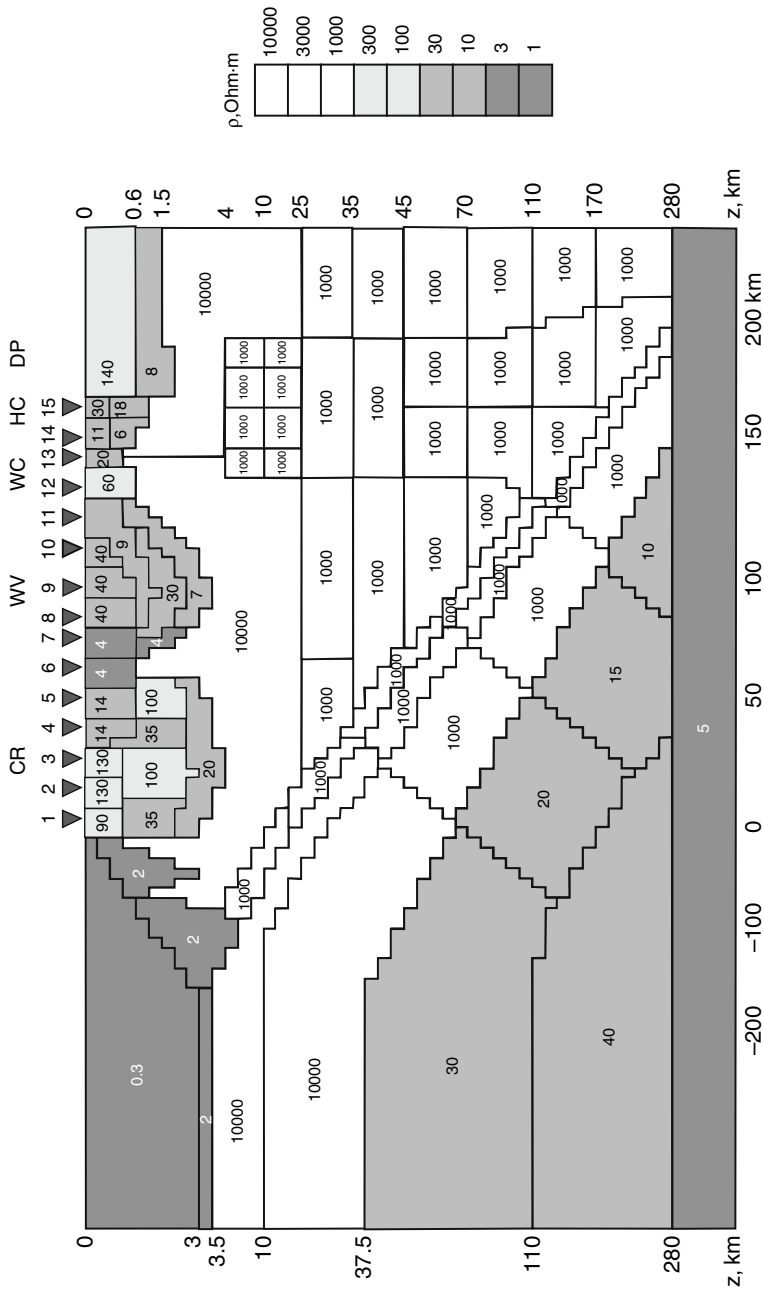

Fig. 12.61 Two-dimensional blocky interpretation model START: CR- Coast Range, WV – Willamette Valley; WC – Western Cascades, HC – High Cascades, DP – Deschutes Plateau. Numbers within blocks are resistivities in Ohm·m

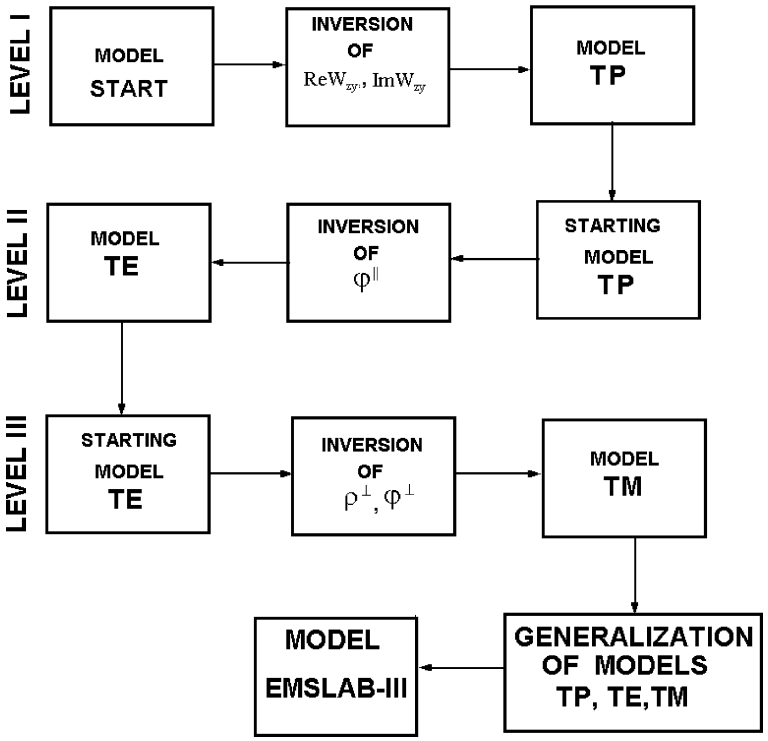

Fig. 12.62 Algorithm of partial inversions

the observed values of the real and imaginary tippers. The TP model seems to agree well with observations: at most stations, the misfits δRe W_{zy} and δIm W_{zy} are at least 5–10 times less than the maximum tipper variations. A noteworthy feature of the model is a conductive continental asthenosphere with a branching-out vertical low-resistivity zone penetrating the continental crust under the High Cascades. This feature of the TP model distinguishes it from EMSLAB-I and EMSLAB-II models and makes it similar to the predictive CASCADIA model, in which a vertical high-temperature zone of wet and dry melting characterized by low resistivities is localized beneath the High Cascades. When eliminating the conductive continental asthenosphere and vertical low-resistive crust-mantle zone, we get the misfits increased by factors of 1.5–2.5. So, we conclude that the tipper inversion settles the dispute among the EMSLAB-I, EMSLAB-II, and CASCADIA model in favor of the CASCADIA model.

Level II**.** Inversion of $\varphi^{\parallel}$ (TE-mode). On this level, we check and edit the results of tipper inversion. The inversion of the longitudinal $\rho^{\parallel}$-curves distorted by near-surface heterogeneities requires a preliminary normalization of the apparent resistivities, which almost always involves the risk of errors (especially in mountains). Therefore, interpreting the EMSLAB data, we limit ourselves to the inversion of the

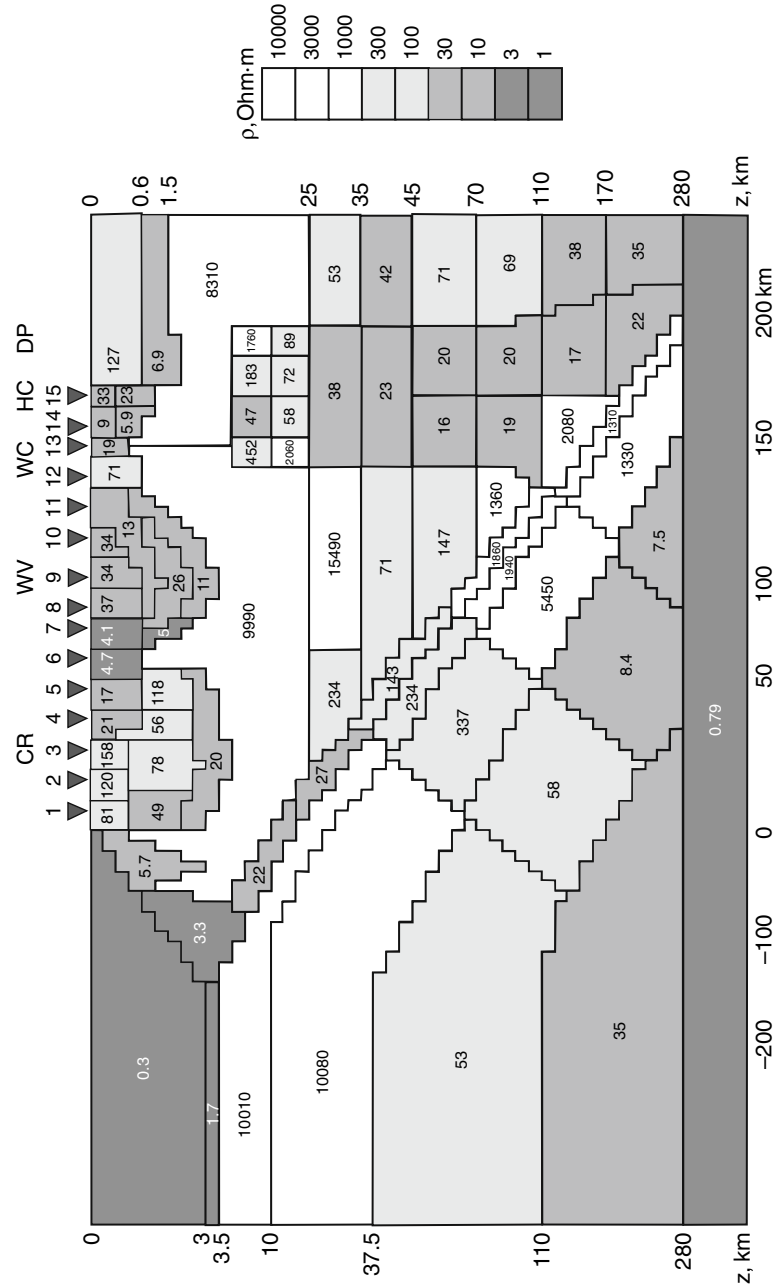

Fig. 12.63 TP model derived from the inversion of tippers Re W_{zy}, Im W_{zy}. Notation is the same as in Fig. 12.60

Table 12.2 Misfits of real and imaginary tippers

Station	1	2	3	4	5	6	7	8	9	10	11	12	13	14	15
δ Re W_{xy}	0.07	0.04	0.03	0.06	0.03	0.02	0.02	0.02	0.03	0.05	0.02	0.04	0.04	0.05	0.02
δ Im W_{xy}	0.05	0.05	0.03	0.04	0.01	0.02	0.02	0.02	0.02	0.03	0.02	0.02	0.05	0.04	0.03
Δ Re W_{xy}	0.39	0.37	0.30	0.47	0.59	0.51	0.24	0.25	0.27	0.23	0.41	0.48	0.42	0.42	0.36
Δ Im W_{xy}	0.37	0.26	0.27	0.23	0.31	0.29	0.10	0.11	0.16	0.17	0.26	0.18	0.26	0.17	0.12

longitudinal phase $\varphi^{\parallel}$-curves whose low-frequency branches are weakly distorted at most stations. If the dispersion relations exist between the apparent-resistivity and phase curves, we hardly lose any substantial information while rejecting the longitudinal $\rho^{\parallel}$-curves. The normalization of the $\varphi^{\parallel}$-curves reduces to an elimination of branches which violate the dispersion relations or are suspected of three-dimensional distortions.

The TP model derived from the inversion of the Re W_{zy}- and Im W_{zy}-curves is used as a starting model for the longitudinal phase inversion. The inversion of the $\varphi^{\parallel}$-curves results in the TE model shown in Fig. 12.64. The model misfits are presented in Table 12.3, where $\delta\varphi^{\parallel}$ is the phase misfit (rms deviation of the model values from the observed values), while $\Delta\varphi^{\parallel} = \left|\max \varphi^{\parallel} - \min \varphi^{\parallel}\right|$ characterizes the maximum variation of the observed phase values. At most stations, the phase misfits are 5 to 10 times less than the phase maximum variation, indicating good agreement between the model and observations.

Compare the continental segments of the TE and TP models. The TE model differs from TP model by better resolving the crustal conductive layer (25–45 km, 14–46 Ohm·m) and the subvertical mantle conductive zone (45–110 km, $\rho = 12$–$46\,\text{Ohm} \cdot \text{m}$). We can consider the TE model as an edited TP model.

Level III. Inversion of $\rho^{\perp}$ and $\varphi^{\perp}$ (TM-mode). The transverse apparent resistivities and phases are less sensitive to crustal and mantle conductive zones but they may provide sharp estimate of the resistivity of the upper consolidated crust and reveal the electric connection between the downgoing oceanic plate and crustal conductive layer.

The inversion of the TM-mode is performed using the TE-2 model derived from the inversion of the TE-mode as a starting model. It results in the TM model shown in Fig. 12.65. The model misfits are presented in Table 12.4, where $\delta\rho^{\perp}$ and $\delta\varphi^{\perp}$ are misfits of transverse apparent resistivities and phases (rms deviation of the model values from the observed values), while while $\Delta\varphi^{\perp} = \left|\max \varphi^{\perp} - \min \varphi^{\perp}\right|$ characterizes the maximum variation of the observed phase values. The apparent resistivity misfits at most stations vary from 6 to 12%, and the phase misfits are 7–10 times smaller than the maximum phase variation.

The TM model inherits the main features of the starting TE model (although with some deviations). What does the TM model indicate? First, there is no continuous ellectrical connecton between the downgoing oceanic plate and the crustal conductive layer (a conductive coupling is absent). Second, the upper consolidated crust in the continental segment of the model has a resistivity of about 2000 Ohm·m (not very high).

To complete the interpretation, we analyze the TP, TE, and TM models and construct the generalized model EMSLAB-III, smoothing out insignificant details and enlarging blocks. All changes are controlled by local misfits. The resulting generalized model EMSLAB-III is shown in Fig. 12.66. Look at Fig. 12.67, where the model and observed curves of $\rho^{\perp}$, $\rho^{\parallel}$, $\varphi^{\perp}$, $\varphi^{\parallel}$, Re W_{zy}, and Im W_{zy} are compared (the static shift in the observed curves of $\rho^{\parallel}$ is eliminated by a vertical displacement

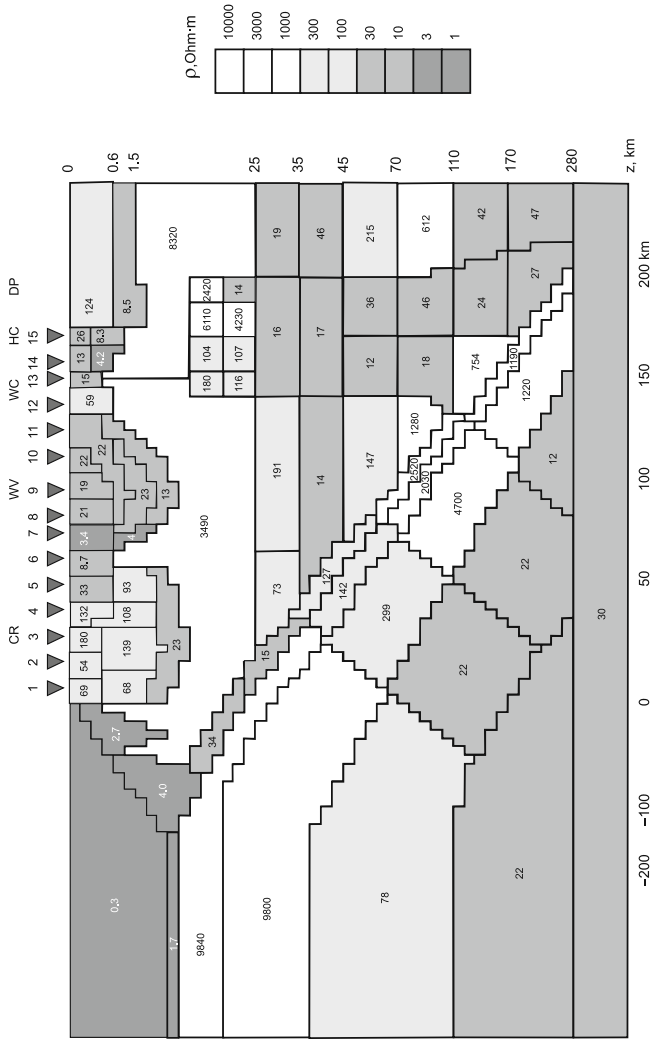

Fig. 12.64 TE model derived from the inversion of longitudinal impedance phases $\varphi^{\parallel}$. Notation is the same as in Fig. 12.61

Table 12.3 Misfits of longitudinal phases

Station	1	2	5	6	7	8	9	11	12	14	15
$\delta\varphi^{\parallel}$, deg	4.0	2.6	3.1	4.6	5.5	4.0	2.0	4.1	2.5	2.3	4.9
$\Delta\varphi^{\parallel}$, deg	23	21	21	23	45	38	29	42	20	29	41

of their low-frequency branches). The remarkable accord between the model and the observation catches the eye.

In its oceanic segment, the EMSLAB-III model is similar to EMSLAB-I and EMSLAB-II models, resolving a thick oceanic asthenosphere in a depth range of 37–110 km.

In the continental segment, the EMSLAB-III model clearly defines a crustal conductive layer (25–40 km, $\rho = 20\,\Omega\mathrm{m}$) and a conductive asthenosphere (100–155 km, $\rho = 30\,\Omega\mathrm{m}$). The crustal and asthenosphere conductors are connected by a columnar conductive body (ρ = 20–30 Ohm·m) that penetrates through the lithosphere and reaches a depth of about 7 km under the volcanic zone of the High Cascades.

The downgoing oceanic plate in a depth range of 4–40 km contains a thin inclined conductor (ρ = 20 Ohm·m) separated from the crustal conductive layer by a zone of higher resistivity (ρ = 200–500 Ohm·m). To all appearance, the fluids in the crustal conductive layer are of internal or mantle origin.

We would like to stress that EMSLAB-III model clearly reflects the fluid regime of the subduction zone. The downgoing plate drags low-resistivity water-saturated rocks of the ocean floor. As the plate sinks, free water is driven out and migrates through the shear zone (at the contact between the subducting oceanic and stable continental plates). Dehydration (release of combined water), beginning at depths of about 30–40 km in the downgoing plate supplies fluids to the mantle and causes wet melting of asthenospheric material. Low-resistivity melts migrate upward through the lithosphere and form the volcanic arc. The heating of the lithosphere activates dehydration in the lower crust, forming the crustal conductive layer.

The new geoelectric model EMSLAB-III of the Cascadia subduction zone recovered from the magnetovariational and magnetelluric data with magnetovariational priority fills the most essential gaps in the previous EMSLAB-I and EMSLAB-II models and is in excellent agreement with the predictive geothermal and petrological CASCADIA model behind which are present-day concepts of geodynamic history of the plate subduction. It seems that the MV-sounding with its rather high sensitivity to horizontal and vertical conductivity variations and rather high immunity to near-surface galvanic distortions can be considered as an efficient tool of the modern geoelectrics. Today the geophysicists have every reason to develop a new magnetotelluric strategy that would realize these attractive potentials of the magnetovariational sounding, especially in the deep geoelectric studies. Do not forget that many things worth doing in the world had been declared impossible before they were done.

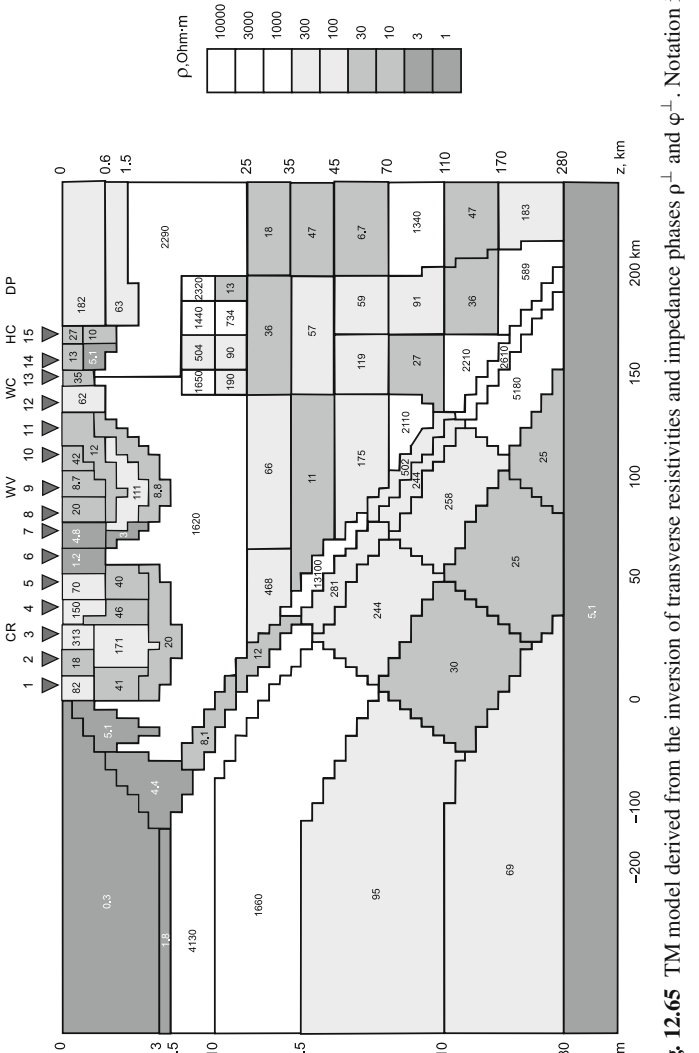

Fig. 12.65 TM model derived from the inversion of transverse resistivities and impedance phases $\rho^{\perp}$ and $\varphi^{\perp}$. Notation is the same as in Fig. 12.61

Table 12.4 Misfits of transverse apparent resistivities and phases

Station	1	2	3	4	5	6	7	8	9	10	11	12	13	14	15
$\delta\rho^{\perp}$, %	12	12	11	10	18	16	13	11	18	7	6	11	12	12	9
$\delta\varphi^{\perp}$, deg	2.5	2.9	2.6	1.9	2.2	3.6	1.0	2.4	4.5	1.8	1.5	2.2	1.9	1.9	1.4
$\Delta\varphi^{\perp}$, deg	20	19	24	18	21	19	22	18	27	21	23	34	22	18	29

12.8 From Two-Dimensional Inversion to Three-Dimensional Inversion

Let us consider two peculiarities that distinguish the three-dimensional inversion of magnetovariational and magnetotelluric data from the two-dimensional inversion discussed above.

The electromagnetic field studied in two-dimensional models is of simple structure. The transverse current flows in the vertical plane perpendicular to the model strike (gathers in the conductive zones and flows over and under the resistive zones), while the longitudinal current flows horizontally (along the model strike). In three-dimensional models the electromagnetic field is dramatically complicated. Considering the three-dimensional models, we observe strong lateral effects (lateral flow-around and current-gathering) and reveal rather complex trajectories, along which the currrent transfers the information on the conductivity distribution. It is evident that adequate description of real asymmetric locally inhomogeneous media requires a great number of the geoelectric and geometric parameters (resistivities and distances in x, y, z). Complication of the interpretation model and an increase in the number of its parameters lead to the extension of the set of equivalent solutions and impair the inversion stability. Thus, we arrive to the conclusion of necessity of strong constraints imposed on the three-dimensional interpretation model.

The properties of the two-dimensional magnetotelluric field depend on its orientation in reference frame formed by the model strike (to separate the induction and galvanic anomalies, it is enough to orient the magnetotelluric field along and across the model strike). In the three-dimensional asymmetric model such a reference frame is absent. So, we lose that simple physical basis, on which the strategy of two-dimensional inversion separating inductive TE mode and galvanic TM mode has been constructed. It would be helpful to use the experience of two-dimensional interpretation and to create the strategy of multicriterion three-dimensional inversion, which is an analog of multicriterion two-dimensional inversion, but takes into account the properties of the three-dimensional magnetotelluric field.

We see the following approaches to the three-dimensional interpretation of magnetovariational and magnetotelluric date.

1. Let a single observation profile cross an elongated three-dimensional structure at acute angle. Here the quasi-two-dimensionality conditions are not observed, but we can accomplish the formal two-dimensional inversion and introduce three-dimensional corrections determined by the hypotheses testing (hypothetical three-dimensional structures of different strike and different elongation are tested).

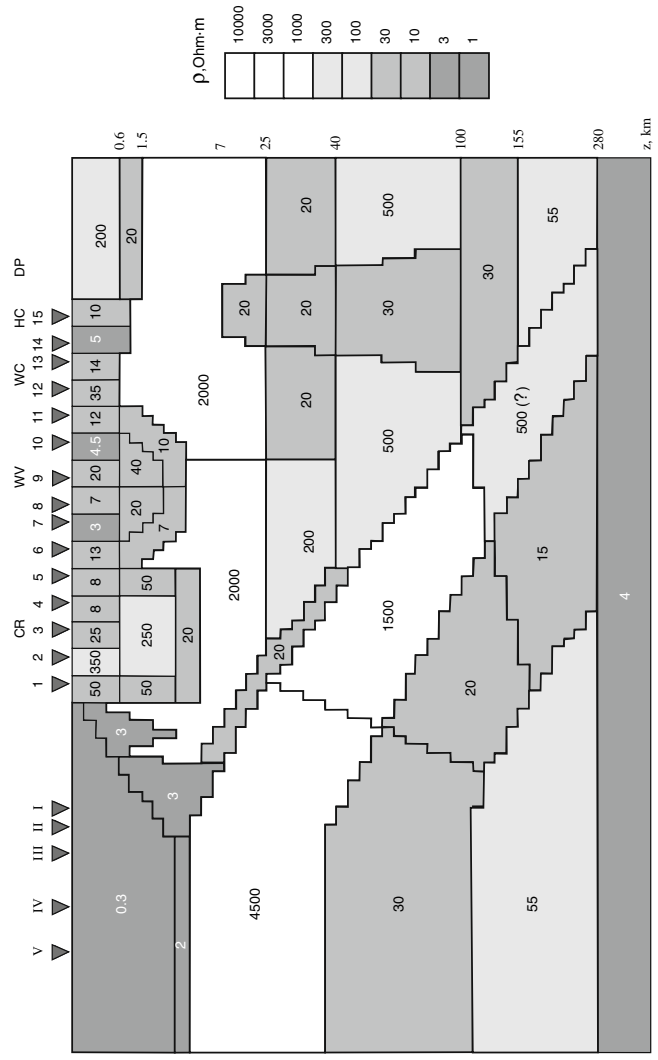

Fig. 12.66 EMSLAB III model. Notation is the same as in Fig. 12.61 (Vanyan et al., 2002a)

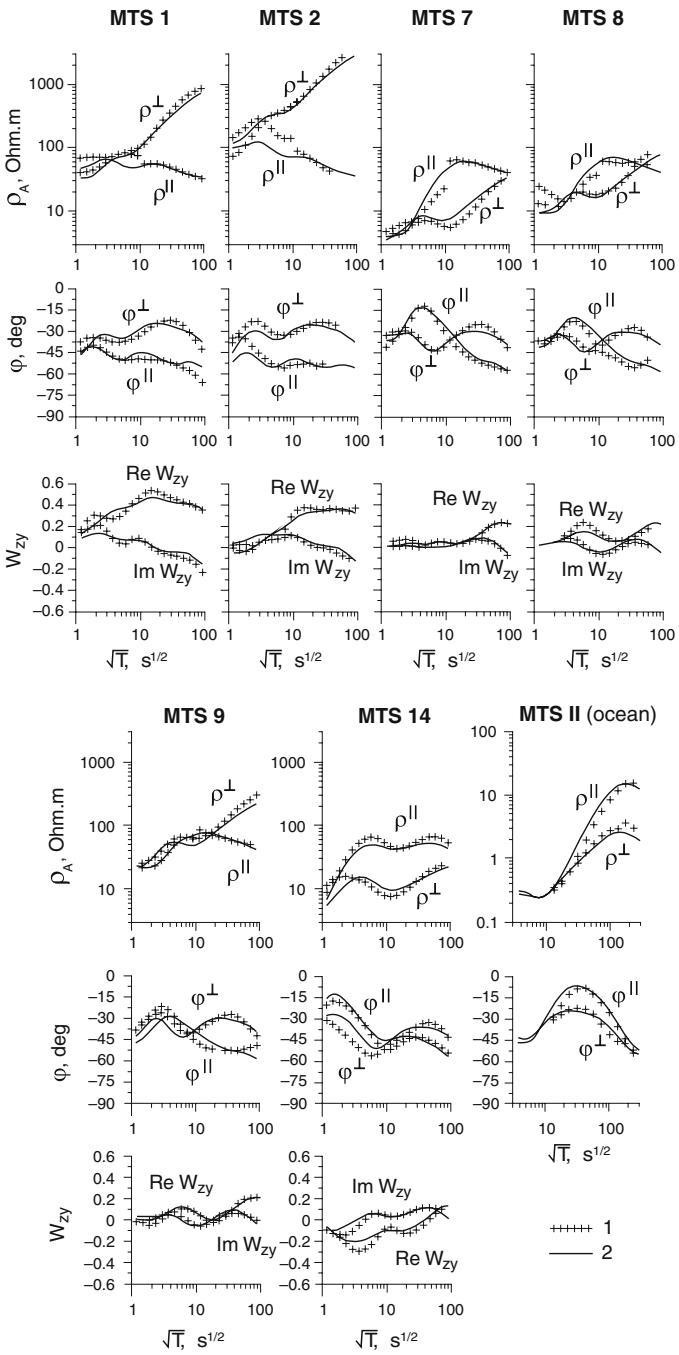

Fig. 12.67 Comparison of the observed MT and MV curves with the curves computed from the model EMSLAB III: 1-observations, 2-model EMSLAB III

On this way we can localize a three-dimensional structure and roughly estimate its depth and strike.

2. Let the quasi-homogeneous geoelectric medium be covered by the areal magnetotelluric survey. In that case the three-dimensional interpretation can be reduced to the quasi-one-dimensional inversion of apparent resistivities ρ_{eff}, ρ_{brd} or ρ_{rms} computed from one of the scalar invariants Z_{eff}, Z_{brd} or Z_{rms} of the impedance tensor. Such an approach is referred to as *scalarization* of the magnetelluric inversion.

3. In the case of the locally inhomogeneous geoelectric medium the three-dimensional interpretation can be accomplished by successive partial inversions informatively connected with each other through starting models and stabilizing functionals. Proceeding from the experience of two-dimensional interpretation, we assume that the most efficient is the following succession of inversions: (1) inversion of the magnetovariational response functions (tipper, horizontal magnetic tensor) – being free of near-surface static distortions, this inversion yields sufficiently reliable image of the geoelectric medium (particularly of its conductive zones), (2) inversion of the magnetotelluric phase response functions (phases of impedance tensor, phase tensor) – this inversion is also free of near-surface static distortions, it controls and edits the results of the magnevariational inversion, and (3) inversion of the magnetotelluric amplitude response functions (apparent resistivities) – this inversion is subjected to strong near-surface static distortions, but it can give additional information on upper layers of the sedimentary cover and galvanic connections that exist in the sedimentary cover and consolidated Earth's crust. Such a three-stage interpretation can be significantly simplified by scalarization of the partial inversion (scalar invariants of tipper, horizontal magnetic tensor, impedance tensor, phase tensor are in use).

4. Method of the successive partial inversion provides necessary stability of the three-dimensional interpretation under condition of sufficiently simple structure of geoelectric medium (single simple-shaped conductive inclusions, absence of strong horizontal and vertical ruptures and dislocations, etc). Studying complex-structured media, we should divide the three-dimensional interpretation into two stages. At the first stage the smoothing (or quasi-one dimensional) inversion is conducted and a simplified schematic model of the investigated medium is constructed. At the second stage this model is included into the blocky starting model as the fixed first approximation. The obtained basis is correlated with the a priori information and with the results of the qualitative analysis of MV-MT data. On this way it is supplemented with a set of local hypothetical inhomogeneities, whose free parameters are determined by the method of successive partial inversions. Hypotheses, which yield the minimal model misfit, are accepted as the most plausible. Thus, the smoothing (or quasi-one-dimensional) inversion is combined with the hypotheses tests. This complex provides stable sufficiently detailed three-dimensional interpretation performed in the class of models with a small number of free parameters.

Magnetotelluric Catechism (Instead of Afterword)

Summing up, we formulate some statetments, which can navigate the interpretation of magnetotelluric and magnetovariational soundings.

1. Presently one cannot entrust the computer (even the supercomputer) with complete self-dependent automatic press-button inversion. Inversion should be conducted in the interactive mode realizing the contact between the geophysicist (a leader) and the computer (a performer). Leader suggests to performer an inversion strategy that can define the interpretation success.

2. The statement of the inverse problem calls for a normal background, which can be given as a mathematical abstraction consistent with magnetotelluric response functions obtained at the boundary of the observation area and with a priori information.

3. The inverse problem is unstable. Its solutions is meaningful provided it is sought within a restricted set of plausible solutions forming the interpretation model. The choice of the interpretation model should be confidently controlled by a priori information and qualitative indications derived from the field observations.

4. The magnetotelluric field is of diffusive nature. Generally it can offer only a smoothed image of the geoelectric medium. Buried sharp conductivity contrasts existing in the Earth are introduced into the interpretation model from a priori information or hypothetically. The most complete interpretation can be performed by a compromise between smoothing (Occam) and contrasting (blocky) inversions.

5. In solving an unstable inverse problem, we come up against the paradox of instability.The more restricted the interpretation model, the more stable the inverse problem and the poorer the detailedness of its solution. On the other hand, the more stable the inverse problem, the higher its resolution. The resolution of the inverse problem and the detailedness of its solution are antagonistic. The inverse problem should be solved with optimum relation between stability, resolution and detailedness. An interpretation model with a small number of layers and structures is preferable. The additional layers and structures can be introduced providing the magnetotelluric and magnetovariational indications demand their presence. Taking advantage of blocky partition, a number of parameters defining the interpretation model should be reduced to a minimum providing a stable solution.

6. The magnetotelluric inverse problem is multicriterion. We can use tippers, magnetic tensors, impedance and phase tensors. These response functions have different sensitivity to different parameters of the interpretation model and different immunity to near-surface distortions. Being inverted simultaneously, they may come into conflict with each other impairing the inversion accuracy. The best approach to the solution of a multicriterion inverse problem is a succession of partial inversions focused upon different elements of the interpretation model. Partial inversions trade their information: the result of a previous inversion is transferred to a next inversion as a starting model. When studying media with sharp horizontal contrasts and strong geoelectric noise, it is profitable to begin with tippers and magnetic tensors which are free from static distortions and nicely resolve the geoelectric medium in the horizontal and vertical directions. It is just tipper and magnetic tensor that under complicated conditions can give a sound reliable basis for further estimates performed by phases and apparent resistivities.

7. The magnetotelluric effects are of integral nature and therefore the large compact bodies can manifest themselves as mosaic alternation of cells of higher and lower conductivity. Such a solution should be considered as one of the equivalent solutions. In agreement with geological expediency, it can be smoothed under condition that the misfits of the response functions do not increase.

8. The inversion adequacy should be estimated by comparing the modeled and measured local response functions. The model elements whose elimination does not increase the misfits of the response functions are considered as unnecessary insignificant artifacts and removed.

9. Magnetotelluric large-scale regional studies of sediments and deep studies of the Earth's crust and upper mantle are usually carried out on the long single profiles which dooms geophysicists to the quasi-one-dimensional or two-dimensional interpretation of the observation data. Admissibility of such simplifications should be verified by a priori and a posteriori analysis of lateral effects. An important part of this analysis is an appraisal and correction of interpretation errors arising due to finite strike of elongated structures considered as two-dimensional ones.

10. The main puzzle of magnetotellurics is a violation of the dispersion relations between apparent resistivities and impedance phases. We have several exotic models that expose these anomalies and occasionally we observe the violations of the dispersion relations in actual practice. But we little understand their physical mechanisms and we cannot tell with distinctness what properties of the geoelectric medium are responsible for violation of the dispersion relations. The study in this field is a challenge for all of us.

References

Adam, A., 1964, *Ueber die Berechnung der magnetotellurusche Anisitropie,* Freiberger Forschugshefte **C-168**, VEB Verlag, Leipzig.

Alekseev, D.A., Palshin, N.A., Berdichevsky, M.N., Varentsov, I.M., 2006, *Violation of dispersion relationship in seafloor TE-impedance*, Abstracts of 18 EMI Workshop, El Vendrel, Spain.

Al'perovich, I.M., Kononov, V.E., Nikiforov, V.M., Sludnev, Yu.G., Kharalinov, V.V., 1980, *Structure of the islands Sakhalin and Iturup from MT-data,* **In:** Nikiforov, V.M., Ed., Deep electromagnetic soundings on the Far East, Vladivostok, Far East Scientific Center Publ. House, Vladivostok 72–90.

Andreeva, E.V., Berdichevsky, M.N., Golubtsova, N.S., Koldaev, D.S., Jakovlev, A.G., 1991 *Controlled transformation of MTS curves,* Izv. Akad. Nauk SSSR, Ser. Fiz. Zemli **10**, 89–95.

Andrieux, P., and Wightman, W.E., 1984, *The so-called static correction in magnetotelluric measurements,* 54th Ann. Int. Mtg., SEG, Abstracts, 43–44.

Avdeev, D.B., Kuvshinov, A.V., Pankratov, O.V., Newman, G.A., 1997, *High-performance three-dimensional electromagnetic modeling using modified Neumann series. Wide-band numerical solution and examples,* J. Geomag. Geoelectr. **49**, 1519–1539.

Backus, G., 1988, *Bayesian inference in geomagnetism,* J. Geophys. **92**, 125–142.

Backus, G., and Gilbert, F., 1968, *The resolving power of gross earth data*, Geophys. J. R. astron. Soc. **16**, 169–205.

Bahr, K., 1985, *Elimination of local 3D distortion of the magnetotelluric tensor impedance*, Seventh Workshop on EM Induction in the Earth and Moon, Nigeria.

Bahr, K., 1988, *Interpretation of magnetotelluric impedance tensor: regional, induction and local telluric distortion*, J. Geophys. **62**, 119–127.

Bahr, K., 1991, *Geological noise in magnetotelluric data: a classification of distortion types*, Phys. Earth planet. Interior **66**, 24–38.

Bahr, K., and Duba, A., 2000, *Is the asthenosphere electrically anisotropic?* Earth Planet. Sci. Lett. **178**, 87–95.

Bahr, K., and Simpson, F., 2002, *Electrical anisotropy below slow- and fast- moving plates: paleoflowing the upper mantle*? Science **295**, 1270–1272.

Barashkov, A.S., 1983, *Reconstruction of the representation domain for the Helmholtz equation with small parameter*, Izv. Vuzov, Mathematics **8**, 3–7.

Barashkov, A.S., 1986, *Reconstruction of the electromagnetic field on the Earth's surface from the impedance tensor*, Izv. Akad. Nauk SSSR, Ser. Fiz. Zemli **5**, 43–52.

Barashkov, A.S., and Dmitriev, V.I., 1987, *On the inverse problem of deep magnetotelluric soundings*, Dokl. Akad. Nauk SSSR **295**(l), 83–86.

Barashkov, I.S., and Dmitriev, V.I., 1990, *Inverse problem of deep MT-sounding for quasi-layered Media*, **In:** Dmitriev, V.I. (ed.), " Methods of mathematical modeling and computing diagnostics", Publishing House of Moscow University, Moscow, 142–153.

Barashkov, A.S., and Jakovlev, A.G., 1989, *On the coastal effect in magnetotellurics*, Izv. Akad. Nauk SSSR, Ser. Fiz. Zemli **5**, 103–107.

Berdichevsky, M.N., 1960, *Theoretical basis of magnetotelluric profiling*, Prikladnaya geofizika **28**, 27–42.

Berdichevsky, M.N., 1961, *Magnetotelluric field in horizontally inhomogeneous medium*, Prikladnaya geofizika **31**, 42–61.

Berdichevsky, M.N., 1963, *Linear relationships in magnetotelluric field*, Prikladnaya geofisika **38**, 74–91.

Berdichevsky, M.N., 1965, *Electrical prospecting with the telluric current method*, Colo. School Mines **60**, 1.

Berdichevsky, M.N., 1968, *Electrical prospecting by the method of Magnetotelluric Profiling*, Nedra, Moscow.

Berdichevsky, M.N., 1996, *On the dynamic corrections of MT-sounding curves*, Phys. Solid Earth **32**(10) 793–795.

Berdichevsky, M.N., and Dmitriev, V.I., 1976, *Basic principles of interpretation of magnetelluric sounding curves*, **In:** Adam, A. (ed.), "Geoelectric and Geothermal Studies", Akademiai Kiado, Budapest.

Berdichevsky, M.N., and Dmitriev, V.I., 1991, *Magnetotelluric sounding of horizontally homogeneous media*, Nedra, Moscow.

Berdichevsky, M.N., and Dmitriev, V.I., 1997, *On deterministic nature of magnetotelluric impedance*, Acta Geophysica Polonica **XLV**(3), 227–236.

Berdichevsky, M.N., and Dmitriev, V.I., 2002, *Magnetotellurics in the context of the theory of ill-posed problems*, Investigations in Geophysics **11**, SEG, Tulsa.

Berdichevsky, M.N., and Jakovlev, A.G., 1984, *Magnetotelluric analog of the Kertz formulae*, Geomagnetism and Aeronomy **XXIV**(5) 805–814.

Berdichevsky, M.N., and Jakovlev, A.G., 1989, *Analytical model of MT-sounding distorted by the S-effect*, Izv. Akad. Nauk SSSR, Ser. Fiz. Zemli **9**, 82–88.

Berdichevsky, M.N., and Jakovlev, A.G., 1990, *Analytical model of magnetotelluric sounding distorted by screening effect*, Phys. Solid Earth **26**, 520–524.

Berdichevsky, M.N., and Jakovlev, A.G., 1991, *Analytical model of MT-sounding distorted by the deep S-effect*, Izv AN SSSR Fiz Zem **4**, 45–51.

Berdichevsky, M.N., and Logunovich, R.F., 2005, *Magnetotelluric polar diagrams*, Izvestia, Phys. Solid Earth **41**(10), 832–843.

Berdichevsky, M.N., and Nechaeva, G.P., 1975, *Suppresion of local distortion in magnetotelluric Sounding*, Prikladnaya Geofizika **79**, 110–116.

Berdichevsky, M.N., and Nguen Tkhan Van, 1991, *Magnitovariational vector*, Izv. Akad. Nauk SSSR, Ser. Fiz. Zemli **3**, 52–62.

Berdichevsky, M.N., and Pokhotelov, D.O., 1997a, *Dispersion Relations in Terms of a Polarizing Medium*, Phys. Solid Earth **33**(7), 539–542.

Berdichevsky, M.N., and Pokhotelov, D.O., 1997b, *Violation of the Dispersion Relations in a Three-Dimensional Magnetotellutic Model*, Phys. Solid Earth **33**(8), 603–612.

Berdichevsky, M.N., and Smirnov, V.S., 1971, *Methods of analyzing magnetovariational profiling data*, Geomagn. Aeron. **11**, 310–312.

Berdichevsky, M.N., and Zhdanov, M.S., 1984, *Advanced theory of deep geomagnetic sounding*, Elsevier, Amsterdam-Oxford-New York-Tokyo.

Berdichevsky, M.N., Vanyan, L.L., Fainberg, E.B., 1969, *On theoretical principles of using electromagnetic variations for the Earth's conductivity study*, Geomagnetism and Aeronomy, **9**, 570–572.

Berdichevsky, M.N., Vanyan, V.V., Kuznetsov, V.A., Levadny, V.T., Mandelbaum, M.M., Nechaeva, G.P., Okulessky, B.A., Shilovsky, P.P., Shpak, I.P., 1980, *Geoelectric model of the Baikal region*, Phys. Earth Planet. Inter. **22**, 1–11.

Berdichevsky, M.N., Bilynsky, A.I., Kobzova, B.M., Moroz, I.P., 1984, *On inductive excitation of deep conductive zones*, Izv. Akad. Nauk SSSR, Ser. Fiz. Zemli **7**, 81–84.

Berdichevsky, M.N., Dmitriev, V.I., Feldman, I.S., Berezinaa, N.I., Demidov, A.I., Jakovlev, S.I., 1988, *Interpretation of deep MT soundings in Tungus Syneclise*, Izv. Akad. Nauk SSSR, Ser. Fiz. Zemli **7**, 73–79.

Berdichevsky, M.N., Bezruk, I.A., Safonov, A.S., 1989a, *Magnetotelluric methods*, **In:** "Electrical Prospecting", Geophysical Reference Book, Part **1**, 261–310, Nedra, Moscow.

Berdichevsky, M.N., Vanyan, L.L., Dmitriev, V.I., 1989b, *Methods used in the USSR to reduce near-surface inhomogeneity effects on deep magnetotelluric sounding*, Phys. Earth Planet. Inter. **53**, 194–206.

Berdichevsky, M.N., Vanyan, L.L., Egorov, I.V., Lebedeva, N.,A., Pal'shin, N.A., Jakovlev, A.G., 1992a, *Analysis of resolving power of electromagnetic sounding*, Izv. Akad. Nauk SSSR, Ser. Fiz. Zemli **1**, 119–128.

Berdichevsky, M.N., Koldaev, D.S., Jakovlev, A.G., 1992b, *MT sounding on the oceanic coast*, Izv. Akad. Nauk SSSR, Ser. Fiz. Zemli **6**, 87–96.

Berdichevsky, M.N., Dmitriev, V.I., Kulikov, V.A., 1993a, *On normalization of magnetotelluric field by fluidized faults,* Izv. Akad. Nauk SSSR, Ser. Fiz. Zemli, **11**, 45–54.

Berdichevsky, M.N., Vanyan, L.L., and Nguen Tkhan Van, 1993b, *Phase polar diagrams of the magnetotelluric impedance*, Izv. Akad. Nauk SSSR, Ser. Fiz. Zemli **2**, 19–23.

Berdichevsky, M.N., Dmitriev, V.I., Kulikov, V.A., 1994, *Sensitivity of deep magnetotelluric sounding in the presence of fluidized faults*, Izv. Akad. Nauk SSSR, Ser. Fiz. Zemli, **6**, 39–49.

Berdichevsky, M.N., Dmitriev, V.I., and Kuznetsov, V.A., 1995, *Bimodal two-dimensional interpretation of MT soundings,* Izv. Akad. Nauk SSSR, Ser. Fiz. Zemli, **10**, 15–31.

Berdichevsky, M.N., Borisova, V.P., Golubtsova, N.S., Ingerov, A.I., Konovalov, Yu.F., Kulikov, A.V., Solodilov, I.N., Chernyavsky, G.A., Spak, I.P., 1996, *Interpretation of Magnetotelluric Soundings in the Lesser Caucasus*, Physics of the solid Earth **32**(4), 352–368.

Berdichevsky, M.N., Dmitriev, V.I., Pozdnjakova, E.E., 1998, *On two-dimensional interpretation of magnetotelluric soundings*, Geophys. J. Int. **133**, 585–606.

Berdichevsky, M.N., Vanyan, L.L., Koshurnikov, A.V., 1999, *Magnetotelluric sounding in the Baikal rift zone*, Phys. Solid Earth **35**(10), 793–814.

Berdichevsky, M.N., Dmitriev, V.I., Mershchikova, N.A., 2000, *On inverse problem of electromagnetic sounding using magnetotelluric and vfgnetovariational data*, Max-Press, Moscow.

Berdichevsky, M.N., Dmitriev, V.I., Golubtsova, N.S., Mershchikova, N.A., Pushkarev, P.Yu., 2003, *Magnetovariational sounding: new possibilities*, Izvestia, Phys. Solid Earth **39**(9), 701–727.

Bernard, G., and Rader, C.M., 1969, *Digital processing of signals*, McCraw-Hill Book Company, New York-London-Sydney-Toronto.

Bibby, H.M., 1986, *Analysis of multiple-source bipole-quadripole resistivity surveys using the apparent resistivity tensor*, Geophysics **51**(4), 972–983.

Bibby, H.M., Caldwell, T.G., Brown, C., 2005, *Determinable and non-determinable parameters of galvanic distortions in magnetotellurics*, Geophys. J. Int. **163**, 915–930.

Bostick, F.X., 1984, *Electromagnetic Array Profiling Survey Method*, US Patent 4.591.791.

Burjanov, V.B., Gordienko, V.V., Kulik, S.N., Logvinov, I.M., 1983, *Integrated geophysical studies of continental tectonosphere*, Naukova Dumka Publishers, Kiev.

Cagniard, L., 1953, *Basic theory of the magnetotelluric method of geophysical prospecting*, Geophysics **18**, 605–635.

Caldwell, T.G., Bibby, H.M., Brown, 2002a, *The magnetotelluric phase tensor – a method of distortion analysis for 3D regional conductivity structures*, Abstracts of 16th Workshop on EM Induction in the Earth, Santa Fe, EM12-4.

Caldwell, T.G., Bibby, H.M., Brown, C., Ogawa, Y., Uchida, T., Takakura, S., Matsushima, N., Bennie, S.I., Tosha, T., Nishi, Y., 2002b, *Phase tensor analysis of MT data from the Taupo volcanic zone*, *New Zealand*, Abstracts of 16th Workshop on EM Induction in the Earth, Santa Fe, EM3-3.

Caldwell, T.G., Bibby, H.M., Brown, 2004, *The magnetotelluric phase tensor*, Geophys. J. Int. **158**, 457–469.

Cantwell, T., 1960, *Detection and analysis of low frequency magnetotelluric signals*, Ph. D. Dissertation, Mass. Inst. Technology.

Chave, A.D., and Jones, A.G., 1997, *Electric and magnetic field galvanic distortion decomposition of BC87 data*, J. Geomag. Geoelectr. **49**, 767–789.

Chave, A.D., and Smith, T., 1994, *On electric and magnetic galvanic distortion tensor decomposition*, J. Geophys. Res. **99**(B3), 4669–4682.

Chave, A.D., Thomson, D.J., and Ander, M.E., 1987, *On the robust estimation of power spectra, coherencies, and transfer functions*, J. Geophys. Res. **92**, 633–648.

Chouteau, M., and Tournerie, B., 2002, *Analysis of magnetotelluric data showing phase rolling out of quadrant*, Abstracts of 16th Workshop on EM Induction in the Earth, Santa Fe, EM4-6.

Constable, S.C., Parker, R.L., Constable, G.G., 1987, *Occam's inversion: a practical algorithm for generating smooth models from electromagnetic sounding data*, Geophysics **52**, 289–300.

Counil, J.L., Le Mouel, J.L., Menvielle, M., 1986, *Associate and conjugate directions concepts in magnetotellurics*, Annales Geophysicae **4**, B2, 115–130.

Dawson, T.W., 1983, *E-polarization induction in two thin half-sheets*, Geophys. J. R. Astron. Soc. **73**, 83–107.

Dawson, T.W., Weaver, J.T., Raval, U., 1982, *B-polarization induction in two generalized thin sheets at the surface of a uniformly conducting earth*, Geophys. J. R. Astron. Soc. **68**, 209–234.

Debabov, A.S., 1980, *On modeling of electromagnetic fields for heterogeneous media*, Dokl. Acad. Nauk SSSR **250**(2), 326–331.

DeGroot-Hedlin, C., and Constable, C.G., 1990, *Occam's inversion: a practical algoritm for generating smooth models from electromagnetic sounding data*, Geophysics **55**, 1613–1624.

D'Erceville, S., and Kunetz, G., 1962, *Some observations regarding naturally occurring electromagnetic field in applied geophysics*, Geophysics **27**, 14–27.

Dyakonova, A.G., Ingerov, A.I., Rokityansky, I.I., 1986, *Electromagnetic Soundings on the Eastern European Platform and in the Urals,* Kiev, Publ. House Naukova Dumka.

Dmitriev, V.I, 1969, *The magnetotelluric field in thin inhomogeneous layers*, **In:** "Computational Methods and Programming", Publishing House of Moscow University **13**, 231–236.

Dmitriev, V.I, 1987, *Inverse Problems in Electrodynamical Prospecting*, **In:** Tikhonov, A.N. (ed.), "Ill-posed Problems in the Natural Sciences", Mir Publishers, Moscow.

Dmitriev, V.I., 2005, *Multidimensional and multicriterion inverse problems of the magnetotelluric sounding*, **In**: Spichak, B.B. (ed.), "Electromagnetic investigations of the Earth's interior", Publishing House "Nauchny mir", Moscow, 33–53.

Dmitriev, V.I., and Berdichevsky, M.N., 1979, *The fundamental model of magnetotelluric prospecting*, IEEE Proc. **67**, 1034–1044.

Dmitriev, V.I., and Berdichevsky, M.N., 1988, *The statistical model of the S-effect*, Abstracts of IX Workshop on EM induction in the Earth and Moon, Sochi, Russia.

Dmitriev, V.I., and Kruglov, I.E., 1995, *Method of synthesized fields in the inverse problems of magnetotellurics*, **In:** Kostomarov, D.T., and Dmitriev, V.I. (eds.), "Mathematical models of natural sciences", Publishing House of Moscow University, Moscow, 115–121.

Dmitriev, V.I., and Kruglov, I.E., 1996, *Synthesized field method in inverse problems of magnetotelluric sounding*, Comput. Math. Model. **7**(4), 217–222.

Dmitriev, V.I., Mershchikova, N.A., 1974, *On the resolving power of deep magnetotelluric sounding*, Izv. Acad. Nauk SSSR, Ser. Fiz. Zemli **8**, 23–38.

Dmitriev, V.I., and Mershchikova, N.A., 2002, *Magnetotelluric field synthesis*, Phys. Solid Earth **38**(11), 968–974.

Dmitriev, V.I., and Zakharov, E.V., 1970, *Methods for solving the problems of electrodynamics of inhomogeneous media*, J. Comput. Math. Math. Phys. **10**(6), 1458–1464.

Dmitriev, V.I., and Zakharov, E.V., 1987, *Integral equations in the boundary problems of electrodynamics*, Publishing House of Moscow University, Moscow.

Egbert, G., 1990, *Comments on "Concerning Dispersion Relations for the Magnetotelluric Impedance Tensor" by E.Yee and K. Paulson*, Geophys. J. Int. **102**, 1–8.

Eggers, D.E., 1982, *An eigenstate formulation of the magnetotelluric impedance tensor*, Geophysics **47**, 1204–1214.

Egorov, I.V., 1987, *Comparison between two-dimensional and axially symmetric three-dimensional magnetotelluric anomalies*, Izv. Acad. Nauk SSSR, Ser. Fiz. Zemli **1**, 106–112.

Everett, J.E., and Hyndman, R.D., 1967, *Geomagnetic variations and electrical conductivity structure in south-west Australia*, Phys. Earth Planet. Int. **1**, 24–34.

Fainberg, E.B., 1983a, *Global Geomagnetic Sounding,* **In:** "Mathematical modeling of electromagnetic field", IZMIRAN Publishers, Moscow, 441–464.

Fainberg, E.B., 1983b, *Global and regional magnetovariational sounding of the Earth,* Dr. Sc. Thesis, IZMIRAN, Moscow.

Fainberg, E.B., and Singer, B.Sh., 1980, *Electromagnetic induction in a non-uniform spherical model of the Earth*, Annal. Geophys. **36**, 127–134.

Fainberg, E.B., and Singer, B.Sh., 1987, *The influence of surface inhomogeneities on deep electromagnetic soundings of the Earth,* Geophys. J. R. Astron. Soc. **90**, 61–73.

Fainberg, E.B., Andrieux, P., Guerin, R., and Poltoratskaya, O.L., 1995, *Dynamic correction of amplitude curves of magnetotelluric sounding distorted by the influence of near-surface inhomogeneities,* Izv. Akad. Nauk SSSR, Ser. Fiz. Zemli **7**, 29–34.

Feldman, I.S., Karev, A.S., Okulessky, B.A., 1988, *Electrical conductivity of the upper mantle of the Russian and Siberian platforms,* IX Workshop of EM induction in the Earth and Moon, Abstracts, 6–6, Sochi, Russia.

Fischer, G., and Schnegg, P., 1980, *The dispersion relations of the magnetotelluric response and their incidence on inverse problem*, Geophys. J. R. Astron. Soc. **62**, 661–673.

Fischer, G., and Schnegg, P., 1993, *The magnetotelluric dispersion relations over 2-D structures*, Geophys. J. Int. **115**, 1119–1123.

Fischer, G., Szarka, L., Aam, A., Weaver, J.T., 1992, *The magnetotelluric phase over 2-D structures,* Geophys. J. Int. **108**, 778–786.

Fiskina, M.V., Singer, B.Sh., Fainberg, E.B., 1986, *On application of the gradient method in deep electromagnetic studies*, Physics of the Earth **12**, 39–43.

Gamble, T.D., Goubau, W.M., and Clark, J., 1979, *Magnetotellurics with a remote reference,* Geophysics **44**, 53–68.

Gao, S., Davis, P.M., Liu, H., Slack, P.D., Zorin, Y.A, Logachev, N.A., Kogan, M., Burkholder, P. D., Meyer, R.P., 1994, *Asymmetric upwarp of the asthenosphere beneath the Baikal rift zone, Siberia,* J. Geophys. Res. **99**(B8), 15319–15330.

Glasko, V.B., 1984, *Inverse problem in mathematical physics*, Nauka, Moscow.

Golubev, N.G., and Varentsov, I.M., 1994, *MT-data inversion: stable optimization methods and interactive graphics*, Abstracts of XII Workshop on EM induction in the Earth, Brest.

Golubtsova, N.S., 1981, *Anomalies of the electromagnetic field over an isometric depression*, Izv. Akad. Nauk SSSR, Ser. Fiz. Zemli **12**, 70–78.

Goltsman, F.M., 1971, *Statistical models of interpretation*, Nauka, Moscow.

Gordienko, V.V., 2002, *Implication of deep geoelectric data for the assessment of tectogenesis hypotheses*, Izvestia, Fys. Solid Earth **38**(10), 846–854.

Grachev, A.F., 1996, *Basic problems of newest tectonics and geodynamics of northern Eurasia*, Phys. Solid Earth, **32**(12), 4–35.

Gregori, G.P., and Lanzerotti, L.J., 1980, *Geomagnetic depth sounding by induction arrow representation*, Rev. Geophys. Space Phys. **18**, 203–209.

Groom, R.W., Bailey, R.C.: 1989, *Decomposition of Magnetotelluric Impedance Tensor in the presence of Local Three-Dimensional Galvanic Distortion*, J. Geophys. Res. **94**(B2), 1913–1925.

Groom, R.W., Bailey, R.C.: 1991, *Analytic investigations of the effects of near-surface three-dimensional galvanic scatters on MT tensot decompositions,* Geophysics **56**(4), 496–518.

Gupta, C.J., and Jones, A.G., 1995, *Electrical conductivity structure of the Purcell Anticlinorium*, Can. J Earth Sci. **32**, 1564–1583.

Gusarov, A.L., 1981, *On uniqueness of solution of inverse magnetotelluric problem for two-dimensional media*: **In** Dmitriev, V.I., (ed.), Mathematical models in geophysics, Moscow University, Moscow, 31–61.

Habashy, T.M., Groom, R.W., Spies, B.R., 1993, *Beyond the Born and Rytov approximation: a nonlinear approach electromagnetic scattering,* J. Geophys. Res. **98**, 1759–1775.

Hansen, C., 1998, *Rank-deficit and discrete ill-posed problems,* Numerical aspects of linear inversion: department of mathematical modeling, Technical university of Denmark, Lyngby.

Heise, W., Pous, J., Munoz, G., 2002, *Phases higher than 90 degrees explained by anisotropic models: application to field data*, Abstracts of 16th Workshop on EM Induction in the Earth, Santa Fe, EM5-16.

Hobbs, B.A., and Dumitresku, C.C., 1997, *One-dimensional magnetotelluric inversion using an 3adaptation of Zohdy resistivity method,* Geophys. Prosp. **45**, 1027–1044.

Hohmann G.W., 1975, *3D IP and EM modeling,* Geophysics **40**, 309–324.

Ingebritsen, S.E., Sherrod, D.R., Mariner, R.H., 1989, *Heat flow and hydrothermal circulation in the Cascade Range*, Science, **243**, 1458–1462.

Jankovski, J., 1972, *Techniques and results of Magnetotelluric and Geomagnetic soundings*, Panstwowe wydawnictwo naukowe*,* Warszawa.

Jankowski, J., Ernst, T., Jóźwiak, W., 2004, *Effect of thin near-surface layer on the geomagnetic induction arrows: an example from the East European Platform*, Acta Geophys Pol **53**(3), 349–361.

Jankowski, J., Praus, O., Jozwiak, W., 2005, *Carpathian anomaly of electrical conductivity: History of its discovery and interpretation*, Publs. Inst. Geophys. Pol. Acad. Sc. **C-95** (386), 17–28.

Jiracek, G.R., Gurtis, J.H., Ramirez, J., 1989, *Two-dimensional magnetotelluric inversion of the EMSLAB Lincoln line,* J. Geophys. Res. **94**, 14145–14151.

Jones, A.G., 1983, *The problem of current channeling a critical review,* Geophys. Surways, **6**, 79–122.

Jones, A.G., 1988, *Static shift of magnetotelluric data and its removal in a sedimentary basin environment*, Geophysics **53**(7), 967–978.

Jones, A.G., and Groom, R.W., 1993, *Strike-angle determination from the magnetotelluric impedance tensor in the presence of noise and local distortion: rotate at your peril!* Geophys. J. Int. **113**, 524–534.

Jones, F.W., and Price, A.T., 1970, *The perturbations of alternating geomagnetic fields by conductivity anomalies,* Geophys. J. R. Astron. Soc. **20**, 317–334.

Jones, A.G., Chave, A.D., Egbert, G., Auld, D., Bahr, K., 1989, *A Comparison of Techniques for Magnetotelluric Response Function Estimation,* J. Geophys. Res. **94**(B10), 14201–14213.

Jupp D.L.B., and Vozoff, K., 1976, *Discussion on "The magnetotelluric method in the exploration of sedimentary basins"*, Geophysics **41**, 325–328.

Jupp, D.L.B., and Vozoff, K., 1977, *Two dimensional Magnetotelluric inversion,* Geophys. J. R. Astron. Soc. **50**, 333–352.

Kaufman, A.A., 1960, *On study of the amplitude and phase characteristics of field in low-frequency electric exploration,* Izv. Vyssh. Uchebn. Zaved., Ser. Geol. Geofiz. **6**, 34–41.

Kaufman, A.A., 1961, *Three methods of field excitation for low frequency exploration,* Izv. Vyssh. Uchebn. Zaved., Ser. Geol. Geofiz. **5**, 13–25.

Kaufman, A.A., 1974, *Basic theory of inductive mineral prospecting*, Nauka, Novosibirsk.

Kaufman, A.A., 1988, *Reduction of the Geological Noise in Magnetotelluric Soundings,* Geoexploration **25**, 145–161.

Kaufman, A.A., 1994, *Geophysical Field Theory and Method, Part C,* Academic Press, INC., San Diego-New York-Boston.

Kaufman, A.A., and Taborovsky, L.A., 1969, *Electomagnetic field above gently slopping structures,* Nauka, Moscow.

Kaufman, A.A., and Keller, G.V., 1981, *The magnetotelluric sounding method,* Elsevier, Amsterdam-Oxford-New York.

Khain, V.E., and Lomize, M.G., 1995, *Geotectonics with Fundamentals of Geodynamics*, Moscow State University, Moscow.

Kovtun, A.A., 1980, *Investigation of the Earth's conductivity using natural electromagnetic field,* Leningrad State University, Leningrad.

Kovtun, A.A., 1989, *Structure of the Earth's crust and upper mantle on the North West of Eastern European platform from MT-data*, Leningrad, Leningrad University.

Krylov, S.V., Mishen'kin, B.P., Puzyrev, N.N., 1975, *Relative characteristics of deep structure-Baikal and other continental rift zones,* Geophysical investigations of the Earth's crust, Nedra Publ. House, 18–25.

Krylov, S.V., Mandelbaum, M.M., Mishen'kin, B.P., Mishen'kina, Z.R., Petrik G.V., Seleznev, V.S., 1981, *Baikal's interior*, Nauka Publ.House, Novosibirsk.

Kuvshinov, A.V., 2004, *Electromagnetic induction in spherical models of the Earth's with three-dimensional distribution of conductivity,* Sc. D. Dissertation, Moscow State University, Moscow.

Kuznetsov, V.A., 2005, *On normalization of the MT-curves distorted by the S-effect,* Izv. Acad. Nauk SSSR, Fiz. Zemli **76**, 91–96.

Lanczos, C., 1961, *Linear Differential Operators*, Van Nostrand, London.

Larsen, J.C., 1977, *Removal of local surface conductivity effects from low frequency mantle response curves,* Acta Geodaet., Geophys. et Montanist., Acad. Sci. Hung. **12**, 183–186.

Larsen, J.C., 1989, *Transfer functions: smooth robust estimates by least squaresand remote reference methods,* Geophys. J. Int. **99**, 645–663.

Larsen, J.C., Mackie, R.L., Manzella, A., Fiodelisi, A., Rieven, S., 1996, *Robust smooth magnetotelluric transfer functions,* Geophys. J. Int. **124**, 801–819.

LaTorraca, G.A., Madden, T.E., Korringa, J., 1986, *An analysis of magnetotelluric impedance for three-dimensional conductivity structures,* Geophysics **51**(9), 1819–1829.

Lavrentyev, M.M., Romanov, V.G., Shishatsky, S.P., 1980, *Inverse problem in mathematical Physics and analysis*, Nauka*,* Moscow.

Ledo, J., 2006, *2-D versus 3-D magnetotellurics data interpretation*, Surveys in Geophysics, **27**, 111–148.

Ledo, J., Pilar, Q., Marti, A., Jones, A., 2002, *Two-dimensional interpretation of three-dimensional magnetotelluric data: an example of limitation and resolution*, Geophys. J. Int. **150**, 127–139.

Leonardon, E.G., 1948, *Geophysical exploration by telluric currents*, Geophysics, **13**(7), 932–949.

Leontovich, M.A., 1948, *Approximate boundary conditions for electromagnetic field on the surface of highly conducting bodies,* **In:** "Propagation of electromagnetic waves", **II**, Moscow-Leningrad, 5–12.

Lilley, F.E.M., 1974, *Analysis of the geomagnetic induction tensor,* Phys. Earth Planet. Inter. **8**, 301–316.

Mackie, R.I., Madden, T.R., 1993, *Three-dimensional magnetotelluric inversion using conjugate gradients,* Geophys. J. Int. **115**, 215–229.

Mackie, R.L., Bennet, B.R., and Madden, T.R., 1988, *Long period Magnetotelluric measurements near the central California coast*, Geophys. J. Int. **95**, 181–194.

Mackie, R.I., Smith, J.T., Madden, T.R., 1994, *Three-dimensional electromagnetic modeling using finite difference equations: the magnetotelluric example,* Radio Science **29**, 923–935.

Mann, J.E., 1964, *Magnetotelluric study of sinusoidal interface,* J. Geophys. Res. **69**(16), 33–45.

Marcuello, A., Queralt, P., Ledo J., 2002, *Applications of dispersion relations to the geomagnetic transfer functions,* Abstracts of 16th Workshop on EM Induction in the Earth, Santa Fe, EM12-10.

Marcuello, A., Queralt, P., Ledo J., 2005, *Applications of dispersion relations to the geomagnetic transfer functions,* Phys. Earth Planet. Inter. (in press).

Marti, A., Queralt, P., Jones, A.G., Ledo, J., 2005, *Improving Bahr's invariant parameters using the WAL approach,* Geophys. J. Int. **163**, 38–41.

Mathews, J., and Walker, R.L., 1964, *Mathematical methods of physics,* W. A. Benjamin, INC., New York.

McNeice, G.W., and Jones, A.G., 2001, *Multifrequency tensor decomposition of magnetotelluric data,* Geophysics **66**(1), 158–173.

Mehanee, S. and Zhdanov, M.S., 2002, *Two-dimensional magnetotelluric inversion of blocky geoelectrical structures*, J. Geophys. Res. **107**(B4), EPM 1–12.

Moroz, Yu.F., 1991, *Electrical conductivity of the crust and upper mantle of Kamchatka,* Publ. House Nauka, Moscow.

Novozhynski K., and Pushkarev, P. Ju., 2001, *Analysis of efficiency of programs for two-dimensional inversion of magnetotelluric data*, Phys. Earth **6**, 72–85.

Obukhov, G.G., 1962, *Magnetotelluric field in the inhomogeneous layer,* Prikladnaya Geofizika, **35**, 61–77.

Obukhov, G.G., Chernjavsky, G.A., Jakovlev, I.A., 1983, *Magnetotelluric surveys in oil-bearing regions of USSR*, Nedra, Moscow.

Oldenburg, D.W., and Ellis, R.G., 1993, *Efficient inversion of magnetotelluric data in two dimension,* Phys. Earth Planet. Inter. **81**, 177–200.

Osipova, I.L., Berdichevsky, M.N., Vanyan, L.L., Borisova, V.P., 1982, *Geoelectric models of North America*, Geomagnetic Studies **29**, Moscow, 117–130.

Park, S.K., 1985, *Distortion of magnetotelluric sounding curves by three dimensional structures*, Geophysics **50**(5), 785–797.

Park, S.K., Orange, A.S., Madden, T.D., 1983, *Effects of three-dimensional structure on magnetotelluric sounding curves*, Geophysics **48**, 1402–1405.

Parker, R.L.,1994, *Geophysical inverse theory,* Princenton University Press, Princeton, New Jercey.

Parkinson, W.D., 1959, *Direction of rapid geomagnetic fluctuation*, Geophys. J. **2**, 1–14.

Parkinson, W.D., 1983, *Introduction to geomagnetism*. Scottish Academic Press, London.

Pellerin L., and Hohmann G.W., 1990, *Transient electromagnetic inversion: a remedy for magnetotelluric static shift,* Geophysics **55**(9), 1242–1250.

Pospeev, V.I., 1976, *Deep magnetotelluric surveys of the south of the Siberian platform and the Baikal rift zone,* **In:** Adam, A. (ed.), "Geoelectric and geothermal studies", Akademiai Kiado, Budapest, 673–681.

Pous, J., Queralt, P., Marcuello, A., 2001, *Magnetotelluric Signature of the Western Cantabrian Mountains*, Geophys. Res. Lett. **28**(9), 1795–1798.

Price, A.T., 1949, *The induction of electric currents in non-uniform thin sheets and shells,* Q. J. Mech. Appl. Math. **2**, 283–310.

Price, A.T., 1962, *Theory of the magnetotelluric field when the source field is considered,* J. Geophys. Res. **67**, 1907–1918.

Price, A.T., 1967, *Electromagnetic induction within the Earth,* in Matsushita, S., and Campell, W.H., (eds.), Physics of Geomagnetic Phenomena, Academic Press, London, 235–295.

Pushkarev, P.Ju., 2002, *Magnetotelluric investigations in the Cascadia subduction zone,* Ph. D. Dissertation, Moscow University, Moscow.

Pushkarev, P., Berdichevsky, M., Vanyan, L., 2002, *EMSLAB interpretation with magnetovariational priority,* The 16th Workshop on EM induction in the Earth, Santa Fe, New Mexico, EM6-38.

Puzyrev, N.N., 1997, *Methods and objects of seismic investigations*, Publ. House of SO RAN, Novosibirsk.

Ranganayaki, R.P., 1984, *An interpretive analysis of magnetotelluric date*, Geophysics, **49**(10), 1730–1748.

Ranganayaki, R.P., and Madden, T.R., 1980, *Generalized thin sheet analysis in magnetotellurics: an extensions of Price's analysis,* Geophys. J. R. Astron. Soc. **60**, 445–457.

Rankin, D., 1962, *The magnetotelluric effect of a dike*, Geophysics **27**, 666–676.

Rasmussen, J. and Humphries, G., 1988, *Tomographic image of the Juan de Fuca plate beneath Wasington Western Oregon using teleseismic P-wave travel times*, Geophys. Res. Lett. **15**, 1417–1420.

Ritter, P., and Banks, R.j., 1998, *Separation of local and regional information in distorted GDS response functions by hypothetical event analysis*, Geophys. J. Int. **135**, 923–942.

Rodi, W.L., and Mackie, R.L., 2001, *Nonlinear conjugate gradients algorithm for 2D magnetotelluic inversion,* Geophysics **66**, 174–187.

Roecker, S.W., Sabitova, T.M., Vinnik, L.P., Burmakov, Y.A., Golovanov, M.I, Mamatkhanova, R., Munirova, L., 1993, *Three-dimensional Elastic Wave Velocity structure of Western and Central Tien Shan*, J. Geophys. Res. **98**(B9), 15579–15795.

Rokityansky, I.I., 1975, *Investigation of electrical conductivity anomalies by the method of magnetovariation profiling,* Naukova Dumka, Kiev.

Rokityansky, I.I., 1982, *Geoelectromagnetic Investigation of the Earth's Crust and Mantle,* Springer-Verlag, Berlin-Heidelberg-New York.

Romanyuk, T.V., Mooney, W.D., Blakely, R.J., 2001a, *Density model of Cascadia subduction zone*, Izvestia, Phys. Solid Earth, **8**, 3–22.

Romanyuk, T.V., Mooney, W.D., Blakely, R.J., 2001b, *Tectonic-Geophysical model of Cascadia subduction zone,* Geotectonika, No. 3, 88–110.

Schmucker, U., 1962, *Erdmagnetische Tiefensondierung in Deutschland.* Abh. Akad. Wiss. Goettingen, Math. Phys., K1, Beitr. IGI **5**, 1–51.

Schmucker, U., 1970, *Anomalies of geomagnetic variations in the southwestern United States*: Univ. of California Press, Berkley.

Schmucker, U., 1971a, *Neue Rechenmethoden zur Tiefensondierung*, Kolloquium "Erdmagnetische Tiefensondierung" vom 14–16 September 1971, Geophysical Institute of Goettingen University, Goettingen, 1–39.

Schmucker, U., 1971b, *Interpretation of induction anomalies above non-uniform surface layer*, Geophysiics, **36**, 156–165.

Schmucker, U., 1979, *Erdmagnetische Variationen und die Electrische Leitfahigkeit in tieferen Schichten der Erde,* Beitrage zur Geowissenschaft, Sonderheft 4, Erich Goltze, Goettingen.

Schmucker, U., 2003, *Inductionsanomalien langperiodischer erdmagnetscher Variationen,* German Elecctromagnetic Workshop, Koenigstein, October 2003.

Schmucker, U., 2004, *Electromagnetic induction studies with long-period geomagnetic variations in Europe – I. Methods*, Geophysical Institute of Goettingen University, Goettingen.

Schultz, A., Fuijii, I., and Uyeshima, A., 1998, *A new 3D Global Mantle Conductivity Reference 3Model,* Proceedings of XIV Workshop on EM Induction in the Earth, Romania.

Semenov, V.Ju., 1998, *Regional conductivity structures of the Earth's mantle,* Proceedings of Geophysical Institute of Polish Academy of Sciences, Warshawa, **C-65**, 302.

Semenov, V.Ju., Vozar, J., Shuman, V.N. , New approach to the gradient magnetovariational sounding, Izvestia, Physics of Solid Earth (in press).

Sharka, L., and Menvielle, M., 1997, *Analysis of rotational invariants of the magnetotelluric impedance tensor*, Geophys. J. Int. **129**, 133–142.

Sheinmann, S.M., 1947, *On diffusion of electromagnetic fields in the Earth*, Prikladnaja Geofizika **3**, 3–57.

Simpson, F., and Bahr, K., 2005, *Practical Magnetotellurics*, Cambridge University Press, Cambridge.

Sims, W.E., and Bostick, F.X., 1967, *Methods of magnetotelluric analysis,* Tech. rep. 58, Electr. Geophys. Res. Lab., Univ. of Texas.

Singer, B.Sh., 1992, *Corrections for distortions of magnetotelluric fields: limits of validity and static approach*, Surveys Geophys. **13**, 309–340.

Singer, B.Sh., Fainberg, E.B., 1985, *Electromagnetic induction in inhomogeneous thin sheets,* IZMIRAN, Moscow.

Singer, B.Sh., Fainberg, E.B., 1997, *Fast 3-D inversion algoritm*, 67th Annual Meeting of SEG, Session 23, paper 364.

Siripunvaraporn, W., *and* Egbert, G., 2000*, An efficient data-subspace inversion method for 2-D magnetotelluric data*, Geophysics **65**, 791–803.

Smith, J.T., 1995, *Understanding telluric distortion matrices*, Geophys. J. Int. **13**, 219–226.

Smith, J.T., and Booker, J.R., 1991, *Rapid Inversion of Two- and Three-dimensional Magnetotelluric Data,* J. Geophys. Res. **96**, 3905–3922.

Smythe, W.R, 1950, *Static and dynamic electricity,* New York-Toronto-London.

Spichak, V.V., 1999, *Magnetotelluric fields in three-dimensional geoelectric models,* Nauchny mir, Moscow.

Spichak, V.V., 2005, *Three-dimensional Bayesian inversion of electromagnetic data*, **In:** "Electromagnetic studies of the Earth's interior Spichak, V.V. (ed.), Nauchny mir, Moscow.

Spichak, V.V., Menville, M., Roussignol, M., 1999, *Three-diimensional inversion of the MT fields using Bayesian statistics,* **In:** Three-dimensional electromagnetics Oristaglio, M., Spies, B. (eds.) SEG, Tulsa, USA, 406–417.

Spitz, S., 1985, *The magnetotelluric impedance tensor properties with respect to rotation,* Geophysics **50**(10) 1610–1617.

Sternberg, B.K., Washburne, J.C., Pellerin, L., 1988, *Correction for the static shift in magnetotellurics using transient electromagnetic sounding*, Geophysics **53**, 1459–1468.

Svetov, B.S.,1960, *On the role of method of field excitation in inductive electrical prospecting*, Izv. Acad. Nauk SSSR, Fizika Zemli, **1**, 115–125.

Svetov, B.S., 1973, Theory, methods, and interpretation of materials of low-frequency inductive electrical prospecting, Nedra, Moscow.

Svetov, B.S., 1991, *Transfer functions of the electromagnetic field*, Izv. Acad. Nauk SSSR, Fiz-ika Zemli **1**, 119–128.

Swift, C.M., 1967, *A magnetotelluric investigation of an electrical conductivity anomaly in the southwestern United States,* Ph. D. Dissertation, MIT, Cambridge.

Tarantola, A., 1987, *Inverse problem theory*, Amsterdam, Elsevier, Amsterdam-London-New York-Tokyo.

Tarantola, A. and Valette, B., 1982, *Inverse problem*: *Quest for formation*, J. Geophys. **50**, 159–170.

Tikhonov, A.N., 1950, *On determination of electric characteristics of deep layers of the Earth crust*, Dokl. Acad. Nauk SSSR **151**, 295–297.

Tikhonov, A.N., 1963, *On solution of ill-posed problem and the regularization method,* Dokl. Akad. Nauk SSSR ,**154**(3), 501–504.

Tikhonov, A.N., 1965, *Mathematical basis for electromagnetic sounding,* J. Comput. Math. Math. Phys. **3**, 207–211.

Tikhonov, A.N., and Arsenin, V.Ya., 1977, *Methods of solution of ill-posed problems*, New York, Wiley.

Tikhonov, A.N., and Berdichevsky, M.N., 1966, *Experience in the use of magnetotelluric method to study geological structure of sedimentary basis,* Izv. Akad. Nauk SSSR, Ser. Fiz. Zemli **2**, 34–41.

Tikhonov, A.N., and Dmitriev, V.I., 1969, *Influence of surface inhomogeneities on deep magnetotelluric sounding,* **In:** "Computing methods and programming" **13**, Moscow university, Moscow.

Tikhonov, A.N., and Samarsky, A.A., 1999, *Equations of mathematical physics,* VI Edition, Publishing House of Moscow University, Moscow, 790.

Tikhonov, A.N., and Goncharsky, A.V., Eds.,1987, *Ill-posed Problems in Natural Sciences*, Mir Publishing House.

Tikhonov, A.N., Dmitriev, V.I., Zakharov, V.I., 1977, *Solution of geoelectric problems for inhomogeneous media,* Phys. Earth, **12**, 9–19.

Tikhonov, A.N., Goncharsky, A.V., Stepanov, V.V., Yagola, A.G., 1983, *Regularizing algo-rithms and a priori information,* Nauka Publ. House, Moscow.

Ting, S.C., and Hohmann G.W., 1981, *Integral equation modelling of 3D MT response,* Geophysics **46**, 182–197.

Torres-Verdin, C., and Bostick, F.X., Jr., 1992, *Principles of spatial surface electric field filtering in magnetotellurics*: *Electromagnetic array profiling* (*EMAP*), Geophysics **57**(4), 603–622.

Trapeznikov, Ju.A., Andreeva, E.V., Batalev, V.Ju., Berdichevsky, M.N., Vanyan, L.L., Volykhin. A.M., Golubtsova, N.S., Rybin, A.K., 1997, *Magnetotelluric soundings in the mountains of the Kirghyz Tien-Shan*, Izvestia, Phys. Solid Earth **1**, 3–20.

Trehu, A.M., Asudeh, I., Broher, T.M., 1994, *Crustal Architecture of the Cascadia Forearc*, Science, **265**, 237–243.

Utada H., and Munekane, H., 2000, *On galvanic distortion of regional three-dimensional magnetotelluric impedances,* Geophys. J. Int. **140**, 385–398.

Vanyan, L.L., 1965, *Principles of electromagnetic soundings*, Nedra, Moscow.

Vanyan, L.L., 1997, *Electromagnetic soundings*, Nauchny mir, Moscow.

Vanyan, L.L., Shilovsky, P.P., 1983, *Deep electrical conductivity of oceans and continents*, Nauka, Moscow.

Vanyan, L.L., Kaufman, A.A., and Terekhin, E.I., 1961, *Calculation of the phase curves of frequency sounding by the transformation method,* Prikl. Geofiz. **30**, 103–113.

Vanyan, L.L., Egorov, I.V., Shilovsky, A.P., 1986, *On magnetotelluric excitation of elongated conducting zones in the Earth's crust and asthenosphere,* Izv. Akad. Nauk SSSR, Ser. Fiz. Zemli **6**, 70–75.

Vanyan, L.L., Egorov, I.V., Shilovsky, A.P., 1988a, *Electromagnetic excitation of axially symmetric asthenospheric zones,* Izv. Akad. Nauk SSSR, Ser. Fiz. Zemli **6**, 67–73.

Vanyan, L.L., Palshin, N.A., Poray-Koshits, A.S., 1988b, *The preliminary interpretation of the EMSLAB MT-soundings,* Abstracts of IX EMI Workshop, Sochi.

Vanyan, L.L., Egorov, I.V., Shilovsky, A.P., 1991, *Induction excitation of deep 3-D conducting zones,* Geophys. J. Int. **105**, 295–300.

Vanyan, L.L., Varentsov, I.M., Golubev, N.G., Sokolova, E.Ju.: 1997, *Construction of inductive magnetotelluric curves from magnetovariational data in experiment EMSLAB*, Phys. Earth **10**, 33–46.

Vanyan, L.L., Varentsov, I.M., Golubev, N.G., Sokolova, E.Ju., 1998, *Determination of synchronous components of magnetic field from inductive vectors*, Phys. Earth **9**, 89–96.

Vanyan, L.L., Berdichevsky, M.N., Pushkarev, P.Yu., Romanyuk, T.V., 2002a, *A geoelectric model of the Cascadia subduction zone,* Izvestia, Phys. Solid Earth **38**(10), 816–846.

Vanyan, L.L., Kuznetsov, V.A., Lyubetskaya, T.V., Palshin, N.A., Korja, T., Lahti, I. and the BEAR Group, 2002b, *Electrical conductivity of the crust beneath Central Lapland*, Izvestia, Phys. Solid Earth **38**(10), 798–815.

Varentsov, I.M., 1999, *Stable nonlinear inversion of magnetotelluric data in the piece-wise continuous 3D media,* Three-dimensional electromagnetics (3DEM-2), Proc. of 3DEM-2 Int. Symposium, Univ. of Utah, Salt Lake City.

Varentsov, I.M., 2002, *A general approach to magnetotelluric data inversion in a piecewise continuous medium*, Izvestiya, Phys. solid Earth **38**(11), 11–33.

Varentsov, I.M., 2004, *The estimation and analysis of horizontal magnetic interstation transfer functions in the EMTESH-Pomerania project,* Abstracts of XVII Workshop on EM induction in the Earth, Hyderabad, India, 153–154.

Varentsov, I.M., 2005, *Method of horizontal magnetovariational sounding:techniques and application in the EMTESH-Pomerania project,* 21 Kolloquim EM Tifenforschung, Wohldenberg, Germany.

Varentsov, I.M., Golubev, N.G., Gordienko, V.V, Sokolova, E.,Yu., 1996, *Study of deep geoelectric structure along the Lincoln line (EMSLAB EXPERIMENT)*, Phys. Earth, **4**, 124–144.

Varentsov, I.M., Sokolova E.Yu., Martanus E.R., Nalivaiko K.V., BEAR Working Group, 2003a*, System of EM field transfer operators for the BEAR array of simultaneous soundings*: *methods and results*, Izvestya, Physics of the Solid Earth, **39**(2), 118–148.

Varentsov, I.M., Sokolova E.Yu., BEAR Working Group*,* 2003b*, Diagnostics and suppression of auroral distortions in the transfer operators of the EM field in the BEAR experiment*, Izvestya, Phys. Solid Earth, **39**(4), 283–307.

Vasseur, G., and Weidelt, P., 1973, *Bimodal electromagnetic induction in nonuniform thin sheets with appplication to the Northern Pyrenean anomaly*, Geophys. J. R. Astron. Soc. **51**, 669–690.

Vozoff, K., 1972, *The magnetotelluric method in the exploration of sedimentary basins*, Geophysics **37**, 98–142.

Vozoff, K., 1991, *The Magnetotelluric Method,* **In:** Nabighian, M.N. (ed.), "Electromagnetic methods in applied geophysics", SEG.

Wait, J.R., 1954, *On the relation between telluric currents and the Earth's magnetic field,* Geophysics, **19**, 281–289.

Wait, J.R., 1962, *Theory of the magnetotelluric field,* J. Res. Nat. Bur. Standards **66D**, 590–641.

Wannamaker, P.E., 2005, *Anisotropy versus heterogeneity in continental solid earth electromagnetic studies,* Surveys Geophys. **26**, 733–765.

Wannamaker, Ph.E., Hohmann, G.W., and Ward, S.H., 1984. *Magnetotelluric responses of three-dimensional bodies in layered earth,* Geophysics **49**(9) 1517–1533.

Wannamaker, Ph.E., Stodt, J.A., Rijo, L., 1987, *A stable finite element solution for two- dimensional magnetotelluric modeling*, Geophys. J. R. Astron. Soc. **88**, 277–296.

Wannamaker, P.E., Booker, J.H., Filloux, J.H., Jones, A.G., Jiracek, G.R., Chave, A D., Tarits, P., Waff, H.S., Young, C.T., Stodt, J.A., Martinez, M., Law, L.K., Yukutake, T., Segava, J.S., White, A, Green, A.W., 1989a, Magnetotelluric observations across the Juan de Fuca subduction system in the EMSLAB project, J. Geophys. Res. **94**(B 10), 14111–14125.

Wannamaker, P.E., Booker, J.R., Jones, A.G., Chave, A.D., Filloux, J.H., Waff, H.S., and Law, L.K., 1989b, *Resistivity cross-section through the Juan de Fuca subduction system and its tectonic implication*, J. Geophys. Res. **94**(B10), 14127–14144.

Wannamaker, P.E., Wright, P.M., Xing, Z.Z., Xingbin, L. and Xiang, Z.J., 1991, *Magnetotelluric transect of Long Valley caldera: resistivity cross-section, structural implications, and the limits of a 2D analysis*, Geophysics, **56**(7), 926–940.

Weaver, J.T., 1963, *The electromagnetic field within a discontinuous conductor with reference to geomagnetic micropulsations near a coastline,* Can. J. Phys. **41**, 484–495.

Weaver, J.T., 1994, *Mathematical methods for Geo-electromagnetic induction,* John Wiley and Sons Inc., New York-Toronto-Singapore.

Weaver, J.T., 2003, *Remarks on the invariants of the magetotelluric tensor*, German EM Workshop, Koenigstein.

Weaver, C.S. and Michaelson, C.A., 1985, *Seismicty and volcanism in the Pacific Northwest: evidence for the segmentation of the Juan de Fuca plate*, Geophys. Res. Lett. **12**, 215–218.

Weaver, J.T., Agarwal, A.K., and Lilley, F.E., 2000, *Characterization of the magnetotelluric tensor in terms of its invariants*, Geophys. J. Int. **141**, 321–336.

Weaver, J.T., Agarwal, A.K., and Lilley, F.E., 2003, *The relation between the magnetotelluric tensor invariants and the phase tensor of Caldwell, Bibby and Brown*, Abstracts of 3D EM III Workshop, Adelaide.

Weidelt, P., 1972, *The inverse problem of geomagnetic induction,* Zeitschrift fur Geophysik **8**(2), 257–290.

Weidelt, P., 1975, *Electromagnetic induction in three-dimensional structure*, J. Geophys. Res. **41**(1), 85–100.

Weidelt, P., 1977, *Numerical study of a conductive channeling effect*, Acta Geodaet.,Geophys. Et Montanist. Acad. Sci. Hung. Volum **12**(1–3), 195–205.

Weidelt, P., 1978, *Entwicklung und Erprobung eines Verfahren zur Inversion zweidimensionalen Leitfaehigkeits in E-polarisation*, Dissertation, Goettingen Universitaet.

Weidelt, P., and Kaikkonen, P., 1994, *Local 1-D interpretation of magnetotelluric B-polarization impedance,* Geophys. J. Int. **117**, 733–748.

Whittall, K.P., and Oldenburg, D.W., 1992, *Inversion of magnetotelluric data for a one-dimensional conductivity,* Geophysical monograph series **5**, SEG, Tulsa.

Wielondek, R., and Ernst, T., 1977, *Application of the method of least squares to determining impulse responses and transfer functions,* Publishing Inst. Geophys. Polish Acad. Sci. **G-1**(110), 3–12.

Wiese, H., 1962, *Geomagnetische Tiefentellurik, Teil 2, Die Streichrichtung der Untergrundstrukturen des elektrischen Winderstandes, ersclossen aus geomagnetischen Variationen,* Geofis. Pura. Appl. **52**, 83–103.

Wiese, H., 1965, *Geomagnetische Tiefentellurik*, Deutsche Akad. Wiss., Belin.

Yanovskaja, T.B., and Porokhova, L.N., 1983, *The inverse problems in geophysics,* Leningrad State University, Leningrad.

Yee, E., and Paulson, K.V., 1987, *The canonical decomposition and its relationships to other forms of magnetotelluric impedance tensor analysis,* Geophys. J. **61**, 173–189.

Yee, E., and Paulson, K., 1988, *Concerning Dispersion Relations for the Magnetotelluric Impedance Tensor*, Geophys. J. **95**, 549–559.

Zhamaletdinov, A.A., 1996, *Graphite in the Earth's crust and electrical conductivity anomalies*, Phys. Solid Earth **32**(4), 265–281.

Zhang, P., Roberts, R.G., Pedersen, L.B., 1987, *Magnetoteluric strike rules,* Geophysics **52**(3), 267–278.

Zhang, P., Pedersen, L.B., Mareschal M, and Chouteau, M., 1993, *Channelling contribution to tipper vectors: a magnetic equivalent to electrical distortion*, Geophys. J. Int. **113**, 693–700.

Zhdanov, M.S., 2002, *Geophysical inverse theory and regularization problems,* Elsevier, Amsterdam-London-New York-Tokyo.

Zhdanov, M.S., and Keller, 1994, *The geoelectrical methods in geophysical exploration,* Elsevier, Amsterdam-London-New York-Tokyo.

Zhdanov, M.S., Spichak, V.V., 1992, Mathematical modeling of electromagnetic fields in three-dimensional media, Moscow, Nauka.

Zohdy, A.A., 1989, *A new method for the automatic interpretation of Schlumberger and Wenner sounding curves*, Geophysics **54**, 245–253.

Zorin, Ju.A., 1971, *Newest structure and isostasy of the Baikal rift zone and adjacent terrain*, Nauka Publ. House, Moscow.

Index